A. Le Pichon
E. Blanc
A. Hauchecorne (Eds.)

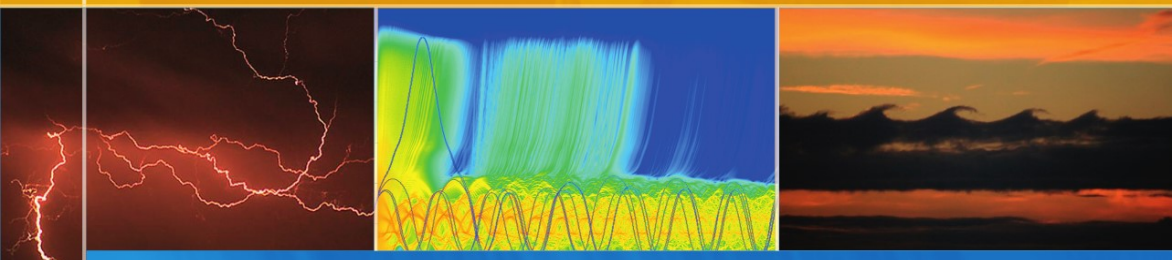

Infrasound Monitoring for Atmospheric Studies

Springer

Infrasound Monitoring for Atmospheric Studies

Alexis Le Pichon · Elisabeth Blanc
Alain Hauchecorne
Editors

Infrasound Monitoring for Atmospheric Studies

Springer

Editors
Alexis Le Pichon
CEA, DAM
DIF, F-91297 Arpajon
France
alexis.le-pichon@cea.fr

Elisabeth Blanc
CEA, DAM
DIF, F-91297 Arpajon
France
elisabeth.blanc@cea.fr

Alain Hauchecorne
Université Versailles-Saint Quentin
CNRS INSU, LATMOS-IPSL, BP3
91371 Verrières-le-Buisson
France
alain.hauchecorne@latmos.ipsl.fr

ISBN 978-1-4020-9507-8 e-ISBN 978-1-4020-9508-5
DOI 10.1007/978-1-4020-9508-5
Springer Dordrecht Heidelberg London New York

Library of Congress Control Number: 2009941470

Cover illustration: Background image, 'Listening to the Earth' @ Shana ParkeHarrison. Images from left to right: Thunderstorms and lightning on May 26th, 2006 Agra, Kansas, USA, courtesy of Oscar van der Velde; Propagation of infrasonic waves from a meteorite exploding in altitude above the Andes Mountain ranges using the NRL-RAMPE parabolic equation method, courtesy of D.P. Drob, NRL, Washington; Kelvin–Helmholtz instability clouds in San Fransisco, courtsey of Lyudmila Zinkova.

Printed on acid-free paper

Springer is part of Springer Science+Business Media (www.springer.com)

Preface

The use of infrasound to monitor the atmosphere has, like infrasound itself, gone largely unheard of through the years. But it has many applications, and it is about time that a book is being devoted to this fascinating subject.

Our own involvement with infrasound occurred as graduate students of Prof. William Donn, who had established an infrasound array at the Lamont-Doherty Geological Observatory (now the Lamont-Doherty Earth Observatory) of Columbia University. It was a natural outgrowth of another major activity at Lamont, using seismic waves to explore the Earth's interior. Both the atmosphere and the solid Earth feature velocity (seismic or acoustic) gradients in the vertical which act to refract the respective waves. The refraction in turn allows one to calculate the respective background structure in these mediums, indirectly exploring locations that are hard to observe otherwise. Monitoring these signals also allows one to discover various phenomena, both natural and man-made (some of which have military applications).

The set-up at Lamont featured a tripartiate array of infrasound sensors of various spacings. The short period (~5 s) array was installed in out-of-the-way locations (like parks) in what is essentially a metropolitan area. This was made more difficult by the necessity to connect some of these sensors to noise reducing pipes. Longer period signals were recorded with microbarovariographs. The signals were transmitted along telephone lines, and captured at Lamont both visually on rotating drums and electronically on large tape-recorders (very similar to what was being done for the seismic wave recordings). Cross-correlation of the signals provided information on direction and phase velocity of the propagating waves. The system required constant attention; if it wasn't a power failure with the acoustic sensors, it was a telephone line going down, or the Ampex tape recorder failing. Fixing the sensor required a trip to its purposely remote location, and that often meant a battle with mosquitoes and other obstacles. Nevertheless this system – and its funding - was maintained for over a decade in the 1960s.

A wide array of phenomena presented itself in the records. Ubiquitously recorded were microbaroms, which represented another seismic connection, as these signals were generated in the air by the same interfering ocean waves that produced microseismic variations in the earth. The simultaneously-recorded microseism activity, in fact, could be used to calibrate the reflection height of

microbaroms by providing an independent assessment of the source amplitude (when the directional effect was taken into account; microseisms did not propagate well onto the continental shelf from the perpendicular off-shelf direction in the near-by Atlantic). Microbaroms were used to monitor the reflection characteristics (i.e., wind and temperature) at the stratopause and lower thermosphere reflection heights on a continual basis, providing evidence of everything from stratospheric warmings to diurnal and semi-diurnal tides. The small dissipation of infrasonic waves even allowed signals from the Pacific to be recorded at Lamont (which is on the New York/New Jersey border), producing information on stratospheric west winds during winter.

Infrasound from sonic booms were recorded when supersonic jets flew to close to shore; example of that were occasional flights of the (French) Concorde, and U.S. military planes. [Both groups denied they were doing it, but the recorded evidence, and refraction properties of the atmosphere, made for a solid case against them!]. Natural oscillations of near-by bridges were observed, at infrasonic frequencies that doctors claimed were harmful to human health. Even signals from lightning were obtained.

There were also military applications. Atmospheric nuclear tests produced long period signals on the microbarovariographs, and rocket launchings from Cape Kennedy were a source of infrasound. There were rumors that infrasound arrays were set up surrounding various countries for the purpose of detecting launches.

Nowadays, as shown by the wide variety of research contained in this book, many of these sources, and more, are still being observed with infrasound recorders. Of course by now both the recording and analysis procedures have advanced notably. The publication of this book should finally make the usefulness of this technique more audible to the scientific community.

New York

David Rind and N.K. Balachandran
Goddard Institute for Space Studies

Foreword

On September 24, 1996 the Comprehensive Nuclear Test Ban Treaty was signed by 71 States Signatories. Its Annexes contained the description of an operational global monitoring system to verify compliance with the Treaty. There were vivid scientific and technical discussions among the delegations on the usefulness of the various technologies to achieve a reliable monitoring system, among which infrasound technologies. For years very little scientific and technical efforts had been developed to detect infrasounds in the atmosphere and questions were numerous. Would it be possible to detect a 1 kt event worldwide with this technology? How should the stations be installed? What about analogue noise filtering? What about sensor specifications and manufacturing capacities? Bringing together existing know-how a monitoring network of 60 stations was design and progressively installed under the responsibility of the Preparatory Technical Secretariat, and by the end of 2010, nearly 80% of the network will be operational. This is a significant achievement considering the conditions required by the Treaty for this network to be considered as operational, and also difficulties linked to the location of some exotic sites.

Sensors specifications were at top level of technology know-how. Today very high quality data is flowing through the International Monitoring System to the users. As never before analysts and scientists have the possibility to monitor and study the acoustic behaviour of the atmosphere and, as always in this type of situation, it brings new insight on the physics involved, with confirmations but also discoveries of acoustic phenomena. Analysis has progressively been enriched, from signals due to occasional natural and anthropogenic events (meteorites, volcanoes, supersonic booms, shuttle and rocket launches, quarry blasts) to interpretation of more continuous background fluctuations. These fluctuations are very often connected to coupling between ocean and atmosphere, like in the case of microbaroms, or between continental relief and atmosphere. Finally, studying the evolution of ray propagation with time allows a better knowledge of the dynamics of the atmosphere upper layers (up to 40 km), which is an essential parameter to locate sources with an increased precision. All these studies are good opportunity to broaden the field of atmospheric research.

But even more than an opportunity, these scientific studies are a necessity. They will allow the International Monitoring System to improve its efficiency, as the data processing is not yet at its full maturity, especially in the field of coupling between

signals generated in the atmosphere, continent and ocean, detected by the various technologies (acoustics, radionuclides, seismics, hydroacoustics). They will also allow new young scientists to be trained in this expending field, scientists that may bring there skills to the Vienna organization sometime in the future.

After the 1995 report on Infrasound, this book is the latest comprehensive report on infrasound science and technology, and much has been done since that early report. I hope it will stimulate interest of geophysicists to get active in this developing field of atmospheric acoustics.

Dr. Yves Caristan
Director of Saclay Research Center
French Atomic Energy Commission

Introduction

Although we are most familiar with sounds we can hear, there is a rich spectrum of acoustic energy that exists at frequencies below our hearing range. These inaudible low-frequency sounds, known as infrasound waves, propagate through the atmosphere for distances of thousands of kilometers without substantial loss of energy. Sounds at these frequencies (below 20 Hz) are almost always present at measurable amplitudes and have been observed since the early ninteenth century at locations distributed around the globe.

Such measurements are now commonly made due to the development of a network of 60 infrasound arrays for the enforcement of the Comprehensive Nuclear-Test-Ban Treaty (CTBT) and the deployment of 20–30 additional arrays for basic research.These arrays give us an unprecedented opportunity for the global study of infrasound. New signal processing methods, highly sensitive microbarometers and efficient and novel array designs allow a precise determination of the wavefront characteristics of low-amplitude signals. This unique recording system continually captures the rich inaudible ambient wavefield, informally referred to as the infrasonic zoo, which includes signals from a wide variety of naturally occurring geophysical phenomena such as tornadoes, volcanic explosions, landslides, thunderstorms, large earthquakes, bolides, ocean waves and aurora. Man-made sources include chemical and nuclear detonations, quarry blasts, supersonic aircraft and industrial activities.

As infrasonic waves propagate through the upper atmosphere, ground-based measurements provide a basis for atmospheric investigations at altitudes where routine measurements by satellite or other ground-based instruments still remain elusive. The global character of the phenomena and the level of knowledge reached today in this science encourage broadening our current fields of research which, in turn, requires a closer cooperation with upper-atmosphere physicists and meteorologists.

With the increasing number of infrasound arrays deployed around the globe, we anticipate that continuing systematic investigations into low-frequency acoustic signals will greatly enhance our understanding of the dynamics of the upper atmosphere, and could be of considerable value for the understanding of large scale atmospheric disturbances and their evolution in relation with climate change studies.

A number of institutions worldwide have active research programs in infrasound. Since 1997, researchers have gathered at technical workshops to present and discuss their latest research results. The response of these researchers to our call for papers has been most gratifying. Fifty-four researchers from twenty-four institutions have contributed to this book. This single volume is a collection of the highest level of research and development achieved today by these experts. This volume reviews the most important areas of infrasound, with emphasis on the latest research and applications, e.g., instrumentation, engineering, signal processing, source monitoring, propagation modeling, atmospheric dynamics, global changes, and remote sensing methods. We believe that this volume presents a comprehensive picture of the present "state of the art" in this technology.

We thank all authors for their motivation in this project and their very valuable contribution. We also thank F. Guillois for the help he provided to design the picture of the book cover. The authors are also grateful to anonymous reviewers for insightful comments on the initial drafts, and to Drs. L. G. Evers, D. N. Green and M. A. H. Hedlin for their supports during the completion of the book. We especially thanks Drs. Rind, N. K. Balachandran, and Y. Caristar for the Preface and foreword.

Henry Ellis "Hank" Bass died on May 28, 2008 after a courageous battle with cancer. Hank had a passion for acoustics that he passed on to his students and colleagues in the United States and around the world. In 1996, when Hank accepted the task of managing the United States infrasound component of the Comprehensive Test Ban Treaty, he began to direct his passion for acoustics toward global infrasound monitoring and research. In the succeeding 12 years Hank became a respected and beloved leader for a diverse, worldwide group of infrasound scientists. The global infrasound community honors Hank's memory and his passion for infrasound by dedicating this book to him.

Alexis Le Pichon
Elisabeth Blanc
Alain Hauchecorne

Contents

Part IV Atmospheric Investigations from Global Continuous Infrasound Monitoring

Contributors

E. Blanc
CEA, DAM, DIF, F-91297 Arpajon, France

Ph. Blanc-Benon
Laboratoire de Mécanique des Fluides et d'Acoustique, Ecole Centrale de Lyon,
LMFA UMR–CNRS 5509, 69134 Ecully Cedex, France

K. Bongiovanni
BBN Technologies, 127 Johnclarke Road, Middletown, RI 02842, USA

L. Bosca
CEA, DAM, DIF, F-91297 Arpajon, France

N. Brachet
CTBTO PTS/IDC
Vienna International Centre, P.O. Box 1200, 1400 Vienna, Austria

D. Brown
CTBTO PTS/IDC
Vienna International Centre, P.O. Box 1200, 1400 Vienna, Austria

Y. Cansi
CEA, DAM, DIF, F-91297 Arpajon, France

L. Ceranna
Federal Institute for Geosciences and Natural Resources, Stilleweg 2,
Hannover, 30655, Germany

M-L. Chanin
Université Versailles-Saint Quentin, CNRS, INSU, LATMOS-IPSL, BP3
91371 Verrières-le-Buisson, France

D.R. Christie
Research School of Earth Sciences, The Australian National University,
Mills Road, Canberra, ACT 0200, Australia

J. Coyne
CTBTO PTS/IDC, Vienna International Centre, P.O. Box 1200,
1400 Vienna, Austria

P. Campus
CTBTO PTS/IDC, Vienna International Centre, P.O. Box 1200,
1400 Vienna, Austria

B. Despres
CEA, DAM, DIF, F-91297 Arpajon, France

D. Drob
Space Sciences Division, U.S. Naval Research Laboratory,
4555 Overlook Avenue, Washington DC 20375, USA

W. N. Edwards
Department of Physics and Astronomy, University of Western Ontario,
London, Ontario, Canada N6A 3K7, USA

L. Evers
Royal Netherlands Meteorological Institute (KNMI),
Wilhelminalaan 10, 3732 GK De Bilt, the Netherlands

T. Farges
CEA, DAM, DIF, F-91297, Arpajon, France

O. Gainville
CEA, DAM, DIF, F-91297 Arpajon, France

M. Garcés
HIGP, SOEST, University of Hawaii Manoa, 73-4460 Queen Kaahumanu Hwy,
#119 Kailua-Kona, HI 96740-2638

R. Gibson
BBN Technologies, 1300N 17th Street, Arlington, VA 22209, USA

K. Gilbert
National Center for Physical Acoustics, The University of Mississippi,
1 Coliseum Drive, MS 38677, USA

D.N. Green
3 AWE Blacknest, Brimpton, Reading
RG7 4RS, United Kingdom

C. D. de Groot-Hedlin
Scripps Institution of Oceanography, La Jolla CA 92093-0225, USA

H. Haak
Royal Netherlands Meteorological Institute (KNMI), Wilhelminalaan 10,
3732 GK De Bilt, the Netherlands

A. Hauchecorne
Université Versailles-Saint Quentin, CNRS INSU, LATMOS-IPSL, BP3,
91371 Verrières-le-Buisson, France

M. Hedlin
Institute of Geophysics and Planetary Physics, University of California, San Diego, 9500 Gilman Drive, La Jolla, CA, 92093, USA

P. Herry
CEA, DAM, DIF, F-91297, Arpajon, France

C. Hetzer
National Center for Physical Acoustics, The University of Mississippi, 1 Coliseum Drive, MS 38677, USA

P. Keckhut
Université Versailles-Saint Quentin, CNRS, INSU, LATMOS-IPSL, BP3, 91371 Verrières-le-Buisson, France

S. Kulichkov
Oboukhov Institute of Atmospheric Physics, Russian Academy of Sciences, Pyzhevsky 3, Moscow119017, Russia

R. Le Bras
CTBTO PTS/IDC, Vienna International Centre, P.O. Box 1200, 1400 Vienna, Austria

A. Le Pichon
CEA, DAM, DIF, F-91297 Arpajon France

F. Le Piver
CEA, DAM, DIF, F-91297 Arpajon, France

P. Lognonné
Institut de Physique du Globe de Paris (IPGP), Equipe Géophysique Spatiale et Planétaire Université Paris Diderot, CNRS, 4 Avenue de Neptune, 94100, Saint Maur des Fossés, France, Paris

F. Lott
Laboratoire de Météorologie Dynamique, Ecole Normale Supérieure, 24 rue Lhomond, 75231 Paris, France

P. Mialle
CTBTO PTS/IDC, Vienna International Centre, P.O. Box 1200, 1400 Vienna, Austria

J. Marty
CEA, DAM, DIF, F-91297, Arpajon, France

R.C. Millet
CEA, DAM, DIF, F-91297 Arpajon, France

T. Mikumo
Disaster Prevention Research Institute, University of Kyoto, Uji, Kyoto 611, Japan

J.P. Mutschlecner
COMPA Industries, 1350 Central Aue Scite 201, Los Alams, NM 87544

D. Norris
Applied Physical Sciences, 4301N, Fairfax Drive,
Arlington, VA22203, USA

J.V. Olson
Geophysical Institute, University of Alaska Fairbanks, Fairbanks,
99775-7320, Alaska, USA

P.F. Piserchia
CEA, DAM, DIF, F-91297 Arpajon, France

D. Ponceau
CEA, DAM, DIF, F-91297 Arpajon, France

D. ReVelle
Geophysics Group, Earth and Environmental Sciences Division,
Los Alamos National Laboratory, Los Alamos, NM, 87545, USA

R. Roche
CEA, DAM, DIF, F-91297 Arpajon, France

C.A.L. Szuberla
Geophysical Institute, University of Alaska, Fairbanks 99775-7320
Alaska, USA

C. Talmadge
National Center for Physical Acoustics, The University of Mississippi,
1 Coliseum Drive, MS 38677, USA

J. Vergoz
CEA, DAM, DIF, F-91297 Arpajon, France

K.T. Walker
Institute of Geophysics and Planetary Physics University of California
San Diego, 9500 Gilman Drive, La Jolla, CA, 92093, USA

S. Watada
Earthquake Research Institute, University of Tokyo,Uji, Kyoto 611 Japan

R. Waxler
National Center for Physical Acoustics, The University of Mississippi,
1 Coliseum Drive, MS 38677, USA

R.W. Whitaker
EES-17 MS J577, Los Alamos National Laboratory, Los Alamos,
NM 87544, USA

M. Willis
National Weather Service, NewPort/Morehead City, NC Weather Forecast Office, 533 Roberts Rd, Newport, NC 28570, USA

C.R. Wilson
Geophysical Institute, University of Alaska, Fairbanks, 99775-7320, Alaska, USA

Part I
History, Instrumentation, Network

Chapter 1
The Characteristics of Infrasound, its Propagation and Some Early History

Läslo G. Evers and Hein W. Haak

1.1 The Physical Characteristics of Infrasound

In general, sound waves are longitudinal waves of which the particle or oscillator motion is in the same direction as the propagation. A sound wave traveling through a gas disturbs the equilibrium state of the gas by compressions and rarefactions. Sound waves are elastic; thus, when particles are displaced, a force proportional to the displacement acts on the particles to restore them to their original position, see e.g. (Pain 1983).

A large range of frequencies of deformations can be facilitated by the gas. Sound waves in the atmosphere become audible to humans if the frequency is in the range of 20–20,000 Hz. Ultrasonic sound is inaudible to humans and has frequencies higher than 20,000 Hz. For example, bats use this high frequency sound as sonar for orientation purposes. At the other end of the spectrum, sound also becomes inaudible when the frequency is lower than roughly 20 Hz. Sound waves are then called infrasound, equivalent to low frequency light which is called infrared and invisible. The lower limit of infrasound is bounded by the thickness of the atmospheric layer through which it travels. When the wavelengths of infrasound become too long, gravity starts acting on the mass displacement. Acoustic-gravity and gravity (or buoyancy) waves are the result if gravity becomes part of the restoring force (Gossard and Hooke 1975). Figure 1.1 schematically illustrates the domains of the different wave types (Gossard and Hooke 1975). The acoustic cut-off frequency N_A is typically 3.3 mHz, and the Brunt-Väisälä frequency N is 2.9 mHz in the lower atmosphere. In addition to frequency, sound waves have other characteristics, such as propagation velocity and amplitude.

Infrasound travels with the speed of sound, 343 m/s at 20°C in air. This velocity increases with temperature and downwind because of advection and vice verse. Furthermore, this velocity depends on the type of gas, i.e. the fundamental property of

L.G. Evers (✉)
Royal Netherlands Meteorological Institute (KNMI),
Wilhelminalaan, 10, 3732 GK De Bilt, The Netherlands
e-mail: evers@knmi.nl

A. Le Pichon et al. (eds.), *Infrasound Monitoring for Atmospheric Studies,*
DOI 10.1007/978-1-4020-9508-5_1,

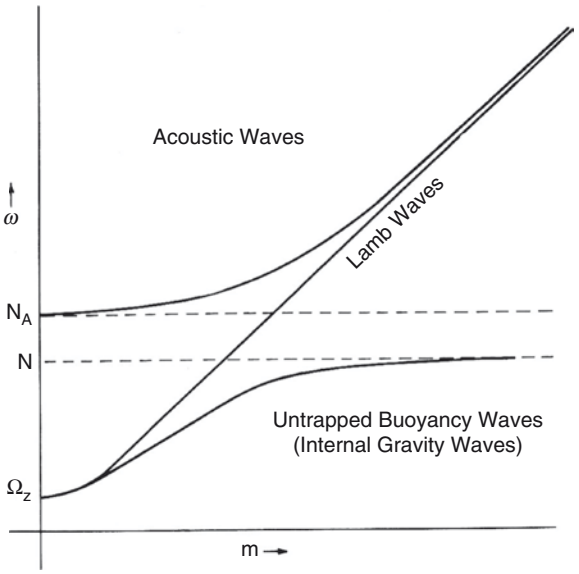

Fig. 1.1 Frequency ω vs. wavenumber *m* plot from Gossard and Hooke (1975). N_A is called the acoustic cut-off frequency, *N* the Brunt-Väisälä frequency, and Ω_z represents the angular frequency of the earth's rotation

the material, which also holds for solids and fluids. Low-frequency waves in the atmosphere with a velocity lower than the sound speed are gravity waves and typically travel with wind speed like velocities in the order of 1–10 m/s. Shock waves are generated when an object travels faster than the speed of sound. These are nonlinear waves that propagate at velocities higher than the sound speed. As the energy of the shock wave dissipates, a linear acoustic wave will remain if sufficient energy is available.

The pressure fluctuations of sound waves are, in general, small with respect to the ambient pressure. For example, an average sound volume setting of a television set in a living room will result in pressure fluctuations of 0.02 Pa (60 dB relative to 20 μPa) against a standard background pressure of 1,013 hPa. Typical infrasound signal amplitudes range from hundredths to tens of pascals.

1.2 The Atmosphere as Medium of Propagation

Infrasound wave propagation is, in first order, dependent on the composition and wind and temperature structure of the atmosphere. The effective sound speed incorporates these effects and, described by [28]

$$c_{\text{eff}} = \sqrt{\gamma_g RT} + \hat{n} \cdot \mathbf{u}, \tag{1}$$

where the multiplication of the ratio of specific heats with the gas constant for air is $\gamma_g R$=402.8 $m^2\ s^{-2}\ K^{-1}$. The absolute temperature is given by T and $\hat{n} \cdot \mathbf{u}$ projects the wind $\mathbf{u}$ in the direction from source to observer $\hat{n}$, through this inner-product. The temperature decreases with altitude in the lower atmosphere, under regular atmospheric circumstances. As a result of this, sound bends upward as function of horizontal distance. Refraction of infrasound may occur from regions where c_{eff} becomes larger than its surface value and depends on the orientation of the wave-front. This can be caused by an increase in wind, or temperature, or a combined effect. Refraction follows from Snell's law and will bend infrasound back to the earth's surface (Mutschlecner and Whitaker 2010).

The atmosphere is composed of 78% molecular nitrogen and 21% molecular oxygen. The remaining 1% consists of water vapor, carbon dioxide, ozone, and other minor constituents. The global mean pressure and density decrease approximately exponentially with altitude. Pressure decreases from 10^5 Pa, at the surface, to 10% of that value at an altitude of 15 km. Consequently, 90% of the atmosphere's mass is present in the first 15 km altitude. The density decreases at the same rate from a surface value of 1.2 kg/m^3. The mean free path of molecules varies proportionally with the inverse of density. Therefore, it increases exponentially with altitude from 10^{-7} m at the surface to 1 m at 100 km (Salby 1996) in the undisturbed gasses.

The absorption of sound in the atmosphere is a function of frequency and decreases with decreasing frequency. The absorption in a molecular gas is caused by two different mechanisms, which are the classical and relaxation effects. The classical effects are formed by transport processes in a gas. These are molecular diffusion, internal friction, and heat conduction. The latter two have the largest contribution. The relaxation effects follow from the compressional energy, which is stored in the internal degrees of freedom of the molecules. It requires time to (de)excitate internal energy states that occur during collisions. The relaxation effects can be split into vibrational and rotational components. Both the classical and relaxation effects are a function of frequency to the power of two (Bass 1972). Because of the fast decrease of attenuation with frequency, infrasound can travel over enormous distances, enabling source identification over long ranges.

The atmosphere is divided into several layers. Naming of these layers can be based on, for example, how well-mixed a certain portion of the atmosphere is. Turbulent eddies lead to a well-mixed atmosphere below 100 km. Above 100 km, turbulent air motions are strongly damped, and diffusion becomes the preferred mechanism for vertical transport. Above an altitude of 500 km, the critical level, molecular collisions are so rare that molecules leave the denser atmosphere into space if their velocity is high enough to escape the earth's gravitational field. Based on the above elucidation, the first 100 km is called the homosphere. Split by the homopause (see Fig. 1.2), the area ranging from 100 to 500 km, is called the heterosphere. The region from 500 km upward is named the exosphere (Salby 1996).

Naming can also be based on the sign of temperature gradients in different parts of the atmosphere. This is more convenient for the study of infrasound since the propagation of infrasound is partly controlled by temperature. The temperature

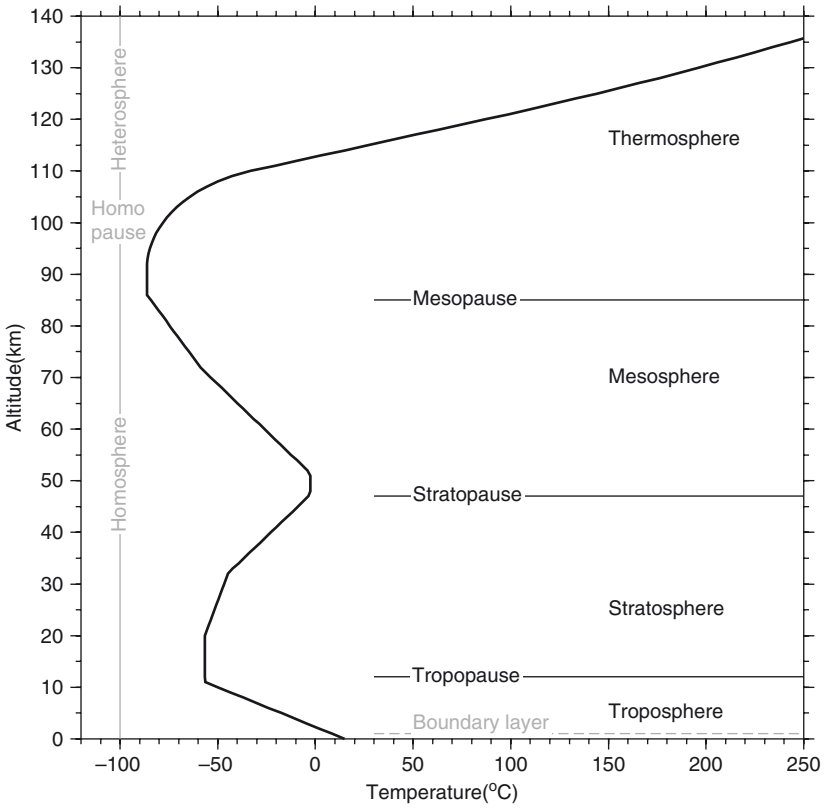

Fig. 1.2 The temperature in the atmosphere as function of altitude based on the average kinetic energy of the atoms, from the U.S. Standard Atmosphere (NOAA, NASA, USAF 1976)

distribution within a standard atmosphere is given in Fig. 1.2. The profile shows a sequence of negative and positive temperature gradients, which are separated by narrow regions of constant temperature. From bottom to top, the atmosphere is divided into layers called the troposphere, stratosphere, mesosphere, and thermosphere; these are separated by the tropopause, stratopause, and mesopause, respectively.

In the standard atmosphere, the temperature decreases with altitude in the troposphere. In a real atmosphere, a temperature inversion may occur when the temperature increases with altitude in the first 100 m up to a couple of kilometers. After a constant temperature in the tropopause, the temperature increases in the stratosphere because of the presence of ozone. The so-called ozone layer consists of this radiatively active trace gas and absorbs UV radiation. After a decrease in temperature in the mesosphere, the temperature rises again in the thermosphere because of highly energetic solar radiation, which is absorbed by very small residuals of molecular oxygen and nitrogen gases. The temperature around 300 km altitude can vary from 700 to 1,600°C depending on the solar activity.

1.3 The Propagation of Infrasound

Figure 1.3 shows the temperature and wind profiles for summer and winter in De Bilt, the Netherlands, at 52°N, 5°E. The wind is split in a West-East component, which is called the zonal wind, and in a South-North component, the meridional wind. The zonal wind is directed positive when blowing from the West toward the East, a westerly wind. The meridional wind has a positive sign if it originates in the South. Two regions in the atmosphere are of importance for infrasound propagation, as far as wind is concerned. First, the jet stream, just below the tropopause, is caused by temperature difference between the pole and equator in combination with the Coriolis force. The temperature gradient is much higher in winter than in summer. Therefore, the maximum zonal wind speed is largest in winter. The other important wind is the zonal mean circulation in the stratosphere. The main features, consistent with the temperature gradient from winter to summer pole, are an easterly jet in the summer hemisphere and a westerly one in winter. The maximum wind speeds of this polar vortex occur around an altitude of 60 km and are again largest in winter (Holton 1979).

Figure 1.4 shows an example of raytracing (Garcés et al. 1998) through the summer profiles presented in Fig. 1.3. Rays are shot from the source at a distance and an altitude of 0 km, each 4° from the vertical to the horizontal. Both westward

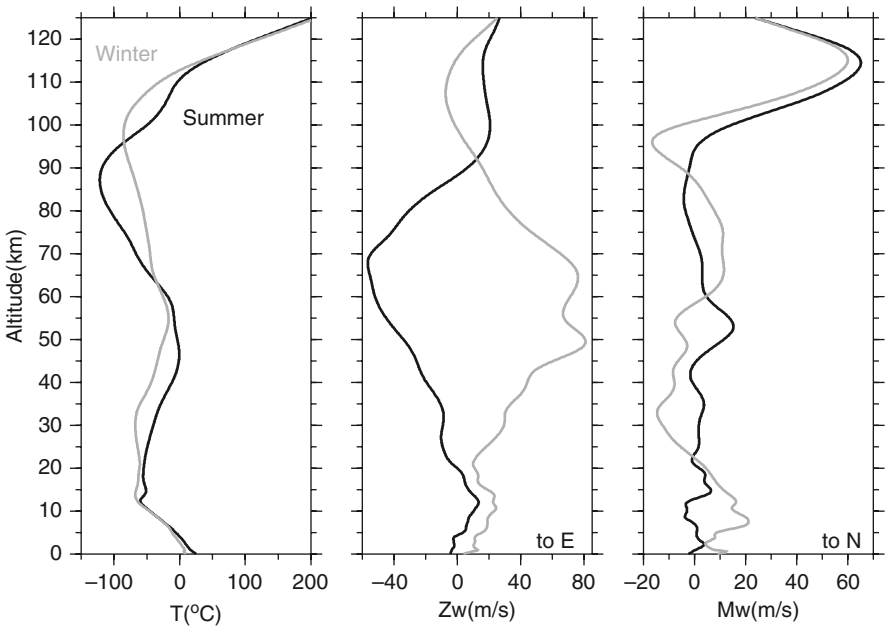

Fig. 1.3 NRL-G2S profiles for 2006, July 01 (in *black*) and December 01 (in *gray*) at 12 UTC in De Bilt, the Netherlands, at 52°N, 5°E (Drob et al. 2003)

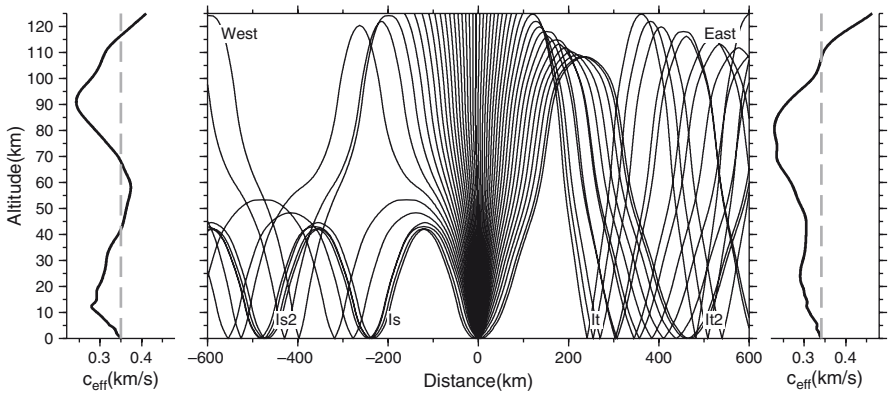

Fig. 1.4 Raytracing for a source at a distance and an altitude of 0 km. Rays are shot each 4° from the vertical to the horizontal in a westward and eastward direction through the summer profiles as given in Fig. 1.3. Effective velocities are given in the *left* and *right frame*; the *dashed vertical line* represents the effective velocity at the surface

and eastward atmospheric trajectories, which are controlled by the effective velocity structure as explained in Equation(1.1) are given. The effective velocity profile for westward propagation is given in the left frame of Fig. 1.4, and the eastward effective velocity is given in the right-hand frame. Infrasound refracts from regions where c_{eff} increases to a value larger than the value at the surface. This surface value of c_{eff} is given by the dashed vertical line in the left and right frames of Fig. 1.4. The polar vortex is directed from East to West. Therefore, stratospheric refractions are predicted for energy traveling to the West. The corresponding arrivals are labeled as Is. A phase that experienced two turns in the stratosphere is indicated by Is2. Some thermospheric paths (It) are also present to the West. The counteracting polar vortex results in solely thermospheric arrivals toward the East.

Figure. 1.4 only represents an West-East cross section, whereas Fig. 1.5 shows the bounce points of the rays on the earth's surface in all directions. The source is located in the center of the figure. Stratospheric arrivals (in orange) are refracted from altitudes of 45 to 55 km, while thermospheric arrivals (in red) result from refractions of altitudes between 100 and 125 km. This image is only valid for 2006, July 01 at 12 UTC for a c_{eff} at 52°N, 5°E and will change as function of time and geographical position. Therefore, Fig. 1.5 also illustrates the challenge in understanding the atmospheric propagation of infrasound.

In summary, wind and temperature conditions that strongly influence infrasound propagation in the lower atmosphere are the occurrence of a temperature inversion in the troposphere and the existence of a jet stream near the tropopause. For the middle atmosphere, important conditions are the strong temperature increase within the stratospheric ozone layer and the polar vortex. Upper atmospheric propagation will be controlled by the positive temperature gradient in the thermosphere.

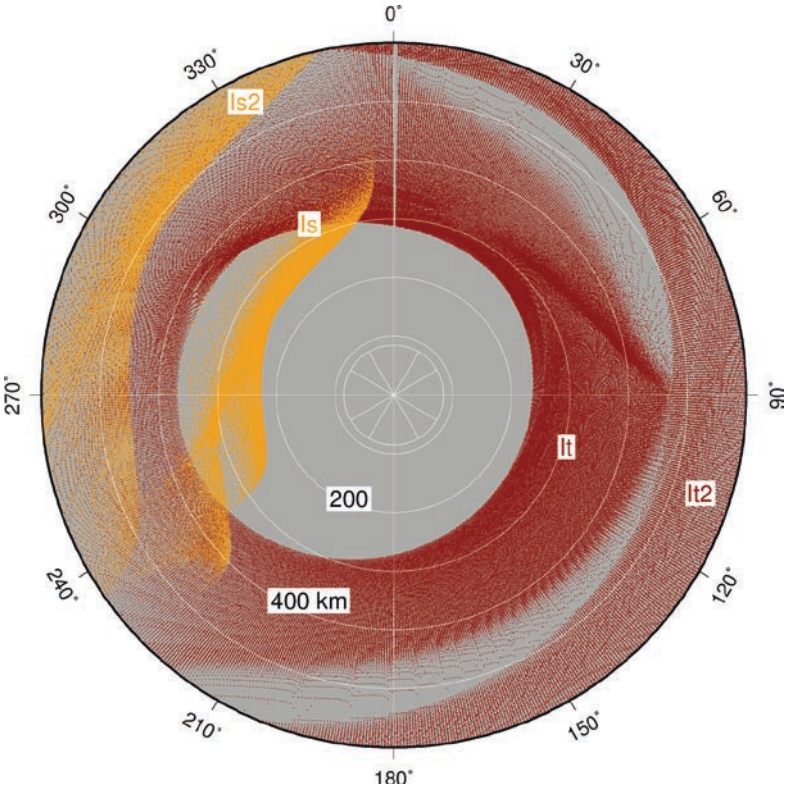

Fig. 1.5 Raytracing through the summer atmosphere from Fig. 1.3 in all directions. The source is located in the center. The bounce points of the rays on the earth's surface are shown as function of distance, up to 600 km, and propagation direction. The North is located at 0° and the East at 90°. The arrivals are labeled using the same convention in Fig. 1.4, where a West (270°) to East (90°) cross section was shown. The stratospheric arrivals are given in *orange*; *red* is used for rays impinging on the earth's surface after being refracted in the thermosphere

1.4 The Early History of Infrasound

1.4.1 The Eruption of Krakatoa in 1883

Krakatoa is a volcanic island in Indonesia, located in the Sunda Strait between Java and Sumatra. The volcano began erupting by the end of July in 1883. Seismic activity and steam venting had already increased during the previous months. Strong canon-like sound had been heard around Krakatoa from May 20, 1883 and onwards (Verbeek 1885). On August 26, the intensity of sounds and ash plume emissions increased drastically. By August 27, the eruption entered its final stage resulting in enormous explosions, large tsunamis, gigantic ash plumes, heavy ash

fall, pyroclastic flows, and pumice deposits. Activity rapidly diminished after this stage, and the last sounds of the volcano were heard on the morning of August 28.

In those days, the area was a colony of the Netherlands and was called the Dutch East Indies. The Dutch mining engineer Verbeek was ordered to do an extensive survey by the Governor-General of the Dutch East Indies. This resulted in a book of 546 pages describing all possible geological and geophysical aspects of the preeruption phase, the eruption itself and the aftermath (Verbeek 1885).

One of the investigations Verbeek made was on the barographic disturbances, which had been measured all over the world. He specifically used barometric readings from an observatory in Sydney where a total of four disturbances were noted. Fig. 1.6 shows the table from Verbeek's book. The propagation directions are given in the left column, where W-O means from West to East. The top rows give the direct wave from Krakatoa to Sydney, where the second row is the one that traveled around the globe. The differential traveltimes between various phases are used in the lower two rows. Verbeek then derives average propagation velocities in the third column of 314.31 and 312.77 m/s being, respectively, dependent and independent of the origin time. He finally averages these values to 313.54 m/s as can be seen in the fourth column. Verbeek notes that this acoustic velocity can only be reached in an atmosphere of −30°C, which leads him to the conclusion that the wave must have traveled at an altitude of 10 km (see the fifth column).

The Royal Society published a beautifully illustrated report of the Krakatoa Committee (Symons 1888). This report also described a variety of phenomena associated with the eruption of Krakatoa. One chapter was dedicated to "the air waves and sounds caused by the eruption of Krakatoa," which was written by Lieut.-General R. Strachey, chairman of the Meteorological Counsel. He analyzed the recordings of 53 barometers from all over the world, where the barometric disturbances appeared up to seven times. Some of the recordings from the original book are shown in Fig. 1.7. On the basis of these observations, he calculates the origin time of the largest explosion that probably caused the barometric disturbances. Differences in the calculated (differential) traveltimes are explained by the

Beweging.	Snelheid in meters per seconde.	Gemiddeld.	Gemiddelde uit alle waarden.	Snelheid 10 kil. boven de oppervlakte der aarde.
Krak.—I.W.-0.	314.16 (**387**)	314.31 afhank. van explosie-tijd	313.54	314.0
Krak.—II.0.-W.	314.47			
I-III. W.-0.	312.66	312.77 onafhank. van explosie.tijd		
II-IV. 0.-W.	312.88			

Fig. 1.6 Propagation velocities of the air-waves from Krakatoa as observed in Sydney. A total of four passes are analyzed, from Verbeek (1885)

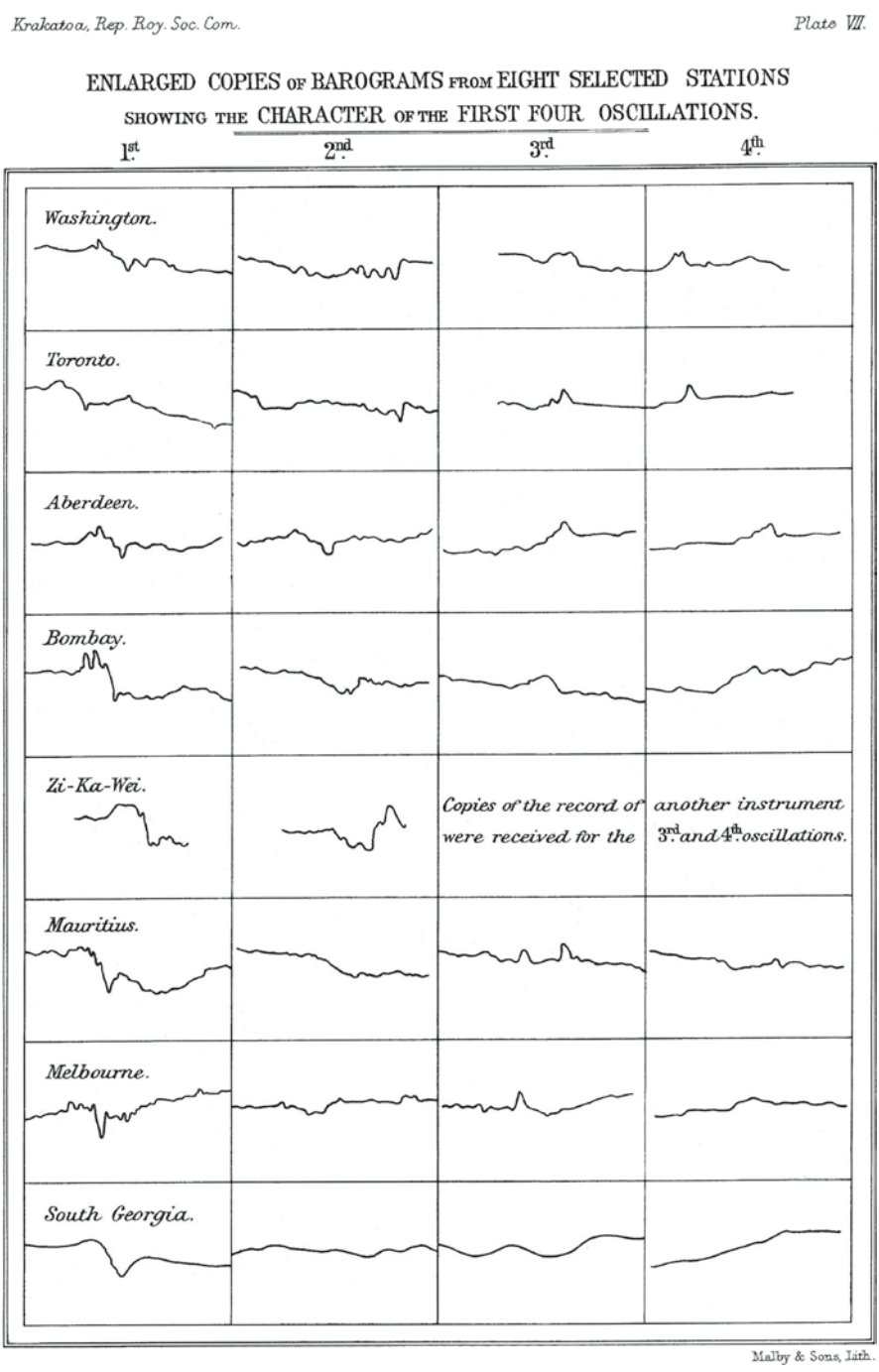

Fig. 1.7 Barograms from all over the world showing the disturbances caused by the eruption of Krakatoa, from Symons (1888)

earth's rotation and a possible influence of unknown winds. The influence of wind is also proposed as possible explanation for the observed difference in propagation velocity for eastward and westward trajectories.

1.4.2 The Great Siberian Meteor in 1908 and the First Microbarometer

A huge meteor exploded presumably a couple of kilometers above the earth's surface in Siberia on June 30, 1908. Seismic and acoustic waves were observed in the Russia and Europe (Whipple 1930). The director of the Irkutsk Observatory, A.V. Voznesenskij, made some investigations and concluded that the meteor must have fallen near a river called Podkamennai (stony) Tunguska. No further investigations were carried out until Leonid Kulik, a Russian geologist, started to undertake expeditions to this area from 1921 and onwards. Kulik identified the actual place, saw the burned vegetation, the broken trees, and collected eyewitness accounts. Although, the Tunguska event remains one of the most dramatic cosmic impacts in recent history, its origin, size, and composition are still debated (Steel 2008).

In 1930, Whipple published a paper dealing with the geophysical phenomena associated with Tunguska meteor. In his paper, Whipple showed the recordings made by microbarographs in the UK (Fig. 1.8). These are probably the first published microbarograms ever. The instruments were developed during the early 1900s by Shaw and Dines, and the details were published in 1904 (Shaw and Dines 1904). They end the introduction of their article with the following statement:

> It is proposed to call the apparatus the Micro-Barograph

They constructed the instrument to get a detailed measurement of small pressure fluctuations associated with severe weather. These fluctuations were identified on traditional barographs as irregularities in the curves of various amplitude and duration. The microbarograph would allow them to establish a connection between the minor fluctuations and meteorological phenomena.

Figure 1.9 shows the operating principles of the first mirobarograph (Shaw and Dines 1904). A hollow cylindrical bell floats in a vessel containing mercury. The interior communicates through thin pipe with a closed reservoir containing air. A very small leak is allowed, i.e. the low frequency cut-off. The reference volume is enclosed in a larger cylinder where in the intervening space is packed with feathers or some other insulating material to avoid pressure fluctuations because of temperature changes. A decrease in atmospheric pressure will raise the cylindrical bell in the mercury. This change is recorded on paper by pen.

The design by Shaw and Dines was based on the earlier work by Wildman Whitehouse who modified the sympiesometer invented by Alexander Adie from

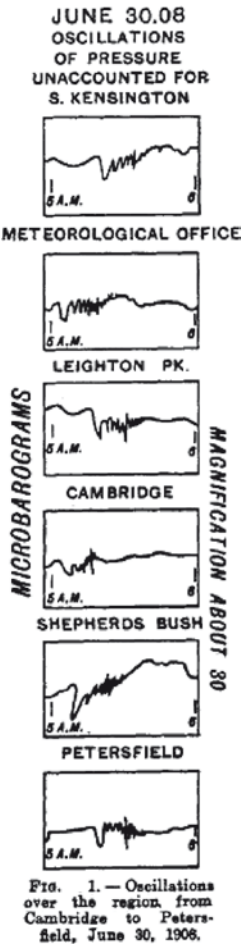

FIG. 1. — Oscillations over the region from Cambridge to Petersfield, June 30, 1908.

Fig. 1.8 Oscillations from the Tunguska meteor observed on microbarographs in the UK, from Whipple (1930)

Edinburgh in 1818. Heavy "ground-swell" on the coast during calm weather prompted Whitehouse just before 1870 to design an instrument based on the sympiesometer but with a better temperature stability (Whitehouse 1870). The whole instrument is based on a simple principle: there are two chambers at maximum temperature stability. In between is a chiffon. The difference in liquid level is a measure of the pressure difference of the two chambers. One chamber is closed, and the other is connected to the outside atmosphere. The dilemma is to follow very small pressure changes on the background of large regular pressure changes. The solution of Whitehouse was a capillary tube connection between the two chambers of the instrument which resets the closed chamber to the ambient pressure with a long time constant.

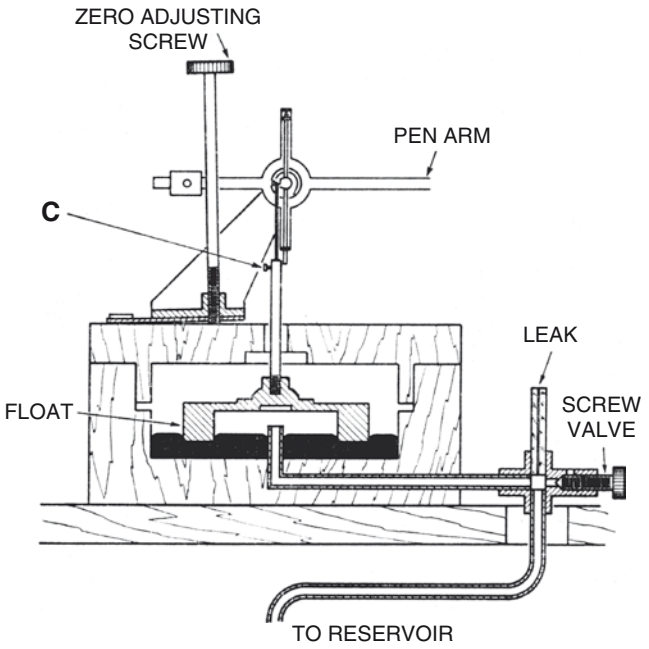

Fig. 1.9 The operating principles of the microbarograph designed by Shaw and Dines, from Meteorological Office (1956). The construction communicates through a thin pipe with a closed vessel containing air. A tuneable and very small leak takes care of the low frequency cut-off

1.4.3 The Shadow Zone Debate

1.4.3.1 The Effect of Composition or Wind?

An explosion occurred in Swiss Alps during the construction of the so-called Jungfraubahn on November 15, 1908. A. de Quervain analyzed the observations of this event and found zones of audibility and inaudibility. It was his conclusion that temperature and wind structure in the atmosphere might serve as possible explanations for the observations.

G. von dem Borne tried to find a theoretical explanation in the composition of the atmosphere. He derived one of the first acoustic velocity profiles for the atmosphere (see Fig. 1.10 from Von dem Borne (1910)). Von dem Borne derived a theoretical explanation for the increase in sound speed with altitude in the transition from an oxygen/nitrogen to hydrogen/helium atmosphere.

Around the same time, sound waves from volcanoes in Japan were analyzed by the famous seismologist Prof. F. Omori and his colleague Mr. S. Fujiwhara. During the four years from 1909–1913, eleven explosions of the volcano Asamayama gave rise to double sound areas (Davison 1917; Grover 1971). Following *Nature* (1914) vol. 92, pg. 592:

> Mr. S. Fujiwhara has recently published an important memoir on the abnormal propagation of sound-waves in the atmosphere.

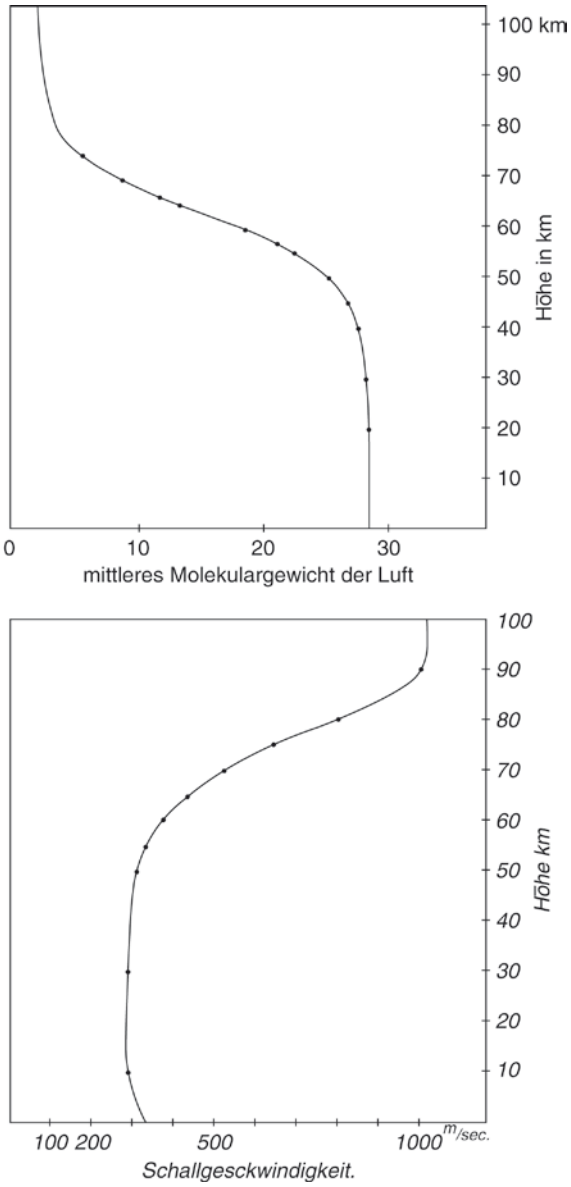

Fig. 1.10 The sound speed in m/s as function of altitude in km as derived by Von dem Borne (1910)

It followed from Fujiwhara's theoretical analysis that the influence of wind could well explain the occurrence of zones of silences (A.D. 1912). By analyzing the winter and summer conditions, Fujiwhara's concluded that sound-areas are single in winter and double in summer (Davison 1917).

1.4.3.2 The Siege of Antwerp During 1914

Prof. Dr. van Everdingen investigated sound and vibrations from the siege of Antwerp during October 7–9, 1914 (Van Everdingen 1914). In those days, Van Everdingen was the director of the Royal Netherlands Meteorological Institute (KNMI). He decided to send an inquiry to lightning observers of the KNMI throughout the Netherlands. Fig. 1.11 (left frame) shows the responses to the inquiries from people who notified rattling of their windows on hearing the canon fires. The arrows indicate the direction from which the sound was observed. Northeastern directions were reported in the northern part of the Netherlands and were correlated with other war activity. A clear shadow zone follows from this study.

The study was extended to the East into Germany by Prof. Dr. Meinardus (1915). His results coincided very well with the earlier observations of Van Everdingen (see the right frame of Fig. 1.11). Furthermore, Meinardus was able to identify a secondary source region near Meppen in Germany, which made him conclude that the secondary sound area reached up to 225 km.

In the same volume of the "Meteorologische Zeitschrift" in which Meinardus presented his results, Dr. Dörr gave similar observations from the Wiener-Neustadt (June 7, 1912) explosion in Austria (Dörr 1915). He concluded that more of these types of studies are necessary to find out whether wind and/or temperature structure leads to refractions (de Quervain, Fujiwhara) or whether reflections occur due to the increase in hydrogen (Von dem Borne).

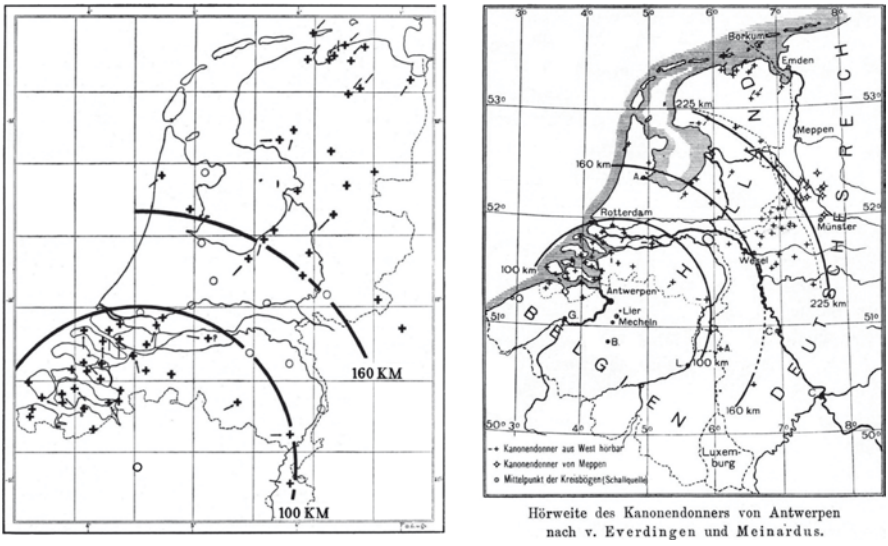

Fig. 1.11 Observations (*crosses*) from canon fires from the siege of Antwerp (*circle*) in the Netherlands (*left*) (Van Everdingen 1914) and Germany (*right frame*) (Meinardus 1915)

1.4.3.3 The Temperature in the Stratosphere

In 1922, Lindemann and Dobson concluded that the density and temperature of the outer atmosphere must be very much higher than what were commonly supposed (Lindemann and Dobson 1922). They show that the temperature above 60 km must again reach surface values. This information is gained from the analysis of the heights, paths, and velocities of some thousands of meteors. The presence of ozone is given as possible explanation for the temperature increase.

Whipple immediately realized the importance of Lindemann's findings for sound propagation (Whipple 1923). The temperature increase in the upper atmosphere will lead to the refraction of sound waves and can also serve as explanation for the zones of audibility.

An excellent review article appeared in 1925 written by Alfred Wegener on the shadow zone (Wegener 1925). Wegener summarizes observations from a wide variety of sources, some of which are described in this chapter, such as the following: canon fire, explosions, volcanoes, and meteors. He then treats four possible explanations:

1. *Temperature*: The work of Lindemann and Dobson needs more proof, for the moment temperature should be regarded as an unlikely candidate.
2. *Wind*: Can not explain the existence of the shadow zone, but has its influence as follows from the observed seasonal variability.
3. *Composition*: Von dem Borne's (1910) work gives a well-funded theoretical explanation for the shadow zone. Although, this theory is hypothetical, it has not been disproved.
4. *Pressure*: Wegener poses a new idea based on the pressure decrease with altitude, which will allow shock waves to exist over longer ranges when traveling at high altitudes.

In later works, Whipple is able to explain the sound observations from explosions by a combined wind and temperature effect (Whipple 1935). An example is given in Fig. 1.12 where the eastward observations of the Oldebroek (the Netherlands) explosion of December 15, 1932 are explained. He also suggested the use of sound to probe the upper atmospheric winds and temperatures (Whipple 1939).

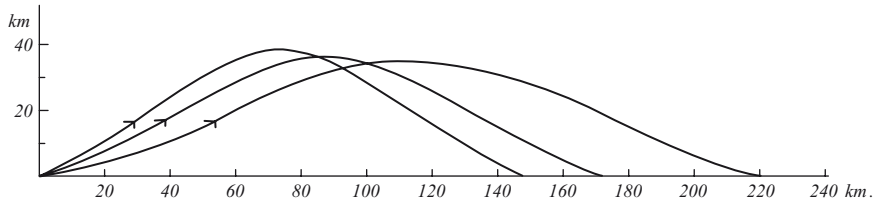

Fig. 1.12 The ray trajectories of sound traveling from the Netherlands to Germany (eastwards) after the Oldebroek explosion of December 15, 1932 (Whipple 1935)

1.4.4 The Work of Victor Hugo Benioff and Beno Gutenberg

A remarkable development took place during 1939 (Benioff and Gutenberg 1935; Gutenberg 1939). The two seismologists Benioff and Gutenberg combined their knowledge from seismology with their interest in atmospheric processes. Benioff had designed an electromagnetic seismograph, and Gutenberg was very much interested in the structure of the Earth and of the layering of the atmosphere. Their instrument, a loudspeaker, mounted in a wooden box connected very easily to the equipment that was in use in the seismological community. The amplifier was a galvanometer with a period of 1.2 s. They used a standard photographic drum recorder, which resulted in a sensitivity of 0.1 Pa per mm on the records. The loudspeaker was used as the moving membrane and had the property of a very low noise output because of its low internal resistance. Besides, the loudspeaker was industrially produced and therefore available at a low price and of constant quality. The loudspeaker has an output that is proportional to the velocity of the membrane and therefore proportional to the pressure change. Therefore, it suppresses the large amplitude low frequency pressure changes and has an output that is almost flat with respect to the pressure noise spectrum. So, Benioff and Gutenberg constructed a low cost and low white noise pressure transducer. This type of microbarograph responds not only to elastic pressure waves but also to variations in momentum of currents or turbulence (see Fig. 1.13). This was the reason why they used two instruments, instead of one, separated a few tens of meters apart. In the end, they used 120 m. The coherent sound waves were clearly separated from the turbulent wind noise. This could be seen as the most elementary array (Benioff and Gutenberg 1939).

The object of their study was an unresolved problem; the origin of microseisms. Microseisms were seen on seismographs all around the world as almost continuous wave trains with a period in the range of 4–10 s. At that time, two hypotheses were used: direct surf on steep shore lines and an atmospheric pressure oscillation. We now know that neither of them is the major cause. But the major effect is caused by interfering (and therefore standing) ocean waves. Benioff and Gutenberg indeed observed oscillations on their microbarograph, which they called microbaroms, a name derived from microseisms that is used in seismology. The lack of coherence between the two phenomena is caused by the differences in the wave paths. In the atmosphere, there is a strong dependence on the wind and temperature profiles. Benioff and Gutenberg were surprised by the rich variety of signals they discovered. They varied from traffic, battleship gunfire, blasting, surf, and possibly earthquakes. Soon they realized that an inversion procedure could be possible, like in seismology, from the study of arrival times to determine the velocity structure of the atmosphere.

Based on the recording of navy gun fire, Gutenberg could find a model for the atmosphere that explained the data and, as a result, earlier observations in Europe of large chemical explosions (see Fig. 1.14). Particular was the explanation of the zones of silence that separated the zones where sounds could be heard clearly. Reflection of the wave signal at high altitude formed the basis of the explanation. This type of behavior was confirmed by the newly acquired Californian data (Gutenberg 1939).

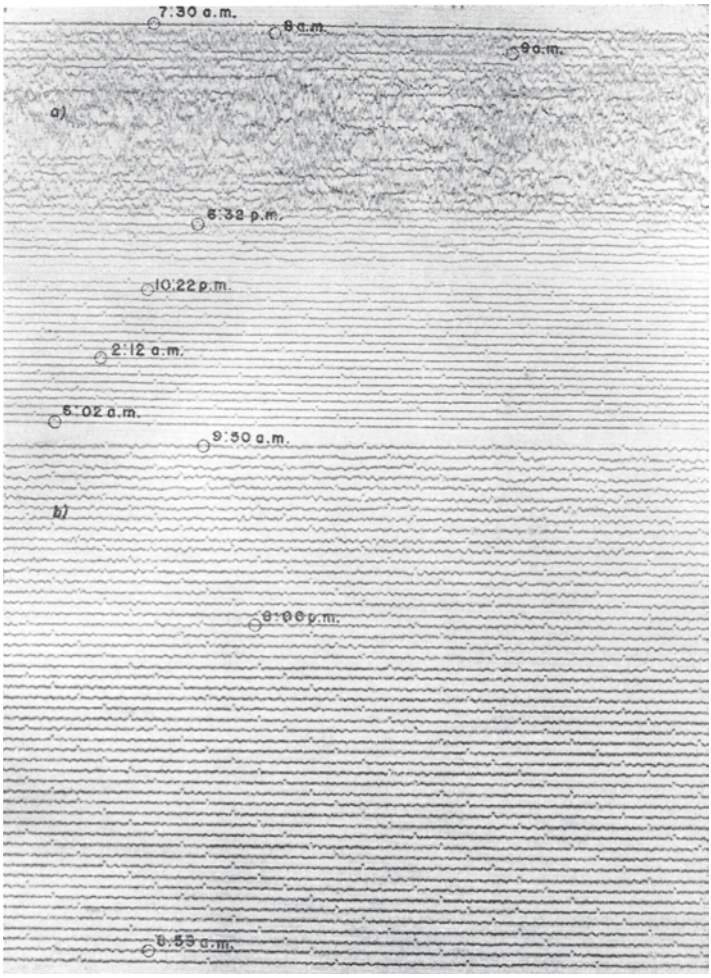

Fig. 1.13 Typical microbarograms on a clear summer day (**a**) 1938, August 13/14) and cloudy winter day (**b**) 1939, January 26/27) from Benioff and Gutenberg (1939)

1.4.5 Infrasound and Nuclear Testing

For over 20 years after World War II, infrasound was mainly developed and used to monitor nuclear explosions. From these studies, it became clear that infrasound and acoustic-gravity waves not only enabled source identification but also contained information on the state of the atmosphere as a whole, i.e. up to thermospheric altitudes.

Controlled experiments started to be conducted by Everett F. Cox in the US (Cox 1947) and Germany (Cox 1949). In the US experiment, six microbarometers, based

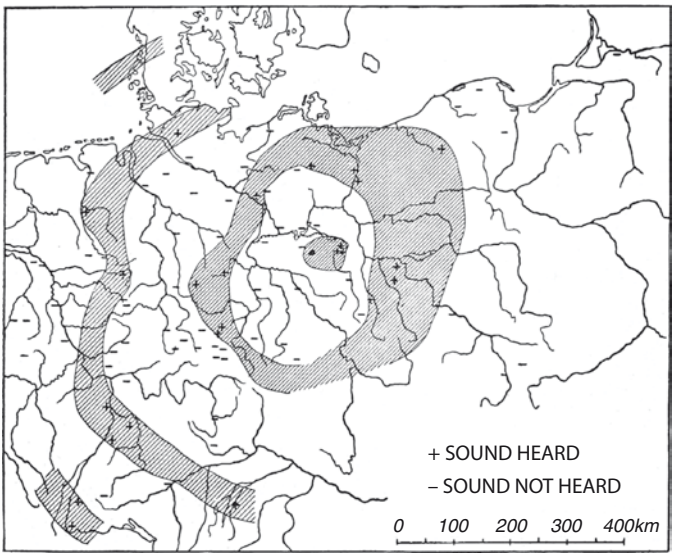

Fig. 1.14 Observations of sound after the explosion of 5,000 kg of ammunition, which was buried on 1925, December 1918 from Gutenberg (1939)

on microphones, were deployed at ranges between 12.9 and 452 km to measure infrasound from explosions with yields between 3.2 and 250 tons TNT. The Helgoland (Germany) experiment involved 5,000 tons of high explosives from which the infrasound was recorded with ten microbarometers at distances of 66–1,000 km. Stratospheric refraction are still labeled as abnormal sound waves based on Gutenberg's work. The temperature in the stratosphere is retrieved from a travel time analysis. Detailed observations of amplitude, frequency, and dispersion are reported.

It was soon realized that wind-noise reduction was an essential element for successfully measuring infrasound. Pioneering work with tapered pipes was performed by Daniels (1959). Long pipes, e.g. 1980 ft, sampled the atmosphere through 100 acoustical resistances. These impedances were matched, by varying the impedances of the pipe through tapering, to make the system nonreflective. Daniels patented his acoustical devices in March 1956 and April 1957 under number 2,739,659 and 2,789,651 with the United States Patent Office. Other systems were also developed, as can be seen in Fig. 1.15, consisting of a ring with discrete inlets.

The development of microbarographs also continued, and an example of a measurement system is described Cook and Bedard (1971). Such a system consisted of a reference volume connected to the atmosphere through a leak, with a diaphragm as pressure-sensing element. A similar sensing technique was based on measuring the length changes from a flexible metal bellows with a linear variable differential transformer (LVDT). A microbarometer based on this principle was, for example,

Fig. 1.15 Thirty-hole ring array at the sonic boom effects recording site in the UK, from Grover (1971)

constructed by Frank H. Grover at the AWRE Blacknest Research Centre in the UK (Grover 1977) (see Fig. 1.16).

Microbarograph records from nuclear tests become available and appear to consist of Lamb waves, acoustic-gravity waves, and acoustic phases. An example is given in Fig. 1.17, which shows the recording of the 50 megaton test on Novaya Zemlya in 1961, October 30. The infrasound traveled around the globe several times, where the travel time was in the same range as observed with the Krakatoa (Symons 1888), i.e. 36 h 20±10 min for Krakatoa and 36 h 27 min for this test. As more observations began to be made, the need for propagation models emerged. Raytracing, as developed by S. Fujiwhara in Japan, was extended to quickly predict atmospheric propagation paths in an atmosphere with varying winds and temperature (Rothwell 1947). This work was later extended to predict azimuthal deviations from cross winds along the ray trajectories (Georges and Beasley 1977). Other theoretical models were developed and validated with observations. Such work is based on Lamb's earlier publications in hydrodynamics (Lamb 1932). The explosive yield can also be determined with these models. This was, for example, done for the Siberian meteor, which resulted in an estimated yield of 10 megaton TNT (Hunt et al. 1960). Allan D. Pierce publishes a large amount of papers on the propagation of acoustic-gravity waves with modes, starting in 1963 (Pierce 1963) and advancing into the seventies (Pierce and Posey 1971).

More and more research groups from various countries get involved in infrasound research (see Thomas et al. 1971 for a complete overview). One of the most productive institutes in terms of publishing their research was the Lamont-Doherty Geological Observatory of Columbia University, Palisades, New York. Here, Nambath K. Balachandran, William L. Donn, Eric S. Posmentier, and David Rind, along with others, discovered and described a

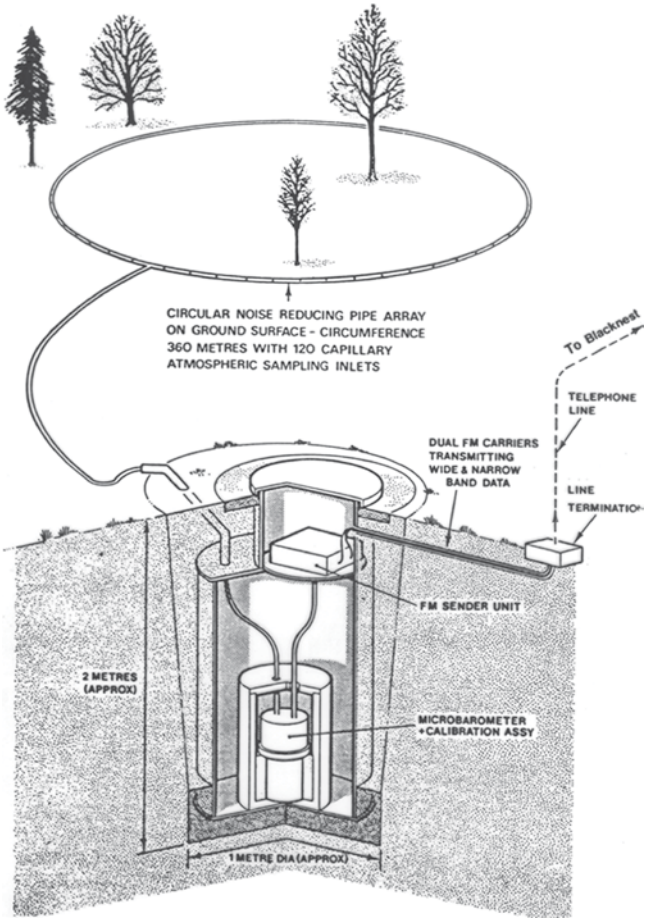

Fig. 1.16 Typical field setup of a microbarometers and its noise reducer at AWRE Blacknest Research Centre in the UK, from Grover (1977)

wide variety of sources of infrasound, propagation characteristics and derived atmospheric specifications. They studied not only nuclear tests (Donn et al. 1963), but also earthquakes (Donn and Posmentier 1964), marine storms (Donn and Posmentier 1967), and microbaroms (Posmentier 1967) and saw the potential of infrasound as atmospheric probe (Donn and Wind 1971). The propagation was studied (Balachandran 1968), paying attention to the effects of wind (Balachandran 1970).

This period of developments came slowly to an end when the Limited (Partial) Test Ban Treaty was signed in 1963 by the Soviet Union, the United States, and the United Kingdom, confining nuclear test explosions to subsurface. To mark the developments, a series of articles on infrasound was published in volume 26 of the

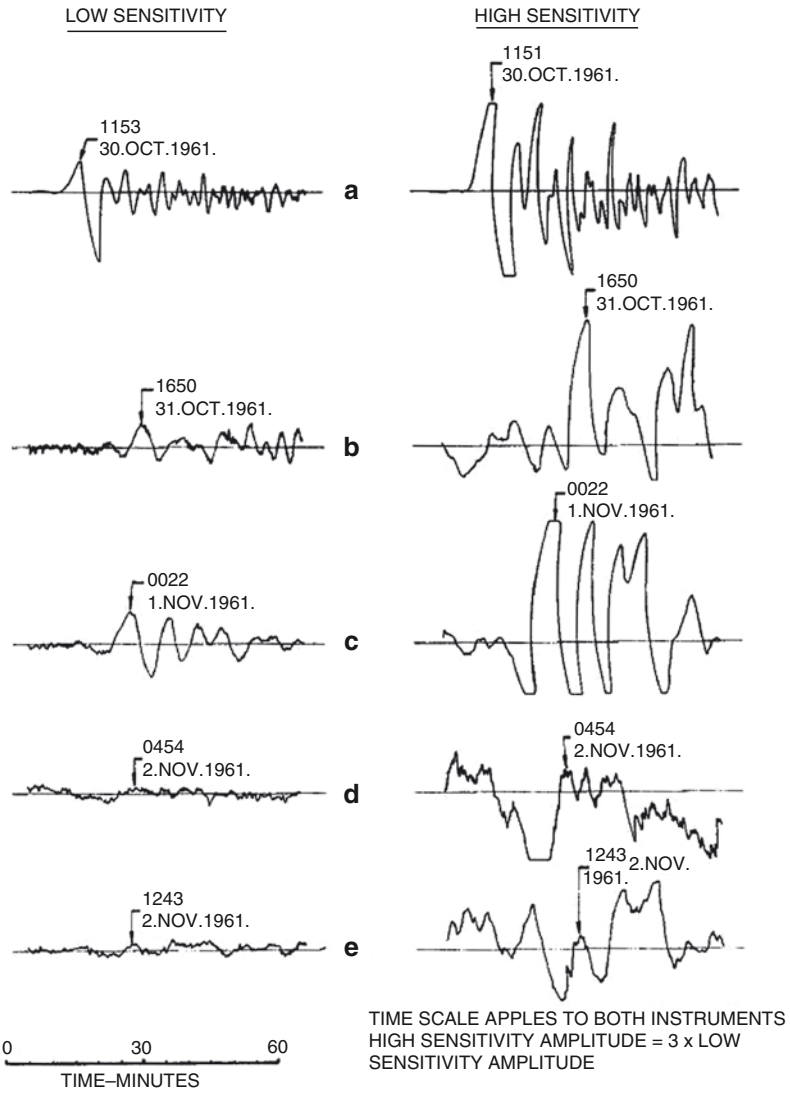

Fig. 1.17 Observations of infrasound from a Russian nuclear test in the UK, from Carpenter et al. (1961) These records consist of measurements from the 50 megaton test on Novaya Zemlya in 1961, October 30, from which the infrasound traveled around the globe, several times

Geophysical Journal of the Royal Astronomical Society (Geoph J R Astr Soc) in 1971. This volume also contains an excellent bibliography on infrasonic waves, which lists the theoretical and observational papers on sources, propagation, and instrumentation up to 1971 (Thomas et al. 1971).

The Lamont-Doherty group continued with studying infrasound and the atmosphere with microbaroms (Donn and Rind 1972), meteors (Donn and Balachandran

1974), bridges (Donn et al. 1974), rockets (Donn et al. 1975), thunder (Balanchandran 1979), volcanoes (Donn and Balachandran 1981), and sonic booms from the Concorde (Balachandran et al. 1977; Donn and Rind 1979), which were also studied by Ludwik Liszka in Sweden (Liszka 1978). Sudden stratospheric warmings were also detected based on the change in infrasonic signature of microbaroms (Rind and Donn 1978).

1.5 The Current Era: Infrasound and the Signature of the CTBT

The series of articles from 1971 from the Geophys J R Astr Soc was taken as a point of departure when, from 1994 to 1996, the Comprehensive Nuclear-Test-Ban Treaty (CTBT) was negotiated. Thus, it became gradually clear that infrasound monitoring should become one of the four techniques used by the treaty's verification system, i.e. the International Monitoring System (IMS) (Brachet et al. 2010). The other techniques are seismological measurements for the solid earth, hydroacoustics for the open waters and oceans, and radionuclide measurements as additional technique for the atmosphere. The fact that two techniques are applied to monitor the atmosphere illustrates the complexity of the medium. The detection of radionuclides serves as definite proof but has the limitation of being slow because the particles have to be transported by the winds to only a couple of collectors, which have been installed world wide. Infrasound is, in that perspective, a relatively fast technique but has some more challenging aspects in source identification.

Between 1971 and 1996, much of the existing knowledge on infrasound had been lost, and only a handful of researchers were working on infrasound. Australia, France, the Netherlands, Sweden, and the US were among the countries that had some activity in the field.

In recent years, since the signing of the CTBT, infrasound research has been rapidly expanding again. Not only do the upcoming 60 IMS infrasound arrays serve as data source, but even the non-IMS arrays that are being deployed. Current research concerns all disciplines of the study of infrasound, i.e. sources (Campus and Cheistie 2010), propagation (de Groot-Hedlin 2010; Kulichkov 2010; Novis et al. 2010; Gainville et al. 2010), and instrumentation (Ponceau and Bosca 2010; Walker and Hedlin 2010). Detailed knowledge on all these aspects is required to accurately identify sources of infrasound. Not only is this of importance from a CTBT point of view, but it also gives rise to various geophysical studies. A large amount of coherent infrasound is continuously being detected from both natural and man-made sources. Applications are foreseen in acoustic remote sensing where in infrasound can be used as passive probe for the atmosphere (Le Pichon et al. 2010; Lott and Millet 2010). Nonacoustic phenomena, such as gravity waves, can also be detected and are of importance for climate modeling (Blanc et al. 2010). This book describes the recent developments in the field of infrasound research and its applications in atmospheric studies.

References

A.D. (1912) S. Fujiwhara über die abnormale Verbreitung von Schallwellen in der Atmosphäre. Meteorologische Zeitschrift November:543–544
Balachandran NK (1968) Acoustic-gravity wave propagation in a temperature- and wind-stratified atmosphere. J Atmos Sci 25:818–826
Balachandran NK (1970) Effects of winds on the dispersion of acoustic-gravity waves. J Acoust Soc Am 48:211–220
Balachandran NK (1979) Infrasound signals from thunder. J Geophys Res 84:1735–1745
Balachandran NK, Donn WL, Rind D (1977) Concorde sonic booms as an atmospheric probe. Science 197:47–49
Bass HE (1972) Atmospheric absorption of sound: analytical expressions. J Acoust Soc Am 52:821–825
Benioff H, Gutenberg B (1939) Waves and currents recorded by electromagnetic barographs. Bull Am Meteorol Soc 20:421–426
Blanc E, Le Pichon A, Ceranna L, Farges T, Marty J, Herry (2010) Global scale monitoring of acoustic and gravity waves for the study of the atmospheric dynamics. This volume, pp. 641–658
Brachet N, Brown D, Le Bras R, Mialle P, Coyne J (2010) Monitoring and earth's atmosphere with the global IMS infrasound network, this volume, pp. 73–114
Campus P, Christie Dr (2010) Worldwide observations of infrasonic waves. This volume, pp. 181–230
Carpenter EW, Harwood G, Whiteside T (1961) Microbarograph records from the Russian large nuclear explosions. Nature 98:857
Cook RK, Bedard AJ Jr (1971) On the measurement of infrasound. Geophys J R Astr Soc 26:5–11
Cox EF (1947) Microbarometric pressures from large high explosives blasts. J Acoust Soc Am 19:832–846
Cox EF (1949) Abnormal audibility zones in long distance propagation through the atmosphere. J Acoust Soc Am 21:6–16
Daniels FB (1959) Noise-reducing line microphone for frequencies below 1 cps. J Acoust Soc Am 31:529–531
Davison C (1917) Sound-areas of great explosion. Nature 98:438–439
Donn WL, Balachandran NK (1974) Meteors and meteorites detected by infrasound. Science 185:707–709
Donn WL, Balachandran NK (1981) Mount St. Helens eruption of 18 May 1980: air waves and explosive yield. Science 213:539–541
Donn WL, Posmentier ES (1964) Ground-coupled air waves from the great Alaskan earthquake. J Geophys Res 69:5357–5361
Donn WL, Posmentier ES (1967) Infrasonic waves for the marine storm of April 7, 1966. J Geophys Res 72:2053–2061
Donn WL, Rind D (1971) Natural infrasound as an atmospheric probe. Geophys J R Astr Soc 26:111–133
Donn WL, Rind D (1972) Microbaroms and the temperature and wind of the upper atmosphere. J Atmos Sci 29:156–172
Donn WL, Rind D (1979) Monitoring stratospheric winds with Concorde generated infrasound. J Appl Meteorol 18:945–952
Donn WL, Pfeffer RL, Ewing M (1963) Propagation of air waves from nuclear explosions. Science 139:307–317
Donn WL, Balachandran NK, Kaschak G (1974) Atmospheric infrasound radiated by bridges. J Acoust Soc Am 56:1367–1370
Donn WL, Balachadran NK, Rind D (1975) Tidal wind control of long-range rocket infrasound. J Geophys Res 80:1162–1164

Dörr JN (1915) Über die Hörbarkeit von Kanonendonner, Explosionen u. dgl. Meteorologische Zeitschrift Mai:207–215

Drob DP, Picone JM, Garcés MA (2003) The global morphology of infrasound propagation. 108:4680

de Groot-Hedlin CD, Hedlin MAH, Drob DP (2010) Atmospheric variability and infrasound monitoring. This volume, PP. 469–504

Gainville O, Blanc-Benon Ph, Blanc E, Roche R, Millet C, Le Piver F, Despres B, Piserchia PF (2010) Misty picture: a unique experiment for the interpretation of the infrasound propagation from large explosive sources. This volume, pp. 569–592

Garcés MA, Hansen RA, Lindquist KG (1998) Traveltimes for infrasonic waves propagating in a stratified atmosphere. Geophys J Int 135:255–263

Georges TM, Beasley WH (1977) Refractions of infrasound by upper-atmospheric winds. J Acoust Soc Am 61:28–34

Gossard EE, Hooke WH (1975) Waves in the atmosphere. Elsevier Amsterdam

Grover FH (1971) Experimental noise reducers for an active microbarograph array. Geophys J R Astr Soc 26:41–52

Grover FH (1977) A survey of atmospheric waves recording at Blacknest. AWRE Report No. O 51/77, UK

Gutenberg B (1939) The velocity of sound waves and the temperature in the stratosphere above Southern California. Bull Am Meteorol Soc 20:192–201

Hunt JN, Palmer R, Penney W (1960) Atmospheric waves caused by large explosions. Phil Trans Roy Soc London A 252:275–315

Holton JR (1979) An introduction to dynamic meteorology. Academic Press, London

Kulichkov S (2010) On the prospects for acoustic sounding of the fine structure of the middle atmosphere. This volume, pp. 505–534

Lamb H (1932) Hydrodynamics. Dover, New York

Le Pichon A, Vergoz J, Cansi Y, Ceranna L, Drob D (2010) Contribution of infrasound monitoring for atmospheric remote sensing. This volume, pp. 623–640

Lindemann FRS, Dobson GMB (1922) A theory of meteors, and the density and temperature of the outer atmosphere to which it leads. Proc Roy Soc 102:411–437

Liszka L (1978) Long-distance focusing of concorde sonic boom. J Acoust Soc Am 64:631–635

Lott F, Millet C (2010) The representation of gravity waves in atmospheric general circulation models (GCMs). This volume, pp. 679–694

Meinardus W (1915) Die Hörweite des Kanonendonners bei der Belagerung von Antwerpen. Meteorologische Zeitschrift Mai: 199–206

Meteorological Office (1956) Handbook of meteorological instruments. Her Majesty's Stationary Office, London

McAdie AG (1912) Taal, Asama-Yama and Katmai. Bull Seism Soc Am 2:233–242

Mutschlecner JP, Whitaker RW (2010) Some atmospheric effects on infrasound signal amplitudes, This volume pp. 449–468

NOAA, NASA, USAF (1976) US Standard Atmosphere, 1976. U.S. Government Printing Office, Washington, DC.

Norris D, Gibson R, Bongiovanni K (2010) Numerical methods to model infrasonic propagation through realistic specifications of the atmosphere. This volume, pp. 535–568

Pain HJ (1983) The physics of vibrations and waves. Wiley, Great Britain

Pierce AD (1963) Propagation of acoustic-gravity waves from a small source above the ground in an isothermal atmosphere. J Acoust Soc Am 35:1798–1807

Pierce AD, Posey JW (1971) Theory of the excitation and propagation of Lamb's atmospheric edge mode from nuclear explosions. Geophys J R Astr Soc 26:341–368

Ponceau D, Bosca L (2010) Specifications of low-noise broadband microbarometers. This volume, pp. 115–136

Posmentier (1967) A theory of microbaroms. Geophys J R Astr Soc 13:487–501

Rind DH, Donn WL (1978) Infrasound observations of variability during stratospheric warmings. J Atmos Sci 35:546–553

Salby ML (1996) Fundamentals of atmospheric physics. Academic Press, San Diego
Shaw WN, Dines WH (1904) The study of the minor fluctuations of atmospheric pressure. Q J R Meteorol Soc 31:39–52
Steel D (2008) Tunguska at 100. Nature 453:1157–1159
Symons GJ (1888) The eruption of Krakatoa and subsequent phenomena, Trübner, London
Rothwell P (1947) Calculation of sound rays in the atmosphere. J Acoust Soc Am 19:205–221
Thomas JE, Pierce AD, Flinn EA, Craine LB (1971) Bibliography on infrasonic waves. Geophys J R Astr Soc 26:399–426.
Van Everdingen E (1914) De hoorbaarheid in Nederland van het kanongebulder bij Antwerpen op 7–9 October 1914. Hemel en Dampkring 6:81–85
Verbeek RDM (1885) Krakatau (Uitgegeven op last van zijne excellentie den Gouverneur-Generaal van Nederlandsch-Indië). Landsdrukkerij, Batavia
Von dem Borne G (1910) Über die schallverbreitung bei Explosionskatastrophen. Physikalische Zeitschrift XI:483–488
Walker KT, Hedlin MAH (2010) A review of wind-noise reduction methodologies. This volume, pp. 137–180
Wegener A (1925) Die äußere Hörbarkeitzone. Zeitsch Geophys I:297–314
Whipple FJW (1923) The high temperature of the upper atmosphere as an explanation of zones of audibility. Nature 111:187
Whipple FJW (1930) The great Siberian meteor and the waves, seismic and arial, which it produced. Q J R Meteorol Soc 56:287–304
Whipple FJW (1935) The propagation of sound to great distances. Q J R Meteorol Soc 61:285–308
Whipple FJW (1939) The upper atmosphere, density and temperature, direct measurements and sound evidence. Q J R Meteorol Soc 65:319–323
Whitehouse W (1870) On a new instrument for recording minute variations of atmospheric pressure. Proc Roy Soc 19:491–493

Chapter 2
The IMS Infrasound Network: Design and Establishment of Infrasound Stations

D. R. Christie and P. Campus

2.1 Introduction

The history of the Comprehensive Nuclear-Test-Ban Treaty (CTBT) is long and involved. After more than four decades on the arms control agenda, the Treaty was finally opened for signature on 24 September 1996 at the United Nations in New York. The Provisional Technical Secretariat (PTS) started work on the establishment of the CTBTO in Vienna on 17 March 1997. As of the end of 2008, 180 States have signed the Treaty and 148 have ratified the Treaty, including 35 of the 44 States whose ratification is required for entry into force. Work on the International Monitoring System (IMS) for Treaty verification is proceeding rapidly and is nearing completion. This state-of-the-art monitoring system comprises 321 seismic, infrasound, hydroacoustic, and radionuclide monitoring stations distributed as uniformly as possible over the face of the globe and 16 radionuclide laboratories. The selection of infrasound as one of the four basic technologies to be used for CTBT verification has led to a rapid advance in infrasound monitoring technology during the last decade.

Infrasound from nuclear explosions can be detected at great distances from the source. Infrasound was widely used during the period from about 1948 to the early 1970s as a means for detecting and locating atmospheric nuclear explosions. The early infrasound monitoring networks were designed to detect fairly large nuclear explosions. In contrast, since the CTBT is a zero-yield treaty that prohibits all nuclear explosions, the technical specifications for the IMS infrasound network are far more stringent than those used in the design of the earlier monitoring systems. For practical purposes, the design of the IMS infrasound network is based on the requirement that the network must be capable of reliably detecting and locating a relatively small atmospheric nuclear explosion with a yield of 1 kiloton (kT) at any point on the globe.

D.R. Christie (✉)
Research School of Earth Sciences, The Australian National University, Mills Road, Canberra, ACT 0200, Australia
e-mail: douglas.christie@anu.edu.au

A. Le Pichon et al. (eds.), *Infrasound Monitoring for Atmospheric Studies,*
DOI 10.1007/978-1-4020-9508-5_2, © Springer Science+Business Media B.V. 2010

Interest in the use of infrasound for monitoring purposes declined rapidly following the signing of the Limited Test-Ban Treaty (LTBT) in 1963, the deployment of satellite-based detection systems in the early 1970s, and the test by China on 16 October 1980, which marked the end of nuclear explosion testing in the atmosphere. In contrast with the other well-developed monitoring technologies, there were only a few infrasound stations in operation when the CTBT was opened for signature in 1996. Much of the technology used to establish the IMS infrasound network has been developed during the last decade. The revival of interest in the field of infrasound in recent years has led to the introduction of infrasonic research programs at several universities and the establishment of independent research arrays at a number of institutions around the world.

The global IMS infrasound network is far larger and much more sensitive than any previously operated infrasound network (Evers and Haak 2010; Brachet et al. 2010). It can be anticipated that data from this unique network could be used as a component in a number of international geophysical hazard-warning systems.

This paper is concerned with the design of the IMS infrasound monitoring network and the design and capability of the array stations in this network. Much of the discussion in this paper will be focused on recent advances in the field of infrasound monitoring that have the potential to significantly improve the detection capability and reliability of the global infrasound network. A brief survey of infrasonic waves detected at stations in the global IMS infrasound network, along with the potential practical applications of data from the global monitoring network, is given in Chap. 6.

2.2 The Global IMS Infrasound Network

The IMS infrasound network (see Fig. 2.1) was designed in 1996 at the Conference on Disarmament in Geneva after careful evaluation of a large number of possible network configurations. The stations in this network are distributed uniformly over the surface of the globe. The final 60-station configuration represents the most cost-effective network design that will guarantee with a high probability two-station detection of infrasonic waves generated by a 1-kiloton explosion located at any point on the globe. Initially, it was specified that the stations in this network would be 4-element array stations with elements arranged in a centered triangle configuration. Later, it was realized that 4-element array configurations may be subject to spatial aliasing and signal-coherence problems (see below), and the restriction on the number of array elements was relaxed to allow construction of arrays with more array elements. As can be seen from Fig. 2.1, the infrasound monitoring stations are located in a wide variety of environments ranging from dense equatorial rainforests to remote wind-swept islands and the exposed ice-covered wastes of the Arctic and Antarctic. The stations illustrated in Fig. 2.1 are located where possible in forests to minimize wind-generated background noise. Many stations are located out of necessity in areas with little protection from the ambient winds. This problem has been

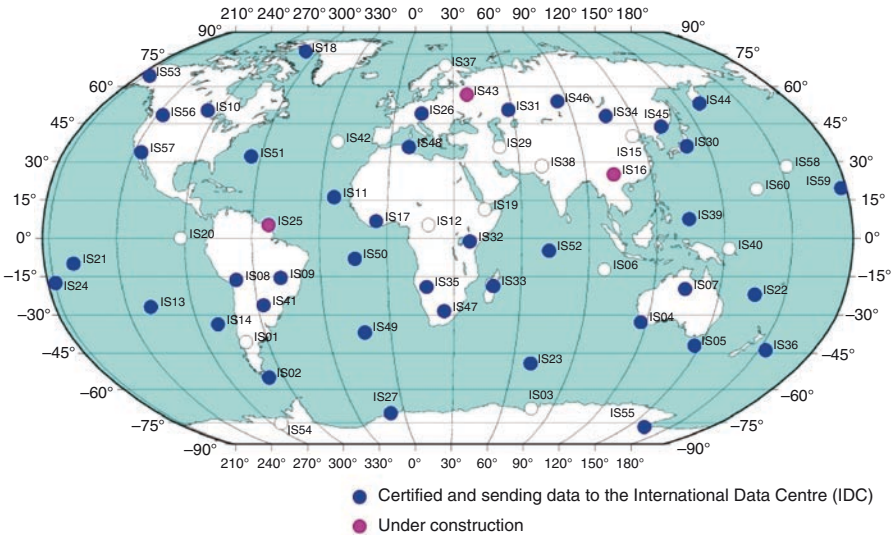

Fig. 2.1 The 60-station International Monitoring System (IMS) infrasound network

partially resolved by using more efficient wind-noise-reducing systems at stations located in high-wind environments [Walker and Hedlin 2010]. Nevertheless, wind-generated noise continues to be a problem at some stations in the IMS infrasound network. The significance of this problem is considered in Sect. 2.6 along with a discussion of some recent advances in wind-noise-reducing technology that have the potential to improve detection capability at infrasound monitoring stations.

At the present time, 41 stations in the IMS infrasound network have been certified. Work has also started on the construction of several other stations.

The performance of the network is governed by the spacing between the stations in the network, the background noise level at each site, the efficiency of the wind-noise-reducing systems, the number of array elements, the sensitivity of the infrasound sensors at all frequencies of interest, the global pattern of the upper atmospheric winds, the uptime of the stations in the network, and the performance of the automatic signal-detection algorithms that are used to routinely analyze the incoming data from the global network. The average spacing between nearest-neighboring stations in the network is 1,920 km in the Northern Hemisphere and 2,027 km in the southern hemisphere. It is clear from Fig. 2.1 that the vast open-ocean areas in the Southern Hemisphere are more difficult to monitor than the continental land mass areas in the Northern Hemisphere. In some cases, the distance across these vast open-ocean regions exceeds 7,000 km. Therefore, the stations that surround these open-ocean regions need to have good detection capability for explosions that occur at distances of up to at least 4,000 km.

A good knowledge of the fundamental relationship that describes wave amplitude as a function of the upper atmospheric winds, source distance, and yield is

essential for the proper design of a global infrasound monitoring system. The upper atmospheric winds (especially the seasonally dependent stratospheric winds) have a strong influence on the propagation properties of infrasonic waves (Mutschlecner and Whitaker 2010; de Groot-Hedlin et al. 2010). Propagation is enhanced considerably when the stratospheric winds are directed along the wave-propagation direction. In contrast, the amplitude of signals that propagate against the stratospheric winds will be attenuated, and the range of detection in the upwind direction will be reduced. On average, however, the stratospheric winds significantly increase the area that can be monitored reliably by an individual array station. The relationship between amplitude as a function of upper atmospheric winds, range, and yield has been studied in considerable detail during the last decade (see, e.g., Mutschlecner et al. 1999), and a number of range–amplitude curves normalized to 1-kT yield with upper-wind-corrected amplitudes (Mutschlecner and Whitaker 1990; Mutschlecner 1998) have been proposed. The most recent work on this subject has been presented by Bhattacharyya et al. (2003) and Whitaker et al. (2003). These authors extend the normalized upper-wind-corrected amplitude–range curves to smaller yields and greater distances. The results of these investigations are summarized in Fig. 2.2. The red curve shown in Fig. 2.2 is computed from the least squares regression given in Whitaker et al. (2003):

$$P_{\mathrm{wca}} = 5.95 \times 10^{4} (R_{\mathrm{s}})^{-1.41}, \tag{2.1}$$

where P_{wca} is the wind-corrected amplitude and R_{s} is the scaled range.

It is worth noting that the results illustrated in Fig. 2.2 include observations of infrasonic waves generated by the relatively small 0.019 kT Watusi test explosion at 21:25:17 UT on 28 September 2002 at the Nevada Test Site (see Bhattacharyya et al. 2003). The detection of signals from this event at IS10 at Lac du Bonnet in Canada at a distance of 2,165 km (denoted by the solid red square in Fig. 2.2) is particularly interesting, because this observation shows that even relatively small-yield explosions can be detected under suitable low-wind-noise conditions at great distances. A second example of the distant detection at an IMS infrasound station of infrasonic waves from a relatively small explosion is the clear observation of signals at IS07 Warramunga, Australia, along an essentially meridional path from the 0.027-kT Woomera test explosion at 00:38:03 UT on 20 September 2002 at a distance of 1,257 km (Brown et al. 2003). A third interesting example of the long-range detection of infrasound from a fairly small explosion is described briefly in Norris and Gibson (2004) and Garcés et al. (2006). In this case, signals from the explosion of a train loaded with chemicals on 18 February 2004 near Neyshabur, Iran, were observed at IS31 Aktyubinsk, Kazakstan, at a distance of 1,579 km and at IS34 Songino, Mongolia, at a distance of 4,078 km. These observations and other similar observations indicate that the IMS infrasound network is potentially capable of detecting explosions with yields that are significantly less than 1 kT. It seems clear that the development and use of improved wind-noise reducing systems that will allow reliable detection of even small-amplitude infrasonic signals at any time of day will substantially lower the global detection threshold, improve network

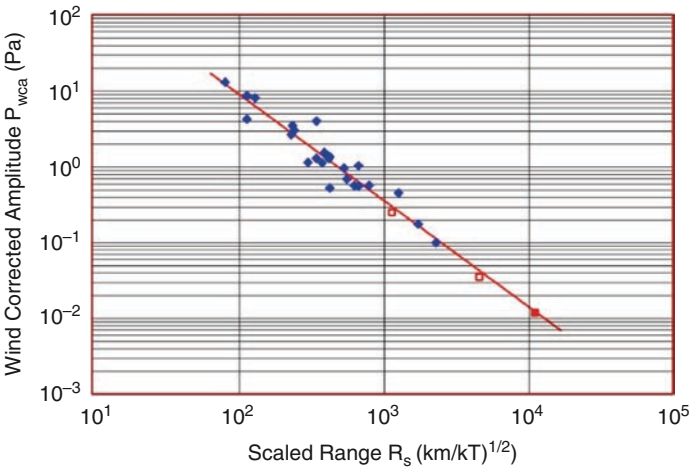

Fig. 2.2 Wind-corrected amplitude, P_{wca} (expressed in Pascals), of infrasonic signals from surface explosions as a function of scaled range R_s. Data for explosion tests at the White Sands Missile Range (*blue diamonds*) are taken from Whitaker et al. (2003). Two results from the Watusi test (*open red squares*) recorded at arrays operated by the Los Alamos National Laboratory are also taken from Whitaker et al. (2003). The *filled red square* corresponds to signals from the 0.019 kT Watusi explosion recorded at IS10 Lac du Bonnet in Canada. This data point is determined from results presented in Bhattacharyya et al. (2003). The scaled range, R_s, is the range in km to the explosion normalized by $(2 \times \text{Yield(kT)})^{0.5}$, where the factor of 2 corresponds to surface explosions. Wind-corrected amplitudes are peak-to-peak amplitudes normalized to zero stratospheric wind conditions by multiplying the observed amplitudes by $10^{-0.019V}$ where V is the wind component in m/s at an altitude of 50 km in the direction of wave propagation (see Mutschlecner and Whitaker 1990; Mutschlecner 1998)

reliability, reduce false alarms, and possibly result in global three-station detection capability. Three-station detection capability is desirable, because this would significantly reduce event-location errors.

All of the early simulations of the performance characteristics of the 60-station IMS infrasound network were based on overly simplified models for the background noise at stations in the network. The background noise at many established stations in the IMS infrasound network have now been documented (see e.g., Bowman et al. 2005, 2007; Woodward et al. 2005). These results should be incorporated into future simulations of the IMS infrasound network performance. Early examples of the simulated performance of the 60-station IMS infrasound network can be found in Clauter and Blandford (1997), Blanc and Plantet (1998) and the National Academy of Sciences (2002). The performance simulations for the IMS infrasound network reported by Clauter and Blandford (1997) and in Figs. 2 to 5 of the National Academy of Sciences report indicate that the threshold for two-station detection should be less than 1 kT for explosions located anywhere on the globe and less than 0.5 kT for all continental land mass areas. The simulations described by Blanc and Plantet (1998), which include a diurnally varying wind-noise model and seasonally varying upper atmospheric winds, indicate a 1-kT threshold

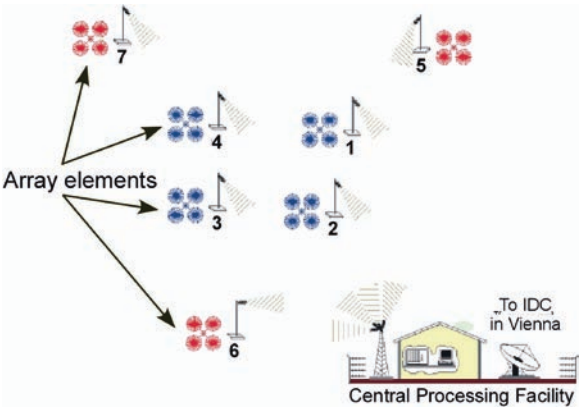

Fig. 2.3 Schematic illustration of a typical IMS infrasound monitoring station with 7 array elements. The diagram shows a rosette wind-noise reducing system (see Fig. 2.17) connected to an infrasonic sensor at each array element, a UHF data transmission tower at each array element, the central processing facility and the satellite dish of the online communications system used to transmit data to the International Data Centre (IDC) in Vienna

Fig. 2.4 Photograph showing the interior of an array element equipment vault at IS04 Shannon, Australia

for two-station detection over much of the globe, but somewhat higher thresholds at certain times of day and in certain seasons over the high latitude open-ocean regions and also over a few low-latitude areas in the Pacific where the upper atmospheric wind speeds are small. All of these simulations assumed 4-element arrays

with wind-noise-reducing systems that are less efficient than those used in the establishment of the IMS network. Since many stations in the IMS infrasound network have more than 4 array elements and all stations have been installed with relatively high-efficiency noise-reducing pipe arrays, it can be anticipated that the actual performance of the network is better than that indicated in the early network simulations noted earlier. This is confirmed in the recent simulations reported by Green (2008) and Le Pichon et al. (2008, 2009).

2.3 Infrasound Monitoring Stations

Where possible, the infrasound stations in the IMS network have been established in sheltered areas located well away from coastal areas, airports, cities, major highways, industrial centers, hydroelectric stations, waterfalls, consistently active volcanoes, and other sources of infrasonic background noise (Campus and Hoffmann 2006; Campus et al. 2007). As noted earlier, the array stations are located in a very wide range of environments. Some stations are located in areas with easy access to technical support; others (such as IS49 Tristan da Cunha) are located in some of the most remote places on the planet. Some stations are located in hot desert environments; others are located out of necessity in the harsh environments of the Arctic and Antarctic. In all cases, the design of each individual station has been tailored to minimize environmental and logistics problems.

An IMS infrasound station consists of a central recording facility (CRF), an infrasonic array with an aperture of 1–3 km, a data-transmission system between the elements in the infrasonic array and the CRF, power supply systems (including backup power supplies) for the array elements and central facility, and an online satellite system (Global Communications Interface or GCI) for the transmission of authenticated data in near real time to the International Data Centre (IDC) in Vienna, Austria. In special cases, out of necessity, a Virtual Private Network (VPN) system is used for transmitting authenticated data in near real time to the IDC.

The following components are installed at each array element:

(a) Equipment vault. These vaults may be buried, partially buried, or located on the surface. The door on each vault is fitted with a tamper-sensing switch that transmits a signal to the CRF and from there to the IDC in Vienna if the door to the vault is opened.
(b) Infrasound sensor located in the equipment vault. The specifications and performance of these sensors are described in Sect. 2.4.
(c) Twenty-four-bit digitizer with antialiasing filter and data authentication located near the infrasonic sensor inside the equipment vault. All infrasound data are sampled at 20 samples per second.
(d) Meteorological equipment. An anemometer, temperature sensor, and absolute barometer are installed at one site (usually the central site) in the infrasonic array. The anemometer is installed at a height of 2.0 m above the surface, and the temperature sensor and absolute barometer are installed at a height of 1.0 m

above the surface. A high-resolution sonic anemometer is installed at almost all of the IMS stations that have been established in the last 8 years. All meteorological data are sampled at 20 samples per second at these stations. A conventional low-resolution cup anemometer is installed at some of the earlier stations in the network. The sampling rate for meteorological data at these earlier stations ranges between 1 and 20 samples per second. It is expected that all anemometers at IMS infrasound stations will eventually be upgraded to sonic anemometers sampled at 20 samples per second.

(e) GPS clock. Time is accurate to within less than 1 ms.

(f) An efficient wind-noise-reducing system (consisting of pipe arrays) that is connected to the inlet of the infrasound sensor. These wind-noise-reducing systems are described in detail in Sect. 2.6.

(g) Regulated array element power supply. In most cases, power for the equipment at each array element in provided by an independent solar power system. This type of power supply has proven to be very reliable. In some cases, power is supplied at each array element using buried cables connected to the central facility power supply. Additional batteries are installed (if required) to provide backup power when the main power supply fails.

(h) Data transmission system. Authenticated data from the array elements are usually transmitted to the central processing system via UHF telemetry. In some cases, a buried optical fiber transmission system is used to connect the digitizer at the array element with the central processing system. Both of these systems are immune to lightning strikes.

Most of the IMS infrasound stations have been constructed as 7- or 8-element arrays. A few stations have been established with only 4 array elements, but it is anticipated that these arrays will be upgraded to 8-element arrays. Two stations have been established with a larger number of array elements (IS27 Neumayer Base in Antarctica with 9 array elements and IS23 Kerguelen with 15 array elements) in order to enhance performance in high-wind environments.

A schematic illustration of a typical infrasound monitoring station is given in Fig. 2.3. Figure 2.4 shows the interior of the equipment vault at IS04 Shannon, Australia.

The stringent specifications for the CTBT verification system require that stations in the IMS network should be mission capable for at least 98% of the time. In practice, this means that at least 70% of the array elements at each station must be operational at any given time. For arrays of more than 4 elements, the configuration and geometry of the array determine the combinations of element failures that may occur before mission capability is lost.

2.4 Infrasound Sensors

The development of suitable infrasonic sensors for nuclear explosion monitoring dates from work on the development of a sensitive capacitor microphone at the National Bureau of Standards in Washington, DC, in the early 1950s (Cordero et al.

1957; Cook 1962; Cook and Bedard 1971). These early infrasonic sensors have been refined considerably in recent years to provide robust, reliable sensors with very high sensitivity. At the present time, two types of high-sensitivity microbarometer infrasonic sensors are in use at stations in the IMS infrasound network. The first of these is an absolute pressure microbarometer (model MB2000 and the recently updated model MB2005) developed at the Laboratoire de Geophysique at the Commissariat à l'Énergie Atomique in Bruyères-le-Châtel and manufactured by Martec Tekelec Systèmes in Les Ulis Cedex, France (Ponceau and Bosca 2010). The operation of this microbarometer is based on the use of a linear variable differential transformer (LVDT) to measure the displacement of a temperature-independent aneroid bellows. A high-sensitivity output for nuclear explosion monitoring in the passband from 0.01 to 27 Hz is obtained by filtering the absolute pressure output signal (0–40 Hz). The updated MB2005 microbarometer has differential outputs, and the electronics have been modified to eliminate sporadic noise bursts on the output signals.

The second infrasonic sensor used at IMS stations is the Chaparral Physics Model 5.1 microbarometer, a refined differential capacitor microbarometer with an aluminized mylar diaphragm. This sensor was developed originally by Chaparral Physics Consultants in Albuquerque, New Mexico, and is now manufactured by Chaparral Physics at the University of Alaska, Fairbanks. The output signal of the Model 5.1 sensor is flat to within 3 dB over the frequency band from 0.02 to 50 Hz. The Chaparral Physics Model 5.1 microbarometer has recently been upgraded to the Model 50 microbarometer with a differential output signal, a flatter response between 0.02 and 50 Hz, a sealed electronics enclosure, and improved thermal stability.

The electronic self-noise of the MB2000/2005 infrasound sensors ($\sim 4 \times 10^{-7}\,Pa^2$/Hz at 10 Hz) is significantly higher than the self-noise of the Chaparral Physics Model 5.1 and Model 50 sensors ($< 1.0 \times 10^{-10}\,Pa^2$/Hz at 10 Hz). However, the MB2000 and MB2005 sensors are used at most IMS infrasound stations because these sensors are very robust and have been tested in a wide variety of environments. In addition, the calibration of these sensors over the complete monitoring passband is very stable. It is clear that a reduction in the electronic self-noise of MB2000/2005 infrasound sensors would be beneficial.

All of these microbarometers meet the specifications for IMS infrasound sensors:

(a) The sensor response must be flat (within 3 dB) over a monitoring passband extending from 0.02 to 4 Hz
(b) The sensor self noise must be ≤18 dB below the minimum acoustic noise at 1 Hz (~5 mPa)

The mechanical sensitivity to both horizontal and vertical motions for the MB2000 and Chaparral Physics Model 5.1 infrasound sensors has been studied in detail by Alcoverro et al. (2005). Both sensors are sensitive to mechanical vibration. The sensitivity of the MB2000 sensor to vertical motions is similar to the sensitivity of a Guralp CMG5T strong motion accelerometer and the mechanical

sensitivity of the Model 5.1 sensor is about 40 times smaller than the sensitivity of the MB2000.

The calculation of the instrumental response of an MB2000 microbarometer connected to a wind-noise-reducing pipe array system is described in detail in Alcoverro (2008). The procedures developed in Alcoverro (2008) to determine the combined pipe array-microbarometer transfer function can be applied to arbitrary pipe array configurations.

A number of other infrasonic sensors have been developed in the last ten years, but the electronic noise floor of most of these sensors does not meet the specifications required for use in the IMS infrasound monitoring network. An exception is the development of an optical fiber infrasound sensor (OFIS) at the University of California (see, e.g., Zumberge et al. 2003; Hedlin et al. 2004; Walker et al. 2005, 2006). OFIS sensors are long compliant tubes wrapped by two pressure sensitive optical fibers that interferometrically detect micropressure fluctuations integrated along the length of the tube. The electronic self-noise of the OFIS sensor is very low and appears to be comparable with the electronic self-noise of the Chaparral Physics Models 5.1 and 50 microbarometers. OFIS sensors can have arbitrary length and can be deployed in a wide variety of configurations to provide very good wind-noise reduction. The response of an OFIS sensor configured in a straight line is wave propagation direction dependent. Higher frequency signals are attenuated when the sensor is aligned along the wave propagation direction. In contrast, there is no distortion or attenuation of signals when wave propagation is perpendicular to the line of the OFIS sensor. Walker et al. (2008) have developed a number of ingenious techniques that use this directional dependence to accurately measure wave propagation direction, elevation, and phase velocity. There are, however, still some issues with the thermal stability of the OFIS sensor that need to be addressed. In addition, the noise level of an 89-m long OFIS sensor (Zumberge et al. 2003) appears to be slightly higher at frequencies below about 0.2 Hz than the noise level found for a 70-m diameter wind-noise-reducing pipe array system (see Fig. 2.17). At the present time, OFIS sensors are buried under gravel in a trench to protect the sensor and to reduce the effect of thermal fluctuations. Tests need to be carried out to evaluate the performance of OFIS sensors in an equatorial monsoonal environment and in the harsh conditions of the Arctic and Antarctic.

2.5 Infrasonic Array Design

Infrasonic arrays at IMS infrasound stations need to be capable of reliably detecting all atmospheric nuclear explosions. A properly designed array should also provide an accurate estimate of signal azimuth for use in source location algorithms. The fundamental principles of array design have been studied for many years (see, e.g., Haubrich 1968; Rost and Thomas 2002). The design of an infrasound monitoring array depends on a large number of factors, including the number and configuration of the array elements, the spatial coherence of signals between array elements and

the amplitude, and coherence properties of background noise. IMS arrays are designed to optimize the detection of signals from regional and distant nuclear explosions with a yield of 1-kT or less. The dominant frequency of signals generated by a low-altitude atmospheric nuclear explosion with a yield of about 1-kT lies in the range from about 0.10 to 0.33 Hz (see, e.g., Whitaker and Mutschlecner 2006) for source distances comparable with the distances between nearest-neighboring stations in the IMS infrasound network. The presence of microbarom signals in this frequency range would therefore appear, at first glance, to seriously complicate the detection of signals from explosions with a yield of around 1 kT. However, small nuclear explosions with yields of around 1 kT also generate infrasonic waves with detectable energy at frequencies both above and below the microbarom passband (0.12–0.35 Hz).

Wind-generated noise is almost always the most important source of background noise at infrasound monitoring stations. Infrasonic arrays are therefore usually designed to ensure that wind-generated background noise is incoherent between array elements. Thus, the signal-to-noise ratio is increased by the square root of the number of array elements. This, however, is a relatively small factor and other techniques are required to reduce background noise at infrasound monitoring stations to acceptable levels. Problems associated with background noise are discussed in detail in Sect. 2.6.

Recent studies of the detection capability at IMS infrasound stations in Australia (Christie et al. 2005b, 2006, 2007; Christie and Kennett 2007) have shown that the most important monitoring passband for the reliable detection of infrasonic signals generated by small regional and distant nuclear explosions with yields of 1 kT or less spans a frequency range from about 0.4 to about 1.2 Hz. This passband, which lies immediately above the microbarom passband, will be referred to as the primary monitoring passband. The lower frequency limit in this passband is governed by the intensity of microbarom background noise and the upper limit is set by problems associated with loss of signal correlation between array elements, spatial aliasing of higher frequency signals, and the loss of higher frequency signal components when the distance to the source is large. The signals that will be detected in this optimal monitoring passband will normally be stratospheric signals. In some circumstances, wave propagation between the source and the IMS infrasound monitoring station may be restricted to a thermospheric waveguide (Christie et al. 2005a; see also Whitaker and Mutschlecner 2008). In this case, since thermospheric signals generally have lower frequencies, the optimum passband for signal detection will usually be in the range from about 0.04 to 0.1 Hz. This longer period passband, which lies immediately below the microbarom passband, will be referred to as the secondary monitoring passband. Most of the observed signals from regional and distant explosions with yields of a few kT or less are detected at IMS infrasound monitoring stations as stratospheric signals in the primary monitoring passband. While it is desirable to design an infrasonic array that provides good detection and azimuthal measurement capability for signals in both monitoring passbands, practical considerations related to the maximum

number of sensors that can be used in the array and the maximum array aperture mean that the design must be tailored to provide an optimal design for detection in the primary monitoring passband. Longer period signals will still be detected reliably, but the errors on azimuthal measurement will be higher than those found for signals detected in the higher frequency primary monitoring passband.

The principal problems in the design of a cost-effective infrasonic array for nuclear explosion monitoring are:

(a) Problems associated with spatial aliasing of higher frequency signals
(b) Problems with loss in signal correlation between array elements

2.5.1 Spatial Aliasing of High Frequency Signals

Spatial aliasing of higher frequency signals is a potentially serious problem for large aperture arrays with a small number of array elements. As noted earlier, to minimize cost, it was initially decided to establish the IMS infrasound network with 4-element arrays in the form of a centered triangle with an aperture in the range from 1 to 3 km. An evaluation of the performance of this initial array design showed that the detection capability could be seriously affected by the spatial aliasing of higher frequency signals. This problem is illustrated in Fig. 2.5, which shows the array configuration and array response (Capon 1969) for a symmetric 4-element centered triangle array with an aperture of 3.0 km. As can be seen from this diagram, the mainlobe in the array response is surrounded by a high density of large amplitude sidelobes. Spatial aliasing of higher frequency signals will therefore be a serious problem with this array configuration. Ideally, the array response should consist of a single symmetrical mainlobe without any nearby sidelobes.

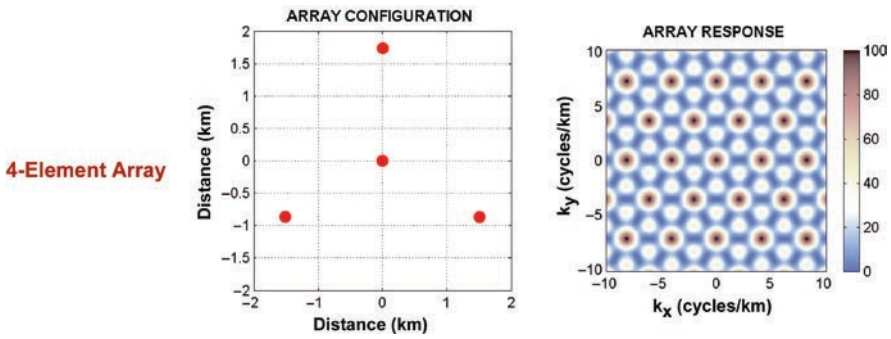

Fig. 2.5 Configuration and response for a 3-km aperture centered triangle array

A poor array response is common to all 4-element infrasonic arrays. Problems with spatial aliasing during the routine processing of data from arrays of this type can be alleviated by using the Progressive Multi-Channel Correlation Algorithm (PMCC) developed by Cansi (1995) (see also Cansi and Le Pichon (2008)), but the use of this technique is problematic in the case where one of the array elements has failed. Spatial aliasing is not the only potentially serious problem with 4-element infrasonic arrays. The degree of signal correlation between array elements may be too small to allow reliable detection of explosion-generated signals using correlation-based processing algorithms (see below).

It is well known that spatial aliasing problems can be resolved by increasing the number of array elements. A thorough investigation of the properties of a wide variety of array configurations was carried out by the authors in 2001 at the CTBTO. The number of array elements in this study ranged from 3 to 16. The results of this study showed that infrasonic arrays should have a minimum of 8 array elements to ensure that spatial aliasing problems are eliminated. Several suitable array designs with 8 or 9 elements have been proposed for use at IMS infrasound stations. Most of these designs take the form of a larger aperture main array with a smaller aperture subarray. Figure 2.6 shows the array configuration and response for 2 arrays with a small aperture triangular subarray enclosed by a larger aperture main array in the form of a pentagon. The first IMS infrasound array of this type was installed at IS55 Windless Bight on the Ross Ice Shelf near McMurdo Station in Antarctica (Wilson et al. 2001). Arrays of this type are now used, where possible, at all recently installed IMS infrasound stations. The array responses for both of the pentagon array designs illustrated in Fig. 2.6 are much better than the array response of the 4-element array shown in Fig. 2.5. The responses for both arrays exhibit fairly good side-lobe suppression, but some fairly low amplitude sidelobes are present, which could result in spatial aliasing at high frequencies when signal-to-noise ratios are small. These sidelobes can be virtually eliminated by introducing small distortions into the symmetrical pentagon main array configuration or by slightly offsetting or distorting the central triangular subarray configuration. We note that the 9-element array illustrated in Fig. 2.6 is more reliable than the 8-element array since the failure of any site in this array has only a slight influence on the performance of the array.

Some of the original 4-element arrays in the IMS infrasound network have now been upgraded to 8-element arrays. It is anticipated that the remaining 4-element arrays in the network will be upgraded to 8-element arrays in the next few years.

It is not always possible to install an ideal array configuration similar to those shown in Fig. 2.6 due to land availability problems, local topography, the distribution of forested areas at the site and other factors such as the supply of power to the array elements. A few examples that illustrate the variability of IMS array configurations are shown in Fig. 2.7. IS04 at Shannon in Australia was installed in a densely forested national park. In this case, a small aperture pentagon array (denoted by elements in red) is located slightly outside a centered triangle main array formed by elements H1, H2, H3, and H8 to facilitate the supply of power to the small aperture subarray. An unusual array configuration in the form of a small

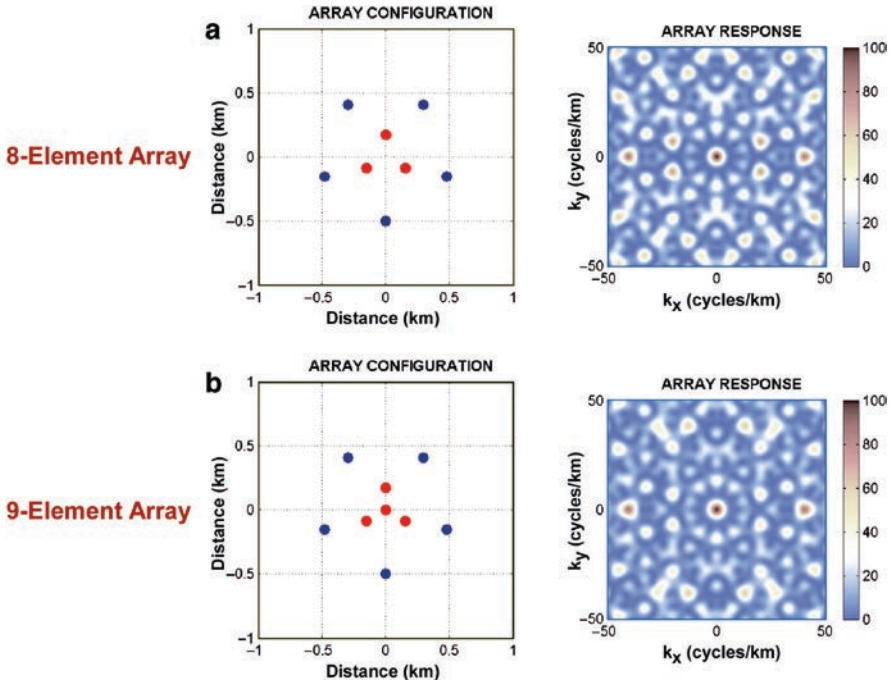

Fig. 2.6 Array configuration and response for (**a**) an 8-element pentagon main array with a triangular subarray and (**b**) a 9-element pentagon main array with a centered triangle subarray

aperture triangular subarray located well outside a large aperture pentagon array was installed at IS05 Hobart on the island of Tasmania. This array configuration was determined by land availability. The array at IS07 Warramunga in the arid interior of Australia is an example of an early IMS array station that was installed with more than 4 array elements in order to improve performance at a site with little shelter from the ambient winds.

All of the configurations illustrated in Fig. 2.7 exhibit a fairly good array response with a pronounced mainlobe surrounded by small amplitude sidelobes. These lower amplitude sidelobes could result in spatial aliasing at higher frequencies when signal-to-noise ratios are small. Spatial aliasing in this case can be reduced by using the technique developed by Kennett et al. (2003). The array at IS07 Warramunga is unique in the IMS network in that sites H1 and L1 are colocated. This was done when this station was installed as a cost-saving measure. It is clear that the array response at IS07 could be improved significantly by moving array element H1 to a site located slightly outside the area defined by H2, H3, and H4 to form a distorted small-aperture quadrilateral subarray. It is worth noting at this point that a good array response does not necessarily mean that the array will have good overall performance characteristics. The following discussion will illustrate this explicitly in the case of the arrays at IS04 and IS05.

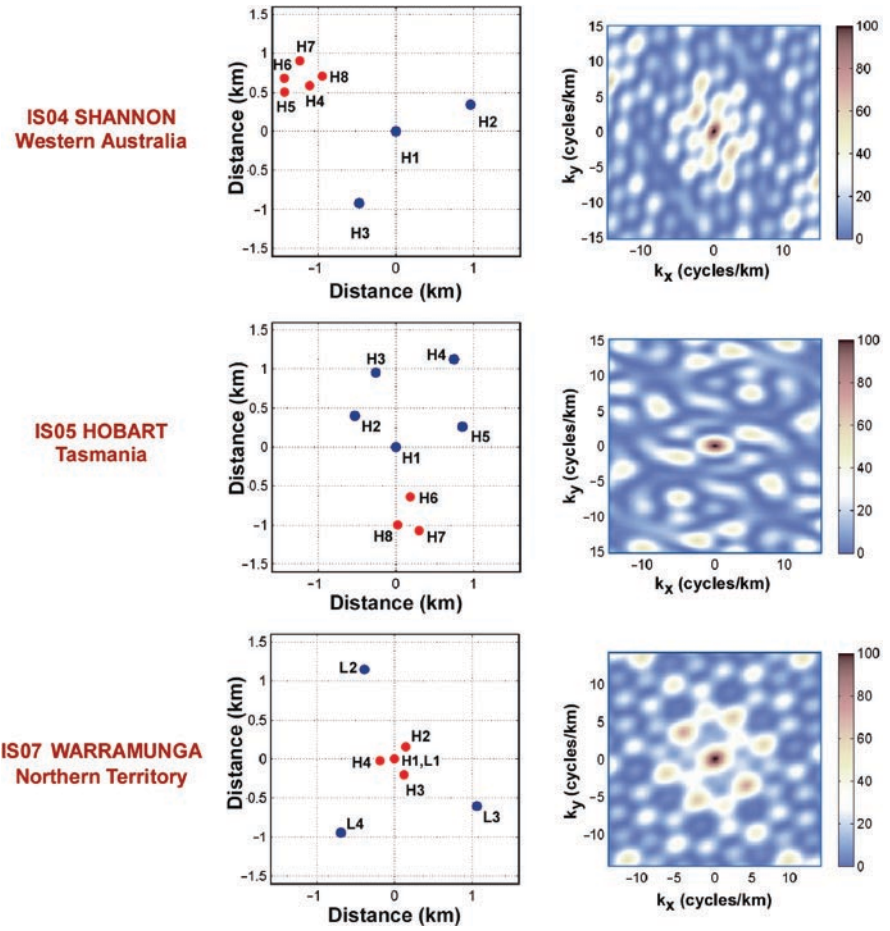

Fig. 2.7 Array configuration and response for 8-element IMS infrasonic arrays at IS04 Shannon, IS05 Hobart and IS07 Warramunga in Australia. Sites in the large aperture main array are shown in blue and sites in the smaller aperture subarray are shown in red. An 18-m diameter 96-port wind-noise-reducing pipe array system is installed at the forested sites at IS04 and IS05. Array elements provided with an 18-m diameter wind-noise-reducing system are identified by "H." The large-aperture main-array elements at IS07 are provided with a 70-m diameter wind-noise-reducing system with 144 ports in order to improve wind-noise reduction. These array elements are identified by "L"

2.5.2 Signal Correlation Between Array Elements

We now turn our attention to the important problem of signal correlation between array elements. The degree of signal correlation between array elements depends critically on the size of the array and the array configuration. The detection capability for small nuclear explosions may be limited at large aperture monitoring arrays with a small number of array elements due to the low degree of signal

correlation between array elements. It is clear that signal correlation needs to be included in the design of a reliable infrasonic monitoring array. Here, we describe and illustrate the use of a new and robust technique that can be used as a measure of the integrated signal correlation properties of infrasonic arrays with arbitrary configurations.

The spatial coherence of infrasonic signals has been studied extensively since the pioneering work of Gossard (1969), Gossard and Sailors (1970) (see also Gossard and Hooke 1975; Mack and Flinn 1971). Mack and Flinn (1971) have provided convincing evidence to show that the observed loss of signal coherence along the direction of wave propagation is due to a small variation, $\pm\Delta c$, in the velocity of the waves, while the observed loss of coherence along the wavefront is due to a small variation, $\pm\Delta\theta$, in the azimuth of the waves. The coherence parameters Δc and $\Delta\theta$ may be frequency- and range-dependent and the loss in coherence parallel to the wavefront is significantly greater than the loss in coherence normal to the wavefront. Mack and Flinn develop a fairly simple, but accurate, signal coherence model that describes signal coherence as a function of frequency and the spacing between array elements. The Mack and Flinn coherence model will therefore be adopted here as a basis for the design of an optimal infrasound monitoring array.

The study of signal coherence is proving to be a fairly complex subject. The physical processes that give rise to a loss in signal correlation between sensors in an infrasonic array remain poorly understood. It seems reasonable to assume that the loss in correlation is mainly due to propagation effects associated with wave propagation through an inhomogeneous medium with turbulence and/or small-scale variations in wind speed. The loss in correlation tends to be larger when the distance to the source exceeds 1,000 km. However, we have found a significant reduction in signal correlation even when the source distance is less than 500 km. The degree of correlation between array elements for signals that are detected as direct arrivals from sources within about 50 km is generally very high.

Mack and Flinn (1971) compared model predictions with observations of relatively long-period infrasound generated by large distant nuclear explosions. Blandford (1997, 2000, 2004) extended the work of Mack and Flinn to higher frequencies and further studies have been reported by Armstrong (1998), McCormack (2002), Christie (2007b), and Christie et al. (2005a, 2006, 2007). Observations of signal correlation between sensors aligned roughly parallel and perpendicular to the wavefront were used by Mack and Flinn to determine the model parameters Δc and $\Delta\theta$. Blandford's parameters for higher frequency infrasound differ slightly from those found by Mack and Flinn. Typically, for large distances, $\Delta c = 15$ m/s and $\Delta\theta = 5°$ (Blandford 1997). However, there is some uncertainty in the choice of Δc and $\Delta\theta$ since the observations exhibit considerable scatter.

The model of Mack and Flinn (1971) is based on the assumption that the signal is described for a given frequency, f, by a uniform distribution, $F(\mathbf{k},f)$, defined by the window $\pm\Delta c$ and $\pm\Delta\theta$ in the wavenumber domain. Mack and Flinn determine the cross-power spectrum between two sensors separated by vector $\boldsymbol{r}$ by evaluating the spatial Fourier transform of the wavenumber spectrum $F(\mathbf{k},f)$ over the area where $F(\mathbf{k},f) \neq 0$. After normalizing the result to unity when $|\boldsymbol{r}| = 0$ and assuming Δc

and $\Delta\theta$ are small and $F(\mathbf{k},f)$ is unity in the window defined by $\pm\Delta c$ and $\pm\Delta\theta$, Mack and Flinn find an expression for the squared coherence, $\gamma^2(\boldsymbol{r},f)$. Using the expression from Mack and Flinn (1971) for the squared coherence, the correlation, C, between two sensors separated by vector $\boldsymbol{r}$ can be written in the form:

$$C(\boldsymbol{r},T)=\sqrt{\gamma^2(\boldsymbol{r},f)}=\sqrt{\left|\frac{\sin(2\pi x\sin(\Delta\theta)/cT)}{2\pi x\sin(\Delta\theta)/cT}\right|^2\cdot\left|\frac{\sin(2\pi y\Delta c/(cT(c+\Delta c))}{2\pi y\Delta c/(cT(c+\Delta c)}\right|^2}\ . \quad (2.2)$$

where, T is the period, c is the mean phase velocity, γ^2 is the squared coherence, Δc and $\Delta\theta$ are the model parameters for the deviations in velocity and azimuth, and x and y are the components of the vector separation, $\boldsymbol{r}$, of the infrasound sensors. Mack and Flinn note that more realistic $F(\mathbf{k},f)$ distributions can be used to define wave amplitudes that gradually reduce to zero from a central maximum, but the results obtained using these distributions are essentially the same as those described by expression (2). The Mack and Flinn model predicts that signal correlation will depend only on Δc when sensors are aligned normal to the wavefront and only on $\Delta\theta$ when sensors are aligned parallel to the wavefront when Δc and $\Delta\theta$ are small.

Expression (2) can be plotted for $y=0$ and constant T to give the Mack and Flinn limiting curve for the variation of correlation between two sensors as a function of sensor separation for sensors aligned parallel to the wavefront. Similarly, a plot of expression (2) with $x=0$ and constant T gives the Mack and Flinn limiting curve for the variation of correlation as a function of sensor separation for sensors aligned normal to the wavefront. Examples that illustrate these two limiting curves are shown in Fig. 2.8 for 0.5, 1, and 2 Hz infrasonic waves. The material in this diagram is adapted, in part, from Blandford (2000) and includes data from two different shuttle launches recorded at DLIAR (2,500 km) and IS10 Lac du Bonnet (2,800 km). The Mack and Flinn limiting curves shown here are calculated for $\Delta c=$ 12, 15, and 18 m/s and $\Delta\theta=5$, 6, and 7°. As can be seen from this figure, signal correlation between 2 array elements is strongly dependent on the separation between the elements and on the frequency of the wave. The data illustrated in Fig. 2.8 for periods of 0.5 and 1.0 s exhibit considerable scatter, but the overall trends are clear. The degree of signal correlation between sensors decreases rapidly as sensor separation increases and as frequency increases. In addition, the degree of signal correlation depends strongly on the alignment of the sensors with respect to the wavefront at large sensor spacing or at high frequencies. The parameters adopted by Blandford (2000), $\Delta c=$ 15 m/s and $\Delta\theta=5°$, provide a reasonably good fit to the data, but they may be slightly too restrictive. We shall, however, continue to use Blandford's parameters in the correlation calculations presented below.

The Mack and Flinn model provides a good description of the observed decrease in signal correlation between two infrasonic sensors as the distance between the sensors is increased, the dependence of correlation on sensor pair orientation with respect to the wavefront, and the rapid decrease in correlation with increasing frequency. In view of the simplified representation, $F(\mathbf{k},f)$, used in the derivation of the Mack and Flinn model to describe the distribution of waves in the wavenumber

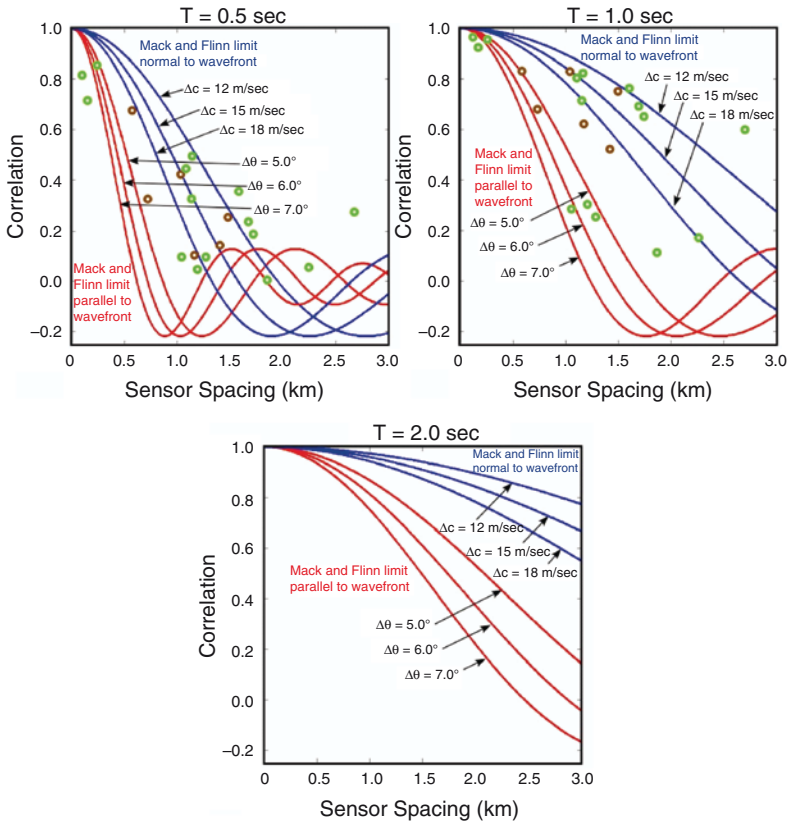

Fig. 2.8 Correlation of 0.5, 1.0 and 2.0 Hz infrasonic signals parallel and perpendicular to the wavefront as a function of sensor spacing (adapted in part from Blandford 2000). The limiting curves for the variation of signal correlation when sensors are aligned parallel and perpendicular to the wavefront are computed from expression (2.2)

domain, it must be expected that the model will only provide an approximate fit to signal correlation observations. However, the functional form of expression (2) does provide a reasonable description of all observed signal correlation properties.

The comparison of data illustrated in Fig. 2.8 is an example of the traditional method that has been used in the past to compare infrasonic wave coherence observations with theory. This method works well when it is possible to find pairs of array elements separated by a range of distances and aligned both along and perpendicular to the wavefront. The method is less useful when data are recorded on an array with a small number of array elements where few, if any, array element pairs are aligned normal and perpendicular to the wave propagation direction. We have therefore decided to use a different comparison method that can be applied directly to any array

configuration and which includes implicitly a contribution from all array element pairs. The method, which is based on the use of the predicted azimuthal variation of the array-averaged correlation coefficient, also allows the model predictions at a specified frequency to be compared directly on the same plot with observed infrasonic wave correlation data corresponding to sources located at any azimuth.

An important feature of the predicted array-averaged correlation coefficient distribution is that this polar distribution provides a unique array characteristic, which can be used to measure array performance. This then provides a basis for the design of an optimal infrasonic array.

Consider first the azimuthal variation of the signal correlation between two sensors as predicted by the Mack and Flinn model. The predicted azimuthal variation as defined by expression (2) is plotted in Fig. 2.9 in polar coordinates as a function of both sensor separation distance and wave period. These curves have been calculated with the same parameters as those used by Blandford (2000), and the results at the extremes can be compared with the limiting Mack and Flinn curves shown in Fig 2.8.

The curves shown in Fig. 2.9a correspond to a sensor separation of 1.0 km. In this case, the azimuthal variation of the predicted correlations is almost isotropic when the period exceeds 2.0 s, although the maximum reduction in correlation along the wavefront direction is still significant for T = 2.0 s. The degree of anisotropy in the azimuthal distribution increases rapidly as period decreases below 2.0 s. This indicates that the dominant contribution to the overall array-averaged correlation coefficient at higher frequencies will come from array element pairs that are aligned more or less in the wave propagation direction and suggests that some array configurations may exhibit azimuthally dependent detection characteristics. This will be illustrated in the results presented below.

The results illustrated in Fig. 2.9b for the azimuthal variation of the correlation between two sensors as a function of sensor spacing are similar in form to those

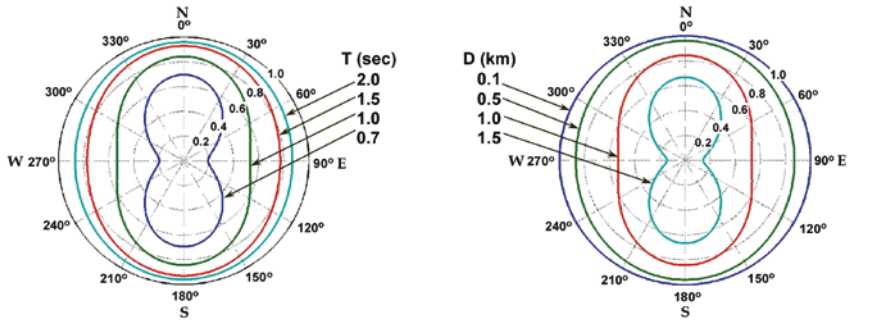

Fig. 2.9 Predicted azimuthal variation of signal correlation between two sensors as a function of wave period, T, and station separation, D. Δc=15 m/s and $\Delta\theta$=5°. The sensors are aligned along the north–south direction

shown in Fig. 2.9a. The azimuthal distribution is essentially isotropic at a frequency of 1 Hz when the sensor separation distance is less than about 0.3 km and highly anisotropic when the separation is more than about 1.0 km. Again these results suggest that certain array configurations may exhibit detection characteristics that are azimuthally biased at higher frequencies.

The predicted degree of correlation between any pair of sensors in an array with a separation vector, r, for infrasonic waves from all azimuths is specified, at a given frequency, by expression (1). Thus, the predicted correlations for all wave back-azimuths can be calculated for each individual sensor pair in the array in a common geographic coordinate system where the wave back-azimuth, φ, is measured from north by rotating the azimuthal distribution defined by (2) to the direction of the pair separation vector, r_{ij}, in the common coordinate system. The results for each sensor pair, $\tilde{C}ij\ (\varphi, T)$, in rotated coordinates can be then be averaged over all pairs of elements in the array to give a predicted normalized array-averaged correlation coefficient for all wave back-azimuths:

$$\bar{C}(\varphi,T) = \frac{2}{N(N-1)} \sum_{j>i}^{N} \tilde{C}ij(\varphi,T). \tag{2.3}$$

The resulting polar distribution of the array-averaged correlation coefficient is thus a unique characteristic of the array configuration, the parameterization of Mack and Flinn theory, and the specified frequency. As noted earlier, each sensor pair in the array contributes to the predicted array-averaged correlation coefficient for any wave back-azimuth direction, and thus the observed normalized array averaged correlation coefficients from all sources can be plotted on the same diagram and compared directly with the theoretical predictions.

We focus initially on the predicted results for arrays with a small number of array elements in order to emphasize potential problems with the reliable detection of infrasonic signals from regional and distant explosions. More specifically, we choose the following tripartite subarrays from IMS infrasound station IS07 Warramunga (see Fig. 2.7): (a) a large aperture (about 2.0-km) array defined by array elements L2, L3, and L4, (b) a medium aperture (about 1.5 km) array defined by array elements H2, L3, and L4, and (c) a small aperture (about 0.3 km) array defined by array elements H2, H3, and H4. The predicted azimuthal distributions of the array-averaged correlation coefficients for this set of subarrays at IS07 with three different apertures are shown in Fig. 2.10.

The results presented in Fig. 2.10 show that the array-averaged correlation coefficient for sparse arrays may be strongly anisotropic at higher frequencies when the array aperture is large. The results also indicate that regional and distant explosions may not be detected reliably on larger aperture triangular arrays at frequencies above 1 Hz.

An example of the comparison between signal correlation observations and model predictions for the large-, medium-, and small-aperture subarrays at IS07 is presented in Fig. 2.11a and b for regional and distant mining and other chemical explosions in Australia. The observations shown in Fig. 2.11 are in fairly good agreement with

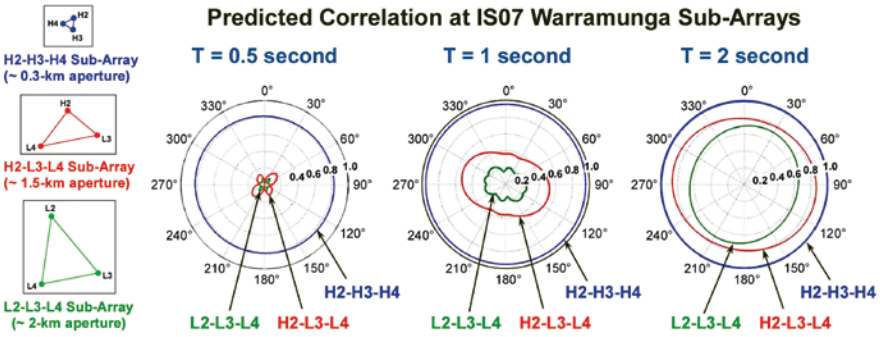

Fig. 2.10 Predicted azimuthal variation of the array-averaged correlation coefficient for a large-aperture (~2 km) subarray (in *green*), a medium aperture (~1.5 km) subarray (in *red*) and a small aperture (~0.3 km) subarray (in *blue*) at IS07 Warramunga, Australia. Azimuth is measured from north. The calculations are based on $\Delta c = 15$ m/s and $\Delta\theta = 5°$ as found by Blandford (1997)

model predictions. Observed signal correlation decreases rapidly with increasing frequency and with increasing array aperture in agreement with theory. The observations confirm that the degree of signal correlation of infrasound from regional and distant explosions is very low on sparse arrays with apertures of about 1 km or more at frequencies above 1 Hz. The degree of signal correlation will also be unacceptably small at all frequencies in the primary monitoring passband (0.4–1.2 Hz) if the array aperture exceeds 2 km.

Similar array-averaged correlation results for naturally occurring regional and distant explosions are described in Christie et al. (2007). The essential conclusion from the results presented in Fig. 2.11 is that the monitoring capability of triangular arrays with apertures of more than 2 km for small nuclear explosions will be, at best, marginal.

We now consider the use of the predicted array-averaged correlation coefficient in the evaluation of the performance of arbitrary array configurations and as a parameter for the design of optimal IMS infrasound monitoring arrays. This discussion will be limited to an evaluation of the detection capability of 4-element centered triangle infrasonic arrays, representative 8-element IMS arrays and 8- and 9-element pentagon arrays with triangular small aperture subarrays.

The array response illustrated in Fig. 2.5 shows that spatial aliasing of higher frequency signals is a potentially serious problem for 4-element centered triangle arrays. We now examine the performance characteristics of centered triangle arrays from a signal correlation perspective. The predicted azimuthal distribution of the array-averaged correlation coefficient for centered triangle arrays with apertures of 1.0, 2.0 and 3.0 km are compared in Fig. 2.12 for signals with frequencies of 0.5, 1.0 and 2.0 Hz.

The predicted azimuthal array-averaged correlation patterns illustrated in Fig. 2.12 for symmetrical centered triangle arrays are all reasonably isotropic. However, the

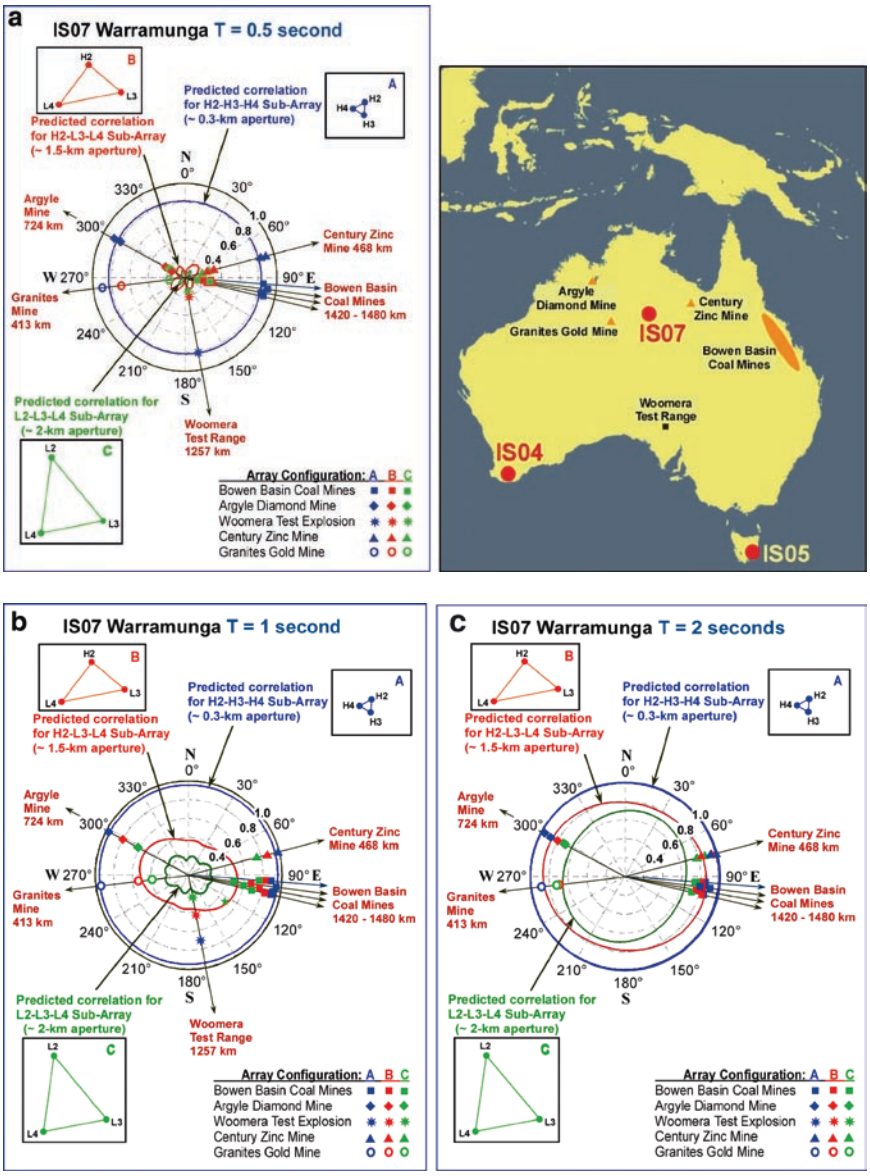

Fig. 2.11 Comparison of predicted and observed array-averaged correlation coefficients for (a) 2.0 Hz, (b) 1.0 Hz and (c) 0.5 Hz infrasonic signals from regional mining and other chemical explosions in Australia recorded on small, medium and large aperture subarrays at IS07

predicted array-averaged correlation coefficient shows that there is a serious loss in signal correlation between array elements in most cases. The signal correlation results indicate that centered triangle arrays will have reasonable signal detection capability (ignoring the spatial aliasing problem) at a relatively low frequency of 0.5 Hz

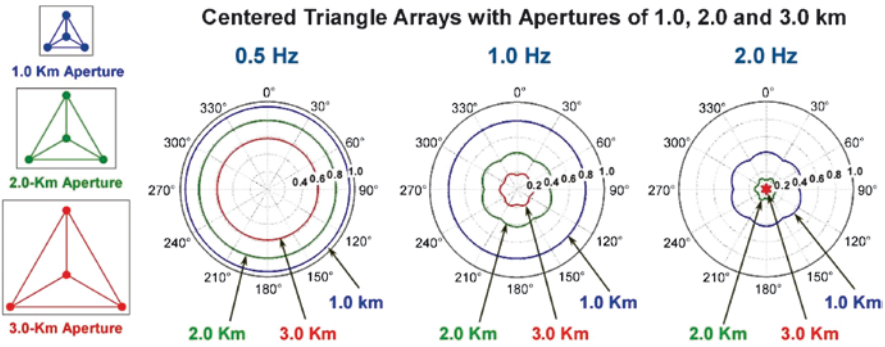

Fig. 2.12 Azimuthal distributions of the array-averaged correlation coefficient predicted by the Mack and Flinn (1971) model for symmetrical centered triangle array configurations at frequencies of 0.5, 1.0 and 2.0 Hz. Results are shown in *blue* for a 1.0-km aperture array; in *green* for a 2.0-km aperture array and in *red* for a 3.0-km aperture array. The correlation model parameters are $\Delta c = 15$ m/s and $q = 5½$ (Blandford 1997)

provided the array aperture is 2.0 km or less. The array correlation coefficient for 3.0-km arrays is significantly attenuated at 0.5 Hz. Detection capability for distant explosions will be reasonably good for 1.0-km aperture arrays, but limited for 2.0- and 3.0-km aperture arrays at 1.0 Hz. The results presented for a frequency of 2.0 Hz show that signal correlation will be very small for all centered triangle arrays with apertures of 1.0 km or more at frequencies of 2.0 Hz or more. These results indicate that higher frequency signals from distant explosions may not be detected reliably on centered triangle arrays with apertures of 1 km or more using automatic processing based on signal correlation algorithms.

It might be expected that infrasound monitoring stations with 8 array elements arranged in a configuration with reasonable side-lobe suppression would have generally acceptable signal correlation properties. However, Christie et al. (2007) have shown that this is not necessarily true. This can be illustrated by the correlation properties for the three operational 8-element IMS infrasound monitoring stations, IS04, IS05, and IS07, located on the Australian continent. As can be seen from the array responses for each of these stations (Fig. 2.6), the array configurations at IS04, IS05, and IS07 exhibit fairly good side-lobe suppression. Each of these stations is configured in the form of a large aperture array with a small aperture subarray. However, the array configurations at each of these stations differ substantially. The calculated polar distributions of the array-averaged correlation coefficients for the arrays at IS04, IS05, and IS07 are shown in Fig. 2.13 for frequencies of 0.5, 1.0, and 2.0 Hz.

As can be seen from Fig. 2.13, the signal correlation properties of all arrays are fairly good at a frequency of 0.5 Hz, but the arrays at IS04 and IS05 exhibit some asymmetry in the azimuthal distribution of the array-averaged correlation coefficient. In addition, the array-averaged correlation in each case is attenuated, which reflects a loss in signal correlation between some site pairs in the array. The loss in signal correlation is much more pronounced at a frequency of 1.0 Hz.

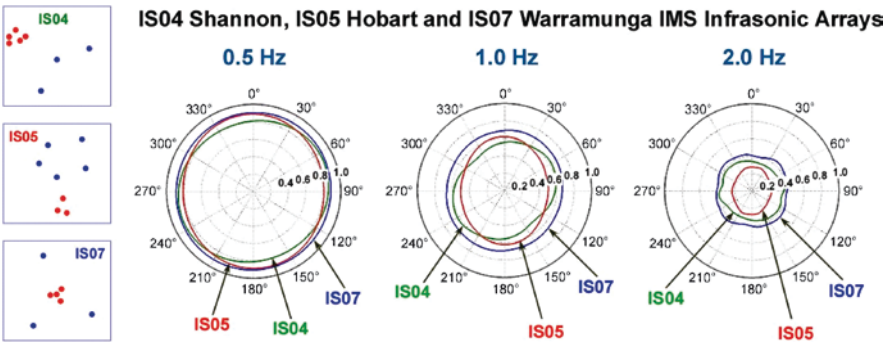

Fig. 2.13 Azimuthal distributions of the predicted array-averaged correlation coefficient for 8-element IMS infrasound arrays at IS04, IS05 and IS07 at frequencies of 0.5, 1.0 and 2.0 Hz. The azimuthal variation of the array-averaged correlation coefficient is shown in *green* for the array at IS04; results in *red* correspond to the array at IS05 and results in *blue* were calculated for the array at IS07. The array configurations are shown on the left hand side of the diagram. Calculations were carried out with $\Delta c = 15$ m/s and $\Delta\theta = 5°$

The polar distributions of the array-averaged correlation coefficient for IS04 and IS05 are also anisotropic at 1.0 Hz, which means that the sensitivity of these arrays is azimuthally dependent. The results for all arrays at a frequency of 2.0 Hz show that contributions to the array-averaged correlation coefficient are almost entirely due to element pairs in the high-frequency subarray. Thus, each of these arrays is reduced effectively to a small aperture subarray at high frequencies. Detection at a frequency of 2.0 Hz is still possible at these arrays, but overall capability is reduced, and the error on azimuthal measurement is increased. The array at IS07 with the small aperture subarray embedded inside the main array has better performance characteristics than the arrays at IS04 and IS05. The essential conclusion here is that small aperture subarrays should not be located outside the main array configuration.

It is easy to design an optimal array with acceptable response and correlation characteristics when the number of array elements is large. However, cost considerations limit the number of array elements at most IMS infrasound monitoring stations to a maximum of about 9. An optimal array design for IMS infrasound monitoring stations should therefore have 8 or 9 array elements with an overall aperture in the range from 1.0 to 3.0 km, and the array should be optimized for detection in the primary monitoring passband (0.4–1.2 Hz). The first step in the design of an infrasound array is to choose a basic array configuration with an acceptable array response. As noted above, this initial problem is essentially resolved for arrays with 8 or more array elements. Arrays with good side-lobe suppression can be designed using a larger aperture pentagon main array with an enclosed smaller aperture triangular subarray, arrays in the form of a logarithmic spiral and arrays with randomly configured array elements. Since most of the arrays installed in recent years at IMS infrasound stations have been 8-element arrays in the form of a small aperture triangular array embedded inside a larger aperture

pentagon array, we will take this well-known basic configuration, along with a similar 9-element array configuration, as basic array configurations that are suitable for use at IMS infrasound monitoring stations. The parameters that need to be optimized are the overall aperture of the main array and the size of the enclosed triangular subarray. Both of these array configurations (see Fig. 2.6) exhibit an acceptable array response. The 9-element array is more robust than the 8-element array. The performance of both arrays will decrease if one of the array elements in the outer pentagon array fails, but the side-lobes that appear in both cases remain relatively small. The 4-element small aperture subarray in the 9-element array will continue to have fairly good performance characteristics even when one of the array elements in the small-aperture array fails.

The predicted azimuthal variation of the array-averaged correlation coefficient for 8-element arrays are given in Fig. 2.14 for overall array apertures of 1.0, 2.0, and 3.0 km, a triangular subarray aperture of 0.3 km and frequencies of 0.5, 1.0, and 2.0 Hz. The results found for the 9-element arrays (not shown) are only slightly better than those found for the 8-element arrays. In all cases, the azimuthal correlation patterns are nearly isotropic, even at high frequencies. However, in the case of the 2- and 3-km aperture arrays, the correlation coefficient at frequencies of 1.0 Hz or higher is attenuated and dominated by contributions from the small aperture triangular subarray. In contrast, the 1.0 km aperture array has fairly good correlation characteristics even at a frequency of 2.0 Hz. The performance of each of these configurations has also been determined for a wide range of subarray apertures. The performance of the 8-element array deteriorates at higher frequency when the aperture of the central triangular subarray exceeds about 250 m. The performance of the 9-element array at higher frequencies is largely independent of the size of the centered triangle subarray up to an aperture of about 300 m. The size of the central subarray should therefore be chosen to be as large as possible in order to minimize

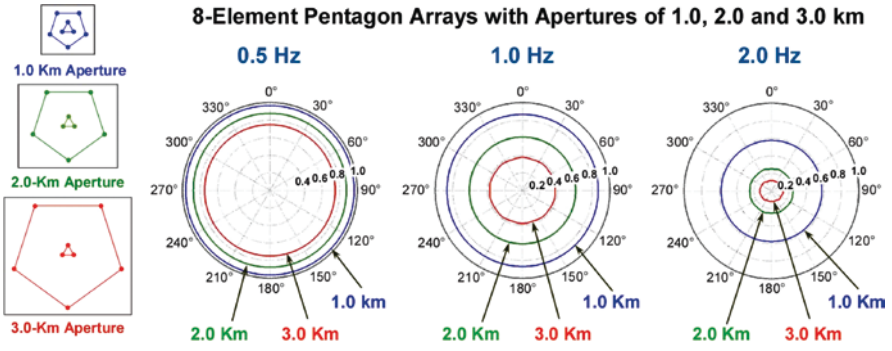

Fig. 2.14 Azimuthal distributions of the array-averaged correlation coefficient predicted by the Mack and Flinn (1971) model for 8-element pentagon array configurations at frequencies of 0.5, 1.0 and 2.0 Hz. Results are shown in blue for a 1.0-km aperture array; in green for a 2.0-km aperture array and in red for a 3.0-km aperture array. The correlation model parameters are $\Delta c = 15$ m/s and $\Delta\theta = 5°$ (Blandford 1997)

the error on azimuthal measurements at high frequencies. Hence, we conclude that the optimal design parameters for 8- and 9-element pentagon arrays are:

(a) 8-element array: 1 km overall aperture with a 0.25-km aperture triangular subarray.
(b) 9-element array: 1 km overall aperture with a 0.30-km aperture centered triangle subarray.

The results presented in this section show that the low degree of signal correlation between array elements in arrays with a small number of array elements may limit the reliable detection of regional and distant explosions at frequencies of 1.0 Hz and higher. The study of the signal correlation properties of typical 8-element IMS arrays with a larger number of array elements shows that, even when the array has good side-lobe suppression characteristics, signal correlation between array elements may be reduced substantially, and the sensitivity of these arrays may exhibit significant azimuthal anisotropy at higher frequencies. These problems can be eliminated by using array configurations in the form of 8- or 9-element pentagon arrays with an overall aperture of 1.0 km and with enclosed subarray apertures of 0.25 km (8-element arrays) or 0.30 km (9-element arrays).

2.6 Background Noise

The primary sources of background noise are given in the following list in order of their importance from a nuclear explosion monitoring perspective:

(a) Wind-generated micropressure fluctuations associated with turbulent eddies in the atmospheric boundary layer (all frequencies)
(b) Microbarom infrasonic waves in the 0.12–0.35 Hz passband
(c) Surf-generated infrasonic noise (usually at frequencies above 1.0 Hz)
(d) Infrasonic noise generated by highway traffic, trains, aircraft, bridges, industry, and other cultural sources (usually high frequency)
(e) Oil and gas refinery flares (high frequency)
(f) Hydroelectric installations (high frequency)
(g) Wind turbines (usually high frequency)
(h) Auroral-generated infrasound (usually at frequencies below 0.1 Hz)
(i) Various naturally occurring infrasonic sources such as ongoing volcanic eruptions, forest fires, waterfalls, etc. (usually at higher frequencies)
(j) Mountain-generated infrasonic waves (frequencies below 0.1 Hz)
(k) Long period pressure fluctuations and wind noise generated by mesoscale density currents
(l) Micropressure fluctuations associated with slowly propagating trapped internal gravity waves (low frequencies); The surface winds associated with highly nonlinear solitary waves and internal bore waves will also generate background noise

(m) Pressure variations at the surface associated with shear instabilities in the upper tropospheric and boundary layer jet streams (low frequencies)

Wind-generated noise is by far the most important source of infrasonic background noise in the primary and secondary monitoring passbands (Walker and Hedlin 2010). This section will therefore be focused on a discussion of techniques that have been used in the past to reduce the influence of wind-generated noise at infrasound monitoring stations and a discussion of new techniques that have been developed recently, which have the potential to significantly reduce or eliminate wind-generated noise at many IMS infrasound monitoring stations. A general review of wind noise reduction methods is given in Part I of this volume in Chap. 5.

Wind noise may be a serious problem at certain times of day at a significant number of infrasound monitoring stations in the global network. At the present time, even with the use of state-of-the-art wind-noise-reducing pipe array systems, turbulent wind noise may prevent the detection of infrasonic signals from atmospheric explosions over significant periods of time if the array elements are exposed to ambient winds of more than a few meters per second. The problem is particularly serious at stations located on remote barren wind-swept islands and at stations located at high latitudes in the Arctic and Antarctic. Continental stations located in open fields or in semidesert areas with sparse vegetation are usually subject to high levels of wind noise during the daytime. Background noise levels at these stations are generally much lower during the night when the winds at the top of the boundary layer are decoupled from the surface by a nocturnal radiation inversion. Wind noise levels will usually be within acceptable limits at all times of day or night at infrasound monitoring stations located in dense forests.

The diurnal variation of background noise conditions at IMS infrasound monitoring stations that are exposed to the ambient winds can be illustrated by the typical background noise conditions found at IS07 Warramunga, Australia (see Fig. 2.15). IS07 is located in a semi-desert environment with sparse vegetation and little shelter from the ambient winds. Wind-generated noise levels are invariably high at this station under daytime convective conditions when the boundary-layer winds are coupled to the surface. The well-mixed boundary layer is replaced at night by a deep stable nocturnal radiation inversion, which effectively decouples the boundary layer winds from the surface and often results in very low noise conditions. The detection capability of this station is fairly poor during the daytime, but may be exceptionally good at night. The diurnal behavior of the background noise levels at IS07 shown in Fig. 2.15 is also characterized by sporadic nocturnal bursts of noise associated with highly nonlinear mesoscale solitary waves and internal bore wave disturbances (Christie 1989) that propagate on the nocturnal inversion layer. The long-period micropressure signatures of a variety of these unusual disturbances can be seen in the records shown in Fig. 2.15. Large amplitude waves of this type are observed frequently at IS07 Warramunga. They are also recorded from time to time at many other infrasound monitoring stations located in areas that favor the formation of stable surface-based inversion layers.

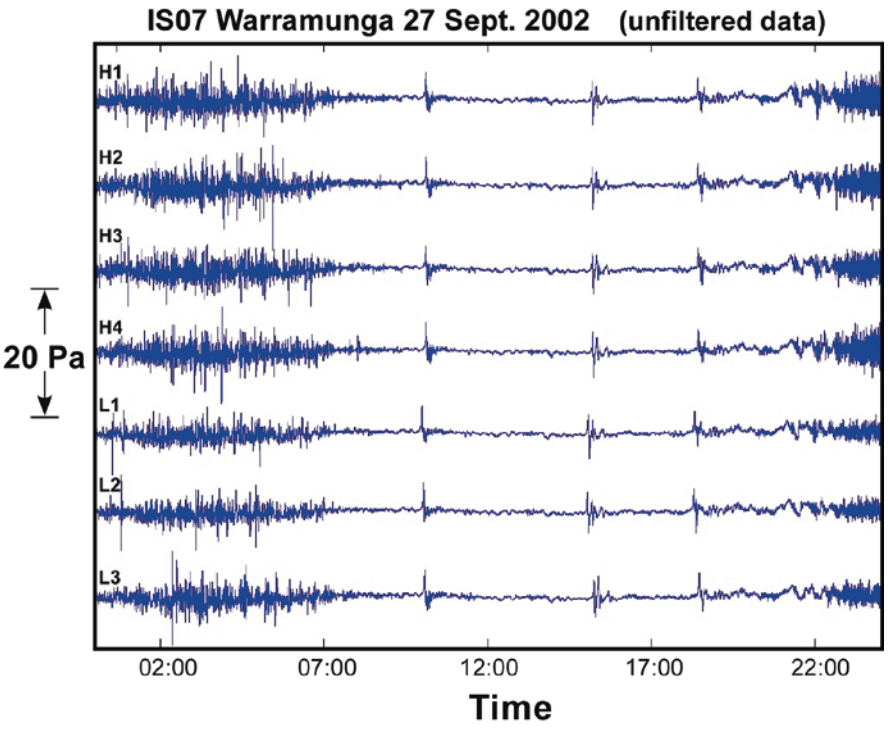

Fig. 2.15 Typical wide-band (0.01–10 Hz) micropressure signatures recorded at IS07 Warramunga over a 24-h period. Time is given in UT (LT = UT + 09:30)

Fig. 2.16 illustrates typical background noise conditions recorded at IS07 Warramunga. A DASE MB2000 infrasonic microbarometer is installed at each array element at IS07. A standard 18-m diameter, 96-port rosette wind-noise-reducing system is connected to the input at all microbarometer sensors in the small aperture H-array (the array configuration for IS07 is shown in Fig. 2.7) and a 70-m diameter, 144-port rosette pipe array is installed at all array elements in the large aperture L-array. A description of the standard CTBTO rosette wind-noise-reducing systems may be found in Christie et al. (2001) and the configuration of both of these pipe array designs are illustrated in Fig. 2.17. The lower limit on the background noise at all array elements at IS07 in very low wind conditions is governed by the electronic noise floor of the MB2000 microbarometer (~4×10^{-7} Pa^2/Hz at 10 Hz). This lower limit is clearly shown by the red curve corresponding to zero wind conditions in Fig. 2.16. For comparison, we have also included power spectral density estimates (blue curve) of background noise recorded simultaneously at IS07 in zero wind conditions using a Chaparral Physics Model 5.1 microbarometer. As discussed in Sect. 2.4, this microbarometer has a very low electronic noise floor

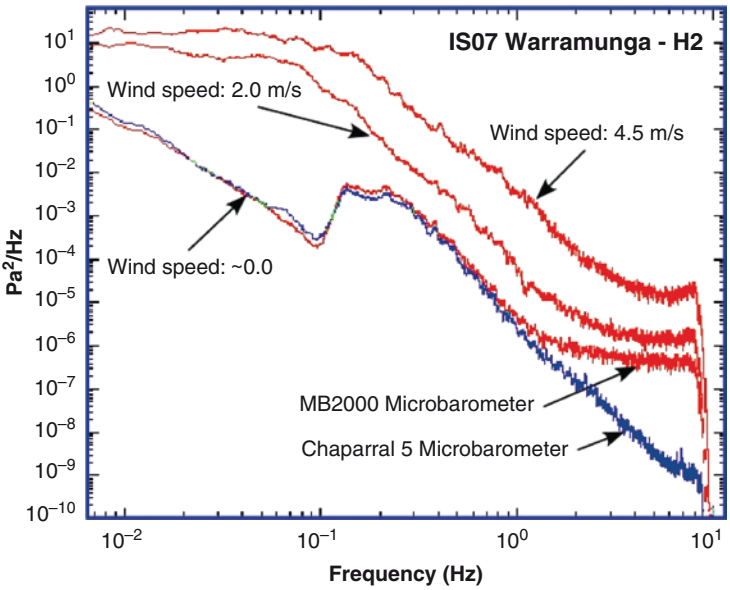

Fig. 2.16 Power spectral density of infrasonic background noise recorded at site H2 at IS07 Warramunga. *Curves* shown in *red* correspond to observations made with the DASE MB2000 microbarometer at site H2 with a standard CTBTO 18-m diameter rosette noise-reducing system installed at the input to the microbarometer. The *blue* curve corresponds to data recorded simultaneously in very low wind conditions using a Chaparral Physics Model 5.1 microbarometer. Wind speed is measured at a height of 2.0 m

(~5×10^{-11} Pa^2/Hz at 10 Hz), and this is reflected in the significantly improved performance of the Chaparral Physics Model 5.1 sensor in low wind conditions at all frequencies above 0.9 Hz. It is interesting to note that the high-frequency observations given by the blue curve in Fig. 2.16 of background noise under very low wind conditions appear to be essentially the same as the lower noise limit reported by Zumberge et al. (2003) in the frequency range from 1 to 10 Hz for observations made under low wind conditions using an OFIS. The Chaparral Physics Model 5.1 sensor observations shown in Fig. 2.16 for very low wind conditions are not limited by the electronic noise floor of this sensor, which is more than one order of magnitude lower than the results shown in this diagram.

The observations presented in Fig. 2.16 show that the average noise levels at 1 Hz at IS07 range from about 2×10^{-6} Pa^2/Hz at night in very low wind conditions to about 3×10^{-3} Pa^2/Hz during the daytime. The microbarom waves recorded in very low wind conditions in this diagram had a peak-peak amplitude of about 0.1 Pa. Note that the microbarom peak has virtually disappeared when winds exceed 2.0 m/s.

Most of the methods that have been used in the past to reduce wind noise have been based on a spatial averaging of the micropressure field over a limited area

surrounding the array element using pipe arrays with a large number of inlet ports or pipe arrays constructed from sections of porous hose (see, e.g., Daniels 1959; Noel and Whitaker 1991; Alcoverro 1998, 2008; Christie 1999, 2002; Christie et al. 2001; Hedlin et al. 2003; Alcoverro and Le Pichon 2005). Examples of pipe arrays that have been designed for use in the IMS infrasound network are illustrated in Fig. 2.17. A photograph of the pipe array installed at IS18 Qaanaaq in northern Greenland is shown in Fig. 2.18. The response of pipe arrays may exhibit resonances at higher frequencies corresponding to organ-pipe modes inside the various pipes that connect the inlet ports to the infrasound sensor (Hedlin and Berger 2001; Alcoverro 2008). These resonances will distort infrasonic signals with frequencies at or near the resonance frequency. However, this potentially serious problem can

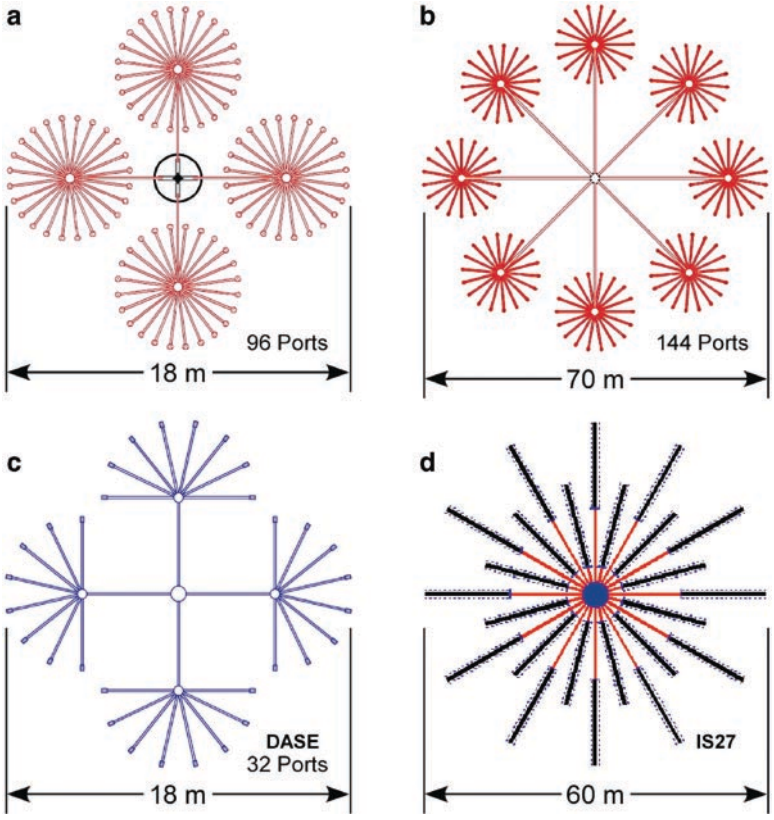

Fig. 2.17 Examples of some of the wind-noise-reducing systems used at stations in the IMS infrasound network. The rosette pipe array designs shown in (**a**) and (**b**) (Christie 1999; Christie et al. 2001) are used widely throughout the IMS infrasound network. The design illustrated in (**c**) (Alcoverro 1998) is also used at a number of IMS infrasound stations. The specialized design illustrated in (**d**) (Christie 2002) is used at IS27 Neumayer Base in Antarctica. This pipe array is constructed from sections of porous hose enclosed in perforated pipes and is designed to operate under snow cover in Arctic and Antarctic conditions

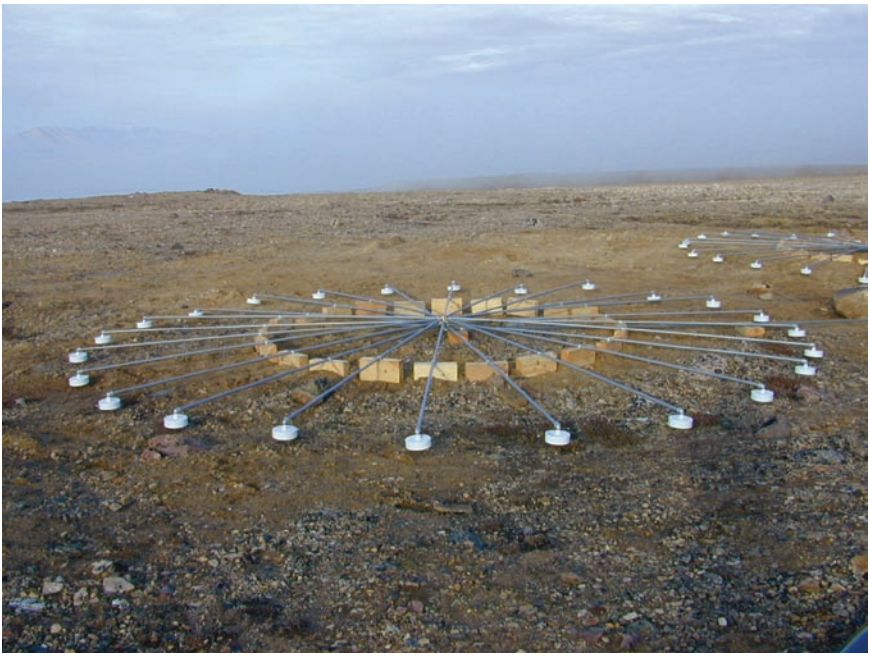

Fig. 2.18 View of one of the four rosettes in the 18-m diameter wind-noise-reducing pipe array installed at site H1 at IS18 Qaanaaq in northern Greenland

be avoided by using impedance matching capillaries in the design of the pipe arrays to ensure that reflections do not occur at the ends of the pipes (Hedlin 2001; Hedlin and Alcoverro 2005). The elimination of resonances may introduce other problems if the high impedance matching capillaries are blocked or partially blocked by moisture or dirt because the resonance-suppressing capillaries result in a much slower phase rotation, and variations in phase could lead to errors in the timing of signals (Alcoverro 2002, 2008). Since pipe arrays integrate the pressure variations at all inlet ports, higher frequency signals may be severely attenuated by large diameter pipe arrays (Hedlin et al. 2003; Alcoverro 2008). The degree of attenuation due to this effect is significant at frequencies above 2 Hz in the case of 70-m diameter pipe arrays, above 4 Hz in the case of 36-m pipe arrays and above 8 Hz in the case of 18-m diameter pipe arrays. Effective noise reduction has also been achieved (Zumberge et al. 2003; Walker et al. 2007) using a distributed OFIS to average pressure fluctuations along a line. The level of noise reduction achieved with an OFIS infrasound sensor in the primary monitoring passband appears to be comparable with the level of noise reduction that can be obtained using a conventional CTBTO rosette pipe array connected to a Chaparral Physics Model 5.1 microbarometer (see Fig. 2.16).

Almost every conceivable wind-noise-reducing pipe array design has been tested during the last 40 years (Christie 2006). It seems very unlikely that further refinements to pipe array design will lead to significant improvements in performance

since the size of the area that can be used, and the number of inlet ports has reached practical limits. The use of compact arrays consisting of a large number of individual sensors and digitizers combined with adaptive signal processing has been proposed as an enhanced noise-reducing technique (Talmadge et al. 2001; Bass and Shields 2004; Shields 2005). This procedure will undoubtedly provide some improvement, and it may eventually lead to a noise-reducing system that is better than existing pipe array systems.

The first attempt to use a wind barrier for infrasound noise reduction was reported by Grover (1971) who evaluated the use of small diameter perforated metal domes for wind-noise reduction at the Blacknest UKAEA infrasonic array. These wind shields provided only marginal noise reduction at high frequencies. Larger diameter wind barriers (5.5-m diameter × 2.0-m high constructed from spaced wooden slats) based on the original design pioneered by L. Liszka at the Swedish Institute of Space Physics in 1972 have been used more successfully to reduce wind noise and enhance signal-to-noise ratios (ReVelle, private communication 2000; Hedlin 2001; Hedlin and Berger 2001, Hedlin and Raspet 2003; Liszka 2008a). Hedlin and Berger (2001) showed that a wire mesh cover over the walls improves the performance of the original wind barriers designed by L. Liszka. However, while these noise-reducing barriers are effective at higher frequencies, they provide relatively little improvement at frequencies in the primary monitoring passband. Another method that has been proposed as a means for the reduction of wind-generated noise is the "sandbox" approach where the microbarometer inlet port is buried in a porous medium (Herrin et al. 2001b). Results using this method with the inlet port buried in a shallow gravel pit have been described briefly by Herrin et al. (2001a). Again, this method provides significant noise reduction at higher frequencies, but only a relatively small reduction at frequencies in the primary monitoring passband. Finally we note the important work of Bedard et al. (2004) who successfully used a porous wind fence with corrugations in conjunction with a porous hose pipe array to reduce wind noise during an investigation of higher frequency infrasound generated by tornadoes.

The development of a more effective wind-noise-reducing system in the form of a turbulence-reducing enclosure has recently been described by Christie et al. (2006, 2007), Christie (2006, 2007a, c), and Christie and Kennett (2007). This system appears to have the potential to effectively eliminate wind-generated background noise in the primary monitoring passband at many of the stations in the IMS infrasound monitoring network. This noise-reducing system is based on the use of a series of screens to mechanically extract energy from turbulent wind-generated eddies in the atmospheric boundary layer and transform these eddies into smaller scale eddies which generate micropressure fluctuations that lie outside the monitoring passband.

All tests on the development of an effective wind-noise-reducing screened enclosure were carried out at IS07 Warramunga located in the arid interior of the Northern Territory of Australia. As noted above, IMS infrasound station IS07 is subject to unacceptably high levels of wind-generated noise during the daytime with average daytime wind speeds in the range from about 2.7 to 4 m/s (as measured at a height of 2.0 m).

The wind noise conditions encountered at Warramunga are typical of wind noise conditions found at many unsheltered IMS infrasound stations. It is clear that the development of a noise-reducing system that is capable of reducing wind noise at IS07 to acceptable levels in the monitoring passband has the potential to resolve wind-noise problems at many IMS infrasound monitoring stations.

A number of different designs for screened enclosures have been tested at Warramunga. The performance of these enclosures were evaluated by comparing the results recorded with a small wind-noise-reducing pipe array and/or a single inlet port located inside an enclosure with simultaneously recorded results for an identical reference pipe array and/or reference single inlet port sited in an area located about 35 m from the enclosure. The location of the reference arrays and the single reference inlet port was chosen to minimize any contamination of the results by turbulence generated in the wake of the enclosure.

The initial open enclosure designs were based on the following criteria:

(a) The interaction of the enclosure with the ambient flow should not create unwanted turbulence. This was achieved by using porous walls, which allow part of the ambient wind to flow through the structure. The precise value of the porosity does not appear to be important provided the screened walls have porosity in the range from about 30 to 50%. Solid walls must not be used since this will generate further unwanted turbulence.
(b) The top of any wall in the structure should not be horizontal since the flow will fold over this boundary normal to the edge and create turbulence at lower levels behind the wall. Bedard et al. (2004) used solid vertical corrugations along the upper edge of their wind fence in an attempt to avoid this problem. The initial experiments at IS07 Warramunga were carried out using a modified version of this technique in which the vertical solid corrugations along the tops of the wall are replaced by deep porous serrations inclined away from the center of the enclosure in order to ensure that any residual turbulence created behind the serrations will have an upwards component which will carry these disturbances into the undisturbed flow aloft that is sweeping over the structure.

Two versions of an open multiple-walled turbulence-reducing enclosure, one with 1.6-m high walls and one with 2.4-m high walls, are illustrated schematically in Fig. 2.19. These wind-noise-reducing systems were evaluated by comparing measured background noise data recorded using a conventional 6-arm porous hose noise-reducing pipe array located on the surface inside the enclosure with data recorded simultaneously using an identical porous hose pipe array located in an open area outside the enclosure.

The 1.6 m high enclosure surrounding the porous hose pipe array improves the overall performance of this noise-reducing system by reducing noise levels at 1.0 Hz in modest winds by about an order of magnitude compared to the noise levels recorded on an identical reference porous hose pipe array located outside the enclosure. However, the efficiency of this enclosure decreases rapidly when wind speeds exceed 3.2 m/s. The results show that this enclosure would probably eliminate wind noise problems when used with existing pipe arrays at IMS infrasound

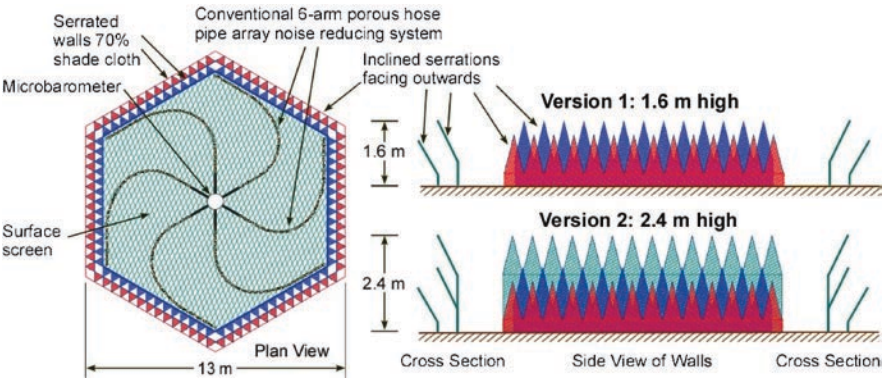

Fig. 2.19 Schematic diagram illustrating two versions of an open turbulence-reducing enclosure. The 1.6-m high enclosure has two porous walls with overlapping deep serrations inclined away from the center. Version 2 of this system is 2.4 m high with three rows of inclined overlapping serrations arranged on two porous walls. The plan view shows the layout of the conventional 6-arm porous hose array system that was used to evaluate the performance of these noise-reducing systems

stations located in sparse forests or other partially sheltered environments where the ambient winds at a height of 2.0 m are less than 3.0 m/s.

The performance of the open enclosure with 2.4-m high walls is significantly better than the performance of the open 1.6-m high enclosure. A detailed evaluation of the performance of the multiple-walled 2.4-m high open turbulence-reducing enclosure (Christie 2006) shows that this enclosure effectively improves the noise-reducing capability of a conventional pipe array by more than two orders of magnitude at 1.0 Hz in winds of up to 4.5 m/s. Since many IMS monitoring stations are subject to average wind speeds of less than 4 m/s, the use of open noise-reducing enclosures of this type in conjunction with existing pipe arrays can potentially resolve wind noise problems at these stations. However, the performance evaluation of this enclosure also shows that the efficiency of the 2.4-m high open enclosure decreases rapidly in ambient winds of more than about 4.5 m/s. Thus, this open enclosure will not resolve wind noise problems at stations located at sites with sustained winds of more than about 5 m/s.

A number of other designs for open turbulence-reducing enclosures are described in Christie (2007c). These include enclosures with 3.2-m high walls. The performance of these higher enclosures proved to be somewhat disappointing. The noise-reducing performance of these higher enclosures was found to be only marginally better than the performance of the 2.4-m high enclosure. This can be attributed to the fairly rapid increase in the ambient boundary layer winds with height above the surface. An examination of the flow inside the enclosure showed that the upper serrations on the top of the 3.2-m walls were interacting with the higher winds at this height, and this in turn resulted in the generation of further unwanted turbulence, which is mixed to lower levels inside the enclosure. The effect of this interaction with the higher winds aloft appears inside the enclosure as a low

intensity induced irregular swirling flow that circulates around the inside of the enclosure. While the overall performance was found to be slightly better than the 2.4-m high enclosure in winds of more than 4.5 m/s, the performance of the 3.2-m high enclosures was again observed to deteriorate rapidly when the ambient winds, as measured at a height of 2.0 m outside the enclosure, exceed about 5.5 m/s.

The design and construction of a significantly improved wind-noise-reducing enclosure is described in Christie et al. (2007) and Christie (2007c). This design is based on a critical examination of the performance of all of the enclosures noted above and a series of separate experiments. A noise survey carried out inside the 3.2-m high open enclosure showed that the maximum noise levels at 1.0 Hz occurred at the midway point between the center and the inside walls of the structure. Noise levels in the corners at the inside walls were slightly higher than the noise levels observed at the center of the enclosure. It was also found from separate experiments that noise levels inside the structure could be reduced using vertical porous radial baffles. However, the most important result from these evaluation experiments was the discovery that noise levels are reduced significantly when the enclosure is completely enclosed by a rigid porous roof.

A schematic illustration of the best version (Version 5B) of the turbulence-reducing enclosure is shown in Fig. 2.20. The principal features of this design are as follows:

(a) The enclosure is limited to a maximum height of 2.0 m to reduce the interaction of the structure with the more intense ambient winds above 2.0 m.
(b) All serrations that protrude into the higher wind regime above 2.0 m have been removed.

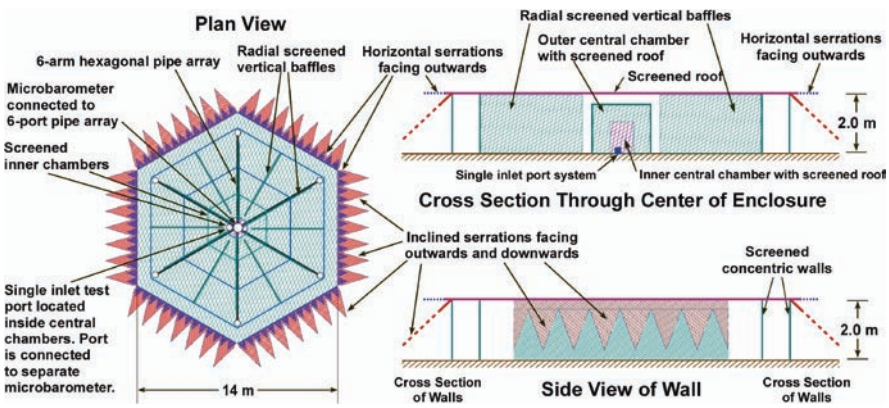

Fig. 2.20 Schematic diagram illustrating Version 5B of the turbulence-reducing enclosure. All higher serrations on the outer walls (see Fig. 2.19) have been replaced by horizontal outward facing serrations and larger scale outward facing and downward inclined serrations along the lower edge of an outer inclined screen attached to the upper edge of the outer wall. Vertical screens aligned radially are included to reduce circulations inside the structure. The enclosure is covered by a screened roof and central concentric enclosed screened chambers have been added to further reduce noise levels at the center of the enclosure

(c) The design includes a row of horizontal outward-facing screened serrations attached to the upper edge of the outer walls inline with the roof of the structure. Since these serrations are horizontal, they do not interact directly with the incoming flow. The purpose of these serrations is to limit the generation of turbulence in the partially blocked flow over the upper edge of the enclosure.
(d) Larger scale downward- and outward-facing serrations are installed along the lower edge of a downward inclined screen attached to the upper edge of the outer wall of the structure. The purpose of these serrations is to degrade incoming turbulent eddies before they reach the outer wall of the structure and also to further limit turbulent flow over the upper edge of the structure. The downward inclined screen attached to the upper edge of the outside of the enclosure also helps to force the blocked ambient airstream to flow around the enclosure, rather than over the roof of the enclosure.
(e) A rigid screened roof is installed over the entire structure.
(f) Vertical screened radial baffles are installed to reduce any circulations inside the enclosure.
(g) Two concentric fully enclosed chambers constructed from porous screens are installed at the center of the enclosure to further enhance noise reduction at the center of the enclosure.

The location of a single-inlet port system near the center of Version 5B of the enclosure and the configuration of a conventional 6-port pipe array are shown in Fig. 2.20. Both of these systems were used to evaluate the performance of this enclosure. These tests were carried out in ambient winds ranging from 0.0 m/s to 6.0 m/s by comparing noise levels recorded on both of the systems located inside the enclosure with simultaneously recorded noise levels recorded on a single-inlet port reference system and an identical 6-port reference pipe array system installed outside the enclosure. A survey of the wind-noise-reducing performance of this simplified, but highly effective, lower profile turbulence-reducing enclosure is presented in Fig. 2.21. The results recorded on the 6-inlet port reference pipe array system located outside the enclosure are not shown in Fig. 2.21 since they are nearly the same as those observed with the external single-port reference system except at longer periods where the noise levels recorded on the 6-port array are a little more than a factor of two lower than those observed on the single-inlet port system. All measurements illustrated in Fig. 2.21 were made with Chaparral Physics Model 5.1 microbarometer sensors to avoid any limitations on low noise observations imposed by the electronic noise floor of the sensor. Wind speed is measured outside the enclosure at a height of 2 m.

The results presented in Fig. 2.21 show that Version 5B of the noise-reducing system has excellent noise-reducing capability. We note that background noise levels recorded inside Version 5B of the enclosure at high frequencies with the single inlet port system are at or below the electronic noise floor of an MB2000 infrasonic microbarometer sensor in winds of up to at least 5.1 m/s. The results shown in Fig. 2.21 appear to indicate that the performance of the single inlet port system located inside the inner chambers near the center of the enclosure is almost

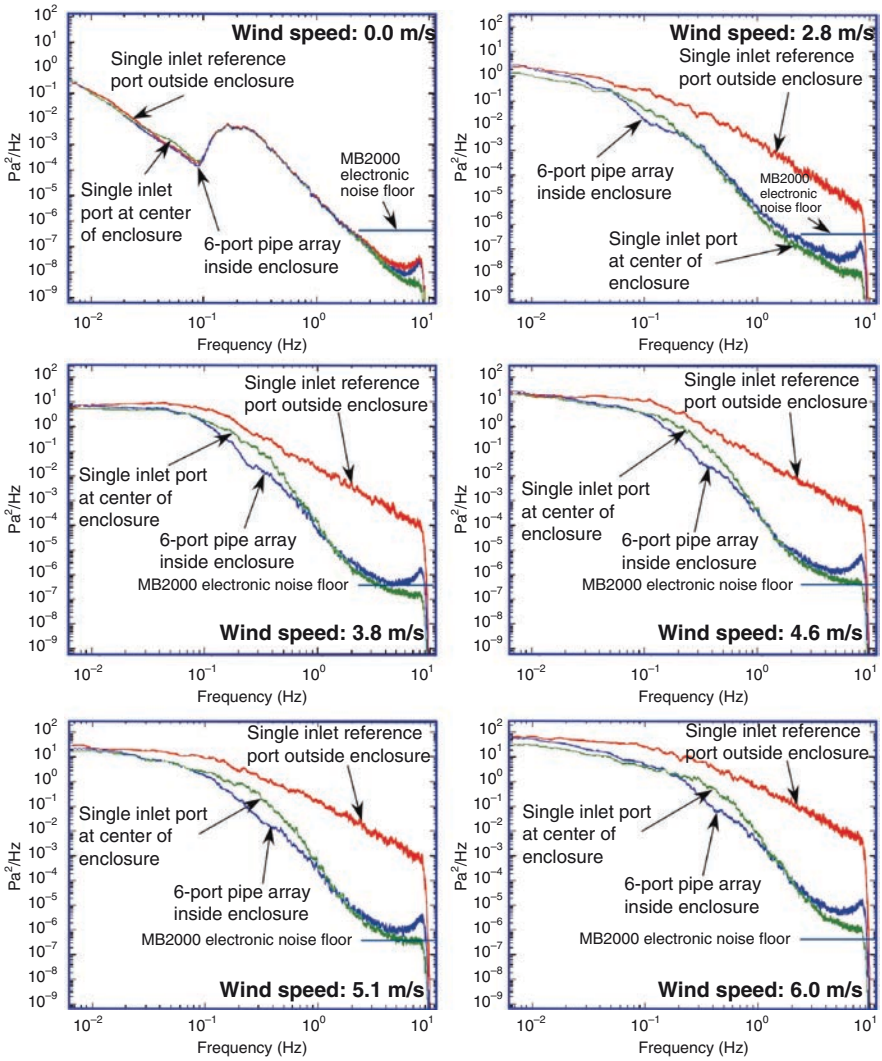

Fig. 2.21 Comparison of power spectral density estimates of infrasonic data recorded with a 6-port pipe array system (*light blue curve*) and a single inlet port system (*green curve*) located inside Version 5B of the turbulence-reducing enclosure with power spectral density estimates of background noise data recorded simultaneously on a single inlet reference port located outside the enclosure (*red curve*)

always better than the performance of the enclosed 6-port pipe array at frequencies above 1 Hz. However, the 6-port pipe array used in these tests did not have resonance-suppressing capillaries installed, and thus the high frequency results shown in Fig. 2.21 for the 6-port pipe array are dominated by the fundamental-mode resonance for this system. Subsequent observations made after the installation of

impedance-matching capillaries show that the degree of noise reduction with the enclosed 6-port array is better than that found for the single-port system at all frequencies. Both systems exhibit very good noise-reduction characteristics at 1.0 Hz in ambient winds of up to about 5 m/s. In this case, wind-generated noise is attenuated by up to 4 orders of magnitude. The performance in higher winds is also significantly better than the performance found for all earlier versions of the enclosure. Version 5B of the system is still very efficient at higher frequencies in ambient winds of 6.0 m/s, but the performance at lower frequencies is starting to diminish at this point.

The high degree of noise reduction achieved in the monitoring passband using the best version of the turbulence reducing enclosure (Fig. 2.20) can be seen in the comparison of waveforms shown in Fig. 2.22, which were recorded near noon in typical daytime wind conditions at IS07 Warramunga. The two upper traces in the

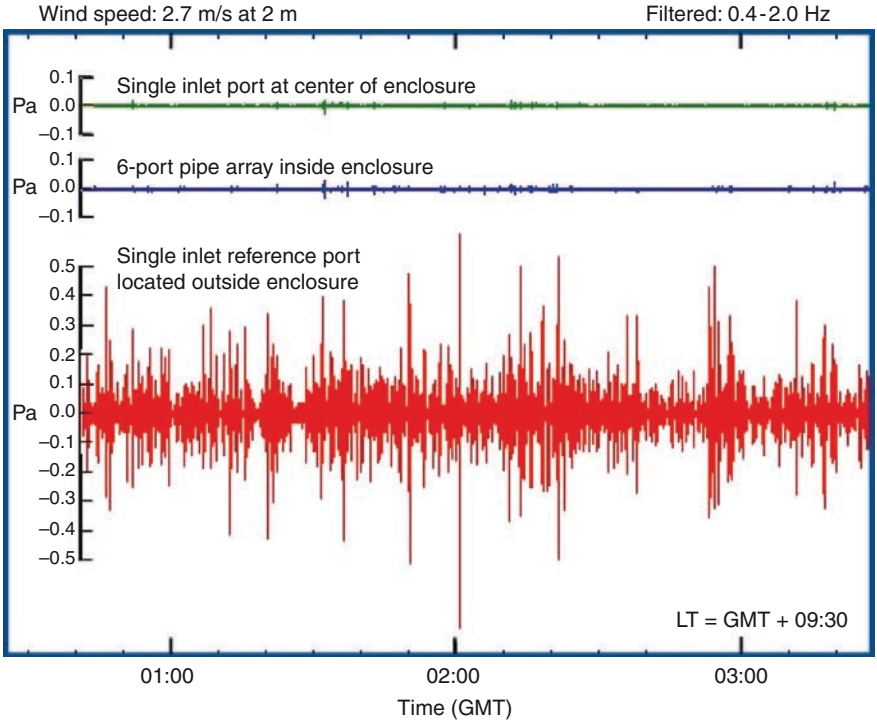

Fig. 2.22 Comparison of background noise in the monitoring passband recorded on a single inlet port system and a 6-port pipe array system located inside Version 5B of the turbulence-reducing enclosure with background noise recorded simultaneously on a single inlet reference port located outside the enclosure. The average wind speed measured outside the enclosure at a height of 2 m during these observations is 2.7 m/s. Note that all traces in this diagram are plotted on the same scale. The noise levels recorded inside the enclosure (*upper traces*) are much less than the noise levels recorded outside the enclosure (*bottom trace*). Some of the barely visible micropressure fluctuations in the top traces may be very weak infrasonic signals

diagram were recorded using the shielded single inlet port system and the 6-port pipe array located inside Version 5B of the enclosure. The bottom trace in this diagram was recorded simultaneously using a single inlet reference port system located outside the turbulence-reducing enclosure. It is clear from the results presented in Fig. 2.22 that wind-generated noise in the primary monitoring passband has been dramatically reduced by Version 5B of the turbulence-reducing enclosure.

In view of the wavelengths involved and the porosity of the screens used in the construction of the turbulence-reducing enclosures, it can be anticipated that these structures will be virtually transparent to infrasonic signals with frequencies in the monitoring passband. The influence of Version 5B of the enclosure on the morphology of recorded infrasound signals has been examined in detail for a wide variety of signals spanning the frequency range from about 0.03 to 6 Hz. In all cases, it was found that enclosures of this type have virtually no observable influence on the waveform of infrasonic waves. This is illustrated in Fig. 2.23 for a signal with frequencies in the primary monitoring passband and in Fig. 2.24 for a higher frequency signal with a dominant frequency of about 6 Hz. These signals were recorded simultaneously inside and outside the enclosure. In both cases the signals recorded inside and outside the enclosure are essentially the same with the same amplitudes and no indication of any phase shifts. Similar results have been found for lower frequency signals. We therefore conclude that the turbulence reducing enclosure is effectively transparent to infrasound and does not significantly attenuate or distort infrasonic signals at frequencies in the monitoring passband.

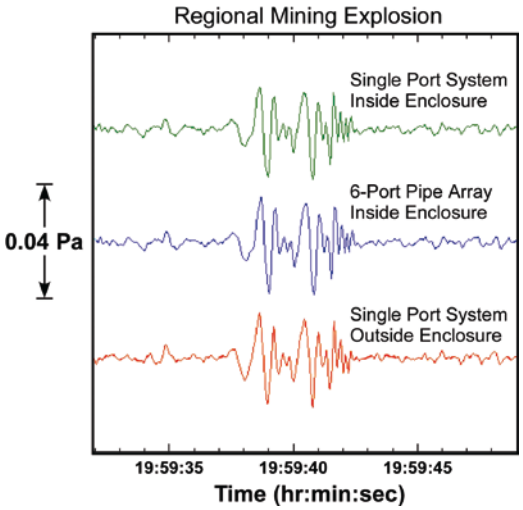

Fig. 2.23 Comparison of infrasonic signals recorded simultaneously on single port systems located inside and outside the turbulence-reducing enclosure and a 6-port pipe array system located inside the enclosure. The signal was generated by a small mining explosion. This comparison indicates that the closed turbulence-reducing enclosure illustrated in Fig. 2.20 does not significantly attenuate or distort infrasonic signals in the primary monitoring passband (0.4–1.2 Hz)

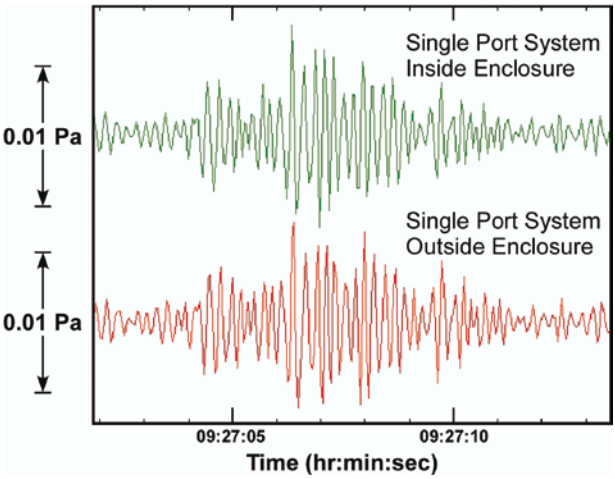

Fig. 2.24 Comparison of high frequency (~6 Hz) infrasonic signals recorded simultaneously on single port systems located inside and outside the turbulence-reducing enclosure. The source of this signal is unknown. This comparison indicates that the closed turbulence-reducing enclosure illustrated in Fig. 2.20 does not significantly attenuate or distort infrasonic signals at frequencies up to at least 6 Hz

The best version of the wind-noise-reducing enclosure illustrated in Fig. 2.20 provides very effective wind-noise reduction in the primary monitoring passband. The noise-reducing performance of this relatively small enclosure when used in conjunction with either a single inlet port or a 6-port pipe array is significantly better than the performance of existing IMS pipe arrays at higher frequencies. The results of a direct comparison of the performance of Version 5B of the enclosure with a standard 96-port 18-m diameter IMS pipe array are presented in Christie (2008). These results show that the degree of noise reduction obtained in winds of 4.3 m/s with a single inlet port located at the center of the enclosure is virtually the same at 1 Hz as the noise reduction obtained using the 96-port 18-m diameter pipe array. However, it is worth noting that the degree of noise reduction obtained with the enclosed single port system is much larger than that found for the 96-port 18-m diameter pipe array at higher frequencies. For example, the degree of noise reduction provided by the single enclosed port system is nearly two orders of magnitude larger than that found for the 18-m diameter pipe array at a frequency of about 5 Hz. The 96-port 18-m diameter pipe array provides slightly better noise reduction at frequencies below 1.0 Hz than the enclosed single port system. Other experimental comparisons have shown that a 12-m diameter 6-port pipe array located inside the enclosure provides almost exactly the same degree of noise reduction at frequencies below 1.0 Hz as a standard 96-port 18-m diameter IMS pipe array. As with the single enclosed port system, it is also found that the degree of noise reduction provided by the enclosed 12-m diameter 6-port system is nearly two orders of magnitude higher than that found for the standard 18-m diameter pipe array at high frequencies

Noise reduction with the enclosed 6-port pipe array is better than that found using only a single inlet port at the center of the enclosure since the 6-port pipe spatially averages the residual surface pressure fluctuations inside the enclosure. If the micropressure signals measured at each of the inlet ports in an N-port array are uncorrelated then the pipe array inside the enclosure should result in a decrease in the power spectral amplitudes by a factor of N over the values found for the single inlet port. The observed reduction in the case of the 6-port array is close to a factor of 6 which suggests that the residual micropressure fluctuations at the vertices inside Version 5B of the enclosure are uncorrelated. Most of the noise reduction seen in the longer period results shown in Fig. 2.21 for the 6-port pipe array is due to the turbulence-reducing properties of the enclosure. It can be anticipated that the degree of noise reduction illustrated in Fig. 2.21 for a 6-port pipe array would be much larger if the enclosure was adapted for use with an 18-m diameter 96-port pipe array. The performance of other types of noise-reducing systems, such as the OFIS, could also be improved by placing the system inside a turbulence-reducing enclosure.

It is worth noting that the performance of a turbulence-reducing enclosure improves as the diameter of the enclosure is increased. This can be seen for example by comparing the performance results for Ludwik Liszka's 5.5-m diameter, 2.0-m high wind fence (see, e.g., Hedlin and Berger 2001; Hedlin 2001) with the performance results for the 14-m diameter, 2.0-m high enclosure illustrated in Fig. 2.20. The 5.4-m diameter wind fence (with screen-covered walls) provides only a very small degree of wind noise reduction at frequencies below 1 Hz in winds of more than 3.0 m/s, and the noise level is reduced to only 1.0×10^{-4} Pa^2/Hz at about 9 Hz in winds in the range from 5.0 to 5.5 m/s. In contrast, the 14-m diameter enclosure (Version 5B) provides a reduction in wind noise at 1 Hz by more than two orders of magnitude in winds in the range from 2.8 to 6.0 m/s, and a reduction in noise level to less than 1.0×10^{-6} Pa^2/Hz at 9 Hz in all winds up to 6.0 m/s. In addition, Version 5B provides useful wind noise reduction down to frequencies below 0.1 Hz in high winds.

The results presented here indicate that wind-noise can be substantially reduced at many IMS infrasound stations by using turbulence-reducing enclosures similar to the enclosure shown in Fig. 2.20 to enhance the performance of existing pipe arrays. We note as well that the latest version of the enclosure can also be used at sites with modest winds of less than 3 m/s as an effective stand-alone noise-reducing system that does not require a pipe array. Version 5B of the turbulence-reducing enclosure is 14 m in diameter. This can be compared with existing pipe arrays at IMS infrasound stations that are usually 18 m in diameter. Since the performance of an enclosure at longer periods is governed by the diameter of the structure, it can be anticipated that turbulence-reducing enclosures that are 18-m in diameter will provide better noise suppression at longer periods (and also at higher frequencies) than the 14-m diameter enclosure shown in Fig. 2.20. Recommendations for the combined use of both wind-noise-reducing enclosures and IMS pipe arrays are given in Christie (2008).

In summary, the results described here and in Christie (2007c), Christie and Kennett (2007), and Christie et al. (2007) show that the performance of conventional wind-noise-reducing pipe arrays can be enhanced significantly by placing the pipe array inside a porous screened enclosure. Enclosures with two screened outer walls are more effective than enclosures with only a single screened outer wall. Additional screened walls do not significantly improve the performance of these enclosures when used with an enclosed pipe array. Noise levels observed at the center of the enclosure using a single inlet port system can, however, be reduced further at high frequencies by including a small enclosed screened chamber around the central inlet port system. Enclosures with a rigid screened roof are much more effective than open enclosures.

The following list provides some practical advice on the construction of turbulence-reducing enclosures for use at permanent infrasound monitoring stations:

(a) The roof and walls, including internal vertical baffles need to be constructed from porous screens. It is essential that the flow in and around the enclosure should not be completely blocked. All screens used in the construction of these enclosures should have a porosity between 30 and 50%. The precise value of the porosity does not appear to be important, but it should probably not be less than 30%. All screens should be as rigid as possible and should be completely stable to ultraviolet radiation.
(b) The screens should be supported on a rigid framework. This can be constructed at permanent stations using stainless-steel cables supported by galvanized fence posts with cement footings.
(c) The supporting structure should be as rigid as possible. Torsional and lateral mechanical resonances need to be suppressed. These resonances can be removed by using appropriate stainless-steel guys at each corner post. Guys should also be used to secure the enclosure in high wind environments.
(d) There should be no holes or gaps in the screening.

The results presented in this section indicate that wind-generated background noise can be substantially reduced in the primary monitoring passband at most IMS infrasound stations by using turbulence-reducing enclosures in conjunction with existing pipe arrays.

2.7 Concluding Remarks

The establishment of the IMS infrasound network is rapidly nearing completion. As of the end of 2008, 41 stations, or 68% of the stations in the IMS infrasound network have been certified and are transmitting data continuously to the IDC in Vienna, Austria. Work has also started on the construction of several other stations in the network. The IMS infrasound monitoring network is far larger and much more sensitive than any previously operated infrasound network.

There have been substantial improvements in infrasound technology during the last 10 years, and many of these improvements have been incorporated into IMS

infrasound monitoring stations. Network simulations of the performance of the IMS infrasound network indicate that all nuclear explosions with yields of 1 kT or more will be detected and located reliably. These simulations also suggest that the detection and location thresholds will be significantly less than 1 kT for explosions that occur over the continental land mass areas. It can be anticipated that recent advances in infrasound monitoring technology and signal processing will result in lower detection thresholds and more accurate location estimates.

2.8 Disclaimer

The views expressed herein are those of the authors and do not necessarily reflect the views of the CTBTO Preparatory Commission.

References

Alcoverro B (1998) Acoustic filters design and experimental results. Proceedings workshop on infrasound. DASE, Commissariat à l'Énergie, Bruyères-le-Châtel, France, 21–24 July 1998

Alcoverro B (2002) Frequency response of noise reducers. Proceedings infrasound technology workshop, De Bilt, The Netherlands, 28–31 October, 2002

Alcoverro B (2008) The design and performance of infrasound noise-reducing pipe arrays. Handbook of signal processing in acoustics, chap. 80, Springer, New York, pp 1473–1486

Alcoverro B, Le Pichon A (2005) Design and optimization of a noise reduction system for infrasonic measurements using elements with low acoustic impedance. J Acoust Soc Am 117:1717–1727

Alcoverro B, Martysevich P, Starovoit Y (2005) Mechanical sensitivity of microbarometers MB2000 (DASE, France) and Chaparral 5 (USA) to vertical and horizontal ground motion. Inframatics 9:1–10

Armstrong WT (1998) Comparison of infrasound correlation over differing array baselines. Proceedings of the 20th annual seismic research symposium, Santa Fe, New Mexico, 21–23 September 1998, pp 543–554

Bass HE, Shields FD (2004) The use of arrays of electronic sensors to separate infrasound from wind noise. Proceedings of the 26th seismic research review, Orlando, Florida, 21–23 September 2004, pp 601–607

Bedard Jr, AJ, Bartram BW, Keane AN, Welsh DC, Nishiyama RT (2004) The infrasound network (ISNET): background, design details, and display capability as an 88D adjunct tornado detection tool. Proceedings of the 22nd conference on severe local storms, Hyannis, MA, American Meteorological Society, Paper 1.1

Bhattacharyya J, Bass HA, Drob DP, Whitaker RW, ReVelle DO, Sandoval TD (2003) Description and analysis of infrasound and seismic signals recorded from the Watusi explosive experiment, September 2002. Proceedings of the 25th seismic research review, Tucson, Arizona, 23–25 September 2003, pp 587–596

Blanc E, Plantet JL (1998) Detection capability of the IMS infrasound network: a more realistic approach. Proceedings workshop on infrasound, Commissariat à l'Énergie Atomique, Bruyères-le-Châtel, France, 21–24 July 1998

Blandford RR (1997) Design of infrasonic arrays. Air Force Technical Applications Center Report, AFTAC-TR-97-013

Blandford RR (2000) Need for a small subarray at IMS infrasound stations – implications of shuttle and S. Pacific nuclear signals. Proceedings infrasound workshop, Passau, Germany, 2–6 October 2000

Blandford RR (2004) Optimal infrasound array design for 1 kt atmospheric explosions. Proceedings infrasound technology workshop, Hobart, Australia, 29 November–2 December 2004
Bowman JR, Baker GE, Bahavar M (2005) Ambient infrasound noise. Geophys Res Lett 32:L09803. doi:10.1029/2005GL022486
Bowman JR, Shields G, O'Brien MS (2007) Infrasound station ambient noise estimates and models: 2003–2006. Proceedings infrasound technology workshop, Tokyo, Japan, 13–16 November 2007
Brachet N, Brown D, Le Bras R, Mialle P, Coyne J (2010) Monitoring the earth's atmosphere with the global IMS infrasound network. This volume, pp. 73–114
Brown D, Collins C, Kennett B (2003) The Woomera infrasound and seismic experiment. Proceedings infrasound technology workshop, La Jolla, California, 27–30 October 2003
Campus P, Hoffmann T (2006) The IMS infrasound network: the challenge continues. Inframatics 13:26–28
Campus P, Demirovic E, Forbes A, Kramer A, Martysevich P, Stefanova S (2007). The IMS infrasound network: current status and future prospectives. Proceedings of the 2007 infrasound workshop, Tokyo, Japan, 13–16 November 2007
Cansi Y (1995) An automatic seismic event processing for detection and location: the PMCC method. Geophys Res Lett 22:1021–1024
Cansi Y, Le Pichon A (2008) Infrasound event detection using the progressive multi-channel correlation algorithm. Handbook of signal processing in acoustics, chap. 77. Springer, New York, pp 1425-1435
Capon J (1969) High resolution frequency wavenumber spectrum analysis. Proc IEEE 57:1408–1418
Christie DR (1989) Long nonlinear waves in the lower atmosphere. J Atmos Sci 46:1462–1491
Christie DR (1999) Wind-noise-reducing pipe arrays. Report IMS-IM-1999-1, International Monitoring System Division, Comprehensive Nuclear-Test-Ban Treaty Organization, Vienna, Austria, 22pp
Christie DR (2002) Wind-noise-reducing pipe arrays for IMS infrasound stations in Antarctica. Report IMS-IM-2002-1, International Monitoring System Division, Comprehensive Nuclear-Test-Ban Treaty Organization, Vienna, Austria, 10pp
Christie DR (2006) Wind noise reduction at infrasound monitoring stations. Proceedings infrasound technology workshop, Fairbanks, Alaska, 25–28 September 2006
Christie DR (2007a) Recent developments in infrasound monitoring technology: application to CTBT verification. CTBTO Spectrum, Issue 10, August 2007 pp 18–19, 24 (available online at http://www.ctbto.org)
Christie DR (2007b) Optimum array design for the detection of distant atmospheric explosions: influence of the spatial correlation of infrasonic signals. Proceedings infrasound technology workshop, Tokyo, Japan, 13–16 November 2007
Christie DR (2007c) Recent progress in wind noise reduction at infrasound monitoring stations. Proceedings infrasound technology workshop, Tokyo, Japan, 13–16 November 2007
Christie DR (2008) Wind-noise-reduction at IMS infrasound stations. Proceedings infrasound technology workshop, Bermuda, 3–7 November 2008
Christie DR, Kennett BLN (2007) Detection of nuclear explosions using infrasound techniques. Final Report AFRL-RV-HA-TR-2007-1151, Air Force Research Laboratory, Hanscom AFB, MA, Available from United States Technical Information Service
Christie DR, Vivas Veloso JA, Campus P, Bell M, Hoffmann T, Langlois A, Martysevich P, Demirovic E, Carvalho J (2001) Detection of atmospheric nuclear explosions: the infrasound component of the International Monitoring System. Kerntechnik 66:98–101
Christie DR, Kennett BLN, Tarlowski C (2005a) Detection of distant atmospheric explosions: Implications for the design of IMS infrasound array stations. Proceedings infrasound technology workshop, Papeete, Tahiti, 28 November –2 December 2005
Christie DR, Kennett BLN, Tarlowski C (2005b) Detection of regional and distant atmospheric explosions. Proceedings of the 27th seismic research review, Rancho Mirage, California, 20–22 September 2005, pp 817–827
Christie DR, Kennett BLN, Tarlowski C (2006) Detection of atmospheric explosions at IMS monitoring stations using infrasound techniques. Proceedings of the 28th seismic research review, Orlando, Florida, 19–21 September 2006, pp 882–892

Christie DR, Kennett BLN, Tarlowski C (2007) Advances in infrasound technology with application to nuclear explosion monitoring. Proceedings of the 29th monitoring research review, Denver, Colorado, 25–27 September 2007, pp 825–835

Clauter DA, Blandford RR (1997) Capability modeling of the proposed International Monitoring System 60-station infrasonic network. Proceedings infrasound workshop for CTBT monitoring, Santa Fe, New Mexico, 25–28 August 1997, p 225

Cook RK (1962) Strange sounds in the atmosphere. Part I. Sound 1:12–16

Cook RK, Bedard AJ Jr (1971) On the measurement of infrasound. Geophys J R astr Soc 26:5–11

Cordero F, Matheson H, Johnson DP (1957) A nonlinear instrument diaphragm. J Res Nat Bur Stand 58:333–337

de Groot-Hedlin CD, Hedlin MAH, Drob DP (2010) Atmospheric variability and infrasound monitoring. This volume, pp. 469–504

Daniels FB (1959) Noise-reducing line microphone for frequencies below 1 cps. J Acoust Soc Am 31:529–531

Evers LG, Haak HW (2010) The characteristics of infrasound, its propagation and some early history. This volume, pp. 3–26

Garcés M, McNamara S, Drob D, Brachet N (2006) A ray-based automatic infrasonic source location algorithm. Proceedings infrasound technology workshop, Fairbanks, Alaska, 25–28 September 2006

Gossard EE (1969) The effect of bandwidth on the interpretation of the cross-spectra of wave recordings from spatially separated sites. J Geophys Res 74:325–335

Gossard EE, Hooke WH (1975) Waves in the atmosphere: atmospheric infrasound and gravity waves, chap. 9, sect. 65. Elsevier, New York

Gossard EE, Sailors DB (1970) Dispersion bandwidth deduced from coherency of wave recordings from spatially separated sites. J Geophys Res 75:1324–1329

Green DN (2008) Assessing the detection capability of the International Monitoring System infrasound network. AWE Report 629/08, AWE Aldermaston, 91pp

Grover FH (1971) Experimental noise reducers for an active microbarograph array. Geophys J R astr Soc 26:41–52

Haubrich RA (1968) Array design. Bull Seis Soc Am 58:977–991

Hedlin MAH (2001) Recent experiments in infrasonic noise reduction: the search for that elusive, broadband, filter. Proceedings infrasound technology workshop, Kailua-Kona, Hawaii, 12–15 November 2001

Hedlin MAH, Alcoverro B (2005) The use of impedance matching capillaries for reducing resonance in rosette infrasonic spatial filters. J Acoust Soc Amer 117:1880–1888

Hedlin MAH, Berger J (2001) Evaluation of infrasonic noise reduction filters. Proceedings of the 23rd seismic research review, Jackson Hole, Wyoming, 2–5 October 2001, pp 121–130

Hedlin MAH, Raspet R (2003) Infrasonic wind-noise reduction by barriers and spatial filters. J Acoust Soc Am 114:1379–1386

Hedlin MAH, Alcoverro B, D'Spain G (2003) Evaluation of rosette infrasonic noise reducing spatial filters. J Acoust Soc Am 114:1807–1820

Hedlin M, Arrowsmith S, Berger J, Walker K, Zumberge M (2004) Experiments in infrasound at the Piñon Flat observatory in California. Proceedings infrasound technology workshop, Hobart, Australia, 29 November–2 December 2004

Herrin E, Golden P, Hedlin MAH (2001a) Investigation of wind noise reducing filters. Proceedings infrasound technology workshop, Kailua-Kona, Hawaii, 12–15 November 2001

Herrin E, Sorrells GG, Negaru P, Swanson JG, Golden P, Mulcahy C (2001b) Comparative evaluation of selected infrasound noise reduction methods. Proceedings of the 23rd seismic research review, Jackson Hole, Wyoming, 2–5 October 2001, pp 131-139

Kennett BLN, Brown DJ, Sambridge M, Tarlowski C (2003) Signal parameter estimation for sparse arrays. Bull Seism Soc Am 93:1765–1772

Le Pichon A, Vergoz J, Green D, Brachet N, Cerranna L, Evers L (2008) Ground-truth events as benchmark for assessing the infrasound detection capability. Proceedings infrasound technology workshop, Bermuda, 3–7 November 2008

Le Pichon A, Vergoz J, Blanc E, Guilbert J, Ceranna L, Evers L, Brachet N (2009) Assessing the performance of the International Monitoring System infrasound network: geographical coverage and temporal variabilities. J Geophys Res 114, D08112, doi:10.1029/2008JD010907

Liszka L (2008a) Infrasound: a summary of 35 years of research. IRF Scientific Report 291, Swedish Institute of Space Physics, Umeå, Sweden, 150pp

Mack H, Flinn EA (1971) Analysis of the spatial coherence of short-period acoustic-gravity waves in the atmosphere. Geophys J R astr Soc 26:255–269

McCormack D (2002) Towards characterization of infrasound signals. Proceedings infrasound technology workshop, De Bilt, The Netherlands, 28–31 October 2002

Mutschlecner JP (1998) Variation and uncertainty in infrasonic signals. Proceedings of the 20th seismic research symposium, Santa Fe, New Mexico, 21–23 September 1998, pp 605–611

Mutschlecner JP, Whitaker RW (1990) The correction of infrasound signals for upper atmospheric winds. Forth international symposium on long range sound propagation, NASA Conference Publication 3101

Mutschlecner JP, Whitaker RW, Auer LH (1999) An empirical study of infrasonic propagation. Los Alamos National Laboratory Technical Report LA-13620-MS

Mutschlecner JP, Whitaker RW (2010) Some atmospheric effects on infrasound signal amplitudes. This volume, pp. 449–468

National Academy of Sciences (2002) Technical issues related to the comprehensive nuclear test ban treaty. National Academy of Sciences Report, National Academy Press, Washington, DC, ISBN 0-309-08506-3

Noel SD, Whitaker RW (1991) Comparison of noise reduction systems. Los Alamos National Laboratory Technical Report LA-12003-MS

Norris D, Gibson R (2004) Validation studies using a TDPE propagation model and near real-time atmospheric specifications. Proceedings Infrasound Technology Workshop, Hobart, Australia, 29 November –2 December 2004

Ponceau D, Bosca L (2010) Specifications of low-noise broadband microbarometers. This volume, pp. 115–136

Rost S, Thomas C (2002) Array seismology: methods and applications. Rev Geophys 40, doi:10.1029/2000RG000100

Shields FD (2005) Low-frequency wind noise correlation in microphone arrays. J Acoust Soc Am 117:3489–3496

Talmadge CL, Shields D, Gilbert KE (2001) Characterization and suppression of wind noise using a large-scale infrasound sensor array. Proceedings infrasound technology workshop, Kailua-Kona, Hawaii, 12–15 November 2001

Walker K, Zumberge M, Berger J, Hedlin M, Matoza R, Durdevic P, Walsh P (2005) Progress in optical fiber infrasound sensor research. Proceedings infrasound technology workshop, Papeete, Tahiti, 28 November – December 2005

Walker K, Zumberge M, Berger J, Hedlin M (2006) Determining infrasound phase velocity direction with a three-arm OFIS. Proceedings of the 28th seismic research review, Orlando, Florida, 19–21 September 2006, pp 882–892

Walker KT, Zumberge M, Hedlin M, Berger J, Shearer P (2007) Resolving infrasound signals with arrays of optical fiber infrasound sensors (OFIS): low wind noise, superb back azimuth (and elevation angle) resolution, and a compact design. Proceedings infrasound technology workshop, Tokyo, Japan, 13–16 November 2007

Walker KT, Zumberge MA, Hedlin MAH, Shearer PM (2008) Methods for determining infrasound phase velocity direction with an array of line sensors. J Acoust Soc Am 124:2090–2099

Walker KT, Hedlin MAH (2010) A review of wind-noise reduction methodologies. This volume, pp. 137–180

Whitaker RW, Mutschlecner JP (2006) Revisiting yield, direction, and signal type. Proceedings of the 28th seismic research review, Orlando, Florida, 19–21 September 2006, 957–963

Whitaker RW, Mutschlecner JP (2008) A comparison of infrasound signals refracted from stratospheric and thermospheric altitudes. J Geophys Res 113, doi:10.1029/2007JD008852

Whitaker RW, Sandoval TD, Mutschlecner JP (2003) Recent infrasound analysis. Proceedings of the 25th seismic research review, Tucson, Arizona, 23–25 September 2003, pp 646–653

Wilson CR, Osborne D, Lawson K, Wilson I (2001) Installation of IS55 array at Windless Bight, Antarctica. Proceedings infrasound technology workshop, Kailua-Kona, Hawaii, 12–15 November 2001

Woodward R, Israelsson H, Bondár I, McLaughlin K, Bowman JR, Bass H (2005) Understanding wind-generated infrasound noise. Proceedings of the 27th seismic research review, Rancho Mirage, California, 20–22 September 2005, pp 866–875

Zumberge MA, Berger J, Hedlin MH, Husmann E, Nooner S, Hilt R, Widmer-Schnidrig R (2003) An optical fiber infrasound sensor: a new lower limit on atmospheric pressure noise between 1 and 10 Hz. J Acoust Soc Am 113:2474–2479

Chapter 3
Monitoring the Earth's Atmosphere with the Global IMS Infrasound Network

Nicolas Brachet, David Brown, Ronan Le Bras, Yves Cansi, Pierrick Mialle, and John Coyne

Disclaimer The views expressed herein are those of the authors and do not necessarily reflect the views of the CTBTO Preparatory Commission

The International Data Centre (IDC) of the Comprehensive Nuclear-Test Ban Treaty Organization (CTBTO) Preparatory Commission receives and processes in near real time data from a globally distributed network of seismic, hydroacoustic, infrasound, and radionuclide stations. In its final configuration, the IMS network will comprise 60 infrasound stations (Fig. 3.1). These stations are arrays of microbarometer sensors that are sensitive to acoustic pressure variations in the atmosphere in the frequency band between 0.02 and 4 Hz. The array configurations typically include 4–8 elements with apertures between 1 and 3 km (Christie et al. 2001; Sec Chap. 2).

Upon receipt at the IDC, the time series data from each seismic, hydroacoustic, and infrasound station are stored and referenced in the IDC database, organized in time blocks, and automatically processed (Fig. 3.2) at the station-level processing. The results of station processing serve as input to network level processing. Network processing results in automatic event locations, which are reported in bulletins known as Standard Event Lists (SELs). Three SELs are successively made at the IDC: SEL1 includes seismic and hydroacoustic data and is produced 1 h after real-time; SEL2 includes seismic, hydroacoustic, and infrasound data and is available 4 h after real-time; SEL3 also includes seismic, hydroacoustic, and infrasound data and is available 6 h after real-time. Seismic data from auxiliary seismic stations are requested after each SEL and are used to refine event locations in subsequent bulletins. The bulletin production deadlines are staggered to accommodate late arriving data and the signal propagation times for all technologies.

Specialized software has been developed to detect infrasound signals, categorize, and identify the most significant detections as phases (as opposed to noise), and subsequently group these phases to form automatic events. The SEL3 bulletin is reviewed

N. Brachet (✉)
CTBTO PTS/IDC, Vienna International Centre, P.O. Box 1200, 1400 Vienna, Austria

A. Le Pichon et al. (eds.), *Infrasound Monitoring for Atmospheric Studies,*
DOI 10.1007/978-1-4020-9508-5_3, © Springer Science+Business Media B.V. 2010

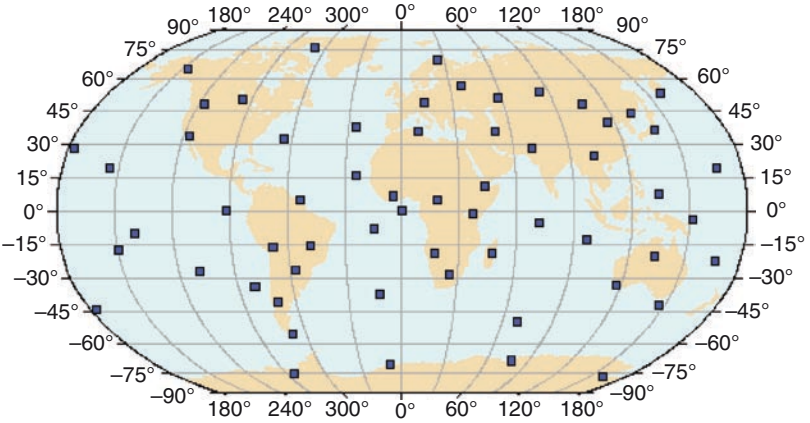

Fig. 3.1 The 60 infrasound stations of the IMS infrasound network

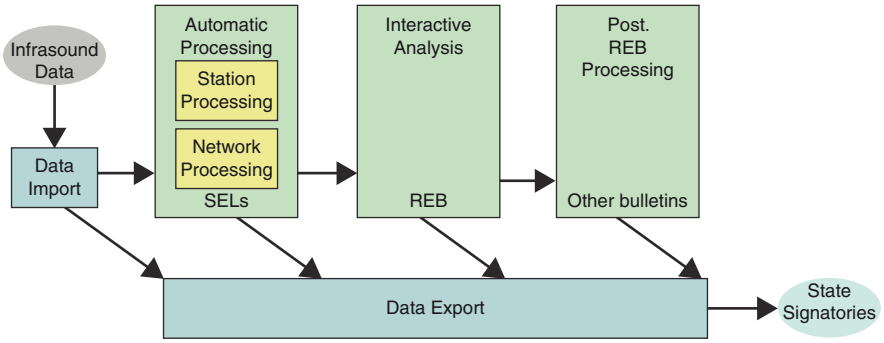

Fig. 3.2 Schematic overview of data processing at the International Data Centre (IDC)

by IDC analysts, who may correct the automatic results or add any late arriving data not available during SEL3 processing. The result of the interactive review process is the Reviewed Event Bulletin (REB), which is typically available in less than 10 days after real time. The creation of the REB triggers a postlocation processing pipeline, which includes processes such as surface wave magnitude estimation and event characterization. Additional bulletins are formed as a result of these processes. After entry into force of the CTBT, the delay for producing the REB is planned to be 2 days.

3.1 Station Processing

The infrasound data frames are received in near real time at the IDC and are organized in 30-min time intervals. Once sufficiently filled with data, these intervals are automatically scheduled for processing. The first stage of automatic

processing is "station processing," where the system attempts to detect signals and extracts their characteristics (e.g., back azimuth, horizontal trace velocity, frequency content, amplitude, and duration) at the individual stations.

3.1.1 Detection of Infrasound Signals

3.1.1.1 Detection Using Waveform Cross-Correlation

The infrasound data are processed using the Progressive Multichannel Correlation (PMCC) algorithm (Cansi 1995; Cansi and Klinger 1997). This array processing method was originally designed for seismic data and proved to be efficient for extracting low-amplitude coherent signals among noncoherent noise.

A temporal signal $s(t)$ can be represented in the frequency domain by its Fourier transform $S(f)=A(f)e^{i\varphi(f)}$, where $A(f)$ represents the spectral amplitude and $\varphi(f)$ is the phase. The background noise is characterized by a rapid variation in both amplitude and phase from one sensor to another, even if they are closer than one wavelength of signal. As opposed to incoherent noise, signal propagates through the array elements without any deformation. In case of a planar wave, the only signal difference observed at different sensors is a time delay, depending on the relative positions of the sensors, and the following formula can be written:

$$A_j(f) = A_i(f)\ \varphi_j(f) = \varphi_i(f) - \vec{k}\cdot(\vec{r_j} - \vec{r_i}), \tag{1}$$

where $\left|\vec{k}\right| = \frac{2\pi f}{c}$ is the magnitude of the wave number $\vec{k}$ which points in the direction of the plane wave's propagation

$\vec{r}$ the sensor position

c the local sound speed

Based on these observations, a signal-processing tool can be used to detect a signal present in the records $s_i(t)$ and $s_j(t)$. The correlation function is used to measure the time delay Δt_{ij} between two records. In case of a wave propagating without distortion, this delay is the same for all frequencies of the signals:

$$\Delta t_{ij} = \frac{1}{2\pi f}(\varphi_j(f) - \varphi_i(f)) \tag{2}$$

The time-delay calculation is not made in the frequency domain, but in the time domain using the correlation function (with values ranging from −1 to 1), which prevents any "wrapping" effect as it uses all possible frequencies. In a given time window, the correlation measures the similarity of the signals shifted in time. The maximum of the correlation function gives the time delay between the signals. This method enables a decision to be made on whether there is a signal in a set of simultaneous records, independently of any information on previous records.

For nonplanar arrays, the travel time differences due to elevation differences between sensors is not negligible for acoustic waves in the air and needs to be taken into account in the processing. At first order, the time delay between sensor j of coordinates (x,y,z) and the center of the array $(0,0,0)$ is:

$$\tau_j = \frac{-x\sin(\theta) - y\cos(\theta)}{V_T} + \frac{z\cos(i)}{c}, \tag{3}$$

where θ is the back azimuth of the wave front, V_T is the horizontal trace velocity, C is the local sound speed, and i is the incidence angle between the direction of the wave front and the vertical.

3.1.1.2 Consistency Used as a Threshold for Detection

To minimize ambiguity problems when correlating the records from sensors too far apart, the analysis is initialized on the smallest groups of three sensors.

The correlation function is used to calculate the propagation time of the wave between sensors i and j. For each subnetwork (i,j,k), the sum of time delays $\Delta t_{ij} + \Delta t_{jk} + \Delta t_{ki}$ is computed.

In case of a planar wave across the array, the closure relation $\Delta t_{ij} + \Delta t_{jk} + \Delta t_{ki} = 0$ should be obtained. In the presence of background noise, the measured delays are the result of random phase combinations and the closure relation given earlier is no longer valid.

The consistency C of the set of delays obtained using all sensors is then defined as a mean quadratic residual of the closure relation, and detection is declared if the consistency value is below a given threshold.

3.1.1.3 Progressiveness

To minimize errors in the calculation of the wave parameters, distant sensors are progressively added using a criterion based on a comparison between their distance to the subnetwork and the computed wavelength. This progressive use of distant sensors has two main effects: the removal of false detections, which could be due to correlated noise at the scale of the starting subarrays, and an improved estimate of the wave parameters by increasing the array aperture.

After being initialized with a small subnetwork of three sensors, to avoid ambiguity problems inherent in the correlation of signals from distant sensors, the wave parameters calculated on the initial subarrays are used when adding other sensors. (Fig. 3.3 presents an example of selected subarrays at the IS53 Fairbanks array.) During this process, a propagation of a planar wave front is assumed. The new measured time delay is given by the maximum of the correlation function, which is the closest to the one that has been estimated. Each elementary detection is therefore defined by several parameters such as the consistency value, the number of sensors participating in the detection, the frequency, the horizontal trace velocity, and the back azimuth.

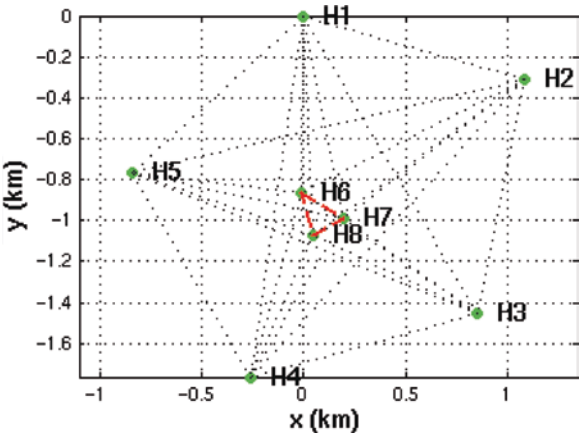

Fig. 3.3 Smallest subnetwork used to initiate progressive multichannel correlation (PMCC processing). Example of (H6,H7,H8) triplet at IS53 array

Such a detector is independent of the signal amplitude and uses only the intrinsic information of the recordings. As long as the closure relation is valid, the use of sensors increasingly further apart gives more precise wave parameters since the aperture of the network increases with each new sensor. The final solution is given by the largest subnetwork in terms of number of sensors.

3.1.1.4 Data Quality Control

Data quality control (QC) is a preprocessing function used by the automatic detection and feature extraction software (DFX) to ensure that subsequent detection processing runs under optimal conditions. The module searches and masks poor quality data waveforms, which are typically single point spikes, data dropouts, and extended sequences of repeated values. The poor quality data samples are repaired whenever possible or discarded before running the detection-processing algorithm.

- Single point spike refers to any isolated sample whose amplitude is anomalously different compared with the amplitudes of the neighboring samples. The signal amplitude differences $\delta_{ij}=s(j)-s(i)$ with $i=1..4$ and $j=2..5$ are measured at five consecutive samples, and the central sample is masked if the following conditions are satisfied: $\delta_{23}*\delta_{34}<0$ and $Min(|\delta_{23}|,|\delta_{34}|)>50*Max(|\delta_{12}|,|\delta_{45}|)$.
-

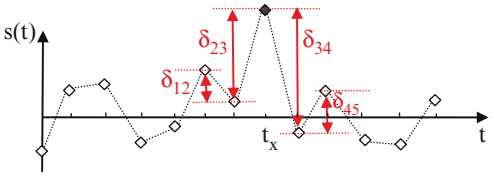

Example of a single point spike masked at time t_x

- Dropouts (missing data) and sequences of identical values, which are composed of four or more samples, are masked by DFX-QC.
- 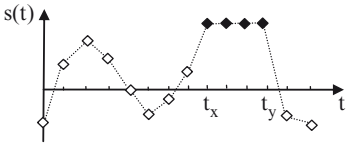

Example of a sequence of four constant values masked at time t_x and t_y

The data QC does not modify the contents of the original waveform data. The function creates a mask structure composed of 0 and 1 values, which characterizes the quality of each waveform data sample during the different stages of station processing.

DFX uses the mask information to repair the poor quality samples. When more than four consecutive samples are masked, the data segment is discarded, and a tapering is applied to attenuate the impact of the data gap on the processing. When fewer (i.e., less than four) samples are masked, a linear interpolation is used to repair the data. DFX-QC declares a data channel unusable if it contains a number of masked samples, which exceeds one third of the samples in the 30-min processing window.

The action of DFX-QC on infrasound data has intentionally been limited to unquestionable data problems (i.e., data gaps and very large spikes), to mitigate any possible bias in cross correlation results introduced by a local change of signal frequency content at repaired samples.

PMCC processing uses the information from data QC for each sliding time window. If the initial subarrays contain sensors with poor quality data, i.e., recordings with consecutive sequences of zeros, then the application automatically searches for alternative triplet combinations among the remaining valid sensors. The best subarrays are selected based on symmetry and aperture criteria. An equilateral triangle of small aperture is the best configuration.

3.1.1.5 Postprocessing: Building PMCC Families

The processing is performed consecutively in 11 frequency bands between 0.07 and 4.0 Hz, and in adjacent time windows covering the whole period of analysis. The duration of the processing window depends inversely on the frequency band. It varies from 60 s for the lowest frequency to 30 s for the highest frequencies (Fig. 3.4a). PMCC uses infinite impulse response filters, configured with Chebyshev filters of orders 2 and 3 and ripples varying between 0.05 and 0.1 (Fig. 3.4b).

This first processing stage produces elementary detections, so-called PMCC pixels, which satisfy the correlation and consistency criteria. The following step is the grouping of individual detection pixels that have similar signal attributes in time, frequency, back azimuth, and horizontal trace velocity. Groups of neighbor pixels constitute a “PMCC family” (see Fig. 3.5).

Only the largest and most stable families are preserved for subsequent processing and give rise to detection. Each detection is characterized by a back azimuth,

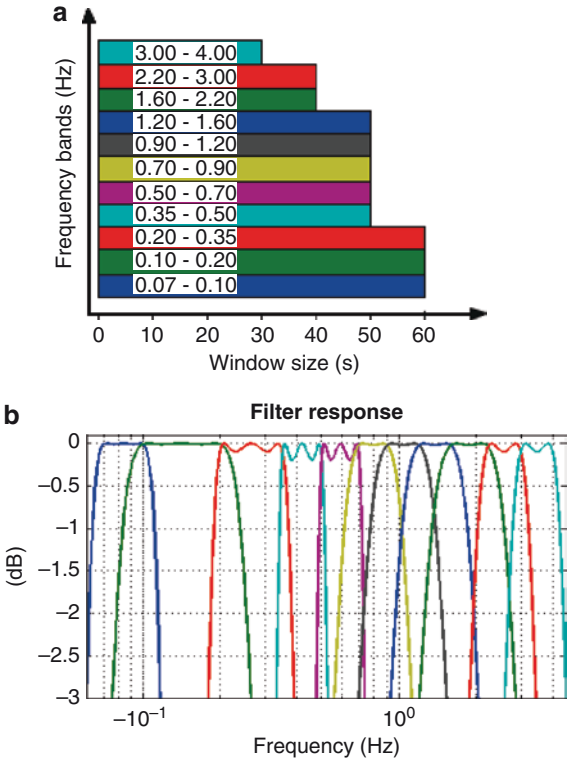

Fig. 3.4 (**a**) Example of a PMCC configuration, showing the duration of processing time windows as a function of frequency band (for 11 bands). (**b**) Response curves of the 11 Chebyshev filters used in the PMCC configuration

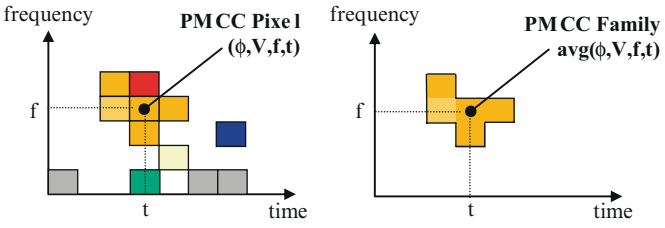

Fig. 3.5 PMCC family formed with pixels with similar back azimuth, horizontal trace velocity, frequency, and time characteristics

horizontal trace velocity, frequency content, consistency, and correlation values, which are the average values of all pixels in the family. Other attributes such as signal duration, Fisher statistics (Fstat), and number of pixels forming the family are also computed.

Several waves with different propagation parameters may coexist in the same time window but in different frequency bands. The PMCC time–frequency analysis permits each detected individual signal to be identified, providing detailed information, particularly on the evolution of the propagation parameters and the frequency content with time.

3.1.2 Feature Extraction of Infrasound Signals

Methods are being explored to enhance the current operational infrasound processing system at the IDC. The aim is to provide both CTBTO and the external users of IDC data products the facility with which to determine more accurate measures of the IMS infrasound network capability (Brown et al. 2008).

This goal is to be achieved through enhancements to the current automatic infrasound processing system that will

(i) Provide infrasound signal amplitudes
(ii) Provide a notion of the background noise characteristics at each station

3.1.2.1 Amplitude Determination

Three different amplitude measures are being determined for each infrasound detection. These are:

(i) Peak-to-peak amplitude
(ii) The maximum RMS amplitude
(iii) The maximum of the instantaneous amplitude as revealed by the analytic trace via the Hilbert transform

The peak-to-peak amplitude is used typically in empirical infrasound amplitude attenuation laws (Whitaker 1995; and Blanc et al. 1997), and so provides a useful addition to the IDC Bulletin. The RMS amplitude, however, is a running average taken over a user-specifiable time interval and is more representative of the average signal strength than the peak signal strength, as revealed by the peak-to-peak amplitude. The RMS amplitude will, for example, assign small-to-modest amplitudes to short-duration spurious signals that consist of a single cycle or oscillation since the neighboring uncorrelated data points will likely figure in the calculation and reduce the measure of the amplitude accordingly. The analytic trace amplitude is the formal definition of instantaneous wave amplitude and its features may be useful (Taner et al. 1979). Assume x(t) is an infrasonic waveform and H(t) its Hilbert Transform (see, e.g., (Bracewell 1986)). The analytic trace A(t) is written simply as the complex time series A(t) = x(t) + iH(t), where i is the unit complex number. The following identifications are then made:

(a) Instantaneous amplitude: $A(t) = \sqrt{\mathbf{x}^2(t) + \mathbf{H}^2(t)}$

(b) Instantaneous phase: $\theta(t) = \arctan\left(\dfrac{\mathbf{H}(t)}{\mathbf{x}(t)}\right)$

(c) Instantaneous frequency: $f(t) = \partial\theta(t) / \partial t$

Here, we take the maximum value of the instantaneous amplitude to be the measure of signal amplitude that is reported.

The analytic trace amplitude, for example, may find application in a future microbarom classifier following Olson's microbarom analysis (Olson 2000) whereas the RMS amplitude may find application in an infrasound detection "measure-of-significance" value.

As an example, amplitudes have been determined for an acoustic signal recorded at station IS26, located in Germany, from the Buncefield Oil Depot explosion in Hertfordshire, UK, in December 2005. The band-pass filtered data are shown in Fig. 3.6.

Figure 3.7 shows the time-aligned beam channel with the analytic trace (red) and a trace derived from the RMS amplitude channel (blue) assuming a 2-s sliding window, superimposed over the beam channel data.

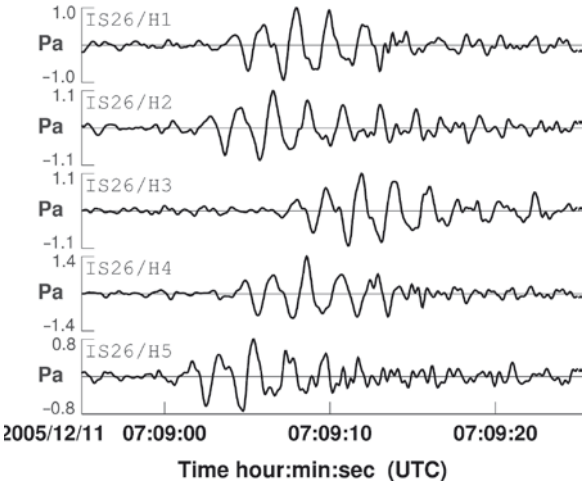

Fig. 3.6 Acoustic waveform recorded on station IS26, Germany from the December 2005 Buncefield oil depot explosion in Hertfordshire UK. Data have been band-pass filtered from 0.5 to 2.0 Hz

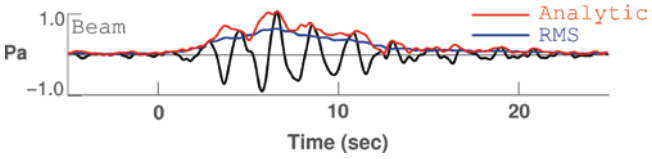

Fig. 3.7 Time aligned beam (*black*) with analytic trace (*red*) and RMS Trace (*blue*) superimposed. The RMS amplitude trace was determined with a 2-s sliding window

For this signal, the peak-to-peak amplitude was found to be 1.90 Pa, maximum analytic trace amplitude 1.04 Pa, and the maximum RMS amplitude 0.62 Pa. As one would expect the analytic trace amplitude agrees exactly with the zero-to-peak amplitude at the maximum point of the signal. As can be seen from the figure, the averaging nature of the RMS amplitude may be useful in discarding less significant signals.

3.1.2.2 Station Noise Characterization

Station ambient noise conditions are represented by the power spectral density (PSD), which provides a measure of the differential power contained in the signal at each frequency. Implicit in the use of the PSD is that both the mean and autocorrelation of the sampled waveform are time independent, which is assumed to hold approximately true in general as the propagating acoustic signals are considered to be short-lived transitory phenomena and will thus provide only a minor impact on the statistics.

Power spectral densities are determined for each station four times per day at hours 03:30, 09:30, 15:30, and 21:30 local station time. A 1-h data interval is used in each case and, except for minor departures, the PSD's are being determined using the processing schema outlined in (Bowman et al. 2005). In this scheme, the 1-h data interval is divided into 21 three-min intervals, each slightly overlapping the adjacent windows and an average PSD determined. A Hanning-type window function is applied to each 3-min interval to dampen spectral leakage and improve amplitude resolution.

Spectral information is recorded in a binary data file in two forms:

(a) The base 10 logarithm of the power spectral density for each sensor for each station. The sample rate is typically 20 samples-per-second, so with the 3,600 data samples in a 3-min window, a PSD using 1,800 frequency pickets is typically computed. As an example, the raw data for day 2007183 h 21:30 on station IS22 (Port Laguerre, New Caledonia) is shown in Fig. 3.8.
(b) Monthly averaged and smoothed logarithmic data, typically with 100 frequency pickets along the abscissa. The data are smoothed with a 6th order 11-point Savitzky–Golay filter. Also recorded is the standard deviation for each data set. The mean and standard deviation data are updated each time when the new data becomes available. The monthly data for stations IS07 (Warramunga, Australia) and IS22 (Port Laguerre, New Caledonia) for July 2007 are shown in Figs. 3.9 and 3.10, respectively.

To provide an indication of the daily variation, spectral data for a single sensor together with the mean μ and standard deviation σ are presented for station IS07 and IS22 for the month of July 2007 in Figs. 3.11 and 3.12, respectively.

The diurnal differences are quite obvious from these figures. Day-time convection has increased wind noise to such a level that the microbarom peak is generally not visible during the day. Interestingly, the night-time hours seem to exhibit most variation, but neither station exhibits a situation in which no microbaroms are present.

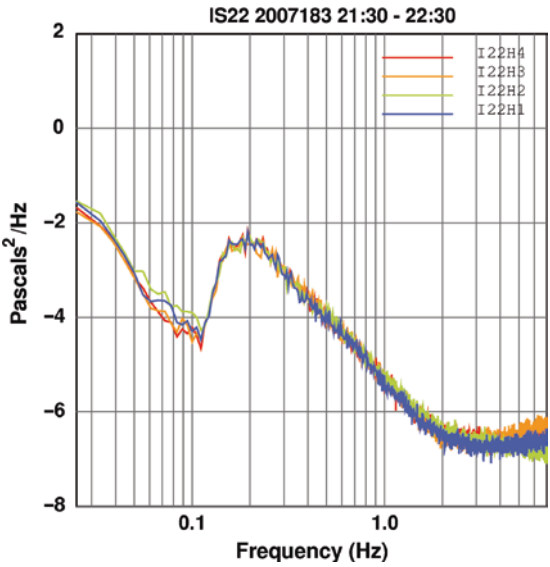

Fig. 3.8 Raw PSD data for station IS22 from 21:30 to 22:30 local time on day 2007183

Spectral data are being written to binary files with the intention that users with access to IDC external data products be able to access them using conventional methods.

3.1.3 Detection Categorization and Phase Identification

The categorization process examines the automatic infrasound detections and classifies them into "phase" or "noise" categories. Phases are detections that can be subsequently associated to others – seismic, infrasound, or hydroacoustic – in order to build events, whereas noise detections are not considered during network processing. The detection categorization strategy has been introduced to mitigate the risk of overwhelming the IDC automatic bulletin with false events caused by misassociation of detections.

The notion of phase and noise applied to infrasound data at the IDC is directly connected to the mission of the CTBTO. The overall mission of the organization is to monitor compliance with the nuclear test-ban treaty, and this is accomplished by routinely producing on a daily basis a bulletin of events that were observed by a global network of seismic, hydroacoustic, and infrasound stations. Given these requirements of a global bulletin of events that are recorded by multiple stations, there are a number of signals recorded at infrasound stations, which are not of interest for CTBT monitoring. Such signals include small local events that can only be observed by single IMS stations – e.g., related to human activity or natural phenomena such as ocean surf and thunderstorms – or multistation events originating from repetitive or long duration

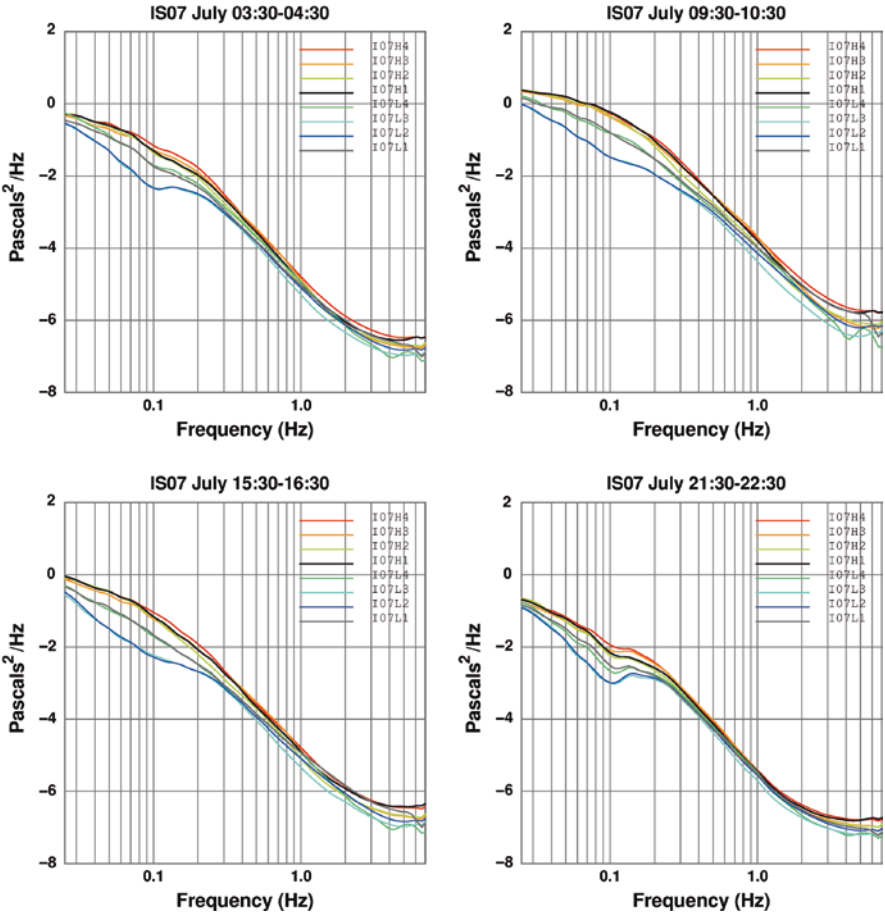

Fig. 3.9 The mean PSD data for station IS07 for the month of July 2007 taken at the four times: 03:30-04:30, 09:30-10:30, 15:30-16:30, and 21:30-22:30 local time. A 6th-order, 11-point Savitzky-Golay filter has been used to smooth the data

sources – e.g., offshore ocean swell, mountain associated waves, industrial activity, and nonexplosive volcanic eruptions. About 90% of the infrasound detections are identified as noise with the current IDC algorithm (Brachet 2004).

3.1.3.1 Categorization on Individual Detections

The categorization algorithm first examines the characteristics of individual infrasound detections based on frequency and horizontal trace velocity criteria. The test identifies as noise all detections with noninfrasonic horizontal trace velocities (values must be ranging between 290 and 450 m/s). Also all infrasound detections with only high-frequency contents (i.e., PMCC families only composed of pixels with

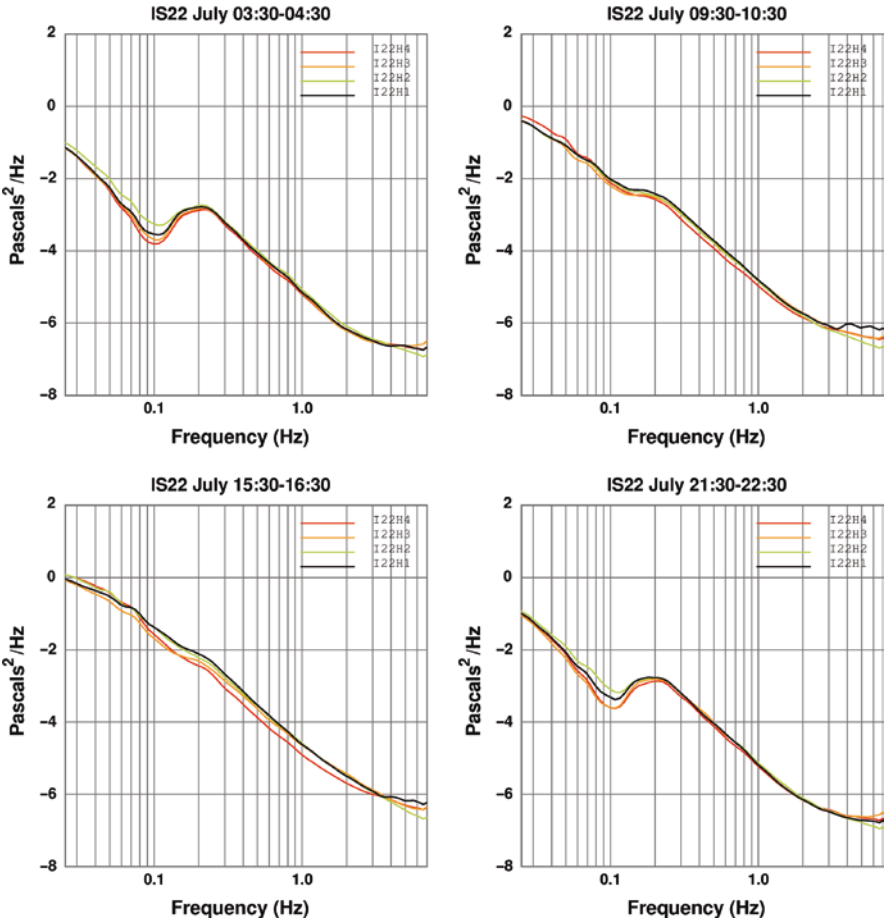

Fig. 3.10 The mean PSD data for station IS22 for the month of July 2007 taken at the four times: 03:30-04:30, 09:3-10:30, 15:30-16:30, and 21:30-22:30 local time. A 6th-order, 11-point Savitzky-Golay filter has been used to smooth the data

frequencies greater than 1.75 Hz), which typically characterize small and usually nonexplosive local infrasound sources, are systematically classified as noise.

Detections with seismic horizontal trace velocities (i.e., values greater than 2,900 m/s) are not considered during the categorization tests. They are systematically identified as phases and put into the phase identification process.

3.1.3.2 Categorization on Clusters of Detections (Meta-Families)

The categorization algorithm then performs a thorough analysis of the infrasound detections taking into account the station detection background in the few hours preceding the detection. This strategy determines whether the reviewed detection

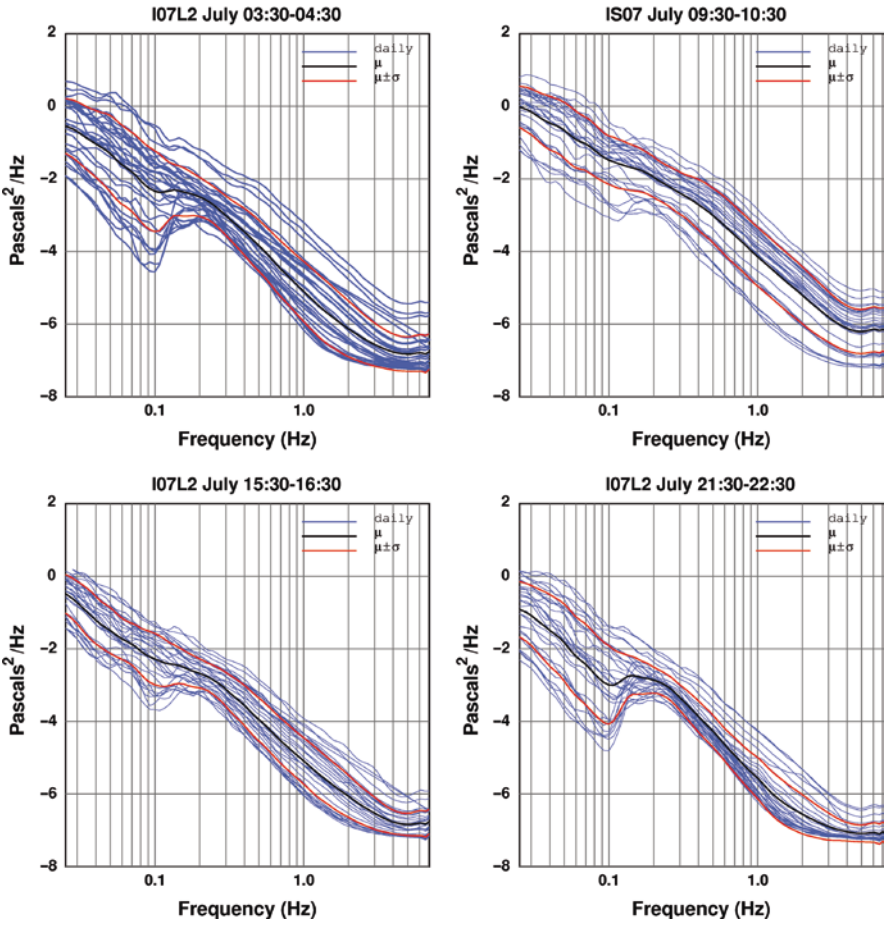

Fig. 3.11 Daily spectral data, the mean μ, and mean ± one-standard deviation σ for sensor I07L2 for all days in July 2007 for the hours 03:30-04:30, 09:30-10:30, 15:30-16:30, and 21:30-22:30 local time

belongs to an isolated infrasound signal or if it can be related to very long duration or repetitive sources that earlier started to produce similar detections.

The first step is to build metafamilies, which are clusters of detections with similar characteristics. Metafamilies are formed with detections that are close in time, back azimuth, and frequency, using the following tests, where *i* and *j* refer to distinct detections:

- abs $(t_j – (t_i + \text{dur}_i)) \leq 3{,}600$ s
- abs $(\text{az}_j – \text{az}_i) \leq \max(1, 2 * \max(\sigma\text{az}_i, \sigma\text{az}_j))$
- abs $(c\text{freq}_j – c\text{freq}_i) \leq \max(2 * \sigma\text{freq}_i, 0.5 * \text{BW}_i)$
- abs $(c\text{freq}_j – c\text{freq}_i) \leq \max(2 * \sigma\text{freq}_j, 0.5 * \text{BW}_j)$

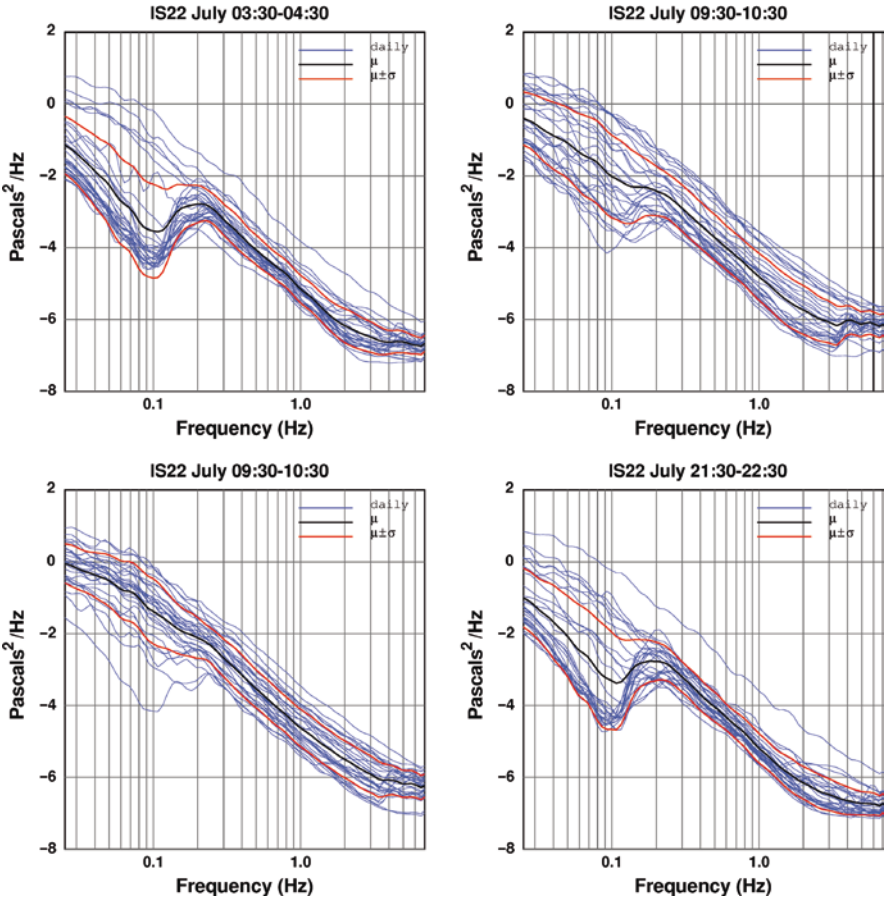

Fig. 3.12 Daily spectral data, the mean μ, and mean ± one-standard deviation σ for sensor I22H1 for all days in July 2007 for the hours 03:30-04:30, 09:30-10:30, 15:30-16:30, and 21:30-22:30 local time

$$\min\left(\frac{\mathrm{BW}_{\mathrm{overlap}}}{\mathrm{BW}_i}, \frac{\mathrm{BW}_{\mathrm{overlap}}}{\mathrm{BW}_j}\right) \geq 30\%$$

with t_i : detection time, dur_i : time duration of the detection family, $\mathrm{az}_i \pm \sigma\mathrm{az}_i$: detection back azimuth and standard deviation, $c\mathrm{freq}_j \pm \sigma\mathrm{freq}_i$: central frequency of PMCC family and standard deviation, BW_i : bandwidth of the detection, and $\mathrm{BW}_{\mathrm{overlap}}$: overlapping bandwidth for the detections i and j

Long duration, short duration, and repetitive series of detection metafamilies are identified as noise. However, some restrictions are applied on the first detection in the cluster. The first detection cannot be tagged as noise to keep a trace of it, and

then, it becomes possible to build an event with the beginning of detection metafamily. Another criterion based on energy (using *F*-statistics values) is also used to avoid any atypical detection in a cluster being categorized as noise. The clusters are defined according to the following criteria:
Long-duration clusters:

- Detection is not the first in a cluster.
- Cluster duration is longer than 3,600 s.
- $\left|\text{Fstat}_i - \overline{\text{Fstat}}\right| \leq 3 \times \sigma_{\text{Fstat}}$,

where Fstat_i is Fisher statistics of detection *i*, $|\text{Fstat}| \pm \sigma_{\text{Fstat}}$ is the mean and standard deviation of *F*-statistics values of all detections included in the cluster.
Short duration and small clusters:

- Cluster duration does not exceed 50 s.
- The total number of pixels in the cluster is below 15.

Repetitive clusters:

- Detection is not the first in a cluster.
- Cluster is comprised of more than five detections.
- $\left|\text{Fstat}_i - \overline{\text{Fstat}}\right| \leq 3 \times \sigma_{\text{Fstat}}$

To illustrate the action of the IDC detection categorization algorithm, Fig. 3.13 shows two views of 1-week detection list (period March 3–9, 2008) for the station IS31, Kazakhstan. The automatic infrasound detections are represented in seven (time and frequency) plots of 24 h duration with frequency bands ranging from 0.1 to 4 Hz. The back azimuths of the detections are displayed with a color scale, which is referenced at the bottom of each side. Figure 3.13(a) shows all PMCC detections for this time period, including long-duration noise signals caused by human activity – oil flares at a back azimuth of 180° – and microbaroms at a back azimuth of 300°. Figure 3.13(b) shows a "cleaned view" of the nonnoise detections remaining after applying the detection characterization and phase-identification algorithm.

3.1.3.3 Phase Identification

The phase-identification process, which follows the detection categorization, assigns phase names to detections. Detections that have been identified as noise during the categorization process are named "N." Seismic detections with speeds more than 5,700 m/s are interpreted as P-type signals, and named "IPx." Seismic detections with speeds between 2,900 and 5,700 m/s are named "ISx." All other detections are interpreted as infrasound arrivals and are named "I."

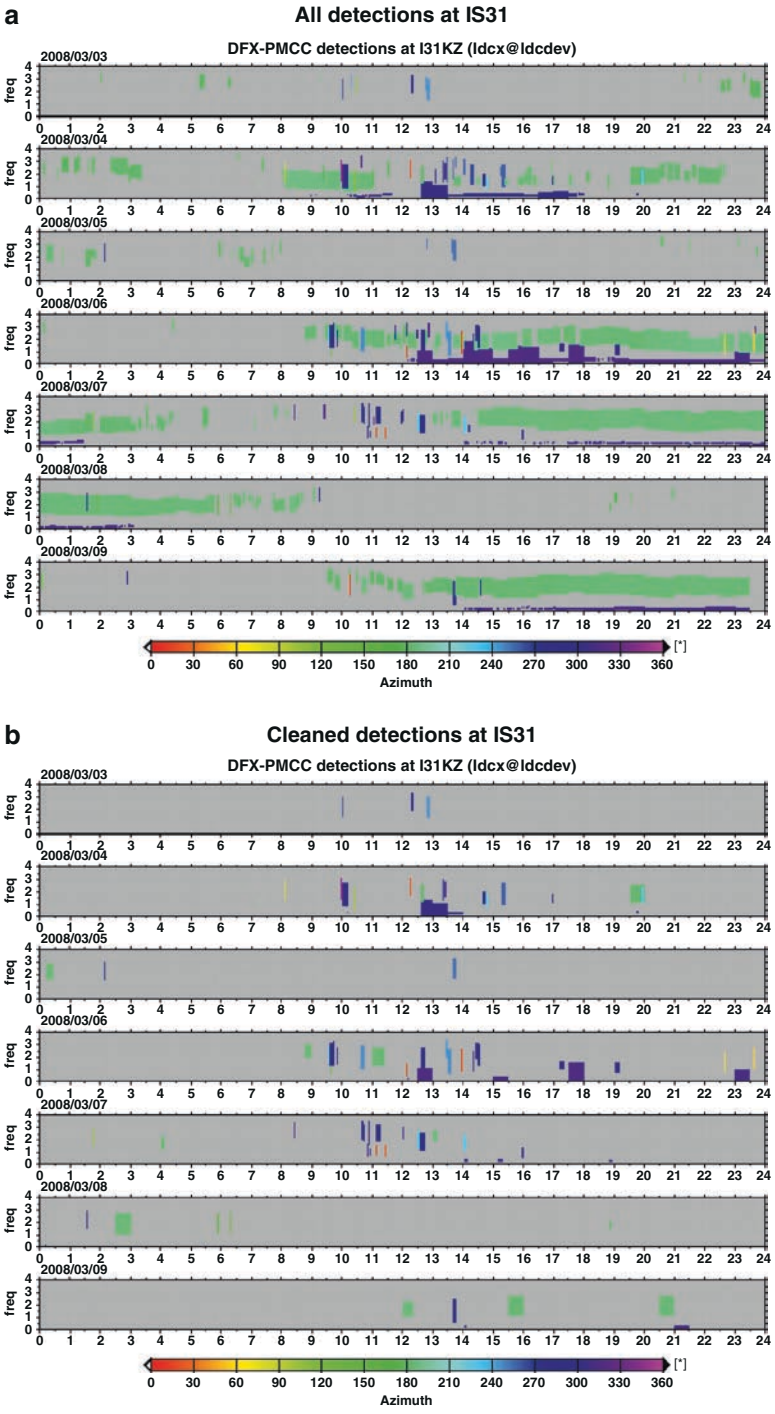

Fig. 3.13 Example of the IDC detection list (**a**) before detection characterization and (**b**) after detection characterization during the period 3–6 March 2008

3.2 Network Processing

Station processing is followed by "network processing," which combines all relevant nonnoise infrasound detections along with detections from seismic and hydroacoustic technologies and attempts to build and locate events from these associations.

3.2.1 Building Candidate Seed Events

Network processing is the IDC automatic subsystem that associates the signal detections at individual IMS stations with events and provides a location and magnitude of these events (Le Bras and Sereno 1996; Le Bras et al. 1999). The location algorithm used at the IDC is an iterative nonlinear least-squares inversion originally developed by Jordan and Sverdrup (1981), which was later modified by Bratt and Bache 1988) to include azimuth and slowness observations.

The association of arrivals is done with a grid search of hypothetical seed events (Fig. 3.14). The grid cells are quasi uniformly distributed at the surface of the Earth and also cover depth zones in geographic areas known for having deep seismicity, as determined by historical seismicity.

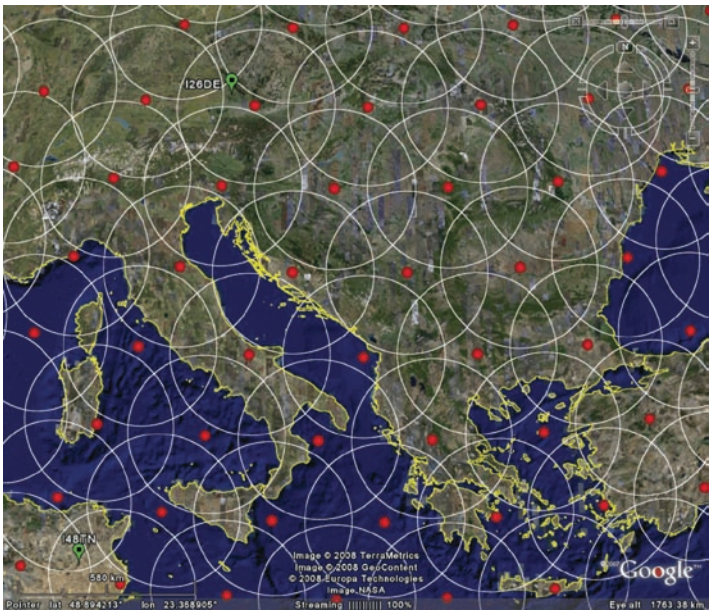

Fig. 3.14 Example of surface grid cells (©Google) used by IDC network processing in South East Europe. Each grid cell is 236 km in radius. There are more than 7,000 cells covering the globe

The arrival detected at the nearest station to the grid cell is called a driver provided the observed slowness matches with the predicted value ± a standard deviation (Fig. 3.15). Contrary to seismic, infrasound slowness is independent of the range between source and receiver, and it is currently calculated as the inverse of the 300 m/s celerity, and the slowness threshold around each grid cell is 45 s/degrees. The driver is used to predict time at the other IMS stations. Stations that are consistent with the driver are added to the seed event (Fig. 3.16).

Once associations have been formed, a location is performed on the association sets. Only association sets surviving this step are further considered. After the location step, some arrivals may be found associated to multiple events, and conflicts need to be resolved by selecting the best quality events (i.e., based on the number of associated defined arrivals, the size of the error ellipse, the distance to the nearest station, and the probability of detection).

3.2.2 *Fusion Between Different Waveform Technologies: Seismic, Infrasound, and Hydroacoustic*

In the current configuration, automatic seed events are created with arrivals detected by stations of the same technology – all seismic, all infrasound, or all hydroacoustic. The association with other technologies is done, for each seed event, by prediction of phase characteristics at other stations: detections that match the

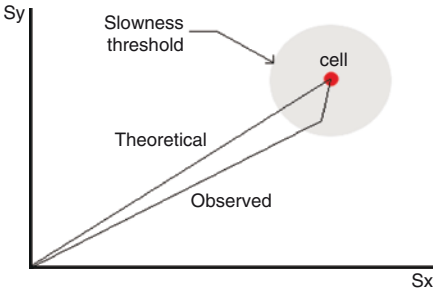

Fig. 3.15 A driver is defined at the closest station to the grid cell if the arrival time and slowness vector match with the predicted values

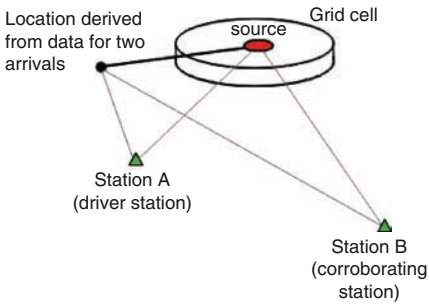

Fig. 3.16 Corroborating stations that are consistent with the driver are added to the seed event

expected time, azimuth, and slowness criteria within certain tolerance thresholds are added to the event and may contribute to the location solution. In contrast with seismic and hydroacoustic, infrasound slowness is not considered during the association process.

The arrival quality test that is applied during this iterative process of phase association and seed event location is based on a comparison of arrival residuals with modeling errors. For infrasound, azimuth and time entities are closely related: an azimuth error $\delta\theta$ in the event epicenter determination at a range of R_k generates a time-equivalent error δT_{Az}, which can be estimated based on geometrical considerations.

$$\delta T_{\mathrm{Az}} = \frac{R_k \delta\theta}{c} \sin(\delta\theta), \tag{4}$$

where c is the infrasound wave celerity (ground speed).

The association process rejects all infrasound data that do not verify the following time relation:

Arrival residuals > tolerance errors

$$\Leftrightarrow \quad \Delta T_{\mathrm{Azimuth}} + \Delta T_{\mathrm{time}} > \delta T_{\mathrm{Azmodel}} + \delta T_{\mathrm{tmodel}} + \delta T_{\mathrm{time}}, \tag{5}$$

where

$$\Delta T_{\mathrm{Azimuth}} = \frac{R_k \Delta\theta}{c} \sin(\Delta\theta) \tag{6}$$

is the time error (in s) associated to the azimuth residual $\Delta\theta$ (in rad), for a source located at a range R_k (in km), and for a celerity c (in km/s). ΔT_{time} is the time residual of the associated PMCC detection

$$\delta T_{\mathrm{Azmodel}} = \frac{R_k \delta\theta}{c} \sin(\delta\theta) \tag{7}$$

is the time error (in s) associated to the azimuth error $\delta\theta$. ($\delta\theta$ includes both measurement and modeling errors, its value is fixed to 5°)

$$\delta T_{\mathrm{tmodel}} = \alpha \times 720 \times \sqrt{\frac{R_{\mathrm{d}}}{90}} + \beta \tag{8}$$

is the travel time modeling error (in s) for a source located at a range R_{d} (in degree). α and β are corrective parameters that reflect three dominating infrasound propagation regimes (cf. Sect. 3.2.4). δT_{time} is the time error associated to the PMCC detection (value fixed to 10 s.)

The candidate events resulting from the automatic association process are examined and validated using an acceptance test based on weighted count of defining phases: the weights for each time, azimuth, and slowness observation at the associated stations are summed up (details of the weights are provided in Table 3.1). Events with a minimum total weight of 3.55 are saved in the automatic SEL

Table 3.1 Weights applied to each type of phase and technology in the acceptance criteria for building IDC automatic events

Station type	Phase type	Time weight	Azimuth weight	Slowness weight	Total weight
Seismic array	P, Pn, Pg, PKP, PKPab, PKPbc, PKiKP	1	0.4	0.4	1.8
	pP, sP, pPKP, pPKPbc, PcP, ScP, SKP, SKPbc PP	0.4	0	0	0.4
	Sn, Lg	0.7	0.4	0.4	1.5
	S	0.7	0	0	0.7
Seismic 3C stations	P, Pn, Pg, PKP, PKPab, PKPbc, PKiKP	1	0.2	0.2	1.4
	pP, sP, pPKP, pPKPbc, PcP, ScP, SKP, SKPbc PP	0.4	0	0	0.4
	Sn, Lg, S	0.7	0	0	0.7
Hydroacoustic	H	1.54	0	0	1.54
Infrasound array	I	0.8	1	0	1.8

bulletins. Given these criteria, infrasound arrivals observed on two arrays are sufficient to build an automatic event.

3.2.3 Limiting the Number of False Infrasound Associations

The number of candidate infrasound events grows exponentially with the number of operating IMS infrasound stations. The IDC has expended some effort to decrease the number of false associations with infrasound arrivals. The introduction of the detection categorization strategy (previously described in station processing) has significantly lowered the number of automatic events with infrasound phases to a more manageable level.

In addition, some criteria have been implemented in IDC network processing to lower the number of false associations of infrasound data:

- The distance for associating infrasound arrivals is limited to 60° from the source
- The range of the first detecting infrasound station should not exceed 40°
- The infrasound events should contain at least one significant infrasound detection (i.e., central frequency between 0.4 and 2.5 Hz; PMCC family of 20 pixels or more; PMCC family with duration above 120s), or should contain at least one seismic phase picked on an infrasound station.
- Small infrasound detections (i.e., PMCC families of 11 pixels or less) are discarded during the weighted count test.
- The frequency–distance attenuation curve obtained empirically with IDC infrasound reference events (IRED) (Fig. 3.17) significantly reduces the false associations of high-frequency detections for large distance events. A first empirical relation has been established using 100 IRED (Brachet et al. 2006):

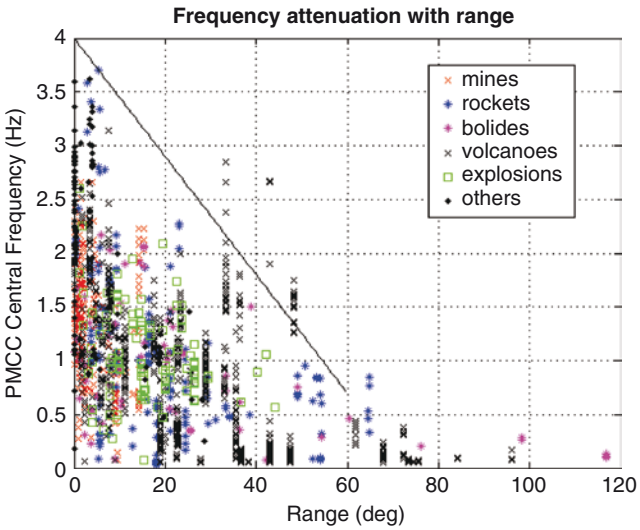

Fig. 3.17 Frequency of the detections contributing to 480 infrasound reference events (IRED). The black curve represents the initial (established with 100 IRED events) empirical frequency–distance attenuation curve ($F>4–0.055*\Delta$) used by the IDC to reject the false association of an infrasound detection to an event. The plot shows that the original curve can still be used as a criterion in the network processing, but the relation could probably be refined to better fit the observed reference events

Reject infrasound association if $F>4.0–0.055*\Delta$ With : $F=$ central frequency of PMCC infrasound detection (in Hz) and Δ = distance from source to station (in degrees). The criterion halved the number of false associations events created with infrasound data.

3.2.4 Atmospheric Modeling

The association of infrasound automatic detections is reliant on achieving good detector performance and a realistic modeling of the wave propagation in the atmosphere. The same set of infrasound travel-time tables is used by the association and location algorithms. At the IDC, the modeling of infrasound wave propagation is currently done using three constant 330, 295, and 303 m/s celerity models, which are range dependent (Fig. 3.18), and no azimuth correction is due to atmospheric winds. This choice for a simplification of the infrasound wave-propagation problem is justified by the currently limited knowledge of the scientific community in this domain and the CPU and time constraints imposed by the IDC real-time operational environment.

Using a simplified celerity model must be seen as an initial step for the IDC, which simplifies the implementation in an automatic system and allows the

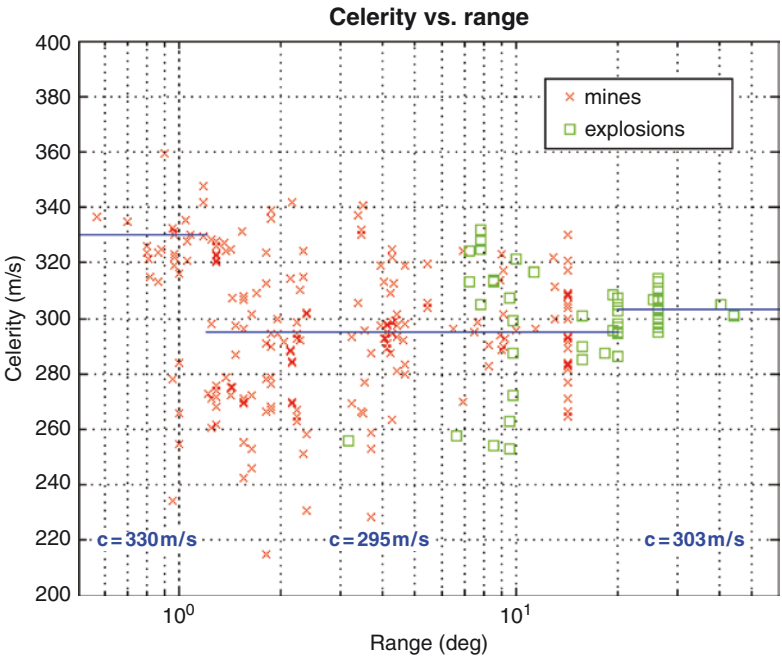

Fig. 3.18 Celerity of the IDC IRED having well constrained location and origin time (i.e., 270 selected mine blasts and chemical explosions). The horizontal *blue line* shows the 330, 295 and 303 m/s celerity values used by the IDC automatic processing

production of fast results during the phase association and event location processes. However, this model is not appropriate for accurately describing the complex propagation of infrasound waves in the atmosphere, and it does not reflect the diurnal and seasonal variations of the atmosphere. The infrasound travel-time tables have been empirically established from a ground truth data set of 270 mine blasts and chemical explosions recorded by the IMS network. 330 m/s is used for short range tropospheric infrasound wave propagation (i.e., range smaller than 1.2°). 295 m/s celerity is used for intermediate range (i.e., range between 1.2 and 20°) where both stratospheric and thermospheric returns may be observed. 303m/s is an average celerity value which fits relatively well with the fastest waves propagating over large distances in the stratosphere (i.e., range larger than 20°).

Travel time modeling error δT_{tmodel} (in s) for infrasound arrivals are function of the range R_{d} (in degrees) and are calculated at the IDC with the empirical formula

$$\delta T_{\text{tmodel}} = \alpha \times 720 \times \sqrt{\frac{R_{\text{d}}}{90}} + \beta, \tag{9}$$

where α and β are corrective coefficients applied for the three different ranges previously identified. (α=1,β=60), (α=2,β=0), and (α=0.8,β=0) correspond

respectively to small, intermediate, and long ranges. The larger model uncertainty remains for intermediate ranges where travel time residuals of the fast stratospheric and slow thermospheric returns are broadly distributed along the central 295 m/s IDC celerity value (Fig. 3.19).

Research is under way to improve the propagation modeling of infrasound waves:

- Using more realistic atmospheric models providing accurate atmospheric parameters in near real time, e.g., global horizontal wind model and mass spectrometer incoherent scatter extended (HWM/MSISE (Drob et al. 2003; Drob et al. 2008a; Hedin 1991; Hedin et al. 1996)) models combined with the European Centre for Medium-Range Weather Forecasts – ECMWF (Fig. 3.20, (Drob et al. 2003)).
- Using ray tracing techniques (e.g., *TauP* (Drob et al. 2008b; Garcés et al. 1998; Garcés and Hetzer 2004) or *WASP-3D* (Dessa et al. 2005; Mialle et al. 2007a; Mialle et al. 2007b; Virieux et al. 2004) software) to better predict travel time and azimuth deviations of different infrasound phases (Fig. 3.21).
- Using more advanced nomenclature, as suggested by (Brown et al. 2002), for various infrasound phases according to the ducting layer in the atmosphere: Iw, tropospheric; Is, stratospheric; It, thermospheric.

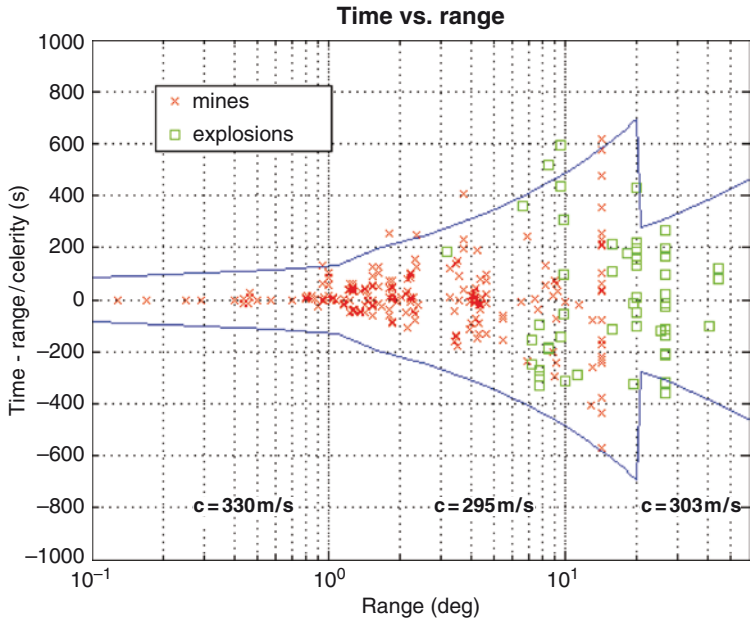

Fig. 3.19 Reduced Travel time modeling error δT_{tmodel} (*blue line*) as a function of range. Celerity values of 330, 295 and 303 m/s have been used respectively for ranges below 1.2°, between 1.2 and 20°, and above 20°. The travel time modeling errors fit with mine blasts and chemical explosions from the IDC IRED database

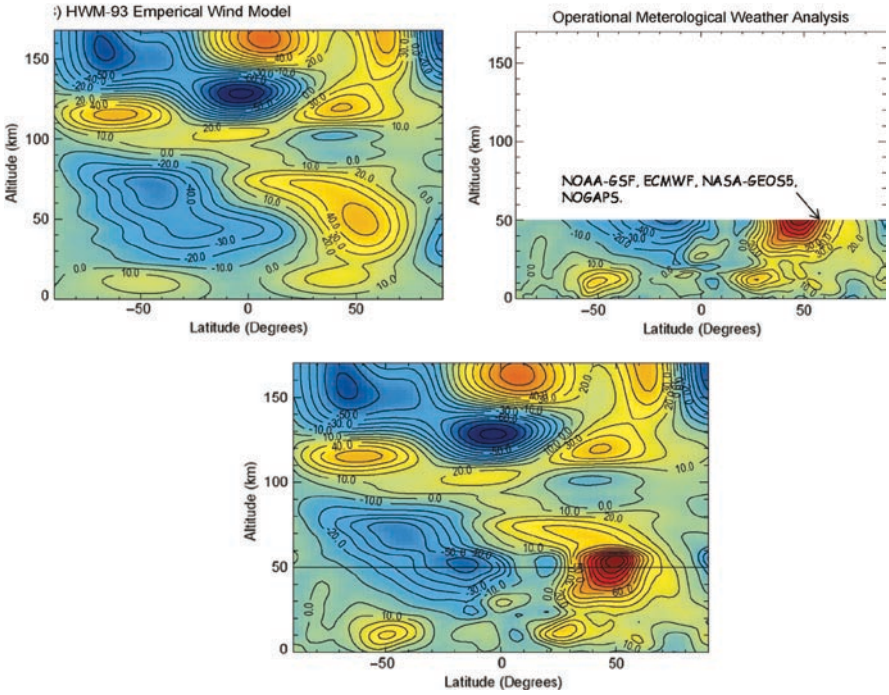

Fig. 3.20 (**a**) HWM-93 model (**b**) numerical weather prediction, e.g., ECMWF atmospheric specifications (**c**) hybrid ground-to-space model, e.g., combining HWM-93 and ECMWF

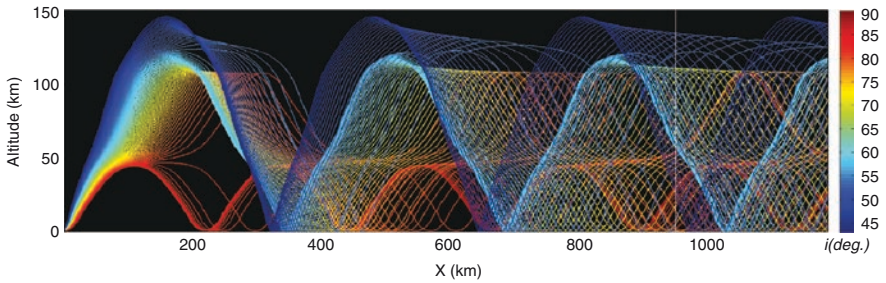

Fig. 3.21 Example of ray tracing simulation of infrasound wave propagation in the atmosphere (stratospheric and thermospheric returns) using WASP-3D

The example presented in Fig. 3.22 illustrates how the complex anisotropic atmosphere impacts the infrasound signal characteristics detected at IMS stations located at different ranges and azimuths.

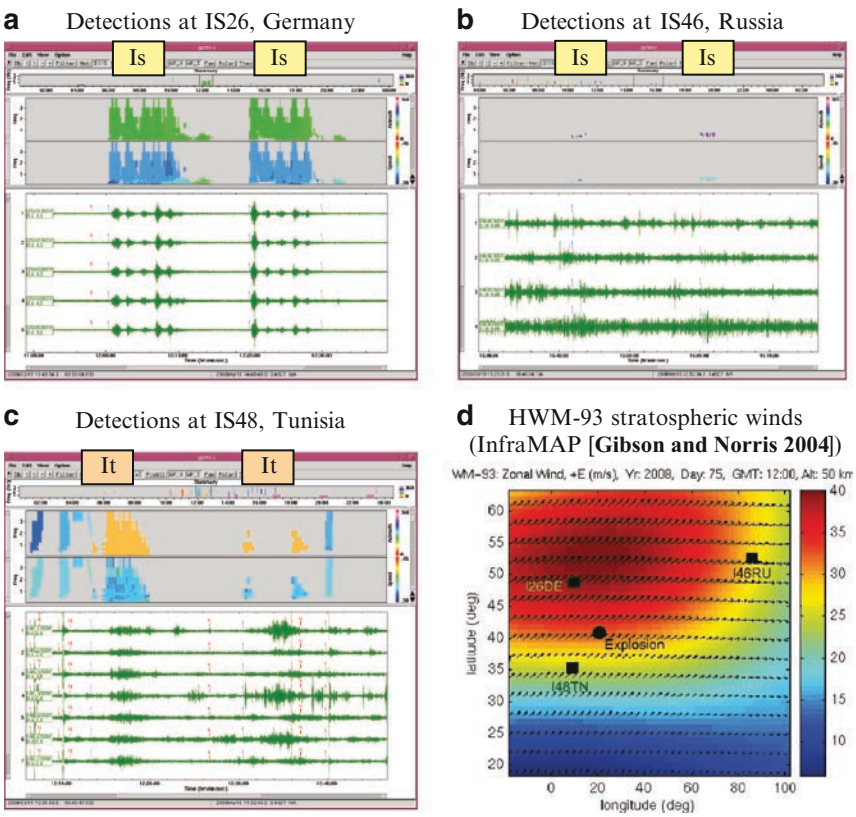

Fig. 3.22 Explosion of an ammunition depot near Tirana, Albania on 15 Mar 2008. Two SEL3 automatic events were built 20 min apart, using **(a)** detections at IMS infrasound arrays IS26-Germany, 950 km, **(b)** IS48-Tunisia, 1,090 km, and **(c)** IS46-Russia, 4,900 km. Stratospheric winds at 50 km (**d**) are favorable for eastward propagation of infrasound signals. A possible interpretation of these arrivals would be thermospheric phases (labeled "It") detected at IS48, and stratospheric phases (labeled "Is") detected at IS26 and IS46. The intensity and wind barbs may explain the azimuth deviations observed at the station and also the very different infrasound waveforms at the two equally distant stations IS26 (clear impulsive signals, winds perpendicular to the wave path) and I48TN (diffused signals, winds against the wave path)

3.3 Interactive Processing

Interactive analysis is the stage of IDC processing where results produced by automatic processing are reviewed and refined by analysts. This stage is concluded by the publication of the REB.

3.3.1 Analysts' Review Tool

The primary tool used by analysts at the IDC to routinely review the seismic, hydroacoustic, and infrasound waveform data is the analyst review station (ARS). ARS allows an analyst to review each SEL3 event and to make corrections and additions as needed. The graphical interface is used to display the waveform data and detections and for calling specialized signal processing tools – e.g., F-k analysis, beam forming, event location, and magnitude computation.

Geotool-PMCC is part of these integrated tools in ARS, which has been specifically developed for infrasound interactive review. The tool allows the analyst to analyze in detail the waveform signals and detections for a selected infrasound station. It graphically displays the PMCC results that were automatically calculated and stored during station processing.

These results are presented as plots of back azimuth and horizontal trace velocities versus time and frequency as well as the raw or filtered time series data, the different phases identified during station processing, and the meteorological observations at the station. This form of display provides a comprehensive picture of the signal properties as they evolve with time, and efficiently helps to comprehend and interpret the detection results. Geotool-PMCC has the ability to toggle the pixel display between all pixels, only pixels that are members of a family, or only pixels that are members of a nonnoise family (Fig. 3.23).

A polar diagram plot is integrated with the main window and displays pixel information in polar coordinates of azimuth and horizontal trace velocity (Fig. 3.24). The frequency polar plot permits a visual separation of the low- and high-frequency events. The time representation is interesting for tracking moving sources, such as large aircraft flying near the array (in such case, the speed representation is also very useful to visualize the changes in horizontal trace velocities with azimuth) or long distance microbaroms sources moving across the ocean.

The analysts may retime, rename, add, or delete infrasound phases in Geotool-PMCC. Each action is synchronized with ARS.

3.3.2 Contribution of Infrasound Data to IDC Event Bulletin

3.3.2.1 Purely Infrasound Events

Rocket Launches and Re-Entries

Rocket launches and re-entries are regular atmospheric sources of infrasound signals that may be recorded at large distances by one or several IMS infrasound

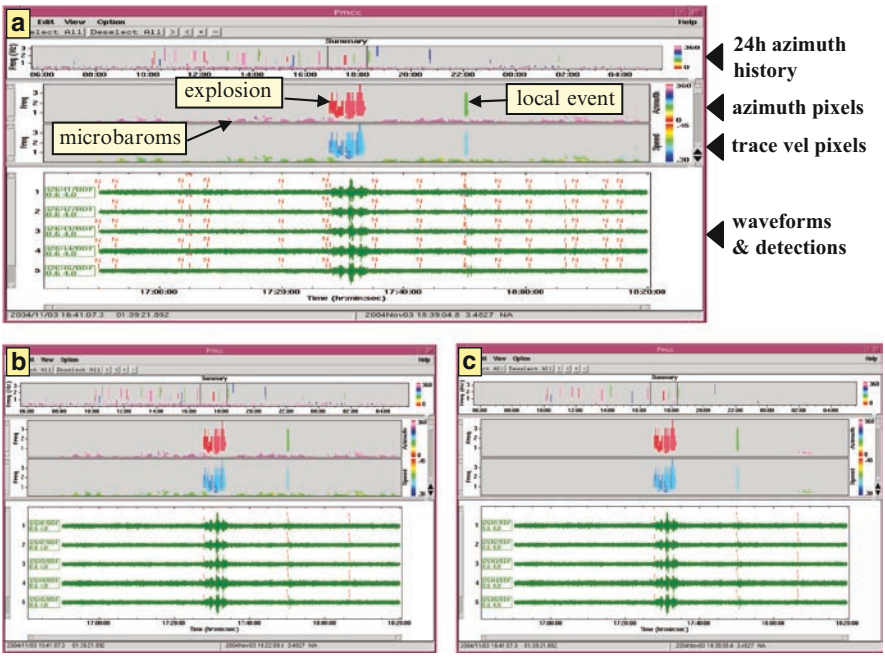

Fig. 3.23 Interactive review of infrasound results related to an explosion in a fireworks factory near Kolding, Denmark (03-Nov-2004) using Geotool-PMCC. The display of detections and PMCC pixel information is configurable, allowing the analyst to highlight the Kolding signal (*red azimuth*) compared to the continuous microbaroms detection background (*pink azimuths*) for example: (**a**) All detections and all family pixels, (**b**) only phase detections and all family pixels, (**c**) only phase detections and related family pixels (cleaned display)

arrays. Although the source is often a generator of large amplitude and long duration infrasound signals, it is not easy to build an IDC event with the detected arrivals. Rockets are supersonic objects – generating infrasound wave fronts in a direction perpendicular to the mach cone – and their flight missions consist of distinct phases like take-off, stage jettisons, and stage re-entries. Therefore, each rocket launch or re-entry can be seen as a combination of distinct events along the trajectory, which are likely to be detected as distinct source points by different IMS infrasound stations.

The example in Fig. 3.25 shows signals associated to the launch of the Space Shuttle Atlantis on February 7, 2008. It has not been confirmed that the infrasound signals detected at the three IMS infrasound arrays correspond to the take-off of the rocket at Kennedy Space Center or any later phase during the flight. However, the REB solution obtained with the three detected arrivals converged to a region located near the launch pad. Considering the small number and the far distance of recording stations, the accuracy is not sufficient to determine which exact phase of the flight is observed.

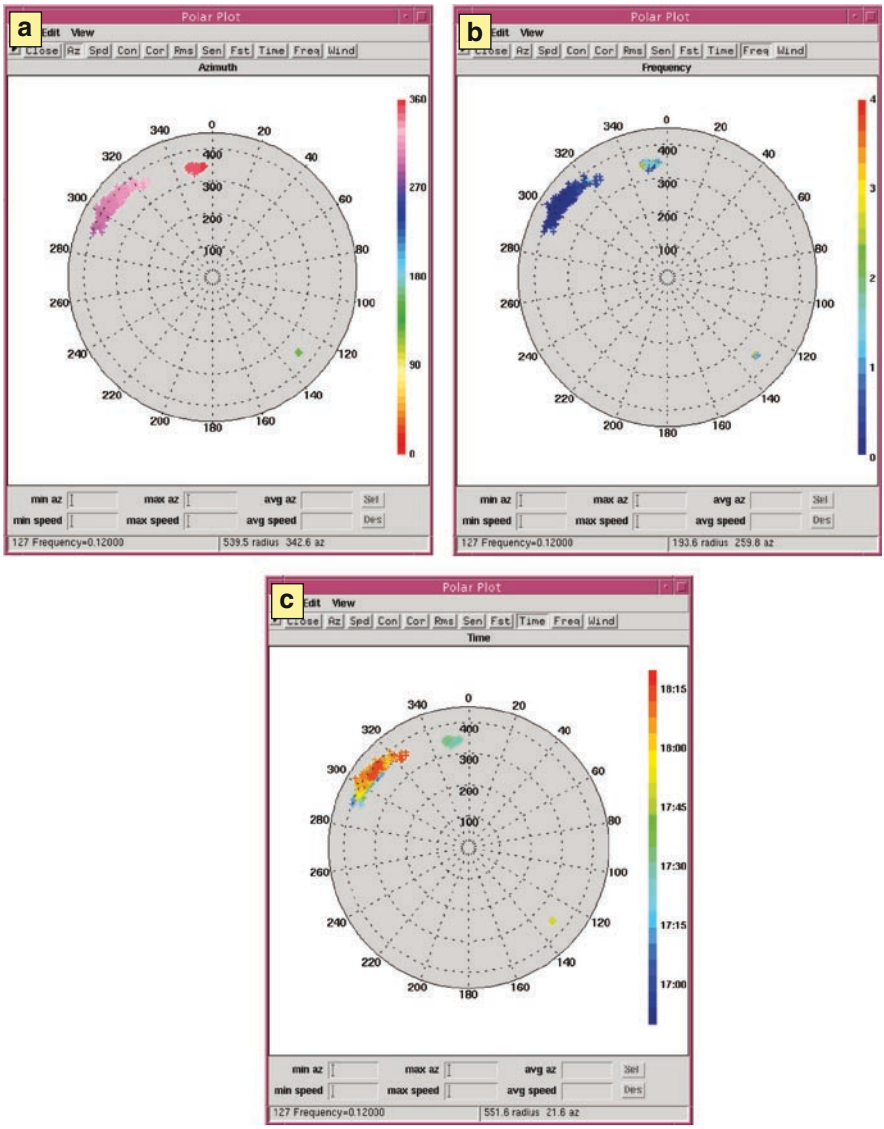

Fig. 3.24 Interactive review of infrasound results related to an explosion in a fireworks factory near Kolding, Denmark (03-Nov-2004) using Geotool-PMCC. The polar diagram plots (back azimuth and horizontal trace velocity) represent the family pixel information for back azimuth (**a**), frequency (**b**), and detection time (**c**)

Bolides

Bolides are large meteor fireballs exploding in the upper atmosphere. For CTBTO, they represent very interesting explosive sources that may release energy of 1 kiloton

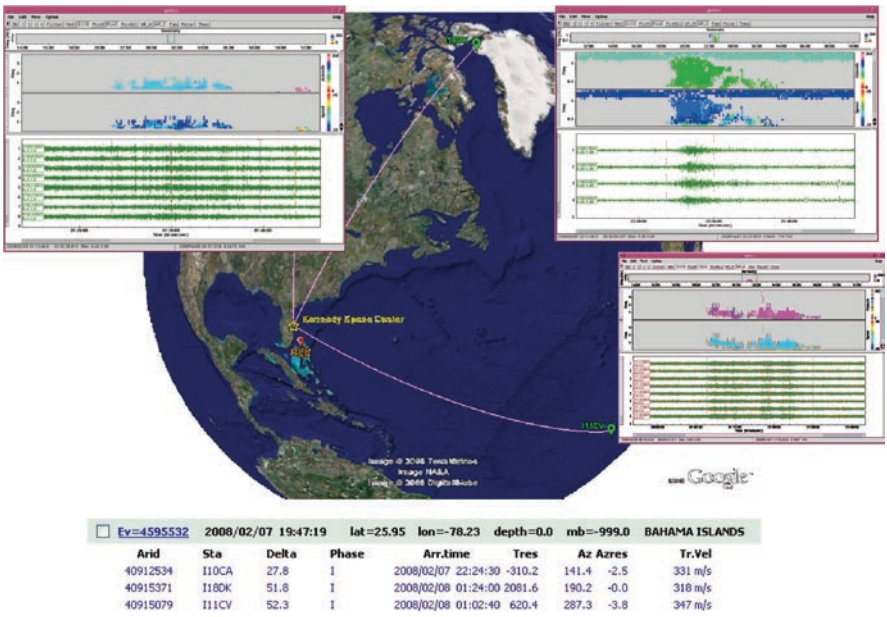

Fig. 3.25 Space Shuttle Atlantis taking off from Kennedy Space Center, Florida on February 7, 2008 at 19:45UTC. Signals related to the rocket launch were detected at three IMS infrasound arrays IS10 (Canada), IS18 (Greenland), and IS11 (Cape Verde). The event was automatically built and included in the REB after analysts review

TNT equivalent or more. The bolide location cannot be constrained easily without satellite data input or seismic data for meteorites impacting the Earth's surface; however, two or more IMS infrasound detections are sufficient to get a first estimate of the location of large bolides. An example of an atmospheric event detected by the infrasound network, probably an exploding meteor, is presented in Fig. 3.26.

Volcanic Eruptions

Volcanic eruptions are natural phenomena distributed worldwide and are powerful sources recorded by the IMS network. Seismic activity is mostly recorded before the eruption during the convective movement of magma in the lava dome, whereas infrasound signals are observed when the eruption has started and vents are opened. It is therefore not common to observe seismic and infrasound signals simultaneously on IMS stations.

The detected infrasound signals have different characteristics according to the type of eruptions:

- Explosive eruptions are sudden releases of material – gas, lava, or rocks – into the atmosphere. Infrasound signals related to such events are usually energetic and their duration rarely exceeds tens of minutes (Fig. 3.27a). The most violent

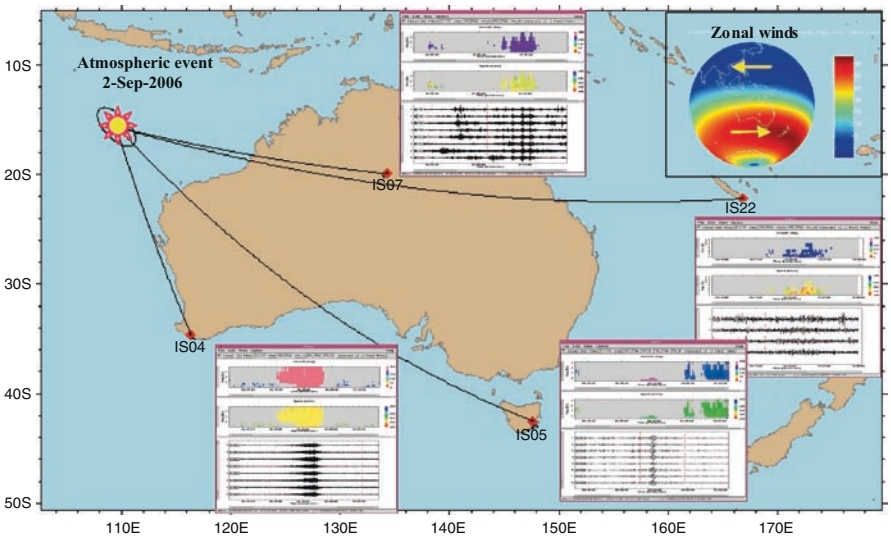

Fig. 3.26 On September 2, 2006, strong signals from an atmospheric event (supposedly meteor explosion, but not independently confirmed) were observed downwind at IMS arrays in Australia and New Caledonia. The event was formed and located in the automatic bulletin in Wharton Basin, North West of Australia

ones may be detected by distant IMS infrasound arrays. An impressive example was the Manam volcano eruption on January 27, 2005, which was detected by eight IMS infrasound stations all over the world (the farthest station was IS33, Madagascar, located 10,675 km from Manam).

- Effusive eruptions are characterized by a burbling activity of the volcano. They are sources of high-frequency infrasound signals, which can only be detected by a local or regional array. The eruptions are usually continuous and may last for hours, days, or months (Fig. 3.27b). The associated infrasound detections are categorized as noise by the IDC categorization algorithm. However, the beginning of each eruption sequence or period of more intense volcanic activity may be picked as a detection phase by the system and may form an infrasound event if several stations detected it.

Volcanic eruptions represent excellent calibration sources for the IMS infrasound network. The location is precisely known, and the energy released during explosive eruptions may be large enough to generate infrasound waves propagating thousands of kilometers. These sources can be used to assess the detection capability of the IMS network and to help validate the atmospheric models (Le Pichon et al. 2005) and infrasound wave propagation tools.

The IMS Infrasound data may be used for civil application for detection of volcanic eruptions and assist in aviation safety. Monitoring volcanic eruptions in remote areas is still challenging, and the possible contribution of infrasound to the early warning program for volcanic ash emission developed by the International

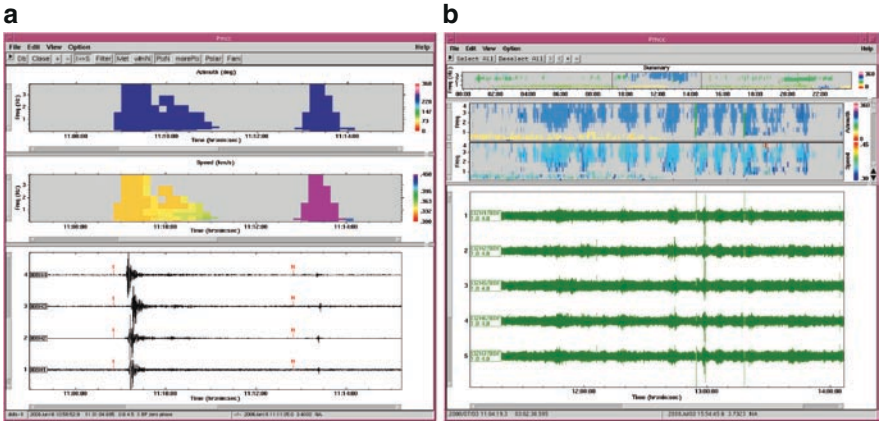

Fig. 3.27 Comparison of the infrasound signals and detections for two types of eruptions: (**a**) Explosive eruption of Ubinas volcano (Peru) recorded by IS08, Bolivia on 18 June 2006. Stratospheric and thermospheric arrivals were clearly detected at the station (**b**) Effusive eruption of Ol Doinyo Lengai volcano (Tanzania) recorded by IS32, Kenya on 3 July 2008

Civil Aviation Organization (ICAO) may help mitigate the risks of catastrophic accidents when aircraft fly through ash clouds (Garcés et al. 2008).

Microbaroms

The interaction of ocean swell with the atmosphere generates energetic long-period infrasound waves, which propagate over large distances, and may be detected by IMS infrasound stations over hours or days. Although considered as noise by the IDC, these microbaroms are interesting sources for infrasound scientific studies. The infrasound signals associated to microbaroms are strongly influenced by the presence of stratospheric wind jets (Le Pichon et al. 2006) and may help better understand the characteristics and temporal fluctuations of the stratosphere. Figure 3.28 shows how the infrasound automatic detections at IS22, New Caledonia, related to microbaroms and volcanic eruptions are dependent on the direction of stratospheric wind jets.

3.3.2.2 Mixed Technology Events

Earthquakes

Earthquakes are among the main sources of mixed technology events – i.e., involving seismic, hydroacoustic, and infrasound detections – in IDC event bulletins.

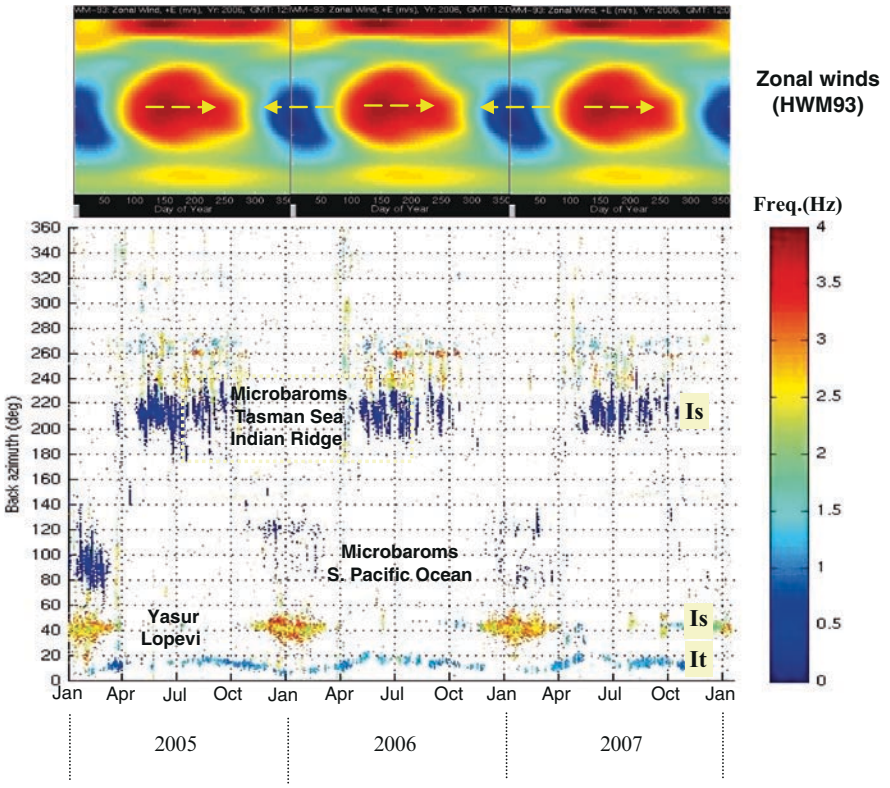

Fig. 3.28 100,000 automatic infrasound detections at IS22, New Caledonia from January 2005 to December 2007. Stratospheric winds blowing in eastward direction from May to October help infrasound waves propagate from the Tasman Sea (back azimuth 210°). In contrast, from December to April, the stratospheric winds blow westward and the station detects signals from South Pacific Ocean or Yasur volcano. The volcanic activity from Lopevi is visible all year round and attributed to thermospheric propagation

For large events, infrasound (ground to air coupled) waves may be detected by IMS infrasound arrays (Le Pichon et al. 2002).

The infrasound sensors behave like seismometers detecting the ground deformation caused by body or surface waves. Seismic waves may be observed at infrasound stations for large events, regardless of the hypocentral depth. They are usually associated to long duration coda waveform signals, which may be energetic but poorly correlated on the small aperture (1–3 km) IMS infrasound arrays.

Topography is a key factor for observing ground to air-coupled infrasound signals. High mountain ranges or volcanic domes located near the epicenter of large earthquakes are shaken by the seismic waves and become themselves secondary sources of infrasound waves that may propagate over hundreds of kilometers before being detected by IMS infrasound stations. The example in Fig. 3.29 shows recent regional earthquakes detected by the Japanese IMS infrasound station IS30.

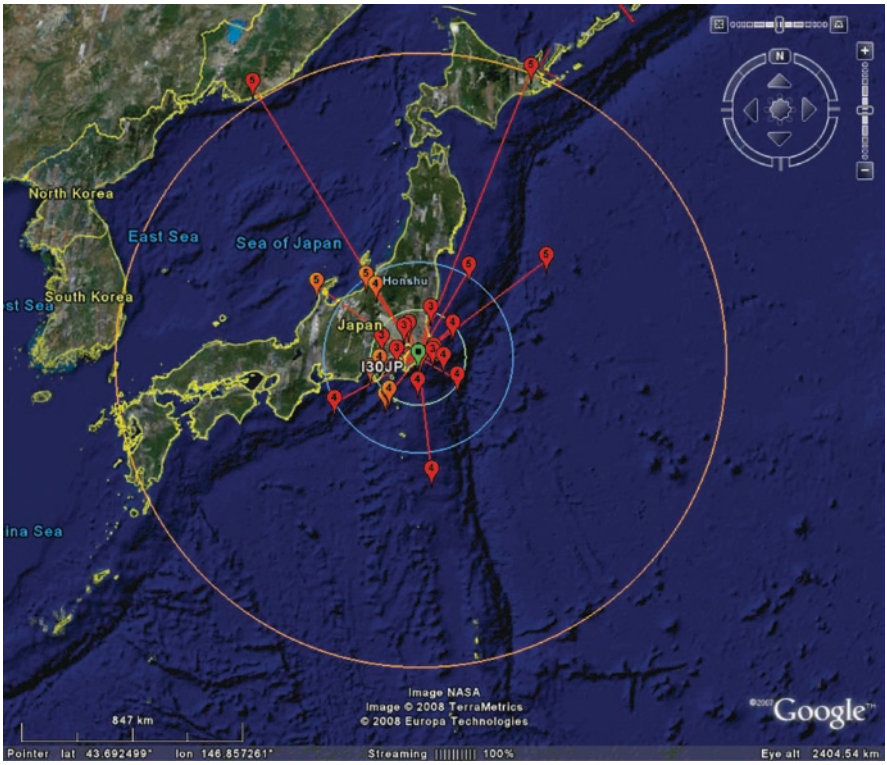

Fig. 3.29 Regional map (©Google) of earthquakes detected by the IMS infrasound station IS30, Japan. Seismic signals were detected for all the events (*red symbols*). Infrasound signals were detected for events located near topographic areas (orange symbols). An indication of the magnitude (IDC mb magnitude) is given for each event, e.g., "4" corresponds to an event with mb between 4 and 5). In this region, magnitudes 3–4, 4–5, 5–6 events can be detected by IS30 within radius of 150 km (*green circle*), 300 km (*blue circle*) and 1,000 km (*orange circle*) respectively

Infrasound signals are detected for epicenters located near topographic areas (mountain range and island), but no infrasound signals originate from earthquakes located off the coast of Japan or in lowland areas.

Deep events with large magnitudes may generate infrasound signals, especially in areas of the globe where topography is favorable for ground to air coupling (mountain ranges and islands). In the IDC automatic network processing, a parameter sets to 150 km the maximal depth for associating infrasound signals to seismic events. This threshold is in agreement with the maximum depth (140 km) recorded so far by infrasound arrays in the IDC REB. However, this depth threshold may possibly be increased, as large events have recently been infrasonically recorded down to a depth of 228 km (Celebes Sea, December 12, 2006, Fig. 3.30). The downside of associating infrasound with deeper events is (1) a risk of increasing the number of false automatic associations of infrasound detections with weak- and low-confidence seismic events, (2) and the coupling areas at the Earth's surface

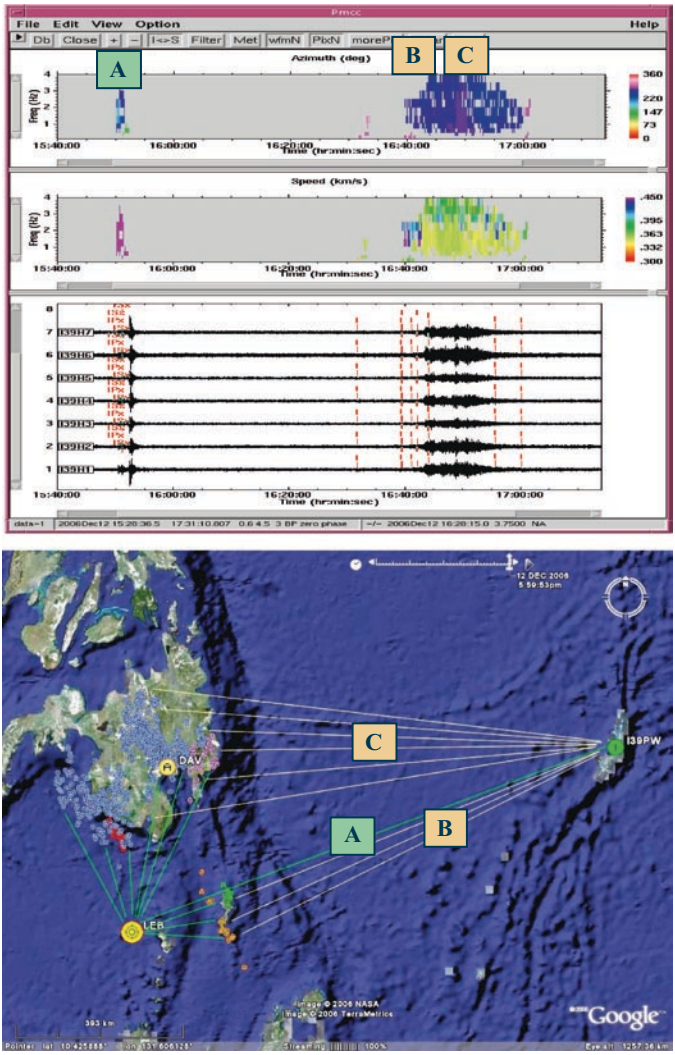

Fig. 3.30 The PMCC detection pixels can either be displayed in Geotool-PMCC with the waveform data, or projected on a topographic map (©Google). The seismic and infrasound waves generated by the Celebes Sea earthquake (December 12, 2006 15:48UTC, REB magnitude 5.6, depth 228 km) have been detected at IS39 Palau infrasound array at a distance of 1,150 km from the source. The signals show clear P and S seismic waves (**a**) followed by a long train of infrasound waves from various azimuths produced by secondary sources at the surface of the globe (mountain peaks, islands) which start vibrating during the passage of seismic waves: (**b**) infrasound from the local islands located in the vicinity of the epicenter (flat terrain reacts as a membrane excited by the vertical incidence seismic wave) and (**c**) infrasound originating from the mountain ranges in Philippines

might be located hundreds of kilometers away from the epicenter and the inclusion of infrasound readings may degrade the automatic seismic location solution.

It can be argued that there is no added value in including infrasound data into the existing IDC seismic event bulletins. Seismic and infrasound arrivals detected on IMS infrasound stations only appear for large earthquakes, which means for events generally recorded and located with good precision by large number of IMS seismic stations. Moreover, large differences in measured infrasound back azimuths due to secondary topographic sources may introduce some bias in the location process. However, the IMS seismic network does not have a complete and uniform coverage of the globe, especially in some oceanic regions where the valuable seismic primary arrays – offering excellent detection capability compared with 3-component seismic stations – are sometimes not so well represented. In such cases, infrasound arrays provide a good complement to the existing seismic network and may help in monitoring the Earth activity and refining the epicenter location in remote areas. The presence of infrasound signals along with seismic signals is always a sign of large earthquakes producing major ground movement at the surface, with sometimes catastrophic consequences for a population living in the area. If infrasound detections are used in combination with seismic information, they could become a reliable indicator for triggering alerts in case of devastating earthquakes (e.g., infrasound waves observed during Banda Aceh "tsunamigenic" Mw9.3 earthquake on December 26, 2004).

Surface Explosions

Most infrasound signals recorded at IMS arrays originate from sources located near the surface of the Earth. Open-pit mine blasts (Fig. 3.31) and chemical explosions are typical examples of fusion between seismic and infrasound data in IDC event bulletins. The coupling of the explosion energy with the ground or the atmosphere may differ from one blast to another, which explains discrepancies in seismic or infrasound observations.

Fig. 3.31 Map (©Google) of open pit mines in Eurasian region detected by the IMS infrasound stations IS31 (Kazakhstan), IS34 (Mongolia), and IS46 (Russia)

The presence of infrasound signals is also strongly dependent on the diurnal and seasonal fluctuations in the atmospheric wind and temperature profiles. The explosions at the Zheleznogorsk open pit mine in Russia have enough yield to produce infrasound signals recorded at 1,500 km distances, detected by IS26 (Germany) during summer months (westward stratospheric wind propagation) and by IS31 (Kazakhstan) during winter months (eastward stratospheric wind propagation).

Infrasound signals associated to explosions are usually composed of a series of impulsive arrivals that correspond to wave reflections from different altitudes of the atmosphere (example of explosion of an ammunition depot near Tirana, Albania in Fig. 3.22). For local blasts, the usage of infrasound back azimuth allows an analyst to substantially refine the location of the event. Research is underway for improving atmospheric modeling as well as determining a better usage of infrasound data in combination with seismic data. In particular, the IDC processing is expected to be enhanced with the introduction of realistic back azimuth corrections due to atmospheric winds as well as a new capability for predicting accurate onset times for different infrasound arrivals.

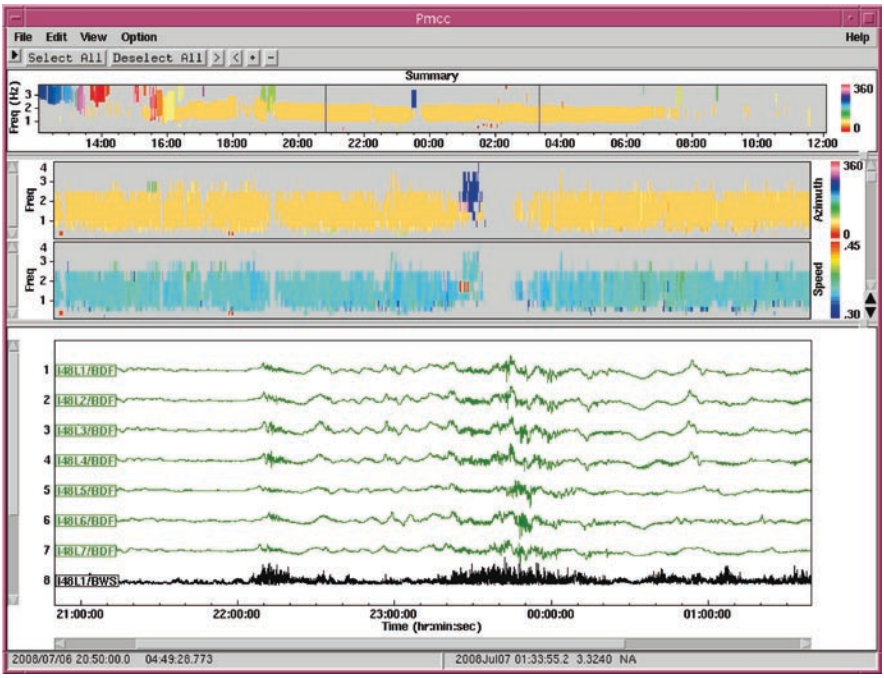

Fig. 3.32 Infrasound (BDF channels) and wind speed (BWS channel) data recorded at IS48, Tunisia, on July 6, 2008. The energetic high-frequency waveforms on BDF channels are caused by wind bursts, as indicated by the BWS wind speed channel. The ocean activity on the Tunisian coast produces a continuous infrasound signal detected in the back azimuth 60–70° (in *yellow*). The detection is interrupted (PMCC pixel gaps) between 23:30 and 23:45 when the wind speed exceeded 3 m/s

3.3.2.3 Importance of Meteorological Data at the Station

The standard IMS configuration for infrasound arrays includes meteorological sensors at one or several elements. Wind speed (and direction) and temperature are key information measured and stored simultaneously with micro pressure data. This meteorological data can be displayed with Geotool-PMCC like any other data time series and may be very helpful for the analysts to understand the detection background at the station.

- The local surface winds strongly influence the detection capability at the station. IMS infrasound stations are equipped with wind-noise reduction systems (rosette pipes), or wherever possible are installed in areas covered by dense vegetation. This has proved to efficiently reduce incoherent high frequency turbulence caused by local wind bursts, but may be insufficient for some stations exposed to very windy conditions. In IDC processing, strong wind bursts generate high-amplitude incoherent infrasound noise, which may mask any other coherent signals occurring at the same time. As the PMCC detection algorithm is based on signal cross correlation, wind bursts do not create false detections but renders the infrasound array blind. Figure 3.32 shows some infrasound and wind speed data recorded at IS48, Tunisia, and PMCC detections interrupted when the wind speed exceeds 3 m/s.
- The local sound speed depends on the temperature at the station. In dry air, at 20°C, the speed of sound is about 343 m/s. In regions like Antarctica or the desert of Australia, temperatures may reach extreme values. The example in Fig. 3.33 shows automatic detections produced at IS55, Windless Bight (Antarctica). The LKO channel indicates a local temperature of −12°C at the time of the recording. Two very local high-frequency transient signals are detected with trace velocities of 319 m/s (i.e., with direct wave propagation in a medium at −12°C). The low-frequency microbaroms show higher horizontal trace velocities (about 345 m/s), which is explained by the propagation in different waveguide (stratospheric phases).

3.3.2.4 Nondefining Infrasound Phases Associated to Events: Ix

The IDC is still at an early stage when identifying infrasound wave types. There is currently no distinction made for tropospheric, stratospheric, and thermospheric phases, all infrasound phases are named “I.” An event cannot include more than one infrasound “I” phase per station. During interactive review, the analysts may decide to associate additional infrasound phases to the event. These phases are named “Ix” and are not used in the location process.

As shown in the previous section, infrasound data may contribute to many types of REB events. In case of very well-constrained source locations (explosive events), the time and azimuth of the automatic detections very well characterize the source. The analysts generally identify the fastest arrival as I-phase and associate it

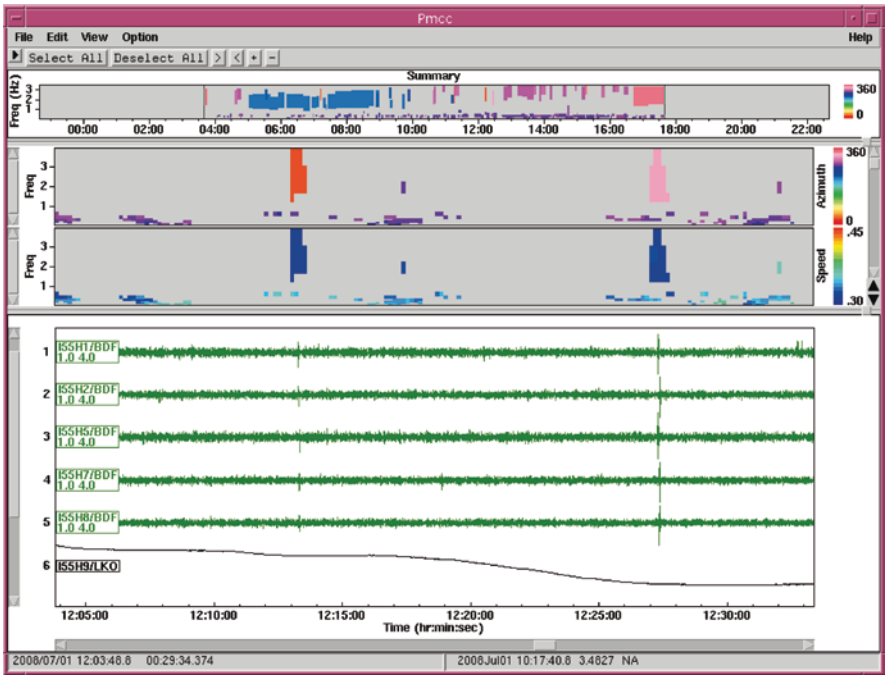

Fig. 3.33 Detections at IS55, Antarctica. The LKO channel indicates the local temperature measured at the array (between −12 and −11°C). The signatures of local sources are characterized by impulsive energetic signals with trace velocities that are of same order as the local sound speed (values represented with a dark blue color). In contrast, the long duration and low-frequency microbaroms that propagate over larger distances have higher trace velocity values (values represented with *light blue* color)

to the event. Later, infrasound phases may also be manually reviewed and associated to the same event, but as there are currently no appropriate travel time tables, these phases are named Ix (Fig. 3.34).

For complex events such as fast moving objects or earthquakes, which involve multiple secondary source points, the current analyst procedure recommends picking and labeling the block of correlated waveforms which better fits with the expected azimuth and time as "I." Any other associated group(s) of infrasound detections should be labeled "Ix." Note that these Ix phases often arrive before the I-phase (due to topographic seismic/infrasound wave coupling, or corresponding to the closest points on the trajectory of a hypersonic moving source).

Concluding Remarks

An automatic and interactive data processing system has been established at the IDC to analyze data from the IMS infrasound network. Specialized software has been developed to automatically detect and categorize infrasound signals at each

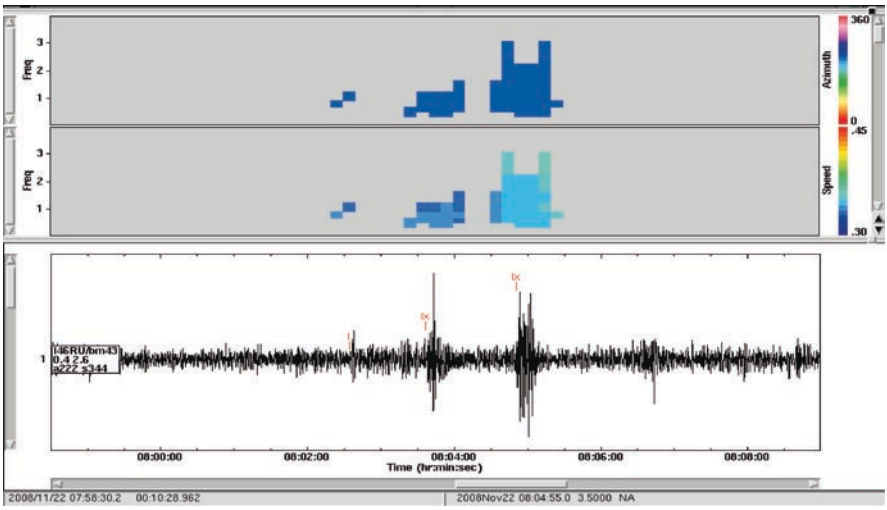

Fig. 3.34 Signal recorded at IS46, Russia related to a blast at Kara Zhyra mine in Kazakhstan (distance of the source: 600 km). The waveforms on the beam channel clearly show a group of three distinct arrivals (two stratospheric and one thermospheric returns, according to ray tracing modeling). The first arrival in the group is identified as "I" and, the two others as "Ix"

individual IMS station, and finally to produce automatic event bulletin together with seismic and hydroacoustic technologies.

The interactive review of the automatic bulletin has demonstrated that the automatic system is functioning at a level whereby infrasound or mixed-technology events can be reliably formed. Various types of infrasound sources have been identified, some of them are energetic enough to be detected by several stations of the IMS network, in particular atmospheric or surface explosions, exploding meteors, rocket launches and re-entries, large earthquakes, and volcanic eruptions.

The production of a good quality automatic infrasound event bulletin requires the correct detection and association of signals and accurate location of the largest number of genuine sources, while keeping the rate of false alarms as low as possible. The IDC will continue working on enhancing the system in order to determine and/or refine the source locations. Additional work is required for producing reliable modeling of the atmospheric specifications and for understanding the impact it has on the infrasound wave propagation. One of the remaining challenges for the IDC will be the integration of these real-time data models into the automatic and interactive operational environment.

Acknowledgements The authors thank the members of the infrasound specialist group at the IDC – Abdou Salam Ndiath, Misrak Fisseha, Mehves Feyza Ocal, Kirill Sitnikov, and Gadi Turyomurugyendo – for their daily contribution to the high quality REB and their dedicated work for promoting infrasound results in IDC operations.

References

Blanc E, Millies-Lacroix JC, Issartel LP, Perez S (1997) Detection of nuclear explosions in the atmosphere. Chocs 17:23–24

Bowman JR, Baker GE, Bahavar M (2005) Ambient infrasound noise. Geophys Res Lett 32:L09803

Bracewell RN (1986) The Fourier transform and its applications, 2nd edn. McGraw-Hill, Reading, NY

Brachet N (2004) Infrasound processing at the IDC – Detection categorization. Infrasound Technology Workshop, Hobart, Tasmania

Brachet N, Coyne J, Le Bras R (2006) Latest developments in the automatic and interactive processing of infrasound data at the IDC. Infrasound Technology Workshop, Fairbanks, Alaska

Bratt SR, Bache TC (1988) Locating events with a sparse network of regional arrays. Bull Seism Soc Am 78:780–798

Brown DJ, Katz CN, Le Bras R, Flanagan MP, Wang J, Gault AK (2002) Infrasonic signal detection and source location at the Prototype International Data Centre. Pure Appl Geophys 159:1081–1125

Brown DJ, Brachet N, Le Bras R (2008) Enhancements to the CTBTO operational automatic infrasound processing system. Thirtieth Monitoring Research Review, Portsmouth, Virginia, September 23–25

Cansi Y (1995) An automatic seismic event processing for detection and location: The P.M.C.C. method. Geophys Res Lett 22:1021–1024

Cansi Y, Klinger Y (1997) An automated data processing method for mini-arrays, CSEM/EMSC European-Mediterranean Seismological Centre. News Lett 11:1021–1024

Christie DR, Vivas Veloso JA, Campus P, Bell M, Hoffmann T, Langlois A, Martysevich P, Demirovic E, Carvalho J (2001) Detection of atmospheric nuclear explosions: the infrasound component of the International Monitoring System. Kerntechnik 66:96–101

Dessa J-X, Virieux J, Lambotte S (2005) Infrasound modeling in a spherical heterogeneous atmosphere. Geophys Res Lett 32:L12808

Drob DP, Picone JM, Garcés M (2003) Global morphology of infrasound propagation. J Geophys Res 108(D21):4680. doi:doi:10.1029/2002JD003307

Drob D et al (2008a) An empirical model of the earth's horizontal wind fields: HWM07. J Geophys Res 113:A12304. doi:doi:10.1029/2008JA013668

Drob DP, Garcés M, Hedlin MAH, Brachet N (2009) The Temporal Morphology of Infrasound Propagation, Pure and Applied Geophysics (in press)

Garcés M, Hetzer C (2004) Infrasonic source location using the tau-p method (update). Infrasound Technology Workshop, Hobart, Tasmania

Garcés M, Hansen R, Lindquist K (1998) Traveltimes for infrasonic waves propagating in a stratified atmosphere. Geophys J Int 135:255–263

Garcés M, Fee D, Steffke A, McCormack D, Servranckx R, Bass H, Hetzer C, Hedlin M, Matoza R, Yepes H, Ramon P (2008) Prototype ASHE volcano monitoring system captures the acoustic fingerprint of stratospheric ash injection. EOS v89:377–378

Gibson RG, Norris DE (2004) Integration of InfraMAP software with near-real-time atmospheric characterizations. BBN Technologies Final Report for Air Force Research Laboratory (AFRL/VSBYE) under Contract DTRA01-01-C-0084

Hedin AE (1991) Extension of the MSIS thermosphere model in the middle and lower atmosphere. J Geophys Res 96:1159–1172

Hedin AE, Fleming EL, Manson AH, Schmidlin FJ, Avery SK, Clark RR, Franke SJ, Fraser GJ, Tsuda T, Vial F, Vincent RA (1996) Empirical wind model for the upper, middle, and lower atmosphere. J Atmos Terr Phys 58:1421–1444

Jordan TH, Sverdrup KA (1981) Teleseismic Location techniques and their application to earthquake clusters in the south-central Pacific. Bull Seism Soc Am 71:1105–1130

Le Bras RJ, Sereno T J (1996) Monitoring nuclear explosion testing in underground and underwater environments, AGU Fall Meeting abstract

Le Bras RJ, Guern JA, Brumbaugh DA, Hansen JA, Sereno TJ (1999) Integration of seismic, hydroacoustic, infrasound and radionuclide processing at the Prototype International Data Center. 21st Seismic Research Symposium, Las Vegas, Nevada

Le Pichon A, Guilbert J, Vega A, Garcés M, Brachet N (2002) Ground-coupled air waves and diffracted infrasound from the Arequipa earthquake of June 23, 2001. Geophys Res Lett 29(18):1886. doi:doi:10.1029/2002GL015052

Le Pichon A, Blanc E, Drob D, Lambotte S, Dessa JX, Lardy M, Bani P, Vergniolle S (2005) Infrasound monitoring of volcanoes to probe high-altitude winds. J Geophys Res 110:D13106. doi:doi:10.1029/2004JD005587

Le Pichon A, Ceranna L, Garcés M, Drob D, Millet C (2006) On using infrasound from interacting ocean swells for global continuous measurements of winds and temperature in the stratosphere. J Geophys Res 111(D11):D11106. doi:10.1029/2005JD006690

Mialle P, Le Pichon A, Vergoz J, Virieux J, and Blanc E (2007) Construction of 3D propagation tables for localizing infrasonic events. Infrasound Technology Workshop, Tokyo, Japan

Mialle P, Le Pichon A, Virieux J, Blanc E (2007) Methodology for infrasound source localization using global propagation tables. Eight International Conference on Theoretical and Computational Acoustics, Heraklion, Crete

Olson JV, Wilson CR, Szuberla CAL (2000) On the analysis of the spatial and temporal structure of natural infrasound signals. Proceedings of the 22nd Annual Seismic Research Symposium, New Orleans, LA

Taner MT, Koehler F, Sheriff RE (1979) Complex seismic trace analysis. Geophysics 44:1041–1063

Virieux J, Garnier N, Blanc E, Dessa J-X (2004) Paraxial raytracing for atmospheric wave propagation. Geophys Res Lett 31:L20106

Whitaker RW (1995) Infrasonic monitoring. Proceedings of the 17th annual Seismic Research Symposium, Scottsdale, AZ, September 12–15, pp. 997–1000

Chapter 4
Low-Noise Broadband Microbarometers

D. Ponceau and L. Bosca

4.1 Background

Infrasound measurements are made thanks to a dedicated set of equipments generally called "infrasound measuring chain". Modern ones generally consist in an infrasound sensor, an acquisition unit and, when necessary, a wind noise reducer.

The term *infrasound sensor* mainly stands for the elements of an infrasound measuring chain which are located between the wind-generated noise reducer and the recorder. It measures atmospheric pressure changes over a very large dynamic range and delivers a dynamic signal adapted to the associated recorder whose input range is limited.

The term *infrasound sensor* mainly stands for the assembly of the mechanics sensitive to pressure and the associated transducer. A mechanics sensitive to pressure or pressure changes induces a motion or stress between two mechanical parts. A transducer converts it into a dynamic signal adapted to the associated acquisition unit, generally a dynamic voltage. Numerous transduction and mechanics principles have been developed for decades, their principle, and some of their specificities are described hereafter (Fig. 4.1).

4.1.1 Self-Noise

During the measurement and when possible, measuring chain self-noise should be negligible relatively to infrasound background noise on site and on the frequency band of interest. It is sometimes considered that sensor self-noise should be more than three times smaller than infrasound background noise.

On noisy or windy sites, signal levels can remain high. On quietest sites, signals to measure can be very weak over some frequency bands.

Thanks to the numerous studies that have been carried out recently in the framework of the International Monitoring System (IMS), Earth's atmosphere's infrasound

D. Ponceau (✉)
CEA, DAM, DIF, F-91297 Arpajon, France
e-mail: damien.ponceau@cea.fr

A. Le Pichon et al. (eds.), *Infrasound Monitoring for Atmospheric Studies,*
DOI 10.1007/978-1-4020-9508-5_4,

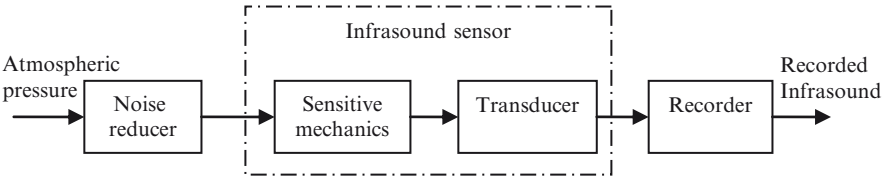

Fig. 4.1 Simplified layout of an infrasound measuring chain

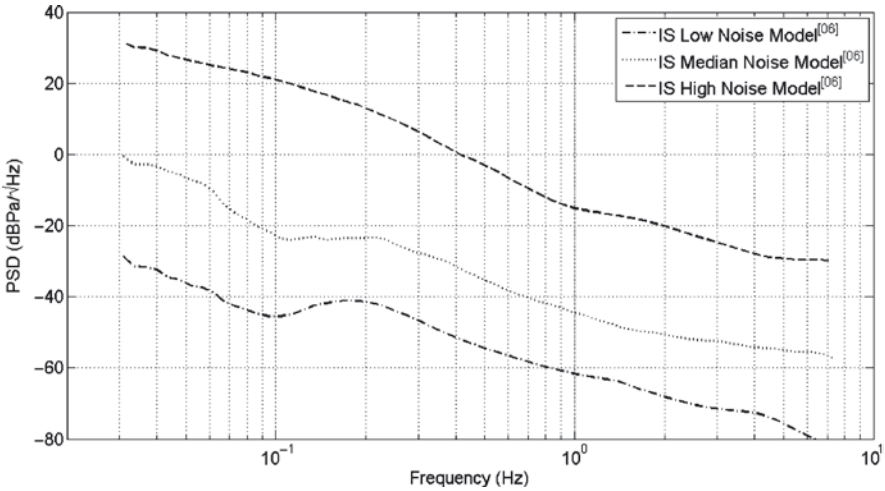

Fig. 4.2 Infrasound noise models established by Bowmann et al. (Bowman et al. 2007)

background noise is better and better known down to frequencies as low as 0.02 Hz. For lower frequencies, it is less true.

Bowman et al. (2007) have recently established models that can be used for infrasound sensors choice or design. Next figure shows three models published in this study. Infrasound Low Noise Model is a fine estimation of the lowest infrasound background noise that can be measured in Earth's atmosphere. It appears that on quietest sites, local noise can be lower than 0.3 mPa_{RMS} over a 1-Hz bandwidth above 3 Hz (Fig. 4.2).

4.1.2 Pressure Range

Infrasound sensors are installed all over the world at a large range of altitudes. This means that infrasound sensor's operating pressure range is several orders larger than infrasound range to measure.

If infrasound range generally does not exceed 1,000 Pa_{cc}, infrasound sensor can be led to deal with absolute pressures from 350 to 1,150 hPa depending on the installation site and meteorological conditions, that's to say a 800-hPa_{cc} range. Obviously, this is highly dependent on the altitude. On a given installation site, with a static altitude, atmospheric pressure changes are much lower, seldom larger than 100 hPa_{cc}.

4.1.3 Dynamic Range

Infrasound sensor's pressure range can be about 800 hPa_{cc}. It is about 80 times larger than biggest infrasound to measure, but it is also more than 200 million times larger than the lowest. It means that infrasound sensors' dynamic range, when expressed in pressure is larger than 200 millions.

It is very hard to realize mechanics, transducers or electronics with such a dynamic range and when possible this led to complex systems with other drawbacks.

This huge dynamic range is the ratio between a large pressure range, from low-frequency pressure changes, and a low infrasound background only above 4 Hz. As a consequence, there is an alternative which consist in differentiating as soon as possible in the pressure measuring chain to measure pressure change or pressure derivate instead of pressure itself.

Here is the main difference between the two main kinds of infrasound sensors: absolute sensors and differential sensors. As absolute sensors are concerned, atmospheric pressure is compared with a known reference in pressure enclosed in a sealed cavity. Some of them use primary vacuum as a reference. Differential sensors compare present atmospheric pressure with an averaged (delayed) image of atmospheric pressure. They use the same acoustic principle as microphones and are sometimes called infrasound microphones. In the same way, classic microphones with low cut-off frequency can be used to measure infrasound.

Differential infrasound sensors can achieve very low noise. Their main drawbacks are their sensitivity to environment due to their low frequency acoustic behavior and the lack of accurate calibration technique suited to them.

4.1.4 Environmental Constraints

Infrasound measuring chains can be installed all over the world, this include very harsh environmental conditions where they can have to fulfill previous requirements.

The IMS is a nice example. Infrasound measuring chains installed on this network have to operate in a very large temperature range (−20, 60°C) not well protected from short period temperature variations. They can be installed in very remote locations where electrical power can be difficult to obtain.

4.1.5 Transfer Function

Up to now, many sensors have been developed, but it looks like there's no perfect infrasound sensor and you still have to choose the sensor best suited to your needs.

This document attempts to introduce major kinds of infrasound sensors and to explain how they operate. This document is not exhaustive as many kinds of sensors have been developed associating many types of mechanics and transducers.

As first infrasound sensors were concerned, dynamic ranges of transducers associated with these absolute microbarometers were too small to measure largest pressure variations associated with long period (e.g., diurnal) pressure changes and smallest infrasounds (Kortschinski et al. 1971). A common solution to this problem was first suggested by Shaw and Dynes (1905), the differential microbarometer. It consists in measuring the difference in pressure between the inside and the outside of a closed cavity in which a small leak is allowed. Short period pressure changes are recorded while flow through the leak equalizes the interior and exterior pressures for long period pressure changes (Kortschinski et al. 1971). Second part of this chapter will introduce the theory of these sensors.

Another difficulty in infrasound sensors design concerns sensors response. The transition between adiabatic and isothermal transformations occurs over infrasound range and can have a noticeable influence on sensor response. This document explains how sensors are affected by this transition.

However, it is difficult to analyze the response of instruments having uncontrolled leaks or needle valves, and their outputs are unknown functions of pressure (Kortschinski et al. 1971).

4.2 Absolute Infrasound Sensors

Infrasounds have been recorded for centuries by barometers (Kortschinski et al. 1971). However, significant advances in infrasound sensing only occurred since last century. Indeed, the fact that nuclear explosions generate infrasounds has stimulated an enhanced interest in infrasound sensors and has led to their application to other fields.

4.2.1 Principle of Operation, Mechanics

Absolute infrasound sensors principle was described by Haak and de Wilde (1996) and Alcoverro and Le Pichon (2005). An absolute infrasound sensor consists in an aneroid capsule deflected by atmospheric pressure changes inside a measuring cavity connected to atmospheric pressure. A motion transducer or a stress transducer converts bellows deflection or stress into a dynamic signal adapted to the associated recorder (Fig. 4.3).

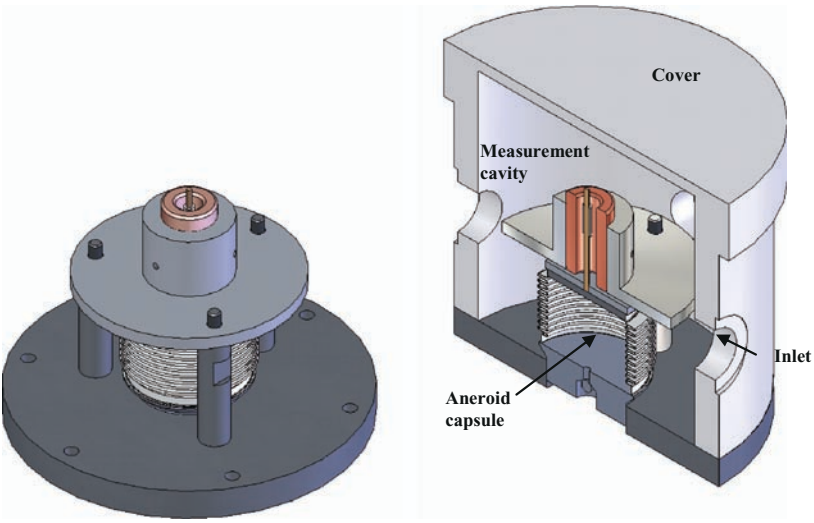

Fig. 4.3 Schematic overviews of an absolute infrasound sensor, the MB2005 from MARTEC

In this chapter, we will describe some influent parameters of an absolute infrasound sensor mechanics in order to estimate its acoustic impedance, Z_{an}, defined as the ratio of the difference in pressure between both sides of the aneroid capsule, p_{an}, to the air flow generated by aneroid capsule motion, q_{an}.

$$Z_{an} = \frac{p_{an}}{q_{an}}[m^2]. \tag{4.1}$$

4.2.1.1 Aneroid Capsule

An aneroid capsule is a metal bellows sealed under vacuum. One end is attached to the frame and includes an inlet used to create a primary vacuum inside the bellows. The other end, the "mobile" end of the aneroid capsule behaves as a piston. The metal bellows can be made of bronze or stainless steel. Modern sensors use specific stainless steel whose thermal coefficient of expansion is adjusted to be very small (CEA/DASE 1998; Martec 2006).

Important parameters of an aneroid capsule include its effective area, stiffness, and mobile mass.

The aneroid capsule's effective area, A_{an}, is the ratio between the force applied on the piston, F_{pi}, and the difference in pressure between both sides of its mobile end, p_{pi}. When the aneroid capsule is deflected it induces an acoustic flow, q_{pi}, proportional to piston velocity relatively to aneroid capsule's frame, v_{pi}. This piston can be modeled as an acousto-mechanical transformer whose mutual constant is its effective area. Piston's mechanical impedance, Z_{mpi}, represents its contribution to aneroid capsule's mobile mass, damping, and spring rate.

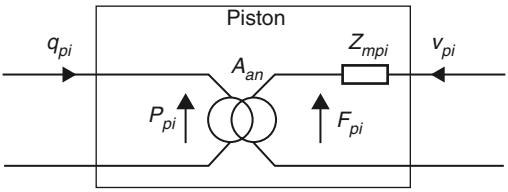

$$\begin{cases} A_{an} = \dfrac{F_{pi}}{p_{pi}} \\ A_{an} = \dfrac{q_{pi}}{v_{pi}} \end{cases} [m^2]. \quad (4.2)$$

The aneroid capsule's spring rate, K_{an}, is the ratio between its deflection, $x–x_0$, and the force applied on it, F_{an}.

$$K_{an} = \frac{F_{an}}{x - x_0}\left[\frac{N}{m}\right] \quad (4.3)$$

The sensitivity to pressure of an aneroid capsule is the ratio of its effective area over its spring rate:

$$S = \frac{A_{an}}{K_{an}} = \frac{x - x_0}{p_{pi}}\left[\frac{m}{Pa}\right] \quad (4.4)$$

The aneroid capsule can be modeled by its acoustic mobile mass, stiffness, and damping coefficient (Fig 4.4).

The acoustic impedance of the aneroid capsule, Z_{aan} is given by the following formula (Alcoverro et al. 2005; Alcoverro and Le Pichon 2002; Alcoverro and Le Pichon 2005):

$$Z_{aan} = R_{aan} + M_{aan} j\omega + \frac{1}{C_{aan} j\omega}[\Omega a] \quad (4.5)$$

The acoustic compliance, C_{aan}, is defined as the ratio of the square of the effective area, A_{an}, of the aneroid capsule to its spring rate, K_{an}:

$$C_{aan} = \frac{A_{an}^2}{K_{an}} \left[\frac{m^3}{Pa}\right] \quad 4.6$$

The acoustic mobile mass, M_{aan}, is defined as the ratio of mechanical mobile mass, m_{an}, of the aneroid capsule over the square of the effective area, A_{an}:

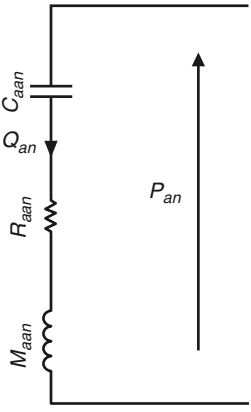

Fig. 4.4 Aneroid capsule acoustic model

$$M_{aan} = \frac{m_{an}}{A_{an}^2} \quad \left[\frac{kg}{m^4}\right] \tag{4.7}$$

The acoustic resistance, R_{aan}, is the acoustic damping of the aneroid capsule.

Infrasound sensors aneroid capsules are designed to minimize acoustic mobile mass and resistance impedances relatively to that of the acoustic compliance over the infrasound frequency band.

The MB2005 aneroid capsule impedance (blue) is plotted on Fig. 4.5 along with the contributions from its stiffness (black), mass (green) and damping coefficient (red).

Over the whole infrasound frequency band and up to 50 Hz, MB2005 aneroid capsule acoustic impedance can be accurately modeled by only the contribution from its stiffness.

4.2.1.2 Measurement Cavity

The measurement cavity is acoustically connected to the atmosphere. Typically, it acts as an acoustic capacitance with losses. Generally, the model used is a resistance in series with a capacitance whose value depends on the thermal process that applies.

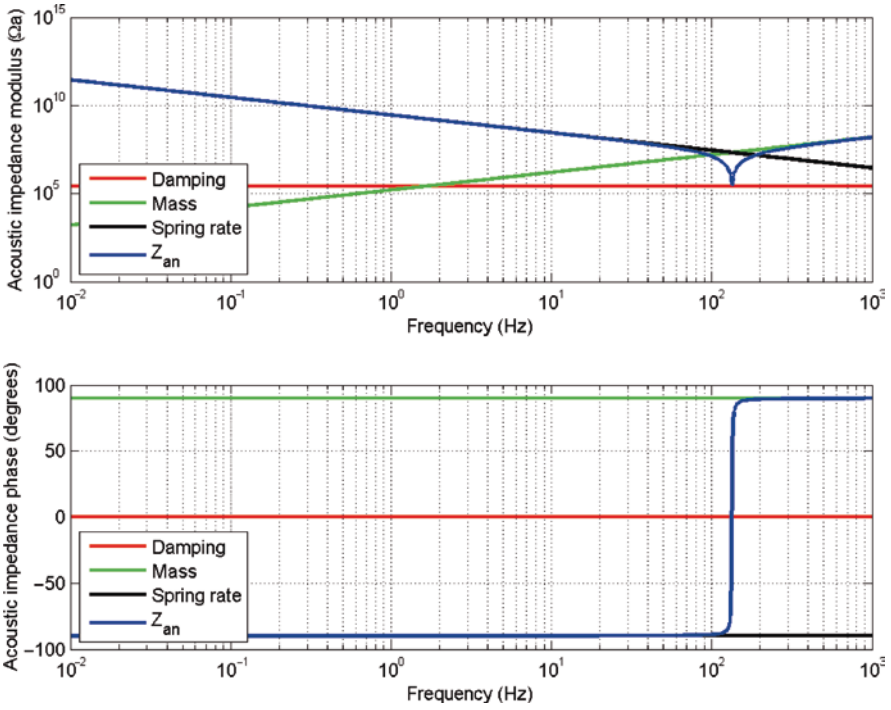

Fig. 4.5 Bode diagram of MB2005 aneroid capsule acoustic impedance (*blue*) with contributions from: damping (*red*), mobile mass (*green*) and spring rate (*black*)

In high frequencies, the thermal regime is adiabatic. Measurement cavity's capacitance is the ratio of its volume, V_{me}, over the product of its pressure, p_m, and the ratio γ of specific temperatures of air.

$$C_{ame} = \frac{V_{me}}{\gamma \bullet p_m} \quad \left[\frac{m^3}{Pa}\right] \tag{4.8}$$

In low frequencies, the thermal regime is isotherm. Cavity's capacitance is the ratio of its volume over its pressure.

$$C_{ame} = \frac{V_{me}}{p_m} \quad \left[\frac{m^3}{Pa}\right] \tag{4.9}$$

To determine the frequency bands where adiabatic or isothermal theory applies, experiments can be performed (Haak and de Wilde 1996). However, the transition is not immediate and could span over octaves within the infrasound frequency band.

Cavity capacitance influence on infrasound measuring chain response needs to be minimized. It cannot be done relatively to that of the aneroid capsule which appears to be negligible. As a conclusion, the acoustic response of the infrasound sensor needs to be as flat as possible over the transition between adiabatic and isothermal transformations frequency bands (Fig. 4.6).

According to both models, the aneroid capsule is equivalent to a cavity. Generally, an equivalent aneroid capsule complex volume can be defined as:

$$V_{an\_e} = \frac{\gamma \bullet p_{\mathrm{m}}}{j\omega \bullet Z_{\mathrm{aan}}} \quad \left[m^3\right] \tag{4.10}$$

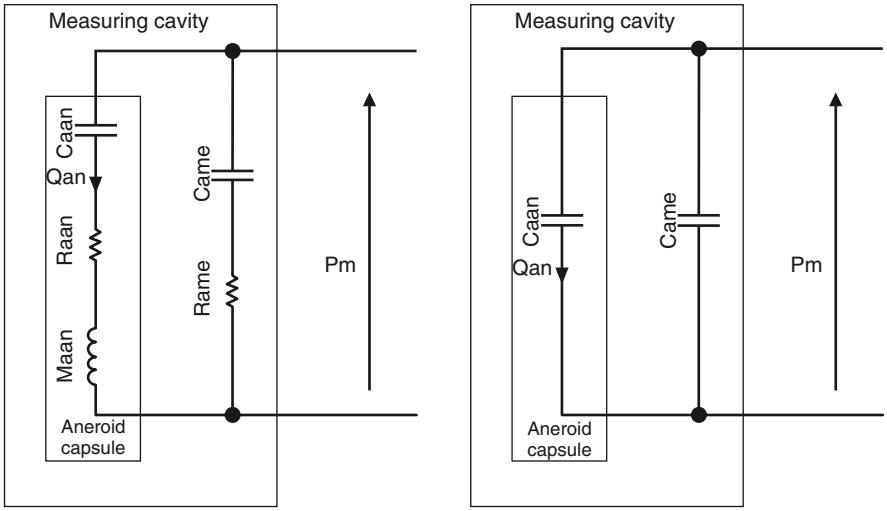

Fig. 4.6 "General" (left) and simplified (right) acoustic models of the aneroid capsule inside the measuring cavity

When aneroid capsule impedance can be simplified to its capacitive part, the aneroid capsule equivalent volume is given by:

$$V_{an\_e} = \gamma \bullet p_{\mathrm{m}} C_{\mathrm{an}} \quad \left[m^3\right] \tag{4.11}$$

4.2.1.3 Inlets and Noise Reducers

Inlets and noise reducers' acoustic impedance can have a major influence on acoustic response of the infrasound measuring chain. Infrasound sensor's inlets are designed not to influence infrasound measuring chain's acoustic response over infrasound bandwidth. These inlets are also designed to match with the noise reducer. Generally, infrasound sensors have one to four inlets but their manufacturers can adapt them on demand.

4.2.1.4 Full Sensor Acoustic Models

Each inlet is represented by losses (R_{ain}) and air mass (M_{ain}). The aneroid capsule is represented by its equivalent acoustic mass, losses, and compliance (M_{aan}, R_{aan}, and C_{aan}). The measurement cavity is represented by its compliance (C_{amc}) and losses (R_{amc}). The figure at right is a simplified model of an absolute infrasound sensor with one inlet as described by Alcoverro and Le Pichon (2005) (Fig. 4.7).

Finally, absolute infrasound sensor mechanics acts as an acoustic low pass filter whose characteristics depend on inlets or noise reducer's acoustic impedance.

If the inlet can be considered as purely resistive R_{ain}, the relation between measured pressure p_{m} and external pressure, p_{e}, is given by:

$$\frac{p_m}{p_e} = \frac{\dfrac{1}{C_{ame} j\omega}}{R_{ain} + \dfrac{1}{C_{ame} j\omega}}. \tag{4.12}$$

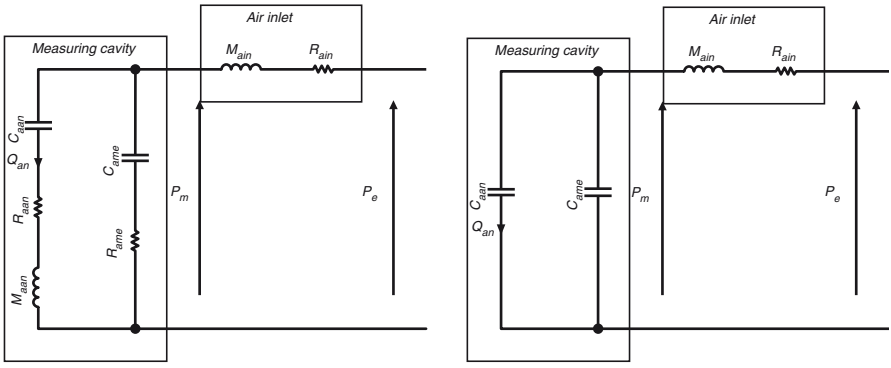

Fig. 4.7 "General" (*left*) and simplified (*right*) acoustic models of an absolute microbarometer

In these conditions, absolute infrasound sensor act as a low pass acoustic filter whose cut-off frequency is dependent on the dimensions of its inlets and of its cavity.

$$\frac{p_m}{p_e} = \frac{1}{1 + \frac{j\omega}{\omega_0}} \quad \text{with } \omega_0 = \frac{1}{R_{in} C_{me}} \tag{4.13}$$

4.2.2 Transducers

The deflection of an aneroid capsule under changes in pressure is converted into an analog voltage by a motion transducer. Various types of transducers can be used depending on the requirements.

Measurement of very long period infrasound requires a transducer with low long period noise. Generally displacement transducers such as LVDT are used.

Displacement transducers are not very appropriated for the upper part of the infrasound frequency range. Indeed, recent studies (Bowman et al. 2007) shown that infrasound minimal noise vs frequency follows a quasi constant slope of about −20 dB/decade (Fig. 4.2).

An adequate infrasound sensor would follow the same slope in order neither to be overspecified in lower frequencies resolution nor underspecified in higher frequencies resolution. Both lead to a decrease in effective dynamic range of the measuring chain.

Many kinds of transducers have been associated with absolute infrasound sensors. Most of them were motion transducers. First ones were pens. More recently, electronic transducers were preferred.

4.2.2.1 Linear Variable Differential Transformer (LVDT)

The LVDT is a type of electrical transformer used for measuring displacement. The transformer has three solenoid coils placed around a tube. One of them, the primary coil, is centered in the central plan. Two others, the secondary coils are symmetrically positioned around this plan. An alternative current is driven trough the primary causing a voltage to be induced in each secondary proportionally to its mutual inductance with the primary. The frequency is usually in the range 1–10 kHz.

A ferritic core, attached to the object whose position is to be measured, slides along the axis of the tube. As the object (and the core) moves, mutual inductances between primary and secondaries change causing voltages induced in the secondary coils to change. The secondary coils are connected in reverse series so that the output voltage is the difference between the two secondary voltages. When the core is in its central position equal voltages are induced in each secondary coil so the output voltage is zero. When the core is moved in one direction, voltage in one coil increases as the other decreases. The magnitude of the output voltage is proportional to the distance between the ferritic core and LVDT central plan, its phase indicates the direction of the displacement.

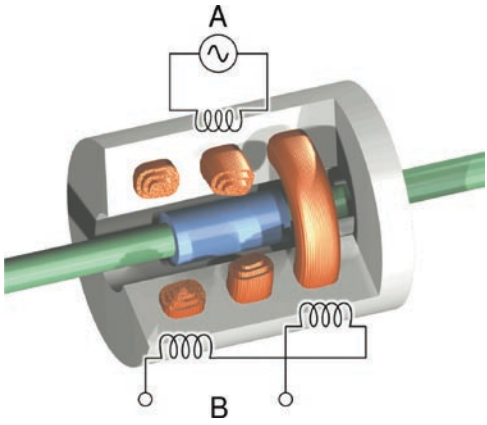

Fig. 4.8 Schematic overview of a linear variable differential transformer. *A* is the excitation for the primary coil. *B* is the output from secondary coils. The ferritic core is represented in *blue*, the mobile element in *green*, the fixed LVDT frame in *gray*

The sliding core does not touch LVDT frame and can move without friction making the LVDT a non contact highly reliable device. The absence of any sliding and rotating contacts allows the LVDT to be completely sealed against the environment (Fig. 4.8).

DASE MB2000 and MB2005 absolute infrasound sensors use a LVDT as displacement transducer. It converts aneroid capsule deflection into a voltage proportional to its mobile end displacement.

Such a transducer has a very wide dynamic range which helps to address issues associated with the dynamic range need for infrasound detectors (e.g., Bowman et al. 2007). For frequencies below 1 Hz, the sensor can measure pressure amplitudes greater than 200 hPa peak to peak (CEA/DASE 1998; Martec 2006). Its response is flat in pressure up to its cut-off frequency that can be adjusted on decades around its nominal cut-off frequency (about 40 Hz). Its electronics is designed to be very stable under IMS conditions.

This signal cannot be digitized totally with common 24 bits recorders as the required dynamic range is too large. A solution consists in filtering signal with a high pass filter but this has to be done with caution as this can induce major phase uncertainties.

An electronic high pass filter is a good solution as it can be made nearly insensitive to environment and aging when properly selected and sealed into a watertight cavity. Furthermore, it can be designed not to induce noise bigger than atmospheric minimum noise down to very low frequencies.

So, LVDT displacement transducers are very suited long range monitoring. They are less suited to temporary measurements because of its power requirements which is generally not smaller than 1.5 W.

4.2.2.2 Magnet and Coil Velocity Transducer

As Haak and de Wilde (1996) first discussed, it is possible to use a magnet and coil velocity transducer as a detector for the aneroid capsule deflection. Such a transducer is robust, has very low noise, and gives the instrument a response in accordance with background noise characteristics. The integration to pressure can be digitally done (Fig. 4.9).

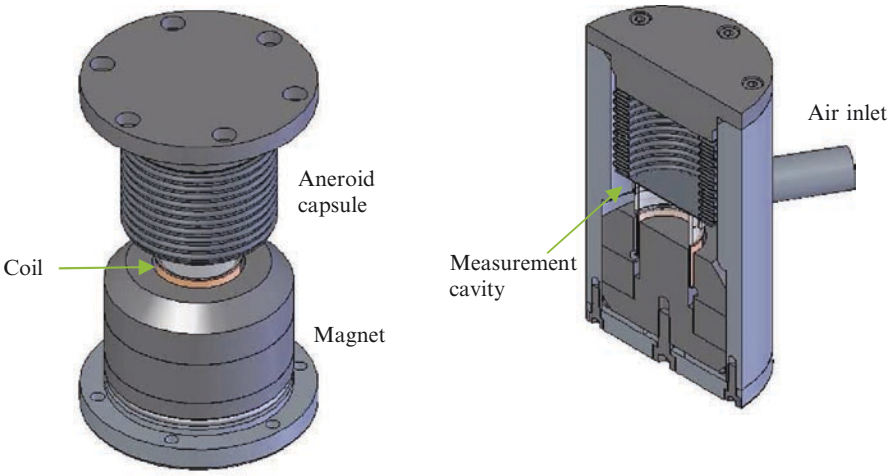

Fig. 4.9 Schematic overview of an absolute infrasound sensor with a magnet and coil velocity transducer (Ponceau 2008)

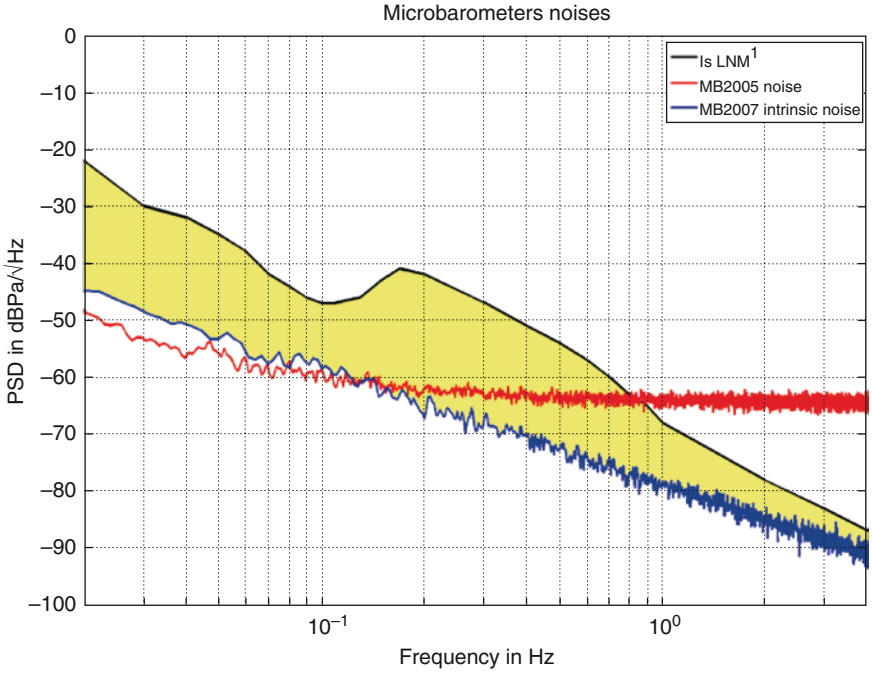

Fig. 4.10 Comparison between MB2007 MB2005 self-noise (Ponceau et al. 2008) and Infrasound Low Noise Model from Bowman (Bowman et al. 2007)

Ponceau et al. (Ponceau 2008; Ponceau et al. 2007) have recently presented a very compact prototype of such a sensor, called MB2007 (Fig. 4.9). Its self noise, plotted on Fig. 4.10, match with Bowman's Infrasound Low Noise Model (Bowman et al. 2007).

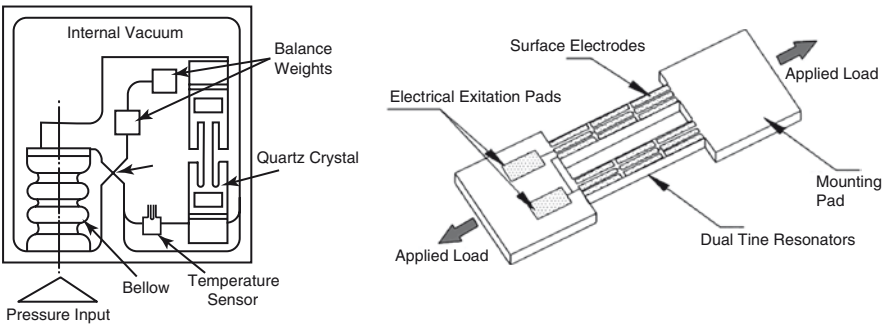

Fig. 4.11 *Left*: Schematic overview of an absolute infrasound sensor with quartz crystal resonator sensing (Paroscientific 2007). *Right*: Schematic overview of a quartz crystal resonator used as a stress transducer (Paroscientific 2007)

Its response in pressure derivate is flat all over the infrasound range. As a result, no phase uncertainties are added and the required recorder dynamic range is smaller.

As a consequence, this passive sensor can be associated with a low power recorder to obtain a measuring chain suitable for temporary experiments.

4.2.2.3 Quartz Crystal Resonator Stress Transducer

Some infrasound sensors use precision quartz crystal resonators (Paroscientific 2007) to sense stress induced by pressure on mechanics. The output of these transducers is the resonant frequency that varies with pressure-induced stress. They are described as transducers with a remarkable repeatability, low hysteresis, and excellent stability (Fig. 4.11).

Marketed sensors are not sensitive enough to solve IS Low Noise Model on the upper part of the infrasound frequency range (Fig. 4.12).

4.3 Differential Infrasound Sensors

Direct measurement of pressure with absolute infrasound sensors induces dynamic range limitations. Electronic solutions have been developed but another common solution to this problem was first introduced by Shaw and Dynes (1905), the differential infrasound sensor. It measures the pressure difference between the inside and outside of a cavity in with a small leak. Short period pressure changes are recorded, while flow through the leak equalizes the interior and exterior pressures for slow changes. Differential infrasound sensors are sometimes called infrasound microphones as they principle of operation is similar to that of acoustic microphones.

Fig. 4.12 Paroscientific DIGIQUARTZ® pressure transducer

One difference is the low frequency bandpass limit, which is lower for infrasound microphones. But the major difference is introduced by Haak and de Wilde (1996), acoustic theory is no longer valid in lower infrasound range where pressure fluctuations are isothermal and not adiabatic.

4.3.1 Principle of Operation, Pressure Sensitive Part

A differential infrasound sensor produces a signal proportional to the difference between the pressure inside the measurement cavity and the pressure in a backing or reference cavity (Figs. 4.13 and 4.14). A small air leak between the two volumes will lead to a pressure equalization over long periods of time. This determines the low frequency response of the system (Rocard 1971).

A differential infrasound sensor is sensitive to temperature differences between both volumes. Thermal insulation need to be carried out with care: a solution is to locate the infrasound sensor a few meters below Earth surface. Furthermore, the volumes can be filled with steel wool or vermiculite as explained by Cook and Bedard (Haak and de Wilde 1996) or Rocard (1971).

A famous example of operational infrasound sensor was described by Rocard (1971). Figures 4.13 and 4.14 show this sensor. Last one is from the original paper.

This sensor consists in two cavities (16 and 18) separated by a bellows (30). Both cavities have similar volumes and are connected through the capillary (31). Front cavity (16) is connected to atmosphere through the capillary (20). Bellows motions induced by pressure changes are measured thanks to an electromagnetic displacement transducer adjusted to match bellows motion range.

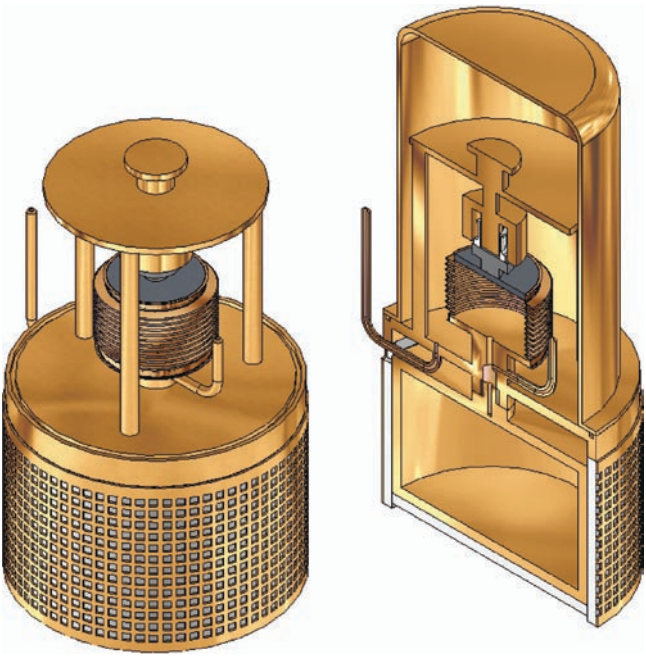

Fig. 4.13 Three dimensions view of the differential infrasound sensor from Rocard (1971)

Here again, thermal insulation was of first interest: reference cavity (18) is covered with a thick thermal insulation, and the sensor was operated inside a thick insulating box (12).

4.3.2 Sensitive Mechanics

The sensitive element may either be a bellows or a diaphragm. Differences in pressure between front inlet and backing volume for long periods are usually small so the bellows can be made quite sensitive to small pressure differences.

4.3.3 Transducers

Mechanics' deflection is converted into an analog voltage by a low noise motion transducer. Many types of transducers have been used. It can be a linear variable differential transducer (LVDT), a capacitive transducer, a magnet and coil velocity transducer, or even an optical transducer as described by Kortschinski et al. (1971).

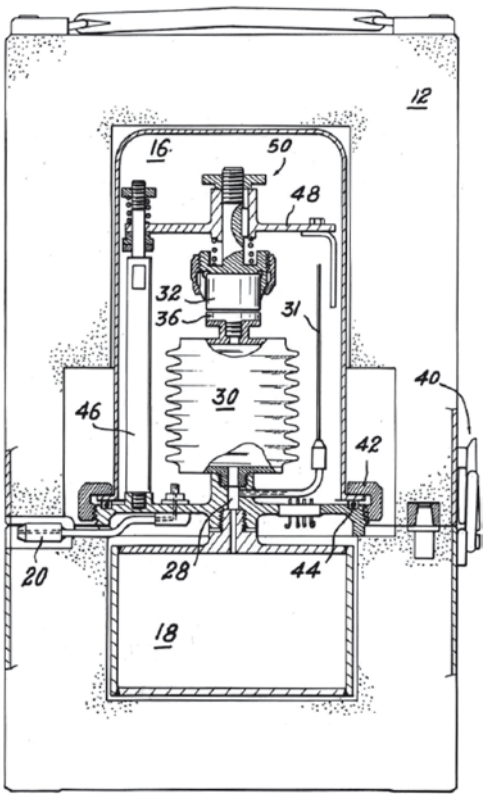

Fig. 4.14 Original view of the differential infrasound sensor from Rocard (1971)

4.3.3.1 Externally Polarized Capacitive Displacement Transducers

Capacitive displacement transducers' principle of operation is well described by Brüel and Kjær (1996). They use the electrical property of "capacitance" to make measurements. Capacitance is a property that exists between any two conductive surfaces within some reasonable proximity. Changes in the distance between surfaces induce changes in capacitance.

These changes in capacitance may be converted to an electrical voltage in two ways. The most simple conversion method uses a constant electrical charge, which is either permanently built into the microphone cartridge or applied to it. Today this method is used for practically all sound measurements.

However, it should be mentioned that the capacitance variations may also be converted to voltage by using high-frequency circuits. High-frequency conversion implies frequency or phase modulation and uses various types of bridge couplings. In principle, such methods work to very low frequencies (even to DC) and therefore are well suited for infrasound measurements. However, in practice the use of these

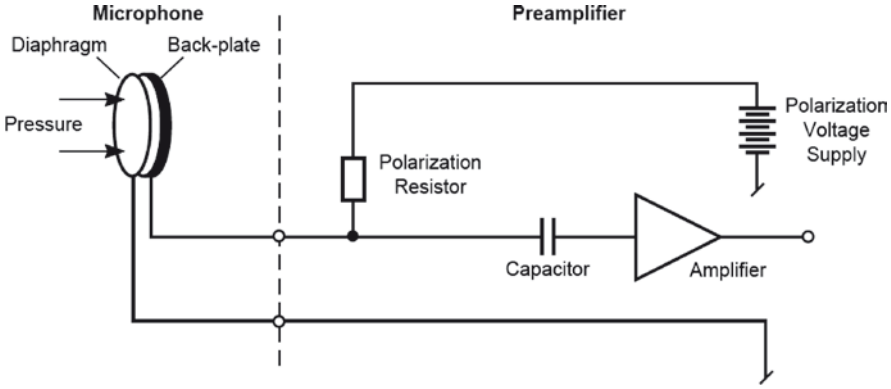

Fig. 4.15 Capacitive Transduction Principle of Brüel and Kjær externally polarized microphones (Brüel and Kjær 1996). The constant electrical charge used for polarization is supplied from an external source

methods is rare because of their complexity, lack of stability, and the relatively high inherent noise levels that these methods imply.

The transduction principle of an externally polarized capacitive displacement transducer is illustrated in Fig. 4.15. For a capacitor formed by two plates: the diaphragm and the back-plate, both plates are polarized by an external voltage source which supplies a charge via a resistor. Movements lead to distance and capacitance changes and to a corresponding AC-voltage across the plates. The AC voltage produced is separated from the polarization voltage by a capacitor placed inside the preamplifier.

4.3.3.2 Prepolarized Capacitive Displacement Transducers

Brüel and Kjær (1996) introduced prepolarized capacitive displacement transducers for measurement microphones in the late seventies and showed by experiments and by extrapolation of measurement results, that such microphones could be made very stable and that they could meet all the requirements set for most applications.

Prepolarized capacitive displacement transducers contain an electret. It consists of a specially selected and stabilized, high-temperature polymer material, which is applied to the top of the back plate. The electret contains trapped or "frozen" electrical charges which produce the necessary electrical field in the air gap. The frozen charge remains inside the electret and stays stable for thousands of years (Fig. 4.16).

Prepolarized microphones are mainly intended for use with battery operated and handheld instruments. Because this type of microphone does not require a polarization voltage it is often selected for temporary measurements to save space and power and allow simpler electronics.

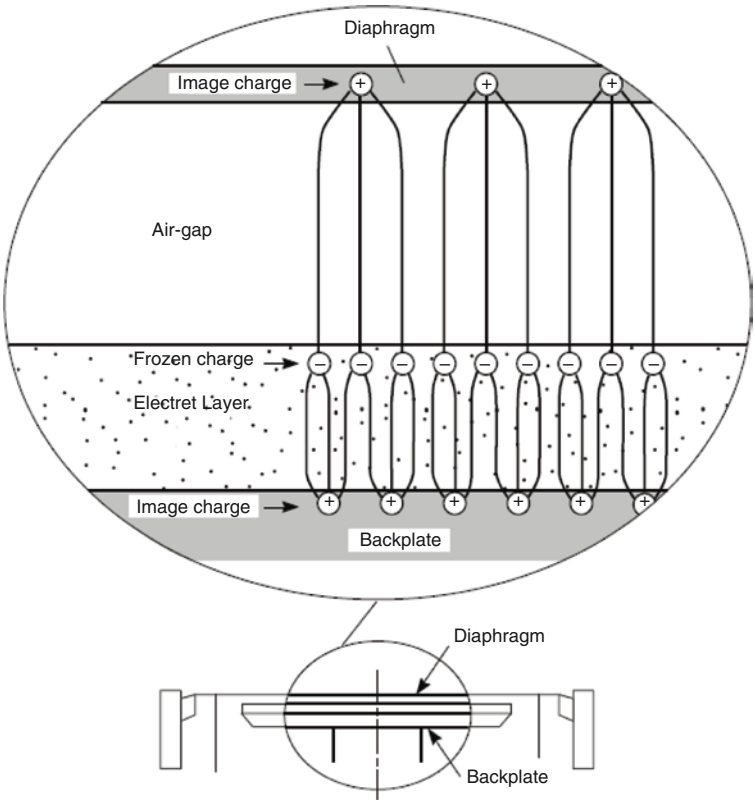

Fig. 4.16 Electret polarization from Brüel and Kjær microphones (Brüel and Kjær 1996). The electret consists of a polymer which contains a permanent or "frozen" electrical charge

4.3.4 Piezoelectric-Based Transducers

Piezoelectric based transducers are now widely used in microphones design. Some of them were characterized by DeWolf (2006) with interesting results.

Such kinds of transducers are now widely used for infrasound measurements and also in distributed arrays (Howard et al. 2008) (Fig. 4.17).

4.3.4.1 Optical Motion Transducer

Kortschinski et al. (1971) presented a differential infrasound sensor using an optical transducer to sense diaphragm deflection. This sensor was not developed to operate on remote locations all over the world (Fig. 4.18), and its self noise was larger than that of modern infrasound sensors. New optics and new interferometry techniques

Fig. 4.17 Piezo-based infrasound sensors from DeWolf (DeWolf 2006)

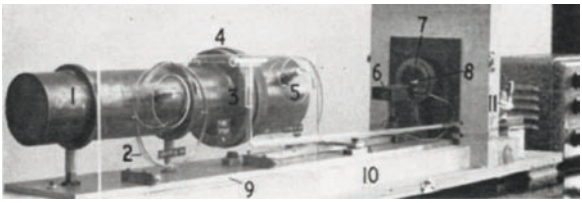

Fig. 4.18 Extract from Kortschinski, 1971 (Kortschinski et al. 1971). The University of Western Ontario (UWO) differential infrasound sensor: *1* chamber 2; *2* capillary tubes; *3* connection to inlet valve; *4* diaphragm tension adjustment nut; *5* chamber 1; *6* photocell housing; *7* condensing lens mount; *8* shaped aperture; *9* aluminum base plate; *10* plywood board; *11* inlet valve

make now possible to consider new developments from motion sensing optical techniques as described by Ponceau et al. (2008).

4.4 Other Infrasound Sensors

4.4.1 Liquid Microbarometer

Kremenetskaya (Bovsherverov et al. 1979; Kremenetskaya et al. 1997) presented liquid infrasound sensors installed in the Apatity seismic array site of Kola Regional Seismological Center of the Russian Academy of Sciences (KRSC). These sensors were selected for their band pass (0.0001–1 Hz) and their ease of operation. Their

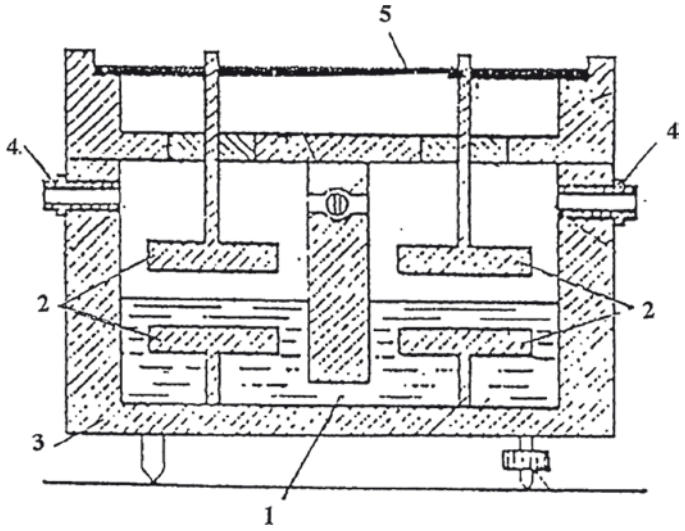

Fig. 4.19 Schematic view of a liquid infrasound sensor from Kremenetskaya (Kremenetskaya et al. 1997): *1* liquid; *2* capacitor plates; *3* body; *4* inlets; *5* electronics

measurements were used in many works (Bovsherverov et al. 1979; Kremenetskaya et al. 1997; Shumilov et al. 2002, 2003).

They were developed by the Institute of Atmospheric Physics RAS (Shumilov et al. 2003). A typical liquid infrasound sensor design is shown in Fig. 4.19. It consists in two measurement cavities. One of the inlets is kept in the atmosphere, other is coupled with a volume (not shown) separated from the atmosphere. Changes in atmospheric pressure induce changes in the relative liquid level in the capacitors. Deviation in liquid level from the balance is transformed into an electric signal by a capacity-voltage converter.

These sensors still may operate with an output sensitivity of about 150 mV/Pa.

4.4.2 Particle Velocity Sensors

A particle velocity sensor is not a conventional infrasound sensor as it does not measure pressure or pressure changes but the velocity of air particles across two tiny, resistive strips of platinum that are heated to about 200°C (de Bree 2007). They also record infrasound waves but through a different physical property, the velocity, which is a vector (and consequently oriented) not a scalar as pressure is.

Van Zon and Evers (2008) recently presented a small aperture high density infrasound array (HDIA) operated by the Royal Netherlands Meteorological Institute (KNMI). This array consists in 80 instruments including 37 pairs of particle velocity sensors closely spaced. Azimuths of the incoming infrasound waves can be calculated from the amplitude ratio between pairs' elements.

4.5 Conclusions

The term *infrasound sensor* mainly stands for the elements of an infrasound measuring chain, which are located between the wind generated noise reducer and the recorder. It measures pressure changes over a very large dynamic range and delivers a dynamic signal adapted to the associated recorder whose input range is limited. No versatile measuring chain is able to solve known Infrasound Low Noise Model and to measure largest infrasound all over infrasound frequency band.

An infrasound sensor can be installed all over the world for a long time under very harsh environmental conditions. Some designs are adapted to operate on worldwide networks and are very robust, reliable, and insensitive to environment but sometimes heavy and power consuming. Others are more adapted to temporary measurements but are not as reliable or insensitive to environment.

On another hand, sensors performances, reliability, and robustness are very different according to the technique used. The sensor to be used has to be chosen with care according to the specifications to reach and the environmental constraints to undergo.

References

Alcoverro B, Heritier T, Martysevitch P, Starovoit Y (2005) Mechanical sensitivity of microbarometers MB2000 (DASE, France) and Chaparral 5 (USA) to vertical and horizontal ground motion. Inframatics 09:1–10

Alcoverro B, Le Pichon A (2002) Frequency response of infrasonic noise reducers. Proceedings of the Infrasound Technology Workshop, KNMI, De Bilt, The Netherlands

Alcoverro B, Le Pichon A (2005) Design and optimization of a noise reduction system for infrasonic measurements using elements with low acoustic impedance. J Acoust Soc Am 117(4): 1717–1727

Bovsherverov BV, Grachev AI, Lomadze CO, Matveev AK (1979) Liquid microbarograph. Izvestiya RAS. Phys Atmos Ocean 15:1215–1218

Bowman JR, Shields G, O'Brien MS (2007) Infrasound station ambient noise estimates and models: 2003-2006, Infrasound Technology Workshop, Tokyo, Japan, 13–16 November 2007

Brüel D, Kjær V (1996) Microphone handbook. Vol. 1, Technical documentation, Juillet 1996

CEA/DASE (1998) MB2000 Technical Manual. October 1998

de Bree HE (2007) The Microflown, E-book. Microflown Technologies, rev. 13-03-2007, www.microflown.com/r&d_books.htm

DeWolf S (2006) Characterizing the mechanical sensitivity of three piezo-based infrasound sensors. Infrasound Technology Workshop, Fairbanks, Alaska

Haak HW, de Wilde GJ (1996) Microbarograph systems for the infrasonic detection of nuclear explosions. Scientific Report WR 96-06, KNMI

Howard W, Dillion K, Shields FD (2008) Locating infrasound events in wind with dense distributed arrays. J Acoust Soc Am 123:3827

Kortschinski J, Murty RC, Curry JC (1971) Microbarograph for meteorological studies: design theory and analysis. J Phys E Sci Instrum 4(4):307–310

Kremenetskaya EO, Kuzmin IA, Raspopov OM, Kulichkov SN (1997) Seismo acoustical equipment complex in Murmansk region. Proceedings of the Infrasound Technology Workshop, Los Alamos National Laboratory, Santa Fe, New Mexico

Martec (2006) MB2005 User manual. Ref: 14643-B, January 2006

Paroscientific Inc (2007) Digiquartz® Pressure Instrumentation
Ponceau D (2008) A low power and low noise infrasound sensor for temporary measurements. J Acoust Soc Am 123:3829
Ponceau D, Millier P, Olivier S (2008) Subnanometric Michelson interferometry for seismological applications. Proceedings from SPIE Photonics Europe 2008, Strasbourg, FR
Ponceau D, Peyraud S, Dupont P (2007) Early developments in absolute infrasound sensors. Infrasound Technology Workshop, Tokyo, Japan, 13–16 November
Rocard Y (1971) Demande de brevet pour procédé et dispositif de détection et d'enregistrement des variations de la pression atmosphérique. DAM/DIREX 0417, 23 November 1971
Shaw WN, Dines WH (1905) The study of fluctuations of atmospheric pressure. Q J R Meteorological Soc 31:39–52
Shumilov OI, Raspopov OM, Kasatkina EA, Kulichkov SN (2002) The high-latitude system for acoustic waves and atmospheric electricity measurements. Proceedings of the Infrasound Technology Workshop, KNMI, De Bilt, The Netherlands
Shumilov OI, Kasatkina EA, Tereshchenko ED, Kulichkov SN, Raspopov OM, Vasiljev AN, Struev AG (2003) Infrasound from the September 24, 2002 Vitim (Siberian) Bolide Detected at Kola Peninsula. Proceedings of the Infrasound Technology Workshop, L2A, La Jolla, California
Van Zon AT, Evers L (2008) A high-density infrasound array of particle velocity sensors in the Nederlands. J Acoust Soc Am 123:3153

Chapter 5
A Review of Wind-Noise Reduction Methodologies

Kristoffer T. Walker and Michael A.H. Hedlin

5.1 Introduction

5.1.1 Importance of Infrasound in Science and Monitoring

Infrasound and longer-period acoustic gravity waves have been of considerable interest since barometers around the world inadvertently recorded infrasound from the 1883 eruption of Krakatau (Evers and Haak 2010). Early recordings showed that, at low frequencies, there is relatively little intrinsic attenuation, facilitating the detection and characterization of large events over great ranges (e.g., Landau and Lifshitz 1959). Infrasound was used to locate enemy artillery in WWI. Infrasound was used as a monitoring tool during the early proliferation of nuclear weapon technologies after WWII when nuclear tests were routinely conducted in the atmosphere. In 1963, the Limited Test Ban Treaty was signed by most nations, and nuclear testing generally went underground. Interest in infrasound as a monitoring tool waned as interest in global seismology increased.

In 1996, the Comprehensive Nuclear-Test-Ban Treaty (CTBT) opened for signature. This treaty is intended to prohibit all nuclear weapon test explosions. Many countries have signed the treaty, but not ratified it. Ratification is an essential step before the treaty can enter into force. The International Monitoring System (IMS) began construction shortly after the treaty was opened for signature. This system will ultimately comprise more than 300 seismic, hydroacoustic, radionuclide, and infrasound stations. Specifically, each of the 60 infrasound stations will comprise an array of infrasound sensors to determine the direction from which signals originated (Christie 1999).

Since the signing of the CTBT and development of the global IMS infrasound network, there has been a renewed interest in infrasound for monitoring and

K.T. Walker (✉)
Institute of Geophysics and Planetary Physics, University of California, San Diego, 9500 Gilman Drive, La Jolla, CA, 92093, USA
e-mail: walker@ucsd.edu

A. Le Pichon et al. (eds.), *Infrasound Monitoring for Atmospheric Studies*,
DOI 10.1007/978-1-4020-9508-5, © Springer Science+Business Media B.V. 2010

scientific research (Christie and Campus 2010; Campus and Christie 2010). In most of these studies, a very limiting constraint is wind; as wind speed increases, the ability to detect infrasound is compromised. For monitoring purposes, this means that each infrasound array in the IMS network has a detection threshold that varies significantly, if not greatly, with local wind speed. Therefore, at any point in time, a certain percentage of the otherwise fully operational network may not be "mission capable." Carefully evaluated and independently verified techniques to reduce the impact of wind on infrasound detection and characterization are of critical importance to the basic infrasound monitoring and research efforts.

5.1.2 Observations of Wind Noise During Measurements of Infrasound

It has been well known for a long time that noise increases on microphones and microbarometers with increasing winds. Figure 5.1 shows a simple example of infrasound in the 1–20 Hz range recorded at Piñon Flat Observatory by a Brüel & Kjær (B&K) microphone with a standard sponge wind filter at a height of 50 cm above the ground in the presence of wind. These spectra are a result of averaging the Fourier transforms of two-minute windows where the median wind speed was in one of four bins (0–2, 2–4, 4–6, and 6–8 m/s). The 7 m/s bin had far fewer spectra than the other three bins. The leveling off at 1 Hz is due to the instrument response of the microphone. The noise in this case generally increases uniformly by ~5 dB per m/s. Estimates at frequencies of 0.01–0.5 Hz vary from 2 to 7 dB per m/s (McDonald et al. 1971; McDonald and Herrin

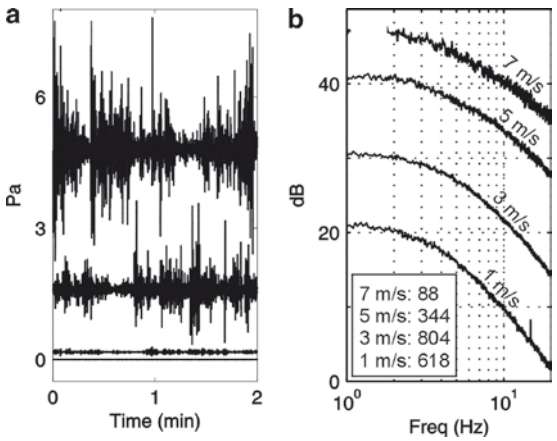

Fig. 5.1 Infrasound recordings in the 1–10 Hz band. Time series (**a**) and average spectra from many 2-min time series (**b**) are shown for four different wind speeds

1974; Hedlin and Alcoverro 2005). Indeed, a 0.05-Pa infrasound signal clearly recorded in 1 m/s winds would be completely masked in 4–5 m/s winds without a better wind filter.

5.2 Wind-Noise Theory

5.2.1 The Physics of Wind

To understand the wind-related noise and design wind-noise resistant technologies or stations, it is helpful to review the basic physics of wind. Wind is caused by spatial differences in atmospheric pressure and is a common part of the diurnal meteorological cycle in most parts of the world. Much of the following discussion comes from Panofsky and Dutton (1984). The first 1–2 km above the ground is called the "friction layer" or the "planetary boundary layer" (PBL), after Lettau (1939). The PBL is defined by the vertical exchange of momentum, heat, and moisture due to surface effects. The top of this layer is often visible to airplane pilots because it contains dust, smoke, and aerosols. The thickness of the PBL can also be detected by acoustic sounders in the 1–3 kHz range and is predicted by a linear relationship with wind speed at 10 m height (e.g., Koracin and Berkowicz 1988).

Wind is intimately related to atmospheric turbulence. There are two types of turbulence: convective and mechanical. Convective turbulence is driven by thermal instability and is the predominant mechanism of mixing in the troposphere. Clouds are often a manifestation of this turbulence. Mechanical turbulence is created by the interaction of the wind with topography and ground-based objects.

A vertical profile in which temperature increases with height is an "inversion" (Fig. 5.2). During the day, solar heating warms the surface and the lower PBL, the top of which occurs at the height z_i. This is the height to the lowest inversion, where the sign of the temperature gradient changes. Because the warmer air near the surface is gravitationally unstable, both convective and mechanical turbu-

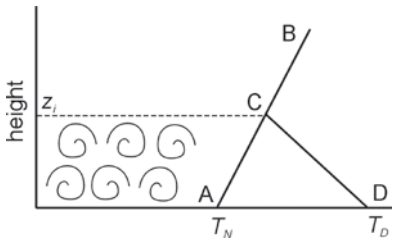

Fig. 5.2 Temperature profiles during the night (AB; inversion) and day (BCD; inversion between CB). The temperature in the surface layer warms during the day, which is one mechanism for driving wind. T_n and T_d are the nighttime and daytime temperatures, respectively

Table 5.1 Surface roughness values (from Panofsky and Dutton 1984)

Ground cover	Roughness length (m)
Water or ice[a]	10^{-4}
Mown grass	10^{-2}
Long grass, rocky ground	0.05
Pasture land	0.20
Suburban housing	0.6
Forests, cities	1–5

[a]Surface roughness increases with wind speed over water

lence occur at a variety of scales producing wind. In some cases, the scales are quite large because of geographical differences in surface heating and can lead to regional horizontal winds. Nonetheless, smaller scale turbulence occurs and defines a mixing layer (surface layer) of thickness h, which is approximately equal to z_i during the day.

An inversion often extends down to the surface at night, making the air gravitationally stable (Fig. 5.2). Consequently, wind and turbulence are often less pronounced at night. However, minor mechanical turbulence still occurs in the lower portions of the surface layer ($h < 100$ m) on clear nights with weak winds.

"Turbules" are defined as self-similar localized eddies (e.g., deWolf 1983; McBride et al. 1992; Goedecke and Auvermann 1997). Wind speed varies as a function of height because of surface friction. In pure mechanical turbulence, the winds in the surface layer are the slowest at the ground level and increase logarithmically with height (e.g., Thuillier and Lappe 1964; Chen 1997). In convective turbulence, the variation of wind speed with height can be much more complex and is often described by a power law over some height range. In either case, the reduction in speed at ground level is a function of the surface roughness, a length that characterizes the size of mechanical turbules (Table 5.1). The surface roughness is also a measure of how efficiently momentum is transferred from the wind into the ground. For example, a dense forest or craggily mountainous terrain has a high roughness and can lead to a great reduction in surface wind. Above relatively smooth surfaces, one can expect a significant increase in wind speed simply between 1 and 3 m height. For example, Berman and Stearns (1977) recorded an ~20–40% difference in wind speed between these two heights in light winds (2–5 m/s).

5.2.2 Predicting Turbulence Potential from Meteorological Data

The potential for turbulence can be calculated from basic meteorological data. Because both mechanical and thermal forcing influences turbulence, a predictive measurement is needed that superimposes the effects of both. Monin and Obukhov

(1954) derived two scaling parameters in the surface layer. The first is the surface friction velocity

$$u_* = \sqrt{\tau / \rho}, \tag{5.1}$$

where ρ is the density and the surface Reynolds stress is $\tau = \rho K_{\mathrm{m}} \partial \overline{u_{\mathrm{x}}} / \partial z$, where $\overline{u_x}$ is the mean wind speed in the wind direction and K_m is the eddy viscosity of the order 1 $\mathrm{m^2\,s^{-1}}$. The second scaling parameter is the Monin-Obukhov length

$$L = -\frac{u_*^3 c_p \rho T}{k_{\mathrm{a}} g H (1 + 0.07 / B)}, \tag{5.2}$$

where c_p is the specific heat at constant pressure, T is the temperature, k_a is the von Karman constant, g is the acceleration due to gravity, H is the vertical heat flux, and B is the Bowen ratio

$$B = -\frac{T_H - T_L + 0.01\Delta z}{2500(q_H - q_L)}, \tag{5.3}$$

where T and q are temperature and humidity at a high and low reference point separated by Δz in the surface layer. In general, L is essentially independent of height, is computed from near-surface measurements, and varies mostly because of variations in u_* and H.

The important parameter that superimposes the effects of thermal and mechanical forcing is the ratio z/L, where z is the height above the ground. This ratio is a measure of the relative importance of mechanical and thermal forcing in the characterization of atmospheric stability. Strongly negative values indicate a dominance of convective turbulence. Smaller negative values are associated with a dominance of mechanical turbulence. Zero means there is pure mechanical turbulence (theoretical case at the ground level). Slightly positive values suggest mechanical turbulence is damped by temperature stratification. Strongly positive values indicate strong damping of turbulence.

5.2.3 *Geographic Influences on Wind*

Careful site selection as a strategy for the abatement of wind noise can benefit greatly from knowledge of the local wind patterns. Much of this section is from Pidwirny and Budikova (2006). As mentioned earlier, wind is derived by spatial differences in atmospheric pressure, which are usually directly related to changes in temperature due to solar heating and surface radiation. Because these differences occur at a variety of scales, they interfere with each other to give rise to the observed local conditions. At a global scale, the equatorial regions experience more solar heating than at the poles. Warming through conduction and convection, the air flows upward and toward the poles, where cooling causes the air to flow

down to the surface and back to the equatorial regions. As viewed from a frame of reference that is fixed in the forward flow, the Coriolis effect deflects the flow toward the right and the left in the northern and southern hemispheres, respectively, leading to three circulation cells in each hemisphere. This system drives most of the global circulation patterns, which are ultimately modulated by regional and local influences.

In the continental interiors, regional variations in solar heating during the day influence convection patterns. Solar heating of the surface warms the air via conduction, the air ascends, horizontal pressure gradients form, and convection pulls in air from other regions that are cooler, such as those beneath cloud cover (Fig. 5.3). The horizontal winds usually do not travel straight lines between the high- and low-pressure regions because of influences by global circulation patterns. This idealized system only works during the day; at night, there is no variation in surface heating or cooling to drive convection and surface winds.

Coastal environments can lead to a similar pattern of convection during the day. Because of the specific heat capacity of water and mixing with deeper layers, the water surface does not heat up as much as the land surface (Fig. 5.4). This can lead to differential surface/air heating, a horizontal pressure gradient, and onshore surface winds.

Unlike continental interiors, coastal environments can also drive convection systems at night. After sunset, the heated land surface continues to radiate heat and eventually becomes cooler than the air temperature, at which point heat is transferred from the air to the ground. Conversely, the water surface stays at a relatively fixed temperature and continues to transfer heat to the air. This reverses the pattern shown in Fig. 5.4, leading to offshore surface winds.

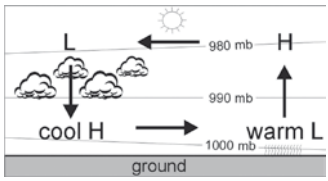

Fig. 5.3 Regional influences on wind in an intracontinental setting during the day. Differences in solar heating at the surface leads to horizontal air temperature and pressure gradients that can lead to a closed convection system

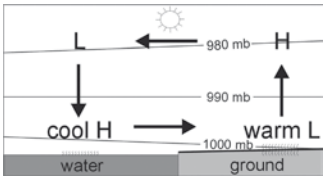

Fig. 5.4 Regional influences on wind in a coastal setting during the day. The specific heat capacity of water leads to differences in solar heating and cooling of the surface, which can drive a close convection system

Whereas the above regional systems are diurnal in nature, there are also seasonal influences on wind over continental spatial scales. In certain equatorial regions, the average daily temperature of the inner continental land surface is greater than that of the adjacent water surfaces. This leads to onshore "Monsoon" winds during the summer that persist diurnally. In some locations and times of the year, these humid winds are diurnally uniform. The situation is reversed during the winter, and the region is dominated by dry offshore winds.

Mountains also affect wind patterns. Despite the obvious obstacle that mountains present to winds driven by global convection systems, mountains also act as sources of heat during the day. Solar heating of their slopes leads to a flow of air up and above the mountain to the height of the surface layer where it is deflected. In the specific case of a valley, heating on both adjacent slopes can give rise to a circulation system with vertical return flow above the axis of the valley. At night, the mountains are heat sinks rather than heat sources; the convection pattern is reversed.

5.2.4 Taylor's Hypothesis

Of fundamental importance to wind-noise theory, Taylor (1938) hypothesized that turbules and their associated observables are spatially fixed time-invariant anomalies. This hypothesis is often called "Taylor's frozen turbulence hypothesis." If correct, this predicts that the statistical properties of flow in time measured at a single point can be used to infer the two-dimensional spatial characteristics of turbulence within the limitations placed by variations of local topography.

There have been numerous verifications of Taylor's hypothesis (e.g., Favre et al. 1962; Frenkiel and Klebanoff 1966; Panofsky 1962). Measurements on aircraft have also been compared to those from towers to test this concept (e.g., Panofsky and Mazzola 1971; Kaimal et al. 1982). These aircraft fly along the mean wind direction so quickly that they effectively sample space instantaneously. The results suggest that short-wavelength structures move with the mean wind (e.g., McDonald et al. 1971), but large-scale structures move at their own velocities in contrast to Taylor's hypothesis.

Although Taylor's hypothesis appears to be generally valid at higher frequencies, studies have shown that turbules are not indefinitely time invariant. Rather, they decay with distance traveled by an amount that is proportional to their length scale; smaller turbules decay faster over shorter distances traveled than larger turbules.

Shields (2005) analyzed pressure data from two strings of microphones located on the ground: one along the wind direction and one perpendicular to it. He calculated the cross-correlation between the reference sensor (the one at the intersection of the two strings) with the other sensors at greater distances in the downwind and crosswind directions (Fig. 5.5). In the downwind direction, what is observed by the reference sensor is observed some time later by the downwind sensors, but the correlation is gradually reduced with time/distance.

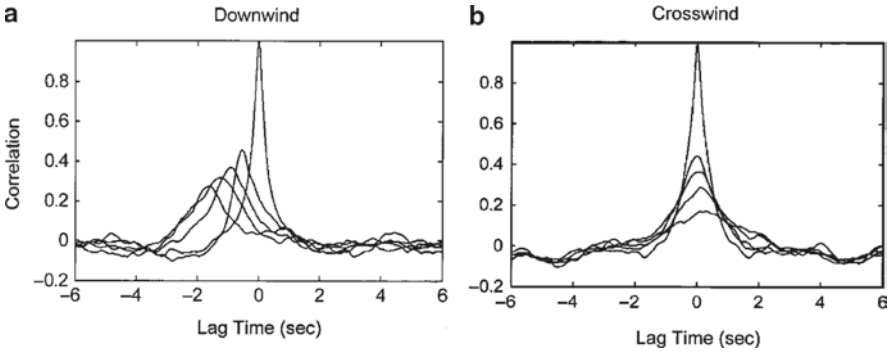

Fig. 5.5 Quantification of Taylor's frozen turbulence hypothesis. Shown are the cross-correlation functions between a reference microphone and microphones at increasing distances in the downwind (**a**) and crosswind (**b**) directions. The sensor separations in the downwind and crosswind directions are 1.2 and 0.6 m, respectively. Modified from Shields (2005)

Indeed, in time/distance space, the slope of the line that connects the points associated with the maxima in (Fig. 5.5a) is equal to the mean advection velocity (~2.7 m/s). If the sensors themselves are not modifying the turbulence, then this suggests Taylor's hypothesis is only a first-order approximation at typical infrasound frequencies. In the crosswind direction, there is also some correlation, but the peak is at zero lag for all sensors, simply reflecting the crosswind spatial coherence length.

5.2.5 Turbulence Length Scales and Noise Spectra

As proposed by Kolmogorov (1941), turbulence velocity spectra are separated into frequency ranges that are associated with three spatial scales of turbulence: source region (large scales and low frequencies), inertial subrange (intermediate scales and frequencies), and dissipation region (small scales and high frequencies). The source region comprises large eddies with length scales of tens of meters to kilometers. The spectral characteristics of this range are not isotropic; the characteristics depend on many variables, including wind, surface roughness, and height of the surface layer. Mixing within the PBL causes energy-containing eddies from the source region to fragment into smaller eddies without energy dissipation. This mixing without dissipation defines the isotropic inertial subrange, with eddy length scales of less than the height above the surface, but larger than the Kolmogorov microscale, which is the smallest scale of turbulence defined by

$$\eta = \left(\frac{\nu^3}{\varepsilon} \right)^{1/4}, \tag{5.4}$$

where ε is the dissipation rate of turbulence into heat and ν is the kinematic (or molecular) viscosity. Continued mixing leads to eddies that are smaller than the Kolmogorov microscale, defining the isotropic dissipation range where molecular mixing dissipates energy over a length scale on the order of millimeter in the surface layer, which is too small to be of concern here.

Wind noise in the infrasound band pertains to the source region and the inertial subrange. Identifying these ranges in spectra of recorded wind noise is important for understanding what type of wind noise is being recorded, which ultimately helps one design or choose the optimum wind-noise filter. For a stationary sensor, the frequency separating the source region on the low side from the inertial subrange on the high side for wind-speed fluctuations in the downwind direction is defined by $fz/\overline{u} > 1$, where f is the frequency, z is the sensor height, and $\bar{u}$ is the mean wind speed (Panofsky and Dutton 1984). Figure 5.6 is a graph depicting this relationship for 10 logarithmically spaced wind speeds. For a fixed wind speed, the inertial subrange moves to lower frequencies as the sensor height increases. For a sensor precisely at the ground level, the inertial subrange is undefined, and the entire infrasound spectrum is in the source region. For a fixed sensor height, the source region moves to higher frequencies as the wind speed increases. The IMS arrays have effective sensor heights from 5 to 40 cm and wind speeds that typically extend up to 5 m/s. Therefore, for any given spectra of recorded pressure, one can expect to find this boundary above ~0.2 Hz. For wind speeds of at least 1 m/s, the boundary is above ~3 Hz.

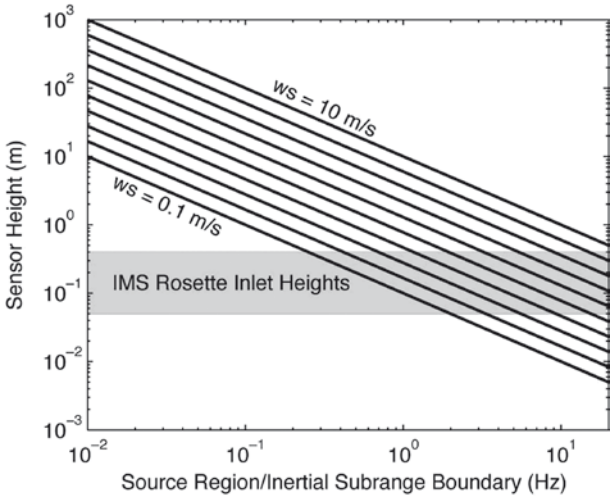

Fig. 5.6 Frequency boundary between the source region at the low end and the inertial subrange at the high end as a function of wind speed and sensor height for wind velocity spectra

5.2.6 *Types of Wind Noise*

In the following section, we discuss four types of wind-related "noise." More detailed discussions of this can be found in Shields (2005), Raspet et al. (2006), and Raspet et al. (2006).

5.2.6.1 Wind Velocity Fluctuations

For the inertial subrange, Monin and Yaglom (1975) show that the power density spectrum of the wind velocity in the downwind direction is

$$V_{11}(k_1) = a_2 \varepsilon^{2/3} k_1^{-5/3}, \tag{5.5}$$

where a_2 is a constant and k_1 is the wave number in the wind direction assuming Taylor's hypothesis

$$k_1 = 2\pi f / \overline{u} \tag{5.6}$$

Recent observations have shown that the −5/3 power laws accurately describes the velocity spectra in the inertial subrange (Shields 2005; Raspet et al. 2006).

5.2.6.2 Interactions Between the Sensor and the Wind

As an object deflects wind, kinetic energy is converted into pressure energy. The pressure at the head of the body directly in front of the wind is called the "stagnation pressure" and is the maximum pressure on the body due to the deflection of the wind. Fluctuating wind velocity can therefore give rise to fluctuating stagnation pressure on pressure-sensing surfaces. Raspet et al. (2006) derived two equations for the stagnation pressure density spectrum in the inertial subrange. Because stagnation pressure depends on the bluffness and geometry of the sensor, effects that are easier to determine empirically than theoretically, they suggest that recorded wind-velocity spectra can be used to predict stagnation pressure and the upper limit of recorded infrasound wind noise in the inertial subrange. Specifically, the stagnation pressure is

$$P_s(k_1) = \rho^2 \overline{u}^2 \left| \overline{V(k_1)} \right|, \tag{5.7}$$

where P_s is the stagnation pressure power density and $\left|\vec{V}\right|$ is the power spectral density of the recorded wind velocity magnitude. A second equation for the stagnation pressure is

$$P_s(k_1) = 1.14\rho^2 \left(\overline{u}^2 + 3.67\overline{u^2}\right) \left(\frac{V_{11}(k_1^0)}{(k_1^0)^{-5/3}} \right) k_1^{-5/3} - 5.89 \left(\frac{V_{11}(k_1^0)}{(k_1^0)^{-5/3}} \right) k_1^{-7/3}, \tag{5.8}$$

where the quantity $V_{11}(k_1^0)$ is the power spectral density of the wind velocity in the downwind direction evaluated for a reference wave number k_1^0 at which there is a good fit of a −5/3 power law curve to the spectra of recorded wind velocity in the downwind direction, and

$$\overline{u^2} = \frac{1}{3}\left(\overline{u_x^2} + \overline{u_y^2} + \overline{u_z^2}\right) \tag{5.9}$$

is the mean of the mean of the squared velocities in the downwind, crosswind, and vertical directions. Predicting P_s is potentially advantageous in the testing of wind-noise reduction methodologies since it eliminates the need for a reference pressure sensor. However, use of the aforementioned equations in the inertial subrange requires a research-grade anemometer that is capable of output sampling rates that are commonly used for microphones (at least 20 Hz). Many of the current IMS anemometers are not capable of such high output rates.

Equations (5.7) and (5.8) are only valid in the inertial subrange. Raspet et al. (2006) extended the turbulence–sensor interaction theory into the source range and introduced

$$P_s(k_1) = \frac{1.44\overline{u}^2 C}{\left[1+(k_1\lambda)^2\right]^{5/6}} + \frac{1.451C^2}{\lambda\left[1+0.1129(k_1\lambda)^2\right]^{5/6}}, \tag{5.10}$$

where C and λ are fit parameters, the latter of which being a length parameter that reflects the location of the transition from the source region to the inertial subrange. These two fit parameters are determined by fitting of the following function to the downwind velocity spectrum

$$V_{11}(k_1) = \frac{C}{\left[1+(k_1\lambda)^2\right]^{5/6}} \tag{5.11}$$

Note that the first term of the pressure equation is simply the velocity spectrum multiplied by $1.44\overline{u}^2$. The second term is constant for low wave numbers and decays as $k_1^{-5/3}$ for high wave numbers. The authors verified that in the inertial subrange, the predictions from equation (5.10) match those from equations (5.7) and (5.8).

5.2.6.3 Pressure Anomalies Advected Across the Sensor

Turbulence–Turbulence Interaction

Taylor's hypothesis predicts that pressure anomalies that develop in turbulent flow in the absence of sensor interference (that is characterized by turbulence–sensor interaction) may be advected with the mean wind speed across a sensor, leading to another type of wind noise. There have been two possible sources of these advected pressure anomalies discussed in the literature. George et al. (1984) describe these sources based on a review of published measurements and identifications of different

pressure fluctuations sources from a turbulent jet without interference from noise associated with wind/sensor interaction. Pressure anomalies can be generated due to the interaction between turbules. Miles et al. (2004) show that this "turbulence–turbulence interaction" is the dominant source of turbulence-induced pressure in the inertial subrange above some threshold sensor height.

Dimensional analysis has been used to derive the pressure power spectral density for turbulence–turbulence interaction, as shown in Monin and Yaglom (1975)

$$P_t(k_1) = a_1 \rho^2 \varepsilon^{4/3} k_1^{-7/3}, \tag{5.12}$$

where a_1 is a constant. This −7/3 pressure power law was also derived by analytical techniques (Hill and Wilczak 1995). However, Miles et al. (2004) found using "Large Eddy Simulation" that this law needs further evaluation for cases where the atmosphere is thermally stratified and stable (strongly positive z/L).

More recently, two equations have been derived that permit the prediction of the turbulence–turbulence pressure spectrum from the velocity spectrum in the inertial subrange. Batchelor (1951) and Raspet et al. (2006) derive

$$P_t(k_1) = 7.60 \left(\frac{V_{11}(k_1^0)}{(k_1^0)^{-5/3}} \right) k^{-7/3} \tag{5.13}$$

Miles et al. (2004) also calculated a velocity and pressure power density from a "large eddy simulation" (LES) and fit their synthetic data and statistics from their simulations to scaling laws based on work by Obukhov (1941). They derive

$$P_t(k_1) = 10.2 \left(\frac{V_{11}(k_1^0)}{(k_1^0)^{-5/3}} \right)^2 k^{-7/3} \tag{5.14}$$

The aforementioned equations are only valid in the inertial subrange, and as with equation (5.8), one must evaluate the velocity spectrum at a reference wave number k_1^0 where the −5/3 power law fits the velocity spectrum well. Raspet et al. (2008) extended the theory to the source region, resulting in

$$P_t(k_1) = 0.811 \frac{C^2}{\lambda} \frac{1}{\left[1 + 0.1792 (k_1 \lambda)^2\right]^{7/6}} \tag{5.15}$$

At low wave numbers, the predicted pressure spectrum is constant, whereas at high wave numbers, the spectrum decays as $k_1^{-7/3}$.

Turbulence–Mean Shear Interaction

The vertical gradient of the average horizontal wind velocity near the ground acts as an impedance to turbules. Turbulence in this region creates another source of pressure fluctuations called "turbulence–mean shear interaction." Raspet et al. (2006) also developed an empirical equation for this that is valid in the source region and inertial subrange,

$$P_{\mathrm{m}}(k_1) = 7.38CK^2 \frac{\lambda^2 (k_1\lambda)^{5/3}}{\left[1+1.622(k_1\lambda)^2\right]^{8/3}} \tag{5.16}$$

In contrast with the constant spectra at low wave numbers for turbulence–sensor and turbulence–turbulence interaction, the turbulence–mean shear interaction spectrum increases as $k_1^{5/3}$ to a peak just before the transition to the inertial subrange where it decays as $k_1^{-11/3}$.

Correlation Distance of Turbulence

Shields (2005) examined pressure and wind data from 28 piezoelectric microphones on the ground and spaced parallel and perpendicular to the dominant wind direction at three field sites. He expanded upon previous results (e.g., Priestley 1966) and derived a model for the narrow-frequency-band correlation of recorded pressure as a function of sensor separation in the downwind and crosswind directions for the 0.2–2.0 Hz range. These correlations are the cross-correlations at zero lag time; these equations have no bearing on Taylor's hypothesis and only describe the spatial structure of turbulence during a snapshot in time.

$$R(x) = \mathrm{e}^{-3.2x} \cos(2\pi x) \tag{5.17}$$

and

$$R(y) = \mathrm{e}^{-7y} \cos(2\pi y) \tag{5.18}$$

where x and y are the separations in unit wavelength, which is defined by the sensor separation divided by the advective wavelength

$$\lambda = \overline{u_x} / 2\pi f \tag{5.19}$$

This is just the inverse of the advective wave number k_1 (5.6). Figure 5.7 shows Shields' results. The similarity between the measurements in each graph indicates that the spatial coherence length is linearly proportional to the size of the turbules over a wide range of length scales. In other words, the spatial characteristics of turbulence have a self-similar appearance. For example, defining the coherence length by the minimum distance to zero correlation, in 3 m/s wind, wind noise at 1 Hz has a coherence length of 0.1 and 0.3 m in the downwind and crosswind directions, respectively. In the same wind, the coherence lengths at 0.1 Hz are 1 and 3 m. Similarly, doubling the wind speed doubles these coherence lengths.

Of fundamental importance, Shields' results confirm the lower and slightly frequency-dependent results of Priestley (1966) that there is an exponential decay in the correlation in all directions (including vertical), but that the downwind direction has an additional periodic factor that oscillates about the zero axis. These results predict that spatial averaging of infrasound along a line parallel to the wind direction, rather than along any other line, results in the greatest attenuation of wind

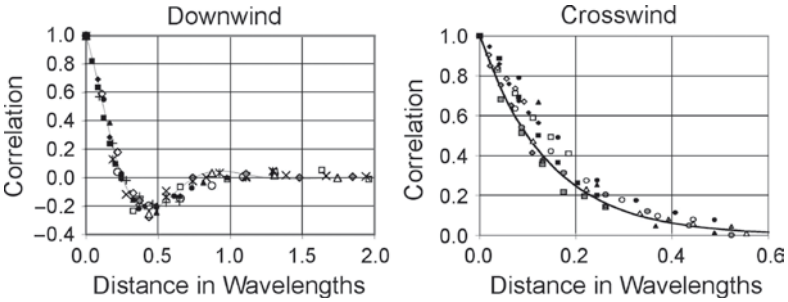

Fig. 5.7 Measured pressure correlation coefficients as a function of unit wavelength in the downwind and crosswind directions for three different field sites and central frequencies from 0.2 to 2.0 Hz. There is a periodicity to the correlation in the downwind direction. The graphed curves are the fits to lower-frequency data in Priestley (1966). Modified from Shields (2005)

noise associated with turbulence–sensor, turbulence–turbulence, and turbulence–mean shear interaction. Specifically, for frequencies where the sensor separation is greater than the coherence length as defined above, one will get approximately $n^{1/2}$ reduction in wind noise for the crosswind direction, but better than $n^{1/2}$ for the downwind direction providing that the sensor separation is not so large as to exclude the negative lobe in the correlation function. Shields specifically reports a "better than $n^{1/2}$" for the 0.5–5.0 Hz range in the downwind direction for his sensor spacing in the 4–8 m/s wind speed range (wind speed was recorded at 3 m height).

5.2.6.4 Acoustic Energy Generated by Wind

It is well known that the interaction of wind with objects can lead to acoustic energy radiation. At larger scales, it has been shown that wind can interact with mountain peaks to radiate infrasound in the 0.01–0.1 Hz band that can travel great continental distances (Larson et al. 1971; Rockway et al. 1974). Turbulent storm systems can also radiate infrasound (e.g., Gossard 1956; Bowman and Bedard 1971; Georges and Greene 1975).

Wind can also indirectly generate infrasound. For example, as the winds increase, so do the size of ocean swells, which can lead to higher surf and more energetic surf infrasound (Garcés et al. 2003; Arrowsmith and Hedlin 2005) and the interaction of intersecting swell patterns (microbaroms; e.g., Garcés et al. 2004). Furthermore, wind also leads to seismic disturbances, which can couple into infrasound via seismic-to-acoustic coupling or create artificial pressure signals if the infrasound sensor is sensitive to seismic shaking.

5.2.6.5 Distinguishing between Wind Noise Types

In designing and testing wind-noise reduction technologies, it is helpful to understand the type of wind noise one is recording and attempting to reduce. Using the

aforementioned equations may help as they predict distinctly different spectra with unique slopes. For example, the recent Raspet et al. (2006) predictions for turbulence–sensor (TS), turbulence–turbulence (TT), and turbulence–mean shear (TMS) interaction suggest that at a height of 1 m, in order of increasing influence in the contribution to wind noise is TMS, TT, and TS for the inertial subrange. In the source range, the contribution to wind noise is TT, TS, and TMS. More observations are required to tests these relations at different heights and at lower frequencies, but Raspet et al. (2006) found that 0.6 and 1.0 m spherical microphone wind screens attenuated wind noise to the same level as that predicted by turbulence–turbulence interaction in the inertial subrange, suggesting that successively larger wind screens would not provide additional improvement.

Similarly, Raspet et al. (2006) analyzed some data presented by Shields (2005). Figure 5.8 shows the pressure spectra recorded by a variety of sensors with different exterior shapes and sizes: (a) a bare B&K 1/2-inch microphone, (b) a piezoelectric sensor, (c) a microphone in a 0.18 m windscreen, and (d) a microphone in a 0.90 m windscreen. Predicted spectra are plotted for turbulence–sensor interaction (a and b), turbulence–turbulence interaction (c and d), and self-noise for the 0.18 and 0.90 m windscreens (E and F). The bare microphone has a spectrum that is fairly close in amplitude and slope to that predicted by the turbulence–sensor interaction. This predicted spectrum serves as an upper limit on the expected wind noise given no wind-noise reduction filters.

Wind noise predicted by turbulence–turbulence interaction correlates with that measured by the 0.9 m windshield sensor (d). However, this may be a coincidence

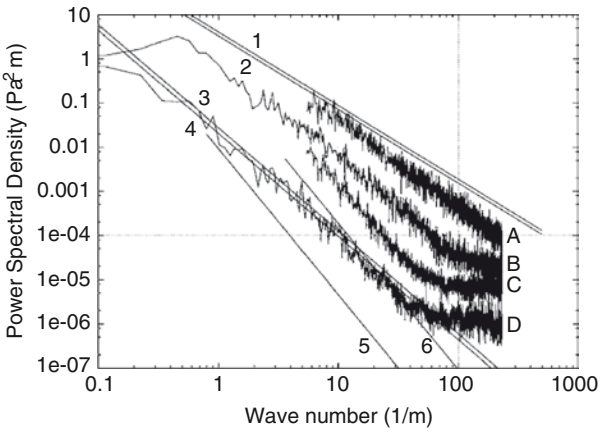

Fig. 5.8 Power spectral densities of wind-noise pressure recordings from four different sensors (A–D) compared with six predictions of wind-noise pressure spectra (1–6). Recordings are made with a bare B&K 1/2-inch microphone (**a**), a piezoelectric sensor (**b**), a microphone in a 0.18 m windscreen (**c**), and a microphone in a 0.90 m windscreen (**d**). Predictions are for Raspet et al. turbulence-sensor interaction (1–2), Batchelor turbulence-turbulence interaction (3), Miles et al. turbulence-turbulence interaction (4), self-noise for the 0.18 m windscreen (5), and self-noise for the 0.90 m windscreen (6). Slightly modified from Raspet et al. (2006)

given that the height of the anemometer was at 1 m while the pressure sensor in the 0.9 m ball was at 0.45 m, meaning that the wind noise predictions were for a higher elevation than those of the sensor.

The pressure spectra recorded by the piezoelectric sensors are about 20 dB greater than that predicted by turbulence–turbulence interaction. If the turbulence–turbulence predictions are accurate, this suggests that the dominant mechanism for the wind noise recorded by Shields is not due to the advection of pressure anomalies across the microphone. Shields collocated one of the piezoelectric sensors with a B&K microphone inserted in a Quad Disk enclosure. A Quad Disk is a tube with four disks mounted over four holes in such as way as to provide a point inside the tube where one can measure pressure that is independent of wind speed and direction (Nishiyama and Bedard 1991). Wyngaard et al. (1994) developed a technique to predict the effect of velocity variations on pressure measurements, and he showed that the Quad Disk should be insensitive to turbulence–sensor interaction. Shields argues that the spectra obtained by both the B&K and the piezoelectric sensors were similar, suggesting that the piezoelectric sensor was not measuring turbulence–sensor noise. Shields also reports that the magnitude of pressure in the 0.5–2.5 Hz band recorded by the piezoelectric sensors at all three sites falls within an upper and lower bounds estimated by Bedard et al. (1992) by analyzing three months of Quad Disk pressure data recorded in various winds. These data show a scatter of up to 10 dB between the bounds, which is considerably less than the 20 dB difference between Shields observations and the turbulence–turbulence prediction, suggesting that the piezoelectric sensors are not greatly influenced by wind–sensor interaction. Based on the good fit of the turbulence–turbulence predictions with the wind-screened microphones, Raspet et al. interprets the piezoelectric sensors to be quite aerodynamic and dominated by fluctuations of a smaller stagnation pressure.

5.3 Wind-Noise Reduction Methodologies

Wind-noise reduction technologies seek to reduce all types of wind noise while preserving signal energy. Most of the strategies to date have focused on reducing turbulence–sensor, turbulence–turbulence, and turbulence–mean shear interaction. As discussed earlier, these types of noise depend on the length scales of the turbules. As predicted by Taylor's hypothesis, the frequency of the noise from a single turbule with largest diameter d scales with the mean wind speed (e.g., Alcoverro and Le Pichon 2005).

The coherence of turbules varies as a function of size and distance traveled. An acoustic signal propagates at much faster velocities and may remain coherent at separations of kilometers. Most of the wind-noise reduction strategies are based on the contrasting spatial coherence lengths of turbules and acoustic signals. The technologies can be grouped into four classes: acoustic integration filters, instantaneous integration sensors, digital filtering with dense microphone arrays, and wind/sensor isolation strategies.

5.3.1 Daniels Filter

There have been a number of mechanical filters developed that attach to microbarometers or low-frequency microphones. If atmospheric pressure is sampled at a number of locations (n) spaced far enough apart so that the pressure variations from wind noise are uncorrelated, but close enough such that the acoustic signal remains coherent and in phase, summing the time series will increase the noise power by n and the signal power by n^2, resulting in a power signal-to-noise improvement of n (or $n^{1/2}$ in amplitude). This is the basis for the seminal work Fred Daniels performed in the 1940s and 50s, leading to the Daniels wind filter, which is also the basis of two other filter designs described later (Daniels 1952, 1959).

The Daniels filter comprises a series of different tapered pipes with sensing inlets distributed uniformly along its length and a microphone connected to its wide end (Fig. 5.9). It is designed to detect coherent infrasound as it propagates from left to right along the length of the filter. Provided that $rf^{1/2}$ is large, where r is the pipe radius and f is the signal frequency, the wave speed inside the pipe will match the wave speed outside, and the signals inside the pipe will sum in phase provided the narrow end of the pipe is pointing directly toward the source. These diameters also acoustically scale the coherent infrasound signals that propagate toward the central microphone such that the acoustic summation of the coherent signals at the microphone yields the outside signal pressure amplitude. While the filter sums signal in phase, incoherent noise from the inlets that travels acoustically inside the pipe is attenuated due to the scaling. The individual pipes have carefully selected diameters and inlet impedances to inhibit internal resonance. A prototype filter was ~600 m long with 100 equally spaced openings. The pipe inner diameter ranged from ~40 mm near the microbarometer to ~8 mm. The noise reduction was reported to be on the order of 20 dB in times of high winds (up to 12 m/s).

The Daniels filter is effectively a line microphone. It has an omnidirectional infrasound instrument response for wavelengths larger than four times the length of the filter ($f < 0.14$ Hz in the 600-m long prototype). For shorter wavelengths, the response is anisotropic and a function of the angle between the signal direction and the pipe (Olson 1947; Daniels 1959; Cook and Bedard 1971; Noel and Whitaker 1991). Figure 5.10 demonstrates the instrument response for three angles. For a broadband signal entering the filter and propagating toward the sensor at the same speed (Fig. 5.10a), the signal is recorded perfectly (flat instrument response). For the opposite direction (Fig. 5.10b), the signals that entered the inlets do not arrive at the sensor in phase, and the response is a boxcar function in time, which is a sinc function in frequency. For the broadside direction (Fig. 5.10c), the signals are also

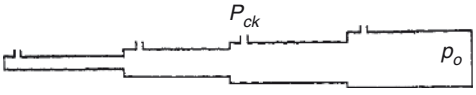

Fig. 5.9 The Daniels wind filter. A microbarometer connects to the wide end of the pipe. From Daniels 1959

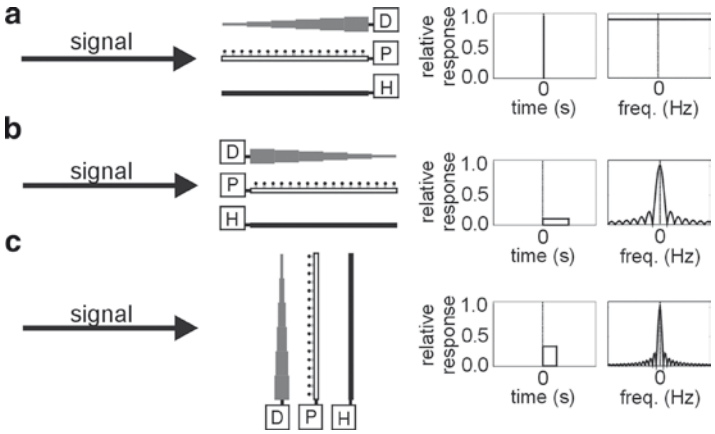

Fig. 5.10 Simplistic view of a Daniels (D), pipe (P), and porous hose (H) filter response to an infrasound signal due to acoustic integration of the signal that enters the filter at various points along its length. For the case of the filter pointing toward the source (**a**), the signal is recorded perfectly leading to a delta function and flat impulse response in the time and frequency domains, respectively. For the opposite case (**b**), one gets the most attenuation of the signal, leading to a wide boxcar and sinc function. For broadside ensonification (**c**), the boxcar is half the width in time of (**b**). In reality, the response for the microporous hose is more complex

out of phase at the sensor, but not by as much, leading to a narrower boxcar function and a broader sinc function. Other more isotropic pipe configurations have been considered (e.g., circular pipes studied by Burridge 1971 and Grover 1971).

5.3.2 Rosette Pipe Filters

A rosette filter is an extension of the Daniels filter and comprises an areal array of solid pipes that are interconnected to a central microbarometer to provide an omnidirectional infrasound instrument response and wind-noise reduction in a frequency band that depends on the aperture of the filter.

The rosette filter is the standard wind-noise filter used at IMS array sites and was designed by Alcoverro in the late 1990s (Alcoverro 1998; Alcoverro and Le Pichon 2005). The original design comprises a number of low-impedance inlets connected by solid pipes to a microbarometer where sound from all inlets is acoustically summed. The along-pipe distance from each inlet to the microbarometer is equal, and thus, at any moment, pressure at the microbarometer is the sum of pressure changes that entered each inlet of the filter simultaneously. The sum is unweighted as each inlet has the same low impedance, which is scaled based on the number of inlets in the filter. In other words, the filter response is a delta function of unity amplitude for vertically incident infrasound.

The inlets are arranged in a geometrically regular pattern around a circle and spaced far enough apart to provide nearly omnidirectional $n^{½}$ noise reduction for a particular frequency band. Alcoverro's prototype filter is shown in Fig. 5.11 and comprises 32 inlets spanning an area 16 m across. The maximum *SNR* gain with this filter is 15 dB. The band of noise reduction possible with each filter scales with aperture. Larger filters provide greater separation of sensors to provide the requirement of incoherent wind noise at lower infrasound frequencies. More recent designs used at IMS sites range in diameter from 18 to 70 m, with considerably more inlets (up to 144). In the filter pictured in Fig. 5.11, noise reduction of 15 dB is observed from 0.1 to 10 Hz. In tests at the Piñon Flat Observatory, Hedlin et al. (2003) found that at wind speeds up to 5.5 m/s, the 18 m filter reduced noise by as much as 20 dB above 0.2 Hz; a 70 m filter reduced noise by a similar amount between 0.02 and 0.7 Hz.

Resonance is an issue inherent in rosette filters. The rosette filter connects each inlet to the microbarometer via two pipes. These pipes are joined at the "secondary summing manifold" (Fig. 5.11). The acoustic impedance of the path is thus not

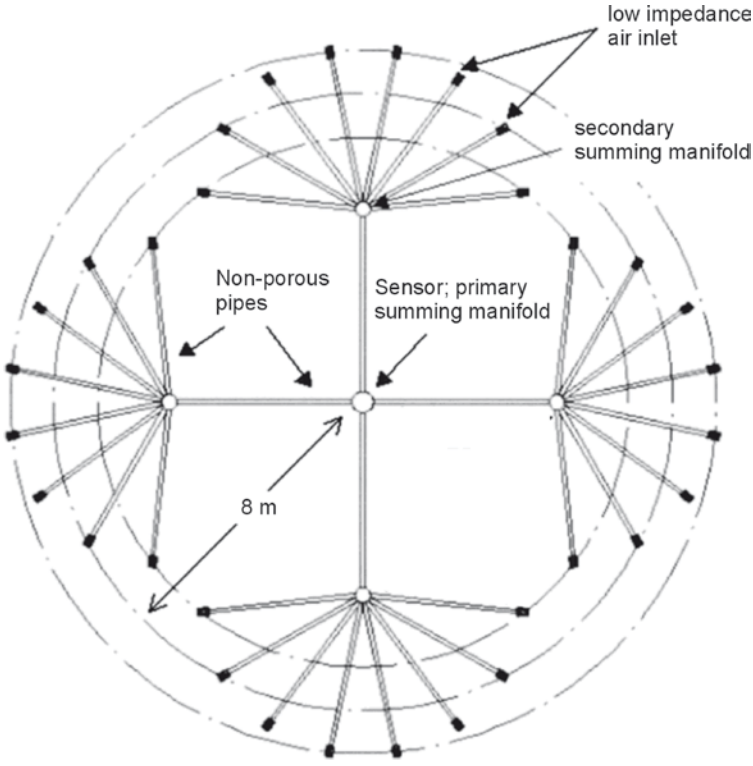

Fig. 5.11 Prototype rosette noise-reduction filter. The salient feature of this filter is that signals and noise are summed at a microbarometer located at the center of the filter after an identical propagation time delay from the inlets for vertically incident signals. Modified from Alcoverro and Le Pichon (2005)

constant giving rise to resonance of different frequencies in each pipe. The fundamental frequency of the resonance scales with the pipe length and is nearly independent of wind speed and temperature. For the 70-m filter, the lowest fundamental frequency is 2.65 Hz, well within the band of interest. Resonance in the shorter pipe is predicted to lie above 9 Hz. Resonance is observed at all wind speeds (Hedlin et al. 2003).

As predicted by Alcoverro and Le Pichon (2005) and demonstrated by Hedlin and Alcoverro (2005) the lower-frequency resonance can be eliminated by installing impedance matching capillary plugs in each pipe that leads away from the microbarometer adjacent to the secondary summing manifolds (Fig. 5.12). These capillary units are solid cylinders of a certain length of PVC that are drilled along their axes to create holes (capillaries) of a certain diameter. The length and diameter of these capillaries are calculated precisely to match the dimensions of the pipe such that they inhibit reflections back to the microbarometer. These small capillaries must be clear of obstructions however, since blockage would close off a significant part of the array from the primary summing manifold. It is unknown how partial or total blockage of one or more capillaries would affect the rosette response. The resonance in the shorter pipes can also be eliminated in a similar fashion, but such a retrofit is costly and usually not necessary if the band of interest is only for frequencies below 5 Hz.

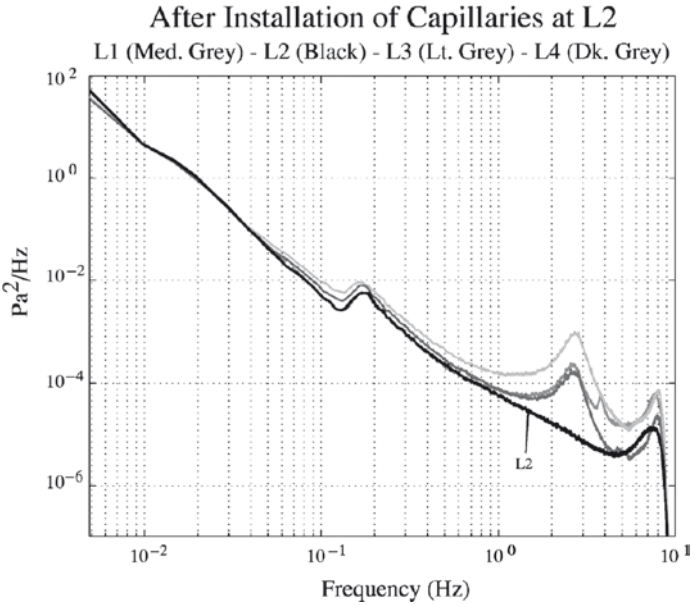

Fig. 5.12 Spectral density estimates taken from data collected without impedance matching capillary plugs (*grey curves*) and with capillary plugs installed at all secondary manifolds (curve labeled "L2"). The microbarom peak can be seen in all spectra at 0.2 Hz. The capillaries effectively remove the resonance in the main pipes between the primary and secondary manifolds. From Hedlin and Alcoverro (2005)

We now return to the omnidirectional instrument response of a rosette. Although the response is a delta function with unity amplitude for vertically incident signals, typical infrasound signals propagate across the filter at grazing elevation angles (<15°; McKisic 1997) and are heavily attenuated because the signals that enter each inlet do not arrive to the central microbarometer in phase. This can be modeled by calculating the travel time it takes for a plane wave that propagates across all the inlets to travel through the pipes to the central sensor. For each of the 32 travel times (for the filter in Fig. 5.11), a delta function of 1/32 amplitude is created and added to the time domain response at the correct time with respect to the time the wavefront crosses the central sensor. The resulting magnitude of the Fourier transform of the response is shown in Fig. 5.13. Smaller 18-m rosettes do not attenuate infrasound below 10 Hz but reduce wind noise by as much as 20 dB above 0.2 Hz. Larger 70-m rosettes do not attenuate infrasound below 2 Hz, but reduce wind noise by up to 20 dB between 0.02 and 0.7 Hz. These "high-frequency" and "low-frequency" rosettes have the fundamental limitation that they can only provide about 20 dB of wind-noise reduction because they cannot be made larger without pushing the flat part of the infrasound signal response to lower frequencies.

An array of small and large rosettes provides the means to monitor the 0.02–10 Hz infrasound band with roughly up to 20 dB wind-noise reduction. Standard array-processing techniques like beamforming can be used to provide an additional *SNR* gain. However, such techniques only work well with array elements that use the same type of rosette filter or in the low-frequency signal band common to all rosettes.

A potential issue with rosette filters is that the pipe diameter can be too small. As the pipe diameter decreases, the pipe should become more dispersive to internally propagating infrasound (Benade 1968). It is our understanding that this effect has not been empirically measured or quantified; the filter responses shown in Fig. 5.13 are approximations (that do not include dispersion) of the actual filter response.

Rosettes are expensive to fabricate and deploy. Depending on the material with which they are constructed and the array location, maintenance costs can also be expensive. Most of the IMS network pipes are either made of PVC or galvanized metal, which usually gets brittle or attacked by corrosion over time. Some of the newly installed IMS rosettes are made of stainless steel pipe and non-corrosive inlets. Because the pipes are open to the atmosphere, occlusions can develop in the capillaries or pipes, the detection and location of which is time consuming. Finally, rosettes occupy a considerable amount of space, which is an especially important consideration for island stations where space is at a premium.

5.3.3 Microporous Hoses

Much infrasound data in recent years has been collected via 1.6-cm diameter microporous or "soaker" hoses that are designed for irrigation. Depending on the objective, configurations vary from linear porous hoses to circular ones, all con-

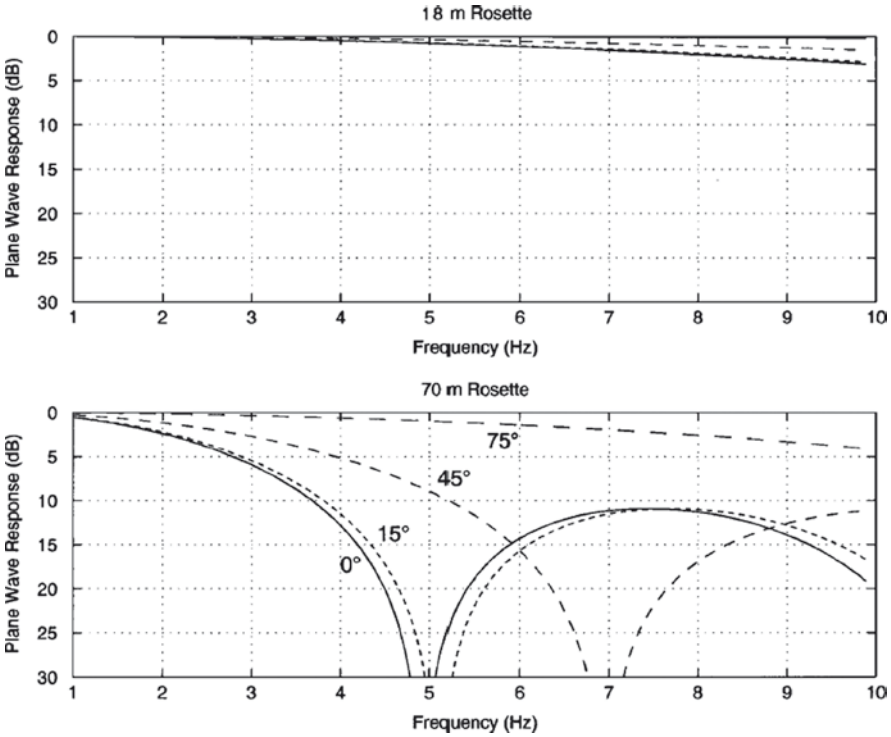

Fig. 5.13 The upper and lower panels show the plane-wave response for the 18- and 70-m rosette filters, respectively, at four arrival angles. The solid curves in each panel represent the response to horizontally propagating signals. The finely to coarsely dashed curves represent signals propagating across the two filters at 15°, 45°, and 75° above the horizontal. The elevation angles are calculated assuming a sound speed of 347 m/s. From Hedlin et al. (2003)

nected to a central or end microbarometer (e.g., Fig. 5.14). There is presumably destructive interference in incoherent wind noise for turbules that are smaller than either the length of the hose for linear configurations or the aperture for areal configurations.

For linear configurations, the instrument response of a porous hose is presumed to be qualitatively similar to that of a Daniels or single pipe filter (Fig. 5.10); as the signal wavefront propagates along the length of the hose toward the microphone, a running acoustic wave presumably propagates inside the hose at the same speed. Ideally, the signal is recorded perfectly, leading to an instrument response characterized by a delta function. The amplitude of this delta function is important. If the signal is originating from the summation of signals that diffused into all parts of the hose, then the hose should have a signal gain factor that increases with hose length. If there is no significant signal gain effect, this suggests that the hose may be analogous to a windscreen commonly found on microphones, which reduces wind noise but may not lead to greater wind-noise reduction with longer hoses.

Fig. 5.14 Photo of a spiraling-outward microporous hose connected to a microbarometer at Piñon Flat Observatory

A circular, spiral, or several linear porous hoses radiating from a central microphone are often used for applications where the source direction is unknown a priori. Such a configuration makes the filter's instrument response and wind-noise reduction isotropic for all signal azimuths and wind directions, which simplifies array processing.

This filter has fared well under some empirical tests. In a study of underground nuclear tests at the Nevada Test Site, Noel and Whitaker (1991) considered various configurations of porous hoses (e.g., "spiders" comprising several microporous arms radiating from the microbarometer, and crosses, a type of spider filter with just four orthogonal arms). They concluded that the spider and cross designs effectively reduced noise while causing relatively little distortion of the signals in the frequency band of interest. Haak and de Wilde (1996) also found significant noise reduction in the band from 10 s to 10 Hz.

These filters are commonly used at temporary recording sites where the goal is to record for a relatively short period of time (e.g., days to weeks/months) for a relatively low cost. The filters are inexpensive, both in terms of raw material cost and manpower. However, using these filters is now being discouraged for long-term installations, and even some short-term ones, for several reasons. First, the theoretical instrument response of a porous hose is not well understood and has not been successfully modeled. Howard et al. (2007) presented results that suggested above ~20 Hz, low-frequency acoustic signals do not penetrate the hose well. They also found that signals coming from the broadside do not have such a simple sinc function response as shown in Fig. 5.10c and are attenuated across the band. Signals propagating along the length were found to be amplified in the 10–20 Hz range

(Fig. 5.10a). They also made measurements at 1, 5, and 10 Hz in an anechoic chamber that suggest infrasound input into the end of the filter is attenuated as it propagates inside at a rate that increases with increasing frequency (up to 1.1 dB/m at 10 Hz). Surprisingly, removing the cap at the end of 18 m long hoses did not appear to significantly affect the response (Hetzer, personal communication, 2008). Finally, they clearly showed that different hoses of the same length and width had significantly different responses and roll-off frequencies, presumably due to different ages or manufacturers. This leads one to wonder if the instrument response is also time dependent, changing with increasing exposure to ultraviolet radiation, dust, and rain.

Porous hoses are also fragile. A single pin-sized hole close to the end where the microphone is can generate high noise levels (Herrin, personal communication, 2006). A kink, which is easy to create and often hard to mend, is also likely to create resonance or other anisotropic instrument-response peculiarities.

5.3.4 Optical Fiber Infrasound Sensor

The previous summation filters relied on acoustic summation of signals that impact many inlets (pipes or flexible hoses) or pores (microporous hoses). The rosettes reduce wind noise, but as they get larger, the omnidirectional instrument response for typical infrasound signals is degraded. The optical fiber infrasound sensor (OFIS) directly measures the integrated pressure change along a path; this sensor does not rely on the propagation of pressure signals through a narrow tube to a central manifold. A laser shines through two optical fibers that are helically wrapped around a long, sealed 2.54 cm diameter silicone tube in such a way as to create a Mach-Zender interferometer that measures diameter change of the tubular diaphragm due to a passing pressure wave. The fiber-wrapped tube is encased in insulation and placed inside a perforated drainage tube of 10 cm diameter (Fig. 5.15). Calibration experiments have been performed demonstrating that the sensor has a flat instrument response down to a frequency dependent on the size of a vent hole (typically 0.05 Hz) and up to the kHz range for broadside signals. Unlike the rosettes, acoustic resonance inside the tube is not measured, since standing waves are averaged to zero by the instantaneous integration along the length. These sensors can lie on the surface, but their sensitivity is currently a function of temperature; they perform well when buried in a trench beneath at least 15 cm of gravel. Lab and field measurements indicate that below 20 Hz there is no attenuation of infrasound by the gravel (Zumberge et al. 2003). Several comparisons with collocated MB2000 sensor recordings show that they are relatively insensitive to seismic shaking likely because such shaking generally modifies the shape of the tube and not the volume that it occupies.

Zumberge et al. (2003) buried a 90-m long linear OFIS beneath 15 cm of gravel at Piñon Flat Observatory and collected several weeks worth of data with which to compare the OFIS to the collocated 70-m L2 pipe rosette of the I57US array.

Fig. 5.15 Photo of the optical fiber infrasound sensor. The sensor is a 2.54 cm diameter silicone tube wrapped with two optical fibers. A laser shines through the fibers. The sensor measures pressure induced diameter changes of the silicone tube with laser interferometry

A microporous hose was laid out around the periphery of the L2 rosette. The I57US L2 and porous hose filters were connected to MB2000 microbarometers. A rocket launch occurred at nearby Vandenberg Air Force Base. The three sensors yielded nearly identical recordings. Figure 5.16 shows the power spectral density computed from a 15 min time window for two mean wind speeds. In 1.4 m/s winds, the OFIS noise floor is about the same as the other systems below 1 Hz. Above 1 Hz, the OFIS is about 10–20 dB lower than that of L2 and the porous hose. In moderate winds (3.4 m/s), the OFIS has a noise floor that is the same as that provided by the porous hose, both of which are lower than L2, likely due to the resonance. Plotting the minimum power for each frequency after computing 440 power spectra shows the same relationships.

The results presented in Zumberge et al. (2003) compare the OFIS to the L2 array element. In moderate winds, the OFIS and porous hose are comparable. As mentioned earlier, the response of the porous hose is unknown, so it is unclear how useful the entire hose was for this comparison. Resonance makes comparison with L2 difficult. Recent comparisons with L2, after it was fitted with capillaries to remove the 3 Hz resonance peak, suggest that in moderate wind a 90-m linear OFIS reduces wind noise at roughly the same level as the 70-m L2 rosette (Walker et al. 2007a, b).

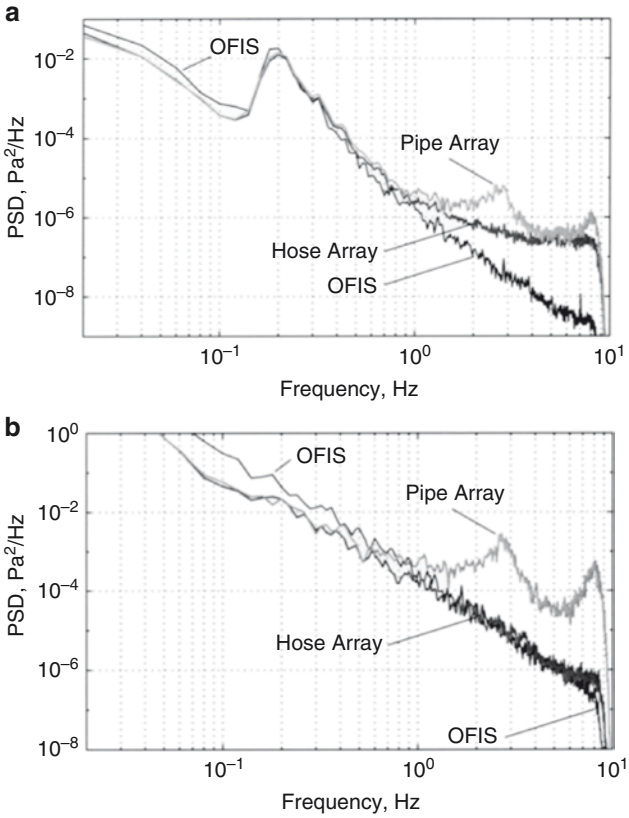

Fig. 5.16 Comparison of the OFIS sensor to the low-frequency element of the I57US array. The power spectral densities are shown for a single 15-min time window for a mean wind speed of 1.4 m/s (**a**) and 3.4 m/s (**b**). The resonance peaks in the L2 rosette are apparent at about 3 and 8 Hz. Modified from Walker et al. (2008)

Recent tests have shown that the minimum noise of L2 is due to the self-noise of the microbarometer. Therefore, once L2 is fitted with a better microbarometer or microphone it should perform better than that shown in Fig. 5.16a in low wind conditions. The self-noise of an OFIS depends on its length, but is generally on the order of $10^{-10}\,\mathrm{Pa^2/Hz}$ for frequencies above 0.2 Hz. For frequencies below 0.2 Hz, the noise floor goes up to $5\times10^{-7}\,\mathrm{Pa^2/Hz}$ at 0.05 Hz presumably due to thermal noise. The noise floor was determined by measuring the noise in the interferometer by helically wrapping the fiber on a stiff mandrill that is not sensitive to atmospheric pressure change. Therefore, the OFIS noise floor in Fig. 5.16b likely represents the acoustic noise floor for that time period at I57US.

An OFIS is similar to the other acoustic summation filters in that it is a directional sensor if used in a linear configuration. Figure 5.17 shows the instrument response of an OFIS as compared to that of a 90-m pipe array. For infrasound with wavelengths larger than $4L$, where L is the length of the linear OFIS, the OFIS is

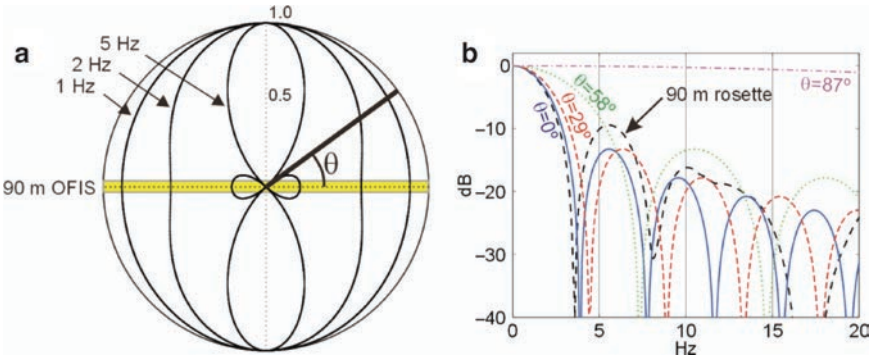

Fig. 5.17 Directivity (**a**) and frequency response (**b**) for a 90-m long OFIS as a function of and frequency. In (**a**) the response is plotted in polar coordinates as a function of θ for three example frequencies. In (**b**) the response is plotted in dB as a function of θ and frequency for four example angles. For comparison purposes, the omnidirectional plane-wave response for a 90-m diameter rosette with eight, 16-m diameter secondary rosettes is also shown for grazing angles in (**b**). Modified from Walker et al. (2008)

effectively a point sensor and has an omnidirectional response (Fig. 5.17a). For shorter wavelengths, the response is more anisotropic. For signals impacting the broadside of the OFIS, the instrument response is a delta function of unity amplitude (flat response in frequency). For signals propagating along the length of the OFIS (endfire), there is a directional attenuation that depends on the frequency and length of the OFIS. The response is the exact opposite to that of the Daniels filter (Fig. 5.10) and has similarities to that of a rosette filter of the same size (Fig. 5.17b). The first node in a 90-m OFIS instrument response for an endfire signal matches the first node in a 90-m diameter rosette for all directions with grazing elevation angles. As mentioned, however, for near broadside signals, the OFIS response is nearly flat. This is a fundamental difference between an OFIS and a rosette; a cluster of several OFIS arms in a radial configuration can each provide wind-noise reduction roughly just as well as a single rosette of the same diameter that occupies the same space, but depending on the number and length of OFIS arms, at least one of the arms can record a broadband signal (0.05–10 Hz) from all directions without attenuation. Therefore, it is probable that a cluster of radially oriented OFIS arms may be an improved alternative to a rosette, since one can make such an OFIS cluster much larger than a rosette to get better wind-noise reduction but without limiting the ability to make broadband infrasound recordings. An additional difference between a rosette and an OFIS is that not only is wind noise from advected turbules attenuated, but wind-induced acoustic noise is also attenuated by the arms that are not oriented favorably to this arriving energy (just like infrasound signals would be).

The new OFIS design uses polarization maintaining fiber, which rectifies an issue with previous OFIS designs where polarization change of the light in the two fibers led to an occasionally uptime problem. Methods and software have been developed to calculate back azimuth and phase velocity by exploiting sensor directivity with a

small array of OFIS arms (Walker et al. 2008). A six-OFIS array near San Diego, California, has been operating since April 2008 for research and monitoring interests. Finally, an automated calibration system has been developed for each OFIS arm.

Current OFIS research is focused on two fronts. The first is on the level of wind-noise reduction provided by a buried OFIS, especially as a function of OFIS length, burial depth, gravel diameter, and wind direction. The second is on determining why the sensitivity to pressure change of an OFIS is a predictable function of temperature and OFIS length. Lab measurements have shown that the mechanical properties of short (1.5 m) silicone tubes do not change significantly with temperature. Field tests have shown that the sensitivity is not related to a buildup of differential pressure across the tube walls. Although the burial of the OFIS with the automated calibration system eliminates this from being a major nuisance, additional experiments and mathematical models are being developed that will likely lead to the fabrication of an OFIS that is insensitive to temperature.

5.3.5 Distributed Sensor (Adaptive Processing with a Dense Array)

Another approach to reducing wind noise is to record pressure simultaneously at many points sampled by a dense array. One could either record to disk all the traces and extract a signal of interest in post-processing, or one could use on-the-fly algorithms to reduce wind noise through filtering or weighted-averaging schemes that adapt to the changing wind conditions, outputting a single trace. This system has been labeled the "distributed sensor" and is being developed by the University of Mississippi and Miltech Research and Technology. The array sensors (Fig. 5.18) comprise similar piezoelectric microphones that are described in Shields (2005). Two configurations are being tested: wired and wireless. The wireless configuration communicates pressure samples through a nearest-neighbor approach, bouncing from one sensor to another until the sample reaches the data-logging hub. If one sensor stops working, communication automatically gets routed around that sensor.

Dillion et al. (2007) deployed a rectangular distributed sensor of 100 elements at Piñon Flat Observatory inside the 70-m L2 I57US rosette, which comprised 144 inlets. They occupied an area of ~500 m^2 inside the ~2,700 m^2 area of the rosette. They confirmed that for simple unweighted-averaging schemes, one gets the expected reduction of wind-noise power by roughly 20 dB. They also confirmed that the larger area and/or number of inlets for L2 reduce wind noise by roughly 5 dB more for frequencies above 0.8 Hz and below 0.4 Hz.

The true potential of the distributed sensor will probably be realized as we learn more about the physics of wind noise. For example, Shields (2005) found that averaging microphones along the wind direction can yield better than $n^{½}$ reduction wind noise. A simple approach would be to have an array of some given size and average only those sensors along a single line that is parallel with the current wind direction. A more sophisticated approach might involve weighted-averaging schemes.

For example, a sensor in the array could be summed with another sensor in the downwind direction a distance of 0.4 wavelengths away by an amount determined by the graph in Fig. 5.7 such that the average cancels the advected wind noise while preserving any energy that propagates across the sensor at a much faster acoustic velocity. Another approach might be a running frequency-wave number (F-K) filter that selectively attenuates slower moving energy that propagates across the array from all directions simultaneously, after which the resulting filtered data could be simply averaged. These are all techniques that might be invoked on a high-speed digital signal processor at the site or back in the lab after the data have been stored to disk. As the availability of faster computational and data storage resources increases with time, it should become easier to manage and process larger amounts of infrasound data.

The distributed sensor is reported to be relatively inexpensive and portable. The individual sensors are very durable, do not have resonance issues in the infrasound band, and have flat instrument responses. Over the next several years, a considerable effort will be spent on investigating if array processing techniques on data from such an array can provide better signal-to-noise ratios than a single rosette or an array of several rosettes.

5.3.6 Porous Media Filters

The last class of filters that we discuss may embody a completely different approach to wind-noise reduction, depending on the type of the wind noise being filtered. Instead of averaging over a number of sensing surfaces, one may be able to isolate the sensor from the advected turbules. Since wind speed decreases with distance toward the ground and the stagnation pressure is not defined on a flat ground for a horizontal wind, it may be that burial of wind sensors in a porous media like sand or gravel may provide a useful wind filter. Herrin et al. (2001) presented theory on wind-noise reduction in rigid, porous media and tested the theory with an experiment in a box of sand. They state that results of Attenborough (1983), Attenborough et al. (1986), and Sabatier et al. (1986, 1993) imply that infrasound pressure decreases exponentially with depth inside a semi-infinite half-space. They also state that "wind-generated atmospheric pressure changes" (presumably those that are advected across the ground) decrease exponentially with depth in this porous medium. Because the attenuation operators are different, the change in signal-to-noise ratio with respect to the observation at the surface, changes with depth

$$\Delta SNR(d) = \mathrm{e}^{d(\alpha_\mathrm{w} - \alpha_\mathrm{i})},$$

where α_i and α_w are the infrasound and wind attenuation operators

$$\alpha_\mathrm{i} = \mathrm{Re}\left(\sqrt{i\frac{\gamma\sigma\omega}{\rho_\mathrm{o}c_\mathrm{o}^2}}\right)$$

and

$$\alpha_{\mathrm{w}} = \mathrm{Re}\left(\sqrt{k_{\mathrm{w}}^2 + i\frac{\sigma\omega}{P_{\mathrm{o}}}}\right),$$

where γ is the specific heat ratio for air, σ is the effective flow resistance of the porous solid, ω is angular frequency, ρ_{o} is the air density, c_{o} is the sound speed, k_{w} is the horizontal wave number characterizing the wind turbules, and P_{o} is the pressure. Herrin et al. (2001) show that the signal-to-noise ratio does not change with depth for frequencies well below

$$f_{\mathrm{c}} = \frac{\sigma c_{\mathrm{w}}^2}{2\pi P_{\mathrm{o}}},$$

where c_{w} is the advective wind speed. For much higher frequencies,

$$\Delta SNR(d,\omega) = 20Log(e)\frac{\omega d}{c_{\mathrm{w}}}$$

The SNR increases with increasing frequency and depth for porous media that have appropriate effective flow resistances.

Herrin et al. (2001) collected data to test the above theory by empirically measuring the attenuation operators. They attached a microphone to a flexible hose, which they placed inside a $2.4\times2.4\times0.6$ m box of sand resting on the surface with the inlet in the center buried beneath 0.36 m of sand. They placed a reference hose and inlet inside the box at a depth of 0.05 m beneath the sand, right above the deeper inlet. They acquired data in both low and moderate winds. They found that they could fit an exponential decay curve to the wind-noise pressure using 6 and 12 m/s wind speeds for the low and moderate wind speed bins into which they separated the data. Unfortunately, no infrasound signals were detected during this trial, and consequently neither the infrasound attenuation operator nor the effective flow resistance could be verified.

Herrin et al. (2001) performed a second experiment where the dimensions of the first were roughly doubled. The burial depth of the test inlet was 0.84 m and the reference inlet was at a depth of 0.1 m. The analysis of this data set was also limited. However, they determined that over the wind speeds sampled, the average attenuation of wind noise was 40 dB at 1 Hz. As with the last data set, broadband infrasound signals were not recorded. However, microbaroms (0.15–0.3 Hz) were recorded during calm periods and used to empirically estimate the theoretical flow resistance of the sand of ~2.0×10^5 N s/m^4. With that flow resistance parameter, an infrasound decay curve was calculated and compared with the mean wind-noise attenuation curve. Although the infrasound transmission decays considerably with increasing frequency, the wind-noise transmission decays much faster beginning at 0.1 Hz and extending to 4 Hz where both curves intersect. This suggests an *SNR* increase of ~20 dB at 1 Hz for their inlet buried at 0.84 m. This also suggests that

above 4 Hz, the infrasound is attenuated more than wind noise. It appears that more work needs to be done in this area, but that porous media filters have significant potential as wind-noise filters, especially when used with sensors that have very low self-noise.

5.3.7 Wind Barriers

Wind barriers share similarities with porous media filters, since they attempt to isolate the sensors from the wind. This should greatly reduce noise from turbulence–turbulence and turbulence–mean shear interaction. The interaction of the barrier walls with the wind may lead to turbulence-sensor noise (i.e., the walls act as pressure sensing surfaces) depending on the wall construction. If the turbulence–sensor noise is negligible and barriers do not create additional noise in the form of turbulence inside the enclosure, then they could be very effective, only measuring the acoustic noise generated by the wind.

There have been several wind barrier designs over the last two decades. Liszka conducted pioneering work with wind barriers for noise reduction at infrasonic frequencies (e.g., Liszka 2008). In Liszka's patented wind barrier design (Swedish Patent No. 7315138-3, October 30, 1975) a sensor is placed inside a semiporous hexagonal barrier. The sides of the fence are not solid to avoid increasing large-scale turbulence downstream of the barrier.

Another design tested by Hedlin and Raspet (2003) included sides that were 50% porous and 2 m high by 5.5 m apart at the base. The entire barrier was coated with a fine wire mesh. The sensor was located inside foam at the center of the fence. The fence reduced wind speed by 90%. Surprisingly, the 10× reduction in wind speed inside the fence did not result in a proportional 20 dB reduction in infrasonic wind noise. In most of the frequency band of interest, the rosettes performed much better in reducing wind noise. However, noise reduction by the barrier was observed to be over 10 dB at frequencies above 0.5 Hz at low wind speeds (<0.5 m/s) and at frequencies above 2 Hz (at wind speeds above 4.0 m/s).

The Hedlin and Raspet (2003) work has an implication for the type of wind noise being created or reduced by the barrier. The wind-noise reduction by the barrier scales much like the wind-noise reduction of the rosettes produced by spatial averaging. Figure 5.19 shows the wind-noise reduction ratio (wind filter spectra divided by spectra from a reference port) for 5.25 m/s wind speed and different filter types with characteristic sizes L (70, 18, and 2.0 m for the rosettes and barrier). As stated by Hedlin and Raspet "If the wind noise and wind-noise reduction are caused by local interactions of the turbulence and the wind-noise reduction device (turbulence–sensor interaction), the wind-noise reductions of similar devices should scale as the ratio of the turbulence scale to a characteristic linear dimension of the device (Strasberg 1988)." Therefore, instead of plotting reduction ratio vs. frequency, they are plotted vs. the scaled "frequency" fL/v, where v is the mean wind speed. Consequently, Fig. 5.19 displays the relative effectiveness of the wind filter in

reducing wind noise generated by turbules with a length scale normalized by the length scale of the assumed spatial averaging filter.

Hedlin and Raspet show that the shapes of the curves, except for that part associated with the 70-m rosette resonance peaks, are independent of wind speed and have roll-offs to the rosettes if the scaling length for the barrier is the barrier height (2.0 m) instead of the barrier diameter (5.5 m). This may suggest that pressure fluctuations are primarily averaged over the front of the barrier in the wind in a similar fashion to being averaged over the surface of the rosettes. However, the barrier displayed a small but significant wind-noise reduction (4 dB) even when the size of the turbulence is greater than the size of the barrier itself (from a scaled frequency of 0.05 to 0.5). This additional noise reduction might be due to a mechanism similar to that of the spherical foam windscreens (Fig. 5.19) in which reductions occur because the pressure measured at the center is the area average of the pressures generated at the surface of the sphere; the wind barrier may serve as a pressure averaging device over the surface of the barrier with negative and positive contributions even for turbulent structures with dimensions much larger than the windscreen. If this is the case, a roof or a more spherical barrier may provide better wind-noise reduction. Regardless, this result suggests that the fundamental issue faced by wind barriers is the reduction in the noise generated by the interaction of the barrier itself with the turbules.

Solid-walled barriers tested by Shams et al. (2005) employed a variety of materials. The guiding principle in this design was that the solid walls, with a low acoustic impedance, would divert atmospheric turbulence away from the sensor while allowing long-period infrasound to penetrate to the interior. One design was found to reduce noise at 0.7 Hz by 10 dB and by greater than 20 dB at 20 Hz. Despite the solid sides, noise from vortex shedding was found to lie above 20 Hz.

A series of barriers have recently been designed and tested by Doug Christie (e.g., Christie et al. 2007; Christie and Campus 2010). The material used is outdoor windscreen that is roughly 50% porous. As of this writing his best design, in terms of experimentally measuring wind-noise reduction at IS07 Warramunga, is shown in Fig. 5.20. The hexagonal barrier has a diameter of 14 m, vertical sides of 2 m height, a roof, internal radial baffles to dampen internal vortices, and serrated edges that extend both outward and downward from the outer upper edge. The serrated edges were a development that came out of work on wind fences designed for an infrasound tornado-warning system network (Bedard et al. 2004) and are designed to reduce the generation of local turbulence as air flows up and over the barrier. Most of the other components of the barrier were designed to minimize air flow within the barrier.

Christie's barrier designs have evolved, with that in Fig. 5.30 being version 5. He reports a dramatic improvement in wind-noise reduction during the transition from a version with an open structure to one with a roof made of the same porous screen. He recorded data with this design using Chaparral Physics microphones and plotted stacked spectra in Fig. 5.21. Comparison of a reference pipe array outside the enclosure (and presumably far enough away to be out of the enclosure's wake) with an identical pipe array and a single inlet microphone inside the enclosure shows a dramatic reduction in wind noise, especially at high frequencies. As was

observed by Hedlin and Raspet (2003), the frequency above which the barrier performs well scales with wind speed. At 1 Hz, the wind-noise reduction is between roughly 5–20 dB for winds up to 5.7 m/s. Remarkably, in most cases, the wind-noise reduction is about the same for the inside pipe array as well as for the inside single inlet microphone, suggesting that a single microphone may be all that is required inside these enclosures.

It is clear that a wind barrier is more effective at reducing some type of wind noise than a 6-inlet pipe array of the same size. However, the technology is still young and there are interesting and practical questions that remain. For example, an 18-m rosette often has as many as 96 inlets, providing a 20 dB reduction in incoherent noise. Since one obtains 5–20 dB reduction at 1 Hz in wind up to 5.7 m/s simply with the enclosure, will that reduction add to that provided by an outside rosette of 96 elements, if that rosette was instead enclosed? In other words, would a rosette of 96 elements outside an 18-m enclosure reduce wind noise to the same base level as that which is provided by the enclosure over an identical 96-element rosette? If so, then there is no benefit to enclosing rosettes. In addressing these questions, spectra predictions from the aforementioned equations for the different types of noise could be invaluable and save lots of time in terms of field experimentation.

The signal-to-noise ratio is ultimately what one seeks to improve. Wind-noise reduction is therefore only half of the problem. The response of the enclosure to infrasound signals should probably be quantified. Christie et al. (2007) compared the time series of an infrasound signal that was recorded in windless conditions by a single port outside the enclosure and the pipe array and single port inside the

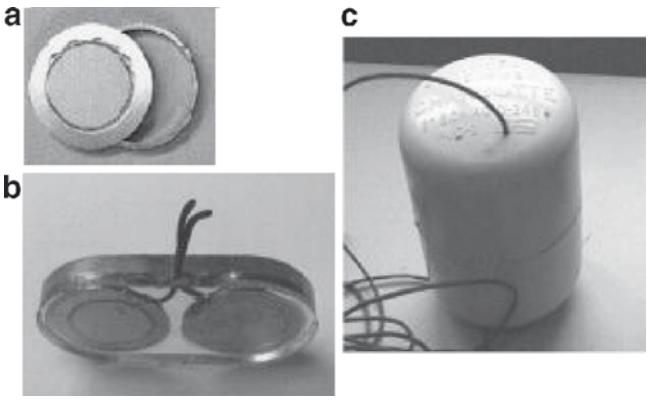

Fig. 5.18 Piezo-electric microphones used in the distributed sensor. (**a**) Pictures a piezoelectric "bimorph" formed by cementing a piezo-ceramic disc to a 3.5 cm diameter brass disc. A pressure sensitive capsule is formed by cementing one of these bimorphs to each side of the brass ring also shown. (**b**) Pictures two capsules, one with the piezo-ceramic turned out and one with it turned in, potted in transparent polyurethane. (**c**) Pictures the housing for the potted capsules. It is made from 5-cm diameter schedule 40 PVC pipe with end caps. The potted capsules are wrapped in fiberglass and enclosed in this PVC housing. Fifty-four holes are bored in the PVC housing in such a way as to make the sensor insensitive to seismic disturbances. From Shields (2005)

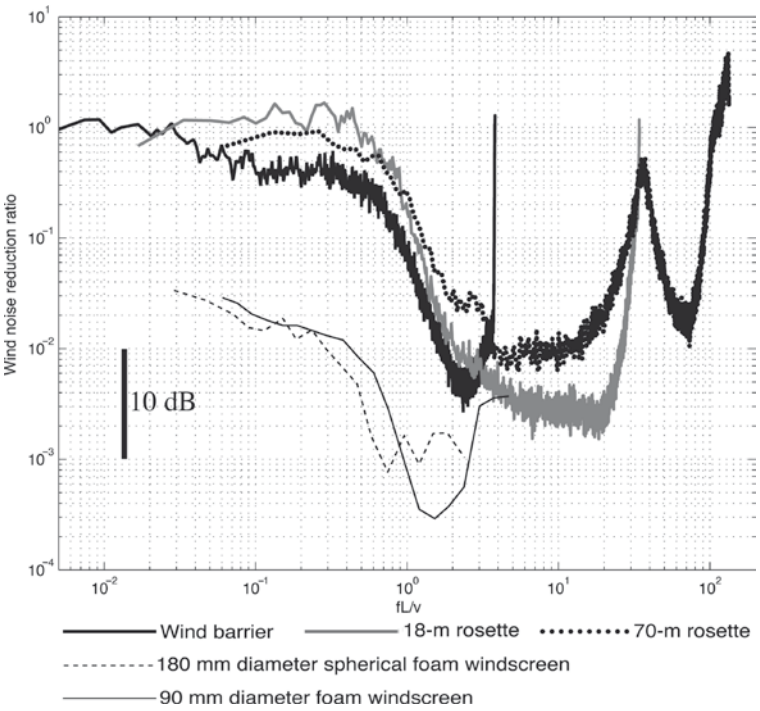

Fig. 5.19 Wind-noise reduction ratio (filter results divided by results from a reference port) vs. scaled frequency at 5.25 m/s for a 70-meter rosette (*bold dots*), for a 18-meter rosette (*bold grey*) and for a wind barrier (*bold black*). Also displayed is the noise reduction produced by a 90-mm-diameter foam windscreen at an average wind speed of 4.84 m/s (*light dashed curve*) and a 180-mm diameter spherical foam windscreen at 4.74 m/s (*light solid curve*). In this figure f is the time frequency, L is the scale length, and v is the wind speed. From Hedlin and Raspet (2003)

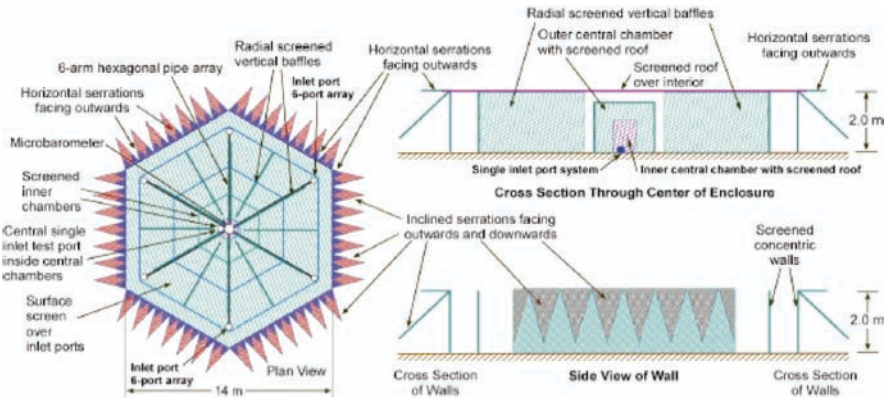

Fig. 5.20 Christie's wind barrier design (version 5). This 14-m barrier encloses a 6-inlet pipe array and a central reference microphone. Modified from Christie et al. (2007)

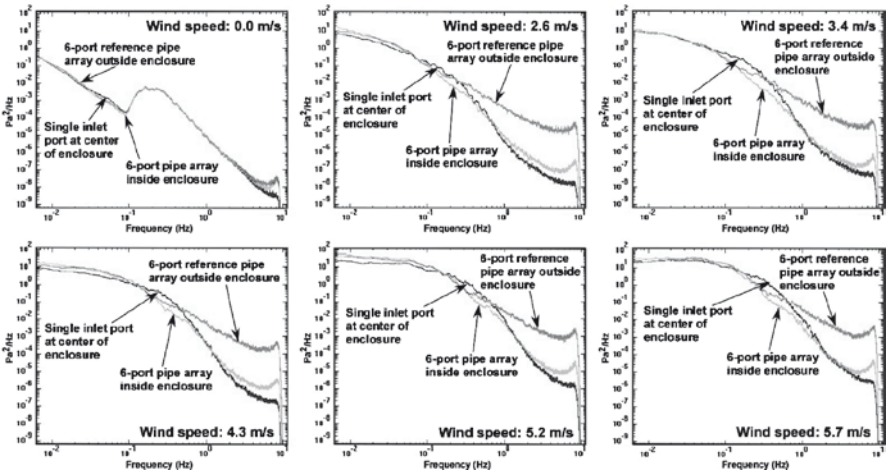

Fig. 5.21 Stacked noise spectra at wind speeds ranging from 0.0 to 5.7 m/s. Spectra are shown for three sensors: a single microphone inside the enclosure, a pipe array inside the enclosure, and the same size pipe array outside the enclosure. The sensors used are Chaparral Physics model 5 microphones with electronic noise floors that are not observed in any of these spectra. Modified from Christie et al. (2007)

enclosure. They showed that there is no attenuation for the dominant frequency of that signal, which was ~1 Hz (Christie et al. 2007). However, subtle differences observed in the structure of the recorded signals may suggest that higher frequencies were attenuated by the enclosure. As with rosette filters, knowledge of the enclosure response function is useful for determining how different properties of the enclosure may impact the ability to hear infrasound throughout the band of interest. For example, would reducing the permeability of the fabric or increasing the size of the enclosure by 20% lead to better wind-noise reduction at 1 Hz without attenuating infrasound at lower frequencies?

A few other questions remain. Can wind barriers (up to 14 m across) be tuned to perform as well as larger 70-m rosettes in the 0.05–0.7 Hz band? What level of improvement can be expected for large 70 m rosettes that have enclosures around the individual subrosettes? Finally, knowing what type of wind noise that is being reduced by these filters, perhaps with the help of the equations above, will help determine how well they will perform at other sites where the predominant wind noise type may be different.

5.4 Discussion

Some characteristics of the ideal infrasound station are that it occupies little space, has a low surface profile, has superb wind-noise reduction at all frequencies while faithfully recording signals, has the ability to determine accurately the direction of

arrival, is maintenance free, and is user-friendly to the station operator and data processor. The many methods discussed earlier exist because there are various situations where some of these characteristics are more important than others. However, many of these techniques are fairly young, not completely understood, and not yet proven to be mission capable.

Two of the technologies above have received considerable attention during the last decade: rosette and porous hose filters. It is probably fair to say that rosettes are currently the standard to which every other technology should be compared. However, it must be remembered that rosettes are inherently flawed by their omnidirectional attenuation of infrasound signals for grazing elevation angles. While this flaw does not affect small pipe arrays, it is debilitating for large arrays that have the ability for better wind-noise reduction, especially at lower frequencies. Porous hoses, although inexpensive and very portable, have been found to be unpredictable at best. Sometimes they provide wind-noise reduction comparable to a rosette. Sometimes they create their own noise. They too suffer from the omnidirectional attenuation of infrasound signals as the rosettes.

The other "younger" technologies may be well poised in the next several years to eventually replace or be used to retrofit aging rosettes and porous hoses arrays. For example, small existing rosettes should probably be retrofitted with wind barriers if such barriers can provide additional wind-noise reduction without signal degradation. This wind noise filter seems to be the most mature of the "young" technologies previously discussed, although outstanding questions still exist. The practical lifetime and maintenance requirements for such barriers are also undetermined.

Rosette footprints could be replaced with buried clusters of n OFIS arms or distributed sensors. The full potential of the distributed sensor may only become clear after different algorithms have been tested on trial data sets. As discussed above, a single OFIS of length L appears to reduce wind noise by about the same amount as a rosette of diameter L. A buried OFIS cluster that occupies the same horizontal area as a rosette should provide greater wind-noise reduction than the rosette if the OFIS time series are summed together or if only the OFIS oriented in the direction parallel to the wind is considered. Since each OFIS arm is a directional sensor that has a flat response for near broadside infrasound signals, one could also make an OFIS cluster much larger than a rosette to get even greater wind-noise reduction without compromising the ability of the sensor to make broadband infrasound recordings of signals from all directions. In this latter case, determining the direction of arrival with several of these OFIS clusters is accomplished with a conceptually simple modification to standard array processing algorithms. For example, the "trial direction" in beamforming would determine which OFIS in each cluster to use for the correlation function, which imparts no additional computation. For even greater directional resolution for signals with good signal-to-noise ratios, one could also take advantage of all OFIS arms by using instrument-response-dependent beamforming (Walker et al. 2008).

Two guiding principles for the design of infrasound stations on islands is to minimize wind noise and the station footprint. A single distributed sensor, OFIS cluster, compact wind barrier array, an array of microphones encased in porous media, or some hybrid of these may work best for these sites.

Site location can of course greatly affect the level of wind noise. Perhaps the optimum natural filter that exists is a dense forest. Forests have a high surface roughness length, greatly reducing wind and likely breaking up large-scale turbules into smaller turbules that can be attenuated better by spatial filters. Although mountains have been associated with low frequency infrasound noise in the 0.01–0.1 Hz range and may cause blockage of higher frequency infrasound, valleys or craggily surfaces may also be locations of relatively slow winds. Given that even stable winds can interact with objects to create infrasound or turbules that can saturate an array, it is important to locate array elements far from obstacles in the path of the wind. Finally, it is clear that wind noise is a site-specific problem. A noise survey at sites of interest for future permanent infrasound stations could be useful in the design of wind filters specifically tailored for those sites.

There are several pitfalls that can arise in wind-noise reduction research that can cause great delays in progress. First, the self-noise floors of the sensors must be significantly lower than that which is possibly achievable with the wind filter. For example, the MB2000 and MB2005 microbarometers have a nominal self-noise floor on the order of 10^{-7} Pa^2/Hz. This sensor noise is apparent at frequencies above ~1 Hz, which happens often when connected to porous hoses or pipe arrays in low wind conditions.

Another problem that can arise is occlusion of the narrow impedance matching capillaries or pipes in reference rosettes. The capillaries are often very narrow, which allows them to become easily occluded. The biggest problem that they present is that such occlusions may remain unnoticed for a long time while quietly degrading the rosette performance and wind-noise reduction comparisons. Perhaps periodically blowing a jet of air through each pipe at the primary summing manifold would be an effective maintenance strategy. A more informative technique may be to impart an instantaneous pressure differential into each pipe and measure the decay rate, which should be predictable and identical for all pipes.

Another potential issue is the development of technologies under the assumption that there is only one type of wind noise. Some types of wind noise may be more important than others depending on the filtering mechanism or atmospheric conditions. Similarly, the same wind speed does not necessarily yield the same level of wind noise. Winds associated with stable atmospheres (non-convecting) are predicted to give rise to significantly lower wind noise levels than winds associated with vigorous diurnal convection. Along the same lines, winds from one direction may give rise to a different level of noise than winds from another direction based on local and regional influences. For this reason, it is probably wise to search for variations in wind-noise spectra for a given wind speed before averaging such spectra. Furthermore, comparing wind-noise reduction spectra obtained at different sites without knowledge of the type of wind noise being attenuated may be deceiving. Although more work remains to be done in quantitatively predicting wind noise, simple equations that predict different types of wind noise are contained in this chapter and explained in more detail in Raspet et al. (2006, 2008). Comparing spectra plotted as a function of advective wave number $2\pi f/\bar{u}$ (or scaled frequency $fL/\bar{u}$) or investigating wind noise with a distributed sensor can be used to determine if the wind noise is acoustic or being advected across the filter (e.g., Hedlin and Raspet 2003).

Testing wind-noise reduction filters is two-sided; such filters are designed to attenuate wind noise more than infrasound such that the signal-to-noise ratio improves. The development of wind-noise filters benefits from quantitative analyses of the effect of the filter on infrasound signals from all directions. This should especially be important if a significant effort is spent on carefully calibrating sensors in the lab that ultimately will be used with these filters. One technique for estimating the infrasound filter response is to calculate the coherence function or transfer function on a time window that contains a broadband infrasound signal recorded by the test sensor/filter and two reference sensors without filters. The three sensors must be spaced far enough apart such that infrasound remains spatially coherent while wind noise is spatially incoherent. Coherence functions are calculated for all three pairs of time series. The near-unity amplitudes of the coherence function between the two reference sensors indicate the spectral bandwidth of the infrasound signal, which provides guidance for how to interpret the other two coherence functions between the test sensor and reference sensors. Used in this way, one can piece together the infrasound filter response by analyzing several signals that together span the frequency band of interest.

It seems clear that continued, paced research and independent validation of results is important to flush out the details of each technology and prove if the technologies are mission capable before great efforts are taken to implement these technologies as part of a routine operational setup. Such efforts would especially benefit from the establishment of one or more "standard" testing facilities, perhaps in different environments, where the nature and character of the wind noise can be quantified and routinely verified with precision instruments such as a high-sample-rate anemometer and a permanent dense microphone array. Such a facility would also benefit from an onsite, active-source infrasound calibration tool such as that provided by a rotary subwoofer (Garcés and Park 2007) or a large weatherproof subwoofer array (Walker et al. 2007b).

5.5 Conclusions

Progress in infrasound science and monitoring efforts suffers from high noise levels created by the wind. There are a number of mature technologies that are routinely employed to reduce wind noise. However, these technologies are of limited usefulness; noise levels in moderate winds are still deafening and instrument responses are not always ideal for typical infrasound signals. The impact to existing monitoring efforts is that at any one time, it is possible that a subset of the IMS network stations will be beset by high noise.

A number of new techniques to reduce wind noise have developed during the last several years. These development efforts were guided by two principles: the need to improve signal-to-noise ratio and the need for compact, low-maintenance designs. In the order in which they are presented earlier, these include the optical fiber infrasound sensor, the distributed sensor, rigid porous media filters, and wind

barriers. The optical fiber sensor is a line sensor, usually buried in gravel, that instantaneously averages pressure along its length. Each arm of a cluster of OFIS arms in a radial configuration has about the same wind-noise reduction as a rosette of the same aperture, but at least one arm can record infrasound from any direction without attenuation. An OFIS cluster can therefore be made larger to provide a better signal-to-noise ratio than what could ever be provided by a rosette. The distributed sensor is a low-profile, generally portable system that comprises many (at least 100) robust, broadband microphones in both a wired and wireless configuration. Methods are being developed and tested to digitally filter wind noise while preserving infrasound. Such algorithms might be run in post-processing or onsite with high-speed digital signal processors. Theoretical work has been carried out and partially tested that predicts rigid porous media like sand and gravel can be utilized with other sensors to improve the signal-to-noise ratio in a part of the frequency band of interest. Finally, wind barriers may act as massive microphone windscreens or as devices that isolate the sensor from advected wind noise. A 14 m prototype has been developed that provides much greater wind-noise reduction above 0.7 Hz than that provided by a 6-port pipe array of the same aperture. These technologies are still young, but may mature during the next five to ten years if paced research and independent validation of results continues, especially if one or more "standard" testing facilities can be agreed upon and developed.

There have been some recent developments in wind-noise theory. It is clear that there are at least four types of wind noise that are important in the infrasound band: turbulence–sensor interaction noise, turbulence–turbulence interaction noise, turbulence–mean shear interaction noise, and acoustic noise generated by the wind. The first three types of noise effectively advect with turbules across the sensor at the mean wind speed. That type of wind noise can be verified if wind-noise spectra plotted as a function of advective wave number collapses onto a single curve. The pressure spectra due to each type of wind noise can also be predicted by wind velocity spectra using simple equations. Wind-noise theory is still evolving and requires more research and validation. However, that which has been discovered should be useful in further development of wind-noise reduction technologies.

Acknowledgements We thank Rich Raspet and Doug Shields for clarifying discussions and an anonymous reviewer for constructive comments that improved this manuscript. This work was supported by the U.S. Army Space and Missile Defense Command.

References

Alcoverro B (1998) Acoustic filters design and experimental results. Proceedings Workshop on Infrasound. DASE, Commissariat à l'Energie, Bruyères-le-Châtel, France, 21–24 July 1998

Alcoverro B, Le Pichon A (2005) Design and optimization of a noise reduction system for infrasonic measurements using elements with low acoustic impedance. J Acoust Soc Am 117: 1717–1727

Arrowsmith SJ, Hedlin MAH (2005) Observations of infrasound from surf in southern California. Geophys Res Lett 32:L09810. doi:10.1029/2005GL022761

Attenborough K (1983) Acoustical characteristics of rigid fibrous absorbents and granular materials. J Acoust Soc Am 73:783–799

Attenborough K, Sabatier JM, Bass HE, Bolen LN (1986) The acoustic transfer function at the surface of a layered poroeleastic soil. J Acoust Soc Am 79:1353–1359

Batchelor GK (1951) Pressure fluctuations in isotropic turbulence. Proc Cambridge Philos Soc 47:359–374

Bedard Jr. AJ, Whitaker RW, Greene GE, Mutschlecner P, Nishiyama RT, and Davidson M (1992) Measurements of pressure fluctuations near the surface of the Earth. 10th Symposium on turbulence and diffusion, Portland, OR, September 29 – October, 1992, American Meteorological Society, 45 Beacon St, Boston, MA, pp. 293–296

Bedard Jr. AJ, Bartram BW, Entwistle B, Golden J, Hodanish S, Jones RM, Nishiyama RT, Keane AN, Mooney L, Nicholls M, Szoke EJ, Thaler E, and Welsh DC (2004) Overview of the ISNET data set and conclusions and recommendations from a March 2004 workshop to review ISNET data. U.S. National Oceanic and Atmospheric Administration, Environmental Technology Laboratory, Boulder, CO, p. 20

Benade AH (1968) On the propagation of sound waves in a cylindrical conduit. J Acoust Soc Am 44:616–623

Berman S, Stearns CR (1977) Near-Earth turbulence and coherence measurements at Aberdeen Proving Ground, Maryland. Boundary-Layer Meteorol 11:485–506

Bowman HS, Bedard AJ (1971) Observations of infrasound and subsonic disturbances related to severe weather. Geophys J Roy Astron Soc 26:215–242

Burridge R (1971) The acoustics of pipe arrays. Geophys J R astr Soc 26:53–69

Chen WF (1997) Handbook of structural engineering. CRC Press, Boca Raton, pp 12–50

Cook RK, Bedard AJ (1971) On the measurement of infrasound. Geophys J R Astr Soc 26:5–11

Christie D (1999) The infrasound segment of the CTBTO's international monitoring system. IUGG, XXII General Assembly, B.7 (abstract)

Christie DR, Campus P (2010) The IMS infrasound network: design and establishment of infrasound stations. This volume, pp. 27–72

Campus P, Christie DR (2010) Worldwide observations of infrasonic waves. This volume, pp. 181–230

Christie D, Kennett BLN, and Tarlowski C (2007) Advances in infrasound technology with application to nuclear explosion monitoring. Proceeding of the 29th monitoring research review. Los Alamos National Laboratory, Los Alamos, New Mexico, pp. 825–835

Daniels FB (1952) Acoustical energy generated by the ocean waves. J Acoust Soc Am 24:83

Daniels FB (1959) Noise-reducing line microphone for frequencies below 1 c/s. J Acoust Soc Am 31:529–531

deWolf DA (1983) A random motion model of fluctuations in a nearly transparent medium. Radio Sci 18:138–142

Dillion K, Howard W, Shields FD (2007) Advances in distributed arrays for detection of infrasonic events [abstract]. J Acoust Soc Am 122:2960

Evers LG, Haak HW (2010) The characteristics of infrasound, its propagation and some early history. This volume, pp. 3–26

Favre AJ, Gaviglio J, Dumas R (1962) Corrélations spatio-temporelles en écoulements turbulents. Mécanique de la turbulence (Coll Intern Du CNRS à Marseille), Paris, ed. CNRS, 419–445

Frenkiel FN, Klebanoff PS (1966) Space-time correlations in turbulence. In: Pai SI (ed) Dynamics of fluids and plasmas. Academic Press, New York. pp. 257–274

Garcés M, Willis M, Hetzer C, Le Pichon A, Drob D (2004) On using ocean swells for continuous infrasonic measurements of winds and temperature in the lower, middle, and upper atmosphere. Geophys Res Lett 31:L19304. doi:10.1029/2004GL020696

Garcés M, Hetzer C, Merrifield M, Willis M, Aucan J (2003) Observations of surf infrasound in Hawaii. Geophys Res Lett 30(24):2264. doi:10.1029/2003GL018614

Garcés M, Park J (2007) A rotary subwoofer as an infrasonic source. Infrasound Technology Workshop. Tokyo, Japan. 13–16 November
George WK, Beuther PD, Arndt REA (1984) Pressure spectra in turbulent free shear flows. J Fluid Mech 148:155–191
Georges TM, Greene GE (1975) Infrasound from convective storms. Part IV. Is it useful for storm warnings? J Appl Meteor 14:1303–1316
Goedecke GH, Auvermann HJ (1997) Acoustic scattering by atmospheric turbules. J Acoust Soc Am 102:759–771
Gossard EE (1956) Gravity waves in the lower troposphere over southern California, Report 709. Naval Electronics Lab, San Diego, CA
Grover FH (1971) Experimental Noise Reducers for an Active Microbarograph Array. Geophys J Roy Astr Soc 26:41–52
Haak HW, de Wilde GJ (1996) Microbarograph systems for the infrasonic detection of nuclear explosions, KNMI publication, WR 96–06
Hedlin MAH, Raspet R (2003) Infrasonic wind noise reduction by barriers and spatial filters. J Acoust Soc Am 114:1379–1386
Hedlin MAH, Alcoverro B, D'Spain G (2003) Evaluation of rosette infrasonic noise-reducing spatial filters. J Acoust Soc Am 114:1807–1820
Hedlin MAH, Alcoverro B (2005) The use of impedance matching capillaries for reducing resonance in rosette infrasonic spatial filters. J Acoust Soc Am 117:1880–1888
Herrin E, Sorrells GG, Negraru P, Swanson JG, Golden P, Mulcahy C (2001) Comparative evaluation of selected infrasound noise reduction methods. Proceedings of the 23rd Seismic Research Review. Los Alamos National Laboratory, Los Alamos, New Mexico, pp. 131–139
Hill RJ, Wilczak JM (1995) Pressure structure functions and spectra for locally isotropic turbulence. J Fluid Mech 296:247–269
Howard W, Dillion K, Shields FD (2007) Acoustical properties of porous hose wind noise filters. J Acoust Soc Am 122:2985
Kaimal JC, Eversole RA, Lenschow DH, Stankov BB, Kahn PH, Businger JA (1982) Spectral characteristics of the convective boundary layer over uneven terrain. J Atmos Sci 39:1098–1114
Kolmogorov AN (1941) Local structure of turbulence in an incompressible fluid at very high Reynolds numbers. Dokl Akad Nauk SSSR 30:299–303
Koracin D, Berkowicz R (1988) Nocturnal boundary-layer height: observations by acoustic sounders and predictions in terms of surface-layer parameters. Boundary-Layer Meteorol 43:65–83
Landau LD and Lifshitz EM (1959) Fluid mechanics: course of theoretical physics, vol. 6. Addison-Wesley Series in advanced physics. London, Paris, Frankfurt: Pergamon Press, p. 536
Larson RJ, Craine LB, Thomas JE, Wilson CR (1971) Correlation of winds and geographic features with production of certain infrasonic signals in the atmosphere. Geophys J R astr Soc 26:201–214
Lettau H (1939) Atmosphärische Turbulenz. Akademische Verlagsgesellschaft, Leipzig
Liszka L (2008) Infrasound: a summary of 35 years of infrasound research. Institutet for rymdfysik, IRF Scientific report 291, ISBN 978-91-977255-0-7
McBride WE, Bass HE, Raspet R, Gilbert KE (1992) Scattering of sound by atmospheric turbulence: Predictions in a refractive shadow zone. J Acoust Soc Am 91:1336–1340
McKisic JM (1997) Infrasound and the infrasonic monitoring of atmospheric nuclear explosions: a literature review, final report submitted to the DOE and Phillips Lab, PL-TR-97-2123
McDonald JA, Douze EJ, Herrin E (1971) The structure of atmospheric turbulence and its application to the design of pipe arrays. Geophys J R astr Soc 26:99–109
McDonald JA, Herrin E (1974) Properties of pressure fluctuations in an atmospheric boundary layer. Boundary-Layer Meteorol 8:419–436
Miles NL, Wyngaard JC, Otte MJ (2004) Turbulent pressure statistics in the atmospheric boundary layer from large-eddy simulation. Boundary-Layer Meteorol 113:161–185
Monin AS, Yaglom AM (1975) Statistical fluid mechanics: mecahnics of turbulence, vol. 2. MIT Press, Cambridge, p. 874
Monin AS, Obukhov AM (1954) Basic laws of turbulent mixing in the ground layer of the atmosphere. Trans Geophys Inst Akad Nauk USSR 151:163–187

Nishiyama RT, Bedard AJ Jr (1991) A Quad-Disc static pressure probe for measurement in adverse atmospheres: with a comparative review of static pressure probe designs. Rev Sci Instrum 62:2193–2204
Noel SD, Whitaker RW (1991) Comparison of noise reduction systems. Los Alamos National Lab report LA-12003-MS
Obukhov AM (1941) Spectral energy distribution in a turbulent flow. Izv Akad Nauk SSSR Ser Georgr I Geofiz 5:453–466
Olson HF (1947) Elements of acoustical engineering, 2nd edn. D. Van Nostrand Company, Princeton, NJ
Panofsky HA (1962) Scale analysis of atmospheric turbulence at 2 meters. Q J R Meteorol Soc 88:57
Panofsky HA, Dutton JA (1984) Atmospheric turbulence: models and methods for engineering applications. John Wiley, New York, p 397
Panofsky HA, Mazzola C (1971) Variances and spectra of vertical velocity just above the surface layer. Boundary-Layer Meteorol 2:30–37
Pidwirny M, Budikova D (2006) Local and regional wind systems. In: Cutler J (ed) Encyclopedia of Earth, Cleveland (Washington, DC: Environmental Information Coalition, National Council for Science and the Environment)
Priestley JT (1966) Calculation of the effectiveness of infrasonic line microphones for reducing wind noise. National Bureau of Standards Report 9380
Raspet R, Webster J, Dillon K (2006) Framework for wind noise studies. J Acoustic Soc Am 199:834–843
Rockway JW, Hower GL, Craine LB, Thomas JE (1974) Applications of ray-tracing to observations of mountain-associated infrasonic waves. Geophys J R astr Soc 35:259–266
Sabatier JM, Bass HE, Bolen LN, Attenborough K, Sastry VVSS (1986) The interaction of airborne sound with the porous ground: the theoretical formulation. J Acoust Soc Am 79:1345–1352
Sabatier JM, Raspet R, Frederickson CK (1993) An improved procedure for the determination of ground parameters using level difference measurements. J Acoust Soc Am 94:396–399
Shams QA, Zuckerwar AJ, Sealey BS (2005) Compact nonporous windscreen for infrasonic measurements. J Acoust Soc Am 118:1335–1340
Shields FD (2005) Low-frequency wind noise correlation in microphone arrays. J Acoust Soc Am 117:3489–3496
Strasberg M (1988) Dimensional analysis of windscreen noise. J. Acoust Soc Am 83:544–548
Taylor GI (1938) The spectrum of turbulence. Proc Roy Soc A164:476–490
Thuillier RH, Lappe UO (1964) Wind and temperature profile characteristics from observations on a 1400 ft tower. J Appl Meteorol 3:299–306
Walker KT, Zumberge MA, Hedlin MAH, Shearer P (2008) Methods for determining infrasound phase velocity direction with an array of line sensors. J Acoust Soc Am 124:2090–2099
Walker KT, Zumberge M, Hedlin M, Berger J, Shearer P (2007) Resolving infrasound signals with arrays of optical fiber infrasound sensors (OFIS): low wind noise, superb back azimuth (and elevation angle) resolution, and a compact design. Infrasound technology workshop. Tokyo, Japan. 13–16 November
Walker KT, Dzieciuch M, Zumberge M, and DeWolf S (2007) M-sequences and an array of speakers form a sensor calibrator down to 8 Hz: Application to the OFIS at the new Camp Elliott OFIS array. Infrasound technology workshop. Tokyo, Japan. 13–16 November
Wyngaard JC, Siegel A, Wilczak J (1994) On the response of a turbulent-pressure probe and the measurement of pressure transport. Boundary-Layer Meteorol 69:379–396
Zumberge MA, Berger J, Hedlin MAH et al (2003) An optical fiber infrasound sensor: A new lower limit on atmospheric pressure noise between 1 and 10 Hz. J Acoust Soc Am 113:2474–2479

Part II
Sources, Observations, and Propagation

Chapter 6
Worldwide Observations of Infrasonic Waves

P. Campus and D. R. Christie

6.1 Introduction

The International Monitoring System (IMS) is designed to ensure compliance with the Comprehensive Nuclear-Test-Ban Treaty (CTBT). Four separate technologies are used in this global monitoring network. A network of 170 seismic stations is used to detect and locate underground nuclear explosions. Underwater explosions are detected with exquisite sensitivity by a network of 11 hydroacoustic stations. A network of 60 infrasound monitoring stations distributed uniformly over the face of the globe is used to detect and locate atmospheric nuclear explosions. Finally, a global network of 80 radionuclide stations is used to detect specific radionuclides that can provide unambiguous evidence for a nuclear explosion.

The infrasound component of the IMS is unique in the sense that all of the stations in this network (with the exception of the station at Warramunga in central Australia) have been established in the last 10 years. The IMS infrasound network is much larger and far more sensitive than any of the earlier infrasound monitoring networks. The stations in this network are located in a wide variety of environments including tropical equatorial rainforests, semi-urban areas with high population densities, semi-desert areas, exposed locations on some of the most remote islands on the globe and the harsh ice-covered Polar regions of the Arctic and Antarctic. A large number of infrasonic signals are detected each day at all stations in the IMS infrasound network. Some of these signals can be easily identified while others can be identified using data from other monitoring networks. However, at the present time, the source of many of the detected infrasound signals is unknown. Several new and interesting infrasound sources have been identified using data from the IMS infrasound network during the last decade. It can be anticipated that the detailed study of data from this unique network will eventually lead to the discovery of other new sources of infrasound.

The establishment of the IMS infrasound network is proceeding rapidly. As of the end of 2008, 41 stations in this global network have been certified and are transmitting

P. Campus (✉)
CTBTO, PTS/IDC, Vienna International Centre, P.O. Box 1200, 1400, Vienna, Austria
e-mail: paola.campus@ctbto.org

A. Le Pichon et al. (eds.), *Infrasound Monitoring for Atmospheric Studies,*
DOI 10.1007/978-1-4020-9508-5_6, © Springer Science+Business Media B.V. 2010

data continuously via satellite or virtual private network (VPN) to the International Data Centre (IDC) in Vienna, Austria. The current status of the IMS infrasound network is illustrated in Fig. 6.1 (Christie and Campus 2010). This chapter also provides an overview of the design and establishment of the stations in the global infrasound network. IMS infrasound stations are array stations with apertures in the range from 1.0 to 3.0 km. The number of elements in each array is usually 7 or 8, but a few stations have only 4 array elements, one station (IS27 Neumayer Base in Antarctica) has 9 array elements and IS23 Kerguelen, which is located in a high-wind environment, has 15 array elements. Infrasound data at all stations in the IMS network are sampled at 20 samples per second. The Nyquist frequency (10 Hz) effectively limits the frequency of detected signals at IMS infrasound stations to less than about 8 Hz. A wind noise-reducing pipe array is connected to the sensor at each array element. Elements with 18-m diameter pipe arrays are denoted by "H" and elements with 36-m or 70-m diameter pipe arrays are denoted by "L." All data are analysed in near real time and archived at the IDC. This high-quality archived data set is by far the largest infrasound data set ever recorded.

The routine analysis of data from the global infrasound network at the IDC has led to the detection of a very large number of infrasound signals from sources distributed over all parts of the globe (Brachet et al. 2010). Most of these detected events originate at local or regional distances from an infrasound monitoring station. Some events are detected, however, at a large number of stations. This chapter is concerned with an attempt to provide an overview of the wide variety of infrasonic waves that are routinely observed at IMS infrasound stations around the globe. This chapter will also include a discussion of a number of possible applications for the use of infrasound data from the global monitoring network.

The overview presented here of signals observed at IMS infrasound stations is limited to a survey of infrasonic waves. It is worth noting, however, that a wide variety of other types of atmospheric waves ranging from highly nonlinear internal trapped waves (Christie et al. 1978; Christie 1989, 1992) to longer period gravity waves created by shear instabilities in the upper tropospheric and boundary layer jets are routinely recorded at stations in this global network.

6.2 Observations of Infrasonic Waves at IMS Infrasound Stations

Infrasonic waves are generated by a large variety of natural and man-made sources (Campus 2004). Natural sources include meteors, auroras, convective storms and lightning, tornadoes, interacting large amplitude ocean waves, earthquakes, icequakes, landslides, avalanches, the calving of icebergs and glaciers, continuously erupting and explosive volcanoes, tsunamis, waterfalls and coastal surf. Man-made sources of infrasound include nuclear explosions, mining and other chemical explosions, the launch and re-entry of satellites, spacecraft and rockets, aircraft, industrial sources such as exhaust fumes from industrial plants, oil and gas refinery flares, hydroelectric dams, wind generators and other cultural sources.

Table 6.1 provides a list of the most important types of observed infrasonic waves, including their typical range of frequencies, observed maximum amplitudes

Table 6.1 Some properties of infrasonic waves

Infrasound source or type	Frequency range (Hz)	Maximum observed amplitude (Pa)	Estimated maximum detection range (km)	References
Atmospheric nuclear explosions	0.002–20	>20	>20,000	Donn and Shaw 1967; Reed 1969 Mutschlecner et al. 1999 Posey and Pierce 1971
Underground nuclear explosions	~1–20	~1	~1,000	Whitaker 2007, 2008
Mining explosions	0.05–20	~5	>5,000	Hagerty et al.2002
Other chemical explosions	0.05–20	~10	>5,000	Reed 1987b Davidson and Whitaker 1992 Grover 1968 Evers et al. 2007
Bridges and other structures	~0.5–20	~0.5	<100	Donn et al. 1974
Gas exhausts from industrial activity	1–20	~0.5	~1,000	Liszka 1974
Launching of rockets and spacecraft	0.01–20	~5	~3,000	Balachandran and Donn 1971 Greene and Bedard 1986
Satellite and spacecraft re-entry	~0.1–10	~1	>2000	Cotten et al. 1971 ; Garcés et al. 2004b
Subsonic aircraft	0.3–20	~2	<100	Evers 2005
Supersonic aircraft	0.3–20	~10	~5,000	Donn 1978; Liszka and Waldemark 1995
Meteors	0.01–20	>10	>20,000	ReVelle 1976
Auroral Infrasound	0.008–20	~2	~4,000	Wilson 1971
Calving of Icebergs and Glaciers	~0.5–8	~1	~200	Campus 2004
Volcanic eruptions	0.002–20	>20	>20,000	Donn and Balachandran 1981
Convective storms	0.01–0.1	~0.5	>1,500	Georges, 1973; Bedard, 1998
Earthquakes	~0.005–10	~4	>10,000	Le Pichon et al., 2003; Mutschlecner and Whitaker, 2005; Young and Greene 1982
Forest fires; large industrial fires	2–20	~2	~4,000	Bedard 1988
Landslides; avalanches	~0.1–20	~1	~1,000	Bedard, 1988, 1993 Arnoult et al. 2005
Microbaroms	0.12–0.35	~5	~10,000	Donn and Rind 1972 Garcés et al. 2004a
Mountain associated waves	~0.007–0.1	~5	~10,000	Rockway et al. 1974 Wilson et al. 2003
Surf	1–20	~0.2	~250	Garcés et al. 2003
Lightning	0.5–20	~2	~50	Few 1970 Lin and Langston 2007
Tornadoes	0.5–20	~0.5	~300	Bedard et al. 1998, 2004a, 2005
Tsunamis	~0.5–2	~0.1	~1,000	Le Pichon et al. 2005c
Waterfalls	0.5–20	~0.2	~200	Bedard 1988

The maximum frequency listed in this table is 20 Hz, the upper frequency limit for infrasound. Some sources may also generate sound at higher frequencies. References are representative only. Many other references exist for most types of infrasound noted in this table.

expressed in Pascals (1 Pa = 10^{-5} bar), estimated maximum range of detection and sample references. A number of relatively minor sources of infrasound have not been included in this table, including hydroelectric power stations, wind turbines, icequakes, microbursts (Bedard 2005), sprites (Liszka, 2004), solar eclipses (Kunhikrishnan and Krishna Murthy 1982; McIntosh and ReVelle 1984) and sources associated with cultural activity such as highways, trains and airports.

"Other references which may be of use concerning observations and theory of infrasound sources include the following:

- Thomas et al. (1971) a summary of articles up until 1970.
- Thomas et al. (1972) a supplement to the above with articles up to 1972.
- Greene and Howard (1975) an observational study of sources with a useful table.
- Axefors et al. (1985) a bibliography of articles up to 1983.
- Backtemans et al. (1985) a general summary including a bibliography.
- McKisic (1996) a comprehensive bibliography of more recent papers.

We note that there are probably many other sources that have not yet been identified or classified. The references are meant to serve only as an introduction to the reader for observations of a given source type; the list of references is by no means comprehensive. In many cases, there are large numbers of papers on a given type. The highest frequency noted in this table is limited to 20 Hz, the accepted upper frequency limit for infrasound. Some of the sources noted in this table may generate higher frequency sound. The upper frequency limit listed in this table for infrasound from some sources is less than 20 Hz. These sources may also generate higher frequency infrasound, but this has not yet been observed. As noted above, IMS infrasound data is digitised at a sampling rate of 20 Hz. Observations of infrasonic waves at IMS stations are therefore limited by the Nyquist frequency to frequencies of less than about 8 Hz. The maximum observed amplitudes are estimates only and are based on a survey of the literature. The maximum detection ranges listed in Table 6.1 are also estimates based primarily on observations reported in the literature. The maximum detection range at a specific station at a particular time depends on a large number of factors including the upper atmospheric wind components in the direction of wave propagation, the degree of signal attenuation along the path between the source and receiver, background noise levels and the efficiency of detection algorithms. It can be anticipated that future improvements in infrasound monitoring technology will lead to lower detection thresholds and maximum detection ranges that are larger than those listed in Table 6.1.

The following sections provide a brief description of typical observations at IMS infrasound stations.

6.3 Natural Sources of Infrasound

Infrasonic signals generated by naturally occurring sources are frequently observed at all monitoring stations in the global infrasound network. Many of these signals, such as microbaroms, signals from ongoing volcanic eruptions, and surf-generated

infrasound are continuous over long periods of time. Signals of this type are normally regarded as background noise from a nuclear explosion monitoring perspective. Other signals such as infrasonic waves generated by bolides and explosive volcanic eruptions may be detected as large-amplitude, short-duration, sharp-onset signals. The morphology of these signals may be similar to the morphology of signals generated by an atmospheric nuclear explosion.

6.3.1 Microbaroms

The nonlinear interaction of large-amplitude storm-generated waves on the surface of the ocean generates standing waves, which radiate continuous infrasonic waves into the atmosphere (Posmentier 1967; Arendt and Fritts 2000). These commonly occurring waves are called microbaroms. Infrasonic waves of this type were first reported by Benioff and Gutenberg (1939) and Gutenberg and Benioff (1941) who describe observations near Pasadena, California, and by Baird and Banwell (1940) who recorded microbaroms at Christchurch, New Zealand. Seismic waves known as microseisms are also generated by standing ocean waves as shown by Longuet-Higgens (1950).

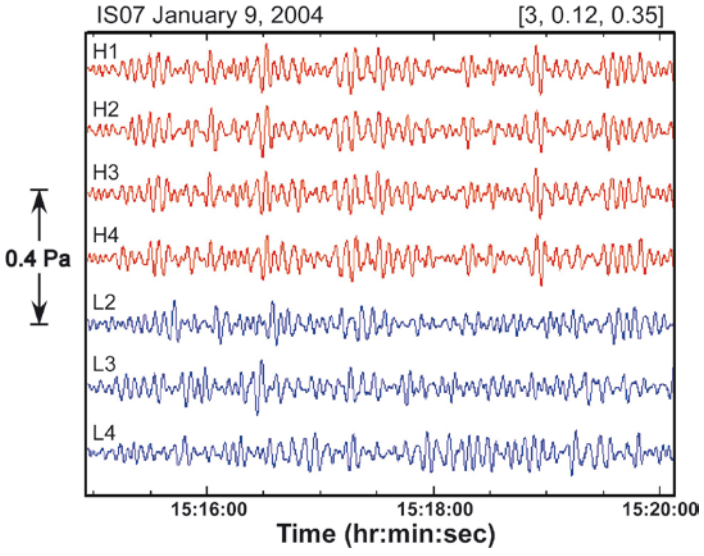

Fig. 6.1 Microbaroms recorded at IS07, Warramunga, Australia. The order and the minimum and maximum frequency of the Butterworth passband filter applied to the data are specified within the brackets in the header of this diagram (and in other diagrams presented below). The microbarom signals illustrated in this diagram were generated by tropical cyclone "Heta" as the cyclone moved to the south of the Cook Islands in the Pacific Ocean. The distance from IS07 to "Heta" at the time of these observations was about 5,400 km. Array elements in the small aperture sub-array are shown in red. Array elements in the large aperture main array are shown in blue. Data from L1 is not shown in this diagram because L1 is co-located with H1 at IS07. The backazimuth is 139º and the apparent velocity is 0.377 km/s

Microbaroms are therefore the atmospheric equivalent of microseisms (Donn and Naini 1973, Barruol et al. 2006). Infrasonic waves of this type are almost always present at any point on the surface of the globe at any time. These ubiquitous waves have frequencies in the range from about 0.12 to 0.35 Hz with amplitudes that can range from tens of mPa up to a few Pa (Donn and Rind 1971). They occur as almost monochromatic wave trains with characteristic modulations in wave amplitude (see Fig. 6.1) and can be detected at distances of up to 10,000 km. Rind (1977) estimates that the energy input into the lower thermosphere due to the dissipation of upward propagating microbaroms is a significant source of heating comparable with the energy input due to upward propagating gravity waves. Hetzer et al. (2007) have recently shown that microbaroms associated with hurricanes, typhoons and tropical cyclones are created in the interaction of storm-generated waves with the ambient wave field surrounding the storm. Thus, the microbarom source does not coincide with the eye of the storm.

The microbaroms illustrated in Fig. 6.1 were recorded on the 8-element IMS infrasonic array at IS07 Warramunga, located in the arid interior of the Australian continent. Microbaroms associated with intense storms over the Southern Ocean are frequently detected at IS07. Microbaroms associated with tropical cyclones in the Indian Ocean to the west and in the Pacific Ocean to the east of the array are also routinely observed at IS07. The microbaroms shown in Fig. 6.1 were generated by large amplitude interacting ocean waves associated with tropical cyclone "Heta" in the South Pacific Ocean. The progress of this tropical cyclone was monitored using microbarom data from IS07 during a five-day period as the cyclone moved south from the Cook Islands over a distance of more than 1,000 km.

The array at IS07 is divided into a large centred triangle array with an aperture of about 2.3 km and a small centred triangle sub-array with an aperture of about 0.38 km. The sensor at each array element in the large aperture array is connected to a 70-m diameter wind-noise-reducing pipe array. These sites are denoted by "L." The sensors in the small aperture sub-array are connected to an 18-m diameter pipe array. These sites are denoted by "H." Sites L1 and H1 are collocated at the centre of the array. The separations between array elements at the vertices of the large aperture array range from a minimum distance of 1.78 km (L3 to L4) to a maximum distance of 2.26 km (L2 to L3). The maximum separation between sites in the H-array is 0.383 km (sites H2 and H4).

The correlation of microbarom signals is very high between sensors separated by up to about 0.5 km and very low when the spacing between sensors exceeds a few kilometres. This can be seen in the microbarom data presented in Fig. 6.1. The degree of signal correlation between sites L2, L3 and L4 in the large aperture L-array is very low. In contrast, the degree of signal correlation between all sites in the small aperture H-array is high.

Microbarom signal amplitudes exhibit characteristic diurnal and semi-diurnal variations, associated with the modulation of the mean upper atmospheric winds by the atmospheric tides. This means that the amplitude of microbarom waves at most stations will vary significantly, depending on the time of day. The detection capability for coherent infrasonic signals with dominant frequencies in the microbarom passband (0.12–0.35 Hz) may be enhanced when signal processing is limited to sites in the large aperture L-array since the microbaroms are incoherent between array elements in this array. Thus, the microbarom signals recorded on the L-array represent incoherent

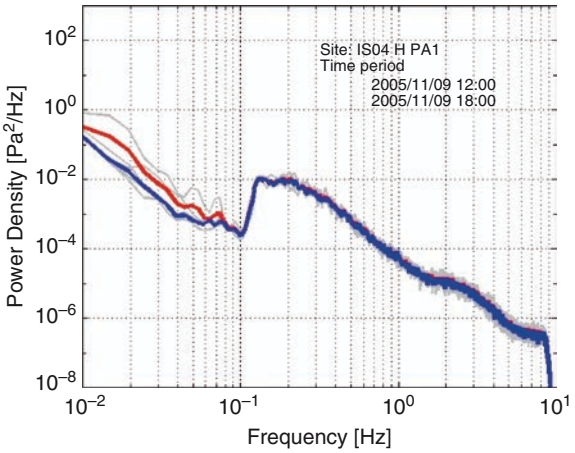

Fig. 6.2 Average (*red curve*) and median (*blue curve*) of the power spectral density of data recorded over a 6-h period during the night at IS04 Shannon, Australia. The microbarom peak is clearly visible during this 6-h period

background noise. In most cases, however, even though the microbarom signals are largely incoherent between sites in the L-array, the high level of background noise due to incoherent microbaroms will limit detection of coherent signals in this passband. It is for this reason that the most important passbands from a nuclear explosion monitoring perspective lie immediately below and immediately above the passband dominated by microbarom waves (~0.12–0.35 Hz). Studies carried out at IMS stations in Australia (see, e.g., Christie et al. 2005; Christie and Kennett 2007) indicate that the most important monitoring passband for the reliable detection of infrasound from small nuclear explosions spans a frequency range of about 0.4–1.2 Hz. This passband will be referred to as the primary monitoring passband.

The observation of microbaroms in the frequency domain may provide a measure of the level of wind-generated background noise at an infrasound array. Since microbaroms are usually observed under relatively low wind noise conditions, the observation of a microbarom peak in the power spectral density plot indicates that noise levels in the primary monitoring passband are low and the array station can potentially detect low-yield nuclear explosions at great distances. Microbaroms will normally be observed at all times of day and night at stations located in tall dense forests. IS04 Shannon is located in a very tall dense forest in the southwest corner of Australia. Figure 6.2 illustrates the power spectral density of data recorded over a 6-h period at IS04 during the night. Similar results are found for data recorded during the day. These results indicate that this station has very good detection capability.

6.3.2 Mountain-Generated Infrasound

Airflow over mountain ranges can generate long period infrasonic waves that propagate for distances of up to 10,000 km (Larson et al. 1971; Rockway et al. 1974; Wilson and Olson, 2003, Wilson et al., 2010). Orographically generated

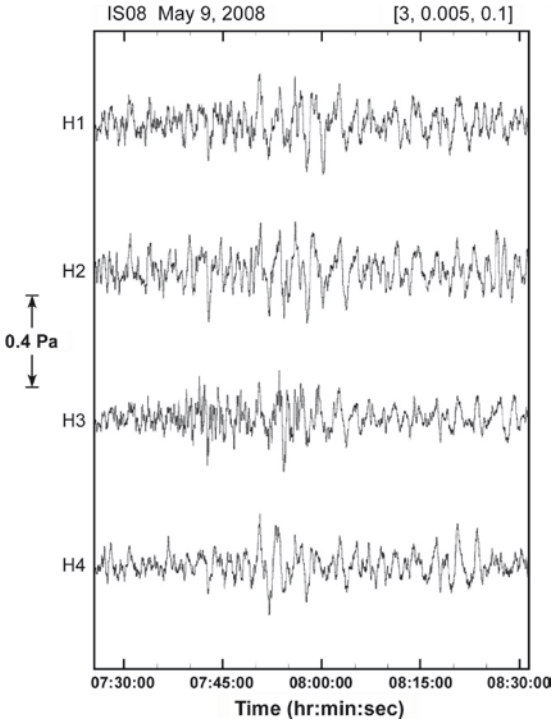

Fig. 6.3 Mountain generated infrasonic waves, recorded at IS08, La Paz, Bolivia

infrasonic waves are continuous with frequencies ranging from about 0.007 to 0.1 Hz. Their amplitudes are usually fairly small, but occasionally reach values above 1 Pa. The precise source mechanism that causes waves of this type is not well understood. The only theoretical work on this subject appears to be that of Chimonas (1977) who developed an idealised model for the generation of mountain-associated infrasound based on the interaction of low-frequency wind oscillations with terrain undulations. Mountain-generated infrasonic waves increase the background noise level at longer periods and contaminate signals recorded at large distances from the source. Figure 6.3 shows an example of mountain-generated infrasonic waves recorded at IS08 La Paz in Bolivia.

6.3.3 Auroral Infrasound

Infrasonic waves generated by auroras are commonly recorded at high latitudes during periods of high geomagnetic activity (see Chrzanowski et al 1961; Wilson 1967, 1971, 2005; Procunier 1971; Wilson and Olson 2005a, Liszka 2008a). Aurora-generated infrasound may also be observed at mid latitudes during strong geomagnetic storms (Maeda and Young 1966; Campus 2003, 2004). As noted in Table 6.1, auroral infrasound has frequencies ranging from about 0.008 Hz up to at least 20 Hz

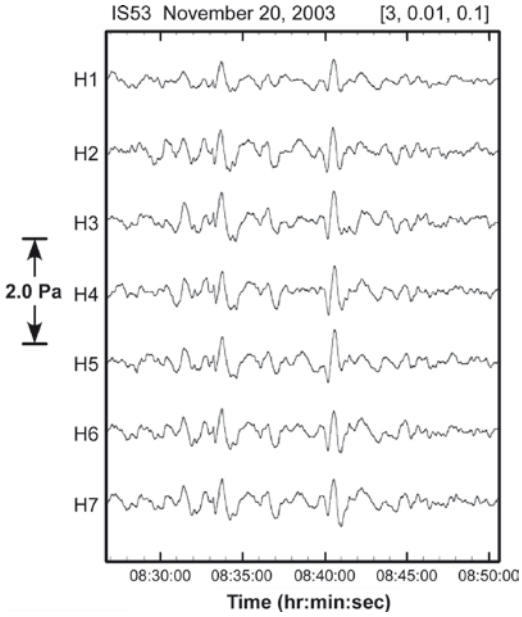

Fig. 6.4 Aurora-generated infrasound recorded at IS53, Fairbanks, Alaska (64.9ºN). The average backazimuth of these waves is about 30º and the average apparent velocity over the array is about 480 m/s

and amplitudes between approximately 0.01 and 2 Pa. Infrasonic signals generated by auroras tend to be continuous with short intervals of higher amplitude. From a nuclear explosion monitoring perspective, auroral-generated infrasound, when present, is part of the continuous background noise at infrasound monitoring stations. These waves often have high apparent velocities (typically 400 to 1,000 m/s), corresponding to a source located at high altitude. Figures 6.4 and 6.5 show two examples of infrasonic waves generated by auroras during a strong geomagnetic storm in November 2003 and recorded at IMS infrasound stations located at high latitude (IS53 Fairbanks) and mid-latitude (IS05 Hobart). We note that visible observations across southern Australia of the aurora (Aurora Australis) were widely reported in the press (including the area where IS05 is located) at the time of this geomagnetic storm. Auroral-generated infrasonic waves are also frequently observed during geomagnetic storms at IS04 Shannon, located in the southwest corner of Australia. The apparent velocities and backazimuths of the events illustrated in Figs. 6.4 and 6.5 confirm the identification of these infrasonic waves.

6.3.4 Infrasound from Meteorological Sources, Lightning and Sprites

Infrasound with frequencies between 0.02 and 0.1 Hz and amplitudes up to about 0.5 Pa may be generated by severe convective storms (Goerke and Woodward 1966;

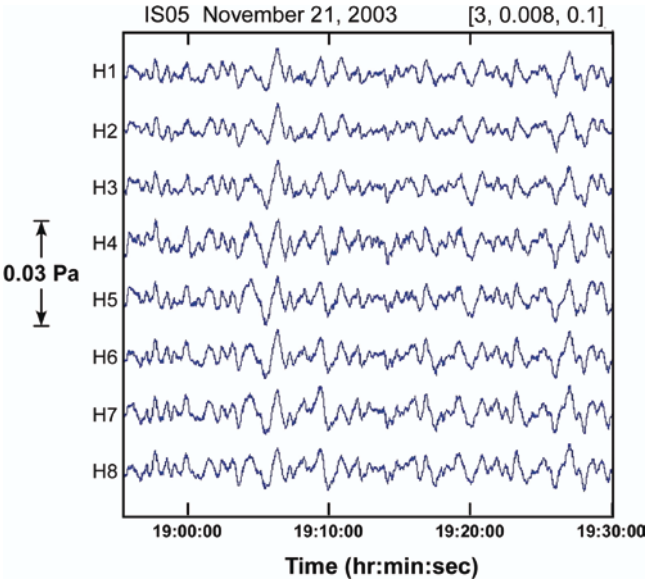

Fig. 6.5 Aurora-generated infrasound recorded at IS05 Hobart, Tasmania, Australia (42.5ºS). The backazimuths of these waves range from 205º to 220º and the average apparent velocity of the signals over the array is 540 m/s

Georges 1973). These signals can be detected at distances of more than 1,500 km. The source mechanism for waves of this type is poorly understood (Bowman and Bedard 1971). Other meteorological sources of infrasound include microbursts, tornadoes, lightning and sprites.

Microbursts are intense highly localised thunderstorm-generated downdrafts of cold air that impinge upon the surface creating a radially spreading outflow density current with a ring vortex along the leading edge. Windshear generated by these intense short-lived disturbances is a serious hazard for aviation, especially during takeoff and landing. Microbursts are characterised by very high winds (up to 75 m/s) that are confined to a small area (less than 4 km in diameter) at or near the surface. Infrasound generated by microbursts will only be detected at relatively small distances from the parent thunderstorm (see Table 6.1) and may be masked by turbulence generated by storm-generated winds.

Most thunderstorm-generated downdrafts are much larger in scale than the intense localised downdraft and outflow that defines a microburst. These larger-scale downdrafts also generate cold outflow density currents at the surface, which propagate away from the thunderstorm for distances of more than 20 km. The surface winds associated with these usually benign large-scale thunderstorm density currents (typically less than 10 m/s) are much less than those associated with a microburst. The winds and wind-generated turbulence associated with a normal thunderstorm outflow are usually sustained over a period of at least 5 min and in some cases over periods of more than 1 h. Observations of infrasonic waves generated by large-scale

thunderstorm outflow density currents have not been reported. Thunderstorm outflow density currents are, however, frequently observed at many infrasonic monitoring stations in the form of a large-amplitude, slowly propagating (typically 10 m/s) signal. The cold outflow in these density currents is also a significant source of wind-generated noise. The morphology of a typical thunderstorm outflow micropressure signature is discussed below.

Tornadoes radiate higher frequency infrasound in the range from about 1 to 20 Hz. Tornado-generated infrasound has been studied in detail by Bedard (1998, 2005) who finds that the properties of infrasonic waves radiated by tornadoes appear to be consistent with the radial vibration model proposed by Abdullah (1966). The results of an evaluation of a prototype infrasonic tornado-detection network are described in considerable detail in Bedard et al. (2004a, b). Several tornadoes were successfully detected during this evaluation experiment. The detection of tornadoes using infrasonic waves provides an important example of the use of infrasound technology.

Infrasonic waves associated with lightning discharges usually occur as short-lived disturbances with frequencies in the range from about 0.5 to 20 Hz and amplitudes ranging from 0.01 up to about 2 Pa (Dessler 1973; Balachandran 1982; Few 1985; Campus 2004; Assink et al. 2008; Liszka 2008a). The dominant frequency of these short-lived disturbances is about 1 Hz. These pulse-like waves often travel almost vertically downwards when the thunderstorm is almost directly overhead. They are also detected as direct arrivals propagating at the local speed of sound when the thunderstorm is some distance from the monitoring station. The maximum range for the detection of lightning-generated infrasound is about 50 km.

An example of the micropressure variations associated with a thunderstorm outflow along with infrasonic signals generated by lightning during this storm is given in Fig. 6.6. This data was recorded at IMS infrasound station IS31, Aktyubinsk, Kazakhstan. The micropressure channels in this diagram are specified by "BDF." Wind speed data (denoted by "LWS") are also included in this diagram. The large amplitude turbulent fluctuations observed on the micropressure channels are a manifestation of wind-generated noise associated with the outflow winds generated by the nearby thunderstorm. The sharp spikes in the data both before and after the onset of the turbulent winds at the surface correspond to infrasonic waves generated by lightning. A detailed examination of the lightning signatures marked by the "spikes" in Fig. 6.6 shows that the vast majority of these signals arrive at the array as direct arrivals with apparent velocities corresponding to the local speed of sound. It appears that the thunderstorm in this case approached the array from the west, passed directly over the array (or slightly to the south of the array) and then departed towards the east. This is shown by the observed backazimuths from lightning generated by the approaching and departing storm. Some of the lightning-generated signals associated with this storm were probably generated when the storm was over (or almost over) the array, but these signals are obscured in this example by thunderstorm outflow wind-generated turbulence.

Figure 6.7 shows in detail a typical example of the micropressure signature of infrasonic waves generated by a lightning discharge during the storm on August 28, 2003.

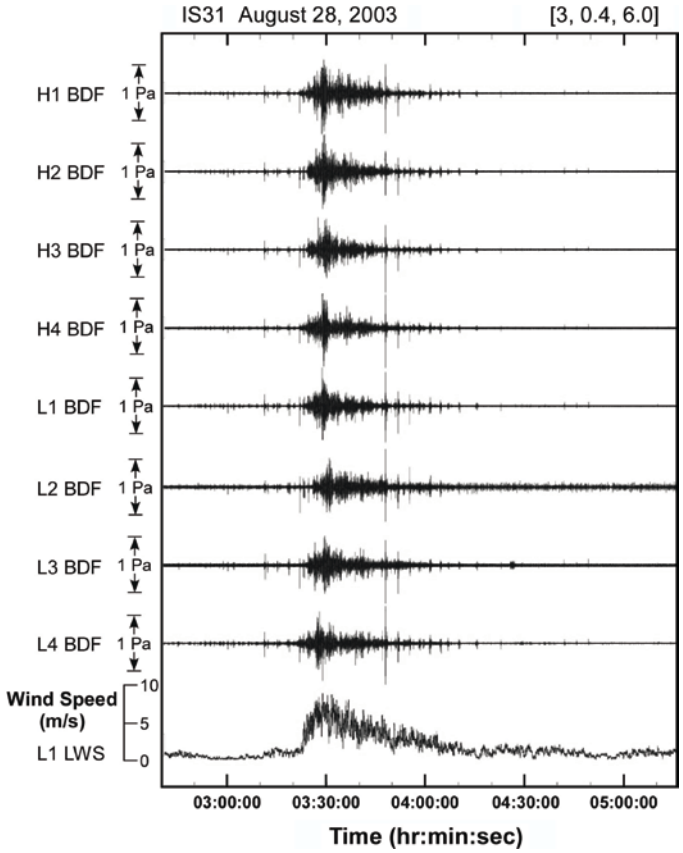

Fig. 6.6 Wind noise and infrasonic signals generated by a local thunderstorm and associated lightning. Data were recorded at IS31, Aktyubinsk, Kazakhstan, on August 28, 2003. Micropressure data is denoted by BDF and wind-speed data by LWS

Sprites are high-altitude discharges into the upper atmosphere, which also generate high-frequency infrasound in the neighbourhood of thunderstorms. Infrasonic signals from sprites typically occur in the form of short-lived chirp-like signatures that may be detected at distances of more than 100 km (Liszka 2004, 2008a; Liszka and Hobara 2006; Farges et al. 2005).

6.3.5 Earthquakes

Infrasonic signals generated by earthquakes are frequently observed at infrasound stations (see, e.g., Grover and Marshall 1968; Cook 1971, Young and Greene 1982;

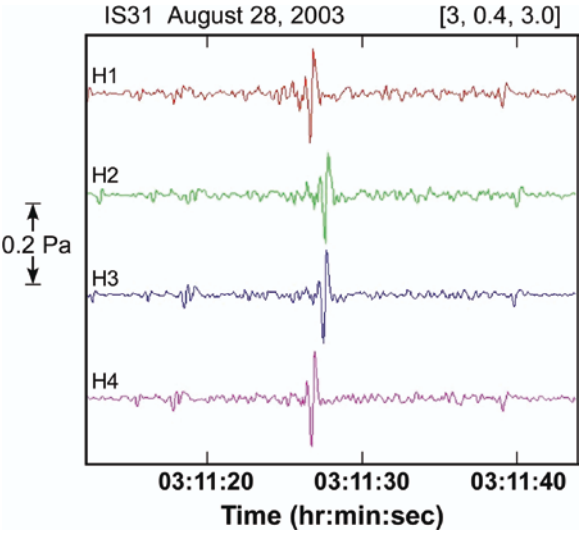

Fig. 6.7 Detailed signature of an infrasonic wave generated by lightning during the thunderstorm on August 28, 2003 at IS31 Aktyubinsk, Kazakhstan. This infrasonic signature was recorded before the thunderstorm outflow winds arrived at the array station. The backazimuth is 286º and the apparent velocity of the signal over the array is 0.349 km/s

Olson et al. 2003; Le Pichon et al. 2003, 2006c; Campus 2004, 2007a; Mutschlecner and Whitaker 2005). Infrasound associated with large earthquakes arises from at least three distinct mechanisms. The first mechanism involves the near vertical radiation of an acoustic wave away from the surface of the Earth during the passage of seismic body and surface waves. Since the vertical particle velocities in the Earth and the air must be identical at the earth–air interface, the apparent horizontal velocities of the airwave and the seismic wave are identical. The apparent velocities of locally generated infrasonic waves of this type are therefore very high, usually in the range from a few km/s up to about 8 km/s, and this characteristic can be used to identify these signals. Violent ground motion at the epicentre of a shallow earthquake provides a second mechanism for the generation of infrasonic waves in the atmosphere. These waves are ducted through the atmosphere at normal atmospheric acoustic velocities and, due to the slower sound speed, arrive at the infrasonic sensor after the ground-coupled airwaves. Long period infrasonic waves may also be generated in the atmosphere when seismic surface waves induce motions in high mountains, causing the mountains to radiate infrasonic waves.

As noted in Table 6.1, the frequency range of earthquake-generated infrasonic waves extends from 0.005 to 10 Hz. Amplitudes vary from about 0.01 Pa to a few Pa. Large earthquakes can be detected infrasonically at distances of up to 10,000 km or more. Examples of infrasonic signals associated with an earthquake in Irian Jaya that occurred on October 10, 2002, with a moment magnitude $M_w = 7.5$, are shown in Figs. 6.8–6.11. Signals from this earthquake were recorded at a distance of about

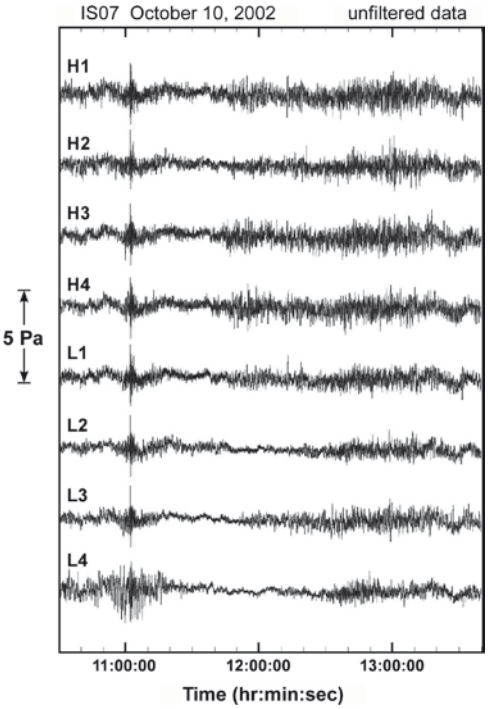

Fig. 6.8 Unfiltered infrasonic data from the Irian Jaya earthquake recorded at IS07, Warramunga, Australia, on October 10, 2002

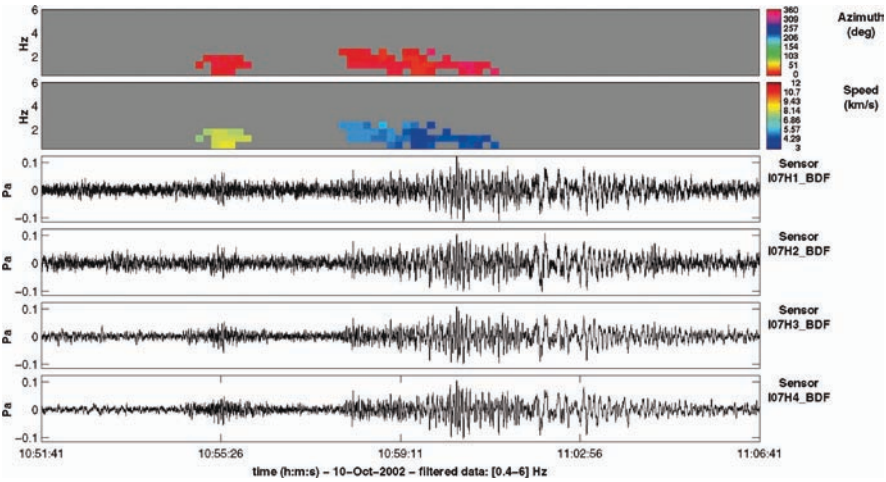

Fig. 6.9 Vertical P and Rayleigh arrivals associated with the Irian Jaya earthquake on October 10, 2002. These ground-to-air coupled waves were detected at IS07, Warramunga, using the progressive multi-channel correlation (PMCC) algorithm. Data are filtered between 0.4 and 6 Hz

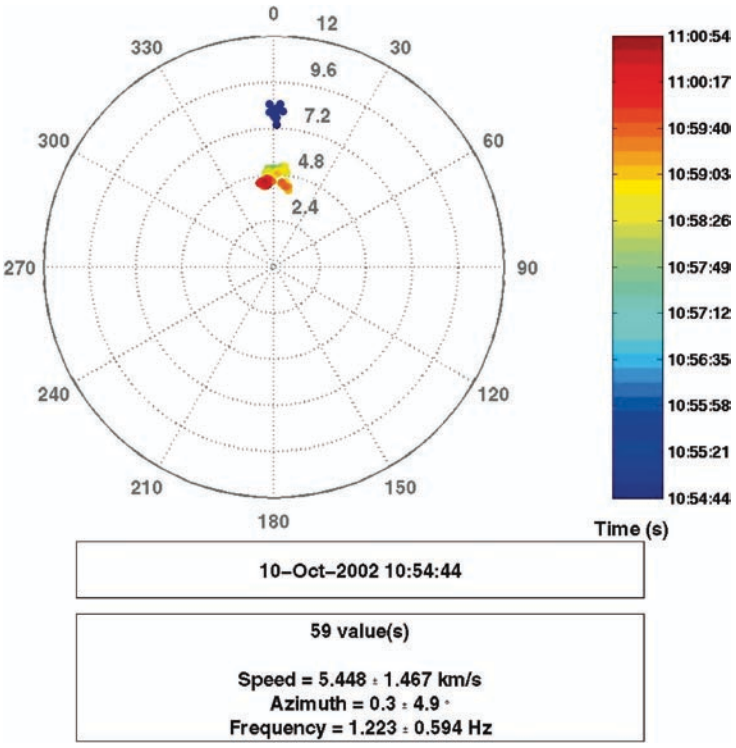

Fig. 6.10 Results of the PMCC analysis for signals generated by the Irian Jaya earthquake on October 10, 2002. The diagram shows the backazimuth (station-to-source) direction and the apparent velocities associated with the two distinct arrivals recorded at IS07 Warramunga, Australia (see Fig. 6.9). The apparent velocities derived from this analysis correspond to seismic P arrivals ($\alpha \sim 8$ km/s) and Rayleigh arrivals ($V_{Ray} = 0.92\beta \sim 4.25$ km/s)

2,000 km at IMS infrasound station IS07 Warramunga, Australia. Two distinct types of arrivals can be seen in Fig. 6.8 at about 1,100 UT and 1,230 UT.

The data shown in Fig. 6.8 have been processed using the progressive multi-channel correlation (PMCC) algorithm (Cansi 1995; Cansi and Le Pichon 2008) applied separately to each group of arrivals. This analysis shows that the first group of waveforms (around 11:00 UT) is associated with the passage of vertical P and Rayleigh waves. The different arrival times and apparent velocities can be clearly seen in Figs. 6.9 and 6.10.

The second group of waveforms, recorded around 12:30 UT is associated with infrasound arrivals propagating at the speed of sound. These arrivals correspond to infrasound generated by the shaking of the area around the epicentre. The results of the PMCC analysis for these arrivals are presented in Fig. 6.11.

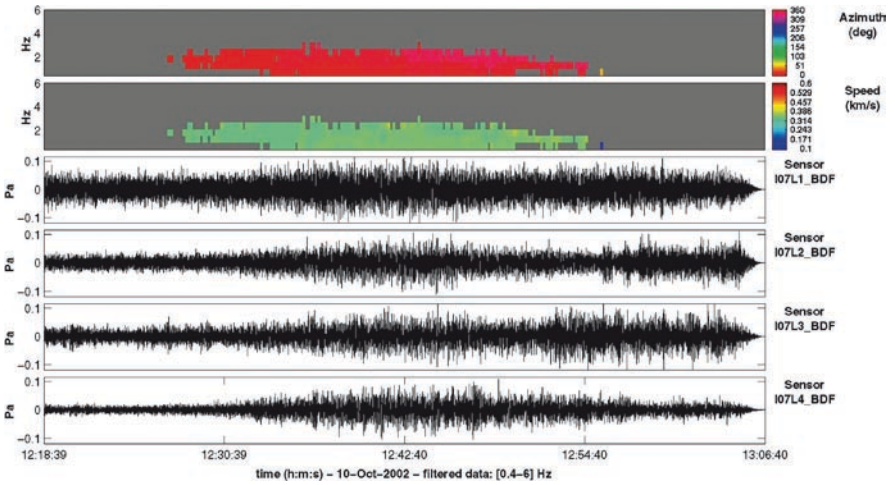

Fig. 6.11 PMCC analysis of infrasound data recorded at IS07, Warramunga, corresponding to infrasound created around the epicentre during the Irian Jaya earthquake on October 10, 2002. Data are filtered between 0.4 and 6 Hz. The observed backazimuth direction (358°) is consistent with the backazimuth derived from data for the ground-coupled vertical P and Rayleigh wave components and the observed apparent velocity (344 m/s) clearly indicates that these waves are atmospheric acoustic waves. The arrival time of these acoustic waves is consistent with a source in the epicentral area of the earthquake

6.3.6 Meteors

Meteors are another important source of infrasonic waves (McIntosh et al., 1976; ReVelle 1976, Evers and Haak 2001; Brown et al. 2002a; Evers and Haak 2003; Campus 2004, 2007a; Edwards et al. 2006; Evers 2008, Liszka 2008b). It has been estimated that the average rate of occurrence of exploding meteors with effective yields of 1 kT or more is greater than two per year over the globe (ReVelle 1997; Brown et al. 2002b). Signals from meteors tend to have frequencies between 0.01 and 20 Hz and amplitudes ranging from 0.01 up to about 10 Pa. The signals are generally quite complex and two or more wave groups corresponding to refractions from different layers in the upper atmosphere are often observed.

An example of infrasonic waves generated by a meteor is given in Fig. 6.12. A few minutes after midnight (local time) on March 27, 2003, a large meteor entered the atmosphere over the north-central United States, moving across Ohio, Illinois, Indiana and Wisconsin and producing a bright luminous blue flash and trail. Fragments of this bolide hit an inhabited area located south of Chicago. A clear signature of this event with several groups of arrivals has been identified in data recorded at IMS infrasound station IS10 Lac du Bonnet, Canada. The records shown in Fig. 6.12 are typical of many meteor-generated infrasound observations.

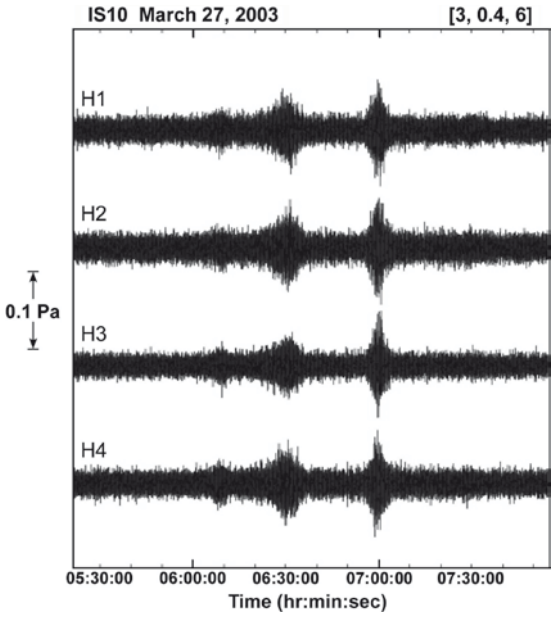

Fig. 6.12 Infrasonic data from the Chicago meteor recorded at IS10 Lac du Bonnet, Canada, on March 27, 2003. Amplitudes are expressed in Pascals. The backazimuth of these waves ranges from about 142° to 148° and the average apparent velocity over the array is 0.340 km/s

6.3.7 Calving of Icebergs and Glaciers

The calving of icebergs and glaciers produces a distinctive infrasonic signal, with sharp-onset high-frequency oscillations ranging between 0.5 and 8 Hz and amplitudes between 0.01 and 1 Pa (Campus 2004, 2007a, 2008). Figures 6.13–6.15 illustrate time series corresponding to signals of this type recorded at IS18 Qaanaaq, Greenland and the results of PMCC analysis.

IMS infrasound station IS18, at a latitude of 77.5ºN, is the northernmost infrasound station in the global monitoring network. The station is located a few kilometres from the isolated settlement of Qaanaaq on the eastern side of Murchison Sound in northwest Greenland. All of the elements of the infrasonic array lie within 1.3 km of the coast. The area around Qaanaaq is surrounded by numerous fjords, which extend inland for distances ranging from about 20 to 40 km to numerous glaciers located along the edge of the Greenland Icecap. Icebergs are shed from the glaciers at the head of these fiords during the summer months and drift in a steady stream down the fjords and then to the south along the eastern coast of the Sound. As a rule, at least half a dozen large icebergs can be seen within a distance of less than 10 km from the sites at IS18 during the summer months. These icebergs frequently break up with an audible sound that can be clearly heard at the infrasonic array. The calving of these icebergs also generates sharp-onset high-frequency infrasonic signals that can be

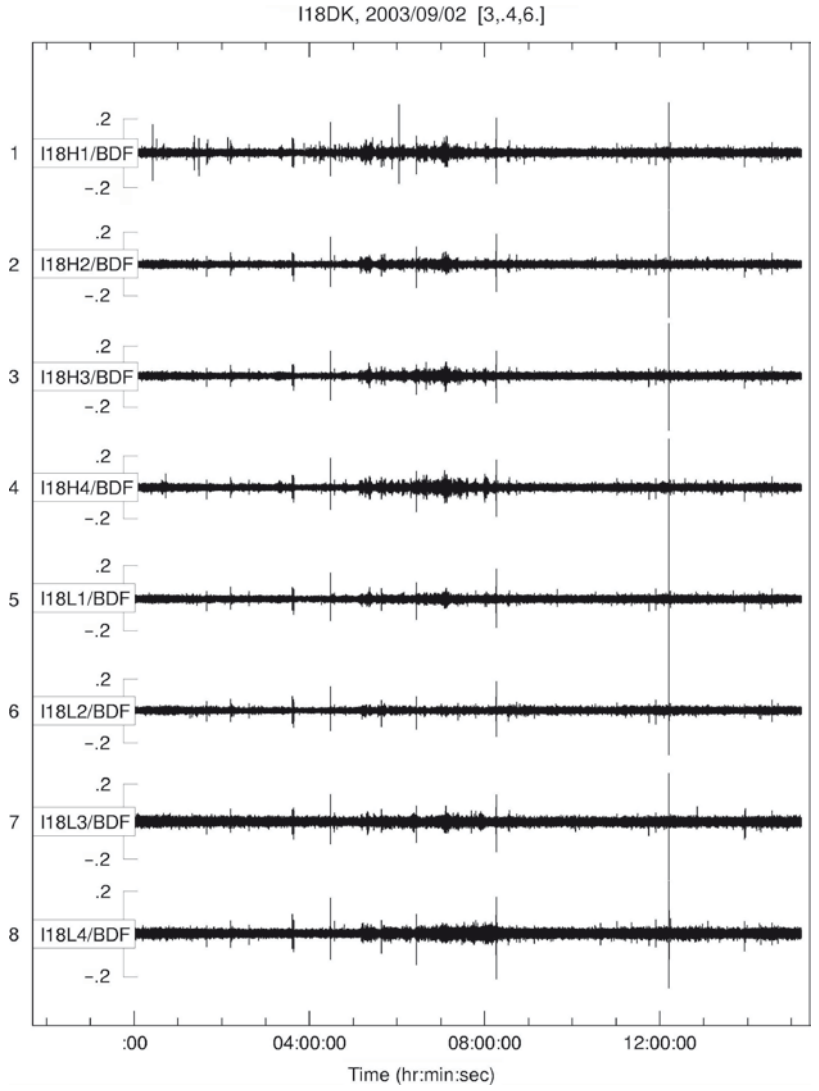

Fig. 6.13 Calving of icebergs and glaciers: infrasonic data recorded over a period of 15 h at IS18 Qaanaaq, Greenland. Amplitudes are expressed in Pascals. Many of the signals illustrated here originate in the breakup of drifting icebergs near the eastern coast of Murchison Sound; a few of these signals may correspond to calving along the face of nearby glaciers

clearly identified in the recorded data. This has been confirmed on numerous occasions by noting the time of a visibly observed calving event and the associated audible sound at the array site and comparing these times with the recorded infrasonic signals. Many of the recorded signals come from the direction of the southward drifting icebergs in Murchison Sound (see Fig. 6.14). The observed backazimuths of

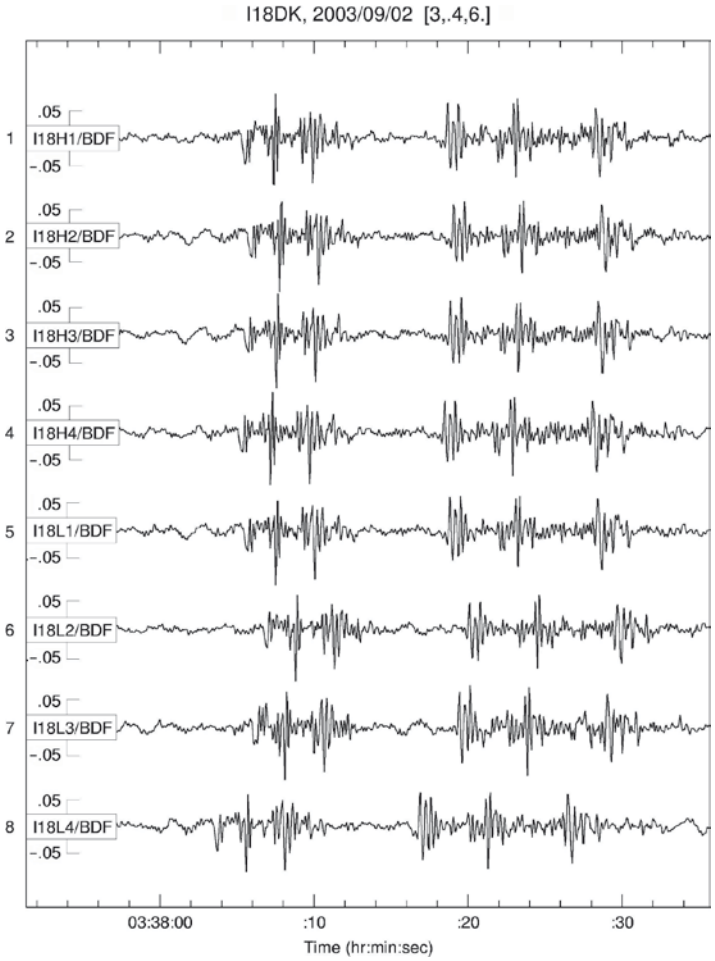

Fig. 6.14 Illustration in detail of the infrasonic signals generated by the calving of icebergs near IS18, Qaanaaq, in northern Greenland. Amplitudes are expressed in Pascals. The high-frequency signals in this diagram are only seconds apart. They all originate from the west-south-west direction with the same backazimuth. This indicates that these signals are generated in either a multiple calving episode associated with a single slowly drifting iceberg or with calving in a group of closely located icebergs in Murchison Sound

other signals (see Fig. 6.15) indicate that these signals are associated with iceberg calving in nearby fjords, especially in the large fjord on the southern side of Qaanaaq that runs from Murchison Sound to the base of Tracy and Helprin Glaciers. It seems very likely that some observed events originate in the calving of these nearby glaciers, but this has not been verified. Recently, Richardson et al. (2008) have reported observations of seismic and infrasonic waves generated by the calving of Bering Glacier in southeast Alaska and also signals generated by the calving of floating and grounded icebergs within a lake near the foot of the glacier.

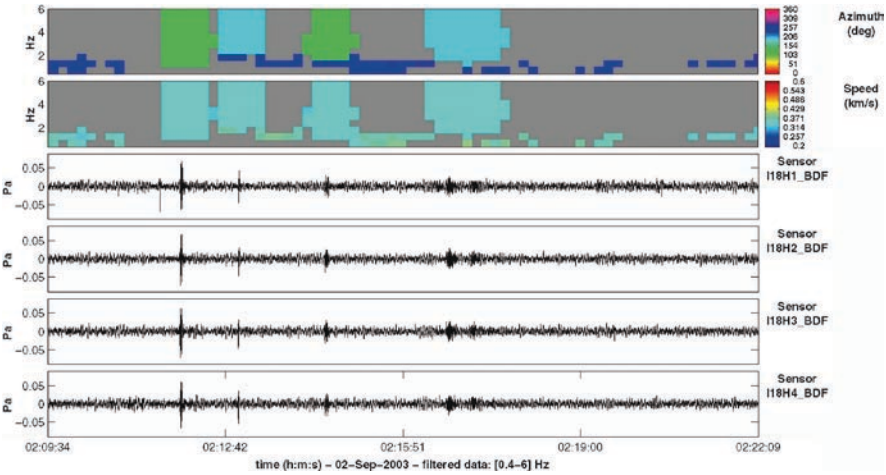

Fig. 6.15 Detection of infrasound generated by the calving of icebergs and glaciers. The data was recorded on September 2, 2003, at IS18 Qaanaaq in Greenland and analysed using the PMCC algorithm. Data are filtered between 0.4 and 6 Hz

The increasing concern with climate change underlines the need for systematic and accurate monitoring of the environment. This is particularly true in the Arctic and Antarctic. In this regard, we note that the high rate of detection of infrasound from calving glaciers and icebergs at IS18 Qaanaaq provides a potentially useful measure of the state-of-health of the Greenland Icecap. The continuous monitoring of data from IS18 over the course of several years could therefore provide a useful indication of global warming. Avalanches and landslides can also be detected at IMS infrasound stations. The detailed monitoring of avalanches and landslides in certain parts of the world using infrasound data might also provide an indication of climate change (Campus 2007a).

6.3.8 Volcanic Eruptions

Volcanic eruptions are a very important source of infrasonic waves (see, e.g., Goerke et al. 1965; Evers and Haak 2001; Le Pichon et al. 2001; Liszka and Garcés 2002; Evers and Haak 2005; Campus et al. 2005; Christie et al. 2005; Campus 2006a, b, 2007b, 2008; Evers 2008). Volcanic infrasound originates primarily in the atmospheric perturbation caused by the explosive ejection of lava and gases from the crater and surrounding vents of the volcano. The quantity of materials discharged during eruptions is dependent on the size of the explosion. The size of an eruption can range, in terms of equivalent yield, from less than 1 kT for small eruptions, to 100 MT for powerful eruptions like those of Krakatoa in 1883 (Symons 1888) and

Mount St. Helens in 1980 (Donn and Balachandran 1981, Reed 1987a). The dominant frequency and amplitude of infrasonic waves from volcanic explosions depends on the size of the explosion and the distance from the source. Large explosions will generate waves that span a very large range of frequencies (from 0.002 Hz up to at least 20 Hz) and the recorded signals may have amplitudes of more than 100 Pa in the near field (less than 50 km) and tens of Pascals at distances of more than 1,000 km. Eruptions of this kind will be detected at great distances (up to at least 20,000 km). The initial impulsive signature of a large volcanic explosion is generally followed by a long train of irregular waves that may extend over periods ranging from hours to weeks. Smaller volcanic eruptions will be dominated by higher frequency waves with smaller amplitudes. There is a large variation in the morphology of infrasonic signals generated by volcanic eruptions. Some signals, especially those associated with small explosions, are very short in duration. These impulsive signals are similar to signals generated by mining explosions. In other cases, the signals generated by small volcanic eruptions may exhibit a coda that extends over a long period of time. A detailed study of the morphology of signals from an active volcano may provide insight into the various source mechanisms for volcano-generated infrasound.

The IMS infrasound network has the potential to provide a significant contribution to the monitoring of volcanic eruptions around the world (Campus 2006a, b; 2007a, b, c). Data from the IMS infrasound network could be incorporated into the existing volcanic ash monitoring systems to provide an enhanced warning system for aviation (Chen and Christie 1995; Campus 2005). Results of a regional study of volcano-generated infrasound in South America with a focus on stratospheric ash injection have recently been reported by Garcés et al. (2008).

A large number of volcanic eruptions have been recorded during the last decade at IMS infrasound stations. Some examples are presented in Figs. 6.16–6.26.

Records of moderate volcanic activity observed during the site survey in April 2001 at IMS station IS40, in Papua New Guinea (Campus 2004) are presented in Figs. 6.16 and 6.17. The observed infrasonic waves were generated by minor volcanic activity at Tavurvur Volcano. Small explosive eruptions were visually seen by observers (including one of the authors) in the area around the crater throughout the site survey period. Infrasound from small explosions at the crater on Tavurvur was detected over a period of several days at the site of IS40 at a distance of approximately 25 km. The volcanic activity at Tavurvur was the dominant signal recorded during the site survey. The backazimuth of the detected signals corresponded in all cases to the direction from the array to the crater at Tavurvur and all signals were detected as direct arrivals with apparent velocities equal to the local speed of sound. In addition, seismic signals generated by the eruptions at Tavurvur during the site survey were recorded and analysed at the Rabaul Volcano Observatory (RVO). This analysis showed that the observed infrasound signals were highly correlated with the observed seismic signals generated by the eruptions at Tavurvur (Itikari et al. 2003).

The detection of the eruption of Mt. St. Helens on March 9, 2005, at 0125 UT is shown in Fig. 6.18. The small but significant explosive eruption, which produced ash falls in the neighbouring towns of Ellensberg, Yakima and Toppenisht, was clearly recorded at IMS infrasound station IS56 Newport in Washington State, USA, at a

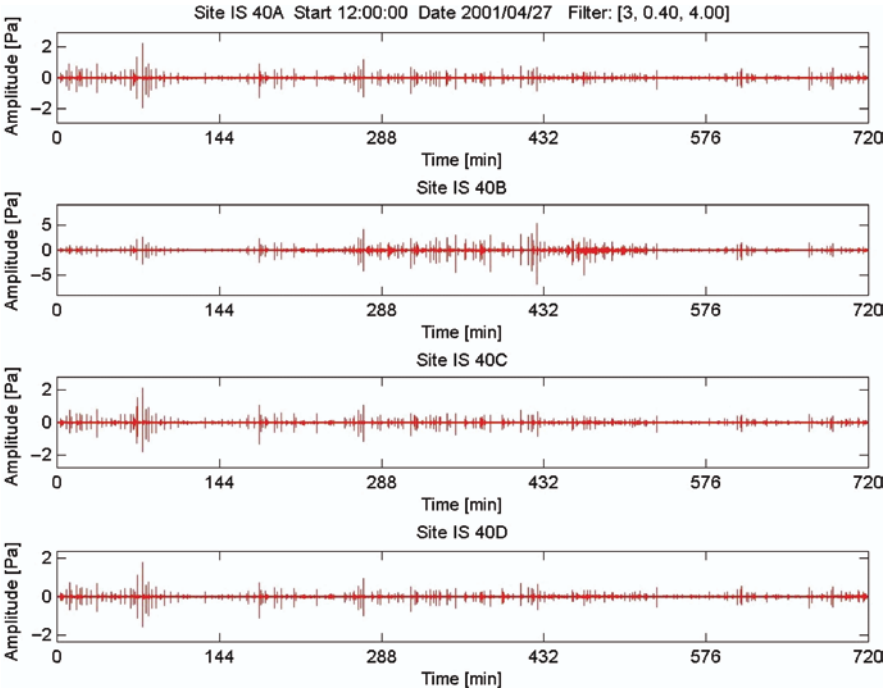

Fig. 6.16 High-frequency infrasonic waves observed in a 12-h window at Keravat, Papua New Guinea, during the site survey for infrasound station IS40. The source of these waves is Tavurvur Volcano located at a distance of about 25 km

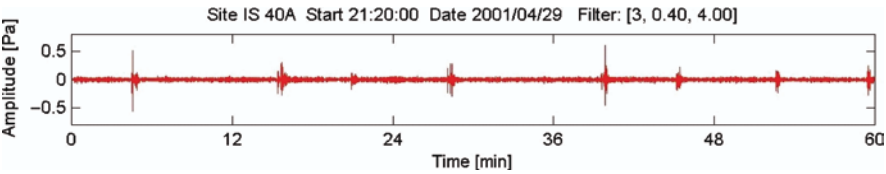

Fig. 6.17 Expanded view of infrasonic waves generated by Tavurvur Volcano. This data was recorded at site IS40A over a 1-h period during the site survey for IMS infrasound station IS40

distance of about 450 km from the volcano (Campus 2005, 2006a). The observed backazimuth of the signals illustrated in Fig. 6.18 (239º) is in good agreement with the actual backazimuth to Mount St. Helens (240º). The onset time of the signals shown in Fig. 6.18 is also consistent with the start of the eruption on March 9, 2005, at approximately 01:26 UT. The detection of infrasonic signals from the eruptions of Mount St. Helens on January 16, 2005, and March 9, 2005, has also been studied by Matoza et al. (2007). These authors describe observations made on the northern flank of the volcano at a distance of about 13 km from the crater and observations made at

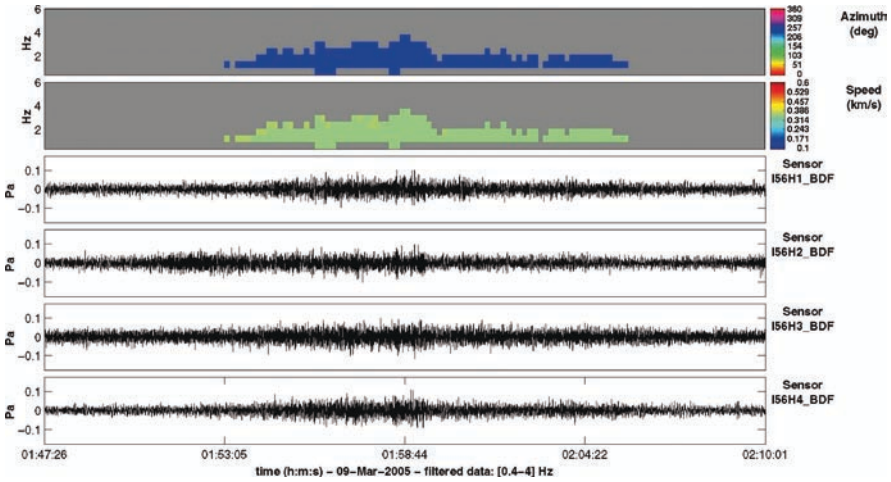

Fig. 6.18 Detection of infrasound arrivals associated with an eruption of Mount St. Helens Volcano on March 9, 2005. These signals were recorded at IS56 Newport, Washington State, and analysed using the PMCC algorithm. Data are filtered between 0.4 and 4 Hz. The observed backazimuth and apparent velocity are 239º and 351 m/s

a site located in Sacajawea State Park about 250 km east of the volcano. The signals generated by the eruption on January 16, 2005, were an order of magnitude smaller than the signals associated with the eruption on March 9, 2005. These signals were not detected at either the Sacajawea site or at IS56 Newport.

The Andes Mountains along the western edge of South America is a very active volcanic region where the IMS infrasound network can provide a significant contribution to volcano monitoring (Campus 2005, 2006a, b, 2007a, b, c). Figure 6.19 shows the detected infrasonic signatures recorded at IS08, La Paz, Bolivia during the eruption of Lascar Volcano on April 18, 2006. This volcano is located in Northern Chile, about 800 km from the IMS station in Bolivia.

A second example of the detection of volcano-generated infrasound at IS08 in Bolivia is shown in Figs. 6.20 and 6.21. The waveforms, observed backazimuths and apparent velocities correspond to an eruption of Ubinas Volcano on April 22, 2006. Ubinas Volcano is located in Peru at a distance of 260 km from IS08. The two distinct apparent velocities shown in Fig. 6.21 might be associated with tropospheric and stratospheric arrivals.

IMS infrasound station, IS44 (Petropavlovsk Kamchatskiy, Russian Federation) is located in a very active volcanic area on the Kamchatka Peninsula. There have been a number of serious encounters by aircraft with volcanic ash generated by volcanic eruptions on the Kamchatka Peninsula during the last 10 years. IS44 is therefore very well located for monitoring hazardous volcanic activity on the Kamchatka Peninsula. Indeed, IS44 lies within good detection range of all active volcanoes on the Kamchatka Peninsula (Campus, 2006b, 2007a, b, c).

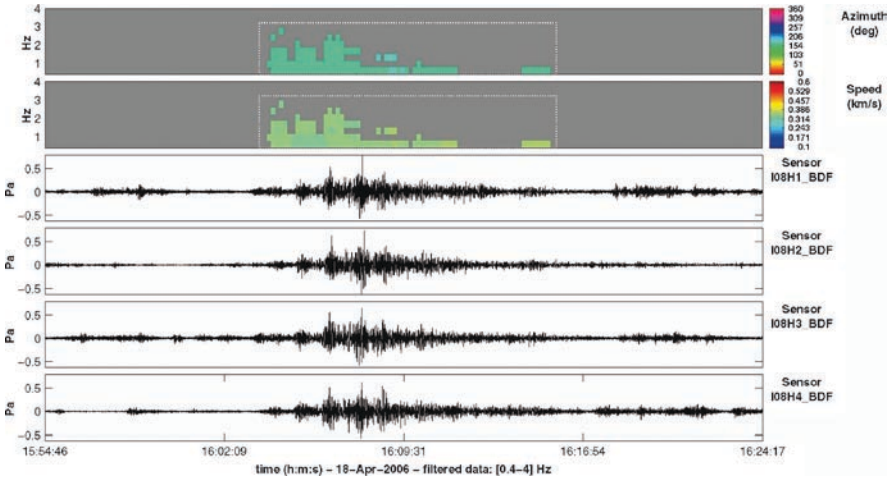

Fig. 6.19 Detection of infrasound signals associated with an eruption of Lascar Volcano in Northern Chile. These signals were recorded at IS08, La Paz, Bolivia, on April 18, 2006, and analysed using the PMCC algorithm. Data are filtered between 0.4 and 4 Hz. The average backazimuth and apparent velocity of the detected signals are 172° and 347 m/s, respectively. Only stratospheric arrivals were observed

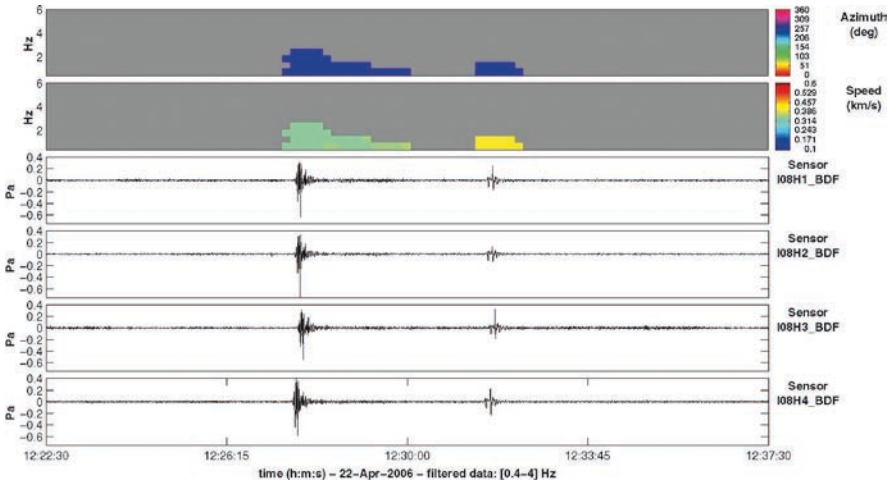

Fig. 6.20 Detection of infrasound signals associated with volcanic activity at Ubinas Volcano in Peru. These signals were recorded at IS08 La Paz, Bolivia, on April 22, 2006, and analysed using the PMCC algorithm. Data are filtered between 0.4 and 4 Hz. The polar diagram illustrated in Fig. 6.21 shows that these signals come from the direction of Ubinas Volcano (267°) but with different apparent velocities (~340 and ~420 m/s)

One of the most active volcanoes in this area is Karymsky Volcano (Lees et al. 2004), located about 160 km from IS44. A typical example of the detection of infrasonic waves from Karymsky Volcano at IS44 is shown in Fig. 6.22.

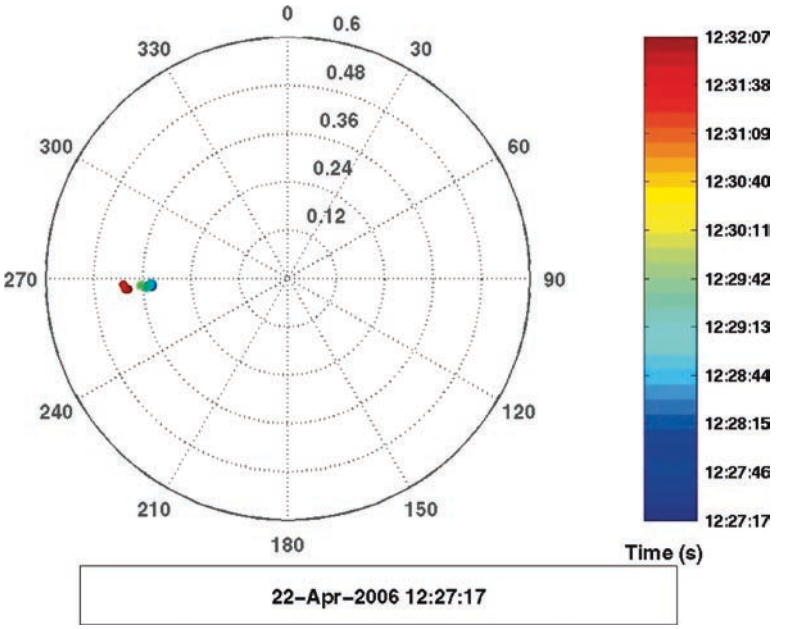

Fig. 6.21 Polar diagram showing the backazimuth (station-to-source) direction and apparent velocities corresponding to the two distinct arrivals illustrated in Fig. 6.20. The data was analysed using the PMCC algorithm

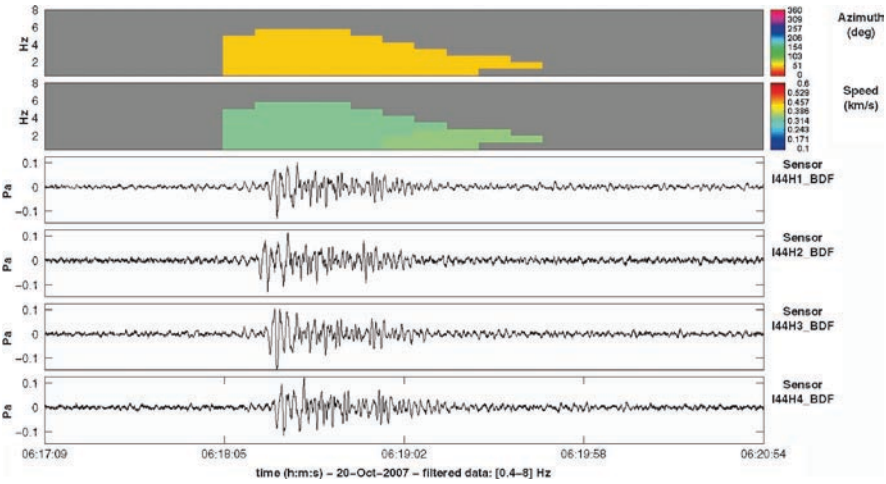

Fig. 6.22 Detection of infrasound signals associated with volcanic activity at Karymsky Volcano. These signals were recorded at IS44 on the Kamchatka Peninsula on October 20, 2007. Data has been analysed using the PMCC algorithm. Data are filtered between 0.4 and 8 Hz. The observed backazimuth (49.8°) is consistent with volcanic activity at Karymsky Volcano. The observed apparent velocity is 338 m/s

Another very active volcano on the Kamchatka Peninsula is Bezymianny Volcano, located about 360 km from IS44. On May 09, 2006, at about 0845 UT, a large eruption at Bezymianny Volcano was noted in several volcanic bulletins. The complexity of the signals recorded at IS44 is illustrated in Fig. 6.23. As can be seen from this diagram, several large amplitude signals were recorded between 0845 UT and 0930 UT and two smaller disturbances were recorded before 08:30. The observed backazimuth and apparent velocities (Figs. 6.23 and 6.24) indicate very clearly that the infrasound signals recorded after 08:30 at IS44 are coming from Bezymianny Volcano. This observation is confirmed by data recorded at another IMS infrasound station, IS53, Fairbanks, Alaska, USA, located about 2,900 km from the volcano.

As can be seen from Fig. 6.23, two clearly defined signals were also recorded at IS44 at about 08:16 and 08:27 UT before the larger amplitude signals from Bezymianny Volcano. It is worth noting that there is no mention in any available volcanic bulletin of any volcanic eruptions on May 09, 2006, on the Kamchatka Peninsula except for the major eruption at Bezymianny Volcano. It is tempting to assume that the earlier signals 08:16 and 08:27 at IS44 are also associated with volcanic activity at Bezymianny Volcano. However, an analysis of these earlier events shows that these signals come from a different direction. Bezymianny Volcano lies at a backazimuth of about 29°. The analysis presented in Figs. 6.25 and 6.26 shows that the backazimuth of the signal at 08:16 in Fig. 6.23 is about 46°, which corresponds to the backazimuth of Karymsky Volcano (see Fig. 6.22). The PMCC analysis (not shown) of the second earlier signal at about 08:27 in Fig. 6.23 also shows that the backazimuth of this signal (46.3°) corresponds to the backazimuth of Karymsky Volcano. We therefore conclude that two different volcanoes were active on the Kamchatka peninsula between the hours of 08:00 and 10:00 on May 09, 2006.

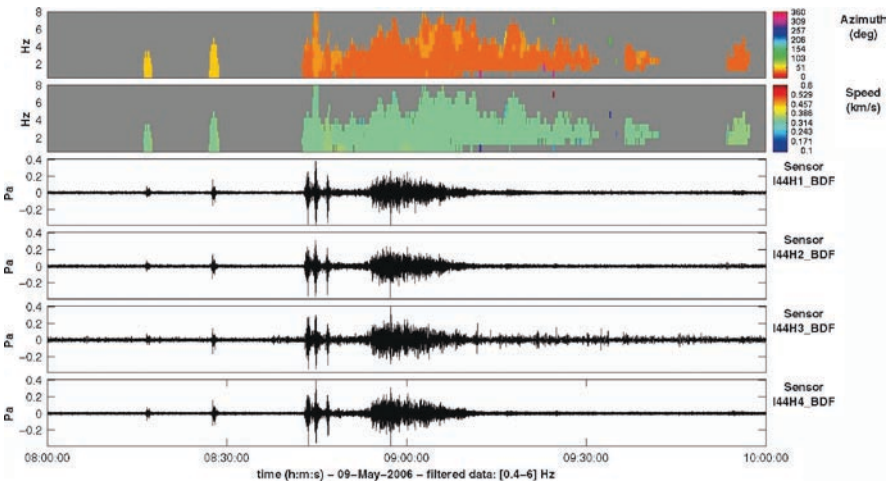

Fig. 6.23 Infrasonic signals at IS44, Petropavlovsk-Kamchatskiy, in the Russian Federation observed between 08:00 and 10:00 on May 09, 2006. The PMCC analysis for this data (see also Fig. 6.24) shows that the large amplitude signals recorded after 08:30 correspond to volcanic activity at Bezymianny Volcano. Data are filtered between 0.4 and 6 Hz

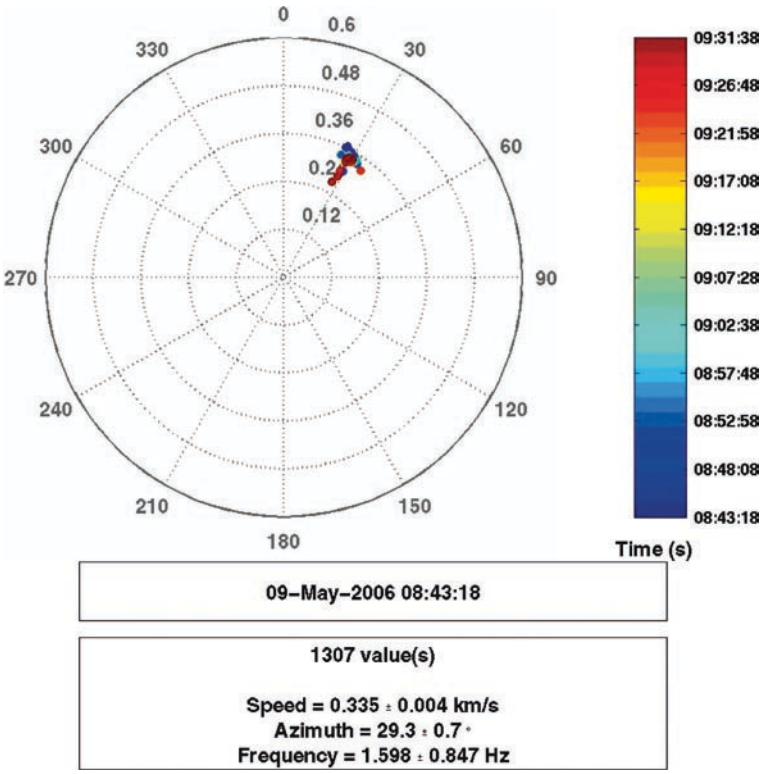

Fig. 6.24 Polar diagram showing the backazimuth directions and apparent velocities associated with the signals observed after 08:30 in Fig. 6.23. The observed backazimuths and arrival times are consistent with signals generated by a documented volcanic eruption at Bezymianny Volcano on the Kamchatka Peninsula

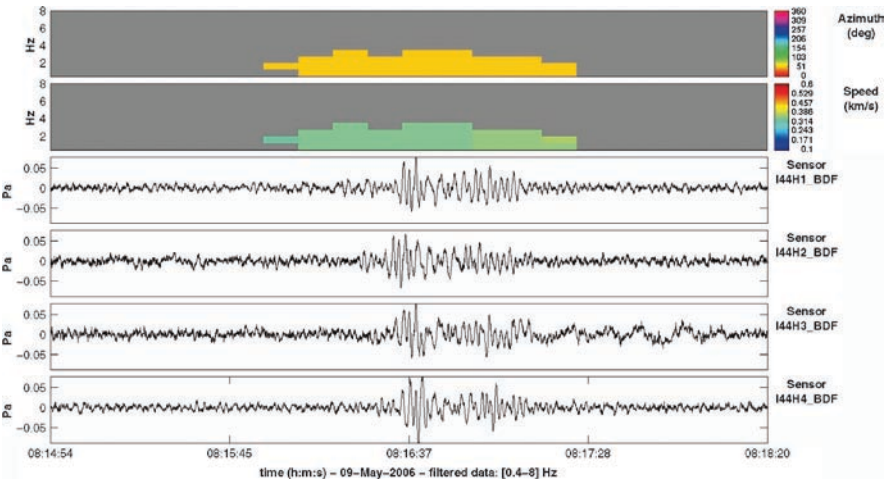

Fig. 6.25 Expanded view of the 1st infrasonic signal illustrated in Fig. 6.23. This data was recorded at IS44, Petropavlovsk-Kamchatskiy on May 09, 2006. The following analysis (Fig. 6.26) shows that this event was not generated by a volcanic eruption at Bezymianny Volcano. Data are filtered between 0.4 and 6 Hz

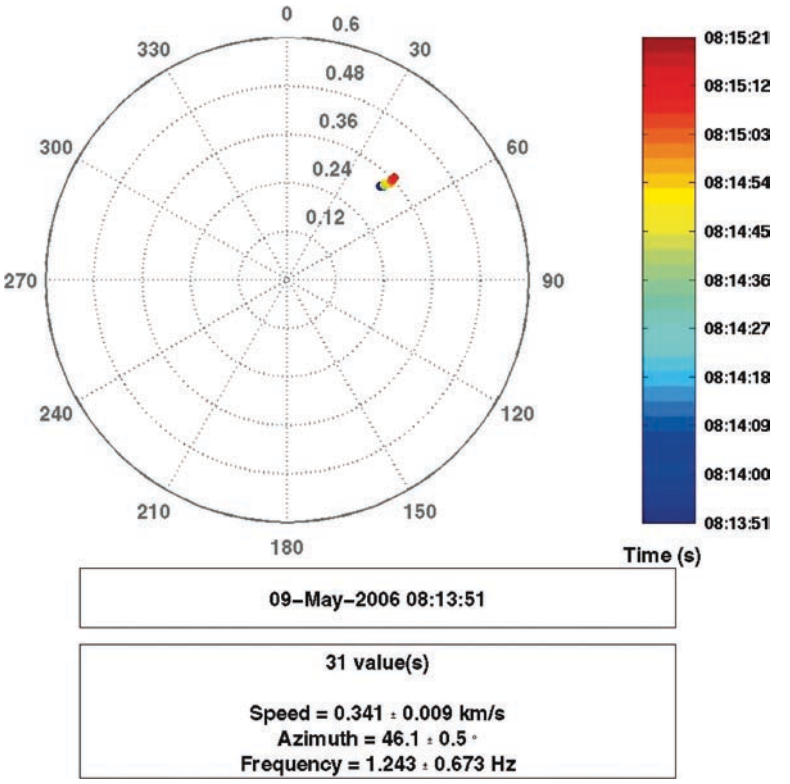

Fig. 6.26 Polar diagram showing the backazimuth directions and apparent velocities associated with the signal illustrated in Fig. 6.25. The observed azimuth (46.1°) indicates that this event originated in a volcanic eruption of Karymsky Volcano on the Kamchatka Peninsula

The results presented here provide a very good example of how the IMS infrasound network can be used to identify and discriminate between volcanic eruptions at two different volcanoes located in the same region. In the present example, neither satellite imagery nor local observations from other monitoring networks identified volcanic activity at two different volcanoes on the Kamchatka Peninsula on May 09, 2006. In contrast, the analysis of IS44 data clearly indicates two different volcanic sources.

Numerous other volcanic eruptions and explosions have been detected during the last decade at IMS infrasound monitoring stations. One noteworthy event that should be mentioned here is the large explosive eruption at approximately 14:00 UT January 25, 2005, of Manam Volcano located close to the equator on the northern side of Papua New Guinea. The initial signals from this event were associated with a series of violent explosions over a period of about 2 h. These signals were detected at a large number of IMS infrasonic stations distributed around the globe (Campus et al. 2005; Christie et al. 2005; Wilson and Olson 2005b). Large volcanic eruptions of this type are relatively rare. The explosive eruption of Manam Volcano in 2005 appears to be the largest explosion in the atmosphere in the last 10 years.

6.4 Man-Made Sources of Infrasound

6.4.1 *Launching of Rockets and the Re-Entry of the Space Shuttle and Space Debris*

Infrasound from the launch of large rockets has been recorded at distances of up to about 3,000 km (see, e.g., Balachandran and Donn 1971; Posmentier 1971; Campus 2004). These long-range signals usually have frequencies extending from 0.01 Hz to more than 10 Hz and durations of several minutes. The amplitudes at distances of about 1,000 km vary from a few tens of mPa to more than 2 Pa, depending on the seasonal component of the stratospheric winds along the direction of wave propagation. Large signals have also been recorded during the overhead passage of large rockets at orbital altitude (about 188 km, Cotton and Donn, 1971; Cotten et al. 1971). These impulsive short-lived signals, which are created in the decay of the rocket-generated N-wave shock cone, have durations of about 2 s. Figures 6.27 and 6.28 show complex signals from the launch of the Soyuz rocket from Baikonur Cosmodrom, as recorded at IS31, Aktyubinsk, Kazakhstan on August 29, 2003, and analysed using the PMCC algorithm. These observations are similar to many other observations of infrasound generated during rocket launches.

The re-entry of the space shuttle, rockets and space debris also generates observable infrasonic signals. Signals associated with the shock front created by the space shuttle during re-entry have often been observed in the United States. These shock front signals are typically sustained along a track below the trajectory that may be more than 8,000 km in length. Sorrells et al. (2002) have studied the seismic and

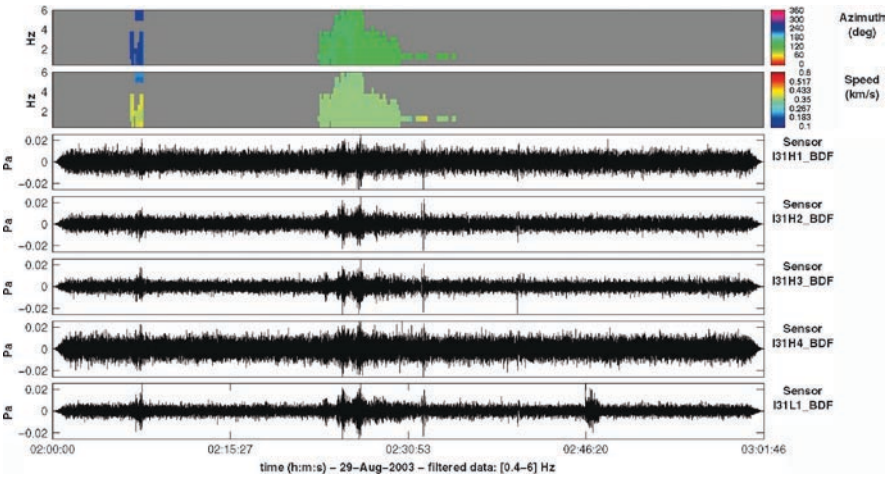

Fig. 6.27 Detection of infrasonic signals generated by the launch of the Soyuz rocket at Baikonur, Kazakhstan, recorded at IS31, Aktyubinsk, Kazakhstan on August 29, 2003, using the PMCC algorithm. Data are filtered between 0.4 and 6 Hz

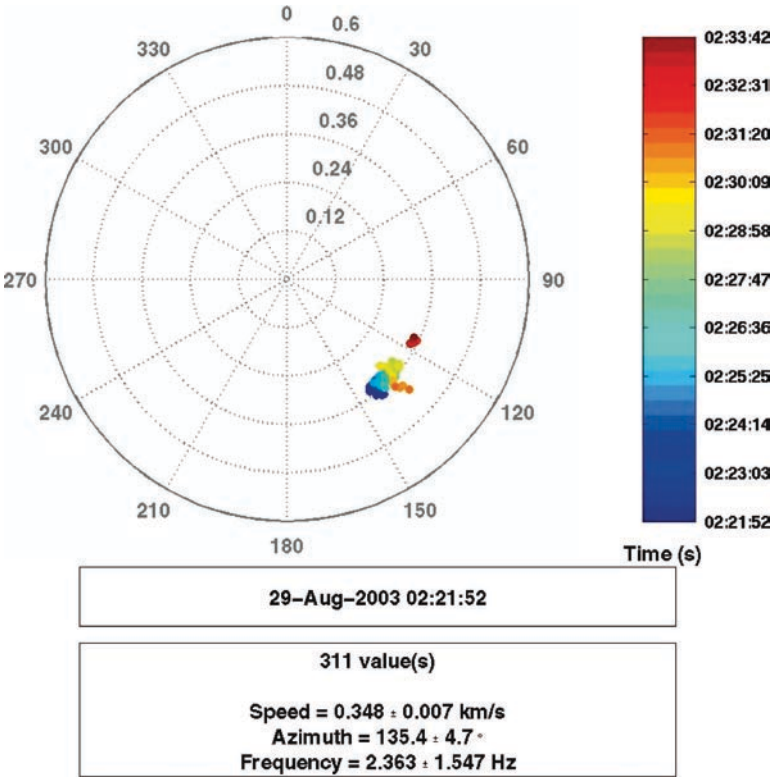

Fig. 6.28 Polar diagram illustrating the backazimuths and apparent velocities associated with the signals shown in Fig. 6.27. Results were computed using the PMCC algorithm

infrasonic signatures created during the re-entry of the space shuttle with an emphasis on the interpretation of seismic precursors to the shock front at the surface. Groot-Hedlin et al. (2007, 2008) describe a very detailed investigation of the shock front signal generated by space shuttle Altlantis during a landing at Edwards Air Force Base in southern California on June 22, 2007. Detections were limited to direct arrivals in the primary acoustic carpet in the area to the east of the trajectory. On the western and northwestern side, both direct and ducted stratospheric arrivals were detected out to distances of several hundred kilometres. Propagation modelling predictions were found to be in good agreement with observations.

6.4.2 Infrasound from Aircraft

Sonic boom signals in the form of an N-wave pressure signature can be detected as direct arrivals over a relatively small area under or near the fight path of a supersonic aircraft (Grover 1973; Donn 1978). Signals from supersonic aircraft are not, however,

limited to this relatively narrow zone (or carpet). As the shock wave propagates away from the aircraft, the higher frequency components are rapidly attenuated and the resulting infrasonic components may be detected, depending on conditions, at distances of up to at least 4,000 km from the flight path of the aircraft (Balachandran et al. 1977; Liszka and Waldemark (1995), Le Pichon and Cansi 2003, Liszka 2008a). As noted in Table 6.1, these long-range signals have frequencies between 0.3 and 20 Hz and amplitudes in the range between 0.01 and 10 Pa. Infrasonic waves generated by a supersonic aircraft are often recorded as a succession of distinct phases corresponding to one or more refractions from the stratosphere and lower thermosphere.

Signals from subsonic aircraft (including helicopters) are also detected routinely at many IMS infrasound stations. In contrast with signals from supersonic aircraft, the detection of signals from subsonic aircraft is limited to direct arrivals with a maximum range of about 40 km. Large-amplitude signals are often generated by aircraft during takeoff and landing. Two examples of signals generated by the take-off and landing of regular flights at the Fairbanks International Airport and recorded at the nearby IMS infrasound station IS53 on June 18, 2008 are presented in Figs. 6.29–6.32. The centre of the 3.6 km long runway at Fairbanks International Airport is located about 5.2 km south of the centre of the IS53 array and the runway is aligned along the 38º/218º direction from true north. The variation in amplitude of the signals shown in Fig. 6.29 for the take-off of Flight AS126 is due primarily to the proximity of sites H2 and H3 to the flight path of the departing aircraft in the 218º direction and possibly to variations in source intensity. The observed backazimuth of infrasonic signals generated during take-off (174.4º) is consistent with a source located close to the nearest end of the runway. The variation in amplitude between sites in the array for signals generated by Flight AS55 during final approach (see Fig. 6.31) is also reflected in the proximity

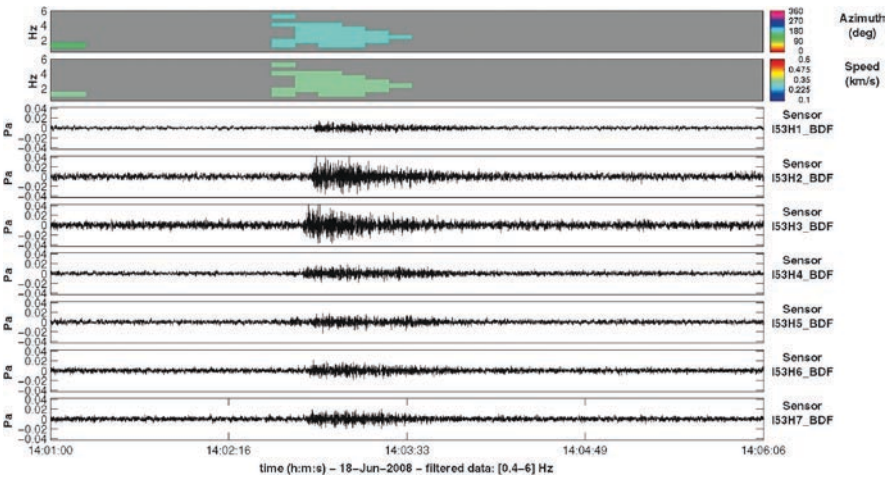

Fig. 6.29 Detection of infrasonic waves associated with the take-off of flight AS126 at Fairbanks International Airport, recorded at IS53, Fairbanks, Alaska on June 18, 2008 using the PMCC algorithm. Data are filtered between 0.4 and 6 Hz

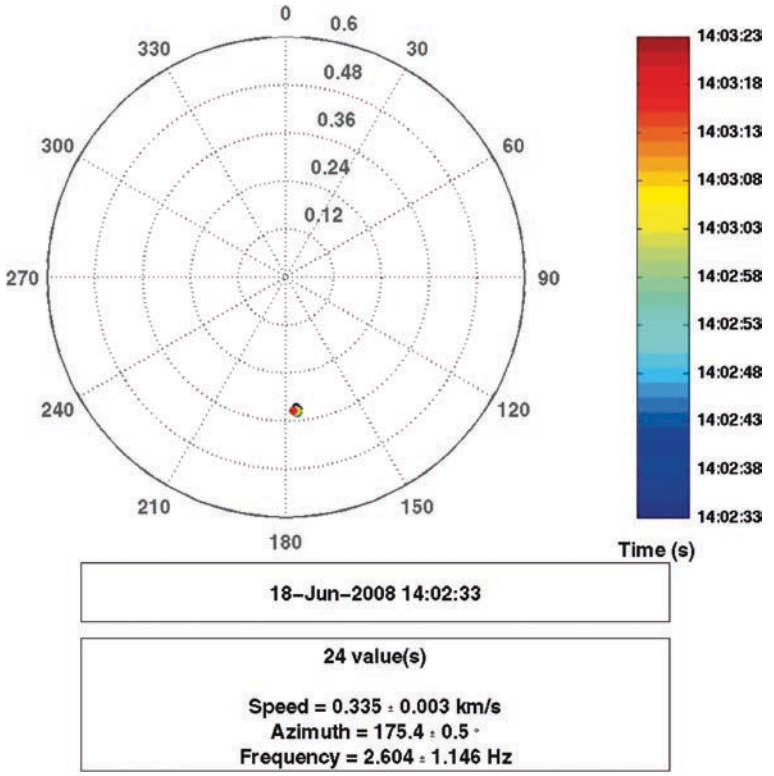

Fig. 6.30 Polar diagram obtained using the PMCC algorithm showing the backazimuths and apparent velocities corresponding to the signals illustrated in Fig. 6.29

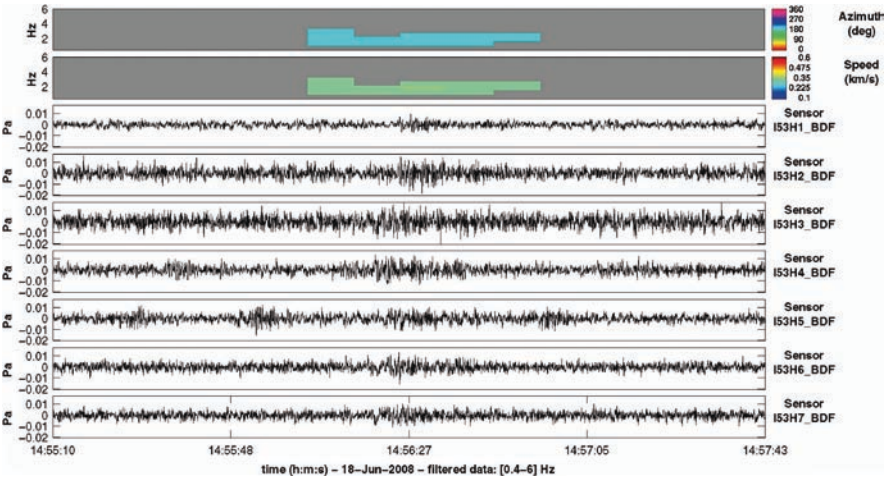

Fig. 6.31 Detection of infrasonic signals associated with the landing of flight AS55 at Fairbanks International Airport, recorded at IS53, Fairbanks, Alaska on June 18, 2008, using the PMCC algorithm. Data are filtered between 0.4 and 6 Hz

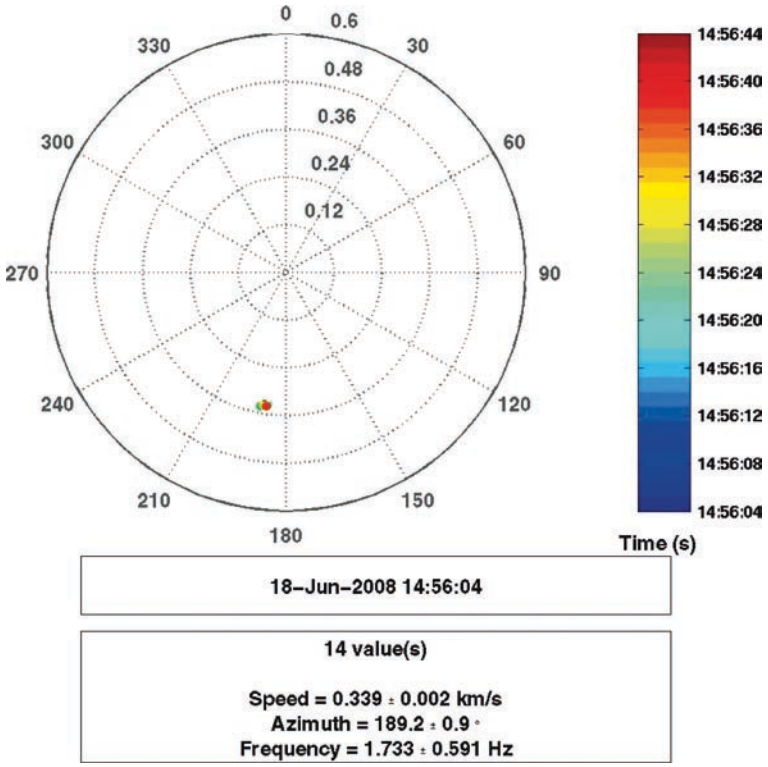

Fig. 6.32 Polar diagram showing the backazimuth directions and apparent velocities associated with the signals illustrated in Fig. 6.31. Results were obtained using the PMCC algorithm

of the array to the airport. Even though the signals illustrated in Fig. 6.31 for the landing aircraft were recorded only 54 min after the signals shown in Fig. 6.29 for the departing aircraft, the background noise levels have increased and the signal-to-noise ratio for the signals shown in Fig. 6.31 is relatively low. Nevertheless, signals were detected and the observed backazimuth for these signals (189.2º) is consistent with signals generated at the far end of the runway during the landing of Flight AS55. Similar results have been recently observed at another IMS infrasound station (IS51 Bermuda) located very close to an airport (Campus 2008).

Infrasonic waves generated by commercial jet aircraft at cruising altitude are also frequently observed at many infrasound stations. In this case, the observed azimuth and apparent velocity of the direct infrasonic arrivals changes rapidly with time as the aircraft passes from one horizon to the other. This characteristic pattern is illustrated in Fig. 6.33 for the flight of a commercial jet aircraft over the infrasonic array at IS07 Warramunga in central Australia (Christie 2004).

Observations of high-frequency signals from subsonic aircraft have also been described briefly by Posmentier (1971). Similar results have been reported by Evers

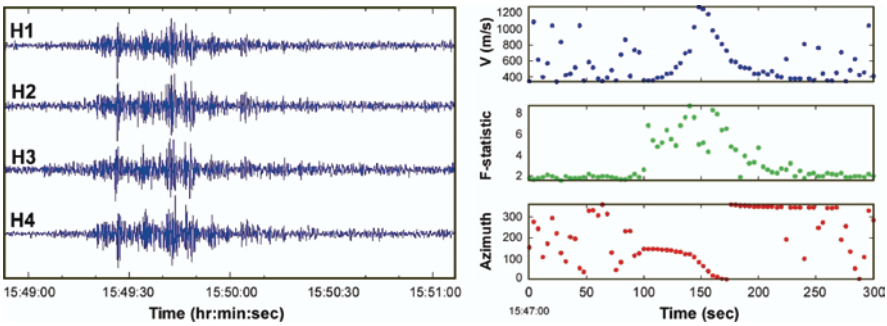

Fig. 6.33 Infrasonic waveforms and observed backazimuth, Fisher *F*-statistic and apparent velocity variations corresponding to the flight of a commercial jet aircraft at cruising altitude over the infrasonic array at IS07 Warramunga, Australia, on 8 March 2002. Data is bandpass filtered between 1.6 and 7.0 Hz. The Fisher *F*-statistic (Melton and Bailey, 1957; Olson, 2004), which is used as a quantitative signal detection indicator here, is related to the signal-to-noise power ratio, P_{snr}, by $P_{snr} = (F-1)/N$, where N is the number of sensors. Since the *F*-statistic is characterised by Fisher's *F*-distribution, it provides a formal statistical measure for signal detection. (This diagram is adapted from Christie (2004))

(2005) corresponding to the flight of a subsonic aircraft over the De Bilt Infrasound Array in The Netherlands and by Walker et al. (2008) for the flight of an aircraft over the array at IS57 Piñon Flats in California.

6.4.3 Chemical Explosions

Chemical explosions generate characteristic sharp-onset infrasonic waves. Waves generated by mining explosions and quarry blasts have frequencies ranging from 0.05 Hz up to at least 20 Hz and amplitudes ranging from a few mPa to more than 5 Pa. The range of detection for large mining explosions may exceed 5,000 km, but is usually less than 2,000 km. Signals from small mining explosions and quarry blasts are frequently detected at most infrasound monitoring stations. Figure 6.34 shows typical examples of mining explosions detected at IS26, Freyung, Germany.

Signals from accidental chemical explosions are also observed from time to time at IMS infrasound monitoring stations. The signature of these events is generally similar to the signature observed from mining explosions. Many of these events are detected only at regional distances, but some larger accidental explosions have been detected at distances of more than 5,000 km. An example of the signals generated by an industrial chemical explosion is shown in Fig. 6.35. A series of three explosions at the Buncefield oil depot near Hemel Hempstead in Hertfordshire, United Kingdom, occurred soon after 0600 UT on December 11, 2005, causing several casualties. The signals from this explosion were recorded at IMS infrasound station IS26 in Freyung, Germany, and at several other European infrasound stations. A number of studies have been reported on the unusual propagation characteristics of the signals from the Buncefield explosion (Ceranna and Le Pichon 2006; Evers and Haak 2006, 2007;

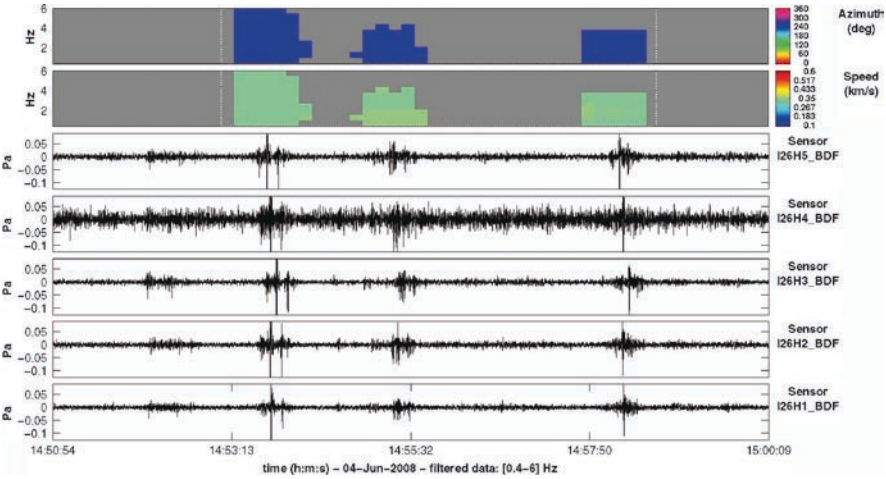

Fig. 6.34 Detection of infrasonic signals associated with local mining activity in data recorded at IS26, Freyung, Germany, on June 04, 2008, using the PMCC algorithm. The source of these events is located at a distance of about 60 km from IS26. Data are filtered between 0.4 and 6 Hz. The observed average backazimuth and apparent velocity of these signals is 265° and 341 m/s, respectively

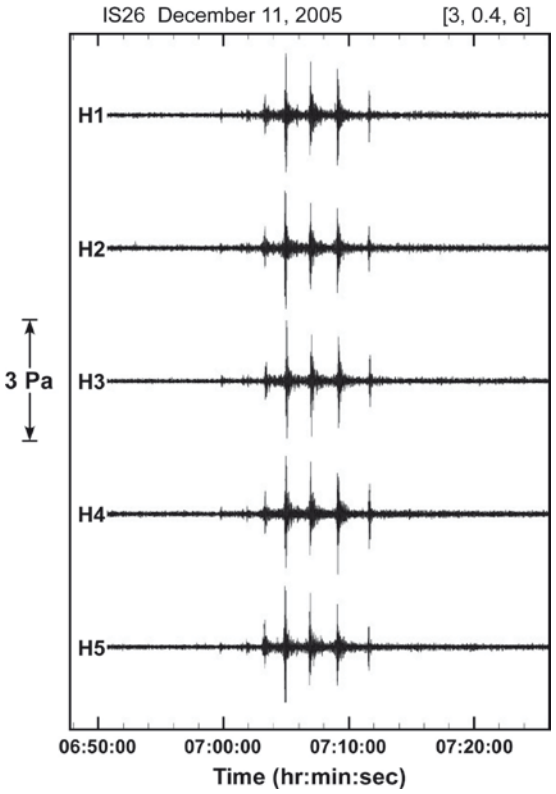

Fig. 6.35 Infrasonic signals generated by the explosion of an oil depot at Buncefield in the United Kingdom and recorded at IS26, Freyung, Germany

Green et al. 2006). The work of Evers and Haak (2006, 2007) is particularly interesting. These authors show that exceptionally fast infrasonic phases can result when energy is trapped for a significant period of time in a stratospheric duct before it is detected at the surface.

6.4.4 Nuclear Explosions

Nuclear explosions also generate sharp-onset infrasonic waves similar to those generated by large chemical explosions. Infrasonic waves generated by very large nuclear explosions in the atmosphere can be detected at any point on the globe (Donn and Shaw 1967). The energy in an atmospheric nuclear explosion is initially confined to a very small volume at extremely high temperatures ($T > 10{,}000{,}000$ ºC) and extremely high pressures ($P > 1{,}000{,}000$ atmospheres). This extremely hot volume radiates large amounts of (soft) X-rays in the first microsecond, which are absorbed within about one metre and this in turn leads to a rapidly expanding, highly luminous fireball, which may reach more than 100 m in diameter at the end of the first millisecond. The fireball continues to expand at supersonic speeds and to rise slowly at a rate of about 100 m/s, changing its form from roughly spherical to toroidal, until the radioactive cloud reaches its neutrally buoyant level, usually near to the top of the troposphere. The supersonic shock wave generated by the explosion is created within the first second and propagates away from the expanding fireball during the first few seconds. After 50 s, the shock wave will have propagated about 20 km from the centre of the explosion. The shock wave gradually decreases in intensity due to geometrical spreading and attenuation, and eventually only the infrasonic components are left as the higher frequency components are absorbed by the atmosphere. The amount of energy that appears in the shock wave depends on the height of the explosion. If the fireball does not touch the ground (this is referred to as an air burst), and if the explosion occurs below 12 km, then approximately 50% of the released energy is carried away by the shock wave. Less energy is carried away by the shock wave when the explosion occurs at higher altitudes (due to an increase in thermal radiation) or when the fireball touches the surface. In the latter case, some of the energy is transferred into the solid Earth or ocean beneath the explosion.

Infrasonic waves generated by atmospheric nuclear explosions are observed with frequencies in the range from about 0.002 Hz to 20 Hz and amplitudes (in the case of large events at regional distances) up to at least 20 Pa. The amplitude of the signal is directly proportional to the square root of the equivalent nuclear explosive yield (in kilotons TNT equivalent). The amplitude of the signal also depends on the component of the stratospheric wind velocity in the direction of propagation. Large nuclear explosions in the Megaton range can be detected at distances of up to at least 20,000 km. The morphology of infrasonic signals from a nuclear explosion will depend on the size of the explosion and the distance from the source. High-frequency signals are attenuated more rapidly than low-frequency signals and hence the waveforms observed at large distance from the source will be dominated by longer period components.

Small atmospheric nuclear explosions with yields of a few kT generate infrasonic waves with frequencies between about 0.02 and 4 Hz. At distances of up to about a thousand kilometres, these relatively high-frequency signals will be observed as a sequence of discrete arrivals corresponding to one or more refractions from the stratosphere and lower thermosphere. The signature from larger nuclear explosions will tend to be dominated by waves with significantly longer periods. These long-period signals propagate with little loss in energy and can be easily detected at great distances from the source in the form of a sequence of modal components consisting of the leading Lamb wave component followed by superimposed dispersed acoustic mode wave trains.

Underground nuclear tests will also generate infrasonic waves in the atmosphere (see, e.g., Whitaker, 2007, 2008). Much of the energy from an underground nuclear explosion is directed upwards, but energy in the sidelobes may be detected at regional distances.

Two examples that illustrate the long-range detection of infrasonic signals from large atmospheric nuclear tests are presented in Figs. 6.36 and 6.37. Infrasonic signals from these two explosions were recorded at WRAI at Warramunga in the Northern Territory of Australia, on November 17, 1976, and October 16, 1980. WRAI was established at Warramunga in August 1975 and was maintained in

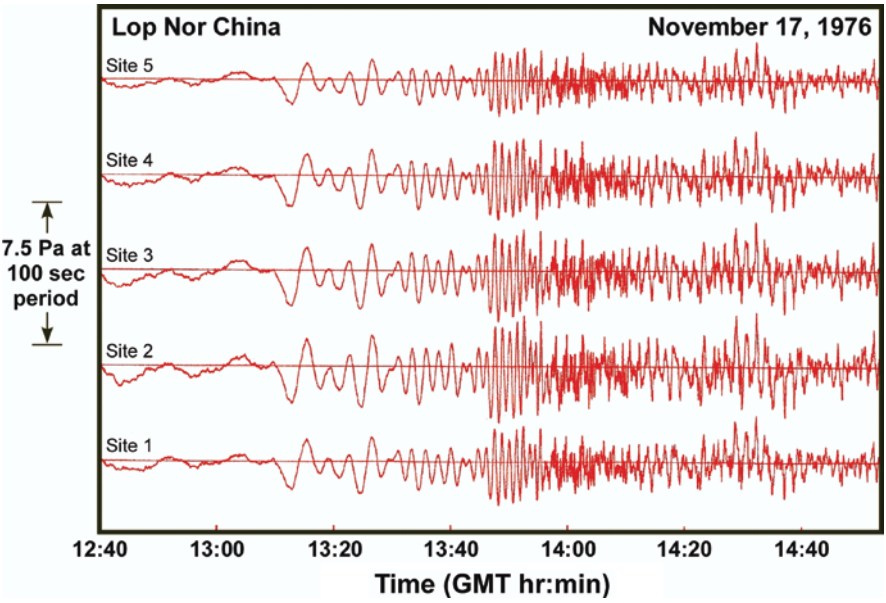

Fig. 6.36 Infrasonic signals recorded at WRAI (Warramunga, Northern Territory, Australia) from the thermonuclear test carried out at Lop Nor, China, on November 17, 1976, at a distance of 8,370 km. Yield is estimated to be 4,000 kT. The first arrival is dominated by very low frequencies and is very likely a Lamb wave. The dispersion of all of the higher frequency modal components is clearly visible. Note that the signal extends over a period of several hours. The data shown in this diagram have not been filtered

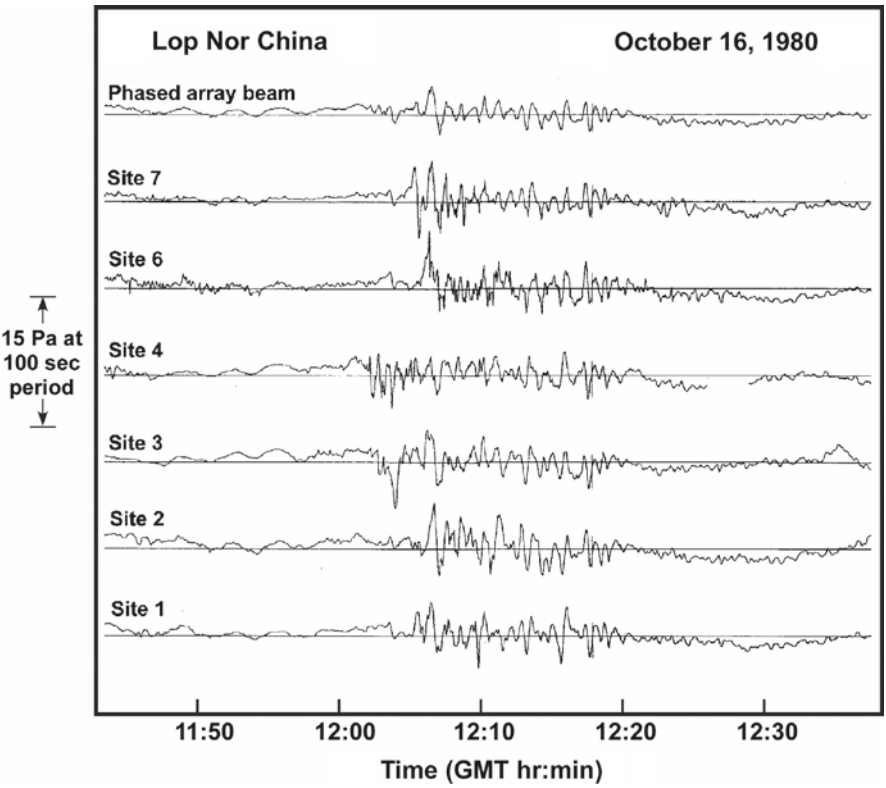

Fig. 6.37 Infrasonic signature of the thermonuclear test at Lop Nor, China, on October 16, 1980 recorded at WRAI (Warramunga, Northern Territory, Australia) at a distance of 8,370 km. Yield is estimated to be between 200 and 1,000 kT. The data have not been filtered. The infrasonic signal illustrated in this diagram corresponds to the last known nuclear test in the atmosphere

continuous operation until 1999 when it was replaced by IMS infrasound station IS07. Both of these nuclear tests were carried out at Lop Nor in China at a distance of 8,370 km. The nuclear test illustrated in Fig. 6.37 is the last known nuclear explosion in the atmosphere.

WRAI was configured initially in the form of a 4-km aperture 5-element centred square array with National Bureau of Standards Mark II differential microbarometer sensors installed at each array element. Later, two more elements were added near site 1 to form a 300-m aperture triangular sub-array. The array data was sampled at 4 samples per second. A description of the response of the differential microbarometer sensors at WRAI is given in Christie et al. (1978). These instruments were designed to detect fairly long period infrasonic waves. The maximum amplitude response is at a period of about 10 s and the gain is reduced by 3 dB at a period of about 100 s. The data presented in Figs. 6.36 and 6.37 have not been filtered in order to illustrate

the modal components (especially in Fig. 6.36) in the recorded infrasonic signals. Since both of the signals shown in Figs. 6.36 and 6.37 include components with periods of about 100 s, the amplitude calibration noted in these diagrams is given for a period of 100 s. The calibration for other periods can be found using the transfer function given in Christie et al. (1978).

The data corresponding to the large thermonuclear test on November 17, 1976 (Fig. 6.36) was recorded under fairly low wind-noise conditions. Background noise levels at WRAI at the time of the last known nuclear test in the atmosphere (Fig. 6.37) were significantly higher and the data shown in Fig. 6.37 is contaminated by longer period wind-generated noise.

6.5 Practical Applications of Infrasonic Data

6.5.1 Tomography of the Upper Atmosphere

The propagation of infrasound depends strongly on the detailed morphology of the atmospheric wind and temperature profiles. This provides the bases for the use of infrasound tomography as a means for determining the structure of the upper atmosphere. The use of infrasound to probe the vertical structure of the atmospheric dates from the work of Gutenberg (1939) who deduced the temperature profile of the atmosphere from infrasonic observations. The interpretation of other early infrasound observations (see, e.g., Cox 1949) revealed the essential features of the vertical wind and temperature profiles. Further refinements were introduced by Donn and Rind (1972), Rind et al. (1973), Rind and Donn (1975) and Rind (1978) to qualitatively measure upper atmospheric winds using microbaroms.

Infrasound tomography can be used to validate the existing upper atmospheric models and to extend the wind profiles to the mesosphere and lower thermosphere where the accuracy of current models is limited. A further advantage of infrasound tomography is that this technique, when used with a global network of uniformly distributed infrasound monitoring stations and modern processing and modelling techniques, has the potential to provide accurate atmospheric profiles at any point on the face of the globe with an unprecedented temporal resolution of a few hours or perhaps even less than 1 h. The use of improved time- and spatially dependent vertical profiles for atmospheric winds and temperatures would significantly improve source location estimates.

The best current estimate of the global atmospheric structure profiles is provided by the Naval Research Laboratory – Ground to Space (NRL-G2S) semi-empirical model, which is based on a self-consistent smooth fusion of operational numerical weather prediction (NWP) lower atmosphere models with the upper atmosphere portion of the Horizontal Wind Model (Hedin et al. 1996)/Mass Spectrometer and Incoherent Radar Model (Hedin 1991) HWM/MSIS climatology (see, e.g., Drob et al. 2003, 2007). Numerous infrasound propagation studies in recent years

(e.g., Le Pichon et al. 2006a) have shown that the NRL-G2S model provides a fairly good description of the temporal and spatial variation of atmospheric wind and temperature profiles up to an altitude of about 55 km. Work is currently underway to improve the Horizontal Wind Model to provide a better estimate of winds in the mesosphere and lower thermosphere (Drob et al. 2006).

Two types of infrasonic sources have been used to refine the upper atmospheric profiles: microbaroms and higher frequency infrasound generated by continuous volcanic eruptions. In principle, microbaroms provide a useful source for global tomography studies since waves of this type are almost always present at monitoring stations in the global IMS infrasound network. However, these waves may be masked by high levels of background noise at some stations (especially during the daytime) and the precise location of the source may not be known with certainty. Nevertheless, microbaroms are potentially very useful for global infrasound tomography studies. Recent examples of the use of microbaroms to delineate the upper atmospheric winds and temperatures using state-of-the-art propagation models are given in Garcés et al. (2004a) and Le Pichon et al. (2006b). An analysis of observations at IS22 in New Caledonia of infrasonic signals generated by continuous eruptions of volcanoes in Vanuatu is described is detail in Le Pichon and Drob (2004) and Le Pichon et al. (2005a, b). These studies show that the observations do not agree with propagation model simulations based on the NRL-G2S climatological profiles and parabolic equation range-dependent modelling assuming a 2 Hz frequency signal. A procedure has therefore been devised to use these observations to correct the NRL-G2S profiles. The main conclusion at this point is that the zonal winds in the upper stratosphere and lower thermosphere are underestimated by the NRL-G2S climatology.

6.5.2 Geophysical Hazard Warning Systems

Data from the global infrasound network can play an important role in a wide variety of international geophysical hazard warning systems ranging from the identification of potential damage from shallow earthquakes, landslides and avalanches in remote areas to the monitoring of global warming and global volcanic activity.

Perhaps the most important potential application the IMS infrasound network is in the use of data from this network to identify, accurately locate and quantify volcanic eruptions in remote areas when data from satellite observations are marginal due to cloud cover. Thus, data from the global infrasound network could provide valuable information that could be used at volcanic ash observatories in parallel with data from other monitoring systems to provide an enhanced warning to aviation of potentially hazardous volcanic ash clouds (Chen and Christie 1995; Campus 2005).

A second potentially important example of the use of infrasound technology in a geophysical hazard warning system is the development of an infrasound tornado-warning system as described by Bedard et al. (2004a, b).

Infrasound can also be used in other more localised geophysical hazard warning systems. For example, the use of infrasound in avalanche warning systems has been studied in detail in recent years (see, e.g., Bedard 1994; Scott et al. 2007).

6.5.3 Observation of Meteors

Detailed infrasonic observations are contributing to our understanding of the frequency, size distribution and dynamics of meteors (see Sect. 3.6) on a global scale. Some of the largest recorded infrasonic signals observed at stations in the global network have originated in meteors that explode in the atmosphere before impact. These exploding meteors (or bolides) sometimes have effective yields of more than 5 kT and signals from these events are observed at a large number of stations in the global network. The signature of a large exploding meteor may be similar to the signature from a nuclear explosion. The generation and propagation of infrasonic signals by large exploding meteors are not yet well understood. Further work on the development of techniques that will provide unambiguous discrimination of bolide-generated infrasound is clearly important from a nuclear explosion monitoring perspective.

6.5.4 Global Warming

It can also be anticipated that data from the global network could be used to monitor global warming. The break-up of icebergs and the calving of glaciers located near Qaanaak are routinely observed at IS18 in northern Greenland. A long-term study of infrasound observations at IS18 could be used to monitor the progress of global warming at high latitudes in the Northern Hemisphere (Campus 2008). Similar studies that focus on ocean-storm-generated infrasound, the prevalence of natural disasters such as landslides and avalanches and infrasound associated with the break-up of the Antarctic ice shelves may also provide a valuable indication of the progress of global warming.

6.5.5 Forensic Investigations

Data from infrasonic arrays can be used in forensic studies of accidental chemical explosions and other disasters to provide a detailed record of the size, timing and sequence of events during the disaster. The detailed analysis of the Buncefield oil depot explosion (Ceranna and Le Pichon 2006; Evers and Haak 2006, 2007; Green et al. 2006) described briefly in Sect. 4.3 is a good example of the usefulness of infrasonic data in investigations of this type.

A second example of the use of infrasonic data as a source of valuable information in a disaster investigation is given by the results of a detailed study of infrasonic waves recorded during the tragic re-entry of space shuttle Columbia over the western United States on February 1, 2003 (Bass et al. 2003).

6.6 Concluding Remarks

The establishment of a global IMS 60-station infrasound network is rapidly nearing completion. The stations in this network are located in a very wide variety of environments ranging from the hot and wet tropics to the icy wastes of the Polar regions. Some of the signals that are detected at stations in the global network are unique to one or perhaps a few nearby monitoring stations located in a specific environment. Other types of signal are commonly detected at almost all stations in the network. This chapter has been concerned with an attempt to provide as many examples as possible of the wide variety of signals that are observed at stations in the global IMS infrasound monitoring network. This survey is not exhaustive. Examples of some relatively minor sources of infrasound have not been included.

The primary purpose of the IMS infrasound network is to detect and locate atmospheric nuclear explosions. There are, however, a number of practical applications where infrasound data may prove to be of value. These potentially important applications are summarised in Sect. 5.

The field of atmospheric infrasound can be regarded as both an old and new area of science. Much of the fundamental research on infrasonic waves was carried out during the period from the late-1950s to the early-1970s. Interest in infrasound started to fade after the signing of the limited test-ban treaty (LTBT) in 1963 and almost all infrasound monitoring networks were closed down in the mid-1970s. There were only a few scientists working in the field of infrasound when the CTBT was opened for signature in September 1996. This situation changed dramatically with the establishment of the global IMS infrasound network. Infrasound research programmes have been established at several universities and institutions and a significant number of scientific papers in infrasound are now published each year in the peer-reviewed literature. There have been a number of improvements in infrasound monitoring technology since 1996, many of which have been incorporated into the global monitoring network. As of the end of 2008, high-quality infrasound data was being recorded at 41 certified stations in the global IMS infrasound network. This data is transmitted directly by satellite (or via VPN) to the IDC in Vienna, Austria, analysed in near real time and permanently archived. The global IMS infrasound network is far larger and much more sensitive than any previously operated infrasound network. Recent studies (Green 2008; Le Pichon et al. 2009) indicate that the IMS infrasound network is capable of detecting and locating any nuclear atmospheric explosion with an yield of 1 kT or more. It can be anticipated that further developments in infrasound monitoring technology will eventually lead to lower detection thresholds and improved location estimates.

We expect that scientific interest in the field of infrasound will continue to increase. A number of problems related to the long-distance propagation of infrasound, the nature of various source mechanisms, and problems associated with the discrimination of signals remain unresolved. A very large number of signals are detected every day by the IMS infrasound network. However, the source of only a small fraction of the detected signals can be identified with certainty. Several new sources of infrasound have been found since work began in 1997 on the establishment of the global infrasound monitoring network. It seems likely that other new and interesting sources will be discovered during the next few years.

6.7 Disclaimer

The views expressed herein are those of the authors and do not necessarily reflect the views of the CTBTO Preparatory Commission.

Acknowledgments Paola Campus expresses her thanks to the Département, Analyse, Surveillance de l'Environment (CEA/DAM/DIF/DASE) for the use of PMCC software.

References

Abdullah AJ (1966) The "musical" sound emitted by a tornado. Mon Weather Rev 94:213–220

Axefors B, Backteman O, Bennerhult O, Nilsson NA (1985) Infrasound: a bibliography of articles up till April 1983, Swedish Defense Materiel Admin., Strockholm, Sweden

Arendt S, Fritts D (2000) Acoustic radiation by ocean surface waves. J Fluid Mech 415:1–21

Arnoult KM, Wilson CR, Olson JV, Szuberla CAL (2005) Infrasound associated with Mt Steller avalanche. Inframatics 12:4–7

Assink JD, Evers LG, Holleman I, Paulssen H (2008) Characterization of infrasound from lightning. Geophys Res Lett 35:L15802

Baird HF, Banwell CJ (1940) Recording of air-presure oscillations associated with microseisms at Christchurch, New Zealand. J Sci Technol 21B:314–329

Balachandran NK (1982) Acoustic and electric signals from lightning. J Geophys Res 88:3879–3884

Balachandran NK, Donn WL (1971) Characteristics of infrasonic signals from rockets. Geophys J R astr Soc 26:135–148

Balachandran NK, Donn WL, Rind DH (1977) Concorde sonic booms as an atmospheric probe. Science 197:47–49

Barruol G, Reymond D, Fontaine FR, Hyvernaud O, Maurer V, Maamaatuaiahutapu K (2006) Characterizing swells in the southern Pacific from seismic and infrasonic noise analyses. Geophys J Int 164:516–542

Bass HE, Tenney S, Clark P, Noble J, Gibson R, Norris D, Bhattacharyya J, Bondar I, Israelsson H, North R, Skov M, Woodward R, Yang X, Whitaker R, Sandoval T, Revelle D, Bedard A, Nishiyama R, Gasiewski A, Drob D, Hedlin M, D'Spain G, Murray J, Rovner G, Berger L, Garcés M, Hetzer C, Herrin E, Hayward C (2003). Report to the Department of Defense on Infrasonic Re-entry Signals from the Space Shuttle Columbia (STS-107) (Revision 3.0). American Geophysical Union, Fall Meeting 2003, abstract #U32B-02

Brackteman O, Kohler J, Sjoberg L (1985) Infrasound: a summary of interesting articles, Swedish Defense Materiel Admin., Stockholm, Sweden

Bedard AJ Jr, (1988) Infrasound from natural sources in Internoise 88. Proceedings from the 1988 International Conference on Noise Control Engineering, Avignon, France

Bedard AJ Jr (1993) Low-frequency sound waves associated with avalanches, atmospheric turbulence, severe weather, and earthquakes. J Acoust Soc Am 94(3):1872

Bedard AJ Jr, (1994) Evaluation of atmospheric infrasound for monitoring avalanches. Proceedings of the 7th international symposium on acoustic remote sensing and associated techniques of the atmosphere and oceans, Boulder, Colorado, 3–5 October 1994.

Bedard AJ Jr, (1998) Infrasonic detection of severe weather. Proceedings of the 19th conference on severe local storms, American Meteor Society, Minneapolis, MN, Paper 6.6

Bedard AJ Jr (2005) Low frequency atmospheric acoustic energy associated with vortices produced by thunderstorms. Mon Weather Rev 133:241–263

Brachet N, Brown D, Le Bras R, Mialle P, Coyne J (2010) Monitoring the earth's atmosphere with the global IMS infrasound network. This volume, pp. 73–114

Bedard AJ Jr, Bartram BW, Keane AN, Welsh DC, Nishiyama RT (2004a) The infrasound Network (ISNET): Background, design details, and display capability as an 88D adjunct tornado detection tool. Proceedings of the 22nd conference on severe local storms, American Meteor Society, Hyannis, MA, Paper 1.1

Bedard AJ Jr, Bartram BW, Entwistle B, Golden J, Hodanish S, Jones RM, Nishiyama RT, Keane AN, Mooney L, Nicholls M, Szoke EJ, Thaler E, Welsh DC (2004b) Overview of the ISNET data set and conclusions and recommendations from a March 2004 workshop to review ISNET data. Proceedings of the 22nd Conference on severe local storms, American Meteor Society, Hyannis, MA, Paper 2.8

Benioff H, Gutenberg B (1939) Waves and currents recorded by electromagnetic barographs. Bull Amer Met Soc 20:421–426

Bowman HS, Bedard AJ (1971) Observations of infrasound and subsonic disturbances related to severe weather. Geophys J R astr Soc 26:215–242

Brown PG, Whitaker RW, ReVelle DO, Tagliaferri E (2002a) Multi-station infrasonic observations of two large bolides: Signal interpretation and implications for monitoring of atmospheric explosions. Geophys Res Lett 29:1636. doi:10.1029/2001GL013778

Brown P, Spalding RE, ReVelle DO, Tagliaferri E, Worden SP (2002b) The flux of small near-Earth objects colliding with the Earth. Nature 420:314–316

Campus P (2003) The CTBT IMS infrasound network: Status of the actual installations and examples of infrasound signals recorded at the existing stations. Proceedings of the American Geophysical Union (AGU) Fall Meeting 2003, San Francisco, California, 8–12 December 2003

Campus P (2004) The IMS infrasound network and its potential for detection of events: examples of a variety of signals recorded around the world. Inframatics 6:14–22

Campus P (2005) The IMS infrasound network and monitoring of volcanoes. Proceedings of the 2005 Infrasound Technology Workshop, Tahiti, 28 November–2 December 2005

Campus P (2006a) Monitoring volcanic eruptions with the IMS infrasound network. Inframatics 15:6–12

Campus P (2006b) Monitoring volcanoes at the CTBT IMS infrasound network. Proceedings of the 2006 Infrasound Technology Workshop, Fairbanks, Alaska, USA, 25–28 September 2006

Campus P (2007a) The IMS infrasound network: detection of a large variety of events, including volcanic eruptions. Proceedings of the 8th International Conference on Theoretical and Computational Acoustics, Heraklion, Crete, 02-06 July 2007.

Campus P (2007b) The IMS infrasound network: detection of a large variety of events including volcanic eruptions. Proceedings of the 2007 Infrasound Technology Workshop, Tokyo, Japan, 13–16 November 2007.

Campus P (2007c) Eruptions detected with the global infrasonic array network of the International Monitoring System. Proceedings of the second international workshop on acoustic remote sensing of volcanoes, Shimabara, Japan, 18 November, 2007

Campus P (2008) The IMS infrasound network and its potential for detections of a wide variety of man-made and natural events. Proceedings Infrasound Technology Workshop, Bermuda, 3–7 November 2008

Campus P, Christie DR, Brown D (2005) Detection of infrasound from the eruption of Manam volcano on January 27, 2005. Proceedings of the 2005 infrasound technology workshop, Tahiti, 28 November – 2 December 2005 and Proceedings of the first international workshop on acoustic remote sensing of volcanoes, Quito, 22 January, 2006

Cansi Y (1995) An automatic seismic event processing for detection and location: the PMCC method. Geophys Res Lett 22:1021–1024

Cansi Y, Le Pichon A (2008) Infrasound event detection using the progressive multi-channel correlation algorithm. Handbook of signal processing in acoustics, Chapter 77, 1425–1435, Springer, New York

Ceranna L, Le Pichon A (2006) The Buncefield fire: a benchmark for infrasound analysis in Europe. Proceedings of the 2006 infrasound technology workshop, Fairbanks, Alaska, USA, 25–28 September 2006

Chen P, Christie DR (1995) Infrasonic detection of volcanic explosions by the International Monitoring System: implications for aviation safety. 2nd meeting international civil aviation volcanic ash warning study group, Montreal, Canada, 2 November 1995

Chimonas G (1977) A possible source mechanism for mountain-associated infrasound. J Atmos Sci 34:806–811

Christie DR (1989) Long nonlinear waves in the lower atmosphere. J Atmos Sci 46: 1462–1491

Christie DR (1992) The Morning Glory of the Gulf of Carpentaria: a paradigm for non-linear waves in the lower atmosphere. Aust Meteor Mag 41:21–60

Christie DR (2004) Observations of infrasound in central Australia. Proceedings Infrasound Technology Workshop, Hobart, Australia, 29 November–3 December 2004

Christie DR, Kennett BLN (2007) Detection of nuclear explosions using infrasound techniques. Final Report AFRL-RV-HA-TR-2007-1151, Air force research laboratory, Hanscom AFB, MA, Available from United States Technical Information Service

Christie DR, Campus P (2010) The IMS infrasound network: design and establishment of infrasound stations. This volume, pp. 27–72

Christie DR, Muirhead KJ, Hales AL (1978) On solitary waves in the atmosphere. J Atmos Sci 35:805–825

Christie DR, Kennett BLN, Tarlowski C (2005) Detection of regional and distant atmospheric explosions. Proceedings of the 27th Seismic Research Review, Rancho Mirage, California, 20–22 September 2005, 817–827

Chrzanowski P, Green G, Lemmon KT, Young JM (1961) Travelling pressure waves associated with geopmagnetic activity. J Geophys Res 66:3727–3733

Cook RK (1971) Infrasound radiated during the Montana Earthquake of 1959 August 18. Geophys J R astr Soc 26:191–198

Cotten DE, Donn WL, Oppenheim A (1971) On the generation and propagation of shock waves from apollo rockets at orbital altitudes. Geophys J Int 26:149–159

Cotton DE, Donn WL (1971) Sound from Apollo rockets in space. Science 171:656

Cox EF (1949) Abnormal audibility zones in long distance propagation through the atmosphere. J Acoust Soc Am 21:6–16

Davidson M, Whitaker RW (1992) Miser's Gold, Los Alamos National Laboratory Technical Report: LA-12074-MS, February

Dessler AJ (1973) Infrasonic thunder. J Geophys Res 78:1889–1896

Donn WL (1978) Exploring the atmosphere with sonic booms. Am Sci 66:724–733

Donn WL, Balachandran NK (1981) Mount St. Helens eruption of 18 May 1980: air waves and explosive yield. Science 213:539–541

Donn WL, Naini B (1973) Sea wave origin of microbaroms and microseisms. J Geophys Res 78:4482–4488

Donn WL, Rind D (1971) Natural infrasound as an atmospheric probe. Geophys J R astr Soc 26:111–133
Donn WL, Rind D (1972) Microbaroms and the temperature and winds in the upper atmosphere. J Atmos Sci 29:156–172
Donn WL, Shaw DM (1967) Exploring the atmosphere with nuclear explosions. Rev Geophys 5:53–82
Donn WL, Balachandran NK, Kaschak G (1974) Atmospheric infrasound radiated by bridges. J Acoust Soc Am 56:1367
Drob DP, Picone JM, Garcés MA (2003) The global morphology of infrasound propagation. J Geophys Res 108, doi:10.1029/2002JD003307
Drob D, O'Brien M, Bowman R (2006) HWM upgrade for infrasound propagation calculations. Proceedings of the 2006 Infrasound Technology Workshop, Fairbanks, Alaska, USA, 25–28 September 2006
Drob DP, Garcés M, Hedlin M, Brachet N (2007) The temporal morphology of infrasound propagation. Proceedings infrasound technology workshop, Tokyo, Japan, 13–16 November 2007
de Groot-Hedlin C, Hedlin MAH, Walker KT (2008) Evaluation of infrasound signals from the shuttle Arlantis using a large seismic network. J Acoust Soc Am 124:1442–1451
de Groot-Hedlin C, Hedlin M, Walker K, Drob D, Zumberge M (2007) Study of infrasound propagation from the shuttle Atlantus using a large sesimic network. Proceedings infrasound technology workshop, Tokyo, Japan, 13–16 November 2007
Edwards WN, Brown P, ReVelle DO (2006) Estimates of metereoid kinetic energies from observations of infrasonic waves. J Atmos Solar-Terrestrial Phys 68:1136–1160
Evers L (2005) Infrasound monitoring in the Netherlands. J Netherlands Acoust Soc (Nederlands Akoestisch Genootschap) 176:1–11
Evers LG (2008) The inaudible symphony: on the detection and source identification of atmospheric infrasound. Ph. D. Thesis, Delft University of Technology, Delft, The Netherlands, ISBN 978-90-71382-55-0
Evers L, Haak H (2001) Recent observations at the Deelen Infrasound array. Proceedings Infrasound Technology Workshop, Kailua-Kona, Hawaii, 12–15 November 2001
Evers LG, Haak HW (2003) Tracing a meteoric trajectory with infrasound. Geophys Res Lett, 30(24): 2246, doi:10.1029/2003GL017947
Evers LG, Haak HW (2005) The detectability of infrasound in The Netherlands from the Italian volcano Mt Etna. J Atmos Sol Terr Phys 67:259–268. doi:10.1016/j.jastp. 2004.09.002
Evers L, Haak H (2006) Seismo-acoustic analysis of explosions and evidence for infrasonic forerunners. Proceedings of the 2006 infrasound technology workshop, Fairbanks, Alaska, USA, 25–28 September 2006
Evers L, Haak H (2007) Infrasonic forerunners: Exceptionally fast acoustic phases. Geophys Res Lett 34:L10806. doi:10.1029/2007GL029353
Evers L, Ceranna L, Haak HW, Le Pichon A, Whitaker RW (2007) A seismoacoustic analysis of the gas-pipeline explosion near ghislenghien in Belgium. Bull Seism Soc Am 97(2):417
Farges T, Blanc E, Le Pichon A, Neubert T, Allin TH (2005) Identification of infrasound produced by sprites during the Sprite2003 campaign. Geophys Res Lett 32:L01813. doi:10.1029/2004GL021212
Few AA (1970) Lightning channel reconstruction from thunder measurements. J Geophys Res 75(36):7517–7523
Few AA (1985) The production of lightning-associated infrasonic acoustic sources in thunderclouds. J Geophys Res 90:6175–6180
Greene GE, Howard J (1975) Natural infrasound: a one year global study, NOAA, TR, ERL 317-WPL-37
Garcés M, Hetzer C, Merrifield M, Willis M, Aucan J (2003) Observations of surf infrasound in Hawai'i. Geophys Res Lett 30(24):2264, doi:10.1029/2003GL018614
Garcés M, Willis M, Hetzer C, Le Pichon A, Drob D (2004a) On using ocean swells for continuous infrasonic measurements of winds and temperature in the lower, middle, and upper atmosphere. Geophys Res Lett 31:L19304. doi:10.1029/2004GL020696

Garcés M, Bass H, Drob D, Hetzer C, Hedlin M, Le Pichon A, Lindquist K, North R, Olson J (2004b) Forensic studies of infrasound from massive hypersonic sources. EOS 85(43):433

Garcés M, Fee D, Steffke A, McCormack D, Servranckx R, Bass H, Hetzer C, Hedlin M, Matoza R, Yepes H, Ramon P (2008) Capturing the acoustic fingerprint of stratospheric ash injection. EOS, Tran Am Geophys Union, 89: 377–378

Georges TM (1973) Infrasound from convective storms: Examining the evidence. Rev Geophys Space Phys 11:571–594

Goerke VH, Woodward MW (1966) Infrasonic observation of a severe weather system. Mon Weather Rev 94:395–398

Goerke VH, Young JM, Cook RK (1965) Infrasonic observations of the 1963 volcanic explosion on the island of Bali. J Geophys Res 70:6017–6022

Green D (2008). Assessing the detection capability of the International Monitoring System infrasound network. AWE Report 629/08, AWE Aldermaston, p. 91

Green D, Bowers D, Drob D, Hort M (2006) The Buncefield oil depot explosion: extending signal coverage using airwaves recorded on seismometers. Proceedings of the 2006 infrasound technology workshop, Fairbanks, Alaska, USA, 25–28 September 2006

Greene GE, Bedard AJ (1986) Infrasound from distant rocket launches, national oceanic and atmospheric administration technical report No: NOAA-TM-ERL-WPL-131, February NTIS Number: PB86-182771/HDM

Grover FH (1968) Research notes: a note on infrasonics at U.K.A.E.A. Blacknest. Geophys J R astr Soc 16:311

Grover FH (1973) Geophysical effects of Concord sonic boom. Q Jl R astr Soc 14:141–160

Grover FH, Marshall PD (1968) Ground to air coupled waves from a distant earthquake. Nature 220:686–687

Gutenberg B (1939) The velocity of sound waves and the temperature in the stratosphere in Southern California. Bull Am Met Soc 20:192–201

Gutenberg B, Benioff H (1941) Atmospheric pressure waves near Pasadena. Trans Amer Geophys Union 22:424–426

Hagerty M, Kim WY, Martysevhich P (2002) Infrasound detection of large mining blasts in Kazakstan. Pure Appl Geophys 159(5):1063–1079

Hedin AE (1991) Extension of the MSIS thermosphere model in the middle and lower atmosphere. J Geophys Res 96:1159–1172

Hedin AE, Fleming EL, Manson AH, Schmidlin FJ, Avery SK, Clark RR, Franke SJ, Fraser GJ, Tsuda T, Vial F, Vincent RA (1996) Empirical wind model for the upper, middle and lower atmosphere. J Atmos Terr Phys 58:1421–1444

Hetzer C, Waxler R, Talmadge C, Garcés M, Gilbert K, Bass H (2007) Hurricane studies using infrasound. Proceedings Infrasound Technology Workshop, Tokyo, Japan, 13–16 November 2007

Itikari I, Campus P, Martysevich P, Hoffman T (2003) IS40 and infrasound waves from volcanic explosions. Proceedings of the 2003 Infrasound Technology Workshop, La Jolla, California, USA, 27–30 October 2003

Kunhikrishnan PK, Krishna Murthy BV (1982) Atmospheric pressure perturbations during total solar eclipse on 16 February 1980, Proceedings of Indian National Science Academy 48A, suppl. 3: 238

Larson RJ, Craine LB, Thomas JE, Wilson CR (1971) Correlation of winds and geographic features with production of certain infrasonic signals in the atmosphere. Geophys J R astr Soc 26:201–214

Le Pichon A, Cansi Y (2003) PMCC for infrasound data processing. Inframatics 2:1–9

Le Pichon A, Drob D (2004) Probing high-altitude winds using infrasound from volcanoes. Inframatics 8:1–16

Le Pichon A, Guilbert J, Cansi Y (2001) Infrasonic waves from natural sources. Proceedings infrasound technology workshop, Kailua-Kona, Hawaii, 12–15 November 2001

Le Pichon A, Guilbert J, Vallée M, Dessa JX, Ulziibat M (2003) Infrasonic imaging of the Kunlun Mountains for the great 2001 China earthquake. Geophys Res Lett 30(15): 1814, doi:10.1029/2003GL017581

Le Pichon A, Blanc E, Drob D (2005a) Probing high-altitude winds using infrasound. J Geophys Res 110:D20104. doi:10.1029/2005JD006020
Le Pichon A, Blanc E, Drob D, Lambotte S, Dessa JX, Lardy M, Bani P, Vergniolle S (2005b) Infrasound monitoring of volcanoes to probe high-altitude winds. J Geophys Res 110:D13106. doi:10.1029/2004JD005587
Le Pichon A, Herry P, Mialle P, Vergoz J, Brachet N, Garcés M, Drob D, Ceranna L (2005c) Infrasound associated with 2004–2005 large Sumatra earthquakes and tsunami. Geophys Res Lett 32:L19802. doi:10.1029/2005GL023893
Le Pichon A, Antier K, Drob D (2006a) Multi-year validation of the NRL-G2S wind fields using infrasound from Yasur. Inframatics 16:1–9
Le Pichon A, Ceranna L, Garcés M, Drob D, Millet C (2006b) On using infrasound from interacting ocean swells for global continuous measurements of winds and temperature in the stratosphere, J Geophys Res 111, doi:10.1029/2005JD006690
Le Pichon A, Mialle P, Guilbert J, Vergoz J (2006c) Multistation infrasonic observations of the Chilean earthquake of 2005 June 13. Geophys J Int 167:838–844
Le Pichon A, Vergoz J, Blanc E, Guilbert J, Ceranna L, Evers L, Brachet N (2009) Assessing the performance of the International Monitoring System infrasound network: geographical coverage and temporal variabilities. J Geophys Res, 114:D08112. doi:10.1029/2008JD010907
Lees JM, Gordeev EI, Ripepe M (2004) Explosions and periodic tremor at Karymsky volcano, Kamchatka. Russia Geophys J Int 158:1151–1167
Lin TL, Langston CA (2007) Infrasound from Thunder: A Natural Seismic Source. Geophys Res Lett 34:L14304. doi:10.1029/2007GL030404
Liszka L (1974) Long-distance propagation of infrasound from artificial sources. J Acoust Soc Am 56:1383
Liszka L (2004) On the possible infrasound generation by sprites. J Low Frequency Noise, Vibration and Active Control 23:85–93
Liszka L (2008a) Infrasound: A summary of 35 years of research. IRF Scientific Report 291, Swedish Institute of Space Physics, Umeå, Sweden, p. 150
Liszka L (2008b) Listening to meteors. IRF Scientific Report 295, Swedish Institute of Space Physics, Umeå, Sweden, p. 66 pp
Liszka L, Garcés MA (2002) Infrasonic observations of the Hekla eruption of February 26, 2000, J. Low Freq. Noise, Vibration, and Active Control 21: 1–8
Liszka L, Hobara Y (2006) Sprite-attributed infrasonic chirps – their detections, occurrence and properties between 1994 and 2004. J Atmos Solar-Terrestrial Phys 68:1179–1188
Liszka L, Waldemark K (1995) High resolution observations of infrasound generated by the supersonic flight of the Concorde. J. Low Frequency Noise and Vibration 14(4):181–192
Longuet-Higgens MS (1950) A theory of the origin of microseisms. Phil Trans R Soc Lond A 243:1–35
Maeda K, Young J (1966) Propagation of pressure waves produced by auroras. J. Geomagn., Kyoto, 18: 275–299
Matoza RS, Hedlin MAH, Garcés MA (2007) An infrasound array study of Mount St. Helens. J Volcanology Geothermal Res 160: 249–262
McIntosh BA, ReVelle DO (1984) Traveling Atmospheric Pressure Waves Measured During a Solar Eclipse. J Geophys Res 89:4953
McIntosh BA, Watson MD, ReVelle DO (1976) Infrasound from a radar-observed meteor. Can J Phys 54:655–662
Melton BS, Bailey LF (1957) Multiple signal correlators. Geophysics 22:565–588
Mutschlecner JP, Whitaker RW (2005) Infrasound from earthquakes. J Geophys Res 110, doi:10.1029/2004JD005067
McKisic JM (1996) Infrasound and the infrasonic monitoring of atmospheric nuclear explosions: an annotated bibliography, Department of Energy and Phillips Laboratory Air Force Materiel Command, PL-TR-96-2282
Mutschlecner JP, Whitaker RW, Auer LH (1999) An empirical study of infrasound propagation, Los Alamos Nat. Lab. Tech Rep. LA-13620-MS

Olson J (2004) Infrasound signal detection using the Fisher F-statistics. Inframatics 6:1–8
Olson J, Wilson CR, Hansen RA (2003) Infrasound associated with the 2002 Denali fault earthquake. Alaska Geophys Res Lett 30:2195. doi:10.1029/2003GL018568
Posey JW, Pierce AD (1971) Estimation of nuclear explosion energies from microbaragraph records. Nature 232:253
Posmentier ES (1967) A theory of microbaroms. Geophys J Int 13:487–501
Posmentier ES (1971) Preliminary observations of 1–16 Hz natural background infrasound and signals from Apollo 14 and aircraft. Geophys J R astr Soc 26:173–177
Procunier RW (1971) Observations of acoustic aurora in the 1–16 Hz range. Geophys J R astr Soc 26:183–189
Reed JW (1969) Climatology of airblast propagations from nevada test site nuclear airbursts, Sandia National Laboratory Report SC-I.R.-69-572 m December
Reed JW (1987a) Air pressure waves from Mount St. Helens eruptions. J Geophys Res 92(11):979
Reed JW (1987b) Climatological assessment of expolosion airblast propagation, Sandia National Laboratory Terchnical Report No. SAND-86-2180C (Conference Proceedings), NTIS Number: DE87010510/HDM
ReVelle DO (1976) On meteor-generated infrasound. J Geophys Res 81:1217–1229
ReVelle DO (1997) Historical detection of atmospheric impacts by large bolides using acoustic-gravity waves. Annals of the New York Academy of Sciences, Volume 822, Near-Earth Objects: The United Nations Conference, 284–302
Richardson J, Fitzgerald K, Pennington W (2008) Seismic and acoustic observations of Bering Glacier calving events. EOS Trans. AGU, 89 (83), Fall Meeting Supplement, Abstract C11A-0479
Rind D (1977) Heating of the lower thermosphere by the dissipation of acoustic waves. J Atmos Terrestrial Phys 39:445–456
Rind D (1978) Investigation of the lower thermosphere results of ten years of continuous observations with natural infrasound. J Atmos Terr Phys 40:1199–1209
Rind D, Donn WL (1975) Further use of natural infrasound as a continuous monitor of the upper atmosphere. J Atmos Sci 32:1694–1704
Rind D, Donn WL, Dede E (1973) Upper air wind speeds calculated from observations of natural infrasound. J Atmos Sci 30:1726–1729
Rockway JW, Hower GL, Craine LB, Thomas JE (1974) Application of ray-tracing to observations of mountain-associated infrasonic waves. Geophys J R astr Soc 35:259–266
Scott ED, Hayward CT, Kubichek RF, Hamann JC, Pierre JW, Comey B, Mendenhall T (2007) Single and multiple sensor identification of avalanche-generated infrasound. Cold Reg Sci Technol 47:159–170
Sorrells G, Bonner J, Herrin ET (2002) Seismic precursors to space shuttle shock fronts. Pure Appl Geophys 159:1153–1181
Symons GJ (ed) (1888) The eruption of Kraktoa and subsequent phenomena. Harrison and Sons, London
Thomas JE, Pierce AD, Flinn EA, Craine LB (1971) Bibliography on infrasonic waves, Geophys J. R. astr Soc 26:399
Thomas JE, Pierce AE, Flinn EA, Craine LB (1972) Supplement to 'Bibliography on Infrasonic Waves, Geophys J. R. astr Soc 30:1
Walker KT, Zumberge MA, Hedlin MAH, Shearer PM (2008) Methods for determining infrasound phase velocity direction with an array of line sensors. J Acoust Soc Am 124:2090–2099
Whitaker R (2007) Infrasound signals as basis for event discriminants. Proceedings of the 29th Monitoring Research Review, Denver, Colorado, 25–27 September 2007, 905–913
Whitaker R (2008) Infrasound signals from ground-motion sources. Proceedings of the 30th monitoring research review, Portsmouth, Virginia, 23–25 September 2008, 912–920
Wilson CR (1967) Infrasonic pressure waves from the aurora; a shock wave model. Nature 214:1299
Wilson CR (1971) Auroral infrasonic waves and poleward expansions of auroral substorms at Inuvik, N.W.T., Canada. Geophys. J. R. astr. Soc., 26: 179-181
Wilson CR (2005) Infrasound from auroral electrojet motions at I53US. Inframatics 10:1–13

Wilson CR, Olson JV (2003) Mountain associated waves at I53US and I55US in Alaska and Antarctica in the frequency passband from 0.015 to 0.10 Hz. Inframatics 3:6–10
Wilson CR, Olson JV (2005a) Frequency domain coherence between high trace-velocity infrasonic signals at I53US and video data from pulsating aurora. Inframatics 9:27–30
Wilson CR, Olson JV (2005b) 153US and 155US signals from Manam Volcano. Inframatics 9:31–35
Wilson CR, Szuberla CAL, Olson JV (2010) High-latitude observations of infrasound from Alaska and Antarctica: mountain associated waves and geomagnetic/auroral Infrasonic signals. This volume, pp. 409–448
Wilson CR, Olson JV, Osborne DL, Le Pichon A (2003) Infrasound from Erebus Volcano at I55US in Antarctica. Inframatics 4:1–8
Young JM, Greene GE (1982) Anamalous infrasound generated by the Alaskan earthquake of 28 March 1964. J Acoust Soc Am 71:334–339

Chapter 7
Infrasonic Observations of Open Ocean Swells in the Pacific: Deciphering the Song of the Sea

M. Garcés, M. Willis, and A. Le Pichon

7.1 Introduction

Microbaroms are continuous infrasonic oscillations produced by ocean waves. They are observed everywhere on Earth and generally determine the ambient noise floor in the 0.1–0.5 Hz frequency band (Bowman et al. 2005). The microbarom peak is in the midst of the detection region for 1-kiloton nuclear explosion tests (Stevens et al. 2002), and thus microbaroms can obscure an important signal of interest. Although microbaroms limit signal detection thresholds in that band, they may be used to remotely sense marine weather and ocean waves, and for passive acoustic tomography of the atmosphere.

The source mechanism for microbaroms is attributed to the nonlinear interaction of ocean surface waves (Hetzer et al. 2010). Multiple swells coexisting at any given point on the ocean surface can radiate infrasonic waves if the ocean-wave spectrum contains swell components that are almost opposite in direction and of a nearly identical frequency. Such interactions commonly occur between ocean waves with ~10 s periods, which are abundant in the open oceans and correspond to the observed 0.2 Hz infrasonic spectral peak. Global ocean-wave spectra, as provided by the National Oceanic and Atmospheric Administration's (NOAA's) Wavewatch 3 (WW3) model, can be used to estimate the acoustic source pressure spectra induced by nonlinear ocean-wave interactions (Willis 2004). Comparison of microbarom observations with surface weather, ocean-wave charts, and WW3-produced acoustic sources suggests that microbarom source regions occur in locations that contain opposing wave trains, instead of exclusively from regions of marine storminess. The arrival azimuths of coherent microbarom signals observed by the global infrasound array network are associated with high ocean-wave activity, the dominant wind directions in the troposphere, stratosphere, and mesosphere, and the thermal structure of the atmosphere. Some of the seasonal trends in the microbarom observations can be explained by the winds in

M. Garcés (✉)
HIGP, SOEST, University of Hawaii, Manoa, 73-4460 Queen Kaahumanu Hwy,
#119 Kailua-Kona, HI 96740-2638
e-mail: milton@isla.hawaii.edu

A. Le Pichon et al. (eds.), *Infrasound Monitoring for Atmospheric Studies,*
DOI 10.1007/978-1-4020-9508-5_7,

the stratosphere and lower mesosphere, whereas some of the daily variability can be explained by the winds in the troposphere and lower stratosphere. However, coherent energy from powerful swells may overcome the wind-carried microbarom signals and arrive to the station through thermospheric ducting (Fig. 7.1).

In this chapter we review contemporary observations and interpretations of microbarom signals recorded by the global infrasound network, and discuss the potential of using these signals for acoustic remote sensing of hurricanes, severe sea states, and the temporal and spatial variability of atmospheric winds.

7.2 Background

Microbaroms were first reported by Sulejkin (1935) and Benioff and Gutenberg (1939), although at the time of their studies there was no accepted hypothesis for microbaroms or their seismic counterparts, microseisms (e.g., Webb and Cox 1986; Webb 1992; Kibblewhite and Wu 1996). Longuet-Higgins (1950) was the first to

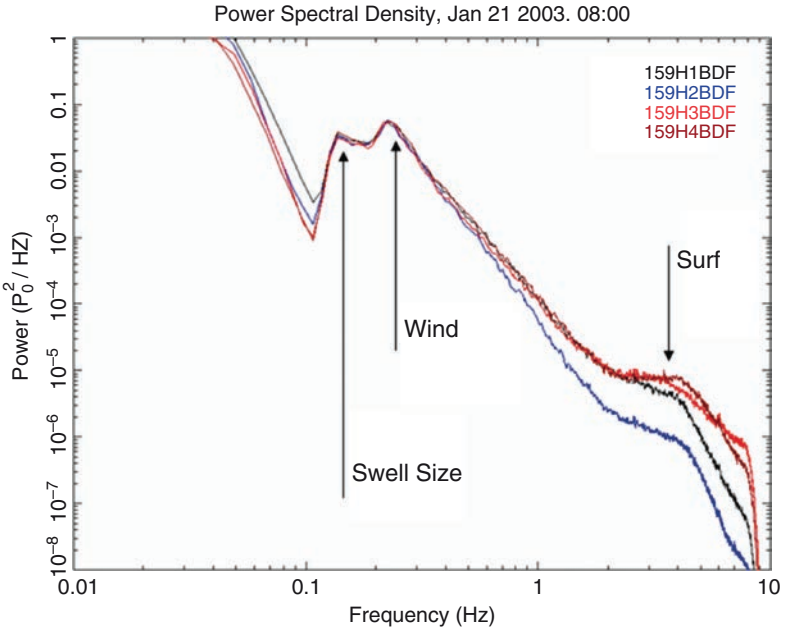

Fig. 7.1 Power spectral density at I59US, Hawaii, showing the frequency partitioning of the persistent ocean infrasound spectrum. The typical microbarom spectrum resides near 0.2 Hz, but occasionally may split and produce multiple peaks. The frequency-dependent microbarom arrival angles derived from array processing suggest that multiple peaks may be attributed to different coexisting storm systems. The lower frequencies correspond to long-period ocean waves radiated by powerful storms, and this energy may arrive to a station through thermospheric ducting. The 0.2 Hz peak may be attributed to stratospheric ducting, which is determined by the global seasonal wind patterns. Above 1 Hz, the ambient noise field is affected by ocean waves breaking by the shoreline [Garces et al. 2003; Le Pichon et al, 2004]

develop a mathematical theory for the excitation of microseisms by ocean waves. Studies by Saxer (1945; 1954), Daniels (1952; 1962), Donn and Posmentier (1967), Donn and Naini (1973) and Rind (1980) suggest that microbaroms and microseisms share a similar source that is related to strong storms over the ocean and the resulting high seas. In addition to major weather systems (cold fronts and high- and low-pressure areas) and significant wave heights, Rind (1980) compared expected source locations of microbaroms and microseisms recorded at Palisades, New York, with dominant wave period and mean propagation charts on a 5° grid provided by the Navy Fleet Numerical Weather Center. Since microbaroms theoretically contain frequencies twice those of the producing ocean waves, Rind attempted to correlate the period of the observed microbaroms with ocean-wave half periods in the expected source regions. Mean propagation charts were used to correlate the expected source regions with areas that contained opposing wave trains. The methods of Rind (1980) were not effective in the case studies presented in this chapter. It should be mentioned that Rind discussed the error potential in correlating microbaroms with mean wave parameters (i.e., significant wave height, dominant period, and propagation directions) on such a coarse grid instead of using an entire spectrum of waves. Substantial advancements have been made in ocean-wave modeling since 1980, which has made contemporary microbarom studies potentially more useful to the monitoring of marine weather and ocean waves.

Microbaroms, like microseisms, are believed to originate from the nonlinear interactions of ocean waves traveling in nearly opposite directions with similar frequencies (e.g., Waxler and Gilbert 2006; Arendt and Fritts 2000; Ponomaryov et al. 1998; Posmentier 1967; Hasselmann 1963). Posmentier (1967) presented a theory that explained the source generation of microbaroms based on the Longuet-Higgins (1950) approach that described the generation of microseisms. Posmentier's theory described a nonlinear pressure perturbation that arises at the air–sea interface when two ocean waves of opposite direction and similar frequencies meet. The corresponding acoustic wave was shown to gain properties of the interfering ocean-wave train where acoustic amplitude is proportional to the product of the opposing ocean waves and frequency is twice that of the individual ocean waves. Waxler and Gilbert (2006) and Arendt and Fritts (2000) extended this theory to an arbitrary spectrum of ocean surface waves. They found that the frequency-doubling nonlinear interactions of pairs of ocean waves traveling in nearly opposite directions produce propagating acoustic waves with a near isotropic radiation pattern. All terrestrial ocean surface waves contain phase speeds and wavelengths much smaller than acoustic phase speeds and wavelengths. Thus, single ocean waves cannot couple sound into the atmosphere. However, sound can be coupled into the atmosphere when ocean waves interact nonlinearly and the sum of the horizontal wave numbers of the ocean surface waves is nearly zero. This occurs only when an ocean-wave spectrum contains components of nearly identical frequencies traveling in nearly opposite directions. Ocean waves propagating with identical frequencies in opposite directions are predicted to radiate sound vertically, leading to efficient ensonification into the ocean and seabed, but ensuring that atmospheric sound never reaches the ground again. Thus, microseisms propagate through the ground as a result of vertical excitation through

the ocean, whereas microbaroms propagate to infrasonic stations after near horizontal radiation from the ocean surface to the atmosphere (Tabulevich 1995).

7.3 Observations

Willis et al. (2004a, b) describe why strong microbarom signals often appear to come from regions of marine storms, but are actually more likely coming from storm-wake regions (Fig. 7.2). This is due to the observation that ocean-wave spectra often become confused upstream of the storm propagation direction, with opposing swell components created ahead of and behind a surface low. Willis et al. (2004a, b) show that the scenario of opposing wave trains interacting with similar frequencies (the prerequisites to microbarom generation) may also occur at large distances from marine storms. The results presented in Garcés et al. (2004) and Willis et al. (2004a, b) show that the detection of microbarom signals by an infrasound array will be dependent on (1) amplitude and frequency of opposing wave trains (which is a byproduct of marine weather), (2) proximity of high-acoustic source regions to array site, (3) mesospheric, stratospheric, and tropospheric winds, (4) thermospheric refraction, and (5) topographic shadowing (Fig. 7.3). The coherence of microbarom wave trains has also been studied to help identify multiple sources or propagation paths (Olson and Szuberla 2005).

Microbaroms have been proposed to recover the characteristics of high-altitude winds (Donn and Rind 1973; Rind and Donn 1975). Donn and Rind (1971) and Rind (1978) related microbarom amplitude variability to solar tide fluctuations in the thermosphere during winter, and stratospheric wind strength during summer. These studies concentrated on the results from an infrasound station in the Eastern United States that was primarily exposed to microbaroms arriving from the North Atlantic. The storm sources considered were between hundreds and one thousand kilometers away. In a more recent study by Le Pichon et al. (2006), microbaroms are used as a natural source for continuous measurements of high-altitude winds over propagation ranges that exceed several thousands of kilometers. In boreal and austral stations, the arrival directions of microbaroms signals reverse from summer to winter and are anticorrelated from the northern to southern hemispheres (Fig. 7.4). A 3D paraxial ray-tracing modeling (Dessa et al. 2005) coupled with high-resolution atmospheric specifications (Drob et al. 2003) was used to explain seasonal trends in the observations. Le Pichon et al. (2006) conclude that the dominant cyclical variations of microbarom azimuths result from the zonal winds reversal in the 35–50 km range and find a clear correlation between the observed signal amplitude and the stratospheric

Fig. 7.2 (continued) but opposite directions. Amplitude will decay, but frequency and direction will remain constant. Swell trains of nearly identical frequencies and in nearly equal but opposite direction meet at point A during Time 3. This scenario supports efficient generation of infrasound in the 0.1–0.5 Hz band. Regardless of the amplitudes of the interfering wave trains, acoustic radiation will still occur

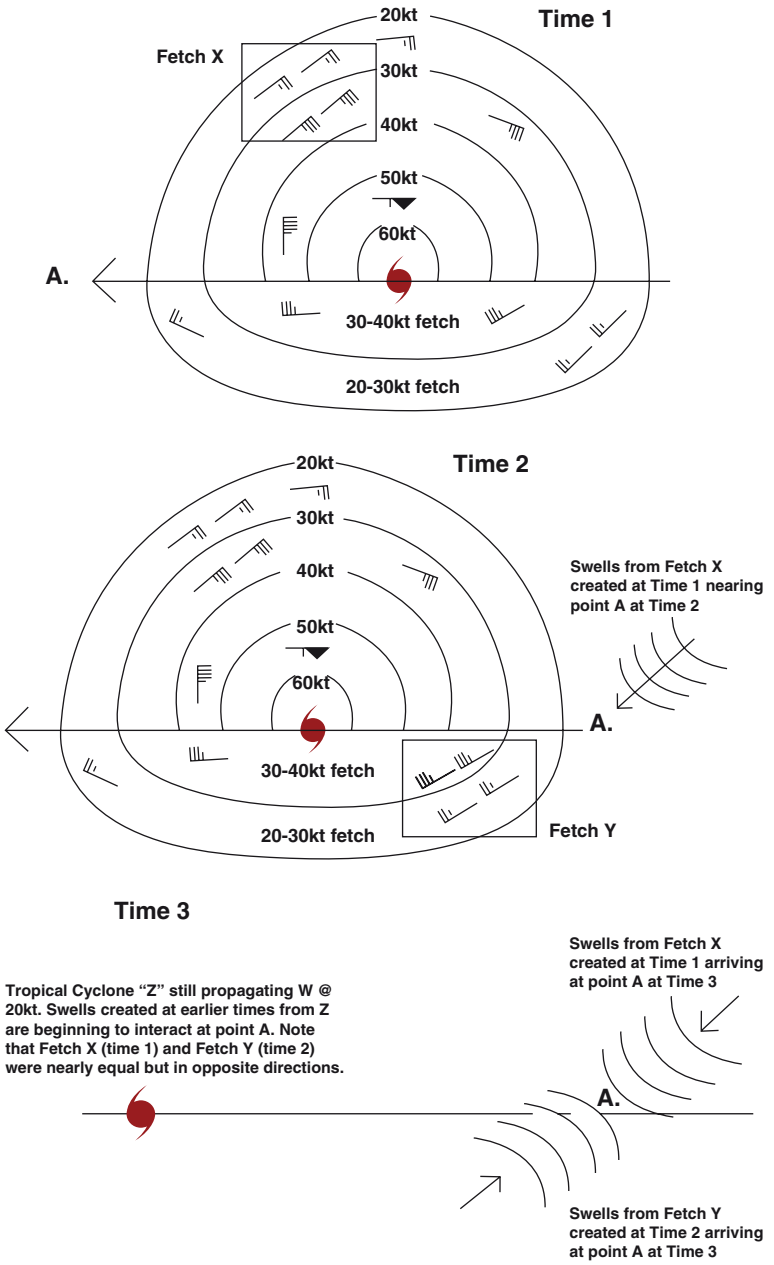

Fig. 7.2 Simplified, idealized flow around tropical cyclone (or mid-latitude low) "Z" moving west at 20 kt in northern hemisphere. In the top figure (Time 1), notice that Fetch X is pointed in the direction of point A. In the bottom figure, Fetch Y is pointed in the direction of point A as well, but a different Time 2. Note that Fetch X and Y are nearly identical in magnitude and fetch length and also pointed in nearly opposite directions. Therefore, the ocean waves these two fetches create will contain nearly identical amplitudes and frequencies and will propagate in nearly equal

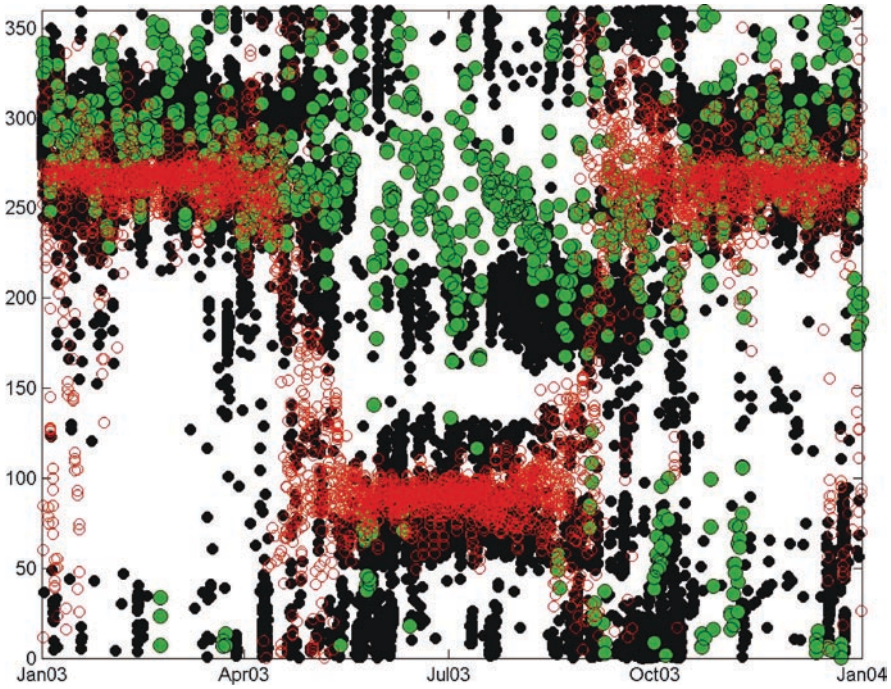

Fig. 7.3 Coherent microbarom (*black circles*) and wind (*green* and *red*) arrival azimuths, clockwise from North, at the Hawaii array for 2003. The transparent circles with the *red rim* represent the winds between 50 and 70 km and the green circles represent the winds between 10 and 20 km evaluated at 18UT. The dominant wind directions match the seasonal variability for some of the arrivals, except for the arrivals from the Southern hemisphere during the Austral winter. These S swells are large, consistent, and powerful, and may overwhelm the 10-s-period swell energy (Figure from Garces et al., 2004)

wind speed (Le Pichon et al. 2010). These results suggest that microbaroms may be used for continuous acoustic remote sensing of the seasonal and short-time scale variability of the state of the atmosphere.

7.4 General Approach

By integrating the NOAA Wavewatch 3 (WW3) model (Tolman 1999; 2002) with recent acoustic source formulations for microbaroms (e.g., Waxler and Gilbert 2006), we demonstrate how we can provide global estimates of microbarom source regions. Such source modeling results would show the relationship between microbarom generation regions with marine storms and high-amplitude standing wave locations. In this section, comparisons between the observed arrivals and modeled microbarom sources will be used together to help present a conceptual model of microbarom generation for a case study in the Pacific.

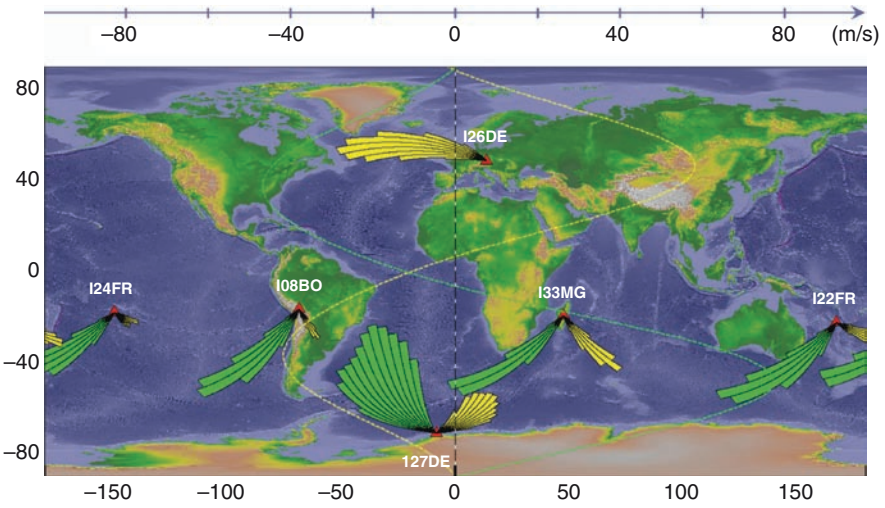

Fig. 7.4 Seasonal variations in the arrival azimuths of microbaroms for several mid- and high-latitude IMS stations in 2003 (figure adapted from Le Pichon et al. 2006). The azimuthal distributions are plotted for each station in Austral winter (*green bars*) and Austral summer (*yellow bars*). The strength of the zonal wind Horizontal Wind Model (HWM-93) is averaged in longitude (180°W–180°E) and in altitude (35–40 km) for the winter and summer seasons (*green* and *yellow curves* respectively, according the scale on the top of the figure). This model provides time-dependent estimates of winds and accounts for the major seasonal variations, daily solar tidal variability, and geomagnetic and solar forcing effects in the mesosphere and lower thermosphere (Hedin et al. 1996). For all stations, the dominant wind directions match the seasonal variability of microbarom detections (Le Pichon et al., 2006).

The Progressive Multi-Channel Correlation (PMCC) algorithm of Cansi (1997) is the signal-detection algorithm we used to process the IMS array data (Brachet et al. 2010). PMCC is used to detect coherent infrasonic energy across the array, which allows the speed, arrival azimuth, and amplitude of the detected arrivals to be extracted. Microbarom arrival azimuth is the main parameter we used to compare with storm and ocean-wave characteristics as well as source modeling results. The arrival azimuth of an infrasound signal is obtained by determining time shifts that yield the highest cross-correlation between waveforms of the array elements and calculating the azimuth from which the waves would have to be arriving in order to achieve those time shifts. Multiple ground truth experiments have confirmed the stability and utility of arrival azimuths for infrasound source location (Garcés et al. 2002). Signals with low PMCC consistency, as well as a steady azimuth and trace velocity, are referred to as coherent arrivals. Infrasonic power spectral densities are used to distinguish peaks within the microbarom passband (normally 0.1 to 0.5 Hz). Power spectra include the combination of both coherent and noncoherent infrasonic signals at each frequency. A more detailed description of the IS59 array, PMCC, and the computation of infrasonic power spectral densities is provided in Willis et al. (2004a, b).

The WW3 ocean-wave model (v1.18) in this study is driven by NOGAPS 10 m surface winds and includes global ice-concentration values. WW3 is used to produce realistic ocean-wave spectra values on a global 1° grid. The wind and ice input files are provided by the Master Environmental Library Homepage (MEL) at http://mel.dmso.mil/. For case studies in large ocean basins (such as the Pacific), WW3 should be initialized at least 6 days ahead of chosen events to produce an accurate background ocean-wave field.

WW3 outputs wave energy densities in 24 directional and 25 frequency bins to produce 600 values at each grid point (Fig. 7.5). These wave spectra are then used to calculate a microbarom source strength spectrum by summing the products of directly opposing wave trains at each frequency. In other words, we used WW3 to evaluate the standing wave field, which has theoretically been shown to be the precursor to microbarom generation. A concise definition of the microbarom source strength spectrum is used in this chapter. WW3 also outputs significant wave height, peak frequency, and dominant ocean-wave propagation directions (wave height shown in Fig. 7.6). These mean parameters are calculated from the wave energy density values in the wave spectrum at each grid point, but do not contain any information about standing waves. Therefore, mean and dominant wave parameters are not useful in suggesting source regions of microbaroms.

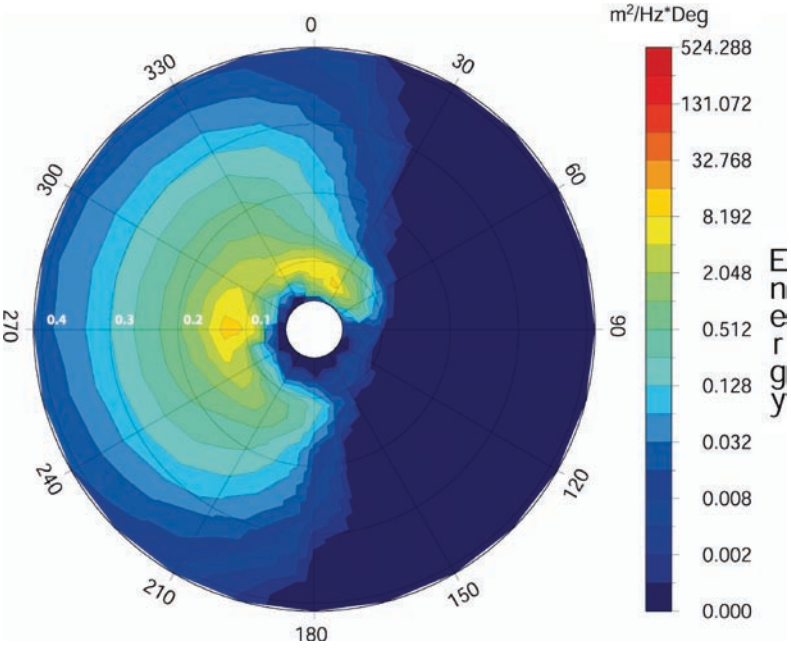

Fig. 7.5 Frequency, directional ocean-wave spectrum for a grid point (38.00 N, 170.00 W) at 18Z on January 4, 2003, in the wake region of the strong marine storm. Frequency (Hz) decreases towards the center, wave energy scale (m²/Hz*Deg) on the right hand side

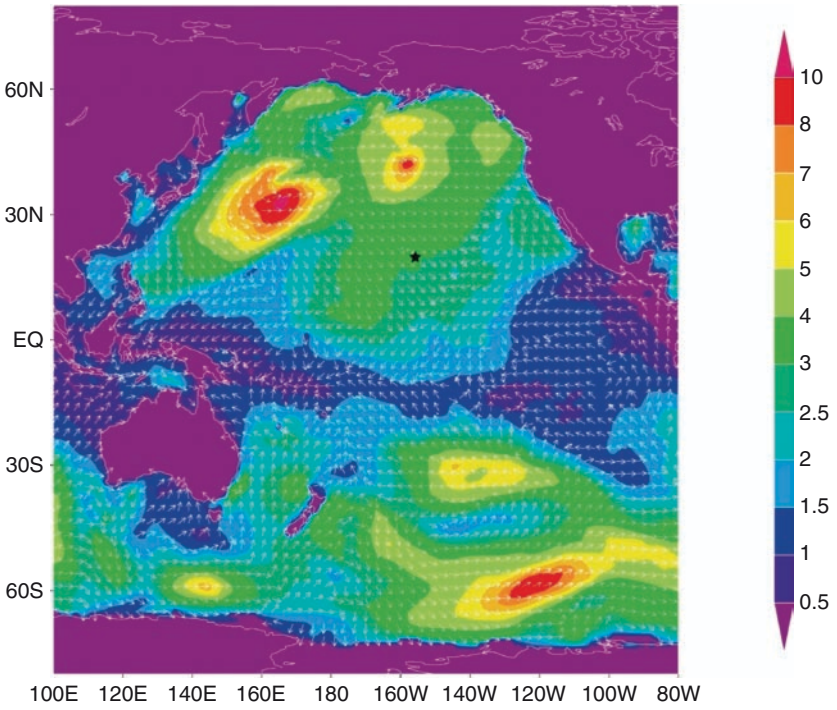

Fig. 7.6 WW3 Significant wave heights (m, *shaded*) and mean-propagation direction vectors (towards) for February 22, 2003. 00Z. *Black star* represents location of I59US array

We concentrated on the case study from February 22, 2003, when the North Pacific was very active with storm and high wave activity. Surface pressure charts were generated using data supplied by the NCEP/NCAR Reanalysis project available in 6 hourly intervals at a resolution of 2.5° (web site at www.cdc.noaa.gov/). The NCEP/NCAR data set provides a good opportunity to examine the synoptic-scale evolution of storm systems. Surface weather and wave charts are compared with microbarom observations and source modeling results to distinguish a relationship between infrasonic source locations and marine storm tracks.

The Wavewatch 3 model outputs the variance density, F, of the surface wave field as a function of frequency, f, and propagation direction, θ, at each grid point of the model (Fig. 7.5). The variance density can be integrated over angle and frequency to provide the total wave energy E

$$E = \int_0^{2\pi} \mathrm{d}\theta \int_0^{\infty} \mathrm{d}f \, F(f,\theta). \tag{7.1}$$

The significant wave height (Fig. 7.6) is defined as

$$H_s = 4\sqrt{E}. \tag{7.2}$$

Thus, the variance density has units of m²/(rad*Hz), and it is a measure of the energy in the surface wave field. The phase of each ocean-wave component is assumed to be random.

Hasselmann (1963) and Waxler and Gilbert (2006) derive a relationship between the microbarom and microseism power spectra and the energy variance of ocean surface waves of the form

$$\left\langle \left| P_{\mathrm{k}}(f_{\mathrm{m}}) \right|^2 \right\rangle \propto \int_0^{2\pi} F\left(\frac{f_{\mathrm{m}}}{2}, \theta \right) F\left(\frac{f_{\mathrm{m}}}{2}, \theta + \pi \right) \mathrm{d}\theta, \tag{7.3}$$

where f_{m} is the microbarom or microseism frequency. Hetzer et al. (2010) describe in greater detail why the microbarom frequency is twice the surface wave frequency, and draw on the work of Waxler and Gilbert (2006) to provide an expression for the microbarom source strength spectrum S, of the form:

$$S(f_{\mathrm{m}}) = \frac{4g\pi^4 \rho_{\mathrm{a}}^2 f_{\mathrm{m}}^3}{c_{\mathrm{a}}^2} \left(\frac{c_{\mathrm{a}}^2}{c_{\mathrm{w}}^2} + \frac{9g^2}{4\pi^2 c_{\mathrm{a}}^2 f_{\mathrm{m}}^2} \right) \int_0^{2\pi} F\left(\frac{f_{\mathrm{m}}}{2}, \theta \right) F\left(\frac{f_{\mathrm{m}}}{2}, \theta + \pi \right) \mathrm{d}\theta, \tag{4.4}$$

where g is the gravitational acceleration (9.8 m/s²), ρ_{a} and ρ_{w} are the air and water densities (approximately 1 and 1,000 kg/m³, respectively), and c_{a} and c_{w} are the air and water sound speeds (approximately 340 and 1,500 m/s, respectively). These equations allow the evaluation of the microbarom source strength from the directional variance density output of ocean surface wave models.

On February 22, 2003, low-frequency energy below 0.6 Hz that originated from a region in the North Pacific was recorded on eight different infrasound stations throughout the Northern Hemisphere and lasted for several hours. This exceptional microbarom burst was much stronger than normal microbarom events (Bhattacharyya et al. 2003) and thus was recorded by eight infrasound arrays: IS10, Canada, IS34, Mongolia, IS53, Alaska, IS56, Washington, IS57, California, IS59, Hawaii, PDIAR, Wyoming, and NVIAR, Nevada. Near the peak of this infrasound event at 00 GMT on the 22nd, three surface low-pressure systems were evident in the North Pacific. The first was an intense cyclone just east of Japan, centered near 40N, 168E with a minimum central pressure below 960 mb. A second, moderately strong and symmetrical surface low (988 mb) was located near 45N, 155W, while a third but much weaker closed low was centered just north of the western Aleutian Islands near 55N, 172W (Willis 2004). The first two cyclones were propagating towards the ENE, whereas the third was moving slowly and erratically.

We used the WW3 output in conjunction with the microbarom source equations to evaluate the expected acoustic source intensity on the ocean surface for the 22 February event. The microbarom back azimuths (Fig. 7.7) extended along great circle routes from 7 of the 8 infrasonic arrays during the peak of this event intersect in a confined region between 25–32N and 168–170W, which is not a region where a surface low or peak in significant wave height is noted. The great circle routes shown in Fig. 7.7 were not corrected for the azimuth errors induced by the wind

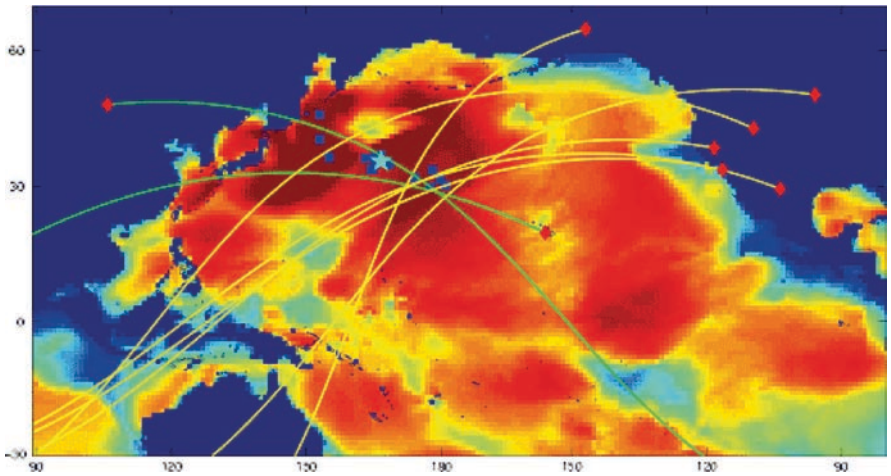

Fig. 7.7 Normalized magnitude of the microbarom source strength spectrum evaluated at a frequency of 0.197 Hz, corresponding to ocean waves interacting with periods of approximately 10 s. *Red shading* represents high acoustic source intensity values whereas *blue shading* represents low intensity values. Great circle paths overlaid correspond to the measured microbarom azimuths at 8 IMS infrasound station. Red diamonds represent infrasound array locations, *blue squares* are infrasound locations derived from travel times and azimuths. The color dynamic range represents 18 dB in intensity

component transverse to the propagation direction. However, by introducing travel times and backazimuth corrections, the inverted infrasonic source locations match well with the predicted high microbarom intensity regions, reinforcing the theoretical and observational concepts presented herein.

7.5 Concluding Remarks

Theory and observations suggest that microbarom source regions occur in locations that contain opposing wave trains instead of from regions of marine storminess. Microbarom source regions are very common and can occur nearly anywhere in the ocean at any given time. All source regions may produce coherent or noncoherent arrivals at an array site, but infrasound stations will generally detect coherent microbarom arrivals from the closest and strongest source whose propagation path is favored by the atmospheric conditions.

Microbarom arrival azimuths and amplitudes exhibit clear seasonal trends mainly driven by the reversal of the zonal stratospheric wind with season (Le Pichon et al. 2006). However, this does not exclude thermospheric arrivals from powerful long-period swells (Garcés et al. 2004) or diffracted arrivals (Godin and Naugolnykh 2005). The continuous microbarom measurements can help refine

evaluations of the global infrasound detection capabilities and also provide new insights to understand and quantify the relationship between infrasonic observables and atmospheric specification problems (Drob et al. 2010).

The following conclusions may be drawn from a careful comparison of microbarom observations with simulated acoustic source pressures derived from the output of the Wavewatch III model (Willis 2004):

1. Case studies show that observed microbarom arrival azimuths coincide well with strong infrasonic source regions predicted by the WW3 model, suggesting that the theoretical basis for the open ocean generation of microbaroms is substantially correct. Mean wave parameters such as significant wave height, peak period, and mean propagation direction are not effective in determining microbarom source regions. Conversely, WW3 is only able to produce an accurate depiction of microbarom source regions generated by open ocean-wave interactions when the entire spectrum is used.
2. Microbaroms are generated wherever ocean surface wave trains with opposite propagation directions and similar frequencies interact. The strongest microbaroms are often generated in the wake regions of marine storms, where the amplitude of the opposing wave trains is greatest. In the case studies considered, propagating surface lows exhibit a modeled wake-region peak in source pressure. However, high-amplitude opposing wave trains can occur almost anywhere in the winter hemisphere where multiple mid-latitude storms may be evident. Thus, high acoustic source pressure regions are often prevalent at a distance from the wave-producing winds.
3. Opposing wave trains and thus microbarom source regions are very common and can occur nearly anywhere in the ocean at any given time. All source regions may produce coherent or noncoherent arrivals at an array site, but the strongest and most coherent signals will be determined by (a) amplitude and frequency of opposing wave trains, (b) proximity of high-acoustic source regions to array site, (c) mesospheric, stratospheric, and tropospheric winds, (d) thermospheric refraction, and (e) topographic shadowing.
4. Infrasound stations receive coherent arrivals from the closest and strongest source whose propagation path is favored by the atmospheric conditions; therefore, weaker signals will be masked, including those generated in wake of distant or weaker storms.

Acknowledgments This work was funded in part by Defense Threat Reduction Agency contracts DTRA01-00-C-0106 and DTRA01-01-C-0077. We express our gratitude to H. Tolman for his guidance on the use of WW3. Many thanks to S. Businger, P. Wittmann, and J. Bhattacharyya for their contributions, and to S. Collins and Surfline, Inc., for their encouragement during this research.

References

Arendt S, Fritts D (2000) Acoustic radiation by ocean surface waves. J Fluid Mech 415:1–21
Bedard A, Georges TM (2000) Atmospheric infrasound. Phys Today 53:32–37

Bhattacharyya J, Hetzer C, Garcés M, Oancea V (2003) Description and analysis of infrasound signals recorded from the North Pacific event of 22 February 2003, presented at the Infrasound Technology Workshop, La Jolla, California, October 27-–30.
Benioff H, Gutenberg B (1939) Waves and currents recorded by electromagnetic barographs. Bull Am Met Soc 20:421
Bowman JR, Baker GE, Bahavar M (2005) Ambient infrasound noise. Geophys Res Lett 32:L09803
Brachet N, Brown D, Le Bras R, Mialle P, Coyne J (2010) Monitoring the earth's atmosphere with the global IMS infrasound network. This volume, pp. 73–114
Brekhovskikh IM, Goncharov VV, Kurtepov VM, Naugolnykh KA (1973) The radiation of infrasound into the atmosphere by surface waves in the ocean. Atmos Oceanic Phys 9:899–907
Cansi Y (1995) An automatic seismic event processing for detection and location: the P.M.C.C. method. Geophys Res Lett 22:1021–1024
Cansi Y, Klinger Y (1997) An automated data processing method for mini-arrays. Newslett Eur-Mediterranean Seismol Center 11:2–4
Daniels FB (1952) Acoustical energy generated by the ocean waves. J Acoust Soc Am 24:83
Daniels FB (1962) Generation of infrasound by ocean waves. J Acoust Soc Am 34:352–353
Dessa JX, Virieux J, Lambotte S (2005) Infrasound modeling in a spherical heterogeneous atmosphere. Geophys Res Lett 32:L12808.1–L12808.5, doi:10.1029/2005GL022867
Drob DP, Meier RR, Picone JM, Garcés MM (2010) Inversion of infrasound signals for passive atmospheric remote sensing. This volume, pp. 695–726
Donn WL, Posmentier ES (1967) Infrasonic waves from the marine storm of April 7, 1966. J Geophys Res 72:2053–2061
Donn WL, Naini B (1973) Sea wave origin of microbaroms and microseisms. J Geophys Res 78:4482–4488
Donn WL, Rind D (1971) Natural infrasound as an atmospheric probe. Geophys J R Astr Soc 26:111–133
Donn WL, Rind D (1973) Microbaroms and the temperature and wind of the upper atmosphere. J Atmos Sci 29:156–172
Drob D, Picone JM, Garcés MA (2003) The global morphology of infrasound propagation. J Geophys Res 108:ACL13.1–ACL13.12, doi:10.1029/2002JD003307.
Garcés M, Hetzer C, Drob D, Woodward R, Bass H, McCormack D, Evers L, Hedlin M, Le Pichon A, Liszka L, Wilson C, Whitaker R (2002) Progress in the development of a ground truth database of infrasonic events. Infrasound Technology Workshop, De Bilt, Netherlands, October 28–31
Garcés M, Willis M, Hetzer C, Le Pichon A, Drob D (2004) On using ocean swells for continuous infrasonic measurements of winds and temperature in the lower, middle, and upper atmosphere. Geophys Res Lett 31:L19304.1–L19304.4, doi:10.1029/2004GRL020696
Godin OA, Naugolnykh KA (2005) Guided propagation of naturally occurring infrasound in the troposphere and stratosphere. Geophys Res Lett 32:L23824. doi:10.1029/2005GL024585
Hasselmann K (1963) A statistical analysis of the generation of microbaroms. Rev Geophys 1:177–210
Hedin AE, Fleming EL, Manson AH, Schmidlin FJ, Avery SK, Clark RR, Franke SJ, Fraser GJ, Tsuda T, Vial F, Vincent RA (1996) Empirical wind model for the upper, middle and lower atmosphere. J Atmos Terr Phys 58:1421–1447
Hedlin M, Garcés M, Bass H, Hayward C, Herrin G, Olson J, Wilson C (2002) Listening to the secret sounds of earth's atmosphere. EOS 83:564–565
Hetzer CH, Gilbert KE, Waxler R, Talmadge CL (2010) Generation of microbaroms by deep-ocean hurricanes. This volume, pp. 245–258
Kibblewhite A, Wu CY (1996) Wave interactions as a seismo-acoustic source. Lecture Notes in Earth Sciences. Springer, Berlin
Le Pichon A, Ceranna L, Garcés M, Drob D, Millet C (2006) On using infrasound from interacting ocean swells for global continuous measurements of winds and temperature in the stratosphere. J Geophys Res 111:D11106. doi:10.1029/2005JD006690

Le Pichon A, Vergoz J, Cansi Y, Ceranna L, Drob D (2010) Contribution of infrasound monitoring for atmospheric remote sensing. This volume, pp. 623–640
Le Pichon A, Maurer V, Raymond D, Hyvernaud O (2004) Infrasound from ocean waves observed in Tahiti. Geophys. Res. Lett. 31:L19103.1–L19103.4. doi:10.1029/2004GL020676
Longuet-Higgins MS (1950) A theory of the origin of microseisms. Phil Trans R Soc Lond 243:1–35
Olson JV, Szuberla C (2005) Distribution of wave packet sizes in microbarom wave trains observed in Alaska. J Acoust Soc Am 117:1032–1037
Ponomaryov EA, Sorokin AG, Tabulevich VN (1998) Microseisms and infrasound: a kind of remote sensing. Phys Earth Planet Inter 108:339–346
Posmentier E (1967) A theory of microbaroms. Geophys J R Astron Soc 13:487–501
Rind D, Donn WL (1975) Further use of natural infrasound as a continuous monitor of the upper atmosphere. J Atmos Sci 32:1694–1704
Rind D (1980) Microseisms at palisades 3. Microseisms and microbaroms. J Geophys Res 85:4854–4862
Rind D (1978) Investigation of the lower thermosphere results of ten years of continuous observations with natural infrasound. J Atmos Terr Phys 40:1199–1209
Saxer L (1945) Electrische Messung kleiner atmospharischer Druckshwankungen. Helv Phys Acta 18:527
Saxer L (1954) Über Entstehung und Ausbreitung quasiperiodischer Luftdruckschwankungen. Arch Meteorol Geophys Bioklum A6:451–457
Sulejkin WW (1935) On the voice of the sea. Dokl Acad Sci USSR 3:259–262
Stevens J, Divnov I, Adams D, Murphy J, Bourchik V (2002) Constraints on infrasound scaling and attenuation relations from Soviet explosion data. Pure Appl Geophys 159:1045–1062
Tabulevich V (1995) On recordings of global microseismic vibrations and observations of microseisms in shore zones of oceans. Phys Earth Planet Inter 91:299–305
Tolman HL (1999) User manual and system documentation of WAVEWATCH-III version 1.19. NOAA/NWS/NCEP/OMB Technical Note Nr. 166, 110 pp
Tolman HL (2002) Validation of WAVEWATCH III version 1.15 for a global domain. NOAA/NWS/NCEP/OMB Technical Note Nr. 213, 33 pp
Waxler R, Gilbert K (2006) The radiation of atmospheric microbaroms by ocean waves. J Acoust Soc Am 119:5
Webb SC (1992) The equilibrium oceanic microseism spectrum. J Acoust Soc Am 92:2141–2158
Webb SC, Cox CS (1986) Observations and modeling of seafloor microseisms. J Geophys Res 91:7343–7358
Willis M (2004) Observations and source modeling of microbaroms in the Pacific. MS thesis, Department of Meteorology, University of Hawaii at Manoa, 77 pp
Willis M, Garcés M, Hetzer C, Businger S (2004a) Infrasonic observations of open ocean swells in the Pacific: deciphering the song of the sea. Geophys Res Lett 31:L19303.1–L19303.4. doi:10.1029/2004GL020684
Willis M, Garcés M, Hetzer C, Businger S (2004) Source modeling of microbaroms in the Pacific preprints, 84th AMS annual meeting. Eighth symposium on integrated observing and assimilation systems for atmosphere, oceans, and land surface (IAOS-AOLS), Seattle, WA, Amer. Meteor. Soc., P2.5

Chapter 8
Generation of Microbaroms by Deep-Ocean Hurricanes

Claus H. Hetzer, Kenneth E. Gilbert, Roger Waxler, and Carrick L. Talmadge

8.1 Introduction

Microbaroms are infrasonic atmospheric pressure waves with a dominant frequency of about 0.2 Hz, first identified by Benioff, Gutenberg (Benioff and Gutenberg 1939; Gutenberg and Benioff 1941), and Baird (1940). Their resemblance to microseisms, a continuous seismic signal at the same frequency, was noted immediately and provided their name. A mechanism for their generation via a nonlinear interaction of opposing ocean surface waves was discovered by Longuet-Higgins (1950) and confirmed by Hasselmann (1963). This theory was then extended into the atmosphere by Brekhovskikh et al. (1973) and Waxler and Gilbert (2006) and is summarized below in Sect. 8.3.2. Microbaroms are observed worldwide (Bowman et al. 2005; Garcés et al. 2010; Hetzer et al. 2010).

The association of microseisms (and, by extension, microbaroms) with severe weather has been known for a century or more (Banerji 1930; Klotz 1910); Klotz (1910) even noted that barographic lows will generate microseisms while over water but not while over land. Some of the first comprehensive studies associating storms and microseisms were carried out by Donn and others starting in the late 1940s (Donn 1951, 1952), demonstrating a clear link between severe weather and microseism "storms." Subsequent work by those and other researchers identified a relationship between water depth below a storm and the microseism period (De Bremaecker 1965; Donn 1954), and that microbaroms and microseisms share a common generation mechanism (Donn and Pasmentier 1967; Donn and Naini 1973) and often a common source (Rind 1980).

Strong microbarom signals are often observed on infrasound arrays when there is a hurricane or other large ocean storm within 500–1,000 km. A common, but puzzling, observation is that microbarom source bearings identified at infrasound arrays rarely point to the center of the storm where the waves are the largest

C.H. Hetzer (✉)
National Center for Physical Acoustics, The University of Mississippi,
1 Coliseum Drive, MS, 38677, USA
e-mail: claus@olemiss.edu

A. Le Pichon et al. (eds.), *Infrasound Monitoring for Atmospheric Studies,*
DOI 10.1007/978-1-4020-9508-5_8, © Springer Science+Business Media B.V. 2010

(Cessaro 1994; Hetzer et al. 2008; Tabulevich 1992; Willis et al. 2004). In this article, we outline the physical mechanism that produces microbaroms and present a hypothesis for why infrasound array bearings do not point toward the hurricane eye. It is hypothesized that microbarom generation results from the interaction of storm-generated waves with the ambient wave field. Observations and wave-action models from Typhoon Usagi (2007) are presented which strongly support this hypothesis.

8.2 Hurricane Monitoring and Modeling

Although much theoretical work was done in the nineteenth and early twentieth centuries, starting with the work of James Pollard Espy in 1841, direct reconnaissance of the interior of a hurricane was not possible until July 27, 1943 when Joseph Duckworth, an American Army Air Corps pilot, became the first to fly an airplane into the eye of a hurricane (Emanuel 2003). Since then a number of technological advances have allowed direct observation, especially improved reconnaissance aircraft, land-based radar, and weather satellites. However, each of these techniques has its limitations, whether it be the temporally discontinuous nature of airplane and satellite observation or the line-of-sight requirement for radar, and all pose considerable expense to any government wishing to implement them.

Similarly, hurricane forecast models have made significant advances, particularly in improving the quality of track predictions. Although statistical prediction models were in use since 1924, routine quantitative track forecasts were first issued in 1954, made possible by the improvements in storm positioning gained from aircraft reconnaissance. Improvements in computer processing power enabled the inclusion of numerical weather-prediction models. Prediction models started as adaptations of the simple barotropic weather models, which consider only horizontal winds and require constant-pressure surfaces to have constant temperatures. The first baroclinic prediction model, wherein wind shear is considered and pressure surfaces can have temperature gradients, was introduced in 1976. Both types of models continue to be run operationally and yield results of comparable accuracy. Currently, the statistical models are, as a group, the least accurate, with barotropic models improving slightly upon them and baroclinic models in turn improving slightly upon the barotropic. Both types of deterministic models forecast tracks accurately within 150 km at 24 h, 280 km at 48 h, and 550 km at 72 h (DeMaria and Gross 2003). Errors at all three timescales have decreased significantly since their introduction, though an idealized experiment with a baroclinic model suggests that the 24-h forecast errors in particular may be converging toward their best-case limits (Leslie et al. 1998). Further improvements may require additional statistical treatments of multiple forecasts with slightly-varying initial conditions (Willoughby 2003).

Intensity forecasting, on the other hand, has been extensively used only since 1988. The best performance in terms of minimum absolute error comes from the

SHIPS model, which uses statistical methods combined with numerical forecast models, and accounts for the effects of land. However, since their introduction, the accuracy of intensity forecasts has only marginally improved, and the 24-h forecast was actually worse in 2000 than it was in 1992–1997 (DeMaria and Gross 2003). Among the shortcomings of the models is an inability to predict rapid intensification, which has been observed in some of the most destructive hurricanes to make landfall in the United States, including Hurricane Katrina (Law and Hobgood 2007).

Infrasound technology has a number of advantages relative to the primary hurricane observation and monitoring technologies. In contrast to the periodic sampling characteristic of airplane and satellite reconnaissance, infrasound records continuously at sampling rates low enough to allow continuous real-time datastreams to be feasible without onerous bandwidth requirements. Infrasound also does not require line-of-sight due to its propagation characteristics, and the equipment required for infrasound monitoring is inexpensive in comparison to radar installations, aircraft and especially satellites, enabling its use in places where extensive radar, airplane, or satellite coverage are not feasible. In addition, to the extent that microbarom signal levels may be related to hurricane intensity, infrasound technology may be able to detect intensity changes in near real time. However, these advantages must be weighed against infrasound's inherent drawbacks. Signals of interest can often be drowned by local noise from wind and turbulence or overwhelmed by nearer, louder sources. Because upwind propagation can increase attenuation significantly, seasonal changes in stratospheric winds have a great deal of control on whether or not infrasound signals are detected (Garcés et al. 2004). One must also address the fact that it is not necessarily the hurricane itself that is being observed; thus, it is vital that the specific sound-generation mechanism be identified so that the acoustic signals can be correctly interpreted and modeled. Since the primary acoustic signal received appears to be a microbarom, first it is necessary to more generally discuss the production of microbaroms.

8.3 Atmospheric Pressure Waves Produced by Ocean Waves

In this section, we will discuss the mechanism for the production of atmospheric pressure waves, specifically microbaroms, by ocean surface waves. We should note that we will not be discussing infrasound from breaking ocean waves, as such signals are generated in a completely different way and occupy a completely separate frequency band (Garcés et al. 2003).

8.3.1 The Ocean Wave Frequency Spectrum

Ocean waves are a continuous superposition of waves of different periods and amplitudes. Generally, the greater the significant wave height, the more long-period waves are present (Goda 2003). The distribution of the wave composition over

frequency (1/period) is expressed as $\bar{F}(f)$ and called the ocean wave "frequency spectrum" and for a fully-developed sea state can be modeled as the Pierson-Moskowitz spectrum (Pierson and Moskowitz 1964),

$$\bar{F}(\omega) = \frac{\alpha g^2}{\omega^5} \exp\left[-\beta \left(\frac{g}{U_{19.5}\omega} \right)^4 \right], \tag{8.1}$$

where $\alpha = 8.1 \times 10^{-3}$ and $\beta = 0.74$ are dimensionless parameters, and $U_{19.5}$ is the wind speed at a height of 19.5 m above the ocean surface. Examples of Pierson–Moskowitz frequency spectra for ocean waves for several wind speeds are shown in Fig. 8.1. Note that, for the greatest wave height, the period of the waves is approximately 10 s. It was later found that the sea state never really becomes fully developed, and the relationship became (Hasselmann and Olbers 1973)

$$\bar{F}(\omega) = \frac{\alpha g^2}{\omega^5} \exp\left[-\frac{5}{4} \left(\frac{\omega_p}{\omega} \right)^4 \right] \gamma^r, \tag{8.2}$$

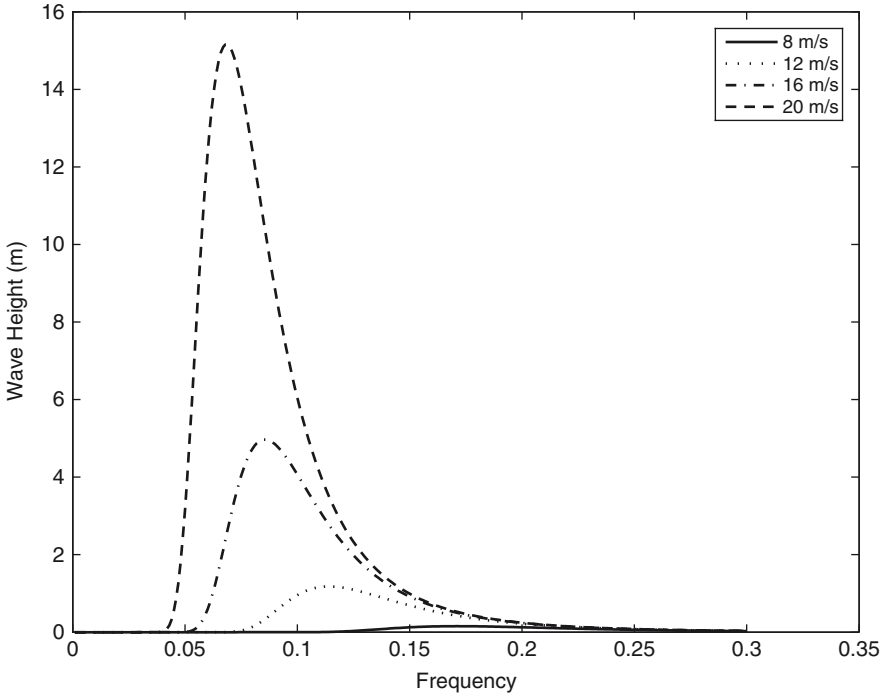

Fig. 8.1 Pierson–Moskowitz surface-wave frequency spectra for various wind speeds (Pierson and Moskowitz 1964)

where

$$r = \exp\left[-\frac{\left(\omega - \omega_p\right)^2}{2\sigma^2\omega_p^2}\right]. \tag{8.3}$$

α, ω_p, γ, and σ are parameters determined from experimental data and are dependent on the wind speed and the fetch, or the length of the water over which the wind has blown. Stronger winds and longer fetch both lead to larger waves.

The dispersion relation for deep-water ocean waves is

$$\kappa = \frac{2\pi}{\lambda_{\text{ocean}}} = \frac{\omega^2}{g}, \tag{8.4}$$

where g is the acceleration of gravity, and λ_{ocean} is the wavelength of the ocean wave. Hence, the wavelength of an ocean wave with a 10 s period is λ_{ocean} = 156 m. The corresponding wavelength of an atmospheric acoustic wave is λ_{air} = 3,400 m. As is discussed below, the fact that λ_{ocean} is much less than λ_{air} has a profound effect on how ocean waves affect pressure waves in the atmosphere.

It should be noted that real ocean wave spectra are a superposition of spectra over multiple directions; the real spectrum is thus a function F (f, θ) of both frequency and direction and is often referred to as the *directional* ocean wave spectrum. This will become important in the following discussion.

8.3.2 Ocean Waves as an Acoustic Transducer

In this section, we outline the basic physics for the interaction of ocean waves with the overlying air. The purpose is to make clear the ocean conditions necessary for the generation of microbaroms.

8.3.2.1 A One-Sided Transducer

For purposes of discussion, we shall regard the moving ocean surface as an ordinary acoustic transducer like the surface on a vibrating wall or ceiling. The main point of this section is that vibrations on the surface of a transducer do not radiate sound unless $\lambda_{\text{transducer}}$, the wavelengths of the pressure variations on the transducer face itself, are greater than or equal to λ_{air}, the wavelength for sound propagating in the air adjacent to the transducer. For the first harmonic, the pressure variations follow the displacement of the transducer, so that if the first harmonic has $\lambda_{\text{transducer}} < \lambda_{\text{air}}$, the transducer does not radiate sound at the frequency of the first harmonic. However, in the case of standing waves on the transducer higher harmonics can radiate, albeit weakly. As explained below, the radiation from higher harmonics results from long-wavelength pressure variations on the transducer face generated by the finite amplitude vibrations of the transducer.

Consider an infinite planar acoustic transducer with one-dimensional transverse harmonic waves. The amplitude of the waves on the surface of the transducer is taken here to be given by

$$A(x,t) = A_0 \cos(\kappa x - \omega t) = \Re\left[A_0 e^{i(\kappa x - \omega t)}\right] = \Re\left[\hat{A}(x,t)\right], \tag{5}$$

where $\hat{A}(x, t) = A_0 e^{i(\kappa x - \omega t)}$ is the complex amplitude, κ is the horizontal wavenumber, ω is the angular frequency, and $\Re$ indicates the real part of the complex argument. It is assumed for now that the amplitude of the transducer vibration is small enough that linear acoustics applies.

The complex pressure on the surface is given by

$$p(x,0,t) = Z_{\text{rad}}(\mathbf{v}\cdot\hat{n}), \tag{6}$$

where Z_{rad} is the specific radiation impedence (Pierce 1989) and

$$\mathbf{v}\cdot\hat{n} = \frac{\partial \hat{A}(x,t)}{\partial t} = -i\omega A_0 \exp[i(\kappa x - \omega t)] \tag{7}$$

is the complex normal velocity of the surface.

For adjacent air with a constant sound speed c_0, the wave number of the sound waves is $k_0 = \omega/c_0$. Now $k_0^2 = \kappa_{\text{air}}^2 + k_{\text{air}}^2$, where κ_{air} and k_{air} are the horizontal and vertical wavenumbers, respective in the air. The vertical wavenumber is thus given by $k_{\text{air}} = \sqrt{k_0^2 - \kappa_{\text{air}}^2}$ and the complex pressure is

$$p(x,y,z,t) = p(x,0,t)e^{i(\kappa_{\text{air}} x + k_{\text{air}} z)} \tag{8}.$$

The key physical element in the analysis is that the trace velocity of the transducer face must match the trace velocity of the acoustic wave (Pierce 1989). Trace velocity matching requires that the horizontal wave number in the air, κ_{air}, be the same as the horizontal wave number κ that exists on the transducer surface, i.e., $\kappa_{\text{air}} = \kappa$. The complex pressure corresponding to outgoing waves generated by the surface is thus given by

$$p(x,y,z,t) = p(x,0)e^{i(\kappa x + k_{\text{air}} z)}e^{-i\omega t} \tag{9}$$

where the vertical wavenumber is $k_{\text{air}} = \sqrt{k_0^2 - \kappa^2}$. To obtain the specific radiation impedance, we use the linearized Euler's equation,

$$\mathbf{v}\cdot\hat{n} = \frac{1}{i\omega\rho}(\hat{n}\cdot\nabla p) = \frac{1}{i\omega\rho}\frac{\partial p}{\partial z} = \frac{\omega\rho}{k_{\text{air}}}\exp(-i\omega t), \tag{10}$$

and obtain $Z_{\text{rad}} = \omega\rho/k_{\text{air}}$. Hence, the pressure on the surface is given by

$$p(x,0,t)\mathrm{e}^{\mathrm{i}(\kappa x-\omega t)}=\frac{-\mathrm{i}\omega^2\rho A_0}{k_{\mathrm{air}}}\mathrm{e}^{\mathrm{i}(\kappa x-\omega t)}=\frac{-\mathrm{i}\omega^2\rho}{k_{\mathrm{air}}}\hat{A}(x,t). \tag{11}$$

The pressure at all values of $z > 0$ is thus given by

$$p(x,y,z,t)=\frac{-\mathrm{i}\omega^2\rho}{\sqrt{k_0^2-\kappa^2}}\hat{A}(x,t)\mathrm{e}^{\mathrm{i}\sqrt{k_0^2-\kappa^2}\,z}. \tag{12}$$

Note that if κ is greater than k_0, the vertical wave number k_{air} is purely imaginary. That is, the sound propagates horizontally but decays exponentially vertically: the surface does not radiate sound for $\kappa > k_0$. Equivalently, we can say that vibrations on the surface of a transducer radiate sound waves only if the pressure fluctuations produced on the surface of the transducer have wavelengths greater than or equal to the acoustic wavelength. When this is not true, air is "dragged" along by the surface vibrations, but no radiating pressure waves are created.

8.3.2.2 Application to Ocean Waves

The above analysis holds for transverse waves of infinitesimal amplitude. Ocean waves are only approximately transverse and have finite amplitudes. Nevertheless, the analysis is relevant to ocean waves. For example, as discussed above in Sect. 8.2.1, a typical period for ocean waves is about 10 s, and the corresponding ocean wavelength is $\lambda_{\mathrm{ocean}} = 156$ m. In contrast, a 10-s acoustic wave in the atmosphere has a wavelength of about 3,400 m. Consequently, the main effect of ocean waves on the overlying air is to produce acoustic waves that propagate horizontally but decay vertically. The trapped pressure variations can be quite large, but they are tightly bound to the ocean surface. Although the linear analysis above was done for a traveling wave, it applies to any superposition of traveling waves and standing waves.

For a sinusoidally vibrating surface, if the amplitude $A(x, t)$ is infinitesimal, only the first harmonic is produced. In reality, any sinusoidally vibrating transducer with a finite amplitude of vibration can produce higher harmonics in addition to the first harmonic (fundamental). As we shall see, for standing waves, it is possible for the second harmonic to have surface pressure variations with horizontal wavelengths greater than the wavelength of sound, so that radiation is possible. We shall consider here only the second harmonic, since the strength of higher harmonics falls off rapidly with the order of the harmonic.

We consider a one-dimensional wave that is composed of the superposition of a right-going and a left-going wave. For this case, the wave amplitude $A(x, t)$ can be written as

$$A(x,t)=A_{\mathrm{R}}\,\sin(\kappa_{\mathrm{R}}x-\omega_{\mathrm{R}}t)+A_{\mathrm{L}}\,\sin(\kappa_{\mathrm{L}}x+\omega_{\mathrm{L}}t), \tag{13}$$

where the wave number and angular frequency for the right-going and left-going waves are labeled by "R" and "L," respectively. In the linear analysis above, the acoustic pressure field of the first harmonic was proportional to $A(x, t)$, and, as discussed, does not propagate vertically. In contrast, the amplitude of the pressure field of the second harmonic is proportional to $A(x, t)^2$. We shall not carry out the full analysis for the second harmonic, but simply indicate how the quadratic dependence on $A(x,t)$ leads to surface pressure variations with wave lengths exceeding λ_{air}, so that vertically propagating pressure waves are possible.

The square of $A(x, t)$ is

$$\begin{aligned} A^2(x,t) &= A_R^2 \sin^2(\kappa_R x - \omega_R t) + A_L^2 \sin^2(\kappa_L x + \omega_L t) \\ &\quad + 2A_L A_R \sin(\kappa_R x - \omega_R t) \sin(\kappa_L x + \omega_L t). \end{aligned} \tag{14}$$

Note that the terms involving $A_{R,L}^2 \sin^2(\kappa_{R,L} x \mp \omega_{R,L} t)$ are equal to, respectively, $(1/2)\ A_{R,L}^2[1 - \cos(2\kappa_{R,L} x \mp 2\omega_{R,L} t)]$. Hence, for these terms, the squaring process leads to functions that are either time independent or have twice the wave number (half the wavelength) of the unsquared term. Consequently, these terms cannot generate a harmonic acoustic wave that propagates vertically.

The cross term, on the other hand, can be written

$$\begin{aligned} &2A_L A_R \sin(\kappa_R x - \omega_R t) \sin(\kappa_L x + \omega_L t) \\ &= A_L A_R \{\cos[(\kappa_R - \kappa_L)x - (\omega_R + \omega_L)t] \\ &\quad + \cos[(\kappa_R + \kappa_L)x - (\omega_R - \omega_L)t]\}. \end{aligned} \tag{15}$$

Defining $\kappa^{\pm} = \kappa_R \pm \kappa_L$, and $\omega^{\pm} = \omega_R \pm \omega_L$, the cross term can be written

$$A_L A_R[\cos(\kappa^- x - \omega^+ t) + \cos(\kappa^+ x - \omega^- t)]. \tag{16}$$

Consider now oppositely directed waves of nearly equal frequency, i.e., $\omega_R \approx \omega_L$ and $\kappa_R \approx \kappa_L$. For this situation, the second term inside the brackets is nearly time independent and has a wave number equal $\kappa^+ \approx 2\kappa_R$, which is greater than $2\pi/\lambda_{air}$, so that it cannot generate a vertically propagating acoustic wave. The first term, however, has a wave number equal to κ^- which goes to zero when $\kappa_R \to \kappa_L$. The effective wavelength, $2\pi/\kappa^-$, thus can be greater than λ_{air} whenever right-going and left-going waves of nearly the same wavelength are superposed, i.e., when standing waves exist. Hence, whenever A_L is nonzero, ocean waves can produce pressure variations in the overlying air with horizontal wavelengths greater than the associated acoustic wavelength. It is these long wavelength pressure variations that radiate and generate microbarom signals. Because of the deep-water dispersion relation, $\omega = \sqrt{g\kappa}$, when $\kappa_R \approx \kappa_L$, we have that $\omega^+ \approx 2\omega_R = \omega_{air}$. Thus, the frequency of the vertically propagating acoustic waves is approximately twice the frequency of the waves that produce them. Since the dominant ocean surface wave frequency is approximately 0.1 Hz, and the microbarom peak occurs at approximately 0.2 Hz, this theory is well supported by observations.

8.3.3 Realistic Ocean Waves

The discussion above describes the basic physics of pressure waves radiated by ocean waves from one side of the air–water interface. From the beginning, ocean scientists have understood that the interface is not a one-sided transducer but rather is a two-sided transducer. When ocean waves radiate pressure waves, the pressure waves propagate into both the atmosphere (microbaroms) and the ocean (microseisms). While one might intuitively assume that the bulk of microbarom energy comes from air compression by the ocean surface, this turns out not to be the case. What has not been generally understood is that the majority of the energy (92%) radiated into the atmosphere comes from pressure waves on the water side of the air-ocean interface that are transmitted upward across the air–water interface. The first researchers to recognize this fact were Brekhovskih et al. (1973) and later, independently, Waxler and Gilbert (2006), who derived a mathematically rigorous expression for the microbarom source function for a statistically defined system of ocean waves. Their derivation treats the air-ocean interface as a two-sided transducer with energy transfer from one side of the interface to the other. For microbaroms of frequency f, the source function is given by

$$S(f) = \frac{4\pi^4 \rho_{\text{air}}^2 g^2 f^3}{c_{\text{air}}^2} \left(\frac{c_{\text{air}}^2}{c_{\text{water}}^2} + \frac{9g^2}{4\pi^2 c_{\text{air}}^2 f^2} \right) W(f), \tag{17}$$

where ρ denotes density (air, water) and c denotes sound speed (air, water). The first term inside the parentheses, $c_{\text{air}}^2 / c_{\text{water}}^2$, is the contribution to atmospheric microbaroms from the water side of the air-water interface and is over ten times the second term which arises from direct compression of the air. Thus, if one neglects the contribution from the ocean itself, the strength of the microbarom signal will be underestimated by approximately a factor of ten.

The function $W(f)$ was first described by Hasselman (1963) and contains information on opposite-going waves in the directional ocean wave spectrum:

$$W(f) = \int_0^{2\pi} F\left(\frac{f}{2}, \theta\right) F\left(\frac{f}{2}, \theta + \pi\right) \mathrm{d}\theta, \tag{18}$$

where $F(f, \theta)$ is the spectrum for ocean wave traveling in the direction given by θ. Note that the frequency spectrum $\bar{F}(f)$ can be expressed as

$$\bar{F}(f) = \int_0^{2\pi} F(f, \theta) \mathrm{d}\theta. \tag{19}$$

The function $W(f)$ is a measure of the intensity of standing waves in a given ocean area. For example, if $W(f) = 0$, there are no standing waves. For a directionally isotropic wave field, $F(f, \theta) = \bar{F}(f) / 2\pi$, and $W(f) = \bar{F}(f)^2 / 2\pi$. In general, $W(f)$ is some value between 0 and $\bar{F}(f)^2 / 2\pi$. The important thing to be noted is that the function $W(f)$ indicates that microbaroms are generated only in regions

where there are oceans waves moving in opposite directions, so that standing waves are created.

8.4 The Microbarom Generation Region of Deep-Ocean Hurricanes

The above discussion has emphasized that microbaroms are generated only in regions where there are waves traveling in opposing directions so that the ocean wave field has a standing wave component. A question that has not been addressed is where such regions exist for a deep-ocean hurricane. A priori, one might expect that the microbarom generation region would be connected with the eye of the hurricane, since the most intense wind and wave activity are there. However, a significant amount of microbarom data indicates that bearings from infrasound arrays rarely point directly toward the center of the generating storm (Hetzer et al. 2008; Tabulevich 1992; Willis et al. 2004). The deviations from the eye are often as large as 20° of azimuth which, at distances from which hurricanes tend to be observed, can be hundreds of kilometers spatially.

Horizontal refraction by the strong concentric winds near the eyewall was first considered for explaining the deflection of signals from the eye so that they appear to originate elsewhere. Calculations based on a wind profile from Hurricane Kerry (1979) (Holland 1980) indicated that deflections of the proper magnitude (10–20°) were possible, but that the strongest curvature was limited to the very close proximity of the eye so that the resultant ray still pointed back toward the eye. It quickly became clear that, in agreement with several other studies (Cessaro 1994; Ponomaryov et al. 1998; Tabulevich 1992), the microbarom generation region and the storm center were not coincident. Keeping the microbarom generation mechanism in mind, the output of the NOAA implementation of the WaveWatch 3 wave action model (Tolman et al. 2002) was applied to Typhoon Usagi. For Usagi, strong infrasound signals in the microbarom band were recorded the International Monitoring System infrasound array I39PW (Palau) with bearings that deviated by approximately 20° from the storm eye (Hetzer et al. 2008). The WaveWatch 3 outputs, which are publicly available, report the direction, period, significant wave height, and other characteristics of the dominant swell at every point in a worldwide grid.

It was immediately clear upon examination of the dominant swell direction plots that for a large region of the ocean, the dominant swell direction was concentrically counterclockwise around the center of the hurricane, and that nowhere in the vicinity of the eyewall were the dominant swells predicted to be in opposition (Fig. 8.2). On the periphery of the area dominated by the hurricane, however, there was an area where the counterclockwise hurricane swell was opposed by the dominant east-to-west swell of the Pacific Ocean, and the infrasound bearings pointed directed to that area. This area was offset from the storm eye by over 500 km, well outside the 200-km radius within which the highest winds tend to be concentrated

(Willoughby 2003). The offset calculated for the infrasound bearings remained consistent in sign and magnitude throughout the time during which strong microbaroms were recorded at I39PW (Fig. 8.3), as did the presence of the interaction region (Hetzer et al. 2008). Even though there is considerable scatter in the

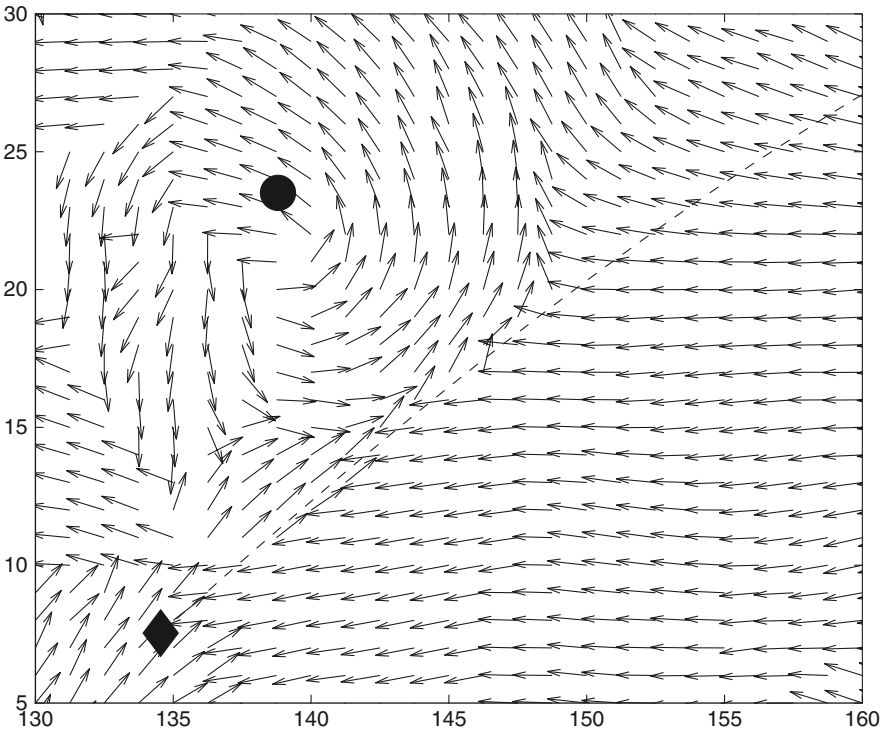

Fig. 8.2 WaveWatch 3 output showing dominant swell direction (*arrows*) on 31 July, 2007, 12:00:00 GMT during Typhoon Usagi. The *dashed line* indicates the infrasound bearing at that time calculated at station I39PW, Palau. Modified from Hetzer et al. (2008), Fig. 8.2, which also shows significant wave height

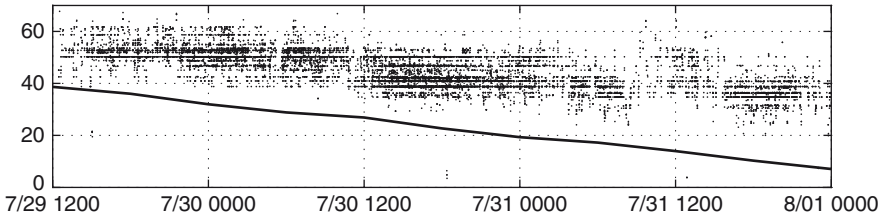

Fig. 8.3 Infrasound bearings (*dots*) and geographic bearing to the eye of Typhoon Usagi (*line*). Vertical scale is 0–100°, horizontal scale is 29 July, 2007 00:00 GMT to 1 August 00:00 GMT, grid every 12 h. Modified from Hetzer et al. (2008)

infrasound bearings, it is clear that the mean infrasound bearing follows the typhoon, lagging initially by about 10° and finally by approximately 25°.

It is obvious from geometry that if complete rotation is achieved in a hurricane's wavefield and the ambient swell is monodirectional there will always be an interaction region along the periphery of the hurricane-dominated swell region. Indeed, if one could achieve the simplest ideal case of a fully-rotated hurricane-driven ocean surface in a wholly monodirectional open ocean wavefield with no other swell components present, this region should be the sole source of microbaroms. Furthermore, since one can think of the distance from the eye to this region as the distance necessary for the hurricane wavefield to "overwhelm" the ambient wavefield, the offset distance may be a function of both the ambient swell strength and that of the hurricane swell. Since the propagation speed of the storm is a function of the surface wind speeds, which in turn controls the ambient swell, an indirect measure of storm intensity could potentially be derived simply from the infrasound measurements and the storm's track. It remains to be seen whether this relationship exists and is of use, and how the offset distance is affected by complicating factors such as coastline reflections, weaker rotation, or multiple interacting swells. Future work, possibly involving triangulation from multiple arrays in concert with higher-resolution surface-wave models, may help confirm and refine this hypothesis.

8.5 Conclusion

A theory to explain the offset between storm location and microbarom bearing based on the interaction of the storm-generated wavefield with the ambient ocean swell has been investigated. In the case of Typhoon Usagi, the theory appears to explain the observations. It remains to be seen whether the proposed theory will hold for more complicated scenarios. Although the improvement in hurricane track forecasting over the past 50 years has been both steady and impressive, the same cannot be said for intensity forecasting. Accurate monitoring, modeling, and forecasting of hurricanes are vital for the well-being of coastal communities worldwide. It is, therefore, of great importance to measure hurricane wind intensity continuously and cost-effectively. The potential use of infrasound for this purpose is actively being investigated.

References

Baird HF, Banwell CJ (1940) Recording of air-pressure oscillations associated with microseisms at Christchurch. N Z J Sci Tech 21B:314–329

Banerji SK (1930) Microseisms associated with disturbed weather in the Indian seas. Phil Trans Roy Soc London Ser A 229:287–328

Benioff H, Gutenberg B (1939) Waves and currents recorded by electromagnetic barographs. Bull Am Meteorol Soc 20:421–426

Bowman JR, Baker GE, Bahavar M (2005) Ambient infrasound noise. Geophys. Res Lett 32:L09803, doi:10.1029/2005GL022486

Brekhovskikh LM, Goncharov VV, Kurtepov VM, Naugolnykh KA (1973) The radiation of infrasound into the atmosphere by surface waves in the ocean. Izv, Atmos Ocean Phys 9:899–907

Cessaro RK (1994) Sources of primary and secondary microseisms. Bull Seismol Soc Am 84:142–148

De Bremaecker J-C (1965) Microseisms from Hurricane "Hilda." Science 148:1725–1727

DeMaria M, Gross JM (2003) Evolution of prediction models. In: Simpson R (ed) Hurricane! Coping with disaster. American Geophysical Union, Washington, DC pp 103–126

Donn WL (1951) Frontal microseisms generated in the western North Atlantic Ocean. J Meteorol 8:406–415

Donn WL (1952) Cyclonic microseisms generated in the western North Atlantic Ocean J Meteorol 9:61–71

Donn WL (1954) The relationship between microseism period and storm position. Science 3080:55–57

Donn WL, Naini B (1973) Sea wave origin of microbaroms and microseisms. J Geophys Res 78:4482–4488.

Donn WL, Posmentier ES (1967) Infrasonic waves from the marine storm of April 7, 1966. J Geophys Res 72:2053–2061

Emanuel K (2003) A century of scientific progress: an evaluation. In: Simpson R (ed) Hurricane! coping with disaster. American Geophysical Union, Washington, DC, pp 177–204

Garcés MA, Hetzer CH, Merrifield M, Willis M, and Aucan J (2003) Observations of surf infrasound in Hawai'i. Geophys Res Lett 30, doi:10.1029/2003GL018614

Garcés M, Willis M, Hetzer C, Le Pichon A, Drob D (2004) On using ocean swells for continuous infrasonic measurements of winds and temperature in the lower, middle, and upper atmosphere. Geophys Res Lett 31, doi:10.1029/2004GL020696

Garcés M, Willis M, Le Pichon A (2010) Infrasonic observations of open ocean swells in the Pacific: deciphering the song of the sea. This volume, pp. 231–244

Goda Y (2003) Revisiting Wilson's formulas for simplified wind-wave prediction. J Waterw Port Coast. Ocean Eng 129:93–95, doi:10.1061/(ASCE)0733–950X(2003)129:2(93)

Gutenberg B, Benioff H (1941) Atmospheric-pressure waves near Pasadena. Trans Am Geophys Union 22:424–426

Hasselmann K (1963) A statistical analysis of the generation of microseisms. Rev Geophys 1:177–210

Hasselmann K, Olbers D (1973) Measurements of wind-wave growth and swell decay during the Joint North Sea Wave Project (JONSWAP). Ergänz Dtsch Hydrogr Z Reihe A 8:1–95

Hetzer CH, Waxler R, Gilbert KE, Talmadge CL, Bass HE (2008) Infrasound from hurricanes: dependence on the ambient ocean surface wave field. Geophys Res Lett 35:L14609, doi:10.1029/2008GL034614

Holland GJ (1980) An analytic model of the wind and pressure profiles in hurricanes. Mon Weather Rev 108:1212–1218

Klotz O (1910) Microseisms. Science 816:252–254

Law KT, Hobgood JS (2007) A statistical model to forecast short-term Atlantic hurricane intensity. Weather Forecast 22:967–981, doi:10.1175/WAF1027.1

Le Pichon A, Vergoz J, Cansi Y, Ceranna L, Drob D (2010) Contribution of infrasound monitoring for atmospheric remote sensing. This volume, pp. 623–640

Leslie LM, Abbey RF, Holland GJ (1998) Tropical cyclone track predictability. Meteorol Atmos Phys 65:223–231

Longuet-Higgins MS (1950) A theory on the origin of microseisms. Philos Trans Royal Soc Lond Ser A 243:1–35

Pierce AD (1989) Acoustics. Acoustical Society of America, Melville, NY

Pierson WJ, Moskowitz L (1964) A proposed spectral form for fully developed wind seas based on the similarity theory of S. A. Kitaigorodskii. J Geophys Res 69:5181–5190

Ponomaryov EA, Sorokin AG, Tabulevich VN (1998) Microseisms and infrasound: A kind of remote sensing. Phys Earth Planet Inter 108:339–346

Rind DH (1980) Microseisms at Palisades 3. Microseisms and microbaroms. J Geophys Res 85:4854–4862

Tabulevich VN (1992) Microseismic and infrasound waves. Research reports in physics Springer, Berlin

Tolman HL, Balasubramaniyan B, Burroughs LD, Chalikov DV, Chao YY, Chen HS, Gerald VM (2002) Development and implementation of wind-generated ocean surface wave models at NCEP. Weather Forecast 17:311–333

Waxler R, Gilbert KE (2006) The radiation of atmospheric microbaroms by ocean waves. J Acoust Soc Am 119:2651–2664

Willis M, Garces MA, Hetzer CH, Businger S (2004) Infrasonic observations of open ocean swells in the Pacific: deciphering the song of the sea. Geophys Res Lett 31:L19303, doi:10.1029/2004GL020684

Willoughby HE (2003) A century of progress in tracking and warning. In: Simpson R (ed) Hurricane! coping with disaster. American Geophysical Union, Washington, DC, pp 205–216

Chapter 9
Acoustic-Gravity Waves from Earthquake Sources

Takeshi Mikumo and Shingo Watada

9.1 Introduction

There are various natural sources that could generate atmospheric pressure waves propagating in the lower atmosphere, which will also propagate up to the upper atmosphere and even to the ionosphere (Garces et al. 2010). Among these sources, atmospheric waves from earthquake sources had been only rarely observed and hence less well-known before the 1964 Alaskan earthquake, except a few early observations of short-period sound waves (Benioff and Gutenberg 1939), as well as air waves coupled with seismic surface waves (Benioff et al. 1951). The great Alaskan earthquake (M_w~9.0) generated unusually long-period atmospheric pressure waves with periods as long as 14 min, which have been clearly recorded at Berkeley and several Californian microbarograph stations (Bolt 1964; Donn and Posmentier 1964; Mikumo 1968).

Since that time, a large number of observations of atmospheric waves related to earthquake sources have been reported to date, with the recent deployment of local and global observation networks including the International Monitoring System (IMS), particularly after the recent 2004 Sumatra-Andaman earthquake. These observations include four different types of waves. The first one is low-frequency acoustic-gravity waves produced from the source region and propagated directly through the lower atmosphere to long distances. The second one is medium- to higher-frequency infrasonic waves, which are radiated also from the source and sometimes converted into somewhat modified forms such as reflected or diffracted waves from earth's topography during their propagation path. The third one is also infrasonic waves coupled with large-amplitude seismic Rayleigh waves during their passage through observation sites along the ground surface. The fourth one is atmospheric gravity waves induced by tsunami waves that are generated from large earthquakes.

T. Mikumo (✉)
Diaster Prevention Research Institute, University of Kyoto, Uji, Kyoto 611, Japan
mikumo@maia.eonet.ne.jp

A. Le Pichon et al. (eds.), *Infrasound Monitoring for Atmospheric Studies,*
DOI 10.1007/978-1-4020-9508-5_9,

In this chapter, emphasis will be placed on the observations and theoretical waveform modeling of the first type of atmospheric pressure waves. Their wave characteristics are closely related to the thermal structure in the lower atmosphere and even part of the upper atmosphere, as well as to the overall source characteristics of large earthquakes that produced the atmospheric perturbations. The observations of the second, third, and fourth types of infrasonic waves will also be briefly reviewed for the sake of comparison. All the pressure waves described here are related to those propagating mainly in the lower atmosphere. Acoustic-gravity waves propagating in the upper atmosphere particularly up into the ionosphere have also been observed after the 1964 Alaskan earthquake, and particularly during the 2004 Sumatra-Andaman earthquake with Doppler sounders and GPS networks, which will provide a new insight into the upper atmospheric structures. These observations, however, will not be included in this review, but will be reviewed in detail in ReVelle (2010).

9.2 Low-Frequency Acoustic-Gravity Waves from Earthquake Source

In general, there are three classes of atmospheric pressure waves propagating from the earth's surface up to the lower to upper atmosphere. One is lower-frequency gravity waves governed primarily by gravitational force or buoyancy, and the second one is higher-frequency acoustic waves governed primarily by compressional force. The other is horizontally propagating Lamb waves trapped near the surface. The cutoff-frequencies for these waves depend on the thermal structure of the atmosphere. The three modes covering different frequencies can propagate together with different velocities and amplitudes, which are called, as a whole, acoustic-gravity waves.

9.2.1 Observations

(a) The first observation was at the time of the 1964 Alaskan earthquake (03 h 36 m1 4 s UT, March 28, 1964; 61.03 N, 147.73 W, M_w~9.0). Analog-type microbarographs operated at that time at several California stations had amplitude responses peaked at 3–5 min and decaying gradually toward longer periods up to 20 min and more rapidly toward shorter periods down to 0.5 min. This response, in addition to favorable atmospheric conditions, made it possible to record unusually low-frequency waves (their corresponding periods up to 14 min) at Berkeley (Bolt 1964; Donn and Posmentier 1964; Mikumo 1968), La Jolla, and at a tripartite network stations of Mission Beach (MB), East San Diego (ESD), and Point Loma (NEL) (Mikumo 1968), all of which were located along the California coast, in addition to College, Alaska. Some of these historical records are reproduced in Fig. 9.1. Their distances from the USGS epicenter to the

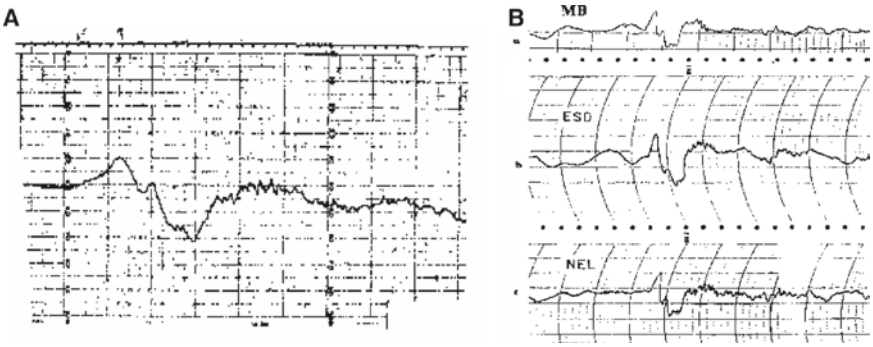

Fig. 9.1 (A). Microbarograph records obtained at California stations during the 1964 Alaskan earthquake. (a) Microbarogram recorded at Berkeley (Bolt, 1964; Reproduced from T. Mikumo, (1968), Atmospheric pressure waves and tectonic deformation associated with the Alaskan earthquake of March 28, 1964, J. Geophys. Res., 73, p.2011, by permission of American Geophysical Union). Vertical thick lines indicate a time interval of every 5 min. The dominant period of the first part is about 14 min, and the maximum peak-to-peak amplitude is about 4 Pa.(40μbars)
(B) Microbarograms recorded at a tripartite network near San Diego, California; (a) Mission Beach (MB), (b) East San Diego (ESD), (c) Point Loma (NEL). (Reproduced from T. Mikumo, (1968), Atmospheric pressure waves and tectonic deformation associated with the Alaskan earthquake of March 28, 1964, J. Geophys. Res., 73, p.2012, by permission of American Geophysical Union). Data were provided by C.T. Johnson. Vertical curved lines indicate a time interval of every 10 min. The maximum peak-to- peak amplitudes are about 5 Pa (50μbars)

California stations were between 3,127 and 3,812 km, and 382 km for College. The recorded amplitude at these stations ranged between 4 and 10 Pa. The arrival times of the first coherent compression peak at 06 h 19 m–06 h 58 m observed at these stations had a group velocity of about 319 m/s, and also their phase velocity estimated from the two stations, Berkeley and ESD, are found consistent with those expected from theoretical prediction of dispersion curves for acoustic-gravity waves (Harkrider 1964).

(b) A second observation came from the recent 2004 Sumatra-Andaman earthquake (01 h 58 m 53 s UT, December 26, 2004; 3.31 N, 95.95 E, M_w=9.2). About 5 h later, four stations on the Japanese Islands, which are located in the distances around 5,600 km from the epicenter, recorded low-frequency atmospheric waves (their corresponding periods up to 12 min) by sensitive microbarographs with a flat frequency response from 0.5 Hz to DC and with a data sampling rate of 1 Hz. The recorded amplitude at the 4 stations ranges between 7 and 12 Pa, and the group velocity of the first compression peak is from 309 to 311 m/s (Mikumo et al. 2008). Figure 9.2 shows the two-channel records obtained at Matsushiro (MAT), and two records at Norikura (NAO and ICRR) stations in central Japan. Daily atmospheric variations have been removed from the records.

In addition, four IMS stations (Cristie and Campus 2010), I52GB, I39PW, I39MG, and I32KY, which are located in and around the Indian Ocean at the distance range between 2,860 and 6,600 km also recorded atmospheric pressure waves between 03 h 39 m and 06 h 34 m with periods of 6–7 min and amplitudes of 0.8 and 2.0 Pa.

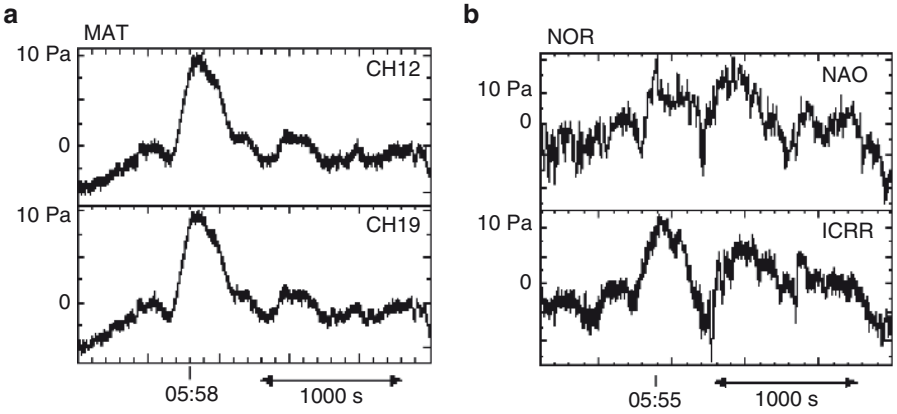

Fig. 9.2 (a) 2-channel microbarograms obtained at Matsushiro (MAT), and (b) two records at Norikura (NAO) and (ICRR), Japan, during the 2004 Sumatra-Andaman earthquake. Daily atmospheric disturbances have been removed from the original records. The dominant period for the first part is about 12 min and the maximum amplitudes are about 9 Pa (Reproduced from T. Mikumo et al.(2008), Low-frequency acoustic-gravity waves from coseismic vertical deformation associated with the 2004 Sumatra-Andaman earthquake, J. Geophys. Res. 113, B12042, p.3, by permission of American Geophysical Union). The total time covers 2400 sec (40 min)

Table 9.1 Observed low-frequency acoustic-gravity waves propagating from two great earthquakes

Earthquake	M_w	Station(s)	Distance (km)	Period (s)	Ampl. (Pa)	Group Vel. (m/s)	Ref.
1964 Alaska	9.0	Berkeley+	3,127	~840	4	309–311	B, M(1)
2004 Sumatra	9.2	Matsushiro+	5,673	~720	9	310	M(2)

1964: + La Jolla, Mission Beach (MB), East San Diego (ESD) and Point Loma (NEL) in California
2004: + Norikura (NAO and ICRR), Kamioka in Japan, and 4 IMS stations.
References: B; Bolt (1964), M(1); Mikumo (1968), M(2); Mikumo et al. (2008)

The waves can be identified by bandpass filtering for the records obtained at their array sensors. The observed group velocity ranged between about 300 and 314 m/s, but the recorded amplitudes are smaller than those at the Japanese stations due to lower sensitivity in the frequency response of the sensors used there (Mikumo et al. 2008).

The observed parameters for the two great earthquakes are listed in Table 9.1. The group velocities estimated at all these stations are found consistent with theoretical dispersion curves given by Press and Harkrider (1962) and Harkrider (1964).

9.2.2 Theoretical Considerations on the Generation Mechanism of Low-Frequency Waves, and Their Waveform Modeling

The low-frequency atmospheric perturbations described above may have been produced by sudden vertical movement of the ground or the sea surface over an extensive source area, and will propagate first upward or obliquely toward the upper atmosphere and after

some time spread horizontally as acoustic-gravity waves through the lower atmosphere. The theory of pressure waves propagating in "a realistic Air Research and Development Command (ARDC) atmospheric temperature structure" can be traced back to Press and Harkrider (1962), Pfeffer and Zarichny (1963), Harkrider (1964), Davis and Archambeau (1998), and others. The so-called ARDC standard model (Wares et al. 1960) has two temperature minima at the tropopause at an altitude of about 15 km and at the mesopause at about 85 km, and then the temperature gradually increases up to the thermosphere. For theoretical treatments, an isothermal half-space continuing upward above an altitude of 220 km has been assumed as one of probable models, for which the phase and group velocity dispersion relations and the dynamic response of the lower atmosphere have been calculated (Harkrider 1964). The standard model has some fluctuations owing to some lateral and seasonal variations of temperature and wind structures, which yields small perturbations to the dispersion relations and dynamic response obtained below. Although the upper thermosphere structure up to 500 km or even higher altitudes such as represented by the CIRA model (e.g., Yeh and Liu 1974; Francis 1975) or the MSISE model (e.g., Hedin 1991) including mass density distribution was not considered at that time, the above ARDC standard model is essentially similar to these recent models, and hence can be used to calculate theoretical waveforms of low-frequency acoustic-gravity waves and also for comparison with the recorded waveforms.

In this chapter, the method of forward waveform modeling is briefly described. The pressure perturbation p_0 due to upward particle velocity of the air w_0, ambient air density ρ_0 and sound velocity c_0 near the ground surface can be approximately related by

$p_0=\rho_0 c_0 w_0$, if the ratio of the time constant of upward displacement of the earth's surface to the local cutoff period (~340 s) is less than 0.3, and if its horizontally expanding velocity is much faster than the sound velocity (Watada et al. 2006; Watada 2009). In this case, the overall system can be treated as a linear system coupled between the ground or sea surface and the atmosphere. The pressure perturbation that would be observed at a station in the far-field compared with the source dimension and the wavelength can be expressed in the frequency domain (Mikumo 1968) as,

$$[p(r, 0, t)]_{Aj} = c(1/2\pi) \int F(\omega) \exp[-i\varphi(\omega)]\, d\omega, \tag{9.1}$$

where $F(\omega)$ is the product of the source time factor $S(\omega)$, source finiteness factor $D(\omega)$, the atmospheric transfer function $A(\omega)$, and the barograph response $B(\omega)$, and $\varphi(\omega)$ is the sum of their phase responses, respectively. c includes an approximate earth's curvature correction for the waves propagating to long distances and also a numerical constant. The atmospheric transfer function $A(\omega)$ includes the dynamic response $A_{Aj}(\omega)$ to a surface point source and receiver and the phase velocity $C_j(\omega)$ for the standard ARDC model, both of which have been calculated by Harkrider (1964) as a function of period. In this case, the actual temperature structure was approximated by 39 isothermal horizontally stratified layers continued up to an isothermal half-space (Model A) or terminated with the free surface (Model B), at an altitude of 220 km. For this temperature model bounded on the top by an isothermal half-space or the free surface and at the bottom by the rigid ground surface, three boundary conditions are required: continuity of the vertical velocity and of total pressure at all interfaces of successive isothermal layers; pressure

perturbation at the ground surface should be equal to p_0 at the source and zero outside the source area; and the propagation coefficient for descending waves at the uppermost layer should be zero. These conditions yield layer matrix formulation for the atmospheric response. Sound velocity at all these heights has been estimated from the square root of the temperature. Air density is assumed to decrease exponentially with altitude from the earth's surface (Press and Harkrider, 1962). The group velocity can also be calculated from the above formulations. The calculations were made for the fundamental and first-higher gravity modes GR_0 and GR_1 and the fundamental, first-, and second-higher acoustic modes S_0, S_1, and S_2. GR_0 has spectral amplitudes over periods from 4.5 to 14 min and S_0 covers from 2 to 4.5 min in this model (Harkrider 1964). This is the reason why low-frequency acoustic-gravity waves can be observed if the frequency response of sensors used at microbarograph stations covers these period ranges.

On the other hand, $S(\omega)$ in (9.1) includes the time-dependence of p_0, which is related to the average displacement a and the rise time τ of coseismic vertical deformation. We also consider that the source area extends over a finite dimension with a rectangle given by the length $2L$ and the width $2W$, with the horizontal expanding velocity v of the source area, by integrating a point-source solution over the area. The source finiteness factor $D(\omega)$ then includes these parameters and also the phase velocity $C_j(\omega)$ and β, the azimuth from the source to the station with respect to the source expanding direction (Mikumo and Bolt 1985). The barograph response $B(\omega)$ appropriate to the station is also included. More detailed expression of the above functions can be found in Mikumo et al. (2008).

9.2.3 *Comparison Between the Recorded and Theoretical Barograms*

The recorded low-frequency acoustic-gravity waves include the effects of the source extended over a wide area. Actually, the source region of the 1964 Alaskan earthquake covers an area of 800 km × 100 km for the uplifted zone and 800 km × 150 km for the subsided zone, both extending southwestward from the epicenter (Plafker 1965), while that of the 2004 Sumatra-Andaman earthquake extends northwestward over curved uplifted and subsided zones for about 1,500 km × 200 km (e.g., Banerjee et al. 2007; Rajendran et al. 2007). In the two great earthquakes both in the plate boundary, the major part of the source region lies beneath the ocean. Large submarine thrust faulting would produce coseismic uplift and subsidence on the sea bottom, and then the deformation would cause swelling and depression of the sea surface. Theoretical studies (Kajiura 1963, 1970) on tsunami generation show that if the wavelength of the deformation is much longer than the water depth and if the deformation takes place within a few minutes, the sea surface behaves almost exactly like the sea bottom deformation. These conditions are met in the present case with the lateral wavelength of deformation over 100–150 km with respect to the water depth of 2,000–4,500 m in the Gulf of Alaska and 3,000–4,000 m in the Indian Ocean, respectively.

For the 1964 Alaskan earthquake, two major zones of uplift, A (a=5 m) and B (a=1.5 m), and two zones of subsidence, C (a=−1.5 m) and D (a=−1.0 m) can be identified. The waveforms produced from each of the four zones have been calculated through the above formulations, including five major acoustic and gravity modes. If the uplift and subsidence took place at almost the same time in the four zones, then the synthetic barograms including these modes radiating from the four zones would be as shown in the second to fourth traces in Fig. 9.3, for different time constants τ=0 ~ 1.0 min. The waveform observed at Berkeley (the uppermost trace) appears more or less consistent with the general features of the theoretical traces with τ=0.3–1.0 min, which means the actual time constant may be in the range between 1 and 3 min (Mikumo 1968).

For the 2004 Sumatra-Andaman earthquake, the major zones of coseismic uplift and subsidence probably may be divided into "eight zones" from the northwestern Sumatra region up to the northern Andaman Islands. In this case, there could

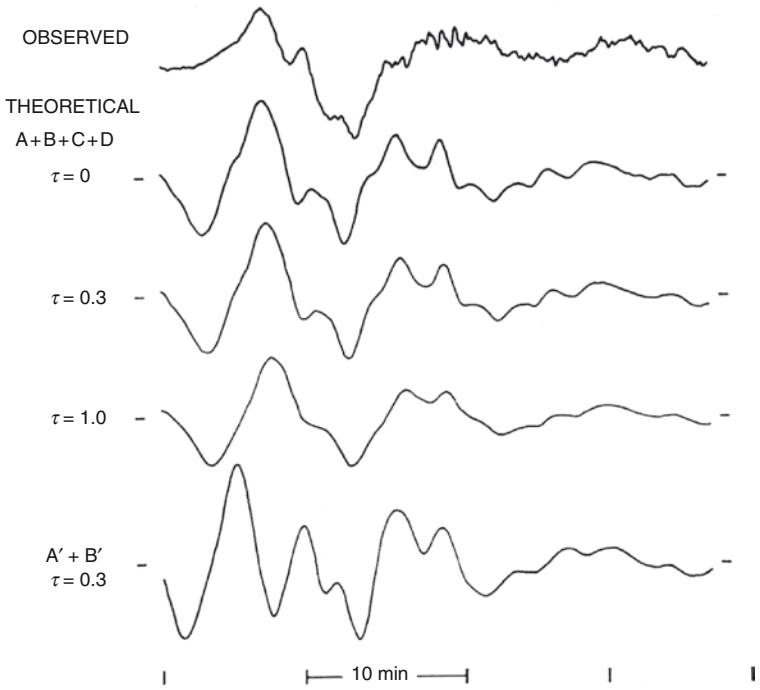

Fig. 9.3 Comparison between the microbarogram recorded at Berkeley and the calculated theoretical waveforms including 5 major acoustic and gravity modes, generated from four major zones of coseismic uplift and subsidence, for a_A = 5 m, a_B = 1.5 m, a_C = -1.5 m and a_D = -1.0 m, with different time constants between τ = 0 and 1.0 min (Reproduced from T. Mikumo, (1968), Atmospheric pressure waves and tectonic deformation associated with the Alaskan earthquake of March 28, 1964, J. Geophys. Res., 73, p. 2023, by permission of American Geophysical Union)

be many different combinations of the source parameters in this forward modeling. It is finally found after a number of calculations that among these combinations, a_{2U}=4 ~ 6 m, a_{2D}=−2 ~ −3 m, τ=1.0 ~ 1.5 min with a_{jU}=1 m, a_{jD}=−0.5 m (j=1,3,4), and v = 2.5 km/s, can produce theoretical waveforms best compared with the general features of observed waveforms at the MAT (see Fig. 9.4). There is, of course, some allowance in the estimated parameters. The above parameters also generate theoretical waveforms generally consistent with the waveforms recorded at the other three Japanese and four IMS stations (Mikumo et al. 2008).

The above model could provide synthetic waveforms well consistent with the observed low-frequency barograms, although there are quite large dilatation precursor and large second peak for Model A. This may come from truncation effects of the synthesis due to sharp cutoff of the theoretical spectral amplitude around 14 min. For Model B, on the other hand, these effects are not apparent, but Model A may be physically more reasonable, because it indirectly includes the thermal structure in part of the upper atmosphere. The absolute amplitude of the theoretical waveforms shown in the middle and bottom traces in Fig. 9.4 (a) for Model A was estimated as 15.4 Pa and 13.3 Pa, respectively, with the pressure perturbation p_0 at the eight source

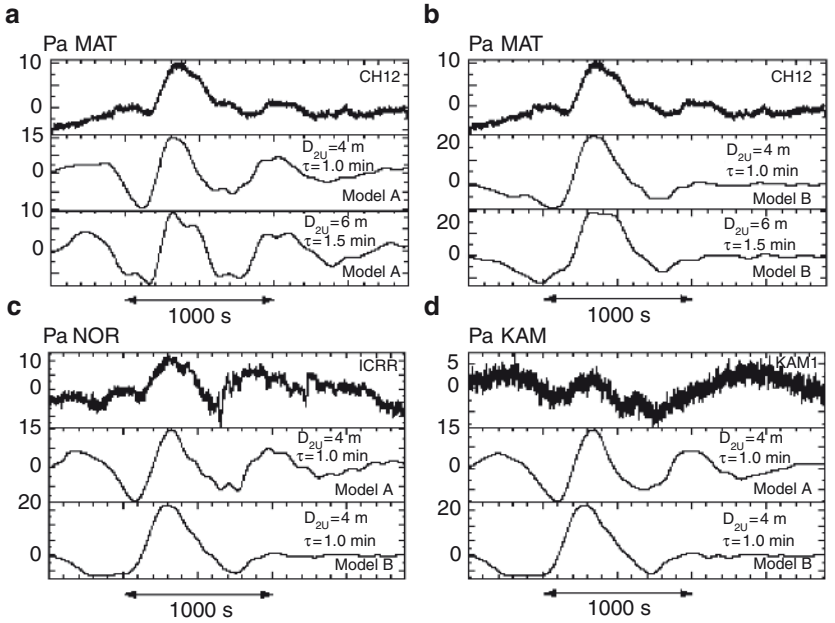

Fig. 9.4 Comparison between the microbarograms recorded at Matsushiro, Norikura, and Kamioka, and the calculated theoretical waveforms including 3 major acoustic gravity modes, generated from eight major zones of tectonic uplift and subsidence, for two possible cases with a_{2U} = 4 m, a_{2D} = -2 m and τ = 1.0 min, and with a_{2U} = 6 m, a_{2D} = -3 m and τ = 1.5 min, together with a_{jU} = 1 m, a_{jD} = -0.5 m (j=1,3,4) and v = 2.5 km/s. The total time covers 2400 sec (40 min). Models A and B are from two different thermal structures at an altitude of 220 km (See text). (Reproduced from T. Mikumo et al., (2008), Low-frequency acoustic-gravity waves from coseismic vertical deformation associated with the 2004 Sumatra-Andaman earthquake, J. Geophys. Res. 113, B12042, p.11, by permission of American Geophysical Union)

regions for $\rho_0 = 1.293 \times 10^{-3}$ gr/cm^3, $c_0 = 320$ m/s, and with the corresponding particle velocities w_0. On the other hand, the recorded maximum amplitude at MAT is 9 Pa, which is somewhat smaller than the above estimates. This difference may be attributed partly to local weather conditions, which could reduce the S/N ratio of observations. Another factor may be possible fluctuations of the spectral amplitude due to thermal and wind structures in the lower atmosphere and also to wave attenuation.

9.2.4 Implications of Propagation of Low-Frequency Acoustic-Gravity Waves to Long Distances

It has now been demonstrated that the sudden vertical movement of the ground or the sea surface can excite atmospheric pressure perturbations with different frequency components. For higher frequency waves, these perturbations will propagate first upward and may be refracted back at an altitude of about 50 km and partly from higher velocity layers down to the earth. The waves may probably be bounced back from the earth's surface and could be again transmitted by multiple refraction–reflection process to long distances (e.g., Mutschlecner and Whitaker 2005), as expected from a ray theory. It is to be noted, however, that the propagation patterns depend strongly on their wavelength. Recent numerical simulations (e.g., Artru et al. 2005; Occhipinti et al. 2006; Shinagawa et al. 2007) incorporating an atmospheric thermal model like the MSISE (Hedin 1991) indicate the wavelength-dependent propagation, suggesting that acoustic waves with periods between 4 and 6 min can be trapped in the lower atmosphere and the earth's surface. The low-frequency waves originated from an extensive source area propagate obliquely toward the upper atmosphere, and after some time spread horizontally as acoustic and gravity waves through the lower to upper atmosphere.

For the observation of atmospheric pressure waves, the frequency response of sensors used at microbarograph stations is a controlling factor as to whether low-frequency acoustic-gravity waves can be detected or only medium- to higher-frequency infrasonic waves will be observed. It is preferable that the frequency response could cover low frequencies to be able to observe such low-frequency acoustic-gravity waves as have been observed from the two great earthquakes, to reveal the lower to upper atmospheric structure as well as to discuss the source process of large earthquakes.

9.3 Medium- to High-Frequency Infrasonic Waves from Earthquake Source

In addition to low-frequency acoustic-gravity waves, medium- to high-frequency infrasonic waves have also been observed, which appear to have originated also from strong upward ground velocity at the source area of large earthquakes and

propagated through the lower atmosphere to short and long distances and sometimes reflected or diffracted by earth's topography.

After the 1964 Alaskan earthquake, this type of waves with periods of 20–27 s and amplitudes between 2 and 3 Pa have also been recorded at three stations, Boulder (3,690 km from the epicenter), Boston, and Washington DC (around 5,280–5,295 km) in central and eastern United States (Young and Greene 1982). The group velocity along the wave path was estimated as 312–316 m/s, although the records did not show unambiguous arrival time of these waves. Similar late arrival of atmospheric pressure waves has been recorded after the time of the 1964 Niigata, Japan, earthquake (M_w=7.5) at Brisbane, Australia (about 7,400 km away from the epicenter) with periods of 60–70 s and a group velocity ranging between 260 and 275 m/s (Bowman and Shrestha 1965).

In addition to these observations at teleseismic distances, infrasonic waves have been identified even at local and regional distances. A convincing evidence is the observation at the IS08 station in Bolivia located at 530 km from the epicenter of the 2001 Arequipa, Peru, earthquake (M_w=8.4) (Le Pichon et al. 2002). The recorded waves, which are believed to come from the main shock, arrived with a group velocity around 330–340 m/s and amplitudes ranging between 2 and 5 Pa for a predominant period of 2 s. Later arrivals with longer periods around 10–20 s probably coming from two aftershocks were interpreted to be associated with high mountain ranges of the Andean Cordillera. During the 2001 Kunlun Mountain, China, earthquake (M_w=8.1), coherent infrasonic waves with periods around 10 s have been recorded at an IMS network of the I34MN station in Mongolia located at 1,800 km away from the epicenter (Le Pichon et al. 2003), where the arrival of the signal with an amplitude of ~2 Pa can be identified with a group velocity ranging between 340 and 380 m/s. The infrasonic waves may have been associated with seismic wave generation over a length of 1,000 km near the fault zone. The 2002 Denali fault earthquake, Alaska (M_w=7.9) also generated strong infrasonic waves, which have been clearly recorded at array sensors of the I53US station in Fairbanks, Alaska, located about 150 km north of the fault (Olson et al. 2003). The signal arriving at the array with a group velocity of 340 m/s indicated large amplitudes reaching 12 Pa. The source of the infrasound has been attributed to the sudden local motion of the mountains in the Alaska Range along the Denali fault.

One of the latest observations of infrasonic waves are from the December 2004 Sumatra-Andaman (M_w=9.2) and the March 2005 Aceh (M_w=8.7) earthquakes in the Indian Ocean. Higher-frequency infrasonic waves produced from the two earthquakes have been recorded at the IMS array, Diego Garcia (I52GB), Palau (I39PW), Australia (I07AU), Madagascar (I39MG), and Kenya (I32KY) stations, and analyzed in two separate frequency bands (0.5–4.0 Hz) and (0.02–0.16 Hz) (Garces et al. 2005; Le Pichon et al. 2005). The analysis reveals three types of infrasonic waves; the first group has a dominant period of 10 s, a group velocity of 350–360 m/s, and a peak-to-peak amplitude of 0.5 Pa, and the second one has a dominant period of 30 s and a p–p amplitude of 2 Pa, and the last one almost overlapping the second group (Le Pichon et al. 2005). The second one implicitly involves the low-frequency acoustic-gravity waves described in Sect. 9.1. An inverse location procedure

suggests that ground movement around the source region efficiently produced the infrasonic waves. The analysis also shows late arrival of longer-period pressure waves generated from the resultant tsunami waves. Another recent observation came from the June 13, 2005, northern Chilean earthquake (M_w=7.8), when coherent infrasonic waves have been detected by 3 IMS stations, I08BO, I09BR, and I41PY, located at distances from 410 to 2,300 km (Le Pichon et al. 2006). These waves arrived at a group velocity ranging between 340 and 370 m/s, and their maximum amplitude is 1.4 Pa for a period of 10 s. The observed azimuth variations and their long signal durations suggest that these waves may have been generated by the ground motion amplified by undulated topography of the Andes Mountains.

More infrasonic observations from 31 large and medium-sized earthquakes during the 20 years from 1983 to 2002 by the network of the Los Alamos National Laboratory at Los Alamos, New Mexico, St. George, Utah and Mercury, Nevada, are summarized in a collective study (Mutschlecner and Whitaker 2005). The distance to these earthquakes ranges between 4,100 km to Alaska and 165 km to New Mexico. Because of the instrumental frequency band between 0.1 and 10 Hz, the recorded signals are mostly high-frequency infrasonic waves with maximum amplitudes ranging between 0.03 and 0.5 Pa, most of which are quite small except two cases with 0.8–1.0 Pa. The phase velocity across the array is estimated in the range between 350 and 450 m/s. In this study, unlike others, it has been shown that the normalized infrasonic amplitude and the duration of the signal depend not only on the epicentral distance but on local earthquake magnitude, although there are quite large variances in these estimates (Mutschlecner and Whitaker 2005).

The main characteristics of medium- to high-frequency infrasonic signals from 12 large earthquakes with magnitudes M_w>7.8 are summarized also by Le Pichon et al. (2006), except the two 1964 earthquakes described above. The observed parameters may be compared with Table 9.1 for the two great earthquakes that produced low-frequency acoustic-gravity waves. An empirical relation between the normalized amplitude and duration of the infrasonic signals and the seismic local magnitude, which is similar to that estimated by Mutschlecner and Whitaker (2005), has also been derived incorporating more data from the listed larger earthquakes (Le Pichon et al. 2006).

It is expected that the use of these infrasonic data would reveal more detailed profiles of stratospheric sound and wind velocity structures

9.4 Ground – Coupled Atmospheric Pressure Perturbations

The third type of atmospheric pressure change observed after large earthquakes are those coupled with strong ground motions due mainly to seismic Rayleigh waves passing by the observation site, which arrive much earlier than infrasonic waves propagating directly from the source. This type of report can be traced back to early observations by Benioff and Gutenberg (1939), and Benioff et al. (1951) at the time of the1951 Imperial Valley earthquake. Another observation came from the 1959 Montana

earthquake (Cook 1971), when the pressure waves have been recorded at a station in Washington DC, which were interpreted to be due to local seismic waves. The observations mentioned in the previous section sometimes include these early arriving infrasonic waves coupled with Rayleigh waves. For the 1964 Alaskan earthquake, there are two observations. One is by Donn and Posmentier (1964) for the observations of ground-coupled pressure waves with Rayleigh wave velocities at Palisades, New York, Berkeley, California, and Honolulu, Hawaii. Another one is shown by Young and Greene (1982) who reported separate observations of infrasonic waves at three stations, Boulder, Boston, and Washington, DC, passing with Rayleigh wave velocities. A similar observation of pressure perturbations at Blacknest, Berkshire, England, with a period around 24 s and amplitude of 0.9 Pa, has been reported to be coupled with seismic Rayleigh waves also from the 1968 Tokachi-Oki earthquake (M_w=7.9) that occurred near the east coast of Honshu, Japan (Grover and Marshall 1968).

The recent infrasonic observations made at IMS stations also recorded pressure changes due to the passage of large amplitude Rayleigh waves. These include the medium- to high-frequency infrasonic waves from the 2001 Kunlun Mountain, China, earthquake recorded at the I34MN station, from the 2001 Arequipa, Peru, earthquake at the IS08 station, from the 2002 Denali, Alaska earthquake at the I53US station, and also from the 2004–2005 large Sumatra earthquakes at the IS52 and 3 other stations. (References for these cases have been given in the previous section). The observed trace velocity in these cases corresponds to that of seismic wave velocity ranging between 3 and 5 km/s. Another local infrasonic signal synchronized with the arrival of seismic waves came from the 2003 Tokachi-Oki, Japan, earthquake (M_w=8.3), which have been recorded at two arrays CHNAR and TJI in Korea, located at distances around 1,500 km (Kim et al. 2004). Although the infrasonic waves can be identified in the bandpass filtered records between 0.01 and 16 Hz, their recorded amplitudes and the group velocity are not explicitly mentioned.

A more comprehensive observation of this type of infrasonic waves has been reported in a recent article by Watada et al. (2006). For the 2003 Tokachi-Oki, Japan earthquake, pressure changes with a dominant period of 15–20 s and amplitudes of a few Pa has been recorded lasting for longer than 20 min by sensitive microbarographs at nine stations on the Japanese Islands. Co-located broadband seismographs also recorded seismic Rayleigh waves at the same time passing through these stations with a group velocity of 3.2 km/s. The high-pass filtered microbarograms and the broadband seismograms are very well correlated for the first 20 min interval, as clearly shown in Fig. 9.5, which clearly indicate that the observed pressure changes are excited by the ground motion due to the passage of Rayleigh waves. From these observations, the seismic-infrasonic pressure transfer function has been calculated from the spectral ratio of the pressure perturbation to the vertical ground velocity as a function of frequency (Watada et al. 2006). The amplitude ratio and the phase difference in the calculated transfer function are found to be nearly constant for the period range between 10 and 50 s. This suggests that the well-known relation between the pressure perturbation p_0, air density ρ_0, sound velocity c_0 near the ground surface, and the vertical velocity of the ground w_0, $p_0=\rho_0 c_0 w_0$ approximately holds for these periods, if the time scale of the vertical motion is short enough when compared with the acoustic cutoff-period. Comparing these results with the theoretical transfer function calculated

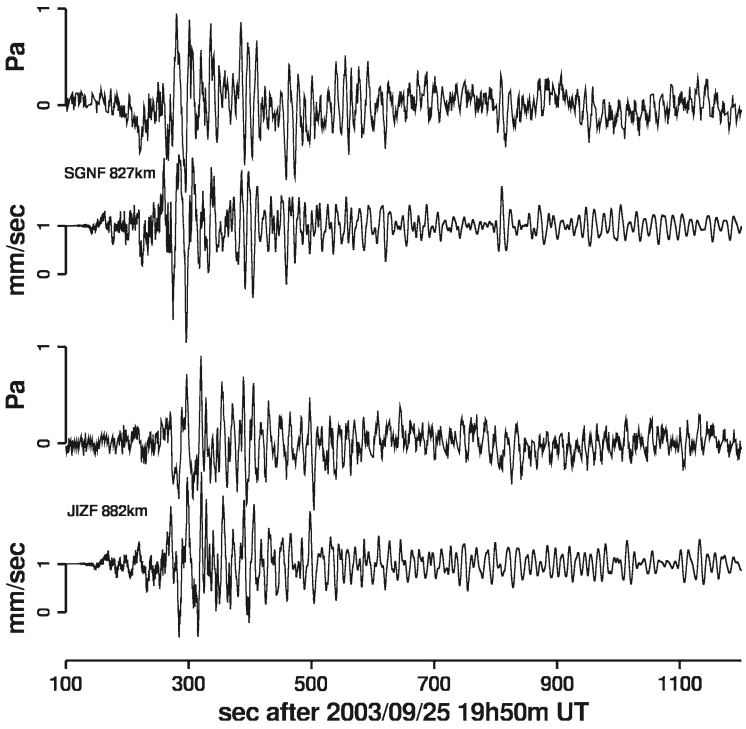

Fig. 9.5 Comparison between the high-pass filtered microbarograms for the period of 50 sec and the original, vertical seismograms at two co-located observation sites, SGNF (upper pair) and JIZF (lower pair). (Reproduced from S. Watada et al. (2006), Atmospheric pressure change associated with the 2003 Tokachi-Oki earthquake, Geophys. Res. Lett., 33, L24306, p.3, by permission of American Geophysical Union)

from acoustic coupling between low-frequency acoustic waves in an isothermal atmosphere and the ground motion, it was concluded that the pressure changes observed during this earthquake are due to nearly vertically upward propagating infrasonic waves generated by the seismic Rayleigh waves.

For more precise waveform modeling for pressure waves, which will be generated from more general, bottom surface deformation including tsunami waves, it is necessary to include the frequency and horizontal wavenumber dependency of pressure variations at the bottom boundary (see Watada 2009).

9.5 Atmospheric Gravity Waves Induced by Tsunami Waves

Although the coupled atmospheric and water gravity waves had been described earlier (Donn and McGuiness 1960), possible arrival of tsunami-induced atmospheric waves has been suggested (Bolt 1964; Mikumo 1968) on the Berkeley microbarograph record obtained at the time of the 1964 Alaskan earthquake. It has

been pointed out that short-period wave trains are superposed with a time delay of about 16 min on the long-period atmospheric pressure waves mentioned in Sect. 9.2.1. An early theoretical work (Peltier and Hines 1976) predicted that atmospheric gravity waves could be generated by tsunami waves under some conditions. Actually, tsunami-induced gravity waves have been clearly observed as ionospheric pressure perturbation by the GPS network in Japan at the time of tsunami arrival from the 2001 Peru earthquake (Artru et al. 2005). During the 2004 Sumatra-Andaman earthquake, infrasonic records at the Diego Garcia station also revealed late arrival of the pressure perturbation related to tsunami waves (Garces et al. 2005; Le Pichon et al. 2005). These pressure perturbations recorded by microbarographs had rather short period and quite small amplitudes, when compared with direct atmospheric gravity waves. It is to be noted, however, that the weak tsunami-induced signals on the earth's surface could be much amplified with altitude toward the ionosphere due to the decrease of air density (e.g., Artru et al. 2005). It has also been confirmed from numerical solutions that long-period tsunami could generate atmospheric gravity waves (Watada 2009). The ionospheric signals attributed to tsunami waves resulting from the 2004 great earthquake have been observed and reported in a number of recent papers, which are summarized by Lognonné (2010).

9.6 Summary

This review summarizes the atmospheric pressure changes due to earthquake sources.

These pressure perturbations include medium- to high-frequency infrasonic waves; one mentioned in Sect. 9.4 is those coupled with seismic surface waves passing through the observation sites with seismic Rayleigh wave velocities, and the other mentioned in Sect. 9.3 is the infrasonic waves with sound speed, which originated from earthquake source and propagated directly to the stations through the atmosphere, and sometimes converted into diffracted or reflected by the earth's surface topography. For a number of large earthquakes, the two types of pressure perturbations have often been recorded together, with the first one arriving much earlier than the second waves. For the case of ground-coupled atmospheric pressure, however, it is important to keep in mind that the microbarograph set up at any stations could record air pressure perturbation but would sometimes be affected directly by strong ground vibration during the passage of large-amplitude seismic waves. To discriminate these two cases, it is necessary to make careful vibration tests for the instrumental response by putting the barograph on a shaking table. Another important check may be to install long-period seismometers and barographs together at the same site to estimate the relationship between the recorded pressure change and the vertical ground velocity, as have been made by Watada et al. (2006).

As described above, very low-frequency acoustic-gravity waves described in Sect. 9.2 generated from large-scale coseismic vertical deformation over the extensive source region have been recorded, with late arrival of tsunami-induced gravity waves mentioned in Sect. 9.5, by microbarographs exceptionally after the two great

earthquakes. It should be noted that the capability for detecting these low-frequency waves depends not only on the frequency response of the instruments used at the observation sites but also on correlations between the observed signals at adjacent sites such as by array sensors used at most IMS stations. It is recommended for future observations that two or three different frequency bands covering very low to high frequencies and array sensors be used at all stations.

In this chapter, only limited observations of atmospheric waves are compared with theoretically predicted waveforms for low-frequency acoustic-gravity waves propagating in the lower atmosphere. As described before, the theory of pressure waves propagated in the lower atmosphere with a realistic thermal structure had been developed earlier in relation to volcanic eruptions and artificial explosions in the air (e.g., Yamamoto, 1957, Press and Harkrider 1962; Pfeffer and Zarichny 1963; Harkrider 1964; Harkrider and Press 1967). More recent theories on acoustic-gravity waves propagating up to the upper atmosphere including the ionosphere can be found in several articles dealing with earthquake and volcanic sources (e.g., Davis and Baker 1965; Leonard and Barnes 1965; Francis 1973, 1975; Yeh and Liu 1974; Kelly et al 1985; Blank 1985; Calais and Minster 1995; Davis and Archambeau 1998; Afraimovich et al. 2001; Artru et al. 2004, 2005; Occhipinti et al. 2006; Tanimoto and Artru 2007; Watada 2009). It is hoped that interested readers could refer also to these original articles.

Theoretical treatment including these atmospheric models, as well as high-altitude observations such as by ionosondes, Doppler sounding, GPS observations, etc. in relation to earthquake-generated acoustic-gravity waves will be essential to explore the structure of the lower to upper atmosphere.

Acknowledgments We thank Alexis Le Pichon, the Editor of this Book, for inviting us to write a chapter and also an anonymous reviewer of this chapter for useful suggestions.

References

Afraimovich EL, Perevalova NP, Plotnikov AV, Uralov AM (2001) The shock-acoustic waves generated by earthquakes. Ann Geophys 19:395–409

Artru J, Farges T, Lognonné P (2004) Acoustic waves generated from seismic surface waves: propagation properties determined from Doppler sounding observations and normal-mode modeling. Geophys J Int 158:1067–1077

Artru JV, Ducic HK, Lognonné P, Murakami M (2005) Ionospheric detection of gravity waves induced by Tsunamis. Geophys J Int 160(3):840–848

Banerjee P, Politz F, Nagarajan B, Burgmann R (2007) Coseismic slip distributions of the 26 December 2004 Sumatra-Andaman and 28 March 2005 Nias earthquakes from GPS static offsets. Bull Seism Soc Am 97:S86–S102

Benioff H, Gutenberg B (1939) Waves and currents recorded by electromagnetic barographs. Bull Am Meteorol Soc 20:421–426

Benioff H, Ewing M, Press F (1951) Sound waves in the atmosphere generated by a small earthquake. Proc Natl Acad Sci., USA 37:600–603

Blank E (1985) Observations in the upper atmosphere of infrasonic waves from natural and artificial sources: A summary. Ann Geophys 3(6):673–688

Bolt BA (1964) Seismic air waves from the great 1964 Alaskan earthquake. Nature 202:1095–1096
Bowman GG, Shrestha KL (1965) Atmospheric pressure waves from the Japanese earthquake of 16, June, 1964. Quart J Royal Meteorol Soc 91:223–224
Calais E, Minster JB (1995) GPS detection of ionospheric perturbations following the January 17, 1994, Northridge earthquake. Geophys Res Lett 22:1045–1048
Cook R (1971) Infrasound radiated during the Montana earthquake of 1959 August 18. Geophys J R Astron Soc 26:191–198
Christie DR, Campus P (2010) The IMS infrasound network: design and establishment of infrasound stations. This volume, pp. 27–72
Davis JB, Archambeau CB (1998) Modeling of atmospheric and ionospheric disturbances from shallow seismic sources. Phys Earth Planet Intr 105:183–199
Davis K, Baker DM (1965) Ionospheric effects observed around the time of the Alaskan earthquake of March 28, 1964. J Geophys Res 70:2251–2253
Donn WL, McGuiness WT (1960) Air-coupled long-waves in the ocean. J Atmos Sci 17:515–521
Donn WL, Posmentier ES (1964) Ground-coupled air waves from the great Alaskan earthquake. J Geophys Res 69:5357–5361
Francis SH (1973) Acoustic-gravity modes and large-scale traveling ionospheric disturbances of a realistic, dissipative atmosphere. J Geophys Res 79:2278–2301
Francis SH (1975) Global propagation of atmospheric gravity waves: A review. J Atmos Terr Phys 37:1011–1054
Garces M, Caron P, Hetzer C (2005) Deep infrasound radiated by the Sumatra earthquake and tsunami. EOS 86(35):317–319
Garcés M, Willis M, Le Pichon A (2010) Infrasonic observations of open ocean swells in the Pacific: deciphering the song of the sea. This volume, pp. 231–244
Grover FH, Marshall PD (1968) Ground to air coupled waves from a distant earthquake. Nature 220(516):686–687
Harkrider DG (1964) Theoretical and observed acoustic-gravity waves from explosive sources in the atmosphere. J Geophys Res 69:5295–5321
Harkrider DG, Press F (1967) The Krakatoa air-sea waves: an example of pulse propagation in coupled systems. Geophys J R astr Soc 13:149–159
Hedin AE (1991) Extension of the MSIS thermosphere model into the middle and lower atmosphere. J Geophys Res 96:1159–1172
Kajiura K (1963) The leading wave of a tsunami. Bull Earthq Res Inst 41:535–571
Kajiura K (1970) Tsunami source, energy and the directivity of wave radiation. Bull Earthq Res Inst 48:835–869
Kelly MC, Livingston R, McCready M (1985) Large altitude thermospheric oscillations induced by an earthquake. Geophys Res Lett 12:577–580
Kim TS, Hayward C, Stump B (2004) Local infrasound signals from the Tokachi-Oki earthquake. Geophys Res Lett 31: L20605, doi:10,1029/2004GL021178
Leonard RS, Barnes RA Jr (1965) Observations of ionospheric disturbances following the Alaskan earthquake. J Geophys Res 70:1250–1253
Le Pichon A, Guilbert J, Vega A, Garces M, Brachet N (2002) Ground-coupled air waves and diffracted infrasound from the Arequipa earthquake of June 23, 2001. Geophys Res Lett 29(18): 1886, doi:10,1029/2002GL015052
Le Pichon A, Guilbert J, Vallee M, Dessa JX, Ulziibat M (2003) Infrasonic imaging of the Kunlun Mountains for the 2001 China earthquake. Geophys Res Lett 30(15): 1184, doi:10,1029/2003GL017581
Le Pichon A, Herry P, Mialle P, Vergoz J, Brachet N, Garces M, Drob D, Ceranna L (2005) Infrasound associated with the 2004–2005 large Sumatra earthquakes and tsunami. Geophys Res Lett 32:L19802. doi:10, 1029/2005GL023893
Le Pichon A, Mialle P, Guilbert J, Vergoz J (2006) Multistation infrasonic observations of the Chilean earthquake of 2005 June 13. Geophys J Int 167:838–844
Mikumo T (1968) Atmospheric pressure waves and tectonic deformation associated with the Alaskan earthquake of March 28, 1964. J Geophys Res 73:2009–2025

Mikumo T, Bolt BA (1985) Excitation mechanism of atmospheric pressure waves from the 1980 Mount St. Helens eruption. Geophys J R astr Soc 81:445–461

Mikumo T, Shibutani T, Le Pichon A, Garces M, Fee D, Tsuyuki T, Watada S, Morii W (2008) Low-frequency acoustic-gravity waves from coseismic vertical deformation associated with the 2004 Sumatra-Andaman earthquake. J Geophys Res 113:B12042. doi:doi.10.1029/2008/JB005710, 2008

Mutschlecner JP, Whitaker RW (2005) Infrasound from earthquake. J Geophys Res 110:1108. doi:10, 1029/2004JD005067

Olson JV, Wilson CR, Hansen RA (2003) Infrasound associated with the 2002 Denali fault earthquake, Alaska. Geophys Res Lett 30(23):2195. doi:doi:10, 1029/29/2003GL018568

Occhipinti G, Lognonné P, Kherani E, Hébert H (2006) 3D waveform modeling of ionospheric signature induced by the 2004 Sumatra tsunami. Geophys Res Lett 33:L20104. doi:10.1029/2006GL026865

Peltier WR, Hines CO (1976) On the possible detection of tsunamis by monitoring of the ionosphere. J Geophys Res 81(12):1995–2000

Pfeffer RL, Zarichny (1963) Acoustic-gravity waves propagation in an atmosphere with two sound channels. Geofis Pura Appl 55:175–199

Plafker G (1965) Tectonic deformation associated with the 1964 Alaskan earthquake. Science 148:1675–1687

Press F, Harkrider D (1962) Propagation of acoustic-gravity waves in the atmosphere. J Geophys Res 67:3889–3908

Rajendran CP, Rajendran K, Anu R, Earnest A, Machado T, Mohan PM, Freymueller J (2007) Crustal deformation and seismic history associated with the 2004 Indian Ocean earthquake: A perspective from the Andaman-Nicobar Islands. Bull Seism Soc Am 97:S174–S191

ReVelle DO (2010) Acoustic-gravity waves from impulsive sources in the atmosphere. This volume, pp. 301–354

Shinagawa H, Iyemori T, Saito S, Maruyama T (2007) A numerical simulation of ionospheric and atmospheric variations associated with the Sumatra earthquake on December 26, 2004. Earth Planets Space 59:1015–1026

Tanimoto T, Artru J (2007) Interaction of Solid Earth, Atmosphere, and Ionosphere. Treatise on Geophysics 4:421–444

Wares, G.W., K.W. Champion, H.L. Pond, and A.E. Cole (1960), Model atmospheres, Hanbook of Geophysics, 1-1-1-37, The Mcmillan Co.

Watada S, Kunugi T, Hirata K, Sugioka H, Nishida K, Sekiguchi S, Oikawa J, Tsujii Y, Kanamori H (2006) Atmospheric pressure change associated with the 2003 Tokachi-Oki earthquake. Geophys Res Lett 33:L24306. doi:10, 1029/2006GL027967

Watada S (2009) Radiation of acoustic and gravity waves and propagation of boundary waves in the stratified fluid from a time-varying bottom boundary. J Fluid Mech 627:361–377

Yamamoto R (1957) A dynamical theory of the microbarographic oscillations produced by the explosions of hydrogen bombs, J Meteorol Soc Japan 35:32–40

Yeh KC, Liu CH (1974) Acoustic-gravity waves in the upper atmosphere. Rev Geophys Space Physics 12:193–216

Young JM, Greene GE (1982) Anomalous infrasound generated by the Alaskan earthquake of 28 March, 1964. J Acoust Soc Am 71:334–339

Chapter 10
Seismic Waves from Atmospheric Sources and Atmospheric/Ionospheric Signatures of Seismic Waves

P. Lognonné

10.1 Introduction

Mikumo and Watada, in the previous chapter of this book, have presented in details the generation of acoustic-gravito waves by quakes and focused their discussion on the waves propagating mainly in the atmosphere, from the earthquake source to the atmospheric recording points. As noted in their section, the observations of these waves, by sensors located at the Earth surface, request most of the time very large quakes, with magnitudes larger than 8.

We focus in this chapter on the waves traveling mostly in the interior or liquid part of the Earth, but nevertheless with a smaller propagation path in the atmosphere. For atmospheric sources (e.g., atmospheric explosions), these waves propagate first in the atmosphere from up to down, reach the ground, and then propagate in the interior of the Earth. Alternatively, for solid Earth sources (e.g., quakes), the waves propagate in the solid earth, then reach the surface, and resume their propagation in the atmosphere, from the surface to the ionospheric heights. The almost propagation in the atmosphere is therefore ranging from 30 km in the first case to about 400–500 km in the second case, while the propagation in the interior of the Earth can be many thousands km, the propagation being worldwide.

The other difference in our approach will be in the observational methods. While Mikomo and Watada are focusing on the observations in the atmosphere, we will concentrate our review on the observation of the waves at the end of their propagation path, and therefore on ionospheric observations, for waves generated by quakes, and on seismic observation, for waves generated by atmospheric sources.

Ionospheric observations, as we will see below, are especially interesting as they can be performed even for "small" magnitude quakes, when compared with the example of Mikumo and Watada in the range of M_s=8–9. The larger sensitivity of

P. Lognonné (✉)
Institut de Physique du Globe de Paris, (IPGP) Equipe Géophysique Spatiale et Planétaire,
Université Paris Diderot, CNRS, 4 Avenue de Neptune, 94100,
Saint Maur des Fossés, France, Paris
e-mail: lognonne@ipgp.fr

A. Le Pichon et al. (eds.), *Infrasound Monitoring for Atmospheric Studies,*
DOI 10.1007/978-1-4020-9508-5_10,

ionosphere when compared with the low atmosphere is related to the exponential decay of the atmospheric density. The amplitudes of acoustic-gravity waves, when they propagate vertically, is indeed proportional to $\rho(z)u^2$, where ρ is the density and u the displacement of the atmospheric particles. When the frequency is low enough (<10mHz), the atmospheric viscosity can be neglected and the amplitude is therefore increasing with altitude, inversely proportional to the square root of density. The resulting amplification can reach factors of about 10^4–10^5 at the altitudes of maximum ionization (~300–400 km), and made observation possible, near the quake for magnitudes as low as 6, and far from the quakes, for magnitudes of about 7.

Many observations of these signals were reported after large quakes in Alaska or Japan in the 60th (Yuen et al. 1969; Weaver et al. 1970; Leonard and Barnes 1965; Davies and Baker 1965) with Doppler techniques sensitive to the vertical oscillations of the ionospheric layers. Much later, Calais et Minster (Calais and Minster 1995) reported ionospheric perturbations of the density of electrons by using another sounding method, based on data from global positioning system (GPS) receivers, and corresponding therefore to electron density perturbations. Since these works, the detection of the associated ionospheric perturbations has benefited from the recent developments in ionosphere remote sensing, in particular of techniques using GPS dense networks, Doppler HF sounder, or even over-the-horizon radar. These tools provide unprecedented capabilities for monitoring the reaction of the ionosphere to seismic waves.

We present in this paper the state of the art in the modeling of these signals, with a review of the theory necessary to model the observations, and present and discuss the perspectives of this new seismological approach.

10.2 Theoretical Modeling of the Seismic Waves in the Neutral and Ionized Atmosphere

10.2.1 Solid Earth–Neutral Atmosphere Coupling

The modeling of waves with a propagation path splitted in the Earth interior and atmosphere has to take into account the two different media, and two approaches are therefore possible. In the first approach, one considers the surface of the Earth as a simple interface (Davies and Archambeau 1998): when waves reach this interface, part of their energy is reflected, while the remaining part is transmitted, either in the atmosphere for upgoing waves or in the solid Earth for downgoing waves. The transmission (t) and reflection (r) coefficients from the interior to the atmosphere can be easily estimated for waves propagating vertically:

$$t = \frac{2\rho_{\text{int}} c_{\text{int}}}{\rho_{\text{air}} c_{\text{air}} + \rho_{\text{int}} c_{\text{int}}} \approx 2,\ r = \frac{\rho_{\text{air}} c_{\text{air}} - \rho_{\text{int}} c_{\text{int}}}{\rho_{\text{air}} c_{\text{air}} + \rho_{\text{int}} c_{\text{int}}} \approx 1,$$

while the energy transmission (T) and reflection (R) coefficients, which verify $R+T=1$, are

$$T = \frac{\rho_{\text{air}} c_{\text{air}}}{\rho_{\text{int}} c_{\text{int}}} t^2, \quad R = r^2.$$

These simplified expressions, as well as the similar expression for a downward propagation, provide the order of magnitude of the energy transfer between the two systems, by using typical values for $\rho_{\text{air}}, \rho_{\text{int}}, c_{\text{air}}, c_{\text{int}}$ (e.g., respectively, 1.2 kg/m^3, 2,600 kg/m^3, 330 m/s, 5,800 m/s). The energy transmitted by one transmission from the interior to the atmosphere or from the atmosphere to the interior is 4 times the acoustic impedance ratio between the air and interior, leading to about 10^{-4} (Lognonné and Johnson 2007). This will be typically the relative energy transferred by a body wave to the atmosphere or by an atmospheric source to the interior. Normal modes associated to surface waves will transmit more energy, as they are stationary waves. The transmitted energy can, however, be estimated for a fundamental surface wave of angular order ℓ easily with this approach. As they have a horizontal wavelength of $\lambda = 2\pi a / (\ell + 1/2)$ and bounce on the surface one time per cycle, with an amplitude decreasing each time by $e^{-\pi/Q}$ due attenuation in the solid part, where Q is the quality coefficient of the mode, the total energy can be expressed as the sum of the term of a geometrical series $e^{-\pi/Q}(e^{-\pi/Q}R)^n T$. During these successive bounces, the portion of energy transmitted to the atmosphere will therefore be $E = \varepsilon \frac{2Q}{\pi} \frac{\rho_{\text{air}} c_{\text{air}}}{\rho_{\text{int}} c_{\text{int}}}$, where ε is the partition ratio between the energy in vertical displacement and the total energy, the latter being typically of the order of 0.5. For a Q value of 100, we find typical values of almost 10^{-3}, showing that almost one per mille of the energy of surface waves is dissipated in the Earth atmosphere, as shown on Fig. 10.1.

A much more detailed and rigorous theory is necessary for the modeling of the observed phenomena, especially because most observations are done for long period seismic waves, with periods of several 10s of seconds or even a few of 100s of seconds, for which the high-frequency approach of propagating waves and rays is not valid anymore: both the surface and the troposphere are indeed within one wavelength for acoustic waves of 100 s (i.e., about 30 km of wavelength). The first theory was developed by Watada (1995) and Lognonné et al. (1998). This approach takes into account the coupling between the solid Earth, the ocean, and the atmosphere. In the latter, the boundary conditions of the elasto-dynamic operator at the solid Earth–atmosphere interface is integrated in the normal modes theory. A radiative boundary condition simulates the escape of acoustic and gravity atmospheric waves in the upper ionosphere, where no refraction of waves is observed. Either variational methods (Lognonné et al. 1998) or iterative methods (Kobayashi 2007) can be used, leading to the computation of normal modes with both eigenfrequency and eigenmodes with complex values. The dissipation related to viscosity in the atmosphere can be easily incorporated, as shown by Artru et al. (2001).

The results for a typical atmospheric model (U.S. Standard atmosphere 1976) and the PREM model for the solid Earth (Dziewonski and Anderson 1981) are shown on Fig. 10.1. The finite wavelength of the long period acoustic waves

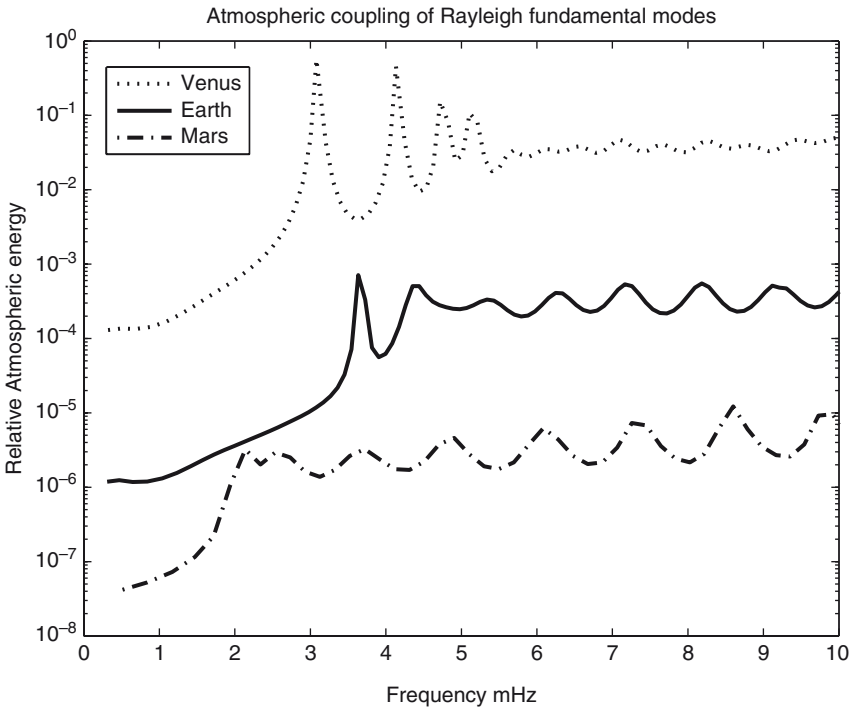

Fig. 10.1 Fraction of the energy of surface waves in the Venus, Earth, and Mars atmospheres for Rayleigh surface waves. Only the first peaks are due to atmospheric resonances. Note that the amplitudes on Mars and Earth are comparable at low frequency (2–3 mHz), due to differences in the atmospheric resonance frequency. US standard atmospheric model (1976) is used for the Earth, whereas the models of Forget et al. (1999) and Hunten et al. (1983) are used for Mars and Venus, respectively (reprinted from Lognonné and Johnson 2007)

generates resonance effects observed at the frequencies associated with the fundamental and overtones of the atmospheric wave-guide. At these frequencies (about 3.7 and 4.44 mHz), a much larger fraction of the seismic waves is transferred in the atmosphere, and this preferential transmission is the major explanation not only for the bichromatic signals observed after volcano eruptions, but also for the large ionospheric waves detected between 3.5 and 5 mHz. The amplitude of the normal modes, either in the atmosphere for the Rayleigh fundamental normal modes, or in the solid Earth for the acoustic normal modes, can be found in Lognonné et al. (1998), Lognonné and Johnson (2007), Lognonné and Clévédé (2002), and Kobayashi (2007). Figure 10.1 also provides a comparison of the coupling between the Earth and other telluric planets. This will be discussed briefly in Sect. 10.5.

The properties of the atmospheric channel in this vertical propagation is, however, significantly depending on the position and local time, as the structure of the atmosphere changes with position and local time (Fig. 10.2) and both the energy transfer and the amplitudes of the normal modes are affected. As the atmosphere/interior coupling is a local effect (i.e., associated with an horizontal propagation much smaller at long period than the wavelength of the seismic waves), a first modeling of this

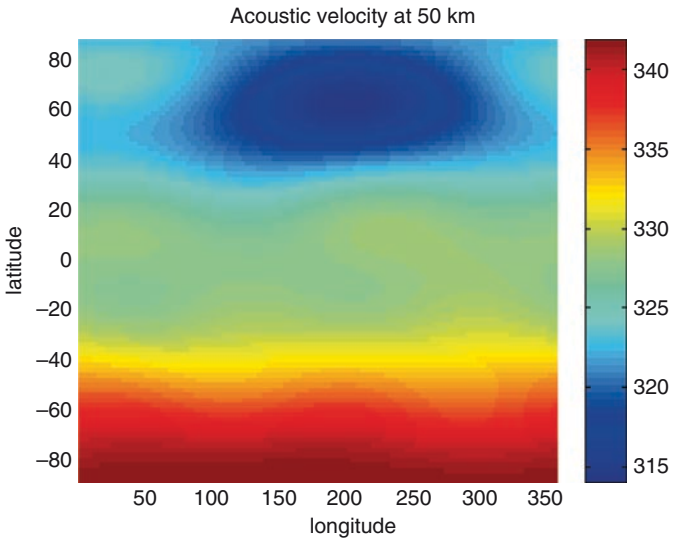

Fig. 10.2 Sound speed in the atmosphere for model NRLMSISE-00 on January 1, a 0 h00 TU, as a function of altitude and longitude, at an altitude of 50 km. Variations are about 10% peak-to-peak and units are in m/s.

variability can be done by using the 1D theory described above on all points of the Earth surface, using on each of these points an empirical 3D atmospheric model, such as the NRLMSIS-00 model (Picone et al. 2002). The first feature observed is related to the crossing between the solid Earth fundamental Rayleigh modes (noted ${}_0S$) and the atmospheric fundamental acoustic modes (noted ${}_0P$). The latter is the main reason for the large energy transfer found around 3.7 mHz between the solid Earth and the atmosphere. Figure 10.3 shows that depending on the local time and location, this crossing can be either between the frequencies of ${}_0S_{27}-{}_0S_{28}$ or ${}_0S_{28}-{}_0S_{29}$. This is generating a dependence of the energetic coupling with local time and location, as shown by Fig. 10.4a: the amount of energy in the atmosphere can vary by a factor of 2 for the fundamental modes and the first overtones at the resonances frequency and the amplitudes are found to be the largest during the night, when the acoustic impedance of the atmosphere is the highest (Fig. 10.4b).

As a first step, spherically symmetric normal modes can be used to compute, with a summation technique, not only seismograms from atmospheric sources, but also atmospheric signals from quakes. We, however, have to keep in mind the effect of the atmospheric variability, which will request the computation of normal modes for a 3D time-dependent atmosphere for more precise studies.

10.2.2 Neutral Atmosphere – Ionospheric Coupling

When the waves reach the ionosphere, they interact with the ionospheric plasma. This interaction is done mainly through collision processes, which transfer the

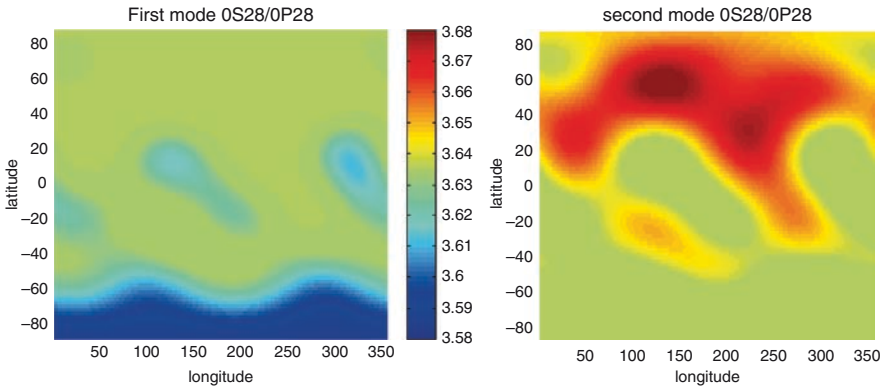

Fig. 10.3 (*Left*) Location of the Earth where the fundamental atmospheric acoustic mode ${}_0P_{28}$ has a frequency below the frequency of the fundamental Rayleigh seismic mode ${}_0S_{28}$. The values of the frequency, with colorscale in mHz, is given in color, the one of ${}_0S_{28}$ being the middle green value of the color scale. (*Right*) The figure shows the location of the Earth where the fundamental atmospheric acoustic mode ${}_0P_{28}$ has a frequency higher than the frequency of the fundamental Rayleigh seismic mode ${}_0S_{28}$. The frequency of ${}_0S_{27}$, ${}_0S_{28}$, and ${}_0S_{29}$ are 3.544, 3.635, and 3.726 mHz, respectively, showing that the acoustic mode is either between ${}_0S_{27}$ and ${}_0S_{28}$ or ${}_0S_{28}$ and ${}_0S_{29}$, depending on the location

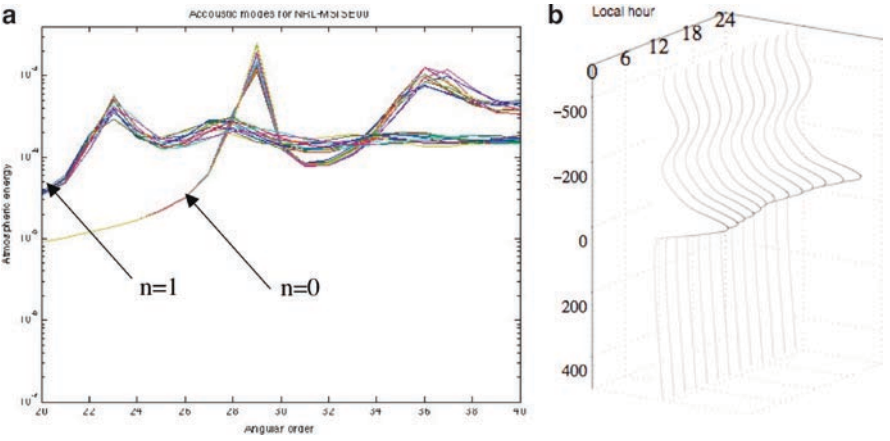

Fig. 10.4a-b (**a**) (Left) Plot of the fraction of energy in the atmosphere for the fundamental Rayleigh waves of angular order up to 50 and for the first harmonics, for different local times of the MSISE-00 atmospheric model. The interior model remains PREM for all cases. The resonances, while occurring for different angular orders, are found at the same frequencies. (*Right*) plot of the amplitude of the vertical component of the fundamental Rayleigh waves near the resonance (angular order 29), as a function of depth in km. The amplitudes, multiplied by the square root of density, are multiplied by 100 in the atmosphere. A minimum of coupling is found near 12 h local time

velocity of the neutral atmosphere, noted δw to the ions or electrons. The electrons/ions are then interacting through electromagnetic forces to maintain the ionosphere neutrality and electric field and magnetic field are therefore perturbed. Both ions and electrons in addition interact with the magnetic and electric field, and to the first order, the velocity of the charged particles is then significant only along the direction of the magnetic field (Kherani et al. 2008; Dautermann et al. 2008, 2009; Ostrovsky 2008). More in details, the Fourier transform of the velocity of a given ionized species is expressed as (Kherani et al. 2008)

$$\delta u^r = \frac{1}{(1+i\eta)\kappa^2}\{[(1+i\eta)^2+\kappa^2 b_r^2]\delta w^r + \kappa^2 b_r b_\theta \delta w^\theta\} \approx \frac{b_r}{(1+i\eta)}\{b_r \delta w^r + b_\theta \delta w^\theta\}$$

$$\delta u^\theta = \frac{1}{(1+i\eta)\kappa^2}\{[(1+i\eta)^2+\kappa^2 b_\theta^2]\delta w^\theta + \kappa^2 b_r b_\theta \delta w^r\} \approx \frac{b_\theta}{(1+i\eta)}\{b_r \delta w^r + b_\theta \delta w^\theta\}$$

$$\delta u^\phi = \frac{1}{\kappa}\{b_\theta \delta w^r - b_r \delta w^\theta\}$$

where we use the Fourier-transformed components of the velocity of a given species δu and the cosine directors of the magnetic field along r, θ, φ, respectively, b_r, b_θ, b_φ and where $\kappa = qB/mv$ is the ratio between the gyropulsation of the ionized species and its collision frequency, $\eta = \omega/v$ is the ratio between the pulsation of the wave and the collision frequency and where the final expression is given to the first order of $1/\kappa$. q, m are the charge and mass of the species, while B is the local amplitude of the magnetic field and i is such that $i^2 = -1$. The typical values of the collision frequencies are given in Fig. 10.5, while the gyrofrequency (2π times smaller than the pulsation) is about 1.4 MHz for electrons and a 50,000 nT magnetic field amplitude, typical of the Earth magnetic field over California or Japan. The gyrofrequency is 30,000 times smaller for O+ ion and therefore about 45 Hz. This shows that for both ions and electrons, κ are much larger than unity, and for the surface waves, η are smaller than unity, which justify these expressions valid to the first order in $1/\kappa$. The ionospheric perturbation in velocity is therefore mainly parallel to the magnetic field and has a smaller component perpendicular to the magnetic field. The electron density variation is expressed by the conservation equation

$$\frac{\partial \delta n}{\partial t} + \mathrm{div}(n_0 \delta \vec{u}) + \mathrm{div}(\delta n \vec{u}_0) = 0$$

in the linearized case and when no perturbation in the production rate is assumed. Here $\vec{u}_0$ is the background and steady-state electron current, such as the equatorial electro-jet. These effects are generating both latitudinal and azimuthal effects on the ionospheric signals.

Figure 10.6 shows the latitudinal effect, for typical amplitudes recoded in the ionosphere, for surface arbitrary vertical amplitude of 1 mm in displacement, at the frequency of 5 mHz. We note the amplification with altitude of the neutral wave, as well as its latitude dependence related to change of the scale height between

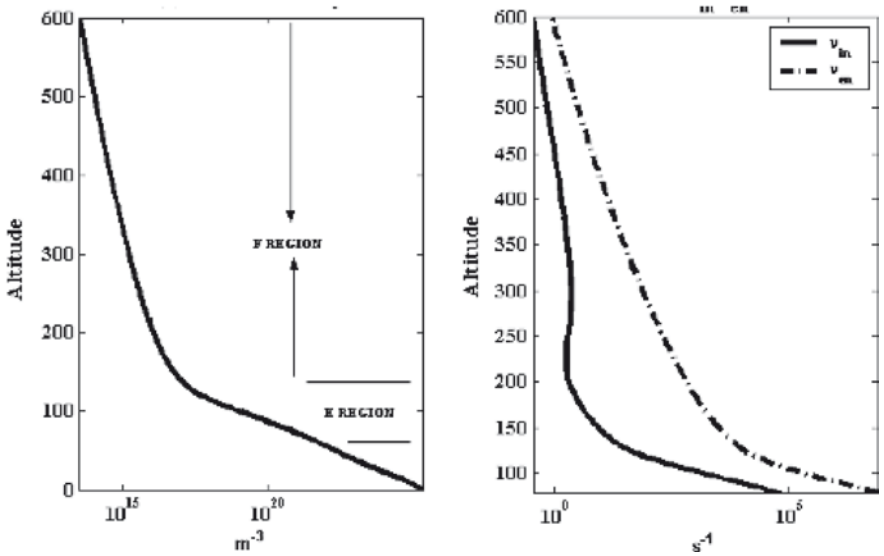

Fig. 10.5 (*Left*) Typical electron density as obtained from IRI (Bilitza 2001) for a morning condition (5 h local time). *Right figure* shows the typical collision frequencies for ion-neutral and electron-neutral, as obtained from model SAMI2 (Huba et al. 2000)

equator and poles. Because of the magnetic field, the vertical charged velocity is canceling at the magnetic equator while the maximum in the electron density perturbation is found at the equator, with a secondary maximum at mid-latitudes. Figure 10.6 also illustrates that the ionospheric perturbation cannot be recorded everywhere with the same efficiency and tools and that both Doppler sounder (sensitive to the velocities) and GPS sounders (sensitive to the electron density) are necessary to perform observations over large range of latitudes.

This azimuth dependence of electron density perturbation is illustrated in Fig. 10.7a, b, for an acoustic expending wave, generated over Japan, where the magnetic inclination is about 50°. During its perturbation, the acoustic ray is bended due to the increase of the sound speed. When propagating southward, it reaches therefore a point where it is parallel to the magnetic field, while a perpendicular configuration is in contrary found for northward propagation path. This azimuth sensitivity, leading to an apparent directivity effect on the observations of ionospheric-seismic signals from quakes (Heki and Ping 2005) or of ionospheric-acoustic signals from volcanic eruptions (Heki 2006) must be taken in the modeling when amplitudes are analyzed and possibly inverted.

10.3 Observation and Inversions

Our review will focus on the observation performed relatively far from the source, when the contributions from the waves propagating in the atmosphere and excited at the source by the piston-like displacement of the ground can be separated from

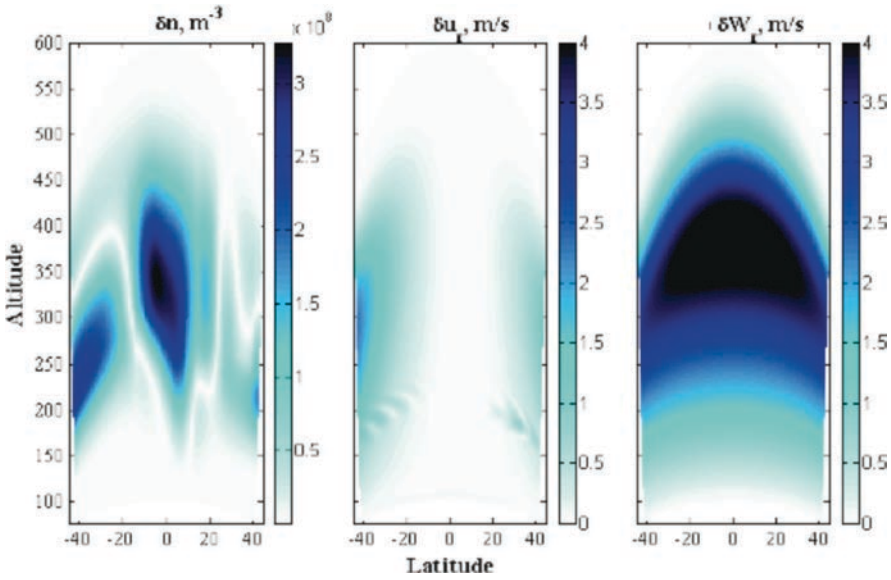

Fig. 10.6 Left and middle figures are the electron density and electron vertical velocity responses to the neutral velocity of the right figure. This neutral velocity field takes into account the amplification of acoustic waves with altitude and its dissipation at high altitude. The period of the acoustic wave is set to 200 s and IRI and SAMI2 models (see Fig. 10.5) are used for the computation of the perturbations

the seismic tele-seismic waves. We will therefore not cover the ionospheric observations of the acoustic waves, the latter being the high altitude counterpart of the waves described in detail by Mikuma and Watada. These waves have however been reported by many studies (e.g., Afraimovich et al. 2001; Heki and Ping 2005; Kiryushkin and Afraimovich 2007; Heki 2006; Astafyeva and Afraimovich 2006) and where probably the waves detected originally by Calais and Minster (1995).

10.3.1 Atmospheric Coupling at the Source

The first illustration of the seismic/acoustic wave coupling can be found in signals detected in an atmospheric-interior path, in which the Rayleigh waves (and theoretically body waves too) are excited at the source by powerful atmospheric sources. They then can propagate in the solid Earth over long distances. The typical sources for such signals are the volcano explosions, like El Chichon in 1982, Pinatubo in 1991, and more recently Montserrat in 2003. This excitation mechanism is very likely contributing also to the continuous excitation of normal modes (see Tanimoto and Artru 2007 for a recent review), even if the oceanic excitation is certainly exiting normal modes at a larger level (Webb 2007).

The first clear observation was made by Pinatubo: by stacking 12 IDA stations during 12 h, Zürn and Widmer (1996) have shown indeed that the recorded signals

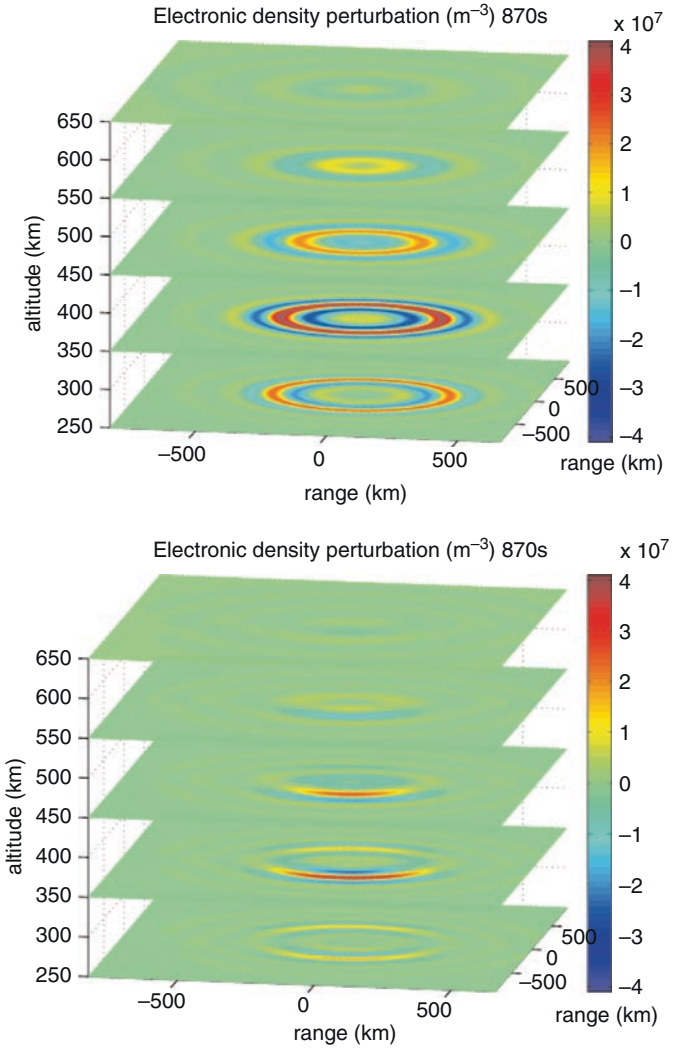

Fig. 10.7 (**a**-**b**): 3D simulation of an acoustic wave generated by a source point at the surface, over Hokkaido, Japan. X and Y direction are along west–east and south–north, respectively. The *top figure* shows the isotropic perturbations in electron density when no magnetic field is taken into account. They reach a maximum at the maximum ionization altitude. The *bottom figure* shows the effect of the magnetic field, which focuses on the perturbation in the south, where the acoustic rays reach a configuration parallel to the magnetic field

have a selective excitation of Rayleigh surface waves around frequencies of 3.7, 4.44 mHz for the two mains peaks. Many papers were published on the explanation of these unusual signals. Some have proposed a feedback regime between the atmosphere and the volcano (Widmer and Zürn 1992; Zürn and Widmer 1996). Other proposed the excitation of two atmospheric waves, the low frequency one being a

gravity wave, and the other being acoustic (Kanamori and Mori 1992; Kanamori et al. 1994). It is now recognized that this bichromatic excitation is just related to the fact that the Rayleigh waves around 3.7 and 4.44 mHz have more energy in the atmosphere and are therefore more excited than the others.

Such views can be consolidated by a waveform source inversion of the Pinatubo data, shown in Fig. 10.8, where 18 stations of the Global Network (Geoscope and Iris) on the VLP channels corresponding to the full day of June 15, 1991 are shown. In such inversions, we have to compute the seismograms, by using the Rayleigh normal modes with their atmospheric extension, as shown in Fig. 10.5. A standard normal mode summation technique (e.g., Lognonné 1991) can be used. For an explosive force, the expression of the seismograms is given by (Lognonné et al. 1994)

$$u(t,\mathbf{r}_s) = \sum_k \Re e\left(\frac{1}{i\sigma_k}\int_0^t dt'\, M_k(r_e,t')e^{i\sigma_k(t-t')}u_k(\mathbf{r}_s)\right)$$

where $\mathbf{r}_s$ r_e are the receiver/explosion coordinates respectively, index k denotes a given mode with quantum numbers ℓ, m, n, σ_k, and $\mathbf{u}_k$ are the normal frequency and normal mode, respectively, associated to index k and where the source term

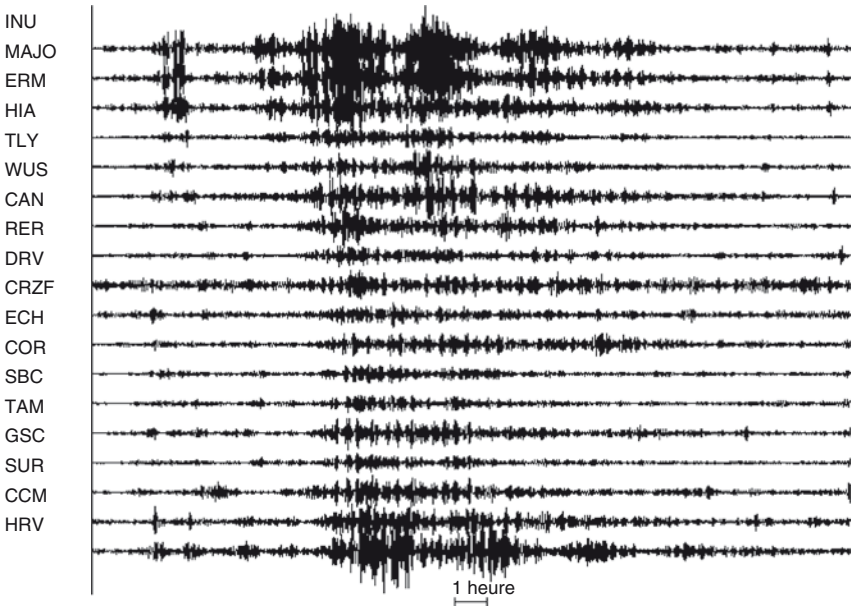

Fig. 10.8 Bandpass filtered vertical data recorded after the Pinatubo eruption by several stations of the global network. Stations have increasing epicentral distance from top to bottom. The Two small quakes recorded on the data and originating from other sources as the Pinatubo region (A M_s=6.1 quake from Causasus and a M_s=6.3 quakes from South Sandwich Islands, occurring, respectively, at 0059TU and 0113TU) are subtracted from the data after CMT inversion of both quakes achieved by a waveform fitting of coupled synthetics computed for the aspherical model M84 (Woodhouse and Dziewonski 1984)

$M_k(\mathrm{r}_{\mathrm{e}}, t)$ is given by the source integrated over the whole source volume and is expressed by $M_k(t) = V_s\, \Delta p(t)\, \mathrm{div}(\mathbf{u}_k)$ when the source is represented as an isotropic pressure glut $\Delta p(t)$ in the source volume V_s. Note that in the source term, the divergence of the normal mode eigenfunction is taken at the source location.

Such an expression allows therefore to test the source altitude. Figure 10.9 shows the result of a least-square inversion of the data with synthetics filtered in the frequency bandpass window from 1 to 8 mHz, assuming that the seismic source is localized at a given altitude/depth z, is isotropic in direction, and is radiating during 10 h starting after June 13, 1991, 22h UT.

The inversion is performed by least-square fitting of the vertical ground displacement after instruments correction and by adding a correlation time to the moment tensor history, in order to stabilize the inversion. We therefore minimize

$$\sum_n \int dt (u^n_{\mathrm{obs}}(t) - u^n_{\mathrm{cal}}(t))^2 + \varepsilon \iint dt \quad dt' \quad m(t) \quad C^{-1}(t-t') \quad m(t')$$

with an exponential correlation function $C(t) = \mathrm{e}^{-(t^2/\tau^2)}$, in order to stabilize inverse problem. Inversions for all altitudes from a few kilometers depth to about 60 km of altitude are then performed and compared. The best variance reduction (about 60%) is found near the surface and at an altitude between 24 and 28 km (Fig. 10.10a, b). To assess the validity of a low-altitude source with respect to a

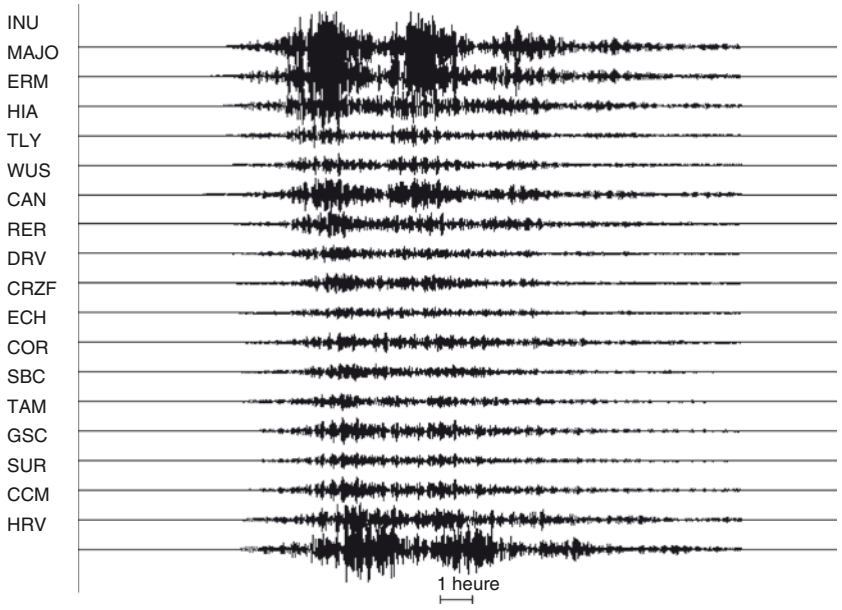

Fig. 10.9 Synthetics found in the inversion, explaining 60% of the variance of the data. The fundamental and the ten first overtones were taken in the normal modes summation and all the normal modes of these branches in the studied frequency window were taken. Note that the main characteristics of the waveforms are retrieved, as well as amplitudes

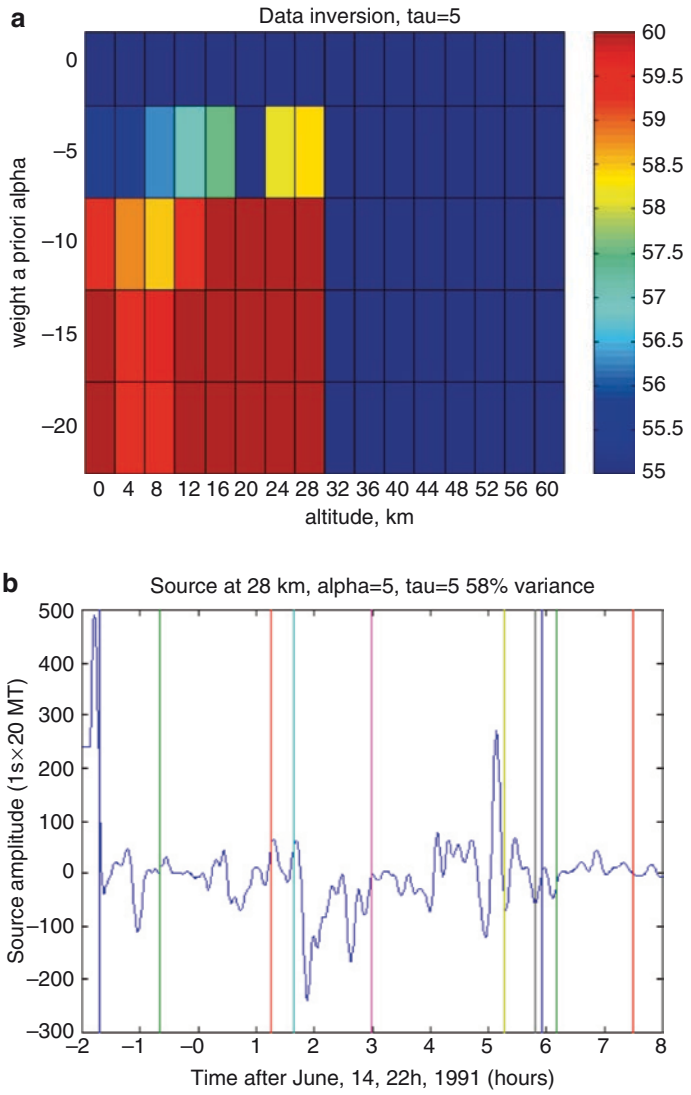

Fig. 10.10 (**a**) Variance reduction for a series of inversion, for different values of altitude, and weighting factor. The best sources are found either at the ground level in the atmosphere or at an altitude between 20 and 28 km corresponding to the altitude reached by the eruptions. (**b**) Source history for a surface pressure glut vs. time. Amplitude is in 20 MT of equivalent TNT times 1 s. The source is at 28 km of altitude, and when compared with the source solution for a shallow atmospheric source, the amplitude of the source is reduced by a factor 100 as well as the complexity of the source. The obtained source function is closer from a series of explosion, each of them of about 20–40 MT and with burst times of the order of 200–500 s. Vertical lines are associated to the reported eruption of the volcano and several fits with the burst found in the source function

high-altitude one, the amplitudes of the two different sources can be compared. The seismic moment of the source ranges between a minimum expressed as $M_0 = \tau_b (\gamma - 1) E$ (Lognonné et al. 1994), where γ is the adiabatic index of the atmosphere and τ_b the duration of the blast and $M_0 = 2\tau_b E$ when all the energy is released in kinetic energy, which might be the case for an eruption where most of the ejecta have a vertical velocity. As shown in Fig. 10.10b, reasonable amplitudes are found only for a source at 24–28 km of altitude, with most of the energy released at the time of the individual explosions. These releases of seismic moment are found near the reported date of the individual eruptions. These eruptions are associated to yields of about 4,000 MTs, corresponding to explosions releasing an energy of about 20 MT equivalent TNT during blast times of about 200–500 s, which corresponds to the order of magnitude of the Pinatubo eruption, whose energy is about 200 MT in several explosions. These results show that the seismic source of the Pinatubo eruption can be relatively well explained by a series of eruptions rather than the complex mechanisms proposed by the previous studies.

In a similar approach, Dautermann et al. 2008, 2009 have recently studied the Montserrat 2003 eruption associated to the explosive lava dome collapse of the Soufriere Hills volcano. Both signal in the ionosphere, associated to the acoustic wave and detected on the TEC GPS data, and signals in the ground, associated to the seismic waves and detected on strain sensors, have been recorded. As for Pinatubo, best results in the waveform fitting are achieved for a source in the atmosphere. Note however that in these cases, both the acoustic and seismic waves must be taken into account in the modeling, as the observations are to close for achieving a separation of the wavetrains, as it was the case for the remote seismic signals of the Pinatubo eruption.

10.3.2 Ionospheric–Atmospheric Coupling of Seismic Waves

Le us now consider the same coupling processes, but in the other propagating direction, i.e., from the Earth interior toward the Earth atmosphere. The classical example will here be a quake, generating seismic waves converted partially to atmospheric waves when the seismic wavefront reaches the Earth surface. In this process, only horizontal S waves, i.e., SH or Love waves, will not generate acoustic waves. All others will be converted and acoustic waves will therefore be launched in the atmosphere for the SV and P body waves and for the spheroidal surface waves, especially the fundamental Rayleigh ones.

The amplitudes of these waves are generally quite small at the Earth surface, as their amplitude, for vertically incident waves, is twice the amplitude of the seismic waves in the interior. The typical amplitude of the associated pressure wave in the atmosphere can be estimated by assuming a vertical propagation, which leads to

$$p = \frac{4\rho c \pi}{T} u \approx \frac{1,600}{T} u$$

for the typical values of the density and sound speed of the atmosphere at the ground level. This shows that even for 20 s surface waves of 1 mm amplitude, corresponding to the typical surface waves of large ($M_s > 8$) quakes at teleseismic distance, the pressure is a fraction of Pa. The same is observed for body waves: one second body waves of 1 cm/s^2, corresponding to the acceleration of a local and shallow 3.5 quake or to a Mercalli scale of II, generates amplitudes of 250 μm and pressure fluctuation smaller than 0.5 Pa. These amplitudes are one order of magnitude smaller than those of the records studied by Mikumo and Watada in the previous section , which correspond to large quakes (e.g., Ms > 8, such as the 2003 Tokachi-Oki earthquake studied by Watada et al. 2006). This shows the difficulties for observing signals for most of the quakes at the ground level and the importance of the amplification in the acoustic waves amplitudes observed when the latter propagate upward towards the ionospheric height, where they are amplified, thanks to the atmospheric density decay.

During more than four decades, the detected signals described above were more or less considered as some "funny" or "exotic" observation in seismology, unable to provide new valuable information, either on the source or on the internal structure of the Earth. However, we are now facing, with the development of new technologies in ionospheric sounding, or with the dense GPS networks progressive changes, which put a new light on these researches and start to point out possible seismological interests and applications.

Following the pioneering works done with analog Doppler sounder (Davies and Baker 1965; Leonard and Barnes 1965; Yuen et al. 1969), observations have been continuously made with improved performances (Namazov et al. 1975; Najita and Yuen 1979; Tanaka et al. 1984; Blanc 1985; Egorov et al. 1990; Parrot et al. 1993). The new generations of sounders, such as the Doppler sounder operated by CEA/DASE in France, can detect most of the earthquakes with M_s greater than 6.5 (Artru et al. 2004). They provide data very similar to seismograms in the sense that they measure directly the vertical motion of an ionospheric layer: both surface waves and body waves are detected in the ionosphere, including SV waves (see Fig 10.11). Many other Doppler sounders are in operation and have collected a large amount of data, especially after the large Sumatra quake with observations in Taiwan (Liu et al. 2004a,b), China (Hao et al. 2006) in addition to those in France. The fine analysis of these data, however, shows that the propagation of the signal at high altitudes is not well explained by acoustic propagation only and that the observed propagation velocities are much lower than the acoustic values (Artru et al. 2005). In Fig. 10.11, this might be observed when we compare the 1 min delay between the waveforms at 186 and 168 km, with the theoretical delay of about 30 s. The full understanding of these data will therefore need further works.

These Doppler instruments remain limited to a small number of point measurements and cannot resolve the 3D structure of the perturbation. Recent studies have therefore used Over-The-Horizon radars, which might provide maps of the ionospheric vertical displacements (Occhipinti 2006). Preliminary results show that the signal-to-noise ratio of these instruments is probably comparable with those obtained by Doppler sounders and that these instruments could therefore be a way

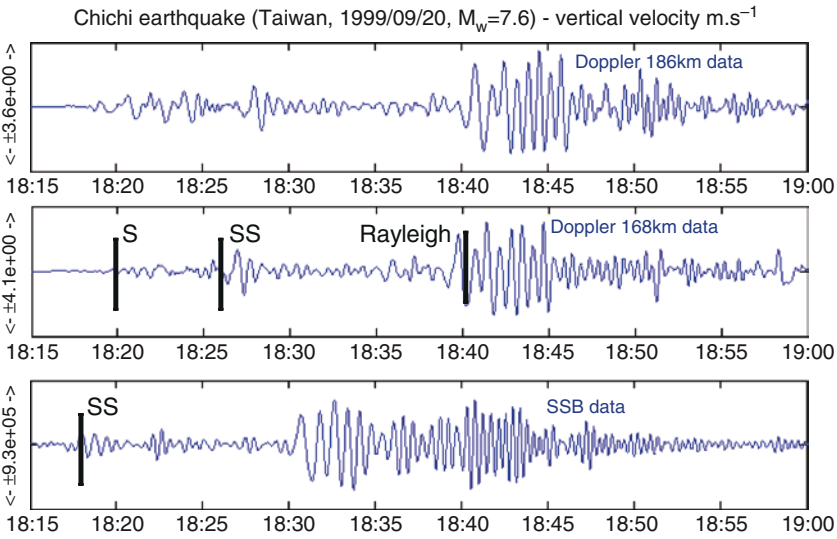

Fig. 10.11 Seismic surface waves after the $M_w = 7.6$ Chi-Chi earthquake (Taiwan, September 20, 1999) as measured on a ground seismometer (bottom panel) at the Geoscope station SSB (Saint-Sauveur, France) and on the CEA ionospheric Doppler sounding network (Francourville, France), corresponding to the vertical motion of ionospheric layers at altitudes 168 and 186 km. These two stations are located at 89.06 and 89.17° of epicentral distance. All traces show the vertical velocity perturbation in the 1–50 mHz frequency band. An amplification of 4.10^4 is observed between the ground and the ionosphere. The ~8 min delay between the ground and the ionosphere at 168 km of altitude corresponds to the propagation time of the acoustic wave. About 28 s are necessary from 168 to 186 km. Because of this delay, body waves are expected to arrive in the ionosphere at about 18 h20, 18 h26 for S and SS waves, respectively, while surface waves arrive at about 18 h39'30''. SV waves, due to SV-P conversion, are therefore possibly detected. Comparison with synthetics obtained with normal modes can be found in Artru et al. (2005). Adapted from Tanimoto and Artru (2007)

to provide dense measurements of the seismic wavefront, with sampling as low as 1 measurement per 25 km^2 over surface of several 10^6 km^2. Their use for scientific application remain, however, challenging.

Another approach is necessary. It can be based on electron density perturbation measurements performed by the GPS networks (see Mannucci 1998 for details on the ionospheric sounding with GPS and Lognonné et al. (2006) for a review on its seismic applications). The first seismic observations were performed by Calais and Minster (1995) after the 1994 Northridge earthquake ($M_s = 6.7$), who detected perturbations in the ionospheric total electron. Afraimovich et al. (2001) detected the acoustic shock waves associated with two earthquakes that occurred in Turkey in 1999. Ducic et al. (2003) have then used data from the dense California GPS networks and detected the ionospheric Rayleigh waves. As Najita and Yuen (1979), they were able to use the ionospheric perturbations for the computation of the group velocity of the long period

oceanic Rayleigh waves. The 3D structure of the Denali ionospheric signal was then characterized by Garcia et al. (2005a, b) and with such an approach, the comparison of signals from identical altitude can be performed. Figure 10.13 illustrates these 3D views of the ionospheric signal and confirms experimentally the maximum electron density altitude, when compared with Fig. 10.6.

The dense and denser GPS networks available around the world, especially in Japan, California, and USA and Europe, allow now numerous observations. Figure 10.12 shows one such example, following the shallow (depth = 27 km), Tokachi-Oki earthquake of September 25, 2003 (M_s = 8.3, latitude and longitude of 41.775°N et 143.904°E). We clearly see on this profile the transition at about 200 km of epicentral distance, between the acoustic waves, propagating mainly in the atmosphere with an acoustic velocity smaller than 1000 m/s, and the acoustic signature of the Rayleigh waves, with an apparent velocity corresponding to the Rayleigh surface waves (3,500 m/s).

Much more studies will probably be performed in the near future on the seismological analysis of these data: in addition to the group velocity measurement already done by Najita and Yuen (1979) and Ducic et al. (2003), we can in particular envisage new seismic source constrain, following the first studies done by Heki and Ping (2005), Kobayashi (2007) for the Tokachi-Oki 2003 quake and Heki (2006) for the large 2004 Sumatra quake.

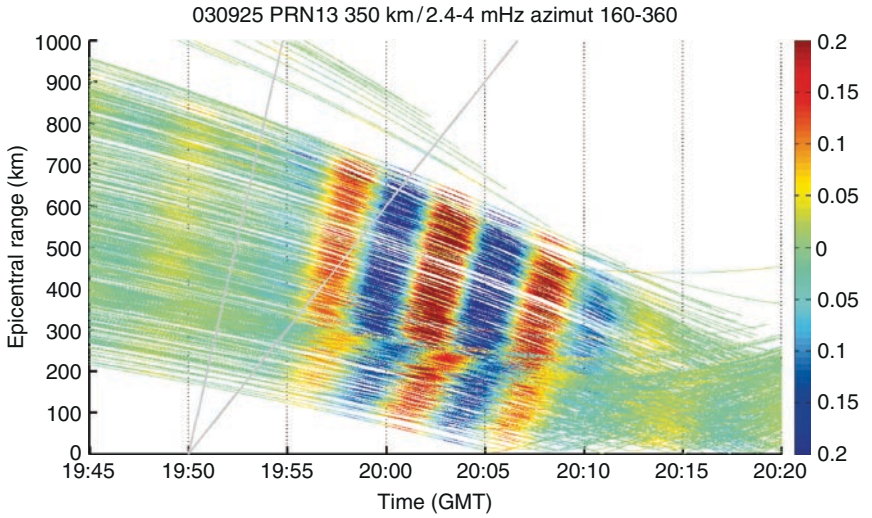

Fig. 10.12 Acoustic and Rayleigh waves detected by the Japanese Geonet GPS network after the Tokachi-Oki earthquake of September 25, 2003. Dates are filtered in the bandpass 2.4–4 mHz, where the atmospheric coupling is the largest. The two gray lines are hodochrons for waves propagating at 3.5 and 1 km/s from the source. Amplitudes are in TEC units. Up to about 300 km of epicentral distance, acoustic waves, propagating mainly in the atmosphere, are detected, while Rayleigh waves appear clearly at distances larger than 300 km

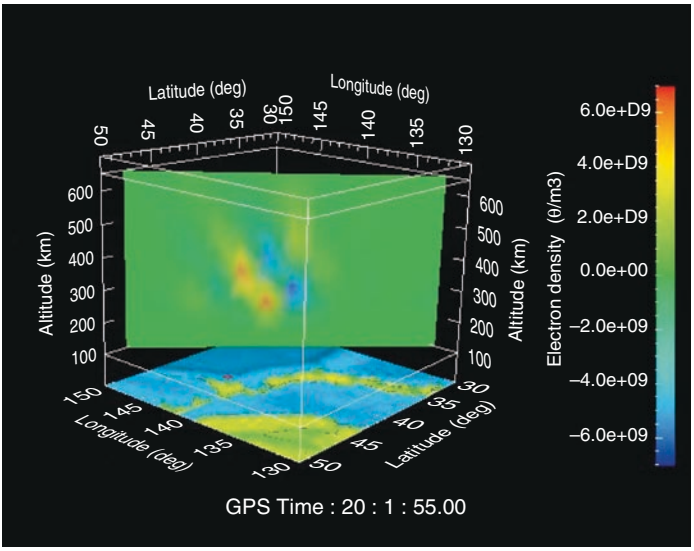

Fig. 10.13 Vertical cut of the 3D Rayleigh waves impact in the ionosphere for the Tokachi-Oki event. The Total Electronic Content amplitudes observed are typically 0.1 TECU peak-to-peak, but 3D local variations reach a few 10^9 e/m^3. No wavefront is observed with a north or northwest propagation direction, due to a poor coverage of the GPS satellite in these directions. The 3D reconstruction is done following methods of Garcia et al. (2005a) and Garcia and Crespon (2008)

10.4 Ionospheric–Atmospheric Coupling of Tsunami Waves

As for surface waves, early theoretical works in the 1970s predicted that atmospheric gravity waves are generated in the wake of a tsunami (Peltier and Hines 1976). About 30 min are needed for the gravity wave to develop its first maximum perturbation in the ionosphere (vs.~10 min for seismic–acoustic waves). But after this delay, the ionospheric perturbation follows the tsunami front and, as for the seismic waves, the atmospheric oscillations are amplified with altitude. It should be noted moreover that, due to their much shorter wavelength and period, the surface noise of ocean swell does not produce significant upward propagating waves in the atmosphere: the atmosphere acts as a filter, enhancing the long wavelength tsunami perturbation over other sources. Figure 10.14 shows the result of simulation, where the tsunami first generates an atmospheric gravity wave, which is then generating, through collisions between neutral atmosphere and ions, perturbations in the electronic density.

The first observation had however to wait almost 30 years. It was performed after the Peru, June 2001 tsunami (Artru et al. 2005). The tsunami arrival was observed on Japanese tide gauges between 20 and 22 h after the earthquake, with wave amplitudes between 10 and 40 cm (open ocean amplitude were estimated to be of 1–2 cm) and dominant periods of 20–30 min. Shortly after, a large ionospheric

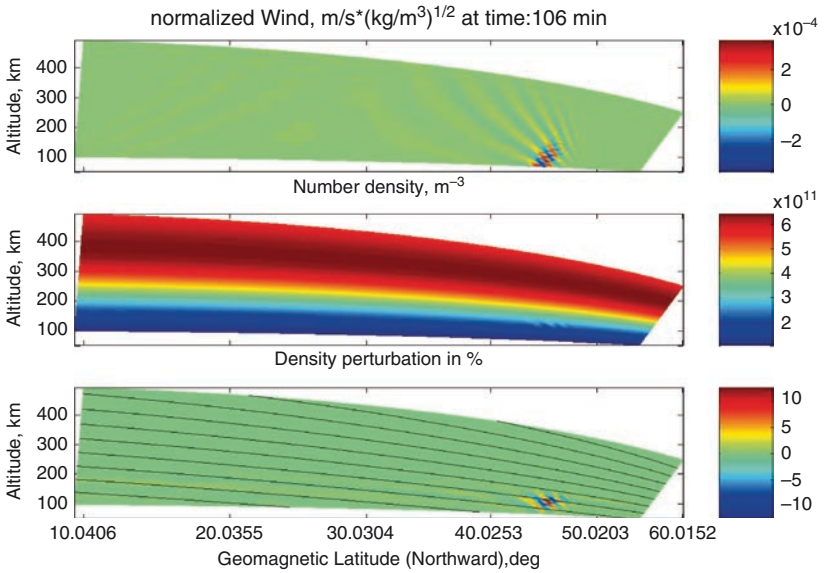

Fig. 10.14 Coupling between the neutral atmosphere gravity wave induced by a tsunami and the ionosphere. The tsunami amplitude has a 0.5 m amplitude and about 13 min period, corresponding to the amplitude of the Sumatra, 2004 tsunami. From top to below are the normalized neutral wind, and the absolute and relative electron density. This shows that large perturbations, reaching 10%, are generated by such tsunamis

perturbation was detected through a specific processing of data from the continuous GPS network in Japan (GEONET). The arrival time, orientation, wavelength, velocity of the wave packet observed are consistent with what is expected for a tsunami-induced perturbation.

The gigantic and dramatic Sumatra tsunami of December 2004 confirmed the possibilities of observing tsunami ionospheric signals, and signals were detected on the Total Electronic Content (TEC) measurement on-board the TOPEX/Poseidon and JASON satellites. The modeling of the ionospheric signal shows that both the waveform and the amplitude observed by Jason and Topex can be reproduced (Occhipinti 2006) when the magnetic field is taken into account (Occhipinti et al. 2008). Other observations were performed worldwide, either on GPS data in the India Ocean (Lognonné et al. 2006; DasGupta et al. 2006; Liu et al. 2004a, b; Otsuka et al. 2006) or even at the Aricebo facility (Lee et al. 2008). All these signals can be associated with the ionospheric perturbation associated to the propagating tsunami. These results confirm the interest of a real-time monitoring of the ionosphere, which could be carried out either with active microwave radar or by optical systems for airglow detection. They open new prospect for future tsunami warning techniques.

10.5 Exporting Remote Sensing Seismology on Venus?

Although on Earth, the technique described above would never provide the same quality of seismic data as a seismic network, they can be the unique way to obtain seismic data on planets too hostile for the deployment of long-lived seismic stations. Venus is the best example (Garcia et al. 2005b; Lognonné and Johnson. 2007). In addition, the coupling strength is proportional to the acoustic impedance of the atmosphere, equal to ρ_c where ρ is the density and c the acoustic speed. As the atmospheric density at the surface of Venus is about 60 kg/m^3 and the acoustic velocity is slightly higher (410 m/s) than on Earth, this leads to an acoustic impedance about 60 times greater than on Earth, where the atmospheric density is 1.2 kg/m^3.

Moreover, at 50 km of altitude, where the Venus pressure is comparable with Earth ground pressure, the decrease by almost two orders of magnitude of the density from its surface value leads already to an amplification of 10 of the waves. Consequently, Venus quakes will generate atmospheric infrasonic waves with amplitudes much larger than on the Earth surface (Fig. 10.15). This profitable effect gives an unique opportunity for a future Venus quakes detection by a satellite sounding the Venus ionosphere.

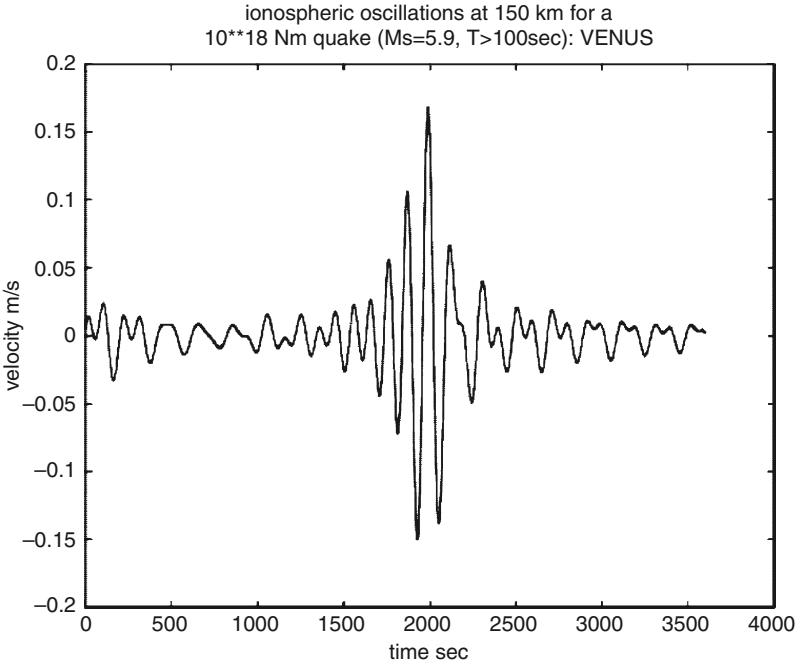

Fig. 10.15 Long period vertical atmospheric oscillations, for a 10^{18} Nm quake (M_w = 5.9) and for period larger than 100 s on Venus. Owing to the difference in the acoustic coupling at the ground, ionospheric signals at 150 km of altitude are about 100 stronger on Venus for the same magnitude and altitude than on Earth

10.6 Conclusion

A significant coupling between the acoustic and seismic waves is observed. This coupling is well understood theoretically. It generates remote seismic waves exited by large atmospheric sources and atmospheric and ionospheric signals coupled to the seismic wavefront. This coupling explains most of the signals recorded by the large volcano eruption, which occurred in the three last decades. It also explains the ionospheric signals, made available by the recent advance in the monitoring of small-scale perturbations of the ionosphere: Rayleigh waves, tsunami-induced gravity waves, and even seismic body waves generate signals, which can be observed by ionospheric sounding based on GPS network, Doppler sounder, OTH radars, and Spaceborne dual-frequency altimeter sounding. These new data open exciting prospects in seismology such as the remote sensing of the Rayleigh seismic wave fronts, especially over the ocean, where the deployment of dense seismic networks is the most challenging. These techniques might also provide in a future a high-resolution picture of the wavefront of body waves. These prospects are also very exciting for tsunamis, as the latter are extremely difficult to observe in the open ocean. The tsunami-generated atmospheric gravity waves have a clear impact on the ionosphere and can be detected by remote sensing systems. Other applications of this technique are also found in planetology, especially with interesting prospects in the remote sensing of quakes on Venus.

Acknowledgment I thank J.Artru, V.Ducic, F.Crespon, R.Garcia, A.Kherani, G.Occhipinti, and L.Rolland for their contributions to the development of the ionospheric seismology project in IPGP. L.Rolland, F.Crespon, R.Garcia, G.Occhipinti, and A.Kherani are acknowledged for providing some figures for this chapter. I thank T.Farges for making available Doppler data from CEA. This work was funded by CNES, ESA, and ANR. This is IPGP contribution 2549.

References

Afraimovich EL, Perevalova NP, Plotnikov AV, Uralov AM (2001) The shock-acoustic waves generated by the earthquakes. Annales Geophysicae 19:395–409

Artru J, Farges T and P. Lognonné (2004) Acoustic waves generated from seismic surface waves: propagation properties determined from Doppler sounding observation and normal-modes modeling. Geophys J Int 158:1067–1077

Artru J, P. Lognonné et E. Blanc (2001) Normal modes modeling of post-seismic ionospheric oscillations. Geophys Res Lett 28: 697–700

Artru J, Ducic V, Kanamori H, Lognonné P, Murakami M (2005) Ionospheric detection of gravity waves induced by tsunamis. Geophy J Int 160:840–848. doi: 10.1111/j.1365-246X.2005.02552.x2005

Astafyeva EI, Afraimovich EL (2006) Long-distance traveling ionospheric disturbances caused by the great Sumatra-Andaman earthquake on 26 December 2004. Earth Planets Space 58:1025–1031

Bilitza D (2001) International reference ionosphere 2000. Radio Science 36:261–275

Blanc E (1985) Observations in the upper atmosphere of infrasonic waves from natural or artificial sources: a summary. Annales Geophysicae 3(6):673–688

Calais E, Minster JB (1995) GPS detection of ionospheric perturbations following the January 17, 1994, Northridge earthquake. Geophys Res Lett 22:1045–1048

DasGupta A, Das A, Hui D, Bandyopadhyay KK, Sivaraman MR (2006) Ionospheric perturbation Observed by the GPS following the December 26th, 2004 Sumatra-Andaman earthquake, EarthPlanet. Space 35:929–959

Dautermann T, Calais E, Mattioli G (2008) GPS detection, modeling and energy estimation of the ionospheric wave caused by the 2003 explosion of the Soufriere hills volcano, Montserrat. J Geophys Res., 114, B02202, doi:10.1029/2008JB005722

Dautermann T, Calais E, Lognonné P, Mattioli GS (2009) Lithosphere-atmosphere-ionosphere coupling after the 2003 explosive eruption of the Soufriere Hills Volcano, Montserrat, Geophys J Int., 179, doi:10.1111/j.1365–246X.2009.04390.X

Davies JB, Archambeau CB (1998) Modeling of atmospheric and ionospheric disturbances from shallow seismic sources. Phys Earth Planet Inter 105:183–199

Davies K, Baker DM (1965) Ionospheric effects observed around the time of the Alaskan earthquake of March 28, 1964. J Geophys Res 70:1251–1253

Ducic VJ Artru and P. Lognonné (2003) Ionospheric remote sensing of the Denali Earthquake Rayleigh surface waves. Geophys Res Lett 30(18): 1951, doi:10.1029/2003GL017812

Dziewonski A, Anderson DL (1981) Preliminary reference Earth model. Phys Earth Planet Inter 25:297–356

Egorov DA, Elizar'ev IN, Novikov VM, Tarashchuk IE (1990) Effects of powerful earthquakes in the earth's ionosphere, Geomagnetizm i Aeronomiia 30:680–682

Forget F, Hourdin F, Fournier R, Hourdin C, Talagrand O, Collins M, Lewis S, Stephen R, Read PL, Huot J-P (1999) Improved general circulation models of the Martian atmosphere from the surface to above 80 km. J Geophys Res 104:24155–24176

Garcia R, Crespon F (2008) Radio tomography of the ionosphere: analysis of an under-determined, ill-posed inverse problem, and regional application. Radio Science 43, RS2014, doi:10.1029/2007RS003714

Garcia R, Crespon F, Ducic V, Lognonné P (2005) 3D ionospheric tomography of the Denali seismo-acoustic waves over California. Geophys J Int 163: 1049–1064, doi: 10.1111/j.1365-246X.2005.02775.x

Garcia R, Lognonné P, Bonnin X (2005b) Detecting atmospheric perturbations produced by Venus quakes. Geophys Res Lett 32:L16205. doi:: 10.1029/2005GL023558

Hao YQ, Xiao Z, Zhang DH (2006) Responses of the ionosphere to the Great Sumatra earthquake and volcanic eruption of Pinatubo. Chinese Phys Lett 23: 1955–1957

Heki K (2006) Explosion energy of the 2004 eruption of the Asama Volcano, central Japan, inferred from ionospheric disturbances Geophys Res Lett 33, doi: 10.1029/2006GL026249

Heki K, Ping J (2005) Directivity and apparent velocity of the coseismic ionospheric disturbances observed with a dense GPS array, Earth Planet. Sci Lett 236:845–855

Huba, JD, Joyce G, Fedder JA (2000) Sami2 is another model of the ionosphere (SAMI2): A new low-latitude ionosphere model. J Geophys Res 105: 23 035

Hunten DM, Colin L, Donahue TM (1983) Venus. Univ of Ariz. Press, Tucson, 1143

Kanamori H, Mori J (1992) Harmonic excitation of mantle Rayleigh waves by the 1991 eruption of mount Pinatubo, Philippines. Geophys Res Lett 19:721–724

Kanamori H, Mori J, Harkrider DG (1994) Excitation of atmospheric oscillations by volcanic eruptions. J Geophys Res 22:21947–21961

Kherani EA, Lognonné P, Kamath N, Crespon F, Garcia R (2009) Response of the ionosphere to the seismie trigerred acoustic waves: electron density and electromagnetic fluetautions. Geophy J Int 176:1–13. doi: 10.1111/j.1365-246X.2008.03818.x

Kiryushkin VV, Afraimovich EL (2007) Determining the parameters of ionospheric perturbation caused by earthquakes using the quasi-optimum algorithm of spatiotemporal processing of TEC measurements. Earth Planets Space 59:267–278

Kobayashi N (2007) A new method to calculate normal modes. Geophys J Int 168: 315–331

Lee MC, Pradipta R, Burke WJ, Labno A, Burton LM, Cohen JA, Dorfman SE, Coster AJ, Sulzer MP, Kuo SP (2008) Did Tsunami-Launched Gravity Waves Trigger Ionospheric Turbulence over Arecibo? J Geophys Res 113:A01302. doi:10.1029/2007JA012615

Leonard RS, Barnes RA Jr (1965) Observation of ionospheric disturbances following the Alaska earthquake. J Geophys Res 70:1250

Liu JY, Tsai YB, Chen SW, Lee CP, Chen YC, Yen HY, Changand WY, Liu C (2006a) Giant ionospheric distrubances excited by the M9.3 Sumatra earthquake of 26 December 2004. Geophys Res Lett 33:L02103

Liu J, Tsai Y, Ma K, Chen Y, Tsai H, Lin C, Kamogawa M, Lee C (2006b) Ionospheric GPS total electroncontent(TEC) disturbances triggered by the 26 December 2004 Indian Ocean tsunami. J Geophys Res 111:A05303. 52

Lognonné P (1991) Normal modes and Seismograms of an anelastic rotative Earth. J Geophys Res 96:20309–20319

Lognonné P, Clévédé E (2002) Chapter 10: Normal modes of the earth and planets, In: Kanamori H, Jennings P and Lee W (ed) Handbook on earthquake and engineering seismology, IASPEI Centennial Publications, International Geophysics series, 81A, Academic Press, New York

Lognonné P, Mosser B, Dahlen FA (1994) Excitation of the Jovian seismic waves by the Shoemaker-Levy 9 cometary impact. Icarus 110:186–195

Lognonné P, Clévédé C, Kanamori H (1998) Normal mode summation of seismograms and barograms in an spherical Earth with realistic atmosphere. Geophys J Int. 135:388–406

Lognonné P, Artru J, Garcia R, Crespon F, Ducic V, Jeansou E, Occhipinti G, Helbert J, Moreaux G, Godet PE (2006) Ground based GPS tomography of ionospheric post-seismic signal., Planet. Space. Science 54:528–540, doi: 10.1016/j.pss.2005.10.021

Lognonné P, Johnson C (2007) Planetary Seismology, in Treatrise in Geophysics, Shubert G (ed), Planets and Moon 10:69-122, Oxford : Elsevier Ltd., doi: 10.1016/B978-044452748-6.00154-1

Mannucci AJ (1998) A global mapping technique for gps-derived ionospheric electron content measurements. Radio Science 33:565–582

Najita K, Yuen P (1979) Long-period Rayleigh wave group velocity dispersion curve from HF doppler sounding of the ionosphere. J Geophys Res 84:1253–1260

Namazov SA, Novikov VD, Khmelnitskii IA (1975) Doppler frequency shift in ionospheric propagation of decametric radio waves. Radiofizika 18:473–500

Occhipinti G (2006) Observations multi-parametres et modéelisation de la signature ionosphérique du grand séisme de Sumatra, Ph.D.Thesis, Institut de Physique du Globe de Paris, December 2006

Occhipinti G, Lognonné P, Kherani E, Hébert H (2006) 3D Waveform modeling of ionospheric signature induced by the 2004 Sumatra tsunami. Geophys Res Lett 33: L20104, doi: 10.1029/2006GL026865

Occhipinti G, Kherani EA, Lognonné P (2008) Geomagnetic dependence of ionospheric disturbances induced by tsunamigenic internal gravity waves. Geophys J Int 753–755:173. doi: 10.1111/j.1365-246X.2008.03760.x

Ostrovsky LA (2008) Ionospheric effects of ground motion: The roles of magnetic field and nonlinearity. J Atmos Solar-Terrest Phys 70:1273–1280

Otsuka Y, Kotake N, Tsugawa T, Shiokawa K, Ogawa T, Effendy SS, Kawamura M, Maruyama T, Hemmakorn N, Komolmis T (2006) GPS detection of total electron content variations over Indonesia and Thailand following the 26 December 2004 earthquake. Earth Planets Space 58:159–165

Parrot M, Achache J, Berthelier JJ, Blanc E, Deschamps A, Lefeuvre F, Menvielle M, Plantet JL, Tarits P, Villain JP (1993) High-frequency seismo-electromagnetic effect. Phys Earth Planet Int 77:65–83

Peltier WR, Hines CO (1976) On the possible detection of tsunamis by a monitoring of the ionosphere. J Geophys Res 81(12):1995–2000

Picone JM, Hedin AE, Drob DP, Aikin AC (2002) NRLMSISE-00 empirical model of the atmosphere: statistical comparisons and scientific issues. J Geophys Res 107(A12): 1468, doi:10.1029/2002JA009430

Tanaka T, Ichinose T, Okuzawa T, Shibata T, Sato Y, Nagasawa C, Ogawa T (1984) HF-Doppler observation of acoustic waves excited by the Urakawa-Oki earthquake on 21 March 1982. J Atmo Terr Phys 46(3):233–245

Tanimoto T, Artru J (2007) Interaction of Solid Earth, Atmosphere, and Ionosphere. Treatrise geophysics, Shubert G (ed), Earthquake seismology 4:421–44

U.S. Standard atmosphere (1976) Committee on the extension to the Standard atmosphere, U.S. Goverment printing office, Washington DC

Watada S (1995) Part 1: Near source acoustic coupling between the atmosphere and the solid Earth during volcanic erruptions, Ph.D. thesis, California Institute of Technology

Watada S, Kunugi T, Hirata K, Sugioka H, Nishida K, Sekiguchi S, Oikawa J, Tsuji Y, Kanamori H (2006) Atmospheric pressure change associated with the 2003 Tokachi-Oki earthquake. Geophys Res Lett 33:L24306

Weaver PF, Yuen PC, Prolss GW, Furumoto AS (1970) Acoustic coupling in the ionosphere from seismic waves of the earthquake at Kurile Islands on August 11, 1969. Nature 226:1239–1241

Webb SC (2007) The Earth's "hum" is driven by ocean waves over the continental shelves. Nature 445:754–756

Widmer R, Zürn W (1992) Bichromatic excitation of long-period Rayleigh and air waves by the mount Pinatubo and El Chichon volcanic eruptions. Geophys Res Lett 19:765–768

Woodhouse JH, Dziewonski AM (1984) Mapping of the upper-mantle: three dimensional modeling of Earth structure by inversion of seismic waveforms, J. Geophys. Res 89:5953–5986

Yuen PC, Weaver PF, Suzuki RK, Furumoto AS (1969) Continuous traveling coupling between seismic waves and the ionosphere evident in May 1968 Japan earthquake data. J Geophys Res 74:2256–2264

Zürn W, Widmer R (1996) Worldwide observation of bichromatic long-period Rayleigh-waves excited during the June 15, 1991 Eruption of Mt. Pinatubo. In: Newhall C, Punongbayan R (ed) Fire and Mud, Eruptions of Mount Pinatubo, Philippines, Philippin Institute of Volcanology and Seismology, Quezo City and University of Washington Press, pp. 615–624

Chapter 11
Acoustic-Gravity Waves from Impulsive Sources in the Atmosphere

D.O. ReVelle

11.1 Atmospheric Modeling and the Acoustic-Gravity Wave (AGW) Spectrum

11.1.1 Introduction to the Atmospheric Medium

The atmosphere is a very complex fluid medium composed of a mixture of compressible gases in a well-mixed (turbulent, but time-varying state) whose detailed parameters vary substantially with altitude above the planetary surface and whose detailed properties can be modeled as being in a state of exact hydrostatic balance for sufficiently large horizontal spatial scales (where the vertical pressure gradient acceleration balances the local acceleration due to gravity along a surface of constant geopotential) as well as *perfect* or *ideal* (free from the influence of van der Waal forces, etc.) at progressively greater geopotential heights (Chapters de Groot-Hedlin et al. 2010; Hauchecorne et al. 2010; Lott and Millet 2010). (It is in fact well known to be composed of the diatomic molecules nitrogen and oxygen at sufficiently low altitudes.) It is also assumed to be in a state of near-geostrophy, i.e., where the flow Rossby number (or where the ratio of the inertial acceleration to the Coriolis acceleration $\cong 0$). These quasigeostrophic horizontal winds themselves are systematically driven by the solar heating differences between the equator and the pole, and their magnitude depends upon the magnitude of the mean, north–south temperature gradients. Over fairly uniform or level terrain, the planetary surface drives convective cells, etc. whose physical effects drive our tropospheric weather patterns, but these properties can also vary substantially due to Planetary, Rossby-gravity, and acoustic-gravity waves (AGWs) generated by mountainous terrain and by ocean–land temperature contrasts, etc. Above about 85 km (depending on latitude, etc.) photoionization and photodissociation readily occurs, and this well-mixed state gives way to a time-varying partially ionized fluid whose properties are dominated

D.O. ReVelle
Geophysics Group, Earth and Environmental Sciences Division, Los Alamos National Laboratory, Los Alamos, NM, 87545, USA
e-mail: revelle@lanl.gov

A. Le Pichon et al. (eds.), *Infrasound Monitoring for Atmospheric Studies,*
DOI 10.1007/978-1-4020-9508-5_11, © Springer Science+Business Media B.V. 2010

by a so-called diffusive separation regime (above the turbopause) with lighter fluids overlaying heavier fluids, i.e., with hydrogen at the outer edge of interplanetary space on top of helium, etc., as the earth's upper atmosphere merges with the outer atmosphere of the sun. At such high altitudes, the atmosphere is nearly isothermal, whereas deeper down in the middle atmosphere the solar heating effects are dominant, and nonisothermal atmospheric effects are very important. These nonisothermal heating effects such as the absorption of incoming solar radiation by ozone near the boundary between the stratosphere and the mesosphere, for example, lead to the formation of vertical sound channels (ducts) of which the atmosphere with horizontal winds possess two such primary channels and numerous subsidiary subducts channels when perturbations in the adiabatic, thermodynamic sound speed (Thompson 1972) are also considered. Furthermore, because of longitudinal irregularities within the atmosphere and its irregular degree of heating, etc., these effects can also vary systematically with horizontal range leading to the concept of range-dependent media, "leaky" waveguide modes, the formation of caustics (from optics indicating focused "burning" regions), etc. In addition, however, fundamental traveling atmospheric phenomena such as traveling cyclones/anticyclones have highly variable horizontal and vertical structure. This structure is also clearly evident in the prevailing horizontal scales in the observed atmospheric temperature and wind fields, etc. Thus, it is extremely natural, and not at all the exception for the atmosphere to have a range-dependent structure. In addition, because of the spherical planet geometry, only half of the available surface area is illuminated by the Sun at any time, which also naturally leads to nonsteady state flow conditions, etc.

When modeling the physical properties of waves emanating from such a complex system, it is obviously not possible to fully account for all these effects simultaneously. Many of these complicated properties can nonetheless be accounted for in varying limits as noted, for example, by Beer (1975), Fleagle and Businger (1980), Gill (1982), Mihalas and Weibel-Mihalas (1999), Thompson (1972) and by Tolstoy (1973) which the reader is invited to consult for further details than can be provided herein.

11.1.2 Key Environmental Parameters: Temperature/Sound Speed and Horizontal Wind Speed

We present below examples of vertical profiles of temperature and of zonal and meridional winds in the atmosphere. These profiles are those indicative of the region near the country of Paraguay on September 15, 2007. This is the date of the entry of the extremely important event, the Carancas meteorite fall and associated cratering record in the high Peruvian Andes as will also be subsequently discussed later on in much greater detail. The profiles in Figs. 11.1–11.3 nonetheless serve to point out the overall waveguide ducting features of the midlatitude atmosphere (in this specific case, a set of atmospheric structure parameters more typical of the Southern hemisphere at the time of the Autumnal equinox).

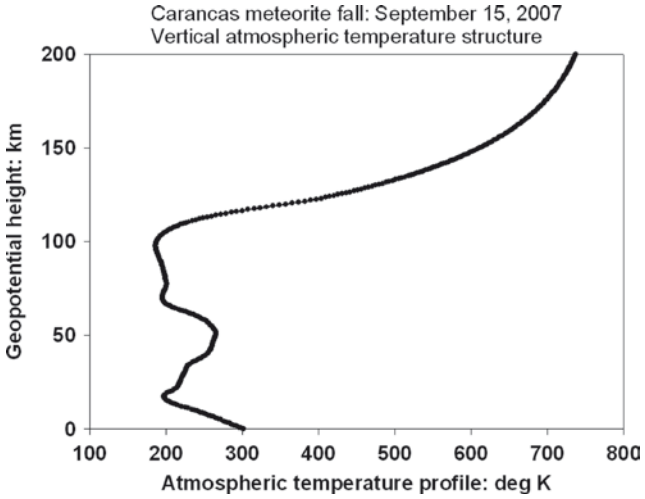

Fig. 11.1 Air temperature as a function of geometric height

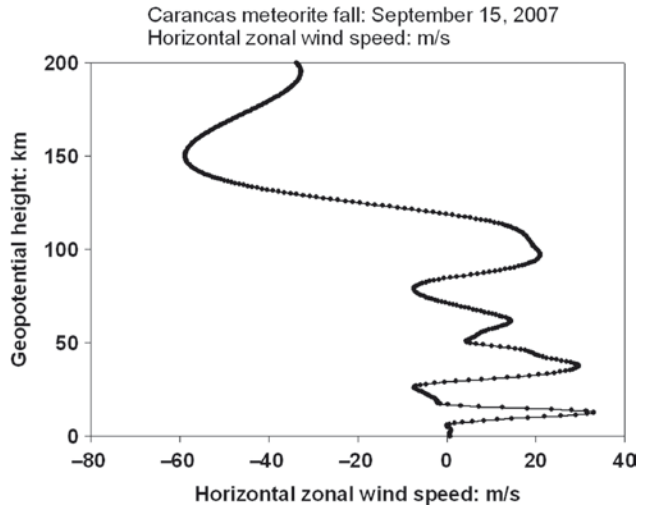

Fig. 11.2 Zonal wind speed as a function of geometric height

In Fig. 11.1, the characteristic behavior of the expected temperature structure can readily be observed, which exhibits a peak value near the ground and again in the vicinity of the stratopause (~50–60 km aloft). Similar structure is also found for the adiabatic thermodynamic sound speed profile, which is derivable from the temperature and the mean molecular weight structure (which is nearly a constant independent of height up to ~85–90 km). In Fig. 11.2, the characteristic zonal wind (east-west) component of the atmosphere is also readily observable,

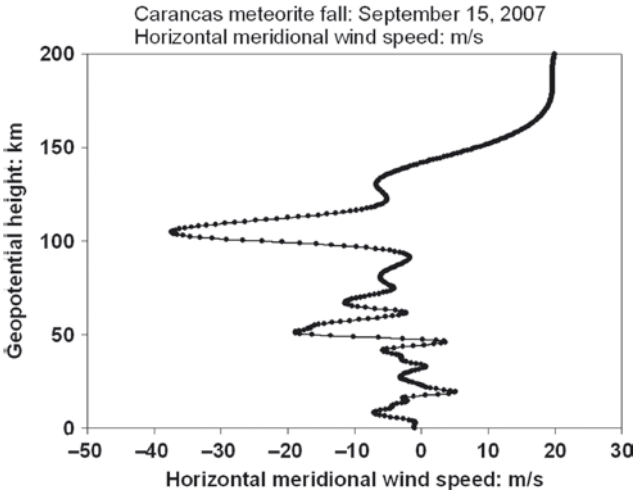

Fig. 11.3 Meridional wind speed as a function of geometric height

which can be expressed in terms of a type of atmospheric jet stream with the approximation that air density times the wind speed is approximately a constant (geostrophy) across vertical regions where the north-south temperature gradient does not change its sign. This behavior was recognized many years ago through a relationship called Egnell's law for the troposphere. In modern terminology, we recognize this behavior through the thermal wind law of meteorology (Gill 1982). From this figure, both the polar tropospheric jet stream at 10–20 km aloft and the polar night jet stream at heights from 40 to 60 km aloft can be readily observed. Finally, in Fig. 11.3, the meridional wind (north-south) component is also plotted. It is generally quite weak in middle latitudes of the earth's atmosphere, except briefly at ~50 and ~100 km. These figures were all generated from data that were extracted from the United Kingdom Meteorological Office (UKMO) for the region transecting Paraguay at the time of fall of the Carancas meteorite and crater-forming event on September 15, 2007.

11.1.3 AGW Resonant Frequencies and Relevant Spatial Scales

The atmosphere has a number of resonant frequencies and also a discrete set of limits that are useful for studying its behavior under varying conditions. In Fig. 11.4, a highly simplified schematic cartoon for AGW sources and the corresponding

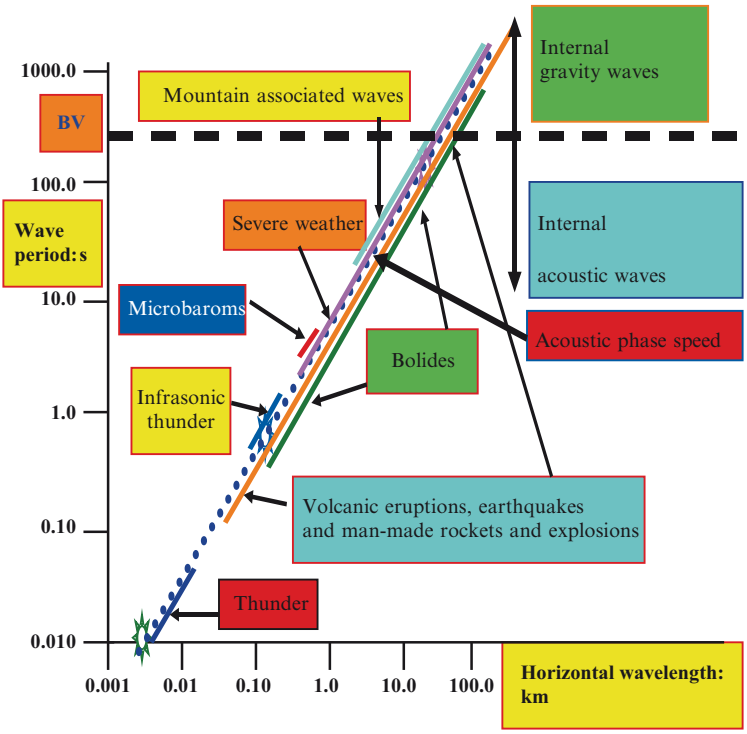

Fig. 11.4 Atmospheric wave sources and regimes

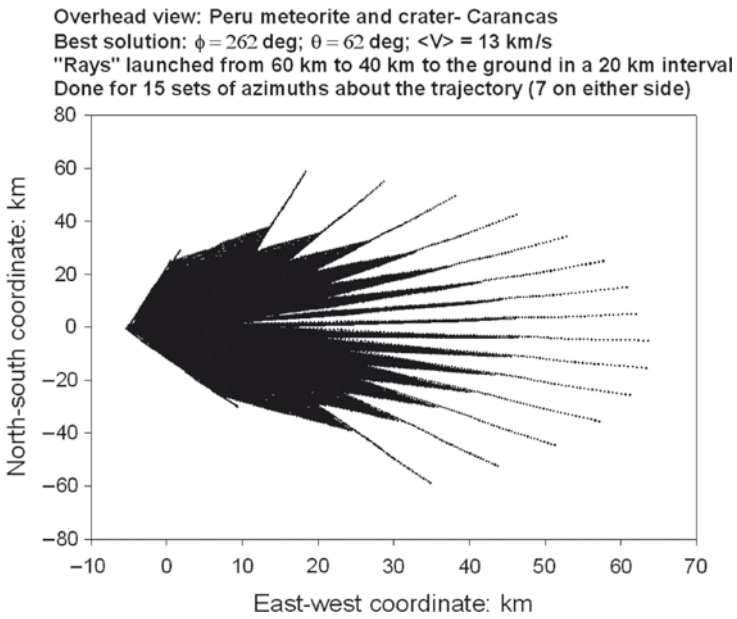

Fig. 11.5 Top view of wave normal paths: θ = 62 deg

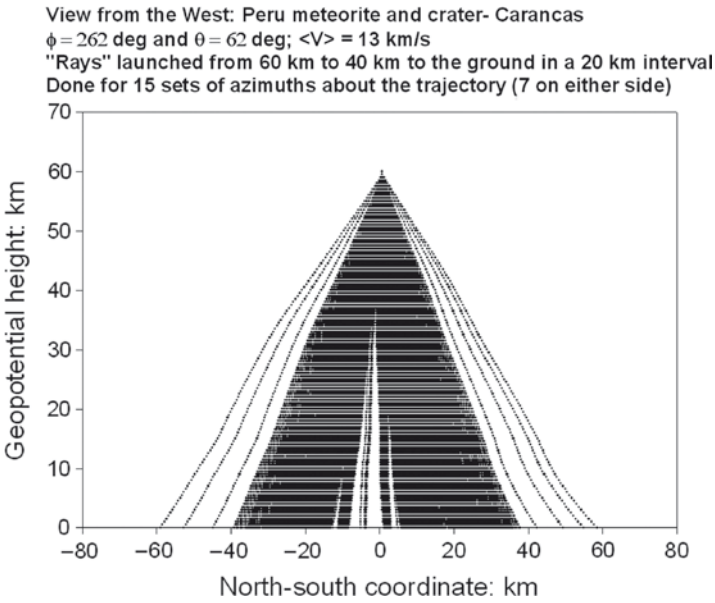

Fig. 11.6 θ = 62 deg: Side view of wave normal paths (viewed from the west)

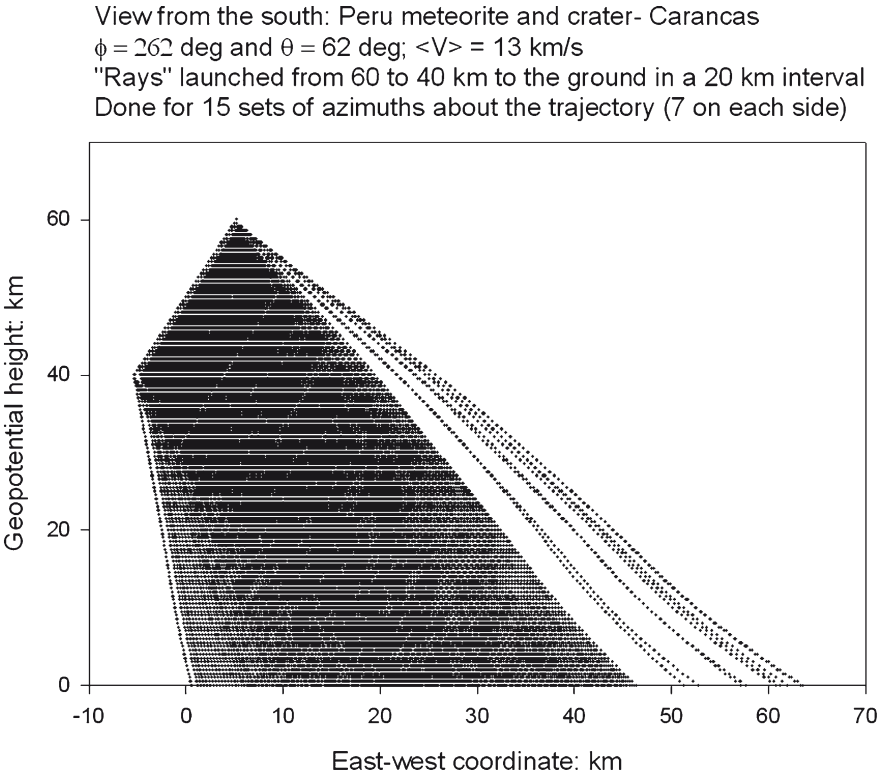

Fig. 11.7 θ = 62 deg: Side view of wave normal paths (viewed from the south)

propagation limits in the atmosphere for a number of atmosphere impulsive sources are plotted.

In middle latitudes where the Coriolis parameter f is $\sim 10^{-4}\,s^{-1}$, the lower period limit (using the longest period, τ, where $\tau = 1/f \sim 10^4$ s) of AGW constructed on a tangent plane in Cartesian coordinates is provided through a self-consistent scaling process by f, as long as fundamental periods that are multiples of the earth's rotation rate as is the case for atmospheric tidal oscillations are also ignored. Additional higher frequency resonant periods where significant amplification of signals is expected, if the atmosphere is driven sufficiently intensely at these frequencies, are the Brunt-Vaisalla (BV) frequency (ω_{BV}) and the atmospheric acoustic waveguide resonant (cut-off) propagation frequency (ω_{ac}). Precise physical definitions of these frequencies are presented in ReVelle (2004, 2005) and thus are not repeated here.

In Fig. 11.4, a highly oversimplified plot of the period (in s) of AGW disturbances vs. their horizontal wavelength scales (in km), it is readily observed that there is actually a complex atmospheric wave zoo composed of numerous zoo (source) members. To be certain that the waves of interest are related to specific impulsive atmospheres sources, we may in fact need additional ancillary information such as detections by additional methods, some of which may not be wave-like in nature or detections in media other than air, for example. In this figure, we have only indicated the presence of the Brunt-Vaisalla frequency (labeled as BV) with internal acoustic waves at frequencies below the BV and internal gravity waves also possible above the BV.

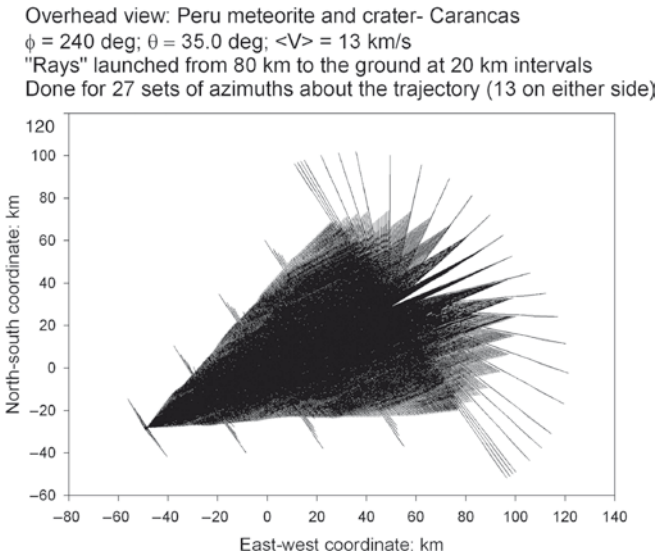

Fig. 11.8 Top view of wave normal paths: θ = 35 deg

Finally, a key measure of the greatest perturbative horizontal scale as a direct result of the impulsive energy deposition process can also be determined by the evaluation of the Barotropic/baroclinic Rossby deformation radius, a key quantity in Meteorology and Atmospheric Dynamics (Fleagle and Businger 1980) that allows an evaluation of the speed of shallow water waves (for long wavelength waves propagating in a fluid medium of constant, i.e., homogeneous density) divided by the Coriolis parameter, f (with the inverse of f also called the atmospheric inertial frequency) or

$$\Lambda = (gH)^{1/2}/f \tag{11.1}$$

where g = acceleration due to gravity, H = fluid depth, likely comparable to the pressure scale height (~7 km), $f = 2 \cdot \Omega \cdot \sin\phi$ = Coriolis parameter (or the atmospheric inertial frequency), $\Omega = 7.292 \times 10^{-5}$/s = earth's solid body rotation rate, and ϕ = latitude

This parameter can be of fundamental importance in examining the effects of geostrophic adjustment processes in the atmosphere due to various types of wave generation by flow over mountains or other perturbative meteorological forcing mechanisms. The process of *geostrophic adjustment* (see for example, Klostermeyer 1976) is also one which also generates Lamb waves as will be discussed in detail for impulsive sources below. Knowledge of this fact allows atmospheric scientists a tool needed to help separate the myriad parts of the atmospheric wave zoo. The Rossby deformation radius provides a measure of the horizontal distance scale over which natural Lamb waves are generated meteorologically and can also indicate plausible directions of wave generation for a specific type of meteorological source. The Rossby radius is a measure of the horizontal scale over which the height field adjusts during the return to an exact state of geostrophic balance after the atmosphere has been perturbed by an external forcing agent.

11.2 Atmospheric Wave Kinematics, Path Dynamics, and Inviscid Energetics

11.2.1 Underlying Physical AGW Regimes

Waves are ubiquitous within all realms of the geophysical environment, and their successful monitoring and interpretation demands that they be properly analyzed to gain full knowledge of their detection time(s) of arrival, as well as locating and characterizing the source region. Atmospheric waves and their wave zoo as discussed earlier and as analyzed in this chapter are a only a small portion of the numerous geophysical phenomena that can be detected within the atmosphere, in the oceans hydroacoustically, using seismic techniques in the lithospheric environment and at the corresponding boundary regions between these various media. It should also

be remembered that the geophysical monitoring of these waves and their sources should be done with full knowledge of the corresponding limitations in terms of analysis assumptions, assumptions regarding the physical state of the propagation medium and its interfacial boundary conditions, various measurement errors, array antenna receiving characteristics, atmospheric synoptic-scale and mesoscale meteorological conditions at the surface and aloft, effects of background noise levels due largely to turbulence on the reliability of the detections, etc. With proper care, it has been previously shown that a large number of sources in the atmospheric wave zoo can be readily identified and rapidly characterized using the numerous techniques now available to analysts of geoacoustic phenomena as will be discussed below.

11.2.1.1 Modeling Approaches for AGWs

The types of modeling approaches used for propagation of AGWs include "ray" or wave normal theory (geometrical acoustics), normal mode waveguide (full wave) theory, Ray-mode theory (see for example Tindle and Guthrie 1974; Jensen et al. 1994), and also various numerical integration techniques, etc. Unlike ray theory, which is typically used only to predict the paths of acoustic disturbances, and waveguide mode theory, which is typically used only to predict AGW amplitudes, ray-mode theory defines the geometrical properties of a normal mode and is used to formally predict the paths of AGWs in terms of its excited normal modes.

The wave normal "ray" tracing equations or geometrical "particle" acoustics (in the nondissipative limit) can be justified by using the size parameter, S, as defined in Optics. If we define:

$$S = 2\pi\{r/\lambda\}, \tag{11.2}$$

where r = "obstacle scale" redirecting the wave, λ = wavelength (at the maximum amplitude of the wave), then we can identify at least three unique physical propagation regimes in terms of S and identified as:

(a) $S >> 1$, Geometrical acoustics
(b) $S \sim O(1)$: Wave diffraction regime
(c) $S << 1$: Wave scattering regime

Furthermore, we can also define the ray vs. a modal transition distance for a horizontally uniform, nonleaky waveguide (Ceplecha et al. 1998):

$$R_{rm} = 2H^2/\lambda \tag{11.3}$$

where H = vertical duct thickness, Then, the current range, R is to be compared with R_{rm} so that if:

(a) $R < R_{rm}$, Geometrical acoustics is applicable (more "rays" than modes exist), whereas if
(b) $R > R_{rm}$, Full wave theory is applicable (more modes than "rays" exist).

11.2.2 Wave Normals and Ray Paths: Tracing the Trajectories of Infrasonic Waves

There are two geometric acoustics kinematic invariants in a horizontally stratified, steady, range-independent medium, namely ReVelle (2004, 2005); (Norris et al. 2010; Gainville et al. 2010):

(a) Wave normal heading angle, ϕ, as defined at the source: ϕ = constant
(b) Characteristic velocity (Snell's law constant), K = constant

We can further subdivide the source types as follows:

(i) For stationary point (nonmoving) sources (for all possible azimuths):

$$K(z) = (c_s/\cos\theta'), \tag{11.4}$$

where θ' = Wave normal launch angle with respect to the local horizontal

(ii) For moving line sources (of effectively infinite speed):

(1) If $V(z) >> c_s$: Hypersonic flow regime:

$$K(z) = (c_s/\sin\theta) \bullet \{\sin^2\theta' + (1–2 \bullet (\Delta\phi/\pi))^2 \bullet \cos^2\theta\}^{½}, \tag{11.5}$$

where θ = Horizontal entry angle of the bolide

(2) For $V(z) > c_s$: Supersonic flow or for supersonically moving point source:

$$K(z) = c_s(z) \bullet V(z) / \{\,|\,(V^2(z) - c_s^2(z))^{½} \bullet \sin\theta - c_s(z) \bullet \cos\theta\,|\,\} \tag{11.6}$$

The aforementioned treatment neglects nonlinear refraction within R_o of the trajectory as recently discussed in Brown et al. (2007).

If steady-state winds are included in the aforementioned treatment, the term, $|V_H| \bullet \cos(\phi - \psi(z))$ must also be added to the right hand side of the various expressions for $K(z)$. In this significant correction term, $|V_H|$ is the magnitude of the horizontal wind speed at any height and the term involving $\cos(\phi - \psi(z))$ represents the projection of the wave vector direction onto the prevailing synoptic-scale wind direction. The characteristic velocity of the "ray" as defined at the source should remain constant during propagation (under the assumed set of circumstances) and thus be observed as the wave trace velocity across the observing array. Similarly, the wave heading should remain constant and be measurable at the observer as well.

The equations needed to describe the propagation paths of "linearized" high-frequency AGWs in a horizontally stratified, range-independent, steady-state atmosphere can be written in the individual x, y, and z group velocity component form (ReVelle 2004, 2005):

$$c_{gx}(z) = dx/dt = c_s(z) \bullet \{\alpha\sin\phi - \beta\cos\phi\} + u(z) + d\phi/dt \bullet y \tag{11.7a}$$

$$c_{gy}(z) = dy/dt = c_s(z) \bullet \{\alpha\cos\phi + \beta\sin\phi\} + v(z) - d\phi/dt \bullet x \tag{11.7b}$$

$$c_{gz}(z) = \mathrm{d}z/\mathrm{d}t = \pm c_s(z) \bullet \gamma + w(z), \tag{11.7c}$$

where

$c_s^2 = \{\gamma \cdot p / \rho$

$c_s = f \bullet \lambda$

f = wave frequency, λ = wavelength, c_s = Adiabatic, thermodynamic phase velocity of acoustical waves, $\{u, v, w\}$ = Zonal, meridional and vertical wind components (time- and space-averaged values)

Equations (10a–10c) have been expressed in terms of the associated direction cosines:

$$\alpha = \cos\theta \tag{11.8a}$$

$$\gamma = \sin\theta \tag{11.8b}$$

which are subject to the summation condition:

$$\alpha^2 + \beta^2 + \gamma^2 = 1 \tag{11.8c}$$

so that $\beta \equiv 0$ for a wave system that is exactly planar.

In the system of equations subsequently being solved below, locally plane waves were assumed with the wave propagation angle θ measured upward from the local horizontal and where ϕ = Wave normal heading angle (measured clockwise from geographic North).

We have considered following (ReVelle 2004, 2005) the possible cases for wave normal tracing:

11.2.2.1 Meteoroid Wave Source Models: "Airwave" Objects

(a) Idealized line source model for an infinite velocity bolide (no deceleration): The Mach cone half angle $\equiv 0°$ so that only a highly direction cylindrical radiation pattern of AGWs is envisioned. This pattern is so directional that bolides entering steeply will have much of their wave energy refracted upward away from the ground.

(b) Modified line source (due to fragmentation effects): There can be significant local ripples in the wave front from fragmentation along the entry path similar to what is found along the tortuous path for ordinary thunder following lightning discharges. In the extreme gross-fragmentation limit, a "leading head emission" for a rapidly moving point source (with radiation generated as quasi-spherical waves) can be envisioned ahead of the trailing regime of an extremely narrow type (a) line source Mach cone.

(c) Supersonic source: Nonzero Mach cone half angle whose value depends on the local sound speed and on the instantaneous meteoroid velocity. In this case, significant deceleration will have occurred and an extremely complicated acoustic radiation and subsequent atmospheric spatial refraction pattern can result.

(d) Supersonic source: Nonzero Mach cone half angle whose value depends on a constant local sound speed (isothermal atmosphere approximation) and on a single average meteoroid velocity over the entire entry.

Data generated by bolides during hypersonic entry into the earth's atmosphere were not anticipated by the early military monitoring networks and came to be known as "airwave" objects (ReVelle 1997). All the early historical records, if it is desirable to trace their detailed origins, are indicated using this naming, which was likely invented by Shoemaker (deceased, but previously at the U.S. Geological Survey, Flagstaff, AZ) and also by Gault (deceased, but previously at the NASA Ames Research Center, Mountain View, CA).

Also, as discussed in ReVelle (1976; 2001), there is a minimum infrasonic detection threshold for bolides corresponding to a blast radius >~5–10 m (Edwards et al. 2008). This corresponds to a minimum peak panchromatic luminosity for a bolide (normalized to a geometric height of 100 km as observed in the zenith and ranging from ~−5 to −6 or brighter) in order to be detectable at ground level by an array of conventional pressure wave sensors.

In addition, the above-mentioned equations can also be used to evaluate the physical development of point and line caustics (due to refractive wave focusing processes) in the atmosphere in the atmospheric propagation environment.

Strictly speaking, the $d\phi/dt$ terms mentioned earlier are all exactly zero in a range independent medium, but we have included them here for completeness sake. We have also included β terms for the possibility of locally nonplane waves. Integration of these equations in a specified medium allows the resulting wave normal paths to be identified. The paths of these "wave normals" (not the corresponding "rays") are Galilean invariant and are the proper quantities to be evaluated. Note that in a windless medium, the ray and wave normal definitions are totally equivalent.

The wave normal paths can be readily identified if we assume an instantaneous source (so that a matching of the wavefront phase with the individual source altitudes can readily be made) and the type of explosion event, i.e., a moving point vs. a line source form for $K(z)$, etc. The basic difference between the two extreme limits of the characteristic velocity is that the infinite speed line sources are very directional unlike the stationary point source problem in which all "ray" launch directions are possible.

As discussed in Revelle (1976, 1997), the launched acoustic wave normal must also satisfy the waveguide conditions in order for long distance ducting of the signal to occur, i.e., $K > c_{\text{eff}}(z=0)$ between the ground and various layers aloft in the earth's atmosphere (Ceplecha et al. 1998). Here, $c_{\text{eff}}\,(z=0)$ is the effective horizontal sound speed at the ground, including the effects of the horizontal winds.

11.2.3 Resulting Wave Normal Paths

In Figs. 11.5–11.11, various views of the expected wave normal paths for the case of the fall of the Carancas meteorites on September 15, 2007, over northeastern

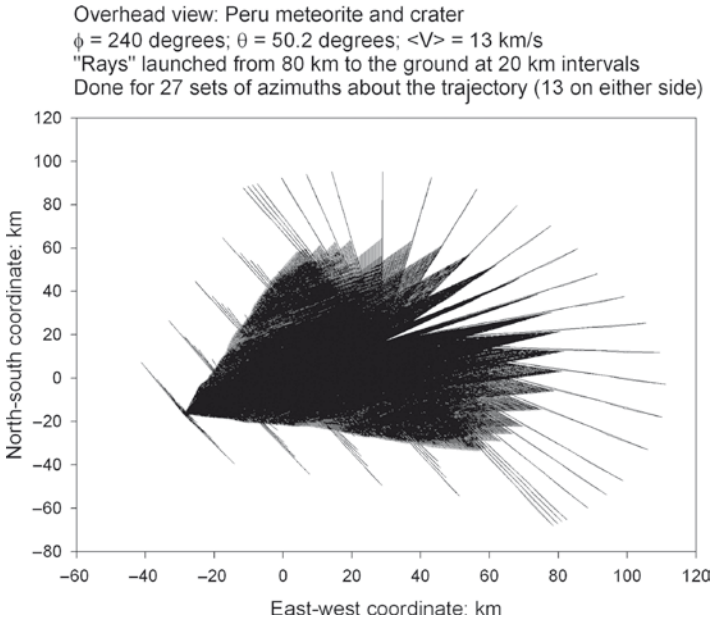

Fig. 11.9 Top view of wave normal paths: θ = 50.2 deg

Peru have been computed. In these computations, source model (d) (supersonic motion with a nonzero Mach cone angle that is constant in an isothermal atmosphere but, in this case, with realistic horizontal winds) of Sect. 11.4.2 has been used. The atmosphere data used for these calculations were displayed in Figs. 11.1–11.3.

In Fig. 11.5, an overhead view of the wave normal paths to the ground for the nominal Carancas meteorite solution for a mean speed, $\langle V \rangle = 13$ km/s with $\phi = 262°$ (bolide heading almost due west) and $\theta = 62°$ has been plotted. In Fig. 11.6, a side view (viewed from the west) with the same set of parameters as is the case with Fig. 11.7, which is the same except viewed from the south is indicated. In Fig. 11.6, the hypersonic boom entry corridor is clearly evident. Throughout these calculations, the wave normals have not been followed beyond the first ground impact conditions for simplicity of the presentations. All of the plots were done for a set of 15 wave azimuths about the cylindrical line source axis with seven sets of headings on either side of the entry plane.

In Fig. 11.8, an overhead view of the wave normal paths to the ground for the Carancas meteorite for a mean speed, $\langle V \rangle = 13$ km/s with $\phi = 240°$ (bolide heading slightly south of west) and $\theta = 35°$ has been plotted. In Figs. 11.9, 11.10 and 11.11, all parameters are the same as in Fig. 11.5, except that the horizontal entry angle, θ, was arbitrarily assumed to be 50.2, 65.2, or 80.2°, respectively. Notice in this progression of plots how the Mach cone projection onto the $\{x, y\}$ plane widens out progressively until by Fig. 11.11, there is very little forward motion of the wave normal paths at all along the original trajectory.

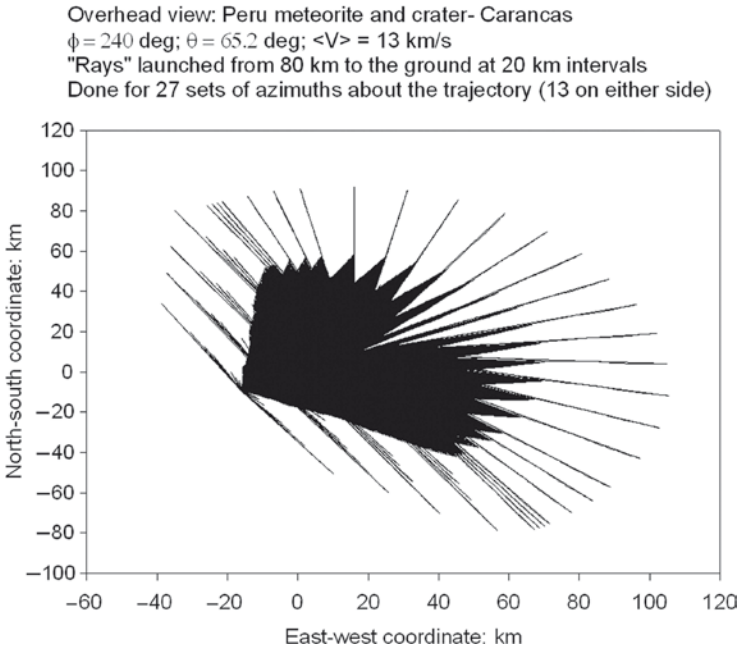

Fig. 11.10 Top view of wave normal paths: θ = 65.2 deg

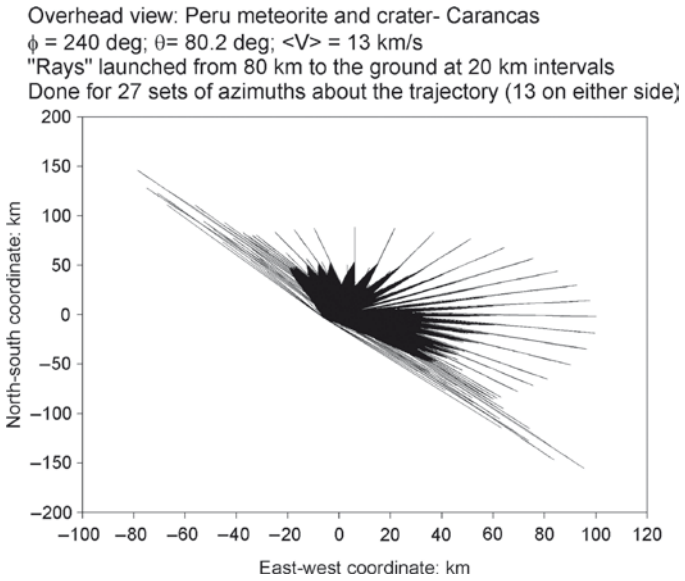

Fig. 11.11 Top view of wave normal paths: θ = 80.2 deg

11.2.4 Wave Kinetic Energy Density Conservation

Wave kinetic energy density conservation in the absence of any internal dissipation can be expressed in the form written below for a medium, which can be stated to be inviscid, nonheat conducting, and with no internal relaxation mechanisms present:

$$\text{Kinetic energy density} \equiv \tfrac{1}{2} \bullet \rho(z) \bullet \{\Delta u^2(z)\} = \text{constant}, \tag{11.9a}$$

where, for plane acoustic (infrasonic waves):

$$\Delta u(z) \equiv \Delta p(z) / \{\rho(z) \bullet c_s(z)\} \tag{11.9b}$$

$\Delta u(z)$ = perturbation wind due to the wave

$$\therefore \tfrac{1}{2} \bullet \Delta p^2(z) / \{\rho(z) \bullet c_s^2(z)\} = \text{propagation constant} \tag{11.9c}$$

and where:

$\rho(z) = \rho_o \bullet \exp(-z/H_p)$ in an isothermal, hydrostatic atmosphere for example; ρ_o = surface air density

Thus, for upward (downward) propagation, it is expected that increasingly (decreasingly) the effects of wave nonlinearity as reflected in the parameter $\Delta u(z)$, should increase (decrease) exponentially whereas $\Delta p(z)$ decreases (increases) exponentially. Knowledge of the wave kinetic-energy density at all points on the entry trajectory and of the infrasonic amplitude, Δp at the ground ($z = 0$) allows a reliable calculation of the source energy (ReVelle et al. 2004). In general, the pressure wave amplitude of the propagating wave is expected to be a function of the range, the blast wave radius, the line source length, and of the differential acoustic efficiency, etc. (Edwards et al. 2006).

In Fig. 11.12, the computed iterated line source blast wave relaxation radius and the corresponding source kinetic energy for the Neuschwanstein meteorite fall in Bavaria (ReVelle et al. 2004) is shown as a function of the geopotential height. The original calculations were done for a strictly isothermal and hydrostatic model atmosphere. In this plot, we have also included the corresponding nonisothermal atmosphere results, where it is clear that the final result can be quite sensitive to the model atmosphere that was used (and in this case with a significantly reduced blast wave radius and source kinetic energy).

This technique is accomplished by first calculating the wave kinetic energy density on the ground from the observed infrasonic amplitude detection. Subsequently, the wave kinetic energy density is calculated iteratively for every possible source height for a bolide entry trajectory that has been modeled, so that the model optical light curve agrees reasonably well with the observed light curve. By subsequently calculating the bolide velocity, kinetic energy, differential acoustic efficiency, etc., we can then find a match within some tolerance between the predicted wave kinetic energy density at ground level from a specific source height and the observed kinetic energy density value. If agreement is not found then it is likely that the phenomenon of dissipation through wave energy absorption has been operative.

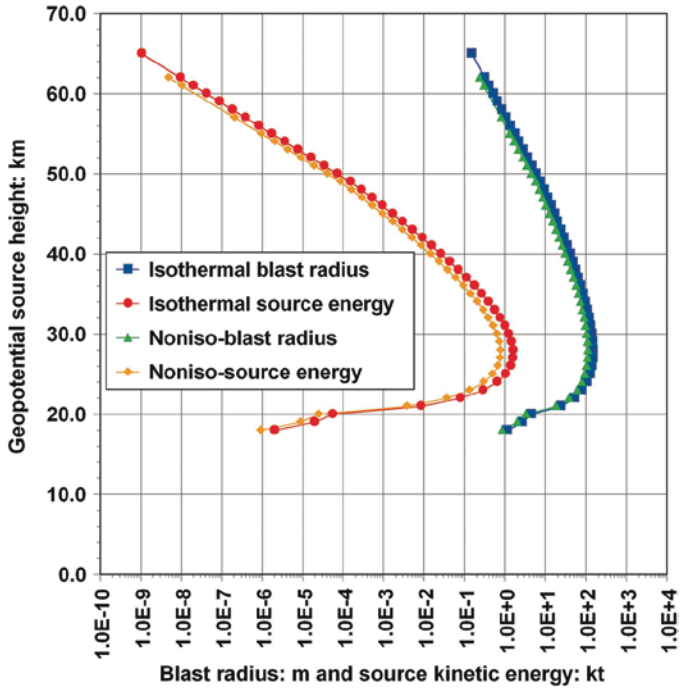

Fig. 11.12 Neuschwanstein meteorite fall: Blast radius and source energy evaluated using the KE density conservation principle for isothermal and nonisothermal model atmospheres

This is only expected to be the case for very small sources (R_o < ~5 m) at very high altitudes (>~90 km) because of the much higher fundamental wave frequencies generated by small sources whose wavelengths physically approach the neutral gas mean free path at such great heights. Physically, as this condition is approached, AGW propagation is no longer possible and wave energy dissipation leading to atmospheric heating is expected to rapidly occur.

11.3 Impulsive Atmospheric Sources: Meteor-Fireballs (Bolides), Rockets, and Missiles, etc.: Systematic Analysis of their AGW Signals

There are numerous impulsive-type elevated sources in the atmosphere, some of which can be readily detected from their AGW signature at ground level. These include, but are not limited to the hypersonic launch entry of manmade sources such as rockets and missiles, and supersonic equatorward motion of the auroral electrojet. The entry of natural objects, gravitationally bound to our solar system, namely large meteor-fireballs or bolides are also a very significant source of such

AGW signals as will be discussed in much greater detail below. The systematic treatment of the linkages between the source entry dynamics/energetics to the generation of atmospheric AGW from such sources is the primary subject of this review chapter. This entry modeling capability includes an approach termed *direct*, which is pursued downward from the top of the atmosphere or an *inverse* entry modeling approach, which is pursued from the lower boundary of the earth's atmosphere ($z=0$) back upward toward the original source location. In addition, the former approach explicitly includes fragmentation processes using our TPFM (Triggered Progressive or Triggered Pressure Fragmentation Model). In addition, the consequences of applying a perturbation conservation principle for the wave kinetic-energy density has also been incorporated as discussed in the previous section of this chapter as has the refractive effects for tracing line source wave normal "rays" emanating directly from the source at very high Mach number (~10–300) and explicitly including the effects of fragmentation on such AGW signals, etc. In addition, the detailed dispersive properties of the nonisothermal atmosphere on the propagation of several types of AGW signals from such sources has also been considered for a medium with two primary resonant frequencies and waveguide ducts (including the horizontal mean winds) as will subsequently be discussed.

11.3.1 Meteor-Fireballs and Bolides as Sources

Meteor-fireballs or more simply bolides have been studied since about the early 1960s as sources of atmospheric AGW ReVelle (1976) and Edwards (2010). These bodies of sizes exceeding ~1 cm across can enter the atmospheric at hypersonic speeds initially ranging from as low as 11.2 km/s (earth's escape velocity) to as high as 73.2 km/s (the parabolic limiting escape speed that gravitationally binds particles to the solar system at the earth's mean distance from the sun). Those bodies that reach the earth's surface intact, we refer to as meteorites and if they maintain their cosmic speeds they can even occasionally form impact or explosion craters at ground level. Quite recently in fact (September 15, 2007) the Carancas meteorite fall actually produced a 13.5 m crater very high in the Peruvian Andes (Brown et al. 2008; Le Pichon et al. 2008; Tancredi et al., 2009-in Press). This impact cratering event itself is quite a rare event by any reasonable account; yet, it was also well observed by many of the local inhabitants. This event also produced AGW airwaves that were subsequently recorded quite close in Bolivia as well as quite far away (~1,560 km) from the event. In addition, seismic waves from the impact itself as well as from propagating surface waves and air-coupled Rayleigh waves were also recorded within a few hundred km of the event. Some of the possible consequences at the time of this event will be discussed subsequently.

Such bodies can have a very wide range of compositions that extend from very strong nickel–iron materials (Fireball Group 0) to ordinary chondrites (Fireball Group I) to carbonaceous chondrites (Fireball Group II) to strong cometary materials (Fireball Group IIIA) to the final extreme of weak cometary

material (Fireball Group IIIB). These bolide groups also have a common compositional origin with the much smaller meteors observed as well (Ceplecha et al. 1998) and that have been analyzed by very different traditional meteor astronomy methods (using beginning heights for meteors vs. using end heights for bolides, etc.). These bodies also have a range of "breaking strengths" as well as weaknesses due to cracks internally due to interplanetary collisions between the liberation of the body from its parent body until its final impact on the upper atmosphere, heralding its arrival at the earth's orbit. One very notable fact remains even after much extensive research by numerous investigators on these bodies and their solar system origins. There is often more dispersion of their fundamental observable properties within two separate individual members of a single fireball group than there is between two separate bolide groups. This apparently has to do with the fact that the devised fireball groups are only statistical inferences and with the fact that these bodies indeed can have very diverse origins leading to large compositional uncertainties and orbital collisional impact histories, etc.

Finally, it is noted here that the current analysis is not in any way limited to the behavior of only very large bolides, but can be extended down to the smallest bodies capable of producing high frequency AGWs. Such small bodies (with peak panchromatic stellar magnitudes as small as ~−6) have recently been observed by the University of Western Ontario (UWO) Southern Ontario Meteor Network (SOMN) by Edwards et al. (2008) for example (see also Chapter 12 by W.N. Edwards in this book).

In Fig. 11.13, a plot of the meteor–atmosphere interaction spectrum is presented, which attempts to provide information on the expected degree of mass loss (ablation) experienced at hypersonic entry velocities for different-sized meteor bodies ranging from a few microns across to a few kilometers across. At the same time, it also provides an estimate of the corresponding peak brightness of the entry (in the standard form expressed at an altitude of 100 km in the zenith). In addition, it also provides a framework of expected atmospheric and cratering phenomena in terms of light emission, sound emission, the corresponding hypersonic and supersonic aerodynamic flow regimes, the development of strong and weak shock waves, atmospheric internal gravity, and infrasonic waves, i.e., AGWs, etc., so that an appreciation of the relative sizes of meteor bodies for each set of phenomena can be expected. Thus, the realm of AGWs from meteors that can be detected at ground level by sensitive microbarometers is only expected from bodies whose initial size is ~1 cm and larger (depending too of course on the possible range of source heights and entry velocities, entry angles, horizontal range, etc.). In this very brief review chapter, we have also not discussed impact into the oceans and the generation of hydroacoustic signals that can be expected to propagate in the oceanic SOFAR channel or the generation of fires on the ground from very extensively penetrating events so that the reader should certainly be appreciative of the fact that there is still much work left to be done in this strongly interdisciplinary research area.

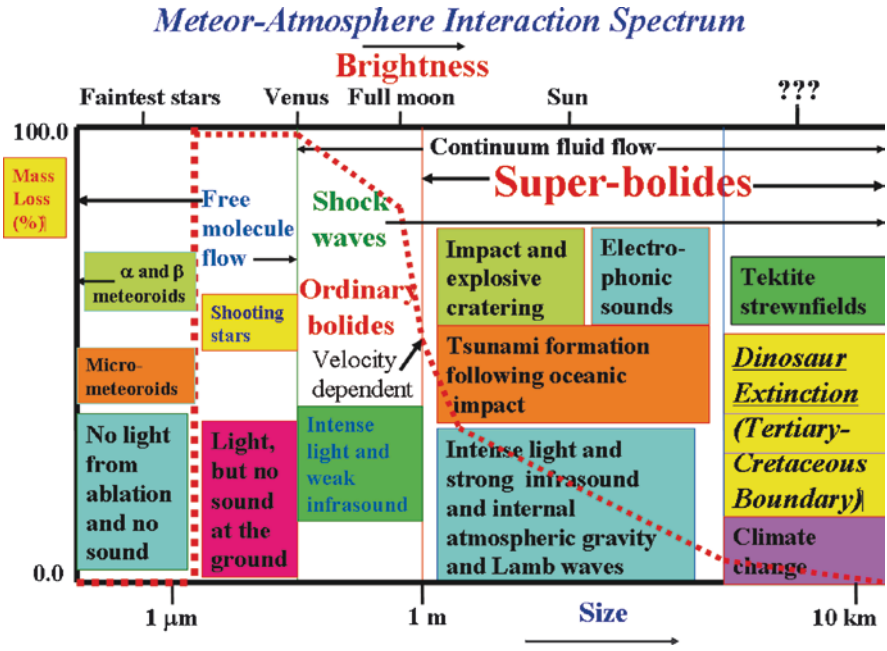

Fig. 11.13 The meteoroid-atmosphere interaction spectrum (mass loss vs. size/brightness) and the phenomena produced and expected in the atmosphere. The heavy dotted line is shown schematically for the expected mass loss which in some regimes is a very strong function of the entry velocity

11.4 Meteor-Fireballs as a Wave Source

11.4.1 Entry Dynamics and Energetics

Entry to the atmosphere at supersonic and hypersonic velocities (corresponding to speeds locally greater than and much greater than the local phase velocity of sound respectively) can produce spectacular atmospheric phenomena including significant optical and infrared light production, ablation or quasicontinuous mass loss of the physical object itself (with the term ablation derived originally from the science of glaciation), fragmentation phenomena or rapid break-up due to mechanical and/or thermal stresses depending on its composition, size and previous collisional history in its orbit about the sun, impact and explosion cratering, electrical effects and lightning, the formation of very strong shock waves and the arrival of very powerful acoustic phenomena, significant deceleration to speeds small enough to allow fragments to arrive at the surface of the Earth in the absence of a significant crater, etc. Analysis of these and additional entry phenomena in terms of the ballistic drag interaction (in the absence of any significant lift forces) between the body and the air and for the radiative, convective and conductive heating of the body by the air (this energy flow is driven by the shock wave itself for a sufficiently large body during entry) can be

conveniently separated into equations for a single-body as well as ones for multiple fragments should break-up occur during entry which at such high speeds is highly likely. Manmade objects (such as reentry space capsules), on the other hand, have purposely been designed to withstand such mechanical stresses during entry within certain physical limits. The single-body approach was the standard that until recently was used by numerous hypersonic entry modeling practitioners, but the models presented below also incorporate the multiple fragment effects after break-up due to the inclusion of a specific wake model for the entry. Here, the current limits are a collective or a noncollective wake limit with the corresponding model largely determining the final optical brightness produced during the entry at any height. In the collective wake, the fragmented particles remain with the main body after fragmentation and continue to interact while in the opposite limit the fragments fall progressively further away from the main body with time and are subsequently "lost" from a dynamical point of view. In what follows the full entry modeling details have been coupled directly to the AGW properties to physically link the source to the subsequent propagation through the atmosphere and make the analyses corresponding much more realistic.

More recently, ReVelle (2001a, 2001b, 2001c, 2001d, 2001e, 2002a, 2002b, 2005, 2007, 2008) has developed a comprehensive entry scheme for modeling the entry of bolides in the atmosphere. In addition, a particularly readable account of numerous aspects of hypersonic re-entry aerodynamics, but including all necessary equations except for many details of the radiation field is provided in the American Institute of Aeronautics and Astronautics (AIAA) monograph by Hankey (1988).

The numerical scheme used by ReVelle numerically solves the fundamental entry modeling equations of hypersonic aerodynamics and of radiation gas dynamics but, in addition, also computes an approximate power balance at all altitudes during entry to examine just how well the entry behavior is being modeled "to completeness" (so that nearly 100% of the energy loss is being accounted for). Below some of the current results of using these procedures in linking the explicit entry dynamics and energetics to the generation of AGW in the atmosphere for both meteor-fireballs as well as for rockets and missiles is presented. Sufficient detail on this aspect of the problem has only been provided so that it can be understood within the context of the generation of AGWs in the atmosphere by such impulsive sources. Further details can be found within the many recent references by ReVelle and others.

11.4.2 Top–Down, Direct Entry Approach

As discussed in ReVelle (1979, 2008), for example, there are two fundamental ways of analyzing the entry dynamics equations, namely a top–down direct entry modeling approach and an inverse approach that will subsequently be discussed below. In the first approach, we specify in advance the bolide composition, shape, initial pre-atmospheric radius, bulk density and/or degree of porosity, entry velocity, entry angle, ReVelle's D parameter for specifying the percentage of the original kinetic energy remaining at the fireball's end height, the wake model (in either the collective or noncollective wake limit, respectively – see below) for distributing the

bolide fragments of the fireball if break up is predicted to occur, the model atmosphere properties by date and/or the season to be used, etc. The model also computes the atmospheric shockwave temperature field as a function of range surrounding the bolide so that an appreciation for the magnitude of the line source explosion and all of its ramifications can be evaluated.

An overview of the numerous the physical processes that are occurring during meteor entry are summarized below in Fig. 11.14 and subsequently described verbally below.

As can be seen in Fig. 11.14, the original kinetic energy of the bolide can be transferred into mass loss (so-called quasicontinuous ablation), deceleration, and into fragmentation processes. These are further coupled together in fact since deceleration rates can change depending on whether or not the collective or the noncollective wake limit has been assigned. These processes then transfer energy eventually into heat (in the viscous fluid approximation) as discussed briefly earlier or into optical light production (or infrared or ultraviolet light production for example) as well as into AGW (or infrasonic waves in the high-frequency acoustic wave limit).

The original bolide energy loss/time can be transferred away from the bolide into a number of distinct physical processes as indicated in Fig. 11.15 for a large meteor-fireball, i.e., the case of the Neuschwanstein meteorite fall. In this figure, we have also indicated a number of important physical processes and their total summation including the deposition/time of heat, light (optical), sound (acoustic limit computation), dissociation, and ionization.

Detailed examples have also been provided in Figs. 11.20–11.23 later on using the direct hypersonic aerodynamic entry modeling procedures for the famous Revelstoke meteorite fall of March 31, 1965, over British Columbia, Canada.

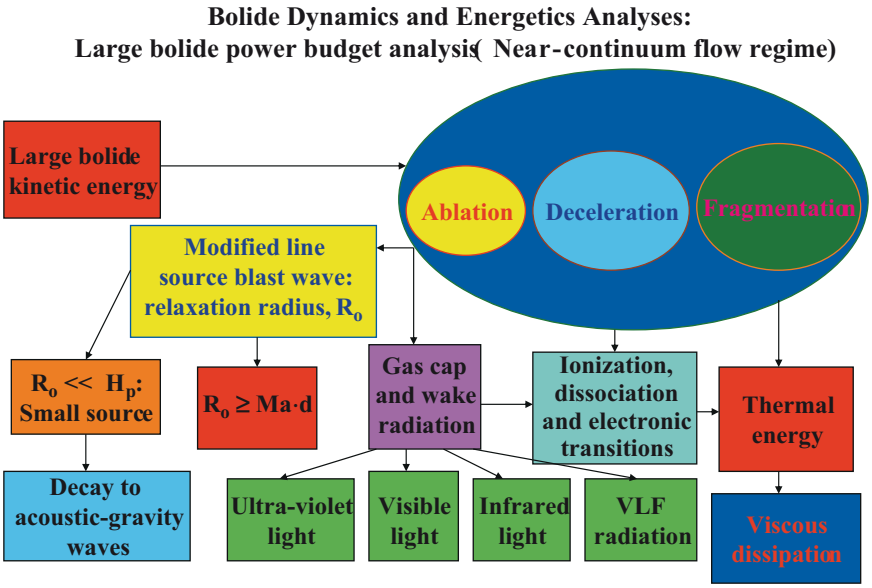

Fig. 11.14 Physical processes occurring during the entry of large meteors in the atmosphere

Many of the necessary inputs used in the direct entry dynamics and energetics model of ReVelle are briefly summarized as a list directly below:

3.75	R_∞	Initial bolide radius (m) [0.000001–1000.0]
13.0	V_∞	Initial entry velocity (km/s) [11.2–73.0]
75.0	Z_R	Zenith angle of entry relative to vertical (deg) [0.0–80.0]
10.0	N_{tot}	Maximum number of pieces produced druing fragmentation [1–1000]
1.209	$S_{f\infty}$	Shape factor (frontal area/volume$^{2/3}$) 1.209 ⇒ sphere [1.209–2.0]
0.667	μ	Shape change factor 2/3 = no shape change [−3–0.6667]
4.605	D	Kinetic energy still at end height [2.303–4.605] i.e., [10–1%]
1.0	BRKTST	Allow breakup 0 = no; 1 = yes [0 or 1]
1.0	FRAGTST	Fragmentation: Remain in wake 0= remain; 1= stay with body [0 or 1]
1.0	PORTST	Allow porous materials 0 = no-porosity; 1 = Fully porous [0 or 1]
1.0	SIGTEST	Ablation parameter σ changes with height; 0 = no change; 1 = Allow change
0.0	MUTEST	Shape changing with height; 0 = same shape factor; 1 = variable [0 or 1]
1.0	ISOTHERM	Atmosphere model treatment; 0 = isothermal; 1 = nonisothermal [0 or 1]
0.0	RHOTST	Atmospheric density profile 0 = winter; 1 = summer [0 or 1]
0.20	Φ	Porosity [0 to 1]; If PORTST= 0, Fireball groups [0 (Iron), 1, 2, 3, and 4]

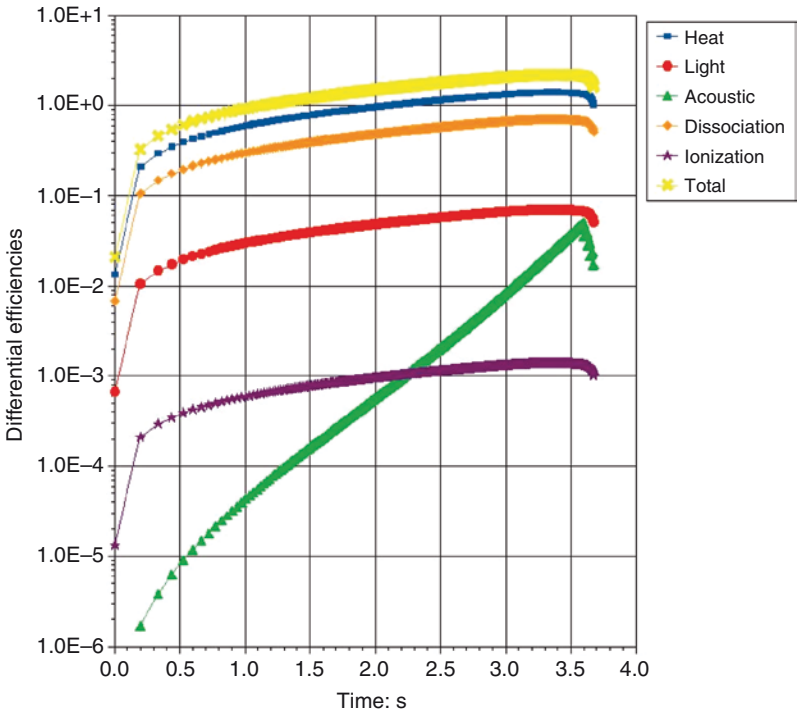

Fig. 11.15 Approximate power balance computed for the Neuschwanstein bolide

Using FRAGTST= 1 (a fragmentation test triggering switch that is used within the entry modeling computer code) in the aforementioned list of settings indicates that the computer run was done using a collective wake TPFM fragmentation model.

Briefly, two model wake options have been provided within the direct entry modeling approach. As indicated in the list earlier, in the collective wake model limit the particles that have fragmented remain nearby the main original body and contribute significantly to the production of optical light by the bolide–atmosphere interaction process. In the opposite limit of the noncollective wake, the fragmented particles rapidly fall away from the original body and are lost with respect to the process of further optical light production. In reality, an oscillation between these two limits probably occurs as well, but this has not yet been incorporated into the numerical entry modeling algorithms. In other words, in the collective wake limit particles are broken off from the main mass (starting only if the stagnation pressure on the front face exceeds the breaking strength of the body) and fall into the near wake while continuing to ablate and accumulate over time, thus changing the frontal cross-sectional area and the overall contribution to the optical fireball luminosity. In the opposite extreme limit, i.e., for the case of the noncollective wake (controlled by setting FRAGTST=0), particles fall into the wake and continue to ablate until finally dissipating their energy far behind the main mass.

The shape factor, S_f, (= the frontal cross-sectional area divided by the total meteor volume raised to the 2/3 power) used in the dynamical and energetics-based entry modeling (and valid for stagnation point heating rates along the center streamline) can range from the spherical value ($S_f = 1.209$) to perhaps the extreme of a hemisphere ($S_f = \sim 1.919$). The shape change parameter, μ, can range from $\mu = 2/3$, which is the self-similar solution where any initial shape will not change during entry (where a sphere remains a sphere throughout entry for example) to possibly relatively small negative values (the so-called pancake fragmentation model limit). A summary of possible μ values based on observations is given in ReVelle (2004, 2005). Currently, the MUTEST option in the computer code is not fully operational because of complications of accurately computing this parameter reliably.

The assignment of ReVelle's D parameter discussed earlier can be used to compute the velocity at the end height during entry using a transcendental solution of the kinetic energy removal equation (ReVelle 2004, 2005). Based on observations of photographs of three meteorites during entry, it can be resonably assigned a value of $D = 4.605$, which corresponds to a 99% kinetic energy removal at the end height. For weaker fireballs a $D = 2.303$, which corresponds to only 90% kinetic energy removal at the end height is more reasonable however. The reader is referred to the original references of ReVelle for explanations of these numerical choices.

In this direct entry modeling, the zenith entry angle of the meteor radiant is assumed to remain constant throughout the entry even though the angle eventually does change. In the absence of significant horizontal winds, it will eventually become nearly vertical at Earth impact (unless the fireball is very energetic and when significant kinetic energy remains even at impact).

The final total number of fragments computed is assigned on the basis of experience and from direct fireball photographic data if available. Since, currently, the meteor is broken into equal-sized pieces (rather than a distribution of sizes for example which is probably more likely in reality), this number may have to be significantly adjusted in the case of very weak cometary-type fireballs (Group IIIA and IIIB types especially) to fully account for the observed brightness that is produced. If PORTST = 0, only the previous, standard nonporous fireball (homogeneous bulk density) model is used, whereas if PORTST = 1, a fully porous meteor model derived by the author in 2001, which accounts for more optical luminosity production (even in the absence of breakup) and correspondingly to even larger ablation coefficients is used.

Finally, we have also included two limiting hydrostatic, nonisothermal atmospheric models within the direct entry dynamics computer code. These include a summer and a winter atmospheric model applicable in middle latitudes to earth's atmosphere, which replicate the US Standard Atmosphere (1976) model up to geopotential altitudes of ~200 km or even higher.

11.4.3 Bottom-Up, Inverse Entry Approach

Using a bottom-up, inverse entry modeling approach as originally developed by McIntosh (and as applied to the fall of the Innisfree meteorite by ReVelle 1979), we can also reliably predict the properties of the original impacting body. In this approach, we can either assume no fragmentation exists at all and proceed with only the single-body solutions or else we can also model each observed piece at its own observed end height as a fragmented fireball and sum the final results as in ReVelle (1979). This approach can also be combined with the cratering diameter equations of Gault (1974) to determine the combined entry solution that satisfies the entry as well as the crater diameter solutions as well at a specified height above the earth's surface. Similar parameters to those discussed earlier are also needed for this approach, which can also be configured to provide error estimates on the original mass, the shape factor, and the hypersonic wave drag coefficient product, etc. (ReVelle 1979, 2008).

As an example of this type of prediction, in Fig. 11.16, a plot of the initial kinetic energy (in kt, TNT equivalent where 1 kt = 4.185×10^{12} J) vs. the terminal mass in kilogram is presented. In Fig. 11.17, a plot of the terminal mass (in kg) vs. the terminal (impact) velocity (in km/s) is also presented. An additional graphical example of this approach is provided in Brown et al. (2008) for the case of the September 15, 2007, Carancas meteorite fall and impact crater in Peru. This specific modeling case included a ground level crater (with a mean diameter = 13.6 m at a termination altitude = 3.826 km above sea level) that was also used along with the observed local soil density and entry angle to heavily constrain the predicted final mass and initial kinetic energy solutions.

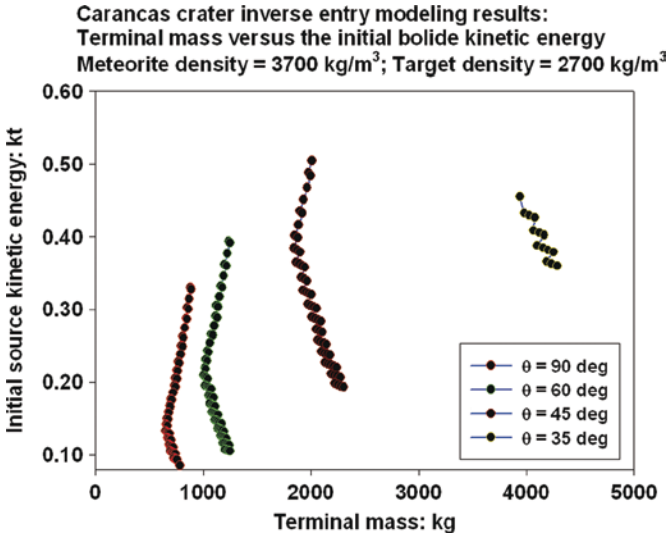

Fig. 11.16 Carancas meteorite fall" September 15, 2007- Initial kinetic energy (kt) versus the terminal mass (kg)

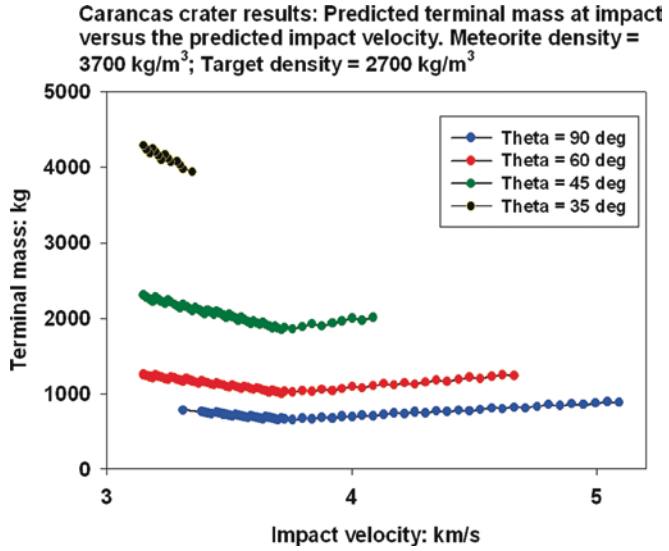

Fig. 11.17 Carancas meteorite fall" September 15, 2007- Terminal mass (kg) versus the terminal impact velocity (km/s)

11.4.4 Wave Source Parameters

The hypersonic aerodynamic entry of sufficiently energetic bodies into the atmosphere guarantees the generation of a quasiline source explosion. Even when the flow is not in a near-continuum state as measured by the local Knudsen number, it will still be in a state of continuum flow with respect to the local pressure or density scale height (ReVelle 2004; 2005). Thus, within a few blast wave radii (to be subsequently discussed below), the impulse provided by the meteor is rapidly transformed into a diffuse weak shock front that can still drive a substantial line source explosion and provide substantial heating in the upper atmosphere (as discussed further in the Appendix).

As a means of providing a measure of the horizontal scale of the line source explosion as well as of its strength, we can compute the line source blast wave relaxation radius. This is a fundamental observable parameter that can be used to specify many of the key physical properties during the energy deposition process. For example, in combination with the line source length, the blast wave radius can be used to specify the complete volumetric scale of the explosion deposition. Within a distance scale of one blast wave radius a very intense nonlinear explosion zone is located where radiation transfer and numerous additional complex physical processes are operative. In addition, the distance scale of an explosion is normally specified with respect to this key parameter, which also provides a measure of the fundamental wavelength of the propagating weak shock disturbance as well as its fundamental wave frequency (or wave period) beyond ~10 blast wave radii from the entry trajectory. The amplitude of the weak shock disturbance can also be readily related to the blast wave radius as well. Given the possible range of entry parameters for meteors, we will compute this quantity later on. Anticipating our findings, we have determined that the blast wave radius can range from values as small as ~1 m to as much as ~30 km or larger (with the latter value more typical of the famous Siberian event of 1908, the so-called Tunguska bolide, which did not produce any ponderable meteorite fragments on the earth). Just for reference, ordinary thunder has an associated blast wave relaxation radius of ~2–3 m and an associated peak fundamental wave frequency of ~50 Hz.

Following continuum flow, line source blast wave treatments by Lin (1954) and Plooster (1971), a nearly complete description of the near-field blast wave can be determined (outside of a reliable prediction of the thickness of the shock wave itself). By relying on a near-field description, the fundamental wavelength generated must be small compared to the distance already propagated, whereas in the opposite extreme, the so-called far-field limit is realized (or mathematically expressed as $2\pi r/\lambda >> 1$, with r = range from the source and λ = wavelength). The energy deposited through the hypersonic drag interaction per unit length of trail can be used to reliably predict the line source blast wave relaxation radius, a quantity that combined with the line source length can be used to completely predict the nonlinear explosion volume surrounding a bolide during reentry.

The definition of the line source blast wave relaxation radius using the drag doubling factor to account for the “TNT equivalence of supersonic/hypersonic

flow" (for details, the reader is referred to the experimental laboratory work of Tsikulin listed in ReVelle (1976):

$$R_o(z) \equiv \{[2m \bullet (dV(z)/dt)]/p(z)\}^{1/2}, \tag{11.10a}$$

where m = meteor mass, dV/dt = meteor deceleration, $p(z)$ = ambient atmospheric pressure, $V(z)$ = meteor velocity, t = time during entry, and z = altitude above the planetary surface.

This characteristic blast radius is thus proportional to the square root of the energy deposited by the bolide per unit length of trail divided by the ambient pressure at any height.

If the range R is sufficiently large and weak shock nonlinear distortion of the waveform is still evident, then the fundamental line source wave period is predicted to increase with range (ReVelle 1976):

$$\tau(x) = 0.562 \bullet \tau_o \bullet x^{1/4}, \tag{11.10b}$$

where

$$x \equiv R / R_o = \text{scaled distance away from the source} \tag{11.10c}$$

$$\tau_o = 2.81 \bullet R_o(z) / c_s(z) = \text{fundamental blast wave period at } x = 10 \tag{11.10d}$$

τ = fundamental wave period, $c_s(z)$ = adiabatic, thermodynamic sound speed as a function of height

For nonbreaking meteors experiencing the hypersonic drag interaction with the atmosphere, the line source blast radius can be shown to be equal to the product of the instantaneous Mach number of the body times the instantaneous bolide diameter. Here, the Mach number is defined as the ratio at any height of the computed speed of the body compared to $c_s(z)$. If break-up is included in the expression, the blast radius is more complex, but increases relative to the nonbreaking bolide limit, by a height variable multiplier of some 5–20 times. Physically, the hypersonic aerodynamic motion combined with the line source blast wave analogy is meaningful only in the limit of zero acceleration in a steady-state medium, but substantial increases in the predicted blast wave radius are predicted at comparatively deep penetration heights after pressure-induced break up is predicted to occur.

Interestingly, analyzing the energetics of the meteor motion and ablation, we can immediately write expressions for the kinetic energy and its time rate of change for spherical bolides in the form (ReVelle et al. 2004):

$$E_k = (\pi / 12 \bullet \rho_m \bullet R_o(z)^3 \bullet \{c_s^3 / V(z)\} \tag{11.11a}$$

$$dE_k / dt = (V^2 / 2) \bullet dm / dt \bullet \{1 + R\} \tag{11.11b}$$

$$dE_k / dt = m \bullet V \bullet dV / dt \bullet \{R^{-1} + 1\} \tag{11.11c}$$

$$R(z) \equiv (\sigma \bullet V(z)^2 / 2)^{-1}, \tag{11.11d}$$

where R = inverse dimensionless ablation efficiency = $m \bullet V \bullet \mathrm{d}V/\mathrm{d}t/\{(V^2/2) \bullet \mathrm{d}m/\mathrm{d}t\}$, R_o = Line source blast wave radius, or alternatively, a useful form of the energy equation can also be rewritten in terms of the line source blast wave relaxation radius (ReVelle and Rajan 1979):

$$\begin{aligned} \mathrm{d}E_k / \mathrm{d}t &= m \bullet V \bullet \mathrm{d}V / \mathrm{d}t \bullet \{(1 / R(z)) + 1) \\ &= \{R_o^{\,2}(z) \bullet p(z) / (2.0)\} \bullet V(z) \bullet \{(1 + R(z))\} \end{aligned} \tag{11.11e}$$

or:

$$\begin{aligned} (1 / E_k) \bullet \mathrm{d}E_k / \mathrm{d}t = -\{6 / \pi\} \bullet \{p(z) / (\rho_m \bullet c_s(z))\} \bullet \\ \{R_o(z) / d^2\} \{1 + R(z)\big) / R(z)\} \end{aligned} \tag{11.11f}$$

or:

$$(1 / E_k) \bullet \mathrm{d}E_k / \mathrm{d}t = -D = -(\alpha + \beta), \tag{11.11g}$$

where d = meteor diameter, ρ_m = bulk density of meteoroid, $R_o(z) = \{V(z)/c_s(z)\} \bullet d(z)$ if there is no fragmentation occurring, D = ReVelle's parameter for the determination of the percentage of the original kinetic energy remaining at the end height (at the height where the optical luminosity is no longer observable), and α = kinetic energy depletion factor due to air drag alone while β = kinetic energy depletion factor due to ablation alone.

Thus, the following new formal expression for D can now be presented from analyses of the (11f) and (11g):

$$D = \{6 / \pi\} \bullet \{p(z) / (\rho_m \bullet c_s(z))\} \bullet \{R_o(z) / d^2\} \{1 + R(z)) / R(z)\} \tag{11.11h}$$

Thus, the time rate of change of the kinetic energy of the body is proportional to either a mass loss term multiplied by a physical constant or by a linear momentum curve multiplied by a different physical constant. This formally proves the very high degree of mathematical separation between ablation and drag processes (with the latter omission including all possible fragmentation effects) as discussed in ReVelle (2004, 2005).

Although the full implications of the above final result in (11.11h) will be elaborated upon at much greater depth in a future publication, the following most important facts can already be concluded here. D depends directly on the ambient atmospheric pressure and the bulk density of the meteoroid and on the blast wave relaxation radius at any height. It also depends inversely upon the diameter of the body. Thus, as either the pressure or bulk density or the blast wave radius increase, so does D, but as the diameter of the body itself increases, D will be predicted to decrease. These values can be combined together to formally predict the D parameter at any height and thus to better understand the associated detailed energetics during bolide entry for a large range of entry conditions.

The earlier approaches are generally equally valid for rockets and missiles (except during powered flight due to thrust or booster separation effects, etc.) as long as appropriate amplitude corrections (ReVelle et al. 2005; ReVelle and Edwards 2006) are made at the lower Mach numbers expected for such sources.

11.4.5 Source Coupling to the Atmosphere: Hypersonic Flow Field Matching of the Pressure Wave Disturbances

To make a simple prediction of the pressure wave amplitude resulting from the bolide energy deposition process vs. range, following Plooster (1968, 1970, 1971) and Jones et al. (1968), there are at least five possible coupling cases that need examination (in all cases, however, these scaled constants were verified by direct numerical hydrocode calculations):

1. Initial condition A: Line source, ideal gas – "C" = 0.70 and "δ" = 1.0; $\Delta p = 0.0805 \bullet p(z)$ at $x = 10.0$ (at 10 blast wave radii)
2. Initial condition B: Isothermal cylinder, constant density, ideal gas – "C" = 0.70 and "δ" = 1.0; $\Delta p = 0.0805\ p(z)$ at $x = 10.0$
3. Initial condition C: Isothermal cylinder, constant density, real gas – "C" = 0.70 and "δ" = 0.66; $\Delta p = 0.0680\ p(z)$ at $x = 10.0$
4. Initial condition D: Isothermal cylinder, low density, ideal gas – "C" = 0.95 and "δ" = 1.61; $\Delta p = 0.0736\ p(z)$ at $x = 10.0$
5. Initial Condition E: Isothermal cylinder, high density, ideal gas – "C" = 0.95 and "δ" = 1.61; $\Delta p = 0.0736 \bullet p(z)$ at $x = 10.0$
6. Initial Condition F: ReVelle (1976), Jones et al. (1968) – "C" = 1 and "δ" = 1.0; $\Delta p = 0.0575 \bullet p(z)$ at $x = 10.0$

where "C" determines the spatial regime (the indicated x value) where the strong shock regime conditions (defined by $\Delta p/p >> 1$) have transitioned to the weak shock regime ($\Delta p/p << 1$)

"δ" = 1 determines the efficiency with which blast waves are generated in comparison with amplitudes indicated in Lin's (1954) original numerical cylindrical line source solution.

Thus, for this range of possible prescribed initial conditions, the predicted amplitude change is 0.0805/0.0575 or as much as ~40% change, which is certainly nontrivial. This uncertainty will certainly affect analyses of the source and its energetics, etc. to some degree.

To illustrate the uncertainty introduced by varying these two parameters, following ReVelle (1976), the detailed amplitude vs. scaled range behavior was predicted using a relationship that approaches nonlinear blast wave behavior at small x and weak nonlinear shock wave behavior as $x \rightarrow \infty$ and is indicated below as a function of "C" and of "δ":

$$f(x) = (3/8)^{-3/5} \bullet C^{-8/5} \bullet \{[1 + (8/3)^{8/5} \bullet C^{-8/5} \bullet \delta^{-1} \bullet x^2]^{3/8} - 1\}^{-1}) \qquad (11.12)$$

where
$f(x) = \{2.0 \bullet (\gamma + 1.0)/\gamma\} \bullet \{\Delta p / p_o\}$
$f(x)$ = pressure amplitude decay factor with range at a fixed altitude, γ = Specific heat of air at constant pressure to that at constant volume, p_o = reference hydrostatic pressure (back pressure for the explosion), $x = R/R_o$ = scaled distance from the line source, R = slant range from the line source, and R_o = line source blast wave relaxation radius.

Finally, the physical coupling of diffuse shock waves at high altitudes where the atmosphere is very viscous and the local neutral gas mean-free path is very large (cm to km in length depending on the geopotential altitude) is discussed further in the Appendix.

11.5 Acoustic-Gravity Wave (AGW) Generation from Impulsive Atmospheric Sources

11.5.1 Previous AGW Modeling Efforts

Some of the AGW modeling efforts of ReVelle (2004, 2005) and of ReVelle (2008) have been recently summarized. This research effort produced a comprehensive pressure wave signature model that incorporated all known linear and quasi-linear atmospheric responses to impulsive Delta function type sources which in this case is just that due to the hypersonic drag interaction of a bolide or a missile with the atmosphere. These pressure wave signature model responses include an Airy function solution corresponding to highly dispersed internal gravity waves (Tolstoy 1973; Gill 1982), highly dispersed internal acoustical waves (Tolstoy 1973), weak shock waves with little or negligible dispersion at sufficiently close range, ducted stratospheric and thermospheric acoustic arrivals, which are very sensitive to the detailed physical structure of the idealized atmospheric waveguide for a specific wave propagation direction, leaky ducted waves, which have not been included yet, etc. Each of these components was separately linked to the model source function (discussed below) that has been formulated on the basis of the most recent and most advanced direct meteor entry models ReVelle (2004, 2005). A further expansion of these and other ancillary topics as well as a detailed summary has also been given in ReVelle (2008).

11.5.2 Most Recent Acoustic-Gravity Wave (AGW) Modeling

The dynamics and energetics of meteoroid entry modeling has been successfully combined with the physics of generation of AGW in the atmosphere ReVelle (2004, 2005) and ReVelle (2007, 2008). In addition, in ReVelle (2008) a very

complete summary of the expected synthesis of all the types of possible AGW signals into a predictive coherent formulation as a function of horizontal range, source height, blast wave radius, etc. has already been presented and will not be repeated here. This formulation includes the Lamb wave associated Airy functions, the internal acoustic wave associated Bessel functions, the close range weak shock waves (with direct paths from the source), the stratospheric and thermospheric ducted acoustical waves, etc.

These possible AGW arrivals are indicated schematically in Fig. 11.22 for the case of two-dimensional modeling of the wave generation processes from impulsive sources and the subsequent complex propagation behavior with height as a function of range for the various types of atmospheric waves listed directly above. The far-field possibilities for a linear wave response in hydrostatic, isothermal, and nonisothermal model atmospheres have been treated theoretically in great detail in Beer (1975) and more recently in Mihalas and Weibel-Mihalas (1999) with respect to wave propagation possibilities for the rapidly expanding fields of Helioseismology and more generally of Stellar-seismology. The basic dispersion equations for simple model atmospheres are well known, but one notable omission is the exact transformation necessary for these isothermal model results to individual layers within a multilayered, nonisothermal medium. Earlier theoretical work by pioneering workers such as Pierce, Posey and Kinney, Press and Harkrider, Pfeffer and Zarichny, Hunt, Palmer and Penny, Hines, Weston, Francis as well as by Meecham and numerous other workers have allowed a linearized full-wave, normal mode treatment for these AGW's to be developed. In addition, Meecham (1965) has separately formulated even more simplified models in a serious attempt to understand the very complex numerical treatments needed to fully predict these waveforms from large energy sources at great range. Earlier work by Richard Scorer and other British geophysicists was groundbreaking in developing the scientific basis for the current predictions in this field. Few individuals have developed their own approach to solving a previously unsolved integral to be able to solve a scientific problem numerically, i.e., such as the Scorer function for example.

With the current work efforts, signals from bolides from very small to very large blast wave sources (from ~1 m to as much as 36 km for the famous Tunguska bolide of June 30, 1908) at ranges from as close as 1 km to <~one Earth radius for both line as well as from point source geometries can now be accurately and reliably modeled for the case of inviscid fluids. Thus, propagation with full dissipation effects at very high altitudes still needs to be successfully incorporated into these modeling procedures in the future. It is further assumed in this analysis that for such sources the waves received at the ground have sufficiently low fundamental frequencies (<~10 Hz) that the acoustic impedance of the ground does not need to be incorporated into the evaluation of the waveform pressure amplitude (Attenborough et al. 1995). For smaller sources at higher wave frequencies some significant portion of the wave energy is absorbed by the ground itself and not perfectly reflected at the ground interface and must be explicitly accounted for during the computation of the pressure wave signature.

First, following Morse and Ingard (1969) and ReVelle (1976), weak shock or linear wave propagation conditions were identified along the AGW propagation path using the concept of a wave distortion distance. Next, it was also implicitly assumed that sufficiently far away from the source (whose characteristic nonlinear blast wave radius can be explicitly modeled using satellite luminosity data in combination with detailed entry modeling analyses), if weak shock conditions were implicitly identified that Gaussian beam theory was used during "wave-front normal" propagation, i.e., in the geometrical acoustics modeling limit, whereas if linearized wave propagation was evident that the full wave theory approach was used during the predicted very small amplitude modeling limit.

Briefly, when the full wave theory was invoked, each signal was assumed first of all to be composed of Lamb waves (internal gravity waves at sufficiently low frequency and internal acoustical waves at sufficiently high frequency guided by the earth's surface) whose amplitude was a function of the source energy, source height and of the horizontal range from the source. The Lamb wave is the fundamental mode of the atmosphere that bridges between the action of internal gravity waves and internal acoustic waves in an isothermal fluid and that allows for transverse waves at low frequencies (below the Brunt-Vaisalla frequency) and longitudinal waves at high frequencies (above the acoustic cut-off frequency). It is strictly a horizontal wave that can develop above a strictly rigid lower boundary, whose wave energy density decreases exponentially upward from that boundary with no vertical motions present. Consequently, its wave energy is concentrated typically at altitudes below ~30 km. The Lamb wave can develop through time under the right conditions away from a source (as discussed in detail further below), and during its propagation, the wave energy subsequently fans out along the earth's surface to typically arrive before other AGW disturbances since it propagates in a region of the greatest atmospheric adiabatic, thermodynamic sound speed (at the acoustic phase velocity).

Further, we will present the results of calculations (ReVelle 2008) that summarize the Lamb wave formation and production for a point source energy release as a function of source height, source energy (or source wave frequency), and range to the source, for two different source heights (and as plotted in Figs. 11.18 and 11.19 respectively). These calculations have all been carried out including an explicit Rayleigh friction, viscous decay term as first suggested by Pierce in 1963. This has made the calculations far more realistic especially at the lower frequencies near the Brunt-Vaisalla frequency, where absorptive effects can be very significant.

An explanation of the symbols used in Figs. 11.18 and 11.19 is necessary. First of all, Ro is the Lamb wave formation distance calculated assuming a viscous fluid. Second, R1 is the Lamb wave dominance distance (in terms of its wave amplitude) if both R1 >> R2 and R1 >> R3 as calculated using either an inviscid or a viscous fluid approximation. R2 and R3 are additional scaled distances developed by Pierce to constrain the Lamb wave formation results. However, it has been previously determined that R1 >> R2 and R1 >> R3 are only generally satisfied at very high altitudes above ~130 km (where the air is very viscous due to the very large neutral gas mean free path). In the absence of formally satisfying this criterion in the real

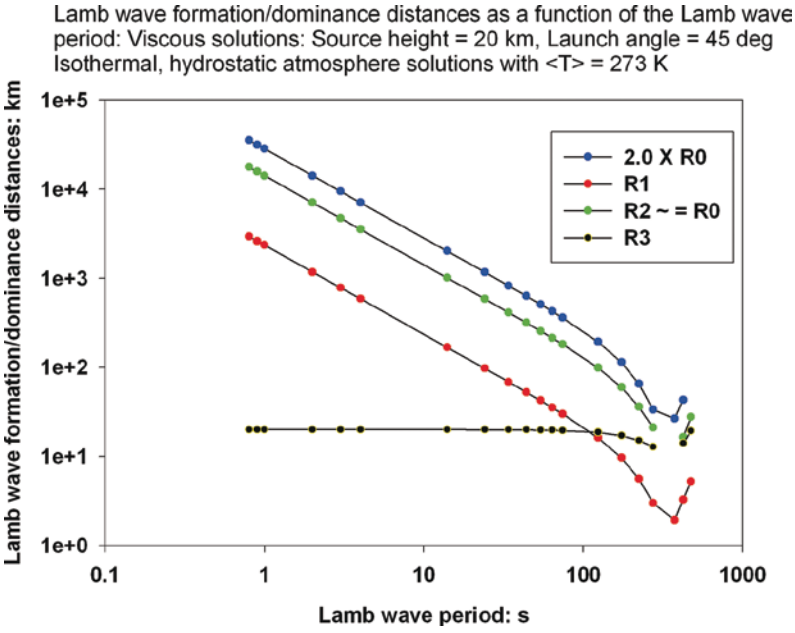

Fig. 11.18 Lamb wave formation and dominance distance (km)- 20 km source height assumed

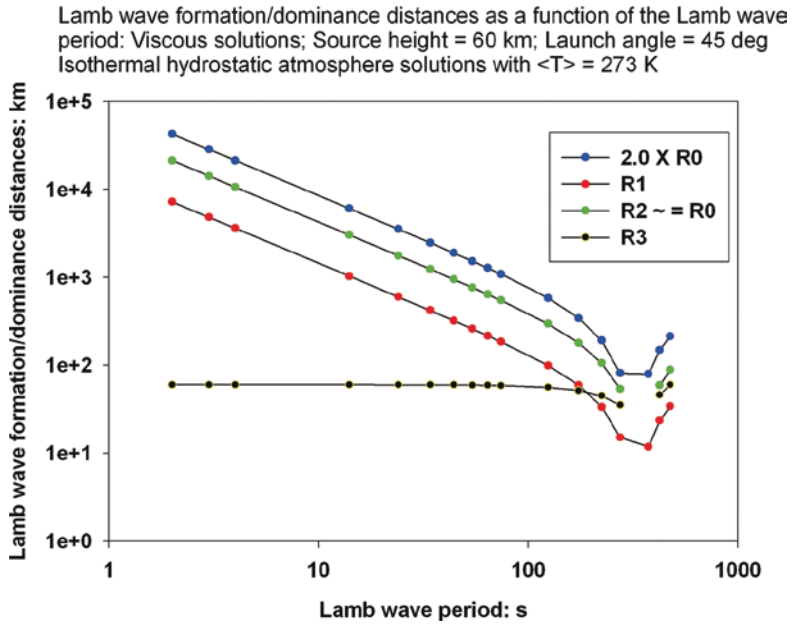

Fig. 11.19 Lamb wave formation and dominance distance (km)- 60 km source height assumed

viscous atmosphere, instead a multiple length of the predicted Ro value has been used to calculate the Lamb wave dominance distance (typically two times Ro has been used for predicting this distance using the atmospheric Rayleigh friction viscous terms that have been evaluated).

Specifically in Figs. 11.18 and 11.19, 2 R_o was used throughout as the criterion for the minimum distance necessary for the development of a significant amplitude Lamb wave contribution to the final atmospheric AGW signal. The results of this new work clearly show that as the wave frequency increases (or equivalently this also corresponds to either a diminished blast wave radius or a diminished source energy input to the atmosphere) or as the source height increases or as the range from the source decreases, the Lamb wave production and/or amplitude dominance is greatly diminished. In the intermediate regime where Lamb waves are still not expected to dominate the observed signal (see the provided propagation summary regime in Table 11.1 below), we have simply included the Lamb wave contribution, but at a greatly diminished amplitude (typically a 90% reduction has been found adequate for comparison against most bolide AGW signals).

More specifically in Fig. 11.18, it can be seen that the Lamb wave from a source at 20 km altitude will not be expected at a wave period of 10 s to dominate the observed AGW signal until a range from the source of ~3,000 km has been achieved, whereas at a period of 100 s, this predicted distance scale has been reduced to only ~300 km. Similarly, in Fig. 11.19, it can also readily be observed that the Lamb wave from a source at 60 km altitude will not be expected at a wave period of 10 s to dominate the observed AGW signal until a range from the source of ~8,000 km has been achieved, whereas at a period of 100 s, this distance scale has been reduced to only ~900 km. Thus, it can be clearly seen in general that as either the source energy decreases (at shorter wave periods) or as the height increases, Lamb wave dominance of the AGW signals at close range is extremely unlikely. For the smaller and less energetic meteors, these predicted distances are all very large to ever expect Lamb wave dominance of the AGW signals, whereas for the extremely rare, but very energetic bolides, the formation and domination of the AGW signal at quite close ranges by the Lamb wave is extremely likely. ReVelle (2008) has discussed this formation and dominance distance scale for Lamb waves further in terms of a constructive interference effect process.

In addition to the Lamb wave contribution, we also expect to observe weak shock waves propagating away from the source (but not significantly dispersed at close range for small sources), except at sufficiently great ranges. In addition, atmospheric acoustical waves are also launched independently by the medium due to the impulsive nature of the source (Tolstoy 1973, Gill 1982) and with additional ducted waves arriving from the stratospheric and thermospheric sound channels either significantly or negligibly dispersed as a function of range (Gill 1982). With the current approach, it has even been found possible to isolate the AGW spectrum in middle latitudes for earth's atmosphere from ~3 h > τ > 0.10 s strictly from the infrasonic spectrum, i.e., $\omega >> \omega_{ac}$ where ω_{ac} is the acoustic waveguide cut-off frequency and τ is the observed wave period. The modeling of the full AGW spectrum adds a significant source of higher frequencies toward the end of the predicted synthesized

Table 11.1 Atmospheric acoustic-gravity wave (AGW) response from impulsive sources such as bolides

CASES:	Lamb waves: Internal gravity waves	Internal acoustical waves	Weak shock blast waves	Stratospheric ducted signals	Thermospheric ducted signals
Close range: Large energy sources	Not yet fully dispersed: Limited Airy function response	Limited Bessel function response	Not yet dispersed, but wave period a function of blast radius	No ducted signals expected; Direct arrivals only	No ducted signals expected; Direct arrivals only
Close range: Small energy sources	No formation at high altitudes; Limited Airy function response	Limited Bessel function response	Not yet dispersed, but wave period a function of blast radius	Ducted signals possible	Ducted signals possible
Intermediate range: Large energy sources	Fully dispersed: Airy function shape, but of limited amplitude	Limited Bessel function response	Fully dispersed with wave period a function of blast radius	Some ducted signals evident downwind: Dispersed wave train	Some ducted signals evident upwind and downwind
Intermediate range: Small energy sources	No formation at high altitudes: Limited Airy function response	Limited Bessel function response	Not yet dispersed, but period a function of blast radius	Some ducted signals evident downwind: Dispersed wave train	Some ducted signals evident upwind and downwind
Great range: Large energy sources	Fully dispersed Airy function shape	Fully dispersed: Bessel function response	No direct signals expected	Ducted signals expected downwind: Fully dispersed with period a function of blast radius	Ducted Signals expected Downwind and upwind: Fully dispersed with period a function of blast radius
Great range: Small energy sources	No formation at high altitudes except for very great ranges	Fully dispersed Bessel function response	No direct signals expected	Ducted signals expected downwind: Fully dispersed with period a function of blast radius	Ducted signals expected downwind and upwind: Fully dispersed with period a function of blast radius

First, we will assign horizontal distance scales from 100 to 300 km as a reasonable *minimum* range for significant atmospheric dispersion, i.e., the minimum range for the Airy phase to fully develop. This distance scale is well known following much earlier work by Pierce and Posey and by Bretherton and Garrett, etc. (see ReVelle 2008 for more details). Next we will assign $R_o \geq 100$ m as a practical value for a *large* source and $R_o \leq 5$ m as a practical value for a *small* source. We can then put physical limits on the regimes identified in the above table. If we use the conventional x definition = $(R^2+z_s^2)^{1/2}/R_o$, we can identify the following regime limits for both a ground level source (where R = range, z_s= source altitude and R_o = blast wave relaxation radius) and one at 50-km altitude in parentheses as indicated later on in (i) to (vi) in section 11.5.5

signal since the dispersion is normal with low frequencies arriving first followed by successive higher frequencies unlike the acoustical signals, which are inversely dispersed and have the highest frequencies arriving at the earliest times followed by progressively longer frequency signals.

Results of our direct entry modeling capabilities (ReVelle, 1976, ReVelle, 2007) for the famous Revelstoke meteorite fall of March 31, 1965 are presented in Figs. 11.20–11.23 below. The predicted panchromatic stellar magnitude (very similar to the optical stellar magnitude) of almost -23 stellar magnitudes is almost as bright as the Sun (as would be observed at 100 km in the zenith) and has been plotted vs. the geopotential height in Fig. 11.20. The large jump in brightness at the lowest heights corresponds to the fragmentation of the body that can also be observed in the blast wave radius in Fig. 11.23. The predicted velocity profile has been plotted in Fig. 11.21, where it can also clearly seen that the terminal speeds at the lowest heights have been predicted to dramatically decrease to those typical of surviving meteorite fragments. The blast wave signature time series (the pressure–amplitude source function) at the corresponding peak blast wave generation altitude has also been plotted in Fig. 11.22. Finally, the computed blast wave radius as a function of altitude has been plotted in Fig. 11.23, where the predicted effects of fragmentation with a correspondingly huge increase in the blast radius at the lowest heights can be clearly identified. This predicted increase in the blast radius also translates into a correspondingly large increase in the predicted wave period.

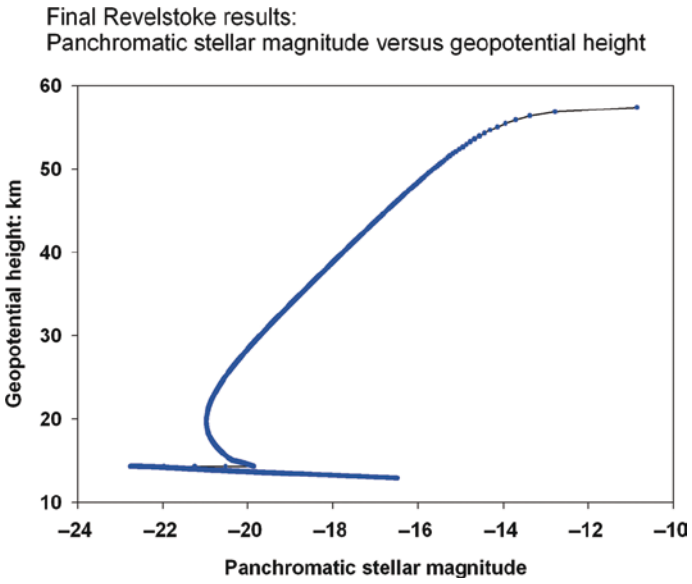

Fig. 11.20 Revelstoke meteorite modeling- Panchromatic stellar magnitude (at a standard height of 100 km in the zenith) as a function of the geopotential height (km)

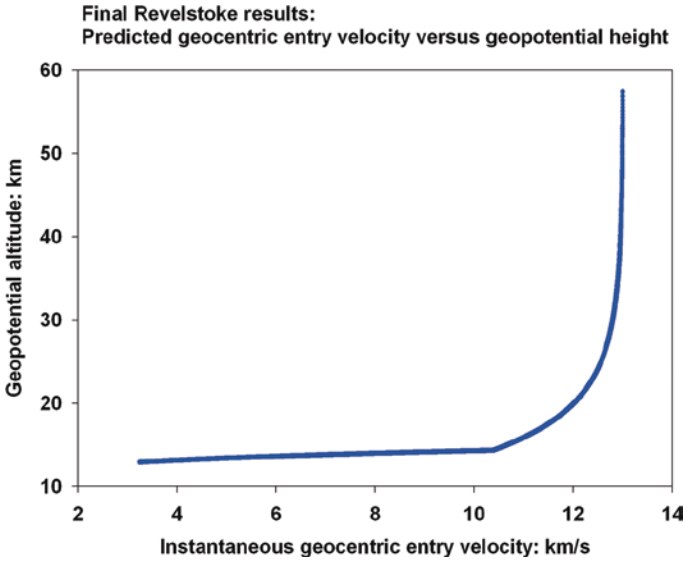

Fig. 11.21 Revelstoke meteorite modeling- Instantaneous velocity (km/s) as a function of the geopotential height (km)

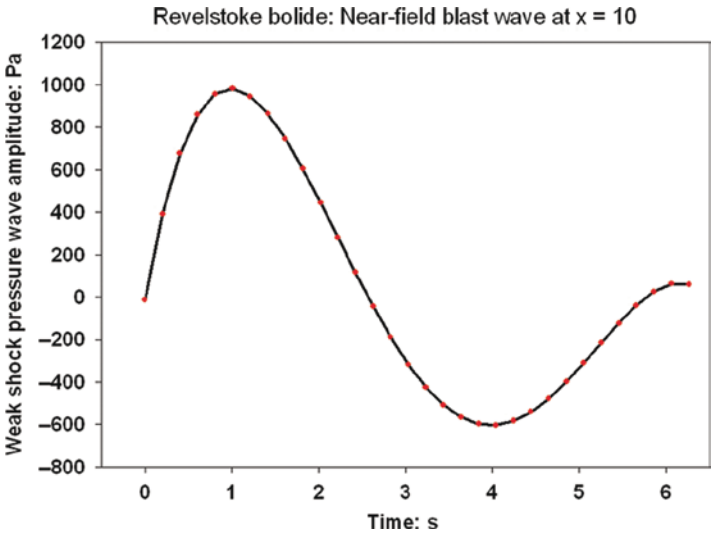

Fig. 11.22 Revelstoke meteorite modeling- Near-field (x = 10) blast wave source amplitude-time series

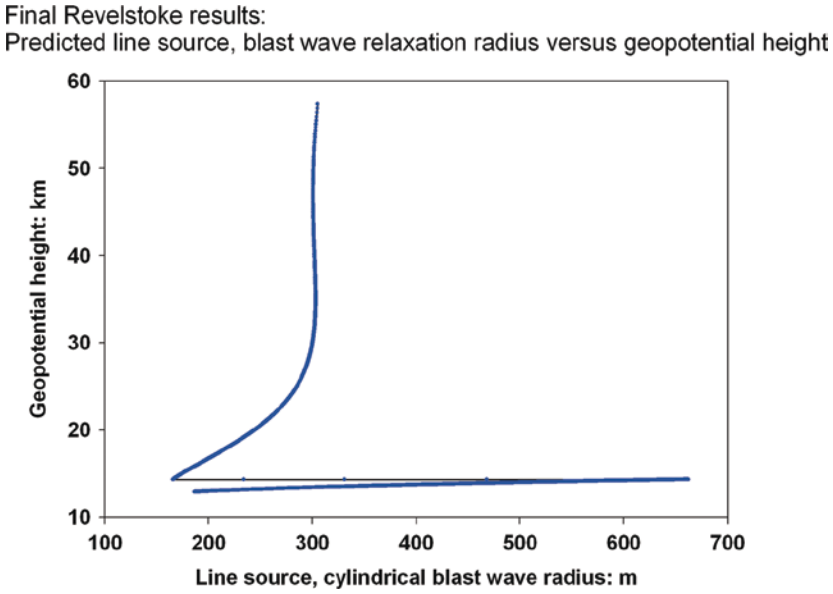

Fig. 11.23 Revelstoke meteorite modeling- Line source blast wave radius (m) including low altitude fragmentation effects as a function of the geopotential height (km)

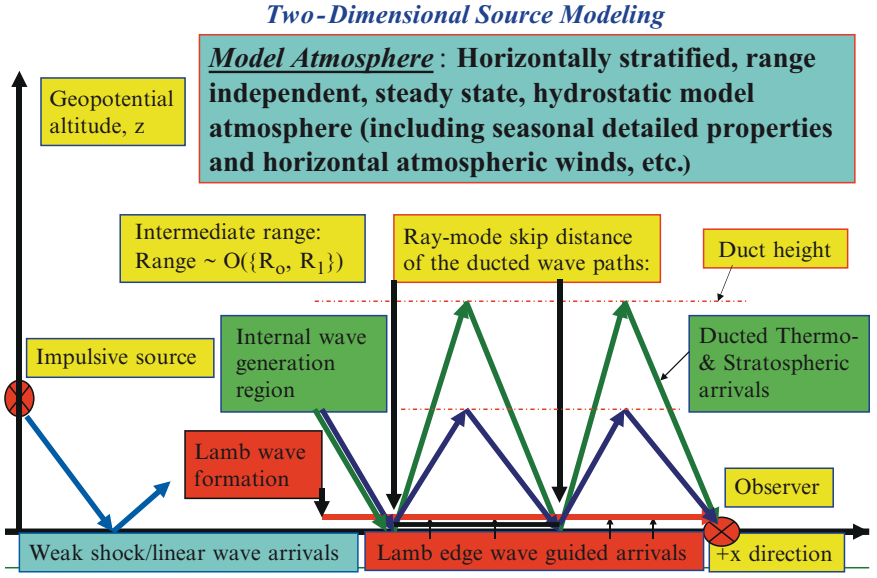

Fig. 11.24 Two-dimensional AGW atmospheric propagation diagram that schematically illustrates the range and height development of various types of signals expected from impulsive sources in middle latitudes

11.5.3 AGW Results for Large and Distant Meteors

In the modeling of these AGW signals, to facilitate comparisons against actual observations, results have been predicted into two separate frequency bins as noted earlier, namely:

1. The full AGW spectrum solution: The total AGW frequency result
2. Acoustic solution: Results for only wave frequencies above ω_{ac}

In what follows below, the results are only presented for the full AGW spectrum.

In Fig. 11.25, the predicted AGW pressure wave signature computed for a range of 3497 km as would be observed at the infrasonic array, PD has been plotted (ReVelle, 2008). Examples of the predicted AGW waveform for downwind ($\alpha = 0°$), counterwind ($\alpha = 180°$) and cross-wind conditions ($\alpha = 90°$) have all been indicated in this figure (in three panels from top to bottom, respectively). These early pressure wave signature results used a far simpler waveguide ducting scheme (including however both strato- and thermospheric ducted phases) than is currently under development (and which will be discussed further below). In the future, all cases will be redone using our more advanced and more realistic, but yet still idealized homogeneous waveguide ducting procedure.

In Fig. 11.25, for example, $\langle L \rangle$ is defined as the atmospheric horizontal dispersion distance scale used for these AGW computations. $\langle L \rangle$ is discussed further in ReVelle (2008). To realistically compare these synthesized AGW signals from the Revelstoke meteorite fall against observations, however, we must also remember that the frequencies allowed by the instrumental band-pass monitoring filters in common use do not include the entire AGW spectrum. These band-pass frequencies range from ~0.01 to 4 Hz for the International Monitoring System arrays and from ~0.04 to 8.2 Hz for both the National Oceanographic Atmospheric Administration (NOAA) arrays still in use and for the Air Force Technical Applications Center (AFTAC) arrays, which were in widespread use up until 1974. Thus, the detailed comparison between observations and theory using a restricted set of filtered AGW signals cannot be fully completed yet, because the effects of the wind-noise reduction filters (after attachment to the microbarographs) has not yet been fully analyzed in terms of the expected frequency modification of the AGW signals. This is not a new problem, but one that has needed resolution by the infrasonic scientific community for a very long time.

In Fig. 11.26, the observed time series of AGW signals from the Revelstoke meteorite fall for all four sensors as recorded at the AFTAC PD array at ~3,497 km range is plotted ReVelle (2008). Although the agreement is in general similar, there are also significant amplitude differences that depend, in part, on exactly what altitude the AGW waves originated from. In this modeling, we have *assumed* that the signals emanated from the altitude of the maximum blast wave relaxation radius, but this simply may not be the case. Detailed testing of signals recorded from a number of additional locations, which is certainly possible for this very well observed bolide event, should be actively pursued. In addition, however, it should be noted that the previous ducted mode solutions used in the computations and shown

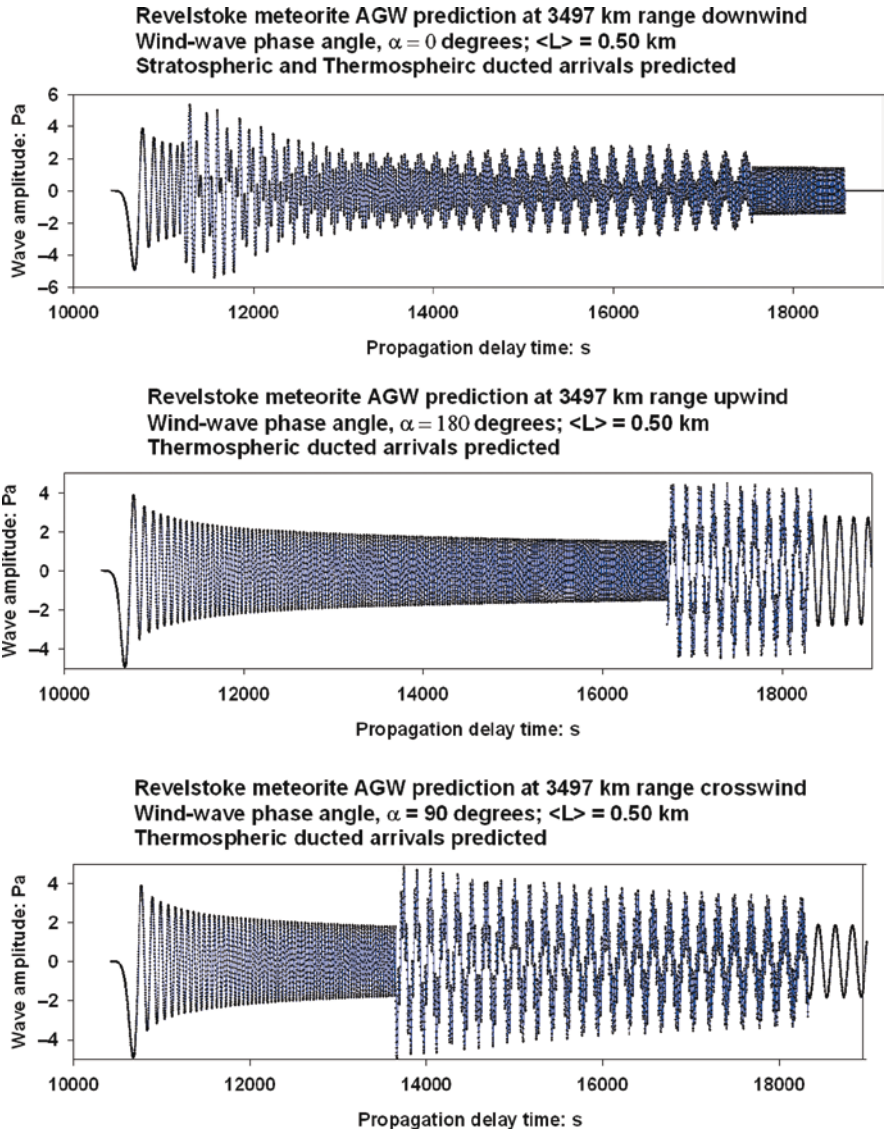

Fig. 11.25 AGW signatures predicted as a function of the wind-wave phase angle, α, for α=0° (downwind), α=180° (counterwind), and α=90° (crosswind) at a horizontal great circle range of 3,497 km from the bolide

in Fig. 11.25 are far simpler than the more realistic ducted solution technique indicated below. The Fortran computer code for these computations is currently undergoing extensive debugging and so the latest Revelstoke AGW solution cannot yet be provided for this important case, but will be completed soon.

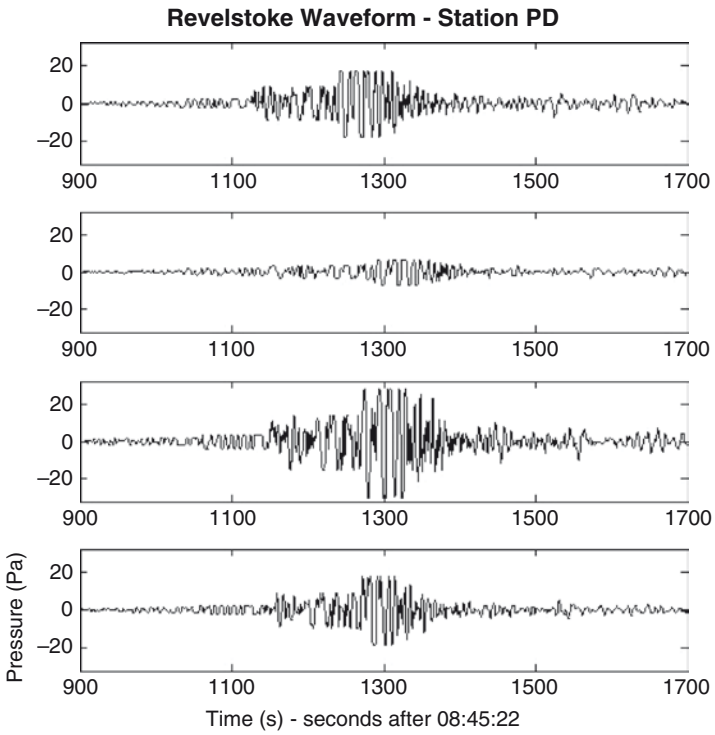

Fig. 11.26 Observed amplitude-time series for four sensors at AFTAC array PD of the arrival of AGW's from the Revelstoke meteorite fall at 3497 km horizontal range (HF bandpass: 8.2 Hz to 25.0 s)

Waveform dispersion in each of the two fundamental branches of the AGW spectrum was modeled by computing the phase and group velocities as a function of wave frequency separately. This allowed the Dirac delta function source (or a Heaviside step function source, etc.) initially composed of a pulse with all frequencies to be dispersed during propagation into a long duration wave train as individual "linear" frequencies traveling with their own individual phase speeds over differing propagation paths. The computed wave train duration is a function of the computed dominant frequency (which also depends on the source blast wave radius or the corresponding source energy input) and on range. In this part of the modeling, the atmosphere was treated as a perfectly stratified, steady state, lossless medium that is in exact hydrostatic balance and that is not range-dependent (using Cartesian coordinate geometry for a specified set of sound and horizontal wind speed variations allowed that will only satisfy the WJKB approximation, i.e., a slowly varying medium). Theoretical work on dissipation due to classical absorption, molecular relaxation, turbulent scattering effects, etc., will be incorporated later. For most low-altitude sources, this is quite a small effect, except perhaps for propagation in the thermospheric waveguide (ReVelle et al., 2009, to be submitted). This atmospheric AGW dispersion problem has previously only been modeled numerically

using very complex and detailed matrix-based algorithms with the exception of the analytic analyses provided in detail in the pioneering work of Meecham (1965) to understand this physical process.

New efforts at AGW modeling discussed further below has made use of two basic atmospheric waveguides (ducts or sound channels) for propagation in any direction with respect to the prevailing, synoptic-scale, mean horizontal winds (with horizontal spatial scales exceeding ~1,000 km). It should be remembered, however, that unlike the thermospheric duct, (extending from the ground to ~110 km), the stratospheric duct (extending from the ground to ~55 km) only exists because of the presence of the mean horizontal wind field and due to small scale sound speed fluctuations. This is because the sound speed profile in the atmosphere nearly always has its maximum value at the ground because of direct solar heating effects. The heights of these ducts in the computations to be discussed are individually computed from the atmospheric data input to our wave source and propagation code (as can be determined by examining Figs. 11.1–11.3). There are certainly other and usually more temporary duct types such as the tropospheric duct (typically extending from the ground to ~15 km), but this can only exist if the vertical gradient of the horizontal tropospheric jet stream wind (which provides the necessary refraction of the signals) is physically present somewhere along the propagation path. In addition, there is also a planetary boundary layer duct (extending from the ground up to the height of the inversion layer aloft and typically this distance is only a few hundred meters for nocturnal radiative temperature inversions in middle latitudes), but for the moment, only the most fundamental atmospheric waveguide ducts have been included since they are expected to significantly influence long distance AGW propagation.

The current procedure that is being used to determine exactly which wave modes could be successfully ducted (which depends quite sensitively upon the atmospheric data for a given date, time and location for a specific event) was modeled using two separate constraints.

This process was treated "exactly," in the limit of an ideal (homogeneous) waveguide, by first assuming that:

(a) Angle of incidence = Angle of reflection

at both the upper and lower duct interfacial boundaries.

Obviously, the wavelengths of the propagating waves are important for this assumption because the local ground topography can significantly change this condition if the corrugated lower boundary has horizontal length scale changes (due to terrain changes or the presence of mountainous regions) comparable with the wavelength of the waves).

Second, a boundary condition was also imposed at both boundaries that demanded that:

(b) The vertical gradient of the pulse amplitude = 0

so that the wave frequency and amplitude would be unchanged upon reflection at both the upper and lower waveguide boundaries

This process resulted in a "geometric fitting" of the dominant wavelength of the dispersed pulse both horizontally as well as vertically within the atmospheric waveguide's structure. This treatment of the possible wave modes (as evaluated below using data in Figs. 11.1–11.3 for the atmospheric sound speed and horizontal wind speed structure at the time of the Carancas meteorite fall on September 15, 2007) included the computation of an integer waveguide mode number for each mode ranging from n = 0 (the low-frequency horizontally propagating Lamb wave) to wave propagation at right angles (upward and downward) to the direction of the two-dimensional waveguide axis at $n = n_{max}$, where n is the mode number and n_{max} is the largest mode number allowed within the duct.

In this newest wave ducting scheme, the lowest order modes travel horizontally, nearly straight down the waveguide with a group velocity almost equal to that of the effective sound velocity (defined to include the thermodynamic sound speed structure as well as the mass average horizontal winds) and the highest order modes travel nearly perpendicular to the two-dimensional waveguide axis with very small group velocity, i.e., with almost no energy transfer down the waveguide. To facilitate the essential correctness of these ducting evaluations that have been indicated in Fig. 11.27, the following constraints have also been imposed that allow for data measurement errors and additional factors:

(c) A near-integer number of hops, n, must be determinable between the source and observer ($\neq 0$). In addition, if the number of hops < some limiting value, these possible solutions were also rejected.
(d) A "miss" distance was also computed for each of these "rays" that satisfied condition (a). The miss distance value was further assigned on the basis of the

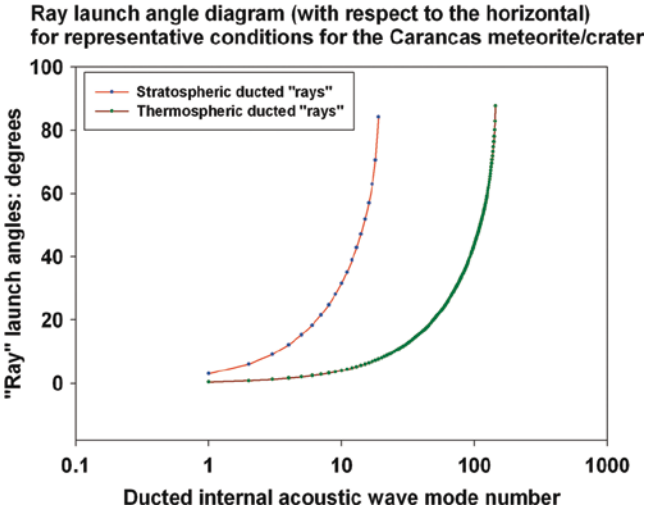

Fig. 11.27 Predicted ducted internal acoustic wave mode number vs. the "ray" launch angle for stratospheric and thermospheric atmospheric ducts that were evident at the time of the Carancas meteorite fall of September 15, 2007

Table 11.2 Ducted wave solution: Carancas meteorite fall at 1,560 km range

Return type	Mode number	Computed no. of hops (n)	Computed miss distance (km)
1[a]	3	0.8823	*2.4493*
1	4	1.1778	*4.3619*
1	7	2.0728	*13.4709*
2	1	~0	–
2	2	~0	–
2	3	~0	–
2	13	0.8047	*9.6443*
2	14	0.8674	*11.2011*
2	15	0.9303	*12.8782*
2	16	0.9935	*14.6768*
2	17	1.0568	*16.5979*
2	*18*	*1.1203*	*18.6428*

[a]Return type = 1: Stratospheric; Type = 2: Thermospheric
[b]For type = 2, Modes 1–3, have n values too close to 0

computed e-folding widths for Gaussian beams as a function of the horizontal range (as discussed briefly below).

Using this new procedure, a graphical modal summary of the full set of possibilities of horizontal "ray" launch angles vs. the internal acoustic mode number is presented in Fig. 11.27.

Also presented below in Table 11.2 are the ducted modal solutions that satisfy our stated criteria (c) and (d) above for the Carancas meteorite fall at a horizontal range = 1,560 km (applicable for signals recorded at the infrasonic array IS041 in Paraguay). This was done using the full set of atmospheric properties in Figs. 11.1–11.3 at the time of the Carancas meteorite fall (and associated crater formation in Peru). Using this new procedure, three stratospheric and nine thermospheric modes were successfully predicted for this case. For these predictions, the number of near-integral hops, n, were only accepted if the numerical values fell between n–0.80 and n+0.20, i.e., within a 20% error bound and with an assumed "Gaussian width" miss distance = 20 km.

Thus, from among the numerous possibilities computed, only a few acoustic ducted modes were found to satisfy both of the aforementioned criteria. This was the case determined for a waveguide with a very specific set of atmospheric properties in which the effective sound speed (including horizontal winds) varies only with height and was independent of time. The computed miss distance criterion was set on the basis of Gaussian beam tracing procedures (for details see Porter and Bucker 1987 and Attenborough et al. 1995).

The predicted ducted ray propagation behavior within each duct could have been treated in at least two fundamentally different ways. First, the mean effective sound speed could have been averaged and combined with the averaged horizontal wind speed for each duct to compute a mean "ray" angle during the propagation. From this angle, the number of hops between source and observer can be

readily computed. Alternatively, the "ray" launch angle could be averaged as it undergoes changes after passage through the entire duct with a varying effective sound speed. For the moment, only the first approach has been used, however, because of its inherent simplicity. Because of the currently imposed boundary conditions, scattering effects due to topography and horizontal waveguide imperfections (resulting in waveguide energy leakage) cannot now be readily modeled, except numerically as noted earlier. Such imperfections will be examined in future modeling efforts.

11.5.4 Results for Small, Quite Close Meteors

In addition, an example of our new AGW modeling capability at close range for the case of very high-speed and high-altitude Leonid meteors with correspondingly smaller blast wave relaxation radii will also be presented. This capability allows the prediction of the same types of arrivals that were also allowed for larger bolides at greater ranges, namely weak shock, direct or ducted arrivals, and the corresponding internal atmospheric acoustical arrivals assuming little or no dispersion for the weak shock arrivals. These weak shock time–amplitude signatures are also derived by modeling the entry dynamics and energetics for individual, but quite small meteors (and with correspondingly much lower luminosity levels).

Work now in progress is using this new AGW capability in combination with direct multi-instrumental detections at the ELFO (Elgin Field Observatory) of the University of Western Ontario at their Department of Physics and Astronomy under the direction of Professor Peter G. Brown (this new work uses CCD all-sky cameras, meteor radar, an infrasound array, seismic data, etc. as part of the SOMN, the Southern Ontario Meteor Network).

Presented in Fig. 11.28 is a calculation of an AGW signature from a very high-velocity Leonid meteor at quite close range for a small blast wave source with signals emanating at high altitudes above the earth.

Note that the earliest predicted arrival in Fig. 11.28 is the very brief and relatively small amplitude (~0.8 Pa peak to peak) weak shock wave emanating directly from the low-density Leonid meteor followed by about 5 min of slightly dispersed atmospheric acoustical waves. The blast wave arrival has a wave period whose value is directly related to the line source blast wave radius as described earlier in the text.

11.5.5 Generalized Results

A summary table is given below for completeness of all possible types of included component atmospheric signals that have been allowed in the treatment by ReVelle (2008) for signal from impulsive sources:

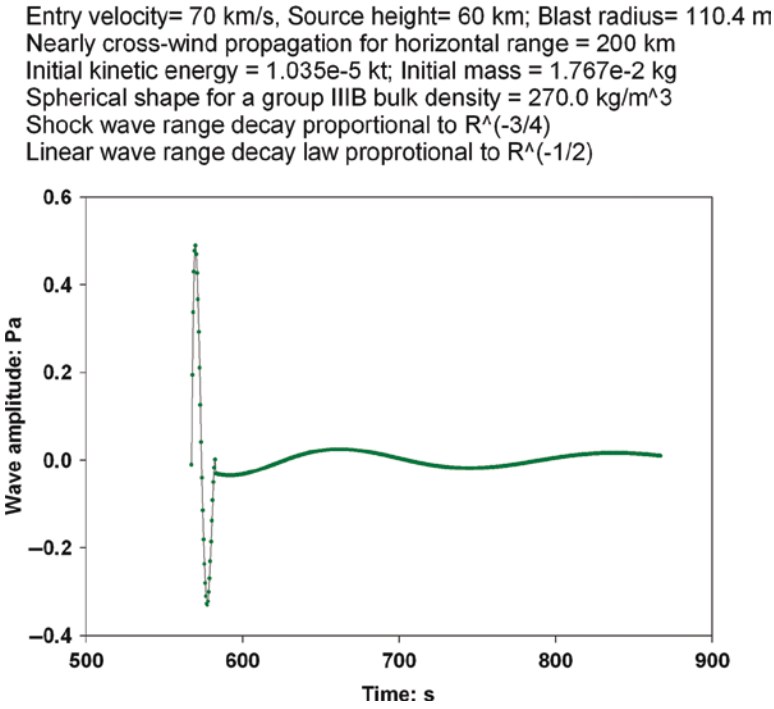

Fig. 11.28 Predicted amplitude-time series of an AGW at relatively close range from a SOMN-type bolide: Entry velocity = 70 km/s, Source height = 60 km, Maximum blast radius = 110.4 m, Horizontal range = 200 km, Initial kinetic energy = 1.035 X 10(-5) kt, Initial mass = 1.767 X 10(-2) kg, Assumed bulk density = 270 kg/m^3 (Weak cometary material)

(i) Large source (LS) – Close range: $R_o \geq 100$ m, $x < 3.0 \times 10^3$ (3.041×10^3)
(ii) Small source (SS) – Close range: $R_o \leq 5$ m, $x < 6 \times 10^4$ (6.083×10^4)
(iii) LS – Intermediary range: $R_o \geq 100$ m, 1.0×10^3 $(1.118 \times 10^3) < x < 3.0 \times 10^3 (3.041 \times 10^3)$
(iv) SS – Intermediary range: $R_o \leq 5$ m, 2×10^4 $(2.236 \times 10^4) < x < 6 \times 10^4$ (6.083×10^4)
(v) LS – Great range: $R_o \geq 100$ m, $x > 1.0 \times 10^3$ $(1.118.0 \times 10^3)$
(vi) SS – Great range: $R_o \leq 5$ m, $x > 2 \times 10^4$ (2.236×10^4)

This transitional set of AGW behavior suggests a simplified, dimensionless scaling index, I_{AGW} can be developed to better understand the possible types of AGW signals that should be expected for various source and range conditions as follows:

$$I_{AGW} = \{R / R_{dis}\} \bullet \exp[-z_s / H_p] \bullet \{R_0 / L\} \tag{11.13}$$

I_{AGW} = AGW behavior index

where

R_{dis} = Distance formation scale for the fully dispersed Airy function of normally dispersed atmospheric internal gravity waves, H_p = Pressure scale height (or more generally the density scale height) = $-p/\partial p/\partial z = RT/g$, where p = air pressure, T = air temperature, g = acceleration due to gravity, and R = universal gas constant divided by the mean molecular weight of the gas

L = Line source length of the bolide

$\rho(z)/\rho_o$ = Air density ratio: The value at the source height to the surface value ($z=0$) where $\rho(z)/\rho_o = \exp[-z_s/H_p]$ in an isothermal atmosphere.

Since the blast wave radius also allows the fundamental wave frequencies of the weak shock wave to be predicted, it also allows an estimate of weak shock effects from a bolide event as a function of range, etc. Some obvious predictions of atmospheric AGW behavior using I_{AGW} are as follows (with obviously many more permutations being possible for all the variables of interest) where weakly nonlinear shock wave distortion effects can be estimated in combination with the distortion distance concept as briefly discussed earlier in this chapter and as discussed at greater length in Morse and Ingard (1969) and in ReVelle (1976):

(a) $I_{AGW} << 1$: $R << R_{dis}$; $R_o << L$; $z_s << H_p$:

Lamb waves are very unlikely to have formed
Dispersed internal acoustic waves are very unlikely
Weak shock wave pulse effects are likely (high frequencies)

(b) $I_{AGW} >> 1$: $R >> R_{dis}$; $R_o < L$; $z_s << H_p$:

Lamb waves are likely very well developed
Dispersed internal acoustic waves are very likely
Dispersed weak shock wave effects are likely

(c) $I_{AGW} < 1$: $R >> R_{dis}$; $R_o < L$; $z_s >> H_p$:

Lamb waves are very likely to have formed, but very unlikely to have significant amplitude
Dispersed internal acoustic waves are very unlikely
Dispersed weak shock waves are likely due to elevated sources

(d) $I_{AGW} > 1$: $R >> R_{dis}$; $R_o < L$; $z_s << H_p$:

Lamb waves are very likely to have formed, but only with moderate amplitude
Dispersed internal acoustical waves are very unlikely
Dispersed weak shock waves are likely

(e) $I_{AGW} \sim O(1)$: $R \sim R_{dis}$; $R_o < L$; $z_s << H_p$:

Lamb waves are unlikely to have formed, but only with small amplitudes
Dispersed internal acoustic waves are unlikely
Weak shock wave pulse effects are likely

(f) $I_{AGW} \sim O(1)$: $R \sim R_{dis}$; $R_o < L$; $z_s >> H_p$:

Lamb waves are very unlikely

Dispersed internal acoustic waves are unlikely
Weak shock wave pulse effects are even more likely

As shown earlier, waveguide ducting possibilities within the atmospheric waveguide can now be evaluated "exactly" (ignoring certain effects like lower boundary terrain irregularities, etc.) with an approach that is a function of the individual atmospheric sound speed and horizontal wind-speed profiles. Thus, such ducting effects may not be more generally clarified using a simplified index approach as suggested earlier. Atmospheric propagation regimes can only be roughly identified with this type of index approach in an attempt to understand when we should expect certain types of various component signals for sources at various altitudes, observed ranges, and differing source energies emanating from the atmospheric wave zoo.

11.6 Future Work

In the future, additional cases of meteoroids monitored by multiple techniques will also continue to be physically modeled to establish well calibrated compositional and physical quantities that can be used to better understand the fundamental origins of these diverse solid particles (that are believed to be very representative of the early solar system). In addition, the inclusion of detailed wave energy dissipation effects is a topic that is next on the list for inclusion in the numerical AGW modeling code that has already been established.

Acknowledgments The author thanks the Ground-based Nuclear Explosion Monitoring (GNEM) program and the personnel in NA-22 at DOE HQ for financial assistance of our infrasonics explosion monitoring work for the past 15 years. He also thanks Professor Peter G. Brown for his continuing interest, support, and financial assistance in making this continuing work on bolides both possible and exciting for both of us and many students over the last several years. He thanks a number of individuals for their help and encouragement in the development of this chapter material. This includes Los Alamos National Laboratory (LANL), Earth and Environmental Sciences (EES) Division and Institute of Space and Response (ISR), LANL Center for Space Science and Exploration (CSSE) and Institute of Geophysics and Planetary Physics (IGPP) personnel as well as individuals at the US Department of Energy (DOE) HQ at NA-22 in Washington, DC. In addition, he also thanks a number of researchers from North America and in Europe who helped encourage him during the lengthy preparation of this material. This includes Professor Peter G. Brown of the University of Western Ontario and Dr. Pavel Spurny of the Czech Academy of Science in Ondrejov, in the Czech Republic, etc.

Appendix: Diffuse Shock Waves at High Altitudes in Isothermal and NonIsothermal Atmospheres

As the meteor interacts at very great altitudes with the exponentially decaying atmospheric environment first while in the outer fringes of the earth's atmosphere, it reacts by electrical charging effects that are poorly understood and by subsequently melting,

vaporizing, undergoing fragmentation, etc. These processes occur directly because the available energy/mass greatly exceeds the energy necessary to completely destroy the body for any reasonable and reasonably well-known composition (Hankey 1988). This interaction type depends, in turn, on the flow regime, i.e., whether the characteristic dimension of the body is greater than or less then the atmospheric neutral gas mean free path. This process can be formally evaluated using the dimensionless combination of parameters called the Knudsen number, Kn (Hankey 1988). In the former regime, continuum flow ($Kn << 1$) has been achieved, and the interaction leads to the formation of a well-developed and largely inviscid shock wave with strong shock radiative properties, whereas in the opposite extreme ($Kn >> 1$), the interaction is termed free molecular. In the latter regime, the interaction is more locally intense in that the shielding provided by a protective air "gas cap" (but still including the ablation products from the mass loss suffered by the body) is largely absent and direct impacts with the body's surface are commonly endured. Diffuse shock waves can still form, however, as discussed in ReVelle (2004, 2005). The Knudsen number can also be scaled with respect to the wavelength of the line source blast wave for the energy deposition process into the atmosphere even though normally, it is scaled with respect to the local neutral gas mean free path with regard to local meteor or bolide heating and ablation effects (ReVelle 2008). Thus, in addition, in the free molecular-flow regime, the meteor and/or bolide energy deposition process also drives intense local atmospheric heating effects, which are progressively stronger at greater altitudes that arise from the decay of the diffuse shock waves formed at somewhat greater distances from the trajectory (ReVelle- Implications of Bolide Entry Solutions for the Condition of One Hundred Percent Differential Acoustic Efficiency: A Numerical and an Analytic Study, to be submitted, 2009). In between these two local ablational heating extremes, the interaction is of the slip-flow or of the transitional-flow type ($Kn \sim O(1)$), where a viscous shock-wave interaction with the frontal cross section of the body occurs, which can also greatly increase localized heating rates (by interference heating effects, etc. as described in Hankey 1988). Through these very intense local meteor heating effects as a function of the Kn, scaled with respect to the local mean free path, the processes of quasi-continuous ablation and air drag (including deceleration) and even discontinuous and often catastrophic fragmentation processes can also typically occur (if the mechanical stagnation pressures on the front face exceed the breaking strength of the body or through conductive heating effects for very small bodies).

Meteor Source Energy Coupling to the Atmosphere: Line Source Blast Waves

From the fundamental hypersonic drag interaction of meteoroids with the atmosphere, the direct entry, dynamical-energetics theory (ReVelle 2004, 2005) can be used, which will fully constrain the deposition of energy in various forms. This includes the deposition of heat, light, waves (infrasound and acoustic waves in the

high-frequency limit, otherwise for the full AGW wave spectrum), ionization, dissociation, etc. Similar modeling efforts have also been made for the re-entry of man-made space capsule reentries (ReVelle et al. 2005; ReVelle and Edwards 2006).

Using this approach, the line source blast wave generated by the bolide in various atmospheric regions (if $\mathrm{Kn} < 1$ so that a quasi-continuous flow regime can be established) can then be readily coupled to the propagation of AGW's. Furthermore, this coupling can be realistically evaluated by examining the conservation properties of the wave kinetic energy density (with small amplitude wave "linearity" assumed) during its propagation from the source to the observer under the assumption of inviscid propagation as discussed earlier in the main body of this chapter. As shown in detail in ReVelle et al. (2004) for the Neuschwanstein fireball and meteorite fall, the wave kinetic energy is dynamically and energetically linked in range to the differential acoustic efficiency (for the original work see ReVelle and Rajan 1979 and ReVelle 1980); as predicted at the fireball at $x = 10$ (10 blast wave radii away from the trajectory). Only for the smaller bolides at progressively greater altitudes do we expect this conservation principle to break down as the wave dissipation heats the atmosphere due to wave energy losses to its surroundings due to classical (molecular shear viscosity and heat conduction) as well as nonclassical mechanisms (molecular internal relaxation, turbulence, etc.). Within certain knowable limits using this type of approach, the initial conditions for the line source blast wave pulse can be fully determined such as its detailed amplitude, wave period, duration of the positive and negative phases of the wave, etc.

Near-Field vs. Far-Field Wave Amplitude Behavior

A pioneering and now quite old breakthrough article by DuMond et al. (1946) and summarized more recently by Snow (1967) showed conclusively the near- and midfield behavior expected for the propagating line source blast wave from small projectiles in a nearly homogeneous (constant density) atmosphere. Within one blast wave radius of the source, the explosion properties of the line source are fully realized, whereas at much greater distances, the wave behavior is in the near-field shock wave regime and still further away the eventual small amplitude, linear wave limit can be fully expected (Thompson 1972). As shown in detail in Morse and Ingard (1969), the degree of waveform distortion becomes progressively greater as the wavelength of the disturbance decreases (progressively higher wave frequencies) or as the overpressure ratio ($\Delta p/p$) becomes larger.

For a ideal diatomic gas including both nitrogen and oxygen molecules predominantly, γ, the ratio of the specific heat at constant pressure to that at constant volume is approximately $\cong 1.40$. Thus, in a homogeneous medium, the predicted overpressure ratio can be written as a function of $f(x)$, which simultaneously allows for both

the nonlinear strong shock blast wave limit as well as the weak shock decay small amplitude limit in the form (ReVelle 1976):

$$\Delta p / p_0 \cong \{\gamma(2.0(\gamma + 1.0))\} \cdot f(x) \tag{A1}$$

and where $f(x)$ has been already been defined in (11.12) in the main body of the chapter.

Allowing for source heights significantly above ground level ($z = 0$) in an isothermal, hydrostatic atmosphere where the air pressure decays exponentially according to the local pressure scale height and simultaneously allowing for large scaled range, the aforementioned expression with "C" = "δ" = 1 as discussed earlier in the main body of this chapter, can be simplified using (11.12) to the limiting far-field form in an isothermal atmosphere, which represents the meteor/bolide blast wave amplitude source function (ReVelle 1976):

$$\Delta p \cong 0.2917 \cdot D_{ws}(r) \cdot x^{-3/4} \cdot \{p^*\};\ x > \sim 10^2 \tag{A2}$$

where

p_o = Surface atmospheric pressure: Pa,
$p(z)$ = Air pressure at the source altitude: Pa,
$p(z) = p_o \cdot \exp[-\int\{dz/H_p(z)\}] = p_o \cdot \exp[-\{z/H_p\}]$,
$\rho(z) = \rho_o \cdot \exp[-\int\{dz/H_\rho(z)\}] = \rho_o \cdot \exp[-\{z/H_\rho\}]$,
H_p = Pressure scale height = $-p(z)/\partial p/\partial z$, and
H_ρ = Density scale height= $-\rho(z)/\partial\rho(z)\partial z$

In an isothermal, hydrostatic atmosphere with $H_p = H_\rho$. $\{p^*\} = \{p_o \bullet p(z)\}^{1/2}$ = geometric mean pressure between source and observer, x = scaled total range from the line source explosion = R/R_o, R = total distance from the explosion: km, R_o = line source cylindrical blast wave relaxation radius: km, and $D_{ws}(r)$ = weak shock dissipation function (assumed = 1, independent of wave frequency or altitude in this analysis).

This pressure scaling for an isothermal atmosphere is proportional to the square root of the surface air pressure value times the pressure value at the source altitude. This scaling comes from the assumption of conservation of the wave kinetic energy density during the AGW propagation as height changes. Thus, in a strictly isothermal, hydrostatic atmosphere ($c_s(z)$ = constant), as the height of the wave increases (decreases) progressively, the velocity amplitude of the wind due to the wave increases (decreases) and are both proportional to the square root of the air density changes (or are also proportional to the square root of the air pressure changes). This fully accounts for the form of the correction factor above.

Further, we will reevaluate the form of this correction factor in a nonisothermal atmosphere. In addition, the indicated parameters ignore a ground reflection factor that is between unity and the amplitude doubling limit, assuming that the wave frequency is sufficiently low so that only a negligible amount of wave energy can actually be transmitted through or absorbed by the local ground surface (Attenborough et al. 1995).

The combination of parameters used in (11.A2) for quasi-linear or for full weak shock propagation insures that the wave kinetic energy density is conserved during atmospheric propagation (see for example, ReVelle et al. (2004) where this concept has been applied to our interpretation of the entry modeling and infrasound recordings from the Neuschwanstein meteorite fall in Germany).

Isothermal vs. Nonisothermal Atmospheric Relationships

From previous treatments of the conservation of the wave kinetic energy density for inviscid fluid flows (which we have implicitly assumed throughout this current analysis), a correction factor is now sought to replace $\{p^*\}$ in (11.A2) that accounts for the behavior of acoustical waves generated aloft in a nonisothermal, hydrostatic atmosphere. However, this limit is not the only one that can readily be analyzed as a detailed theoretical analysis of the behavior of infrasonic signals from four, very high altitude (>~90–100 km), but quite bright shower meteors that incorporates classical dissipation (using realistic molecular heat conduction, shear viscosity, and molecular internal relaxation coefficients) in the limit of "quasilinear" wave propagation has already been completed ReVelle, Edwards, Brown and Spurny (2009).

To evaluate the nonisothermal effects expected, we now rely on (11.9c) that has already been formulated for locally plane waves in Sect. 11.2.4. in the main body of this chapter. From this relationship, it is clear that in the more general nonisothermal atmospheric case, the product of the square root of the air density times the adiabatic, thermodynamic sound speed is proportional to the pressure wave amplitude if the wave kinetic energy density is to remain a constant. Thus, the linear wave relationship for an ideal gas can readily be formulated in a fully nonisothermal, hydrostatic model atmosphere in the far-field limit in the form:

$$\Delta p = 0.2917 \bullet D_{ws}\,(r) \bullet x^{-3/4} \bullet \{[\rho(z_o) / \rho\,(z_s)]^{1/2} \bullet [c_s(z_o) / c_s(z_s)]\} \qquad \text{(A3)}$$

which is applicable again for $x > \sim 10^2$ and where z_o is the lower boundary of the atmosphere ($z=0$) and z_s is the corresponding blast wave source altitude.

Thus, the linear correction factor for correctly predicting the wave amplitude as a function of height in a nonisothermal, hydrostatic model atmosphere is given by the quantity in the curly brackets on the extreme right-hand side of (11.A3), replacing the expression p^* for an isothermal, hydrostatic model atmosphere.

Of course, none of these wave energy correction factors directly account for the focusing (or defocusing) effects of the horizontal wind field in the downwind (upwind) direction in a stratospheric waveguide for example. These amplitude considerations are a separate problem not treated within this chapter at all, but one that has been recently solved by the author after modifying the classical ocean-acoustics version of ray-mode theory to include the mean horizontal winds at all heights in a

medium with two permanent sound channels and while allowing for the full range of AGW frequencies (ReVelle 2009).

References

Attenborough K, Taherzadeh S, Bass HE, Di X, Raspet R, Becker GR, Gudesen A, Chrestman A, Daigle GA, L'Esperance A, Gabillet Y, Gilbert KE, Liu YL, White MJ, Naz P, Noble JM, van Hoof HAJM (1995) Benchmark cases for outdoor sound propagation models. J.A.S.A 97:173–191

Beer T (1975) Atmospheric waves. Adam-Hilger, London, p 300

Brown PG, Edwards WN, ReVelle DO, Spurny P (2007) Acoustic analysis of shock production by very high-altitude meteors-i: infrasonic observations, dynamics and luminosity. J.A.S.T.P 69:600–620

Brown PG, ReVelle DO, Sukara EA, Edwards WN, Arrowsmith S, Jackson LE, Tancredi G, Eaton D (2008) Analysis of a crater forming meteorite impact in Peru. J Geophys Res 113:E09007

Ceplecha Z, Borovicka J, Graham Elford W, ReVelle DO, Hawkes RL, Porubcan V, Simek M (1998) Meteor Phenomena and Bodies, Space Science Reviews, 84:327–471

DuMond JWM, Cohen ER, Panofsky WKH, Deeds E (1946) A determination of the waveforms and laws of propagation and dissipation of ballistic shock waves. J.A.S.A 18:97–118

de Groot-Hedlin CD, Hedlin MAH, Drob DP (2010) Atmospheric variability and infrasound monitoring. This volume, pp. 469–504

Edwards WN, Brown PG, ReVelle DO (2006) Estimates of meteoroid kinetic energies from observations of meteoroid airwaves. J.A.S.T.P 68:1136–1160

Edwards WN, Brown PG, Weryk RJ, ReVelle DO (2008) Infrasonic observations of meteoroids. Preliminary results from a coordinated optical-radar-infrasound observing campaign. Earth Moon Planets 102:221–229

Edwards WN (2010) Meteor generated infrasound: theory and observation. This volume, pp. 355–408

Fleagle RG, Businger JA (1980) Atmospheric physics, Second edn, International Geophysics Series. Academic Press, New York, NY, p 432

Gault DE (1974) Impact Craters, In a Primer in Lunar Geology, (R. Greeley and P. Schultz editors), NASA TMX 62359, pp. 137–175

Gainville O, Blanc-Benon Ph, Blanc E, Roche R, Millet C, Le Piver F, Despres B, Piserchia PF (2010) Misty picture: a unique experiment for the interpretation of the infrasound propagation from large explosive sources. This volume, pp. 569–592

Gill AE (1982) Atmospheric-ocean dynamics. Academic Press, Orlando, p 662

Hankey WL (1988) Re-entry aerodynamics. In: Przemieniecki JS (ed) AIAA Education Series, AIAA, Washington, DC, p 144

Hauchecorne A, Keckhut P, Chanin M-L (2010) Dynamics and transport in the middle atmosphere using remote sensing techniques from ground and space. This volume, pp. 659–678

Jensen FB, Kuperman WA, Porter MB, Schmidt H (1994) Computational ocean acoustics, American Institute of Physics, New York, pp. 300

Jones DL, Goyer GG, Plooster MN (1968) Shock wave from a lightning discharge. J Geophys Res 73:3121–3127

Klostermeyer J (1976) Lamb waves originating in non-geostrophic perturbations. Nature 260:32–34

Le Pichon A, Antier K, Cansi Y, Hernandez B, Minaya E, Burgoa B, Drob D, Evers LG, Vaubaillon J (2008) Evidence for a meteoritic origin of the September 15, 2007. Carancas Crater Meteoritics Planetary Science 43:1797–1809

Lin S-C (1954) Cylindrical shock waves produced by an instantaneous energy release. J Appl Phys 25:54–57

Lott F, Millet C (2010) The representation of gravity waves in atmospheric general circulation models (GCMs). This volume, pp. 679–694
Meecham WC (1965) Simplified normal mode treatment of long-period acoustic-gravity waves in the atmosphere. Proc IEEE 53:2079–2087
Mihalas D, Weibel-Mihalas B (1999) Foundations of radiation hydrodynamics. Dover Publications, Mineola, NY 718
Morse PM, Ingard KU (1969) Theoretical acoustics. McGraw-Hill, New York, NY, p 556
Norris D, Gibson R, Bongiovanni K (2010) Numerical methods to model infrasonic propagation through realistic specifications of the atmosphere. This volume, pp. 535–568
Plooster MN (1968) Shock waves from line sources, NCAR Report TN-37, NCAR, Boulder, CO, p 93
Plooster MN (1970) Shock waves from lines sources. Numerical solutions and experimental measurements. Phys Fluids 13:2665–2675
Plooster MN (1971) Numerical simulation of spark discharges in air. Phys Fluids 14:2111–2123
Porter MB, Bucker HP (1987) Gaussian beam tracing for computing ocean acoustic fields. J.A.S.A 82:1349–1359
ReVelle DO (1976) On meteor generated infrasound. J Geophys Res 81:1217–1230
ReVelle DO (1979) A quasi-simple ablation model for large meteorite entry: theory versus observations. J.A.S.T.P 41:453–473
ReVelle DO (1980) A predictive macroscopic, integral radiative efficiency model. J Geophys Res 85:1803–1808
ReVelle DO (1997) Historical detection of acoustic-gravity waves from atmospheric impact of bolides. In: Remo J (ed) Near-Earth objects, vol. 822, New York Academy of Sciences, United Nations and United Nations Explorer's Club, pp. 284–302
ReVelle DO (2001a) Theoretical Leonid Entry Modeling, Meteoroids 2001, Kiruna, Sweden, European Space Agency, ESA-SP-495, ESTEC, Noordwijk, the Netherlands, Editor: B. Warmbein, 149–154
ReVelle DO (2001b) Large Leonid Entry Modeling: Application to the Bolide of 11/17/1998, Meteoroids 2001, Kiruna, Sweden, European Space Agency, ESA-SP-495, ESTEC, Noordwijk, the Netherlands, Editor: B. Warmbein, 179–184
ReVelle DO (2001c) Global Infrasonic Monitoring of Large Bolides, Meteoroids 2001, Kiruna, Sweden, European Space Agency, ESA-SP-495, ESTEC, Noordwijk, the Netherlands, Editor: B. Warmbein, 483–490
ReVelle DO (2001d) Bolide Fragmentation Processes: Single-body Modeling versus the Catastrophic Fragmentation Limit, Meteoroids 2001, Kiruna, Sweden, European Space Agency, ESA-SP-495, ESTEC, Noordwijk, the Netherlands, Editor: B. Warmbein, 491–496
ReVelle DO (2001e) Bolide Dynamics and Luminosity Modeling: Comparisons between Uniform Bulk Density and Porous Meteoroid Models, Meteoroids 2001, Kiruna, Sweden, European Space Agency, ESA-SP-495, ESTEC, Noordwijk, the Netherlands, Editor: B. Warmbein, 513–518
ReVelle DO (2002a) Fireball Dynamics, Energetics, Ablation, Luminosity and Fragmentation Modeling, Asteroids Comets Meteors 2002, Berlin, Germany, European Space Agency, ESA-SP-500, ESTEC, Noordwijk, the Netherlands, Editor: B. Warmbein, 127–136
ReVelle DO (2002b) Porosity: A Natural Alternative Explanation of Bolide Types, their Atmospheric Behavior and the Implications, Asteroids Comets Meteors 2002, Berlin, Germany, European Space Agency, ESA-SP-500, ESTEC, Noordwijk, the Netherlands, Editor: B. Warmbein, 233–236
ReVelle DO (2005) Recent advances in bolide entry modeling: a bolide potpourri. Earth Moon Planets. doi:10.1007/s11038-005- 9064-4. Also available in the standard print vol. 95, No. 1–4, pp. 441–476, December, 2004
ReVelle DO (2007) NEO fireball diversity- energetics-based entry modeling and analysis techniques, near-Earth objects: our celestial neighbors- opportunities and risk. In: Milani A, Valsecchi GB, Vokrouhlicky D (ed) Proceedings IAU Symposium No. 236, 2006, pp. 95–106

ReVelle DO (2008) Acoustic-gravity waves from bolide sources. Earth, Moon and Planets 102:345–356

ReVelle (2009) Modified Ray-Mode (Phase) Theory- Understanding Counter-wind Propagation Effects from Atmospheric Explosions, D.O., Accepted to J.A.S.T.P.

ReVelle DO, Edwards WN, Brown PG, Spurny P (2009) Acoustic Analysis of Shock Production by Very High Altitude Meteors – II: Entry Dynamics and Infrasound Analyses, to be submitted to J.A.S.T.P.

ReVelle DO, Edwards WN, Sandoval TD (2005) Genesis- An artificial, low velocity, "meteor" fall and recovery: September 8, 2004, Meteorit Planet Sci 40(6):819–839

ReVelle DO, Edwards WN (2006) Stardust-an artificial, low velocity "meteor" fall and recovery: 15 January 2006. Meteorit Planet Sci 42(2):155–304

ReVelle DO, Rajan RS (1979) On the luminous efficiency of meteoritic fireballs. J Geophys Res 84:6255–6262

ReVelle DO, Brown PG, Spurny P (2004) Entry dynamics and acoustic/infrasonic/seismic analysis for the Neuschwanstein fireball. Meteorit Planet Sci 39:1–22

ReVelle DO, Edwards W, Sandoval TD (2005) Genesis – an artificial low velocity "meteor" fall and recovery: September 8, 2004. Meteorit Planet Sci 40:819–839

ReVelle DO, Sukara EA, Edwards WN, Brown PG (2008) Reanalysis of the historic AFTAC Bolide infrasound database. Earth Moon Planets 102:337–344

Snow WB (1967) Survey of Acoustic Characteristics of Bullet Shock Waves. IEEE Transactions on Audio and Electroacoustics, AU-15 (4), 161–175

Tancredi G, Ishitsuka J, Schultz PH, Harris RS, Brown P, ReVelle D, Antier K, Le Pichon A, Rosales D, Vidal E, Varela ME, Sanchez L, Benavente S, Bojorquez J, Cabezas D, Dalmau A (2009) A meteorite crater on Earth formed in September 15, 2007: the carancas hypervelocity impact. Meteorit Planet Sci, In the Press

Thompson PA (1972) Compressible-fluid dynamics. McGraw-Hill, New York, NY 665

Tindle CT, Guthrie KM (1974) Rays as interfering modes in underwater acoustics. J Sound Vib 4:291–295

Tolstoy I (1973) Wave propagation. McGraw-Hill, New York, NY 466

Chapter 12
Meteor Generated Infrasound: Theory and Observation

Wayne N. Edwards

12.1 Introduction and the History of Meteor Infrasound

The infrasonic region of the acoustic spectrum in the Earth's atmosphere is filled with a wide variety of natural sources (Garcés et al. 2010). These sources include such energetic processes as severe weather systems (tornados, hurricanes, etc.) (Mikumo et al. 2010), oceanic waves (surf, microbaroms) (Hetzer et al. 2010; Kulichkov 2010; Blanc et al. 2010), volcanic eruptions, earthquakes (de Groot-Hedlin et al. 2010), lightning (Hauchecorne et al. 2010), and aurora (Mutschlecner and Whitaker 2010). One of the more unusual, but constant, sources of natural infrasound is that of interplanetary debris, or meteoroids, colliding with the Earth's atmosphere at hypersonic velocities, in a process commonly referred to as a meteor. Meteoroids are most commonly the remnant materials of the minor bodies of the solar system, comets, and asteroids, which have been released from their parent body (e.g., during active phases of comets passing near the Sun or during collisions between bodies) and orbit independently about the sun. Meteoroids range greatly in size, more than nine orders of magnitude, from tiny interplanetary dust particles (IDP) of only a few 10s of micrometers to asteroidal-sized objects many kilometers in dimension. For the purposes of generating infrasound, however, we will focus upon the upper end of this scale, on meteoroids of centimeter sizes and larger.

The history of meteor infrasound dates back to the early twentieth century and is nearly as old as the beginning of research in the subaudible spectrum of atmospheric waves near the end of nineteenth century. By the early 1900s, microbarometers were in scattered scientific use throughout England and Europe, when on June 30, 1908, an extremely energetic meteoroid exploded at an altitude of ~10 km over the Tunguska River in central Siberia (Chyba et al. 1993). Despite burning and leveling more than 2,000 km^2 of the local boreal forest, word of this substantial atmospheric impact traveled slowly, due, in part, to both the remoteness of the region and the

W.N. Edwards
Department of Physics and Astronomy, University of Western Ontario, London, Ontario London, Ontario, N6A 3K7, Canada
email: wayne.edwards@nrcan.gc.ca

A. Le Pichon et al. (eds.), *Infrasound Monitoring for Atmospheric Studies,*
DOI 10.1007/978-1-4020-9508-5_12,

general turmoil after the event during World War I (1914–1918) and Russian Revolution (1917). When eventually the event reached the scientific community in the early 1920s and investigations commenced (Kulik 1927), it was discovered that, like the eruption of the Krakatoa volcano decades earlier (Strachey 1888; Kanamori 1994), the Tunguska event had generated both infrasound and large-scale oscillations of atmosphere (i.e., gravity waves) (Evers and Haak 2010; Edwards 2010; Drob et al. 2010), which were recorded (Fig. 12.1) throughout Russia, Europe, and as distant as Washington, DC (Whipple 1930, 1934). From seismic and infrasonic recordings of the event and comparisons to nuclear explosions, the Tunguska meteor has been estimated to have released an equivalent energy of between 10 and 12.5 Mt of TNT (Hunt et al. 1960; Ben-Menahem 1975) (1 Mt = 4.185×10^{15} J).

After the Tunguska event, meteor-generated sound returned to general anonymity. While investigators of potential meteorite falls recognized that large meteors produced audible sounds (often reported by eyewitnesses during investigations) and recognized the likely sources of these sounds as originating from either the hypersonic shock waves of a meteoroid's atmospheric entry or from explosive gross fragmentation of the body of the meteoroid at altitude (e.g., Wylie 1932), much was anecdotal in terms of the recording of these sounds. Not until the escalation of the Cold War during the 1950s and the requirement to monitor for atmospheric nuclear weapon tests, did significant progress on recording meteor infrasound occur. Recognizing that infrasound was an efficient means of monitoring and characterizing surface and airborne nuclear weapons tests conducted by the Soviet Union, the United States Air Force Technical Applications Center (AFTAC) developed a global network of infrasound stations for just this purpose. As a consequence of the monitoring of low-frequency sound for nuclear explosions, this network also detected at least ten incidences of large (1–10 m and larger) meteoroid atmospheric impacts located globally between 1960 and 1974 (ReVelle 1997). These detections,

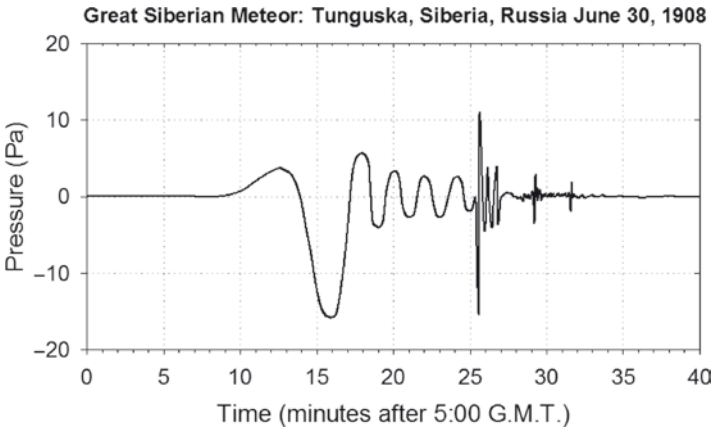

Fig. 12.1 Composite trace of the atmospheric pressure signals recorded across Europe of the Great Siberian Meteor, on June 30, 1908 (after Whipple 1930)

like the Tunguska bolide half a century earlier, were detected but remained generally unrecognized as meteor infrasound until some time later. More recently with the construction of the Comprehensive Nuclear Test-Ban-Treaty global network of infrasound stations as part of the larger multisensor suite (seismic/hydroacoustic/infrasound/radionuclide) of the International Monitoring System (IMS) (Christie et al. 2001; Christie and Campus 2010), the number of these large meteoroids or bolides being detected is once more on the rise (e.g., Brown et al. 2002a, 2004; Le Pichon et al. 2002; Klekociuk et al. 2005; Edwards et al. 2006).

In contrast to these larger 1–10 m class meteoroids, until the late 1970s, infrasound from smaller, more common, meteoroids had rarely been recorded in audible sound (Millman 1970; Öpik 1970) and not yet recognized in the subaudible, despite meteoroids at these small sizes being significantly greater in number and thus more frequent (Ceplecha et al. 1998; Brown et al. 2002b). Indeed, in the early 1970s (ReVelle 1974), during a theoretical investigation into meteor infrasound, predicted that up to 60 meteors (typically centimeter sized) might be observable over the course of a year according to meteoroid flux measurements of the time. This paucity of observation of smaller meteors was likely due, in part, to the selective nature of infrasound monitoring and the general system design at that time. AFTAC infrasound stations monitored two specific infrasonic bands for nuclear explosions, 0.04–8.2 Hz and 44–440 s (ReVelle 1997). As the dominant infrasonic period of meteor infrasound scales with a meteoroid's kinetic energy (see Sects. 12.2 and 12.3), these systems were generally only sensitive to the largest of bolides, since the interest of AFTAC was directed at the low frequencies and longer durations typical of nuclear explosions. Broader band systems used for scientific research (e.g., Kraemer 1977) avoided this limitation, but instead suffered from primarily analog recording and manual analysis methods of the data. As will be shown (Sect. 12.4), these small meteor infrasound detections are often very short in duration and have very low amplitudes (< few hundredths of Pascal). Yet, despite these difficulties, progress was made by the efforts of the former Wave Propagation Laboratory in Boulder, Colorado, USA, as apparent meteor infrasound signals were identified from occasional very bright meteors or large bolides observed by eyewitnesses, and more rarely with ground-based all-sky cameras, providing only moderate source location and time constraints (Goerke 1966; Bedard and Greene 1981).

During the mid-late 1970s and early 1980s, the two predominant meteor networks in North America, the Meteorite Observation and Recovery Program (MORP) in Western Canada (Halliday et al. 1978) and the U.S. Smithsonian Institution's Prairie Network (PN) (McCrosky and Boeschenstein 1965) teamed up with the Springhill Meteor Observatory (SMO) (Watson et al. 1976; McKinley 1961) and the University of Michigan (UofM), respectively, to begin comprehensive monitoring programs to record and identify meteor infrasound from these centimeter-sized meteoroids and larger, using both optical and radar systems to observe bright meteors. Over the approximately 5 years of simultaneous monitoring, two observations were made were made by the individual groups. The first was made by the SMO on December 14, 1974, where during the annual Geminid meteor shower a strong radar echo from a meteor was observed at ranges between 240 and 280 km.

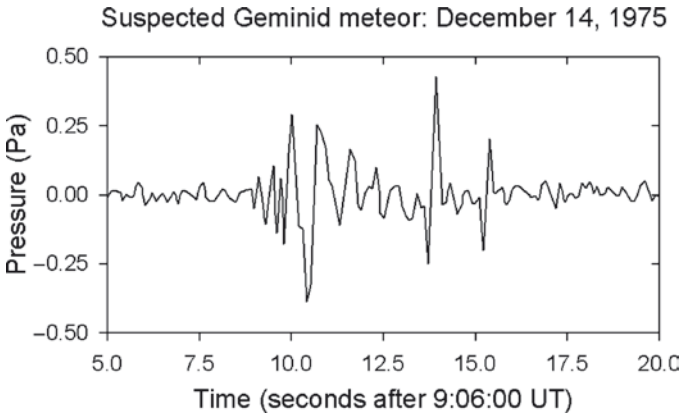

Fig. 12.2 Suspected infrasonic signal from a radar observed Geminid meteor ($v = 35$ km/s) on December 14, 1974, by the Springhill Meteor Observatory (SMO). Although the coincident radar/infrasound observations were suggestive, a definitive association could not be made. Estimates, based on radar echo duration, indicated a meteoroid mass of ~1 kg (from McIntosh et al. 1976)

Approximately 14 min later, a coherent infrasonic signal lasting ~7 s was observed by the SMO infrasound array in Ottawa, Canada (Fig. 12.2). While the time delay between the two detections in general fit the observed radar range to the meteor, a lack of directional information from the radar system meant that the association could not be confirmed (McIntosh et al. 1976).

Soon after the identification of McIntosh et al. (1976), the UofM/PN collaboration produced the first confirmed meteor infrasound observation from a meteor with a well-determined trajectory (Kraemer and Bartman 1981). The meteor, observed on May 24, 1975, was observed between 68.5 and 49.2 km altitude had an initial velocity of 16.5 km/s and lasted for ~2.1 s reaching a brightness of −5.1 magnitudes (McCrosky et al. 1979), about 2.5 times brighter than the planet Venus (magnitude −4). After this meteor event, two distinct arrivals were observed on a nearby infrasonic array (Fig. 12.3). Using the arrival azimuths and apparent velocities of the two signals observed by the station, reverse ray tracing was performed and the two signals were found to pass within 1.6 and 0.4 km from the observed meteor trajectory, delimiting the source regions of the infrasound signals to 54.5 ± 1.6 km and 66.7 ± 0.2 km altitude, respectively. For the next ~25 years, this would remain the only confirmed observation of infrasound from a common centimeter-class meteor.

With infrasonic monitoring and research reviving in the late 1990s due, in large part, to the inception of the CTBT/IMS global infrasound network, infrasonic detections of meteors have begun to once more accumulate. While some of these observations continued to be made by the chance occurrence of bright meteors identified near infrasound stations with few direct observations on the source meteor (e.g., ReVelle and Whitaker 1999; Evers and Haak 2003; Le Pichon et al. 2002), more and more meteor infrasound detections are being associated with constrained meteor locations, trajectories, velocities, energies, and in some cases,

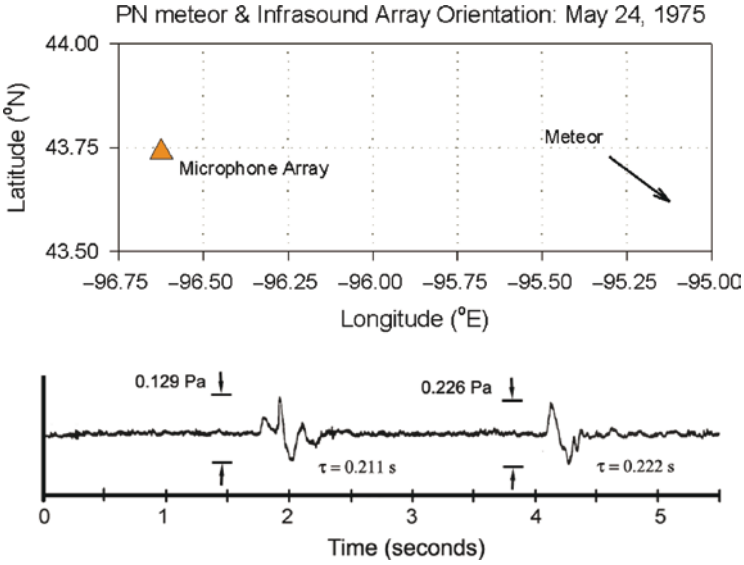

Fig. 12.3 The first observation of infrasound from a well-constrained meteor trajectory (Kraemer 1977; Kraemer and Bartman 1981). Prairie Network (PN) meteor trajectory was photographically observed traveling from 65.5 to 49.2 km altitude, at an inclination of 55.66° from the horizontal, at an initial velocity of 16.5 km/s. From meteor light production, the meteoroid's mass was estimated to be 0.320 kg (McCrosky et al. 1979)

even recovered meteorites (e.g., Brown et al. 2002c, 2004; ReVelle et al. 2004; Llorca et al. 2005). The advent and adoption of new and inexpensive visual technologies amongst both professionals and the public (i.e., camcorders, security cameras, and digital/photographic cameras) have provided new means for acquiring visual meteor observations. In addition, space-based visual and infrared satellite systems (Tagliaferri et al. 1994) have proved to be a powerful means of identifying and characterizing infrasound from large (> 1 m sized) meteoroid impacts around the globe (see Sect. 12.5), which would otherwise be unobservable by conventional observing methods (Brown et al. 2002a; Edwards et al. 2006).

Finally, like their predecessors, modern regional meteor networks such as the European Fireball Network (EN) (Oberst et al. 1998), Spanish Meteor Network (SPMN) (Trigo-Rodríguez et al. 2004) and the Southern Ontario Meteor Network (SOMN) (Weryk et al. 2007), have begun to once more monitor for the elusive sounds from centimeter-sized meteoroids. Armed with significant advancements in computers and modern digital data acquisition, storage, and processing, these monitoring campaigns are achieving significant results (e.g., Llorca et al. 2005; Brown et al. 2007; Edwards et al. 2007). With photographic and video cameras systems providing accurately measured meteor occurrence times, trajectories, velocities, and photometric masses, we are now just starting to be able to explore and test the predictions of meteor generated infrasound theory developed by ReVelle (1974, 1976). These new observations of source heights, propagation patterns, and signal

characteristics are the focus of Sect. 12.4. With this renewed interest in infrasound monitoring and research, we are beginning to understand the process of this naturally occurring source of infrasound in far greater detail than ever before.

12.2 A Primer on Single-Body Meteor Physics

As we proceed throughout this chapter, it is necessary to be familiar with various aspects, terminology, and the general physical theory of meteoroid entry and interaction with the atmosphere to fully understand how this relates to meteor-generated infrasound. Although various aspects of meteor entry remain fields of active research and uncertainty remains in various quantities, the physics of a simple, single body, meteoroid entry is well known and is still commonly used to describe and compare the dynamics of meteor observations (e.g., Ceplecha et al. 2000).

The single-body theory of a meteor motion (Öpik 1933, 1937; Whipple 1938) is a set of linked differential equations, which describe the atmospheric motion and ablation of a generalized, single-body meteoroid (i.e., nonfragmenting), with mass, m, bulk density, ρ_m, and velocity, v. The meteoroid encounters the Earth at hypersonic velocities between 11.2 and 72.8 km/s, bounded by the Earth's escape speed (11.2 km/s) and the escape speed of the Sun at the Earth (42.5 km/s) plus the Earth's orbital speed (30.3 km/s). At such high velocities, the force of gravity may be neglected as the time of this interaction, or typical meteor durations, are generally short (< 1 s to a few seconds) and gravity does not have sufficient time to significantly affect a meteor's path. Thus, the trajectory of the meteor may be approximated as a line in space with only the atmospheric drag force acting on the meteoroid. If the surface of the Earth is approximated as a sphere, the motion and ablation (mass-loss) of the meteoroid may be described as (Ceplecha et al. 1998):

$$\frac{dv}{dt} = -\Gamma A \rho_m^{-2/3} \rho m^{-1/3} v^2, \tag{12.1}$$

$$\frac{dm}{dt} = -\frac{\Lambda A}{2\xi} \rho_m^{-2/3} \rho m^{2/3} v^3, \tag{12.2}$$

where

$$\mathrm{A} = S m^{-2/3} \rho_m^{\ 2/3} \tag{12.3}$$

is the so-called shape-change factor. In (12.1)–(12.3), S is the frontal cross-sectional area of the meteoroid, Γ is the coefficient of drag, ρ is the atmospheric density, Λ is the heat transfer coefficient (a measure of how efficient frictional heat is transferred to the meteoroid), and ξ is the ablation energy of the meteoroid (the energy necessary to ablate a unit mass). The geometry of the meteor trajectory is then described by:

$$\frac{dh}{dt} = \frac{l - \frac{a}{2}}{\frac{b}{2} + h} v, \tag{12.4}$$

$$z(t) = \cos^{-1}\left(\frac{\frac{a}{2} - l}{\frac{b}{2} + h}\right), \tag{12.5}$$

$$al + bh + c = l^2 - h^2 \tag{12.6}$$

where t is time, h is height, l is distance along the trajectory, z is the zenith distance of the meteor's radiant (direction in the sky from which the meteor originates), and a, b, and c are constants related to the geometry of the trajectory.

Numerical solutions of (12.1) through (12.6) provide physical insight into the process of meteoroid ablation and kinematics within the framework of single-body meteor theory, as well as a fundamental means of comparison to meteor observations and estimation of the physical characteristics of the associated meteoroid. If observations are of sufficient quality as to measure a meteoroid's deceleration, (12.2) may be used with these observations to infer the meteoroid's mass (given assumptions of the meteoroid's density). This inferred mass is often termed the meteoroid's *dynamical mass* in that it originates from the observed meteor dynamics. In reality, however, the meteoroid is never actually observed during its entry, instead the products of the atmospheric friction and ablation of the meteoroid (the meteor) are observed (i.e., light, ionization, and sound).

Light and ionization are fundamentally related to the meteoroid ablation process. When the meteoroid collides with atmospheric molecules, the collisional friction heats the surface of the meteoroid resulting in melting, vaporization, and potentially general ablation in the form of fragmentation of the meteoroid surface. This process produces ionization of the meteoric atoms being ablated creating a plasma that quickly surrounds the parent meteoroid. As the electrons in these excited atoms drop back to their ground state, photons are given off, forming the visual phenomena commonly associated with the meteoroid entry (i.e., the meteor) and commonly recorded by the photographic and/or video methods used to determine the meteor's trajectory and velocity. The luminosity, I, of the meteor is assumed to be related to the mass loss of the meteoroid via:

$$I = -\tau_L \frac{v^2}{2} \frac{dm}{dt}, \tag{12.7}$$

where τ_L is the efficiency of the process or the *luminous efficiency*. A more general form relates luminosity to the change in kinetic energy in time, which includes the added energy due to the meteoroid's deceleration (Ceplecha et al. 1998):

$$I = -\tau_L \left(\frac{v^2}{2} \frac{dm}{dt} + mv \frac{dv}{dt} \right). \tag{12.8}$$

As meteor light production is linked with the change in meteor mass, by integrating the meteor's change in luminosity over time, often referred to as the meteor's *light-curve*, an estimate of the initial mass can be made given some estimate of the luminous efficiency. Such mass estimates are referred to as *photometric masses*. The luminous efficiency, however, is not a well-known quantity and is certainly not constant for all meteors. It is often inferred or measured through comparison of the photometric mass with the dynamic mass and, where possible, recovered meteorites (e.g., Ceplecha 1996). Only a few direct experiments with artificial iron meteoroids have been made to date, and these have all been made at the slowest of meteor velocities (McCrosky and Soberman 1963; Ayers et al. 1970).

Meteor ionization, measured using radio techniques, is also linked to mass loss in a similar way to that of light. Ionization is created during inelastic collisions as ablated meteoric atoms encounter atmospheric molecules. These collisions may result in the release of free electrons as part of the plasma surrounding the meteoroid during entry and then are subsequently left behind along the meteor's trail as entry proceeds. Thus, the number of these free electrons per unit length the meteors trail, q, is also assumed to be linked with meteoroid ablation according to (McKinley 1961):

$$qv\eta = -\frac{1}{2}\tau_I \frac{dm}{dt} v^2, \tag{12.9}$$

where τ_I is the *ionization efficiency*, and η is the mean ionization potential per atom involved in the collision. Thus, in a similar way to the photometric methods discussed previously, integration of the line density of ionization (number of electrons per meter) of a meteor trail may be used to again estimate meteoroid mass. This mass estimate is typically called the *radar mass*. The relationship of radar mass to the photometric and dynamic masses discussed earlier, despite early simultaneous optical/radar meteor observations (Kaiser 1953; McKinley 1961), remains a topic of active research.

Unlike light and ionization production, meteor sound production is not directly linked to ablation in general (12.2), rather it is atmospheric drag (12.1) that is of fundamental importance. This is because sound generation is related to the atmospheric shock that is produced as the meteoroid passes through the atmosphere at hypersonic speeds. The degree of this separation between ablation and drag processes is shown mathematically by inspecting the rate of change of the kinetic energy in time (bracketed factor in (12.8)), where the change in the meteoroid kinetic energy is proportional to either a mass loss term multiplied by a physical constant or by the linear momentum multiplied by a different constant. First developed by ReVelle (1974, 1976), meteor generated sound theory approximates the generally conical, ballistic shock (*Mach cone* – equivalent to the sonic boom produced by supersonic aircraft) as an instantaneously produced line source blast wave with cylindrical symmetry (Fig. 12.4). Such a simplifying approximation is

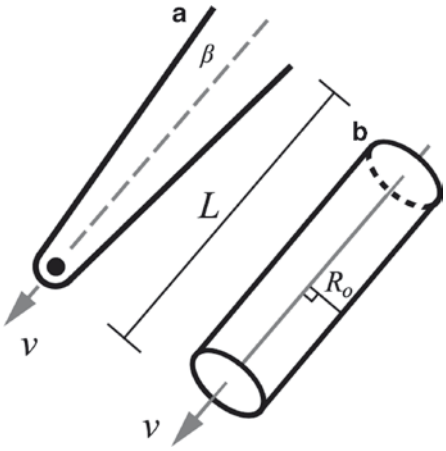

Fig. 12.4 In classical meteor infrasound theory, the (**a**) narrow, generally conical, hypersonic ballistic shock of meteors (characterized by the Mach angle β) are approximated as (**b**) an instantaneous cylindrical line source explosion of radius, R_o, and length, L

valid for meteors because their speeds far exceed the local thermodynamic sound speed of the atmosphere. These hypersonic velocities result in very narrow (<1°) Mach cones since:

$$\sin\beta = \frac{C_S}{v} = \frac{1}{M}, \tag{12.10}$$

where β is the half angle of the Mach cone and C_S is the local ambient thermodynamic sound speed (Beyer 1997). In Earth's atmosphere, between 0 and 100 km, the sound speed slowly varies with an average mean of $C_S \approx 305$ m/s ± 15%. M is simply the ratio of the object (meteoroid) velocity and sound speed, often referred to as the *Mach number*.

Classical line source blast wave theory (Tsikulin 1969) shows that the radius of this cylindrical blast or blast radius, R_o, which physically represents the initial zone of highly nonlinear wave propagation, is defined as:

$$R_o = \left(\frac{E_o}{p}\right)^{1/2}, \tag{12.11}$$

where E_o is the energy per unit length along the cylindrical shock, and p is the ambient atmospheric pressure. Physically, R_o is the point at which the ambient atmospheric kinetic energy density equals that of the shock; the overpressure at one blast radius thus is very close in magnitude to that of the local atmospheric pressure.

For meteors, E_o is simply the atmospheric drag force, and it follows that we can write (12.11) as:

$$R_o \approx M d_m, \tag{12.12}$$

where d_m is the physical diameter of the meteoroid (ReVelle 1976). This R_o is then associated with the dominant or fundamental frequency, f_0, of the resulting propagating ballistic shock wave by the relationship:

$$f_0 = \frac{C_S}{2.81 R_O} \tag{12.13}$$

after the blast wave has traveled a distance of $10R_o$ (ReVelle 1976). Inspection of the definitions of the meteor blast radius and fundamental frequency shows that increasingly faster and/or larger meteoroids will produce increasingly lower frequencies. For representative meteor velocities, centimeter-sized and larger meteoroids should then produce frequencies less than ~100 Hz. The bulk of this frequency range lies below the range of human hearing (< 20 Hz) in the regime of infrasound (analogous to infrared radiation, where the wavelength of light is longer than visible radiation). This does not imply that all meteor shocks are inaudible at the ground; larger meteors, in particular may produce large amounts of acoustic energy, some of which will fall in the low end of human hearing (though the peak in the frequency spectrum will be much lower). Thus, if it were possible to measure this initial peak frequency of the ballistic shock wave it would, in principle, be a straight forward means of determining the size of the meteoroid given measurements of the meteor velocity and some assumption of the meteoroid's bulk density. Unfortunately, measurements of meteor ballistic shock waves are made from the surface of the Earth, for economic and technical reasons. By the time the shock reaches low altitudes, it will have propagated significant distances from this source region, so the behavior and attenuation of the shock wave over distance must be understood to achieve this ultimate goal of acoustic measurement of meteoroid size.

As a meteor's ballistic shock propagates outward after formation, it undergoes several phases of propagation. Initially, the propagation is as a highly nonlinear shock wave characterized by R_o with a large overpressure (the difference between the pressure amplitude of the shock to the ambient atmosphere), Δp, and having propagation faster than the local speed of sound. After several R_o distances, this nonlinear shock smoothly transitions into a state of weak nonlinearity. The shock wave propagation approaches the local thermodynamic sound speed and the initially high overpressures have decreased by several orders of magnitude. Nevertheless, the overpressure at this weak-shock stage is still large enough that significant wave attenuation exists such that as wave amplitude decreases, dispersion modifies the wavefront, rounding the initially sharply defined front and increasing its period (Fig. 12.5). This weakly nonlinear state exists for a variable amount of time, depending upon the height and frequency of the shock, until amplitudes have decreased sufficiently and the wave transitions into effectively linear propagation where attenuation is much reduced (ReVelle 1974). A complete discussion of where and how these transitions are found will be discussed in Sect. 12.3.

By synthesizing theoretical and experimental work on cylindrical shock waves produced by high-velocity projectiles and lightning, ReVelle (1976) showed that the increase in the weakly nonlinear shock wave period, τ, follows the relationship:

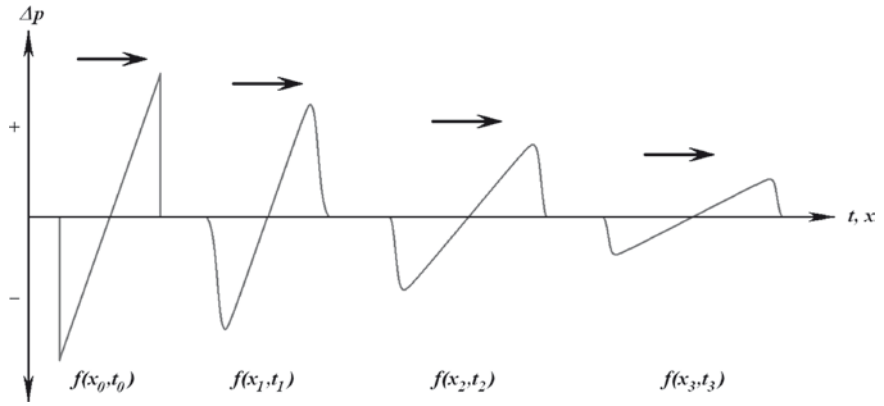

Fig. 12.5 Schematic diagram of the weakly nonlinear modification of an initially highly nonlinear ballistic shock wave. As the ballistic shock propagates (to the *right*), initially sharp features are smoothed as the overpressure decreases (resulting smaller perturbations to the ambient atmosphere) and variable dispersion at different parts of the wavetrain gradually increase the fundamental period of the shock (after Dumond et al. 1946)

$$\tau = 0.562\ \tau_{\mathrm{o}} x^{1/4} \text{ for } x \geq 10 \tag{12.14}$$

where $\tau_{\mathrm{o}} = f_{\mathrm{o}}^{-1}$, the initial fundamental period of the shock wave, and x is the distance traveled in units of R_{o} (i.e., $x = R/R_{\mathrm{o}}$, where R is the distance or range from the source). Similarly, the overpressure of weakly nonlinear waves is found to decay at a rate of:

$$\frac{\Delta p}{p} \cong \frac{2©}{\gamma+1}\left(\frac{0.4503}{\left(1+4.803x^2\right)^{3/8}-1}\right) \quad \text{for } x \geq 0.05, \tag{12.15}$$

where $\gamma = 1.4$, is the ratio of specific heats for air. For consistency between (12.13), (12.14) and (12.15), calculations are typically started at an initial distance of $10R_{\mathrm{o}}$ from the source. Yet, this only expresses the decay of the wavefront as a function of geometrical distance from the source region. The shock wave becomes further modified when losses due to classical thermal and viscous atmospheric absorption (loss of organized wave energy to equivalent random molecular translational energy) and molecular relaxation (loss of wave energy to molecular internal rotational and vibrational energy) (Sutherland and Bass 2004) mechanisms are included. Finally, as the processes of geometrical spreading and absorption progress, the ballistic wavefront continues propagating throughout the atmosphere, subject to atmospheric refraction (which may produce shadow zones – regions of silence where the wave cannot propagate, and caustics – points of wavefront convergence that result in amplification) and the anisotropic effects of upper air winds on the local speed of sound (Groves 1955; Thompson 1971). More complete discussions on the development and application of cylindrical line source theory are provided in Sect. 12.3.

At the end of propagation, presuming the wave has not been completely attenuated and a path to the sensor exists, the resulting signal detected by sensitive low-frequency microphones or microbarometers at the Earth's surface may be substantially modified from the initial blast wave. Since these modifications and losses can be quantified, it is possible to reconstruct and estimate the initial blast wave (and the properties of the source meteoroid) through the measured properties of the detected signal. If a meteor's velocity and trajectory orientation can be provided by independent observations by optical and radar systems, using accurate upper-air data provided through meteorological data and atmospheric models (e.g., Swinbank and O'Neill 1994; Hedin 1991; Hedin et al. 1996; Drob et al. 2003), observed meteor infrasound can be localized to its source (e.g., Kraemer 1977; Brown et al. 2007). Such coordinated observations enable calibration of observed meteor infrasound characteristics, eventually providing another independent method of estimating properties of the source meteoroid (e.g., size, mass, and kinetic energy) as it existed at this source region.

12.3 Cylindrical Line Source Theory: Inhomogeneous Stratified Atmosphere

In the preceding section, the fundamentals of meteor-generated infrasound and its relationship to the interaction between the entry of a high-velocity meteoritic body and the atmosphere were briefly discussed, with several fundamental relationships presented. In this section, we will take these relationships further and layout the general algorithm used for predicting the infrasonic signal properties of an arbitrary meteor using the cylindrical line source approximation developed by ReVelle (1974). In the first part of this section, the development of the cylindrical line source approximation as applied to meteors is described for the general case of a meteor propagating through an inhomogeneous, vertically stratified atmosphere, while in the second part, the general method of implementation of this theory is provided. While the following section is intended to demonstrate the methods used to implement and therefore predict and compare cylindrical line source theory to observations of meteor-generated infrasound (Sect. 12.4), aspects of the reasoning behind particular approximations and discussions of their implications, have been summarized only where appropriate. For more complete derivations, along with detailed discussions of elements and approximations of the theory, the reader is directed to the works of ReVelle (1974) and Kraemer (1977). A detailed description of the theory as applied to a simple isothermal atmospheric model is also provided by ReVelle (1976).

12.3.1 Meteor Generated Infrasound: The Cylindrical Line Source Approximation

Meteoroids entering the 's atmosphere do so at very high velocities, ranging between 11.2 and 72.8 km/s or equivalently between Mach numbers of ~35–240.

Such extreme velocities coupled with the typically short durations of meteors, lasting between < 1 to a few seconds (Ceplecha et al. 1998), means that Earth's gravity does not play a significant role in perturbing the meteor trajectory. Additionally the generally conic ballistic shock front produced by the meteor's passage may be approximated as cylindrical due to the narrowness of the Mach cone (12.10). Thus, in nearly all cases, a meteor can be approximated as an instantaneous cylindrical line source blast located in the upper atmosphere (Fig. 12.4). Cylindrical symmetry results in the propagation of the generated wave front primarily perpendicular to the trajectory of the source meteor. Yet, because meteors may occur at random orientations, and the length of a meteor's trajectory, L, may extend for several 10s to 100s of kilometers, this preferred propagation direction results in a highly directional source. Thus, detection of meteor generated infrasound is quite variable from meteor to meteor. To orient the meteor source in space and the direction of propagation of the wave front relative to the meteor's trajectory, a coordinate system is used (Fig. 12.6) where following ReVelle (1976):

φ is the azimuth of the meteor heading (i.e., direction in which the meteor is traveling) measured clockwise from North.

θ is the elevation of the meteor trajectory as measured from the horizon.

$d\varphi$ is the deviation of the infrasonic ray (perpendicular to the wave front) from the meteor heading (e.g., $d\varphi = 0°$ when ray is in heading direction, 180° when opposite heading, and 90° perpendicular to heading).

ε is the zenith angle of the acoustic ray as measured from the vertical.

The relationship among ε, θ, and $d\varphi$ may be expressed in radians as:

$$d\varphi = \frac{\pi}{2}(1 - \tan\theta \cot\varepsilon) \quad \text{with } \theta \neq \frac{\pi}{2},\ \varepsilon \neq 0 \text{ and } \varepsilon \geq \theta. \tag{12.16}$$

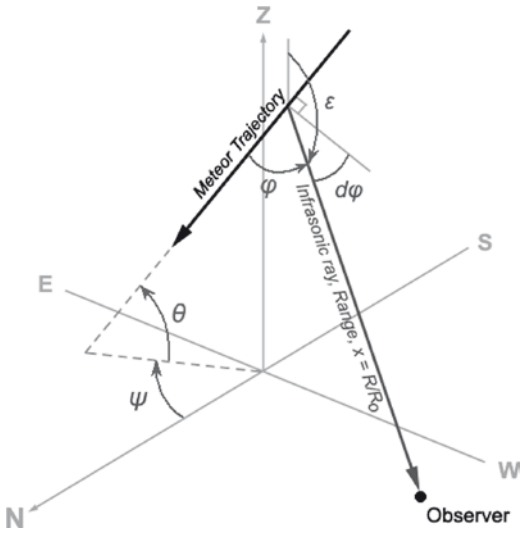

Fig. 12.6 Coordinate system used to describe propagation of the generated ballistic shock wave from a meteor trajectory approximated as a cylindrical line source

In addition to this coordinate system, calculations of the acoustic ray path through the atmosphere are simplified by assuming that the path the wave takes to the observer is straight. While in general this not the case, gradients in the sound speed structure will cause these wave fronts to refract (Groves 1955), in the immediate region of the meteor where direct source to receiver geometry is possible (the region of interest) refraction is typically moderate and this assumption is generally reasonable. In practice, the region to which this assumption is valid is ~200 km ground range from the source meteor (see Sect. 12.4). While refraction may be explicitly included in the following procedure, the result will only lengthen the path the wave must travel to the observer, with the overall effect of slightly increasing the absorption and spreading losses the wave front will experience.

With the coordinate system and path geometry defined, cylindrical line source theory as applied to meteors begins with a thought experiment that will outline the algorithm employed. Suppose an arbitrary meteor occurs in the atmosphere. This meteor produces an initially strong atmospheric shock wave where the pressure of the shock front greatly exceeds the surrounding ambient pressure of the atmosphere. This strongly shocked wave propagates rapidly as a highly nonlinear disturbance and will persist until the pressure of the front decays to a value comparable to that of the surrounding ambient atmosphere. From this position onward, the wave front transitions into a state of weak nonlinearity where the front pressure is still large, but begins to propagate at near acoustic velocities all the while its form modifies with a decaying pressure front and lengthening period. This weakly nonlinear state continues until the wave at some point transitions to linearity where the pressure of the disturbance is greatly less than the surrounding atmosphere and its period no longer changes significantly. Where this second transition to linearity occurs, however, is unclear.

To determine or at least estimate where the linearity transition occurs, the concept of a distortion distance is invoked. Towne (1967) showed that a plane sinusoidal wave will distort in its fundamental period by 10% in a distance of:

$$d' = \frac{C_S \tau}{34.3 \dfrac{\Delta p}{p}}, \tag{12.17}$$

where C_S is the speed of sound, τ is the period of the wave, and $\Delta p/p$ is the ratio of the wave overpressure, Δp, to that of the ambient atmospheric pressure, p. If we compare this distortion distance, d', with the distance the wave is to travel to the observer, then the condition of the transition to linearity occurs when,

$$d' > d_r, \tag{12.18}$$

when the distortion distance, d', is greater than the distance remaining to travel to the observer, d_r. The maximum altitude at which this transition may occur can be estimated by assuming an unphysical condition. If we assume that initially, after the highly nonlinear phase, the wave begins to propagate as a linear wave (rather than as weakly nonlinear), then condition (12.18) represents the altitude at which this linear

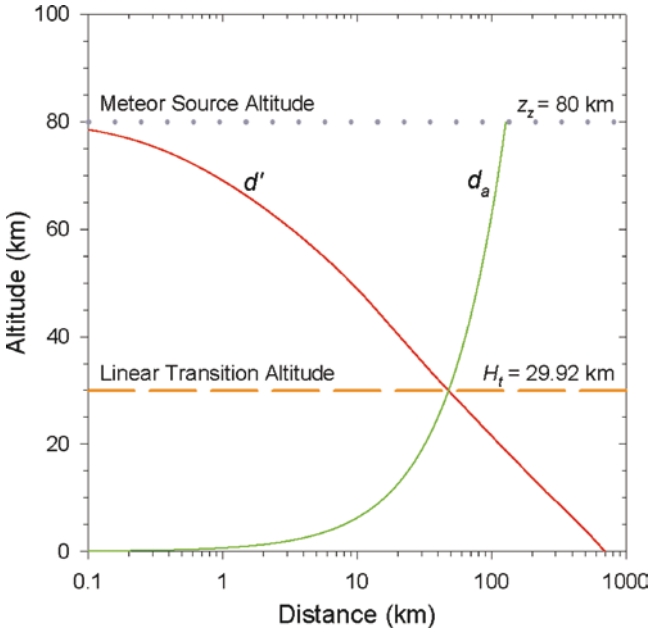

Fig. 12.7 Determination of the transition altitude from weakly nonlinear to linear wave propagation for an example meteor (Table 12.2). The initial ballistic shock wave propagates from the meteor source region, it continually decreases in overpressure ratio (amplitude) resulting in progressively longer distortion distances. When d' exceeds the remaining distance to the observer, d_a, the wave may be considered thereafter in a steady linear state as further distortion of the wave (lengthening of its dominant period) will not occur before the wave reaches the observer

wave becomes a shock wave (Fig. 12.7). Therefore, by inference, as initial state of the wave is in fact as a weakly nonlinear shock, it should remain a shock to *at least* this altitude, whereupon either the wave will transition to a linear state, or continue on as a weak shock and potentially transitioning at some later time and altitude.

To determine this transition altitude, we must first construct how a cylindrical line source shock wave will attenuate and modify itself during propagation. To this end ReVelle (1974) appealed to the observations of shock waves produced by lightning (i.e., thunder), aircraft, and experimental results from cylindrical line sources (Lin 1954; Sakurai 1965; Few 1968; Jones et al. 1968) to extrapolate how a similar blast wave produced at altitude by a meteor, would be generated and decay from its source. To begin, we examine the fundamental period of the initial shock wave. As discussed previously, the initial highly nonlinear shock wave propagates outward until the pressure or kinetic energy density of the shock equals that of the surrounding atmosphere. Thus, the following equality exists at this point, where the energy of the surrounding atmosphere balances the energy output of the meteoroid on the atmosphere (i.e., atmospheric drag):

$$pV = F_D L \quad \text{or} \quad p\pi R_o^2 L = C_D \pi r_m^2 \rho v^2 L, \tag{12.19}$$

where the cylindrical volume, V, of the shock front (produced along the meteor's trajectory) of length, L, and radius, R_o, is equal to the drag force, F_D, exerted on the atmosphere by the meteoroid traveling at a velocity, v, over the same distance, L, assuming a spherical meteoroid of radius, r_m. Here, p and ρ are the ambient atmospheric pressure and density, respectively, and C_D is the atmospheric drag coefficient hereafter assumed to be equal to unity. This reduces, after some algebra, to the familiar equation (12.12) quoted constantly in meteor infrasound literature (ReVelle 1976). This equality is then simply the physical redefinition of the line source explosion blast radius, R_o, described in Sect. 12.2 and (12.11) and requires that the meteoroid body is whole (single-body). If break up, or fragmentation of the single body, is included the expression for the blast radius is more complex, but increases relative to the nonfragmenting limit by a constant multiplier of some 10–20 times. It is of interest here to point out that (12.11) is not the only blast radius definition used for line sources. Indeed several definitions have been proposed by various authors, but typically differ by simply a multiplicative constant. From ReVelle (1974):

Basic definition (Tsikulin 1969):

$$R_O = \left(\frac{E_O}{p}\right)^{1/2}. \tag{12.20}$$

Modified definition (Tsikulin 1970):

$$R_O = \left(\frac{2E_O}{p}\right)^{1/2}. \tag{12.21}$$

Sakurai (1965):

$$R_O = \left(\frac{E_O}{2\pi p}\right)^{1/2}. \tag{12.22}$$

Few (1968):

$$R_O = \left(\frac{E_O}{\pi p}\right)^{1/2}. \tag{12.23}$$

Jones et al. (1968):

$$R_O = \left(\frac{4E_O}{\gamma bp}\right)^{1/2}, \tag{12.24}$$

where $b = 3.94$ for a diatomic gas, $\gamma = 1.40$.

Here again, E_o is the source's energy per unit length. Also, since the line source blast wave radius, R_o, is fully meaningful only in the limit of zero accelerations for as a steady state medium, substantial increases in the blast radius can also be expected for meteors observed at comparatively deep penetration heights, where meteoroids may rapidly decelerate over wide altitude ranges.

Once the blast radius of the disturbance is determined, it is readily related to the period (or frequency) of the resulting ballistic shock wave via (12.13). This initial period, τ_o, of the ballistic shock wave (referred to as an *N*-wave for aircraft sonic booms due to the *N*-like appearance of the pressure waveform, Beyer 1997) then begins to slowly widen or spread as it propagates outward in its weakly nonlinear state according to (12.14) of Sect. 12.2 (DuMond et al. 1946). Therefore, by the time the ballistic wave reaches the observer, the dominant period will have been significantly altered from its original state at the source. Note that by definition, if the wave has transitioned to a linear wave the period will remain constant at the value it had at the time of transition.

Now that the period and is modification during propagation are defined, attention is turned to the behavior of the pressure or amplitude of the ballistic shock wave during propagation to the surface. From the work of Jones et al. (1968) with shock waves from lightning discharges, it was found that in the strongly nonlinear region close to the source ($x \to 0$) according to the pressure ratio:

$$\frac{p'}{p} = \frac{\gamma}{2(\gamma+1)x^2}, \tag{12.25}$$

where p', is the absolute pressure of the strong shock and $p' \gg p$. In the weakly nonlinear regime, however, where $p' \leq p$, the overpressure ratio, $\Delta p/p$, is used instead to measure amplitude and decays more slowly at a rate of $x^{-3/4}$. Thus, a limiting equation was needed, which behaved such that at $x < 1$ the decay is as a function of x^{-2}, but as x increases this rapid attenuation slows to $x^{-3/4}$. A fit to these two limits was then given and experimentally verified for $10 \leq \Delta p/p \leq 0.04$ (Jones et al. 1968; Tsikulin 1969), by the function:

$$\frac{\Delta p}{p} = \frac{\gamma}{2(\gamma+1)}\left(\frac{\left(\frac{3}{8}\right)^{-3/5}}{\left(1+\left(\frac{8}{3}\right)^{8/5}x^2\right)^{3/8}-1}\right) \quad \text{for } x \geq 0.05 \tag{12.26}$$

and adopted by ReVelle (1974) for its similarity to the theoretical and experimental $x^{-3/4}$ decay of sonic booms associated with projectiles and aircraft. This is a more complete version of (12.15) given is Sect. 12.2. Yet, decay for linearly propagating waves from a cylindrical line source is not the same. Linear waves from a cylindrical source are predicted to decay according to $x^{-1/2}$ (Officer 1958). To correctly account for this change in attenuation when the propagating wave changes states, a correction term of $x^{1/4}$ is simply applied to the numerator in (12.26) upon satisfying condition (12.18). An additional correction to (12.26) is then applied to account for the difference between the actual nonuniform (i.e., refracting) ray path to that of the straight source-receiver path assumed by (12.26) (Pierce and Thomas 1969). This correction has the form:

$$N^{*} = \left(\frac{\rho_0}{\rho_Z}\right)^{1/2} \frac{C_{S0}}{\overline{C}_S} N_C, \tag{12.27}$$

with,

$$\overline{C}_S = \frac{\int_{z_0}^{z_S} C_S(z)\,dz}{z_S - z_0}, \tag{12.28}$$

where ρ_0, C_{S0} and z_0 are the atmospheric density, sound speed, and altitude of the observer, and ρ_z and z_z are the density and altitude of the source, respectively. $\overline{C}_S$ is simply the average sound speed between the observer and the source. The small nonlinear propagation correction term, N_C, in (12.27) is given values by Pierce and Thomas (1969) of $N_C < 2.1$ below ~100 km and $N_C < 1.55$ below 50 km. Yet this small correction factor in this application is considered minor in comparison to the general uncertainty and variation in the atmospheric density of any given atmospheric model. Thus, for simplicity hereafter a value of $N_C = 1$ is used throughout the following procedure (ReVelle 1974). With this functional form for spreading losses of weakly nonlinear, as well as linear, ballistic waves away from the source region defined, ReVelle (1974) turned attention to the additional attenuation of the wave front overpressure due to atmospheric absorption.

The two different states of the shock wave (weakly nonlinear and linear) required two different approaches to determining the effects of absorption. For weakly nonlinear waves ReVelle (1974) appealed to the results of Morse and Ingard (1968), which showed that for shocked acoustic waves at distance from their source:

$$\frac{dp_S}{ds} = -\left(\frac{\gamma+1}{\gamma^2\lambda}\right)\left(\frac{\rho C_S^2}{p_o^2}\right) p_S^2 - \left(\frac{3\delta}{2\rho_o C_S \lambda^2}\right) p_S \tag{12.29}$$

with

$$\delta = 4\left[\frac{4}{3}\mu + \eta + \frac{K(\gamma-1)}{C_P}\right], \tag{12.30}$$

where p_S is the pressure amplitude of the wave, p_o and $\rho_o \approx \rho$ are the average ambient pressure and density of the fluid (i.e., atmosphere), λ is the wavelength of the shock, μ and η are the ordinary (shear) and bulk (volume) viscosities of the fluid respectively, K is thermal conductivity of the fluid, and C_p is the specific heat of the fluid at constant pressure, with integration required over the path length s. The general solution to (12.29) can then be written as:

$$\frac{\Delta p}{\Delta p_Z}\left[\frac{\Delta p + \frac{B}{A}}{\Delta p_Z + \frac{B}{A}}\right] = \exp\left(-\int_{z_0}^{z} \frac{B}{\cos\varepsilon}\,dz\right), \tag{12.31}$$

with

$$A = \frac{(\gamma + 1)}{\gamma \lambda p_0} \quad \text{and} \quad B = \frac{3\delta}{2\rho_0 C_S \lambda^2} \tag{12.32}$$

after integrating the path length from the source altitude, z_0, to the observation altitude, z. Δp and Δp_z are then the overpressures of the ballistic wave at the observer and at the meteor source altitude, respectively. The atmospheric attenuation or damping factor to be applied to (12.26) for a weak shock is then:

$$D_{WS} = \frac{\Delta p}{\Delta p_Z} = \frac{\frac{B}{A}\exp\left(-\int_{z_0}^{z} \frac{B}{\cos\varepsilon} dz\right)}{\Delta p_Z \left(1 - \exp\left(-\int_{z_0}^{z} \frac{B}{\cos\varepsilon} dz\right)\right) + \frac{B}{A}} \tag{12.33}$$

this is a more generalized version of the weak shock damping function provided for an isothermal atmosphere by ReVelle (1976). Note, however, that the solution to (12.33), requires some knowledge of Δp_z. To determine an appropriate value for this initial amplitude condition, studies of line source shock waves and lightning in the near field are examined.

From the work of Plooster (1968, 1970, 1971) and Jones et al. (1968), the degree of sensitivity in the initial amplitude is dependent upon the values of two dimensionless constants they term "C" and "δ" (not to be confused with the uses of C and δ used previously). Physically, "C" determines the spatial regime (x value) where the strong shock regime conditions (defined by $\Delta p/p >> 1$) have transitioned to the weak shock regime ($\Delta p/p << 1$), while "δ" determines the efficiency with which blast waves are generated in comparison to amplitudes indicated in Lin's (1954) original numerical cylindrical line source solution.

According to Plooster (1968, 1970, 1971) and Jones et al. (1968), there are at least four cases (combinations of "C" and "δ") that need further examination, each of which has been extrapolated from its prediction at $x = 1$ ($R = R_o$) to $x = 10$ (for consistency in the algorithm of Part B of this section):

1. Line source, constant density, ideal gas: "C" = 0.70, "δ" = 1.0
   $\Delta p_z = 0.0805 \cdot p(z)$ at $x = 10$.
2. Isothermal cylinder, constant density, real gas: "C" = 0.70, "δ" = 0.66
   $\Delta p_z = 0.0680 \cdot p(z)$ at $x = 10.0$.
3. Isothermal cylinder, high or low density, ideal gas: "C" = 0.95, "δ" = 1.61
   $\Delta p_z = 0.0736 \cdot p(z)$ at $x = 10.0$.
4. Lightning, Jones et al. (1968): "C" = 1, "δ" = 1.0
   $\Delta p_z = 0.0575 \cdot p(z)$ at $x = 10.0$.

Thus, for this range of possible initial conditions, the predicted variation in initial amplitude is from 0.0805 to 0.0575 or as much as ~40%, which is certainly nontrivial and will effect analyses of the source and its energetics. From here onward, the Jones et al. (1968) value of $\Delta p_z = 0.0575 \cdot p(z)$ is adopted as the lower limit to this range of variation (ReVelle 1976). Note that this is a correction to the

original value of $\Delta p_z = 0.563 \cdot p(z)$ given by ReVelle (1976), as this was originally evaluated at $x = 1.0$.

For a linearly propagating wave, derivation of the absorption or damping function is more straightforward. From Evans and Sutherland (1970) the absorption decay law for plane sinusoidal linear waves has the form:

$$\frac{\Delta p}{\Delta p_Z} = \exp(-\bar{\alpha}\Delta s), \tag{12.34}$$

where $\bar{\alpha}$ is the total amplitude absorption coefficient with the functional form of (Morse and Ingard 1968):

$$\bar{\alpha} = \frac{\pi^2}{2\rho C_S \lambda^2}\delta. \tag{12.35}$$

Therefore, following a similar procedure for solving (12.29), the linear damping function, D_L, has the general form of:

$$D_L = \frac{\Delta p}{\Delta p_Z} = \exp\left(-\int_{z_0}^{z} \frac{\bar{\alpha}}{\cos\varepsilon} dz\right). \tag{12.36}$$

Equation (12.36), like (12.33), is a generalized form of the ReVelle's linear damping function for an isothermal atmosphere (ReVelle 1976).

With these two absorption or damping functions for weakly nonlinear and linear waves, nearly all that is required to determine both the overpressure amplitude and period of a meteor generated shock wave is available, using the cylindrical line source approximation. Only one last term is required. In (12.26), the decay of the overpressure ratio, $\Delta p/p$, was derived by Jones et al. (1968) assuming a uniform ambient pressure, p, against which the expanding shock wave propagates. In practice, however, since the source altitudes of meteor generated infrasound may be quite high (i.e., many atmospheric scale heights), this pressure can assume a wide range of ambient values as the shock wave propagates downward through the atmosphere. Thus, the following correction term is required to be applied to (12.26) before proceeding (Pierce and Thomas 1969).

$$Z^* = \frac{\rho_z C_{Sz}^2}{\rho_0 C_{S0}^2}, \tag{12.37}$$

where again ρ_0 and C_{S0} are the atmospheric density, sound speed at the altitude of the observer, z_0, and similarly ρ_z and C_{Sz} are the density and sound speed at altitude of the source, z_z, respectively. Thus, the source altitude correction term is physically the ratio of the acoustic impedances at the observing and source altitudes, which corrects (12.26) for any altitude difference between the source region and the observer. In the special case of an isothermal atmosphere (12.37) combines with (12.27) and reduces to the root of the ratio of observer and source pressures. When the overpressure ratio is then used to determine the final wave overpressure, the altitude correction becomes simply geometric mean pressure between source and receiver (ReVelle 1976).

With the inclusion of this final altitude correction term, the cylindrical line source approximation theory as applied to meteor generated infrasound is complete. In the following section, these relationships are used to construct a simple algorithm for predicting the overpressure amplitude and fundamental period for any given meteor trajectory and propagation orientation.

12.3.2 Implementation of Cylindrical Line Source Theory

In the preceding half of this section, the general relationships among the generation, propagation, and absorption of meteor infrasound were given using the approximation of a cylindrical line source blast wave for the more generally conical hypersonic shockwave generated by a meteoroid entry into the atmosphere. Here, we will use these relationships to develop the algorithm used to predict the observed amplitude and period of the resulting shock wave at the location of the observer, be that at ground level or at altitude. An example of the procedure will be followed using an arbitrary meteor as we progress through the section, while comparisons of these same calculations are made, using observational constraints, to actual observed meteor infrasound data in Sect. 12.4.

We begin by considering the meteor example provided in Table 12.1. Although many of these parameters, as will be explained further in the following section, are not necessarily known immediately, several such as meteor velocity, inclination, heading, and ground range to the observer are readily measurable. Others such as meteoroid mass may be inferred from meteor lightcurve or ionization analysis, while meteoroid density, source altitude and ray deviation may be arrived at by either appropriate physical assumptions or through forward modeling (e.g., Brown et al. 2007; Edwards et al. 2007). For simplicity, we will also use the 1976 U.S. Standard Atmosphere for mid-latitudes (U.S. Government Printing Office 1976) as our atmospheric model.

To begin, the physical size of the meteoroid must first be determined. If a spherical meteoroid shape (for simplicity) is assumed, the characteristic diameter is then:

Table 12.1 Physical properties and orientation for an arbitrary meteor observation

Meteor characteristics	
Velocity (v)	20 km/s
Meteoroid mass (m)	1 kg
Meteoroid density (ρ_m)	3,700 kg/m^3
Source altitude (z_z)	80 km
Trajectory inclination (θ)	45°
Ray deviation from heading (dφ)	89°
Observation characteristics	
Ground range (R_g)	100 km
Elevation (z_0)	0 m

$$d_{\mathrm{m}} = \sqrt[3]{\frac{6m}{\pi\rho_{\mathrm{m}}}} \quad \text{or} \quad d_{\mathrm{m}} = 0.0802\,\mathrm{m}.$$

Knowing the diameter of the meteoroid, the approximate size of the resulting cylindrical blast radius may be determined from (12.12) and the known sound speed at the source altitude:
at 80 km altitude: $T = 198.63$ K, $C_{\mathrm{S}} = 0.282$ km/s,

$$R_o \approx (20\mathrm{km/s}) / (0.282\mathrm{km/s}) \times (0.0802\mathrm{m}) = 5.68\mathrm{m}.$$

With this blast radius, R_{o}, the initial period of the shock wave, τ_{o}, is then (12.13):

$$\tau_o = 2.81 \times (5.68\mathrm{m}) / (282\mathrm{m/s}) = 0.057 \text{ seconds}$$

or an initial frequency of

$$f_o = \tau_o^{-1} = 1/(0.058 \text{ sec.}) = 17.7\mathrm{Hz}$$

while the total distance from the meteor source region to the observer in units of R_{o} is then:

$$x_{total} \cong \frac{\sqrt{R_g^2 + z_Z^2}}{R_O} = ((100\,\mathrm{km})^2 + (80\,\mathrm{km})^2)^{1/2} / (0.00568\,\mathrm{km}) = 22{,}546\,R_{\mathrm{o}}.$$

In determining the initial period, the process of computing the overpressure of the shock wave and modification of its period as it propagates from the source region, can now begin. As discussed previously, there are two distinct types of possible propagation; as a weakly nonlinear shock wave, or as a linear propagating wave. The methods of determining both are similar, however, due to the integration terms in (12.28), (12.33) and (12.36), the process of evaluating these functions are typically achieved through numerical integration. For compactness the geometrical spreading function (12.26) is represented as $f(x)$ below. With this noted, the general form of the propagation of a weakly nonlinear shock wave is (from (12.26), (12.33) and (12.37)):

$$\frac{\Delta p}{p} = f(x) D_{\mathrm{WS}} Z^* \tag{12.38}$$

while for linear wave propagation the form is (12.26), (12.36) and (12.37):

$$\frac{\Delta p}{p} = f(x) D_{\mathrm{L}} Z^* x^{1/4}. \tag{12.39}$$

To determine where these two modes of propagation are dominant along a path to the surface, the altitude of transition (where condition (12.18) is satisfied) must be found. Beginning at an initial distance of $x = 10$, to ensure both (12.25) and (12.26) are applicable, (12.39) is evaluated assuming the wave initially begins as a linearly decaying wave, with its period slowly increasing according to (12.25). For the purposes of these calculations, C_{p} of air is taken as 1008.56 $\mathrm{J\,kg^{-1}\,K^{-1}}$ and the

following functions are used for determining the shear viscosity, μ, and thermal conductivity, K, for the atmosphere as a function of temperature, T (Pierce 1989):

$$\mu(T) = \mu_o \frac{(T_o + T_S)}{(T + T_S)} \left(\frac{T}{T_o}\right)^{3/2}, \tag{12.40}$$

$$K(T) = K_o \left(\frac{T}{T_o}\right)^{3/2} \left(\frac{T_o + T_a \exp\left(-\frac{T_b}{T_o}\right)}{T + T_a \exp\left(-\frac{T_b}{T}\right)}\right) \tag{12.41}$$

with
$\mu_o = 1.846 \times 10^{-5}$ Pa s
$K_o = 2.624 \times 10^{-2}$ Wm^{-1}K^{-1}
$T_o = 300$K
$T_a = 245.4$K
$T_b = 27.6$K
The bulk viscosity, η, of air is then simply related to the shear viscosity via the relationship:

$$\eta = \frac{2}{3}\mu. \tag{12.42}$$

Although there remains a great deal of uncertainty and dispute regarding the actual value of the bulk or volume viscosity of the atmosphere (Zuckerwar and Ash 2006), this particular form is employed in part due to its general simplicity and, more importantly, the agreement between the calculated overpressure amplitudes that result from its use with those of recorded observations (next section).

Following each step in the propagation of this linear wave, the distortion distance, d', is then calculated via (12.17) and compared with the remaining distance to the observation point. Where condition (12.18) is satisfied then defines the upper limit to the transition altitude, H_t, where the more rapidly decaying weakly nonlinear shock transitions to a more slowly decaying linear wave. In our example, this transition occurs at an altitude of 29.92 km or equivalently at a range of $x = 14{,}123$ (Fig. 12.7). Although the step size in altitude to be used in the integration is arbitrary, often it is desirable to use a small enough step such that the model atmosphere chosen at that scale may be considered slowly varying and thus locally homogeneous and isothermal. In practice, step sizes on the order of 10 m have been found to be sufficient to adequately determine H_t.

With the upper limit to H_t now known, the final overpressure amplitude and period calculations to the observer may now be computed. Once more, we begin by propagating the disturbance from an initial distance of $x = 10$, however, this time we compute the decay of the overpressure ratio via (12.38), as a more physically correct weakly nonlinear shock wave, with the same slowly increasing period determined by (12.25). This integration continues onward toward the point of observation

until the transition altitude, H_t, is reached. At the transition point, one of two options may be exercised (a) the weakly nonlinear wave may continue to propagate onward to the observation point or (b) the weakly nonlinear wave transitions to that of a linear wave. If the first option is chosen, the calculations may proceed as they had started and the final overpressure ratio and period may be calculated at the final observation point. If, however, the second option is chosen, then further calculations of the decay of the overpressure ratio to the observation point must be that of a linear wave defined by a decay, which follows (12.39) with the wave period now fixed at its value at H_t. As such, the final calculations for the linear wave proceeds from H_t to the final observation point according to:

$$\frac{\Delta p}{p}_{z_Z - g} = \frac{\Delta p}{p}_{z_Z - H_t} D_{L\ H_t - g} \left(\frac{Z^*_{z_Z - g}}{Z^*_{z_Z - H_t}} \right) \left(\frac{x_{z_Z - H_t}}{x_{z_Z - g}} \right)^{1/2} \text{ with } z_z > H_t \geq g \qquad (12.43)$$

with

$$\tau\,(x) = \tau\,(H_t)$$

where g is the altitude of the final observation position. This is a modification of (12.39), where the subscripted terms $z_z - H_t$ represent the previous weakly nonlinear decay of the wave computed from the source to the transition altitude and take the place of $f(x)$. Following (12.43), the integration continues the remaining distance to the point of observation, $H_t - g$, and final overpressure ratio and period of a linear wave are determined.

With the successful calculation of the theoretical overpressure ratio, it is a straightforward matter to calculate the theoretical overpressure amplitude of the wave by multiplying this ratio by the ambient atmospheric pressure at the point of observation, p. With this procedure an interesting phenomenon occurs. The decay of the meteor shock wave has thus far been determined via the dimensionless ratio $\Delta p/p$, which decays either as $x^{-3/4}$ or $x^{-1/2}$, yet atmospheric pressure, p, increases exponentially as the altitude decreases; the end result is that the overpressure, Δp, turns over at altitude and begins to increase with decreasing altitude (Fig. 12.8). This is not unphysical, however, as the wave's energy is continuously removed from the wave as it propagates outward from the source via (12.38) and (12.39) (ReVelle 1976); yet, the decay is always in relation to the ambient atmospheric pressure. Thus, if the pressure of the ambient air through which the wave is propagating grows, so does the wave overpressure. This growth in overpressure is then limited by the maximum atmospheric pressure at the Earth's surface.

Comparison of the two possible types of observed waves (weakly nonlinear and linear) shows that the transition to linearity can greatly influence the final observed value depending upon where the transition to linearity occurs (Fig. 12.8). The further this transition occurs from the observer, the greater the difference between the two wave types becomes. In our example (Table 12.2), although the dominant periods of the two types of waves are similar, varying by just more than 10%, the predicted amplitudes of the two wave types are significantly different with the

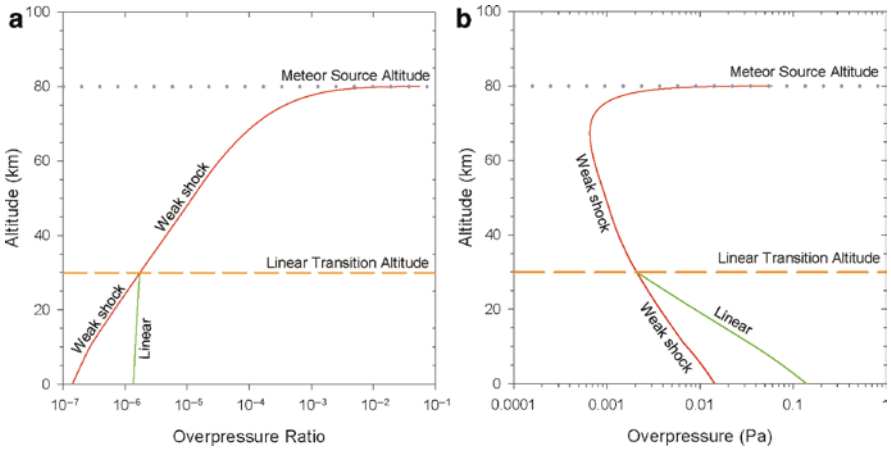

Fig. 12.8 (**a**) Overpressure ratio, $\Delta p/p$, and (**b**) overpressure, Δp, as a function of altitude for a meteor (Table 12.2) ballistic wave using the cylindrical line source blast wave approximation. Significant decreases in the attenuation of the wave occur upon reaching a state of linearity at the transition altitude, H_t, while exponentially increases in ambient atmospheric pressure at lower altitudes cause observed overpressures (**b**) of both states to grow

Table 12.2 Predicted meteor infrasound signal characteristics as predicted by cylindrical line source blast wave theory as applied to a trial meteor (Table 12.1) in the 1976 U.S. Standard Atmosphere

	Overpressure ratio ($\Delta p/p$)	Overpressure amplitude (Δp) (Pa)	Period (τ) (s)	Frequency (f) (Hz)
Weakly nonlinear	1.42×10^{-7}	0.014	0.389	2.57
Linear	1.37×10^{-6}	0.139	0.346	2.89

linear wave nearly an order of magnitude larger than that of the weakly nonlinear shock. In practice, both signals are within the realm of detection by modern microbarometers (Sect. 12.4); however, the significantly larger amplitude of the linear wave would allow for a greater ease of recognition and detection, even in noisy conditions, relative to the weakly nonlinear shock. To determine which of these states may be reaching the surface as well as verifying the general applicability of the cylindrical blast wave approach to meteor generated infrasound, comparisons of these predicted signal properties must be made against observed meteor infrasound detections of well-constrained meteors and meteor trajectories. Such comparisons are a topic of discussion in the following section.

Finally, the development of this algorithm makes no assumption regarding the location of the point of observation, other than that the observer is somewhere below the meteor trajectory. As the observer may be located either at altitude or at the surface, the algorithm ignores the potential for a ground reflection factor for an observer at the surface of the Earth. Therefore, it is noted that for a surface observer

the reflection factor may vary between a factor of 1–2 of the predicted overpressure amplitude, Δp; assuming that the wave frequency is sufficiently low so that only a negligible amount of wave energy can be transmitted through or absorbed by the local ground surface. Thus, the specific value the reflection factor will take will be a function of the local surface conditions where the observation is being made.

12.4 Regional Observations of Meteor Infrasound

In the previous section, the theoretical groundwork for the cylindrical line source blast wave approximation as applied to meteor generated infrasound was presented and the general algorithm for its application to a single body, nonfragmenting, meteor, as developed by ReVelle (1974, 1976) and revised by Kraemer (1977). In this section, the predictions of this theoretical model will be compared with actual observations of meteor infrasound and provide a basis for the observational characteristics of meteor infrasound generated by common, centimeter-sized meteoroids as recorded at regional (less than ~200 km) distances.

12.4.1 Identification and Detection of Meteor Infrasound

To identify meteor infrasound, it is beneficial to be familiar with the general form and characteristics of a ballistic shock wave. A ballistic shock wave is produced anytime the motion of an object through the air (or any fluid) is faster than the medium can carry the wave (produced by the object's motion) away from this moving source. This results in a build up of compression in the fluid in front of the object that propagates outward into the conical shape (Fig. 12.4a) described by (12.10) (Beyer 1997). The resulting pressure waveform of this motion induced shock wave has the appearance shown in Fig. 12.9, which was termed initially by DuMond et al. (1946) as an *N-wave*, due to its similarity in time to the shape of the capital letter *N*. This is also more commonly referred to as a sonic boom. As much of this terminology initially originated from studies of supersonic aircraft, these terms have become

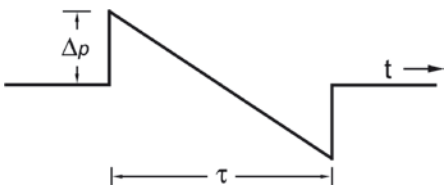

Fig. 12.9 Idealized pressure waveform as a function of time, *t*, for a ballistic *N*-wave (DuMond et al. 1946)

synonymous with these manmade sources; yet, the same basic waveform should also be produced by the equivalent ballistic shock front, or sonic boom, of a meteor.

To be able to observe and identify regional meteor infrasound it is important to understand the various elements that are required of a meteor for it to be able to produce detectable infrasound at the observer's location. Simply knowing what type of pressure waveform is likely to be associated with meteor infrasound generated by its ballistic trajectory is not enough to identify it with a meteor, as other natural and artificial sources can also produce similar waveforms (e.g., lightning and supersonic aircraft). To observe meteor-generated infrasound at the location of the observer, three basic requirements must be met:

1. The source meteoroid must be of sufficient size and/or velocity such that the initial ballistic wave generated may propagate to the observer without being completely attenuated by the atmosphere.
2. The position and orientation of the meteor trajectory must be such that an acoustic path in the atmosphere (at the time of the meteor event), to connect the source meteor and observer, is available.
3. Acoustic/infrasonic background noise levels at the point of observation must be of a sufficiently low level that the arriving meteor infrasonic wave is detectable.

As the third condition depends on the choice of the observer's location, the characteristics of that site and the equipment used, and not of the source meteor itself, nothing further will be discussed of this requirement other than to say that it is a requirement that is common throughout infrasound research, regardless of the source.

The first condition, regarding the meteoroid's size and velocity, may be addressed from the point of view of the predictions of cylindrical line source blast wave theory (Sect. 12.3). As was discussed in the preceding section, the characteristics of the initial ballistic shock wave of a meteor is related to the size of its blast radius, R_o, and therefore the product of a meteoroid's physical size and its velocity ((12.12) and (12.19)). Although atmospheric sound speed also plays a role (12.12), its influence may in general be neglected for the purposes of this discussion as the sound speed does not vary significantly over the range of potential source heights for meteor infrasound and so may be thought of as effectively constant. By inspection of (12.12) and (12.13), it is observed that by increasing either the diameter of the meteoroid, its velocity, or both, the size of the blast radius of the cylindrical line source increases and with this increase, the dominant frequency, f_0, of the initial ballistic shock correspondingly decreases (or equivalently its period, τ_0, increases). As higher frequencies are more greatly affected by atmospheric absorption (Pierce 1989), in general, the lower the initial fundamental frequency, the greater the chance the resulting ballistic wave may reach the observer.

Yet, meteors may be observed to propagate over a broad range of altitudes, from ~120 to ~20 km (Ceplecha et al. 1998), with the result that a blast radius produced at low altitude is more likely to produce observable infrasound at the surface than it would if produced at a higher altitude. This is due, in part, to the greater absorption experienced due to the increase in range to the observer, which comes with an increase in source height, but more so due to the greater absorption of high frequencies

in the upper atmosphere as a consequence of the longer mean-free paths of atmospheric molecules at altitude. This variability in ability to observe meteor infrasound, due to the combination of blast radius and source altitude, can be seen in Fig. 12.10, where the linear transition distance, H_t, is used as a means of measuring the overall shock wave absorption and dissipation. At high altitudes and small blast radii, the meteor ballistic waves are rapidly absorbed, reaching linearity very close to the source and thus will not survive long before complete attenuation, never to be recorded by ground observers. Yet, larger blast radii at increasingly lower source altitudes reach linearity at greater distances from the source region, increasing the likelihood of observation (Fig. 12.10). From this theoretical basis and observations of infrasound from high-altitude rocket-launched grenades (Procunier and Sharp 1971) ReVelle (1976) predicted that the minimum blast radius required to be able to produce observable infrasound at the surface would be on the order of $R_o \approx 10$ m. This minimum limit may also be expressed in terms of a meteoroids kinetic energy by making assumptions of the meteoroid's density and velocity.

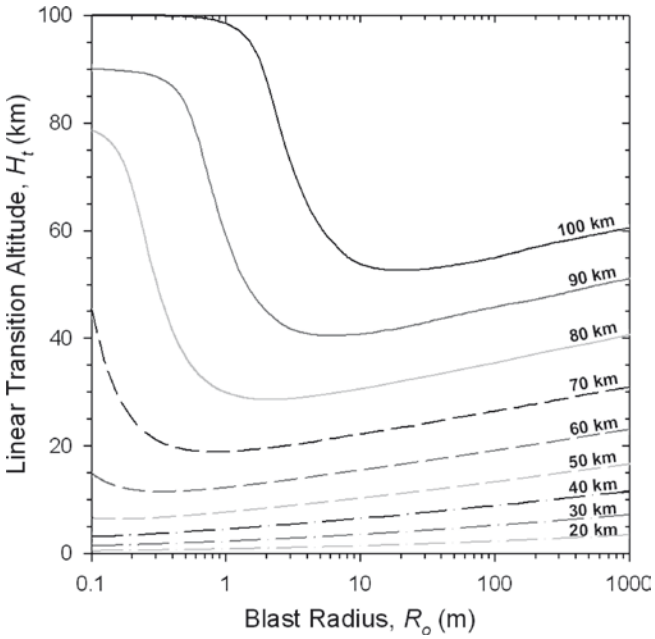

Fig. 12.10 Behavior of the linear transition altitude, H_t, as a function of the cylindrical line source blast radius, R_o, for multiple meteor source altitudes as seen from an observer at a range of 100 km. At high altitudes and small R_o, linearity is achieved rapidly due to the extreme attenuation of high frequencies in the rarefied upper atmosphere. As R_o increases, the shock wave frequency decreases and linearity is achieved at lower altitudes as attenuation lessens. At larger R_o, for high altitude sources, the wave can propagate further in a weakly nonlinear state, until it is forced to linearity by both its decaying overpressure and the increasingly thicker atmosphere, as it propagates to lower altitudes. In reality, however, at 100–1,000 km R_o (particularly at low source heights) at this range are likely to behave predominantly as weakly nonlinear shocks

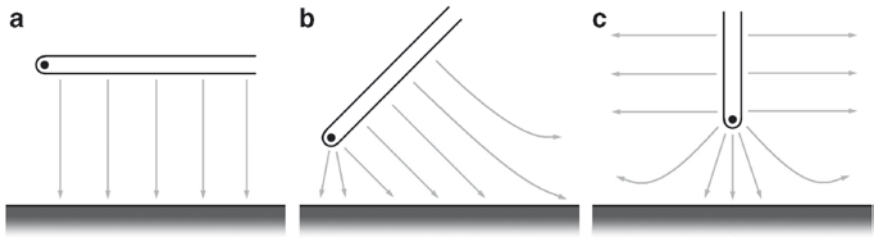

Fig. 12.11 Schematic variation of the extent of a meteor hypersonic boom corridor at the surface as a function of meteor trajectory orientation. (**a**) Horizontal, (**b**) inclined, (**c**) vertical

Using average cometary-type properties Brown et al. (2007) found this to be on the order of at least $W = 6.2 \times 10^{-5}$ kt of TNT (1 kt of TNT $= 4.185 \times 10^{12}$ J).

The second condition required to observe meteor infrasound, regarding the source meteor's position and orientation relative to the observer, is a direct result of the propagation geometry of a cylindrical line source. Cylindrical symmetry of the line source results in the predominant propagation of the ballistic wave in directions that are perpendicular to the orientation of the trajectory. This propagation condition results in a wide variability in the area over which ballistic waves may be observed. This region or zone of audibility (including nonaudible frequencies) at the surface is often referred to as a sonic boom carpet in supersonic aircraft studies (e.g., Cates and Sturtevant 2002) or in the case of meteors, a hypersonic boom corridor (e.g., ReVelle et al. 2004). The hypersonic corridor, demonstrated in Fig. 12.11, is generally composed of only that portion of the wave front whose rays are oriented toward the surface ($\varepsilon > 90°$) and thus propagating from the lower half of the meteor trajectory. Initially upward propagating rays, while potentially possessing a route to the ground via the upper thermosphere, will in general experience severe attenuation by the greatly rarefied regions of the upper atmosphere. This severe attenuation often results in these thermospheric paths being ill-suited for the survival of meteor infrasound to the surface, except for the largest and most energetic of meteors (discussed in Sect. 12.5). In Fig. 12.11, the dependence on the elevation of the meteor's trajectory, θ, relative to the horizontal is also demonstrated. As propagation of the ballistic wave front is perpendicular to the trajectory, increases in θ have the effect of decreasing the total area of the hypersonic boom corridor by sending greater portions of the ballistic wave along paths that will not reach a surface observer. Therefore, in general, it may be stated that a horizontally propagating meteor will have a larger hypersonic boom corridor than a similar meteor with an inclined trajectory, with the minimum occurring when the meteor is at the vertical with only the omnidirectional blunted end of the ballistic wave (i.e., the air cap preceding the meteoroid) producing viable paths to the surface as most of the ballistic wave remains in the upper atmosphere. Any refraction experienced by ballistic waves in the troposphere, which will tend to refract these waves back toward the stratosphere (Groves 1955), increases this effect, while upper atmospheric wind structure complicates propagation even further. An example of a

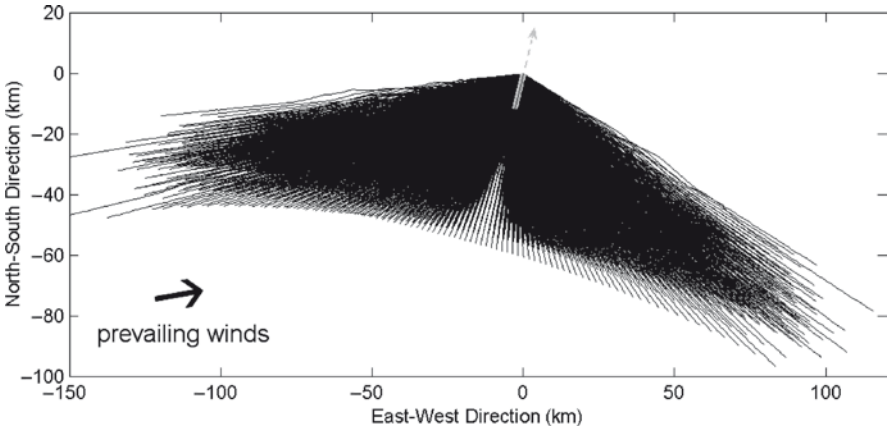

Fig. 12.12 A typical meteoric hypersonic boom corridor as seen from above. In this case the theoretical corridor is calculated for SOMN# 20060419 (*short gray line at 0, 0*), a meteor with a descent trajectory azimuth of 13.8° East from North (*dashed arrow*) and inclination of 26.1° from the horizontal. Ray paths initially spread perpendicularly outward from the lower half of the cylindrical source (extending from 80.1 to 66.9 km altitude), producing a butterfly-type pattern of arrivals on the surface. Note that prevailing winds create a slight asymmetry

typical hypersonic boom corridor is shown in Fig. 12.12, where, viewed from above, the corridor appears as a butterfly or wing-shaped pattern with its axial symmetry (about the plane of the meteor's trajectory) slightly distorted due to prevailing winds. In practice, how much of this theoretical hypersonic boom corridor is observable will depend upon the meteor shock wave's frequency content and atmospheric attenuation during its propagation (Sect. 12.3), as well as local noise conditions at the site of observation.

The overall result to be taken from this discussion is that the detection of meteor infrasound is the result of the convergence of several favorable conditions. As the occurrence rate of meteors favorable to produce infrasound is random, it is often only a matter of time before such a convergence will occur; yet, this greatly depends upon the flux of meteors at favorable sizes. If current estimates of the flux of meteoroids at the Earth (at the sizes likely capable of producing infrasound) are inspected, the occurrence rate over the entire surface of the Earth of a 10 cm sized sporadic meteoroid is on the order of 1 every 30 min. At 1 m, this rate is ~2–3 per month; 10 m sized objects occur on average only once per decade, while finally, events the size of the Tunguska meteor (~40 m) may be expected to recur approximately once a millennia (Brown et al. 2002b). During prominent meteor showers, such as the Leonids, Perseids, and Geminids, the rates of smaller, infrasound-producing meteoroids, increases even further (Ceplecha et al. 1998; Brown et al. 2007). Therefore, while large meteoroids (>1 m in dimension) may produce significant amounts of infrasound detectable over 100s to 1,000s of kilometers (see Sect. 12.5), smaller centimeter-scale meteoroids likely represent the majority of meteor generated

infrasound due to their vastly greater numbers, even though only a small proportion of meteors of these sizes (i.e., meteors/fireballs with visual magnitudes brighter than −2) will produce detectable infrasound at the surface (Brown et al. 2007; Edwards et al. 2007).

12.4.2 Observations of Regional Meteor Infrasound

So far much of the discussion in this chapter has been largely theoretical. In this section, however, recent observations of regional meteor infrasound will be compared with the predictions made by the preceding sections and cylindrical line source theory. Such comparisons have only recently been made possible due to the general paucity of meteor infrasound from well-observed and constrained meteors prior to the mid-2000s (Sect. 12.1). In the following observations, it is to be noted that each observation presented has been confirmed to be associated with an optically or radar observed meteor whose trajectory, velocity, and in many cases, its photometric mass have been constrained using standard methods (Ceplecha and McCrosky 1976; Ceplecha 1987; Borovička 1990; Ceplecha et al. 1998). To determine and delimit propagation geometries and source altitudes for these observed signals, numerical ray tracing from the observed meteor positions to the observing station were performed and compared with observed time delays, arrival azimuths, and trace velocities (incidence angles) (Brown et al. 2007; Edwards et al. 2007), using model atmospheres constructed for the time and region of the event from available meteorological data (Swinbank and O'Neill 1994; Hocking 1997) and standard atmospheric models (Hedin 1991; Hedin et al. 1996). Since 2000, dozens of cases of such confirmed meteor infrasound have been identified between the ongoing monitoring campaigns in Canada and Europe (see Sect. 12.1), a significant advancement since the early monitoring efforts of the late 1970s. It is from these more recent observations that this section draws upon.

In the preceding section, it was remarked that ballistic meteor infrasound should take the general form of an *N*-wave (DuMond et al. 1946) or ballistic wave (Fig. 12.9) and that this wave is defined to be ballistic by its perpendicular propagation geometry with respect to the source meteor's trajectory, rather than more random acute or obtuse angles that result from an omnidirectional point source. Point-like sources are not uncommon in meteors as these sources can be generated during the gross fragmentation of meteoroids (e.g., Qamar 1995; Arrowsmith et al. 2007). Complicating this apparently clear-cut distinction between ballistic and point-like sources, Brown et al. (2007) demonstrated theoretically that the high temperatures of the initial nonlinear shock wave, within the first ten blast radii of the meteor, may produce deviations in a ray's geometry of up to ~25° from the ideal perpendicular. To provide a means of distinguishing between both ballistic and nonballistic waves from meteors, Edwards et al. (2007) proposed a three category system based on the determined ray deviations: (1) The ballistic regime, which lies

between ray deviations: 90 ± 20°, where most ballistic waves predicted by theory should reside, (2) a quasiballistic regime, bordering the ballistic at: 55–70° and 110–125° ray deviations, for those observations with significantly larger deviations than theory would predict, yet, may exhibit ballistic wave features, and (3) the nonballistic regime relegated to those observations with deviations most likely to be associated with omnidirectional point-like sources.

Using the Edwards et al. (2007) classification scheme, 23 observations of confirmed meteor infrasound recorded by the SOMN monitoring program between 2006 and 2007 are subdivided in Fig. 12.13. Of these events, a majority of 61% (14 events) are found to classify as ballistic, 17% (4 events) quasiballistic, with the remaining 22% (5 events) appearing to originate from distinctly nonballistic sources. Such a clear majority of ballistic events confirms the initial hypothesis that a meteor's hypersonic shock wave, produced by the entry into the Earth's atmosphere of a meteoroid at extreme velocities, is the primary source of meteor generated infrasound. In addition, these observations demonstrate the preferred propagation geometry of meteor infrasound (discussed in the preceding section) with ray deviations, $d\varphi$, that originate from the lower half of the meteor's trajectory (Note: as defined in Sect. 12.3.1, $d\varphi = 0$ represents propagation in the direction of the meteor's heading).

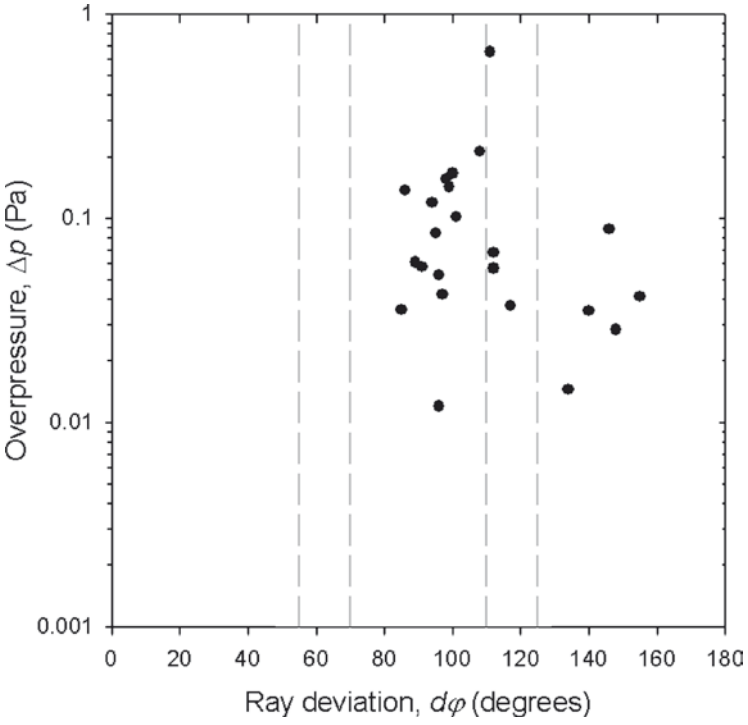

Fig. 12.13 Observed variation in infrasonic ray deviation from 23 meteors observed by the SOMN. *Dashed lines* indicate the current boundaries of ballistic, quasi-ballistic and nonballistic regimes

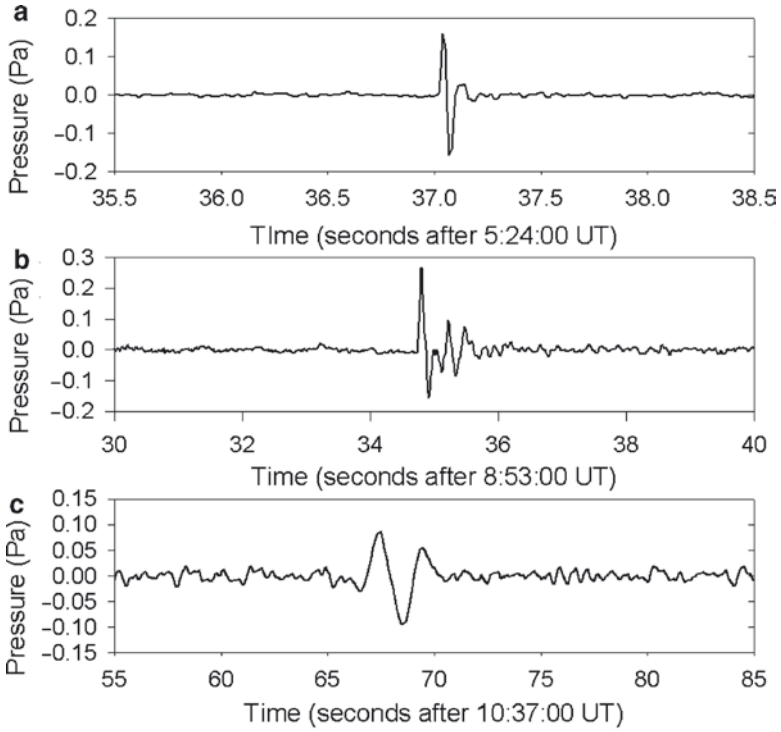

Fig. 12.14 Examples of observations of "classical" *N*-wave-type ballistic waves associated with meteors. (**a**) SOMN# 20071004b: velocity 16.26 km/s, $R_o \approx 2.4$ m, (**b**) SOMN# 20060213: velocity = 12.70 km/s, $R_o \approx 4.5$ m (**c**) SOMN# 20071021, velocity = 68.0 km/s, $R_o \approx 5.7$ m

With the classification of observations, inspection of the various observed waveforms can be made in context. In Fig. 12.14, several examples of meteor ballistic waves are shown for a variety of different blast radii, R_o. In general, these observations show the anticipated structure to that of the *N*-wave, yet in many cases the overpressure amplitude of the initial shock front exceeds that of the trailing rarefaction (unlike the classical *N*-wave shown in Fig. 12.9). This is often (but not always) followed by a slowly decaying wavetrain series. These decaying wavetrains have been observed to slowly vary in arrival (or back) azimuths in a manner consistent with originating from higher positions along the source meteor's trajectory (Brown et al. 2007), which suggests that these persisting wavetrains represent scattering of acoustic energy from the cylindrical blast wave as it propagates to the surface. Yet, not all meteor infrasound observations classified as ballistic, show *N*-wave-like patterns, and instead appear almost reverberatory in structure. These quite often brief pulses (few seconds duration) of infrasound show distinct periodic oscillations of two or three cycles of nearly equal amplitude which abruptly terminate (Fig. 12.15). The mechanism behind the creation of these waveforms is not well understood, but may reflect on the relaxation of the atmosphere as it restores itself to ambient levels

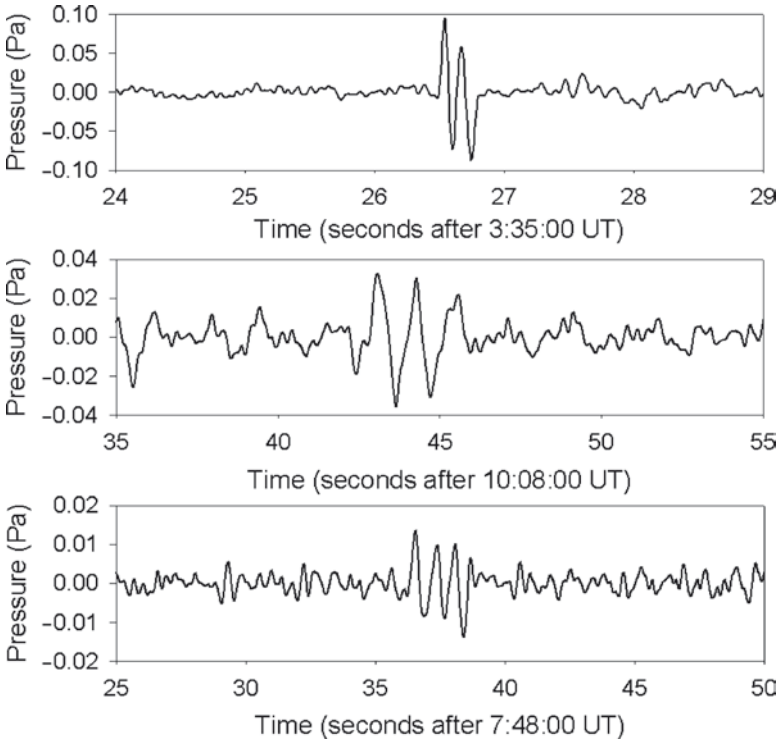

Fig. 12.15 Examples of observed reverberatory-type ballistic waves associated with meteor infrasound. Unlike singular *N*-type ballistic waves (Fig. 12.14), these ballistic waves recur several times before abruptly terminating. (**a**) SOMN# 20061104: velocity = 29.93 km/s, $R_o \approx 2.7$ m (**b**) SOMN# 20070125: velocity = 68.63 km/s, $R_o \approx 7.4$ m (**c**) SOMN# 20070511: velocity = 64.72 km/s, $R_o \approx 3.2$ m

at high altitude after the creation of a cylindrical blast wave by a meteor. Unanticipated signal structure such as the observations in Fig. 12.15 demonstrate the still largely unexplored field of meteor infrasound.

Observations which fall into the nonballistic regime typically do not show the recognizable *N*-wave-like signature of ballistic waves, instead often appearing structurally complicated or as dispersed pulses (Fig. 12.16). This is a likely result of a change in the source mechanism as nonballistic observations are quite often found to be associated with meteors undergoing gross fragmentation (large-scale break-up of the parent meteoroid) and so do not fit the simple single body model of a cylindrical line source blast wave. Instead, gross fragmentation of a meteor appears to act like a quasipoint source; with propagation that is omnidirectional, but may be extended along the direction of decent. The extent of this stretching of the source region becomes velocity dependant, such that the slower the meteor travels, the better an approximation to a true point-source explosion the fragmentation becomes. When several or continuous fragmentations occur one can likely anticipate a quite complicated signal to be observed.

The third category of quasiballistic observations, as the name implies, are a transitional type that separates the ballistic and nonballistic regimes. This results in quasiballistic signals exhibiting the characteristics of either of the two bordering regimes (Fig. 12.17). As greater numbers of quasiballistic observations are

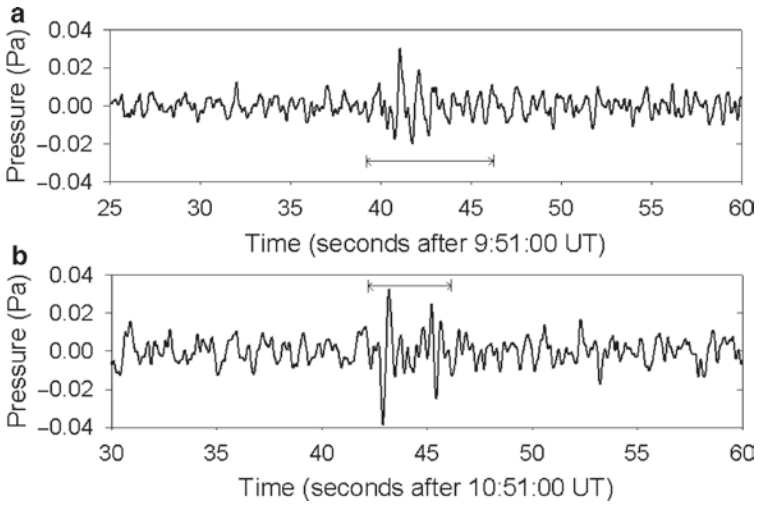

Fig. 12.16 Examples of nonballistic meteor infrasound. These type of observations are often associated with meteors undergoing gross fragmentation and do not display the well-characterized waveforms of ballistic waves, instead appearing less structured or dispersed. *Horizontal bars* indicate the durations of the meteor signals (SOMN# 20060813 (*above*), SOMN# 20070102 (*below*))

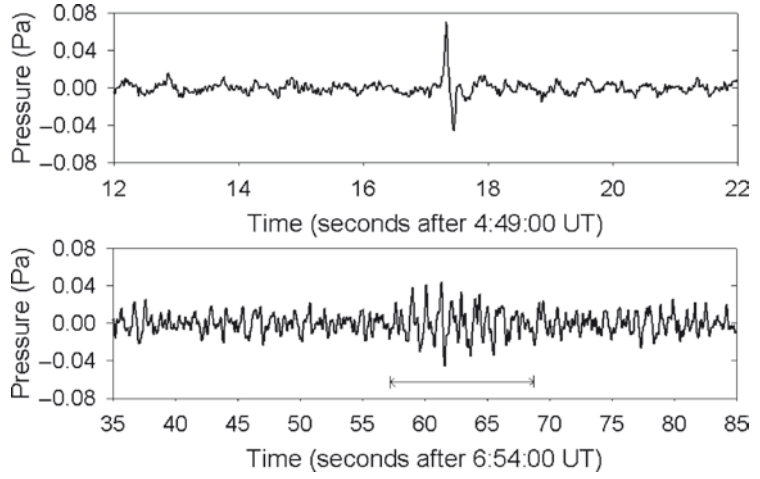

Fig. 12.17 Examples of quasi-ballistic meteor infrasound. This transitional category of meteor infrasound displays the characteristics of both ballistic (*above*: SOMN# 20070725) and nonballistic (*below*: SOMN# 20061101) waves and may in the future be able to more fully delimit the two categories. *Horizontal bar* indicates the duration of the signal

observed, it should become possible to better define the boundaries of ballistic observations, as the current limits of how far ballistic waves may deviate from the perpendicular of a meteor's trajectory are not well known. In time as further observations of this transitional type are made, it is likely the quasiballistic category will narrow or perhaps, even be eliminated altogether.

While structural and mechanistic differences between observed meteor infrasound signals can be readily pointed out, common properties between signals also exist. One of the greatest similarities for regional meteor infrasound may be found in the dominant period (or frequency) of observed waves and the source regions where these waves are produced in the atmosphere. As cylindrical line source theory predicts ((12.12) and (12.13)), the dominant period produced by these sources, will be proportional to both the altitude at which the wave is generated as well as the kinetic energy of the meteoroid and through the kinetic energy, its mass and velocity. For nonballistic waves, the physical basis upon which (12.12) and (12.13) are derived should also apply, though the geometry of the source may vary. As the observed amplitude, period, and meteor velocity and source region are all readily measurable or determinable properties (cf. Ceplecha 1987; Borovička 1990; Brown et al. 2007; Edwards et al. 2007), while meteoroid mass in practice is inferred based on dynamics, light or ionization production (Sect. 12.2, Ceplecha et al. 1998), only the relations between the first four properties will be discussed in greater detail.

According to the predictions of cylindrical line source theory (Sect. 12.3), it should be anticipated that the dominant periods of meteor infrasound are directly proportional to the extent of the initial blast radius, R_o, (12.13) and therefore also to meteor velocity, v (12.12). Although the period of the shock wave will slowly increase as the wave propagates outward during the weakly nonlinear phase, the kernel of the initial period and its proportionality to meteor velocity should remain (12.25). Comparable relationships are also to be anticipated for nonballistic meteor infrasound. While the geometry of the source region result in more gradual increases in R_o with v (e.g., spherical, $R_o \propto v^{2/3}$ vs. cylindrical, $R_o \propto v$), the energy available for blast wave production in these cases (i.e., kinetic energy) will in general scale with the square of meteor velocity.

Such a general trend can be seen in Fig. 12.18, where the observed periods of ballistic, quasiballistic, and nonballistic regional observations are shown as a function of observed meteor velocity for observed regional meteors with masses between 0.001 and 1 kg. Scatter in this trend is produced by variations in meteor mass, range and source altitude, all of which when increasing will tend to increase the initial (and therefore the observed) period of the shock wave. Yet, despite these additional factors, the strong dependence on meteor velocity remains quite apparent.

These strong correlations between the general predictions of cylindrical line source blast wave theory and recent observations suggest that the theoretical model developed several decades ago by ReVelle (1974, Sect. 12.3) may indeed be reasonable. Using the observed trajectories, velocities, and determined photometric masses and infrasonic source regions for the ballistic and quasiballistic series of SOMN meteors, the amplitude (overpressure) and period predictions of the meteor cylindrical

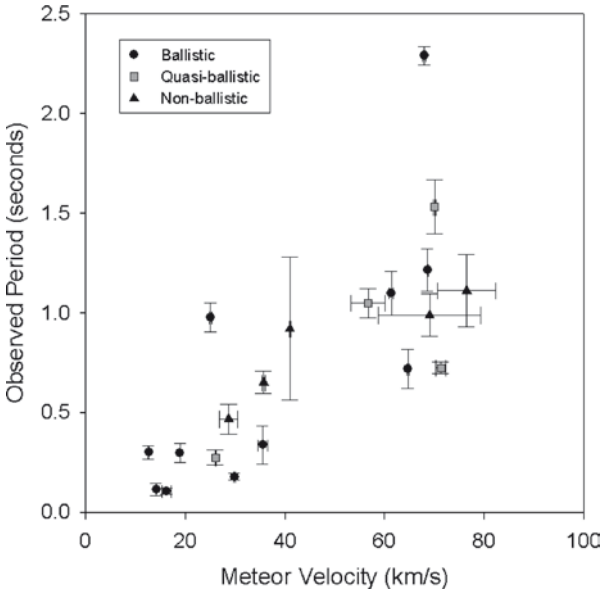

Fig. 12.18 Observed periods of meteor generated infrasound from centimeter sized meteoroids, as a function of observed meteor velocity

line source model are compared with observations (Fig. 12.19). Comparison between the observed and calculated amplitudes of weak shock and linear waves, it is seen that weak shocks in general underestimate the observed overpressure with gradually better agreement as overpressure increases; however, better agreement is observed for linear waves. Although generally over-predicting the observed amplitudes, the behavior is more systematic by a factor of two or three on average. Predictions of the fundamental periods by cylindrical line source theory in contrast show a progressive underestimation of the observed period. As both weak shock and linear modes follow the same functional form to determine the period growth (12.25), both modes show similar patterns (Fig. 12.18c, d). These comparisons suggest the following points. (1) The current estimation of the altitude of transition to linearity, is close to reality but is likely systematically too high. This is consistent with this calculation being the minimum altitude at which this may take place (Sect. 12.3). (2) The current growth in the fundamental period of the cylindrical blast wave, derived from the early work of DuMond et al. (1946), is underestimated for weakly nonlinear shock waves propagating from these altitudes. As the work of DuMond et al. (1946) focused on measurements of shock waves propagating through generally homogeneous, isothermal conditions at surface pressures, such an observation should not be unanticipated for shock waves propagating significant distances and altitudes through an inhomogeneous atmosphere. Thus, these comparisons show that in general the cylindrical line source blast wave model is a valid means of approximating meteor ballistic shock waves and their propagation, but that revisions on the theory will be necessary in the future if theoretical agreement to observation is to be reached.

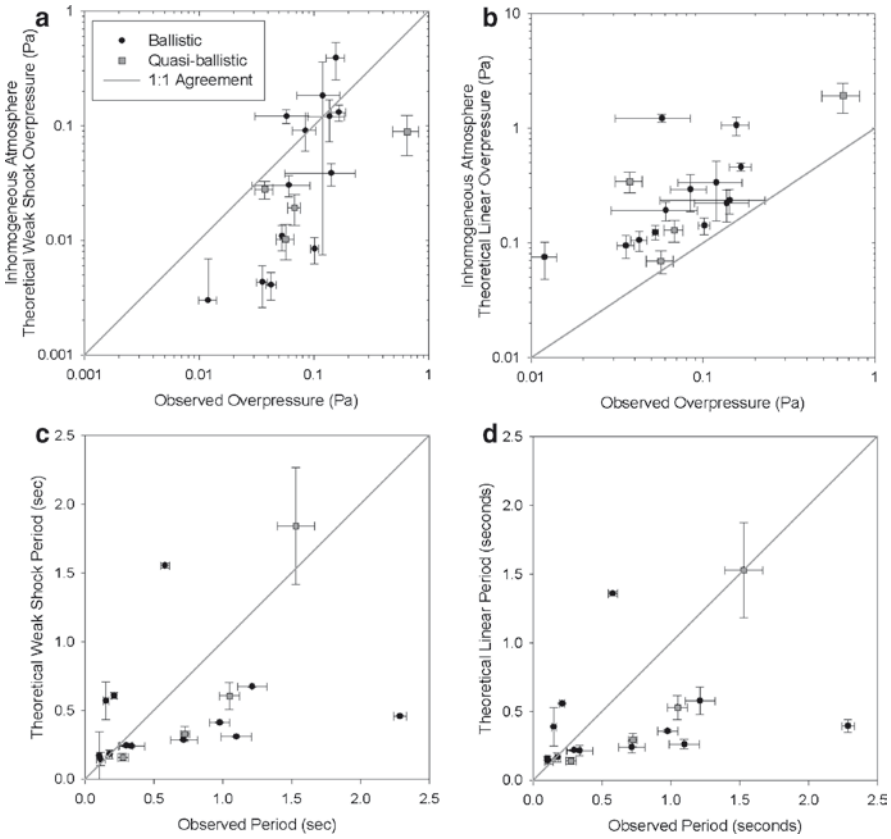

Fig. 12.19 Comparison of the amplitude and fundamental period predictions of cylindrical line source blast wave theory, as applied to meteors, to observations of meteor ballistic and quasi-ballistic shock waves. (**a, c**) Predicted arrival as a weakly nonlinear shock wave, (**b, d**) Predicted arrival as a linearly propagating wave

We conclude this section on regional meteor infrasound by investigating the source regions where these shock waves are generated. The altitudes at which regional meteor infrasound can originate is a complex function of several factors regarding the properties of the meteoroid, the geometry of its entry, and the conditions of the atmosphere in which the meteoroid is propagating. While a detailed discussion of the properties of meteoroids and the heights at which they are observed to produce meteors is beyond the scope of this section, detailed discussions on the subject may be found in Ceplecha and McCrosky (1976), Halliday et al. (1989), and Ceplecha et al. (1998). In terms of meteor infrasound, however, the general rule is that a meteoroid must first be of sufficient size, strength and velocity to reach altitudes where the atmosphere may respond fluidly to its passage. Too high and the meteoroid encounters the atmosphere in the free molecular flow regime, where encounters are with individual air molecules and the surface of the

meteoroid and production of a significant blast wave is negligible. Instead, a state of continuum flow must exist. This state occurs at altitudes where the local Knudson number, Kn (the ratio of the neutral gas mean-free path to the characteristic dimension of the meteoroid (i.e., diameter)) is much less than unity ($Kn \ll 1$) (Ceplecha et al. 1998). In this regime, the meteoroid–atmosphere interaction leads to the formation of a well-developed largely inviscid shock wave with strong radiative properties, while the formation of protective air gas caps in front of the meteoroid shield it, in part, from direct atmospheric molecule impacts. In between free molecular and continuum flow a state of slip-flow (a transitional flow type) exists where a viscous shock-wave body interaction occurs that can greatly increase localized heating rates (so-called interference heating). However, it is in continuum flow where cylindrical (or other blast geometries) become more feasible. By observing the distribution of source altitudes determined for the regional observations of meteor infrasound by the SOMN (Edwards et al. 2007) and EN (Brown et al. 2007), the typical altitudes where this condition is met appears to exist below ~100 km, peaking at an altitude of ~80 km (Fig. 12.20) for centimeter-sized meteoroids. Note, however, that the previous discussion regarding the necessity of a meteoroid to produce a sufficiently large blast radii, as well as have favorable geometry to produce detectable at the surface, still applies.

Also shown in Fig. 12.20 are the observed amplitudes of these meteor infrasound signals as a function of source altitude. While the amplitude in and of itself is a

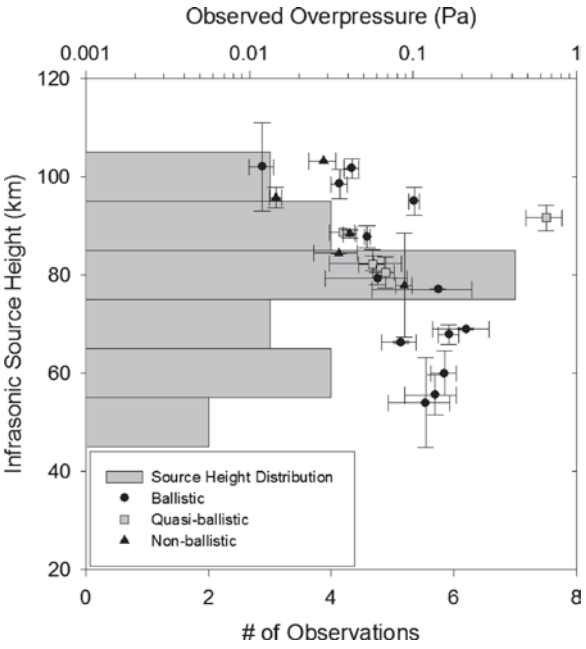

Fig. 12.20 Histogram of observed regional meteor infrasound source altitude and the variation in observed amplitude at the surface

complex function of observational range, wavelength, and the state of the atmosphere during a wave's propagation to the surface, all of which are likely contributors to the observed scatter in Fig. 12.20, a general trend of decreasing amplitude with source altitude can be identified. This trend of decreasing amplitude with increasing source altitude is a result of the conservation of wave energy and has been observed for other sources of infrasound, which may also vary significantly in altitude such as nuclear and chemical explosions (e.g., Glasstone and Dolan 1977). The physical reasoning for this trend is that wave energy must be conserved. As the blast wave propagates to the surface from altitude, it encounters increasingly denser regions of air to conserve energy, while still continuing to propagate in this increasingly denser medium, the wave must lower its amplitude. Thus, in addition to the losses in wave amplitude due to geometrical spreading and absorption that occur as a result of an increase in source altitude, in general, the greater the source altitude, the lower the observed amplitude will be at the surface for equivalent sources. This effect of source altitude will be revisited once more in the next section.

12.5 Long Range Observations of Meteor Infrasound

Unlike regional infrasound from small, centimeter-sized meteoroids, long-range meteor infrasound has been an almost continuous source of signal detections for as long as the infrasound band of the acoustic spectrum has been monitored (e.g., Whipple 1930; Folinsbee et al. 1967; ReVelle 1997; Brown et al. 2002a–c). To distinguish these types of observations from those of regional meteors discussed in the preceding section, long range meteor infrasound hereafter is defined as those meteor observations detected at ranges >250 km. At these more distant ranges meteor infrasound is less likely to reach the observer along a direct path from the source meteor, as often typifies the regional observations discussed previously. Instead, the generated infrasonic waves reach the observer after either being ducted along the waveguide that exists between the stratosphere and troposphere (stratospheric arrivals) or after refraction back to the surface from high in the thermosphere (thermospheric arrivals), the same means by which long distance observations are made of many other types of infrasonic sources (Drob et al. 2003). Indeed, as a typical observer's range for this type of meteor infrasound lies between ~2,000 and 3,000 km from the source (Edwards et al. 2006), the infrasonic wave front may have propagated between these regions (often referred to as a skip or hop) more than a dozen times before reaching the observer. In the following section, the sources of long range meteor infrasound, various observational aspects and its current limitations will be discussed.

12.5.1 The Sources of Long Range Meteor Infrasound

To generate infrasound, such that it may be observable at distances that vary from a few 100 to >10,000 km, an infrasonic source must be extremely energetic.

As kinetic energy is the means by which meteoroids produce infrasound (Sects. 12.2 and 12.3), an increase in meteoroid mass (and size) is necessary to provide this energy, since the maximum observed meteoroid velocities reach only ~73 km/s (Ceplecha et al. 1998). From observation, the dominant periods for these observations typically range between ~1 and 15 s (or 0.067–1 Hz) with source energies between 0.01 and 20 kt of TNT (Edwards et al. 2006), consistent with low-atmospheric attenuation at long periods and the large source energies necessary for long distance propagation. Assuming the observed range of meteor velocities apply, such periods and energies are consistent with the atmospheric impacts of large meteoroids meters in dimension. It becomes apparent, therefore, that meteors producing infrasound at these distances represent the largest of meteoroids, with diameters ranging from 1 to 10s of meters as in the specific case of the Tunguska Meteor (Whipple 1930; Ben-Menahem 1975). As the largest particles likely to be ejected from cometary sources are not anticipated to greatly exceed centimeters or decimeters in extent (de Pater and Lissauer 2001), barring direct impact of a cometary nucleus, the source of objects at these sizes are likely primarily of asteroidal origin. This conclusion generally constrains the sources of these long distance infrasound producing meteoroids to likely be Apollo-type (Earth crossing with origins in the main asteroid belt) and Aten-type (Earth crossing with orbits interior to the Earth's) Near Earth Asteroids (NEA). Yet this conclusion seems to be in contradiction to extrapolations made from a number of observations of smaller 0.1–1 m sized meteoroids where it is predicted that fragile cometary-type material should dominate in the 1–10 m regime (Ceplecha 1994). The resolution to this apparent disagreement is simple; while the orbital properties of these objects may be predominantly asteroidal-type, the physical properties and general strength of the impacting body may variety quite a bit, with perhaps very frail objects dominating the population.

As discussed in Sect. 12.3A, meteoroids of 1–10 m sizes recur typically on the timescales of months to decades. As these rates are averages computed over the entire surface of the Earth, the long distances to which these events are typically observed are a product of low influx rates and the broad spatial distribution of modern global infrasound networks (Christie et al. 2001) and regional focus of research networks (e.g., Evers and Haak 2003), resulting in a low probability that such an event will occur near an observer. A secondary consequence, as these objects are equally likely to occur anywhere over the Earth, it may be expected that >70% of these events will occur over the oceans rather than continental landmasses, where direct observation of the source meteor by ground-based observers is unlikely. This lack of direct observation makes identification of instances of large meteoroid atmospheric impacts (henceforth referred to as bolides) particularly difficult, as both the time and location of such events are random and not readily constrained to an area or region like an earthquake or erupting volcano. Indeed, documented instances of large meteoroid atmospheric impacts occurring over water and detected infrasonically have often been assisted by modern space-based optical and infrared observations by U.S. Department of Energy (DoE) and Department of Defense (DoD) satellites (e.g., Brown et al. 2002a–c; Klekociuk et al. 2005).

Although satellite-based observations have proved to be a valuable source of identifying bolide impacts in remote areas and thus their infrasonic signatures, it is when bolides occur over land and are observed across multiple suites of instruments (e.g., optical, seismic, and radar) as well as infrasonically, that a better understanding of the nature of these sources can be made (e.g., Brown et al. 2002c, 2004; ReVelle et al. 2004; Klekociuk et al. 2005; Arrowsmith et al. 2007), providing a means of calibrating similar infrasonic and space-based observations for more remotely located bolide events (Brown et al. 2002a–c; Edwards et al. 2006). From such well-observed bolides, it is found that meteoroids at these sizes experience: (1) almost continuous gross fragmentation (e.g., Brown et al. 2003) or (2) distinct episodes of explosive fragmentation (e.g., Brown et al. 2004; Arrowsmith et al. 2007) upon reaching low altitudes ranging from ~40 to 15 km, often referred to as terminal bursts due to their close proximity to the end of the luminous part of the meteor's trajectory. These instances of general break-up, results not only in the destruction of the bolide into fine micron-sized particles (Klekociuk et al. 2005) and small fragments which may fall to the surface as meteorites (e.g., Borovička et al. 2003), but also the production of significant amounts of infrasound. Such sources are distinctly different than that of the cylindrical line source discussed in Sect. 12.3.

In cases of bolide fragmentation, or terminal bursts, the cylindrical line source model of meteor infrasound is often abandoned and these fragmentations are instead approximated as quasi-point source explosions. The term "quasi" is added to remind us that since the source is not exactly stationary in space during episodes of gross fragmentation, the source region is elongated slightly along the trajectory. As the duration of these explosive events typically last<< 1 s, this elongation is typically small in comparison to the observer's range and so the point source approximation is valid. In cases where fragmentation is not anticipated (or observed) and a cylindrical-type source is more appropriate, a point source approximation may still be used when the range of the observer greatly exceeds the length of the bolide's trajectory (i.e., $R >> L$). As typical trajectories do not often exceed 100 km in length (except in cases of very low inclination or grazing meteors (e.g., Llorca et al. 2005)) and the acoustic coupling efficiency for a bolide increases with decreasing altitude (cf. Brown et al. 2003), effectively shortening the infrasound-producing region of the trajectory, at ranges of several 100 km and certainly >1,000 km, the cylindrical line source closely approximates that of a point source at altitude. With these concepts regarding long range meteor infrasound sources in mind, the observations of this type of meteor infrasound is examined in the following section.

12.5.2 Observations of Long-Range Meteor Infrasound

In Sects. 12.3 and 12.4, the concept of meteor infrasound as a cylindrical line source blast wave was introduced. With this model of infrasound generation, the ballistic wave and its features were shown to be typical of meteor infrasound at close range. At long ranges, however, this ballistic wave and its features are susceptible

to, and become heavily modified by, the effects of absorption, dispersion, and various modes of propagation (stratospheric vs. thermospheric) as the wave propagates to the observer. This is common to many types of infrasonic sources observed at great range. In the end, at long ranges, the recognizable features of regional meteor infrasound (Figs. 12.14 and 12.15) produce a wide variety of signal variations as singular or multiple wave arrivals from the same event may be recorded by the observer all traveling along separate, or slightly different atmospheric paths (Fig. 12.21) (Garcés et al. 1998; Arrowsmith et al. 2007). This variety makes recognition of long range meteor infrasound difficult when no observation of the bolide (instrumental or eyewitness) is available to constrain the location or time of the source.

Yet, at long distances, the transient and energetic nature of these bolides allows these events to be treated much like naturally occurring point source explosions. Thus, when arrivals are detected by multiple, well-separated stations, arrival azimuths at each station may be used to delimit the location of the source (via great-circle intersection, often weighted by the acuteness of the intersection). This is where the randomness of bolides stands out as an identifier, as bolides will not often coincide with known sources of natural infrasound (e.g., volcanoes and seismic fault lines) or regions where artificial explosives are expected (e.g., open pit mines and military test sites) (Fig. 12.22). From this position, the time of the event may be estimated using average propagation velocities and observational range, or arrival time delays calculated from atmospheric propagation models, and observed arrival times. This has been (ReVelle 1997) and continues to be a common means of identifying bolides by global networks even today (e.g., Arrowsmith et al. 2008). Indeed, relationships between infrasonic period and amplitude with source energy, observed for chemical and nuclear explosions, remain a common means of also characterizing a bolide's kinetic energy (Edwards et al. 2006). The most common of these being the period-energy relationship developed by AFTAC:

$$\log\left(\frac{W}{2}\right) = 3.34\log(\tau) - 2.58, \quad \frac{W}{2} \le 100\,\text{kt}, \tag{12.44}$$

$$\log\left(\frac{W}{2}\right) = 4.14\log(\tau) - 3.61, \quad \frac{W}{2} \ge 40\,\text{kt}, \tag{12.45}$$

where τ is the observed period at maximum amplitude of a signal in seconds and W is the energy or yield of the source in kt of equivalent TNT (Ceplecha et al. 1998).

More recently, since the mid-1990s, assistance in localizing and characterizing bolides has come at times from space-based satellite Earth-observing systems of the DoD and DoE (Tagliaferri et al. 1994; Brown et al. 1996). These optical and infrared observations have assisted in the identification of bolide infrasound by providing details of location and time of events (Brown et al. 2002a–c), and periodically velocity estimates and lightcurves, allowing further constraint of a bolide's mass and kinetic energy (e.g., Brown et al. 2004; Klekociuk et al. 2005). In a study of 31 bolide events observed by these satellite systems as well as infrasonically, Edwards

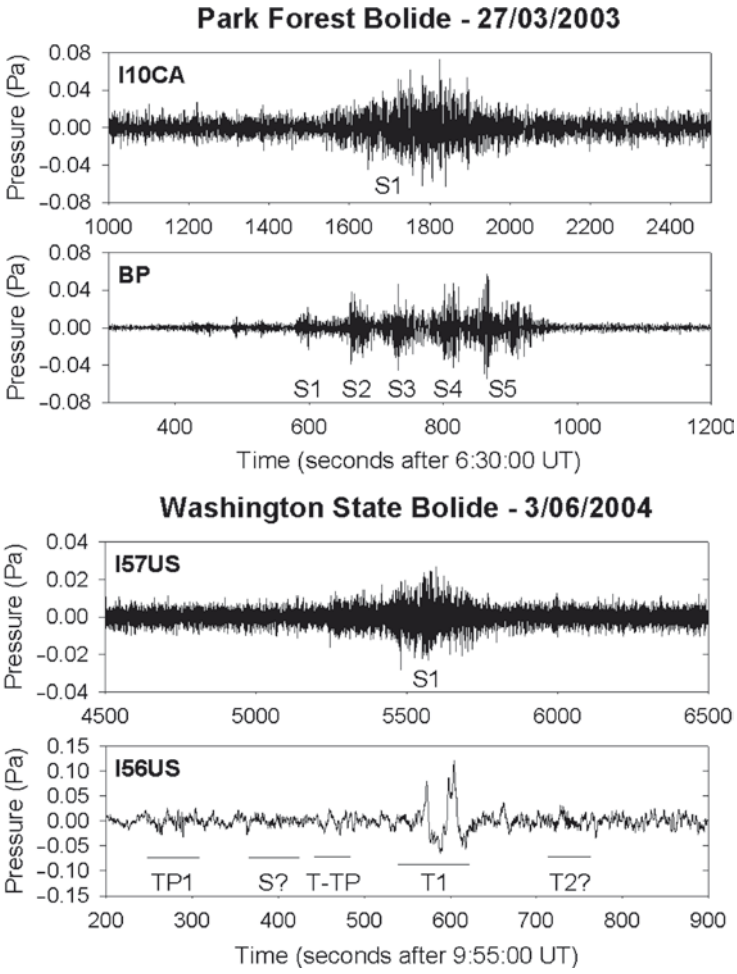

Fig. 12.21 Examples in the variety of observed long distance infrasound. (*Top*) Observations of the Park Forest bolide on March 27, 2003 (Brown et al. 2004). (*Bottom*) Observations of the Washington state bolide on June 3, 2004 (Arrowsmith et al. 2007). Although some observations may be the result of sound propagation along a singular path (e.g., I10CA, I57US), infrasound may also reach the same station along a variety of different paths (e.g., BP, I56US). S – stratospheric, T – thermospheric, TP – tropospheric, T-TP – converted Tropospheric from thermospheric

et al. (2006) examined long distance meteor infrasound statistically using similar methods employed to examine large nuclear and chemical explosions (e.g., Davidson and Whitaker 1992; Blanc et al. 1997) by calibrating satellite-derived estimates of bolide kinetic energies with well-documented multi-instrumental meteor observations, for which meteorites were recovered for some (Brown et al. 2002b). In their analysis, Edwards et al. (2006) were able to demonstrate several aspects of long range meteor infrasound that were previously unknown or only suspected upon theoretical grounds prior to the study.

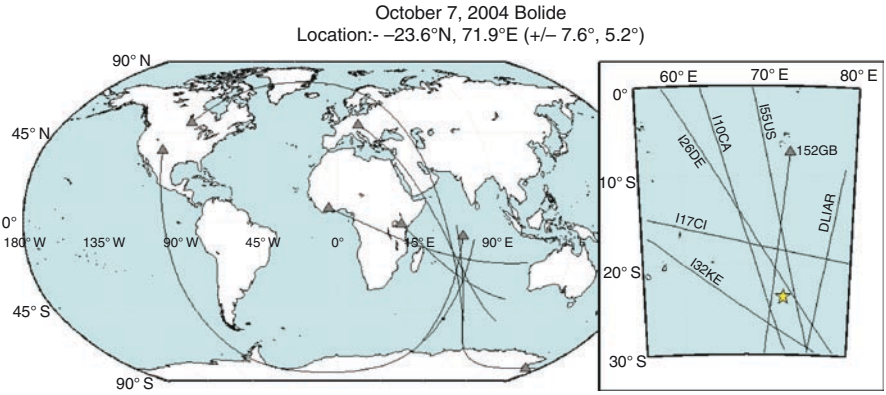

Fig. 12.22 Source location determination of a bolide over the Indian Ocean on October 7, 2004 (Arrowsmith et al. 2008). Infrasound detection was observed by seven stations at distances ranging from 2,200 to ~19,000 km. The estimated energy and random location of the event, unassociated with natural or known artificial sources of infrasound, help identify this as a bolide event. Based on a simple average infrasonic propagation velocity of 305 m/s, the time of the event would be at 13:33 UT ± 8 min on October 7, 2004. Using the amplitude-energy relationship (12.46) and measured amplitudes and ranges of the various signals (Arrowsmith et al. 2008), a source energy of ~14 kt is determined for the bolide, with approximately a factor of 2 uncertainty

Observations of infrasonic signal amplitudes as a function range (scaled by source energy or yield) for these bolides were found to fit the power law functions:

$$\log W = \frac{3}{b}(a - kw) + 3\log R - \frac{3}{b}\log A \tag{12.46}$$

with

$$a = 3.36 \pm 0.60, \quad b = -1.74 \pm 0.24, \quad k = -0.0177\,\mathrm{s/m}, \quad \text{for } W < 7\,\mathrm{kt},$$

$$a = 2.58 \pm 0.41, \quad b = -1.35 \pm 0.18, \quad k = -0.0018\,\mathrm{s/m}, \quad \text{for } W > 7\,\mathrm{kt},$$

where w is the average component of stratospheric wind, between 30 and 60 km altitude, directed along the great circle path connecting the bolide source and observer (+ in direction of propagation). Comparison of the bolide amplitude-range relations (12.46) to similar relationships derived from nuclear and chemical explosions (e.g., American National Standards 1983; Reed 1977; Whitaker 1995; Clauter and Blandford 1998; Blanc et al. 1997), show that bolide infrasound is consistently observed at lower amplitudes at equivalent ranges (Edwards et al. 2006). As discussed previously for regional observations (Sect. 12.4B), these lower observed amplitudes are a consequence of the high altitudes at which bolide's generate infrasound relative to equivalent surface sources. Correcting (12.46) for source altitude, Edwards et al. (2006) found that for these 1–10 m sized meteoroids source altitudes varied on average between 20 and 30 km altitude. This range in source altitude is a significant departure from the ~80 km altitude peak in source altitude observed for

smaller centimeter-sized regional meteor infrasound (Sect. 12.4, Fig. 12.20), but is consistent with visual observations (Halliday et al. 1989) and physically with the survival of larger meteoroids able to penetrate deep into the atmosphere at these 1–10 m sizes (Bland and Artemieva 2003).

A similar comparison of the AFTAC period-energy relationships ((12.44) and (12.45)) to observed bolide infrasound fundamental periods also shows good agreement between 0.05 and 7 kt, suggesting the approximation to a point source in this energy range is not altogether unreasonable; however, large departures from these explosion relationships are observed at energies >7 kt (Fig. 12.23). Edwards et al. (2006) suggest this may be the result of the gross fragmentation of these large meteoroids during entry, with multiple fragments traveling as a cloud during entry creating multiple blast cavities, which merge to form a much larger effective cavity (R_o), in effect generating longer periods than would a single body (Sect. 12.3, (12.13)). It is difficult to ascertain the validity of this hypothesis as such large events occur so infrequently and to date none have been observed in sufficient detail to discern such behavior, leaving the verification of this attribute of bolide infrasound to theoretical modeling (Ceplecha and ReVelle 2005) and future observations.

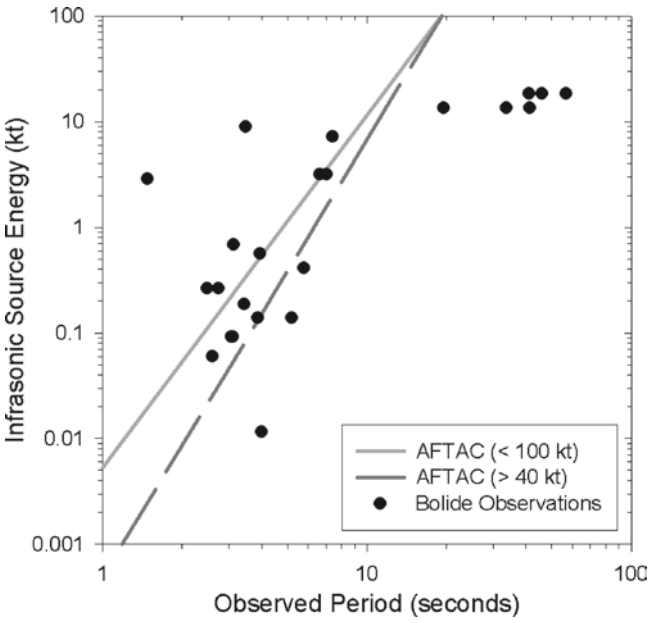

Fig. 12.23 Comparison of the States Air Force Technical Applications Center (AFTAC) period-energy relations for large (> 100 kt) and small (< 40 kt) nuclear explosions (Edwards et al. 2006). Moderate agreement between these relationships is observed for bolides between ~0.05 and 10 kt, but as energies increase greater deviation from the AFTAC curves is observed. This deviation may be due to dynamical changes experienced during entry, creating dominantly larger periods as the large parent meteoroids fragment

As a final observation regarding long distance bolide infrasound, it is interesting to note that in general thermospheric arrivals do not appear to be at all common, with >95% of observations (Edwards et al. 2006) appearing to propagate along stratospheric channels based on average observed propagation velocities, $\overline{v}$, from the source (Table 12.3, Ceplecha et al. 1998). This is in contrast to observations other natural and artificial surface explosions where thermospheric phases are observed with regularity, even for relatively small energies (e.g., Ottemöller and Evers 2008). In cases where thermospheric arrivals are observed for bolides (e.g., Brown et al. 2003), amplitudes are often observed to be relatively weak in comparison to stratospheric arrivals (Fig. 12.24), demonstrating the severe attenuation of infrasound propagating along thermospheric paths. Yet, for other events, often in the intermediate ranges between regional and long distance meteor infrasound, thermospheric arrivals appear to be the dominant phase open to observation along a given geometry (Fig. 12.21, Arrowsmith et al. 2007).

This apparent preferred mode of propagation may once more be due in part to the higher altitudes at which large 1–10 m class bolides produce much of their infrasound. From analysis of observed amplitude offsets (Edwards et al. 2006), source altitudes of 20–30 km are common. At these altitudes, significantly more

Table 12.3 Typical ranges of average propagation, $\overline{v}$, and trace velocities, V_{tr}, for the four primary modes of atmospheric propagation (from Ceplecha et al. 1998)

Designation	Average propagation velocity ($\bar{v}$) (km/s)	Trace or apparent horizontal velocity (V_{tr}) (km/s)	Primary propagation mode
L	0.330–0.340	0.340	Lamb (horizontal) wave
TP	0.300–0.320	0.320–0.340	Tropospheric wave
S	0.280–0.310	0.340–0.450	Stratospheric wave
T	0.220–0.240	0.450–1.100	Thermospheric wave

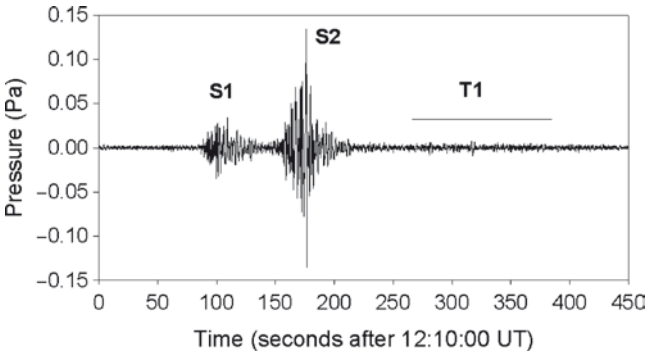

Fig. 12.24 Infrasonic observations of the Morávka fireball by the International Monitoring System (IMS) infrasound station in Freyung, Germany (I26DE). From the known trajectory of the fireball and ray propagation modeling, the first two arrivals, S_1 and S_2 are identified as stratospherically propagating waves, while the third significantly lower amplitude arrival, T_1, propagated along a higher altitude thermospheric path (Brown et al. 2003)

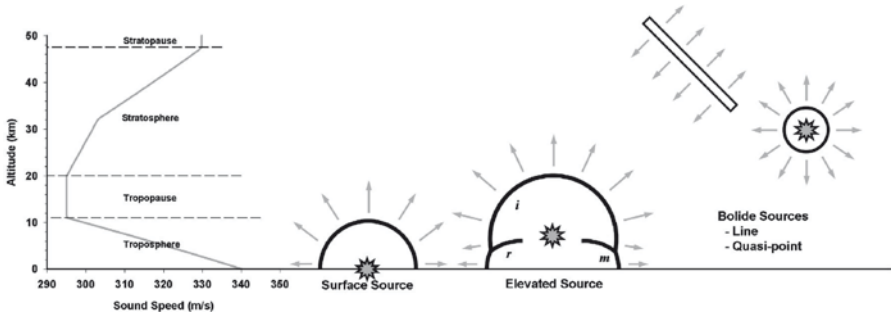

Fig. 12.25 Schematic diagram of the differences in the deposition of acoustic/infrasonic energy between high altitude bolide and surface/elevated sources. Where surface and elevated (< 10 km from surface) sources primarily direct their acoustic radiation initially upward and horizontally due to reflection with the ground (Glasstone and Dolan 1977). Bolide sources (*cylindrical line* source, quasi-point), by virtue of their high altitudes regions (15–40 km), often deposit significant portions of their acoustic radiation directly into the stratosphere. Labels for elevated source indicate the initial (incident) shock wave, *i*, the surface reflected wave, *r*, and horizontally propagating Mach stem, *m*, formed by constructive interference of incident and reflected waves

acoustic energy will be deposited directly into the stratosphere where it may efficiently propagate along stratospheric waveguides producing detectable signals for 1,000s of km (Brown et al. 2002a–c; Edwards et al. 2006; Arrowsmith et al. 2008) or become trapped (e.g., Arrowsmith et al. 2007) depending on atmospheric conditions (temperature/wind). Proportionally less acoustic energy from bolides is then available to thermospheric paths relative to a surface or near-surface sources where much of the acoustic propagation is typically directed upwards by reflection with ground or horizontally along the surface requiring appropriate atmospheric conditions to emplace acoustic energy in stratospheric channels (Fig. 12.25). As attenuation in the upper atmosphere (e.g., Sutherland and Bass 2004), global propagation of infrasound (e.g., Bass et al. 2007; Millet et al. 2007; Kulichkov 2004), and measurement of upper atmospheric condition using infrasound (e.g., Le Pichon et al. 2005) remain topics of active research, this difference in propagation methods makes bolide events a unique means of probing the upper atmosphere, validating atmospheric models and exploring low frequency sound propagation over the entirety of the globe. This property, if nothing else, will continue to make detection of meteor/bolide infrasound and the characterization of their source bodies highly desirable to the future of infrasound research.

12.6 Conclusions

Over the course of this discussion of meteor generated infrasound, it has been shown that the history of regional and global meteor and bolide detections parallels the development and usage of infrasound as a monitoring technology from the beginning of the twentieth century, to the modern day. As advancements in technology and

monitoring capabilities has expanded, our ability to detect the entire range of meteoroid sizes and energies, from the very small (centimeter; ~10^{-5} kt) to the very large (10s of meters, >10 kt), has also increased. With the assistance of visual, radar, and space-based sensor suites, the source regions and generation mechanisms of meteor-related infrasound are being identified and constrained, allowing the predictions of cylindrical line source blast wave theory and other dynamical meteor entry models to be put to the test at explaining the wide range of ground-based observations. These new constraints are opening a new methodology for studying the physics of the hypervelocity entry of meteoric material in the upper atmosphere and meteor physics in general by independently estimating luminous efficiencies and providing estimates of meteoroid masses and kinetic energies (e.g., Edwards et al. 2006, 2007).

Yet the study of meteor or bolide infrasound holds interest of many fields of investigation and research beyond meteor physics. The observations and study of these naturally energetic sources are providing estimates of the flux of large meteoroids at the Earth (ReVelle 2001; Brown et al. 2002b); provide a mechanism for studying interaction of material at hypersonic velocities, important for the design and engineering of re-entering spacecraft (e.g., ReVelle et al. 2005; ReVelle and Edwards, 2007); allow testing and calibration for infrasonic propagation and atmospheric models (e.g., Drob et al. 2003; Arrowsmith et al. 2007; Brown et al. 2007); provide the potential for inversion of wind structure at stratospheric and lower mesospheric altitudes (cf. Le Pichon et al. 2005); and finally provide a means of testing the monitoring capabilities of growing global infrasound network of the CTBT/IMS used for the identification and enforcement of the nonproliferation of nuclear weapons testing worldwide (Christie et al. 2001).

While it is clear that not all aspects of meteor generated infrasound are as yet well known, with the growing capabilities, incorporation and collaboration between multiple sensors, technologies and researchers, our understanding of this type of natural infrasound is advancing rapidly.

Acknowledgements The author extends his appreciation to David McCormack and the personnel at Natural Resources Canada (NRCan) for their assistance in obtaining and collecting data. Thanks also to Peter Brown and Douglas ReVelle for both their assistance and encouragement in pursuing meteor infrasound over the course of the past 5 years. To the meteor physics research groups at the University of Western Ontario, Canada, the Ondrejov Observatory, Czech Republic, and the Spanish Meteor Network for their past and continued cooperation at identifying and characterizing meteor infrasound. Thanks also to the British Atmospheric Data Center (BADC) for access to weather and upper atmospheric data and the Ontario Graduate Scholarship (OGS) program for financial assistance.

References

American National Standards Institute (1983) Airblast characteristics for single point explosions in air, ANSI Standard S2.20-1983. Acoustical Society of America, New York

Arrowsmith SJ, Drob DP, Hedlin MAH, Edwards WN (2007) A joint seismic and acoustic study of the Washington State bolide: observations and modeling. J Geophys Res 112, doi: 10.1029/2006JD008001

Arrowsmith SJ, ReVelle DO, Edwards W, Brown P (2008) Global detection of infrasonic signals from three large bolides. Earth Moon Planets 102:357–363
Ayers WG, McCrosky RE, Shao CY (1970) Photographic observations of 10 artificial meteors. Smith Astrophys Obs 317:1–40
Bass HE, Hetzer CH, Raspet R (2007) On the speed of sound in the atmosphere as a function of altitude and frequency. J Geophys Res 112, doi: 10.1029/2006JD007806
Bedard AJ, Greene GE (1981) Case study using arrays of infrasonic microphones to detect and locate meteors and meteorites. J Acoust Soc Am 69:1277–1279
Ben-Menahem A (1975) Source parameters of the Siberian explosion of June 30, 1908, from analysis and synthesis of seismic signals at four stations. Phys Earth Planet Int 11:1–35
Beyer RT (1997) Nonlinear acoustics. American Acoustical Society of America, Woodbury, NY
Blanc E, Millies-Lacroix JC, Issartel JP, Perez S (1997) Detection of nuclear explosions in the atmosphere. Chocs 17:23–34
Bland PA, Artemieva NA (2003) Efficient disruption of small asteroids by Earth's atmosphere. Nature 424:288–291
Blanc E, Le Pichon A, Ceranna L, Farges T, Marty J, Herry P (2010) Global scale monitoring of acoustic and gravity waves for the study of the atmospheric dynamics. This volume, pp. 641–658
Borovička J (1990) The comparison of two methods of determining meteor trajectories from photographs. Bull Astron Insc Czech 41:391–396
Borovička J, Spurný P, Kalenda P, Tagliaferri E (2003) The Morávka meteorite Fall: 1: Description of the events and determination of the fireball trajectory and orbit from video records. Meteorit Planet Sci 38:975–987
Brown PG, Hildebrand AR, Green DWE, Page D, Jacobs C, ReVelle D, Tagliaferri E, Wacker J, Wetmiller B (1996) The fall of the St-Robert meteorite. Meteorit Planet Sci 31:502–517
Brown PG, Whitaker RW, ReVelle DO (2002a) Multi-station infrasonic observations of two large bolides: signal interpretation and implications for monitoring of atmospheric explosions. Geophys Res Lett 29, doi: 10.1029/2001GL013778.
Brown P, Spalding RE, ReVelle DO, Tagliaferri E, Worden SP (2002b) The flux of small near-Earth objects colliding with the Earth. Nature 420:314–316
Brown PG, ReVelle DO, Tagliaferri E, Hildebrand AR (2002c) An entry model for the Tagish Lake fireball using seismic, satellite and infrasound records. Meteorit Planet Sci 37:661–675
Brown PG, Kalenda P, ReVelle DO, Borovicka J (2003) The Morávka meteorite fall: 2. Interpretation of infrasonic and seismic data. Meteorit Planet Sci 38:989–1003
Brown PG, Pack D, Edwards WN, ReVelle DO, Yoo BB, Spalding RE, Tagliaferri E (2004) The orbit, atmospheric dynamics and initial mass of the Park Forest meteorite. Meteorit Planet Sci 39:1781–1796
Brown PG, Edwards WN, ReVelle DO, Spurný P (2007) Acoustic analysis of shock production by very high-altitude meteors – I: infrasonic observations, dynamics and luminosity. J Atmos Solar-Terr Phys 69:600–620
Cates JE, Sturtevant B (2002) Seismic detection of sonic booms. J Acoust Soc Am 111:614–628
Ceplecha Z (1987) Geometric, dynamic, orbital and photometric data on meteoroids from photographic fireball networks. Bull Astron Ins Czech 38:222–234
Ceplecha Z (1996) Luminous efficiency based on photographic observations of the Lost City fireball and implications for the influx of interplanetary bodies onto Earth. Astron Astrophys 311:329–332
Ceplecha Z, McCrosky RE (1976) Fireball end heights: a diagnostic for the structure of meteoric material. J Geophys Res 81:6257–6275
Ceplecha Z, ReVelle DO (2005) Fragmentation model of meteoroid motion, mass loss, and radiation in the atmosphere. Meteorit Planet Sci 40:35–54
Ceplecha Z, Borovička J, Elford WG, ReVelle DO, Hawkes RL, Porubcan V, Simek M (1998) Meteor phenomena and bodies. Space Science Rev 84:327–471
Ceplecha Z, Borovička J, Spurný P (2000) Dynamical behaviour of meteoroids in the atmosphere derived from very precise photographic records. Astron Astrophys 357:1115–1122

Christie DR, Vivas Veloso JA, Campus P, Bell M, Hoffman T, Langlois A, Martysevich P, Demirovic E, Carvalho J (2001) Detection of atmospheric nuclear explosions: the infrasound component of the International Monitoring System. Kerntechnik 66:96–101
Christie DR, Campus P (2010) The IMS infrasound network: design and establishment of infrasound stations. This volume, pp. 27–72
Chyba CF, Thomas PJ, Zahnle KJ (1993) The 1908 Tunguska explosion: atmospheric disruption of a stony asteroid. Nature 361:40–44
Clauter DA, Blandford RR (1998) Capability modeling of the proposed International Monitoring System 60-station infrasonic network, LAUR-98-56, Los Alamos National Labs Report, Los Alamos, New Mexico
Davidson M, Whitaker RW (1992) Miser's Gold, LA-12074-MS, Los Alamos National Laboratory Report, pp 1–28
de Pater I, Lissauer JJ (2001) Planetary sciences. Cambridge University Press, Cambridge, UK
de Groot-Hedlin CD, Hedlin MAH, Drob DP (2010) Atmospheric variability and infrasound monitoring. This volume, pp. 469–504
Drob DP, Picone JM, Garcés MA (2003) Global morphology of infrasound propagation. J Geophys Res 108, doi: 10.1029/2002JD003307
Drob DP, Meier RR, Picone JM, Garcés MM (2010) Inversion of infrasound signals for passive atmospheric remote sensing. This volume, pp. 695–726
DuMond JWM, Cohen RE, Panofsky WKH, Deeds E (1946) A determination of the wave forms and laws of propagation and dissipation of ballistic shock waves. J Acoust Soc Am 18:97–118
Edwards WN, Brown PG, ReVelle DO (2006) Estimates of meteoroid kinetic energies from observations of infrasonic airwaves. J Atmos Solar-Terr Phys 68:1136–1160
Edwards WN, Brown PG, Weryk RJ, ReVelle DO (2007) Infrasonic observations of meteoroids: preliminary results from a coordinated optical-radar-infrasound campaign. Earth Moon Planet, 102, doi: 10.1007/s11038-007-9154-6
Edwards WN (2010) Meteor generated infrasound: theory and observation. This volume, pp. 355–408
Evans LB, Sutherland LC (1970) Absorption of sound in air. Wylie Labs, Huntsville, Alabama
Evers LG, Haak HW (2003) Tracing a meteoric trajectory with infrasound, Geophys Res Lett 30, doi: 10.1029/2003GL017947
Evers LG, Haak HW (2010) The characteristics of infrasound, its propagation and some early history. This volume, pp. 3–26
Few AA Jr (1968) Thunder, Ph.D. Dissertation, Rice University, Houston, TX
Folinsbee RE, Douglas JAV, Maxwell JA (1967) Revelstoke, a new Type I carbonaceous chondrite. Geochim Cosmochim Acta 31:1625–1635
Garcés MA, Hansen RA, Lindquist KG (1998) Traveltimes for infrasonic waves propagating in a stratified atmosphere. Geophys J Int 135:255–263
Garcés M, Willis M, Le Pichon A (2010) Infrasonic observations of open ocean swells in the Pacific: deciphering the song of the sea. This volume, pp. 231–244
Glasstone S, Dolan PJ (1977) The effects of nuclear weapons. United States Department of Defense and Department of Energy, Washington DC
Goerke VH (1966) Infrasonic observations of a fireball. Sky and Telescope 32:313
Groves GV (1955) Geometrical theory of sound propagation in the atmosphere. J Atmos Terr Phys 7:113–127
Halliday I, Blackwell AT, Griffin AA (1978) The Innisfree meteorite and the Canadian camera network. J R Astron Soc Canada 72:15–39
Halliday I, Blackwell AT, Griffin AA (1989) The typical meteorite event, based on photographic records of 44 fireballs. Meteoritics 24:65–72
Hauchecorne A, Keckhut P, Chanin M-L (2010) Dynamics and transport in the middle atmosphere using remote sensing techniques from ground and space. This volume, pp. 659–678
Hedin AE (1991) Extension of the MSIS thermosphere model into the middle and lower atmosphere. J Geophys Res 96:1159–1172

Hedin AE, Fleming EL, Manson AH, Schmidlin FJ, Avery SK, Clark RR, Franke SJ, Fraser GJ, Tsuda T, Vial F, Vincent RA (1996) Empirical wind model for the upper, middle and lower atmosphere. J Atmos Terr Phys 58:1421–1447

Hetzer CH, Gilbert KE, Waxler R, Talmadge CL (2010) Generation of microbaroms by deep-ocean hurricanes. This volume, pp. 245–258

Hocking WK (1997) Strengths and limitations of MST radar measurements of middle-atmosphere winds. Annal Geophys 15:1111–1122

Hunt JN, Palmer R, Penny W (1960) Atmospheric waves caused by large explosions. Philos Trans Roy Soc London 252:275–315

Jones DL, Goyer GG, Plooster MN (1968) Shock wave from a lightning discharge. J Geophys Res 73:3121–3127

Kaiser TR (1953) Radio echo studies of meteor ionization. Philos Mag Supp 2:495–544

Kanamori (1994) Excitation of atmospheric oscillations by volcanic eruptions. J Geophys Res 99(B11):21947–21961

Klekociuk AR, Brown PG, Pack DW, ReVelle DO, Edwards WN, Spalding RE, Tagliaferri E, Bernard YB, Zagari J (2005) Lidar, satellite and acoustic measurements of an asteroidal air-burst in Earth's atmosphere. Nature 436:1132–1135

Kraemer DR (1977) Infrasound from accurately measured meteor trails, Ph.D. Dissertation, University of Michigan, Ann Arbor, MI

Kraemer DR, Bartman FL (1981) Infrasound from accurately measured meteor trails. In: Mathews T, Hicks RB (eds) Proceedings of the International Symposium of Acoustic Remote Sensing of the Atmosphere and Oceans, vol. 31–49. University of Calgary Press, Calgary, Canada

Kulichkov SN (2004) Long-range propagation and scattering of low-frequency sound pulses in the middle atmosphere. Meteorol Atmos Phys 85:47–60

Kulichkov S (2010) On the prospects for acoustic sounding of the fine structure of the middle atmosphere. This volume, pp. 505–534

Kulik (1927) On the history of the bolide of 1908 June, 30. J Russian Acad Sci 127A:393–398

Le Pichon A, Guerin JM, Blanc E, Raymond D (2002) Trail in the atmosphere of the 29 December 2000 meteor as recorded in Tahiti: characteristics and trajectory reconstitution. J Geophys Res 107, doi: 10.1029/2001JD001283

Le Pichon A, Blanc E, Drob D (2005) Probing high altitude winds using infrasound. J Geophys Res 110, doi: 10.1029/2005JD006020

Lin SC (1954) Cylindrical shock waves produced by instantaneous energy release. J Appl Phys 25:54–57

Llorca J, Trigo-Rodríguez JM, Ortiz JL, Docobo JA, García-Guinea J, Castro-Tirado AJ, Rubin AE, Eugster O, Edwards WN, Laubenstein M, Casanova I (2005) The Villalbeto de la Peña Meteorite Fall: I. fireball energy, meteorite recovery, strewn field and petrography. Meteorit Planet Sci 40:795–804

McCrosky RE, Boeschenstein H (1965) The Prairie Meteorite Network, Smithsonian Astrophysical Observatory Special Report #173, pp 1–26

McCrosky RE, Soberman RK (1963) Results from an artificial iron meteoroid at 10 km/s. Smith Contrib Astrophys 7:199–208

McCrosky RE, Shao CY, Posen A (1979) The Prairie Network bolide data. II – Trajectories and light curves. Meteoritika 38:106–156

McIntosh BA, Watson MD, ReVelle DO (1976) Infrasound from a radar-observed meteor. Canad J Phys 54:655–662

McKinley DWR (1961) Meteor science and engineering. McGraw-Hill, New York

Millet C, Robinet JC, Roblin C (2007) On using computational areoacoustics for long-range propagation of infrasounds in realistic atmospheres. Geophys Res Lett 34, doi: 10.1029/2007GL029449

Millman PM (1970) Meteor news. J R Astron Soc Canada 64:55–59

Mikumo T, Watada S (2010) Acoustic-gravity waves from earthquake sources. This volume, pp. 259–276

Morse PM, Ingard KU (1968) Theoretical acoustics. McGraw-Hill, New York

Mutschlecner JP, Whitaker RW (2010) Some atmospheric effects on infrasound signal amplitudes. This volume, pp. 449–468
Oberst J, Molau S, Heinlein D, Gritzner C, Schindler M, Spurny P, Ceplecha Z, Rendtel J, Betlem H (1998) The "European Fireball Network": current status and future prospects. Meteorit Planet Sci 33:49–56
Officer CB (1958) Introduction to the theory of sound transmission – application to the ocean. McGraw-Hill, New York
Öpik EJ (1933) Atomic collisions and radiation of meteors. Acta Comment Univ Tartuensis 26:1–39
Öpik EJ (1937) Basis of the physical theory of meteors. Acta Comment Univ Tartuensis 33:1–66
Öpik EJ (1970) The sonic boom of the boveedy meteorite. Irish Astron J 9:308–310
Ottemöller L, Evers LG (2008) Seismo-acoustic analysis of the Brucefield old depot explosion in the UK, 2005 December 11. Geophys J Int 172:1123–1134
Pierce AD (1989) Acoustics: an introduction to its physical principles and applications. Acoustical Society of America, Melville, New York
Pierce AD, Thomas C (1969) Atmospheric correction factor for sonic-boom pressure amplitudes. J Acoust Soc Am 46:1366–1380
Plooster MN (1968) Shock waves from line sources, NCAR Report TN, pp 1–93
Plooster MN (1970) Shock waves from lines sources. Numerical solutions and experimental measurements. Phys Fluid 13:2665–2675
Plooster MN (1971) Numerical simulation of spark discharges in air. Phys Fluid 14:2111–2123
Procunier RW, Sharp GW (1971) Optimum frequency for detection of acoustic sources in the upper atmosphere. J Acoust Soc Am 49:622–626
Qamar A (1995) Space shuttle and meteoroid – tracking supersonic objects in the atmosphere with seismographs. Seismol Res Lett 66:6–12
Reed JW (1977) Attenuation of explosion waves. J Acoust Soc Am 61:39–47
ReVelle DO (1974) Acoustics of meteors – effects of the atmospheric temperature and wind structure on the sounds produced by meteors, Ph.D. Dissertation, University of Michigan, Ann Arbor, MI
ReVelle DO (1976) On meteor generated infrasound. J Geophys Res 81:1217–1229
ReVelle DO (1997) Historical detection of atmospheric impacts by large bolides using acoustic-gravity waves. In: Remo JL (ed) Annals of the New York academy of sciences, near-earth objects – the United Nations international conference, New York Academy of Sciences, vol. 822, pp 284–302
ReVelle DO (2001) Global infrasonic monitoring of large bolides, in Proceedings of the Meteoroids 2001 Conference, 6 – 10 August 2001, Kiruna, Sweden, ESA SP-495, pp. 483–489, ESA Publ. Div., Noordwijk, Netherlands, ISBN:92-9092-805-0
ReVelle DO, Edwards WN (2007) Stardust – an artificial, low-velocity "meteor" fall and recovery: 15 January, 2006. Meteorit Planet Sci 42:271–299
ReVelle DO, Whitaker RW (1999) Infrasonic detection of a Leonid bolide: 1998 November 17. Meteorit Planet Sci 34:995–1005
ReVelle DO, Brown PG, Spurný P (2004) Entry dynamics and acoustics/infrasonic/seismic analysis for the Neuschwanstein meteorite fall. Meteorit Planet Sci 39:1605–1626
ReVelle DO, Edwards W, Sandoval TD (2005) Genesis – an artificial, low velocity "meteor" fall and recovery: September 8, 2004. Meteorit Planet Sci 40:895–916
Sakurai A (1965) Blast wave theory. In: Holt M (ed) Basic developments in fluid dynamics, vol. 1. Academic Press, New York, pp 309–375
Strachey R (1888) On the air waves and sounds caused by the eruption of Krakatoa in August, 1883. In: Simkin T, Fiske RS (eds) Krakatau 1883. Simthsonian Institution Press, pp 368–374
Sutherland LC, Bass HE (2004) Atmospheric absorption in the atmosphere up to 160 km. J Acoust Soc Am 115:1012–1032
Swinbank R, O'Neill AA (1994) Stratosphere-troposphere data assimilation system. Month Weather Rev 122:686–702
Tagliaferri E, Spalding R, Jacobs C, Worden SP, Erlich A (1994) Hazards due to comets and impacts. University of Arizona Press, Tucson, Arizona, p 199

Thompson RJ (1971) Ray theory for an inhomogeneous moving medium. J Acoust Soc Am 51:1675–1682

Towne DH (1967) Wave phenomena. Addison-Wesley, Reading, MA

Trigo-Rodríguez JM, Castro-Tirado AJ, Llorca J, Fabregat J, Martínez VJ, Reglero V, Jelínek M, Kubánek P, Mateo T, De Ugarte Postigo A (2004) The development of the Spanish Fireball Network using a new all-sky CCD system Earth Moon Planets, 95, doi: 10.1007/s11038-005-4341-9

Tsikulin MA (1969) Shock waves during the movement of large meteorites in the atmosphere. Nauka Izadatel'stvo, Moscow (English Translation: AD 715-537, National Technical Information Service, Springfield, Virginia, 1970)

United States Committee on Extension to the Standard Atmosphere 1976. *U.S. Standard Atmosphere 1976*, U.S. Government Printing Office, Washington.

Watson M, McIntosh B, ReVelle D (1976) A meteor infrasound recording system. In: IEEE international conference on ICASSP'76 acoustics, speech, and signal processing, pp 786–789

Weryk RJ, Brown PG, Domokos A, Edwards WN, Krzeminski Z, Nudds SH, Welch DL (2007) The Southern Ontario All-sky Meteor Camera Network. Earth Moon Planets, doi: 10.1007/s11038-007-9183-1

Whipple FJW (1930) The Great Siberian meteor and the waves, seismic and aerial, which it produced. Quart J R Meteorol Soc 56:287–304

Whipple FJW (1934) On phenomena related to the great Siberian meteor. Quart J R Meteorol Soc 60:505–513

Whipple FL (1938) Photographic meteor studies I. Proc Am Philos Soc 79:499–548

Whitaker RW (1995) Infrasonic monitoring. In: Proceedings of the 17th Seismic research symposium on monitoring a Comprehensive Test Ban Treaty, pp 997–1000

Wylie CC (1932) Sounds from meteors. Popul Astron 40:289–294

Zuckerwar AJ, Ash RL (2006) Variational approach to the volume viscosity of fluids. Phys Fluid 18(047101):1–10

Chapter 13
High-latitude Observations of Infrasound from Alaska and Antarctica: Mountain Associated Waves and Geomagnetic/Auroral Infrasonic Signals

Charles R. Wilson, Curt A. L. Szuberla, and John V. Olson

13.1 Introduction

Mountain associated waves (MAW) are generated as hydrodynamic infrasound in the turbulent wind-stream in the lee of high mountain ranges during periods of severe winter storms (Meecham 1971). MAW events are observed worldwide. At any one infrasonic station, such as I53US in Alaska, MAW signals arrive at an infrasonic array from various azimuth-bands, each of which subtends an extensive mountain range. The characteristics of MAW events, both in Alaska and Antarctica, are described in Sect. 1 in terms of typical event morphology as well as the specific waveform characteristics of: pressure amplitude, mean and variance of trace-velocity, back azimuth of arrival, waveform coherence across the array, and spectral content of the MAW signals.

Infrasonic wave episodes of long-duration high coherency wave trains with very high trace-velocities have been observed, in the pass band from 0.015 to 0.10 Hz, over the past 35 years at many different high latitude infrasonic arrays in Alaska, Canada, Sweden, and Antarctica. These high trace–velocity infrasound episodes are often directly associated with periods of geomagnetic and auroral activity. They have recently been observed throughout the year at the infrasonic arrays at I53US in Fairbanks and I55US in Antarctica. In Sect. 2.1, AIW infrasound that is directly associated with auroral electrojet motions is described. In Sect. 2.2, GAIW infrasound is described that is associated with large fluctuations in the H and D components during intervals of magnetic disturbance with examples from both Alaska and Antarctica.

C.R. Wilson (✉)
Geophysical Institute, University of Alaska Fairbanks, 99775-7320, Alaska, USA
e-mail: crw@gi.alaska.edu

A. Le Pichon et al. (eds.), *Infrasound Monitoring for Atmospheric Studies,*
DOI 10.1007/978-1-4020-9508-5_13,

13.2 Mountain Associated Waves

Atmospheric turbulence generated by mountain ranges that interrupt the troposphere wind flow can produce aerodynamic infrasound that propagates thousands of kilometers from the source regions (Larson et al. 1971). These mountain associated infrasonic waves (MAW) have been observed for many years by infrasonic arrays operated by the University of Alaska in Antarctica and in interior Alaska. At the two new CTBT/IMS infrasonic arrays: I53US at Fairbanks and I55US at Windless Bight, Antarctica, we have accumulated a very large data set of MAW events at both stations from 2002 through 2007. The CTBT infrasonic arrays at both I53US and I55US have eight sensors that are arranged in a pentagonal pattern of five microphones with an aperture of 1.7 km and with an inner triangular pattern of three microphones with an aperture of 173 m. The geometry of the I53US array at Fairbanks is shown in Fig. 13.A below. That of the I55US array in Windless Bight, Antarctica is shown in Fig. 13.B below.

The microphones used at these two arrays are Chaparral Model 5 sensors. The microphones are vented to the atmosphere by systems of noise reducing pipes.

The detection algorithm that we use in searching for coherent MAW infrasonic waves that propagate across the sensor array is based upon the mean of each of the maxima of all the 28 microphone-pairs of inter-microphone cross-correlations. That is, the normalized cross-correlation function is computed for each microphone pair and its maximum is identified. Next, the mean of all of these maxima is then defined to be the output value of the detection algorithm, or mean cross-correlation maximum (MCCM). For search analysis, the data are segmented into small windows a few

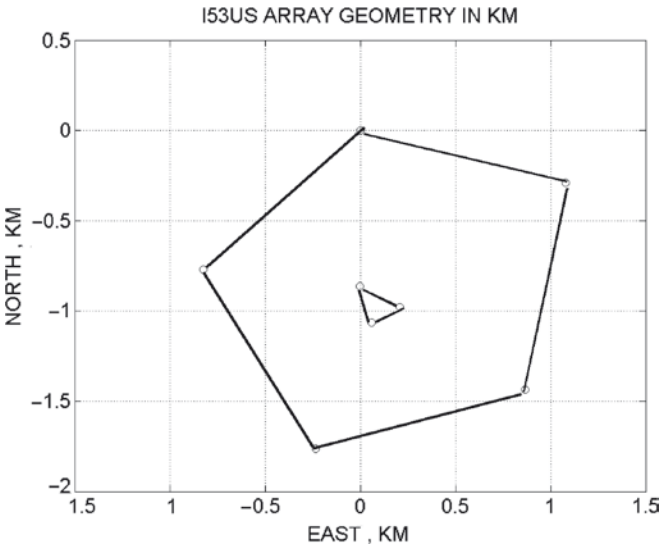

Fig. 13.A I53US array geometry in km East and North of 0,0

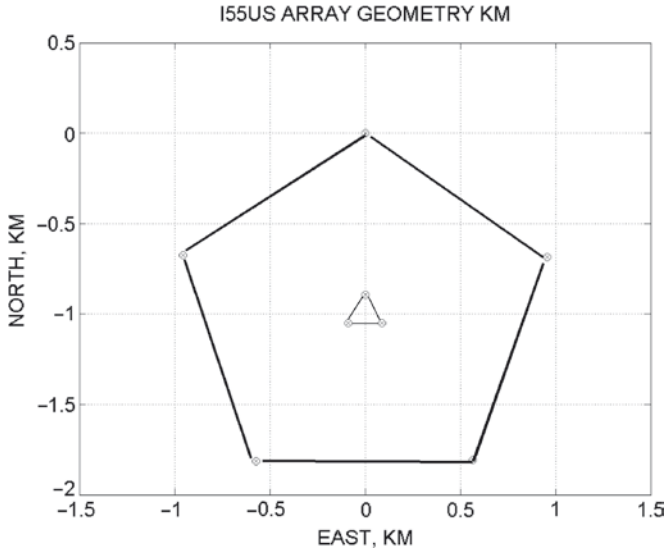

Fig. 13.B I55US array geometry in km East and North from 0,0

minutes long and the detection algorithm is applied to each window resulting in a series of detection values of the following parameters: (1) The F-Stat which is a measure of the signal to noise ratio for coherent signals in the analysis window, (2) MCCM, (3) the apparent (trace) velocity in km/s, (4) back azimuth of arrival in degrees, and (5) a binary measure of the planarity of the wave packet for each data window in the time series of data (see description of σ_τ in Szuberla and Olson (2004)). The upper left panel in Fig. 13.1 depicts the histogram of MCCM values with a threshold value shown via the red line. The threshold was determined empirically from the analysis of multiple years of MCCM values calculated at the station. The upper right panel is a similar representation of the F-statistic value for the same data. This set of five values is then the final output of the MCCM detection algorithm. For the MAW signal search, we scan an entire 24 h record of eight-sensor pressure data with a sliding window that is 10,000 points or 500 s in length. MAW are long period waves; therefore, all the I53US and I55US data were first pass band filtered from 0.015 to 0.10 Hz before application of the detection algorithm for signal search. An example is shown in Fig. 13.1 with the output of the MCCM detection algorithm for the MAW event of January 12, 2007 at I53US.

13.2.1 MAW at I53US in Fairbanks, Alaska

Thus far, we have found many examples of MAW events at I53US that are characterized by: (1) long period waves in the range from 70 to 20 s periods, (2) long durations of quasi-sinusoidal wave trains, amplitudes of a few tenths of a Pa, lasting

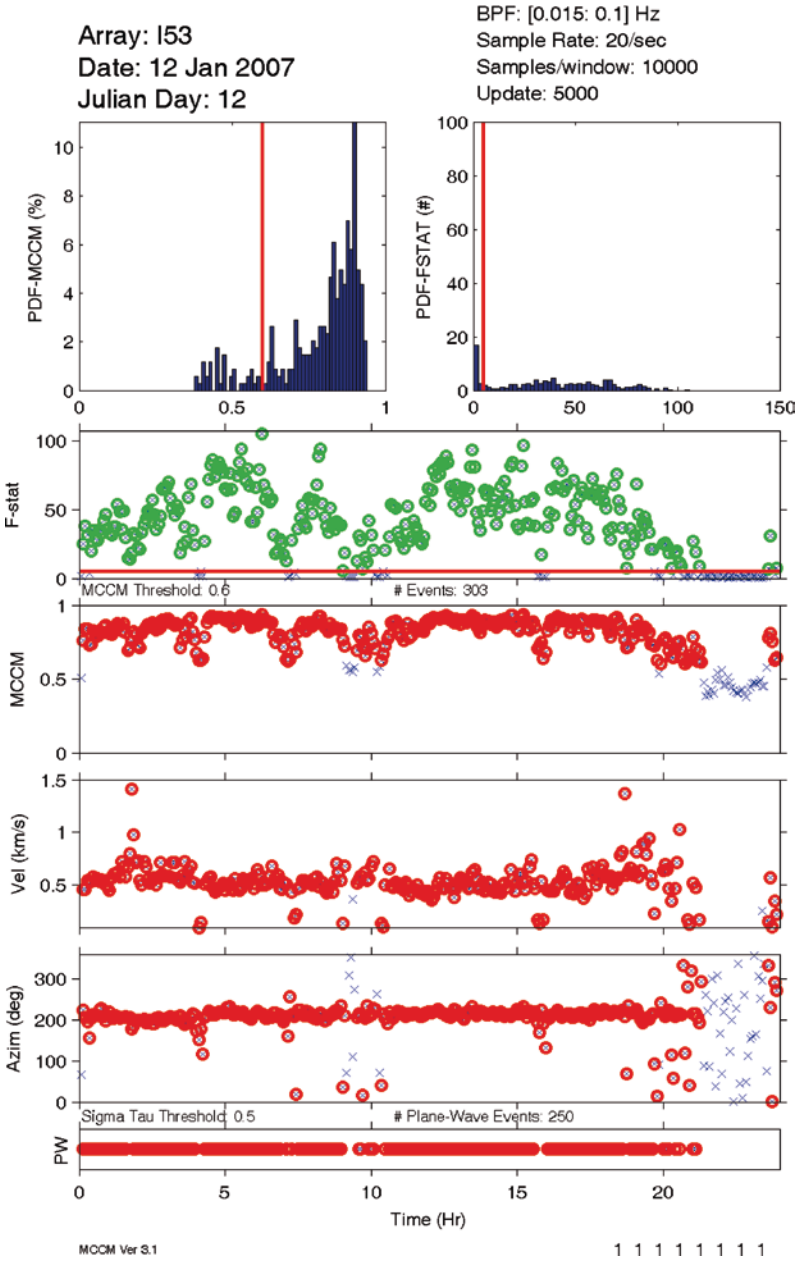

Fig. 13.1 Mean cross-correlation maximum (MCCM) detector plot for a typical mountain associated waves (MAW) event January 12, 2007, recorded at the I53US array

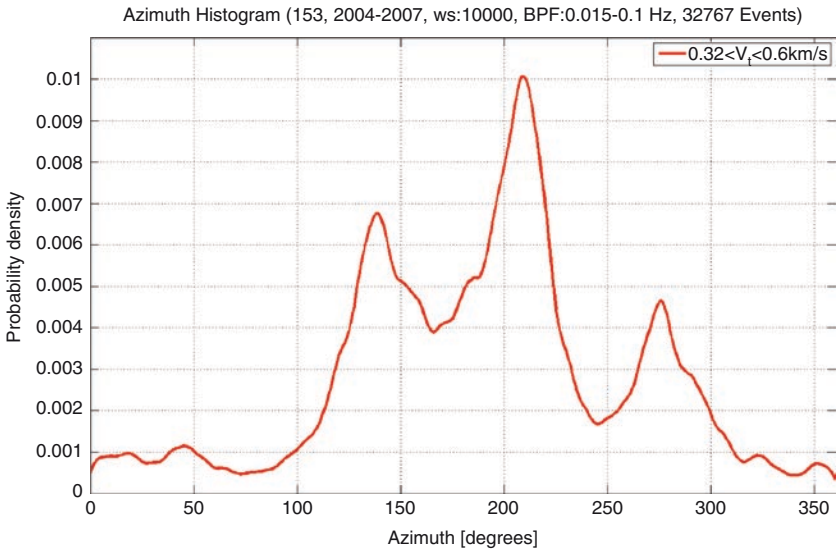

Fig. 13.2 I53US MAW signals as a function of azimuth for the period 2004 through 2007

up to several days, (3) a total lack of diurnal variation of frequency of occurrence, (4) a strong tendency to be observed only during winter months, and (5) a fixed azimuth of arrival from definite direction bands. The three principal direction bands for MAW at Fairbanks are Band-1 110° to 150°azimuth (St. Elias Range), Band-2 170° to 230°(Alaska and Aleutian Ranges), and Band-3 275° to 300°(Seward and Chukotsk peninsulas). A histogram of the azimuthal distribution of MAW at I53US is given in Fig. 13.2. Although there are mountain ranges located at virtually every direction, as seen from Fairbanks, it is principally within the three bands listed above that most of the MAWs are observed at I53US.

A sampling of individual MAW events at I53US is displayed in Fig. 13.3 from 2005, 2006, and 2007 in plots of azimuth of arrival vs. trace-velocity. Each data point in the plot represents the estimate from successive data windows from the MCCM analysis. For a single stationary source, there is an intrinsic scattering of the data points associated with the MCCM analysis process that depends on the I53US array geometry and also on the three input parameters: trace velocity, azimuth, and σ_τ. For the December 30, 2006 MAW event, shown in blue in Fig. 13.3, the mean value of azimuth was 140° with standard deviation of 18°. The mean trace-velocity (v_t) was 0.42 km/s with standard deviation 0.08 km/s. The uncertainty in the trace-velocity estimate becomes very large as v_t increases. For more distant sources of MAW, the scattering in the points becomes larger in Fig. 13.3 due to multiple propagation path effects.

At I53US, there have been dozens of MAW events observed during the Northern Hemisphere winter months. A few of the MAW events have been selected in Table 13.1 for illustration as typical of what occurs at Fairbanks, Alaska. Table 13.1

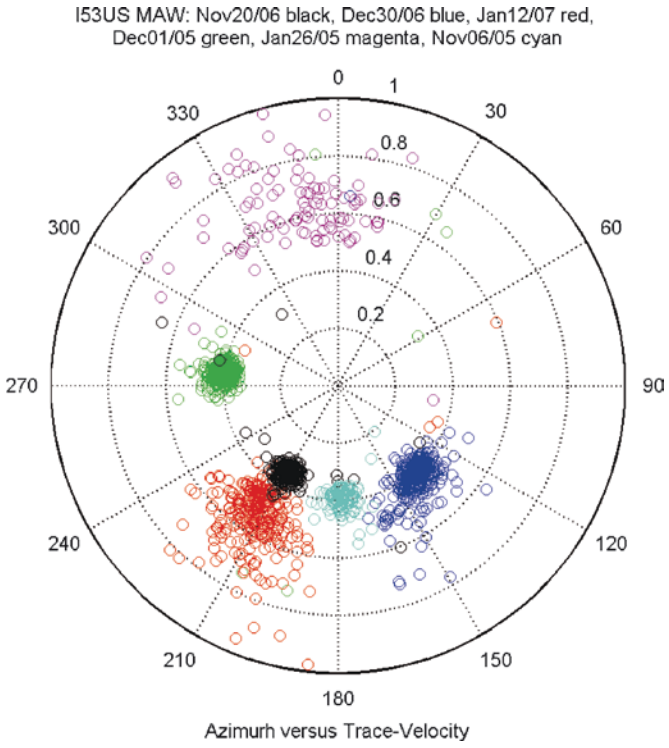

Fig. 13.3 Azimuth vs. trace-velocity plots for six individual MAW events at I53US from 2005 to 2007

Table 13.1 Parameters for MAW events at I53US from 2005 to 2007

	UT		Degrees		km/s		
Date	Start time	End time	Median Azimuth	Std (A)	Mean Vt	Std (Vt)	MCCM
12/01/05	0:00	10:00	276	11	0.422	0.056	0.925
11/06/05	0:00	10:00	178	7.8	0.41	0.155	0.847
11/20/06	11:00	20:00	210	7	0.319	0.089	0.832
12/30/06	0:00	24:00:	138	5.8	0.415	0.059	0.908
01/12/07	0:00	20:00	213	16	0.526	0.072	0.849

lists the MAW signal parameters of azimuth, trace-velocity, and mean coherence for five of the MAW events that are displayed in Fig. 13.3 as color-coded plots of azimuth vs. trace velocity. The intervals of time included in the plots are given to the nearest hour of UT time in the table. Each point in the plots represents the estimates of azimuth and trace-velocity from successive sliding data windows of length 10,000 points, or 500 s of time. The best beams are shown in Fig. 13.4 below for

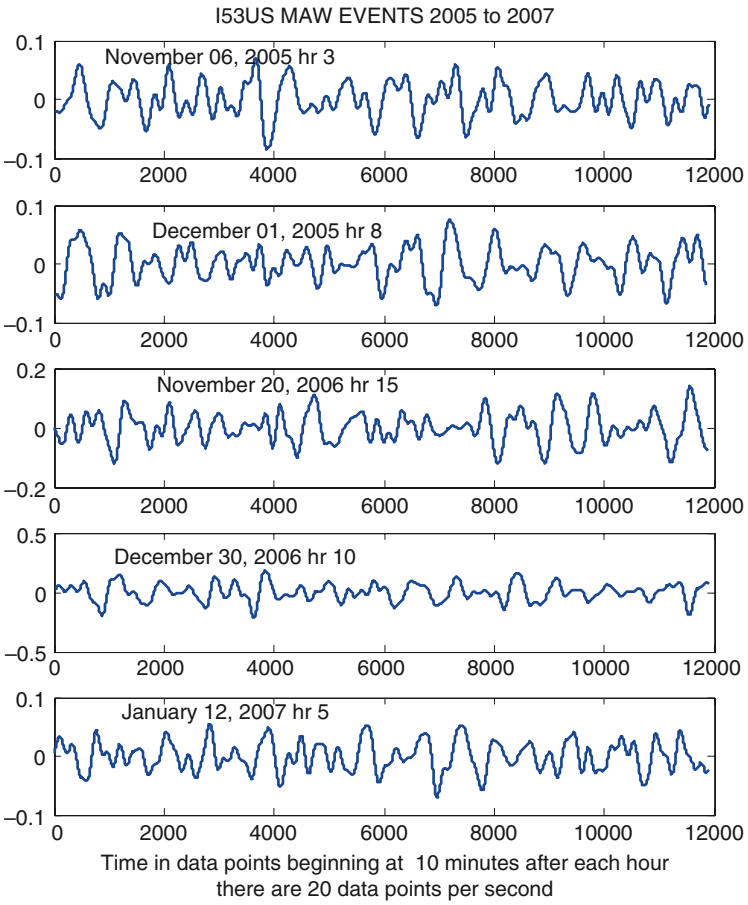

Fig. 13.4 Five MAW examples best beam pressure waveforms for 10 min of time as observed at I53US. The vertical scale in all five panels above is in Pascal

the waveforms of microphone pressure vs. time for each of the five MAW events that are listed in Table 13.1 below. The best beam time series represents the phase-aligned average for all eight microphone waveforms. For example, the best beam in the bottom plot of Fig. 13.4 for the January 12 MAW event is essentially the same as the phase-aligned waveform of all eight microphone traces shown in the bottom panel of Fig. 13.5. The various MAW waveforms shown in Fig. 13.4 exhibit the irregular nature of the pressure time series that is characteristic of all MAW event signals. In spite of the irregular waveform of MAW signals, all eight microphones have virtually the identical waveform that results in an average coherence of 0.872 for the five events listed in Table 13.1.

Mount McKinley in the Alaska Range stands alone, rising 5,800 m above the surrounding plain to a height of 6,190 m. The mountain is roughly 250 km from

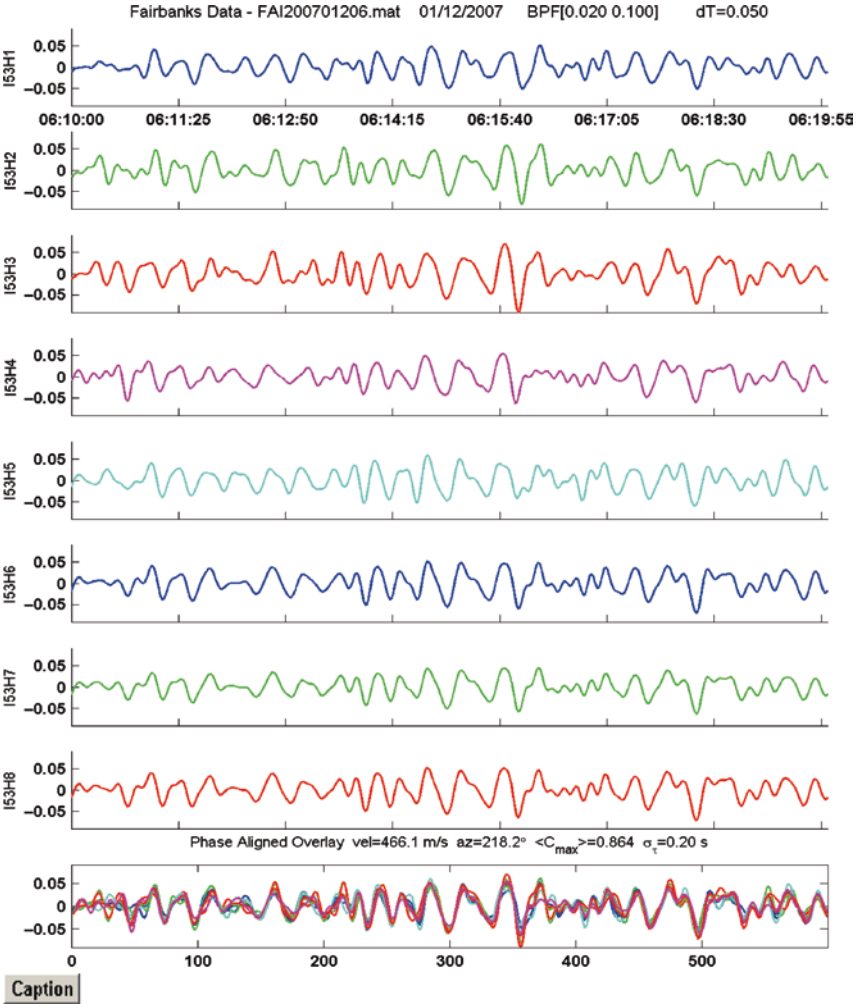

Fig. 13.5 Plot of the January 12, 2007 MAW signal from Mt McKinley showing the same irregular wave form at all eight sensors: I53H1 through I53H8. The best beam superposition of all eight waveforms is shown in the bottom panel. The azimuth is 218°, trace-velocity 0.466 km/s, and coherence 0.864

I53US at an azimuth of 219°. During the winter, McKinley is a frequent source of MAW observed at I53US. Two MAW events from McKinley are shown in Fig. 13.3 in black circles for November 20, 2006 and in red circles for January 12, 2007.

The MCCM detector plot of F-Statistic, MCCM, trace-velocity, azimuth, and sigma-tau for day 12/07 is shown in Fig. 13.1. A continuous plot, from 00:00 to 20:00 UT, of the five MAW signal parameters can be seen in Fig. 13.1 with an

azimuth of 213°, a trace velocity of 0.526 km/s, a mean MCCM value of coherence of 0.849 and a σ_τ of 0.21 s.

In Fig. 13.5 the I53US microphone pressure time series are given for the January 12, 2007 MAW event for the time period 06:10–06:20 UT. The maximum peak-to-peak amplitude of the wave train is about 0.10 Pa in the frequency pass band from 0.02 to 0.10 Hz. The irregular waveform of the MAW signal that can be seen in Fig. 13.5 is basically the same at all eight microphones. This characteristic of irregular waveform is an important distinguishing feature of all MAW infrasonic events. The MCCM value for this signal was 0.864 that is typical of MAW events, whereas Volcanic eruption signals and Mine excavation signals frequently have coherence values of 0.95 or higher.

The McKinley MAW event on November 20, 2006, as shown in black in Fig. 13.3, continued for several days at I53US.This MAW event began on the November 16 and lasted through the 22nd, as can be seen in Fig. 13.6 in a plot of azimuth vs. time. In Fig. 13.6 time is expressed in terms of the data window number from 1 to 2,419, spanning the 7 days of data. The persistent azimuth of about 210° for the McKinley MAW in November 2006 is most prominent in Fig. 13.6 from 0 to 345 points for November 16; from 1,250 to 1,750 points for November 19–20; and 2,000 to 2,419 for November 21–22. Changing propagation conditions and time fluctuations in the MAW source can account for the sporadic behavior of the Mount McKinley MAW signals shown in Fig. 13.6.

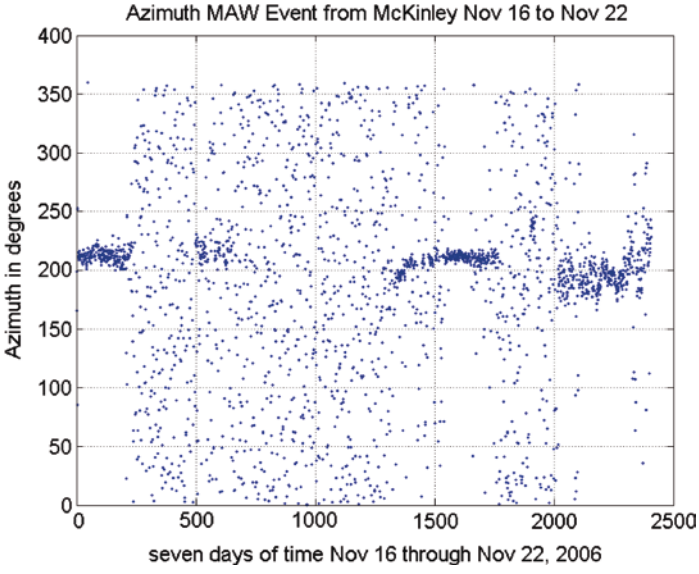

Fig. 13.6 Azimuth vs. time plot for a persistent Mount McKinley MAW event from an azimuth of 216° from November 16–22, 2006 at I53US.The drop-out of the MAW signal may be due to either changing propagation conditions and/or source fluctuations with time

Verification of McKinley as the source of MAW events observed at I53US can be established by ray-tracing simulations. This method makes use of a model atmospheric profile of sound velocity and along-track winds. The Naval Research Laboratory (NRL) Ground to Space (G2S) Model (Drob et al. 2003; Drob 2004) was used to provide range-dependent atmospheric profiles of static sound speed and wind speed along the great circle path from McKinley to I53US for the ray trace simulations. A comprehensive range-dependent calculation for the January 12, 2007 I53US MAW signal was then preformed with the NRL RAM-PE/2 DC code. These range-dependent codes utilize entire data matrix of sound speed and wind speed from the G2S atmospheric model from McKinley to I53US. The eigenrays were estimated by the RAM-PE/2 DC code. The eigenrays in Fig. 13.7 are superimposed on a color plot of the acoustic wave energy from the RAM-PE analysis. The color bar defines the acoustic wave energy loss in dB. The rays propagating into region of greater than 100 dB loss, as indicated by the PE code, were not considered in this calculation. The PE full wave calculations results are shown in color in Fig. 13.7 for the

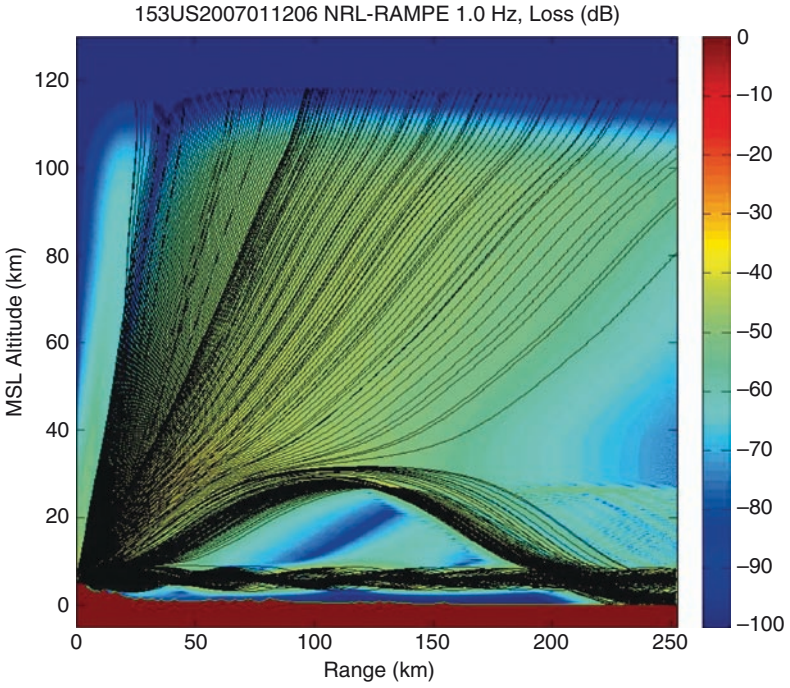

Fig. 13.7 Ray tracing plot for MAW signals from Mount McKinley at 0 km at left edge of plot to the location of I53US at 250 km at right edge of plot. The plot was done using atmospheric data for hour 06 UT on January 12, 2007. The color plot represents acoustic wave energy loss in dB per kilometer of propagation of the infrasonic waves at a frequency of 1.0 Hz

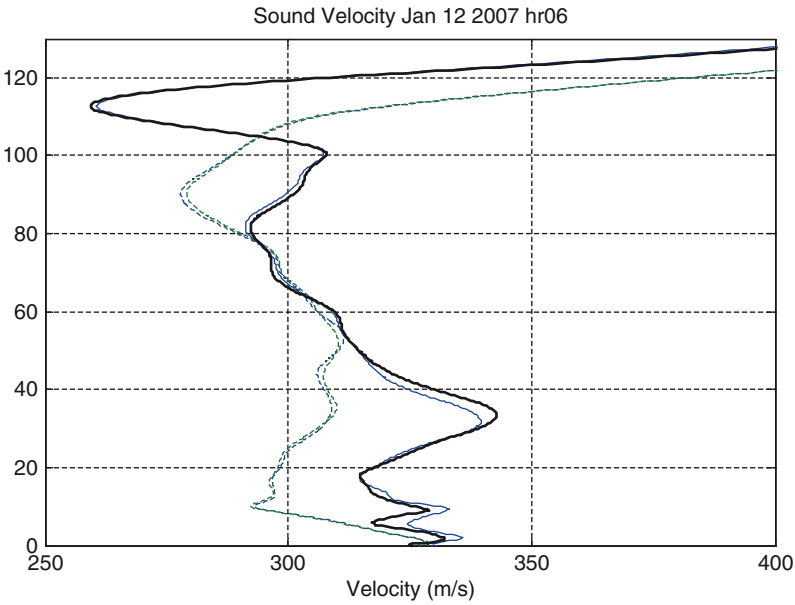

Fig. 13.8 Sound velocity vs. height averaged along track from Mt. McKinley to I53US. Vertical scale is in km

I53US MAW signals. In Fig. 13.7, the eigenrays from the RAM-PE/2 DC calculations are shown in black starting from the location of McKinley at 0 km on the left of the plot, at an elevation 6.2 km, to I53US at 250 km on the right of the plot at the surface. The ducting of most of the MAW acoustic energy into the stratospheric sound channel can be seen clearly within the altitude region from 0 to 30 km.

The altitude profiles of sound velocity and static sound speed, as averaged along the 250 km path, used in the ray tracing simulations of Figs. 13.7 and 13.4 are shown in Figs. 13.8 and 13.9, respectively. There is a troposphere sound duct at an elevation from about 5 to 10 km due to the strong wind speed of 35 m/s in the direction of propagation along the path from McKinley to I53US. This along-track wind speed duct can be seen clearly in Fig. 13.9 at an elevation of about 10 km. The ray tracing simulation depicted in Fig. 13.7 does not show any wave propagation down to the surface of MAW signals from this troposphere sound duct.

In the winter at I53US examples of MAW events have been observed wherein the azimuth of the MAW signals received changes systematically with time in an eastward direction as the winter storms that generate the mountain associated turbulence seem to drift eastward across the interior Alaska Range of mountains and then down across the Alaska Costal mountains. An eastward drifting MAW event

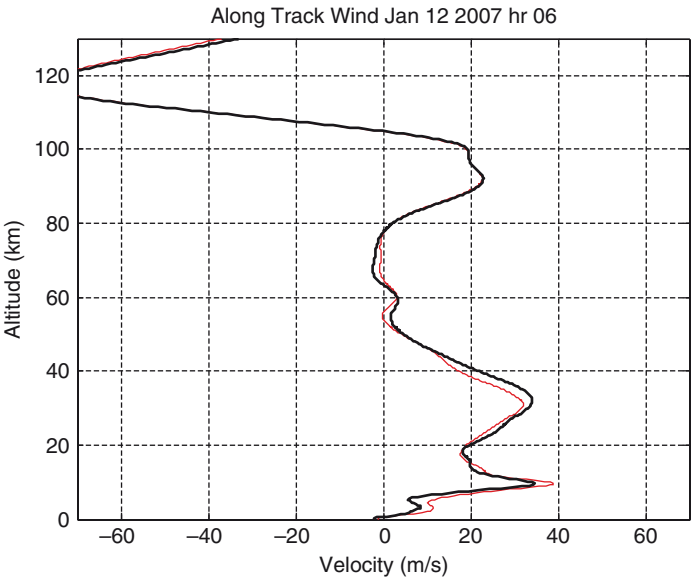

Fig. 13.9 Along-track wind component as a function of height at 06 h on January 12, 2007 as averaged from McKinley to I53US along the propagation path. Vertical scale is in km

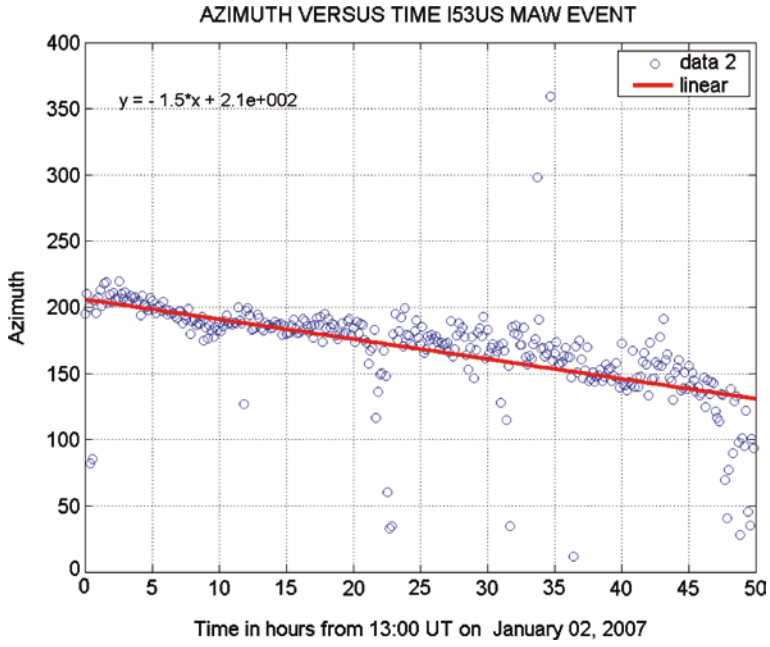

Fig. 13.10 Azimuth vs. time I53US MAW event on January 2–4, 2007. The eastward drift of the azimuth of the source from 210 to 150° can be seen in this plot

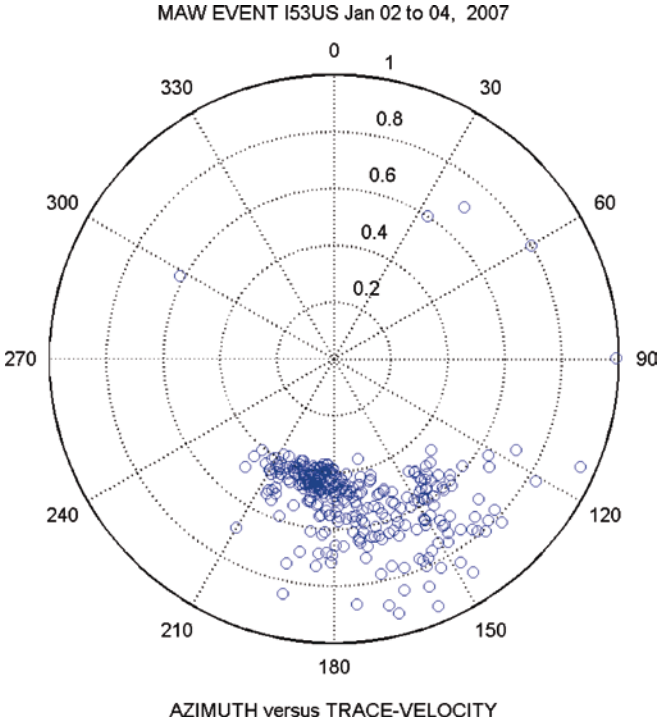

Fig. 13.11 Azimuth vs. trace-velocity MAW event on January 2–4, 2007

from I53US is shown in Fig. 13.10 as a plot of azimuth of MAW wave packets vs. time beginning at 13:00 on January 2, 2007 and lasting for 50 h. The azimuth drifted eastward from 210° to 150° at a rate of about 1.5° per hour. The different character of this January 2, 2007 MAW event, as opposed to the more or less stationary source events depicted in Fig. 13.3, can be clearly seen in Fig. 13.11 in the Azimuth vs. trace-velocity plot. The larger scattering in trace-velocity for data points with azimuths from 170 to 135° toward the end of the MAW event on January 4 is consistent with the greater distance from I53US of the Alaska Costal range as compared to the Alaska Range of mountains of interior Alaska at azimuths from 170 to 210°.

There is a very strong seasonal variation observed in the occurrence of MAW events at I53US in Alaska. During many years of infrasonic observations at Fairbanks, MAW have been found to occur only during the boreal winter. This seasonal characteristic of MAW at I53US is clearly evident from the data displayed in Fig. 13.12.

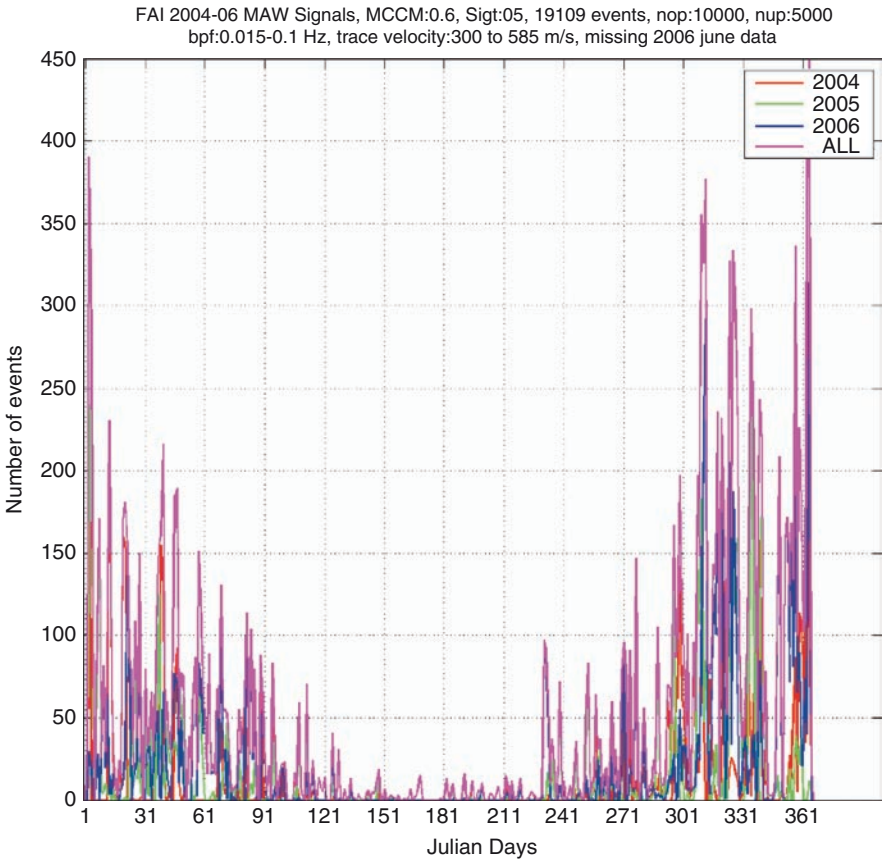

Fig. 13.12 Seasonal variation of MAW signals at I53US for 2004 through 2006. The number of MAW signals as a function of Julian Day for 2004 (*orange*), 2005 (*green*), 2006 (*blue*), and all 3 years together (*purple*) is depicted. The pressure data were band pass filtered from 0.015 to 0.10 Hz and then trace-velocity selected for V_t [0.3, 0.585] km/s. Each MAW signal was of length 10,000 data points and of duration 500 s

13.2.2 MAW at I55US in Windless Bight, Antarctica

At I55US in Windless Bight, Antarctica, there are fewer MAW events observed during any 1 year than in Alaska at I53US. In Antarctica there are high mountain regions in almost all directions as seen from the array. The Trans Antarctic Range extends all across Antarctica from the Shackleton Range to the south all the way to the mountains of the Borchgrevink Coast to the north. Just to the west of I55US, the Royal Society Range is a known source of MAW events. Overall, the principal sources of MAW events observed at I55US are located northward of I55US. There is a possible distant MAW source in the Mount Cook alpine region on the South Island of New Zealand (azimuth 3.3°). Also, in the same general northerly direction, there is a probable MAW source in the Antarctic mountainous region of Victoria

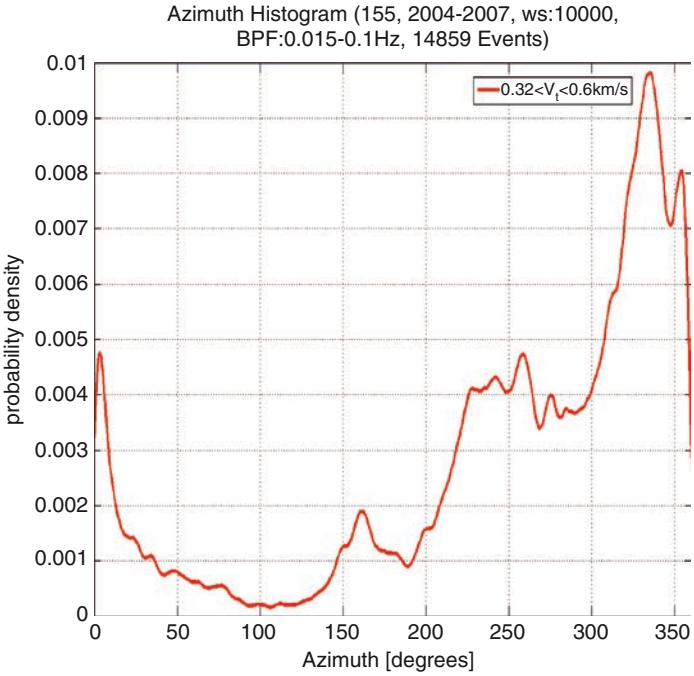

Fig. 13.13 Probability density of observing MAW as a function of azimuth at I55US in Windless Bight, Antarctica

Land along the Borchgrevink Coast. These particular Antarctic mountains subtend an azimuth range from 350 to 10°. With observations from only one infrasonic array at I55US, it is not possible to resolve the ambiguity in the location of possible sources of MAW received from the northerly direction. In New Zealand there are frequently very strong winds from the Tasman Sea blowing across the high Southern Alps Range that could certainly produce the turbulence responsible for the generation of MAW. Although this source in New Zealand is several thousand kilometers away, it could produce strong MAW signals of high coherence at I55US. It is not uncommon to observe MAW events at infrasonic arrays around the world that are at such great distances from their sources.

In Fig. 13.13 a plot is given of the probability density of observing MAW as a function of azimuth at I55US. The azimuth of the highest probability of observing MAW at I55US is about 330° in the direction of Mt Melbourne (elevation 3,600 m) in the Borchgrevink Mountains of Victoria Land. The next most often observed MAW source at I55US is the Royal Society Range, located across McMurdo Sound from Windless Bight, subtending an azimuth range from 230 to 300°. Mount Lister, at an azimuth of 249°, with a height of 4,025 m is the highest peak in these mountains and appears to be a strong nearby source of MAW at I55US. The Queen Maud Mountains at an azimuth of 165° has peaks with heights up to 4,100 m and is probably the MAW source seen at 165° in the plot in Fig. 13.13. The peak in the plot at the far left in Fig. 13.13 with an azimuth of about 5° could represent MAW either from New Zealand or Mt. Admiralty in the Borchgrevink Mountains in Victoria Land.

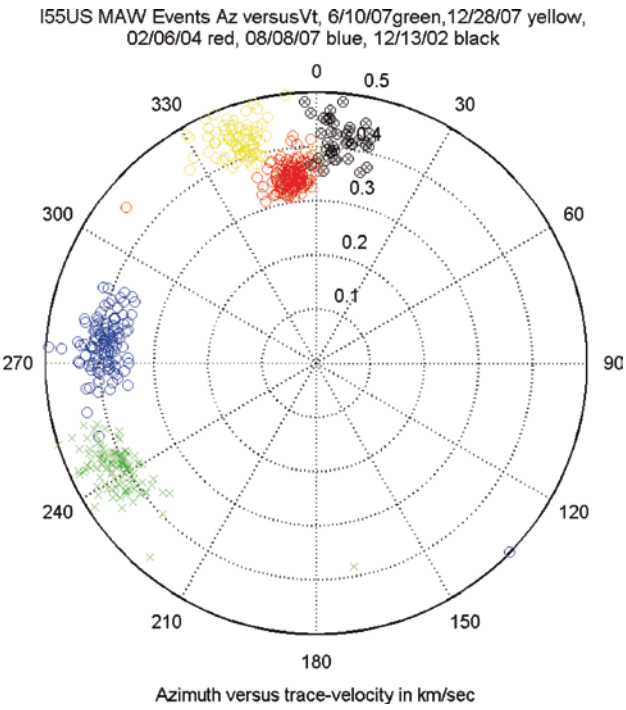

Fig. 13.14 Azimuth vs. trace-velocity for five MAW events at I55US from 2002 to 2007. The radial scale of trace-velocity is in km/s

In Fig. 13.14 a polar plot is given for MAW events at I55US of azimuth vs. trace-velocity for seven events from 2002 to 2007. Each data point represents the estimate of azimuth and trace-velocity, from an analysis window of 10,000 points of pressure data, for each successive sliding data window throughout the MAW event. The pressure data for the MAW analysis were band pass filtered from 0.02 to 0.10 Hz. The MAW signals in Antarctica have smaller amplitude and lower cross correlation values than those at I53US. Initially no MAW events were ever detected in the data at I55US until after we began to pure-state (Olson 1982) and band pass filter the pressure data before the detector analysis was applied.

In Fig. 13.14 the MAW signals shown in black for December 13, 2002 at an azimuth of about 5.7° are either from New Zealand or Mt. Admiralty in the Borchgrevink Mountains of Victoria Land. The two MAW signal groups shown in red at an azimuth of about 352° on February 6, 2004 and those shown in yellow at an azimuth of about 341° on December 28, 2007 are probably both from the Royal Society Range near Mt Melbourne. The MAW signals shown in green from the southwest west at an azimuth of about 243° on October 6, 2007 are from the direction of Mt. Lister. The signals shown in blue from the west from 260 to 280° are from the Royal Society Range across McMurdo Sound from I55US. The signal parameters for the MAW events shown in Fig. 13.14 are given in Table 13.2 below.

Table 13.2 Parameters for MAW events in Antarctica at I55US 2002–2007

Date	UT Start time	UT End time	Degrees Median A	Degrees Std (A)	km/s Mean V_t	km/s Std (V_t)	MCCM
12/13/02	3:00	7:00	5.7	_	0.435	0.029	0.898
09/08/03	5:00	15:00	275	14.9	0.395	0.027	0.85
02/06/04	0:00	0:00	352	29	0.348	0.023	0.833
01/00/00	9:00	22:00	243	8.7	0.416	0.027	0.714
12/28/07	0:00	6:00	341	5	0.435	0.029	0.859

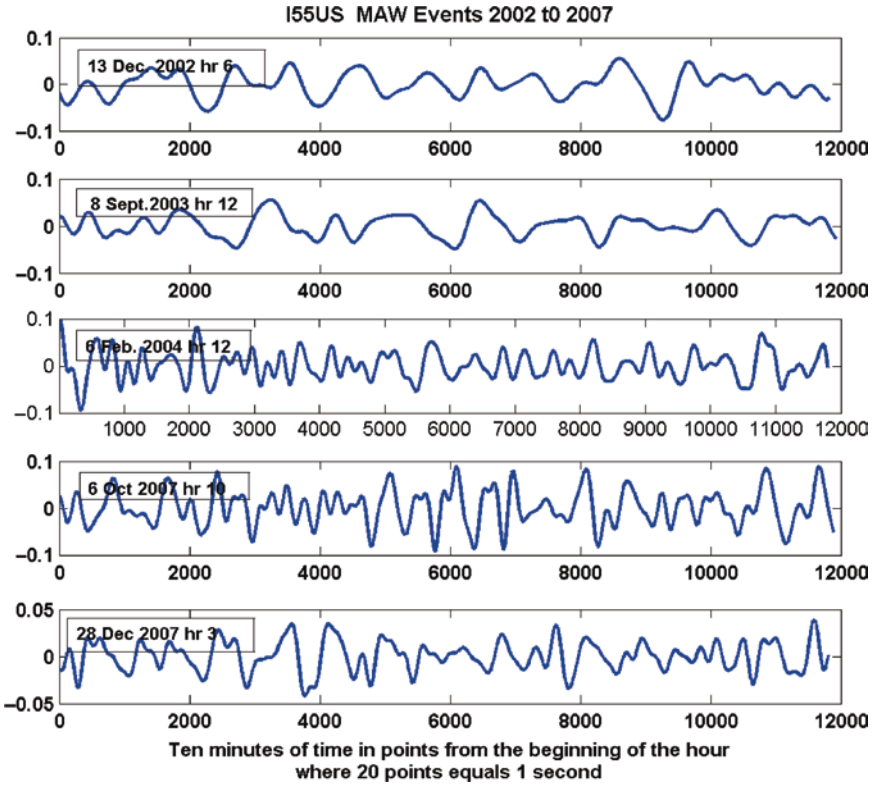

Fig. 13.15 MAW events at I55US best beam waveforms for 10 min of time. Vertical units are in Pa

The best beam waveforms for the MAW events at I55US shown in Fig. 13.14 are plotted in Fig. 13.15. The waveform plots are for 10 min of pressure data beginning at 10 min after the start time for the signals listed in column two of Table 13.2. The pressure scale ordinate is in Pa and the time scale is in samples. The amplitude of the MAW signals varies from a minimum of ±0.05 Pa for the December 28, 2007 event to a maximum of ±0.1 Pa for the other four events in the top four panels of Fig. 13.15. The spectral characteristics of the MAW signals shown in the bottom three panels of Fig. 13.15 clearly differ from those of the top two panel events.

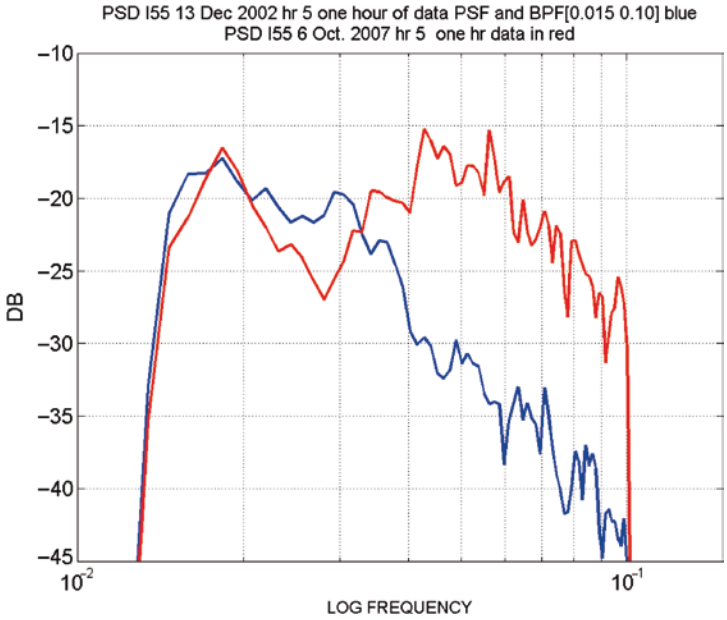

Fig. 13.16 Power spectra of the MAW signals are shown in blue for the December 13, 2002 event and in *red* for the October 6, 2007. The pressure data were band pass filtered from 0.015 to 0.10 Hz and pure state filtered. One hour of data of 72,000 samples was used in determining the spectra

The higher frequency MAW signals are probably from sources closer to I55US in the Trans Antarctic and Royal Society mountain ranges. This difference in the frequency content of the MAW signals is shown in Fig. 13.16. The same effect is observed in Alaska at I53US where Mt. McKinley, at a distance of only 250 km from I53US, produces higher frequency MAW signals than those from sources that are farther away.

An example of MAW from December 13, 2002 observed in Windless Bight at I55US is shown in Fig. 13.17. The figure is formatted as per Fig. 13.1. This event was observed for about 10 h with maximum peak-to-peak amplitude of about 0.16 Pascal with an average coherence $C=0.890$. The periods of the waves with maximum energy are: 53, 31 and 28 s. The duration of the MAW event is shown clearly in the day-long period covered by the figure. Thus, from about 07 to 09 UT, the value of MCCM is highest at about 0.90, the azimuth trace has a constant value at 5° and the trace velocity averages about 0.435 km/s. A 12-min sliding window, for the period 05 to 06 UT was used to determine the average parameters for this MAW event as follows: $C=0.898$, $V=0.44$ km/s (±0.04 km/s), and $Az=6°$ (±3°). The azimuth vs. trace-velocity plot for this December 13 MAW event is shown in Fig. 13.14 as the black data points.

The second example of a MAW event at I55US is shown in Fig. 13.18 as the detector plot for September 2003. Plane waves are detected, as indicated by the bottom panel, from about 05 to 16 UT. The plots of trace-velocity and azimuth in Fig. 13.18 show consistent values of trace-velocity of 0.395 km/s and azimuth of 275°, respectively.

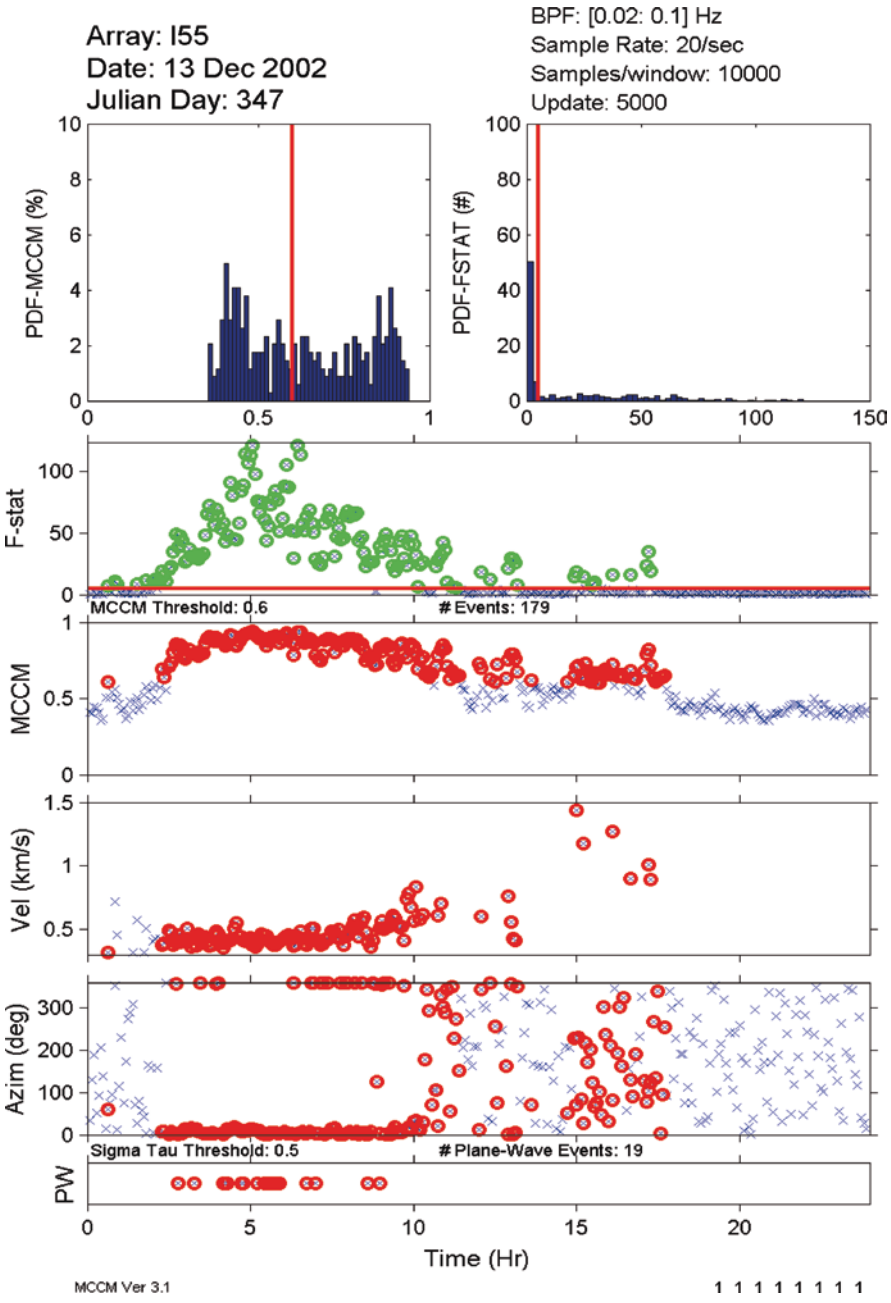

Fig. 13.17 Detector plot for MAW event at I55US for December 13, 2002. The constant azimuth and trace-velocity plots from 7 to 10 h and the high MCCM and F-Stat values in this interval show the presence of MAW waves that are from north of I55US

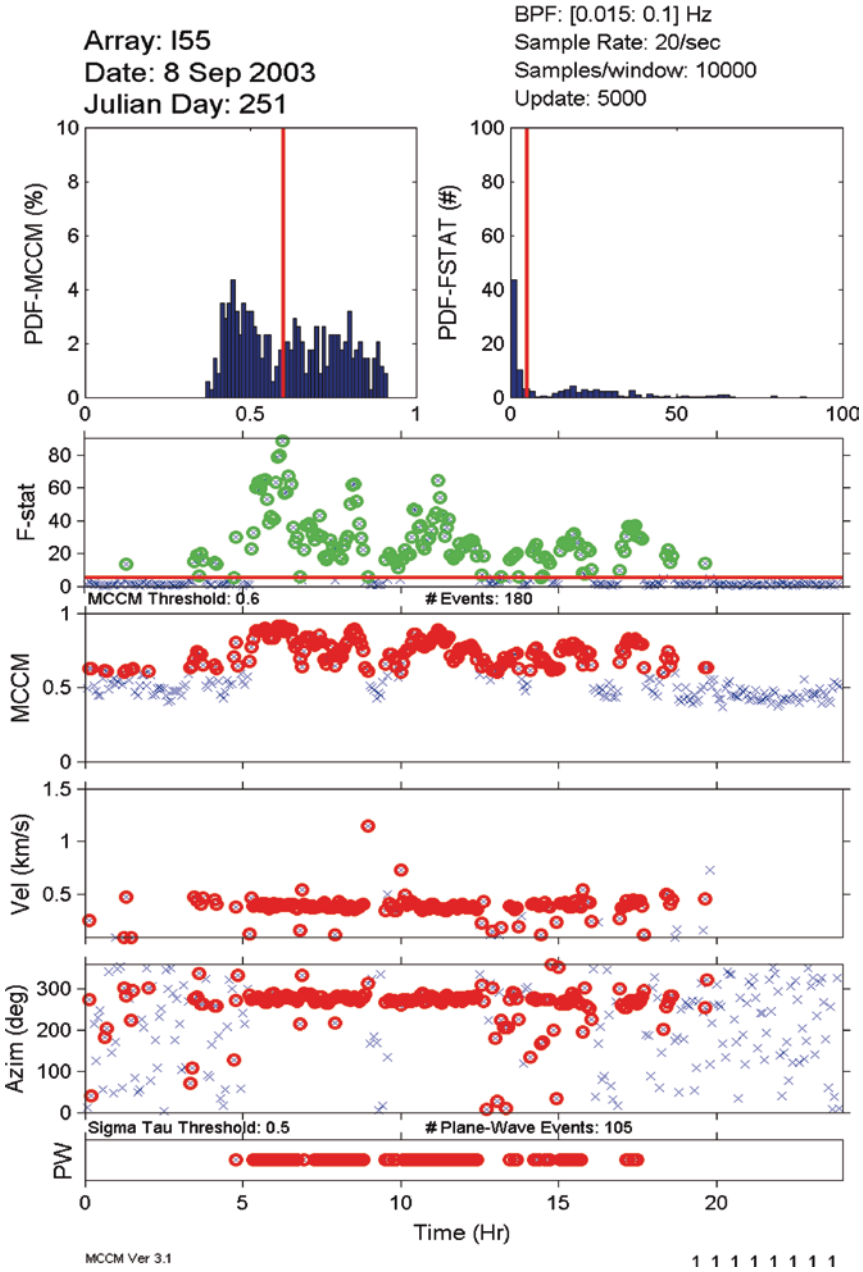

Fig. 13.18 Detector plot for MAW event at I55US for September 8, 2003. The constant azimuth and trace-velocity plots from 5 to 16 h and the high MCCM and F-Stat values in this interval indicate the presence of plane-wave MAW signals from an azimuth 275°.

This event from the west at 275° is shown in Fig. 13.14 as the blue data points of azimuth vs. trace velocity.

13.3 Auroral Infrasound Waves

13.3.1 AIW Bow Waves from Auroral Electrojet Motions

At infrasonic arrays in Alaska, at Inuvik NWT, Canada, and at Kiruna in Sweden, many impulsive, large amplitude, auroral infrasound signals have been found to be related to specific auroral arcs in the auroral displays overhead. These signals have been identified as acoustic bow-waves that are generated by the supersonic motion of auroral arcs that contain strong electrojet currents as they move in the neutral atmosphere, (Wilson 1969a). These Auroral Infrasonic bow-Waves were named AIW. AIW infrasound signals are highly anisotropic, propagating as a bow-wave moving in the same direction as that of the auroral arc motion. The AIW trace velocity across the microphone array is the same as lateral velocity of the supersonic auroral arc. Because of the anisotropic nature of the propagation of infrasonic bow-waves, it is not possible to triangulate on the auroral AIW source region by the use of data from two highly separated infrasonic arrays sites where the same AIW signals are observed.

In 2002 when the I53US array was established in Fairbanks, a new and different type of high trace-velocity auroral infrasound signal episode was discovered. These new high trace-velocity auroral signals were named GAIW (for Geomagnetic substorm Associated Infrasonic Waves) because they appear to be associated with geomagnetic activity. The characteristics and morphology of both the AIW and the GAIW infrasound events are described below using examples from the I53US array.

An example of the wave-train of a very large AIW bow-wave that was observed at I53US on September 11, 2005 (day 254) at 08:47 UT is shown in Fig. 13.19. The pressure traces from all eight sensors at I53US have been phase-aligned and superimposed in Fig. 13.19 to show the high average coherence of 0.98 for the signal across the array. The observed AIW trace velocity and back-azimuth are 0.56 km/s and 46.7°, respectively. The peak-to peak amplitude of this AIW is about 0.9 Pascal. There was daylight at I53US at the time of the signal in Fig. 13.19, thus no aurora video data are available. The geomagnetic data from the Poker Flat magnetic observatory, 30 km north of I53US, show large fluctuations in the H and Z magnetic components that indicate the presence of strong auroral electrojet currents that could have been the source of this AIW.

The geomagnetic traces of the H, D, and Z components from Poker Flat observatory for September11, 2005 are shown in Fig. 13.20. Very large fluctuations can be seen in H (north-south), D (east-west), and Z (vertical) components that are typical of those associated with strong auroral electrojet currents during an auroral substorm. The presence of an auroral electrojet arc moving across the zenith at Poker

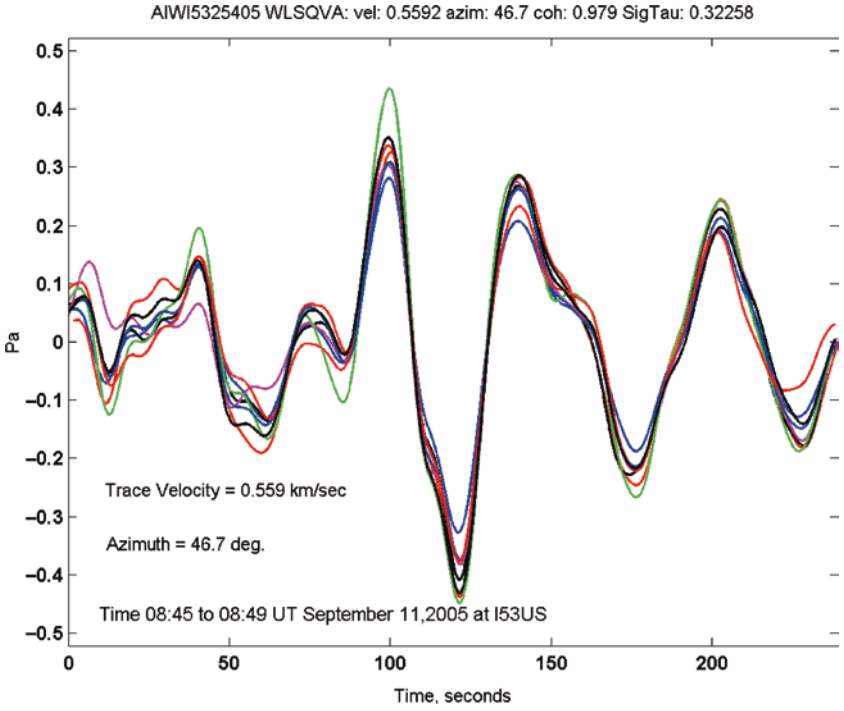

Fig. 13.19 AIW bow wave observed at the I53US infrasound array in Fairbanks, Alaska on September 11, 2005

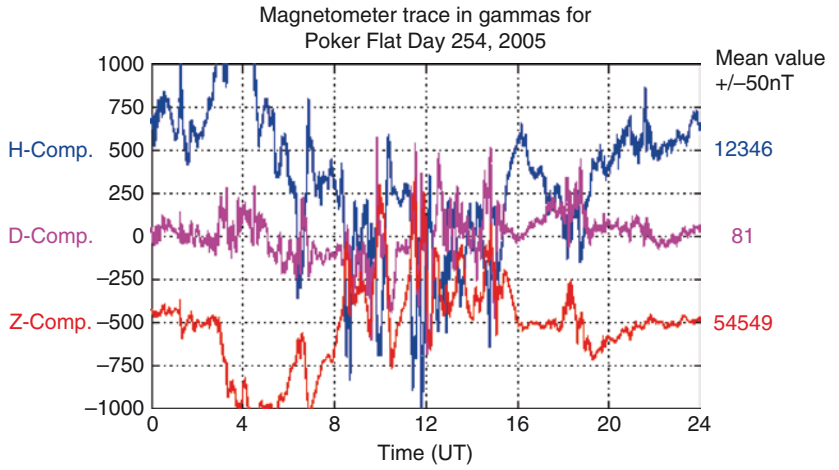

Fig. 13.20 Magnetometer traces recorded at Poker Flat, Alaska on September11, 2005. The entire day shows the presence of magnetic disturbances associated with magnetospheric substorms

Flat toward the I53US infrasonic array at Fairbanks can be inferred from an analysis of the magnetic data. For a westward flowing auroral electrojet current, as the arc moves laterally toward the magnetic observatory, the H component should show a southward change that becomes a maximum as the arc crosses the zenith. At zenith, crossing time the Z component should change from negative (upward) to positive (downward) values.

The magnetic data from Poker Flat for the interval 08:38–08:45 UT of Day 254 was detrended to enable the analyst to separate the permanent geomagnetic field from the magnetic induction resulting from the auroral line current. The Total Horizontal Disturbance vector (THD) was formed from the detrended H and D: $THD = \sqrt{(H^2 + D^2)}$. In Fig. 13.21 the THD vector and the detrended Z component are plotted to show that as THD becomes a maximum, the Z component changes from negative to positive. These changes are used to infer that the line current was moving from north to south, crossing the zenith at Poker Flat at about 08:41 UT.

The direction of the THD vector is perpendicular to the auroral line current axis and should, therefore, be parallel to the direction of the propagation of the bow-wave created by the supersonic motion of the auroral arc as is predicted by the simple AIW generation model (Wilson 1969b). Fig. 13.22 shows a plot of the time evolution of the THD vector for the interval between 08:38 and 08:45 UT. The black arrow gives the direction of the THD vector at the time of its maximum value. The red arrow gives the direction of propagation of the AIW signal as it

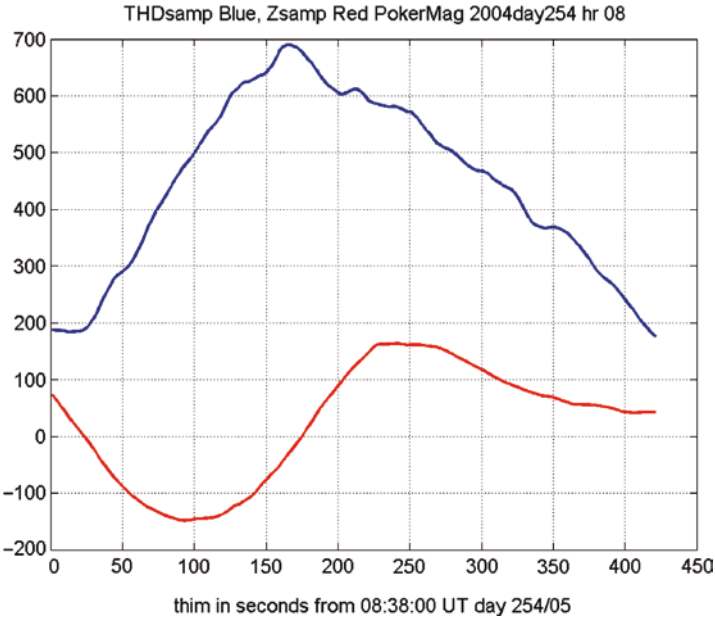

Fig. 13.21 The magnetic induction observed at Poker Flat, Alaska from 08:38 to 08:45 UT, THD in blue Z comp in *red*. Vertical scale in nT. These changes are consistent with the overhead passage of a westward electrojet near the time that the Z component changes sign

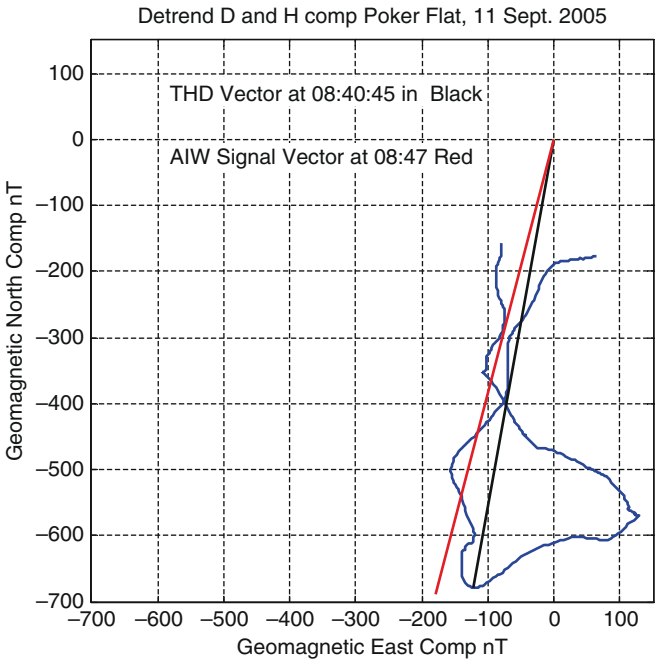

Fig. 13.22 The trajectory of the THD vector in the horizontal plane at Poker Flat, Alaska, on September 11, 2005 for the period 08:38 to 08:45 UT (*blue*). The *red arrow* shows the direction of propagation of the infrasound AIW and the *black arrow* shows the THD vector at 08:40 UT

crossed the I53US array at 08:47 UT. For this particular example of an AIW associated with an auroral electrojet source, there is excellent agreement between the directions of the THD vector at maxima and that of the AIW bow-wave propagation. The time of arrival of the AIW at I53US at 08:47 UT is consistent with the propagation time expected from an auroral arc at 110 km altitude that crosses the Poker Flat zenith at 08:41 UT.

It is also possible to determine the speed of the lateral motion of the line current from its magnetic field components variations with time. For a line current at a height h above the earth's surface, the speed of lateral motion is given by: $V = h\,(d/dt)(Z/THD)$ where Z is the vertical component of the magnetic field perturbation and THD is the total horizontal component. This determination of arc speed has been made for the AIW event on September 11, 2005. The results are shown in Fig. 13.23 as a plot of the ratio of the detrended Z component to the detrended THD component for the period 08:39:40–08:41:40 UT. A linear fit has been done to the blue data line resulting in the red line with a slope of 0.0046 (s^{-1}). Assuming a height of 110 km, a lateral motion speed of 0.506 km/s is obtained. The trace-velocity of the received AIW signal shown in Fig. 13.19 was found to be 0.559 km/s with an uncertainty of ±0.047 km/s. These two numbers agree well and support the basic assumptions of the source model. Many similar examples of AIW and their associated auroral line-current magnetic fluctuations have been found at I53US

since its operation began in 2002. Table 13.3 is given below of 15 examples of AIW signals observed at I53US from 2002 to 2005.

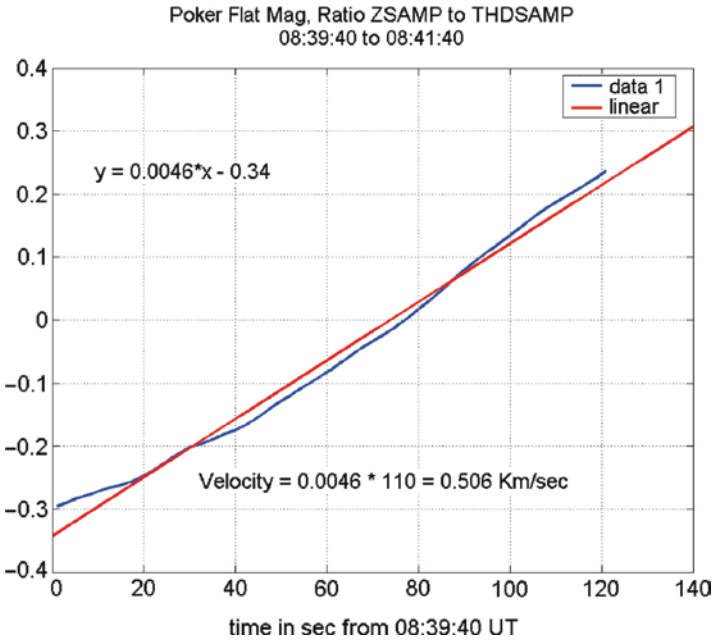

Fig. 13.23 Plot of the ratio of Z comp to THD comp for September 11 AIW

Table 13.3 AIW Bow Waves observed at I53US 2002 to 2005

Date	Time UT	p-t-p AmpPa	Trace Vel. Km/Sec	Azim	MCCM	Sig.T
12/19/02	11:14	0.54	0.578	344	0.984	0.18
2/2/03	15:12	0.45	0.623	344	0.934	0.16
3/6/03	16:54	0.7	1.611	310	0.973	0.3
3/8/03	13:50	0.4	0.767	16.5	0.925	0.62
3/17/03	14:58	0.65	1.44	358	0.929	0.9
4/14/03	15:50	0.6	0.603	263	0.949	0.21
8/18/03	18:09	1.64	1.21	303	0.91	0.7
8/18/03	15:21	0.85	0.793	31.7	0.968	0.44
2/11/04	14:23	0.75	0.595	339	0.989	0.16
2/11/04	14:07	0.6	0.561	304	0.837	0.38
7/25/04	16:09	0.75	0.534	353	0.957	0.15
7/27/04	15:14	0.5	0.715	323	0.949	0.38
7/27/04	16:28	0.65	0.809	350	0.988	0.25
8/30/04	16:14	0.65	0.84	341	0.988	0.2
3/14/05	5:52	0.45	0.715	91	0.934	0.24
Average Values		0.678Pa	0.826 km/sec		0.95	

13.3.2 High Trace-Velocity GAIW Infrasound Signals

Recently a new type of auroral infrasound signal has been identified at both I53US in Alaska and I55US in Antarctica that, when first described, often seemed to be associated with the pulsating auroras that occur during an auroral substorm's final hours (see for example, Akasofu 1968). However, after further research, using a larger database of aurora video tapes, these high trace-velocity I53US infrasonic signals were found to occur many times when there were no pulsating auroras visible. At the present time, the ongoing research at the Geophysical Institute of UAF indicates that long intervals of high trace-velocity infrasound at I53US are closely associated with periods of a specific type geomagnetic disturbance that is observed at the College International Geophysical Observatory (CIGO) and Poker Flat magnetic observatories in Fairbanks. This specific type of magnetic disturbance consists of large, simultaneous, geomagnetic fluctuations occurring in both the H and D magnetometer components. The amplitude of the H and D fluctuations about the local mean can be as large as 1,000 nT. The average period of these H and D fluctuations is approximately 10 min. This type of magnetic disturbance with accompanying high trace-velocity infrasound at I53US can last for several hours.

On April 14, 2003, there was a strong infrasonic event consisting of high trace-velocity signals at I53US that lasted from 12:00 to 16:00 UT. Simultaneously, magnetic disturbances were observed from 12:00 to 16:00 UT in Alaska at all seven of the magnetic observatories in the Alaskan Magnetometer Chain from Kaktovik in the north, located on the coast of the Arctic Ocean, to Gakona far to the south of Fairbanks. The H component traces for all seven magnetometer sites in the Alaska observatory chain for day 104 can be seen in Fig. 13.24. The sudden onset of the southward H component began at 12 UT and lasted for until 16 UT. During this time interval, high trace-velocity infrasonic signals were observed.

The infrasound detector plot from I53US for April 14, 2003 is shown in Fig. 13.25 to illustrate the simultaneous occurrence of high trace-velocity signals with the magnetic disturbance from 12 to 16 UT. The eight-channel infrasound data were band-pass filtered between 0.02 and 0.10 Hz and analyzed with a 10 min sliding window. At each window location, values of the F-statistic and mean correlation (MCCM) are computed and shown in the top two panels. At the same time, estimates of the signal trace-velocity and azimuth of arrival are computed and shown in the lower two panels. For intervals in which the detectors exceed pre-defined thresholds, the estimates of trace-velocity and azimuth are tagged with red circles. It can be seen that signals with significant detector values occur in the interval near 12–16 UT. During that interval, the trace-velocity of the signals is near 1 km/s with azimuths that decrease slightly across the interval. This variation of azimuth of arrival with time is consistent with the source area drifting westward with respect to the I53US array. The decrease in trace-velocity with time from 1.025 km/s at hour 12 to a lower value of 0.672 km/s in hour 15 is consistent with the source region being closer to the infrasonic array at hour 12 and farther away to the west in hour 15.

Examples of the infrasound waveforms observed during the interval between 12 and 16 UT are given in Fig. 13.26 as the best beam traces from the eight

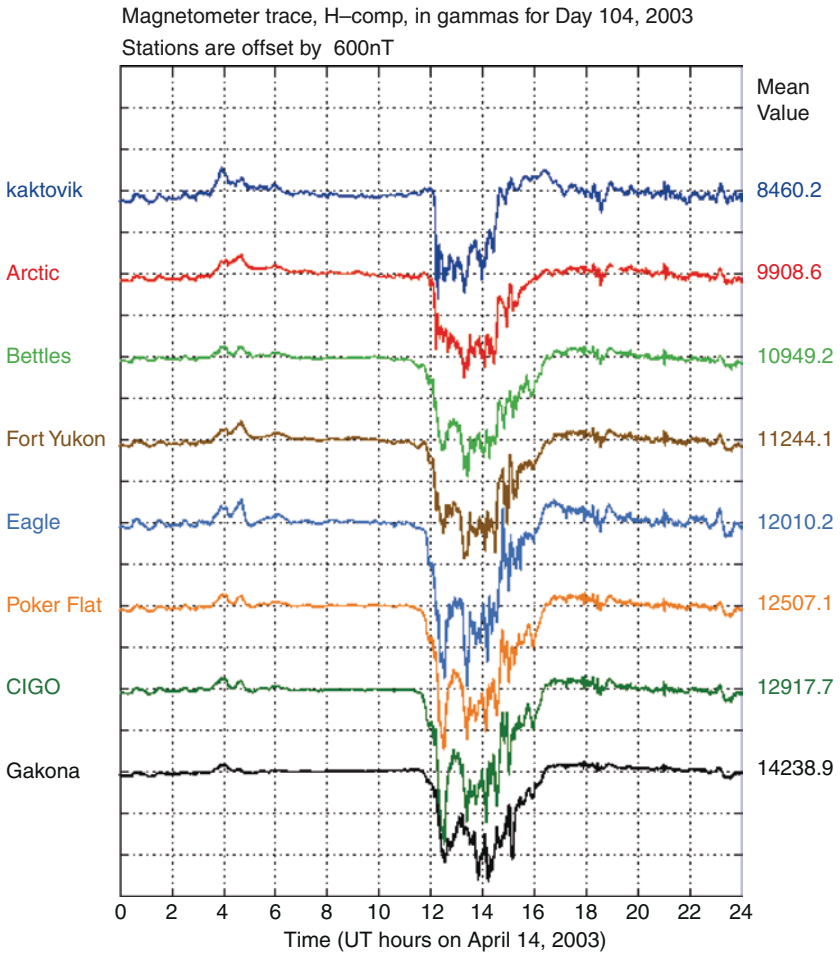

Fig. 13.24 Alaskan Magnetometer Chain H component traces for April 14, 2003. Note the sudden onset of activity near 12:00 UT that lasts for several hours. Analysis of the magnetometer data indicates that initially the center of the substorm electrojet lay just poleward of the CIGO site and subsequently began rapid north/south excursions

microphones of the I53US infrasound array. Each panel contains the data for 1 h between 12 and 16 UT. While coherent signals are present throughout each hour, as evidenced in Fig. 13.26, there are short intervals of time that exhibit large amplitude signals. For example, the wave packets at 15:46 UT (panel four) have peak-to-peak amplitudes of about 0.7 Pa. The source of the infrasound signals on April 14, 2003 was active throughout the 4-h interval of the magnetic disturbance in Alaska.

The type of continuous radiation of infrasound during a geomagnetic disturbance, such as on April 14, 2003, has been seen many times at I53US over the years of

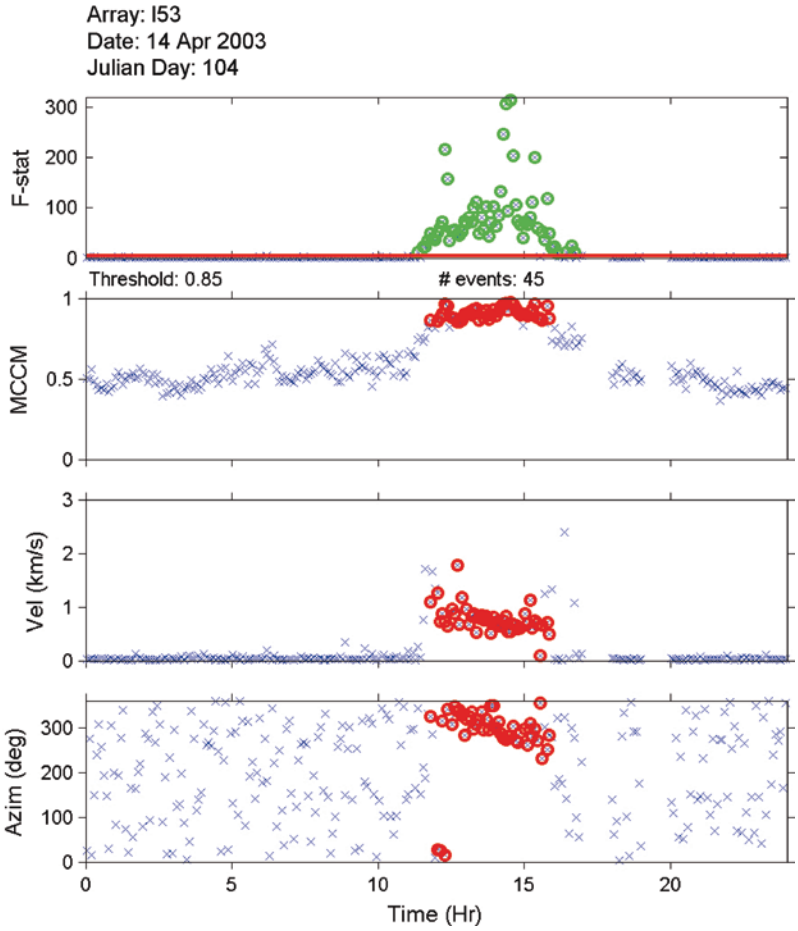

Fig. 13.25 Detector plot I53US April 14, 2003 for 24 h. The top two panels show the F-statistic and mean correlation (MCCM) values computed from a small window that slides across the 24 h of data. At the same time, values of the trace-velocity and azimuth of arrival are estimated. For times when the detector values rise above pre-defined thresholds, the estimates are tagged with *red circles*

operation of the Fairbanks infrasonic array. Formerly, if there was supersonic motion of an auroral electrojet arc observed on the video camera and a simultaneous typical magnetic signature of a moving line current was observed at the local magnetic observatory, then an associated AIW bow wave was usually observed at I53US. It now appears that for very large geomagnetic disturbances in Alaska, there is a source of infrasound from the upper atmosphere in the auroral regions that can produce almost continuous radiation of high trace-velocity wave packets. If this infrasound source is due to many successive bow-waves produced by a series of electrojet currents undergoing supersonic motion, then the direction of propagation of the received infrasound wave packets should be parallel to the total horizontal magnetic disturbance vector (THD). Thus, a useful tool for illustrating the relation of the THD and the azimuth of propagation of GAIW signals is a map of the locus of the end point

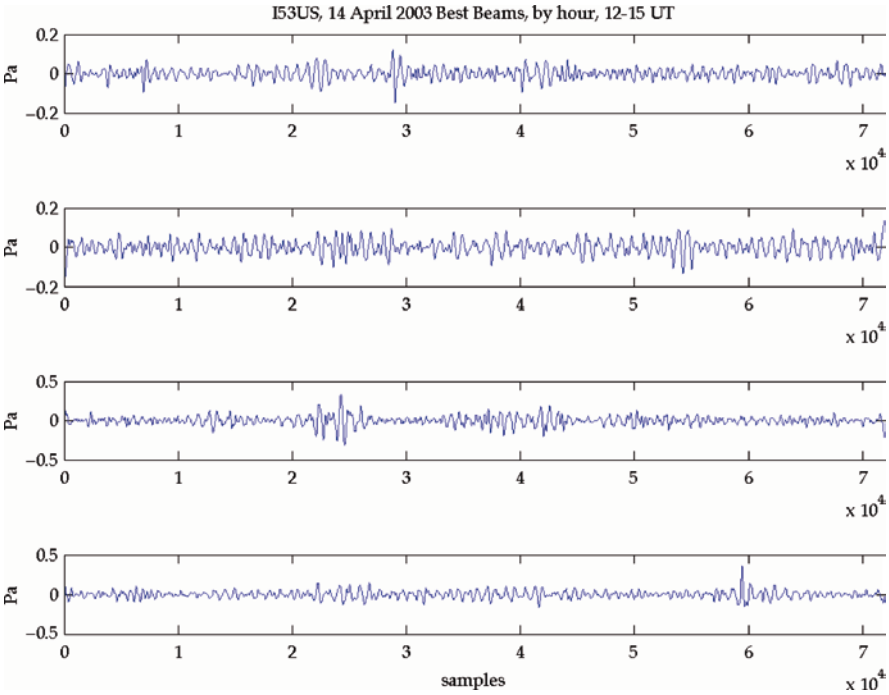

Fig. 13.26 Best beam traces of GAIW signals on April 14, 2003 for 12–15 UT, by hour from top to bottom panel

of the THD vector in the geomagnetic plane and a vector representing the propagation direction of the associated GAIW infrasound. This has been done for the April 14, 2003 GAIW event at I53US for the four largest signals that were observed during successive hours of the April 14. These THD vector locus maps can be seen in Figs. 13.27–13.30 below. The locus of the end point of the THD vector in time is shown in blue and the location at the time of a GAIW event is shown in black. The infrasound azimuth vector (labeled INF SIG) is shown in red. There is an uncertainty in the estimates of signal azimuth that increases with trace-velocity and a range in the THD vector direction that depends on the choice of delay time for the infrasound to propagate to the ground from the source region. Figures 13.27–13.30 show that the GAIW wave packet directions are approximately consistent with direction of the maximum in the THD, and thus, consistent with the view that the infrasound might be generated by the motions of multiple electrojet arcs.

Three further examples of GAIW infrasonic events at I53US from May 8, 2005, July 25, 2004, and September 13, 2005 are shown in Figs. 13.31 through 13.35. The detector plot in Fig. 13.31 for May 8, 2005 shows the only infrasonic signals for the day during the period from 14 to 18 UT with high trace-velocities coming from the north and high correlation values. In Fig. 13.32 the magnetogram from the CIGO magnetic observatory at Fairbanks shows very large magnetic disturbance in the H and D components from 14 to 17 UT on May 8. In Fig. 13.33 the detector plot from I53US for July 25, 2004 and the CIGO magnetogram plot in Fig. 13.34 show

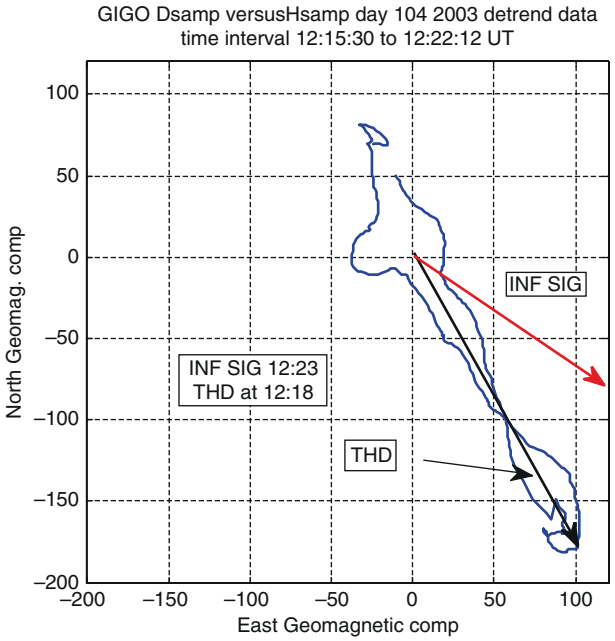

Fig. 13.27 Map of THD vector locus in geomagnetic plane with THD vector in *black* at 12:18 UT and GAIW signal direction vector in *red* at 12:23 UT April 14, 2003 hour 12 CIGO magnetic data and I53US infrasound data

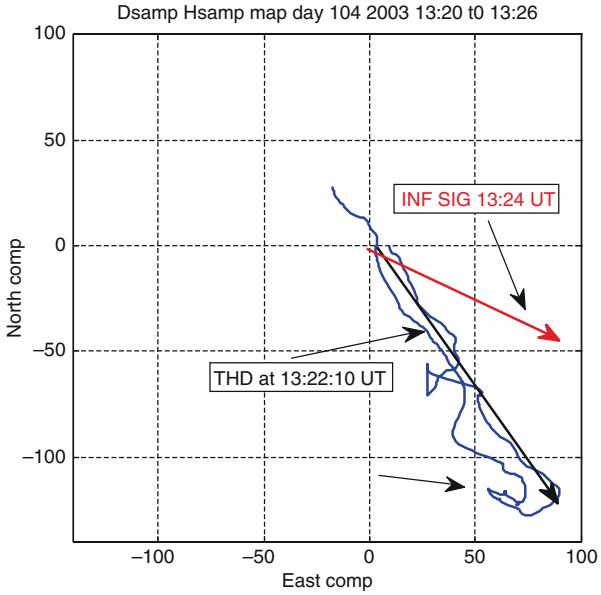

Fig. 13.28 Map of THD vector locus in geomagnetic plane with THD vector in *black* at 13:22 UT and GAIW signal direction vector in *red* at 13:24 UT April 14, 2003 hour 13 CIGO magnetic data and I53US infrasound data

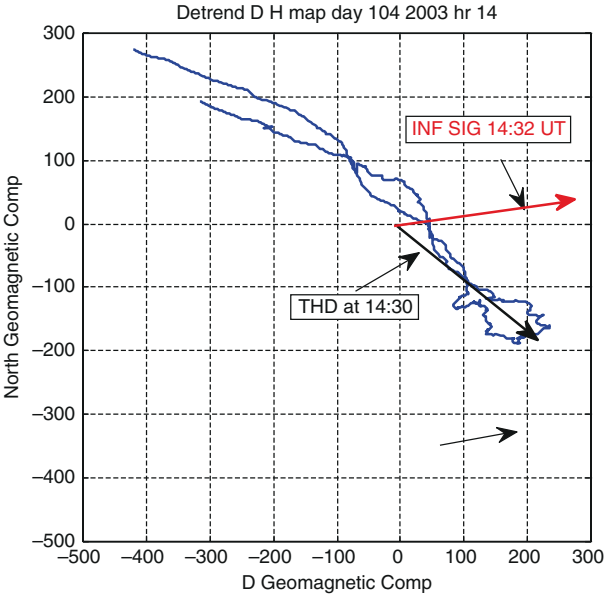

Fig. 13.29 Map of THD vector locus in geomagnetic plane with THD vector in *black* at 14:30 UT and GAIW signal direction vector in *red* at 14:32 UT April 14, 2003 hour 14 CIGO magnetic data and I53US infrasound data

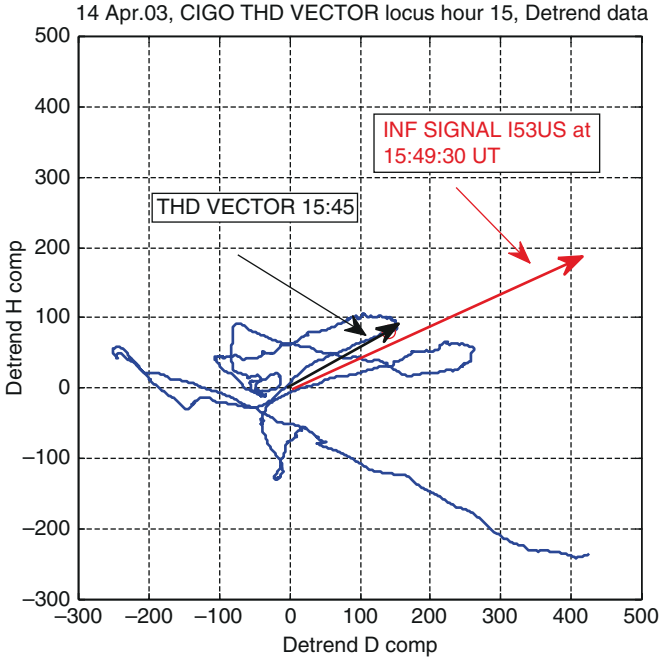

Fig. 13.30 Map of THD vector locus in the geomagnetic plane with THD vector in *black* at 15:45 UT and GAIW signal direction vector in *red* at 15:49:30 UT. April 14, 2003 hour 15 CIGO magnetic data and I53US infrasound data

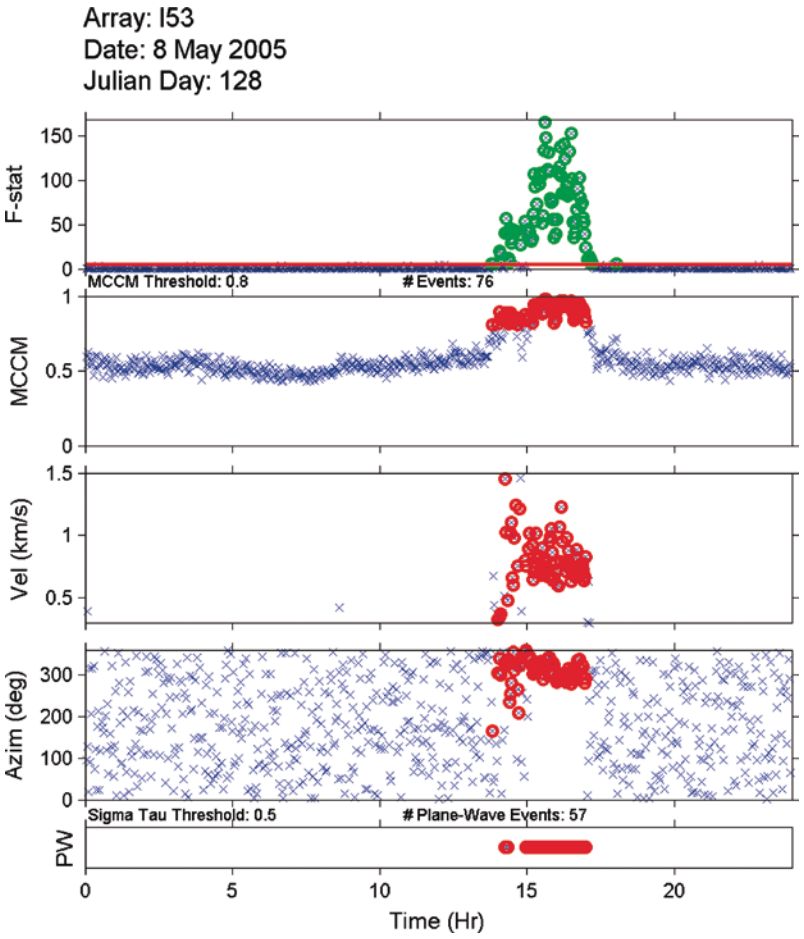

Fig. 13.31 Detector plot I53US for May 8, 2005, GAIW signals 14 to 17 UT

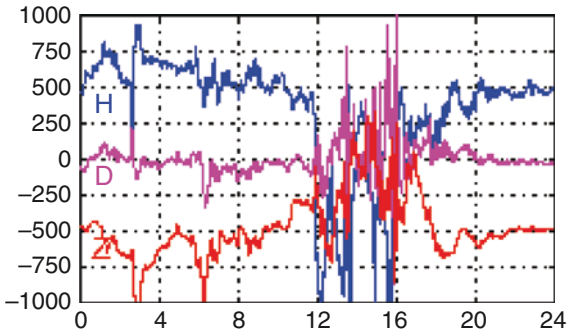

Fig. 13.32 CIGO Magnetograms for May 8, 2005. Magnetic disturbance at the same time as GAIW signals in Fig. 13.31

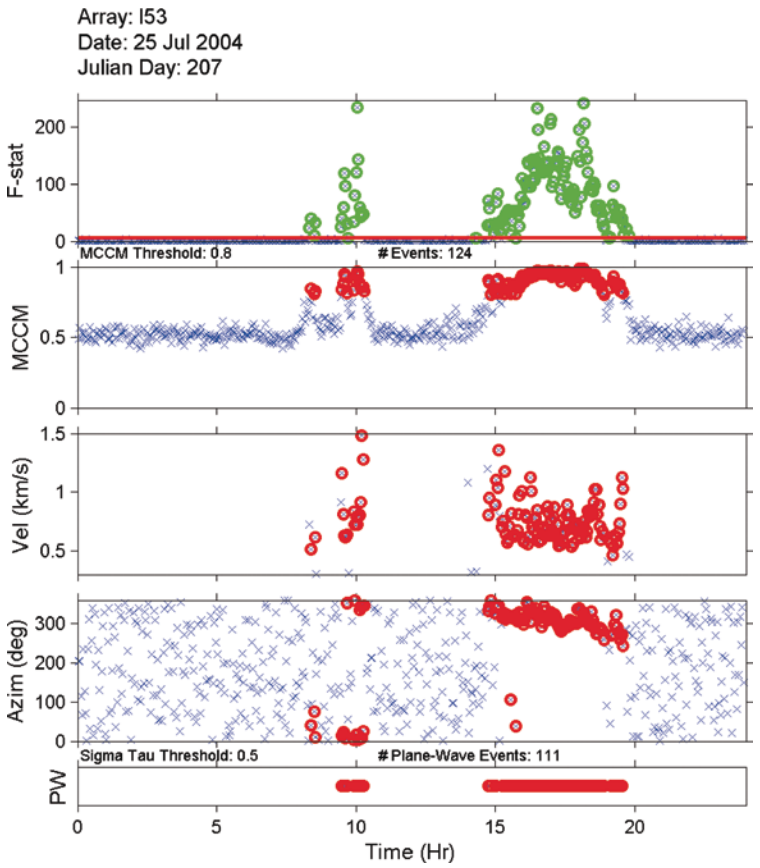

Fig. 13.33 Detector plot at I53US for July 25, 2004, GAIW signals from 14 to 19 UT

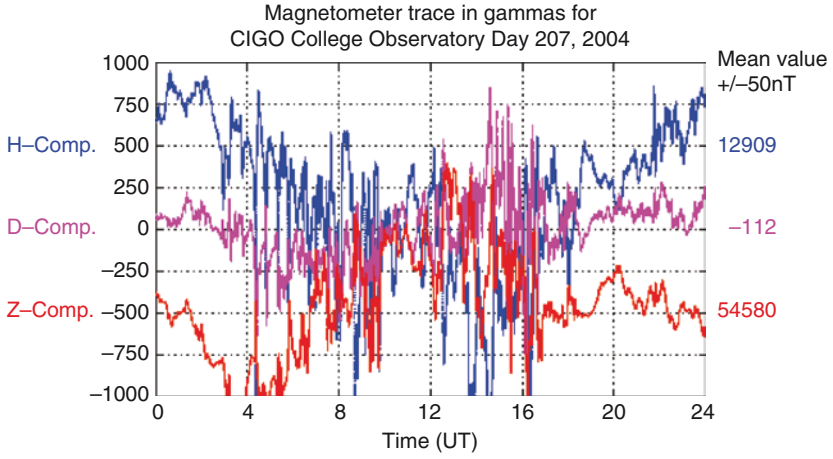

Fig. 13.34 CIGO magnetogram for July 25, 2004 with magnetic disturbance in H and D components 14–18 h

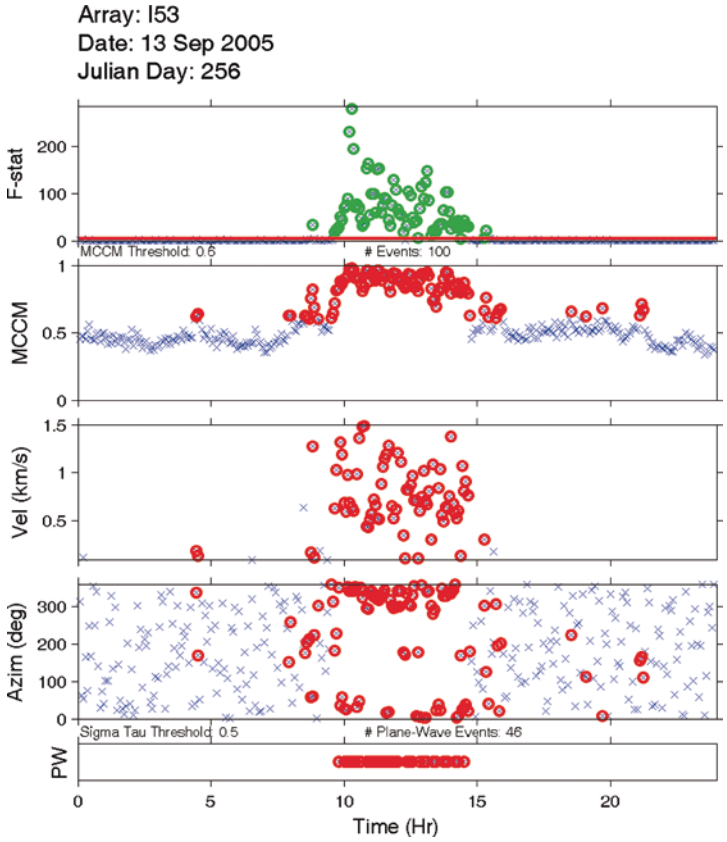

Fig. 13.35 Detector plot I53US for September 13, 2005, GAIW signals 10–14 UT

respectively GAIW signals and strong H and D magnetic disturbance in the same time period from about 14 to 18 UT. The GAIW signals have high trace-velocity, very high correlation values, and signal azimuths from the north that drift from east to west with time in a manner similar to that shown in Fig. 13.7, for the GAIW event of April 14, 2003 that is described above. In Fig. 13.35 the detector plot at I53US for September 13, 2005 shows the presence of high trace-velocity GAIW signals from the north during the interval from 10 to 15 h UT. There is no infrasound signal at any other time during this day. In Fig. 13.36 the magnetogram plot from Poker Flat magnetic observatory shows a simultaneous magnetic disturbance in the H and D components in the period 10 to 15 h.

The 1961 infrasonic observations from Washington D.C. indicated that there was an infrasound source, moving across northern auroral regions from east to west throughout the night during times of strong geomagnetic disturbance (Chrzanowski et al. 1961). The exact nature of this polar infrasound source was not known. In 1972, at UAF in a study of infrasound observed from four stations, Johnson (1972) found that it was possible to trace the east-west motion of polar

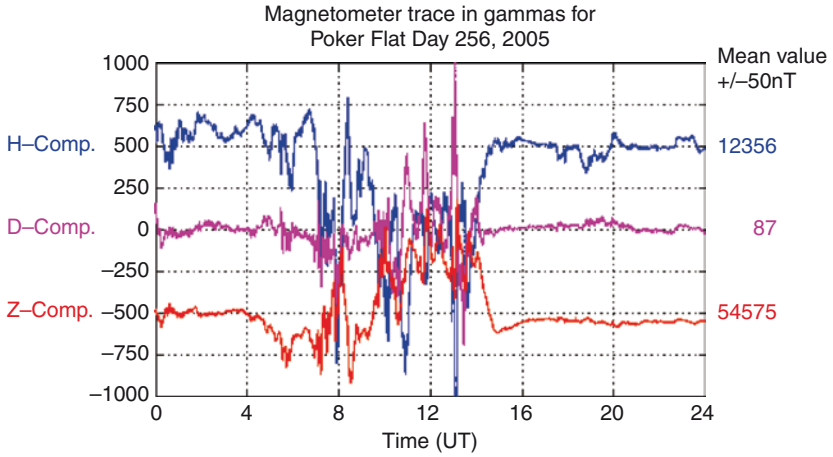

Fig. 13.36 Poker Flat magnetogram for September 13, 2005

substorms using auroral infrasonic data from four widely spaced infrasonic arrays at Washington DC, Boulder, Colorado, Pullman, Washington, and College, Alaska. It is our contention that this infrasound source, which was observed at lower latitude infrasonic arrays and moved westward across the northern sky, was from the GAIW signals associated with westward moving auroral substorm activity.

Because of the large positive temperature gradient with increasing height in the atmosphere above the 100 km level, infrasound radiated from the aurora/electrojet regions at a height of 120 km will be refracted strongly downward. Ray tracing, using an atmospheric model with a stratified temperature profile and no wind, indicates that a infrasonic wave packet from the 120 km level will arrive at the surface with a horizontal trace velocity that increases rapidly to infinity as the horizontal distance of the source patch from the array zenith point decreases to zero. Thus, the observed trace velocity of a GAIW wave packet can vary from about 0.40 km/s for a source patch that is 100 km away from the zenith to infinity for a source that is directly overhead. However, from a study of twenty one infrasonic wave events observed at I53US in 2003 for signals with trace-velocity greater than 1.00 km/s and less than 5.0 km/s, the average horizontal trace velocity was found to be 1.69 ± 0.27 km/s. The GAIW ray path travel times from the 120 km level to the surface vary from 250 s for a source overhead to 320 s for a source 100 km from the zenith.

13.3.3 Simultaneous Observation of GAIW at both I53US in Alaska and I55US in Antarctica

Continuous type GAIW auroral infrasound signals, as distinct from discrete AIW bow waves, are also observed at I55US in Windless Bight, Antarctica. The

geomagnetic latitude of a particular site determines its location with respect to the auroral oval where auroral infrasound is generated. The geomagnetic latitude of I55US in Antarctica is 79.72° south, while I53US in Fairbanks is at 65.12° north. Thus, I55US is almost 15° closer to the South magnetic pole than I53US is to the North magnetic pole. Therefore, one should not expect the auroral infrasound to be identical at I53US and I55US. However, on October 29, 2003, during a global magnetic storm following a very large solar flare, the simultaneous observations of GAIW infrasound, in the time period from 15 to 17 UT, occurred at both I53US and I55US. The detector plot from I55US in Antarctica is shown in Fig. 13.37 where the only sustained coherent signals during the day were high trace-velocity GAIW from the northwest that occurred from 15 to 17 h. In Fig. 13.38 a 30 min segment of the GAIW signals at I55US is shown as the best-beam for the pressure traces from 15:25 to 15:55 UT. For these signals, the trace-velocity was 0.77 km/s, the

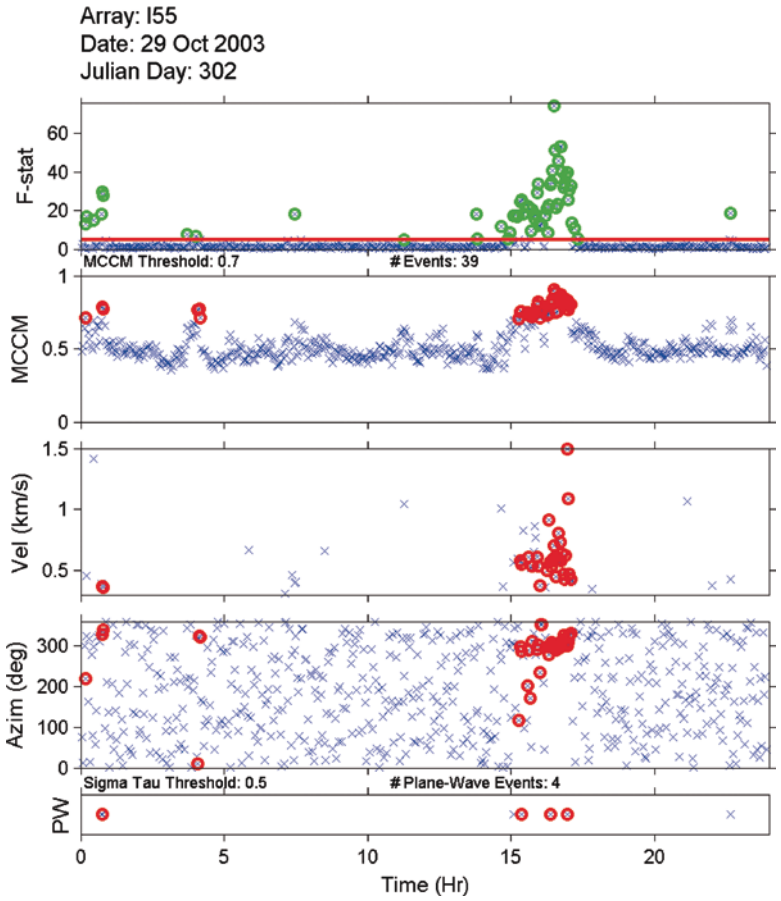

Fig. 13.37 Detector plot I55US October 29, 2003 with GAIW signals from 15 to 17 h

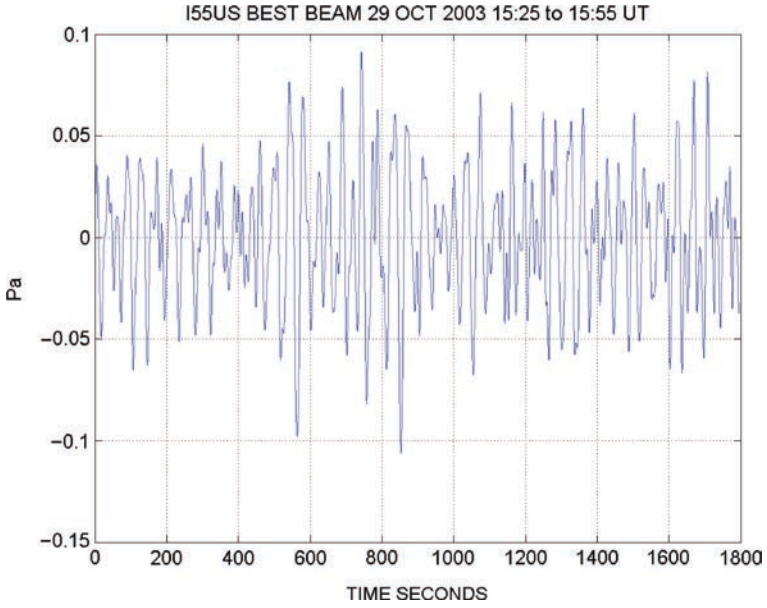

Fig. 13.38 Best Beam GAIW signals I55US October 29, 2003 15:25 to 15:55 UT

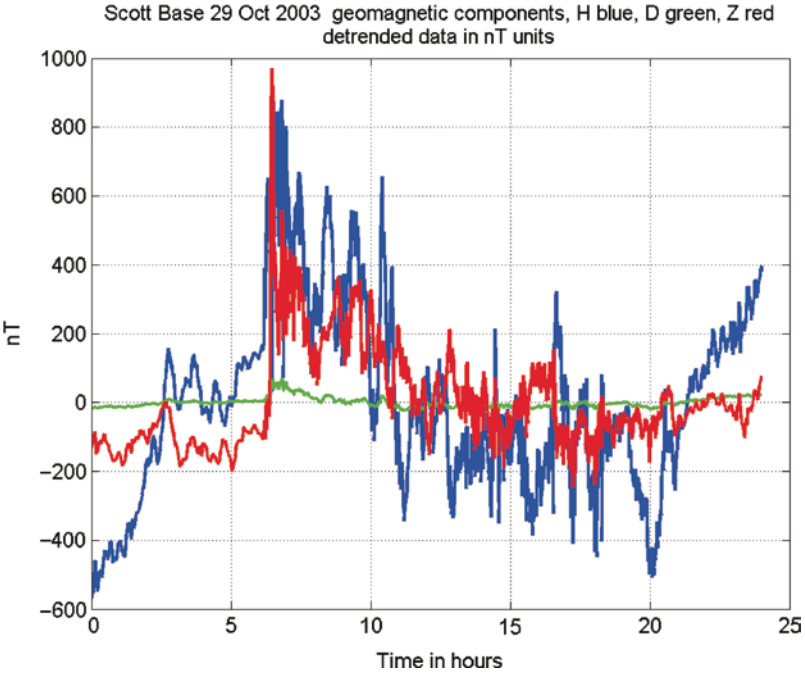

Fig. 13.39 Scott Base Magnetic data for October 29, 2003, H component *blue*, D component *green,* and Z comp *red*

azimuth was 293°, and the coherence was 0.64. The magnetic disturbance on October 29, 2003 in Antarctica was recorded at Scott Base, (that is within 23 km of I55US), which is shown in Fig. 13.39. Fig. 13.39 can be compared with Fig. 13.42 from the northern hemisphere magnetogram from CIGO in Fairbanks to see the simultaneous onset of the magnetic substorm.

For the same 24 h period on October 29, 2003, the detector plot for I53US is shown in Fig. 13.40 for the Northern Hemisphere. In Alaska on the 29th, there was also infrasound from MAW from an azimuth of 130° from 3 to 13 h and also from 200° azimuth from 22 to 24 h. The trace-velocity of these MAW signals can be seen in Fig. 13.40 to be much lower than that of the GAIW signals from 15 to 18 h. The GAIW signals at I53US are shown in Fig. 13.41 as the best-beam plot for the same period of time as that at I55US: from 15:25 to 15:55 UT. The trace-velocity for the GAIW shown in Fig. 13.40 was 0.75 km/s from an azimuth of 330° with a coherence

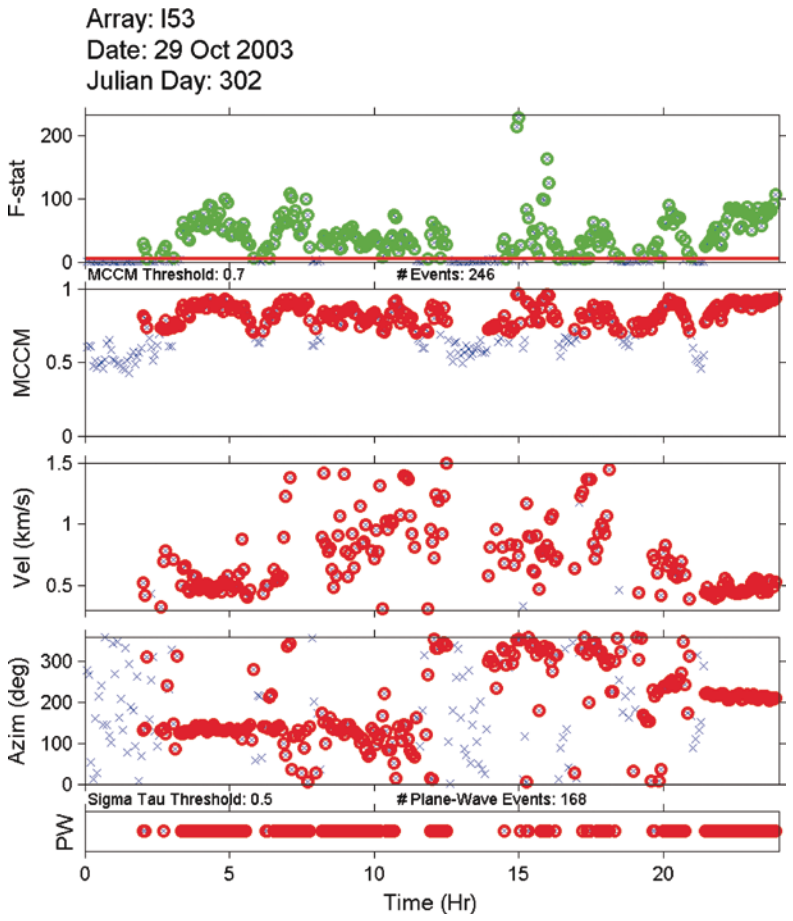

Fig. 13.40 Detector plot I53US October 29, 2003. MAW signals from azimuth 130°. 03–13 UT, MAW from azimuth 200° 22–24 UT, and GAIW signals 15–20 UT from the north

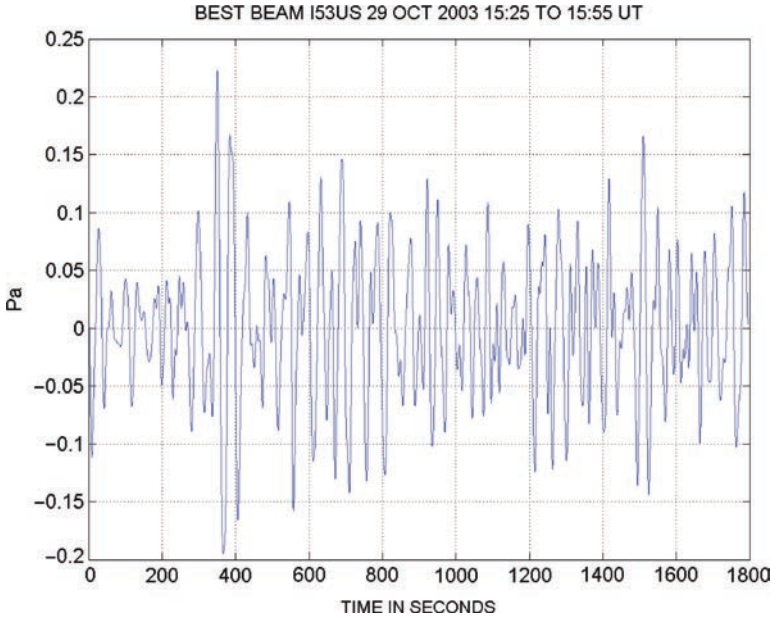

Fig. 13.41 Best Beam I53US October 29, 2003, GAIW signals from 15:25 to 15:55

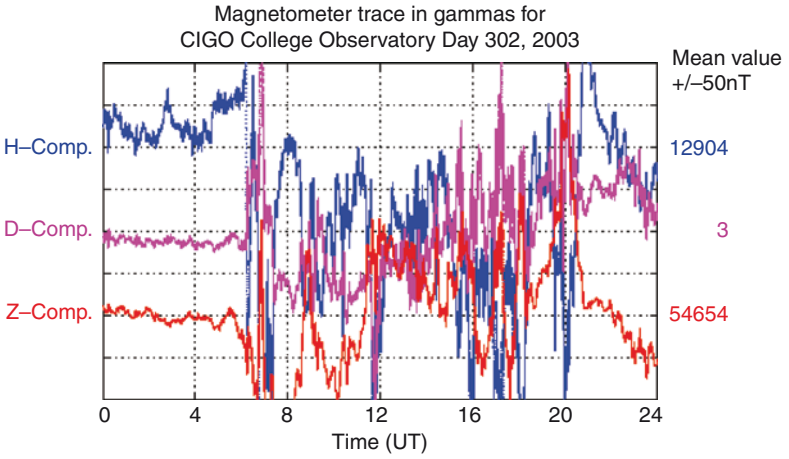

Fig. 13.42 CIGO magnetic observatory H, D, and Z components for October 29, 2003. The large fluctuations in H and D can be seen during the period 15–17 h when the GAIW were observed at I53US

of 0.91. The pressure amplitude for the Alaskan signals is about twice as large as those from Antarctica. The large geomagnetic disturbance associated with the GAIW event on October 29, 2003 can be seen in Fig. 13.42 from the CIGO magnetic observatory in Fairbanks. Thus, these I55US infrasound signals are almost certainly

associated with the auroral and magnetic storm that produced similar GAIW signals in Alaska at I53US. Studies of auroral infrasound will be continued at I53US and I55US over the next few years during their winter auroral seasons.

13.3.4 Conclusion and Future Research

Very recent studies of the polarization, in the H component-D component plane, of the geomagnetic THD vector during periods of auroral infrasound reception have indicated that both AIW bow waves and continuous GAIW infrasound signals observed at I53US may both be the result of auroral electrojet motions. These studies are described in an article posted on an online journal in the InfraMatics Newsletter that can be accessed at www.inframatics.org. The article by C. R. Wilson and J. V. Olson is titled "Auroral Infrasound and local Geomagnetic Disturbance at I53US." This article can be found in Issue number 22 for September 2008 on pages 2–9 of the InfraMatics Newsletter. We are led to the conclusion that much of the high trace-velocity auroral infrasound observed at I53US can be explained in terms of both the lateral supersonic motion of the auroral-electrojet arcs, of either linear or curved shapes, and the Lorentz-force coupling between the ionospheric currents and the neutral atmospheric gas. Whether or not pulsating auroral forms can be an additional source of auroral infrasound has not yet been determined, but awaits further collection of auroral video data and silultaneous infrasound observations at I53US in Fairbanks, Alaska in 2009.

References

Akasofu SI (1968) Polar and magnetospheric substorms. Springer, New York, NY

Chrzanowski P, Green G, Lemmon KT, Young JM (1961) Traveling pressure waves associated with geomagnetic activity. J Geophys Res 66:3727–3733

Drob DP, Picone JM, Garcs MA (2003) The global morphology of infrasound propagation. J Geophys Res 108, doi:10.1029/2002JD003307

Drob DP (2004) Atmospheric specifications for infrasound calculations, Inframatics Newsletter, No. 5, March 2004

Johnson RE (1972) An infrasonic pressure disturbance study of two polar substorms. Planet Space Sci 20(3):313–329

Larson RJ, Craine LB, Thomas JE, Wilson CR (1971) Correlation of winds and geographic features with production of certain infrasonic signals in the atmosphere. Geophys J Int 26:201–214

Meecham WC (1971) On aerodynamic infrasound. J Atmos Terr Phys 33:149

Olson J (1982) Noise suppression using data-adaptive polarization filters: Applications to infrasonic array data. J Acoust Soc Am 72:1456–1460

Szuberla C, Olson J (2004) Uncertainties associated with parameter estimation in atmospheric infrasound arrays. J Acoust Soc Am 115(1):253–258

Wilson CR (1969a) Auroral infrasonic waves. J Geophys Res 74:1812–1836

Wilson CR (1969b) "Infrasonic waves from moving auroral electrojets". J Planet Space Sci 17:1107–1120

Chapter 14
Some Atmospheric Effects on Infrasound Signal Amplitudes

J.P. Mutschlecner and Rodney W. Whitaker

14.1 Infrasound Sources

There are numerous sources of infrasonic pressure waves, or signals, which have been documented and, in some cases, carefully researched (Garcés et al. 2010). Many of these are of natural origin, while several have an origin in artificially produced circumstances. In both cases, the waves from the sources travel through the atmosphere and are consequently affected by this propagation. A review of sources is provided in a bibliographic form by McKisic (1997a), Greene and Howard (1975), and McIntosh (1982). We concentrate on three classes of infrasound sources for which attributes connected with the atmosphere have been found. The first of these are atmospheric nuclear explosions which, because of their great power, generated large signals at distances of up to several thousand kilometers. Thus, these sources can be uniquely useful for studying long-range propagation in the atmosphere. For explosions at the Nevada Test Site (NTS), Nevada, USA, a data summary has been provided by Reed (1969). Data from these nuclear, and also chemical, explosions are particularly relevant today because of the advent of the International Monitoring System (IMS) of the Comprehensive Test Ban Treaty Organization (CTBTO) that has deployed infrasound arrays worldwide to monitor such explosions (http://www.ctbto.org/) (Christie and Campus 2010).

Chemical explosions represent a second class of source type and, like the nuclear class, have the advantage of a well controlled known source size when used for dedicated tests. In general, they may not provide signals at the ranges of nuclear explosions, but good signals are detected at distances of hundreds of kilometers or more. A study of these signals has been given by Whitaker et al. (1994).

R.W. Whitaker (✉)
EES-17 MS J577, Los Alamos National Laboratory,
Los Alamos, NM 87544, USA
e-mail: rww@larl.gov

A. Le Pichon et al. (eds.), *Infrasound Monitoring for Atmospheric Studies*,
DOI 10.1007/978-1-4020-9508-5_14, © Springer Science+Business Media B.V. 2010

A third class of infrasound sources is earthquakes. Earthquakes produce infrasound signals due to the interactions of the atmosphere with the ground motion near the fault associated with the earthquake. While earthquake strengths can be defined by their seismic magnitudes, they are much more complex infrasound sources than explosions because of variations in the seismic mechanisms and the ground motions. Depending upon magnitude, earthquake signals can be observed at distances of up to a few thousand kilometers. Figure 14.1 gives an example of the relation of the log of normalized infrasound signal amplitude to seismic magnitude, M_L, as given by Mutschlecner and Whitaker (2005). Section 14.3 of this chapter explains the process that normalizes the signals for the effects of distance and atmospheric propagation. In effect, the signal amplitudes have been adjusted to a standard distance (in this case 250 km), with the effects from atmospheric winds removed. Throughout this chapter, the signal units are in Pascals of peak-to-trough pressure amplitude at maximum strength (1 Pascal = 10 dynes/cm^2 = 10 μbars). Unlike explosive sources that have signal durations of seconds to about a minute, earthquake signal durations may last from minutes to about an hour. Figure 14.1 shows that durations can be related to seismic magnitude. Mutschlecner and Whitaker (2005) have provided a model to explain this relation in terms of the spreading of the seismic ground motion region with time.

In order to study the interactions of the propagating signal with the atmosphere through which it passes, there is an obvious necessity of knowing the source and the source size-signal strength relation. For these reasons, in this chapter use is made of controlled explosive sources and earthquakes for which both conditions are met.

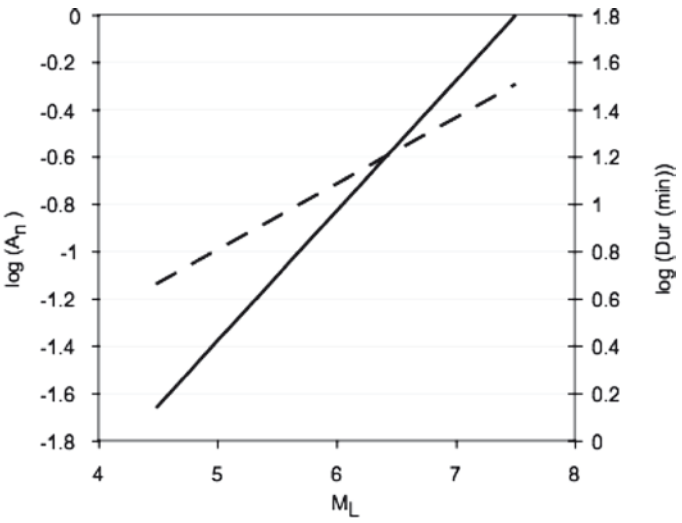

Fig. 14.1 The empirical relation for log of normalized amplitude, A_n, and seismic magnitude, M_L, (solid line) and the empirical relation for log of signal duration and seismic magnitude (dashed line) are shown for earthquakes

14.2 The Influence of the Atmosphere

The ability of infrasound to communicate signals from a source to a distant receiver relies upon two characteristics of the atmosphere. The first is the fact that over much of the infrasound wavelength spectrum, the absorption of sound energy is very low, especially as compared to the auditory part of the spectrum. The second is the ability of the atmosphere to refract waves that travel upward from a source back downward toward the earth. This second property, in turn, is the result of the vertical temperature profile of the atmosphere, which leads to a variable sound speed with altitude. Figure 14.2(a) illustrates this characteristic with a typical sound speed profile. A ray trace simulation of the effects of the varying sound speed on infrasound propagation is shown in Fig. 14.2(b) (see also Figs. 1.2 and 1.4 in Evers and Haak 2010). It is seen that the rays are bent back toward Earth and by reflection at the surface, are able to achieve multiple "bounces" in their trajectories. The analog of infrasound with optical rays is obvious.

Two other factors are essential for the successful propagation of infrasound over long distances; one of these is the ability of the Earth to reflect the waves with very little loss. The other, again relating to the atmosphere, is the presence of organized high velocity winds that add to or subtract from the sound speed as a function of altitude. Two wave types are considered: (1) those that are returned from stratospheric levels at about 50 km, here called S waves; and (2) those returned from thermospheric levels at about 110 km, or T waves. Three other propagation modes, tropospheric waves, Lamb waves, and gravity waves, are not considered here.

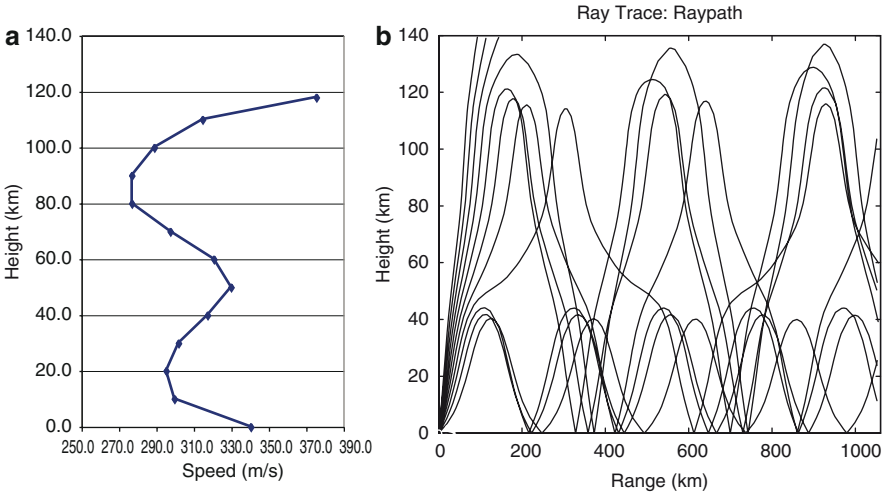

Fig. 14.2 (**a**) The sound speed in the atmosphere which results from the temperature profile is shown vs. altitude. S signal returns result from the lower peak centered at about 50 km and T signals from the speed rise beginning at about 100 km (**b**) An example is shown for a ray-trace simulation of infrasound propagation in the atmosphere for S and T returns. Multiple returns or "bounces" from the earth's surface are shown in the result

While the characteristics of the atmosphere just described are responsible for the successful long-range propagation of infrasound, the atmosphere also modifies an infrasound signal's characteristics in important ways. An account must be taken of these effects in signal analysis. To illustrate some of the effects upon signals, we use a set of data compiled by Reed (1969). This is a remarkable data set because it consists of infrasound observations conducted consistently over a long time at multiple observing stations. The sources were atmospheric nuclear explosion tests conducted at the NTS from 1951 to 1958. The explosions ranged in size from 0.6 to 74 kilotons (kt) in TNT equivalent yield, where 1 kiloton (kt) is 4.18×10^{12} joules. Observations were carried out at a total of nine stations, though not all were employed for all tests. Figure 14.3 shows the location of the stations with respect to the NTS. Single microphones were employed generally at each site and had wide band sensitivity from about 0.05 to 30 Hz. The recorded signal types were S, T, and tropospheric. In addition to the nuclear explosion signals, high explosive calibration shots preceded many of the nuclear explosions. Mutschlecner et al. (1999) have provided a detailed analysis of this data set. The limitations of the data set are that (1) single microphones, not arrays, were deployed at the sites so that the signal azimuths and trace velocities were not determined, (2) only amplitude and timing values, not wave forms, are generally available, and (3) most of the stations are located within or close to a single "bounce" distance, about 220 km. In connection with the last restriction, it is a curiosity that the program for these observations was not primarily for purely scientific research, but to help assure that blast damage (e.g., window breakage) off the NTS was avoided.

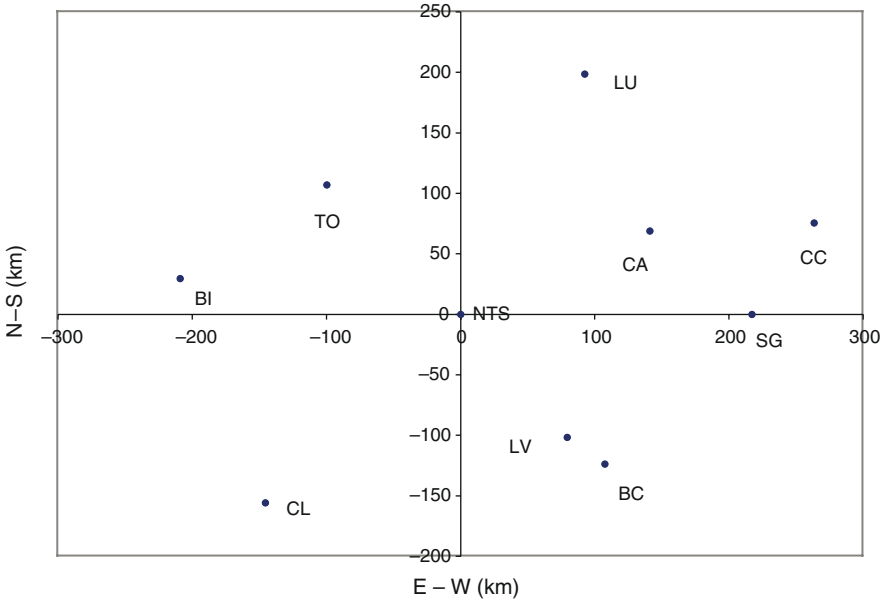

Fig. 14.3 The microphone locations surrounding the Nevada Test Site (NTS) are shown. The primary data in this discussion came from the sites at St. George, UT (SG); Bishop, CA (BI); China Lake, CA (CL); and Lund, NV (LU)

In order to compare signal amplitudes from differing yield explosions, it is necessary to normalize to a standard yield, in this case 1 kt. The observed amplitude, A_o, is normalized by

$$A_w = A_o W^{-n} \tag{14.1}$$

where W is the explosion yield and A_w is the normalized amplitude. The value of n used here is 0.456 (± 0.05) based upon the earlier analysis of Mutschlecner et al. (1999). Figure 14.4 displays the values of log A_w for S signals vs. day of the year for three of the stations: St. George, UT (part a), Bishop, CA, (part b), and Lund, NV, (part c). Data from all of the years are merged. In the data from St. George and Bishop, variations in

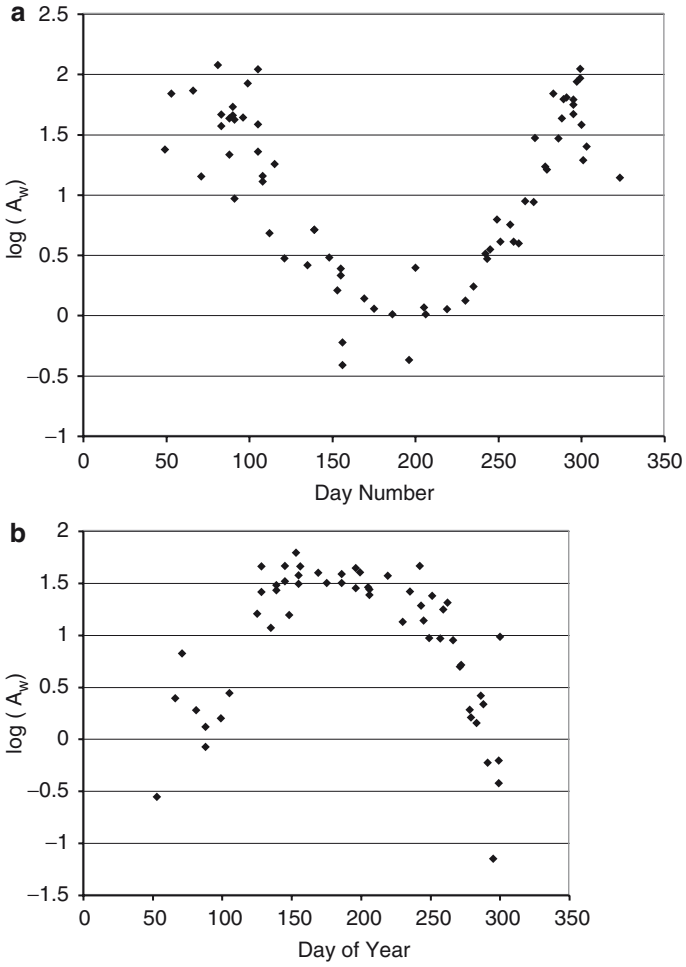

Fig. 14.4 Shown is the log of observed amplitude normalized for yield, A_w, vs. day of year of nuclear atmospheric explosions for the stations at: (a) St. George, (b) Bishop, and (c) Lund. The strong seasonal variations in amplitude and dependence upon station location with respect to the NTS are seen

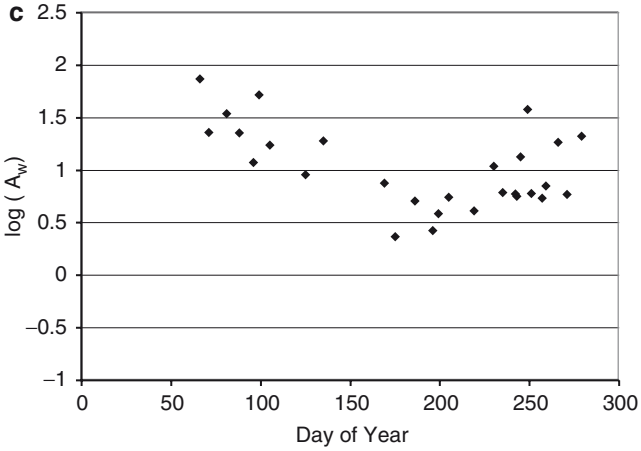

Fig. 14.4 (continued)

A_w are over two orders of magnitude. For St. George, the maxima in amplitude are found near the mid-winter to end-of-the year period and minimum values occur in the mid-summer period. In contrast, the Bishop data have a phase difference from St. George of about one-half year with the maximum in amplitude during the summer and minimum in the winter. The data for Lund have a reduced seasonal dependence, but with the same phase as for St. George. Thus, two critical characteristics are seen: (1) a potentially very large annual effect in amplitude which cannot be ignored, and (2) a seasonal effect which is dependent upon direction to the source. By contrast, it is found that T signal amplitudes appear to have no seasonal dependence.

The explanation for these effects upon amplitude lies in the seasonal variation of the zonal wind in the stratosphere. Figure 14.5 shows the seasonal variation of the zonal (East-West) component, V_z, and the meridional component (North-South), V_m, of the wind averaged over the altitude range of 45–55 km. This has been termed the Stratospheric Circulation Index (SCI) by Webb (1966). The North-South or the meridional component, V_m, is much smaller in amplitude than V_z, but also has a seasonal variation. The Fig. 14.5 shows V_z and V_m from a model developed for the Southwestern US by Mutschlecner et al. (1999). For St. George, almost directly east of the NTS, V_z adds to the sonic velocity in the atmosphere during the winter period and reduces the effective sonic velocity during the summer period. This results in more effective returns of infrasound signals during the winter period and less effective returns during the summer. By contrast, Bishop, nearly directly west of the NTS, has the most effective zonal wind during the summer period and least effective during the winter. Lund, to the northeast of the NTS, receives only a component of the V_z wind and so has a reduced seasonal effect as seen in Fig. 14.3. A detailed description of these effects requires an atmospheric propagation model including wind effects. It is important to note that the stratospheric wind not only varies seasonally, but has a very strong geographic variation. Webb (1966) has provided a description of these variations and McKisic (1997b) provides a useful summary.

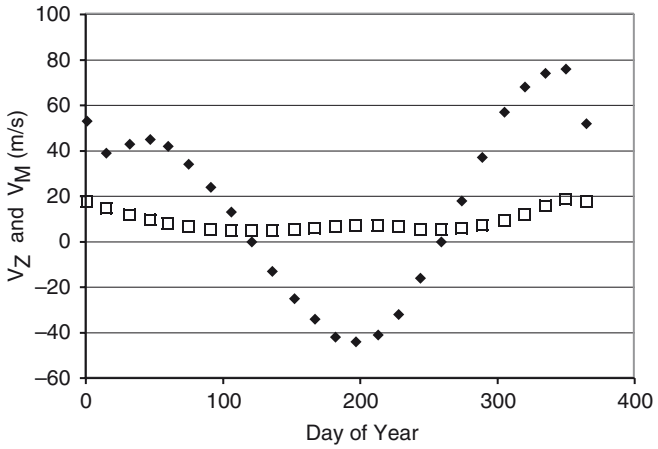

Fig. 14.5 The zonal, V_z, (*diamonds*) and meridional, V_m, (*squares*) components of the SCI are displayed vs. day of year. The values are for a model of the SCI for the southwestern US

From the size and variability of the effects of the atmosphere and winds upon amplitudes, it is clear that analysis of signals for source information or other purposes will require that these effects be taken into account or removed. There are two possible approaches to this effort. One is a detailed modeling of the propagation of the signal through the atmosphere with accounting for the effects of both temperature profile and of wind profile. The second possibility is an empirical procedure that is presented in this chapter. Ideally, future work will make use of some combination of the two methods, especially since the use of the first method for each signal of interest could be laborious and time-consuming.

14.3 Quantifying the Effects of Wind on Infrasound Signals

It has been shown in an earlier section and in other chapters that stratospheric winds can have a profound effect on the pressure amplitudes of infrasound signals (Chapters Evers and Haak 2010; Kulichkov 2010; Norris et al. 2010). This is particularly true of those signals which return to Earth by refraction from the stratospheric region, that is, S signals. It also has been shown that the effect is seasonally dependent in accord with the seasonal variation of the stratospheric winds. In this section the effect is quantified and later a method is presented to "correct" or normalize the pressure amplitudes for the effects of wind.

As in the earlier section, the data used are signals from atmospheric nuclear explosions at the NTS observed at stations at about one bounce location distances (~220 km). Figure 14.6 shows the logarithm of pressure amplitude normalized for explosion size, or yield, A_w, at St. George vs. the zonal component, V_z, of the SCI model. The SCI is an appropriate definition for the wind profile in the present context since it is in the altitude domain of the SCI definition that the S signals are fully refracted for return to the earth. However, other similar definitions could be used for the purpose.

Figure 14.6 shows a linear relation between the two variables. In the present example, the zonal component of the SCI is used because the St. George station is nearly directly east of the NTS (the convention is that positive wind values are to the east). As a second example, the logarithms of signal yield-normalized amplitudes from the NTS observed at Bishop, CA, are shown vs. the SCI V_z in Fig. 14.7. The Bishop station is almost directly west of the NTS. A comparison of Figs. 14.6 and 14.7 shows that the amplitudes at St. George increase as V_z increases, while

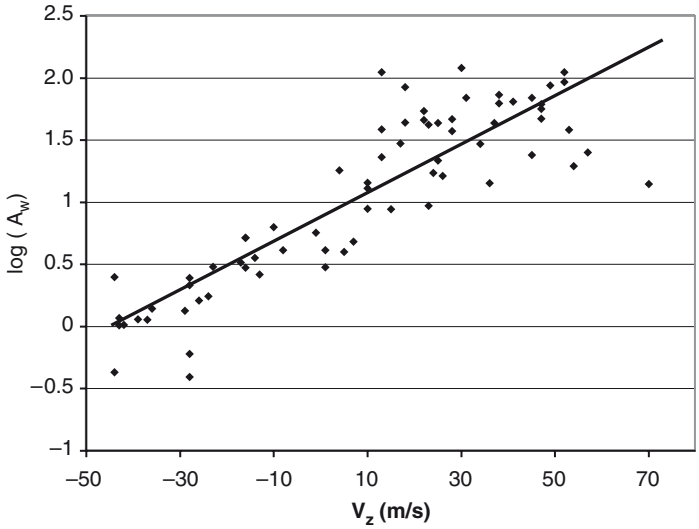

Fig. 14.6 The log of yield-normalized nuclear explosion amplitudes, A_w, for St. George is shown vs. the corresponding values of zonal SCI, V_z , from the model. A least squares fit line is shown

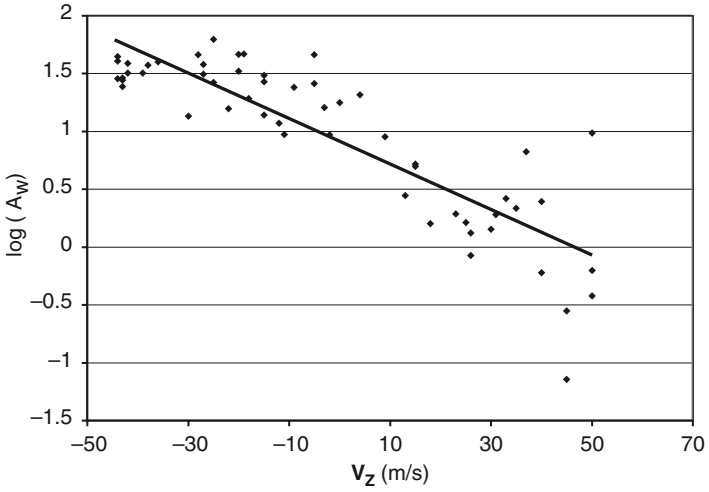

Fig. 14.7 The same plot as in Fig. 14.6, but for Bishop

those at Bishop decrease with V_z. This effect results from the fact that for St. George a positive value of V_z enhances the propagation of S signals because the wind is toward the station, while for Bishop, negative values of V_z will be toward the station.

For more general circumstances where the observer is at some azimuth, θ, with respect to the source the appropriate value of the SCI will be a component of the SCI, V_d, directed from the source to the observer given by

$$V_d = V_z \sin\theta + V_m \cos\theta, \tag{14.2}$$

where for V_m the convention is that positive winds are to the North.

Then, from the types of relations seen in Figs. 14.6 and 14.7, we can write for the wind and distance normalized amplitude, A_n:

$$A_n = A_o \, 10^{-k V_d} \, (R/R_o)^{-\alpha} \tag{14.3}$$

where k represents the slope seen in the Figs. 14.6 and 14.7. The third factor gives normalization for the effect of distance; R is the great circle distance on the ground to the source, R_o an arbitrary standard scaling distance (here 250 km, i.e., about one bounce distance), and α is a distance normalizing parameter. Thus, A_n represents the pressure amplitude normalized for the effects of wind and distance. This normalization permits a comparison among various observations of the same source or, with proper compensation, among various sources. For example, we have been able to compare infrasound signals among numerous earthquakes (Mutschlecner and Whitaker (2005)). This wind normalization formulation originally was presented by Mutschlecner and Whitaker (1990).

From a detailed analysis of all of the observations of the atmospheric nuclear events, at several stations a statistically optimum value of k is:

$$k = 0.018 \; (0.002) \; s/m. \tag{14.4}$$

Numbers in parenthesis are 1-sigma RMS values. This analysis was presented by Mutschlecner et al. (1999). In a similar way, we have deduced an optimum value for α as

$$\alpha = 1.45 \; (\; 0.15). \tag{14.5}$$

Others have determined values for k independently. Blanc et al. (1997) find 0.0116 s/m and Edwards et al. (2006) find 0.0177 s/m.

14.4 The Los Alamos He Data Set

Infrasound measurements of high explosive (HE) sources have been made by the Los Alamos National Laboratory over a period of years. The measurements have been made in a consistent way and the sources were well-defined. As a result, this set provides a reliable base of ground-truth infrasound data.

Table 14.1 HE event information

Event	Date/Doy	Weight (Tons)	Sites
Mill race	9/16/81 259	600	1
Predirect course	10/7/82 280	24	2
Direct course	10/26/83 299	600	4
Minor scale	6/27/85 178	4,800	2
Misty picture	5/14/87 134	4,880	5
Misers gold	6/01/89 152	2,400	8
Distant image	6/20/91 171	2,400	2
Minor uncle	6/10/93 161	2,400	3
Watusi	9/28/02 271	19	3

The sources were masses of ANFO explosive (fuel oil and ammonium nitrate mixture) that were used in tests at the White Sands Missile Range, New Mexico, USA. The tests were conducted by the US Defense Nuclear Agency (now the Defense Threat Reduction Agency) for purposes of the measurement of blast and seismic effects at short to intermediate ranges. The DNA tests were carried out over a period from 1981 to 1993. The explosive charges were shaped as hemispheres and were at ground level with the exception of two (pre-Direct Course and Direct Course) in a spherical configuration at an elevation above the ground. Table 14.1 provides details of the tests including the code names, dates, and weights in tons of ANFO. The masses varied from 24 to 4,880 tons. Thus, a substantial range in source size is available for understanding of charge size dependence. Note that one ton of ANFO is approximately equivalent to 1.42 tons of TNT with respect to blast effects. An additional explosive test, Watusi, (not done by DNA) was carried out at the NTS and is included in Table 14.1. The test was in a cylindrical excavation with the top of the explosive flush with the surface.

The infrasound measurements were conducted with arrays of four Chaparral II sensors or their equivalent using porous hose-type noise reducers. The array size was typically about 50–100 m in diameter. There were several fixed array locations at Los Alamos, NM, St. George UT, and Boulder, CO (for one event). For several events, temporary arrays were deployed at a variety of locations toward the west of White Sands. Table 14.1 provides the number of arrays used in each case. The distances from the arrays ranged from 250 to 5,300 km.

The data were analyzed with standard beam-forming software over a pass band of 0.1–3 Hz, which provided amplitudes, trace velocities, spectra, celerities (average travel speeds), and back azimuths. Generally, multiple signal arrivals were seen at the arrays. In this report only the dominant S arrivals are used. A portion of these data were previously discussed by Davidson and Whitaker (1992) and Whitaker et al. (1994).

This database can provide a useful ground-truth set. One limitation is that the dates of the tests are not uniformly distributed during the year. This set of HE data has been used to test the methods for the normalization of wind effects given in Sect. 14.3. The logarithms of the observed amplitudes, A_o, are displayed vs. explosion-size-scaled range, R_s, in Fig. 14.8. The scaled range is defined by

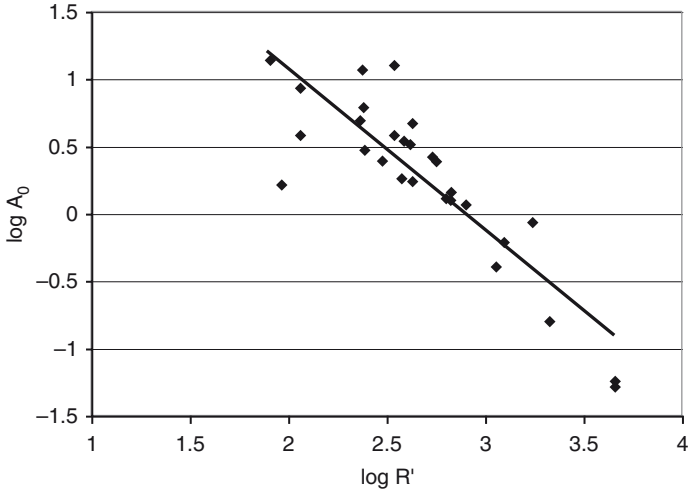

Fig. 14.8 The log of observed amplitudes, A_o, vs. log of yield-scaled range, R_s, for high explosive tests. A least-squares fit line is shown

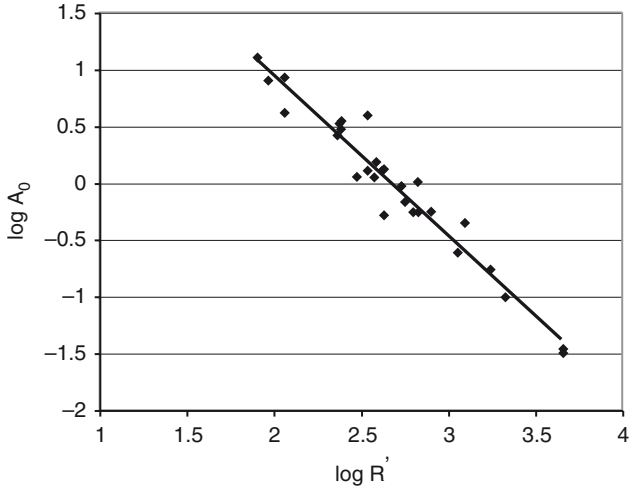

Fig. 14.9 The same plot as in Fig. 14.8, but with log of amplitudes normalized for the effects of wind, A'_0. The improvement of the fit to a least-squares line is seen

$$R_s = R / \sqrt{2W / 1000}, \tag{14.6}$$

where W is the explosive charge weight (tons). This protocol for display is conventional for observations of explosions (see ANSI (1983)). Figure 14.9 shows the same data but with the pressure amplitudes normalized for the effects of wind, with A'_0, the wind-normalized amplitudes given by

$$log\left(A'_0\right) = \log\left(A_o\right) - kV_d, \tag{14.7}$$

Comparison of Figs. 14.8 and 14.9 shows that a substantial improvement in the relation is achieved after the wind effect normalization. The correlation measure, R^2, is 0.75 for the un-normalized data and 0.95 for the normalized data, with standard deviations of 0.31 and 0.15, respectively. The relation seen in Fig. 14.9 is

$$log\left(A'_0\right) = 4.61\left(.23\right) - 1.34\left(.09\right) log\left(R'\right). \tag{14.8}$$

Equation 14.8 can be inverted to provide estimates of explosive size from wind-normalized amplitudes, provided the distance from the source is known:

$$log(W) = 1.49\left(0.10\right) log\left(A'_0\right) + 2.00\left(0.20\right) log(R) - 4.18\left(.23\right), \tag{14.9}$$

where the units are: W in tons of ANFO equivalent, A'_0 in microbars, and R in kilometers.

An example of the use of this estimator for explosive weight, W, is found in an accidental explosion which occurred on May 4, 1988 at a chemical plant at Henderson, Nevada, USA, close to Las Vegas, Nevada. Two distinct explosions occurred minutes apart in very large stores of ammonium perchlorate (AP), which is used for rocket fuel. As an aside, it was thought at the time that AP was not an explosive material. Details of the circumstances have been given by Reed (1992).

These explosions were observed at the St. George, Utah, and Los Alamos, New Mexico infrasound arrays operated by the Los Alamos National Laboratory. The St. George array was too close to the source for confidence in the propagation modes, but the Los Alamos array, at a distance of 774 km, observed both explosions with S signal amplitudes of 6.8 and 12.9 μbars. After minor corrections for wind effects, the amplitudes were used in Eqn. (14.9) to give explosive weights of 800 and 2,100 tons ANFO equivalent or a total of 2,900 tons. The actual charge masses of AP totaled 4,250 tons. The conversion from AP to ANFO explosive equivalent is poorly known. Reed (1992) made a separate estimate based upon the local blast effects and found 3,700 tons of nuclear free-air equivalent explosive size. This example shows the important possible use of the estimator in determining the explosive masses involved in surreptitious or unknown explosions.

It was indicated in an earlier section that thermospheric return, or T, signals show no effect due to the stratospheric wind. This is because these signals are robustly returned by the sound velocity gradients at about 110 km, regardless of the wind profiles. As a result, the T signal from a source will be roughly constant throughout the year at a given station. The ratio, R_{st}, between the wind-normalized S signal amplitude, $A_o(S)$, and the T signal amplitude, $A_o(T)$, for an event is

$$R_{st} = A_o(S) 10^{-kV_d} / A_o(T). \tag{14.10}$$

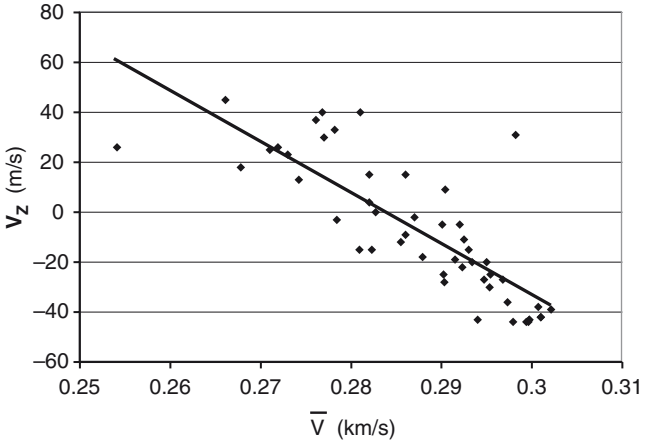

Fig. 14.10 Average travel velocities, $\bar{V}$, are shown vs. the model zonal wind, V_z, for the Bishop data

For explosive sources such as chemical or nuclear, we find (Whitaker and Mutschlecner (2008)) the value ranges from about 2 to 7 depending upon the circumstances. For other types of sources, such as earthquakes, the ratio differs, probably due to variations in the source radiation patterns.

In addition to the effects of wind upon pressure amplitudes, winds may also affect other observed signal parameters. For example, we have shown in Mutschlecner et al. (1999), using the nuclear explosion data, that the average travel velocity, $\bar{V}$, of S signals is influenced by the stratospheric wind. $\bar{V}$ is the great circle distance to the source divided by the signal transit time. Figure 14.10 shows that there is an inverse relation between $\bar{V}$ and V_z for the nuclear data at the Bishop station. This result follows because Bishop is to the west of NTS, and hence, a positive V_z will degrade the efficiency of the waveguide. Unfortunately, the data for the other stations with nuclear observations, while suggesting such relations, are not of sufficient clarity for quantification. Future efforts to quantify the effects of the stratospheric winds upon $\bar{V}$ could help to provide another means to help determine wind characteristics by infrasonic observations.

14.5 Determination of Wind Characteristics

As the previous section has shown, the atmospheric winds have a profound influence on S signals; as a result, it is necessary to have knowledge of the wind structure in order to carry out propagation calculations to determine these effects or, at least, to have some parameterization such as the SCI as shown in Eqn. (14.3). Historically, several observational methods have been used to determine wind profiles with altitude. Primary examples are rocketsondes, which can measure atmospheric properties up

to altitudes of about 90–100 km and atmospheric grenade experiments. Details of these methods are covered in detail by Webb (1966). Unfortunately these methods are expensive and, while for a period there was a continuing program of this research, there are now few such measurements. Interestingly, observations of infrasound signals may themselves, in some cases, provide measures of wind parameters as will be outlined in this section.

Because the stratospheric wind structure strongly affects the amplitude of S signals while the T signal strength is unaffected, it is possible to deduce from their relative strengths a measure of the stratospheric wind. In effect, the T signal strength is used as a base which removes from the analysis the effects of source size and of distance. Equation (14.10) can be rewritten as

$$V_d = \log\left[A_o(S)/A_o(T)\bar{R}_{st}\right]/k, \tag{14.11}$$

where $\bar{R}_{st}$ is an adopted average value for a given source type. Thus, with the ratio of the S and T amplitudes, the value of the directed wind, V_d, can be determined when values of $\bar{R}_{st}$ and k are adopted.

As an example of this method, we use the signals from atmospheric nuclear tests observed at the Bishop, CA array. The parameters used in the example are

$$k = 0.018\,\mathrm{s/m} \tag{14.12}$$

$$\bar{R}_{st} = 4.69\ (0.60) \tag{14.13}$$

Because Bishop is nearly directly to the west of the NTS, the values of V_d are equivalent to $-V_z$. Figure 14.11 shows the derived values of V_z vs. day of year; a few end-of-year observations were deleted since this is an unstable period. For comparison, the V_z relation from the SCI model cited earlier is shown. The general agreement in the derived values with the model is good. The RMS departure of the V_z values from the model is about 16 m/s, excepting a few end-of-year values when variations in the winds are known to be very large. The RMS value is very close to the RMS spread of rocketsonde observations taken at the White Sands Missile Range over a period of years, 16.7 m/s, as given by McCullough and Novlan (1977). It is likely that much of the variation between the model and the derived values of V_z, thus, are caused by the actual variations of the wind from the model mean values.

This method for determination of the SCI parameter for stratospheric wind from a ratio of amplitudes of S and T signals appears to be promising. However, it is subject to the quality of the adopted values of k and $\bar{R}_{st}$. The value of k can be improved with the use of other data sets or perhaps theory. As indicated previously, the value of $\bar{R}_{st}$ appears to be source dependent. For example, Whitaker and Mutschlecner (2008) find that for earthquakes the average value is between 0.40 and 0.60. Thus, further work is needed in the determination of optimum values of $\bar{R}_{st}$ for differing cases. Earthquake S and T signal amplitudes have been used to test the method with a different kind of source. Figure 14.11 shows the values of V_z and the SCI V_z for comparison. There are relatively few T signals available here, but the

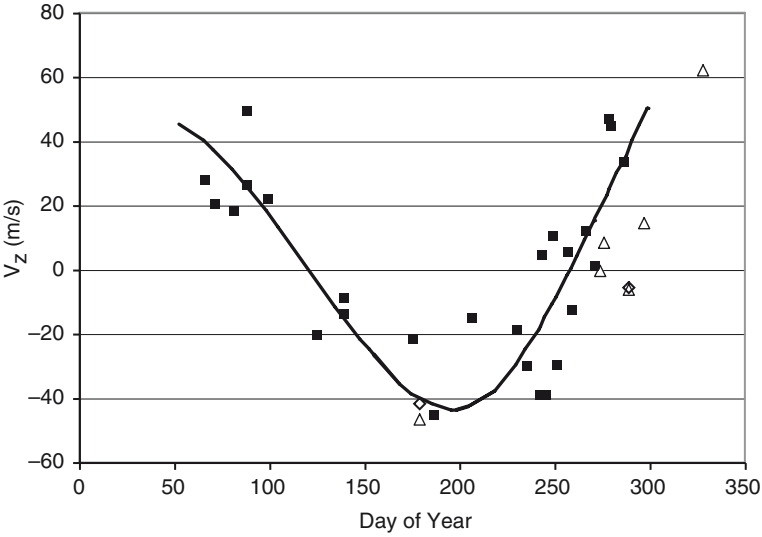

Fig. 14.11 Values for V_z obtained by the use of S and T amplitudes for Bishop data vs. day of year (squares). Values obtained from earthquake S and T amplitudes are also shown (*open triangles and open diamonds*). For comparison, the V_z-day of year relation from the SCI model is shown

comparison shows fair agreement. The RMS for the fit is about 22 m/s, but this is sensitive to the value of $\overline{R}_{st}$ used.

Another method for wind determination relies on the special circumstance in which two stations are positioned on either side of a source directly to the east and to the west. This situation is found for the atmospheric nuclear test signals at St. George, UT, and Bishop, CA. In this circumstance, we can write for the two stations

$$A_{sg} = C\,10^{kV_z}, \tag{14.14}$$

$$A_{bi} = C\,10^{-kV_z}, \tag{14.15}$$

where A_{sg} and A_{bi} are the S signal amplitudes observed at St. George and Bishop, respectively, C is a constant containing the source and distance-scaling data (identical for the two stations), and V_z is the relevant zonal SCI value. Then Eqs. (14.14) and (14.15) can be combined as a solution for V_z:

$$V_z = (\log A_{sg} - \log A_{bi})/2k. \tag{14.16}$$

Thus, in this method there is dependence only on values of the S amplitudes. Figure 14.12 shows the resulting values of V_z for the St. George-Bishop pairs vs. day number and compares these values with V_z given in the model. The agreement is good in terms of the general trends and the RMS variance between the derived

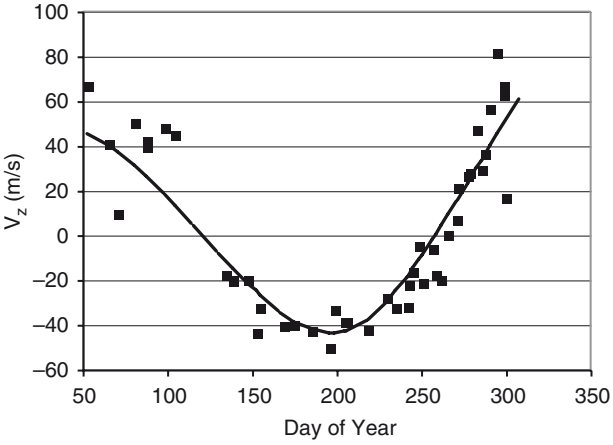

Fig. 14.12 Values of V_z determined using amplitudes from pairs of St. George and Bishop S amplitude observations of the same nuclear event vs. day of year. For comparison, the SCI V_z from the model is shown

values and the model is 14.3 m/s . While this method is rather unique in application in terms of the required placement of the observing sites, it has the advantage in relying only on S signals.

A more general method can be applied in circumstances where the same event's S signals are observed at three or more stations. For example, for two stations labeled *m* and *n*

$$\log (A_m^{'}) - \log (A_n^{'}) = k\ [(\sin\theta_m - \sin\theta_n)V_z + (\cos\theta_m - \cos\theta_n)V_m], \quad (14.17)$$

where $A_{m'}$ and $A_{n'}$ are the S amplitudes at stations *m* and *n* normalized to an arbitrary standard distance, R_o, by the formulas

$$A_m^{'} = A_m\ (R_m / R_o)^{-\alpha} \quad (14.18)$$

$$A_n^{'} = A_n\ (R_n / R_o)^{-\alpha} \quad (14.19)$$

where θ_m and θ_n are the respective azimuths from the two stations. Similarly, we can write for two stations *p* and *q* observing the same event

$$\log (A_p^{'}) - \log (A_q^{'}) = k\ [\ (\sin\theta_p - \sin\theta_q)V_z + (\cos\theta_p - \cos\theta_q)V_m\ ]\ . \quad (14.20)$$

Then, from pairs of Eqs. like (14.17) and (14.20) for three or more stations, simultaneous solutions can be achieved for V_z and V_m. This method has been tested for the nuclear atmospheric data taken at St. George, UT; Bishop, CA; China Lake, CA; and Lund, NV. Figure 14.3 shows the locations of these stations. A number of combinations of these stations were used as tests, some with three and some with

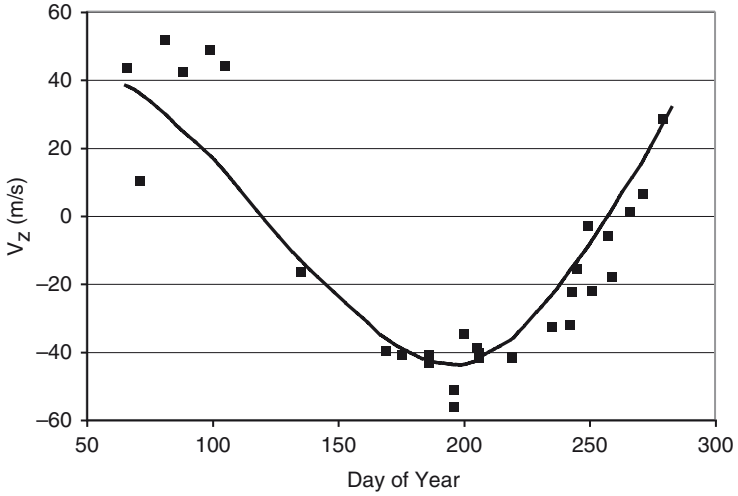

Fig. 14.13 Example of values of V_z determined from the multistation method (using St. George, Bishop, China Lake, and Lund) with S amplitudes vs. day of year. For comparison, the model SCI V_z is shown

four stations. In general, the solution for V_z appears to be about as satisfactory as those of the other methods previously described. Figure 14.13 shows an example solution for V_z compared with the model V_z vs. day number. The fit is not as good in the first part of the year as later and the data set available lacks points for a portion of the year. The RMS of the fit in this example is about 13 m/s.

Unfortunately, the method cannot determine values of V_m with any quality in these tests. This results from the fact that V_z is so much larger than V_m during most of the year that there is little leverage in determining the latter. Figure 14.5 illustrates this circumstance. In addition, it was found that two sets of station pairs were unable to recover values of V_z. These were examples in which two pairs of stations formed lines that were nearly parallel to each other in which case the solutions become indeterminate. However, this method offers the possibility of a more general solution for V_z than the earlier two more restricted methods.

Table 14.2 contains a comparison of the four methods discussed for wind determination. Each method is applicable to a particular observational circumstance and in some cases can provide confirmatory values. Methods have been developed to provide global wind specifications based upon various lower altitude measurements and upper atmospheric models. The G2S specification, described by Drob et al. (2003), is becoming the basis of atmospheric wind data used in propagation modeling. With the G2S data, one may obtain global profiles of wind and sound speed using inputs from operational numerical weather prediction and empirical models for the upper atmosphere. It may be an advantage to these methods to have key parameters, such as the SCI V_z, for comparison with G2S results or as values to use in the modeling.

Table 14.2 Methods for obtaining atmospheric parameters

Method	Requirement	Result	Example	Fit to model
S/T Signal Ratio	S and T signal amps. for single station, k, R_{st}	V_d of SCI	Fig. 14.11	16 m/s
E-W station pairs	S amps. for 2 stations to E and W of source, k	V_z of SCI	Fig. 14.12	14 m/s
Multiple Station	3 or more station S amps, k	V_z (potentially V_m) of SCI	Fig. 14.13	13 m/s
Travel Velocity	Single station, $\bar{V}$	V_z of SCI		Untested

14.6 Some Recent Studies Using IMS Data

The advent of the infrasound arm of the International Monitoring System (IMS), supporting the Comprehensive Test Ban Treaty (CTBT), provides a powerful new means of both (1) determining atmospheric structure and (2) establishing new ground-truth data sets. The data from the arrays, of course, also will support studies of many sources both of a natural type such as volcanoes, and of artificial types such as mining explosions. The IMS global network now consists of about 50 infrasound arrays which are in operation or soon to be. The ultimate system is designed to have 60 arrays.

There are several examples of such uses of the infrasound IMS data already in the literature. Le Pichon et al. (2005a) used one IMS array for studies of the atmospheric winds from observations of a volcano and a similar study was made by Le Pichon et al. (2005b). Le Pichon et al. (2006a) used observations of microbarom signals at six stations of the IMS for atmospheric structure studies. Le Pichon et al. (2006b) used multiple IMS stations for the study of earthquakes. Antier et al. (2007) also used observations of a volcano to study atmospheric structure.

It seems likely that this use of the IMS infrasound stations will continue to be very useful for future improvements in the knowledge of the atmosphere needed for infrasound propagation. In addition, new knowledge concerning source characteristics will become available and help to support the core mission of the CTBT.

14.7 Conclusions

The nature of the earth's atmosphere is responsible for the ability of infrasound waves to travel very large distances from a source to a receiver depending upon the size and character of the source. At the same time, the atmosphere can modify signals in a number of different ways. The primary effect on signals explored in this chapter is modification of amplitudes. However, there are other effects including modification of (1) celerity or average travel velocity (briefly documented here), (2) trace velocity or horizontal speed of the waves across an array, and (3) apparent azimuth of a signal's source. The last of these has been explored by Le Pichon et al. (2005a) and Le Pichon et al. (2005b). No doubt the character of a signal such as its frequency content is also modified by atmospheric transmission. This means that to

fully analyze a signal, it is desirable to have some knowledge of how to either remove the effects or understand their nature. In this chapter we have attempted to provide a methodology for the correction or normalization of amplitudes. In past infrasound research, the signals were largely accepted as detected, and for some purposes, this was sufficient. In the future there should be greater effort made in accounting for atmospheric effects on signals (Kulichkov 2010).

A key requirement for such understanding of the atmospheric effects is a knowledge of the structure of the atmosphere, particularly that of the temperature and wind, along the propagation path. Fortunately great progress has been made in this area of atmospheric research. The strong difficulty here is that the structure has large variability, both geographically and temporally. An interesting corollary of the atmospheric effects on signals is that signals may, in some circumstances, be used to obtain a parametric measure of the winds along the propagation path (Drob et al. 2010). In this chapter we have shown some methods for doing this. This ability may be useful to the technique of modeling the atmospheric structure; however, this connection has yet to be explored.

The advent of the International Monitoring system of the CTBTO offers the promise of much more research on the atmosphere through the interaction of multiple stations observing a source. Earthquakes, volcanoes, and bolides, in particular, seem to offer sources that can be observed at multiple arrays. The years ahead should be exciting ones in the area of infrasound-atmospheric interactions.

Acknowledgments This work was supported in part by the U.S. Department of Energy. We wish to dedicate this chapter to the late Jack W. Reed, who was instrumental both in observing much of the data used here and archiving them for future research.

References

American National Standards Institute (ANSI) (1983) Estimating airblast characteristics for single point explosions in air, with a guide to evaluation of atmospheric propagation and effects, ANSI S2.20-1983. American Institute of Physics

Antier K, Le Pichon A, Vergniolle S, Zielinski C, Lardy M (2007) Multiyear validation of the NRL-G2S wind fields using infrasound from Yasur. J Geophys Res 112:D23110. doi:10.1029/2007JD008467

Blanc E, Perez S, Issartel J-P, Millieres-Lacroix J-C (1997) Revue Scientifique et Technique de la Direction des Applications Militaires 17 23

Christie DR, Campus P (2010) The IMS infrasound network: design and establishment of infrasound stations. This volume, pp. 27–72

Davidson M, Whitaker RW (1992), Miser's Gold, Technical Report, LA-12074-MS, Los Alamos National Laboratory, Los Alamos, N.M

Drob Douglas P, Picone JM, Garces M (2003) Global morphology of infrasound propagation. J. Geophys. Res 108:ACL13.1–ACL13.12. doi:10.1029/2002JD003307

Drob DP, Meier RR, Picone JM, Garcés MM (2010) Inversion of infrasound signals for passive atmospheric remote sensing. This volume, pp. 695–726

Edwards Wayne N, Brown Peter G, ReVelle Douglas O (2006) Estimates of meteoroid kinetic energies from observations of infasonic airwaves. J Atmos Solar-Terrestrial Phys 68:1136–1160

Evers LG, Haak HW (2010) The characteristics of infrasound, its propagation and some early history. This volume, pp. 3–26

Garcés M, Willis M, Le Pichon A (2010) Infrasonic observations of open ocean swells in the Pacific: deciphering the song of the sea. This volume, pp. 231–244

Greene GE, Howard J (1975) Natural infrasound: A one year global study, NOAA TR, ERL-317-WPL-37

Kulichkov S (2010) On the prospects for acoustic sounding of the fine structure of the middle atmosphere. This volume, pp. 505–534

Le Pichon A, Blanc E, Drob D (2005a) Probing high-altitude winds using infrasound. J Geophys Res 110:D20104. doi:10.1029/2005JD006020

Le Pichon A, Blanc E, Drob D, Lambotte S, Dessa JX, Lardy M, Bani P, Vergniolle S (2005b) Infrasound monitoring of volcanoes to probe high-altitude winds. J Geophys Res 110:D13106. doi:10.1029/2004JD005587

Le Pichon A, Ceranna L, Garces M, Drob D, Millet C (2006a) On using infrasound from interacting ocean swells for global continuous measurements of winds and temperature in the stratosphere. J Geophys Res 111:D11106. doi:10.1029/2005JD006690

Le Pichon A, Mialle P, Guilbert J, Vergoz J (2006b) Multistation infrasonic observations of the Chilean earthquake of June 13. Geophys J Int 167:838–844

McCullough D, Novlan DJ (1977) Atmospheric structure white sands missile range, New Mexico, Part 6, 25–65 kilometers, DR-942. Atmospheric Sciences Laboratory, WSMR

McIntosh Bruce A (1982) Natural and unnatural infrasound, Herzberg Institute of Astrophysics, National Research Council Canada, SR-82-1

McKisic JM (1997a) Infrasound and the infrasonic monitoring of atmospheric nuclear explosions: An annotated bibliography, Phillips Laboratory Technical Report, PL-96-2282

McKisic JM (1997b) Infrasound and the infrasonic monitoring of atmospheric nuclear explosions: Supporting environmental data, Phillips Laboratory Technical Report, PL-97-2124

Mutschlecner J Paul, Whitaker Rodney W (1990) The correction of infrasound signals for upper atmospheric winds, in the fourth international symposium on Long-Range Sound Propagation, NASA Conference Publication, 3101, (1990)

Mutschlecner JP, Whitaker RW (2005) Infrasound from earthquakes. J Geophy Res 110:D01108. doi:10.1029/2004JD005067

Mutschlecner JP, Whitaker RW, Auer LH (1999) An empirical study of infrasonic propagation, Los Alamos National Laboratory Technical Report, LA-13620-MS. Los Alamos, NM

Norris D, Gibson R, Bongiovanni K (2010) Numerical methods to model infrasonic propagation through realistic specifications of the atmosphere. This volume, pp. 535–568

Reed JW (1969) Climatology of airblast propagations from Nevada Test Site nuclear airbursts Tech. Rep. SCRR-69-572, Sandia Laboratory, Albuquerque, NM

Reed JW (1992) Analysis of the accidental explosion at PEPCON, Henderson, Nevada, on May 4,1988. Propellants, explosives, pyrotechnics 17:88–95

Webb WL (1966) The structure of the stratosphere and mesosphere. Elsevier, New York, pp 141–145

Whitaker Rodney W, Mutschlecner J. Paul (2008) A comparison of infrasound signals refracted from stratospheric and thermospheric altitudes. J Geophys Res 113, doi:10.1029/2007JD008852

Whitaker RW, Noel SD, Meadows WR (1994) Infrasonic observations and modeling of the Minor Uncle explosive event, Sixth International Symposium on Long-Range Sound Propagation, National Research Council, Canada, 480–497

Chapter 15
Atmospheric Variability and Infrasound Monitoring

Catherine D. de Groot-Hedlin, Michael A.H. Hedlin, and Douglas P. Drob

15.1 Introduction

The modern era of infrasound studies was ushered in by the nuclear age, and the attendant needs to monitor the Earth and its atmosphere for clandestine nuclear tests. Monitoring requirements became more urgent with the initiation of the Comprehensive Nuclear Test Ban Treaty (CTBT), which sought to ban all nuclear tests. The treaty calls for the development of an International Monitoring System (IMS), consisting of radionuclide, seismic, hydroacoustic, and infrasound stations distributed nearly uniformly over the globe (PrepCom 1997; Christie and Campus 2010). The selection of infrasound as one component of the IMS was guided by the fact that low frequency acoustic energy can be detected at distances of hundreds to thousands of kilometers because attenuation decreases with decreasing frequency. Consequently, infrasonics – the study of infrasound – is an effective technology for monitoring Earth's atmosphere for nuclear explosions (Brachet et al. 2010).

The infrasound component of the IMS is still under construction, but will ultimately consist of a network of 60 infrasound stations that measure pressure at frequencies from roughly 0.01– 5 Hz (Fig. 15.1). An ancillary benefit of this network is that it detects a much broader range of atmospheric and geophysical phenomena than had previously been observed. Largely for this reason, infrasound is emerging as a means of conducting basic research into a variety of natural phenomena (Bass et al. 2006). Recent studies to have made use of infrasound have focused on disparate sources: meteors (Revelle et al. 2004; Revelle 2010; Edwards 2010), oceans swells (Garcés et al. 2004, 2010; Hetzer et al. 2010), surf noise (Arrowsmith and Hedlin 2005), tsunamis (Le Pichon et al. 2005c), earthquakes (Olson et al. 2003; Mutschlecner and Whitaker 2010), sprites which correlate with infrasound chirps

C.D. de Groot-Hedlin (✉)
Scripps Institution of Oceanography, La Jolla, CA,
92093-0225, USA
e-mail: chedlin@ucsd.edu

A. Le Pichon et al. (eds.), *Infrasound Monitoring for Atmospheric Studies,*
DOI 10.1007/978-1-4020-9508-5_15, © Springer Science+Business Media B.V. 2010

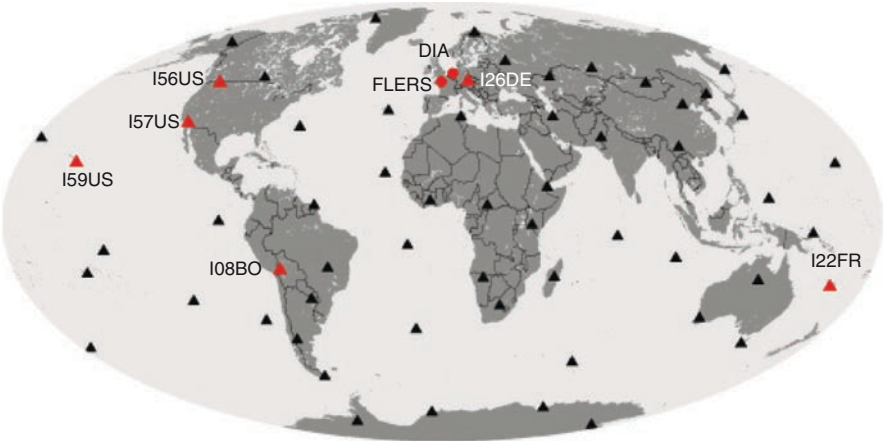

Fig. 15.1 The International Monitoring System (IMS) infrasound network, shown by *triangles* (Christie and Campus 2010). The IMS infrasound stations mentioned in this chapter are shown as *red triangles*. Other infrasound stations mentioned in the document are shown as *red circles*

associated with thunderstorms (Liszka and Hobara 2006; Blarc et al. 2010), and volcanoes (Le Pichon et al. 2005a; Matoza et al. 2006; Fee and Garcés 2007). Monitoring at these stations has also been used to infer atmospheric properties at high altitudes (Le Pichon et al. 2005a, 2006, 2010; Le Pichon 2005b).

Research is progressing on the use of infrasound as a warning system for natural hazards. Since acoustic energy propagates long distances, only a few observing sites may be required to monitor a broad area. The Acoustic Surveillance for Hazardous Eruptions (ASHE) program (Garcés et al. 2008) has examined the efficacy of using infrasound to detect explosive volcanic eruptions that can hurl ash into the air, creating hazards for nearby communities and for aircraft flying in the vicinity (Perkins 2003). Infrasound signals generated by small bursts of steam venting at Mount St. Helens have been detected at observing sites deployed under this program (Matoza et al. 2006; Moran et al. 2008). The value of volcano-acoustic monitoring in forecasting major eruptions has been documented (Garcés et al. 1999; Johnson et al. 2003). Further tests are in progress on detecting avalanche hazards using infrasound data (Scott et al. 2007).

The challenges of infrasound monitoring lie in the detection of signals in determining the location of their source, and in estimating the source size. However, each of these aspects of monitoring depends critically on propagation through the atmosphere. Temporal and spatial variations in atmospheric temperature and wind speed gradients affect the number and magnitude of infrasonic detections. For instance, it has been observed that sources that generate strong signals at a given time of day (Fee and Garcés 2007) or year (Le Pichon et al. 2002; Arrowsmith and Hedlin 2005) are detected weakly or not at all at other times, and that infrasound signals recorded at one location may not be detected nearby (e.g. de Groot-Hedlin et al. 2008). Seasonal variability in winds at high altitudes can affect the apparent source

azimuth (Le Pichon et al. 2005a; Le Pichon et al. 2005b), and hence, apparent location (Evers and Haak 2005). These observations, or lack thereof, depend on variations in atmospheric temperatures and wind. Thus, efforts to monitor anthropogenic and natural acoustic sources using infrasound rely on an understanding of the effect of spatiotemporal variations in the atmosphere on propagation. This chapter focuses primarily on acoustic propagation and its impact on monitoring capability.

Our success in infrasound monitoring efforts depends upon our understanding of acoustic propagation through an atmosphere that varies both spatially and temporally. Infrasound propagation is, thus, inextricably linked with atmospheric conditions, specifically, with wind and temperature variations. We begin the next section with some history of our understanding of acoustic propagation within the atmosphere and how advances in our knowledge of vertical gradients in winds and temperatures have led to further insight into sound propagation, and vice versa: how the study of sounds at audible frequencies has led to advances in our understanding of the atmosphere. We continue with a detailed explanation of spatiotemporal variations in atmospheric characteristics. The following section outlines a number of case studies that have shown the effects of seasonal and diurnal variations in the atmosphere on infrasound monitoring efforts, as well as other studies that have shown the effect of spatial variations in the atmosphere on infrasound detections. We conclude with a discussion on the impact of atmospheric variability on infrasound monitoring efforts, and conversely, how infrasound recordings can be used to improve our knowledge of the atmosphere.

15.2 The Atmosphere and Infrasound Propagation

15.2.1 A History of Our Understanding of Acoustic Propagation

Early efforts to understand long-range acoustic transmission through the atmosphere were advanced by studies of audible sound propagation (Evens and Haak 2010). Reynolds (1874) conducted an experiment to determine changes in sound intensity with wind direction, wind speed gradient, as well as the height of both the source and the listener. Equipped only with an anemometer to measure wind speeds and an electric bell to produce repeatable sounds, Reynolds and an assistant listened for sounds at elevations up to 25 ft. (about 8 m), with the intention of determining the extent to which sound propagation is controlled by refraction. They found that in the downwind direction, there was little difference in perceived sound intensities as a function of the observer's elevation, but at a distance upwind, sounds that were inaudible on the ground could be heard with much greater intensity by an observer at higher elevations, where winds are stronger. In this way, Reynolds demonstrated that acoustic energy is refracted by wind velocity gradients; sound bends downward in the direction of the wind, extending the range to which it may be heard, and bends upward, away from the ground, producing an acoustic shadow zone in the opposite direction. Reynolds (1874) also reasoned that sound is refracted by

vertical temperature gradients since sound velocity varies as the square root of the temperature. Consequently, acoustic waves propagating near the ground bend upward under standard atmospheric conditions in which temperature decreases with altitude. He later conducted an experiment that lent weight to this hypothesis (Reynolds 1876); sounds generated by pistol shots and by rockets that detonated charges of 12 oz (about 340 g) of gunpowder at a height of approximately 300 m were heard by observers at large distances from the source. Reynolds attributed this to the downward refraction of sound caused by a temperature inversion.

The studies explained several phenomena that had puzzled early observers. For instance, it had long been known that sounds are less intense during the day than at night. Reynolds (1874) argued that this was due to greater upward refraction of sound during the day resulting from a larger decrease in temperature with altitude. In addition, cases had been documented in which observers had seen but not heard the firing of cannons or guns. Samuel Pepys wrote of a yacht captain who fled at the sight of a naval battle between British and Dutch fleets in 1666, though he had not heard a sound (Ross 2000). Reynolds (1874) noted that guns might not be heard at a distance of about 500 m against a strong wind. In these cases, observers were located in a sound shadow created by the upward refraction of sound. The presence of sound shadows had significant effects in warfare; before reliable communications were available, the sounds of gunfire and cannons were often used to gauge a battle's progress. In several instances reported by Ross (2000), battles in the US civil war were lost when reinforcements were directed to join in combat when they heard the sounds of engagement. Unfortunately for the commanders, the strategy failed because the backup forces were located in sound shadows and so they arrived too late or not at all.

Reynolds' studies described sound propagation within the troposphere – the lowest layer of the atmosphere where wind and temperature gradients were known from balloon sonde measurements – to distances of tens of kilometers. Anomalous patterns of sound detections at larger distances required an understanding of winds and temperatures at higher altitudes. By the early last century, very loud sounds generated by explosions or gunfire were known to produce zones of audibility alternating with sound shadows, so that an observer hundreds of kilometers from an explosion might hear it clearly, while observers much nearer would not. During World War I, it was recognized that there was a zone of audibility in the region nearest a battlefield, ringed by a zone of silence, with a second full or partial ring of audibility outside it. These anomalous sound patterns were observed to vary seasonally, with sounds of gunfire in northwestern Europe propagating to great distances to the east in winter and to the west in summer (Whipple 1935). The fact that these effects were due to the distribution of wind and temperature at high altitude was only a hypothesis at that time (Nature 1922).

Shortly after World War I, a decision was made to conduct experiments in which aural observations were augmented by instrumental recordings of explosions, to allow for accurate measures of travel time. To that end, arrangements were made for recordings of explosions in Oldebroek, the Netherlands (Nature 1922, 1923) and gunfire at a site near London, England (Whipple 1931, 1934). Gutenberg (1939) used gunfire from

United States Navy ships' offshore target practice near southern California as sound sources in a long-range acoustic propagation study. These studies confirmed the presence of acoustic shadows between zones of audibility, and showed that sound detections in the outer zones of audibility were delayed with respect to sounds in the inner region. Only sounds in the inner ring appeared to correspond to direct waves from the origin to the detector (Whipple 1935; Gutenberg 1939). Whipple (1931) conducted an experiment involving the use of small arrays of microphones to derive the arrival's angle of incidence, and thus, to estimate the sound velocity at the turning point. In this way, he inferred the presence of a zone of increasing sound velocities above the troposphere to altitudes of 50–60 km. At the time, these long-range sound propagation experiments were the only way to derive the temperature distribution in the upper atmosphere (Whipple 1934). These experiments also confirmed the annual variability in acoustic detections down to infrasound frequencies.

15.2.2 Application to Infrasound Propagation

The derivation of atmospheric temperatures from studies of long-range propagation of audible sounds was limited to the troposphere and stratosphere because, as first shown by Schrodinger's study on classical absorption (Schrodinger 1917), sound transmission at heights above 60 km is too severely attenuated for observation. Further studies have shown that attenuation can be categorized in terms of classical losses, which involve the irreversible transfer of kinetic energy from the acoustic wave into heat, and molecular relaxation losses, involving the excitation of the constituent gas molecules within the air (e.g. Evans et al. 1972; Ejakov et al. 2003). The total atmospheric absorption increases approximately with the square of the frequency over a wide range of altitudes (de Groot-Hedlin 2008), thus the atmosphere acts as a low pass filter to acoustic energy. At sea level, a 1 Hz signal undergoes approximately 0.002 dB of absorption over a path length of 100 km, increasing gradually to about 0.05 dB/100 km at 50 km altitude (Sutherland and Bass 2004), characteristic of turning altitudes within the stratosphere. By comparison, an audible 100 Hz signal is attenuated by nearly 200 dB/100 km at 50 km altitude. Attenuation increases more rapidly at higher altitudes, supporting the use of infrasound frequencies to investigate sound speeds within the upper atmosphere.

The early sound experiments demonstrated that acoustic propagation is controlled primarily by winds and the adiabatic sound speed, which varies as the square root of the air temperature (Mutschlecner and Whitaker 2010). Since then, infrasound studies have confirmed that acoustic energy is ducted between the ground and the upper atmosphere, allowing infrasound waves to propagate to distances of hundreds to thousands of kilometers. Infrasound arrivals may be classified into three types, tropospheric, stratospheric, or thermospheric, depending on whether they arise from ducting between the ground and the lower, middle, or upper atmosphere. Tropospheric infrasound arrivals propagate within the lower atmosphere through transient ducts created by

temperature inversions or the tropospheric jet stream. Stratospheric arrivals, resulting from ducting between the ground and stratopause, are governed by seasonal variations in east–west (zonal) stratospheric winds. In the northern hemisphere, stratospheric winds flow to the west in summer and to the east in winter, enhancing ducting along the wind direction and diminishing propagation along the opposite bearing. Thermospheric arrivals, resulting from downward refraction by the steep sound speed gradients of the upper atmosphere, are always predicted, but are quite rarely observed due to high acoustic absorption within the thin upper atmosphere (Sutherland and Bass 2004; Norris et al. 2010).

Infrasound propagation is often represented by ray tracing, as illustrated in Fig. 15.2 (see also Fig. 15.4 in Evers and Haak 2010), which shows ducting within the stratosphere and thermosphere for sound and wind speeds derived from the Naval Research Laboratory Mass Spectrometer and Incoherent Scatter Radar Model-00/Horizontal Wind Model-93 (NRLMSISE-00/HWM-93) empirical models (Picone et al. 2002; Hedin et al. 1996) for a summer date (July 21, 2006) in the northern hemisphere. Infrasound signals can be observed at the surface when the combined sound speed and wind speed (the effective sound speed) is greater than the effective sound speed on the ground. Thus, stratospheric ducting is predicted to the west for this example, and thermospheric ducting is predicted in all directions. Tropospheric returns are not predicted in this case as there is no temperature inversion. The rays were computed for a source at 100 m altitude, using equations derived for 3-D ray tracing through an advected medium (Garcés et al. 1998). Although ray methods offer a high frequency approximation to acoustic propagation, their value in modeling low frequency infrasound propagation has been confirmed by many studies (e.g. Ottemöller and Evers 2008; de Groot-Hedlin et al. 2008; Evers and Haak 2005; Le Pichon et al. 2005a).

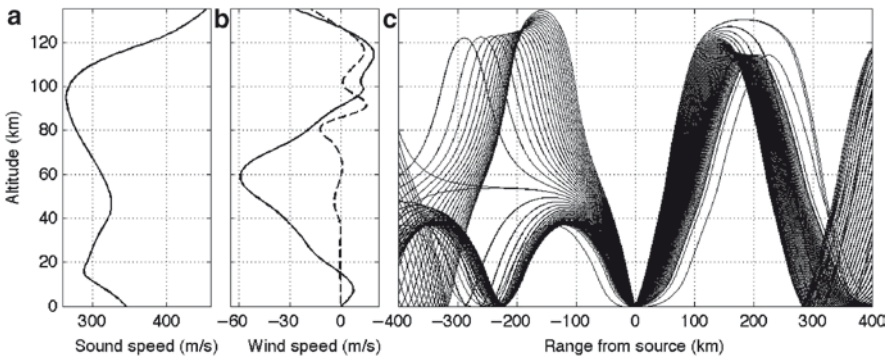

Fig. 15.2 (**a**) 1D sound speed profile. (**b**) Zonal (*black*) and meridional (north–south, *dotted*) wind speed profiles. Profiles are based on climatological predictions for a source at 33.2°N, 106.5°W on July 21. (**c**) Ray diagram showing refraction of sound in an advected medium, for 1D sound and wind speed profiles shown in (**a**) and (**b**). The source is at 100 m altitude. Only rays that reach the ground are shown. Rays are refracted within the stratosphere and thermosphere and undergo reflection at the ground. Regions in which rays are refracted upward before reaching the ground are shadow zones

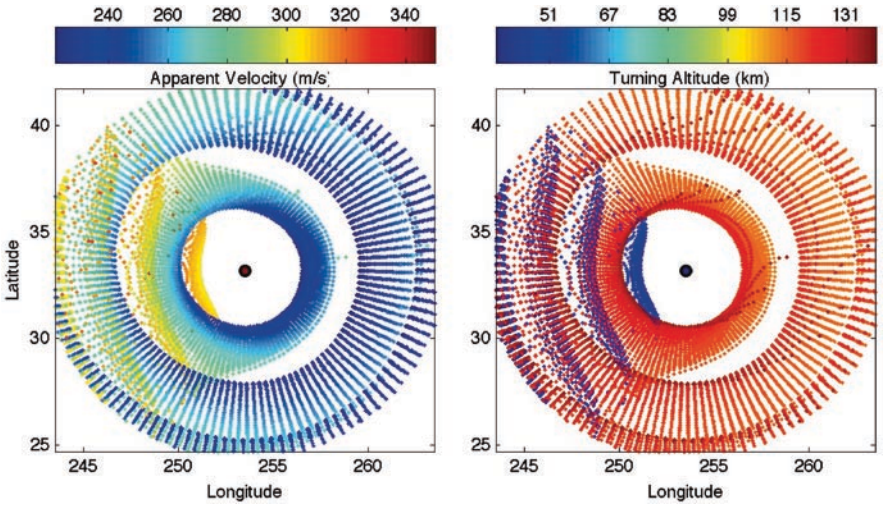

Fig. 15.3 Maps of ray endpoints that reach the ground for the atmospheric profiles shown in Fig. 15.2. Results are shown up to a distance of 990 km for a source at 33.2°N, 106.5°W, at an elevation of 100 m. The source location is marked by a *circle* at the center. The ray endpoints are shown color-coded according to apparent velocity (*left*) and turning point altitude (*right*)

Ray-tracing over a uniform series of azimuths and declination angles from the source highlights regions where rays intersect with the ground surface (Fig. 15.3) and emphasizes spatial variability in predicted signal characteristics. Rays were launched at equal increments in azimuth and declination, thus the density of ray endpoints to reach the ground is indicative of signal strength and hence detectability. Apparent velocities (the distance from the source divided by the travel time) are plotted to emphasize the difference between stratospheric and thermospheric returns. The alternating zones of ensonification and shadow zones for stratospheric arrivals, first noted during World War I, are evident to the west. As shown, stratospheric arrivals to the west of the source would be followed by thermospheric arrivals.

Ray theory relies on a high frequency approximation to wave propagation. That is, its use assumes that sound speeds vary on a scale length much larger than the propagation wavelength. This approximation starts to break down at infrasonic frequencies for typical atmospheric conditions, where sound speed gradients of 4 m/s per km of altitude are common. A more complete description of infrasound propagation includes finite wavelength effects like diffraction, scattering (Embleton 1996), and surface waves (Attenborough 2002), and temporal effects like turbulence and propagating gravity waves. Fortunately for the purposes of infrasound monitoring, these effects lead to a penetration of acoustic energy into shadow zones at amplitudes much greater than that predicted by ray theory (Embleton 1996; Attenborough 2002). Thus, infrasound detections have been reported at distances of up to tens of kilometers within areas predicted by ray theory to be shadow zones (e.g. Ottemöller and Evers 2008; de Groot-Hedlin 2008; Kulichkov et al. 2002).

15.3 Spatiotemporal Variability of the Atmosphere

In order to understand the spatiotemporal variability of infrasound, it is useful to describe the temperature structure of the atmosphere, followed by its general circulation, the seasonal modulations, the day-to-day variations caused by planetary waves and eddies, the migrating and nonmigrating tides produced by solar heating, and internal gravity waves. Each of these dynamical processes influences acoustic propagation in one way or another. More specifically, the seasonal variations of infrasound propagation characteristics are determined by corresponding variations in general circulation. Superimposed on these variations are day to day changes caused by planetary waves and eddies, commonly referred to as weather. It is also known that local time variations of the thermospheric ducting characteristics result from migrating solar tides. At the smallest scales, the gravity wave fluctuations cause scattering of the acoustic wave energy into shadow zones, as well as into and out of various atmospheric ducts. Other processes such as land/sea breezes, marine/nocturnal inversion layers, and evolution of the planetary boundary layer (PBL) are also known to be relevant for infrasound propagation.

This section seeks to answer the following questions: Why does atmospheric temperature vary with altitude? What causes the winds to vary? How does the spatiotemporal variability of the atmosphere (from the ground to space) affect acoustic propagation? In this section we will work our way from the largest spatiotemporal scales to the smaller spatiotemporal scales. Although relevant to the attenuation of infrasound at thermospheric altitudes, details regarding atmospheric composition are not discussed. The following academic texts on the physics of global atmospheric general circulation and related topics are recommended: Holton (1992), Chamberlain and Hunten (1987), Andrews et al. (1987), and Brasseur and Solomon (1986).

With respect to the observational specification of the atmospheric state for describing infrasound propagation, the atmosphere's overall structure can typically be described by climatologies such as the COSPAR International Reference Atmosphere (CIRA) (Fleming et al. 1988), and the afore mentioned NRLMSISE-00 and HWM-93 empirical models (Drob et al. 2010). For applied work, the day-to-day variability of planetary waves and tidal oscillations can be described well in a "nowcast" or "hindcast" sense by operational numerical weather prediction data assimilation systems. Examples are NOAA Global Forecast System (GSF) (Kalnay et al. 1990), NASA Goddard Earth Observing System (GEOS5) (Bloom et al. 2005), the European Centre for Medium Range Weather Forecasting (ECMWF) (Molteni et al. 1996), and Navy Operational Global Atmospheric Prediction system (NOGAPS) (Hogan and Rosmond 1991). These systems provide specifications at 6 h real-time update cycles for altitudes up to between 35 and 80 km, limited by available meteorological data altitude coverage. A hybrid approach which combines empirical climatologies with these specifications to create a seamless global ground-to-space atmospheric specification from 0 to > 150 km for infrasound propagation modeling was developed by Drob et al. (2003). A number of other ground-to-space atmospheric models are being developed for general purpose use by the scientific community (Akmaev et al. 2008; Richter et al. 2008).

Mesoscale weather models such as the Coupled Ocean Atmosphere Mesoscale Prediction System (COAMPS) (Hodur 1997), the NOAA rapid update cycle (RUC) (Benjamin et al. 2004), and the Weather Research and Forecasting (WRF) system (Skamarock et al. 2005) are receiving much attention by the operational and atmospheric research communities. Although limited to the first 25 km of the atmosphere, observational coverage and physical knowledge are sufficient to provide accurate specifications with horizontal resolutions to better than 10 × 10 km over most geographic regions. Operational specifications for regions such as the continental United States are available on 1-h update cycles. Effects such as the diurnal cycle of sea breezes, upslope and down slope winds, and topographically induced wind storms are resolved by these systems. Even some large scale gravity waves, such as those generated by flow over topography can be resolved deterministically by these models. At present, however, the internal spectrum of gravity waves from 0 to 120 km relevant to infrasound propagation physics can only be described parametrically, i.e., in a statistical sense (see for example Fritts and Alexander 2003).

15.3.1 Vertical Temperature Structure

To describe the processes relevant to infrasound propagation, it is useful to start by considering the globally averaged (spherically symmetric) temperature profile. The temperature profile for the US standard atmosphere NASA-TM-X-74335 (1976) is shown in Fig. 15.4 (see also Fig. 15.2 in Evers and Haak 2010). This vertical structure is effectively the result of the radiative balance between outgoing

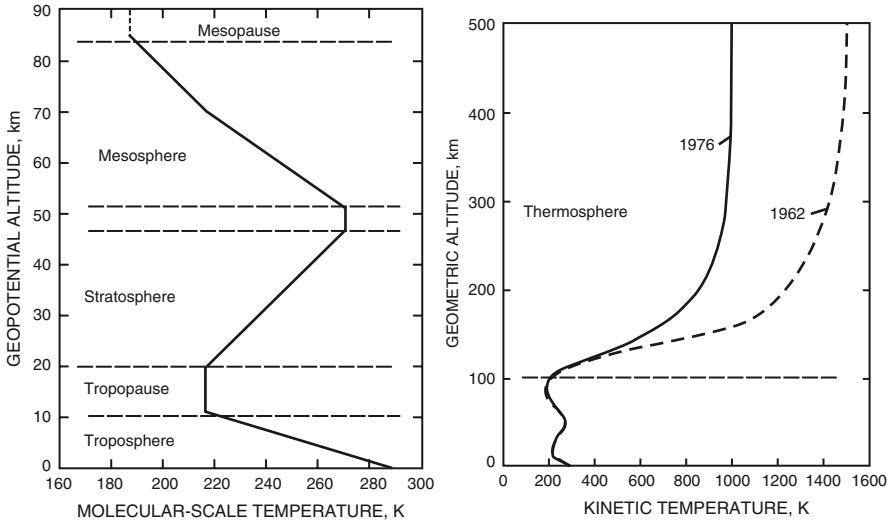

Fig. 15.4 Basic structure from the US Standard atmosphere (independent of latitude, longitude, or season)

infrared (IR) thermal cooling and the incoming solar ultraviolet (UV) heating process. This temperature structure provides the rationale for the atmospheric nomenclature, "sphere" for the specific layers – troposphere, stratosphere, mesosphere, and thermosphere, and "pause" for the interfaces between those layers – tropopause, stratopause, and mesopause . On average, this vertical profile is responsible for the formation of two basic infrasound ducts, one from the stratospheric temperature inversion and one from the thermospheric increase.

The fundamental heat source to the lower atmosphere is the absorption of solar energy by the surface followed by reradiation in the infrared into the lower thermosphere. This heat is transported away from the lower troposphere by convection. At mean sea level, the average temperature is 288.2 K, corresponding to a mean adiabatic sound speed (c) of 340.4 m/s ($c^2 = 401.875\ m^2 s^{-2} K^{-1} T$, where T is the temperature in degrees K. This is a very good approximation below 95 km.). As altitude increases and the atmospheric mass density decreases, the temperature decreases with an average adiabatic lapse rate of approximately 6 K/km. Increased absorption of solar UV radiation, itself a product of UV absorption, causes the temperature gradient to change sign above the tropopause. The stratopause temperature maximum occurs roughly at the altitude of maximum absorption; about 270 K at 50 km corresponding to an average adiabatic sound speed of 329.4 m/s. Above this altitude, temperature decreases again as O_3 concentrations decrease. This is further accelerated by the increase of infrared cooling by CO_2, resulting in the temperature minima of 186.9 K at the mesopause. This corresponds to an adiabatic sound speed of 186.9 m/s. In the thermosphere, the effects of the absorption of extreme ultraviolet (EUV) radiation by various atomic and molecular species [e.g. O, O_2] result in an isothermal temperature maximum beginning at about 300–500 km. The maximum temperature ranges from 600 to 1,200 K (c = 491– 694 m/s), depending on the phase of the 11 year solar Sun spot cycle.

15.3.2 General Circulation

The dynamics of the atmosphere, which result from the fact the Earth is a tilted, rotating, uneven sphere, create a rich complexity that is observed in the spatiotemporal variability of infrasound propagation (Hauchecorne et al. 2010). Atmospheric dynamics are the result of the uneven diurnal and seasonal distributions in radiative heating and cooling. Seasonal and latitudinal variations determine the overall nature of the general circulation patterns; the many surface variations in longitude result in the weather systems (i.e., synoptic scale planetary waves) and, due to solar heating under rotation, the diurnal (local-time) variations of the vertically propagating migrating tides.

First we consider the zonally averaged features of the atmosphere's general circulation (i.e., the average of the wind fields around a circle of constant latitude). Salient features of the Earth's general circulation are surface currents, such as the trade winds, the tropospheric jet streams, and the stratospheric wind jets. The average tropospheric jet stream zonal velocity is about 40 ± 20 m/s, while the average zonal velocity of the stratospheric wind jet is 80 ± 40 m/s. The zonally averaged meridional (north–south) winds are on the order of a few m/s, while the planetary scale vertical

winds are on the order of cm/s. Thus, the vertical winds are irrelevant to infrasound propagation, but the meridional winds are significant when considering departures from the zonal average.

The surface temperature is maximum at the equator and decreases toward the poles. Near the surface, trade winds are driven by upward and poleward motions of air heated at the surface in the tropics. These maintain the low and midlatitude surface westerlies (west to east). This advection carries large amounts of water vapor toward the equator producing enhanced rainfall there, where the additional latent heat supplies additional drive to the low latitude general circulation cells. Similar processes produce corresponding polar tropospheric circulation cells, along with the midlatitude (Ferrel) circulation cells. These circulation cells are illustrated in Fig. 15.5. The Hadley cell is highly asymmetric with respect to the equator in the winter and summer. The winter hemisphere cell dominates with strong cross equatorial transport into summer hemisphere near the surface. These dynamical processes primarily influence surface wind noise at the IMS infrasound arrays.

The latitudinal temperature gradients, which result from differential solar heating of the globe, are responsible for the tropospheric and stratospheric jet streams. The structure of the tropopause varies with latitude and season – at the equator, the tropopause is located at an altitude of 18 km with a minimum temperature of 190 K,

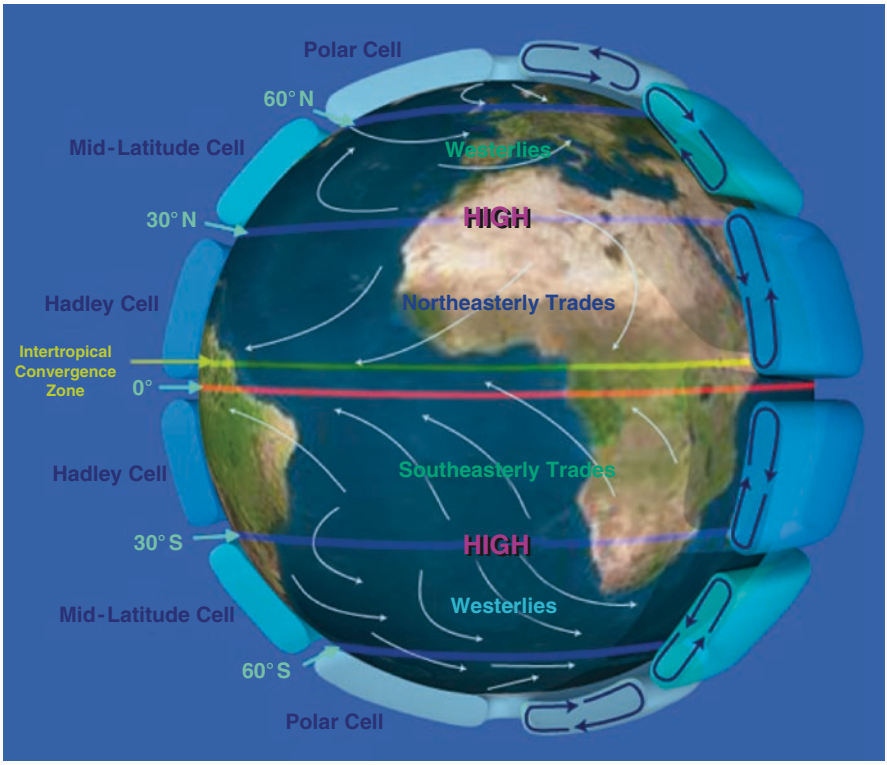

Fig. 15.5 Tropospheric general circulation cells

while at the polar latitudes it is lower and colder, located at 8 km with a minimum temperature of 220 K. This temperature distribution drives the tropospheric jet streams in both hemispheres, with the strongest one located furthest equatorward during winter. A split jet stream is occasionally observed, typically in August or September in the Southern Hemisphere.

The meridional temperature structure of the stratosphere is somewhat different than in the troposphere. The lower stratosphere has a temperature minimum at the equator with a maximum at the summer pole and in the midlatitude of the winter hemisphere. Above about 35 km, the temperature decreases uniformly from the summer pole to winter pole in accordance with radiative equilibrium considerations; however, eddy (planetary wave) motions can induce substantial local departures in the winter stratosphere and during both solstices in the mesopause as we shall see in the next section. The net radiative heating has a strong seasonal dependence with maximum heating in the summer hemisphere, and maximum cooling in the winter hemisphere. The result is a diabatic circulation – rising in the summer hemisphere, meridional drift to winter hemisphere, with sinking downward there. Under the influence of Coriolis torque from the Earth rotation, westerlies (eastward winds) are produced in the winter hemisphere and easterlies (westward winds) in the summer hemisphere in approximate balance with the meridional pressure gradient. Figure 15.6

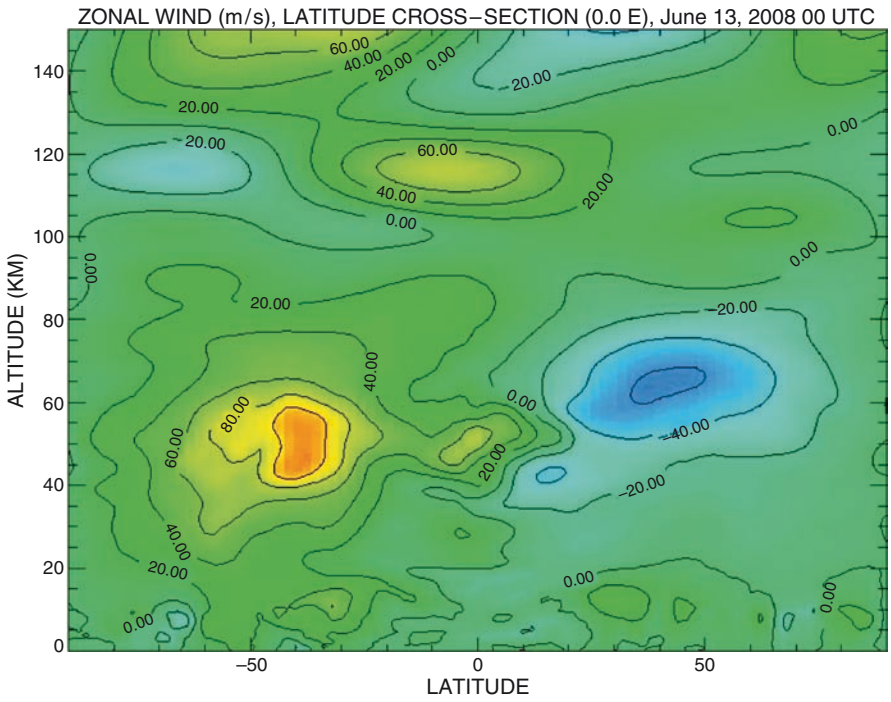

Fig. 15.6 A typical Northern hemisphere summer cross section of the zonal winds field at a single longitude, taken from the G2S model (Drob et al. 2003)

illustrates a typical slice of the zonal wind field during Northern Hemisphere Summer conditions. There is also a diabatically induced circulation during the equinoxes with upward motion in the equatorial region and poleward drift in both the spring and autumn hemispheres.

The observed latitudinal temperature distribution in the mesosphere arises from a balance between the net radiative drive and the heat transport plus local temperature changes produced by these motions. Owing to gravity wave drag, the latitudinal temperature distribution and wind jets in the mesopause region actually reverse from what they are in the stratosphere during the solstices. The summer mesopause is actually colder than the winter mesopause. As a result of these processes, two counter propagating wind jets of a slightly weaker magnitude close off and form above the stratospheric jets.

A rigorous mathematical description of the geophysical fluid dynamics of the general circulation patterns including various approximation to primitive hydrodynamic equations such as the hydrostatic balance, the geostrophic approximation, and gradient winds can be found in for example Holton (1992), Chamberlain and Hunten (1987), Andrews et al. (1987), and Brasseur and Solomon (1986).

15.3.3 Planetary Waves – Synoptic Scale Meteorology

The next level of detail in describing the atmospheric variations that influence infrasound propagation are the global asymmetries and anomalies caused by stationary waves, freely propagating planetary waves, and eddies (Hauchecorne et al. 2010). Commonly referred to as the synoptic scale motions or terrestrial weather, these are generated by nonlinear dynamical instabilities, land/sea contrasts, and interaction of the general circulation with topography. These waves and gyres have global wave numbers (number of waves at a given latitude) between 1 to 5 and periods from 3 to 16 days. They cause the day-to-day variability of observed infrasound propagation characteristics (e.g. Le Pichon et al. 2002, 2005a). Vertical structure in these waves may also result in waveform complexity from the infrasound analog of seismic low-velocity zones. Over the length scale of these waves, the pressure gradients are *nearly* balanced by geotropic winds arising from the Coriolis force. At mid-latitudes, consideration of the lateral (horizontal) pressure gradient and the Coriolis forces dictates that the wind patterns associated with synoptic scale disturbances flow counter clockwise around regions of low pressure in the Northern hemisphere; and clockwise around regions of high pressure. The converse of this relationship holds in the southern hemisphere.

The large scale wave features relevant to infrasound propagation are the Rossby/Planetary waves, which are free or normal mode oscillations of the atmosphere. These extratropical planetary waves result from longitudinal variations in radiation, convection or latent heating, nonlinear cascades from shorter scale disturbances, and mechanical disturbances from topographic variations. These waves have a westward phase velocity with respect to Earth's atmosphere. In the equatorial region, in addition

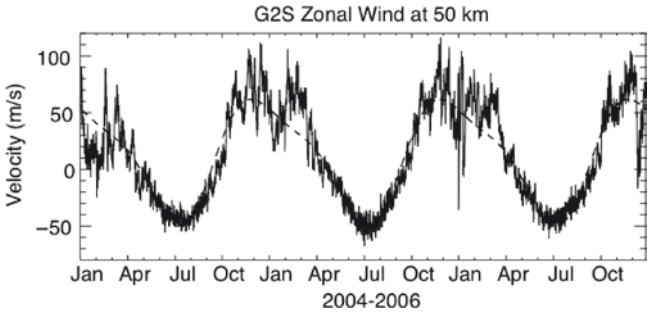

Fig. 15.7 The zonal (east–west) wind field at 50 km above a typical midlatitude location (33°N) as given by the HWM-93 (*dashed*) and G2S model (*solid*)

to Rossby waves, Kelvin waves that propagate eastward with respect to the atmosphere are possible. These equatorial waves often have shorter periods and higher wave numbers relative to midlatitude planetary waves. Again, for a rigorous discussion, we refer the interested reader to the general atmospheric science texts.

Owing to the fact that the planetary waves only propagate westward, they can only propagate vertically from the troposphere into the stratosphere and mesosphere when zonal mean winds are eastward. As explained in Holton (1992), "The vertical propagation of stationary waves can occur only in the presence of westerly winds weaker than a critical value that depends on the horizontal scale of the waves." Thus, large amplitude planetary waves are only observed in the stratosphere in the winter hemisphere. This is why the flow becomes zonally symmetric in the summer hemisphere. From the observational perspective of single site location, an example of a multiyear time series of the zonal wind field at an altitude of 50 km above a typical midlatitude station (e.g. I56US) is shown in Fig. 15.7. Note that during Northern hemisphere summer, departures from climatology are infrequent, while during the winter time departures can be significant. This is relevant when comparing results from infrasound propagation calculations against observations using either climatology or an actual specification of the atmospheric state of a given day, i.e., climatology may produce reliable results in the summer and equinoxes, but not in the winter. Owing to more continental land masses, the prevalence of vertically propagating planetary waves is more significant in the northern hemisphere.

15.3.4 Migrating and Nonmigrating Solar Tides

The migrating solar tides are coherent global-scale atmospheric waves (disturbances), which propagate westward with the apparent motion of the Sun at periods that are harmonics of a solar day. These are the dominant mechanism of the meteorological variability in the mesosphere and lower thermosphere (MLT). These tidal oscillations are the result of solar EUV heating of H_2O and O_3 by absorption in the IR and O_3

absorption of UV radiation in the stratosphere. This results in repeatable 24 and 12 h oscillations in the MLT (Forbes 1995; Hagan 1996). In the lower-thermosphere, there is an in situ component forced by O_2 absorption by the Schuman-Runge bands and continuum, which gives rise to both evanescent and freely propagating modes.

The amplitude of these tidal oscillations increases with altitude as they propagate from the source region into regions of ever-decreasing neutral density. The strongest tidal signatures are found in the MLT between 80 and 120 km as observed in all variables by satellite and ground-based instruments. As a result of their repeatability, the salient features of these global scale oscillations can be reasonably well parameterized by empirical and theoretical models. In addition, there is a quadrature relationship between the temperature, zonal, and meridional wind velocity perturbations. The diurnal tide (24-h harmonic) dominates near the tropics, where the meridional wind has a maximum at ± 22° with a vertical wavelength of ~20 km and an average amplitude of 30–50 m/s at 100 km depending on season. The migrating diurnal tide has a maximum during the spring and fall equinoxes when the solar heating is symmetric with respect to the equator. This tide begins to dissipate above 115 km. The semidiurnal oscillations (12-h harmonic) dominate at midlatitudes (± 42°), with peak amplitudes of approximately 30 m/s at 100–115 km. The semidiurnal tide propagates deeper into the lower thermosphere due to the longer vertical wavelength ~60 km. The amplitude of all of these tides also exhibits a fair amount of some day-to-day variability as a result of nonlinear wave-wave and wave-mean flow interaction.

These waves result in hourly (diurnal and semidiurnal) variations of the infrasound propagation characteristics as shown by several authors; e.g. Donn and Rind (1972), Rind and Donn (1975), Rind (1978), Garces et al. (2002), and Le Pichon et al. (2005a). Figure 15.8, from Le Pichon et al. (2005a), presents the diurnal variations

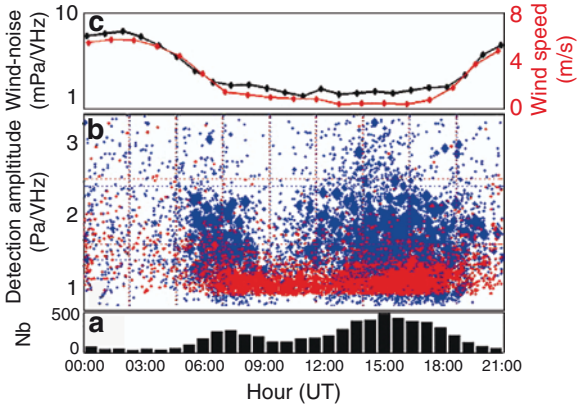

Fig. 15.8 Statistics on the number of detections from June 2003 to May 2004 compared with wind-noise variation measured at I22FR. (**a**) Histograms on the number of detections vs. time of day. (**b**) Measured amplitude of signals for Lopevi (in *blue*), and Yasur (in *red*) vs. time of day. (**c**) Diurnal variations of infrasound noise level at 1 Hz (*black*) and hourly averaged wind speed (in *red*) measured at the central array element (from Le Pichon et al. 2005a)

of the number of detections from June 2003 to May 2004 compared with wind-noise variation measured at I22FR. Statistics are correlated to the daily fluctuations of the wind-related noise. The highest value of the noise level at 1 Hz is obtained during daytime when the local wind speed reaches ~5 m/s (0000 UT corresponds to 1100 local time). As a result, due to the low amplitude of the signals, the number of detections significantly decreases during the daytime. There is no signal from Lopevi from 0900 to 1200 UT, though the wind-noise remains at a low level.

Recent upper atmospheric research observations indicate that there are also significant nonmigrating tidal oscillations; see for example Forbes et al. (2003) and Oberheide et al. (2006, 2007). These tidal oscillations can be thought of as longitudinally dependent enhancements of the migrating tides, which result from the longitudinal variations in the latent heating forcing function via the distribution of O_3 and H_2O. The predominant nonmigrating tidal mode is a diurnal eastward propagating oscillation, with global wave number 3. The temperature perturbations resulting from this oscillation can be on the order of 16 K at 86 km, peaking during equinox. At 110 km near ± 30° latitude, the semidiurnal perturbations can be on the order of 25 K. Currently, the significance/influence of these tidal modes on infrasound propagation characteristics remains unknown.

15.3.5 Gravity (Internal Buoyancy) Wave Spectrum

The last atmospheric phenomena relevant to infrasound propagation physics is the internal gravity wave spectrum (Mikumo and Watada 2010; Lott and Millet 2010). These internal waves result from the stratification or buoyancy of the atmosphere. They are produced by a variety of sources in the lower and middle atmosphere, including cumulous convection, flow over topography, and fluid instabilities. A typical gravity wave has a vertical wavelength that ranges from 5 to 15 km, a horizontal phase speed up to 80 m/s, a horizontal wavelength between 10 to 200 km, and periods which range from 5 to 120 min. There are three subclasses of gravity waves, from the low to high frequencies depending on the scale of ω (intrinsic frequency) to the Brunt–Väisälä frequency (high frequency limit) and the Coriolis frequency (*f*) (low frequency limit): acoustic gravity waves, gravity waves, and inertio-gravity waves.

Gravity waves are known to be responsible for internal scattering of acoustic energy into and out of ducts, as well as into the classical zones of silence. The vertical wavelengths and amplitudes of these will also cause infrasound waveform complexity via the transient low velocity zones that they generate. Recent theoretical studies on this subject have been presented by Chunchuzov (2004) and Ostashev et al. (2005). As mentioned earlier, gravity wave dynamics also affect the temperature structure and general circulation of the middle atmosphere, transporting energy and momentum. They also contribute to turbulence and mixing. The basic linear theory of these waves is described in for example Holton (1992). See Fritts and Alexander (2003) for a complete review of the current understanding of atmospheric gravity waves – the main points are summarized here.

The primary sources of gravity waves are topography, convection, wind shear, and nonlinear wave-wave instabilities. Topographic gravity waves from flow over topography have horizontal wavelength from 10 to 100 km. The waves may vary from nearly undetectable to large amplitude waves that may even become dynamically unstable (nonlinear). The typical phase speeds are near zero, with the vertical wavelengths governed by static stability and the background mean flow. As noted by Fritts and Alexander (2003), the horizontal velocity and temperature gravity wave variances are 2–3 times higher over significant topography compared to the plains and oceans; independent of other sources and 5 times higher than those regions have no obvious meteorological sources. There is some controversy with respect to the physical mechanisms of the convective generation of gravity waves (i.e., by storm fronts and cumulous convection). Observations of high ω gravity waves show close correspondence with deep convective clouds. Convectively generated waves have a complete range of phase speeds, frequencies, and wavelengths. Microphysical generation mechanisms proposed depend on the local shear, vertical wind profile, and time dependence of latent heating. Shear generation is predominantly propagation away from shear layers and Kelvin-Helmholtz instabilities. These processes are not well understood as today's theories for this mechanism require computationally intensive nonlinear, numerical simulations. Yet another generation mechanism known to generate gravity waves is geostrophic adjustment. In this mechanism, gravity wave excitation occurs from the restoration of significant perturbations to the global balance flow, which then relaxes to a new balance state by the redistribution of momentum, energy, and the radiation of excess energy via gravity waves. For this, the tropospheric jet stream could be one possible source; frontal-genesis, and baroclinic instability are other examples of unbalanced flow which may be sources for intertio-gravity waves. For these sources, the vertical scales – λ_z greater than a few or more, $\lambda_{x,y}$ approximately 10–100 times larger, periods on the order of a hour or so.

Relevant to the influence of gravity wave on infrasound propagation is the question of whether there is a continuous spectrum of gravity waves or a discrete number of them? There is observational evidence for both. Development of the characteristics of the gravity wave spectrum as a function of altitude is an important consideration for both infrasound propagation modeling as well as the atmospheric science community in general. For the latter, gravity waves excite a net body force that has the same sign as the local wind shear. For example, topographically forced gravity waves exert a westward drag above the tropospheric jet peak winds. In the mesosphere, gravity waves exert a force that is generally opposite to the background winds and that is strong enough to influence the atmospheric circulation and structure, causing the reversal of the zonal mean and driving the mean meridional transport. This circulation leads to a warm winter mesopause and a cold summer mesopause (i.e., reversal of the latitudinal temperature gradient). In these processes, gravity wave variability or blocking via wave-wave and wave-mean flow interactions as a function of latitude, season, and altitude are all important consideration in these processes.

As a consequence, there are at least eight gravity wave parameterization schemes proposed or implemented in atmospheric general circulation models. Specification of the characteristics at the source level, wave propagation (spectral evolution) as a

function of height, and calculation of effects (forcing/drag) on the background atmosphere are all taken into account. Typically the vertical variation of the spectral shape and amplitude are physically characterized by wave saturation conditions. This includes the variations with space and time, as well as the various wave components (k, m, and ω). The energy spectrum has the general form $E(\omega) = \omega^{-5/3}$. Doppler shifts of the spectrum, both internal and external, are considered by the best theories. Measurement of all of the parameters and validation of the theories is somewhat challenging, but not impossible. Again see Fritts and Alexander (2003) for detailed references and discussion. Climatologies and statistics have been developed from Space Based observations throughout the atmosphere, radiosonde profiles, rocket soundings, lidars, radars, and aircraft measurements. The observations show strong seasonal and latitudinal variations; these are related to source function and background wind variation filtering effects.

Lastly, at the very smallest scale as an internal dynamical phenomena, the presence of upward propagating gravity waves can result in instability and turbulent dynamics, often associated with breaking. There are a convective instability limit (see Fritts and Alexander 2003) and a dynamical instability limit that are related to the Richardson number. By comparison, Kelvin-Helmoltz instabilities are among the most common sources of turbulence in the atmosphere. These can result from wind shears induced by inertio-gravity waves. While direct observations are difficult, most of the current research on Kelvin-Helmholtz instabilities is performed by numerical simulations.

15.4 The Effect of the Atmosphere on Infrasound Monitoring: Case Studies

15.4.1 Temporal Variations in Signal Characteristics

Many long-term observational studies conducted at IMS infrasound stations have shown seasonal variations in recorded signal characteristics. One such study (Arrowsmith and Hedlin 2005) was a year long investigation of surf-generated infrasound detections at the I57US array in southern California. Ocean-generated infrasonic waves at frequencies between 1 and 5 Hz are attributed to waves breaking along the shore (Kerman 1988). Surf-generated infrasonic waves had previously been reported at the I59US IMS array in Hawaii, located about 7.5 km from the coastline (Garcés et al. 2003), and signal amplitudes were shown to correlate with offshore wave heights. At the I57US array, arrival angles obtained using the Progressive Multi-Channel Correlation (PMCC) algorithm (Cansi 1995) pointed to an ocean source; however, the signal amplitudes were correlated with wave heights only over the winter months. The correlation broke down in summer. Arrowsmith and Hedlin (2005) demonstrated that arrivals were stratospherically ducted between the source region along the coastline and the array – a distance of approximately 200 km. They concluded that the number and amplitude of detected signals depended

on two things: the wave height, which relates to source amplitude, and the strength of the stratospheric duct.

Figure 15.9 shows the number of surf-generated signals detected in this study over a year, as well as meridional and zonal wind speeds along the propagation path. There is an obvious seasonal trend in the number of detections that correlates to the strength of the stratospheric winds to the west. Westward stratospheric winds strengthen the stratospheric duct, enabling propagation of surf-generated infrasound to the I57US array in winter. The far lower number of detections in summer is due in part to the smaller number of periods of high surf activity, but also to the disappearance of the stratospheric duct.

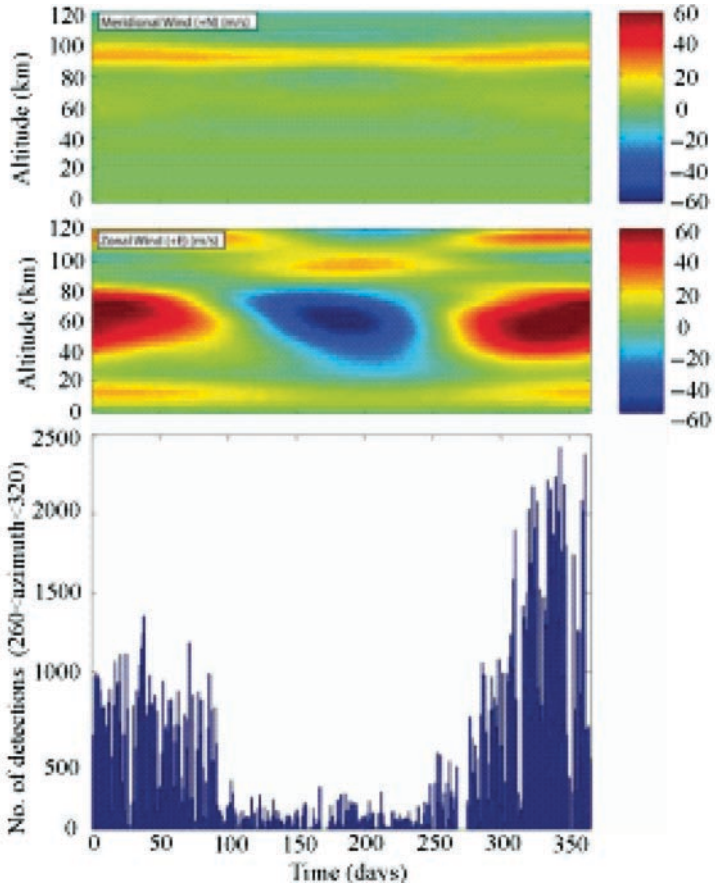

Fig. 15.9 (*Top* and *middle panels*) Meridional and zonal wind speeds along the propagation path, averaged along the path from source to receiver, for each day of the year. These values were derived from the HWM climatological model (Hedin et al. 1996). (*Bottom panel*) The number of detections per day from the west (from Arrowsmith and Hedlin 2005)

Other investigations to show seasonal variations in signal detection rates include a study of infrasonic waves generated by the Concorde (Le Pichon et al. 2002), and several studies of microbaroms detected at Hawaii (Willis et al. 2004; Garcés et al. 2004), and at infrasound stations in Bolivia and Germany (Le Pichon et al. 2006).

In the Concorde study, infrasonic waves excited by the regularly scheduled flights with known flight routes were detected at an infrasound array at Flers, in northwest France. The Concorde traveled at supersonic speeds, generating shock waves near the aircraft (Whitham 1974). The pressure disturbance resulting from supersonic objects in the atmosphere decreases rapidly with distance from the source so that propagation is acoustic over almost the entire source-receiver path. Thus, transmission is governed by wind and sound speed gradients in the atmosphere. Concorde flights have been recorded at infrasound sensors at distances from hundreds to thousands of kilometers (Liszka 1978). The Le Pichon et al. (2002) study specifically addressed the affects of upper atmospheric fluctuations on the infrasonic waves. They found both seasonal and diurnal trends in the number of Concorde-generated phases detected daily, in the apparent phase velocities, and the width of the frequency bands. Large numbers of arrivals were detected from October through April, with fewer phases recorded from May to September and none in August. Signal amplitudes were also lower and had a narrower frequency range in summer. They concluded that infrasonic arrivals had been refracted in the stratosphere and thermosphere in winter, but only in the thermosphere in summer. Weaker diurnal trends in the number and amplitude of arrivals were attributed to daily tidal fluctuations in atmospheric winds at about 120 km in altitude. These results further confirm the influence of atmospheric winds on long-range sound propagation.

Microbaroms are infrasonic waves generated by ocean swells and are ubiquitous at IMS infrasound arrays, with a peak frequency of 0.2 Hz. Arendt and Fritts (2000) proposed a source mechanism involving the nonlinear interaction of ocean swells with atmospheric pressure waves. Microbaroms dominate the ambient infrasound field at I59US (Willis et al. 2004). Willis et al. (2004) demonstrated that arrival azimuths vary annually; they arrive from the east or south from June through September, and predominantly from the northwest from October through March. These seasonal patterns in arrival directions not only relate to regions of dominant storm activity, but also to wind directions in the atmosphere at altitudes of 10–20 km and from 50 to 70 km (Garcés et al. 2004).

Monitoring at I08BO, a midlatitude infrasound IMS stations in Bolivia, and at I26DE, an IMS station in Germany, over a 5-year period showed clear annual cycles in the number, arrival azimuth, and amplitude of microbaroms recorded at these stations (Le Pichon et al. 2006). The numbers of arrivals at each station show a clear correlation with the direction of the zonal stratospheric winds in each hemisphere. The stratospheric winds blow to the east between June to November in the southern hemisphere, consistent with observed arrivals from the antarctic circumpolar current (ACC) to the south-southwest, and blow westward the rest of the year, leading to arrivals from ACC regions to the southeast of the array from December through April. In Germany, microbaroms arrive from the North Atlantic to the west to northwest of the array between October to June, consistent with the eastward flow of stratospheric winds at this time.

Infrasound generated by three active volcanoes on the Vanuatu archipelago was monitored over a 1-year period at the I22FR infrasound station south of the archipelago (Le Pichon et al. 2005a). Between them, the three volcanoes provided a frequent source of infrasonic waves. The PMCC algorithm (Cansi 1995) was applied to the data to estimate the direction of each arrival. Le Pichon et al. (2005a) found that the arrival of azimuth from these fixed sources varies seasonally, with fluctuations of up to 15° over the course of a year. They used 3-D ray-tracing through a moving atmosphere, using temperatures and wind speeds from NRL-Ground-To-Space (NRL-G2S) specifications to find that simulated azimuth deviations failed to predict the observed swings in arrival azimuth over the span of a year. They concluded that the mesospheric winds are underestimated. In a follow-up study, Le Pichon et al. (2005b) showed that these observations could be used to investigate the structure of high altitude winds. They applied an iterative algorithm to reconstruct wind speed profiles at altitudes above 60 km, such that differences between observed and predicted azimuths were minimized. The results showed that mesospheric wind speeds were underestimated by 20–50 m/s, and that stratospheric winds extend to the lower thermosphere (see Fig. 15.6 in Le Pichon et al. 2010).

Infrasonic waves generated by eruptions of Mt Etna in Italy were observed over the summer of 2001 at the Deelen Infrasound Array (DIA) in The Netherlands and at IS26 in Germany (Evers and Haak 2005). Mt Etna was almost continuously active over this period. A detailed examination over 24 h at the DIA array showed a clear diurnal pattern in the number of detections; the detection rate rose significantly in the late evening and decreased again about 10 h later. Evers and Haak (2005) attribute this, in small part, to the decrease in human activity at this time. However, they ascribed this primarily to the increased stability of the atmosphere at night, which arises due to the decrease in turbulence and atmospheric convection caused by the solar heat flux. This diurnal variation in detection rate was not observed at IS26.

Evers and Haak (2005) also observed that the measured azimuths to source were deflected by about 3.5° at the nearer stations, IS26, and about 2.6° at DIA, leading to an error in the source location estimated using the crossing of the two bearing estimates (Fig. 15.10). They used 3-D ray-tracing through an advected medium (Garcés et al. 1998) to confirm that zonal cross winds within the stratosphere deflect the infrasonic waves westward, leading to the observed azimuth deviations.

Fee and Garcés (2007) observed a clear diurnal cycle in infrasound arrival amplitudes arising from shallow volcanic tremor excited by an active vent of Kilauea Volcano. They deployed the sensor array approximately 12.5 km to the northwest of the active vent; this location was chosen because ray theory predicts a shadow zone starting at a distance of 12 km from the source for much of the day. Spectrograms were computed for seven days of beam-formed data. They showed that spectral amplitudes between 0.02–0.3 Hz were a proxy for wind speed, and were anticorrelated with infrasonic tremor in the 0.5–3 Hz band. The amplitudes of the tremor arrivals peaked in the early morning hours, about 0000–0500 local time. The spectrograms are shown in Fig. 15.11. Fee and Garcés (2007) concluded that the arrival amplitudes were highest at night due to a temperature inversion created by the rapid cooling of the Earth's surface. The temperature inversion creates a stable layer of atmosphere characterized by light winds, and results in a waveguide that ducts infrasound energy.

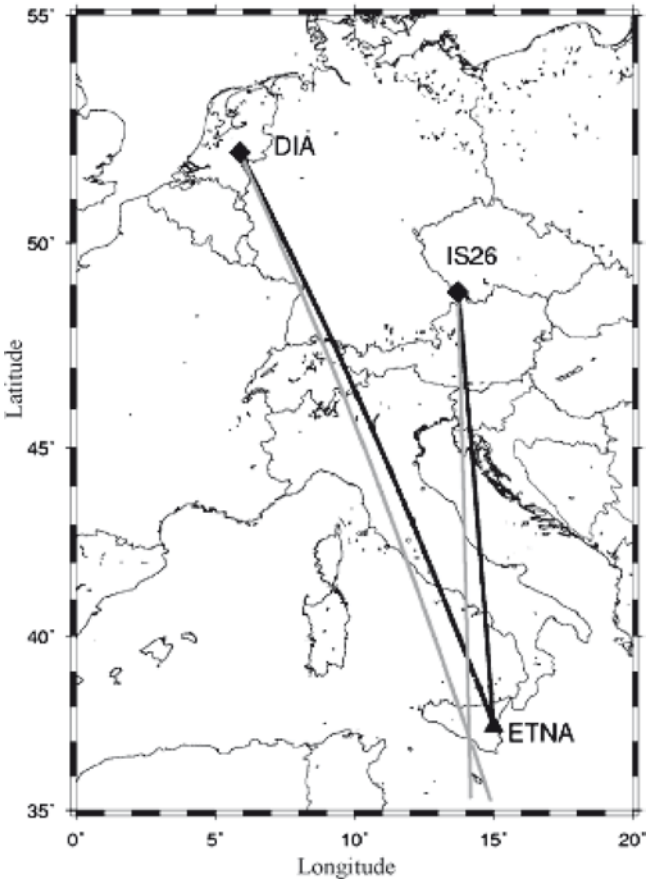

Fig. 15.10 Map showing observed azimuths to source (*gray*) and true values (*black*) for DIA and IS26 toward Mt. Etna, in Sicily (from Evers and Haak 2005)

15.4.2 Spatial Variations in Signal Characteristics

Relatively few studies have shown clear spatial variations in observed signal arrivals. One difficulty is that the sparse distribution of infrasound stations makes it difficult to delineate the edges of shadow zones. However, comparatively dense distributions of seismic networks exist worldwide, and have been used to record infrasound energy for a variety of sources (e.g. Cates and Sturtevant 2002; Cochran and Shearer 2006; Arrowsmith et al. 2007; Ottemöller and Evers 2008). Although seismic waveforms do not yield an accurate measure of the infrasound amplitude due to local variations in the efficiency of air to ground coupling, they provide both travel times and a lower limit on the ground exposure to the sonic boom.

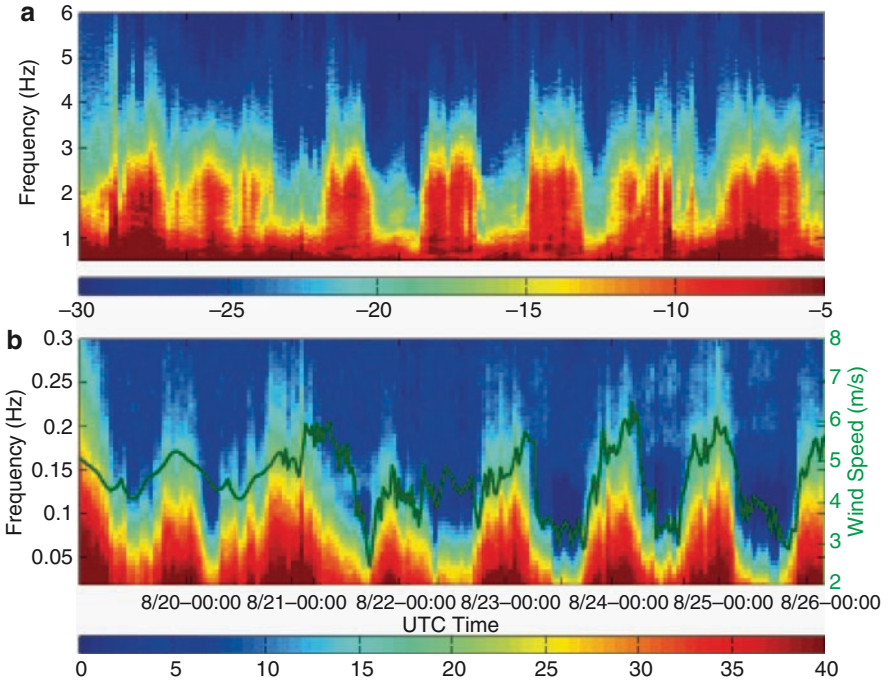

Fig. 15.11 Spectrograms of beamed signals at a temporary station near Kilauea Volcano. (**a**) Spectrograms at 0.5–3 Hz, showing infrasonic tremor from the volcano and (**b**) 0.02–0.3 Hz. The latter spectra serve as a proxy for wind speed at the station. The green line in (**b**) is the wind speed at a nearby tower. The signal and wind spectra are anticorrelated due to the rise of a nocturnal boundary layer at night, which results in low winds and infrasound ducting from the volcano to the nearby infrasound station (from Fee and Garcés 2007)

A recent study to make use of the dense networks in the western United States was an infrasound analysis of the reentry of the space shuttle Atlantis by de Groot-Hedlin et al. (2008). The space shuttle usually lands at the Kennedy Space Center (KSC) in Florida, but severe weather in that area on June 22, 2007 forced NASA to direct Atlantis to the alternate landing site at Edwards Air Force Base in the Mojave Desert in southern California. The infrasound generated by the shuttle was examined at over three hundred three-component seismic stations in the USArray, various regional seismic networks, and three infrasound stations in southern California and western Nevada. The temporary presence of the transportable USArray in this region provided this study with a much broader and denser array of sensors than would otherwise be available. A time and position record of its trajectory, accurate to 25–50 m, was recorded with a GPS receiver onboard the space shuttle. This yielded a rare opportunity to evaluate present-day atmospheric models over a dense network using infrasound signals for which we know when and where the source occurred.

Over one hundred seismic sensors and all three infrasound stations recorded the signal, and arrival times were picked. For comparison, travel times were computed for 3-D rays propagated through atmospheric specifications provided by the NRL-G2S model (Drob et al. 2003) and by climatology data. The source model was similar to that of Le Pichon et al. (2002), that is, rays were launched at right angles to infinitesimal Mach cones along the flight trajectory. The results were quite similar for both sets of atmospheric specifications, and observed arrival times are compared to arrival times predicted based on ray propagation through an NRL-G2S atmospheric model (Fig. 15.12). Comparison of predicted vs. observed travel times shows agreement over much of the study area. To the east of the shuttle trajectory, there were no detections beyond the primary acoustic carpet, but infrasound energy was detected hundreds of kilometers to the west and northwest of the shuttle trajectory, consistent with the predictions of ducting due to the westward summer-time stratospheric jet. To the northwest, regions of ensonification are predicted to alternate with shadow zones. However, infrasound energy was detected to distances of tens of kilometers within predicted shadow regions.

These results were confirmed, in part, by an infrasound study of an accidental explosion at an oil depot, one of Europe's largest explosions since the Second World War (Ottemöller and Evers 2008). Seismic stations in the UK and the Netherlands,

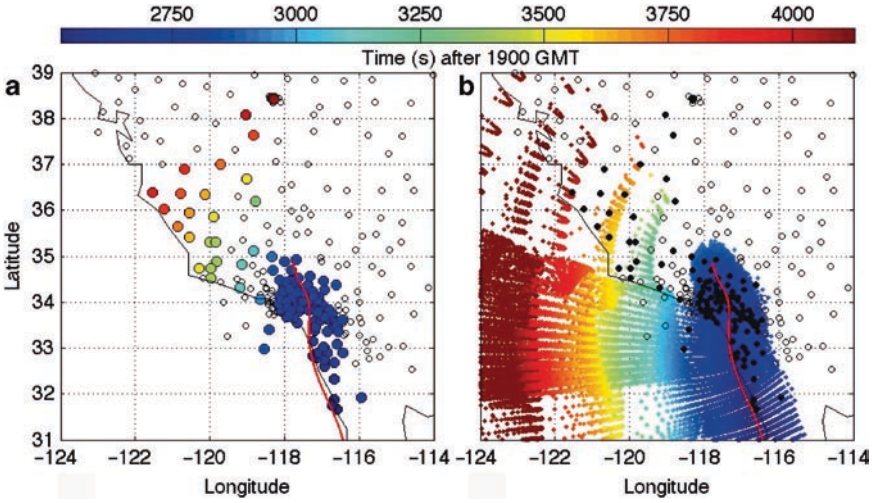

Fig. 15.12 (**a**) Map of stations used in the study by de Groot-Hedlin et al. (2008). *Filled circles* indicate seismic and infrasound stations that recorded an arrival, color-coded according to observed first arrival time, in seconds after 1900 GMT. For comparison, the shuttle speed drops below Mach 1 at 2,732 s after 1900 GMT. The supersonic portion of the shuttle trajectory is shown in red. Empty circles indicate station locations where signal were not detected. (**b**) Map of ray endpoints that reach the ground, for rays starting along the supersonic portion of the shuttle trajectory. Only stratospheric and tropospheric arrivals were considered. The endpoints are color-coded according to the predicted arrival time. Empty circles mark stations where signals were not observed. Filled circles indicate stations where arrivals were detected

and infrasound stations in the Netherlands recorded infrasonic waves from the explosion. Ottemöller and Evers (2008) noted that the predicted shadow zone was roughly 20 km larger than the observed shadow zone. They concluded that in other respects, the observed infrasound arrivals validated predictions based on ray-tracing through NRL-G2S atmospheric models.

However, another investigation did not find evidence of predictable shadow zones. A study of a bolide observed over a wide region of the northwestern United States and southwestern Canada was recorded at approximately one hundred seismometers in the area and at the I56US and I57US IMS arrays (Arrowsmith et al. 2007). The seismic data indicated that the source of the infrasound energy was a terminal burst rather than a hypersonic transit through the atmosphere. It was noted that the infrasound propagated at approximately 330 m/s, consistent with propagation near the surface. Arrivals were also detected well within areas predicted to be shadow zones, based on propagation through a NRL-G2S atmospheric model.

15.4.3 Spatial and Temporal Variations in Signal Characteristics

One experiment may be used to examine both spatial and temporal detectability of infrasound. Rockets were launched from the White Sands Missile range (WSMR) in New Mexico on three dates during 2005 and 2006, and detonated in the atmosphere at altitudes ranging from about 30 km to 50 km (Herrin et al. 2008). The dates were chosen, in part, to examine infrasound propagation through several characteristic high altitude wind patterns; in fall, when stratospheric winds transition from westward flow in the summer to eastward flow in the winter; in spring, when stratospheric winds transition back to the west; and in summer. The rocket trajectories were provided by radar data that gave the rocket's position as a function of time. The actual detonation locations were determined to within several seconds and several kilometers. Two rockets were launched on each date to take advantage of relatively calm atmospheric conditions. A relatively dense network of temporary infrasound arrays was deployed for each date to augment five permanent stations in the study area. A map (Fig. 15.13) shows where infrasound sensors were deployed for each date, and which stations recorded a signal associated with the detonations. Infrasonic waves were detected at distances of nearly 1,000 km. The data acquired in this experiment are still under study; some further details are given in Herrin et al. (2008).

15.5 Discussion

The seismic velocity structure of the Earth's interior does not change very rapidly, at least not on human time scales. Decades of observations of travel times from thousands of earthquakes to hundreds of seismic stations distributed worldwide have allowed seismologists to define this structure in exquisite detail. The models we have

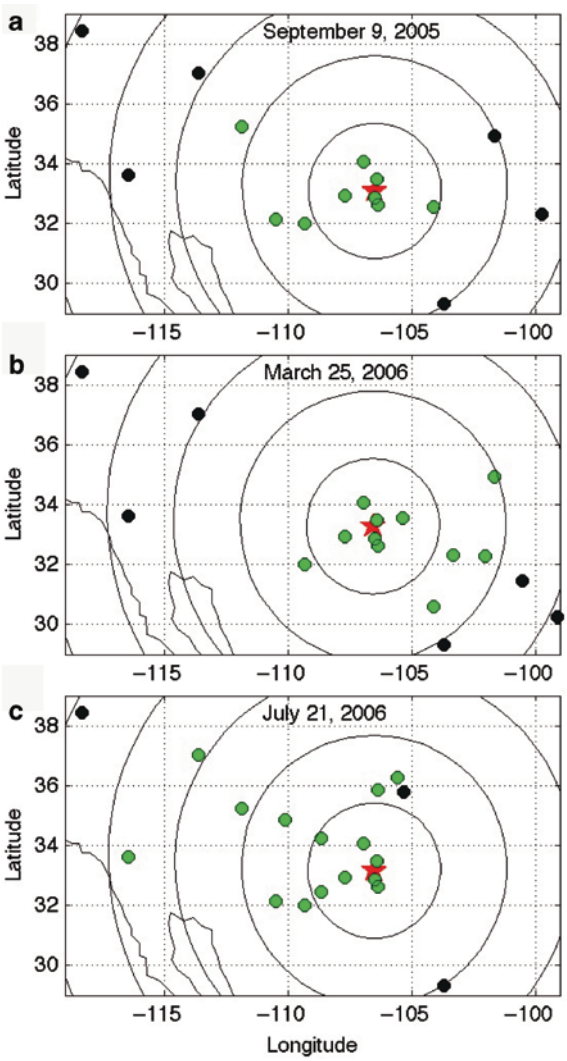

Fig. 15.13 Locations of infrasound stations for high altitude infrasound experiments on (**a**) September 2005, (**b**) March 25, 2006, and (**c**) July 21, 2006. The *green circles* indicate stations that measured a signal, and the *black circles* indicate those that did not

of the seismic velocity structure of the Earth's interior are rooted in travel time observations. Studies of the structure of the Earth's atmosphere are significantly different, however, in that change occurs continuously on all timescales. The manner in which we probe atmospheric structure is also entirely different. The bulk of our knowledge of the atmosphere's structure is not based on acoustic travel times, but is determined by various operational and research measurements; synthesized into mesoscale, global, and climatological atmospheric specifications (as described in section III).

Atmospheric change is ultimately driven by solar heating. Heating varies seasonally as a function of latitude, diurnally, and with altitude. The broad optical spectrum of the sun's photons is absorbed first by the atoms and molecules at the top of the atmosphere primarily at the EUV wavelengths, then those remaining wavelengths (UV) and photons are absorbed by ozone in the stratosphere, and finally what is left reaches the surface. Atmospheric dynamics result from the fact the Earth is a tilted, rotating, uneven sphere – resulting in uneven heating. While the large-scale structures evolve slowly with season, other finer-scale structures present one moment may be entirely gone the next. Some of the structures are repeatable from year-to-year and day-to-day in the average sense, while others are purely stochastic/random. These atmospheric changes vary with location as well as season. Zonal stratospheric winds, which have a significant influence on the nature of observable propagation characteristics, reverse twice each year at midlatitudes in both the northern and southern hemisphere. Near the equator and the poles, zonal winds have little in the way of seasonally varying atmospheric characteristics, and instead are influenced by vertically propagating planetary waves which can result in the creation of ducts that can last for a few days. Other significant variations include the surface winds which influence wind noise at the detectors, the migrating solar heating driven tides which can produce local time variations in the upper stratospheric and thermospheric ducts, as well as internal gravity waves which can result in scattering of infrasound into and out of various ducts often in places where classically they are not predicted to exist.

This ongoing change poses a great challenge to those whose studies rely on the propagation of sound through the atmosphere. Zonal winds might enhance propagation through the stratosphere along a given latitude at one time of the year (such as from west to east in the northern hemisphere winter) and inhibit propagation along the same path a few months later after the stratospheric wind jets reverse directions. The same winds may not enhance or inhibit propagation along a north-south path at the same latitude, but will deflect the energy from the great-circle plane connecting the source and the receiver and cause a bias in the arrival direction. It is well known that the structure of acoustic recordings can be highly time-variant. This variable nature of infrasound recordings is often attributed to finer-scale temperature and wind structure of the intervening atmosphere. Propagation ducts open and close, and fine-scale structures may scatter acoustic energy. Energy from an impulsive source might be multipathed and arrive at a recording station several times after taking markedly different paths. Amplitudes of infrasound signals can be significantly altered, complicating efforts to estimate source energy.

The atmospheric science community is making great strides in providing accurate specifications of the atmospheric from the ground to space (Drob et al. 2010). They are demonstrating operational data assimilation capabilities with compilations of recent historical data sets. Scientific knowledge of the dynamical processes of the atmosphere that is relevant to infrasound propagation research is continuing to advance on many fronts.

Atmospheric variability is of central importance when analyzing local or remote recordings of infrasound from man-made or natural phenomena. Key questions in many such studies are what caused this sound, and where did it happen. These questions

are of paramount importance to those in the nuclear monitoring community. Infrasound data are collected worldwide for the goal of not only detecting signals from explosive sources, but also for providing the basis for identifying the event as an explosion and then giving a location accurate enough to be of use for more thorough investigations. There is growing interest in the use of infrasound as a tool for monitoring a plethora of natural hazards such as tornadoes, hurricanes, volcanic eruptions, ocean swell, tsunami, wildfires, avalanches, etc. All of these phenomena are significant sources of infrasound energy. Understanding propagation is essential in assessing the utility of infrasound for these events as well as for longer-lived phenomena, to track them as they evolve from their embryonic stages until they no longer pose a threat.

Much progress has been made in defining atmospheric structure, though this is another area in which our field is significantly different than seismology. In seismology, the structure is defined by direct measurements of travel times. Available models of atmospheric structure come from the assimilation of diverse multiinstrument data sets and provide hourly conditions at any location and at any time of the year (e.g. Kalnay et al. 1990; Bloom et al. 2005; Hogan and Rosmond 1991; Molteni et al. 1996). Recent hybrid models (e.g. G2S; Drob et al. 2003) bring together these specifications with empirical models to allow us to estimate atmospheric wind and temperature structure as it varies over all relevant altitudes. Perhaps the ultimate goal in atmospheric modeling is to develop the tools needed to define atmospheric structure to a scale fine enough in time and space to permit us to synthesize the larger features in infrasound recordings (such as first arrival time, arrival direction, number of arrivals) that are essential for us to be able to answer the questions posed earlier, namely what generated the sound and where the source was located.

Given that our atmospheric models are not developed from direct measurements of acoustic travel times, infrasound sources that have been "ground truthed," or defined accurately in terms of time of occurrence, geographic location, and altitude, are essential for validating our atmospheric modeling methods and our techniques for simulating the propagation of sound. Ground truth databases (e.g. the GINA database maintained by Canada's Geological Survey of Canada, McCormack and Evers 2003) – data collected at the WSMR by a consortium of universities in the United states – (Herrin et al. 2008) continue to grow (Green et al. 2010). The pressing need for such events underscores the importance of metadata that can give us the much-needed information on these sources. These data sources include satellite observations (e.g. providing location and time of bolide explosions) and telemetry on man-made supersonic aircraft (such as discussed by de Groot-Hedlin in their study of the Atlantis shuttle – de Groot-Hedlin 2008). This gives us an opportunity to directly test our modeling methods.

There is a keen need to validate our models and modeling methods. This is hampered somewhat by the rather low density of infrasound stations. Atmospheric variability is such that it is the norm to observe significant differences in waveforms between these stations. Increasing the station density is a worthy goal, but the question arises: how can we do so at a reasonable cost? In seismically active regions, such as along the western US and Japan, seismic station density is high. Currently, a network of 400 seismic stations is "rolling" across the continental US – the USArray.

The average separation between seismic stations is 70 km. We are now seeing preliminary uses of the USArray to look up, rather than down, to probe the Earth's atmosphere. If sound waves from large ground-truthed atmospheric sources couple effectively to seismic and are recorded well above noise, the seismic network stations can significantly increase the density of paths through the atmosphere along which we directly measure the travel time of sound and compare these observations with predictions. As these studies accumulate and as we record progressively larger, more rare, sources, we should be able to subject our atmospheric models to progressively more stringent tests. More advanced studies of coupled acoustic-seismic waveforms require a much deeper analysis and consideration of how this coupling occurs. Perhaps the network of the future will be designed not to just look down into the solid Earth with seismic instruments and not to just look up into the atmosphere with microbarometers, but to probe in both directions with colocated sensors.

We have relatively good information on the atmospheric temperature and wind structure below 55–60 km. Above that altitude range, the G2S model with its supporting lower atmospheric operational data sets effectively melds in situ observations (e.g. Kalnay et al. 1990; Bloom et al. 2005) with climatology models (e.g. Picone et al. 2002; Hedin et al. 1996). Thus, high-altitude winds and temperatures are more poorly constrained. As the next generation of ground-to-space models are developed and evolve (e.g. Akmaev et al. 2008; Richter et al. 2008), validation of these new specification is another area in which infrasound studies might be useful. We have commonly used our best atmospheric models to extract as much information from our infrasound data as possible to accurately locate and identify sources. With long-lived, stationary sources, such as active volcanoes, recorded remotely by infrasound stations (as described by Le Pichon 2005b), we can probe the atmosphere where other methods give us relatively little control. We can simultaneously do infrasound research and atmospheric research.

So, looking into the future, the field of infrasound is bound to mature as the density of recording sites increases, as we use progressively more data to accurately model our atmosphere in space and time, and as we subject our models to progressively more stringent tests in more seasons, at more locations using ground truthed sources. As our computational resources continue to expand, we expect our improved atmospheric models will be paired by synthesis methods that mimic actual propagation more faithfully.

Acknowledgements We thank L. Evers, David Fee and Milton Garces, and Steven Arrowsmith for giving us permission to use figures from their papers. We also thank an anonymous reviewer for a careful review.

References

Akmaev RA, Fuller-Rowell TJ, Wu F, Forbes JM, Zhang X, Anghel AF, Iredell MD, Moorthi S, Juang H-M (2008) Tidal variability in the lower thermosphere: comparison of whole atmosphere model (WAM) simulations with observations from TIMED. Geophys Res Lett 35:L03810, doi:10.1029/2007GL032584

Andrews DG, Holton JR, Leovy CB (1987) Middle atmosphere dynamics. Academic Press, San Diego, CA

Arendt S, Fritts D (2000) Acoustic radiation by ocean surface waves. J Fluid Mech 415:1–21

Arrowsmith SJ, Hedlin MAH (2005) Observations of infrasound from surf in southern California. Geophys Res Lett 32:L09810, doi:10.1029/2005GL022761

Arrowsmith SJ, Drob DP, Hedlin MAH, Edwards W (2007) A joint seismic and acoustic study of the Washington state bolide: observations and modeling. J Geophys Res 112:D09304, doi:10.1029/2006JD008001

Attenborough K (2002) Sound propagation close to the ground. Annu Rev Fluid Mech 34:51–82

Bass HE, Bhattacharyya J, Garcés MA, Hedlin M, Olson JV, Woodward RL (2006) Infrasound. Acoust Today 2:9–19

Benjamin SG, Devenyi D, Weygandt SS, Brundage KJ, Brown JM, Grell GA, Kim D, Schwartz BE, Smirnova TG, Smith TL, Manikin GS (2004) An hourly assimilation-forecast cycle: the RUC. Month Weather Rev 132:495–518

Bloom S, da Silva A, Dee D, Bosilovich M, Chern J-D, Pawson S, Schubert S, Sienkiewicz M, Stajner I, Tan W-W, Wu M-L (2005) Documentation and validation of the goddard Earth observing system (GEOS) data assimilation system – version 4, Technical Report Series on Global Modeling and Data Assimilation, NASA/TM-2005-104606

Blanc E, Le Pichon A, Ceranna L, Farges T, Marty J, Herry P (2010) Global scale monitoring of acoustic and gravity waves for the study of the atmospheric dynamics. This volume, pp. 641–658

Brachet N, Brown D, Le Bras R, Mialle P, Coyne J (2010) Monitoring the earth's atmosphere with the global IMS infrasound network. This volume, pp. 73–114

Brasseur G, Solomon S (1986) Aeronomy of the middle atmosphere. Reidel Publishing, Dordrecht, Holland

Cansi Y (1995) An automated seismic event processing for detection and location: The P.M.C.C. method. Geophys Res Lett 22:1021–1024

Cates JE, Sturtevant B (2002) Seismic detection of sonic booms. J Acoust Soc Am 111:614–628

Chamberlain JW, Hunten DM (1987) Theory of planetary atmospheres; an introduction to their physics and chemistry, 2nd edn. Academic Press, San Diego, CA

Christie DR, Campus P (2010) The IMS infrasound network: design and establishment of infrasound stations. This volume, pp. 27–72

Chunchuzov IP (2004) Influence of internal gravity waves on sound propagation in the lower atmosphere. Met Atmos Phys 85(1–3):61–76

Cochran ES, Shearer PM (2006) Infrasound events detected with the southern California seismic network. Geophys Res Lett 33:L19803, doi:10.1029/2006GL026951

de Groot-Hedlin CD (2008) Finite-difference time-domain synthesis of infrasound propagation through an absorbing atmosphere. J Acoust Soc Am 124:1430–1441

de Groot-Hedlin CD, Hedlin MAH, Walker KT, Drob DP, Zumberge MA (2008) Evaluation of infrasound signals from the shuttle Atlantis using a large seismic network. J Acoust Soc Am 124:1442–1451

Donn W, Rind D (1972) Microbaroms and the temperature and wind of the upper atmosphere. J Atmos Sci 29:156–172

Drob DP, Picone JM, Garcés M (2003) Global morphology of infrasound propagation. J Geophys Res 108(D21):4680, doi:10.1029/2002JD003307

Drob DP, Meier RR, Picone JM, Garcés MM (2010) Inversion of infrasound signals for passive atmospheric remote sensing. This volume, pp. 695–726

Edwards WN (2010) Meteor generated infrasound: theory and observation. This volume, pp. 355–408

Ejakov SG, Phillips S, Dain Y, Lueptow RM, Visser JH (2003) Acoustic attenuation in gas mixtures with nitrogen: experimental data and calculations. J Acoust Soc Am 113:1871–1879

Embleton TFW (1996) Tutorial on sound propagation outdoors. J Acoust Soc Am 100:31–48

Evans LB, Bass HE, Sutherland LC (1972) Atmospheric absorption of sound: theoretical predictions. J Acoust Soc Am 51:1565–1575
Evers LG, Haak HW (2005) The detectability of infrasound in The Netherlands from the Italian volcano Mt. Etna. J Atmos Solar-Terr Phys 67:259–268
Evers LG, Haak HW (2010) The characteristics of infrasound, its propagation and some early history. This volume, pp. 3–26
Fee D, Garcés M (2007) Infrasonic tremor in the diffraction zone. Geophys Res Lett 34:L16826, doi:10.1029/2007GL030616
Fleming EL, Chandra S, Shoeberl MR, Barnett JJ (1988) Monthly mean global climatology of temperature, wind, geopotential height and pressure for 0–120 km, National Aeronautics and Space Administration, Technical Memorandum 100697, Washington, DC
Forbes JM (1995) Tidal and planetary waves. In: Johnson RM, Killeen TL (eds) Geophysical monograph on the upper mesosphere and lower thermosphere. American Geophysical Union, Washington, DC
Forbes JM, Zhang X, Talaat ER, Ward W (2003) Nonmigrating diurnal tides in the thermosphere. J Geophys Res 108, doi:10.1029/2002JA009262
Fritts DC, Alexander JM (2003) Gravity wave dynamics and effects in the middle atmosphere. Rev Geophys 41:3.1–3.64
Garcés M, Hansen RA, Lindquist KG (1998) Travel times for infrasonic waves propagating in a stratified atmosphere. Geophys J Int 135:255–263
Garcés M, Iguchi M, Ishihara K, Morrissey M, Sudo Y, Tsutsui T (1999) Infrasonic precursors to a Vulcanian eruption at Sakurajima volcano, Japan. Geophys Res Lett 26:2537–2540
Garcés M, Drob DP, Picone JM (2002) A theoretical study of the effect of geomagnetic fluctuations and solar tides on the propagation of infrasonic waves in the upper atmosphere. Geophys J Int 148:77–87
Garcés M, Hetzer C, Merrifield M, Willis M, Aucan J (2003) Observations of surf infrasound in Hawai'I. Geophys Res Lett 30:2264, doi:10.1029/2003GL018614
Garcés M, Willis M, Hetzer C, Le Pichon A, Drob (2004) On using ocean swells for continuous infrasonic measurements of winds and temperature in the lower, middle, and upper atmosphere. Geophys Res Lett 31:L19304, doi:10.1029/2004GL020696
Garcés M, Fee D, Steffke A, McCormack D, Servranckx R, Bass H, Hetzer C, Hedlin M, Matoza R, Yepes H, Ramon P (2008) Prototype ASHE volcano monitoring system captures the acoustic fingerprint of stratospheric ash injection. EOS 89:377–388
Garcés M, Willis M, Le Pichon A (2010) Infrasonic observations of open ocean swells in the Pacific: deciphering the song of the sea. This volume, pp. 231–244
Green DN, Le Pichon A, Ceranna L, Evers L (2010) Ground truth events: assessing the capability of infrasound networks using high resolution data analyses. This volume, pp. 593–622
Gutenberg B (1939) The velocity of sound waves and the temperature in the stratosphere in Southern California. Bull Seis Soc Am 20:192–201
Hagan ME (1996) Comparative effects of migrating solar sources on tidal signatures in the middle and upper atmosphere. J Geophys Res 101:21213–21222
Hauchecorne A, Keckhut P, Chanin M-L (2010) Dynamics and transport in the middle atmosphere using remote sensing techniques from ground and space. This volume, pp. 659–678
Hedin AE, Fleming EL, Manson AH, Schmidlin FJ, Avery SK, Clark RR, Franke SJ, Fraser GJ, Tsuda T, Vial F, Vincent RA (1996) Empirical wind model for the upper, middle and lower atmosphere. J Atmos Solar-Terr Phys 58:1441–1447
Herrin G, Bass H, Andre B, Woodward B, Drob D, Hedlin M, Garcés M, Golden P, Norris D, de Groot-Hedlin C, Walker K, Szuberla C, Whitaker R, Shields D (2008) High-altitude infrasound calibration experiments. Acoust Today 4:9–21
Hetzer CH, Gilbert KE, Waxler R, Talmadge CL (2010) Generation of microbaroms by deep-ocean hurricanes. This volume, pp. 245–258
Hodur RM (1997) The Naval Research Laboratory coupled ocean/atmosphere mesoscale prediction system (COAMPS). Month Weather Rev 125(7):1414–1430

Hogan T, Rosmond T (1991) The description of the navy operational global atmospheric prediction system's spectral forecast model. Month Weather Rev 119:1786–1815
Holton JR (1992) An Introduction to dynamical meteorology. Academic Press, San Diego, CA
Johnson JB, Aster RC, Ruiz MC, Malone SD, McChesney PJ, Lees JM, Kyle PR (2003) Interpretation and utility of infrasonic records from erupting volcanoes. J Volc Geotherm Res 121:15–63
Kalnay E, Kanamitsu M, Baker WE (1990) Global numerical weather prediction at the National Meteorological Center. Bull Amer Meteor Soc 71:1410–1428
Kerman B (1988) Sea-surface sound. Springer, New York
Kulichkov SN, Bush GA, Svertilov AI (2002) New type of infrasonic arrivals in the geometric shadow region at long distances from explosions. Izv Atmos Ocean Phys 38:397–402
Le Pichon A, Garcés M, Blanc E, Barthelemy M, Drob D (2002) Acoustic propagation and atmosphere characteristics derived from infrasonic waves generated by the Concorde. J Acoust Soc Am 111:629–641, doi: 10.1121/1.1404434
Le Pichon A, Blanc E, Drob D, Lambotte S, Dessa JX, Lardy M, Bani P, Vergnoille S (2005a) Infrasound monitoring of volcanoes to probe high-altitude winds. J Geophys Res 110:D13106, doi:10.1029/2004JD005587
Le Pichon A, Blanc E, Drob D (2005b) Probing high-altitude winds using infrasound. J Geophys Res 110:D20104, doi:10.1029/2005/D006020
Le Pichon A, Herry P, Mialle P, Vergoz J, Brachet N, Garcés M, Drob D, Ceranna L (2005c) Infrasound associated with 2004–2005 large Sumatra earthquakes and tsunami. Geophys Res Lett 32:L19802, doi:10.1029/2005GL023893
Le Pichon A, Ceranna L, Garcés M, Drob D, Millet C (2006) On using infrasound from interacting ocean swells for global continuous measurements of winds and temperature in the stratosphere. J Geophys Res 111:D11106, doi:10.1029/2005JD006690
Le Pichon A, Vergoz J, Cansi Y, Ceranna L, Drob D (2010) Contribution of infrasound monitoring for atmospheric remote sensing. This volume, pp. 623–640
Liszka L (1978) Long-distance focusing of Concorde sonic boom. J Acoust Soc Am 64:31–635
Liszka L, Hobara Y (2006) Sprite-attributed infrasonic chirps – their detection, occurrence and properties between 1994 and 2004. J Atmos Solar-Terr Phys 68:1179–1188
Lott F, Millet C (2010) The representation of gravity waves in atmospheric general circulation models (GCMs). This volume, pp. 679–694
Matoza RS, Hedlin MAH, Garcés MA (2006) An infrasound array study of Mount St. Helens. J. Volcanol Geothermal Res 160:249–262, doi:10.1016/j.jvolgeores. 2006.10.006
McCormack D, Evers L (2003) The global infrasound archive – GINA. Inframatics 1:6–7
Mikumo T, Watada S (2010) Acoustic-gravity waves from earthquake sources. This volume, pp. 259–276
Molteni F, Buizza R, Palmer TN, Petroliagis T (1996) The ECMWF ensemble prediction system: methodology and validation. Quart J Roy Meteor Soc 122:73–119
Moran SC, Matoza RS, Garcés MA, Hedlin MAH, Bowers D, Scott WE, Sherrod DR, Vallance JW (2008) Seismic and acoustic recordings of an unusually large rockfall at Mount St. Helens, Washington. Geophys Res Lett 35:L19302, doi:10.1029/2008GL035176
Mutschlecner JP, Whitaker RW (2010) Some atmospheric effects on infrasound signal amplitudes. This volume, pp. 449–468
NASA, U.S. Standard Atmosphere, U.S. Government Printing Office, Washington, DC, http://ntrs.nasa.gov/archive/nasa/casi.ntrs.nasa.gov/19770009539_1977009539.pdf
Nature News (1922) Propagation of the sound explosions. Nature 110:619–620
Nature News (1923) The Oldebroek explosion of October 28, 1922. Nature 111:619–620
Norris D, Gibson R, Bongiovanni K (2010) Numerical methods to model infrasonic propagation through realistic specifications of the atmosphere. This volume, pp. 535–568
Oberheide J, Wu Q, Killeen TL, Hagan ME, Roble RG (2006) Diurnal nonmigrating tides from TIMED Doppler interferometer wind data: monthly climatologies and seasonal variations. J Geophys Res 111:A10S03, doi:10.1029/2005JA011491

Oberheide J, Wu Q, Killeen TL, Hagan ME, Roble RG (2007) A climatology of nonmigrating semidiurnal tides from TIMED Doppler Interferometer (TIDI) wind data. J Atmos Solar-Terr Phys 69:2203–2218
Olson JV, Wilson CR, Hansen RA (2003) Infrasound associated with the 2002 Denali fault earthquake, Alaska. Geophys Res Lett 30:2195, doi:10.1029/2003GL018568
Ostashev VE, Chunchuzov IP, Wilson DK (2005) Sound propagation through and scattering by internal gravity waves in a stably stratified atmosphere. J Acoust Soc Am 118(6):3420–3429
Ottemöller L, Evers LG (2008) Seismo-acoustic analysis of the Buncefield oil depot explosion in the UK, 2005 December 11. Geophys J Int 172:1123–1134
Perkins S (2003) Danger in the air, 163, 168, http://www.sciencenews.org/articles/20030913/bob8.asp, 9/13/03
Picone JM, Hedin AE, Drob DP, Aiken AC (2002) NRLMSIS-00 empirical model of the atmosphere: statistical comparisons and scientific issues. J Geophys Res 107:1468, doi:10.1029/2002JA009430
Preparatory Commission for the Comprehensive Nuclear-Test-Ban Treaty Organization (PrepCom) (1997) Comprehensive Nuclear-Test-Ban Treaty (CTBT), V.97-28276, Austria, 139pp
Revelle DO (2010) Acoustic-gravity waves from impulsive sources in the atmosphere. This volume, pp. 301–354
Revelle DO, Brown PG, Spurny P (2004) Entry dynamics and acoustics/ infrasonic/seismic analysis for the Neuschwanstein meteorite fall. Meteor Planet Sci 39:1605–1626
Reynolds O (1874) On the refraction of sound by the atmosphere. Proc Roy Soc London 22:531–548
Reynolds O (1876) On the refraction of sound by the atmosphere. Phil Trans Royal Soc London 166:315–324
Richter JH, Sassi F, Garcia RR, Matthes K, Fischer CA (2008) Dynamics of the middle atmosphere as simulated by the Whole Atmosphere Community Climate Model, version 3 (WACCM3). J Geophys Res 113:D08101, doi:10.1029/2007JD009269
Rind D (1978) Investigation of the lower thermosphere results from ten years of continuous observations with natural infrasound. J Atmos Sci 40:1199–1209
Rind D, Donn WL (1975) Further use of natural infrasound as a continuous monitor of the upper atmosphere. J Atmos Sci 32:1694–1704
Ross CD (2000) Outdoor sound propagation in the US Civil War. Appl Acoust 59:137–147
Schrodinger E (1917) Zur Akustik der Atmosphare. Phys Z 18:445–453
Scott ED, Hayward CT, Kubichek RF, Hamann JC, Pierre JW, Comey B, Mendenhall T (2007) Single and multiple sensor identification of avalanche-generated infrasound. Cold Reg Sci Technol 47:159–170, doi:10.1016/ j.coldregions.2006.08.005
Skamarock WC, Klemp JB, Dudhia J, Gill DO, Barker DM, Wang W, Powers JG (2005) A description of the advanced research WRF Version 2. NCAR Tech Notes-468+STR
Sutherland LC, Bass HE (2004) Atmospheric absorption in the atmosphere up to 160 km. J Acoust Soc Am 115:1012–1032, doi:10.1121/1.1631937
Whipple FJW (1931) The investigation of air waves from explosions. Progress in England. Quart J Roy Meteor Soc 57:331–335
Whipple FJW (1934) Propagation to great distance of airwaves from gunfire. Progress of the investigation during 1932. Quart J Roy Meteor Soc 60:80–88
Whipple FJW (1935) The propagation of sound to great distances. Quart J Roy Meteor Soc 61:285–308
Whitham GB (1974) Linear and nonlinear waves. Wiley, New York
Willis M, Garcés M, Hetzer C, Businger S (2004) Infrasonic observations of open ocean swells in the Pacific: deciphering the song of the sea. Geophys Res Lett 31:L19304, doi:10.1029/2004GL020684

Part III
Propagation Modeling in a Realistic Atmosphere

Chapter 16
On the Prospects for Acoustic Sounding of the Fine Structure of the Middle Atmosphere

Sergey Kulichkov

16.1 Introduction

The method of acoustic sounding of the atmospheric middle and upper layers is a bistatic method. In this method, the sources (continuous and pulsed) and receivers (acoustic microphones) of sound are located on the land surface at distances of hundreds to thousands of kilometers from each other. Acoustic signals recorded during the so-called long-range sound propagation (LRSP) in the atmosphere are informative: they provide information on atmospheric structure at different altitudes.

In the literature, LRSP in the atmosphere is considered to be sound that covers a distance equal to hundreds or thousands of kilometers from its source (Kulichkov 1992; (Norris et al. 2010; Gainville et al. 2010). The physical basis for LRSP is the refraction of sound rays by the layered atmospheric temperature and wind speed inhomogeneities. Due to refraction, acoustic signals propagate through the atmosphere along cyclic ray trajectories, turning toward the ground surface in regions of increasing (with height) effective sound speed $c_{\text{eff}}(z)$ (adiabatic sound speed plus wind speed in the direction of sound wave propagation). The ray turning heights may be within the atmospheric boundary layer (ABL) and the troposphere (if both temperature and wind inversions occur along the propagation direction) and the middle ($20 < z < 120$ km) and upper (120 km $< z$) atmosphere.

In the case of LRSP, zones of acoustic audibility and silence are formed on the land surface (Fig. 16.1). The dimensions and spatial configuration of these zones depend significantly on the form of the mean vertical profile of the effective sound speed $c_{\text{eff}}(z)$ and on the type of ray paths forming the corresponding types of infrasonic arrivals (surface, tropospheric, mesospheric, and thermospheric) (Kulichkov 2004). Infrasonic arrivals in the audibility zone significantly differ in amplitude and structure from those in the geometric shadow zone. In the audibility zone, acoustic arrivals are a combination of both localized (I) and continuous (P) components. Component P corresponds

S. Kulichkov (✉)
Oboukhov Institute of Atmospheric Physics, Russian Academy of Sciences, Pyzhevsky 3, Moscow, 119017, Russia
e-mail: snk@ifaran.ru

A. Le Pichon et al. (eds.), *Infrasound Monitoring for Atmospheric Studies,*
DOI 10.1007/978-1-4020-9508-5_16,

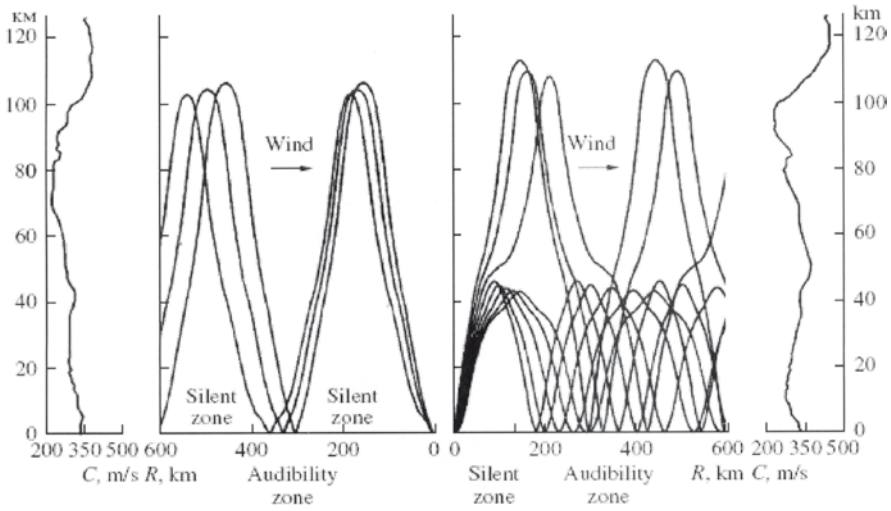

Fig. 16.1 Sound ray paths and the profiles of the effective speed of sound for its propagation against (*left*) and along (*right*) the direction of the prevailing wind

to partial reflection of acoustic signals from atmospheric inhomogeneities. Only the components *P* are usually recorded in the geometric shadow region.

The localized (one or two signals period) component *I* of a signal is formed by infrasonic waves propagating along the rays and turning (due to refraction) toward the ground surface. The duration of this component is approximately equal to that of the acoustic pulse at the ray turning altitude.

The component (*P*) occurs as a sequence of acoustic arrivals partially reflected from the anisotropic locally stratified temperature and wind inhomogeneities in the stratosphere and mesosphere. The partial reflections occur along the entire ray path (at different *z*) when the acoustic energy crosses the boundaries of the stratified structures. These partial reflections result not only in a significant increase of the total duration of an infrasonic arrival in the audibility zone, but also in its penetration into the geometric shadow zone (Bush et al. 1997; Kulichkov 1998; Kulichkov and Bush 2001).

Fig. 16.2 shows an example of an infrasonic signal recorded in the geometric shadow region at a distance of 300 km from an explosion equivalent to 20–70 tons of TNT (below, the shadow zones are taken to mean only the regions on the ground surface that are in zones of silence for both stratospheric and mesospheric ray trajectories). The signal in Fig. 16.2 illustrates almost all the known types of recorded infrasonic arrivals at long distances from ground explosions. Among these arrivals are the so-called Lamb waves *L* propagating in the acoustic waveguide formed by the wind inversion in the lower troposphere, and also oscillating, strato-mesospheric P_{sm} (corresponding to the partial acoustic pulse reflection from both stratospheric and mesospheric thin-layered inhomogeneities), localized mesospheric I_m, and thermospheric I_t infrasonic signals.

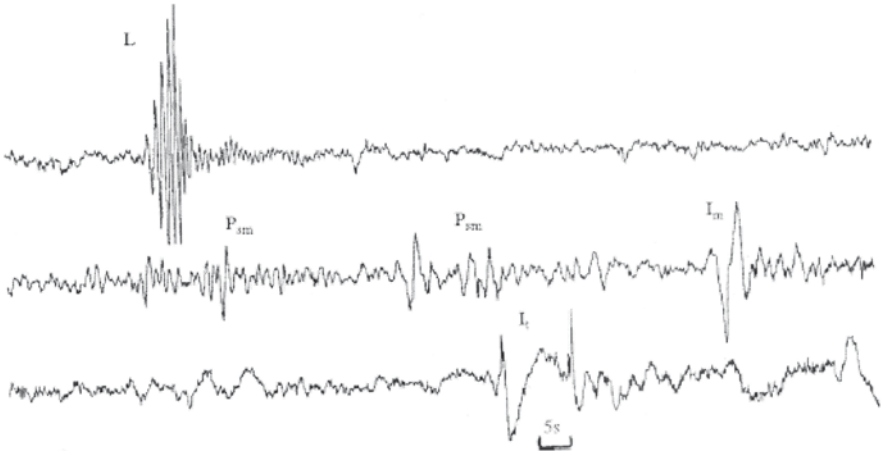

Fig. 16.2 Sample of infrasonic signal in the zone of acoustic shadow at a distance about 300 km from a surface explosion with yield of 20–70 tons TNT. L – Lamb wave; P_{SM} – strato-mesospheric arrival; I_M – mesospheric arrival; I_t – thermospheric arrival

As noted above, the infrasound sources used in the method of acoustic sounding of the atmosphere may be continuous (polar aurora, storm waves in the ocean, thunderstorms, atmospheric fronts, etc.) or pulsed (Kulichkov 1992; Campus and Christie 2010). Among the pulsed sources are explosions of different types and energy (Kulichkov 1992), shock waves from airplanes and rockets (Balashandran et al. 1977; Donn 1978; Posmenteir 1971; Liszka and Olsson 1971), volcanic eruptions (Fujiwara 1914a, Tahira 1982, 1988), and others. Infrasonic waves (from such sources) propagate throughout the atmosphere to distances of hundreds or thousands of kilometers (Kulichkov 1992) and may be used in sounding the middle and upper atmosphere (Balashandran et al. 1977; Le Pichon et al. 2010).

The history of studying LRSP in the atmosphere, the basic data on infrasound sources and on the effect of the atmospheric structure on infrasonic wave propagation, and also the basic principles of the theory and the results of experimental investigations are given in the reviews (Kulichkov 1992; Ingard 1953; Cox 1958; Georges and Young 1972; Gossard and Hooke 1975; Brown and Hall 1978; Wilson et al. 1995; McKisic 1997). One of the most remarkable historical mentions of LRSP in the atmosphere is the sound from a powerful artillery salute fired in London in 1837 on the occasion of Queen Victoria's crowning. This salute was heard on the continent at a distance of 200–300 km from London, though this salute was not heard at a distance of 50–100 km from its source.

The phenomenon of LRSP in the atmosphere has already been known over several centuries; however, its systematic study was started in the latter half of the nineteenth century. At that time work by Stokes (1857) was published, in which the effect of temperature and wind stratifications in the atmosphere on sound wave propagation was studied. Later, the necessity of explaining the reasons for increased audibility of sound in the downwind direction and its decreased audibility in the upwind direction

gave impetus to the appearance of the works by Reynolds (1874) and Rayleigh (1944), who were the first to introduce the notion of acoustic rays and formulate the law of refraction of the normal to the phase front in the stratified moving atmosphere. These notions are of fundamental importance for acoustics as a whole.

The studies made in the first half of the twentieth century should be especially noted. In these works, LRSP was used to sound the upper layers of the atmosphere (Fujiwara 1914a). Long before the development of other sounding methods (rocket, optic, and radiophysical), studies were made in Japan and Germany (Fujiwara 1914a, b, b) (observations of long-range propagation of sound from explosions equivalent to a few hundreds of kilograms of TNT, where 100 kg TNT ~ 4×10^8 J) from which it follows that there are regions of increasing (with height) temperature in the stratosphere. The region of strong winds was also observed in the stratosphere. Moreover, our analysis (Kulichkov 1992) of the results obtained in Fujiwara (1914a, b) on the basis of the current knowledge of temperature and wind stratifications in the upper atmosphere shows that the authors have also recorded infrasonic signals reflected from the lower thermospheric layers. Therefore, as far back as the first third of the twentieth century, the data obtained with the acoustic method indicated the occurrence of the thermosphere (the region of increased temperature at altitudes above 90 km), which, a few decades later, was confirmed by the studies of the upper atmosphere with the use of geophysical rockets.

After World War II, the wind field in the stratosphere was studied experimentally using ground explosions equivalent to 100 kg of TNT (Crary 1950, 1952). Moreover, the rocket-grenade method of acoustic sounding of the atmospheric upper layers was also developed (Reed 1972), with the aid of which the data on the structure of wind and temperature fields in the middle and upper (up to a height of about 90 km) atmosphere were obtained. These data were used in constructing a basic atmospheric model, which remains important at present. Later, with the development of balloon, rocket, radiophysical, and optical methods of sounding the middle and upper atmosphere, interest in the acoustic methods was, to a large extent, lost. Since this time, the phenomenon of LRSP in the atmosphere has been studied mainly to monitor nuclear tests.

16.2 Prospects for Using the Method of Acoustic Sounding to Study the Middle Atmosphere

In spite of evident progress in the studies of the atmospheric middle and upper layers with the use of radars and lidars, the acoustic method remains important nowadays and has a number of advantages as compared to remote radiophysical and optical methods. To use the acoustic method in studying the atmosphere, the development and maintenance of expensive equipment and complex infrastructure are not needed. Different natural (sea storm, lightning discharges, volcanic eruptions, etc.) and man-caused (research and industrial) phenomena may be used as sound sources (Kulichkov 2004; Campus and Christie 2010).

One more advantage of the acoustic method is that it allows one to study not only the lower stratosphere, but also the little-investigated atmospheric layers located above the lower stratosphere. Radiolocating and optical methods used in sounding these layers are not efficient, because the reflectivity of electromagnetic waves is small at heights of 30–80 km due to an insufficient intensity of turbulence and insignificant electronic concentration.

In the absence of a regular rocket sounding of the thermosphere, the acoustic method can be used to obtain data on the vertical gradients of air temperature and wind velocity at heights of 90–110 km (Le Pichon et al. 2010; Drob et al. 2010). It is important to study the indicated range of heights of the thermosphere, because within this range, the occurrence of sporadic layers in the region *E* of the ionosphere with anomalously high values of electronic concentration is noted.

The acoustic method is also promising in studying different variations in average vertical temperature and wind distributions in the stratosphere and the lower thermosphere, which are caused by internal gravity waves (IGVs), tidal phenomena, and seasonal and climate changes (Le Pichon et al. 2010; Blanc et al. 2010).

A new line in the remote sensing of a fine structure of the middle and upper atmosphere is the possibility of using the acoustic method of partial reflections, which is based on an analysis of the characteristics of the oscillating component of acoustic signals at long distances from their sources. A similar method was used earlier in our studies (Kulichkov 1998; Kulichkov et al. 2002) for the qualitative estimates of the parameters of a fine inhomogeneous structure of the middle atmosphere.

The advantage of the method of partial reflections is that the amplitude and frequency characteristics of recorded infrasound signals bear a simple relationship to the characteristics of atmospheric inhomogeneities (vertical gradients of air-temperature and wind-velocity variations with height, thicknesses of atmospheric layers). In the radiophysical and optical methods, energetic summation of sounding signals reflected from atmospheric inhomogeneities is needed to determine these parameters. In these methods, the thicknesses of averaging layers reach a few tens of meters (Whiteway and Carswell 1994, 1995; Widdel and von Zahn 1990; Rottger 1987), which naturally leads to errors in measuring vertical air-temperature and wind-velocity gradients (the most important characteristics of atmospheric inhomogeneities in various practical problems).

The acoustic method allows one to study the statistical characteristics of fine-structure anisotropic temperature and wind inhomogeneities in the atmospheric middle and upper layers. For this purpose, data regarding fluctuations in the amplitude and phase of infrasonic signals propagating in the middle atmosphere with anisotropic turbulence can be used. The theory of similar fluctuations is developed in Chunchuzov (2002).

One unique advantage of using the acoustic method for remote sensing of the atmosphere is that, with its aid, one will be able to obtain data on a global distribution of fine-structure inhomogeneities in the middle atmosphere. This will be facilitated using data obtained from the International Monitoring System infrasound network, which is being set up and shall consist of 60 stations distributed around

the globe (Christie and Campus 2010). By now, infrasonic signals from a few millions of different events have already been recorded at this network (Brachet et al. 2010). It is evident that such unique data are appropriate for use in the problems of acoustic sounding of the atmospheric middle and upper layers.

Thus, long-range acoustic sounding is used primarily in two ways to study the structure of the middle and upper atmospheres: (1) studies of the mean vertical profiles of air-temperature and wind-velocity fluctuations with height and their variations caused by different natural phenomena (IGVs, atmospheric tides, and seasonal and climate changes); and (2) studies of anisotropic turbulence and the fine inhomogeneous structure of the vertical profiles of air temperature and wind velocity in the middle and upper atmospheres, and the global distribution of this structure.

Below, we will dwell upon some results obtained with the acoustic method in the current studies of the middle atmosphere.

16.3 Rapid Variations in Infrasonic Signals at Long Distances from Repeated Explosions

In its acoustic properties, the atmosphere is essentially an inhomogeneous, nonlinear, dissipative, and nonstationary medium subjected to both external and internal factors (solar flares, the interplanetary magnetic field, and meteorological, seismic, and other disturbances). In addition to the regular seasonal changes in the atmosphere, fluctuations are also observed in its acoustic parameters due to tidal phenomena, planetary and IGWs, turbulence, etc., which result in significant distortions of the structure of the atmospheric sound field and in qualitative and quantitative changes of its characteristics.

The combination of both the medium-scale and fine structures of the profile of temperature and wind stratification (the effective acoustic speed) significantly affects the properties of the long-range propagation of infrasonic waves. This is reflected in the fact that signals even from repeated sources may have significantly different characteristics due to time variations in the vertical effective acoustic speed profile $c_{\text{eff}}(z)$. This hinders the prediction of infrasonic wave propagation at long distances in the atmosphere and also results in errors in detecting and identifying explosions. This problem is distinguished in National Research Council (1997) as one of the most important problems of infrasonic monitoring of explosions.

The so-called "rapid" (at several-minute intervals) variations in the structure of infrasonic arrivals from pulsed sources are the most difficult to study (Kulichkov and Bush 2001). For this reason, our experiments with series of explosions equivalent to 50–100 kg and 20–70 tons of TNT are of special interest. These experiments are described in detail by the authors in Bush et al. (1997), Kulichkov (1998), and Kulichkov and Bush (2001). The time interval among the explosions varied from 10 to 20 min within each series, which allowed one to study rapid time variations in infrasonic arrivals at the intervals indicated. Such variability may be, for example, due to IGWs and also ordered (coherent) structures horizontally transported by

wind in turbulent fluxes throughout the upper stratosphere and mesosphere. The occurrence of IGWs at both stratospheric and mesospheric heights is supported by the results of numerous experiments (e.g. Rottger 1987), while coherent structures in both temperature and wind fields are mainly studied in the ABL and in the lower troposphere (Mikhailova and Ordanovich 1991; Petenko and Bezverkhnii 1999).

In the zones of audibility and geometric shadow, infrasonic arrivals were recorded with tripartite infrasound arrays. In all the cases, the desired signal had large amplitude and was reliably detected above natural noise. In the zones of audibility and geometric shadow, variations were revealed not only in the amplitude, but also in the structure of infrasonic arrivals. These variations in structure occurred in time intervals whose duration coincided with the periods of IGWs and some global geophysical phenomena, such as planetary waves and tides. Some results are given in Figs. 16.1–16.6.

In the winter experiments (January 24, 1991) with explosions equivalent to 50–100 kg of TNT, stratospheric infrasonic signals (Fig. 16.3) were recorded in the city of Vladimir at a distance of 124 km to the east of its sources. Fig. 16.3 also shows an acoustic pulse in the vicinity of a source. It follows from Fig. 16.3 that a stratospheric infrasonic arrival consists of two quasi-periodic groups of waves that arrived at an interval of about 7 s. The maximum spectral density of the signal corresponds to a frequency of about 7 Hz.

The sound ray trajectories in the inhomogeneous moving atmosphere were calculated on the basis of the data obtained from the rocket sounding of the atmosphere during the periods closest to those during which the experiments were conducted.

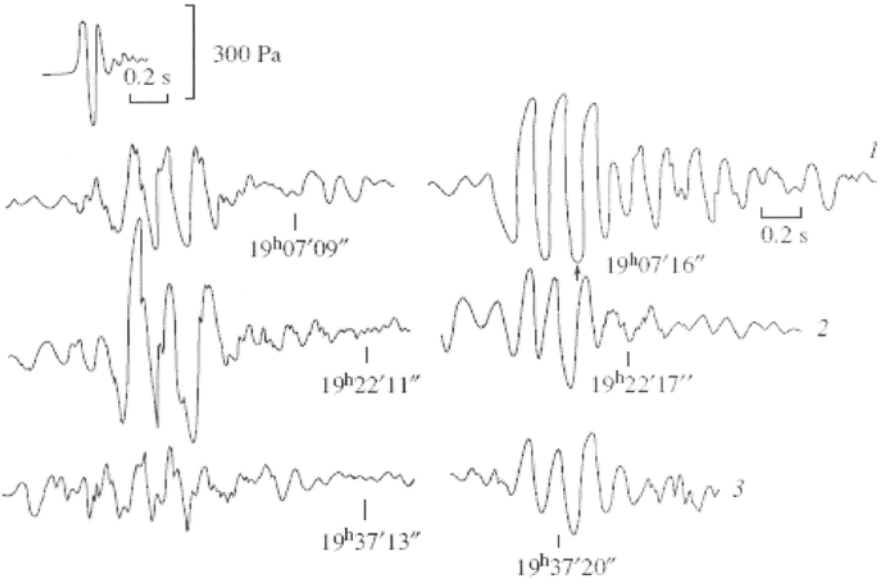

Fig. 16.3 Acoustic pulse at a distance of 1 km from an explosion equivalent to 50–100 kg of TNT. Records of stratospheric infrasonic arrivals at a distance of 124 km to the east of three explosions (1–3) (equivalent to 50–100 kg of TNT) implemented at 15-min intervals on January 24, 1991

According to these calculations, the groups of sound rays turning toward the ground surface at heights H of about 36 and 30 km (at grazing angles α of 41° and 26°, respectively) arrive sequentially at the recording site at a distance of 124 km from their source. The results of ray-path calculations mainly correspond to the experimental results. Here, it should be noted that *any* calculations of the trajectories of LRSP in the atmosphere are very rough; therefore, in interpreting experimental data, one should consider them as an illustration. (The rocket sounding station is situated in a neighborhood of the city of Volgograd, but not in the region where the experiments were conducted; the accuracy in determining the temperature and the wind speed and direction is not absolute.)

Time variations in the ratio between the amplitude values of the first and second arrivals are a special feature of the results obtained. For example, for the experiments conducted on January 24, 1991 (Fig. 16.3), the time interval between two basic arrivals varied within the range $\Delta t = 6.65$–8 s (i.e., apparently, the interval between the heights (H) of ray turning also varied for different grazing angles α). Such variability is characteristic of experiments carried out even within 1-h interval (in Fig. 16.3, the time interval between the explosions is equal to 15 min). This points to the fact that rapid variations in the stratospheric stratification on time scales less than 15 min noticeably affect the characteristics of infrasonic signals.

The arrivals of infrasonic signals from the explosions equivalent to 20–70 tons of TNT (the initial acoustic pulse in the vicinity of one of the sources is shown in Fig. 16.4) had a complex structure in different seasons (Figs. 16.4–16.8).

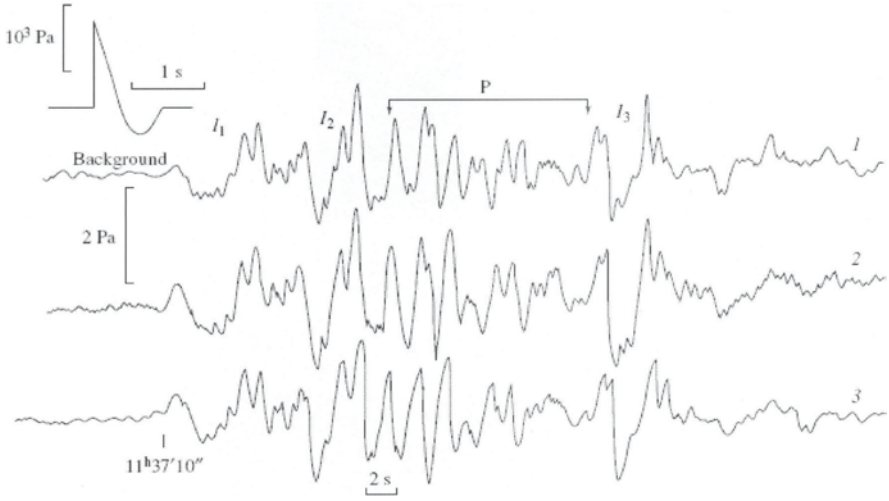

Fig. 16.4 Acoustic pulse at a distance of 2 km from an explosion equivalent to 20–70 tons of TNT. Records of infrasonic arrivals for three microphones (1–3) spaced about 100 m apart in the zone of refractive acoustic audibility at a distance of 300 km from the explosion equivalent to 20–70 tons of TNT implemented on July 7, 1990. I_{1-3} denotes localized (pulsed) arrivals, and P denotes oscillating arrivals

The recorded signals were a combination of localized (*I*) and continuous (*P*) components (coherent for three microphones) with amplitudes significantly exceeding the background values (Fig. 16.4). According to the results of ray-path calculations, the altitudes of reflection of infrasonic waves for the types of signals considered below are within the stratosphere and mesosphere.

The pulsed component of a signal is formed by infrasonic waves propagating along the rays turning (due to refraction) toward the ground surface at the heights z at which the condition $c_{\text{eff}}(z) > c_{\text{eff}}(0)$ is fulfilled. The duration of the pulsed component is approximately equal to that of the acoustic pulse at the height of ray turning. This is the case of *total* reflection. Such arrivals are formed only in the zones of refractive acoustic audibility. It is seen from Figs. 16.4–16.6 and 16.8 that the localized component (*I*) has a complex structure consisting of individual arrivals I_{1-3}. In the experiments carried out on July 7, 1990, the first two arrivals I_{1-2} were recorded with a time interval of about 7 s. The third arrival I_3 was recorded 27 s after the first one I_1. The height of ray turning (the black extrema in the vertical profile of the effective sound speed $s_{\text{eff}}(z)$ in Fig. 16.5) could range from 46 to 56 km for I_{1-2} and was 77 km for I_3.

The oscillating component *P* was observed in the zones of audibility (Figs. 16.4–16.6) and geometric shadow (Fig. 16.7; in this case, *partial* reflection occurs) and

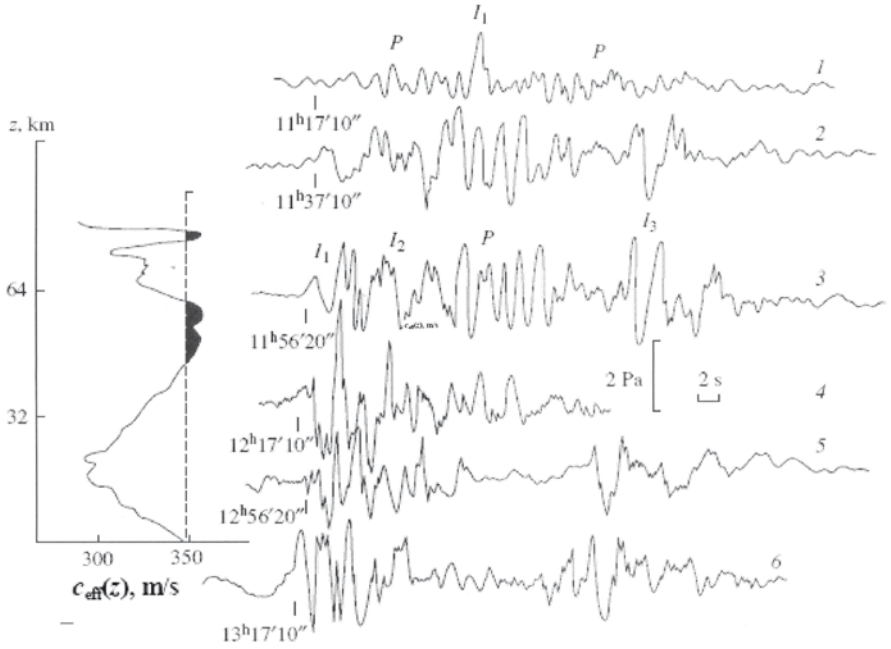

Fig. 16.5 Records of infrasonic arrivals in the zone of refractive acoustic audibility at a distance of 300 km from six explosions (1–6) equivalent to 20–70 tons of TNT implemented at a 20-min interval during daylight hours on July 7, 1990 (on the *right*). Profile of the effective acoustic speed $c_{\text{eff}}(z)$ (on the *left*; the region of ray turning is *shaded*)

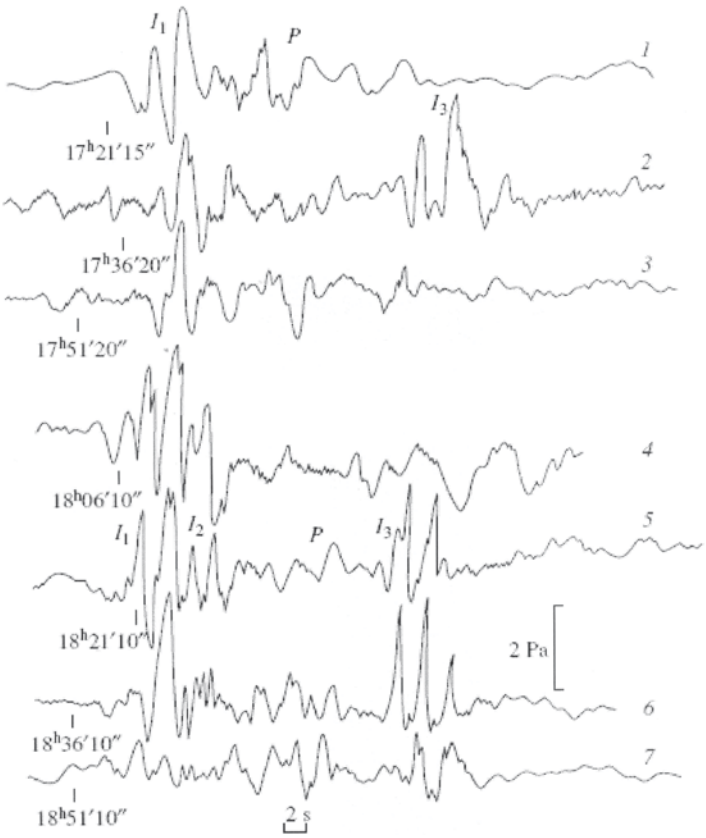

Fig. 16.6 Records of infrasonic arrivals in the zone of refractive acoustic audibility at a distance of 300 km from seven explosions (1–7) equivalent to 20–70 tons of TNT implemented at a 15-min interval in the evening of July 7, 1990

was *coherent* (see, for example, Fig. 16.4) for the three spaced microphones during a long (sometimes exceeding 3 min) time interval. The coherence of the signals suggests that the reflective structures that occupy an extensive region at the stratomesospheric altitudes are also *coherent* (ordered), and their horizontal scale is many times longer than the distance between the receiving microphones. In our case, this distance was about 100 m; however, similar long *coherent* signals from explosions are also (almost always) recorded on the microphones spaced a few kilometers apart on the ground surface.

The results of numerous studies of the inhomogeneous strato-mesospheric structure support (directly or indirectly) the occurrence of the ordered (*coherent*), long-lived, and limited (in size) locally stratified inhomogeneities in both temperature and wind fields, whose vertical and horizontal dimensions vary from tens to hundreds of meters and from a few to several tens of kilometers, respectively. These results were obtained with the use of the rocket method (the falling-sphere method), MST radars (Balsley

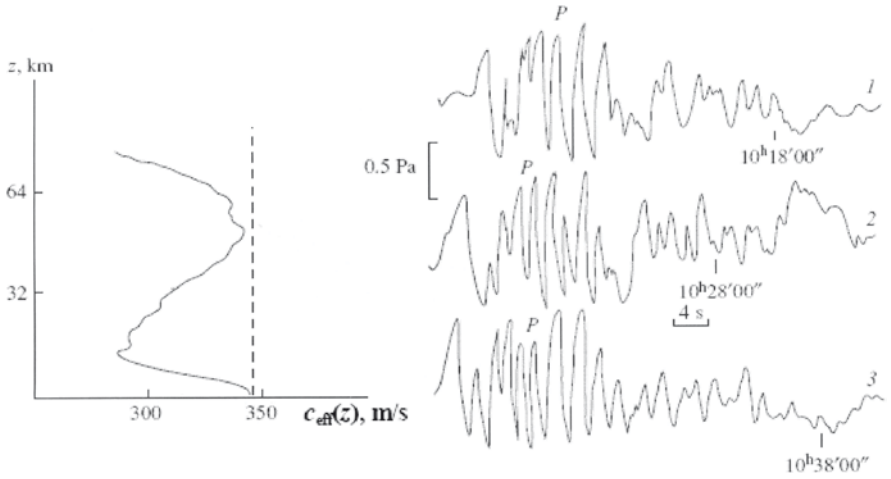

Fig. 16.7 Records of infrasonic arrivals in the zone of geometric shadow at a distance of 300 km from three explosions (1–3) equivalent to 20–70 tons of TNT implemented at a 10-min interval in the morning of May 21, 1989 (on the *right*). Profile of the effective acoustic speed $c_{eff}(z)$ (on the *left*). *P* denotes oscillating arrivals

and Gage 1980), optical lidars (Chunchuzov 2002), and refractive measurements (Grechko et al. 1981, 1997). In this case, it is noted that the values of the vertical temperature and wind gradients in such ordered stratified formations significantly (several times) exceed those of the corresponding average gradients (for example, for wind velocity, they reach 40–70 $m s^{-1}$/km, Sofiev 1986; Collins et al. 1992).

The partial reflection/scattering of infrasonic waves by coherent inhomogeneities, which are significantly extended in the horizontal direction, results in their penetration into the geometric shadow zone at long distances from explosions. The above-mentioned oscillating component appears because reflection/scattering occurs in all the portions of the ray paths (at different *z*) crossing the boundaries of the stratified structures. This component also significantly increases the duration of an infrasonic arrival in the audibility zone. Similar effects in oceanic acoustics were considered in Gostev et al. (1989)and Gostev and Shvachko (1998). Rapid variations are characteristic of the pulsed and oscillating components of signals recorded from explosions equivalent to 20–70 tons of TNT as well as from lower energy explosions (Kulichkov and Bush 2001) (see Fig. 16.3). In Figs. 16.5 and 16.6, it is seen that in the audibility zone during a rather short time period, some significant changes were observed not only in the amplitude, but also in the *structure* of arrivals, which, at one moment, had the form of the sequence of the localized components I_1–I_3 (corresponding to the sound ray turning in the strato-mesosphere at different altitudes) and, at another moment, had the form of the oscillating signal *P*. At some moments, the amplitudes of the localized I_1–I_3 (total reflection) and oscillating *P* (partial reflection) components proved to be comparable (curves *2*, *3* in Fig. 16.5 and curve *7* in Fig. 16.6). Moreover, the first arrivals I_{1-2} also had internal structure that varied during the time taken to conduct the experiments. In this case, the third arrivals I_3

sometimes disappeared and sometimes reoccurred in the experiments carried out during a 1-h period in the daytime (Fig. 16.5) and in the evening (Fig. 16.6). In Figs. 16.5 and 16.6, the oscillating components *P* change their structure. Note that in Figs. 16.5 and 16.6, the time interval between the first two arrivals I_{1-2} also varies during both daylight and evening hours. This is apparently due to the influence of atmospheric tides on the effective acoustic speed profile.

It is evident that variations in the structure of infrasonic signals are caused by changes in the form of the average effective acoustic speed profile and its fine structure. Different types of the $c_{\text{eff}}(z)$ profiles are shown in Figs. 16.5, 16.7, and 16.8, together with the examples of signals. Below, we shall consider a simple model which allows one to explain the basic properties of time variations in infrasonic arrivals from explosions.

Even in the case of total reflection, the amplitude and form of pulses depend significantly on the characteristics of the inhomogeneous structure of the atmosphere in the region of ray turning. If the ray turning height h_1 is in the vicinity of the height h of a local minimum of the acoustic refractive index squared $n^2(z)$ – maximum of $c_{\text{eff}}(z)$ (Fig. 16.9) – a portion of acoustic energy may penetrate to the above layers (Yu and Kravtsov 1965; Kulichkov 1989). In the general case, for a smooth profile $n^2(z)$, this problem was studied, for example, in Yu and Kravtsov (1965). In Kulichkov (1989), we considered a model of the piecewise-linear profile of $n^2(z)$ changes with height z. It is shown that the amplitude $|V|$ and the phase ψ of the reflection coefficient depend significantly on the ratio between the gradients q and

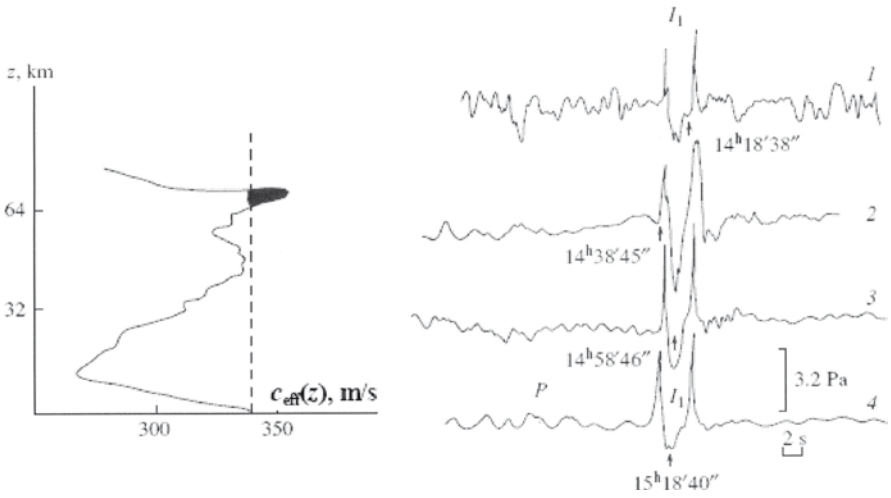

Fig. 16.8 Records of infrasonic arrivals in the zone of refractive acoustic audibility at a distance of 300 km from four explosions (1–4) equivalent to 20–70 tons of TNT implemented at a 20-min interval in the daytime of May 19, 1990 (on the *left*). Profile of the effective acoustic speed $c_{\text{eff}}(z)$ (on the *left*; the ray turning region is *shaded*). *P* denotes oscillating arrivals, and I_1 denotes localized (pulsed) arrivals

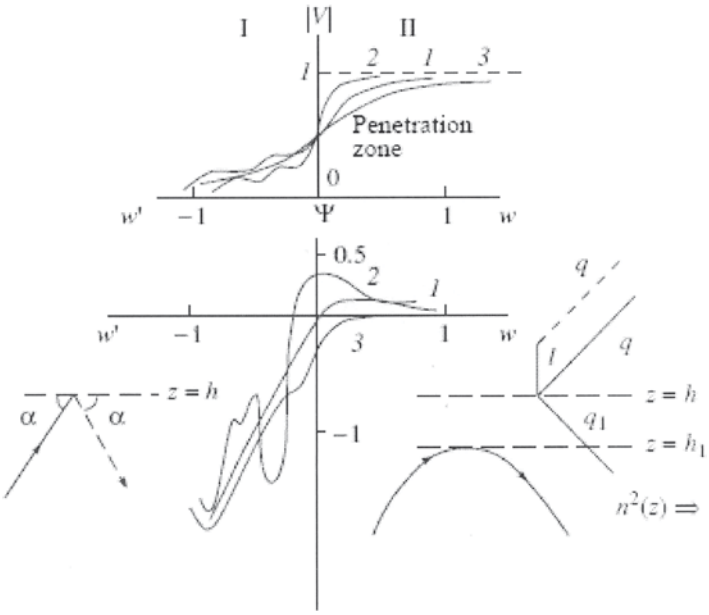

Fig. 16.9 Amplitude V and phase Ψ of the coefficient of sound wave reflection by an inhomogeneous atmospheric structure modeled with a bilinear height profile of the acoustic refractive index squared n^2 (z) at (1) $q_1/q=1$, (2) $q_1/q=4$, and (3) $q_1/q=0.25$. $z=h$ is the interface between the layers with different dn^2/dz; h_1 is the height of ray turning under total reflection, when the condition $c_{eff}(z)>c_{eff}(z=0)$ is fulfilled; l is the depth of the transition layer; α is the grazing angle; X-axis: $w'=(2/3)\,[k\sin^3\alpha/q_1]$; $w=(2/3)[k/q](h_1-h)^{3/2}q_1^{3/2}$; $q=dn^2/dz$ if $z>h$; and $q_1=dn^2/dz$ if $z<h$. **I** indicates the region of partial reflection**,** and **II** indicates the region of total reflection

q_1 below and above the ray turning height h_1 and also on the transition layer depth l (transition layer with vertical gradients equal to zero may exist between the layers with vertical gradients q and q_1 as indicated in Fig. 16.9) and the value of $\Delta h=h-h_1$ (Fig. 16.9). Changes in the values of Δh and q/q_1 (the vertical gradients q and q_1 of the square of the refractive index $n^2(z)$ are indicated in Fig. 16.9) result in the corresponding changes in the amplitude and form of a reflected pulsed signal.
When the condition

$$\Delta h = h_1 - h > k^{-2/3} q^{-1/3} \sim 1\,\text{km} \tag{16.1}$$

is fulfilled, such penetration is insignificant (Kulichkov 1989). The presence of the transition layer hinders this penetration. To estimate the depth l, we obtain an expression similar to (16.1). Here, the following values were taken for the variables entering (16.1): $k_0 \sim 5.8$ km^{-1} is the value of the wave vector for a sound pulse 3 s in duration at the upper stratospheric heights (Figs. 16.4–16.6), and $q \sim 0.03$ km^{-1} is the typical mean value of the vertical gradient of the acoustic refractive index squared.

Over minor time intervals, the value of Δh (or l) may oscillate with amplitudes of a few hundreds of meters, for example, due to the IGW effect (Kulichkov and

Bush 2001). In practice, this may result in noticeable changes in the structure of infrasonic arrivals from repeated sources even if the time interval among them is insignificant. This is supported by the experimental results given in Figs. 16.3–16.6.

The extent to which the variability of infrasonic arrivals from repeated sources (sources having the same parameters) is affected by IGWs and other types of waves depends apparently on the form of the average effective sound speed profile.

Let us conditionally differentiate four types of the $c_{\text{eff}}(z)$ profiles with different shapes and amplitudes of the maximum effective sound speed (Figs. 16.5, 16.7 and 16.8): (1) the value of the $c_{\text{eff}}(z)$ maximum significantly exceeds the surface values of $c_{\text{eff}}(z=0)$, and this maximum is extended along the height z (the lower black maximum in Fig. 16.5); (2) the same, but this maximum is narrow (the profile in Fig. 16.8); (3) the value of the $c_{\text{eff}}(z)$ maximum slightly exceeds either the surface values of $c_{\text{eff}}(z = 0)$ or the values of the maxima located below, if the stratification profile has a few extrema of $c_{\text{eff}}(z)$ (the upper black maximum of the $c_{\text{eff}}(z)$ profile in Fig. 16.5); and (4) the maximum values of $c_{\text{eff}}(z)$ are smaller than the surface values of $c_{\text{eff}}(z = 0)$ (Fig. 16.7).

Different types of infrasonic signals (from explosions) observed in the experiments correspond to different types of $c_{\text{eff}}(z)$ profiles. A stable recording of infrasonic signals consisting of both localized and oscillating components is characteristic of the type 1 profile (the $c_{\text{eff}}(z)$ maximum is well pronounced, and its changes do not violate the condition $c_{\text{eff}}(z) > c_{\text{eff}}(0)$; therefore, the localized component is stably recorded). At the same time, due to an increase/decrease of the ray turning height under the influence of IGWs or due to the transport of coherent structures by wind in the temperature and wind fields, the case may occur when these heights are in the vicinity of a local minimum of the acoustic refractive index squared (Fig. 16.9). In this case, the phenomenon of *penetration* becomes significant, and the coefficients of the total and partial reflections may take comparable values. This results in an equalization of the amplitudes of different components of a signal. In Figs. 16.5 and 16.6, the arrivals I_{1-2} correspond to the type 1 profile. For the type 2 profile, a recorded signal has a similar structure (Fig. 16.8), but the amplitude of the pulsed component of arrival significantly exceeds that of the oscillating component (since partial reflection is effective only in a rather narrow region in the vicinity of the $c_{\text{eff}}(z)$ maximum, the duration of the oscillating component is shorter than that in the previous case for the type 1 profile). For the type 3 profile, due to the effect of IGWs or the transport of coherent structures, the ray turning condition $c_{\text{eff}}(z) > c_{\text{eff}}(z=0)$ may be violated; therefore, the recorded signal is unstable (the third arrivals I_3 in Figs. 16.5–16.6). In the case of the type 4 profile, the pulsed component of a signal is absent, because the total reflection condition $c_{\text{eff}}(z) > c_{\text{eff}}(z=0)$ is not fulfilled. Only the oscillating component corresponding to partial reflection/scattering of infrasonic waves by coherent inhomogeneous structures of the acoustic refractive index in the strato-mesosphere is recorded (Fig. 16.7). This signal is very long and stable. In this case, the region of small grazing angles (i.e., relatively high values of the reflection coefficient V) is rather extensive in height because of a wide $c_{\text{eff}}(z)$ maximum.

16.4 Partial Reflection of Infrasonic Pulses from Anisotropic Inhomogeneities in the Middle Atmosphere

As noted above, in the audibility zone, acoustic arrivals are a combination of both the localized (*I*) and oscillating (*P*) components. Only the oscillating components (*P*) are usually recorded in the geometric shadow region. Nevertheless, in parallel with the oscillating infrasonic arrivals (*P*), signals having the form of localized pulsed components (*I*) usually observed only in the audibility zone may be recorded even in the geometric shadow zone. This is suggested by the results of our experiments carried out in different seasons (Bush et al. 1997; Kulichkov and Bush 2001). According to ray-path calculations, the reflection altitudes for the indicated types of infrasonic signals are within the mesosphere ($z > 50$ km).

Fig. 16.10 gives the most illustrative example of such a localized mesospheric arrival I_m, recorded in late fall within the geometric shadow region at a distance of 200 km to the west of a surface explosion equivalent to 260 tons of TNT (Kulichkov et al. 2002). Fig. 16.10 also shows the thermospheric arrival I_t (whose *U*-wave form is typical of the localized pulsed acoustic arrivals observed in the audibility zone) and the vertical profile of the effective sound speed $c_{eff}(z)$ (adiabatic sound speed plus wind velocity in the direction of sound wave propagation) estimated using data obtained from the rocket sounding of the atmosphere during the periods closest to those during which the experiments were conducted. The difference between the values of the effective sound speed at the ground surface ($c(0) = 326$ m/s) and the corresponding values for the stratosphere and mesosphere exceeded 70 m/s (see Fig. 16.10), which excluded the possibility of a ray turning toward the ground surface at these altitudes. It follows from the calculations that the time of I_m appearing

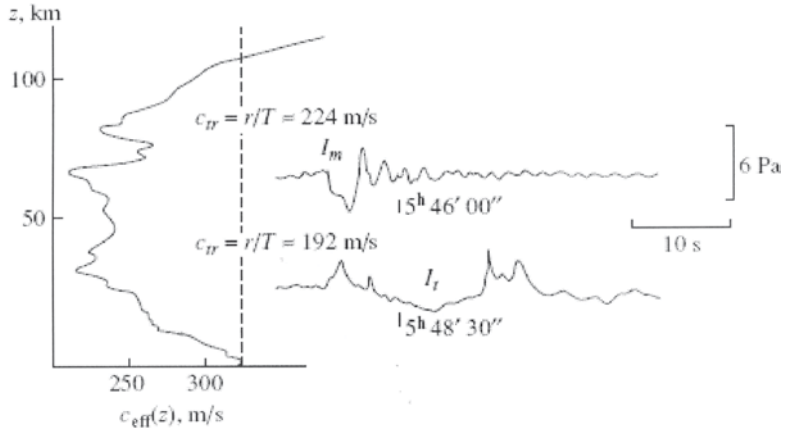

Fig. 16.10 Acoustic signals recorded at a distance of 200 km (mesospheric and thermospheric arrivals) to the west of the explosion equivalent to 260 tons of TNT implemented on November 28, 1981 (on the *right*); the effective sound-speed profile (on the *left*); and c_{tr} is the mean horizontal propagation speed

corresponds to the reflection of infrasonic waves from the inhomogeneities at an altitude (z_{ref}) of about 60 km. For the thermospheric signal I_t, the ray turning altitude is estimated at z_{ref} ~ 115 km (in this case, the reflection coefficient is equal to unity).

This previously unstudied, localized type of infrasonic arrival I_m in the geometric shadow region was observed in the experiments carried out in 1989–1990. In this case, the measurements in the acoustic shadow region were taken at a distance of 300 km to the north of the surface explosions equivalent to 20–70 tons of TNT. Some results are given in Figs. 16.2 and 16.11. Figure 16.11 shows the infrasonic signals recorded from three explosions implemented at a 20-min interval in 1989. The presence of both the quasi-periodic (P_{sm}) and localized (I_m) signal components is seen. The effective sound-speed profile and some ray paths for the 1990 experiments are shown in Fig. 16.12 (Kulichkov et al. 2002). For grazing angles α smaller than 10°, acoustic signals propagate in the acoustic waveguide formed by wind inversion in the lower troposphere (Lamb wave – L in Fig. 16.2). It is seen from Fig. 16.12 that the effective sound-speed values for the stratosphere and mesosphere are smaller than those for the ground surface. Because of this, for both stratospheric and mesospheric infrasonic signals, the geometric shadow zone is formed on the ground surface. In this case, stratospheric and mesospheric acoustic arrivals (observed in the geometric shadow region) from surface explosions are formed under partial sound reflection from coherent locally stratified inhomogeneities of the acoustic refractive index in the upper stratosphere-lower mesosphere (Bush et al. 1997). The dashed lines in Fig. 16.12 correspond to the supposed ray paths. A thermospheric signal is formed at refractive (according to Snell's law) ray turning in the thermosphere. The long-term oscillating infrasonic signals P_{sm} were observed in the shadow region in all the experiments and in all seasons (Kulichkov 1998, 2004; Bush et al. 1997; Kulichkov and Bush 2001), which suggest the constant presence of long-lived inhomogeneous structures that have a significant reflectivity (for example, a stably large value of the vertical gradient of the effective sound speed) and occupy a rather extensive altitude region in the stratosphere and mesosphere.

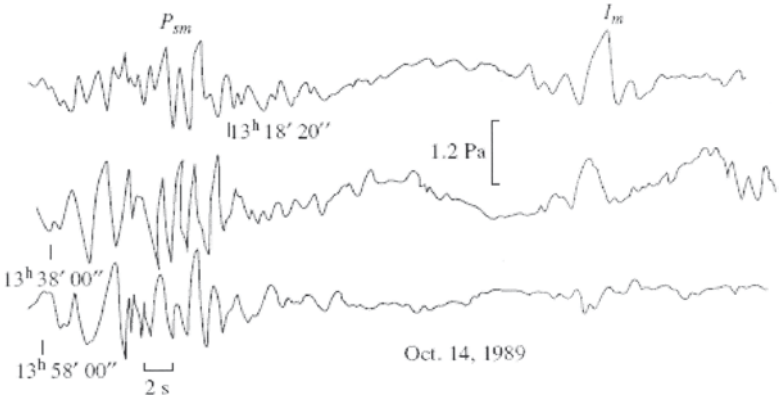

Fig. 16.11 Infrasonic signals recorded at a distance of 300 km to the north of the explosions equivalent to 20–70 tons of TNT implemented on October 14, 1989; P_{sm} and I_m denote the oscillating and pulsed mesospheric arrivals, respectively

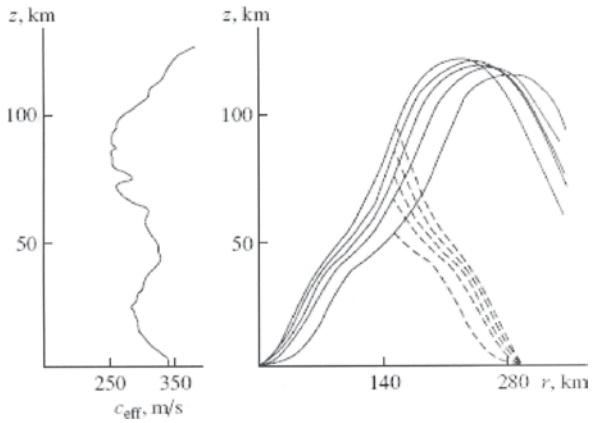

Fig. 16.12 Examples of ray paths for the experiments carried out on October 20, 1990. The *dashed lines* correspond to the supposed paths under the partial reflection of acoustic signals from locally layered inhomogeneities in the stratomesosphere. The effective sound-speed profile is on the *left*

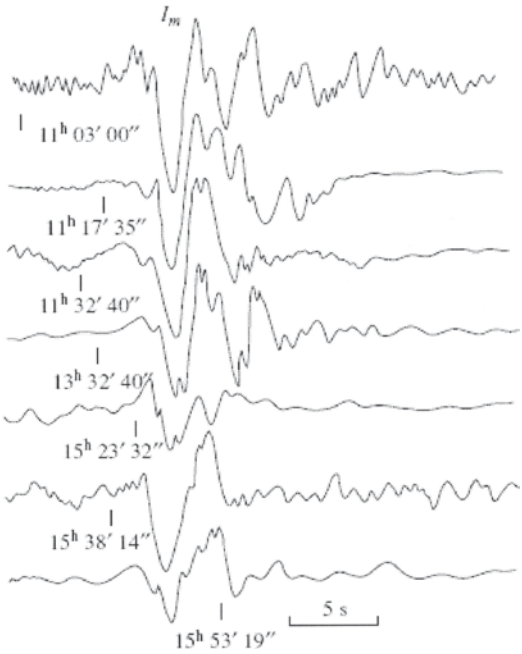

Fig. 16.13 Localized (pulsed I_m) infrasonic signals recorded in the geometric shadow zone at a distance of 300 km from the explosions equivalent to 20–70 tons of TNT implemented on October 20, 1990

An example of the localized infrasonic arrivals I_m recorded during a set of experiments is shown in Fig. 16.13. In this case, the explosions were implemented at intervals of 15-min. It is seen that such arrivals are observed during the whole set

of the experiments for more than 4 h, which suggests the occurrence of localized reflecting layers in the mesosphere during a time period longer than 4 h. Variations in the form of acoustic arrivals are also seen, though their localized pulsed structure is conserved. Variations in the form of the signals shown in Fig. 16.13 apparently suggest the evolution of the reflecting layers due to the effect of IGVs and tides (Kulichkov and Bush 2001).

Let us assume that the occurrence of the localized infrasonic arrivals I_m in the shadow zone is determined by the presence (in the middle mesosphere) of a thin localized layer (or a system of such layers) with a high value of the vertical gradient of the effective sound speed. Such a localization may be due to the occurrence (in the mesosphere) of the so-called wind-corner layers, within which a rapid change is noted in wind direction with altitude (Yu and Kravtsov 1965; Kulichkov 1989; von Zahn and Widdel 1985).

The occurrence of wind-corner layers in the mesosphere was first noted in analyzing rocket sounding data (von Zahn and Widdel 1985). The authors of von Zahn and Widdel (1985) defined the wind corner as a thin layer (less than 1 km in depth) within which the wind direction may change with a gradient more than 50°/1 km (compared to the mean value of the indicated gradient of no more than 10°/1 km). In the center of this layer, the values of the horizontal wind velocity have their local minimum. In Hooper and Thomas (1997), the same authors made a more detailed analysis of the wind-corner data obtained from rocket measurements, which allowed them to assume that (1) the frequency of occurrence of wind corners is approximately the same in summer and winter; moreover, a strong wind corner was noted in each third rocket measurement; (2) wind corners may occur at any time of day; (3) wind-corner layers were observed at altitudes below the mesopause ($z \sim 80$ km) in winter and above the mesopause in summer; several wind-corner layers may occur within an altitude interval of about 5 km in summer and 3–3.5 km in winter; (4) characteristic of a strong wind corner is that, in summer, wind tends to change its north direction to westward, and in winter, the wind direction is reversed; and (5) at altitudes below 90 km, the wind corners tend to form within or close to the layer in which the Richardson number $\mathrm{Ri} < 1/4$ (where $\mathrm{Ri} = N^2/(du/dz)^2$; $N^2 = \{g(d\rho/dz) + g^2/c^2\}$-Brunt-Väisälä frequency, ρ – atmospheric density, u – wind velocity, z – height, c – sound velocity. When Ri is small (typically considered below 1/4), then velocity shear is considered sufficient to overcome the tendency of a stratified fluid to remain stratified, and some mixing will generally occur. When Ri is large, turbulent mixing across the stratification is generally suppressed).

The wind-corner layers were observed during radar sounding of the middle atmosphere. According to Hooper and Thomas (1997), the values of the vertical wind-velocity gradients may reach about 100 $\mathrm{m\,s^{-1}}$/ km within these layers. Very high values of the vertical wind-velocity gradients in the wind-corner layers were also noted by Collins et al. (1992), who, with the aid of the EISCAT 224-MHz radar measurements taken in March 1990, revealed the occurrence (at an altitude of about 68 km) of a thin layer whose vertical dimension was noticeably smaller than 1 km, and within which the meridional wind rapidly changed its direction, so that the value of its projection along the northward direction changed to 38 m/s.

Infrasonic waves from localized (in altitude) coherent locally stratified inhomogeneities, having significant horizontal dimensions and such high values of the vertical wind-velocity gradients, may have coefficient of partial reflection values sufficient for the corresponding signals to be recorded at the ground surface. These signals will have the form of localized pulses (Kulichkov 2003).

To estimate the coefficient of partial reflection of infrasonic signals from inhomogeneous structures in the mesosphere, let us use the recorded data on infrasonic arrivals from an explosion (see Fig. 16.2). According to the acoustic "momentum" conservation law, which has been experimentally substantiated for the case of LRSP in the atmosphere (Gostev et al. 1989), the "momentum" $\boldsymbol{I}$ (equal to the product of the wave profile area $\int p\,\mathrm{d}t$ in the coordinates p (pressure) and t (time) and the distance r to the source) takes the same (to within the ray focusing factor) values for the acoustic signals corresponding to all the types of ray paths. Taking into account the fact that the reflection coefficient for a thermospheric arrival is equal to unity (because this arrival is formed at ray turning in the thermosphere – the case of total reflection) and comparing between the "momentum" $\boldsymbol{I}$ values for the thermospheric I_t and mesospheric I_m infrasonic arrivals, one can roughly estimate the coefficient of partial reflection V_m of mesospheric signals from mesospheric inhomogeneities. For the localized mesospheric arrival I_m in Fig. 16.2, we have $V_m \sim I_m/I_t \sim 0.25$. In obtaining this relation, we neglected the insignificant differences in the sound ray focusing factors for the thermospheric and mesospheric acoustic arrivals in Fig. 16.2. According to the experimental data, the mean horizontal mesospheric arrival speed $c = r/T$ (r is the distance between the source and the receiver, and T is the time of propagation) is approximately equal to 0.275 km/s. According to the calculations of the ray paths shown in Fig. 16.4, such values of $c = r/T$ correspond to reflection altitudes of 74–75 km. The ray incidence angle α_0 for the indicated altitudes is approximately equal to 56°. Here, it should be noted that the resulting estimates are conventional because significant errors in the measurements taken at the mesospheric altitudes are characteristic of any data obtained by rocket (or other) sounding of the atmosphere. Moreover, the data presented in Fig. 16.12 were obtained during the time closest to (but not within) the observation period. This leads to errors in the ray-path calculations. It follows from Fig. 16.2 (see also Fig. 16.13) that the mesospheric arrival I_m under consideration, unlike the earlier arrivals P_{sm}, is localized, which suggests the reflection from a rather thin layer. Below, we shall obtain rough estimates of the vertical scale of this layer and the vertical gradients of the effective sound speed, which may correspond to the observed coefficients of the partial reflection of infrasonic waves from a localized mesospheric heterogeneity ($V_m \sim 0.25$).

Let us consider the case of the partial reflection of infrasonic waves from an Epstein symmetric layer (Fig. 16.14), which is most appropriate (in our opinion) for the description of the wind-corner layer, when, in its center, the horizontal wind velocity takes on minimum values. Note that the models of the wind velocity profile in the form of Epstein layers are widely used in oceanic acoustics in studying the penetration of acoustic signals into the geometric shadow region (Gostev et al. 1989; Gostev and Shvachko 1998).

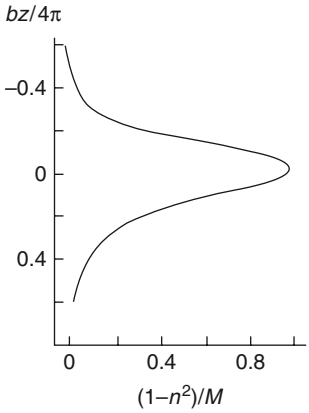

Fig. 16.14 Epstein symmetric layer (Rottger 1987). *X*-axis: $(1-n^2)/M$. *Y*-axis: $bz/4\pi$

The acoustic refractive index $n(z)=c_0/c(z)$ (hereafter, by the sound speed $c(z)$ we mean its effective values $c_{\text{eff}}(z)$) as a function of some conventional altitude z in the Epstein symmetric layer has the form

$$n^2(z) = 1 - 4M \times e^{mz} \left(1 + e^{mz}\right)^{-2}, \tag{16.2}$$

where $m \quad 4\pi/S\lambda_0$, S is the wave layer depth, λ_0 is the length of the wave incident on the layer, $M=1-n_1^2$; $n_1^2=[c_0/c_1]^2$; c_1 is the sound speed in the center of the layer ($z=0$).

The coefficient of the partial reflection V of acoustic waves from the Epstein symmetric layer at $M<0$ (we consider the case of reflection from the layer in whose center the refractive index takes its maximum values, and the effective sound speed is minimum) is written as (Kulichkov et al. 2002)

$$V^2 = \cos^2 \pi d_2 \,/\, \{\cos^2 \pi d_2 \mathrm{ch}^2(\pi S \cos\alpha_0) + \sin^2 \pi d_2 \mathrm{sh}^2(\pi S \cos\alpha_0)\}, \tag{16.3}$$

where $d_2 = 0.5(1 - 4S^2M)^{1/2}$; and α_0 is the angle of wave incidence on the layer. Assuming that at a (presumed) reflection altitude of 74–75 km, the effective sound speed c_0, the wavelength λ_0, and the angle of incidence α_0 are roughly equal to 0.288 km/s, 1.44 km, and 56°, respectively, we can estimate the conventional range of variations in the wave layer thickness S and the acoustic refractive index (within this layer) squared M. We have $S = 1.15$ at $M = -0.4$ and $S = 0.7$ at $M = -0.3$. With a decrease in S, the absolute values of M also decrease, while the partial reflection coefficients remain unchanged. We shall estimate the range of variation in the reflecting layer depth $h = 2l$ from the relation $l \sim 0.4 \times \lambda_0 \times S$. As follows from (16.2) (see also Fig. 16.14), at such values of l, the acoustic refractive index n ($\pm\, l$) at the layer boundaries differs from $n_0 = 1$ by only 0.5%. We shall estimate the vertical effective sound-speed gradient $\partial c/\mathrm{d}z$ at $\partial c/\mathrm{d}z \sim \Delta c/l$, where Δc is the variation of the effective sound speed in the layer, which corresponds to the values obtained for M. As a result, we shall obtain the range of variations in the vertical gradients of the effective sound speed and the depth of the Epstein symmetric layer for the experimental value of the coefficient of partial reflection ($V_m \sim 0.25$) of acoustic signals

from the inhomogeneous layer at an altitude of 74–75 km. We have $\partial c/\mathrm{d}z \sim 66$ (m/s)/km if $h = 2l = 1.324$ km and $\partial c/\mathrm{d}z \sim 87$ (m/s)/km if $h = 2l = 0.8$ km. The variations in the vertical gradients of the effective sound speed and layer depths, which are necessary to obtain the values of the partial reflection coefficient $V_m \sim 0.25$, are within the range $66 < \partial c/\mathrm{d}z < 87$ (m/s)/km under the corresponding changes $1.324 > h > 0.8$ km (with a decrease of h, the necessary values of the vertical effective sound-speed gradient $\partial c/\mathrm{d}z$ increase). The calculations performed for other types of Epstein layers and also for a bilinear profile of the acoustic refractive index squared yield $\partial c/\mathrm{d}z$ and h values, which, in the order of magnitude, correspond to those given above. The results obtained are in agreement with the data obtained from rocket and radar measurements of the vertical gradients of wind velocity and wind-corner layer depths (von Zahn and Widdel 1985; Turner 1973; Hooper and Thomas 1997).

The temporal variability of infrasonic signals scattered from the fine-layered structure of the middle atmosphere and observed in shadow zone was studied in Kulichkov (2004). The values of the coefficients of partial reflection (V) of infrasonic waves by inhomogeneous structures in the middle atmosphere are given in Fig. 16.15a. The maximum values of the coefficients V for infrasonic arrivals recorded in the geometric shadow region were observed in July. Figure 16.15b shows the radar data used to estimate the zonal (in the radar beam direction) wind velocity component variance, due to the effect of IGWs within the range of periods between 5 min and 2 h in the height region between 65 and 85 km (Murayama et al. 1992). Here, the IGW intensity in the mesosphere has its local maximum in July as well.

16.5 On the Potential for Studying Anisotropic Turbulence in the Atmosphere Using the Acoustic Sounding Method

It is known that atmospheric turbulence significantly affects the amplitudes and phases of acoustic signals at long distances from explosions. Therefore, one can assume that the characteristics of atmospheric turbulence can be determined by using the reciprocity relation between these characteristics and the values of the amplitude and phase distortions of acoustic signals propagating in the turbulent atmosphere. An example of the influence of atmospheric turbulence on errors in determining the azimuth and grazing angle of sound rays for infrasonic signals propagating in a stratospheric acoustic waveguide is shown in Figs. 16.16a, b.

The effect of turbulent inhomogeneities on the characteristics of acoustic signals was studied earlier in the approximation of the theory of local homogeneous and isotropic turbulence. The first studies in this area were conducted by Krasil'nikov (1945) in the 1940s. The well-known studies by Tatarskii (1971) and others are also devoted to this problem.

The effects of mesoscale anisotropic inhomogeneous structures of temperature and wind velocity (with horizontal sizes of 100 m to 2–3 km and a lifetime of 1–30 min) on the characteristics of pulsed acoustic signals propagating in the

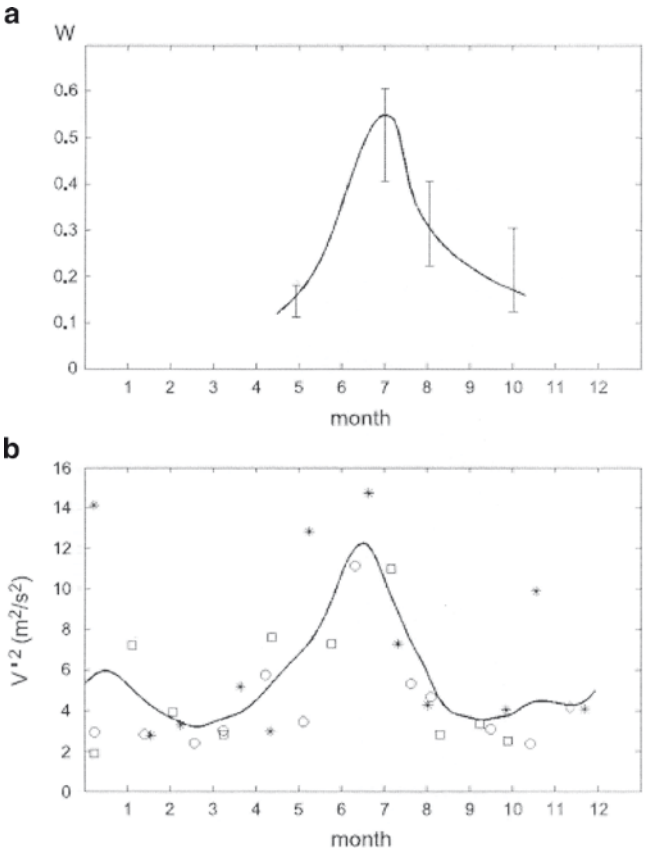

Fig. 16.15 Coefficient (W) of partial reflection of infrasonic signals from fine-layered structure of the middle atmosphere obtained in different seasons (Bush et al. 1997) (**a**). Error bars correspond to variations of the coefficient W in different experiments. The variance (V'^2) of zonal radial wind velocities in the altitude regions of 65–85 km averaged for periods of 5 min–2 h and observed in different seasons and years (*circle* – 1986; *circle with dot* – 1987; *astericks* – 1988) (**b**)

troposphere and stratosphere over long distances from their sources remain insufficiently studied. Some aspects of the theory of the effect of anisotropic turbulence on the characteristics of acoustic signals are considered in Ostashev et al. (2005) without relation to real experimental data.

The relation between observed fluctuations in the parameters of acoustic signals (τ is the signal duration, θ is the azimuth, and α is the grazing angle) and the characteristics of anisotropic turbulence in the troposphere was analyzed on the basis of the results obtained in Chunchuzov (2002), where the spectra of anisotropic fluctuations in (temperature) density and wind velocity were studied.

In our experiments (Chunchuzov et al. 2005), the angles of acoustic signal arrivals were measured with the aid of a conventional scheme of sound recording

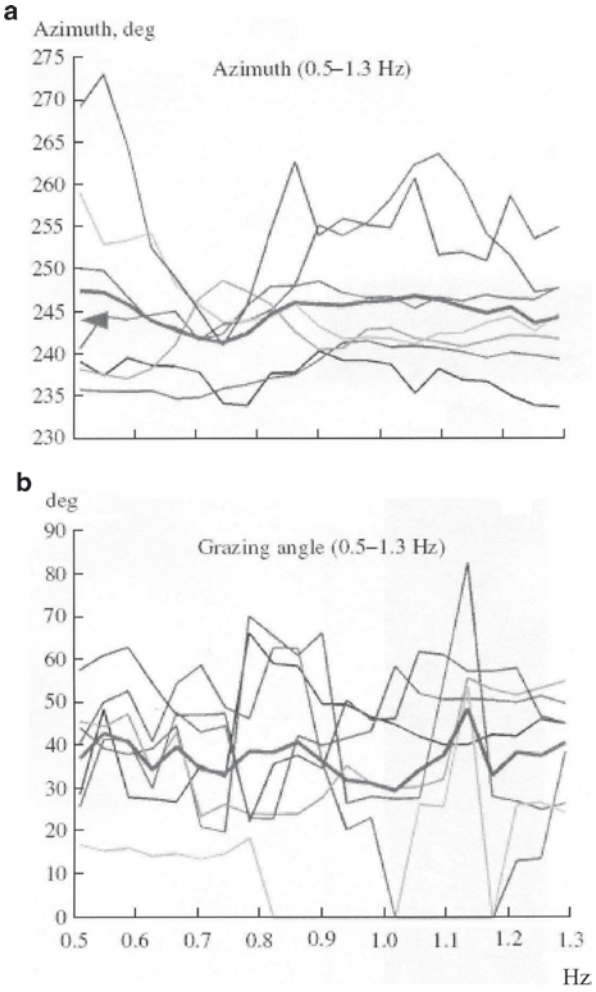

Fig. 16.16 Fluctuations in the (**a**) azimuths and (**b**) grazing angles of infrasonic signals (in the frequency range 0.5–1.3 Hz) recorded at a distance of about 300 km from the point of setting off surface explosions equivalent to 20–70 tons of TNT in different years (*thin curves*). The mean grazing angle (*thick curve*). *X*-axis: acoustic frequency in Hz

by a system of three receiving microphones (Fig. 16.17). Errors in measuring the azimuth (θ) and grazing angle (the α angle of tilting of the sound ray about the horizon) are due mainly to the fluctuations $\delta\Delta t_2$ and $\delta\Delta t_1$ in the time delays of signal-front arrivals Δt_2 and Δt_1, about their mean values $<\Delta t_2>$ and $<\Delta t_1>$. With consideration for the form of the three-dimensional spectra of fluctuations in the horizontal (x) projection of wind velocity and vertical displacements, it is possible to obtain the following expression for the variance of travel-time fluctuations $\delta\tau^2(x_1)$, which are caused by anisotropic inhomogeneities within the range of small vertical scales:

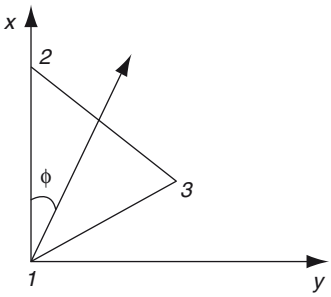

Fig. 16.17 Conventional scheme of location of acoustic microphones 1–3. *Arrow* corresponds to wave front propagation. The axis *X* is directed to the north

$$\left\langle \delta\tau^2 \right\rangle = 2\pi R_0 \left[\left(2\beta \left\langle \mu_T{}^2 \right\rangle + \gamma \left\langle \mu_\sigma{}^2 \right\rangle \right) / m^* \right]_0 / 3c_0{}^2 \quad (\alpha \neq 0), \tag{16.4}$$

$$\left\langle \delta\tau^2 \right\rangle = 4\pi^{1/2} r \left(2\beta \left\langle \mu_T{}^2 \right\rangle + \gamma \left\langle \mu_\sigma{}^2 \right\rangle \right) / \left(3k_0 c_0{}^2 \right) \quad (\alpha \approx 0), \tag{16.5}$$

where (16.4) is obtained for a waveguide ray with a small vertical angle $\alpha \neq 0$, and with the radius of ray-path curvature $R_0 = |z''(x_0)|^{-1}$ at the turning point with the coordinates $(x_0, z(x_0))$, and where (16.5) is obtained for the case of an almost horizontal ray $\alpha \approx 0$, grazing along the land surface to the receiver located at the distance r from the source. The radius of curvature can be determined from the following formula:

$$R_0 = \left| z''(x_0) \right|^{-1} = \left| \mathrm{d}(\mathrm{tg}\alpha)/\mathrm{d}x \right|^{-1}_{x=x0}. \tag{16.6}$$

In (16.4) and (16.5), $\left\langle \mu_T{}^2 \right\rangle = \left\langle \delta c^2 (x,t) / c_0{}^2 \right\rangle$ and $\left\langle \mu_\sigma{}^2 \right\rangle = \left\langle vx^2 / c_0{}^2 \right\rangle$ denote the contributions made by the relative fluctuations in temperature (or sound speed) and wind-velocity projection, respectively, to the variance of fluctuations in the acoustic refractive index, and r is the horizontal distance from the source to the receiver. The brackets $|\ldots|_{x=x0}$ in (16.6) imply that the expression inside them is taken at the point of ray turning.

The constants γ and β in (16.4) and (16.5) are the proportionality coefficients in the laws of decrease ($\sim k_z^{-3}$) for the vertical spectra of horizontal wind-velocity and temperature inhomogeneities with an increase in the vertical wave number k_z. Their numerical values are in the range between 0.1 and 0.3 (Chunchuzov et al. 2005).

The theoretically predicted range of vertical scales in which the vertical spectra of anisotropic inhomogeneities of wind-velocity and temperature decrease according to the law k^{-3} is determined by the interval $m^* < k_z < m_M$, where m^* is the characteristic vertical wave number above which the nonlinearity forms a spectral tail with the law of decrease k_z, and $m_M = m^* \exp(\beta^{-1})$ is the critical wave number, above which the spectral tail becomes unstable.

Note that the relation $2\langle v_x{}^2 \rangle = N_1{}^2 \nu_v{}^2$ (where ν_v is the variance of the medium's vertical displacements caused by IGWs) is valid for the field of internal waves; therefore, both of the contributions to the refractive index can be expressed through $\langle v_x{}^2 \rangle$ (Kulichkov et al. 2008):

$$< \mu_T^2 >= (N_1^2 v_v / g)^2 / 4 \approx (N_1^2 < v_x^2 > / 2g^2, < \mu_\sigma^2 >= N_1^2 v_v^2 / c_0^2 = < v_x^2 > / c_0^2.$$

Thus, for waveguide rays, the value of $<\delta\tau^2>$ increases as the variance of fluctuations in wind velocity in the vicinity of the point of ray turning and the characteristic vertical scale $2\pi/m^*$ increase. It is the critical wave number m_M that determines the minimum vertical scale $2\pi/m^*$ on which the spectral components become unstable. It is assumed that, on the one hand, if $k_z \geq m_M$ (k_z – vertical wave number) turbulence is generated owing to wave-field breaking in certain spatial regions where wave instability occurs. On the other hand, the generated turbulence leads to a turbulent diffusion of the wave components of the spectrum with $k_3 < m_M$, thereby stabilizing the increase in the gradients of the wave field because of its nonlinearity.

From measurements of $<\delta\tau^2>$ at different distances from the source, we obtain data on the root mean square values of wind-velocity projection $(<v_x^2>)^{1/2}$ at different heights of ray turning and, hence, on the vertical gradient of this quantity. For typical fluctuations in wind velocity and under the conditions of a stably stratified ABL, for the mean square of fluctuations in signal travel time $<\delta\tau^2>$ in the lower troposphere at a distance of 2.5 km from the source, it can be found that

$$\left(\left\langle \delta\tau^2 \right\rangle\right)^{1/2} = 4.5 \times 10^{-3} \text{ sec.} \tag{16.7}$$

In order to calculate (16.7), we used the following parameter values characteristic of the lower atmosphere:

$R_0 \sim 35$ km; $<\mu_\sigma^2 = v_x^2>/c_0^2 \approx (0.6/340)^2 = 3.1 \times 10^{-6}$; the root mean square wind velocity $(<v_x^2>)^{1/2} - 0.6$ m/s; the Brunt Väisälä frequency $N_1 = 0.025$ rad/s; $<\mu_T^2> = 0.025^2 \times 0.6^2 / 19.6^2 = 5.9 \times 10^{-7}$; the characteristic vertical wave number for tropospheric anisotropic inhomogeneities $m^* = N_1/(<2v_x^2>)^{1/2} \approx 0.03$ rad/m, which corresponds to the vertical scale $2\pi/m^* \approx 210$ m; and the numerical value of the coefficient $\beta \sim 0.22$.

The values obtained for $(<\delta\tau^2>)^{1/2}$ are in good agreement with the root mean square fluctuations in signal travel time, which were obtained experimentally at a distance of 2.5 km under the conditions of a stably stratified ABL (Chunchuzov et al. 2005; Kulichkov et al. 2008). Figure 16.16a shows some example of fluctuations in the azimuths of acoustic signals.

To estimate fluctuations in the azimuth of signal arrival θ, we obtained the following expression:

$$\left[\left\langle (\delta\theta)^2 \right\rangle\right]^{1/2} / \left|\left\langle \theta \right\rangle\right| \approx 2\left[\left\langle (\delta\Delta t_2)^2 \right\rangle\right]^{1/2} / \left|\left\langle \Delta t_2 \right\rangle\right|, \tag{16.8}$$

where Δt_2 is the delay time between signals on the remote microphones of the receiving system. A theoretical estimate of the root mean square error in measuring the signal time delay between the receivers yields $[(<\delta\Delta t_2)^2>]^{1/2} = [D_\tau(0, \Delta y_0)]^{1/2} \approx 0.6 \times 10^{-3}$ s, which does not exceed the accuracy of measurements of time delays (1 ms). Here, $D_\tau(0, \Delta y_0)$ denotes the horizontal structure function of fluctuations in signal travel time for two receivers located at the distance Δy_0 from each

other in the direction transverse to the direction of sound-wave propagation. In our experiments, the mean azimuth $<\theta>$ of signal arrival at a distance of 2.5 km was (−15)°, and the mean delay between the moments of signal arrival was $|\langle \Delta t_2 \rangle| = 0.0228$ s (at a sound speed of 340 m/s in the vicinity of the land surface). In this case, we have the relative error $[(<\delta\Delta t_2)^2>]^{1/2}/|<\Delta t_2>|=0.026$; therefore, the root mean square value of fluctuations in the azimuth of signal arrival is $[(<\delta\theta)^2>]^{1/2} \approx 1°$, which corresponds to the experimental data given in Fig. 16.16a.

The fluctuations $\delta\alpha$ in the grazing angles α of acoustic signals were estimated in a similar way:

$$\left(\left\langle \delta\alpha^2 \right\rangle\right)^{1/2} \approx \left(c_0 / x_1\right)\left(\left\langle \delta\Delta t_1^{\,2} \right\rangle\right)^{1/2} / \left|\left\langle \sin(\alpha) \right\rangle\right|. \tag{16.9}$$

It follows from (16.9) that the error $(<\delta\alpha^2>)^{1/2}$ increases with a decrease of the angle α therefore, a correct determination of the small angles α, whose values are comparable to the very error in their determination, becomes almost impossible. For the experiments carried out on August 9, 2004, it is found that $(<\delta\alpha^2>)^{1/2} \approx 0.11$ rad (≈6.5°), which is in agreement with the experimental data (Kulichkov et al. 2008).

In order to calculate fluctuations in the azimuths and grazing angles of acoustic signals propagating in a stratospheric acoustic waveguide at a distance of several hundreds of kilometers from their sources, we will use the following values for the characteristic parameters of anisotropic fluctuations in wind velocity at the stratospheric altitudes of acoustic-ray turning (35–40 km): $\sigma = (\langle v_x^{\,2} \rangle)^{1/2} = 5$ m/s is the root mean square value of wind-velocity fluctuations; $m^* = N/(2^{1/2}\sigma) = 0.02$ rad/s/ ($2^{1/2}$ 5 m/s) = 0.0035 rad/m; $L = 2\pi/m^* \sim 1{,}800$ m is the outer vertical scale of the fluctuations; $e_0 = 0.0065$ is the squared ratio between the vertical and horizontal scales of inhomogeneities (for the stratosphere, this ratio is in the range 0.0001–0.001); $\Delta y = 300$ m is the distance between the receiving microphones; and $<\delta\tau^2> = 0.078$ s^2 is the mean square of fluctuations in the travel time of a stratospheric arrival at the horizontal distance $r = 300$ km from the source.

In this case, $D_\tau(0, \Delta y_0) \approx 6 <\delta\tau^2> (e_0 m^{*2} \Delta y^2) \approx 3.35\times10^{-3}$ s^2; therefore, at a typical signal delay $|<\Delta t_2>| \sim 0.9$ s between the receiving microphones, we obtain:

$$\left[\left\langle (\delta\Delta t_2)^2 \right\rangle\right]^{1/2} = [D_\tau(0, \Delta y_0)]^{1/2} \approx 0.058, \quad \left[\left\langle (\delta\Delta t_2)^2 \right\rangle\right]^{1/2} / \left|\left\langle \Delta t_2 \right\rangle\right| \approx 0.06,$$

and, thus, the root mean square value of fluctuations in the azimuth of signal arrival is

$$\left[\left\langle (\delta\theta)^2 \right\rangle\right]^{1/2} \approx 8^0. \tag{16.10}$$

For the root mean square values of fluctuations in the grazing angle α at its mean $\alpha = 35°$, we obtain the following estimate:

$$\left(\left\langle \delta\alpha^2 \right\rangle\right)^{1/2} \approx \left(c_0 / x_1\right)\left(\left\langle \delta\Delta t_1^{\,2} \right\rangle\right)^{1/2} / \left|<\sin(\alpha)>\right| = (2.27)(0.057)/(0.57) \sim 0.227 (\sim 13^0). \tag{16.11}$$

The above theoretical estimates of the root mean square fluctuations in the azimuths and grazing angles of acoustic signals propagating in a stratospheric acoustic waveguide are in good agreement with the averaged experimental data (Figs. 16.16a, b) obtained for infrasonic signals recorded at a distance of about 300 km from the site of series of surface explosions equivalent to 20–70 tons of TNT.

16.6 Conclusions

In conclusion, let us note the main prospects for using infrasonic waves in sounding the middle and upper atmospheres within the height range 20–150 km.

The available methods for long-range sounding of the middle atmosphere with the aid of radars, lidars, and especially with the use of satellites, make it possible to obtain sufficiently reliable data on the vertical profiles of air temperature and wind velocity for the whole globe. However, the methods based on the use of electromagnetic waves within both radio and optical ranges applied to the problems of atmospheric sounding have significant physical limitations (weak turbulence and insignificant electronic concentration) within the height interval of the upper mesosphere to the lower and middle thermosphere (70–150 km). For infrasonic waves within the indicated height region of the atmosphere, such limitations are absent.

The acoustic method is not only complimentary to the rocket, radiophysical, and optical methods of investigating the atmosphere, but has a number of advantages. This method does not require the development and maintenance of any expensive equipment and complex infrastructure. Different natural (oceanic storms, lightning strikes, volcanic eruptions, etc.) and man-caused (research and industrial explosions) phenomena can be used as sound sources. A new promising direction in the development of the acoustic method of atmospheric sounding is the use of infrasonic waves to study the fine inhomogeneous structure of the middle atmosphere and the thermosphere within the vertical scales 10–100 m.

The advantage of the acoustic method, as compared to the optical and radio methods, is that the amplitude and frequency characteristics of recorded signals depend simply on the characteristics of atmospheric inhomogeneities (vertical air-temperature and wind-velocity gradients and atmospheric-layer thicknesses). To determine these parameters, no energetic summation of sounding signals reflected from atmospheric inhomogeneities is required as in the radiophysical and optical methods. In these methods, the averaging-layer thicknesses reach a few tens of meters, which naturally results in errors in measuring the vertical gradients of air temperature and wind velocity.

In recent years, this problem has become especially urgent in relation to the establishment of a continuously operating network consisting of 60 infrasonic stations uniformly distributed over the globe and used for the infrasonic method of monitoring the observance of the Comprehensive Nuclear Test Ban Treaty. By now, using this network, infrasonic signals from a few million different events have been recorded.

The results obtained using the international infrasonic monitoring network provide reason for further development of the acoustic method for long-range sounding of the fine inhomogeneous structure of the atmosphere.

Acknowledgments This study was supported by the Russian Foundation for Basic Research, project nos. 08-05-00445, and the International Scientific and Technological Center, project no. 2845.

References

Balashandran NK, Donn WL, Rind DN (1977) On Concorde sonic booms as an atmospheric probe. Science 197:47–49

Balsley BB, Gage KS (1980) The MST radar technique: potential for middle atmospheric studies. Pure Appl Geophys 118:452–493

Blanc E, Le Pichon A, Ceranna L, Farges T, Marty J, Herry P (2010) Global scale monitoring of acoustic and gravity waves for the study of the atmospheric dynamics. This volume, pp. 641–658

Brachet N, Brown D, Le Bras R, Mialle P, Coyne J (2010) Monitoring the earth's atmosphere with the global IMS infrasound network. This volume, pp. 73–114

Brown EH, Hall FF (1978) Advances in atmospheric acoustics. Rev Geophys Space Phys 16:47–110

Bush GA, Kulichkov SN, Svertilov AI (1997) Some results of the experiments on acoustic wave scattering from anisotropic inhomogeneities of the middle atmosphere. Izv Atmos Ocean Phys 33(4):445–452

Campus P, Christie DR (2010) Worldwide observations of infrasonic waves. This volume, pp. 181–230

Christie DR, Campus P (2010) The IMS infrasound network: design and establishment of infrasound stations. This volume, pp. 27–72

Chunchuzov IP (2002) On the high-wavenumber form of the Eulerian internal wave spectrum in the atmosphere. J Atmos Sci 59:1753–1772

Chunchuzov IP, Kulichkov SN, Otrezov AI, et al. (2005) Acoustic study of mesoscale fluctuations in the wind velocity in the stable atmospheric boundary layer. Izv Akad Nauk Fiz Atmos Okeana 41:761–782 [Izv Atmos Ocean Phys 41:693–712]

Collins PN, Rietveld MT, Rottger J, Hocking WK (1992) Turbulence scattering layers in the middle-mesosphere observed by the EISCAT 224-MHz radar. Radio Sci 27(2):97–107

Cox EF (1958) Sound propagation in air. In: Handbuch der Physik, vol. 48, chap. 22. Springer, Berlin, pp 455–461

Crary AD (1950) Stratospheric winds and temperatures from acoustical propagation studies. J Meteorol 7:233–242

Crary AD (1952) Stratospheric winds and temperatures in low latitudes from acoustical propagation studies. J Meteorol 9:93–109

Donn WL (1978) Exploring the atmosphere with sonic booms. Or how I learned to love concorde. Am Sci 66:724–733

Drob DP, Meier RR, Picone JM, Garcés MM (2010) Inversion of infrasound signals for passive atmospheric remote sensing. This volume, pp. 695–726

Fujiwara S (1914) On the abnormal propagation of sound waves in the atmosphere, second part. Bull Centr Meteorol Observ Japan 2(1):1–43

Fujiwhara S (1914) On the abnormal propagation of sound waves in the atmosphere, second part. Bull Centr Meteorol Observ Japan 2(4):1–82

Gainville O, Blanc-Benon Ph, Blanc E, Roche R, Millet C, Le Piver F, Despres B, Piserchia PF (2010) Misty picture: a unique experiment for the interpretation of the infrasound propagation from large explosive sources. This volume, pp. 569–592

Georges TM, Young JI (1972) Passive sensing of natural acoustic-gravity waves at the Earth's surface. In: Derr US (ed) Remote sensing of the troposphere, chap. 21. Government Printing Office, Washington, DC

Gossard EE, Hooke WH (1975) Waves in the atmosphere. Elsevier, New York

Gostev VS, Shvachko RF (1998) Methods of calculating the spatiotemporal and angular characteristics of the sound field in a shadow zone. Akust Zh 44(2):274–277

Gostev VS, Neklyudov VI, Chuprov SD, Shvachko LV, Shvachko RF (1989) Illumination of shadow zones. In: Brekhovskikh LM, Andreeva IB (eds) Akustika okeanskoi sredy (acoustics of the oceanic medium). Nauka, Moscow, pp 88–97

Grechko GM, Gurvich AS, Lyakhov VA, Savchenko SA, Sokolovskii SV (1981) Results of refraction studies during the third expedition on board the Salyut 6 space station. Izv Akad Nauk SSSR Fiz Atmos Okeana 17(11):1123–1133

Grechko GM, Gurvich AS, Kan V, Pakhomov AI, Podvyaznyi YaP, Savchenko SA (1997) Observations of the atmospheric turbulence at altitudes of 20–70 km. Dokl Akad Nauk 357(5):683–686

Hooper DA, Thomas L (1997) The small-scale structure of VHF mesospheric echo layers observed at mid-latitudes. Ann Geophys 15:1037–1047

Ingard UA (1953) Review of the influence of meteorological conditions on sound propagation. J Acoust Soc Am 25:405

Krasil'nikov VA (1945) Sound propagation in the turbulent atmosphere. Dokl Akad Nauk SSSR 47(7):486

Kravtsov YuA (1965) Modification of the geometrical-optics method for a wave penetrating through a caustic. Izv Vyssh Uchebn Zaved Radiofiz 8(4):659–667

Kulichkov SN (1989) Coefficient of reflection of acoustic waves from the upper stratosphere. Izv Akad Nauk SSSR Fiz Atmos Okeana 25(7):688–694

Kulichkov SN (1992) Long-range propagation of sound in the atmosphere (review). Izv Akad Nauk Fiz Atmos Okeana 28:3–20

Kulichkov SN (1998) Acoustic sounding of inhomogeneous structures in the middle atmosphere. Izv Atmos Ocean Phys 34(1):5–11

Kulichkov SN (2003) Conservation of "acoustic momentum" during long-range infrasonic propagation in the atmosphere. Izv Atmos Ocean Phys 38(5):582–587

Kulichkov SN (2004) Long-range propagation and scattering of low-frequency sound pulses in the middle atmosphere. Meteorol Atmos Phys 85(1–3):49–60

Kulichkov SN, Bush GA (2001) Rapid variations in infra-sonic signals at long distances from one-type explosions. Izv Atmos Ocean Phys 37(3):306–313

Kulichkov SN, Bush GA, Svertilov AI (2002) New type of infrasound arrivals in the zone of geometric shadow at the long distances from explosions. Izv Atmos Ocean Phys 38(4):397–402

Kulichkov SN, Chunchuzov IP, Bush GA, Perepelkin VG (2008) Physical modeling of long-range infrasonic propagation. Izv Atmos Ocean Phys 44(2):175–186

Le Pichon A, Vergoz J, Cansi Y, Ceranna L, Drob D (2010) Contribution of infrasound monitoring for atmospheric remote sensing. This volume, pp. 623–640

Liszka L, Olsson S (1971) On the generation of artificial atmospheric waves. J Atmos Terr Phys 33: 1933–1939

McKisic MJ (1997) Infrasound and the infrasonic monitoring of atmospheric nuclear explosions: a literature review, Final Report, Department of Energy, Office of Non-Proliferation and National Security, Washington, DC, p 310

Norris D, Gibson R, Bongiovanni K (2010) Numerical methods to model infrasonic propagation through realistic specifications of the atmosphere. This volume, pp. 535–568

Mikhailova LA, Ordanovich AE (1991) Coherent structures in the atmospheric boundary layer: a review. Izv Akad Nauk SSSR Fiz Atmos Okeana 27(6):593–613

Murayama Y et al. (1992) Seasonal variation of gravity wave activity in the middle atmosphere observed with the MU Radar. Proc Symp Middle Atmos Sci G(2–3):24–25

National Research Council (1997) Research required to support comprehensive nuclear test ban treaty monitoring, National Academy Press, Washington, DC

Ostashev VE, Chunchuzov IP, Wilson DK (2005) Sound propagation through and scattering by internal gravity waves in a stably stratified atmosphere. J Acoust Soc Am 118(6):256–262
Petenko IV, Bezverkhnii VA (1999) Temporal scales of convective coherent structures derived from sodar data. Meteorol Atmos Phys 71(1–2):105–115
Posmenteir ES (1971) Preliminary observation of 1–16 Hz Natural background and signals from Apollo 14 aircraft. Geophys J Astron Soc 26:173–177
Rayleigh JWS (1944) The theory of sound, 2nd edn. OGIZ, Leningrad
Reed JW (1972) Air blast overpressure decay at long ranges. J Geophys Res 77(9):1623–1629
Reynolds O (1874) On the reflection of sound by the atmosphere. Proc R Soc 22:531
Rottger J (1987) VHF radar measurements of small-scale and meso-scale dynamical processes in the middle atmosphere. Philos Trans R Soc Lond Ser A 323:611–628
Sofiev EN (1986) Wind pause structure in the vicinity of a mountain ridge. Meteorol Gidrol 5:37–41
Stokes GG (1857) On the effect of wind on the intensity of sound. British Associations Report, p 22
Tahira MA (1982) Study of the infrasonic wave in the atmosphere (II). Infrasonic waves generated by the explosions of the volcano Sakura-Jima. J Meteorol Soc Japan 60(3):896
Tahira MA (1988) Study of the long range propagation of infrasonic waves in the atmosphere (I). Observation of the volcanic infrasonic waves propagating through the thermospheric duct. J Meteorol Soc Japan 66(1):17–26
Tatarskii VI (1971) The effects of the turbulent atmosphere on wave propagation. US Department of Commerce, Springfield, Moscow
Turner JS (1973) Buoyancy effects in fluids. Cambridge University Press, Cambridge
von Zahn U, Widdel HU (1985) Wind corners in the winter mesosphere. Geophys Res Lett 20:673–676
Whiteway J, Carswell AI (1994) Rayleigh lidar observations of thermal structure and gravity wave activity in the high arctic during a stratospheric warming. J Atmos Sci 51(21):3122–3136
Whiteway J, Carswell AI (1995) Lidar observations of gravity wave activity in the upper stratosphere over Toronto. J Geophys Res 100(D7):14113–14124
Widdel HU, von Zahn U (1990) Wind corners in the 70– 100 km altitude range as observed at andenes (69-degrees latitude). J Atmos Terr Phys 52:995–1015
Wilson CR, Olson JV, Spell BD (1995) Natural infrasonic waves in the atmosphere: their characteristics, morphology and detection, University of Alaska. Technical Report ARS-95-039, Prepared for ENSCO Corporation, October 16

Chapter 17
Numerical Methods to Model Infrasonic Propagation Through Realistic Specifications of the Atmosphere

David Norris, Robert Gibson, and Kevin Bongiovanni

17.1 Introduction

Infrasound stations around the world continuously record a wealth of man-made and natural infrasonic signals (Brachet et al. 2010; Campus and Christie 2010). To discriminate between the various signals, researchers and analysts need insight into the physical processes that affect the observations. Atmospheric and propagation modeling has proven to be extremely useful in supporting this need because it can be applied to predict signal characteristics, localize source regions, and infer properties of the source itself (Bass et al. 2006).

This chapter provides a review of numerical methods for prediction of infrasonic signal characteristics. As mentioned above, effective infrasound modeling requires specifying the state of the atmosphere and capturing the relevant physics that affect the propagating signal. Our intention is to provide an overview of the progress that has been accomplished to date, complete with references that may be consulted by the interested reader who seeks more details. In general, theoretical derivations and model equations are avoided in place of a more descriptive review. The focus is on the propagating infrasonic wavefront subsequent to generation by a given source. Specific source types and mechanisms are beyond the scope of this review.

The chapter begins by reviewing the key relevant physical processes and how they are resolved numerically. They are grouped into the areas:

- Mean state of the atmosphere
- Fine-scale structure of the atmosphere
- Sound speed and moving medium
- Refraction
- Diffraction
- Absorption and dispersion
- Terrain

D. Norris (✉)
Applied Physical Sciences, 4301N, Fairfax Drive, Arlington, VA 22203, USA
e-mail: dnorris@aphysci.com

A. Le Pichon et al. (eds.), *Infrasound Monitoring for Atmospheric Studies,*
DOI 10.1007/978-1-4020-9508-5_17, © Springer Science+Business Media B.V. 2010

The chapter concludes by addressing separately three specific topics of interest:

- Full-wave modeling
- Nonlinear effects
- Spectral methods

For each topic area, the approaches developed to model it are reviewed. The advantages and disadvantages are discussed, and examples are provided where possible.

17.2 Mean State of the Atmosphere

Infrasound propagating in the atmosphere is primarily affected by temperature and horizontal wind, and secondarily by density, average molecular weight, specific heat ratio, and air composition. Temperature establishes the static sound speed. Two components are required to describe horizontal wind: a zonal component (parallel to the equator), and a meridional component (along a meridian). Horizontal wind can be added to the static sound speed in a given direction to define an effective sound speed. The presence of wind also creates a moving medium through which the sound propagates via advection. Molecular weight and specific heat ratio, like temperature, affect the static sound speed, though to a smaller degree. Air composition, including the presence of water (humidity), determines in part the sound absorption levels, and thus, influences attenuation.

The existence of multiple atmospheric layers and large spatial and temporal variability in the atmospheric temperature, wind speed, and wind direction results in a complex and dynamic infrasound propagation environment. Characterizations of temperature and wind are required in the lower, middle, and upper atmosphere in order to predict long-range infrasound propagation paths. In assessing atmospheric characterizations to determine a suitable estimate of the environmental conditions that affect infrasound propagation, one must consider factors including breadth of coverage (latitude, longitude, and altitude), temporal resolution (on annual, seasonal, and diurnal time scales), and spatial resolution.

Climatological models have been used to characterize atmospheric profiles since the earliest days of infrasound propagation modeling. Climatological models predict mean environmental profiles, typically as a function of latitude and longitude, based on assimilation of many years of observed data. In the simplest implementation, a single set of profiles (a temperature profile, a zonal wind profile, and a meridional wind profile) is used to characterize the atmospheric propagation environment over an entire infrasound propagation path. Climatological models that are based solely on historical data do not capture fine-scale temporal and spatial atmospheric structure. However, climatology remains an essential element of estimating the propagation environment, particularly in the mesosphere and thermosphere, where observational data are sparse.

The climatological models that have been most widely employed in recent years are the following:

- Horizontal wind model (HWM) (Hedin et al. 1996)
- Extended mass spectrometer – incoherent scatter radar (MSISE) model (Picone et al. 2002)

HWM provides zonal and meridional wind components, and MSISE provides temperature, density, and atmospheric composition. These empirical atmospheric models have global coverage from the ground into the thermosphere and capture dominant seasonal and diurnal atmospheric variability. HWM and MSISE include characterization of the effects of variations in solar flux and geomagnetic disturbances from solar activity, which influence temperature and winds above 100 km. Because the models define temperature and wind values at all latitudes, longitudes, and altitudes, they are well-suited for defining a range-dependent environment that can be used over a long propagation path.

As an example of climatological model output, Fig. 17.1 shows a set of temperature profiles from MSISE at a series of locations along a meridian. In Fig. 17.2, an image of the magnitude of the zonal wind from HWM is shown, as a function of day of year, above a fixed location in the continental U.S. Note the seasonal dependence of stratospheric wind direction; the large variation in stratospheric wind over the annual cycle has a significant effect on the presence or absence of a stratospheric duct for infrasound propagation.

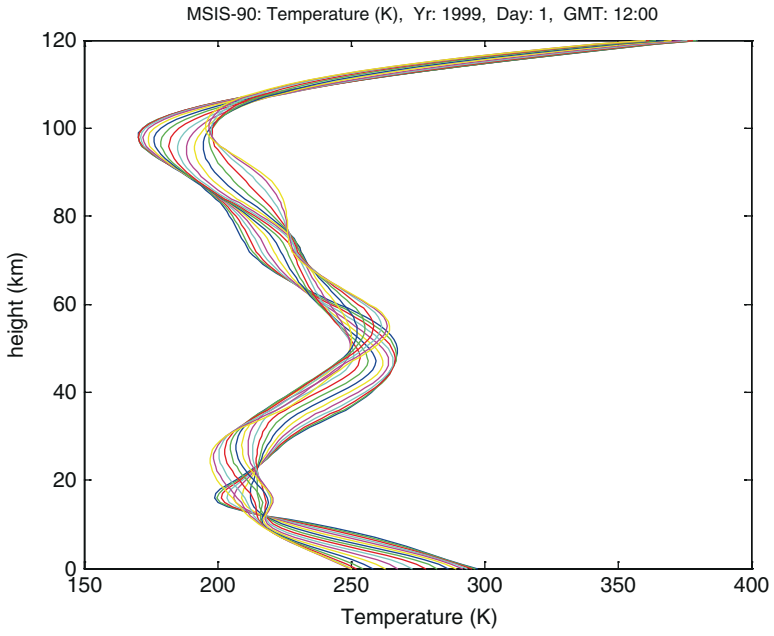

Fig. 17.1 Profiles of MSISE temperature along a profile from the equator to the North Pole

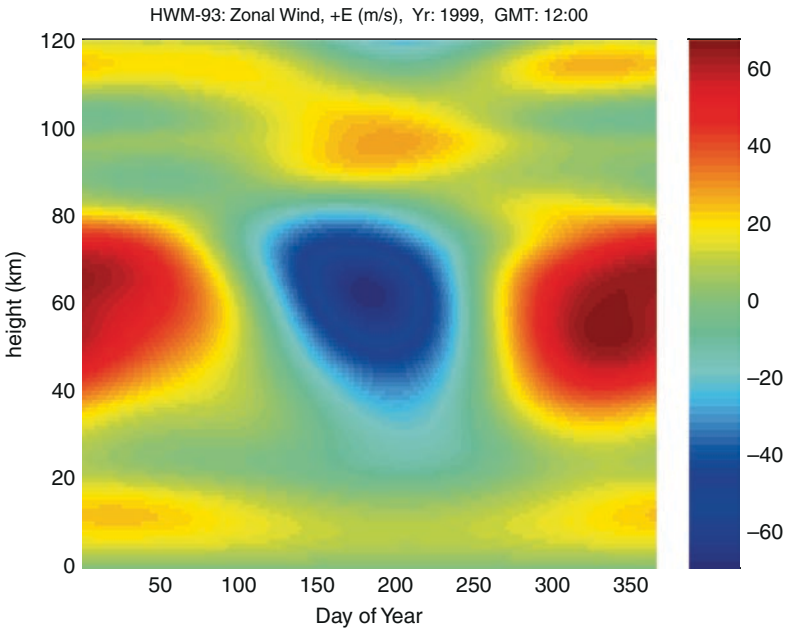

Fig. 17.2 Variation in zonal wind with time of year over continental U.S. Note the strong seasonal shift corresponding to westward winds in the summer and eastward in winter

Global climatological models such as HWM and MSISE that are based solely on historical data do not capture fine-scale temporal and spatial atmospheric structure. The strong relationship between infrasound propagation and atmospheric variability has been known since at least the early 1970s. Donn and Rind (1971) identified several unexpected periods of strong infrasound from otherwise relatively steady microbarom sources, and these periods were found to coincide with abnormal stratospheric warming events that were not predicted by climatology (Garce's etal. 2010; Hetzer et al. 2010). Since that time, significant progress has been made in the understanding of infrasound propagation and atmospheric effects, and improved modeling tools are now available for predicting infrasonic propagation through the variable atmosphere.

Supplementing climatological models with updated atmospheric characterizations, for example, near-real-time observations, can result in an estimate of the environment that captures more details that are relevant to infrasound. This is particularly true for propagation paths that dwell primarily in the lower and middle atmosphere, where updated observational data are more readily available. Updated atmospheric characterizations include raw data such as in situ profiles obtained from radiosondes or rocketsondes, and assimilated data such as the output from a numerical weather prediction (NWP) system or synoptic model. However, these updated characterizations typically do not span all altitudes that are necessary to define the infrasound propagation environment. Therefore, in previous efforts, spline functions have been applied over

a transition region to merge in situ profile data or synoptic model output with climatological model output at higher altitudes.

The use of an in situ profile, e.g., from a radiosonde, can be advantageous when the sounding coincides with a specific location and event time of interest. However, the availability of high-quality soundings is typically somewhat sparse across the globe. Furthermore, the use of a single profile does not allow the definition of a range-dependent environment.

The current state-of-the-art for integrating the output from operational NWP models with climatological models is the Naval Research Laboratory Ground to Space (NRL-G2S) specification (Drob et al. 2003; Lott and Millet 2010). NRL-G2S is a semi-empirical spectral model that defines the global atmosphere and that is widely used with infrasound propagation models. The G2S atmospheric characterizations from the surface to approximately 55 km utilize the output of multiple NWP systems and other relevant global data sets. Above this region, upper atmospheric characterizations are based on the MSISE and HWM climatologies. NRL-G2S employs spherical and vector spherical harmonics in the data assimilation process to produce a set of model coefficients for each day and time of interest. Coefficient sets can then be used to reconstruct fields of each atmospheric state variable as well as spatial derivatives. The NRL-G2S specification can be used to characterize the entire infrasound propagation environment in a range-dependent format.

Although global atmospheric models such as NRL-G2S have met with much success in recent years at defining the infrasound propagation environment, particularly for relatively long propagation paths, they do not capture all spatial and temporal variability that is important at local and regional scales. Synoptic models like G2S can capture many important regional features such as stratospheric jets. However, smaller-scale, lower-altitude structure in the atmosphere that is not predicted by either climatology or near-real-time global modeling can be relevant, as it can contribute to phenomena such as tropospheric ducting and scattering of infrasound. For example, Kulichkov et al. (2000) have presented evidence that environmental conditions varying over a short time scale can result in anomalous propagation effects. Specifically, these investigators have attributed a tropospheric class of infrasonic arrivals, over relatively short range, to the effects of a jet stream at 10–20 km altitude.

Furthermore, terrain elevation is a potentially important issue for infrasound propagation calculation. The NRL-G2S system references atmospheric specifications to mean sea level. Variable terrain adds to the complexity of the characterization of winds near the earth's surface. Environmental specification issues relative to terrain that should be considered include: correctly accounting for terrain altitude above mean sea level when evaluating atmospheric characterizations, and characterizing near-surface winds in the vicinity of rapidly varying terrain such as mountain ranges and islands. Propagation modeling considerations, discussed later in this chapter, include consistently modeling ground reflections from terrain features using physically valid assumptions, and determining spatial length scales that are appropriate for evaluating terrain elevation and slope at infrasonic frequencies of interest.

In order to address research questions related to regional atmospheric effects and variable terrain elevation, the NRL-G2S system is currently being upgraded to include operational mesoscale NWP analysis products (Gibson et al. 2006). These advances are intended to improve the temporal, horizontal, and vertical resolution in the 0 to 35 km region. Regional atmospheric specifications from operational weather centers have a high spatiotemporal resolution and accuracy compared to comprehensive global specifications. This is achieved by focusing additional efforts on the meteorological observations and atmospheric physics specific to a given geographic region. The new regional specifications also provide extra information at the surface by utilizing a terrain-following coordinate system, including high-resolution topography and additional atmospheric boundary layer effects.

17.3 Fine-Scale Structure of the Atmosphere

The atmospheric structure responsible for the propagation of infrasound can change rapidly. Fine-scale atmospheric structures can be responsible for infrasonic refraction, advection, and scattering. Global or mesoscale specifications that characterize the mean state of the atmosphere are unable to resolve all fine-scale stochastic phenomena, e.g., atmospheric irregularities smaller than the model resolution, fine-scale structures above 35 km, and gravity wave fluctuations that cannot be deterministically measured or internally generated by the model. Fine-scale atmospheric structure not characterized by near-real-time atmospheric models such as NRL-G2S has been identified as a likely source of refraction and scattering effects that may play a significant role in infrasound propagation.

Acoustic propagation through various types of inhomogeneous media has been studied (e.g., Ostashev 1997), but fundamental issues have not been thoroughly investigated or validated for infrasound. Propagation through turbulence in the ocean and atmosphere has been treated using phase screen methods, which are computationally efficient but do not incorporate all of the relevant physics. Much progress has been made in understanding propagation through locally homogeneous and isotropic turbulence in the atmosphere, but many problems still remain related to the effects of turbulence intermittency and mesoscale anisotropic coherent structures (Kallistratova 2002).

Atmospheric properties vary in both space and time. Coherent spatial variability is observed at length scales from meters to thousands of kilometers, and temporal variability occurs over diurnal and seasonal time scales. The variability in wind and temperature makes modeling infrasound propagation a challenging problem. Since the environment is dynamic and cannot be measured over the entire region through which the infrasonic signals propagate, stochastic modeling methods are necessary to account fully for the environment's influence on propagation.

The dominant source of variability affecting infrasonic propagation is believed to result from gravity waves because their spatial scales are of the same order as

infrasonic wavelengths (Lott and Millet 2010). Gravity waves result from oscillations of air parcels displaced by buoyancy and restored by gravity. The oscillations have time scales ranging from minutes to tens of hours. Vertical length scales of gravity waves are in the range of 0.1–10 km, and horizontal scales can span from 100 to 10,000 km. The multiscale nature of gravity waves presents a challenge to quantification of their properties. Owing to the important influences of gravity waves on the atmosphere's general circulation, vertical structure, and spatiotemporal variability, gravity wave dynamics are a significant atmospheric science research topic area. Recent research progress includes a better understanding of gravity wave source characteristics, evolution with altitude due to changes in wind conditions, and atmospheric stability (e.g., Fritts and Alexander 2003). The development of high-fidelity physically-based gravity wave parameterizations is an active research area (Gibson et al. 2008).

A significant body of research has been carried out to define the spectral character of gravity waves. The spectral model of Gardner (1995, 1993) has been investigated for applicability to atmospheric specification for infrasound propagation (Norris and Gibson 2002). Gardner's model is based on scale-independent diffusive filtering theory. A source spectrum is defined near the ground. As the spectrum is propagated up in height, attenuation is modeled by introduction of diffusive damping. The key spectral properties are increase in energy with height, shift toward larger length scales with height, and attenuation of smaller length scales with height.

Wind perturbations due to gravity waves can be modeled in the spectral domain (Norris and Gibson 2002). Both height and range-dependent gravity wave dependencies are modeled. The spectral model can be used to generate multiple realizations of the perturbed environment, and propagation can be evaluated through the sum of mean and perturbed profiles. Model predictions can, therefore, be made through atmospheric "snapshots" of the inhomogeneities. The Gardner spectral model, evaluated at four discrete heights, is shown in Fig. 17.3. These heights capture the dominant gravity wave variability from the troposphere up to the lower thermosphere. Gravity waves are not fully developed below the troposphere. In the thermosphere, diffusion increases dramatically and gravity waves are damped out. Predicted standard deviations of wind perturbations are listed in the figure alongside the spectral heights.

Fourier inversion using random phase is applied to the spectra to generate realizations of wind perturbation profiles that can then be used for Monte Carlo type analyses (Norris and Gibson 2002). A wind perturbation profile is generated for each of the five spectra. A composite profile is then computed by shading each profile spatially with a Gaussian filter and then summing them together, where Gaussian filter half-power points are set to the midpoint between each of the spectral heights. To model range-dependent variability, a dominant horizontal length scale is defined, and Gaussian weighting functions are used to combine the wind perturbation profiles.

Although research on this topic is still in progress, there is evidence of the importance of gravity waves on infrasound propagation. As discussed later in this chapter, when gravity wave perturbations are included in the atmospheric characterization,

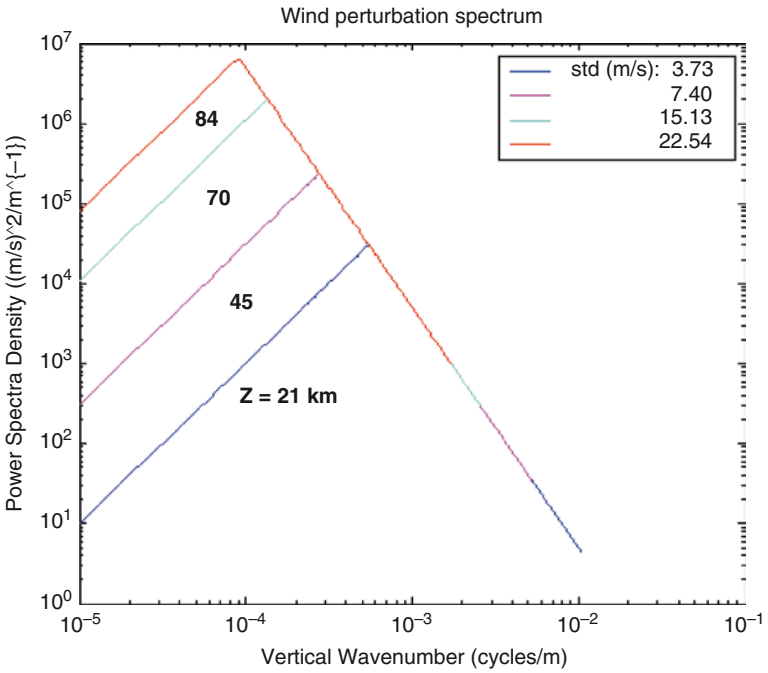

Fig. 17.3 Wind perturbation spectra from Gardner's gravity wave model evaluated at four discrete heights

scattered infrasound energy can predicted to penetrate shadow zones, consistent with a growing body of observational data. Scattering of sound from tropospheric gravity waves is discussed by Kallistratova (2002) as a mechanism for explaining observed infrasound signals. Kulichkov (2004) has long observed "partial reflection (scattering)" of low-frequency acoustic or infrasonic pulses from fine-layered inhomogeneities in the middle atmosphere. Both signal variations, with time scales similar to the periods of internal gravity waves, and also intermittent observations of signals in shadow zone regions, are attributed to inhomogeneous coherent structure in the atmosphere.

In addition to gravity waves, there exists other fine-scale structure in the atmosphere that has spatial scales on the same order as infrasound and that may also influence infrasonic propagation. One example is Kelvin-Helmholtz waves or shear instabilities. These waves are coherent perturbations of both scalar and vector fields in the boundary region. They start as rolling undulations and then evolve to a wave-like structure that eventually breaks down into vortices or billows. Kelvin-Helmholtz waves are often present within layers of moderate and severe clear air turbulence. Their effect on infrasound propagation is a topic of current research (Gibson et al. 2008).

17.4 Sound Speed and Moving Medium

The speed of sound in a fluid can be derived from the state equation that relates the fluid's pressure to density. For seawater, no simple state equation exists, due to its complex composition, and therefore, there are no closed form sound speed expressions. The underwater acoustics community has to rely on empirical expressions that are a function of temperature, pressure, and salinity. For atmospheric studies, the air composition is also quite complex, consisting mainly of Nitrogen, Oxygen, and a variety of trace gasses. However, the ideal gas law can be applied to equate pressure to density, where the average molecular weight of the air is used. From this expression, a closed form solution for the sound speed can be derived. In fact, the sound speed is simply proportional to the square root of temperature.

Up to this point, we have assumed that the air is dry and contains no humidity (which is a second order correction to the sound speed expressions). For infrasound, humidity is generally neglected, in part due to its second order effect, but also since the amount of humidity drops off dramatically above the troposphere. Since typical infrasonic paths may extend significantly above this region, refracting back toward the ground either in the stratosphere or thermosphere, the percentage of the total path length in the troposphere is small, further reducing any effect humidity may play on the propagation.

The atmospheric sound speed defined by temperature is referred to as the *static* sound speed. Since propagating acoustic waves are longitudinal pressure disturbances within the fluid medium, wind also has an effect on speed. There are two classical approaches for dealing with fluid motion (e.g., wind). In the simpler approach, the wind velocity in the direction of propagation is added to the *static* sound speed to produce an *effective* sound speed. The resulting effective sound speed accounts for the combined refractive effects of temperature and wind.

The effective sound speed approach is an approximation, however, as it only accounts for one effect the wind has on the propagation. As an illustration, imagine you are rowing a boat and crossing a river. As you row across the river, the current of the river perpendicular to your boat pushes you in the direction of the flow. When you arrive at the opposite shore, you are some distance downstream from your original launch point. This same effect occurs for propagating acoustic waves in the atmosphere. As the sound propagates, it travels with the fluid being pushed around by the wind. In the horizontal plane, this is called horizontal translation or advection. The effect occurs in all directions, but it is most pronounced in the horizontal plane perpendicular to the propagation. Just like the rowboat, sound emanating from a source can be advected "downstream" from the direction it was launched, dependent on the wind strength and direction.

Translational wind effects are not captured by the effective sound speed. Models that fully account for winds are referred to as including the effects of the *moving medium*. We include examples of moving medium models in the rest of this chapter.

17.5 Refraction

Refraction describes the change of direction of a propagating wavefront. The effects of refraction can perhaps best be seen by using a ray model. Refraction effects are represented by tracing the vector that is normal to the wavefront, and the trace over time produces the ray path. The ray paths are independent of frequency, as ray theory is a high frequency approximation to the more complex wave equation. It is generally valid if the acoustic amplitude varies only slightly over distances comparable to a wavelength, and if the curvature of the wavefront is much larger than a wavelength. Figure 17.4 shows an example of a fan of rays launched from a source.

Ray theory has found great utility in the infrasound community. It is attractive because the computational loading is small compared to other models, and three-dimensional effects can be modeled in a straightforward manner. Ray paths are easily interpreted because they provide a clear visualization of the path the sound traverses. In addition, phase identification of infrasonic arrivals is facilitated by overlaying ground bounce locations from a fan of rays launched at the source. Figure 17.5 illustrates an application of this technique, in which the observations and ray predictions are plotted vs. range from the source.

Two-dimensional ray solutions over range and height have been used, but three-dimensional implementations are much more common. This is because propagation effects are not solely limited to the range-height vertical slice. Refraction is most pronounced in the vertical plane, but also occurs in the horizontal plane from horizontal wind and temperature gradients. Horizontal translation of the ray path due to moving medium effects is also important. These horizontal effects have been shown to significantly alter propagation paths (Georges and Beasley 1977).

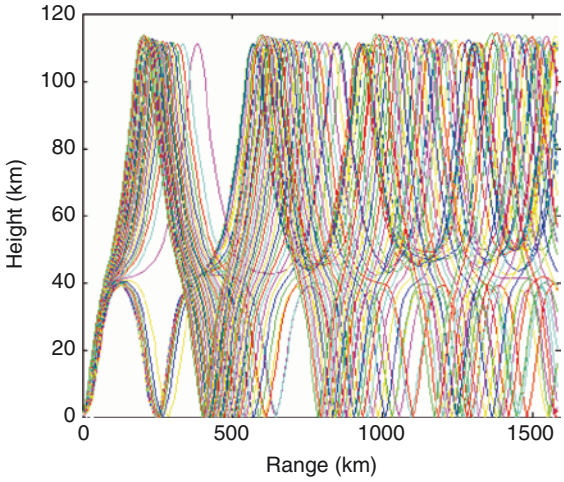

Fig. 17.4 Example of a fan of rays launched from a source. Rays fill both the stratospheric and thermospheric ducts

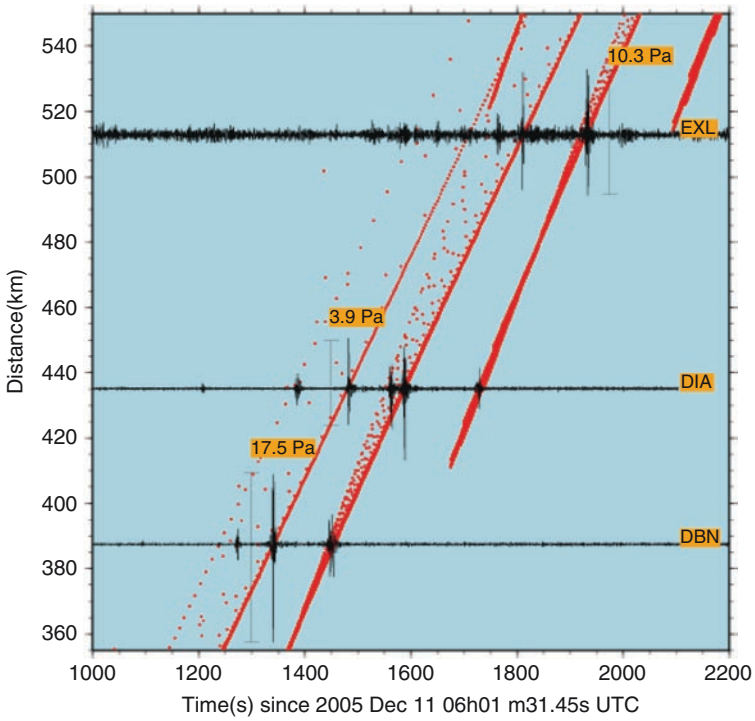

Fig. 17.5 Waveform observations (*black*) and ray trace ground bounces (*red*) plotted vs. range from the source (adapted from Evers and Haak 2006)

Numerically, ray theory takes the form of the following: (1) the Eikonal equation, a generalization of Snell's law, from which the refracted ray paths are computed; and (2) the transport equation, which can be used to predict amplitude. (For a good overview, see Jensen et al. 1994.) Amplitude predictions are problematic at caustics, regions where adjacent rays cross, because of a singularity in the solution. In addition, zero amplitude is predicted in ray shadow zones, since the propagation effects of diffraction and scattering are not accounted for and must be repaired heuristically.

Three ray models have enjoyed widespread application in the infrasound community:

- HARPA
- WASP-3D
- Tau-P

HARPA is a full three-dimensional ray model that numerically solves a Hamiltonian formulation of the ray equations in spherical coordinates (Jones et al. 1986). It accounts for the range dependence of the atmosphere and moving medium effects. WASP-3D is another Hamiltonian solution that provides similar capabilities (Dessa et al. 2005). Both models are cast in spherical coordinates to account for the Earth curvature, which can have a nonnegligible effect over very long ranges of thousands of kilometers.

Although these models are numerically efficient, a large number of rays must generally be computed to characterize the propagation paths for a given scenario. Further, eigenray solutions, those rays that connect source and receiver locations within a given tolerance or "miss distance," require iterating over a large subset of ray elevation and azimuth angles. These applications can make ray calculations time consuming.

Tau-P was developed as a fast alternative to other ray models for computation of travel times. It was originally developed for seismic applications (Buland and Chapman 1983) and reformulated for atmospheric applications (Garcés et al. 1998). The computational gain is made by assuming, in part, a stratified atmosphere (no range-dependence).

As an example of some applications, ray models have been used to compute seasonal travel-time tables for the infrasound stations that make up the CTBT monitoring network (Brown et al. 2001). Ray travel times have also been used to evaluate the performance of this network (O'Brien and Shields 2004). Total travel time divided by ground range is defined as the group velocity or celerity. Ray-based celerities have been used to successfully explain exceptionally fast infrasonic arrivals from an oil depot explosion (Evers and Haak 2007).

Azimuthal deviation is an important three-dimensional effect that has been extensively modeled using ray theory. It is defined as the difference between the ray launch azimuth and the ray azimuth orientation at its endpoint. It results from horizontal refraction and translation, the latter due to the moving medium. For infrasonic observations, it can be used to "correct" the observed back azimuth to determine the direction of the source. Back azimuth comparisons have been effectively used in evaluating atmospheric specifications and estimating upper-level wind corrections (Le Pichon et al. 2006, 2005).

Ray theory cannot be used to predict waveforms directly. However, a numerical technique has been used to predict synthetic waveforms. A time series is first created by defining impulse functions at ray arrival times. Each impulse function is assigned the amplitude of its associated ray. The time series is then convolved with a predefined source function to generate a synthetic waveform. This approach has been used effectively in comparison studies of bolide observations (Norris and Gibson 2004a). Figure 17.6 shows a waveform comparison technique. The predictions were computed over a range of candidate source heights, and a best fit was used to estimate the actual value of source height.

17.6 Diffraction

In the previous section, we discussed refraction, in which propagation is approximated by ray paths. In reality, the wave nature of sound results in a continuous field of sound spread through space, not confined to a single path. As an example, consider an environment where the sound speed decreases with height. The sound rays will refract upward and there will be a "shadow zone" downrange where no rays penetrate. Refraction-based models predict zero amplitude in this region. However, in reality, the sound penetrates into shadow zones, through diffraction, among other mechanisms.

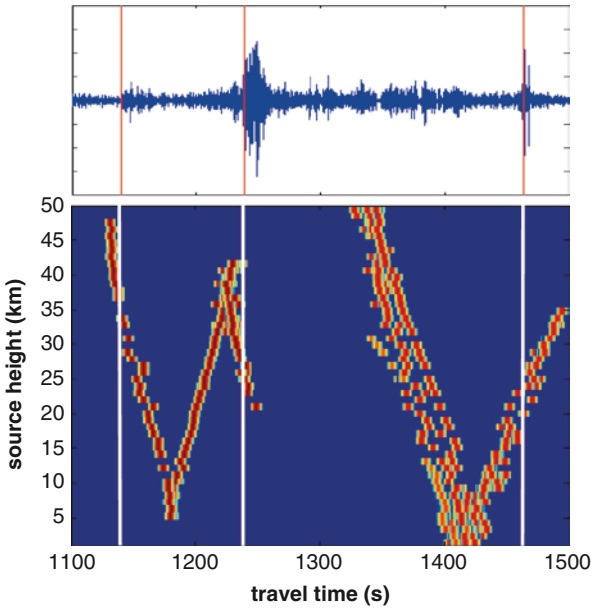

Fig. 17.6 Comparison of measured arrival times (*above*) with synthetic waveform predictions from eigenrays solved over source heights of 0–50 km (*below*)

Diffraction is a frequency-dependent phenomenon. As the frequency of the propagating wave increases, the diffraction effects extend over a smaller and smaller region, until eventually geometric or ray theory can be used. Parabolic equation (PE) methods capture diffraction effects and have been widely applied to infrasonic studies.

The continuous-wave PE model is derived by assuming a single harmonic frequency of propagation. Substitution into the linear wave equation produces the Helmholtz equation, which is expressed in the frequency domain. The Helmholtz equation is factored into a forward propagating wave and a backward propagating wave. Only the forward propagating wave is retained, which means that backscattered energy is not modeled. Backscatter for infrasound is generally not a concern because the forward propagation dominates over the long atmospheric paths that are typically of interest. In addition, significant interaction with scattering bodies of sizes comparable to the long wavelengths of infrasound is not common.

The forward propagation function in the frequency domain can be solved by a variety of numerical methods, including finite difference, Padé, Green's function, and spectral approaches. Simpler numerical techniques result in *narrow angle* formulations. The narrow angle refers to the extent of vertical angles over which the source can be realized, and it is typically in the range of 20°. More complex *wide angle* formulations extend the vertical angle to 60° or more. In infrasound, the presence of thermospheric paths, which have, in ray terms, large source elevation angles, necessitates the selection of wide-angle PE models.

PE models are used to generate predictions of acoustic amplitude fields at a given frequency over a vertical slice (range-height) of the atmosphere. By restricting the propagation to the vertical plane, azimuthal symmetry is assumed. The PE formulations are solved for a wave function that has the property of cylindrical spreading, with the amplitude falling off as a function of the square root of range. The final pressure amplitude field is then computed by adding an additional spreading loss factor to ensure spherical spreading proportional to the reciprocal of range ($1/r$).

Sources are characterized using a PE starter field, which defines the acoustic field over all heights at a small distance from the source. Starter fields have been computed for simple point sources, with or without directivity, and for line sources. Numerically, the starter field is marched forward in range by solving the forward propagation frequency-domain equation. The range step size, as well as the height step size, is generally limited by the acoustic wavelength and length scales of the inhomogeneities in the atmosphere. Thus, higher frequency PE predictions can take considerably longer to run than lower frequencies.

The split-step Fourier (Jensen et al. 1994, West et al. 1992) and Padé PE (Collins 1993) numerical approaches have been commonly applied to infrasound. For example, PE predictions at various frequencies have been computed to characterize propagation loss for infrasound from mining activity (McKenna et al. 2007). Figure 17.7 provides an example of a split-step Fourier PE solution at 0.2 Hz. Note the fuzzy boundary between strong and weak amplitude regions. This smooth variation in the field is due in part to diffraction.

The preceding PE examples use effective sound speed, in which the wind is assimilated into the static sound speed. Thus, moving medium effects are not accounted for. Wind Mach numbers, the ratio of wind speed to static sound speed, can reach 0.3 or greater along infrasound propagation paths, and therefore, moving

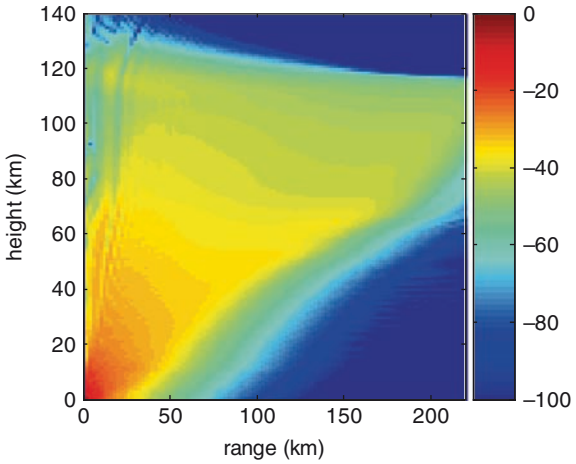

Fig. 17.7 Amplitude field from parabolic equation (PE) model at 0.2 Hz

medium effects can potentially be important for certain scenarios. A PE version has been derived that accounts for moving medium effects within the range-height vertical plane (Lingevitch et al. 2002). This version is a wide-angle solution, valid for a range-dependent atmosphere and the weak shear limit, the latter valid for frequencies above 0.1 Hz. The authors cite an infrasound example where the moving medium significantly alters the predicted amplitude field of thermospheric paths.

An important numerical feature of PE models is that they can properly account for the propagation effects of small-scale atmospheric inhomogeneities. One caveat is that the height and range steps in the formulation must be a fraction of the length scales of the smaller inhomogeneities. This fraction is typically between one-fourth and one-sixth (Jensen et al. 1994). One interesting application in this regard is the modeling of gravity wave effects. Atmospheric inhomogeneities due to gravity waves have been discussed in a previous section. Here, the PE model can be applied to predict their effect on the amplitude field for a given frequency. Figure 17.8 shows a PE prediction at 0.2 Hz similar to Fig. 17.7, but with the addition of wind inhomogeneities due to gravity waves. The inhomogeneities result in energy in the stratopause region of approximately 50 km propagating down to the ground. Depending on the specific nature of the inhomogeneities, the physical processes that produce this effect are some combination of strong refraction, diffraction, and forward scattering.

Theoretically, the PE model can be applied over three dimensions to generate amplitude predictions over an entire region of the atmosphere. However, three-dimensional PE predictions for infrasound have not been pursued due to the long propagation distances and computational limitations. The so-called "N-by-2D" approaches have been used in their place. In this approach, the vertical slice PE is

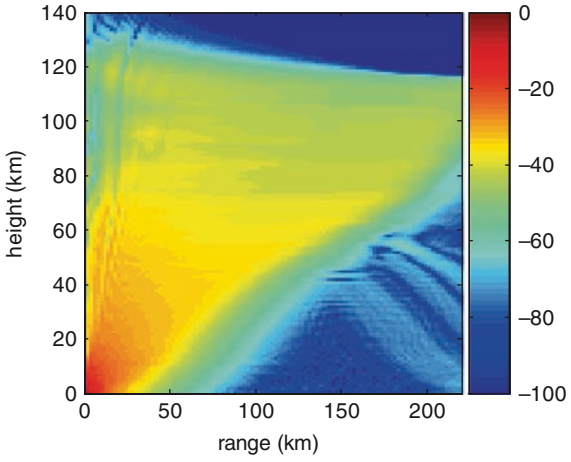

Fig. 17.8 Amplitude field from the PE model with gravity waves included in the atmospheric specification

solved over a range of azimuths and then a composition image is created of the amplitude field in the horizontal plane at a given altitude. It is important to note that N-by-2D techniques do not account for any horizontal coupling of the acoustic energy, but they do provide very useful visualizations of the acoustic geographical "footprint." The prediction footprint is at the ground and extends out in range to 1,000 km (Gainville et al. 2006). An example of transmission loss predictions using a continuous-wave PE model is shown in Fig. 18.7 (Gainville et al. 2010).

17.7 Absorption and Dispersion

As sound propagates in a fluid, it experiences absorption through two main mechanisms: classical losses and relaxation losses. Classical losses are associated with the transfer of energy between molecules as the wave propagates. Translational or shear effects generally dominate this term, but there is also a small contribution from diffusion associated with thermal conduction. Relaxation losses are related to the redistribution of energy within a molecule, both through molecular rotation and vibration (Kinsler et al. 1984).

The state-of-the-art absorption model for the low frequencies and high altitudes relevant to infrasound is that formulated by Sutherland and Bass (2004). The Sutherland and Bass model accounts for all the dominant loss mechanisms: translation, diffusion, molecular rotation, and molecular vibration. Figure 17.9 gives an example of absorption coefficient profiles for these components as well as the total. The classical losses used here refer to the sum of translation and diffusion losses. A general overview of these loss mechanisms and detailed derivation of the absorption formulations can be found by the interested reader in the literature (Bass et al. 1984).

The atmosphere must be specified in significant detail to calculate absorption. Required atmospheric profiles at a given location include temperature, total density, total pressure, viscosity, specific heat ratio, and mean molecular weight. Mole fractions are required for those components that comprise most of the atmosphere: N_2, O_2, CO_2, O_3, O, and H_2O. The four primary components, O_2, N_2, CO_2, and O_3, are used to compute vibration losses, for which relaxation frequencies are needed. Much of these data can also be specified in higher-fidelity using the MSISE model, discussed in a previous section. MSISE also specifies the minor air components N, HE, AR, and H, which are used to generate a finer estimate of mean molecular weight and total density.

Absorption models, such as that of Sutherland and Bass, can be numerically incorporated into propagation models by straightforward means. For ray tracing, the total absorption is simply found by integrating the absorption coefficient along a given ray path. Figure 17.10 provides an example. The left panel shows representative stratospheric and thermospheric ray paths, and the right panel shows the associated absorption as a function of range. Stratospheric absorption is generally negligible for low frequencies and moderate ranges. Thermospheric absorption, on the other hand, is nonnegligible, over 35 dB in this example. Almost all of the absorption occurs over a

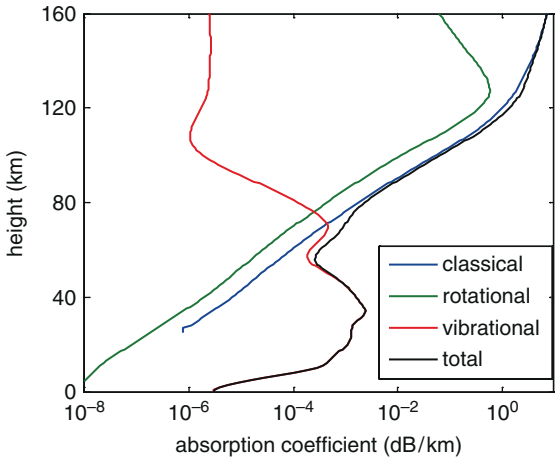

Fig. 17.9 Example of total absorption coefficient at 0.4 Hz, with contributions from individual loss mechanisms shown separately

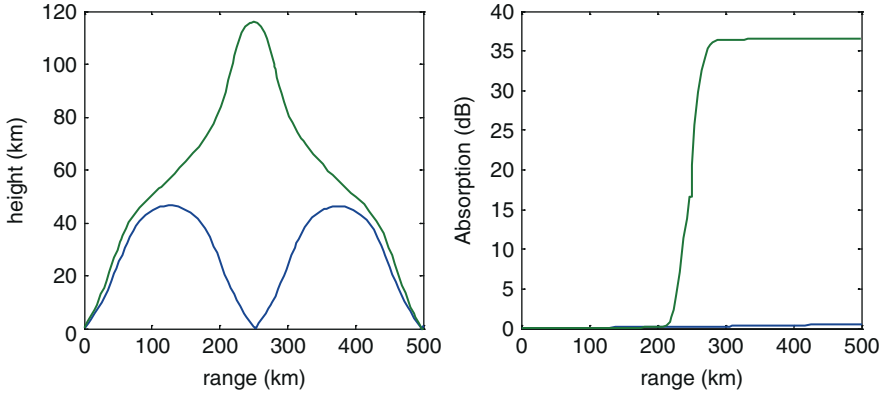

Fig. 17.10 Representative stratospheric (*blue*) and thermospheric (*green*) ray paths, and associated absorption at 0.4 Hz

very small portion of the path, when the ray is sampling the thermosphere above 100 km.

This example illustrates the inherent sensitivity of absorption calculations to both the path the infrasound traverses in the thermosphere as well as the thermospheric composition. Error in either of these specifications can result in significant mismatch between predicted absorption and that observed. As a result, absorption predictions have shown inconsistent results when compared to observations (McKenna 2005). To date, comprehensive sensitivity studies have not been performed to fully quantify these effects.

Incorporating absorption into PE models is also straightforward. Recall the PE formulation is expressed in the frequency domain. The wave function variable can be represented as an exponential function raised to the power ikr, where i is the imaginary number, k is the wavenumber, and r is range. By modifying this function to $i(kr + i\alpha)$, we introduce a loss term $\exp(-\alpha)$, where alpha is computed directly from the absorption model. PE model comparisons that incorporate absorption have shown similar results to ray theory studies. An overprediction of thermospheric losses is apparent that has not been fully resolved.

One physical phenomenon that may affect the thermospheric paths is dispersion. Dispersion is defined as a dependence of sound speed on frequency. Atmospheric dispersion results from classical and rotational absorption losses. The same formulations used to compute absorption also can be applied to characterize dispersive effects (Sutherland and Bass 2004). Dispersion effects are generally considered negligible for atmospheric propagation. However, within the high absorption region of the thermosphere, they can potentially be important. Dispersion has been shown to alter the refractive properties of thermospheric rays and amplitude fields of PE predictions (Bass and Hetzer 2006).

Figure 17.11 shows dispersive sound speed profiles over a range of frequencies. The computations were made for a typical atmospheric state computed from the MSISE model. At 0.1 Hz, the dispersive effects are negligible, but at higher

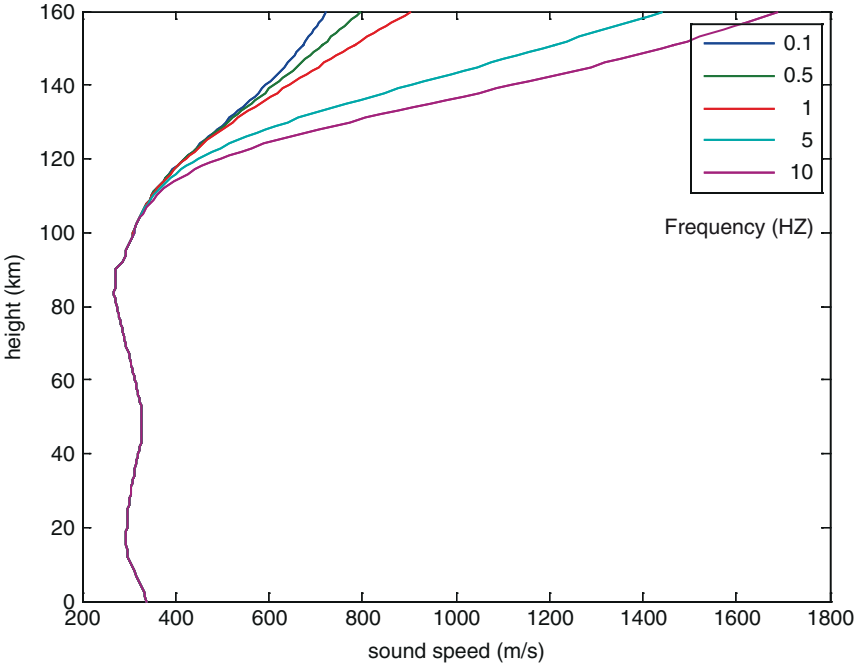

Fig. 17.11 Static sound speed profiles that include the effects of dispersion over a range of frequencies (adapted from Bass and Hetzer 2006)

frequencies and above 100 km, the change in sound speed is significant. It should be noted that those situations where dispersive effects are most pronounced are also where absorption is very large. The influence of dispersion on observed thermospheric signals is still an open research issue.

17.8 Terrain

Terrain effects with regard to atmospheric specification have been introduced in a previous section. In this section, we consider how to incorporate terrain into propagation formulations. The baseline modeling domain for infrasonic propagation models is a flat Earth in either spherical coordinates or range-height coordinates.

When terrain effects are integrated, care must be taken in defining the atmospheric values near and at the terrain surface for purposes of propagation modeling. For some specifications, atmospheric variables are defined down to mean sea level, whereas terrain elevation may be above or below mean sea level. Regional or mesoscale specifications based on the output of NWP models generally use a terrain-following coordinate system. In such a specification, atmospheric variables may be defined on pressure surfaces rather than at constant heights. At each surface or contour of the specification, all variables necessary for propagation calculations are available. Atmospheric variables are defined down to the lowest contour level, which is at or near the local terrain elevation.

The terrain-following nature of atmospheric specification surfaces can be seen in Fig. 17.12, which shows horizontal wind magnitude for a vertical slice of a high-resolution regional atmospheric specification. The specification contours

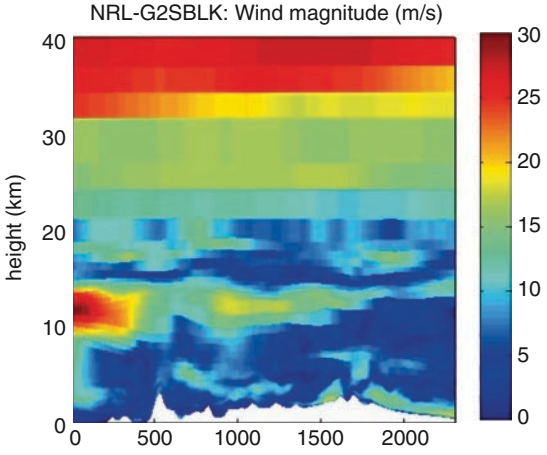

Fig. 17.12 A vertical slice of the horizontal wind magnitude (m/s) for an atmospheric specification based on the output from numerical weather prediction (NWP) models. Horizontal axis is range in km

closest to Earth's surface can be seen to follow the major terrain features. The vertical resolution of the specification is on the order of 10–50 m near the surface, increasing to larger, yet variable values with height.

The next step in the integration is assimilating the terrain-following atmospheric specifications into the propagation models. For ray tracing, it involves redefining the lower boundary over which the ray will interact. If the ray model does not account for the moving medium, then the interaction is computed by reflecting the ray specularly at the boundary, where the specular angle is computed from the local terrain gradient. For moving medium ray models, the interaction is more complicated. The advection of the ray due to the winds introduces additional terms in the boundary calculations that produce a reflected angle that can differ from specular. To compute the properties of the reflected ray, the local wind field and gradients must also be known at the interface (Jones et al. 1986).

In general, as the propagation range decreases and the frequency range of interest increases, the importance of ray interaction with variable terrain becomes greater. Figure 17.13 displays ray paths for propagation from an elevated source, showing interaction with terrain. At local interactions between the rays and earth's surface, a topographic database is used to compute the local terrain height and the local first and second derivatives in latitude and longitude. These data, which may be computed using cubic spline interpolation, are needed in the ray tracing formulations to resolve the angle of reflection of the ray at the surface.

Terrain effects have been integrated in three-dimensional ray tracing and PE predictions to study bolides. Ray trace interaction with nearby mountains was found to explain observations successfully (Arrowsmith et al. 2007). However, the relative significance of terrain for various ranges and conditions has yet to be fully quantified.

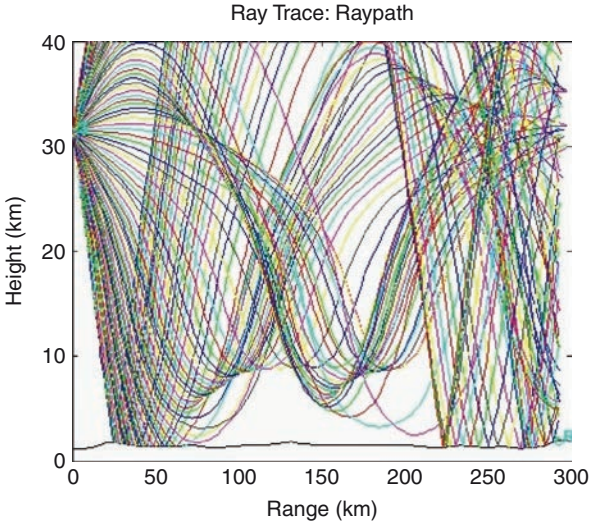

Fig. 17.13 Modeled infrasound ray paths for an elevated source. Reflection of rays off complex terrain elevation is shown

PE modeling over a vertical slice also incorporates terrain by modifying the lower boundary condition. Three common solutions are (Donohue and Kuttler 1997):

- Stair-stepping/terrain masking
- Piecewise conformal mapping
- Piecewise linear shift mapping

In the stair-stepping or terrain masking approach, the terrain is realized as a series of stair steps. The PE solution is marched through range as before, but now with a stair-step lower boundary. In this implementation, the terrain becomes a series of knife-edge diffractors, where all surface reflections are approximated by tip diffraction. The implementation assumes perfectly reflecting surfaces, which is generally a good assumption for infrasound.

Piecewise conformal mapping transforms the boundary into terrain-following arcs. Each arc is applied over a defined piece of the total terrain profile. The PE formulation does not change, but the index of refraction is modified to incorporate the effects of each arc.

The piecewise linear shift mapping approach is the most numerically intensive of the three. A new coordinate system is defined based on shifting the height to follow the terrain. The Helmholtz equation is rederived for this system and the new terms must be numerically addressed in the final PE solution.

Another alternative to incorporating terrain involves the use of finite-difference PE models. In these formulations, the terrain can easily be integrated into the finite-difference mesh already established for the finite difference calculations. This approach has been used successfully to model terrain effects associated with above-ground controlled explosions (de Groot-Hedlin 2006).

Figure 17.14 shows an example of PE predictions with a stair-step terrain model. The terrain is simply modeled as a wedge of height 10 km. The frequency dependence of the acoustic field down-propagation from the source is apparent.

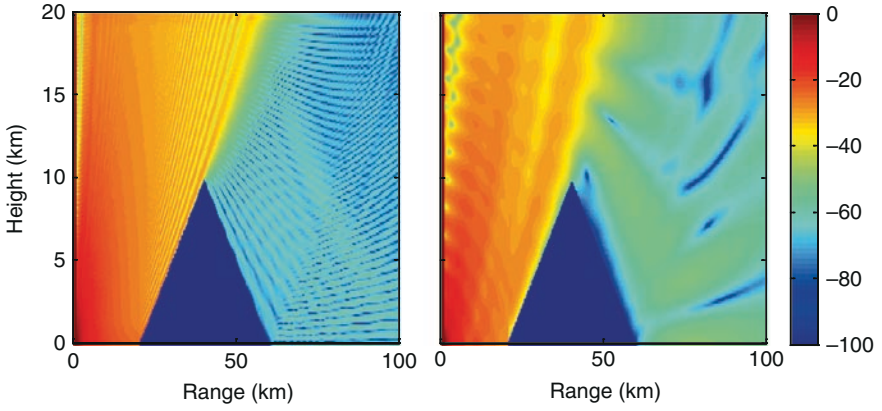

Fig. 17.14 Terrain effects using the stair-step mapping for 2 Hz (*left panel*) and 0.2 Hz (*right panel*) (adapted from Norris 2007)

An example of PE model predictions with and without specifying variable terrain elevation is shown in Fig. 17.15. The modeled scenario is the 2004 bolide explosion in Washington State, USA, with source height of approximately 40 km, studied by Arrowsmith et al. (2007). The figure above shows a portion near the earth's surface of the calculated amplitude field at 1 Hz using an atmospheric specification that does not include variable terrain elevation. The similar figure below, also for 1 Hz, uses a high-resolution atmospheric specification that includes variable terrain elevation. Significant differences in the details of predicted energy near the earth's surface can be seen.

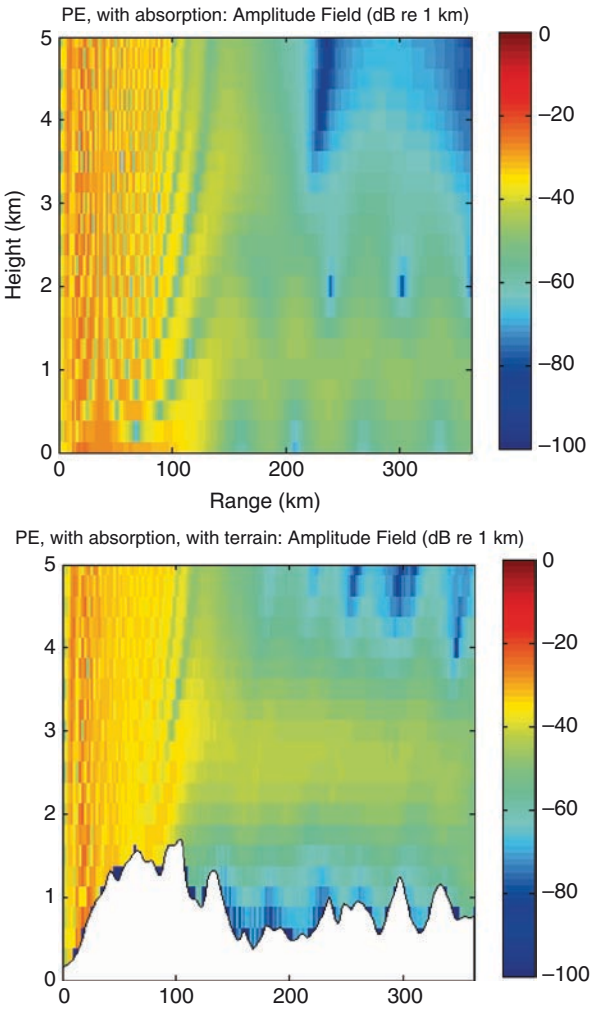

Fig. 17.15 PE amplitude fields (1 Hz) near earth's surface for propagation from an elevated source. No variable terrain (*top*); variable terrain (*bottom*)

17.9 Full-Wave Models

In the preceding sections, we review various physical phenomena and models well suited to address those propagation effects. In this section, we diverge from this outline and directly address full-wave models. Full-wave approaches are developed to capture the entire waveform properties of the source and propagate them forward in time. Generally, they start with a source waveform predefined in the near field, and solve for the waveform at some downrange distance and time. All propagation effects, including spreading loss, refraction, diffraction, absorption, and terrain, can potentially be included in the numerical solution.

Full-wave models that have been used in infrasound studies include:

- Normal modes
- Time-domain parabolic equation (TDPE)
- Finite-difference time domain

Each will be discussed in turn below.

17.10 Normal Modes

Infrasound can be interpreted as propagating through two acoustic ducts, the lower capped at approximately 50 km (in the stratosphere) and the other at approximately 120 km (in the thermosphere). Normal mode models provide a natural numerical approach to address this ducted propagation.

For a range-independent environment, normal mode formulations are derived from the Helmholtz equation in cylindrical coordinates. The solution can be expressed as the sum of two eigenfunctions that are functions of range and height, respectively. Key to the solution is solving, as each mode in the sum, the relation between the horizontal wavenumber and angular frequency. This solution can be expressed in a dispersion curve, which plots the functional dependence between these two variables.

During the 1970s, normal mode models were developed to study very large yield explosions (Pierce and Kinney 1976), and the dominant frequencies for these events were 0.1 Hz and below. More recently, normal mode approaches were modified to analyze smaller events with dominant frequencies above 0.1 Hz (Dighe et al. 1998). The solution of the dispersion curve was simplified by incorporating the WKB approximation. The WKB approximation is valid for the higher frequencies of interest, and it can be interpreted geometrically as expressing each mode as the combination of upward and downward traveling plane wave, each described by a ray path.

Since the normal mode solution is for a range-independent atmosphere, the modes are solved through stratified atmospheric layers. This can potentially limit their application to longer ranges where range-dependent effects are significant. In general, the computational load for normal mode models is small, but can increase depending on the number of layers and modes solved for. The bottom boundary of the duct is assumed hard and absorption effects are not easily integrated into the solution.

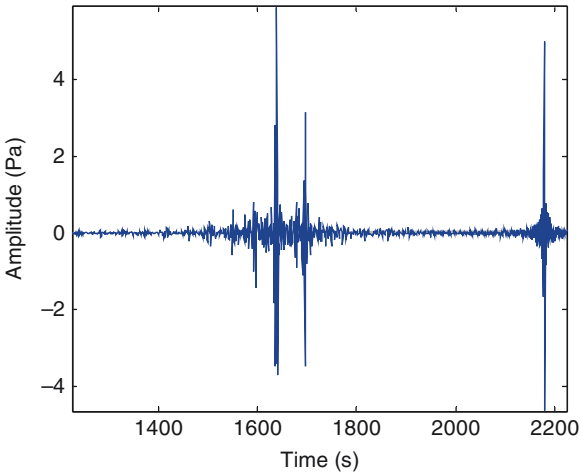

Fig. 17.16 Example waveform prediction using the normal mode model. Both stratospheric (early arrival) and thermospheric (last arrival) are modeled in this case

Figure 17.16 gives an example of a normal mode waveform prediction over a 450 km path. In this case, both stratospheric and thermospheric arrivals are evident.

Recently, normal mode analysis of infrasound propagation has become less popular than finite difference and parabolic methods described below. However, in one interesting study, repeated signals from a single infrasound source were observed to exhibit dispersive properties. The propagation was modeled using a simple low-velocity waveguide, and predicted group velocities were used to estimate source range (Herrin et al. 2006).

17.11 Time-Domain Parabolic Equation

PE methods can be utilized to generate full-wave solutions. The two main approaches to achieving these TDPE solutions are finite difference and Fourier synthesis. The first approach uses finite difference methods to solve the propagation equations directly in the time domain (Collins 1998). The main advantage is a (potentially) significant reduction in computational loading. Additional properties such as nonconstant density gradients and nonlinear effects can also be more easily incorporated into the characterizations. The main disadvantage is that the formulation must be carefully examined for numerical stability. Boundary conditions can also be more complicated to define.

The second TDPE approach utilizes Fourier synthesis. This method involves running a version of the continuous wave PE at each frequency bin that spectrally defines the source waveform. An inverse Fourier transform of the synthesized spectrum is then computed to derive the received waveform (Tappert et al. 1995). The main advantage of Fourier synthesis is that all capabilities of the continuous

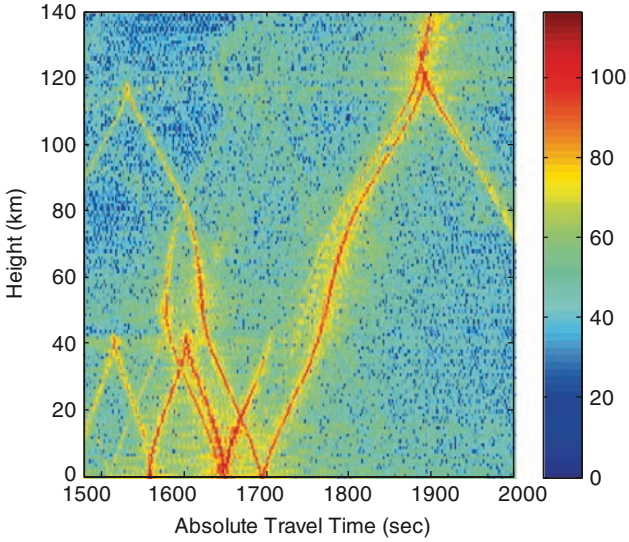

Fig. 17.17 Waveform arrival structure as a function of height along a 300 km propagation path and over a source bandwidth of 0–1 Hz. Both stratospheric and thermospheric arrivals are evident

wave model are maintained. The main disadvantage is the high computational loading, especially for large frequency bandwidths and acoustic arrivals that are widely dispersed in time. In both of these scenarios, the spectral bin size can become very small, meaning a large number of continuous-wave PE solutions must be computed.

Figure 17.17 shows an example of the waveform arrival structure at the receiving end of a 300 km propagation path. It is important not to confuse these images with PE amplitude fields. The ordinate is time, and the received waveform at the ground or any height can be found by taking a horizontal slice through the image. The first dominant arrival in this figure is stratospheric as the arrival energy is capped at approximately 40 km. The second dominant arrival is thermospheric with the energy extending up to 120 km.

In infrasound, Fourier-synthesis TDPE models have been widely applied. They have been used in validation studies of train explosions (Norris and Gibson 2004b) and in studying the properties of waveform observations from controlled surface explosions (Kulichkov et al. 2004, 2003).

17.12 Finite Difference Time Domain

Fundamental to all propagation models reviewed to this point is the establishment of the linear wave equations as a starting point in the theoretical derivation. Finite-difference methods can be directly applied to a discrete version of the wave

equation before any derivations are carried out, such as factorization or frequency-domain transformation. More fundamentally, finite difference can be applied to first principles fluid equations used to derive the wave equation, namely Euler's momentum equation, the continuity equation, and the state equation.

The primary challenge in finite difference methods is managing the computational loading. Selection of the spatial grid size and time steps is critical to ensure convergence and stability in the solution. In addition, defining the boundary conditions can add additional complexity. Since the solution is marched forward in time, "snapshots" of the acoustic field can be plotted as the acoustic field evolves. Multiple snapshots can be combined to generate animation of the evolving waveforms.

Finite difference time domain (FDTD) models have been derived from the fluid equations to model low frequency acoustic propagation as well as acousto-gravity wave propagation (de Groot-Hedlin 2007). This solution includes topography and it has been compared to finite-difference frequency domain solutions for consistency. An example of the FDTD solution for an evolving waveform from a harmonic source is shown in Fig. 17.18.

FDTD methods can also be used to account for the effects of the moving medium, discussed in a previous section. A general solution has been derived for

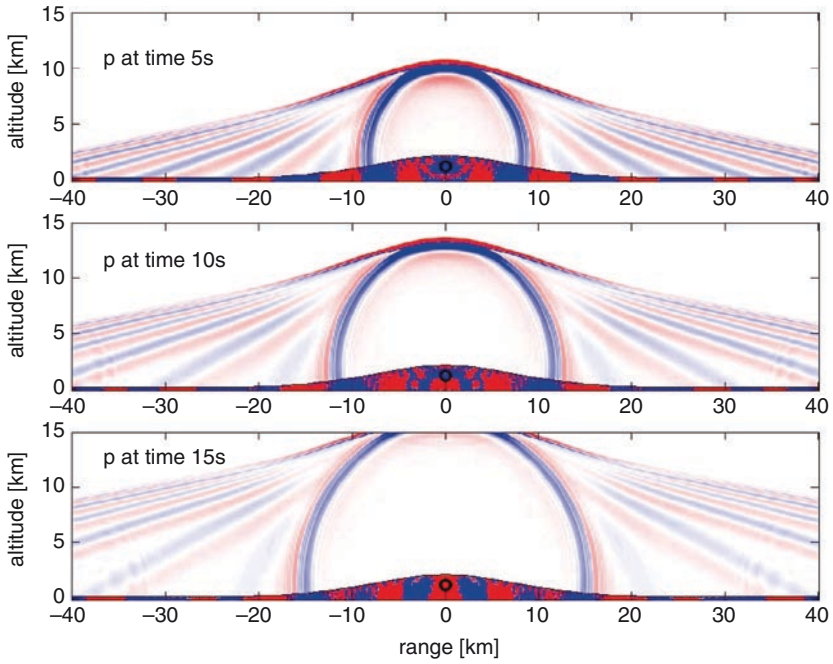

Fig. 17.18 Snapshots of the acoustic field propagating outward from a 0.5 Hz harmonic source (adapted from de Groot-Hedlin 2007)

use in two-dimensions (Ostashev et al. 2005). This solution has been adapted for infrasound studies by accounting for the exponential decay in density with height that may affect the propagation (de Groot-Hedlin 2005). Density is accounted for by utilizing a transformation that is used in formulating a PE model for deriving acousto-gravity wave (Lingevitch et al. 1999).

17.13 Nonlinear Effects

The propagation models discussed above are all based on the linear wave equation. The linear assumption breaks down for high-intensity, impulsive sources such as nuclear and nonnuclear explosions (Pierce et al. 1973; Kinney and Graham 1985). Properties of refraction, diffraction, dissipation, and ground-interaction all have different characteristics for nonlinear propagation when compared to linear propagation (Hamilton and Blackstock 1998).

The theory of nonlinear acoustics has been well developed over the years, and the fundamental equations that define the different characteristics of the nonlinear propagation have been derived. The challenge arises in being able to analytically or numerically solve the defining equations for a particular problem of interest. In underwater acoustics, great progress has been made in the ability to model the evolving wave front of a weakly nonlinear shock wave. For example, some successful modeling has been achieved through the solution of the Nonlinear Progressive wave Equation (NPE).

The NPE model was developed to model the time-dependent evolution of a nonlinear wave as it propagates. It includes separate terms for the physical processes of refraction, steepening, radial spreading, and diffraction (McDonald and Kuperman 1985). Initially, it was only solved numerically for a few simple cases (McDonald and Kuperman 1987). In a later work, however, the NPE model was successfully used to predict nonlinear propagation of a weak shock front in an ocean acoustic waveguide (Ambrosiano et al. 1990). The nonlinear effects were quantified by comparing the waveform predictions with the nonlinear terms turned on and off. It was observed that the nonlinearities caused energy loss near the source. This loss was attributed to shock formation, steepening in the evolving waveform, and unique interaction with the lower boundary that included a smaller effective grazing angle.

The study of nonlinear effects in infrasound is an active research area. Initial attempts have focused on using the NPE formulations described above (van der Eerden et al. 2004; Norris et al. 2008). More recent efforts are focused on deriving a new system of nonlinear governing equations that accurately account for the low density and high attenuation seen in the thermosphere (Krasnov et al. 2007). In addition, studies of sonic boom propagation through turbulence using the KZK approach may have further applications to infrasound (Blanc-Benon et al. 2002).

17.14 Spectral Methods

Important numerical techniques that can be applied to solving partial differential equations (PDEs) are spectral methods (Fornberg and Sloan 1994; Trefethen 2000 Hesthaven et al. 2007). Spectral methods have significant potential to numerically solve a large variety of complex formulations derived from fluid and wave equations. This potential results from their numerical efficiency, accuracy, and flexibility. The challenge in applying these methods is that the implementation can sometimes be complex, though resources are available, such as libraries of spectral operators and algorithms (e.g., see Trefethen 2000). This section provides an introduction to spectral methods, followed by a recent infrasonic application. Interested readers should consult the aforementioned references for more detailed presentations.

Spectral methods are categorized as global numerical methods as opposed to finite-difference methods, which use local approximations for derivatives. Spectral methods are *global* in the sense that they use all available data points, and provide expressions that can be differentiated *exactly*. Often this is accomplished with the assistance of a set of basis functions to construct an *interpolant*. Common choices are Chebyshev polynomials for nonperiodic data and trigonometric functions for periodic data. The key point is that for a spectral method, convergence can be exceedingly fast (exponential order) compared to finite-difference methods (polynomial order convergence) and is, therefore, a better choice than local methods when very accurate solutions or long time integrations on coarse grids are required (Hesthaven et al. 2007).

The application that is perhaps most responsible for the widespread use of spectral methods is the accurate and efficient solution of the incompressible Navier-Stokes equations. However, hyperbolic problems, which include some nonlinear wave propagation, were traditionally viewed as problematic. Fortunately, significant progress has been made to date, and this is an active research domain (Gottlieb and Hesthaven 2001). In general, there are two primary issues that must be addressed in developing a numerical spectral procedure: first, how to choose the basis functions for the interpolant such that the approximation converges rapidly; and second, how to determine the expansion coefficients from among three major approaches: Tau, Galerkin, and Collocation. From an infrasound perspective, the third approach, spectral collocation (also called pseudospectral) – a technique where the coefficients are selected to satisfy the boundary conditions and the residual (difference between the expansion and true solution) must be zero at the spatial grid points, appears to be the most appealing. This is because it is particularly easy to apply to equations with variable coefficients (range-dependence) and nonlinearities, as pseudospectral methods only give rise to products of numbers (rather than products of expansions) for determining the expansion coefficients.

In recent years, pseudospectral methods have gained popularity in solving propagation problems in infrasound. Chebyshev pseudo spectral methods (CPSM) have been used in a version of the continuous-wave PE applied to the

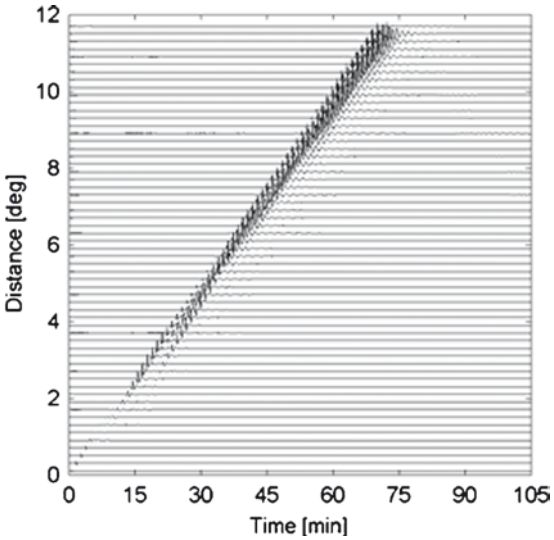

Fig. 17.19 Sample output of predicted waveforms vs. range from CPSM model (adapted from Ceranna 2003)

study of surface blasts (Gainville et al. 2006). CPSM have also been used to solve more fundamental fluid equation derivations. In one case, the derivation starts with the aero-acoustic equations. Two dimensional fields are then formulated at Gauss-Lobatto points, and the evolving acoustic pressure field is solved in time using a third-order Runge-Kutta algorithm. Figure 17.19 shows a sample output of the CPSM model at a successive series of ranges (Ceranna 2003). One advantage of this approach is that the evolving waveform can be easily displayed as a function of time. This model has been used in a detailed study of the Buncefield oil plant explosion (Ceranna and Le Pichon 2006). CPSM have also been adapted for use in modeling supersonic moving sources such as bolides, through representation of the source function as a line source (Arrowsmith et al. 2005; Ceranna and Le Pichon 2004).

17.15 Summary

Successful modeling of infrasound requires a combination of atmospheric specifications that capture the spatial and temporal structure of the medium with propagation models that capture the dominant physics. This chapter has provided an overview of the previous work in these areas, current tools available, and research areas that are being pursued. A summary of the methods covered is given in Table 17.1, along with comments on applicability and limitations.

Table 17.1 Summary of infrasound modeling methods

Method	Application	Limitations
Mean atmospheric specifications (HWM, MSISE, NRL-G2S)	Wind, temperature, density specification from ground to thermosphere	Less accurate at higher altitudes due to sparse data
Numerical weather prediction (NWP) models	High-fidelity regional or mesoscale atmospheric specifications	Generally not available above ~50 km. Cannot resolve fine-scale phenomena smaller than the model resolution
Fine-scale atmospheric specifications (e.g., gravity wave models)	Wind perturbation fields driven by atmospheric instabilities	Geospatial dependence of perturbation strength not fully quantified
Ray theory (HARPA, Tau-P, Gaussian beam)	Ray path predictions as driven by refraction. Solved in both two and three dimensions	Amplitude predictions problematic
Parabolic equation (PE) methods	Amplitude field predictions as driven by refraction and diffraction	Three-dimensional formulations computationally expensive
Absorption models (e.g., Sutherland and Bass)	Attenuation and dispersion specification applicable to low frequencies and high altitudes	Relies on detailed specification of atmospheric state
Full-wave models (normal mode, TDPE, FDTD)	Waveform predictions downrange of given source	Source waveform must be specified. More validation needed to bound performance
Nonlinear methods	Waveform predictions that account for nonlinear effects neglected in linear formulations	Active research area. Effects for infrasound domain not fully quantified

In conclusion, it should be noted that this overview is not inclusive of all the research that has been accomplished within the infrasound modeling community. It has provided a roadmap of the major thrusts that have been completed to date, and identifies some promising research areas that should bear fruit in the future.

References

Ambrosiano J, Plante D, McDonald B, Kuperman W (1990) Nonlinear propagation in an ocean acoustic waveguide. J Acoust Soc Am 87:1473–1481

Arrowsmith S, Hedlin M, Ceranna L, Edwards W (2005) An analysis of infrasound signals from the June 3rd, 2004 fireball over Washington State. Inframatics 10:14–21

Arrowsmith S, Drob D, Hedlin M, Edwards W (2007) A joint seismic and acoustic study of the Washington State bolide: observations and modeling. J Geophys Res 112:D09304

Bass H, Hetzer C (2006) An overview of absorption and dispersion of infrasound in the upper atmosphere. Inframatics 15:1–5

Bass H, Sutherland L, Piercy J, Evans L (1984) Absorption of sound by the atmosphere. In: Mason W., Thurston R (eds) Physical acoustics academic, vol. XVII, chap. 3. Orlando, FL: Academic

Bass H, Bhattacharyya J, Garcés M, Hedlin M, Olson J, Woodward R (2006) Infrasound. Acoust Today 2(1):9–19

Blanc-Benon P, Lipkens B, Dallois L, Hamilton M, Blackstock D (2002) Propagation of finite amplitude sound through turbulence: modeling with geometrical acoustics and the parabolic approximation. J Acoust Soc Am 111:487–498

Brachet N, Brown D, Le Bras R, Mialle P, Coyne J (2010) Monitoring the earth's atmosphere with the global IMS infrasound network. This volume, pp. 73–114

Brown D, Gault A, Geary R, Caron P, Burlacu R (2001) The Pacific infrasound event of April 23, 2001. Proceedings of the 23rd seismic research review, Jackson Hole, WY

Buland R, Chapman C (1983) The computation of seismic travel times. J Acoust Soc Am 73:1271–1302

Campus P, Christie DR (2010) Worldwide observations of infrasonic waves. This volume, pp. 181–230

Ceranna L (2003) Simulating the propagation of infrasound in the atmosphere. Infrasound Technology Workshop, La Jolla, CA

Ceranna L, Le Pichon A (2004) Simulating acoustic wave propagation in the atmosphere. Infrasound Technology Workshop, Hobart, Tasmania

Ceranna L, Le Pichon A (2006) The Buncefield fire: a benchmark for infrasound analysis in Europe. Infrasound Technology Workshop, Fairbanks, Alaska

Collins M (1993) A split-step Padé solution for the parabolic equation method. J Acoust Soc Am 93:1736–1742

Collins M (1998) The time-domain solution of the wide-angle parabolic equation including the effects of sediment dispersion. J Acoust Soc Am 84:2114–2125

de Groot-Hedlin C (2005) Modeling infrasound waveforms in a windy environment. Inframatics 11:1–7

de Groot-Hedlin C (2006) Finite difference methods for acoustic and acousto-gravity wavefields: application to low frequency infrasound propagation. Proceedings of the 28th seismic research review, Orlando, FL

de Groot-Hedlin C (2007) Finite difference modeling of infrasound propagation to local and regional distances. Proceedings of the 29th seismic research review, Denver, CO

Dessa J, Virieux J, Lambotte S (2005) Infrasound modeling in a spherical heterogeneous atmosphere. Geophys Res Lett 32:L12808

Dighe K, Whitaker R, Armstrong, 1998: Modeling study of infrasonic detection of a 1 kT atmospheric blast. Proceedings of the 20th annual seismic research symposium, Santa Fe, New Mex

Donn W, Rind D (1971) Natural infrasound as an atmospheric probe. Geophys J Roy Astron Soc 26:111–133

Donohue D, Kuttler J (1997) Modeling radar propagation over terrain. Johns Hopkins APL Tech Dig 18(2):279–287

Drob D, Picone J, Garcés M (2003) The global morphology of infrasound propagation. J Geophys Res 108(D21):4680

Evers L, Haak H (2006) Seismo-acoustic analysis of explosions and evidence for infrasonic forerunners. Infrasound Technology Workshop, Fairbanks, Alaska

Evers L, Haak H (2007) Infrasonic forerunners: exceptionally fast acoustic phases. Geophys Res Lett 34:L10806

Fornberg B, Sloan D (1994) A review of pseudospectral methods for solving partial differential equations. Acta Num 3:203–267

Fritts D, Alexander J (2003) Gravity wave dynamics and effects in the middle atmosphere. R Geophys 22:275–308

Gainville O, Piserchia P, Depres B, Have P, Blanc-Benon P, Aballea F (2006) Numerical modeling of infrasound propagation in a realistic atmosphere. Infrasound Technology Workshop, Fairbanks, Alaska

Gainville O, Blanc-Benon Ph, Blanc E, Roche R, Millet C, Le Piver F, Despres B, Piserchia PF (2010) Misty picture: a unique experiment for the interpretation of the infrasound propagation from large explosive sources. This voslume, pp. 569–592

Garcés M, Hansen R, Lindquist K (1998) Travel times for infrasonic waves propagating in a stratified atmosphere. Geophys J Int 135:255–263
Garcés M, Willis M, Le Pichon A (2010) Infrasonic observations of open ocean swells in the Pacific: deciphering the song of the sea. This volume, pp. 231–244
Gardner C (1993) Gravity wave models for the horizontal wave number spectra of atmospheric velocity and density fluctuations. J Geophys Res 98:1035–1049
Gardner C (1995) Scale-independent diffusive filtering theory of gravity wave spectra in the atmosphere, the upper mesosphere and lower thermosphere: a review of experiment and theory. Geophysical Monograph Series, 87, AGU, Washington, DC
Georges T, Beasley W (1977) Refraction of infrasound by upper-atmospheric winds. J Acoust Soc Am 61:28–34
Gibson R, Drob D, Norris D (2006) Advancement of infrasound propagation calculation techniques using synoptic and mesoscale atmospheric specifications. Proceedings of the 28th seismic research review, Orlando, FL
Gibson R, Norris D, Drob D (2008) Investigation of the effects of fine-scale atmospheric inhomogeneities on infrasound propagation. Proceedings of the 30th monitoring research review, Portsmouth, VA
Gottlieb D, Hesthaven J (2001) Spectral methods for hyperbolic problems. J Comput Appl Math 128:83–131
Hamilton M, Blackstock D (1998) Nonlinear acoustics. Academic Press, San Diego
Hedin A, Fleming E, Manson A, Scmidlin F, Avery S, Clark R, Franke S, Fraser G, Tsunda T, Vial F, Vincent R (1996) Empirical wind model for the upper, middle, and lower atmosphere. J Atmos Terr Phys 58:1421–1447
Herrin E, Kim T, Stump B (2006) Evidence for an infrasound waveguide. Geophys Res Lett 33:L07815
Hesthaven J, Gottlieb S, Gottlieb D (2007) Spectral methods for time-dependent problems. Cambridge University Press, Cambridge, MA
Hetzer CH, Gilbert KE, Waxler R, Talmadge CL (2010) Generation of microbaroms by deep-ocean hurricanes. This volume, pp. 245–258
Jensen F, Kuperman W, Porter M, Schmidt H (1994) Computational ocean acoustics. AIP Press, New York
Jones M, Riley J, Georges T (1986) A versatile three-dimensional Hamiltonian ray-tracing program for acoustic waves in the atmosphere above irregular terrain. NOAA Special Report, Wave Propagation Laboratory, Boulder, CO
Kallistratova M (2002) Acoustic waves in the turbulent atmosphere: a review. J Atmos Ocean Technol 19:1139–1150
Kinney G, Graham K (1985) Explosive shocks in air. Springer, New York
Kinsler L, Frey A, Coppens A, Sanders J (1984) Fundamentals of acoustics. Wiley, New York
Krasnov V, Drobzheva Y, Lastovicka J (2007) Acoustic energy transfer to the upper atmosphere from sinusoidal sources and a role of nonlinear processes. J Atmos Solar-Terr Phys 69:1357–1365
Kulichkov S (2004) Long-range propagation and scattering of low-frequency sound pulses in the middle atmosphere. Meteorol Atmos Phys 85:47–60
Kulichkov S, Bush G, ReVelle D, Whitaker R, Raspopov O (2000) On so called "tropospheric" arrivals at long distances from surface explosions. Infrasound Technology Workshop, Passau, Germany
Kulichkov S, Avilov K, Popov O, Baryshnikov A (2003) Experience in using the pseudodifferential parabolic equation method to study the problems of long-rang infrasound propagation in the atmosphere. Inframatics 3:1–5
Kulichkov S, Avilov K, Bush G, Popov O, Raspopov O, Baryshnikov A, ReVelle D, Whitaker R (2004) On anomalously fast infrasonic arrivals at long distances from surface explosions. Izv, Atmos Ocean Phys 40:1–9
Le Pichon A, Blanc E, Drob D, Lambotte S, Dessa J, Lardy M, Bani P, Vergniolle S (2005) Infrasound monitoring of volcanoes to probe high-altitude winds. J Geophys Res 110:D13106
Le Pichon A, Antier K, Drob D (2006) Multi-year validation of the NRL-G2S wind fields using infrasound from Yasur. Inframatics 16:1–9

Lingevitch J, Collins M, Siegmann W (1999) Parabolic equations for gravity and acousto-gravity waves. J Acoust Soc Am 105:3049–3056
Lingevitch J, Collins M, Dacol D, Drob D, Rogers J, Siegmann W (2002) A wide angle and high Mach number parabolic equation. J Acoust Soc Am 111:729–734
Lott F, Millet C (2010) The representation of gravity waves in atmospheric general circulation models (GCMs). This volume, pp. 679–694
McDonald B, Kuperman W (1985) Time domain solution of the parabolic equation including nonlinearity. J Comput Math Appl 11:843–851
McDonald B, Kuperman W (1987) Time domain formulation for pulse propagation including nonlinear behavior at a caustic. J Acoust Soc Am 81:1406–1417
McKenna S (2005) Infrasound wave propagation over near-regional and tele-infrasonic distances. PhD Dissertation, Southern Methodist University, Dallas, TX
McKenna M, Stump B, Hayek S, McKenna J, Stanton T (2007) Tele-infrasonic studies of hard-rock mining explosions. J Acoust Soc Am 122:97–106
Norris D (2007) Waveform modeling and comparisons with ground truth events. Infrasound Technology Workshop, Tokyo
Norris D, Gibson R (2002) InfraMAP enhancements: Environmental/propagation variability and localization accuracy of infrasonic networks. Proceedings of the 24th seismic research review, Ponte Vedra Beach, FL
Norris D, Gibson R (2004a) Advanced tools for infrasonic modeling. Inframatics 5:13–19
Norris D, Gibson R (2004b) Validation studies using a TDPE propagation model and near real-time atmospheric specifications. Infrasound Technology Workshop, Hobart, Tasmania
Norris D, Bongiovanni K, Masi J (2008) Nonlinear propagation modeling of infrasound. J Acoust Soc Am 123:3829
O'Brien M, Shields G (2004) Infrasound source location using time-varying atmospheric models. Proceedings of the 26th seismic research review, Orlando, FL
Ostashev V (1997) Acoustics in moving inhomogeneous media. E & FN Spon, London
Ostashev V, Wilson D, Liu L, Aldridge D, Symons N, Marlin D (2005) Equations for finite-difference, time-domain simulation of sound propagation in moving inhomogeneous media and numerical implementation. J Acoust Soc Am 117:503–517
Picone J, Hedin A, Drob D, Aiken A (2002) NRLMSISE-00 empirical model of the atmosphere: Statistical comparisons and scientific issues. J Geophys Res 107:1468
Pierce A, Kinney W (1976) Computational techniques for the study of infrasound propagation in the atmosphere. Air Force Geophysics Laboratories Technical Report AFGL-TR-76-56, Hanscom AFB, MA
Pierce A, Moo C, Posey J (1973) Generation and propagation of infrasonic waves. Air Force Cambridge Research Laboratories Technical Report AFCRL-TR-73-0135, Bedford, MA
Sutherland L, Bass H (2004) Atmospheric absorption in the atmosphere up to 160 km. J Acoust Soc Am 115:1012–1032
Tappert F, Spiesberger J, Boden L (1995) New full-wave approximation for ocean acoustic travel time predictions. J Acoust Soc Am 97:2771–2782
Trefethen L (2000) Spectral Methods in MATLAB. SIAM, Philadelphia
van der Eerden F, Védy E, Salomons E (2004) Prediction of shock waves over a large distance: a hybrid method. Proceedings of the 11th symposium on long range sound propagation, Fairlee, VT
West M, Gilbert K, Sack R (1992) A tutorial on the Parabolic equation (PE) model used for long range sound propagation in the atmosphere. Appl Acoust 37:31–49

Chapter 18
Misty Picture: A Unique Experiment for the Interpretation of the Infrasound Propagation from Large Explosive Sources

O. Gainville, Ph. Blanc-Benon, E. Blanc, R. Roche, C. Millet, F. Le Piver, B. Despres, and P.F. Piserchia

18.1 Introduction

A strong motivation for continuing infrasonic research is for understanding atmospheric acoustics in the context of the Comprehensive Nuclear-Test-Ban Treaty. The International Monitoring System develops a sixty barometric station network which should be able to detect one kiloton yield explosion anywhere on the globe (Christie and Campus 2010). Explosion studies are necessary to evaluate the detection capability of this network and to develop tools for infrasound record analysis. In this context, the Commisariat à l'Energie Atomique, in collaboration with the Laboratoire de Mécanique des Fluides et d'Acoustique, has developed a capability for discrimination and characterization of large explosive sources.

Barometric recordings made during the second half of the twentieth century allow us to understand the atmospheric propagation of infrasound as presented in McKisic's review of published natural and human made explosions (Mckisic 1997). The most energetic artificial explosions are atmospheric nuclear tests and high explosive experiments performed to simulate nuclear explosion effects. Barometric records of these events were used to characterize the atmospheric propagation of infrasound. Tropospheric, stratospheric and thermospheric infrasound waveguides are observed in the atmosphere (Evers and Haak 2007; 2010) with various average speeds over a great circle. Explosion experiments allow the calibration of empirical laws which link source yield W to the maximum overpressure measured at the station (Whitaker et al. 1990; Mutschelener et al. 1999). These empirical laws are based on a cylindrical scaling law $R/W^{1/2}$, with R the distance to the source. They also include mean atmospheric absorption effects and take into account mean wind

O. Gainville (✉)
CEA, DAM, DIF
F-91297, Arpajon, France
e-mail: olaf.gainville@cea.fr

A. Le Pichon et al. (eds.), *Infrasound Monitoring for Atmospheric Studies*,
DOI 10.1007/978-1-4020-9508-5_18, © Springer Science+Business Media B.V. 2010

effects. In addition to explosion experiments, International Monitoring System barometric stations record various other explosions such as industrial accidents. The study of these accidents allows to evaluate the validity of empirical laws (Green et al 2010; Ceranna et al. 2009; Evers and Haak 2007).

From the early modeling of Pierce (1967), Reed (1977) or ReVelle and Whitaker (1996) it is apparent that it is necessary to take into account the seasonal atmospheric time variability to model the long-range propagation of explosion associated infrasound. Classical ray tracing methods (Jones et al. 1986; Drop et al. 2003; Gainville et al. 2006) are often used in this way, mainly to compute arrival time and geometrical wave characteristics. Linear parabolic equation approximations are used to include scattering effects in infrasound propagation simulation (Dallois et al. 2001; Lingevitch et al. 2002; Kulichkov et al. 2004; Norris 2006), with particular interest in wide-angle approximation quite important in turbulent media. Nonlinear effects, important for energetic explosions, are included in ray tracing methods (Cleveland et al. 1996; Gainville et al. 2006) and parabolic equation methods (Blanc-Benon et al. 2002; Aver'yanov et al. 2006; Coulouvrat 2008). Research to model the infrasound propagation from explosive sources has recently focused on mixed asymptotic methods (Coulouvrat 2008) or on direct simulation methods (Bailly and Bogey 2008; Marsden et al. 2008; Wilson and Liu 2004; Del Pino et al. 2009).

In this chapter, we are interested in the propagation of infrasound emitted by a chemical explosion, known as Misty Picture experiment, which occurred in 1987 in New Mexico (USA). Infrasound was recorded by 23 sensors up to a distance of 1,200 km in a quiet background noise condition. Because of the difficulties to undertake such an energetic explosion and the extensive documentation of the event (Reed et al. 1987; Whitaker et al. 1974; Blanc 1988), this event provides a unique opportunity to study the propagation of infrasound. In addition to long-range measurements, Reed et al. (1987) installed microphones at approximatively 10 km from the source which give a useful source waveform reference. This experiment provides an opportunity to characterize the long-range propagation of infrasonic waves for low frequency source (0.1 Hz). We investigate effects of various phenomena, such as the wind, the atmospheric absorption, nonlinearities, refraction and scattering by small atmospheric heterogeneities on observed phases kinds, their travel time and their waveform signature. In this chapter, after a presentation of the Misty Picture experiment and of the available measurements, we describe the modeling of this event. The analysis of simulation results is performed in order to compare with measurements, first to describe geometrically the propagation of infrasound and secondly to study the pressure signature at long range.

18.2 The Misty Picture Experiment

Misty Picture was a high explosive test sponsored by the US Defense Nuclear Agency. It was detonated at 10:00 MDT (16:00 UT) on 14th May 1987 at White Sands Missile range in New Mexico (USA). The explosive charge consisted of

4,685 tons of (ammonium nitrate and fuel oil ANFO) arranged into a 27 m diameter fiberglass hemisphere container installed on the ground. The resulting airblast provided the scaled equivalent airblast of an 8 kt nuclear explosion. The primary objective of the test was to provide an airblast, dust cloud and ground shock environment for the US Department of Defense (Lehr 1987).

Three laboratories recorded infrasound emitted by this explosive test at distances from 7 to 1,200 km as presented in Fig. 18.1: the Sandia National Laboratory (Reed et al. 1987), the Los Alamos National Laboratory (Whitaker et al. 1990) and the French Commissariat à l'Energie Atomique (Blanc 1988). The event was instrumented with 23 barometric stations for which maximum overpressure and arrival time are available. Because of background wind noise, only 21 of the 23 pressure signatures allow an observation of arrivals. Six stations between the source and 100 km detected a tropospheric arrival. Five stations between 100 and 220 km detected both stratospheric and tropospheric arrivals whereas the four stations between 220 and 450 km detected thermospheric arrivals. The six farthest stations, between 700 and 1,200 km in the West direction, detected multiple stratospheric arrivals only. Los Alamos National Laboratory stations are four multi-sensor microbarographic arrays allowing a more sensitive detection and a higher signal-to-noise ratio.

CEA barometric records shown in this chapter have not been previously published and were performed by Blanc. Ten barometric stations were installed around the source up to a distance of 1,000 km. Numerous arrivals are observed at each station with low background noise levels except at Tatum station. All these stations were composed of a single barometer. The sampling frequency is 4 Hz and the amplitude response of the sensor is a band pass filter with cutoff frequencies of 0.03 and 1 Hz.

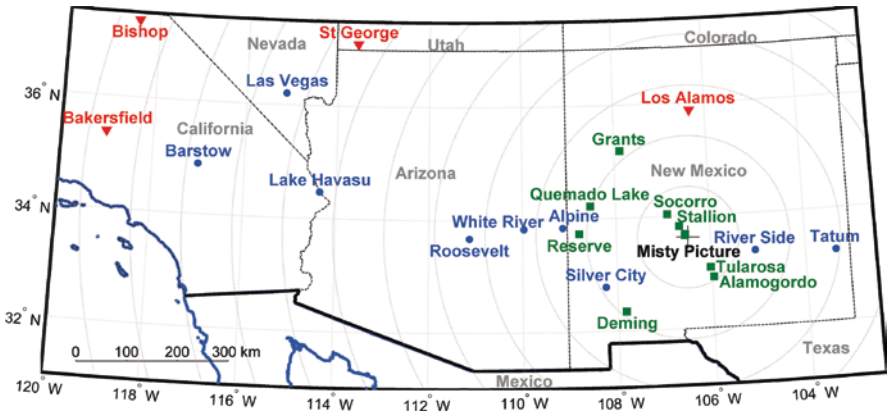

Fig. 18.1 Map of the Misty Picture event. Three laboratories performed infrasound measurements: (▼) Los Alamos National Laboratory (Whitaker et al. 1990), (■) Sandia National Laboratory (Reed et al. 1987) and (●) Commissariat à l'Energie Atomique (Blanc 1988). The *square* close to the source (Misty Picture) shows the location of two infrasonic stations: Admin park and Observer area

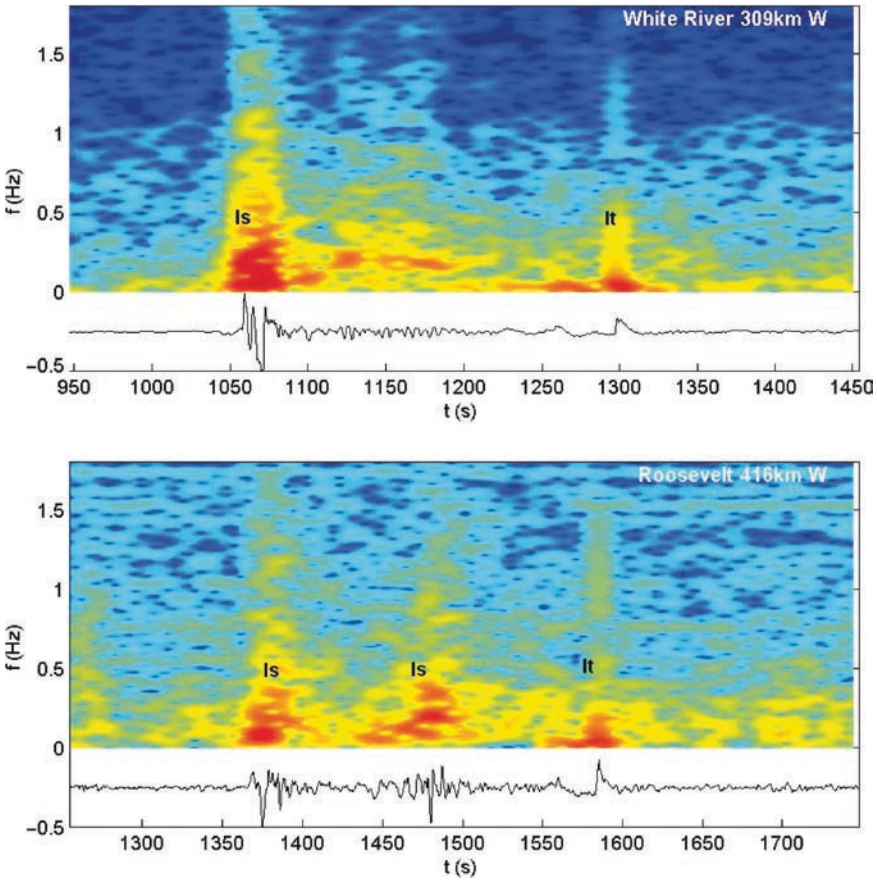

Fig. 18.2 Spectrograms of measured overpressure signature at White River (309 km) and Roosevelt (416 km) stations (normalized amplitude). For both signals, the later arrivals have a lower central frequency than previous ones. This observation allows the identification of stratospheric arrivals I_s and thermospheric arrivals I_t

Signal analysis allows the identification of arrivals using spectrograms (see Fig. 18.2) and cross-correlation for array stations. Acoustic energy due to the Misty Picture experiment is in the 0.05–0.5 Hz spectral range. Signal central frequency shifts from 0.2 Hz close to the source to 0.1 Hz at long range.

In spite of previous analysis of these measurements (Blanc 1988; Peyret 1995; Rascalou 1989; Reed et al. 1987), these data are of particular interest because it seems to be the most instrumented barometric event recorded. Source informations, meteorological measurement and numerous barometric measures at various distances and in various directions are of particular interest. This explosion allows the study of infrasound propagation with comparison between simulations and measurements.

18.3 Infrasonic Wave Propagation Modeling

To model the long-range propagation of infrasound generated by the Misty Picture event, we need to describe the source, the atmosphere and the Earth surface. Using these informations, we model the infrasound propagation using a ray tracing model and a parabolic equation model. The goal is to understand the propagation of infrasound and to compare computed and measured pressure signatures at receivers. Simulations allow us to investigate the influence of the various phenomena which affect the propagation of infrasound.

18.3.1 Source

The Misty Picture event is located on the Earth surface, 1,505 m above the sea level, at 33° 37′ 11.5″N latitude and the 106°38′26.3″W longitude. The Misty Picture explosion is equivalent to 3,840 tons of trinitrotoluene (TNT) using the 82% ratio of ANFO mechanical efficiency (Koper et al. 2002). The air temperature close to the source was approximatively 20°C and the atmospheric pressure was 860 hPa (Reed et al. 1987).

The shock wave pressure signature close to the source is described by the maximum overpressure p_{peak}, the positive phase duration t_d and the waveform (Reed 1977; Kinney and Graham 1985; Drobzheva and Krasnov 1999). The shock wave characteristics are estimated using empirical models defined for an explosion in a free space homogeneous standard atmosphere. These empirical models used scaling laws which defined a scaled distance $Z = RW^{-1/3}$, where R is the distance to the source and W is the source yield. These models can be applied to an inhomogeneous atmosphere using energy conservation laws (Kinney and Graham 1985; Drobzheva and Krasnov 1999; Korobeinikov 1985). For an explosion located on the ground surface the yield is doubled ($2W$) if we assume that no energy is lost in the crater formation.

For the Misty Picture explosion, we used the Kinney empirical models (Kinney and Graham 1985) for both the maximum overpressure p_{peak} and the positive phase duration t_d. These empirical models are in agreement with measures performed at Admin park (7.26 km) and Observer area (8.38 km) (Reed et al. 1987) as shown in Fig. 18.3. Differences are associated to tropospheric temperature and wind inhomogeneity effects that create local focusing of waves (Reed et al. 1987). Maximum overpressure and time duration values are given in Table 18.1 for the Misty Picture event.

The initial pulse signature is modeled using the waveform proposed by Reed (1977):

$$p(t) = p_{peak}\left(1-\frac{t}{t_d}\right)\left(1-\frac{t}{t_{tot}}\right)\left(1-\frac{t}{t_{tot}}\right)^2, \quad (1)$$

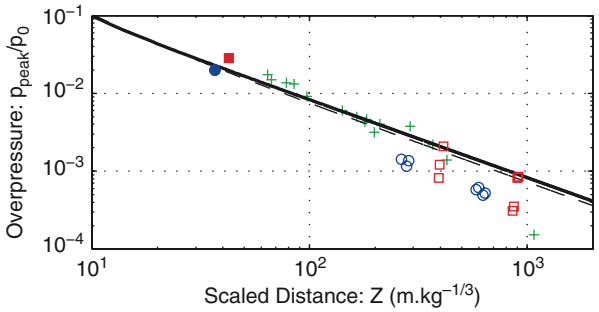

Fig. 18.3 Scaled overpressure vs. Scaled distance given by the Kinney model (Kinney and Graham 1985) (*solid line* —) and Korobeinikov model (Drobzheva and Krasnov 2003) (*dashed line* - -). *Red squares* and *blue circles* are respectively Admin park and Observer area measures. *Filled symbols* are relative to the Misty Picture explosion whereas the others are relative to pre explosion events (2 h, 1 h and 1 mn before Misty Picture event) (Reed et al. 1987). Measure analysis is performed as proposed by Koper et al. (2002). For comparison, Koper et al. analysis results are indicated with *green crosses*

Table 18.1 Comparison between Kinney's model and measures of the maximum overpressure and the pulse duration at Admin park and Observer area stations. Kinney's model parameters are computed for an effective charge weight of $2 \times 3{,}840 t_{TNT}$. The analysis of measured pressure signatures is performed as presented by Koper et al. (2002). The 4.0 km Kinney's model parameters are used as initial condition in our simulations

		Measurements		Kinney's model	
Station	Distance (km)	p_{peak} (Pa)	t_d (s)	p_{peak} (Pa)	t_d (s)
	4.0			3,900	0.822
Admin park	7.26	1,700	0.855	2,990	0.856
Observer area	8.38	2,410	0.862	1,800	0.868

with $t_{tot} = 3.565 t_d$, p_{peak} the maximum overpressure and t_d the positive phase duration. This waveform shape and its spectrum are in agreement with measurements at Admin park and Observer area (see Fig. 18.4). The agreement of this model with the measurements appears better than for the classical waveform used by Kinney and Graham (1985) in Fig. 18.4, particularly for the central frequency. We note that Drobzheva and Krasnov (1999) use a modified Reed's model which improves the pulse shape but not the pulse spectrum. A low frequency analytical approximation of Reed's model is used for linear codes. This simple function presented in Fig. 18.4 is defined by

$$p(t) = -0.33\, p_{peak} \sin(2\omega_d t + 4\pi\Delta) \frac{1 - \cos(\omega_d t + 2\pi\Delta)}{2}, \tag{2}$$

with $\omega_d = \pi/4t_d$ and $\Delta = 0.355$. The amplitude, the central frequency and the time reference of this signal are fitted to agree with the low frequency filtered Reed's

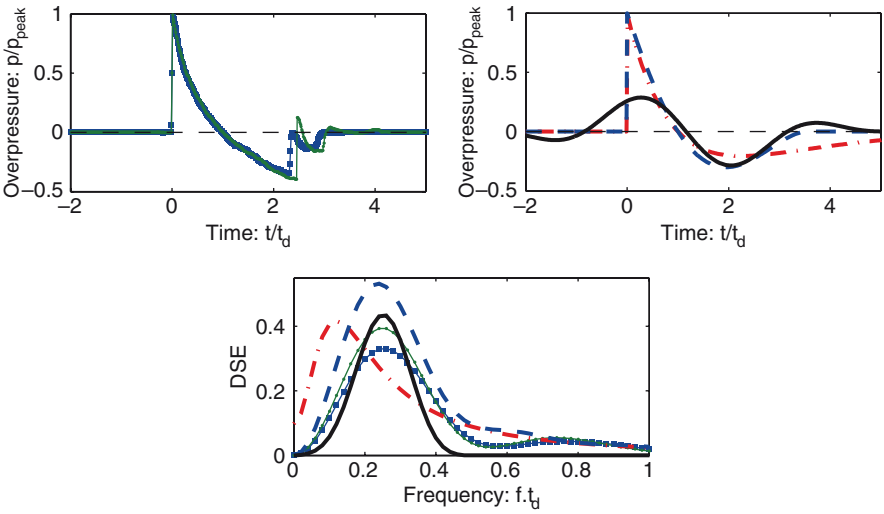

Fig. 18.4 Pressure signature at the source. In the *upper* figures the scaled overpressure is plotted as a function of the scaled time. The *left hand panel* shows the measurements at Admin park (-•-) and Observer area (–). The *right hand panel* shows the predictions made for Kinney's model (-.-), Reed's model (- -) and the low frequency model (–). In the *lower panel* the scaled energy spectral density (dimension less) is shown for each signal

model. All these models have well-calibrated energy amplitude at low frequency. Differences in the spectrum and in the pulse signature are essentially due to the second shock which is not present in models.

For the Misty Picture event, the central frequency at 4 km from the source is around 0.3 Hz and its limit is 0.1 Hz at long range. The Misty Picture event is a low frequency propagation problem.

18.3.2 Atmosphere

To model the long-range propagation of infrasound, we use an inhomogeneous stratified atmosphere which is a combination of measurements with empirical models (see Fig. 18.5). Numerous weather observations were made before and after the explosion (Reed et al. 1987). The rawinsonde launch at 10:00 (MDT) from Stallion station gives the temperature and wind profiles between the ground and an altitude of 19 km. The rocketsonde launch from White Sand Missile Range at 10:02 (MDT) gives temperature and wind profiles every kilometer between 29 and 73 km altitude. These measurements are linking with statistical temperature MSIS-90 and wind HMW-93 (Hedin et al. 1996) profiles. These statistical profiles are consistent for high altitude, whereas measurements are more representative of the low atmosphere. Moreover, weather measurements introduced fine structures representative of media turbulence and gravity waves not modeled by statistical profiles. These structures are

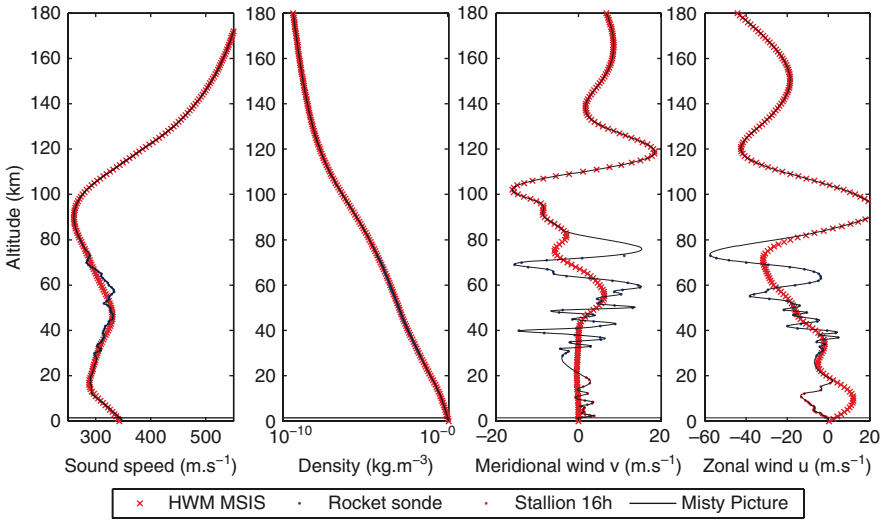

Fig. 18.5 Sound speed profile, density profile and wind profiles (*black line*) used to model the long-range propagation of infrasound emitted by the Misty Picture event. They are composed of measurements (Reed et al. 1987) (*green* and *blue points*) for low altitudes and of statistical models (Hedin 1991; Hedin et al. 1996) (*red crosses*) above 73 km (sea level). The matching between profiles and their interpolation is performed with splines

assumed to be presented as an infinitely stratified approximation of gravity wave models (Kulichkov 2004; Ostashev et al. 2005). This is in agreement with the observations that the horizontal scale of atmospheric gravity waves is much greater than the vertical scale. Our atmospheric model is used as an atmospheric turbulence case which allows the study of infrasound wave scattering by gravity wave inhomogeneities. The use of measurements in our atmospheric model increases qualitatively the interpretation of the long-range propagation of infrasound but not quantitatively.

In addition to the temperature and horizontal wind profiles, the atmospheric model includes the composition profiles and thermodynamic relations of Sutherland and Bass (2004). Using the hydrostatic equilibrium hypothesis and a sea level density of 1.17 kg m^{-3}, we define the density profile showed in Fig. 18.5.

Atmospheric sound absorption is also described in Sutherland and Bass's (2004) paper. Absorption and wave dispersion take into account shear viscosity, bulk viscosity and molecular vibrational relaxation.

18.3.3 Geometry and Earth Surface Modeling

In our study, the Earth surface is assumed to be spherical or planar at the altitude of the point source, i.e. 1,500 m above the sea level. For a spherical surface, the Earth radius is assumed to be constant at 6,371 km. The topography is not

included and the reflection of infrasound is assumed specular and total both on the ground and the ocean. The infrasound propagation is studied up to a distance of 1,000 km mainly in the West direction, where most of the barometric stations were located.

18.3.4 Propagation Models

To study the propagation of infrasound generated by the high explosive Misty Picture event, we use a nonlinear ray tracing method and a linear wide-angle parabolic equation (WAPE) method.

The ray tracing method models the propagation of acoustic waves in the geometrical acoustics limits. Geometrical acoustics is the study of acoustic wave fronts propagating in the high frequency hypothesis. In atmospheric propagation, the high frequency hypothesis is based on the assumption that space and time scales of atmospheric properties (temperature, wind, density) are much larger than acoustic wave scales. For a detailed presentation of the geometrical acoustic theory, we refer the reader to Whitham (1974) and Candel (1977). For a detailed presentation of the ray tracing code, its validation, we refer the reader to Gainville et al. (2006) or Gainville (2008). Our ray tracing code solves ray tracing equations and geodesic element equations to compute ray trajectory and amplitude variations using the wave action conservation law. We use an efficient shooting method to determine all the eigenrays that link the source to the station. Each eigenray is associated with an arrival at the station. The group velocity of the ray at the station provides the trace velocity and the azimuth of the wave. The global pressure signature at the receiver is the sum of eigenray pressure signature contributions. These pressure signatures are obtained by solving a generalized Burgers equation along each eigenray. This generalized Burgers equation takes into account nonlinear effects, shear and bulk viscosity absorption and molecular vibrational relaxation mechanisms. This equation is solved using a Fourier Galerkin spectral scheme. Specific developments are performed to pass through caustics and take into account ground reflection. This method is particularly efficient in modeling the propagation of infrasound, particularly in three dimensions. But, it is limited in the case of low frequency sources, such as the Misty Picture event, because the model does not incorporate wave diffraction.

The WAPE method (Dallois et al. 2001) models diffraction effects such as Fresnel diffraction at shadow zone boundaries and scattering by small atmospheric inhomogeneities. The propagation problem is simplified in a two-dimensional problem using a local cylindrical symmetry assumption. The wind convection is included using the effective celerity computed in the azimuth propagation direction. The method includes density variations and atmospheric absorption and dispersion. The ground surface is assumed planar with an infinite impedance. This method allows us to compute acoustic pressure level on the ground for a sinusoidal source and the pressure signature at receivers for a transient source.

18.4 Infrasound Propagation Interpretation

In this section, we study the propagation of infrasound waves emitted by the Misty Picture event by analyzing measurements and numerical simulations. We study mainly the West-East direction of propagation because of the alignment of the barometric stations following this line. We identified measured arrivals with either geometrical energy paths or diffracted energy paths. Effects of various mechanisms, such as scattering and atmospheric absorption, on the pressure level are also evaluated.

18.4.1 Propagation Results

The propagation of infrasound for the Misty Picture experiment in the West–East direction is shown in Fig. 18.6. The overpressure level computed by the parabolic equation method for sinusoidal sources of 0.1 and 1 Hz central frequencies and ray tracing results are represented as a function of the distance and the altitude. The

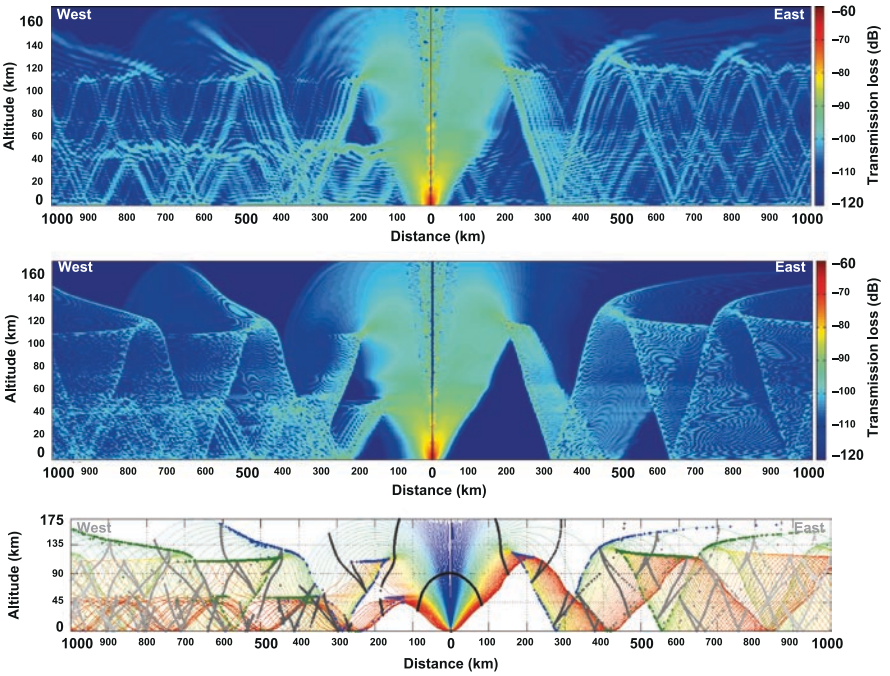

Fig. 18.6 Propagation in the West–East direction of infrasound emitted by a motionless point source on the ground. *Top* and *middle graph* show the transmission loss computed using the parabolic equation at 0.1 and 1 Hz, respectively. The *bottom graph* shows ray-trace mapping of the acoustic field. Ray colors depend on the ray launch parameter, wave fronts are showed by *gray points* every 600 s and caustics by *blue* and *green points*

West–East propagation of infrasound shows two main altitudes of refraction which are linked to the well-known stratospheric I_s and thermospheric I_t phases. Thermospheric phases evolve between the ground and the low thermosphere. The high positive thermospheric gradient of sound speed refracts infrasound and the ground reflects infrasound with low dissipation. Because of atmospheric thermo-viscous dissipation, wave energy absorption increases with altitude. Thermospheric phase I_{ta} which is refracted under the thermospheric cusp caustic (around 100 km height) is often observed contrary to the thermospheric phase I_{tb} refracted above the thermospheric cusp caustic, which is most attenuated. Wave energy above 140 km is often assumed totally dissipated. Stratospheric phases are trapped between the ground and the relative maximum of sound speed located at 50 km of altitude. However, stratospheric phases are visible only in the West. This is the most significant effect of the wind on infrasound propagation. In this figure, singularities of geometrical acoustics like caustics and shadow zones are also visible. The pressure level at 1 Hz is in agreement with ray tracing results with well-defined shadow zones and caustics whereas at 0.1 Hz results are not consistent with the geometrical structure, with arrivals observed in the shadow zones.

The infrasound propagation directivity is observed on maps in Fig. 18.7. This directivity effect is associated with the wind and is season-dependent. On these maps, the transmission loss is computed on the Earth surface using the parabolic equation method and the ray tracing method up to a distance of 1,000 km. Low arrival overpressure amplitudes (dark blue) are associated with shadow zones and high amplitudes are associated with caustics (red). In addition to thermospheric and stratospheric phases, tropospheric phases which evolve between the ground and approximatively 10 km are observed in the North–West direction. The ray tracing method overestimates the amplitude of these phases because of ground reaching caustics. Caustic overestimated amplitudes are observed for stratospheric and thermospheric phases as rings of high amplitude. Directivity maps show that stratospheric paths are only in the West direction whereas thermospheric paths are all around the source with a higher amplitude in the East direction. The parabolic equation computation at 0.1 Hz shows no shadow zone whereas the 0.5 Hz map appears in good agreement with geometrical results except close to the source and caustics.

The atmospheric infrasound propagation study shows three kinds of paths: tropospheric path (I_w), stratospheric path (I_s) and thermospheric path (I_t). Various reflections of these paths can be observed at a given distance from the source. To identify paths between the source and a receiver on the ground in the West direction, we use the representation of Fig. 18.8. In this figure, ground ray arrival times, West barometric station overpressure measurements and parabolic computed overpressure energy are superimposed. Multipaths are distinguished by their distinct arrival times at a given distance. Tropospheric paths are observed at a distance less than 100 km and travel within the lower 10 km of the atmosphere at a speed close to the ground sound speed. These paths are observed only with the parabolic equation method and on the measurements. Various stratospheric path reflections arrived with different retarded times. The retarded arrival time of these paths is independent of the distance and each path appears close to vertical in the

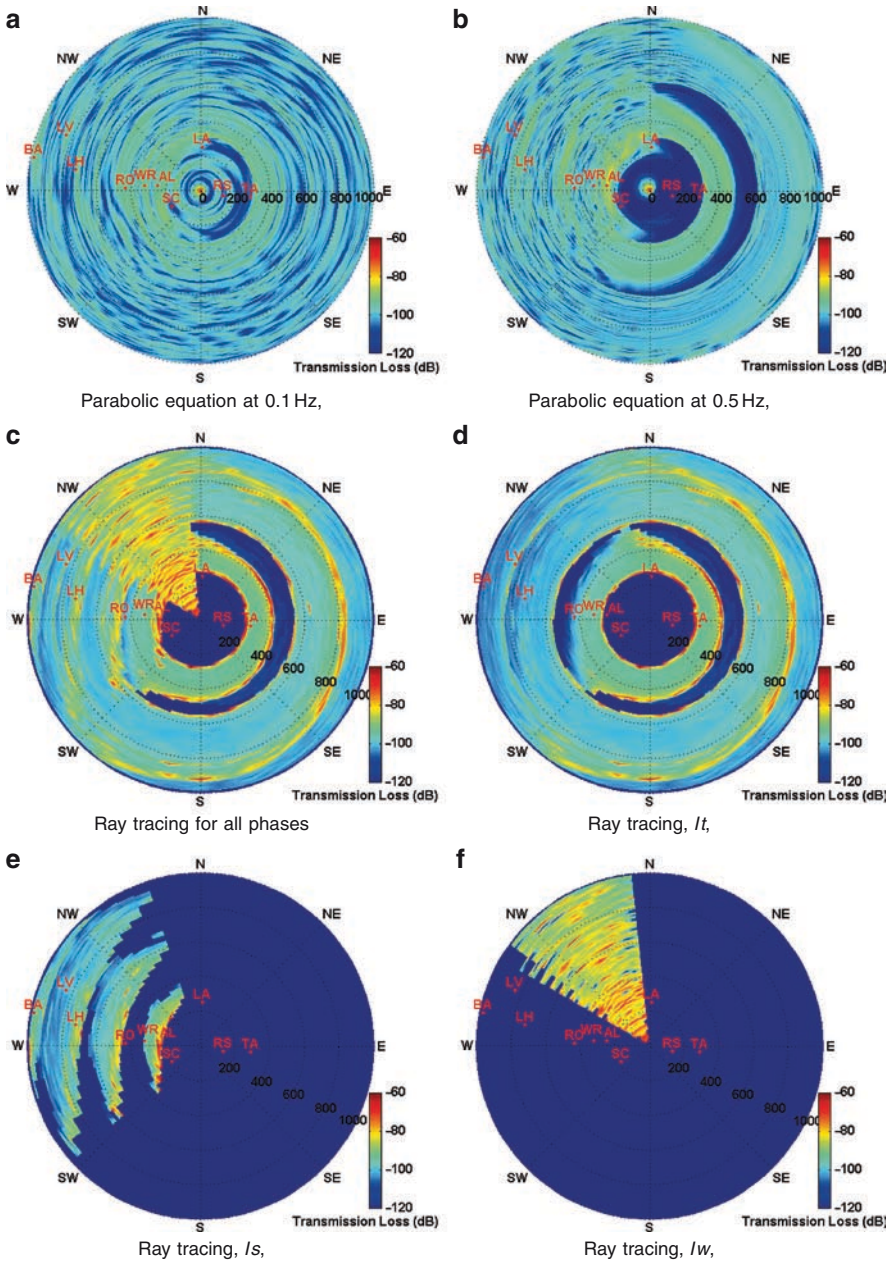

Fig. 18.7 Transmission loss at the ground surface computed with parabolic equation at 0.1 and 0.5 Hz and with the ray tracing method for the maximum of all the phases and for the maximum of each phase independently. The positions of the stations are indicated by *red dots*. (a) Parabolic equation at 0.1 Hz, (b) parabolic equation at 0.5 Hz, (c) ray tracing for all phases, (d) ray tracing, I_t, (e) ray tracing, I_s, (f) ray tracing, I_w

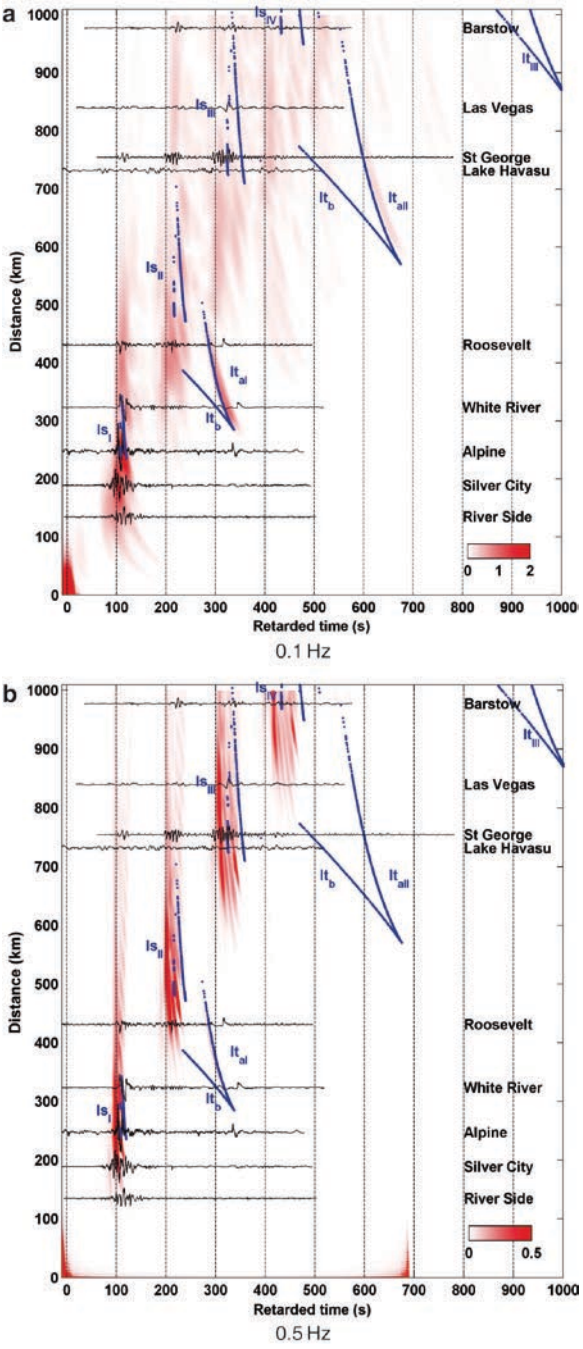

Fig. 18.8 Measured pressure signature (*black*), ray tracing arrival times (*blue*) and parabolic equation pressure signature energy (*red*) are plotted as a function of a retarded time for various distances from the source in the West direction. The retarded time is referenced relatively to the ground sound speed (i.e. 340 m s^{-1}). The parabolic method computations are performed for the low frequency source signature model with 0.1 and 0.5 Hz central frequencies. The normalized energy is estimated within a time window of 3.5 s. Because of the periodicity of the parabolic equation method signature, energy of the tropospheric path appears as an artifact at 700 s

representation of Fig. 18.8. The first stratospheric path, noted I_{sI}, arrived 100 s later than a ground sound speed reference direct wave and the gap between each reflection of this path is of 100 s. Geometrical acoustics predicts smaller stratospheric path observation distance ranges than those predicted by the parabolic equation method at the source frequencies (around 0.1 Hz) or observed. For instance, whereas geometrical acoustic predicts first reflection stratospheric path I_{sI} between 200 and 300 km, parabolic equation method predicts energy for this path between less than 100 km and up to 1,000 km. Geometrical acoustics allows the identification of two thermospheric paths I_{ta} and I_{tb}, but parabolic equation method shows that the I_{tb} path is totally attenuated by atmospheric absorption. Various reflections of the thermospheric path I_{ta} are observed with an arrival time gap of approximatively 300 s. So, the representation of Fig. 18.8 seems to be a good way for the identification of arrival paths. Alpine station records one stratospheric path and one thermospheric path whereas Roosevelt station measures two stratospheric paths and one thermospheric path. Stations at long-range record mainly stratospheric paths and possibly a second reflection thermospheric path. Each measured arrival is clearly associated with a stratospheric reflection or a thermospheric one.

18.4.2 Diffraction and Scattering in Shadow Zones

In shadow zones, the geometrical acoustics and parabolic equation computation at 1 Hz do not predict arrivals where measurements are performed (see Fig. 18.6 and 18.8). These measurements are confirmed by parabolic equation computation at 0.1 Hz, which is the source frequency.

The first shadow zone is defined by the horizontally emitted ray and the cusp caustic which reaches the ground close to 240 km in the West direction (see Fig. 18.6). Three mechanisms can explain energy arrival in this shadow zone. (i) Creeping wave (Pierce 1994) are associated to the diffraction at the geometrical amplitude discontinuity located along the horizontally emitted ray. Creeping wave ground relative speed is the ground sound speed and these waves are associated to the direct wave noted I_w which is observed between the source and 100 km with a retarded arrival time of 0 s. (ii) Caustics are another kind of amplitude discontinuity predicted by geometrical acoustics (Pierce 1994). Diffraction at caustics can explain a shadow zone reduction of some kilometers where the cusp caustic reaches the ground. (iii) The most important mechanism of diffraction is the wave scattering by small atmospheric temperature and wind inhomogeneities. As presented before, these inhomogeneities are associated to internal gravity waves and they are included in our atmospheric model. Ostashev et al. (2005) and Kulichkov et al. (2007) show that scattering by a horizontally stratified turbulence can be interpreted as a partial reflection of acoustic waves by inhomogeneities. The arrival time of a partially reflected wave is quite in agreement with arrival times computed by the parabolic equation method and measured. This result is true for each stratospheric reflection but it is not observed for the thermospheric path (see Fig. 18.8). Ostashev

et al. (2005) show that the more the wave travel direction is horizontal, the more the wave is scattered. This explains why thermospheric paths are not partially reflected.

Diffraction occurs not only before the illuminated zone but also after, i.e., for the first stratospheric reflection I_{sl}, from 320 km up to more than 1,000 km (see Fig. 18.8). Diffraction in this zone is associated with creeping waves generated at the caustic which pass along the ground in the illuminated zone (see Fig. 18.6). This diffraction mechanism generates a closely vertical wave which propagates at the ground sound speed like a tropospheric wave. This wave is clearly observed on finite difference simulation (cf. Bailly and Bogey 2008). This wave is observed for all the stratospheric reflections and both at 0.1 and 0.5 Hz (see Fig. 18.8).

Moreover, diffraction is an important mechanism in the conversion between stratospheric path and thermospheric path. At low frequency (0.1 Hz, Fig. 18.8), we observe an arrival at a retarded time between 400 and 500 s at distances between 400 and 600 km. This arrival can been explained geometrically as a stratospheric refraction of the first thermospheric reflection (I_{tl}). This kind of path, which has often low amplitude, is rarely observed and is called diffracted path I_d. Other conversions exist at longer distance from the source but they cannot be distinguished using classical path arrival times.

18.4.3 Discussion

In this section, we have summed up various effects which affect the long-range propagation of infrasound. The main effect on the overpressure level is associated with the wind. The propagation is anisotropic because of the increase of refraction in the downwind direction and a decrease in the opposite direction. This effect is season-dependent on a dominant wind in the West direction in summer and an opposite wind in winter at the Misty Picture location (Le Pichon et al. 2005). The atmospheric absorption is responsible of the strong attenuation of thermospheric path I_{tb}. Density fluctuations affect the amplitude of the wave only if the source and the receiver are not at the same height. Refraction by the density gradient is very weak. The Earth curvature modified the arrival time of the first stratospheric path by 2.5 s and the arrival time of the first thermospheric path by 8.5 s relative to a flat ground propagation model. The Earth curvature has a weak effect on phase amplitudes. Finally, the source frequency is an important factor because of diffraction and scattering mechanisms. In the Misty Picture configuration, which is a standard atmosphere, no shadow zones are observed at frequencies lower than approximatively 0.5 Hz.

The Misty Picture event appears as a reference atmospheric infrasound propagation problem. All measured arrivals are identified both in geometrical zones and in shadow zones. Amplitudes of scattered and diffracted arrivals are, at low frequency, of the same level as geometrical arrivals. The path identification method is particularly efficient to stack ray tracing and parabolic equation methods results with

measurements (Fig. 18.8). Comparisons of measurements with simulations show that, up to a 4 kt yield ground explosion, which is the Misty Picture yield, linear models give arrival time path in agreement with measurements. However, nonlinear effects, scattering and atmospheric absorption have significant effects on the waveform signature evolution during the propagation.

18.5 Pressure Signature Analysis

In the previous section, we identified measured arrivals with acoustic wave paths and studied effects of various mechanisms on the global acoustic energy level. In this section, we investigate the waveform evolution from the source to the receiver and the effects of nonlinearities, atmospheric absorption and scattering on the pressure signature. We focus on Alpine, White River and Roosevelt stations and perform comparisons between measured signatures, parabolic equation method simulations and ray tracing method simulations.

18.5.1 Waveform Evolution During the Propagation

Phase identification at barometric station located between 200 and 400 km in the direction West of the source allows us to find: a stratospheric path I_{sI} and a thermospheric path I_{ta} at Alpine station, two stratospheric paths I_{sI} and I_{sII} and a thermospheric path I_{ta} at White River and Roosevelt stations. However, the ray tracing method predicts only stratospheric path waveform signatures at Alpine and White River and thermospheric path waveform signatures at White River and Roosevelt. Pressure signatures measured and computed using linear ray tracing, nonlinear ray tracing and parabolic equation for these three stations are plotted in Fig. 18.9 with the eigenrays between the source and stations. Simulations are performed using the atmospheric model of Sect. 18.3.2, the Reed's waveform signature for the ray tracing code and the low frequency waveform signature for the parabolic equation method (cf. Sect. 18.3.1). Parabolic equation method simulations are limited to low frequencies below 0.5 Hz (i.e. a sampling frequency of 1 Hz).

Arrival times are globally in agreement with measurements, ray tracing and parabolic equation methods except for modeled thermospheric paths which arrived approximatively 50 s before measurements. This difference is due to the atmospheric models which should underestimate effective celerity in the high atmosphere. Uncertainties on meteorological conditions can also explain the miss, on ray tracing and parabolic equation results, of the thermospheric arrival measured at Alpine 1,060 s after the explosion. Signature amplitudes are globally in good agreement except near caustics where the amplitude is overestimated with the ray tracing method. This is the case of the Alpine stratospheric path (I_{sI}). Ray tracing simulations overestimate the amplitude whereas the parabolic equation method amplitude

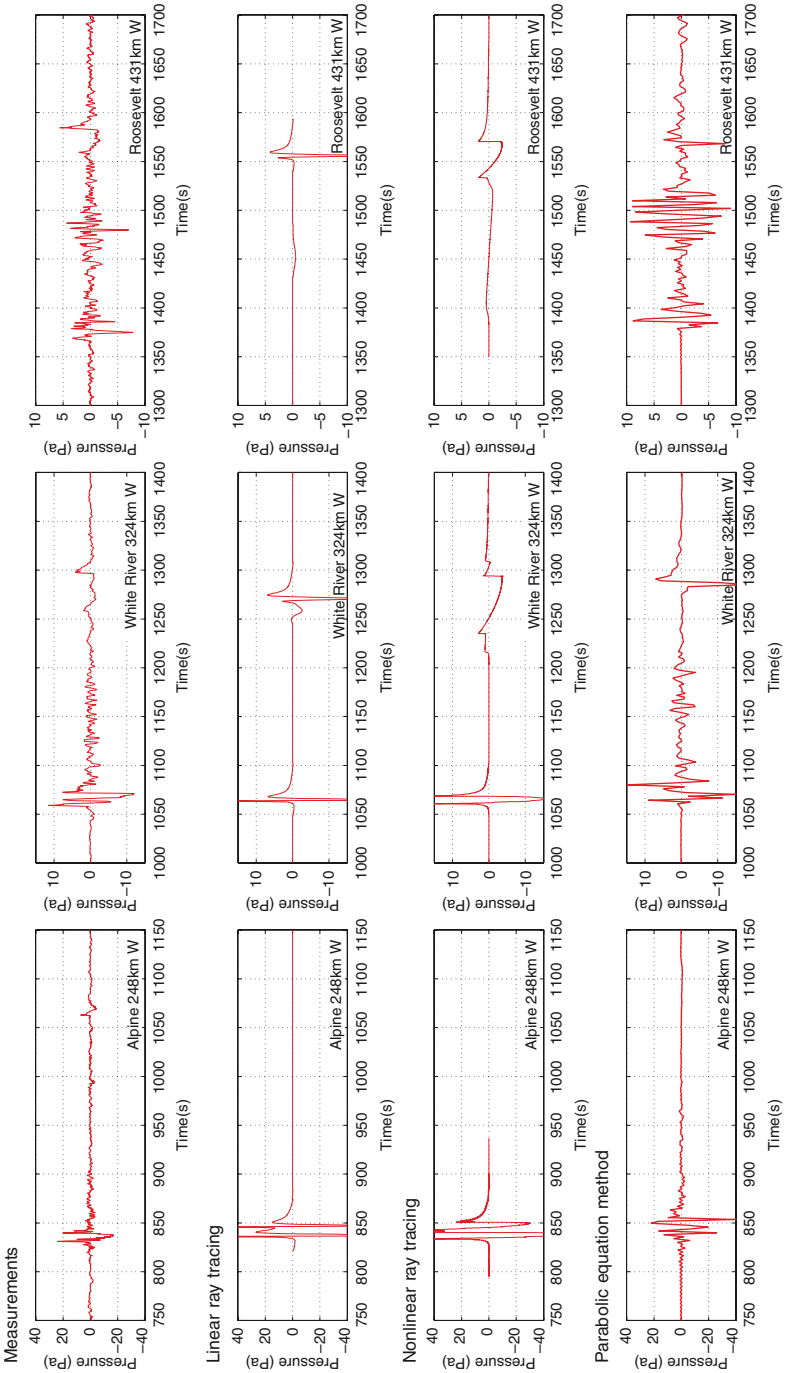

Fig. 18.9 Pressure signatures at Alpine, White River and Roosevelt stations. From the *top* to the *bottom*, the measured, linear ray tracing, nonlinear ray tracing and parabolic equation method pressure signatures are plotted

is realistic. Linear simulations overestimate the amplitude of thermospheric arrivals at White River and Roosevelt whereas nonlinear ray tracing agrees with the measurements. The nonlinear computation of the waveform allows the reconstitution of a "U" pressure signature at Alpine and White River for the stratospheric path and of a "N" at White River and Roosevelt for the thermospheric path. At the Alpine station, the ray tracing method finds two stratospheric paths with the same number of reflections and same arrival times. These two arrivals are linked with two effective sound speed local maxima within the effective celerity profiles. This double arrival is not observed on the parabolic equation simulation at Alpine nor on measurements. This difference is due to the high frequency approximation of the ray tracing method which implies a high sensitivity to sound speed variation which is not real for low frequency waves because of wave scattering.

The comparison of pressure signature amplitudes is difficult because of scattering effects and because of filtering effects both on measurements and on simulations. Measured and simulated pressure signature spectra allow a comparison of pressure signature energy level for each frequency. In Fig. 18.10, the spectral density of energy (DSE) is plotted for each infrasound arrival independently. For each arrival, the frequency range and amplitude are of the same order for simulations and measurements. Linear ray tracing DSE amplitude is higher than nonlinear ray tracing DSE amplitude and overestimates measured amplitude. For the stratospheric path (both top graphs of Fig. 18.10), parabolic equation results appear closer to the measurements than nonlinear ray tracing results at low frequency whereas at high frequency nonlinear ray tracing results are more realistic. For thermospheric paths (both bottom graphs of Fig. 18.10), the nonlinear results compare best with the measured spectrum particularly for the White River thermospheric path.

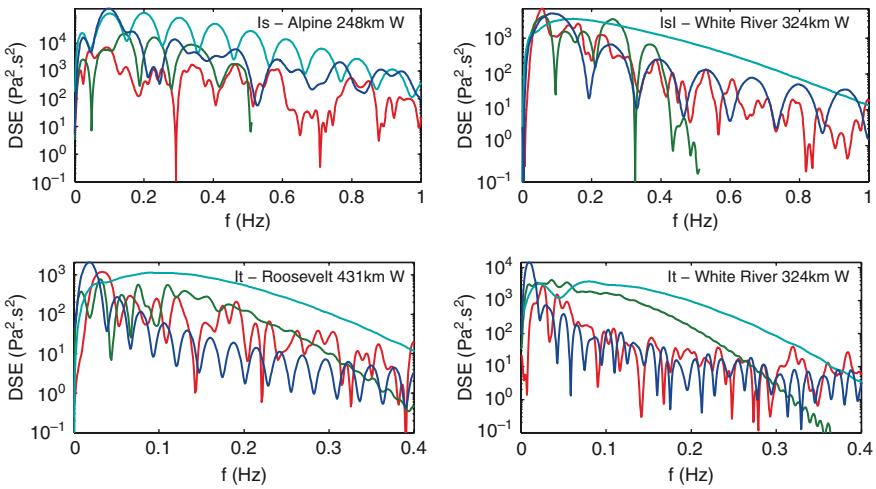

Fig. 18.10 Spectrum of measured arrivals (– *red*), nonlinear ray tracing simulation (– *blue*), linear ray tracing (– *turquoise*) and parabolic equation method simulation (– *green*) at Alpine, White River and Roosevelt stations. Spectra deduced from parabolic equation simulations are truncated at 0.5Hz

18.5.2 Nonlinearity and Atmospheric Absorption

For the global acoustic pressure level, atmospheric absorption is an important phenomenon whereas nonlinear effects are not significant. For the waveform signature, both of these competitive mechanisms are important. The effects of these two phenomenon are observed experimentally for the Misty Picture event. Because of atmospheric absorption, only low frequencies propagate at long range. Barometric stations record signal only between 0 and 0.5 Hz whereas the source pressure signature spectrum is composed of high frequencies too. Nonlinear effects are observed on stratospheric arrivals with the "U" signature shape and on thermospheric arrivals with the "N" shape.

In this subsection, we evaluate nonlinear and atmospheric absorption effects on the pressure signature evolution along ray paths for the Misty Picture event. The shock formation time t_{shock} quantifies nonlinearity effects relative to the propagation distance. The Gol'dberg number G (Rogers and Gardner 1980) quantifies nonlinearity effects relative to linear dissipative effects for a given pressure signature. These numbers are defined from Burgers' equation as

$$t_{\text{shock}} = \frac{\rho_0 c_0^2}{\beta f_w p_w} \quad \text{and} \quad G = \frac{\beta p_{\text{w}}}{\delta \rho_0 f_{\text{w}}},$$

where β is the nonlinear coefficient (Pierce 1994), δ is the absorption coefficient (Pierce 1994), c_0 is the sound speed, ρ_0 is the density, p_{w} is the wave amplitude and f_{w} is the wave central frequency. These two numbers are evaluated for the Misty Picture event along eigenrays which arrived at Alpine, White River and Roosevelt stations. Pressure signatures computed along these rays by solving generalized Burgers' equation are used to evaluate the central frequency f_{w} and the amplitude p_{w}. The shock formation time and the Gol'dberg number are plotted in Fig. 18.11.

The shock formation time mainly increases during the propagation whereas the Gol'dberg number decreases. This is associated to the increase of the pressure signature duration and the decrease of its amplitude. The shock formation time evolves quickly close to the source from 0 to 100 s and after 10 km of propagation it stays between 100 and 1,000 s except near caustics where it decreases to 0 because of caustic signature amplitude singularity. The Gol'dberg number evolves symmetrically with a singularity close to caustics and to the source.

As presented in Fig. 18.11, the shock formation time is of the order of 100 s i.e. a distance of 30 km. With only nonlinear mechanisms, after a propagation time of 100 s, the pressure signature evolves as a "N" wave, independently of the waveform source shape. As for the sonic boom propagation (Plotkin 2002), nonlinearities are weak and it is a cumulative process efficient at long range. The propagation time to the barometric station (~1,000 s) is 10 times the shock formation time. Then, pressure signatures at the station, in absence of competitive processes, are close to an "N" wave.

The Gol'dberg number is greater than approximatively 17 (cf. Fig. 18.11), which means that nonlinearities are dominant relatively to linear absorption mechanisms.

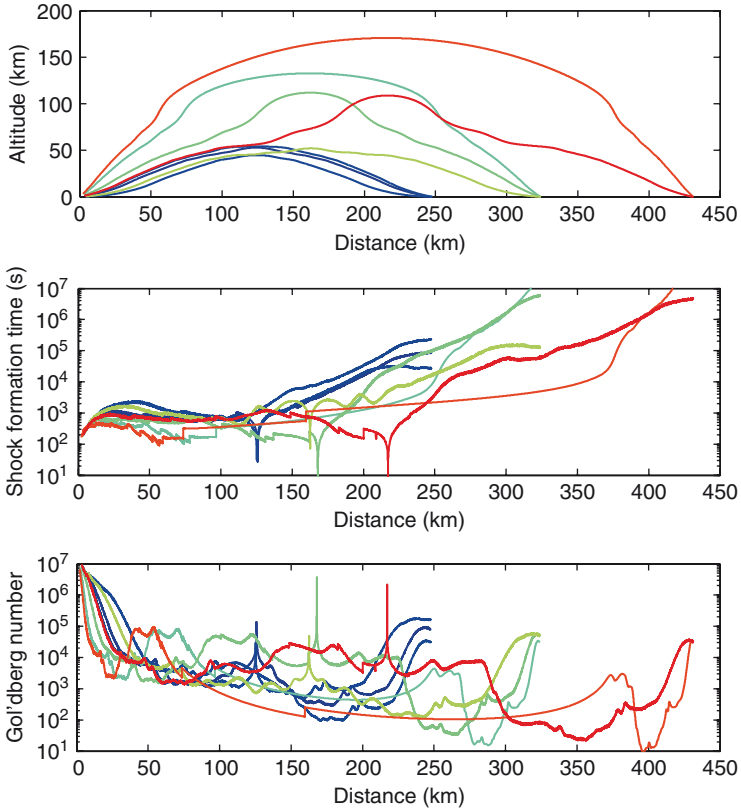

Fig. 18.11 Nonlinear effects for the Misty Picture event. From *top* to *bottom*, ray paths, the shock formation time and the Gol'dberg number are plotted for Alpine, White River and Roosevelt station eigenrays

This Gol'dberg number limit is obtained by Rogers and Gardner (1980) by equalizing nonlinear absorption with linear viscosity and molecular relaxation absorption mechanisms. This number can be found numerically by a parametric study of Burgers' equation. The pressure signature at receiver is mainly dependent on nonlinearities, but absorption mechanisms are important to study the shock rise time or for lower amplitude sources. When, in an application, the Gol'dberg number is a priori unknown, full generalized Burgers' equation should be solved.

18.5.3 Discussion

We observe that both nonlinearity and scattering have influence on the waveform evolution and that nonlinearity is more important for the thermospheric path. Nonlinearities allow to find the 'N' and the 'U' waveforms measured for respectively

thermospheric and stratospheric paths. Nonlinearity is a weak mechanism which dominates linear absorption effects during the propagation for an event of the Misty Picture energy class. Scattering influences the pressure signature especially for the stratospheric path and its energy level as well. In spite of these qualitative results, comparisons between simulations and measurements remain difficult because of uncertainties on meteorological conditions of propagation.

18.6 Conclusion

The Misty Picture experiment is a unique opportunity for the interpretation of the infrasound propagation from High Explosive sources. This infrasonic event is one of the most instrumented with records close to the source and at long range. Most of the 23 barometric records are of good quality with a good signal-to-noise ratio. Numerous documentations of the event supply accurate descriptions of the source, of the atmosphere and of barometric recorded signatures. Our study is focused on high explosive events of approximatively 4 kt yield which enable us to investigate the propagation of 0.1 Hz central frequency infrasound.

The Misty Picture event allows us both to study the geometric long-range propagation of infrasound and to study the waveform signature generated by high explosive events. We identify infrasonic arrivals and match them with geometrical phases or diffracted phases. For each phase, arrival times, apparent velocity, duration and amplitude are in agreement between measurement and simulation. The study shows the importance of scattering in shadow zones for stratospheric phases. This is the main mechanism of wave diffraction in shadow zones and its effects are important at low frequencies (0.1 Hz). This mechanism explains that stratospheric phases are observed on a zone larger than the geometrical zone. All the stratospheric phases are observed numerically and experimentally up to 1,000 km with frequencies in the range 0.01–0.5 Hz. This result should be used in the interpretation of barometric station records. On the other hand, thermospheric paths are only observed in the geometrical zone and can be completely described using a ray tracing model. Linear acoustic appears efficient to model the propagation path of infrasound emitted by high explosions up to, at least, 4 kt yield.

However, nonlinear mechanisms are quite important to model the waveform signature evolution of infrasound. The “N” and the “U” measured waveform shape of thermospheric and stratospheric paths respectively are associated with nonlinear mechanisms. Nonlinearities are weak but the development of nonlinear models is necessary in order to characterize the source energy from station measurements.

The study of the Misty Picture event shows that the modeling of infrasound propagation at long range should take into account thermal atmospheric structure, the wind, the atmospheric absorption and scattering to explain arrival type and arrival time. The model should also include weak nonlinear mechanisms to model the waveform signature. However, ray tracing validity is limited because of diffraction mechanisms whereas the linear parabolic equation is limited because of

nonlinearities. The complementarity of these methods is useful to investigate the propagation of infrasound. The development of a nonlinear propagation method which includes all physical effects is an unsolved problem. Such a model is necessary for a full analysis of the propagation of infrasound. The modeling of the propagation of infrasound is also highly dependent upon the knowledge of the atmosphere, at small and global scales. To improve atmospheric models, infrasound networks can be used for atmospheric remote sensing.

Acknowledgments The authors show their gratitude to Abraham R. Jacobson which allowed Blanc et al. to perform barometric and ionospheric measurements of the Misty Picture event. Our gratitude comes to R.W. Whitaker for the profitable conversations during the preparation and the realization of measurements.

References

Aver'yanov MV, Khokhlova VA, Sapozhnikov OA, Blanc-Benon P, Cleveland RO (2006) Parabolic equation for nonlinear acoustic wave propagation in inhomogeneous moving media. Acoust Phys 52(6): 623–632

Bailly C, Bogey C (2008) Direct computation of infrasound propagation in inhomogeneous atmosphere using a low-dispersion and low-dissipation algorithm. In: Proceeding of the 10th ICFD conference on numerical methods for fluid dynamics

Blanc E (1988) Mesures ionosphériques et microbarographiques – Expérience Misty Picture. Technical Report 370/88, CEA, Sept. 1988

Blanc-Benon P, Lipkens B, Dallois L, Hamilton MF, Blackstock DT (2002) Propagation of finite amplitude sound through turbulence: modeling with geometrical acoustics and parabolic approximation. J Acoust Soc Am 111(1): 487–497

Candel SM (1977) Numerical solution of conservation equations arising in linear wave theory: application to aeroacoustics. J Fluid Mech 83(3): 465–493

Ceranna L, Le Pichon A, Green DN, and Mialle P (2009) The Buncefield explosion: a benchmark for infrasound analysis across central europe. Geophys J Int 177(2): 491–508

Christie DR, Campus P (2010) The IMS infrasound network: design and establishment of infrasound stations. This volume, pp. 27–72

Cleveland RO, Hamilton MF, and Blackstock DT (1996) Time-domain modeling of finite-amplitude sound in relaxing fluids. J Acoust Soc Am 99(6): 3312–3318

Coulouvrat F (2008) Parabolic approximation in ray coordinates for high-frequency nonlinear waves in a inhomogeneous and high speed moving fluid. Wave Motion 45(6): 804–820

Dallois L, Blanc-Benon P, and Juve D (2001) A wide-angle parabolic equation for acoustic waves in inhomogeneous moving media: applications to atmospheric sound propagation. J Comput Acoust 9(2): 477–494

Del Pino S, Després B, Havé P, Jourdren H, and Piserchia P (2009) 3D finite volume simulation of acoustic waves in the Earth atmosphere. Comput Fluids 38, 765777.

Drob DP, Picone JM, and Garcés M (2003) Global morphology of infrasound propagation. J Geophys Res 108(D21): 4680

Drobzheva Y, and Krasnov V (1999) The model of acoustic disturbances in atmosphere and ionosphere for Mill Race explosion. Phys Chem Earth (c) 24(8): 963–967

Drobzheva Y, Krasnov V (2003) The acoustic field in the atmosphere and ionosphere caused by a point explosion on the ground. J Atmos Solar-Terr Phys 65, 369–377

Evers L, Haak H (2007) Infrasonic forerunners: exceptionally fast acoustic phases. Geophys Res Lett 34, L10806

Evers LG, Haak HW (2010) The characteristics of infrasound, its propagation and some early history. This volume, pp. 3–26

Gainville O, Piserchia PF, Blanc-Benon P, and Scott J, (2006) Ray tracing for long range atmospheric propagation of infrasound. In 12th AIAA/CEAS aeroacoustics conference, Cambridge, MA, 8–10th May 2006, in AIAA Paper No. 2006–2451

Gainville O (2008) Modélisation de la propagation atmosphérique des ondes infrasonores par une méthode de tracé de rayons non linéaire. PhD thesis, Ecole Centrale Lyon, No. 2008-07

Green DN, Le Pichon A, Ceranna L, Evers L (2010) Ground truth events: assessing the capability of infrasound networks using high resolution data analyses. This volume, pp. 593–622

Hedin AE (1991) Extension of the MSIS thermospheric model into the middle and lower atmosphere. J Geophys Res 96, 1159

Hedin AE, Fleming EL, Manson AH, Schmidlin FJ, Avery SK, Clark RR, Franke SJ, Frasera GJ, Tsuda T, Vial F, and Vincent RA (1996) Empirical wind model for the upper, middle and lower atmosphere. J Atmos Terr Phys 58, 1421–1447

Jones RM, Riley JP, and Georges TM (1986) Harpa: A versatile three-dimensional Hamiltonian ray-tracing program for acoustic waves in the atmosphere above irregular terrain. Technical Report, National Oceanic and Atmospheric Administration, Boulder, CO

Kinney GF, Graham KJ (1985) Explosive shocks in air. Springer, New York, Tokyo

Koper KD, Wallace TC, Reinke RE, and Leverette JA (2002) Empirical scaling laws for truck bomb explosions based on seismic and acoustic data. Seismol Soc Am 92(2): 527–542

Korobeinikov VP (1985) Problems of point-blast theory. American Institute of Physics, New York 1985

Kulichkov SN (2004) Long-range propagation and scattering of low-frequency sound pulses in the middle atmosphere. Meteorol Atmos Phys 85, 47–60

Kulichkov SN, Avilov KV, Bush GA, Popov OE, Raspopov OM, Baryshnikov AK, ReVelle DO, and Whitaker RW (2004) On anomalously fast infrasonic arrivals at long distances from surface explosions. Izv, Atmos Ocean Phys 40(1): 1–9

Kulichkov S, Chunchuzov I, Perepelkin V, Svertilov A, and Baryshnikov A (2007) On the influence of anisotropic turbulence on fluctuations in the azimuths and grazing angles of acoustic signals in the lower and middle atmosphere. InfraMatics (The newsletter of Subaudible sound) 18, 1–5

Le Pichon A, Blanc E, Drob D, Lambotte S, Dessa J-X, Lardy M, Bani P, Vergniolle S (2005) Infrasound monitoring of volcanoes to probe high-altitude winds. J Geophys Res 110, D13106

Lehr LD (1987) Misty Picture event – test execution report. Technical Report ADA283521, Defence Nuclear Agency, Washington, November 1987

Lingevitch JF, Collins MD, Dacol DK, Drob DP, Rogers JCW, and Siegmann WL (2002) A wide angle and high mach number parabolic equation. J Acoust Soc Am 111(2): 729–734

Marsden O, Vayno L, Boger C, and Bailly C (2008) Study of long-range infrasound propagation with high-performance numerical schemes applied to the Euler equations. In: 13th long range sound propagation symposium, Lyon, France, 16–17 Oct 2008

McKisic JM (1997) Infrasound and the infrasonic monitoring of atmospheric nuclear explosions: a literature review. Final Report PL-TR-97-2123, Department of Energy and Phillips Laboratory

Mutschlecner JP, Whitaker RW, and Auer LH (1999) An empirical study of infrasonic propagation. Technical Report, Los Alamos National Laboratory, Los Alamos, NM (US)

Norris DE (2006) Recent advances in prediction infrasound using the time-domain parabolic equation (TDPE) model. In: 12th long range sound propagation symposium, New Orleans, USA, 25–26 Oct, 2006, CD-Rom

Ostashev VE, Chunchuzov IP, and Wilson DK (2005) Sound propagation through and scattering by internal gravity waves in a stably stratified atmosphere. J Acoust Soc Am 118(6): 3420–3429

Peyret C (1995) Propagation des ondes de choc dans l'atmosphère. PhD thesis, Universit Paris VI, Paris, Juin

Pierce AD (1967) Guided infrasonic modes in a temperature and wind stratified atmosphere. J Acoust Soc Am 41, 597–611

Pierce AD (1994) Acoustics: an introduction to its physical principles and applications. Acoustical Society of America, New York

Plotkin KJ (2002) State of the art of sonic boom modeling. J Acoust Soc Am 111(1): 530–536

Rascalou B (1989) Étude détaillée des mesures microbarographiques – Expérience Misty Picture. Technical Report 24/89/Et, CEA, Bruyères-le-Châtel, Nov. 1989

Reed JW (1977) Atmospheric attenuation of explosion waves. J Acoust Soc Am 61(1): 39–47

Reed JW, Church HW, and Huck TW (1987) Misty Picture weather-watch and microbarograph project: experiments 9412-14-18. Sand–87-2978c, Sandia National Laboratories

ReVelle DO, Whitaker RW (1996) Lamb waves from airborne explosion sources: Viscous effects and comparisons to ducted acoustic arrivals. In: 7th international long-range sound propagation symposium (July 1996), Ed. Juvé D, Bass HE and Attenborough K, École Centrale Lyon, Ecully, France, pp 323–337

Rogers PH, Gardner JH (1980) Propagation of sonic booms in the thermosphere. J Acoust Soc Am 67(1): 78–91

Sutherland LC, and Bass HE (2004) Atmospheric absorption in the atmosphere up to 160 km. J Acoust Soc Am 115(3): 1012–1032

Whitaker RW, Mutschlecner JP, Davidson MB, and Noel SD (1990) Infrasonic observations of large-scale HE events. In: 14th long range sound propagation symposium, Virginia, USA, 16–17 May 1990, pp 133–141

Whitham GB (1974) Linear and nonlinear waves. Interscience series of texts, monographs and tracts. Wiley, Hoboken, NJ, USA

Wilson DK, Liu L (2004) Finite-difference, time-domain simulation of sound propagation in a dynamic atmosphere. Technical Report ERDC/CRREL TR-04-12, US Army Corps of Engineers, May 2004

Chapter 19
Ground Truth Events: Assessing the Capability of Infrasound Networks Using High Resolution Data Analyses

David N. Green, Alexis Le Pichon, Lars Ceranna, and Läslo Evers

19.1 Infrasound and Ground Truth

The purpose of building and maintaining an infrasound network is to be able to detect, identify, and locate low-frequency atmospheric pressure disturbances. In order to assess the capability of such a network, and to recognise potential weaknesses, the system must be tested using signals from well understood sources. Events which generate such signals are referred to as ground truth and are defined as being events for which the source location, origin time and acoustic generation mechanism are known through independent means. In ideal circumstances, a measure of the source magnitude should also be ascertained, and parameters influencing the acoustic radiation pattern such as local terrain and ground cover should be identified. Similar to seismic ground truth parameters (e.g., Bondar et al. 2004a), the infrasound ground truth parameters are associated with only the source. Meteorological parameters which influence the propagation of the acoustic waves (e.g., temperature and wind) are not considered ground truth, and it is often the accuracy of these atmospheric parameters that we wish to test using signals from ground truth events.

A successful infrasound analysis will take recordings from one or more microbarograph arrays and process the data to provide estimates of the signal arrival time, horizontal trace velocity, back-azimuth, amplitude, and spectra. These parameters, used in conjunction with state of the art modelling techniques and atmospheric specifications are subsequently used to provide estimates of the source location, origin time and some measure of the acoustic magnitude. In infrasound studies, the acoustic magnitude is most often described in terms of equivalent explosive yield, measured in kilotonnes (kt) of TNT; we adopt this measure in this chapter. Each of these estimates relies in some manner on accurate predictions of the propagation path the infrasonic waves take through the atmosphere. The location estimate, if based on back-azimuth intersections, is sensitive to the along-path azimuth

D.N. Green (✉)
AWE Blacknest, Brimpton, Reading
RG7 4RS, United Kingdom
e-mail: dgreen@blacknest.gov.uk

A. Le Pichon et al. (eds.), *Infrasound Monitoring for Atmospheric Studies*,
DOI 10.1007/978-1-4020-9508-5_19, © Springer Science+Business Media B.V. 2010

deviations, whereas the magnitude, or yield, calculations rely on accurate specification of the along-path wind speeds in the stratosphere to correct for propagation effects. Testing the accuracy and repeatability of these calculations requires ground truth data, which constrain the source information such that the differences between the true and predicted atmospheric propagation paths may be found. Ground truth data can be used in two ways: as the initial conditions for forward modelling where the acoustic propagation is simulated and the results compared to the data, or as the observed parameters against which the results of inversion techniques can be compared. An example of forward modelling is the identification of the different phases (tropospheric, stratospheric, or thermospheric) present in an infrasonic wavetrain, and an example of an inversion technique is the estimation of the source location parameters.

Interest in infrasound has grown over the last decade in response to the design and deployment of a network of microbarograph arrays in support of verifying the Comprehensive Nuclear-Test-Ban Treaty (CTBT), which is described in Christie and Campus 2010 Chapter 2. This provides a key motivation for understanding more about the details of infrasound propagation; we wish to know how best to exploit the infrasound data for CTBT verification. Other motivations for studying infrasound, for example, characterising volcanic eruptions and the implications for aviation safety (Garces et al. 2008) or understanding upper atmospheric dynamics (Le Pichon et al. 2005) also require tested, reliable atmospheric velocity models.

The major challenge for infrasound modelling is contending with the continuously changing atmospheric velocity structure, with the consequence that two events whose locations are the same, but have different origin times, sample different propagation paths. This makes the assessment of the velocity specifications quite unlike that from research areas, such as seismology, where time-independent velocity structure allows the combination of velocity estimates from time separated events; these can constrain an absolute velocity model which is refined as more data become available. In infrasound studies, although the propagation characteristics from each event are unique, the time-dependent velocity models can be constrained by independent meteorological parameters which are already collected for purposes including weather forecasting, climate modelling and aircraft travel. One consequence of this is that it is difficult to attribute a set uncertainty to each model; instead, we learn about the limitations of our models through testing against ground truth events. As the number of ground truth events in our databases increases, we can begin to describe these limitations within a statistical framework. Therefore, the gathering and careful archiving of ground truth data are essential for future reassessments of infrasound analysis capabilities.

In this chapter, we review the methods which are employed to gather ground truth information and the rapidly expanding literature regarding such events. We show how the emphasis of ground truth studies has changed over time and provide examples of the information that have been acquired from these analyses. To illustrate these points, and to highlight the improvements in resolution that can be made using networks of arrays, we provide a case study from a large chemical explosion that occurred at the Buncefield oil depot, UK.

19.2 Ground Truth Data–A Historical Perspective

The nature of ground truth studies has changed over time, in response to the scientific problems that are deemed most relevant during different periods. During the 1940s and 1950s, the focus was on identifying the modes of propagation from the observed multiple arrivals and understanding the atmospheric velocity structure (e.g., Cox 1947; Richardson and Kennedy 1952). As the 1950s continued, atmospheric nuclear tests became the most prevalent localised infrasonic sources and the focus of study switched to understanding the very low-frequency acoustic-gravity waves generated by megaton-yield explosions (e.g., Press and Harkrider 1962). Once the propagation modes had been established, further research effort went into relating pressure amplitudes to the explosive yield (Posey and Pierce 1971; Flores and Vega 1975).

After the cessation of atmospheric nuclear testing, initiated by the signing of the Partial Test Ban Treaty by the USSR, USA and UK in 1963, the number of infrasound studies decreased in response to dwindling interest in infrasonic monitoring. Ground truth events were limited to those either recorded as part of military chemical explosive tests (e.g., Al'Perovich et al. 1985; Whitaker et al. 1990), industrial accidents (e.g., Grover 1974) or from large natural events, such as the eruption of Mount St. Helens in 1980 (Donn and Balachandran 1981).

Interest in infrasound was rekindled during the negotiations for a CTBT in the mid-1990s. It was decided that a network of microbarograph arrays would be necessary, within the framework of an International Monitoring System (IMS), to support radionuclide detection in verifying that no clandestine atmospheric nuclear tests had occurred. Here, the focus is different again: rather than the very large events studied previously, explosions with yields in the sub-kiloton to a few kilotons range are of interest. For a CTBT to be successful, it would be necessary for effective verification technologies (seismic, infrasound, hydroacoustic and radionuclide detection) to identify and locate any events of interest. Therefore, infrasound studies in the past decade have concentrated on smaller explosions, which the infrasound network of the IMS has been designed to detect; these studies have improved event detection methods alongside location and yield estimation techniques (Whitaker et al. 2003; Evers et al. 2007; Ceranna et al. 2009). The global atmospheric coverage has increased as the IMS network has been constructed, ensuring that the number of ground truth events detected has steadily increased over the last ten years (Fig. 19.1).

In addition, as the events of interest have become smaller, the dominant signal frequencies of interest have increased. This has meant that more detailed atmospheric parameterisations are required to facilitate accurate propagation analyses. The atmospheric specifications are generated from well validated atmospheric models; however, as Drob et al. (2003) makes clear, the ultimate test of the applicability of these specifications to infrasound analyses is how well they predict arrivals recorded over microbarograph networks. The knowledge of how accurately

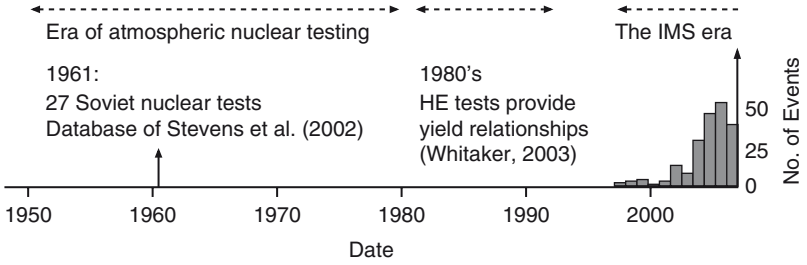

Fig. 19.1 A timeline showing the major changes in focus for infrasound research over the last 50 years. Between 1945 and 1963 the U.S. conducted 212 atmospheric nuclear tests compared with 216 conducted by the USSR (Mikhailov 1999). Consequently, between the 1960s and late 1970s, much of the work was driven by attempting to understand the signals from atmospheric nuclear tests of large yield (100s kt). In the 1980s, infrasound research slowed, although the Los Alamos group worked on eight high explosive (HE) tests between 1981 and 1993 to determine the pressure vs. yield relationships. Since the late 1990s, infrasound research has been buoyed by the advent of the International Monitoring System (IMS) network, with the number of ground truth events within the Space and Missile Defence Command (SMDC) database steadily increasing with the increased number of stations

the acoustic propagation models simulate the infrasound arrivals from unknown events is a crucial issue for CTBT era infrasound monitoring.

Because of the sparse global coverage of microbarograph arrays, many events are recorded at only one station. Indeed, 88% of the U.S. Space and Missile Defence Command (SMDC) infrasound database consists of events recorded by one array. Although these single-station events are undoubtably useful, as they provide single propagation paths for atmospheric specification validation, they do not allow the breadth of analysis of a multi-station recording. For example, multi-station recordings allow location estimates to be made and yield estimation uncertainty for the event to be assessed. Both location and yield parameters are important, especially in the context of CTBT verification.

In some areas of the globe, notably central Europe and western USA, networks with higher density than the proposed 60 station IMS network (Christie and Campus 2010) have been achieved. In central Europe, ten arrays are currently operational, with a mean spacing between nearest neighbour stations of approximately 280 km, compared with 2,000 km for the proposed IMS network. Observations from this network have been combined to provide evidence of highly active infrasound source regions (Le Pichon et al. 2008), with a number of ground truth events recorded across multiple stations (e.g., Evers and Haak 2007; Ceranna et al. 2009).

Another advantage of having recordings over a dense network is understanding why signals were not recorded at a particular station, rather than just understanding the signals recorded. By having the higher station density, the zones of infrasound ground returns become more well defined. Well constrained ground truth events, ideally recorded over multiple stations, will play a major role in constraining the

effects that uncertainties in the atmospheric velocity structure have on the estimation of source parameters from infrasound analyses.

19.3 Process of Obtaining Ground Truth

As progress in data analyses is made, and the focus of investigations changes, it is important to be able to test new ideas or search for evidence within the old data. Therefore, it becomes essential to carefully archive the event information and pressure waveforms to enable such analyses. This has been done successfully for the high explosive (HE) tests conducted at White Sands Missile Range from which infrasound was recorded by researchers at Los Alamos National Laboratory (LANL), U.S.; as more data have become available, refinements have been made to the pressure vs. yield relationships (e.g., Whitaker et al. 1990, 2003). Other analysts have conducted careful research into past events in order to generate ground truth databases. For example, Stevens et al. (2002) compiled records from twenty-seven Soviet nuclear tests and compared the results with a variety of yield estimation formulae.

At present, the U.S. SMDC maintains a well designed infrasound event catalogue and waveform database,[1] of which many events can be considered ground truth (e.g., O'Brien et al. 2006). Choosing which events should be classified as ground truth depends upon the accuracy with which the source location and origin time are known. Here, we restrict ground truth to be events whose source was stationary. Therefore, from the variety of phenomena listed in the infrasound database, only mine blasts, volcanic eruptions, chemical explosions and gas pipeline explosions can be considered ground truth events (Fig. 19.2). Bolides, landslides and rocket launches and re-entries all have moving sources and are not considered to be ground truth. The source locations of earthquake generated infrasound signals are also difficult to define. Mutschlecner and Whitaker (2005) give a comprehensive overview of signals from 31 earthquakes; for earthquakes with local magnitudes less than 7.0 the strongest stratospheric arrivals are aligned with the epicentre to within three degrees. These signals also have travel-times consistent with propagation from the earthquake epicentral region. However, many secondary infrasonic arrivals generated by earthquakes can be associated with the interaction of seismic surface waves with pronounced topography up to hundreds of kilometres from the epicentre (Le Pichon et al. 2003; Mutschlecner and Whitaker 2005). These secondary arrivals complicate the infrasonic wavetrain such that it can be extremely difficult to decipher which signals can be associated with ground truth information from the epicentral region. Therefore, although some very well constrained earthquake generated signals may be useful for ground truth analyses, we do not consider earthquake sources to be suitable as ground truth events.

[1] www.rdss.info, operational at time of writing.

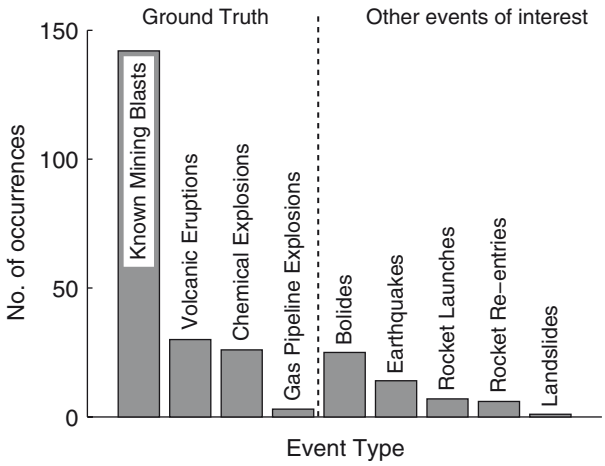

Fig. 19.2 A histogram showing the numbers of events within the SMDC infrasound database which have at least one recording station listed within the bulletin entry. The events span the time period between February 1997 and July 2007. Ground truth events are defined to be those for which the source is stationary

The parameters required for ground truth metadata are the source location and origin time. Explosive yield data are also useful, although it is difficult to determine and therefore only available in a few cases. For controlled explosions, gathering ground truth data is a trivial matter; the source location is known to an arbitrary accuracy, the origin time can be accurately measured from the detonation timings, and the yields are predetermined. For accidental explosions, or for explosions controlled by a party not associated with the infrasound network, the gathering of ground truth metadata can be a painstaking and time consuming process. If the infrasound was generated near ground level, some energy may couple into the ground generating seismic waves allowing the origin time to be estimated. Often these origin time estimates are accurate to within two seconds. For the majority of mining blasts reported in the SMDC database, the seismic arrival method is used to provide the origin times; however, when these are unavailable, the reports of the mine management must be relied upon, which can be of variable quality. The estimate of the location is more problematic. Most well-constrained seismic location estimates, if available, are accurate to within a few tens of kilometres (e.g., Bondar et al. 2004b), which can be up to 20% of the infrasonic path length for a one bounce stratospheric arrival. This uncertainty is unacceptably large for ground truth events which are to be used in model validation. This problem leads to the question: what is the sufficient accuracy for ground truth data? Often the shortest path lengths for recorded stratospheric arrivals are between 100 and 200 km, depending upon atmospheric conditions. Therefore, accepting a location accuracy of two kilometres or better would ensure that the error was less than 2% of the shortest path length, without excluding large numbers of events for which locations within a few metres are not known.

Because of the problems of constraining the source location seismically, finding the location often becomes detective work. News reports give clues regarding the location, and satellite imagery available via the internet allows closer inspection of proposed source locations. Often, if the explosion is an industrial accident occurring at a factory, this is relatively straightforward to locate on a map. More novel techniques are sometimes required when the source is less obvious. Bowman et al. (2007) described a case of using a combination of newspaper pictures and satellite imagery to constrain the location of a gas pipeline explosion close to St. Petersburg. Using such techniques, it is often possible to reduce the location uncertainties to within a few hundred metres.

19.4 Ground Truth Examples

Ground truth events have been an integral part of infrasonic studies since the early attempts to explain long-distance propagation of sound through the atmosphere. For example, early work by Cox (1947) utilised chemical explosions to explore the detectability of "abnormal" sound, which we now accept as refracted infrasound, at a series of ranges from the source. Furthermore, in April 1947 when British engineers destroyed the fortifications on the island of Helgoland using approximately 5,000 tons of TNT, ten microbarographs were sited across Germany and northern Italy to record the airwaves (Cox 1949; Cox et al. 1949). The recordings, which included direct airwaves and refractions from both the stratosphere and thermosphere allowed the researchers to make an attempt at estimating the upper atmospheric temperature structure, which was poorly constrained at the time.

Although instrumentation and knowledge of the atmospheric velocity structure are much improved since the mid-twentieth century, ground truth studies are still concerned with mapping out the acoustic propagation paths through the atmosphere. With increased knowledge of the general structure, research has been able to focus on the fluctuations from the mean state of the atmosphere. Russian researchers have been particularly active in this pursuit, with experiments involving repeated explosions designed to probe changes in stratospheric wind structure over periods of minutes and hours. For example, Kulichkov and Bush (2001) provide examples of stratospheric arrival amplitude changes of a factor of two occurring over a 20 min period, and the occurrence and disappearance of distinct arrivals over an hour and a half. Kulichkov (2004) suggests that one mode of variability that may explain these fluctuations are internal gravity waves which, through movement of air masses, can change the stratospheric acoustic velocity structure over timescales on the order of those observed (Kulichkov 2010). Detailed studies such as these have prompted researchers to include the variability, in the form of velocity perturbations, within their models (e.g., Norris et al. 2006).

In addition, with the accumulation of data from ground truth events, it has been possible to identify a wider range of propagation paths. For example, weak infrasonic returns from the stratosphere that arrive earlier than propagation models

predict have been recorded when stratospheric winds are high (Kulichkov et al. 2004; Evers and Haak 2007). These have been attributed to headwave-like propagation along the effective velocity maximum in the stratosphere. Another example is the recording of strong, pulsed stratospheric returns within the geometric shadow zone predicted by ray theory. Kulichkov et al. (2002) provide a number of examples and suggest that they are the result of partial reflection of acoustic pulses from coherent, locally-stratified inhomogeneities of the acoustic refractive index. It is suggested that these are a consequence of layers of rapidly changing wind direction which generate vertical gradients in the horizontal wind speed of over 50 m/s/km. Only with accurate knowledge of the source location and origin time can we compare predicted and actual travel-times, allowing the atmospheric propagation paths to be identified.

Although many ground truth studies have shown the effects of the stratospheric winds on the arrival times (e.g., Evers et al. 2007; Ceranna et al. 2009), very few studies are extended enough to show the seasonal variations that occur in signal detectability and propagation path. One superb example is given by Antier et al. (2007), who utilise continuous recordings of the highly repetitive volcanic explosions at Yasur volcano on the Vanuatu archipelago. Recordings from a near-vent microbarograph provide the ground truth information, and recordings of the stratospheric recordings at a range of 399 km on the New Caledonia IMS infrasound array (IS22) clearly show repeated seasonal variations over a three year period.

In addition to identifying the atmospheric propagation paths and understanding their variability, a key use of infrasound measurements, especially in terms of verifying the Comprehensive Test Ban Treaty, is to locate atmospheric events and estimate their yield. There are very few examples within the literature in which well-constrained ground truth events have been located using only infrasound data. This may be a consequence of many factors, including the sparse nature of regional infrasound networks leading to few detections per event, and the influence of stratospheric winds which can reduce the azimuthal coverage of recorded signals. For example, only 12% of the ground truth events archived within the SMDC database are recorded at two or more stations.

Two examples of multi-airwave location are given by Evers et al. (2007) for a gas pipeline explosion in Belgium, and by Ceranna et al. (2009) for the Buncefield oil depot explosion, which is detailed in Sect. 19.6. The example given by Evers et al. (2007) shows the importance of accounting for the specific propagation characteristics at the time of the explosion. For this study, location estimates were made using cross-bearings, which is often advisable because of the uncertainties in travel-times; when the azimuthal deviations generated by the stratospheric winds are accounted for the area of the location uncertainty ellipse is reduced by approximately a factor of two.

A relationship between recorded pressure and yield proved elusive for early researchers (e.g., Cox 1947). However, work both at the Air Force Technical Applications Center (AFTAC) and LANL in the United States showed that relatively simple formulae could describe the expected pressure from an explosion of given yield. The LANL relationship was derived empirically from a number of chemical explosions for which ground truth parameters (location, origin time and yield) were

well constrained (e.g., Whitaker et al. 1990, 2003). The relationship shows that the pressure amplitude of a stratospheric return is dependent upon the explosive yield, the source to receiver range, and the stratospheric wind speed (which is usually taken to be the average along-path wind speed at an altitude of 50 km). If the infrasonic wave propagates in the same direction as the wind, the arrival amplitude is enhanced; if the wave propagates against the wind, the arrival amplitude is reduced. This relationship has been used in subsequent analyses to provide estimates of explosive yield for events where no independent yield estimates are available (e.g., Evers et al. 2007; Ottemöller and Evers 2008; Ceranna et al. 2009).

In the future, it may become possible to produce artificial acoustic sources that can be used to generate infrasound, providing acoustic ground truth in an easily controllable manner. For example, Garces and Park (2007) have been experimenting with a commercially available rotary subwoofer to generate infrasound for instrument calibration, a technology which may be expanded to atmospheric soundings. Such low frequency sources would open up the possibility of extending experiments which acoustically explore the lower atmospheric boundary layer (e.g., Chunchuzov et al. 2005) to probe the upper atmosphere.

The examples given above are testament to the fact that infrasound is best measured using dedicated microbarograph arrays that record atmospheric pressure perturbations, and which allow the source direction to be calculated using back-azimuth estimates from array processing. However, in certain circumstances, synergy between infrasonic and seismic data can provide further information regarding the acoustic source or the manner in which acoustic waves propagate through the atmosphere.

For example, seismic data may be used to provide well constrained source locations, such that the event may be considered as ground truth for infrasound purposes (e.g., Arrowsmith et al. 2007; McKenna et al. 2007) or the combination of the seismic and infrasound data may be able to improve the estimated receiver to source range (e.g., Stump et al. 2004). A good example of this is the Washington State bolide (Arrowsmith et al. 2007); usually bolides would not be included in ground truth studies used for model validation because of the complications of interpreting the moving source. However, in this instance, visual evidence and the recordings of the event on approximately 100 seismometers allowed the acoustic source to be identified as a single (terminal) airburst, rather than a hypersonic shock. Therefore, there was a single source location, which was located to within ±3 km in the horizontal plane and within ±1 km in the vertical plane. Although the location error is greater than desired for ground truth, this explosion is an excellent example of an elevated event recorded at multiple sensor locations. The estimated source location was used by Arrowsmith et al. (2007) to test the applicability of a number of different propagation models, including range-dependent ray tracing with and without ground surface topography (Jones et al. 1986) and a parabolic equation solver (e.g., Lingevitch et al. 2002).

Other studies have used acoustic arrivals recorded on seismometers to provide extra azimuthal coverage of an event (e.g., Ottemöller and Evers 2008; Ceranna et al. 2009), especially for the tropospheric arrivals often not recorded by the regional scale IMS infrasound network. However, seismic recordings of airwaves

can only be used to provide arrival time information. Pressure amplitudes, although related to the amplitude of the seismic signals (e.g., Sorrells 1971), are difficult to calculate from the air-coupled seismic arrivals.

In areas where mining explosions are common, the combination of infrasound and seismic data has been shown to be especially useful, with the infrasound data being used to discriminate between explosions that vent to the atmosphere and other seismic disturbances including small earthquakes and contained explosions (e.g., Stump et al. 2002; Sorrells 1997). An example is given in Fig. 19.3 for a blast from a mine in southern Siberia (details can be found in the SMDC database). The mine is located 143 km from the co-located seismic and infrasound arrays. Using a simple travel-time formulation and assuming that the infrasound has a celerity, $\overline{v}$, equal to 0.3 km/s and the regional seismic *P* wave velocity is 6 km/s, an estimated range to the station is calculated as 148 km. Therefore, using both seismic and infrasound data, an approximate location can be found using the calculated back-azimuth and range, and the event can be identified as a near-surface disturbance due to the presence of both a regional seismic signal and a high amplitude infrasonic signal.

The identification of infrasound for a given event implies that, in most cases, either the source occurred in the atmosphere or close to the Earth's surface. The major exception are large earthquakes which are easily identified using seismic methods. Discriminating between different acoustic source types in the atmosphere is a more difficult problem, primarily due to the large influence the time dependent atmospheric conditions have on the infrasonic waveforms. However, modern array processing techniques combined with propagation modelling provide means of

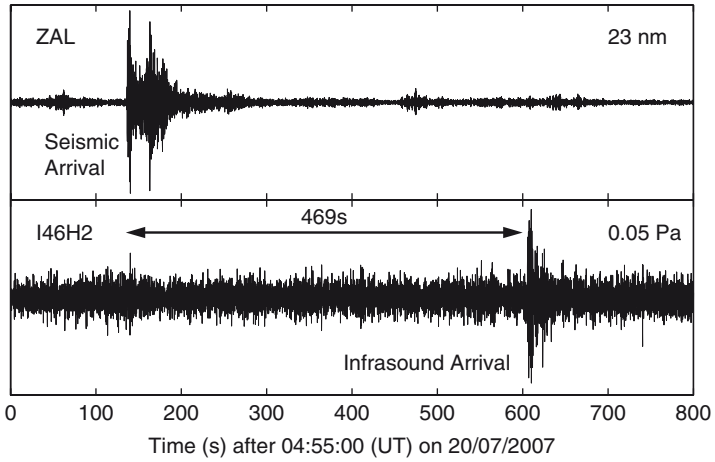

Fig. 19.3 An example of seismo-acoustic data from the co-located IMS arrays, Zalesovo (Seismic) and 146RU (Infrasound) located in southern Russia. The seismic recording is the first element of the seismic array; the recording is from element H2 of the infrasound array. The values in the *top right* of the panels show the maximum amplitude recorded. The source of the signals was a mining explosion that occurred 143 km to the north-east of the stations

identifying important source characteristics; the applicability of these as source discriminants is tested using ground truth events.

One example of a source type discriminant is the determination of whether the source is moving or stationary. This characteristic is often identified by modelling the arrival times and back-azimuths. If the acoustic source is moving, the data are often only explainable using a moving point source or extended line source model (e.g., Brown et al. 2003; ReVelle et al. 2004). However, if the source is a stationary point source a static model will, if the atmospheric parameterisation is accurate, provide the best result. The most common moving sources are meteorite falls, where infrasound can be generated by either the ballistic shock wave or fragmentation events. Such events are common, with the largest event annually having on average an energy equivalent to a 5 kt explosion (Brown et al. 2002). Therefore, it is important to be able to identify such events in the CTBT era where infrasound signals from these explosions might be considered suspicious. Examples of other moving source phenomena, often with lower source energies, are rocket launches (Kaschak et al. 1970) and supersonic aeroplane flights (Balachandran et al. 1977; Liszka 1978; Le Pichon et al. 2002).

It is difficult to use other signal characteristics, including amplitude and duration, as signal discriminants because the time-dependent atmospheric parameters have a large influence on the resultant waveforms. These atmospheric effects must be deconvolved from the signal before the source signature is obtained. However, one possible discriminant, identified from ground truth studies of explosions and earthquakes (Whitaker and Mutschlecner 2008), is the amplitude ratio of stratospheric and thermospheric arrivals from a given event, once the stratospheric arrival amplitude has been corrected for the effect of the wind. For explosions, the stratospheric arrivals are on an average approximately 4 times bigger than the thermospheric arrivals, whereas for earthquakes they are on an average 2.5 times smaller. Whitaker and Mutschlecner (2008) tentatively suggest that this is a consequence of the different source mechanisms generating complex radiation patterns. This example of a discriminant requires the identification of both the stratospheric and thermospheric arrivals, and the association of these phases with the correct source; this is another example of the importance of deploying microbarograph arrays for back-azimuth and trace velocity determination, coupled with reliable atmospheric velocity models. This discriminant is an encouraging step forward, as it shows that by analysing an extensive ground truth dataset significant relationships may be found. As more data become available from the IMS stations, and more ground truth events are identified, it is hoped more source discriminants will be identified.

19.5 Common Propagation Paths

Ground truth events, due to their known locations and origin times, allow confident assessments to be made of the propagation paths that acoustic waves travel along through the atmosphere. By combining the results from many such events, a

description of the most likely waveguides through which infrasound will travel can be developed.

One example of this is a combined study of signals from nuclear explosions, chemical explosions and earthquakes (Mutschlecner et al. 1999; Whitaker and Mutschlecner 2008). The work draws upon the experience gained from recording acoustics generated by explosive testing, including the series of atmospheric nuclear tests conducted at the Nevada Test Site between 1951 and 1962 (Reed 1969). The infrasound recorded from these explosions illuminated three dominant waveguides; one in the troposphere (0–10 km altitude), one between the ground and the stratosphere (0 to ~50 km altitude) and one between the ground and the thermosphere (0 to ~110 km altitude). The stratospheric and thermospheric waveguides are occasionally referred to in the literature as the ozonospheric and ionospheric waveguides, respectively (e.g., Reed 1969).

The tropospheric waveguide can be formed by temperature inversions or shallow wind shears that are often prevalent in night-time conditions (e.g., Thorpe and Guymer 1977). However, for regional studies, these arrivals are of little interest as they are seldom observed at ranges greater than 300 km from the source. Therefore, in the era of CTBT monitoring, most of the focus is placed on the waveguides that can transport infrasound over hundreds and thousands of kilometres: the stratospheric and thermospheric waveguides.

The detection of arrivals within the stratospheric waveguide, denoted I_s, and arrivals within the thermospheric waveguide, denoted I_t, is dependent upon the orientation of the source and receiver. Nevertheless, in a study of 24 source/receiver pairs recording a series of chemical explosions, Whitaker and Mutschlecner (2008) report stratospheric arrivals can be identified on 100% of the records, whereas thermospheric arrivals are only identified on 45%. Similar results were found for the set of 183 measurements from U.S. atmospheric nuclear explosions with a range of yields between 0.6 and 74 kt: stratospheric arrivals are identified on 95% of the recordings and thermospheric arrivals on 52%. Unlike the chemical explosions which were conducted at the surface, the nuclear explosions had heights of burst ranging between the surface and approximately 12 km altitude. However, Mutschlecner et al. (1999) showed that the height-of-burst has little effect on the amplitude decay with distance for stratospheric or thermospheric arrivals, suggesting that detectability will not be greatly influenced by different source altitudes throughout the troposphere.

These results suggest that most infrasonic arrivals recorded by arrays at regional or tele-infrasonic distances will have propagated in the stratospheric waveguide, a hypothesis supported by the predominance of seasonally dependent detection azimuths observed at many infrasound stations (e.g., Le Pichon et al. 2008). However, this is in disagreement with the predicted ducting fractions of Drob et al. (2003), which suggest that thermospheric arrivals should dominate across the globe. The difference may be due to the current generation of infrasound arrays being more sensitive to stratospheric arrivals. For example, the relatively small array aperture (~ 1 km) might allow little signal-to-noise improvement to be made at low signal frequencies associated with thermospheric arrivals, decreasing the probability of detection. Or it may be that a bias towards identifying high frequency signals might

be present in automatic detectors, or that the present models incorporate insufficient thermospheric absorption; future research will hopefully resolve this issue.

When analysing stratospheric infrasonic returns, the direction of the stratospheric wind relative to the propagation direction is the dominant factor controlling infrasound detectability, a phenomenon that is shown clearly in a study of volcano generated acoustics in the Vanuatu archipelago (Le Pichon et al. 2005). Here, recordings are made over the same time period at one IMS station in New Caledonia (I22FR) from two volcanoes: Lopevi volcano located approximately north (14°) of the recording station at a range of 650 km and Yasur volcano located to the north-east (43°) at a range of 400 km.

Refraction of the signals from the north is not strongly influenced by the zonal stratospheric winds which travel perpendicular to the acoustic propagation path. Therefore, as the stratospheric effective acoustic velocity along this propagation path is not high enough to cause the infrasound to refract back to the ground, the waves travel up to the thermosphere where the energy is turned back towards the Earth's surface due to the high acoustic velocities at these altitudes. This refraction from the thermosphere is not strongly seasonal dependent because it is not governed by wind parameters; therefore, the arrivals are observed throughout the year. However, this series of ground truth events provides confirmation of semidiurnal variations in thermospheric detectability due to solar driven atmospheric tides, a phenomenon that has been described theoretically by Garces et al. (2002). Detections from Lopevi show that when the tides increase the temperature of the thermosphere, the increased acoustic velocities cause refraction at lower altitudes and ground returns are observed. Conversely, when the tidal heating is at its lowest, causing the acoustic rays to be turned in the higher, hotter but more rarefied thermosphere, detections are not observed. The non-observation is attributed to acoustic waves in the higher thermosphere being rapidly attenuated due to strong atmospheric absorption (Sutherland and Bass 2004).

In contrast to the Lopevi case, infrasound from the Yasur volcano to the north-east is strongly influenced by the zonal stratospheric winds. In the Southern Hemisphere, the dominant stratospheric wind direction is westward in the months between November and March, whereas it is eastward between May and September. Therefore, on the south-westerly propagation path from Yasur to I22FR, the wind increases the along path stratospheric effective acoustic velocity in the Southern hemisphere summer and decreases the effective velocity in the winter. Therefore, refractions back to the ground from the stratosphere only occur during the months between November and March (Le Pichon et al. 2005).

The example given above highlights the complexity of infrasound propagation; each infrasound detection must be considered within the framework of a time-dependent atmospheric model through which the simulated propagation paths are highly azimuthally-dependent. However, the continual improvement of atmospheric specifications allow these propagation paths to be modelled with improved accuracy; ground truth events can then be used to validate the models and highlight areas for further improvement. In Sect. 19.6, we introduce a case study where arrivals at many azimuths allow us to take advantage of signals travelling through all three major waveguides to help constrain the source parameters.

19.6 A Case Study: The Buncefield Oil Depot Explosion

A large explosion occurred at the Buncefield Oil Depot, UK, on 11th December 2005, when an accidentally released petrol vapour cloud was ignited. Prior to the explosion, the depot, located 35 km north-west of central London at 51.766°N 0.427°W, was a primary distribution centre for oil in the UK. It received fuel via pipeline from coastal refineries which was subsequently stored in large tanks above ground level before being distributed to customers via road or pipe.

Detailed accounts of the events leading up to the explosion, and the subsequent aftermath, are given in the reports of the Buncefield Major Investigation Board, directed by the UK Health and Safety Executive (HSE 2006; Powell 2006a–c). These reports are an excellent source of ground truth information, regarding both the nature of the event and its location. On-site damage suggests that the vapour cloud should be considered a distributed source, as it spreads over an area of ~ 80,000 m^2. The documents include maps of the vapour cloud extent allowing us to locate a point source for the explosion that will be within a couple of hundred metres of the true ignition location. Seismic records and eyewitness accounts indicate that there was only one large explosion as the vapour cloud ignited. The seismic analysis, using the UK national network operated by the British Geological Survey, also allows the origin time information to be estimated as 06:01:31.45±0.5 s UTC (Ottemöller and Evers 2008).

Information regarding the magnitude of the event is less well constrained, and due to the uncertainties, this cannot be considered ground truth information. However, the following short summary, compiled from the HSE reports, provides some comprehension of the event size. On the morning of the explosion, a valve mechanism that prevented the overfilling of the storage facilities failed on a tank that was being supplied with unleaded petrol. This led to ~300 tons of fuel being spilt over the top of the tank. The flow of petrol off the edge of the tank allowed entrainment of air to occur, forming a vapour. The resulting vapour cloud is estimated, from on-site damage, to have spread over an area of ~80,000 m^2 with a thickness between 1 and 7 m. The atmospheric overpressures generated have been estimated from blast damage at between 0.7 and 1 bar in the vicinity of the main blast (Powell 2006c), dropping two orders of magnitude at a distance of 2 km. These overpressure estimates are large in comparison with those inferred from previous vapour cloud explosions (Lenoir and Davenport 1993), and when combined with the unconfined nature of the Buncefield explosion suggest that the incident was well suited for producing high amplitude infrasonic waves.

The Buncefield explosion also provides an example of how supposed ground truth information can be very misleading, due to garbled reporting. Hinzen (2007) stated that part of Luton airport terminal was destroyed in the blast; this is incorrect. Luton airport is located 13 km away from the explosion site, and if the reported damage was assumed to be true then the yield would have had to be much larger.

In order to analyze the infrasound propagation paths, an understanding of the atmospheric velocity structure is required; at the time of the explosion two

atmospheric parameterisations were available for this purpose. The MSISE/HWM model is a hybrid of the Mass Spectrometer and Incoherent Scatter Radar model (Picone et al. 2002), which provides temperature data, and the Horizontal Wind Model (Hedin et al. 1996), which provides vertical profiles of the horizontal wind. This model is a seasonally varying empirical model, and although easy to implement does not explain the large variability that often occurs in the atmospheric variables. The second model is the state of the art NRL-G2S (Ground to Space) model (Drob et al. 2003) which fuses operational weather data from the lowermost 50 km of the atmosphere with the MSISE/HWM coefficients for the upper atmosphere to provide acoustic velocity and wind profiles. This is based on high resolution meteorological models and therefore has the ability to explain more of the observed variations.

The infrasound analysis and ground truth information are contained within three main publications. Ottemöller and Evers (2008) detail a seismo-acoustic analysis; this provides the origin time estimate and also illustrates methods of phase identification and yield calculation. Ceranna et al. (2009) use more infrasound data, and further ground-coupled airwaves, to provide a comprehensive analysis including phase identification, atmospheric model comparison, source location and yield estimation. Further work by Evers and Haak (2007) illustrate the unusual fast stratospheric arrivals that were a consequence of the strong stratospheric winds present at the time of the explosion.

19.6.1 Observations

It was fortuitous for infrasound research that the Buncefield explosion occurred during the northern hemisphere winter, due to the high density of infrasound stations located downwind of the source. Seven microbarometer arrays, across France, Germany, the Netherlands and Sweden, recorded the airwaves (Fig. 19.4). In addition, 54 seismic stations also recorded the airwaves as air-to-ground coupled arrivals (one of which, the GERESS array in south-east Germany, recorded the signals on 19 of the 25 separate instruments in the array). Each infrasound array detected multiple arrivals, indicating that the acoustic energy propagated through numerous atmospheric paths between the source and the stations; Fig. 19.5 provides some examples. The celerities (0.250–0.360 km/s) and apparent velocities (0.338–0.435 km/s) of the arrivals were consistent with a wide range of signals, including returns from the troposphere, stratosphere and thermosphere (e.g., Evers and Haak 2007; Ceranna et al. 2009). The extremely high celerities of some of the arrivals (>0.34 km/s) were interpreted by Evers and Haak (2007) as evidence of acoustic energy critically refracted at the stratospheric velocity maximum being returned to the ground (headwave propagation). Three stations in northern Sweden did not record the event, indicating the edge of the zone of detectability.

Combined with the well constrained, independently gathered, ground truth information, this comprehensive set of observations provides a benchmark dataset

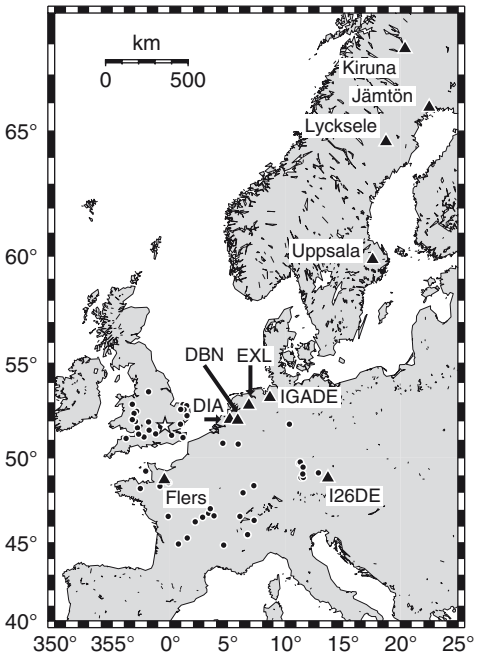

Fig. 19.4 A map showing the location of the Buncefield explosion (*star*) with respect to the locations of the infrasound stations in Europe (*triangles*); all stations except the northern most three (Lycksele, Jämtön and Kiruna) recorded the event. *Black circles* indicate the locations of seismometers that also recorded the passage of the airwaves

for exploring the suitability of different atmospheric parameterisations, investigating location algorithms and probing the consistency of yield estimation calculations.

19.6.2 Analysis Results

One consequence of having the large geographical spread of recording stations is that the predicted regional distribution of different types of signals can be tested against the observations. Ottemöller and Evers (2008) show the regions in which the tropospheric, stratospheric and thermospheric arrivals are predicted from the NRL-G2S model for ranges up to 600 km away from the source. This study shows good correspondence between the observed arrivals and the predicted zones of infrasonic ground returns, especially for the tropospheric and stratospheric arrivals. In the direction upwind of the stratospheric winds, the model fit is less well constrained, with the arrivals starting at ranges 20 km prior to the predicted thermospheric bounce. Ceranna et al. (2009) also identify the zones in which different arrivals will be observed, out to ranges of approximately 2,000 km. This study

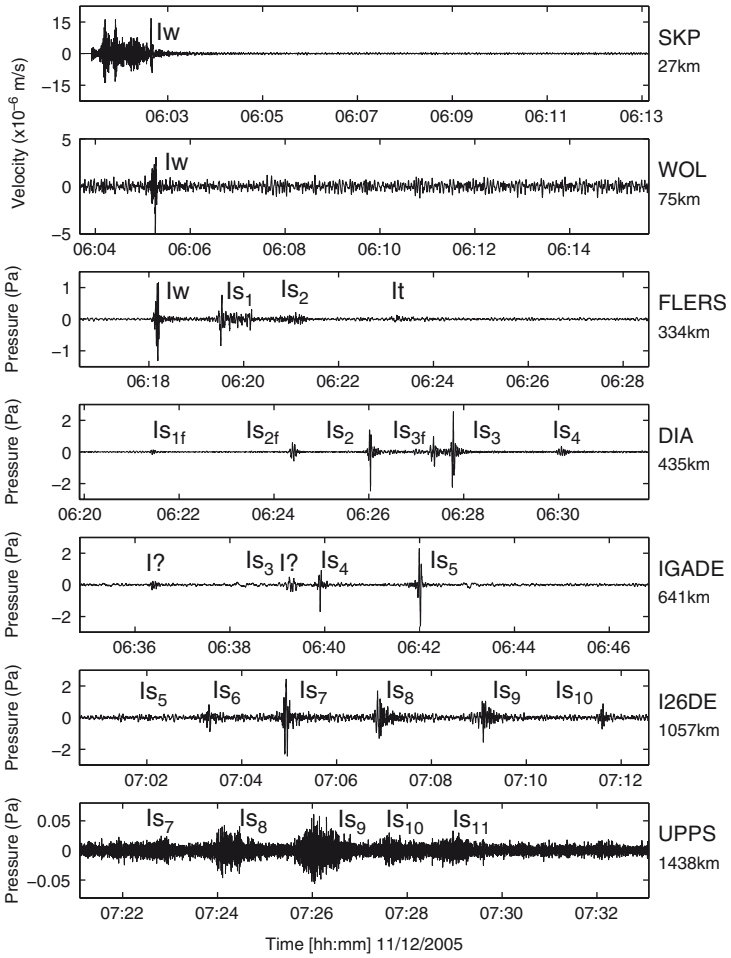

Fig. 19.5 Pressure waveforms recorded from the Buncefield oil depot explosion (after Ceranna et al. 2009) filtered between 0.1 and 4 Hz. The phases attributed by Ceranna et al. (2009) are indicated: I_w is a tropospheric phase, I_s is a stratospheric phase and I_t is a thermospheric phase. Numerical subscripts refer to the number of ground returns on the path since the source. The range to the station is given beneath the station name. *I*? refers to two arrivals at IGADE that are not easily explainable but are consistent with the fast infrasonic returns (indicated by "f" in the DIA annotation subscripts) analysed by Evers and Haak (2007). Stations SKP and WOL are seismometers, FLERS, DIA, IGADE, I26DE and UPPS (Uppsala) are microbarograph arrays

shows the pronounced differences between the regions of different arrivals predicted by the MSISE/HWM and NRL-G2S specifications. For example, models incorporating the MSISE/HWM model predict that the northern Swedish stations (Fig. 19.4) would have observed stratospheric arrivals, and the station FLERS, at an azimuth approximately aligned with the meridional wind, would only observe thermospheric phases; neither scenario matches the observations (Fig. 19.5). When

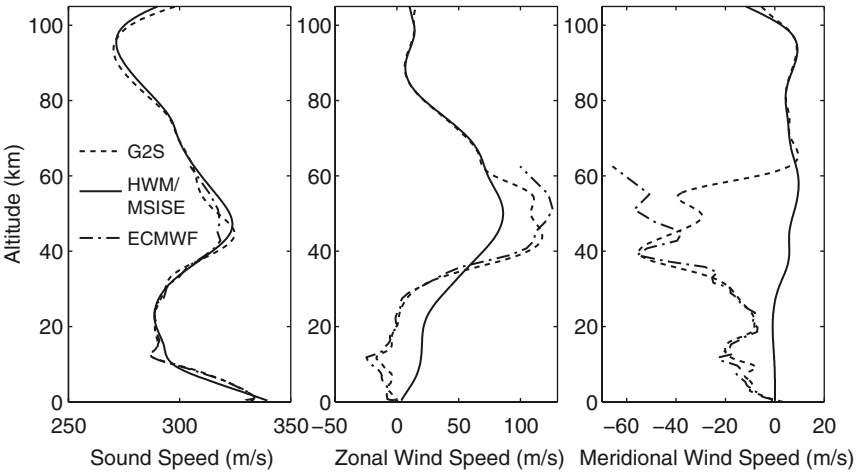

Fig. 19.6 The differences between the seasonal MSISE/HWM empirical model and the numerical weather model from the ECMWF for location 50°N, 6°E at 6AM 11th December 2005. The Ground-to-Space model used in the infrasound raytracing takes the numerical weather model in the lower 50 km and spline fits this to the upper atmospheric specifications given by HWM/MSISE using a spherical harmonic decomposition (Drob et al. 2003). Note the large differences between the stratospheric wind speeds in the two underlying models, and that the zonal component dominates

the NRL-G2S model is used, the fast stratospheric jet present in this model (Fig. 19.6) predicts the observed tropospheric, stratospheric and thermospheric arrivals at FLERS and indicates that the Northern Swedish stations are close to the region in which stratospheric arrivals are not observed. Although it does not predict the observed phases exactly in all locations, the NRL-G2S model provides a much more accurate picture of the geographical regions associated with the different arrival types.

In Fig. 19.7, we show the predicted travel-time variations with range, using a 1D raytracing model and both the G2S model and the empirical MSISE/HWM model as atmospheric parameterisations. We have transformed each travel-time, t_a, into a reduced time t_r, defined as,

$$t_r = t_a - \frac{R}{v_{ref}}, \tag{1}$$

where R is the station range and v_{ref} is a reference velocity (0.34 km/s). This transformation separates the arrivals with different celerities and allows the various stratospheric returns to be traced across central Europe between ranges of 200 and 1,100 km. To aid the clear interpretation of the different stratospheric arrivals, we adopt the I_{sx} notation (e.g., Ceranna et al. 2009), where x is the number of ground returns between source and receiver.

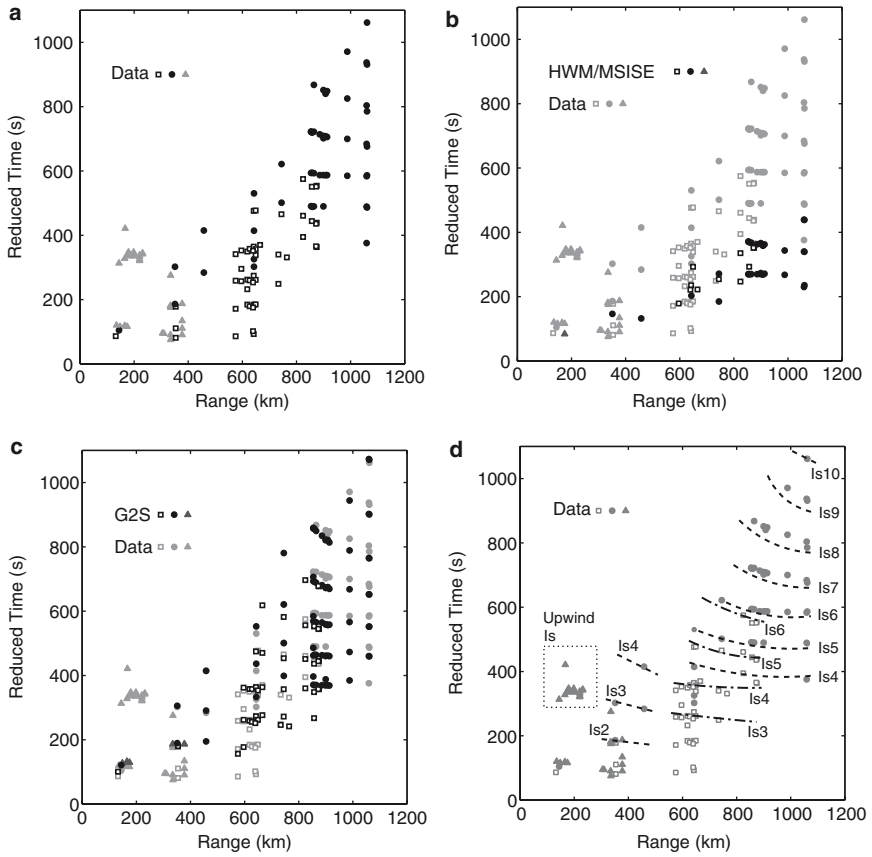

Fig. 19.7 A comparison of the travel-time data, and those predicted by 1D ray-tracing. Travel-times, t_a, have been transformed into reduced times, t_r, defined as $t_r = t_a - (R/v_{ref})$ where R is the source to receiver range and v_{ref} is a reference velocity taken as 0.34 km/s. (**a**) shows the travel-time data; in all panels, the marker shape refers to the source to station azimuth: *circles* between 60 and 120°, *squares* between 120 and 180°, all others depicted as *triangles*. (**b**) shows the comparison between the data (*light shades*) and the HWM/MSISE predictions (*dark shades*). Similarly, (**c**) shows the comparison between the data (*light shades*) and the G2S predictions (*dark shades*). (**d**) shows the interpretation of the G2S arrivals in terms of the stratospheric bounces, I_{sx}, where x is the number of ground returns between source and receiver

Because of the high density of stations, the different stratospheric bounces can be identified, and a clear azimuthal pattern is observed. The results are split into two azimuthal swaths, between 60–120° and 120–180°. This split is based on the geometry of the stratospheric high velocity jet present in the NRL-G2S model which propagates almost directly eastwards; the arrivals along the two paths have recognisably different arrival times. Along the more easterly path, the arrival times are greater for a given stratospheric return due to the geometry of the acoustic ray path. For example, in Fig. 19.7d, it can be seen that arrival I_{s4} (the fourth stratospheric bounce) at a range of 800 km arrives with a reduced time, t_r, of

approximately 400 s for the 60–120° path and approximately 350 s for the 120–180° path, equivalent to travel-times of approximately 2,750 and 2,700 s, respectively. The increase in travel-time along the more easterly path is due to the influence of the stronger along-path stratospheric wind component in this direction, causing stratospheric refraction to be more pronounced. This causes infrasound with a given take-off angle to refract and return to the ground surface at a shorter range along the easterly path compared with the southerly path. In the example given, four stratospheric bounces occur along both paths between the source and a range of 800 km. Because stratospheric refraction is stronger along the easterly path, a more vertical take-off angle is required in this direction compared with the southerly path to ensure the correct number of bounces within the given range. A consequence of the more vertical take-off angle is that the acoustic energy travels higher into the stratosphere before being returned to the ground surface, compared with the shallower take-off angle required in the more southerly direction. As the waves travel higher into the atmosphere in the easterly direction, the ray-path is longer, resulting in larger travel-times along the easterly path for a given arrival (e.g., I_{s4} at 800 km).

The Buncefield explosion is unusual because signals from up to the tenth stratospheric bounce (I_{s10}) are observed at the relatively short range of 1,050 km (at station I26DE). These multiple arrivals are a consequence of the stratospheric waveguide formed by the strong zonal stratospheric winds, whose speeds exceeded 100 m/s (Fig. 19.6). This highly efficient waveguide returned acoustic energy at relatively short ranges from the source (Ottemöller and Evers (2008) estimate ranges between 100 and 160 km for I_{s1}), allowing large numbers of bounces to occur in a given range.

The accuracy of the models can be considered more quantitatively through studying the arrival times; Ottemöller and Evers (2008) show that the average residual for stratospheric arrivals across the UK and the Netherlands is 3.8 s. In comparison, the results across central Europe shown in Fig. 19.7 have travel-time residuals with a mean value of 17 s over the 75% of the stratospheric arrivals explained by the G2S model. However, the residuals show a strong dependence on distance from the source due to compounding model errors. Therefore, it is more comparable to consider residuals normalised by the true travel-times (e.g., O'Brien et al. 2006). Applying this to the results of Fig. 19.7 gives a mean residual of 0.68% of the true travel-times, only slightly greater than that of Ottemöller and Evers (2008) which is approximately 0.45% of the true travel-times. Comparing the true and predicted travel-times shows that the model consistently predicts faster propagation than that observed, suggesting that for this particular case the G2S model slightly overestimates the wind speeds. We do not calculate residuals for the MSISE/HWM model because only 13% of the observed arrivals are predicted in this case, compared with the 75% using the G2S model (Fig. 19.7).

Much of the arrival time data in the above analysis came from ground-coupled airwaves, i.e., measurements of an airwave passage on a seismometer. However, these arrivals are limited in the information they give; they only provide arrival time data. In contrast, arrays of microbarographs provide information on the direction of

the arrival, both in the sense of azimuth and incidence angle. Whereas azimuth can be used in location analyses, the incidence angle, which is often expressed in terms of the apparent velocity across the array, provides clues about the height attained by the acoustic waves. For example, Ceranna et al. (2009) show that across the three infrasound arrays with kilometre size apertures the apparent velocities of the 13 arrivals can be predicted to within, on average, 3 m/s or 1% of the measured velocities. This gives extra confidence in the modelled propagation paths. Also, unusual combinations of high celerity and high apparent velocities provided the evidence for Evers and Haak (2007) to postulate the existence of the headwave propagation in the stratosphere due to high winds.

Examples within the literature comparing source locations made with infrasound data to well constrained ground truth data are sparse. The Buncefield explosion is ideal for such studies, due to the large number of distinct phases recorded over a number of infrasound arrays. Ceranna et al. (2009) explored the effect of using different arrivals and data-derived parameters to locate the event. The location results were obtained using a least-squares inversion method (Geiger 1910), for which the functions to be minimised were either the differences between the observed and calculated arrival times, the differences between the observed and calculated back-azimuths, or a weighted sum of both. A subset of the results, showing only the results using the NRL-G2S atmospheric specification, are illustrated in Fig. 19.8. Ceranna et al. (2009) showed that for the Buncefield explosion the NRL-G2S model consistently provides the most accurate results compared to using a constant velocity or the MSISE/HWM models.

The results show that adding the arrival time data into the location estimates makes a significant improvement to the location estimates, with the residual between the estimate and the ground truth locations being only 35% of the residual obtained using the back-azimuth alone. Also, by including the arrival time data, it is possible to estimate the origin time, which in the best cases is within a few seconds of the ground truth estimate. In addition, the results show the advantage of using multiple arrivals (e.g., the different stratospheric bounces) to constrain the location, rather than just the first arrival. This advantage is especially pronounced when there are few contributing stations. For the examples using only the data from infrasound arrays, the use of multiple arrivals improved both the location and origin time estimates by between a factor of 2.5 and 10.

A novel use of the multiple arrivals was to locate the event using just the arrivals from one array (Ceranna et al. 2009). The back-azimuth estimate was used to provide a bearing, whereas the difference between the arrival times of the individual phases were used to estimate the range to the source. This method was used for two examples: the data at FLERS where tropospheric, stratospheric and thermospheric arrivals were observed, and the data at I26DE where six stratospheric arrivals were observed. The location using the FLERS data was much better constrained than that at I26DE because of the large variety of arrival celerities due to the observation of infrasound that had propagated through different waveguides; indeed, the single station location for FLERS provided epicentre and origin time estimates that were comparable in accuracy to those made with all available data

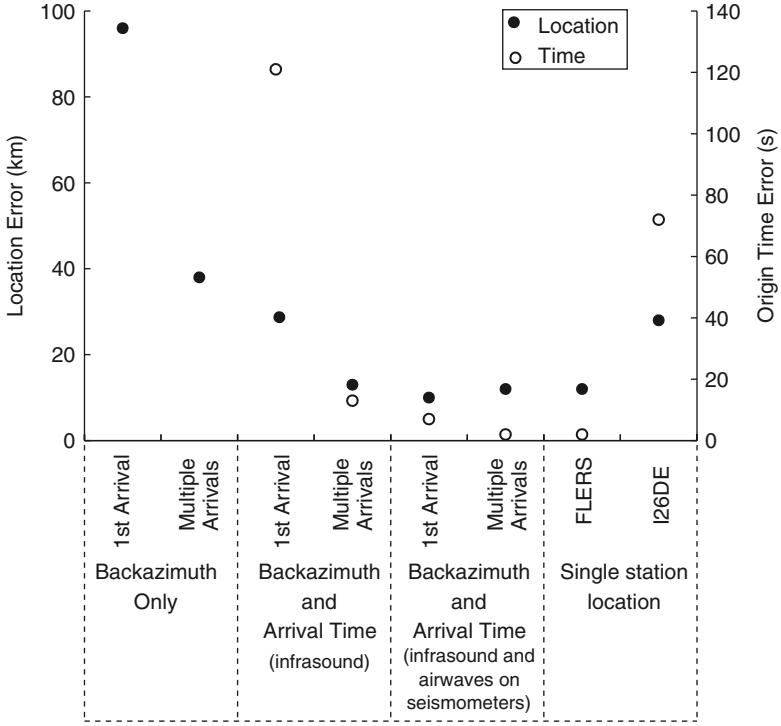

Fig. 19.8 A subset of the location results of Ceranna et al. (2009), showing both the difference between the predicted and true locations (*full circles*) and the predicted and true origin times (*open circles*). All models use the NRL-G2S atmospheric model. The different *columns* on the horizontal axis refer to the different data used. For those referred to as "1st Arrival," only the first arrival at each station is used in the location estimate, for the "multiple arrival" estimates all arrivals at the stations are used. The single station locations use only the data from FLERS and I26DE, respectively (Fig. 19.4 and 19.5)

(Fig. 19.8). The single station location using I26DE was not as well constrained because the celerities of all the stratospheric arrivals were very similar, with the consequence that the minima in the residuals was less pronounced. However, the ability to locate atmospheric events using multiple arrivals at a single station may prove extremely useful in locations where the density of infrasound arrays is less than in central Europe.

Although we have no ground truth information regarding the yield of the explosion, the well-constrained location parameters and atmospheric specifications allow the yield to be estimated using the Whitaker et al. (2003) formulation. As there are multiple observations, the consistency of the estimates can be tested for a number of stations at different ranges and azimuths from the explosion. Ceranna et al. (2009) show that the yield estimates are spread over almost an order of magnitude, from 19 to 153 metric tons of HE with a mean value of 51 tons.

For the results shown in Ceranna et al. (2009), the variability in yield estimates can be explained by two mechanisms: the position of the observing station with respect to the centre of the stratospheric arrival's ground return footprint and the magnitude of the along path wind speed. The first mechanism is highlighted by the difference in amplitude of different stratospheric arrivals at the same station (e.g., 126DE in Fig. 19.5). As suggested by Evers et al. (2007), it is expected that the amplitude will be larger at the centre of the stratospheric arrival's ground return footprint. The second mechanism is likely to have caused much of the variability in yield estimation for the Buncefield explosion, as large azimuthal differences in stratospheric wind speed were present in the atmospheric models. It appears that at stations which are located along paths with very high (>90 m/s) wind speeds the Whitaker formulation overcompensates and provides low yield estimates. As the stratospheric wind speeds are 40% larger in the G2S compared with the HWM model (Fig. 19.6), and the Whitaker yield estimation is very sensitive at high wind speeds, this suggests that there is an upper wind limit in which the formulation is applicable. It is only through testing the consistency of the formulation using multi-station ground truth events where such systematic differences to the formula will be found.

19.7 Future Considerations

With the expansion of the IMS infrasound network, set up to support the verification of the CTBT, the identification of more ground truth events appears probable. In the era of CTBT monitoring the focus of ground truth analysis is likely to become how accurately the infrasound source can be located, whether the event can be identified as an explosion, and how well the equivalent explosive yield can be estimated. However, these parameters are directly linked to the accuracy of the atmospheric models used, and therefore ground truth events will continue to play a vital role in model validation. The example of the Buncefield oil depot explosion illustrates these types of analyses.

Future advances in infrasound analysis must be considered when collecting and archiving ground truth data. At the time of writing, the state-of-the-art atmospheric models have a time resolution of a few hours; in the future it may be important to assess models which attempt to simulate atmospheric acoustic velocity changes on the timescales of infrasound propagation from a source to a distant receiver. Also, most present studies attempt to match arrival times and back-azimuths; the next generation of propagation models will also need to explain amplitudes, in order to improve the estimation of source magnitude or yield. These models will be assessed using the ground truth data collected in the coming years, in conjunction with the recordings already archived. However, this will only be possible if a comprehensive ground truth database is maintained. Waveform data, as well as event metadata, should be stored to ensure any future developments can be tested.

19.8 Summary

Ground truth events provide an opportunity to quantitatively assess both the performance of a network of infrasound sensors and the performance of acoustic propagation models. Two of the parameters that can be assessed in such analyses are the residuals between observed and predicted travel-times and the residuals between the true and estimated source location. In this chapter, we have provided an example of such an analysis, using the Buncefield oil depot explosion as a case study. Infrasound from this event was recorded at seven microbarograph arrays and as air-to-ground coupled waves on 54 seismic stations; 75% of the 102 recorded stratospheric phases could be explained using the NRL-G2S atmospheric model of Drob et al. (2003). The mean travel-time residual for these arrivals is 17 s, but these residuals show a correlation with the source to receiver range. Therefore, it may be more useful, especially when comparing to other events, to calculate the travel-time residual as a percentage of the travel-time, which was 0.68% for the Buncefield signals. The location analysis clearly showed that arrival-times as well as back-azimuths should be incorporated into epicentral determination routines, as using the arrival-times reduced the location residuals to 35% of the residuals found when using back-azimuth alone. Using both arrival-times and back-azimuths placed the estimated epicentre within 15 km of the true location.

The number of microbarograph arrays being deployed is currently increasing, especially with the continued development of the 60-station IMS network. It is expected that with this higher density of stations many more infrasonic arrivals from known sources will be detected. For these infrasound sources, the ground truth data need to be collected and archived. This will allow future developments in infrasound analysis to be quantitatively tested against the performance of current procedures.

References

Al'Perovich LS, Afraymovich EL, Vugmeyster BO, Gokhberg MB, Drobzhev VI, Yerushchenkov AI, Ivanov EA, Kalikhman AD, Kurdryavtsev VP, Kulichkov SN, Krasnov VM, Mordukhovich MI, Matveyev AK, Nagorskiy PM, Ponomarev EA, Salikhov NM, Tarashchuk YE, Troitskaya VA, Fedorovich GV (1985) The acoustic wave of an explosion. Izv-Phys Solid Earth 21(11):835–842

Antier K, Le Pichon A, Vergniolle S, Zielinski C, Lardy M (2007) Multiyear validation of the NRL-G2S wind fields using infrasound from Yasur. J Geophys Res 112(D23110), doi:10.1029/2007JD008462

Arrowsmith SJ, Drob DP, Hedlin MAH, Edwards W (2007) A joint seismic and acoustic study of the Washington state Bolide: observations and modelling. J Geophys Res 112(D09304), doi:10.1029/2006JD008001

Balachandran NW, Donn WL, Rind D (1977) Concorde sonic booms as an atmospheric probe. Science 197(4298):47–49

Bondar I, Engdahl ER, Yang X, Ghalib HAA, Hofstetter A, Kirichenko V, Wagner R, Gupta I, Ekström G, Bergman E, Israelsson H, McLaughlin K (2004a) Collection of a reference event set for regional and teleseismic location calibration. Bull Seism Soc Am 94(4):1528–1545

Bondar I, Myers S, Engdahl E, Bergman E (2004b) Epicentre accuracy based on seismic network criteria. Geophys J Int 156(3):483–496

Bowman JR, Shields G, O'Brien MS, Israelsson H (2007) The infrasound database of the SMDC monitoring research program. In: Proceedings of the 2007 infrasound technology workshop, Japan Weather Association, Tokyo, Japan, p 89

Brown P, Spalding RE, ReVelle DO, Tagliaferri E, Wordon SP (2002) The flux of small near-Earth objects colliding with the Earth. Nature 420:294–296

Brown PG, Kalenda P, ReVelle DO, Borovička J (2003) The Morávka meteorite fall: 2. Interpretation of infrasonic and seismic data. Meteorit Planet Sci 38(7):989–1003

Ceranna L, Le Pichon A, Green DN, Mialle P (2009) The Buncefield explosion: a benchmark for infrasound analysis across central Europe. Geophys J Int 177(2):491–508

Christie DR, Campus P (2010) The IMS infrasound network: design and establishment of infrasound stations. This volume, pp. 27–72

Chunchuzov I, Kulichkov S, Otrezov A, Perepelkin V (2005) Acoustic pulse propagation through a fluctuating stably stratified atmospheric boundary layer. J Acoust Soc Am 117(4):1868–1879

Cox EF (1947) Microbarometric pressures from large high explosive blasts. J Acoust Soc Am 19(5):832–846

Cox EF (1949) Abnormal audibility zones in long distance propagation through the atmosphere. J Acoust Soc Am 21(1):6–16

Cox EF, Atanasoff JV, Snavely BL, Beecher DW, Brown J (1949) Upper-atmosphere temperatures from Helgoland big bang. J Meteorol 6(5):300–311

Donn WL, Balachandran NK (1981) Mount St. Helens eruption of 18 May 1980: air waves and explosive yield. Science 213(4507):539–541

Drob DP, Picone JM, Garces M (2003) Global morphology of infrasound propagation. J Geophys Res 108(D21):4680,doi:10.1029/2002JD003307

Evers LG, Haak HW (2007) Infrasonic forerunners: exceptionally fast acoustic phases. Geophys Res Lett 34(L10806), doi:10.1029/2007GL029353

Evers LG, Ceranna L, Haak HW, Le Pichon A, Whitaker RW (2007) A seismoacoustic analysis of the gas-pipeline explosion near Ghislenghien in Belgium. Bull Seism Soc Am 97(2):417–425

Flores JS, Vega AJ (1975) Some relations between energy-yield of atmospheric nuclear tests and generated infrasonic waves. J Acoust Soc Am 57(5):1040–1043

Garces M, Park J (2007) A rotary subwoofer as an infrasonic source. In: 2007 infrasound technology workshop: program and abstracts, Tokyo, Japan, p 85

Garces M, Drob DP, Picone JM (2002) A theoretical study of the effect of geomagnetic fluctuations and solar tides on the propagation of infrasonic waves in the upper atmosphere. Geophys J Int 148:77–87

Garces M, Fee D, Steffke A, McCormack D, Servranckx R, Bass H, Hetzer C, Hedlin M, Matoza R, Yepes H, Ramon P (2008) Capturing the acoustic fingerprint of stratospheric ash injection. EOS 89(40):377–378

Geiger L (1910) Herdbestimmung bei Erdbeben aus den Ankunftszeiten. Nachrichten von der Königlichen Gesellschaft der Wissenschaften zu Göttingen. Mathematisch-physikalische Klasse, pp 331–349

Grover FH (1974) Infrasonic and seismic wave records from the Flixborough and St Bridget explosions. Technical Report O 46/74, AWRE

Hedin AE, Fleming EL, Manson AH, Schmidlin FJ, Avery SK, Clark RR, Franke SJ, Fraser GJ, Suda T, Vial F, Vincent RA (1996) Empirical wind model for the upper, middle and lower atmosphere. J Atmos Terr Phys 58(13):1421–1447

Hinzen KG (2007) London fuel tank explosion recorded by short-period seismic stations at 500-km distance. Seism Res Lett 78(3):383–388

HSE (2006) Buncefield major incident investigation: initial report to the health and safety commission. Health and Safety Executive Report, http://www.buncefieldinvestigation.gov.uk

Jones RM, Riley JP, Georges TM (1986) HARPA: A versatile three-dimensional hamiltonian ray-tracing program for acoustic waves in the atmosphere above irregular terrain. Technical report, NOAA, Boulder, CO

Kaschak G, Donn WL, Fehr U (1970) Long-range infrasound from rockets. J Acoust Soc Am 48(1):12–20

Kulichkov SN (2004) Long-range propagation and scattering of low-frequency sound pulses in the middle atmosphere. Meteorol Atmos Phys 85:47–60

Kulichkov SN, Bush GA (2001) Rapid variations in infrasonic signals at long distances from one-type explosons. Izv, Atmos Ocean Phys 37(3):306–313

Kulichkov SN, Bush GA, Svertilov AI (2002) New type of infrasonic arrivals in the geometric shadow region at long distances from explosions. Izv, Atmos Ocean Phys 38(4):397–402

Kulichkov SN, Avilov KV, Bush GA, Popov OE, Raspopov OM, Baryshnikov AK, ReVelle DO, Whitaker RW (2004) On anomalously fast infrasonic arrivals at long distances from surface explosions. Izv, Atmos Ocean Phys 40(1):1–9

Kulichkov S (2010) On the prospects for acoustic sounding of the fine structure of the middle atmosphere. This volume, pp. 505–534

Le Pichon A, Garces M, Blanc E, Barthelemy M, Drob D (2002) Acoustic propagation and atmospheric characteristics derived from infrasonic waves generated by the concorde. J Acoust Soc Am 111:629–641, doi:10.1121/1.1404434

Le Pichon A, Guilbert J, Vallee M, Dessa JX, Ulziibat M (2003) Infrasonic imaging of the Kunlun Mountains for the great 2001 China earthquake. Geophys Res Lett 30(15):1814

Le Pichon A, Blanc E, Drob D (2005) Probing high-altitude winds using infrasound. J Geophys Res 110:D20, 104, doi:10.1029/2005JD006020

Le Pichon A, Vergoz J, Herry P, Ceranna L (2008) Analyzing the detection capability of infrasound arrays in central Europe. J Geophys Res 113(D12115), doi:10.1029/2007JD009509

Lenoir EM, Davenport JA (1993) A survey of vapor cloud explosions: second update. Process Saf Prog 12(1):12–33

Lingevitch JF, Collins MD, Mills MJ (2002) A two-way parabolic equation that accounts for multiple scattering. J Acoust Soc Am 112:476–480

Liszka L (1978) Long-distance focusing of concorde sonic boom. J Acoust Soc Am 64(2):631–635

McKenna MH, Stump BW, Hayek S, McKenna JR, Stanton TR (2007) Tele-infrasonic studies of hard-rock mining explosions. J Acoust Soc Am 122(1):97–106, doi:10.1121/1.2741375

Mikhailov VN (ed) (1999) Catalog of worldwide nuclear testing. Begell-Atom, LLC, New York

Mutschlecner JP, Whitaker RW (2005) Infrasound from earthquakes. J Geophys Res 110(D01108), doi:10.1029/2004JD005067

Mutschlecner JP, Whitaker RW, Auer LH (1999) An empirical study of infrasonic propagation. Technical Report, Los Alamos National Laboratory

Norris D, Bhattacharyya J, Whitaker R (2006) Development of advanced propagation models and applications to the study of impulsive infrasonic events. In: 28th monitoring research review: ground-based nuclear explosion monitoring technologies, pp 919–925

O'Brien MS, Bowman JR, Drob DP (2006) Improved infrasound locations through refining atmospheric models using wind data and ground-truth infrasound events. In: 28th seismic research review: ground-based nuclear explosion monitoring technologies, pp 926–935

Ottemöller L, Evers LG (2008) Seismo-acoustic analysis of the Buncefield oil depot explosion in the UK, 2005 December 11. Geophys J Int 172:1123–1134

Picone JM, Hedin AE, Drob DP, Aikin AC (2002) NRLMSISE-00 empirical model of the atmosphere: statistical comparisons and scientific issues. J Geophys Res 107(A12):1468,10.1029/2002JA009430

Posey JW, Pierce AD (1971) Estimation of nuclear explosion energies from microbarograph records. Nature 232:253

Powell T (2006a) The Buncefield investigation, First Progress Report. Technical Report, Health and Safety Commission, http://www.Buncefieldinvestigation.gov.uk

Powell T (2006b) The Buncefield investigation, Second Progress Report. Technical Report, Health and Safety Commission, http://www.Buncefieldinvestigation.gov.uk
Powell T (2006c) The Buncefield investigation, Third Progress Report. Technical Report, Health and Safety Commission, http://www.Buncefieldinvestigation.gov.uk
Press F, Harkrider D (1962) Propagation of acoustic-gravity waves in the atmosphere. J Geophys Res 67(10):3889–3908
Reed JW (1969) Climatology of airblast propagation from Nevada test site nuclear airblasts. Technical Report, Sandia Laboratories, Albuquerque
ReVelle DO, Brown PG, Spurný P (2004) Entry dynamics and aoustics/infrasonic/seismic analysis for the Neuschwanstein meteorite fall. Meteorit Planet Sci 39(10):1605–1626
Richardson JM, Kennedy WB (1952) Atmospheric winds and temperatures to 50-kilometers altitude as determined by acoustical propagation studies. J Acoust Soc Am 24(6):731–741
Sorrells GG (1971) A preliminary investigation into the relationship between long-period seismic noise and local fluctuations in the atmospheric pressure field. Geophys J R Astr Soc 26:71–82
Sorrells GG (1997) Construction of regional ground truth databases using seismic and infrasound data. Seism Res Lett 68(5):743–752
Stevens J, Divnov I, Adams D, Murphy J, Bourchik V (2002) Constraints on infrasound scaling and attenuation relations from Soviet explosion data. Pageoph 159:1045–1062
Stump BW, Hedlin MAH, Pearson DC, Hsu V (2002) Characterization of mining explosions at regional distances: implications with the international monitoring system. Rev Geophys 40(4), doi:10.1029/1998RG000048
Stump BW, Jun MS, Hayward C, Jeon JS, Che IY, Thomason K, House SM, McKenna J (2004) Small-aperture seismo-acoustic arrays: design, implementation, and utilization. Bull Seism Soc Am 94(1):220–236
Sutherland LC, Bass HE (2004) Atmospheric absorption in the atmosphere up to 160 km. J Acoust Soc Am 115(3):1012–1032, doi:10.1121/1.1631937
Thorpe AJ, Guymer TH (1977) The nocturnal jet. Quart J R Met Soc 103:633–653
Whitaker RW, Mutschlecner JP (2008) A comparison of infrasound signals refracted from stratospheric and thermospheric altitudes. J Geophys Res Doi:10.1029/2007JD008852, in press
Whitaker RW, Mutschlecner JP, Davidson MB, Noel SB (1990) Infrasonic observations of large scale HE events. Technical Report, Los Alamos National Laboratory
Whitaker RW, Sondoval TD, Mutschlecner JP (2003) Recent infrasound analysis. In: Proceedings of the 25th annual seismic research symposium, Tuscon, AZ, pp 646–654

Part IV
Atmospheric Investigations from Global Continuous Infrasound Monitoring

Chapter 20
Contribution of Infrasound Monitoring for Atmospheric Remote Sensing

A. Le Pichon, J. Vergoz, Y. Cansi, L. Ceranna, and D. Drob

20.1 Introduction

Infrasonic waves propagate in the atmosphere over very large distances in the waveguide formed by the atmosphere, its temperature gradients, and vertical wind profiles. Ducting is especially efficient in the ground to stratosphere and thermosphere waveguides. It can be reinforced or reduced by the high altitude winds (Kulichkov et al. 2004; Garcés et al. 2004; Mutschlener and Whitaker 2010; de Groot-Hedlin et al. 2010). As acoustic waves propagate in the upper atmosphere, the wavefront characteristics reveal, in addition to information about the source, significant features of the vertical structure of the winds. The interpretation of these data motivated studies on sources of infrasonic waves and their propagation in the upper atmosphere. Infrasonic waves from naturally occurring geophysical phenomena have been observed since early in the last century (Evers and Haak 2010). The interpretation of these data motivated studies on their propagation in the upper atmosphere (e.g. Rind 1978).

Interest in infrasound technology and research was revived after the Comprehensive nuclear-Test-Ban Treaty (CTBT) was adopted and opened for signature in 1996. In order to monitor compliance with the CTBT, an International Monitoring System (IMS) has been designed and is in the process of being deployed (Christie and Campus 2010). The IMS network will include sixty infrasound stations designed to detect atmospheric nuclear tests (PrepCom 1997). The design goal is a system able to detect and locate explosions with a yield equivalent to one kiloton TNT equivalent anywhere in the world with at least two stations (Christie et al. 2001). Even though the 60 station network is not yet fully established, it now provides global coverage of infrasound generated by natural phenomena (Hedlin et al. 2002). Numerous studies have demonstrated the capability of the IMS network to detect and locate large infrasound events (Campus and Christie 2010). Regular acoustic detection of large bolides has been reported (Brown et al. 2002;

A. Le Pichon (✉)
CEA, DAM, DIF, F-91297, Arpajon, France
e-mail: alexis.le-pichon@cea.fr

A. Le Pichon et al. (eds.), *Infrasound Monitoring for Atmospheric Studies*,
DOI 10.1007/978-1-4020-9508-5_20, © Springer Science+Business Media B.V. 2010

Arrowsmith et al. 2007; Revelle 2010; Edwards 2010), as well as infrasound observations of large-scale earthquakes (Mutschlecner and Whitaker 2005; Le Pichon et al. 2006a; Mutschlecner 2010), interacting open-ocean swells (Garcés et al. 2004, 2010; Le Pichon et al. 2006b; Hetzer et al. 2010), or volcanic eruptions (Wilson and Forbes 1969; Liszka and Garcés 2002). Taking advantage of new signal processing methods and efficient array design (Brachet et al. 2010), measurements of permanent sources of infrasound are now available and provide a basis for accurate atmospheric investigations (Drob et al. 2010).

In the first part, we evaluate the effects of the atmospheric dynamics on the signals routinely observed by the infrasound IMS network. In more detail, we focus on the 0.2–2 Hz frequency band where signals from atmospheric explosions are more likely to be detected (Stevens et al. 2002). Below 0.5 Hz, infrasonic waves from open-ocean swells are the prominent source of the signals detected by operating IMS arrays. These infrasonic waves, referred to as microbaroms, are related to nonlinear interaction of standing ocean waves near low-pressure systems and the resulting high ocean surface waves (Posmentier 1967; Arendt and Fritts 2000; Willis et al. 2004). In addition to information about the source, microbarom waveform characteristics reveal significant features of the vertical structure of the winds (Rind and Donn 1975). Rind (1978) rselated microbarom amplitude variability to the solar tide fluctuations in the thermosphere during winter, and stratospheric wind force during summer. Garcés et al. (2004) demonstrated that microbarom observations in Hawaii match the seasonal distribution of large swells in the Pacific and the dominant upper-wind direction up to the lower mesosphere. At larger scale, other studies highlighted a clear correlation between the prevailing direction of the stratospheric winds and microbarom arrival azimuths observed by Austral stations (Le Pichon et al. 2006b). Microbaroms are then valuable potential source for global atmospheric monitoring since pressure waves can be generated continuously over long duration, allowing investigations in the seasonal and diurnal fluctuations of the atmosphere.

In the second part, we focus on signals from volcanic eruptions. As repetitive ground truth events, volcanic eruptions are outstanding natural sources of infrasonic waves for atmospheric studies. The equivalent yield of explosive eruptions may vary from a small fraction of a kiloton of TNT, for many eruptions, up to a few Megatons for rare events such as the Mount St. Helens eruption (USA, 1980) (Donn and Balachandran 1981; Reed 1987; Delclos et al. 1990). A continuous monitoring of such signals has been proposed to address new insights on quantitative relationships between infrasonic observables and atmospheric specifications (Guilbert et al. 2005; Le Pichon et al. 2005a; Garcés and Le Pichon 2009). We concentrate on the capability of measuring small temporal wind fluctuations from the ground to the stratosphere thanks to a continuous monitoring of active volcanoes in the Vanuatu regions.

Studying the atmosphere in the 40–90 km altitude range is still a great challenge since conventional airplanes and balloons cannot reach this high altitude, which is too low for direct satellite measurements. Satellites traveling at orbital speeds encounter enough particles to burn up, and suborbital rockets are limited to studying

just one specific area before falling back to Earth. In the last part, we discuss the potential of infrasound remote sensing to provide meaningful information in the mesosphere and thermosphere where there is a lack of routine measurements.

20.2 Monitoring Ocean Swells for Continuous Stratospheric Wind Measurements

20.2.1 Deciphering the Song of the Oceans

Infrasound recordings of operating IMS arrays are routinely processed at the International Data Center (IDC) (Brachet and Coyne 2006). The wave parameters of the detected signals are calculated with the Progressive Multi-Channel Correlation Method (PMCC) (Cansi 1995). Used as a real-time detector, this method proved to be very efficient for routinely monitoring low-amplitude coherent waves within noncoherent noise. In this study, the detection results of the automatic processing for a set of IMS infrasound stations are analyzed over several years. All detections lasting several hours with a dominant frequency of 0.1–0.3 Hz and stable azimuths are identified as microbarom signals and selected from the detection bulletins.

Figure 20.1 presents the results of 5-years of continuous processing of microbaroms at stations I08BO (Bolivia) and I26DE (Germany). Microbaroms are consistently detected throughout the year with clear seasonal trend in the arrival azimuths. At I26DE, detections around 270–320° originate from ocean swells in the North Atlantic. They are mainly observed from October to June, while southwest signals are poorly detected in Bolivia. At I08BO, azimuths range between 200 and 225° from May to November, and less prominently between 130 and 155° from December to April. The Antarctic Circumpolar Current (ACC) links the major southern oceans in the 50°–60°S range. Large swell systems, driven by strong continuous eastwards surface winds, move along this peri-Antarctic belt and generate microbaroms. As for the arrival azimuths, there is an anticorrelated annual variation of the amplitude from the southern to northern hemispheres. In Bolivia, the amplitude increases during the Austral winter, while in Germany it decreases during the same period.

The seasonal transition in the bearings along with the stratospheric general circulation between summer and winter is clearly shown by Fig. 20.4 in (Garcés et al. 2010). The main bearings follow the reversal in the prevailing zonal wind direction. In the southern hemisphere, around and above the stratopause (altitude of 40–50 km), zonal winds reverse from east to west during the transition between Austral winter to summer (green and yellow curves, respectively). These results show that the empirical HWM-93 model provides a good description of the general seasonal changes. During the Austral winter, the number of detections is on average 2–3 times larger than the number of detections observed in the Austral summer. Similarly, around latitude of 50°S, stratospheric wind speeds decrease from ~80 to ~40 m/s from winter to summer. In the northern hemisphere, it is the opposite.

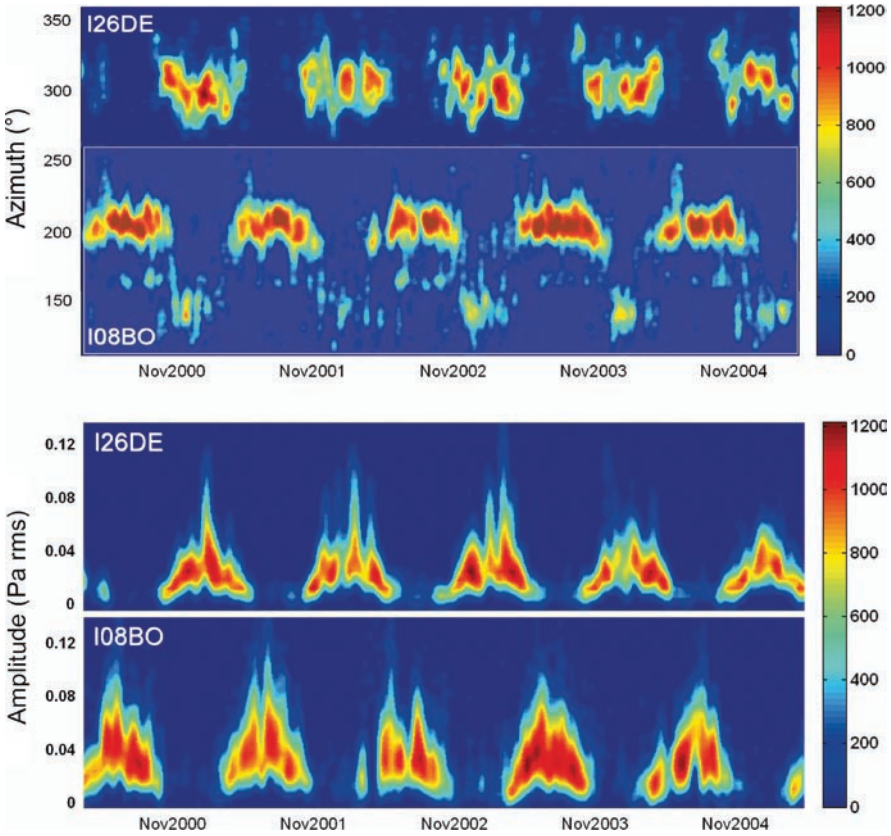

Fig. 20.1 Results of automatic PMCC processing at I08BO and I26DE in the 0.05–0.5 Hz band from June 2000 to June 2005. The *color scale* codes the number of detections. *Top*: Azimuthal variation of microbaroms. Arrival azimuths are clockwise from North. Detections at I08BO are contained within the *white rectangle*. *Bottom*: Variation of signal amplitude

20.2.2 Infrasound Globally Driven by the Stratospheric General Circulation

Such trends in the observations are confirmed on a global scale. A cumulated yearly summary of the IDC detection results from 2004 to 2008 is presented in Fig. 20.2. Depending on the detection capability of each station, which varies according to local meteorological conditions and the deployment environment, the averaged daily number of detections ranges between 10 and 400. Microbarom signals are consistently detected throughout the year at all IMS stations. In the northern hemisphere, detections mainly originate from ocean swells in the Pacific, Atlantic, and Indian oceans. In the southern hemisphere, the main sources of signals are the large swell systems driven by strong continuous eastwards surface winds along the ACC,

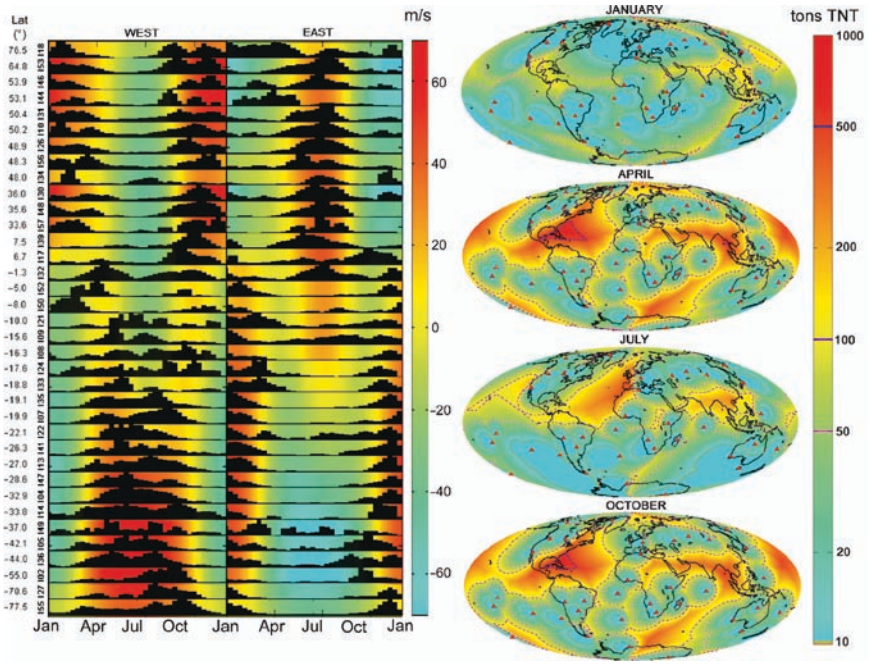

Fig. 20.2 Infrasound globally driven by the stratospheric general circulation. *Left*: Annual variations of 4-year cumulative distributions of the IDC detections with frequency lower than 2 Hz. The 36 IMS stations are sorted by increasing latitude. WEST/EAST: Eastwards (arrival azimuths from 180 to 360°) and westwards (from 0 to 180°) propagation, respectively. At each station site, the eastwards and westwards yearly variation of the HWM-93 zonal wind at 50 km altitude are superimposed to the detections with color referring to the stratospheric wind strength (positive values toward East, in m/s). The HWM-93 empirical model provides time-dependent estimates of vertical wind profiles, and accounts for the major seasonal variations (Hedin et al. 1996). As a result of the seasonal zonal wind reversals in the stratosphere, clear seasonal variations of back-azimuths are observed. In the northern hemisphere and during summer (from June to August), signals from easterly directions dominate and vice versa during winter (from November to January). In the southern hemisphere, it is the opposite. *Right*: Threshold maps of the IMS network composed of 36 stations using HWM-93 and a uniform wind noise of 0.02 Pa distribution at all stations on the 1st of January, April, July, and October 2003. The *red triangles* indicate the location of the 36 IMS stations. This indicates the geographical coverage of the minimum energy detectable by at least one IMS station (in ton of TNT-equivalent). The threshold intervals are logarithmically spaced (Le Pichon et al., 2008)

showing approximately a 6-month delay. The seasonal variation in the number of detections is well correlated with the variation of the stratospheric wind strength along the source-receiver path, while perturbations from this seasonal trend can either be related to short time-scale variability of the atmosphere, or explained by changes in the nature of the source (amount of ocean swell energy, local sources). This global scale analysis confirms that the primary factor controlling the signal detectability is the seasonal variability of the prevailing zonal wind, since at most arrays, ~80% of the detections in the 0.2–2 Hz bandpass are associated with propagation downwind of the dominant stratospheric wind direction.

As microbaroms are permanently detected on a global scale, they provide means to evaluate the detection capability of the IMS network throughout the year. Figure 20.2 compares the geographical coverage of the minimum energy detectable by at least one station and a uniform noise distribution at different periods of the year using the current 36 station network. The Appendix details the methodology used to compute the detection capability maps. The yearly summary of the IDC detection lists is consistent with the yearly variations of the one-station coverage detection capability, which follow the general stratospheric wind circulation. These comparisons show that the empirical wind model used explains well the eastward and westward detections. During the transition between winter and summer, the observed bearing transitions are driven by the seasonal reversal of the stratospheric winds. During Austral winter months, downwind propagation yields a significant enhancement of the performance and explains the dominant westwards and eastwards bearings in the northern and southern hemispheres, respectively. During summer months, it is the opposite. A significant performance enhancement is predicted in January and July when the steady prevailing stratospheric jet currents favor long-range propagation. During the transition between winter and summer, zonal winds reduce and reverse, yielding higher detection thresholds. The larger spatial gradients of the threshold values are explained by the unstable and much weaker stratospheric wind strength during these periods, causing the detectability to drop at a greater rate with increasing range from a given station. For some geographical areas and at a given time of the year, depending on the stratospheric wind model used, thresholds may vary in a range of 200 tons.

20.3 Multiyear Validation of Upper-Wind Models

20.3.1 Context and Observations

The I22FR IMS infrasound array installed in New-Caledonia continuously detects coherent infrasonic waves originating from active volcanoes in the Vanuatu region. The Vanuatu archipelago, located in the South Pacific between New-Caledonia and Fiji, is composed by more than 80 islands. Although the large majority of volcanoes in that tectonic context produce an explosive activity with silicic magmas, magmas emitted around Vanuatu are largely basaltic, but more viscous, allowing explosions at their vents (Robin and Monzier 1994; Lardy et al. 1999). The three most active volcanoes of Vanuatu present various degrees in explosivity (Fig. 20.3). The Lopevi volcano (16.50°S, 168.34°E) produces pyroclastic flows as well as Strombolian and Vulcanian explosions (Lardy et al. 1999; Vergniolle and Brandeis 1996). Ambrym (16.25°S, 168.12°E, ~10 km wide) is the most voluminous active volcano in Vanuatu. It produces the largest magma volume, with more than 50 eruptions reported since 1774 (Robin and Monzier 1994). Although eruptions have been explosive in the past, the current activity consists in a lava lake; a cooler layer of magma slowly develops at the surface until that thin layer is disrupted by the arrival

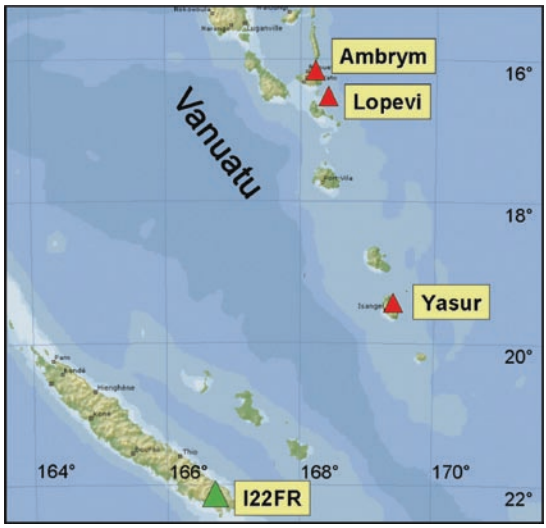

Fig. 20.3 Geographic situation of the Archipelago of Vanuatu in Oceania. The green triangle indicates the location of the I22FR infrasound station (22.19°S, 166.84°E). This station consists of four MB2000-type microbarometers, 1–3 km apart. The three most active volcanoes of Vanuatu indicated by the *red triangles* (Map source: Encarta) are Lopevi (16.50°S, 168.34°E, 1,410 m high, azimuth of 14.3°N from I22FR), Ambrym (16.25°S, 168.12°E, 1,330 m high, azimuth of 11.8°N from I22FR), and Yasur (19.52S, 169.42E, 360 m high, azimuth of 42.7°N from I22FR) (Le Pichon et al. 2004)

of large bubbles. Yasur (19.52S, 169.42E), after 800 years of continuous activity (McClelland et al. 1989), is now producing a series of explosions. The nearest one, Yasur, is located at 399 km to the north-northeast (42.7° clockwise from North) of I22FR. It produces a series of explosions, whose characteristics vary between Strombolian and mild-Vulcanian (McClelland et al. 1989). These are triggered by the sudden decompression of the inner magmatic gas, which expels magma fragments at the vent with large velocities. Its regular activity (several hundred explosions per day are generally measured) combined with its accessibility makes it one of the most studied volcanos (geological, seismic, and thermal surveys).

Figure 20.4 presents the results of continuous PMCC processing of the background noise continuously recorded by I22FR. Due to the geographic situation of I22FR, most of the detected infrasonic waves are produced by standing ocean waves near low-pressure systems in the south Pacific. From 0.1 to 0.3 Hz, microbaroms are permanently observed and their monitoring over 1 year exhibits a clear seasonal trend correlated with changes in the stratospheric wind direction (Sect. 20.2). From 0.2 to 2 Hz, for azimuths ranging from 0 to 50°, permanent detections from Ambrym, Lopevi, and Yasur are observed. As for microbaroms, seasonal changes in the bearings of these signals are noted. From austral summer to austral winter, the azimuth variations approach 8° and 15° for Yasur and Lopevi, respectively. Due to the low particle density and nonlinear dissipation in the upper

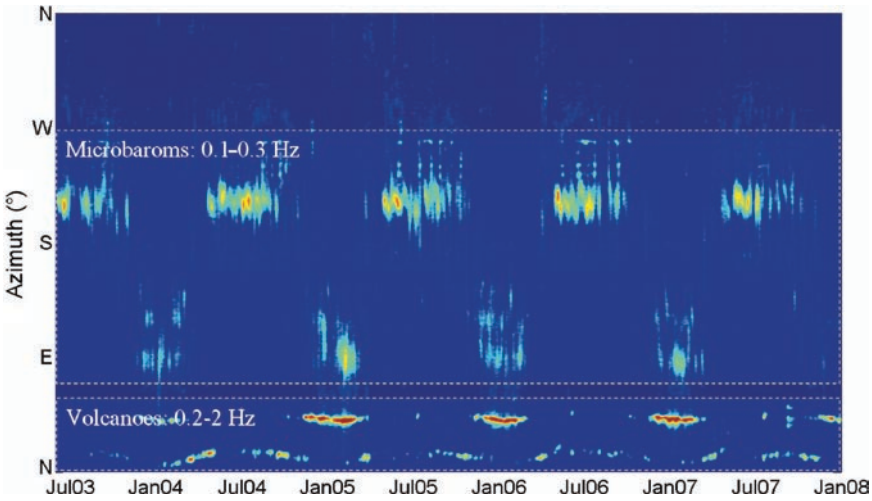

Fig. 20.4 Results of continuous automatic processing of infrasonic waves at I22FR in the [0.1–4] Hz band showing the temporal variation of the arrival azimuths from June 2003 to January 2008. Color refers to the number of detections per day (*dark blue* and *red colors* correspond to 0 and 200 detections per day, respectively)

atmosphere, thermospheric returns are strongly attenuated at a range of hundreds of kilometers. Considering the relative high frequency content of the measured signals from Yasur (greater than 1 Hz), thermospheric arrivals are unlikely because of severe absorption in the upper atmosphere (Bass and Sutherland 2004). Thus, most of the acoustic energy propagates in the stratospheric duct. A multiyear monitoring of Yasur has been proposed to investigate the effects of seasonal and short-time scale atmospheric changes on the propagation, as well as to consistently validate the Naval Research Laboratory Ground to Space (NRL-G2S) semi-empirical atmospheric model up to the stratosphere (Antier et al. 2007).

20.3.2 Propagation Modeling

The long range propagation is simulated using the windy atmospheric sonic propagation ray theory-based method (WASP-3D), which accounts for the spatio-temporal variations of the horizontal wind terms along the ray paths in spherical coordinates (Virieux et al. 2004). This method provides all needed kinematic parameters of each ray (travel time, incidence angle, azimuthal deviation) for comparisons with measurements. The NRL-G2S model was run to provide a self-consistent climatological database in the Vanuatu region from May 2003 to May 2006, at 6-h intervals (Drob et al. 2003). The atmospheric profiles are defined over a grid ranging from 164 to 170°E in longitude, 14 to 24°S in latitude, and 0 to 170 km in altitude with a step resolution of 1°. Following a shooting procedure, simulations are carried out with ray parameters (slowness values) derived from the measured horizontal trace velocities. Ray trajectories are calculated each day at 0, 6, 12, and

18 h UT. Only rays with bounces contained within a circle of radius 50 km centered on I22FR are selected. This range allows focusing on all rays reaching the array for comparisons with measurements.

Figure 20.5 presents the observed azimuth of the infrasonic waves generated by Yasur as detected at I22FR. Measurements are compared to ray tracing results from September 2003 to May 2007 along with the temporal variation of the NRL-G2S

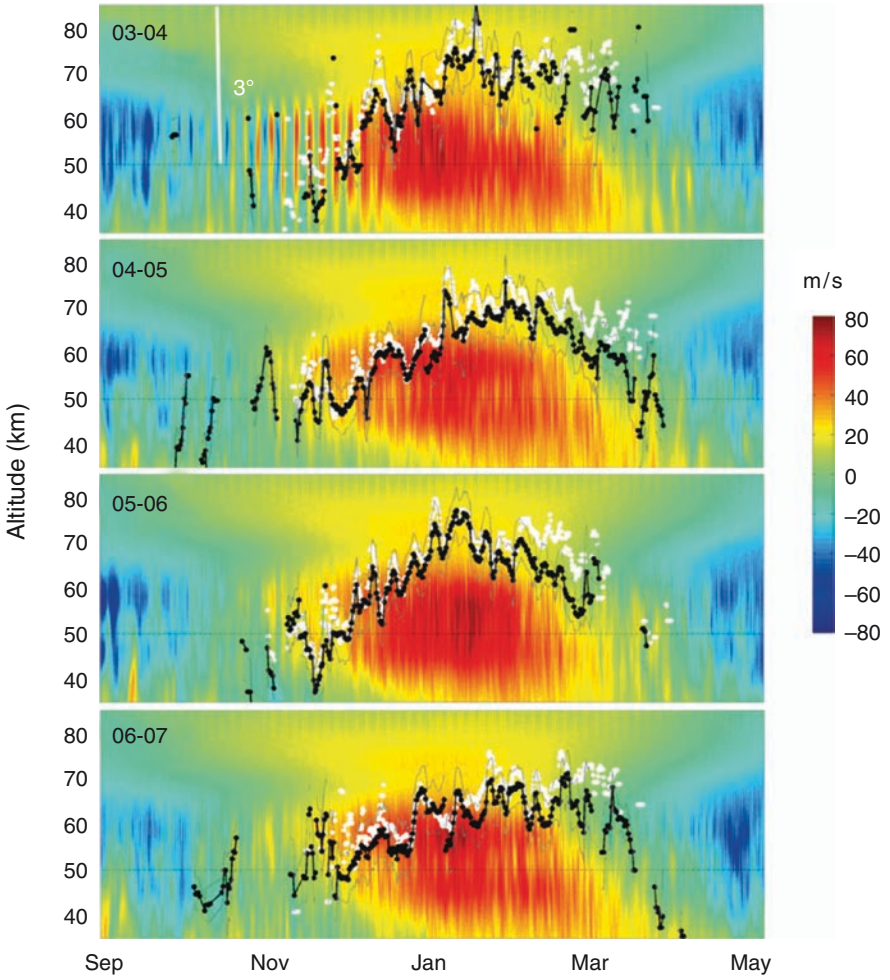

Fig. 20.5 Comparisons between the observed and simulated arrival azimuths of signals from Yasur. Temporal variation of the azimuthal deviation (*white y*-scale on the *left*) from September 2003 to May 2007, superimposed on the vertical structure of the G2S sound speed corrected for the wind in the propagation direction, relative to the sound speed at the ground level (color scale on the *right*). The *black dotted lines* indicate the true bearing of Yasur as seen from I22FR (42.7°). *Black* and *white dots* are the PMCC and ray tracing results, respectively. The *gray* lines indicate the range of uncertainties of the measured azimuths. Simulations are carried out each 6 h. Measurements are averaged over consecutive periods of length 6 h

effective sound speed (wind-corrected sound speed along the propagation path). During the austral summer, from November to March, the prevailing westward winds allow the formation of a stratospheric waveguide below 40–50 km altitude. Due to the seasonal variations in the strength of the transverse wind component, the apparent arrival direction of these waves does not correspond to the original launch direction. The large observed variations in the bearing of the detected signals are mainly driven by the reversibility of the zonal stratospheric wind with season. From summer to winter, the amplitude of the observed azimuthal deviation approaches 5°. From November to January, the azimuth decreases from 43 to 39° when the zonal winds are the strongest, before rising up to the true bearing (42.7°) in March when stratospheric winds reverse. Comparison between the observed and the predicted azimuths shows a similar seasonal trend. Furthermore, the simulation results are in very good agreement with the observations even down to time scale of a few days. The errors are generally lower than 0.5° (less than 0.2%) for more than 90% of the time.

The simulation results accurately explain seasonal changes as well as short-time scale variations of the infrasonic observables. Second-order azimuthal oscillations are observed and well predicted down to a time scale of a few days. They are associated to modulations of the general circulation in the stratosphere. In our region of interest, zonal wind reversals often result from significant quasi-stationary subtropical planetary waves. Such disturbances are formed in connection with large stationary ridges in the polar winter stratospheric wind jet (Le Pichon et al. 2005a).

20.4 How Infrasound can Probe High-Altitude Winds?

20.4.1 Where Models Fail to Explain the Observations

Even though good agreements were found between observations and simulations (Fig. 20.5), some discrepancies can be noted. Noticeable gaps are found at the end of the downwind season when winds reverse (in March–April). Furthermore, for some periods (e.g. October–November 2007), no stratospheric return is predicted though clear signals from Yasur are observed. Also, at the end of the austral summer, the azimuthal deviation bias in the February–March time frame needs to be understood. Although there is not a complete set of detections throughout the year, there is some indication – though questionable in terms of statistical significance – that the azimuthal deviations are underpredicted during the eastward stratospheric wind phase and overpredicted during the westward stratospheric wind phase, with good agreement during the reversals. This could, thus, be explained by an over/under estimation of the specified stratospheric wind magnitudes for which a correction could be made. Further studies should investigate the origin of these discrepancies. For example, one could extract the temperature profile from the NASA missions in the mesosphere and lower thermosphere (MLT) regions (http://stp.gsfc.

nasa.gov/) for comparison with the background specifications utilized for the propagation calculations.

It is important to note that the instantaneous atmospheric conditions deviate from the climatological average on a daily basis, especially in a range of altitude (50–110 km) that is inaccessible to operational ground-based weather stations and meteorology satellites. The largest part of the observed discrepancies between the observations and the theory can be explained by either the underestimation of the wind speed between the stratopause and the lower thermosphere, or the inaccuracy of the current predictions of stratospheric wind velocities. Compared to the strong temporal variability of the upper wind fields, the sound speed variations induced by temperature changes are of second order (Hedin et al. 1996); an increase of 50 m/s in the sound speed would correspond to a temperature variation greater than 80°C, which is unrealistic at short-time scales. Given the advanced state of numerical weather prediction systems, it is assumed that the wind fields below 50 km are essentially correct. Above 120 km, the influence of the solar heating on the atmospheric circulation is also well described (Picone et al. 2002; Drob et al. 2003).

20.4.2 Inversion of Infrasound Measurements

We focus here on the development of inversion procedures in order to retrieve the wind profile in the MLT. As a first attempt, a basic inversion routine has been proposed to delineate the vertical structure of the wind field (Le Pichon et al. 2005b). We apply scaled Gaussian correction factors to the prevailing zonal wind component, centered at 80 km with a half width of 30 km. An iterative algorithm is used for the correction of NRL-G2S winds (Coleman and Li 1996). Winds are then adjusted in order to minimize residuals between the observed and predicted azimuthal deviations. The process stops when, after convergence, residuals become less than 0.2°. The final solution fuses the initial NRL-G2S model (0–50 km and 110–180 km) with the reconstructed wind profiles (50–110 km) using B-spline functions.

The temporal variations of the observed azimuthal deviations from the Lopevi volcano located to the north of the station are used for monitoring the fluctuations of the zonal wind. The result of the inversion shows that the original wind model underestimates the speed of the mesospheric wind jet by at least 20 m/s for extended periods of time; the largest differences amounting to around 50 m/s (Fig. 20.6). Furthermore, the strong wind region in the stratosphere should be extended to the lower-thermosphere with wind speeds approaching 100 m/s. Quasi-stationary subtropical disturbances are found to extend to higher altitudes. For example, between the 5th and 20th of August 2003, wind reversals from −20 to 20 m/s are observed in the 40–55 km region, thereby breaking the seasonal trend in zonal wind direction (Fig. 20.6a). An extension of this large circulation cell up to 70–80 km provides here a good match between the measured and simulated azimuthal deviation (black arrow on Fig. 20.6b). More generally, naturally occurring stochastic variations in the mesosphere are overshadowed by the seasonal variations

of the original NRL-G2S model. In particular, the steady eastward wind jet predicted by available wind models during the Austral summer in the lower thermosphere (~120 km, Fig. 20.6a) is replaced by a series of fluctuating irregular wind cells (Fig. 20.6b).

These results show that propagation modeling above the stratosphere cannot be accurately carried out with the current atmospheric models. The use of infrasound inversion as described here to retrieve the fine temporal fluctuations of the upper atmospheric winds provides a foundation for more realistic azimuth and travel time estimates. This, in turn, will result in a significant reduction in the errors in source

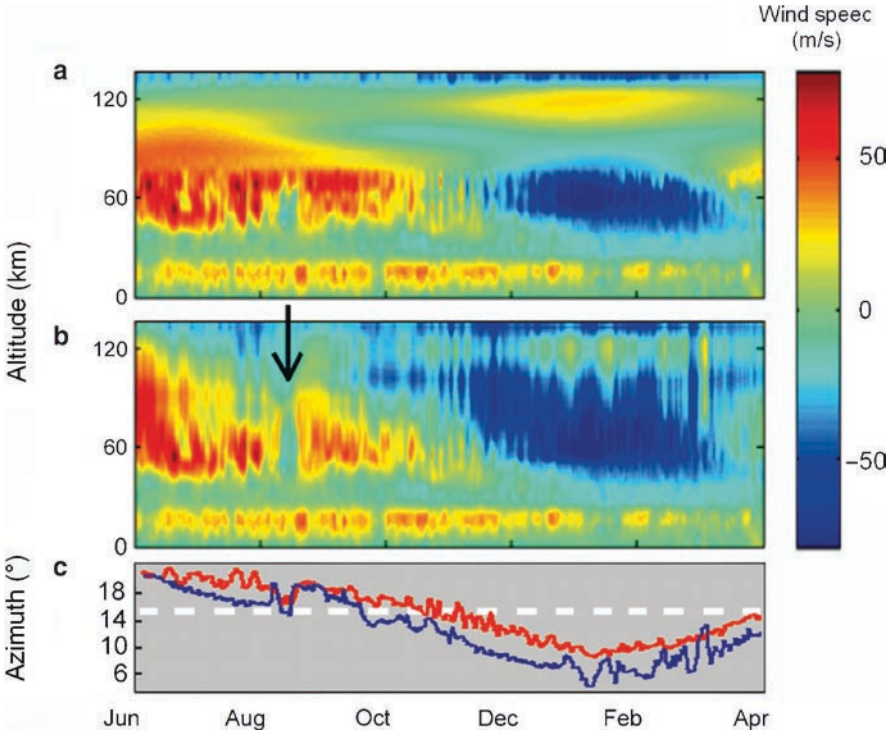

Fig. 20.6 Seasonal correction of the NRL-G2S zonal winds using infrasonic measurements from the Lopevi volcano from June 2003 to April 2004. Winds are specified at 12 h UT (night time in New-Caledonia), when noise levels at the infrasonic array are lowest and allow good detectability. (**a**) Original wind profiles; the artificial junction lines at 65 and 110 km between the smoothed HWM-93 empirical and the NRL-G2S models are clearly seen. (**b**) Result of the inversion. The original model underestimates the speed of the mesospheric wind jet while stochastic variations are reconstructed. (**c**) Measured and predicted azimuths using the corrected wind model (*red* and *blue curves*, respectively) compared to the true azimuth of the volcano (14.3°, *white dashed line*) (Le Pichon et al. 2005)

location procedures. It is also worth noting that these results indicate that a general enhancement of the winds above the stratosphere may lead to the formation of previously unrecognized mesospheric waveguides. More studies like the one presented here will better determine the role of different factors that influence propagation predictions and could estimate more precisely how large are the errors in the upper wind models. Ideally, the amplitude of a number of empirically derived vertical eigenfunctions can be estimated from infrasonic measurements, and the physical self-consistency of the inferred atmospheric corrections could be improved by including additional infrasonic observables.

20.5 Concluding Remarks

Infrasound signal from ocean swells can be used as a natural source for continuous measurements of high-altitude winds over propagation ranges that exceed several thousands of kilometers. We suggest that the cyclical variations of microbarom azimuths essentially result from seasonal zonal wind reversals in the 35–50 km range, since for large ranges thermospheric returns are strongly attenuated, and tropospheric ducts are unstable due to the high variability of the wind in that region. The analysis of the IDC detection results for 36 IMS stations over a 4-year period clearly reveals seasonal transitions in the dominant bearing. A global scale comparison with empirical stratospheric wind models confirms that long-range infrasound propagation is essentially driven by the seasonal zonal wind reversals in the stratosphere. Simulations of detection capability maps explain these trends and point out the strong influence of the stratospheric wind on the network performance. In order to get more realistic thresholds, site, time, and frequency-dependent noise models, as well as improved specifications of high-altitude winds (Drob et al. 2003) should be incorporated in the calculations (Clauter and Blandford 1997; Bowman et al. 2005; Le Pichon et al. 2008).

In conjunction with other technologies, microbaroms may yield further information on the seasonal and short time-scale variability of the atmosphere below ~50 km. By taking advantage of new signal processing methods and recent advances in modeling techniques, continuing investigations into global monitoring of natural infrasound may allow continuous, passive acoustic tomography of the stratosphere and lower mesosphere. Furthermore, it is expected that a global monitoring of microbaroms could detect stratospheric warming at mid and high latitudes, which significantly affects the structure of the stratospheric waveguide.

From the multiyear monitoring of active volcanoes and propagation modeling results, we can safely say that the Tropospheric/Stratospheric Numerical Weather Prediction analysis fields incorporated into the G2S specifications provide a faithful representation of the atmosphere up to ~50 km. The simulation results presented here provide a good description of the general seasonal changes as well as short-time scale fluctuations of the measurements. Such signals can capture the atmospheric variations with a higher level of detail since smaller oscillations associated to large scale propagating stratospheric planetary waves are well predicted – e.g., errors generally remain lower than 0.5° for the azimuthal deviation. For large

propagation range, most of the acoustic energy produced by the ocean swells and active volcanoes efficiently propagates in the stratospheric duct due to very weak attenuation. Thus, one can expect that the use of appropriate propagation tools along with the NRL-G2S specifications would provide accurate enough simulations for most infrasound observations in the frequency range of interest to detect atmospheric explosion.

A continuous infrasound monitoring of active volcanoes has been proposed as a remote sensing method of the upper atmosphere. A first attempt has been carried out to adjust the vertical structure of the wind in the upper stratosphere and mesosphere. Although a rigorous statistical analysis of the inversion procedure is needed (Drob et al. 2010), the first results of the inversion suggest that the speed of the mesospheric wind jet in the climatological wind model is significantly underestimated, and the strong wind region in the stratosphere should be extended to the lower thermosphere.

Combined with all available MLT observations, such as those already provided by the NASA thermosphere, ionosphere, and mesosphere energetics and dynamics (TIMED) mission, it is expected that a global infrasound tomography would help to develop better predictive atmospheric models and could be of considerable value for climate change studies and applications to the space industry.

These observations will probably occur more frequently in the future because of the increasing number of IMS stations being deployed. Continuing investigations into natural and permanent sources of infrasound as detected by the IMS network will better determine the role of different factors that influence propagation predictions and could help to estimate more precisely how large the errors in the upper wind models are. More studies like the ones presented here will also certainly help advance the development of automated source location procedures for operational infrasound monitoring.

Acknowledgement The authors are grateful to Drs. E. Blanc and J. Guilbert from CEA/DASE for their interests in these studies and helpful discussions, and Dr. Nicolas Brachet from CTBTO PTS/IDC for providing bulletins. We would also like to thank the NASA Goddard Space Flight Center, Global Modeling and Assimilation Office (GSFC-GMAO), and the NOAA National Centers for Environmental Prediction (NCEP) for providing the NWP data that went into the NRL-G2S atmospheric specifications. Support was also provided by Institut de Physique du Globe de Paris, Coordination de la Recherche Volcanologique, and Ministère de l'Ecologie et Développement Durable to install instruments close to the Yasur volcano.

Appendix

In order to estimate the detection capability of a geographically distributed network of stations, it is essential to predict the amplitude of an infrasound signal at any location, and to further evaluate whether the signal is detectable above the noise levels at the recording stations. Assuming that the signals of interest are produced by high explosive tests, we use for the yield estimation the scaling relation derived

from the LANL database covering charge weights of ~20–4,880 tons (Whitaker et al. 2003),

$$P_{\mathrm{wca}} = 5.95\times10^{4}(\mathrm{SR})^{-1.4072}, \tag{A. 1}$$

where P_{wca} is the wind corrected pressure and SR is the scaled range (in km) between station and receiver. P_{wca} is calculated from the observed peak-to-peak pressure (in microbars) at the dominant period of a stratospheric infrasound arrival, P_{raw}, using,

$$P_{\mathrm{wca}} = P_{\mathrm{raw}}10^{-0.018V_{\mathrm{s}}}, \tag{A. 2}$$

where V_{s} is the along-path horizontal component of the wind speed (in m/s) at an altitude of 50 km. To estimate V_{s}, the along-path stratospheric wind component is extracted at each node of the source grid along the great circle arc, and the mean is calculated. The scaled range, SR, is defined as,

$$\mathrm{SR} = \frac{R}{\sqrt{2\times E}}, \tag{A. 3}$$

where R is the source to receiver range (in km) and E is the charge weight (in kt). Overall, it follows from (20.1) to (20.3),

$$E_{\mathrm{min}} = 8.1871\times10^{-8}\times P_{\mathrm{threshold}}^{1.4213}\times R^{2}\times10^{-0.0256V_{\mathrm{s}}}, \tag{A. 4}$$

where E_{min} is the minimum detectable charge weight for a measured amplitude $P_{\mathrm{threshold}}$ of a coherent signal.

To evaluate the detection capability of the IMS network, we consider the constraints on evaluating the smallest measurable signal amplitude $P_{\mathrm{threshold}}$ at the receivers.

Due to the high sensitivity of infrasound stations to a large variety of signals including coherent signals with very low SNR, and in order to minimize the number of missed events and reduce the false alarm rate, we set a minimum value for SNR equal to 1 for all stations (Evers and Haak 2004). As the SNR value is taken equal to 1, $P_{\mathrm{threshold}}$ in (20.4) is in essence the background noise level.

The detection capability is estimated using a $1^{\circ}\times1^{\circ}$ source grid covering the globe. For one specific date and time, the stratospheric wind is averaged along the great circle path between each grid node location (i, j) and each array (k). From (20.4), we compute $E_{\mathrm{min}[k']}(i, j)$, where $(1\le k'\le N)$ is the index of sorted values of energy. For sources located with a threshold of N stations, the minimum detectable energy is given by $E_{\mathrm{min}[k'=N]}(i, j)$.

For the 36 station network, we consider a time independent and geographically uniform noise distribution of 0.02 Pa RMS. This value corresponds to the average noise level for frequencies greater than 0.5 Hz and local wind speeds generally lower than 2 m/s (Bowman et al. 2005). The stratospheric wind term V_{s} (20.4) is derived from HWM-93. Using these parameters, the network performances with one-station coverage are simulated.

References

Antier K, Le Pichon A, Antier K, Vergniolle S, Zielinskin C, Lardy M (2007) Multi-year validation of the NRL-G2S wind fields using infrasound from Yasur. J Geophys Res 112:D23110. doi:10.1029/2007JD008462

Arendt S, Fritts D (2000) Acoustic radiation by ocean surface waves. J Fluid Mech 415:1–21

Arrowsmith SJ, Drob DP, Hedlin MAH, Edwards W (2007) A joint seismic and acoustic study of the Washington State bolide: observations and modeling. J Geophys Res 112, doi:10.1029/2006JD008001

Bass HE, Sutherland LC (2004) Atmospheric absorption in the atmosphere up to 160 km. J Acoust Soc Am 115:1012–1032

Bowman JR, Baker GE, Bahavar M (2005) Ambient infrasound noise. Geophys Res Lett 32, 10.1029/2005GL022486

Brachet N, Coyne J (2006) The current status of infrasound data processing at the international data Centre. In: Proceeding of the 28th seismic research review: ground-based nuclear explosion monitoring technologies, Orlando

Brachet N, Brown D, Le Bras R, Mialle P, Coyne J (2010) Monitoring the earth's atmosphere with the global IMS infrasound network. This volume, pp. 73–114

Brown PG, Whitaker RW, ReVelle DO, Tagliaferri E (2002) Multi-station infrasonic observations of two larges bolides: Signal interpretation and implications for monitoring of atmospheric explosions. Geophys Res Lett 29, doi:10.1029/2001GL013778

Campus P, Christie DR (2010) Worldwide observations of infrasonic waves. This volume, pp. 181–230

Cansi Y (1995) An automatic seismic event processing for detection and location: the PMCC method. Geophys Res Lett 22:1021–1024

Christie DR, Veloso V, Campus P, Bell M, Hoffmann T, Langlois A, Martysevich P, Demirovic E, Carvalho J (2001) Detection of atmospheric nuclear explosions: the infrasound component of the International Monitoring System. Kerntechnik 66:96–101

Christie DR, Campus P (2010) The IMS infrasound network: design and establishment of infrasound stations. This volume, pp. 27–72

Clauter DA, Blandford RR (1997) Capability modeling of the proposed International Monitoring System 60-Station infrasonic network. In: Proceedings of the infrasound workshop for CTBT monitoring, LA-UR-98-56, Santa Fe, New Mexico

Coleman TF, Li Y (1996) An interior, trust region approach for nonlinear minimization subject to bounds. SIAM J Optim 6:418–445

Delclos C, Blanc E, Broche P, Glangeaud F, Lacoume JL (1990) Processing and interpretation of microbarograph signals generated by the explosion of Mount St. Helens. J Geophys Res 95:5485–5494

de Groot-Hedlin CD, Hedlin MAH, Drob DP (2010) Atmospheric variability and infrasound monitoring. This volume, pp. 469–504

Donn WL, Balachandran NK (1981) Mount St. Helens eruption of 18 May 1980: air wave and explosive yield. Science 213:539–541

Drob DP, Picone JM, Garcés M (2003) The global morphology of infrasound propagation. J Geophys Res 108, doi:10.1029/2002JD003307

Drob DP, Meier RR, Picone JM, Garcés MM (2010) Inversion of infrasound signals for passive atmospheric remote sensing. This volume, pp. 695–726

Edwards WN (2010) Meteor generated infrasound: theory and observation. This volume, pp. 355–408

Evers LG, Haak HW (2004) The detectability of infrasound in the Netherlands from the Italian volcano Mt. Etna. J Atmos Sol Terr Phys 67, doi:10.1016/j.jastp.2004.09.002

Evers LG, Haak HW (2010) The characteristics of infrasound, its propagation and some early history. This volume, pp. 3–26

Garcés M, Le Pichon A (2009) Infrasound: applications for earthquakes, tsunamis and volcanoes. In: Lee WHK (ed) Springer section on earthquakes, tsunamis, and volcanoes, Encyclopedia of complexity and systems science (in press)

Garcés M, Willis M, Hetzer C, Le Pichon A, Drob DP (2004) On using ocean swells for continuous infrasonic measurements of winds and temperature in the lower, middle, and upper atmosphere. Geophys Res Lett 31, doi:10.1029/2004GRL020696

Garcés M, Willis M, Le Pichon A (2010) Infrasonic observations of open ocean swells in the Pacific: deciphering the song of the sea. This volume, pp. 231–244

Guilbert J, Prih Harjadi PJ, Heritier T, Le Pichon A (2005) The first results of infrasound array in Kalimantan: an original approach for an automatic bulletin of volcanic activity in Indonesia, European Geophysical Union Meeting, 7, Abstract A-09100, Vienna

Hedin AE, Fleming EL, Manson AH, Schmidlin FJ, Avery SK, Clark RR, Franke SJ, Fraser GJ, Tsuda T, Vial F, Vincent RA (1996) Empirical wind model for the upper, middle and lower atmosphere. J Atmos Terr Phys 58:1421–1447

Hedlin MAH, Garcés M, Bass H, Hayward C, Herrin G, Olson J, Wilson C (2002) Listening to the secret sounds of earth's atmosphere. EOS 83:564–565

Hetzer CH, Gilbert KE, Waxler R, Talmadge CL (2010) Generation of microbaroms by deep-ocean hurricanes. This volume, pp. 245–258

Kulichkov SN, Avilov KV, Popov OE, Otrezov AI, Bush GA, Baryshnikov AK (2004) Some results of simulation of long-range infrasonic propagation in the atmosphere. Izv Atmos Ocean Phys 40:202–215

Lardy M, Priam R, Charley D (1999) Lopévi : Résumé de l'activité historique et de l'activité récente, LAVE, Technical Report 77, ORSTOM, New-Caledonia, Nouméa, 5pp

Le Pichon, A., E. Blanc, D. Drob, S. Lambotte, J. X. Dessa, M. Lardy, P. Bani, and S. Vergniolle, Infrasound monitoring of volcanoes to probe high-altitude winds, J. Geophys. Res., 110, D13106, DOI:10.1029/2004JD005587

Le Pichon, A., E. Blanc, and D. Drob, Probing high-altitude winds using infrasound, J. Geophys. Res., 110, D20104, DOI:10.1029/2005JD006020

Le Pichon A, Blanc E, Drob D, Lambotte S, Dessa JX, Lardy M, Bani P, Vergniolle S (2005a) Infrasound monitoring of volcanoes to probe high-altitude winds. J Geophys Res 110:D13106. doi:10.1029/2004JD005587

Le Pichon A, Blanc E, Drob D (2005b) How can infrasound listen to high-altitude winds? J Geophys Res 110:D20104. doi:10.1029/2005JD006020

Le Pichon A, Mialle P, Guilbert J, Vergoz J (2006a) Multi-station infrasonic observations of the Chilean earthquake of June 13, 2005. Geophys J Int 167:838–844

Le Pichon A, Ceranna L, Garcés M, Drob DP, Millet C (2006b) On using infrasound from interacting ocean swells for global continuous measurements of winds and temperature in the stratosphere. J Geophys Res 111, doi:10.1029/2005JD006690

Le Pichon A, Vergoz J, Blanc E, Guilbert J, Ceranna L, Evers LG, Brachet N (2009) Assessing the performance of the International Monitoring System infrasound network: Geographical coverage and temporal variabilities. J Geophys Res 114, D08112, doi:10.1029/2008JD010907

Le Pichon A, Vergoz J, Cansi Y, Ceranna L, Drob D (2010) Contribution of infrasound monitoring for atmospheric remote sensing. This volume, pp. 623–640

Liszka L, Garcés MA (2002) Infrasonic observations of the Hekla eruption of February 26, 2000. J Low Freq Noise Vib 20:1–8

McClelland L, Simkin T, Summers M, Nielsen E, Stein TC (1989) Global volcanism: 1975–1985. Prentice-Hall, Englewood Cliffs, NJ 655 pp

Mutschlecner JP, Whitaker RW (2005) Infrasound from earthquakes. J Geophys Res 110, doi:10.1029/2004JD005067

Mutschlecner JP, Whitaker RW (2010) Some atmospheric effects on infrasound signal amplitudes. This volume, pp. 449–468

Picone JM, Hedin AE, Drob D, Aikin AC (2002) NRLMSISE-00 empirical model of the atmosphere: statistical comparisons and scientific issues. J Geophys Res 107, doi:10.1029/2002JA009430

Posmentier E (1967) A theory of microbaroms. Geophys J R Astr Soc 13:487–501

Preparatory Commission for the Comprehensive Nuclear-Test-Ban Treaty Organization (PrepCom) (1997) Comprehensive Nuclear-Test-Ban Treaty (CTBT). V.97-28276, Austria, 139pp
Reed JW (1987) Air pressure waves from Mount St. Helens eruptions. J Geophys Res 92:11979–11992
Revelle DO (2010) Acoustic-gravity waves from impulsive sources in the atmosphere. This volume, pp. 301–354
Rind D (1978) Investigation of the lower thermosphere results of ten years of continuous observations with natural infrasound. J Atmos Terr Phys 40:1199–1209
Rind D, Donn WL (1975) Further use of infrasound as a continuous monitor of the upper-atmosphere. J Atmos Sci 32:1694–1704
Robin C, Monzier M (1994) Volcanics hazards in Vanuatu, Technical Report 16, ORSTOM Geology and Geophysics, New-Caledonia, Nouméa, 15pp
Stevens JL, Divnov II, Adams DA, Murphy JR, Bourchik VN (2002) Constraints on infrasound scaling and attenuation relations from soviet explosion data. Pure Appl Geophys 159:1045–1062
Vergniolle S, Brandeis G (1996) Strombolian explosions: a large bubble breaking at the surface of a lava column as a source of sound. J Geophys Res 101:433–448
Virieux J, Garnier N, Blanc E, Dessa JX (2004) Paraxial ray-tracing for atmospheric wave propagation. Geophys Res Lett 31, DOI:10.1029/2004GL020514
Willis M, Garcés M, Hetzer C, Businger S (2004) Infrasonic observations of open ocean swells in the Pacific: deciphering the song of the sea. Geophys Res Lett 31, doi:10.1029/2004GL020684
Whitaker RW, Sondoval TD, Mutschlecner JP (2003) Recent infrasound analysis. In: Proceedings of the 25th seismic research review – nuclear explosion monitoring, Tucson, Arizona
Wilson CR, Forbes RB (1969) Infrasonic waves from Alaskan volcanic eruption. J Geophys Res 74:4511–4522

Chapter 21
Global Scale Monitoring of Acoustic and Gravity Waves for the Study of the Atmospheric Dynamics

E. Blanc, A. Le Pichon, L. Ceranna, T. Farges, J. Marty, and P. Herry

21.1 Introduction

The infrasound technology has been mainly used to study specific events as auroras (Wilson 1973, 1975; Wilson et al. 2010), severe weather (Bowman and Bedard 1971), manmade disturbances (Liszka 1974; Campus and Christie 2010), meteorites (Revelle 1976, 2010; Edwards 2010), solar eclipses (Farges et al. 2003), or volcanic eruptions (Delclos et al. 1990). In parallel to such observations, it appeared in the pioneer works of Rind et al. (1973), Rind and Donn (1975, 1978), Rind (1978), and Rind et al. (1981) that the monitoring of quasi-continuous infrasound sources such as ocean swell could be used to extract atmospheric parameters. Bush et al. (1989) proposed to use acoustic sounding from engineering blasts at the ground to study the fine structure of the upper atmosphere. The possibility of tracking cyclones by infrasound monitoring was proposed by Ponomaryov et al. (1998). Strong variations in the sound velocity deduced from infrasound parameters were related to circulation changes produced by stratospheric warming (Rind and Donn 1978). However, the analysis of atmospheric parameters was constrained, most of the time, by the use of single sensor and limited processing methods, which did not allow the determination of the horizontal scale length and the spatial coherency, thereby limiting the accuracy of the results.

The development of the International Infrasound Monitoring System (IMS) for the verification of the Comprehensive nuclear Test Ban Treaty (CTBT) offers permanent and global measurements with a high data quality (Christie and Campus 2010). The stations act as very sensitive acoustic antennas providing the azimuth angle and the horizontal phase velocity of any coherent signals extracted from the ambient noise (Brachet et al. 2010). Many infrasound events have been analyzed with unprecedented precision, such as the Sumatra earthquake (Garcés et al. 2005), large super bolides (Garcés et al. 2004), hurricanes (Hetzer et al. 2008, 2010), earthquakes (Le Pichon et al. 2003), and volcanoes (Evers and Haak 2001). Infrasound

E. Blanc (✉)
CEA, DAM, DIF, F-91297, Arpajon, France
e-mail: elisabeth.blanc@cea.fr

A. Le Pichon et al. (eds.), *Infrasound Monitoring for Atmospheric Studies,*
DOI 10.1007/978-1-4020-9508-5_21, © Springer Science+Business Media B.V. 2010

produced by the daily Concorde flights between North America and Europe has been systematically used to quantify the azimuth changes produced by the stratospheric and thermospheric winds (Le Pichon et al. 2002). Using similar changes in infrasound signals from volcanoes, the mesospheric winds were determined with a precision which was not achieved by the available wind models (Le Pichon et al., 2005 a, b). This work and ongoing new observations open a new area of large scale atmospheric studies carried out with the network (Blanc et al. 2008).

The purpose of this paper is to show, through several examples, how the network can continuously monitor the acoustic gravity waves and the atmospheric circulation, with the objective to permanently contribute to the understanding of the dynamics of the atmosphere at regional and global scales in relation with climate.

21.2 Atmospheric Waves and Dynamics of the Atmosphere

21.2.1 Properties of Acoustic and Gravity Waves

The atmospheric waves can be distinguished as acoustic or gravity waves according to their frequency range (Blanc 1985; Fig. 21.1). Acoustic waves are characterized by frequency higher than the acoustic cut-off frequency. The restoring force is the compression force, while in gravity waves, characterized by frequencies between the Coriolis frequency (12 h at the pole) and the Brunt-Väisälä frequency, the restoring force is the gravitational force (Hines 1960). The properties of both wave systems are very different. Acoustic waves propagate at the sound velocity, they are ducted in the acoustic wave channel formed by the different atmospheric gradients of the atmosphere (Kulichkov 2010; Norris et al. 2010). Gravity waves, characterized by larger scales, propagate at a velocity lower than the sound velocity and their group and phase vertical velocities are in opposite directions.

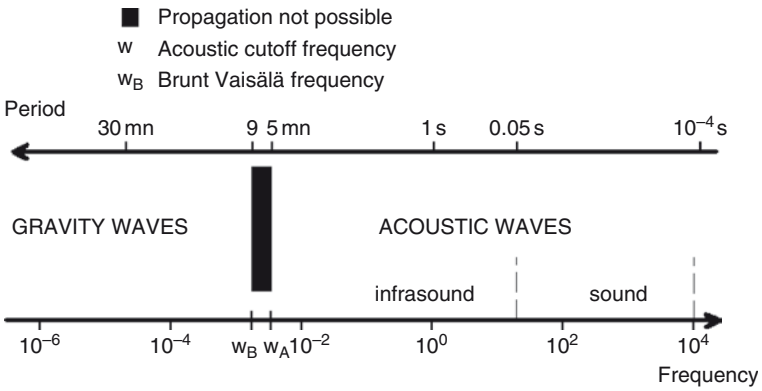

Fig. 21.1 Frequency range of acoustic and gravity waves

Both wave systems are submitted, when they propagate upwards, to an increase of their amplitude when the altitude increases. The reason is that, for maintaining constant energy flux, the amplitude must grow exponentially with the altitude z as $\rho(z)^{-1/2}$ to compensate the upward decrease of the atmospheric density ρ. This amplification is about 10^4 for propagation up to 150 km. In the acoustic wave domain, the energy dissipation is produced by viscosity and thermal conductivity, and becomes increasingly important at increasing heights. This process competes with the amplification process. The wave amplitude reaches a maximum before vanishing at altitudes of about 110 km for wave periods of 1 s and of 160 km for periods of 10 s. Gravity waves break through either convective or shear instability. Waves can also be filtered and dissipated by stratospheric wind systems when the phase speed matches the background wind speed.

The sources of infrasound are ocean swells, volcanoes, earthquakes, and manmade activity (Bass et al. 2006), while the sources of gravity waves are related to topography, convective systems, and geostrophic adjustment occurring near the jet stream or wave interactions. Gravity waves can transport energy and momentum from one region to another, produce turbulence and mixing, and influence the mean circulation and thermal structure of the middle atmosphere (Fritts and Alexander 2003). Their amplitude is very large and their horizontal wavelength ranges from kilometers to thousands of kilometers. As it has been observed in the wind profiles measured by rockets (Kulichkov and Bush 2001), they can modulate the wind systems. Gravity waves affect all the layers of the atmosphere, where they are observed by microbarometers, lidar, balloons, ionospheric sounding, or satellites (Blanc., 1985; Rees et al. 2000; Hertzog et al. 2008; Plougonven et al. 2008; Chum et al. 2008; Wu et al. 2006; Hauchecorne et al. 2010).

21.2.2 Impact of Acoustic and Gravity Waves on the Atmosphere

The impact of most acoustic waves on the atmosphere is expected to be limited due to their small time and space scales. However, quasi-continuous infrasound sources like ocean swells affect a large surface over oceans. Rind (1977) estimated that the dissipation of infrasound at 5 s period produced by ocean swells in the Atlantic ocean could produce heating rates up to 30 K/day in the 110–140 km altitude range. Similar results were found by Hickey et al. (2001): waves at 10 s periods produce a heating of 11 K/day at 140 km altitude.

Models predict that the troposphere also influences the stratosphere through large scale upward propagating waves. This wave forcing drives a global scale tropical pumping which withdraws air upward and poleward from the tropical lower stratosphere (Holton et al., 1995). The air masses are then transmitted poleward and downward in the high latitude regions, leading to fluctuations in the strength of the polar vortex (Baldwin et al. 2003a). This effect is large throughout the Northern winter where continental planetary waves generated over mountains

propagate upward in the stratosphere and contribute to the general circulation flow (Fig. 21.2, Plumb 2002). Gravity waves are responsible for the mesospheric meridional and vertical circulation and for the transport of atmospheric constituents in this region. They deposit their momentum and decelerate the zonal wind inducing a vertical upward transport at the summer pole. The resulting strong adiabatic cooling leads to the formation of polar mesospheric clouds (Thomas and Olivero 2001), a meridional transport from the summer to the winter pole and a downward transport at the winter pole. This transport may be amplified in some particular dynamical situations. For instance, a strong air descent has been observed by satellite in Northern Polar Regions, transporting a large quantity of NO2, due to a pure atmospheric dynamical phenomenon (Hauchecorne et al. 2007).

Disturbances in the polar stratosphere are Sudden Stratospheric Warmings (SSW) characterized by a rapid increase of the polar cap temperature, which can reach several tens of degrees in a week. The inverse phenomenon, characterized by a cooling of the polar stratosphere, is called Vortex Intensification (VI). Recent studies showed that SSW significantly influences the tropospheric climate. The effects can last more than two months after the occurrence of SSW (Baldwin and Dunkerton 2001, Baldwin et al. 2003b). Changes in the tropospheric climate have been predicted from polar to tropical regions in relation with SSW and VI by Kuroda (2008).

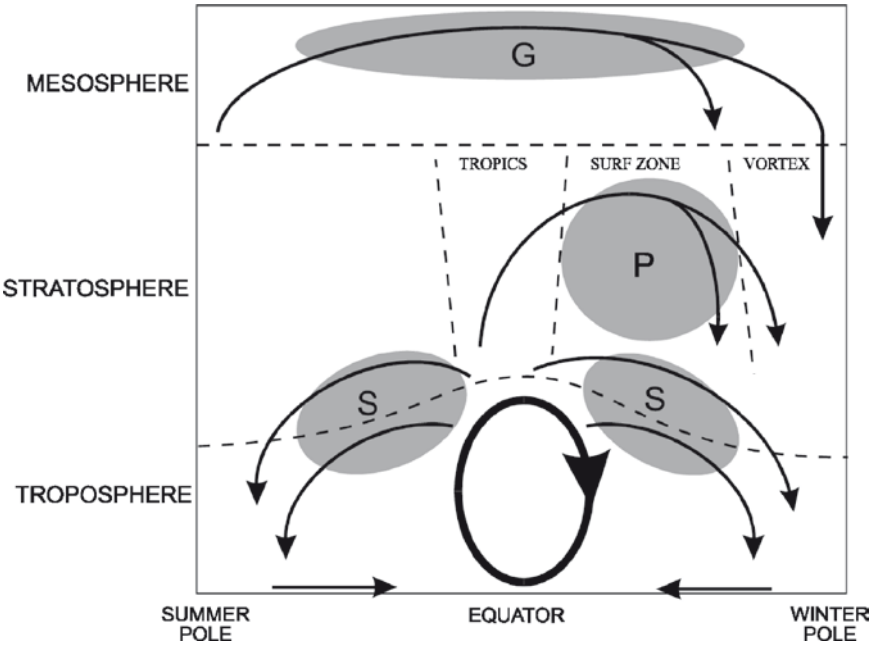

Fig. 21.2 Dynamics of the troposphere-stratosphere-mesosphere exchanges (Adapted from Plumb et al., 2002). The *shaded regions* denote breaking regions of Synoptic, Planetary, and Gravity waves

21.3 Parameters Measured with Infrasound Arrays

The IMS infrasound network developed for the verification of the CTBT is composed of 60 stations located as uniformly as possible over the surface of the globe. More than 70% of the stations are now in operation. It is larger and much more sensitive than any previously operated infrasound network. This network offers a unique system for a global monitoring of atmospheric waves over long time periods with a time resolution of 0.2 s. In order to detect signals from different sources in a large distance range, the microbarometers have been designed for having a good sensitivity (1 mPa) and a large dynamic range (80 dB, 24 bits). Measurements are performed using arrays of microbarometers. Each station is built according to the same technical specifications. It consists of an array of 4–9 sensors, arranged in an optimal configuration with an aperture of 1–3 km. To improve the station detectability, the number of sensors is larger in noisy sites. The sensors are equipped with acoustic filtering systems (microporous hoses or pipes), which reduce the noise produced by local surface winds (Alcoverro and Le Pichon 2005).

The stations form sensitive acoustical antennas, providing azimuth and apparent wave velocity. The recent technical advances and the development of efficient algorithms for detecting coherent waves within noncoherent noise allow characterizing routinely and in real-time low-amplitude pressure signals (Cansi 1995). Using such an approach, a large set of infrasound signals has been identified during the last few years. Different wave systems can be differentiated from their wave signature in time and frequency and from their wave azimuth and phase velocity.

The processed frequency range is 0.02–5 Hz; however, large amplitude gravity waves can be observed, in spite of the instrumental filtering. At frequencies lower than 0.01 Hz, the filter produces an amplitude reduction of about 20 dB per decade (Fig. 21.3). The spectrum of Fig. 21.3, measured at the Antarctica IS27 station, shows the typical microbarom infrasound peak at 0.2 Hz produced by ocean swells. It also shows gravity wave activity permanently observed at frequencies lower than 3×10^{-3} Hz. The spectrum amplitude in this frequency range is highly variable. Figure 21.4 presents an example of

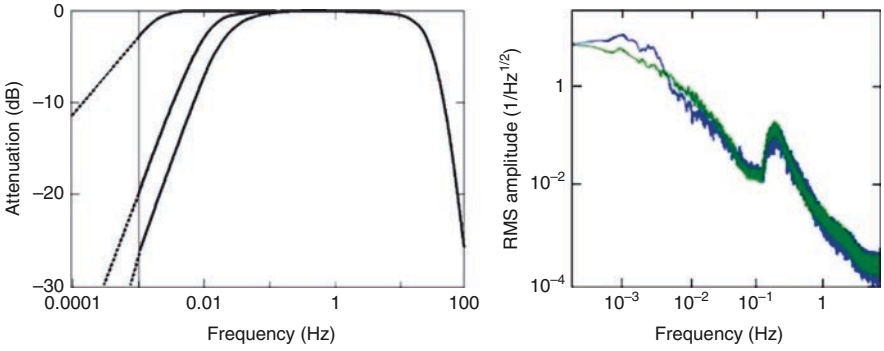

Fig. 21.3 Frequency bandwidth of the microbarometer and example of atmospheric wave spectrum. The microbarom peak near 0.2 Hz is clearly observed. For periods greater than 3 min, gravity wave activity can be observed in the spectrum in (*blue*) compared to a period of weaker activity in (*green*)

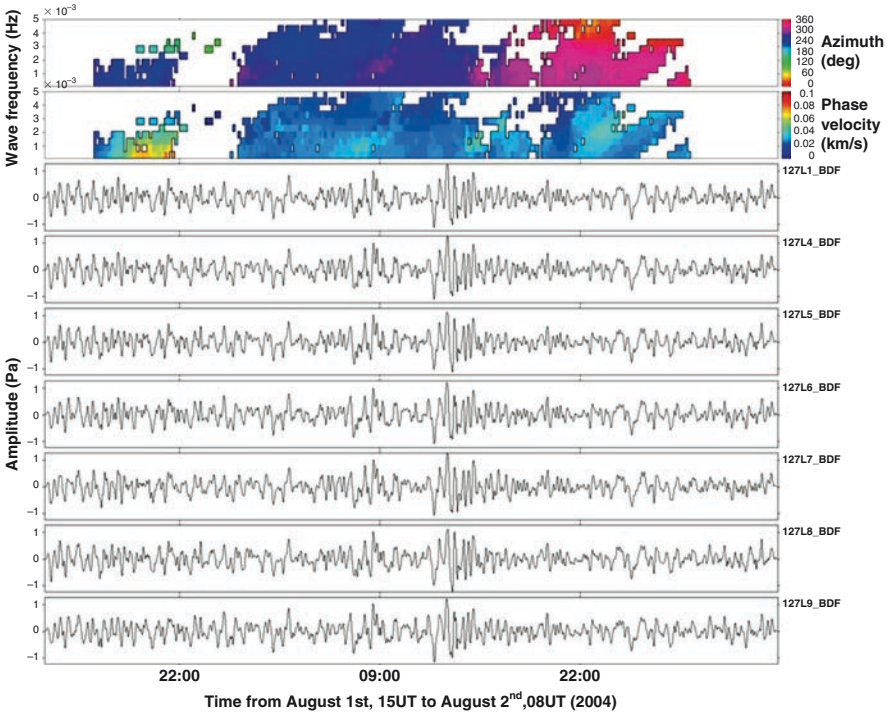

Fig. 21.4 Example of gravity wave observations at the station IS27 analyzed with the PMCC processing method. The waveforms are shown for each sensor. The wave azimuth varies from 240 to 360°. The phase velocity is lower than 60 m/s

the PMCC processing adapted to gravity waves (frequency range lower than the Brunt Väisälä frequency, and phase velocity lower than the sound velocity). For a wave period of ~30 mn, the 2 Pa measured amplitude actually corresponds to an amplitude of 28 Pa after being corrected by the frequency response of the sensor.

The IMS infrasound network constitutes the first global infrasound network ever built with such performances. It is much larger and much more sensitive than any previously operated network and constitutes the first network with a global and uniform distribution of stations. This network provides a global and homogeneous state of the atmosphere and of its diurnal and seasonal variability. It may also provide relevant information about changes in infrasound propagation and wave activity over a large time scale with possible relation with climate change.

21.4 Monitoring of the Atmospheric Wave Guide

The first way of atmospheric imaging consists in the monitoring of the atmospheric wave guide. This can be performed by using microbarom signals produced by ocean swells, which are constantly and globally observed at all IMS infrasound stations.

Figure 21.5 compares microbaroms in Northern (Alaska) and Southern (Antarctica) Polar Regions. Microbarom waves propagate in the ground to stratosphere waveguide and present a typical seasonal trend in the azimuths and amplitudes driven by the seasonal reversal of the zonal stratospheric wind (Le Pichon et al. 2006). In addition to this seasonal trend, signals show amplitude fluctuations at a scale of several days. These fluctuations are larger in winter in both hemispheres. This is an effect of the

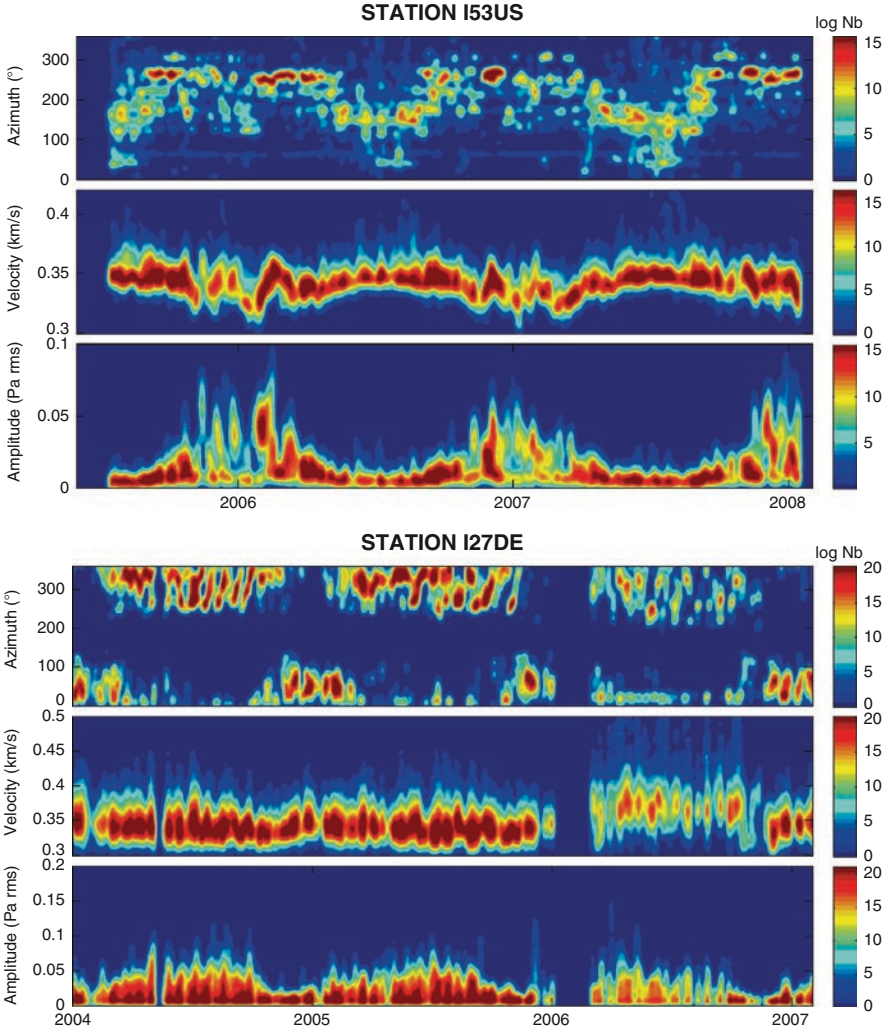

Fig. 21.5 Azimuth, phase velocity (related to the elevation angle) and amplitude of infrasound from ocean swells. *Bottom*: IS27 Antarctica station. *Top*: IS53 Alaska station. The seasonal azimuth variations are produced by the seasonal change of stratospheric winds. Amplitude fluctuations are more frequent and of shorter duration in the Northern hemisphere. An anomaly in the velocity variations is observed during the 2006 austral winter at the IS27 station

stratospheric winds, stronger in winter, which reinforce the stratospheric ducting of the waves. The seasonal amplitude variations are larger in the Northern hemisphere than in the Southern hemisphere, and the amplitude fluctuations over scales of several days are also larger. In the Northern hemisphere, midlatitude gravity waves are constantly generated by atmospheric storms and orographic forcing in the troposphere. As continental areas are smaller in the Southern hemisphere, the excitation of gravity waves by such processes is weaker. Also, the Antarctic plateau provides few obstructions for local orographic forcing. Antarctica represents the interesting specific conditions for the analysis of gravity waves in relation with waves propagating from other regions or other altitude ranges.

In parallel, another kind of disturbances, acting at a seasonal scale, has been identified. An anomaly lasting the whole 2006 austral winter is characterized by increasing phase velocities and decreasing signal amplitudes (Fig. 21.5). Details are shown in Fig. 21.6 (Ceranna et al. 2008). The increase of the velocity indicates a change in the incidence angle of the detected waves. The observed anomaly cannot be explained by signal processing, instrumentation, or station parameters, which remained unchanged during that period. As microbaroms propagate at large distances in the stratospheric wave guide (Le Pichon et al. 2006), the increasing velocity can be explained by a change in the reflection height produced by temporal fluctuations in the stratospheric wave guide parameters. A stratospheric cooling could produce a reflection at higher altitudes by decreasing the effective sound speed in the stratosphere.

This demonstrates the possibility of using infrasound data for atmospheric remote sensing. Other possibilities are the use of the azimuthal deviations produced by the winds on the infrasound propagation path to determine wind parameters in the mesosphere where there is a lack of operational observations (Le Pichon et al 2005a, b).

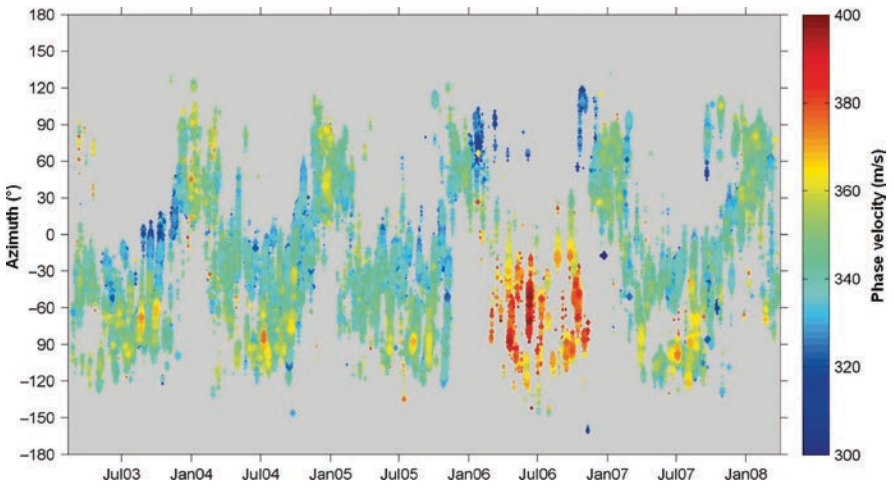

Fig. 21.6 Details of the velocity anomaly observed at the IS27 station during the 2006 Austral winter (Ceranna et al. 2008)

21.5 Monitoring of Wave Activity

Observations of waves and dynamical disturbances in the polar troposphere are very rare. Gravity waves in Antarctica were previously observed by microbarometers, but only during observation campaigns that are limited in time. Two events were observed by Egger et al. (1993) which are explained as trapped neutral mode and propagating wave of orographic origin. Other observations performed during a 9 months campaign by Rees et al. (2000) showed the presence of gravity waves mainly propagating from Southeast directions.

21.5.1 Gravity Waves in Antarctica

Gravity waves were researched within four years of data recorded at station IS27. Figure 21.7 shows the uncorrected measured amplitude, the phase velocity, and the mean frequency of the waves. The frequency band ranges from 2×10^{-4} to 2×10^{-3} Hz. This excludes planetary and tidal waves. Two wave systems with slightly higher amplitudes in winter can be observed. The direction of propagation is mainly North to North-West (260–330°N), but a weaker Eastwards activity is also observed (90–120°). These waves are not related to the surface winds, which is in agreement with previous observations performed by Rees et al., (2000) at frequencies lower than 0.004 Hz. Rees et al. suggested that such waves were generated in regions aloft driven by dynamical instabilities. Balloon observations in the stratosphere (Innis et al. 2004) also showed no correlation between surface winds and stratospheric gravity wave activity.

A large gravity wave activity has been observed by satellite over southern Andes, Antarctica peninsula, and sub-Antarctica islands by Wu et al. (2006) from June to August 2003 (Fig. 21.8). These observations have been compared with IS27 observations, available during the same period of time. The satellite shows that gravity wave activity was mainly concentrated in the latitude range from 40 to 70°S over South America and Antarctic peninsula. The satellite did not report any activity at higher latitudes. This is in good agreement with previous observations of stratospheric gravity waves by balloons, showing a large gravity wave activity over the Antarctic peninsula (Hertzog et al. 2008). Gravity waves recorded at IS27 during the same period have been analyzed and a large activity has been observed in the North-West direction. The azimuths of the gravity waves have been converted into longitudes, assuming that the wave origin is located at the same latitude for all events in the 40–70°S latitude range. The number of detections versus longitude is shown in the lower part of Fig. 21.8 where the different colors correspond to different ranges of latitudes. The wave direction roughly corresponds to the gravity wave location observed by satellite with, however, a small longitude shift. The distance between the station and the wave activity observed by the satellite is at least

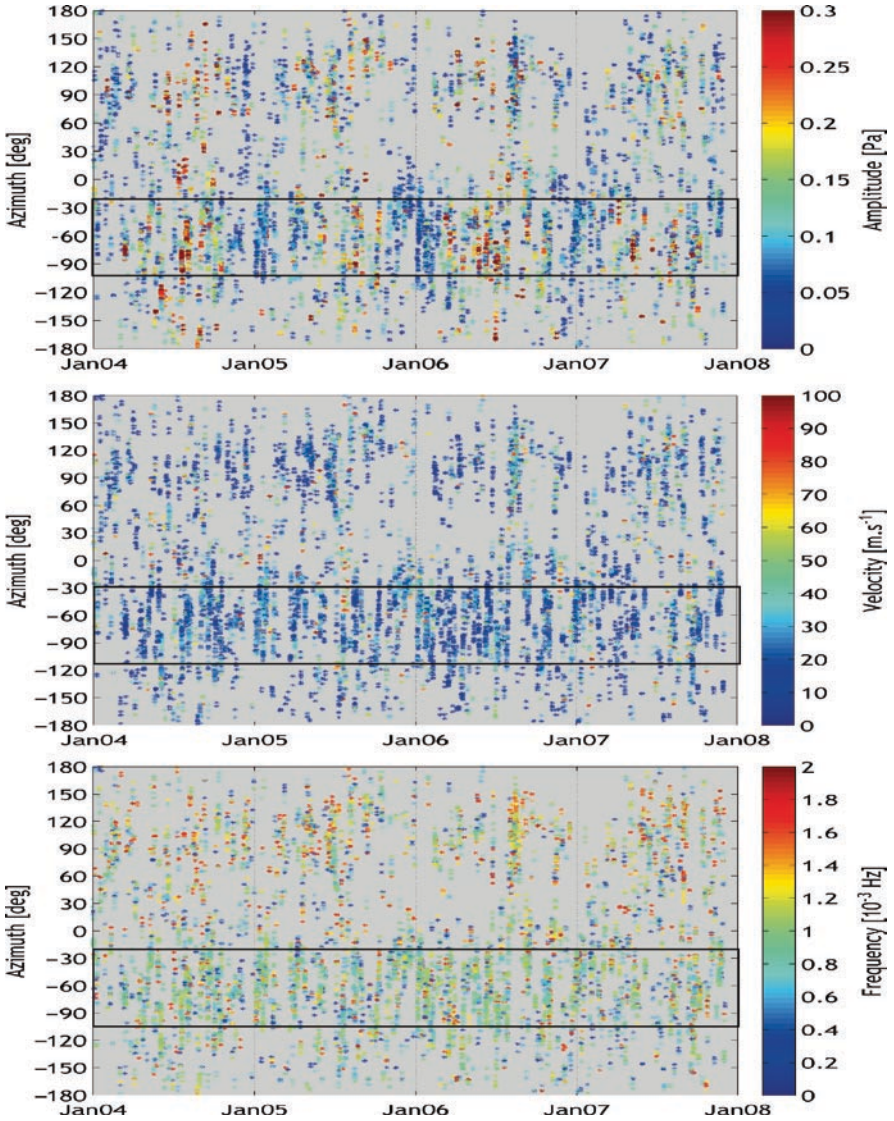

Fig. 21.7 Four years of gravity waves observed at the IS27 Antarctica station. The color indicates the wave amplitude (*top*), the phase velocity (*middle*), and the wave frequency (*bottom*)

1000 km. A long range propagation of such gravity waves is not suggested by their upward propagation predicted by models (Watanabe et al. 2006). Weaker orographic gravity waves originating at shorter distances can also be considered. However, the lack of correlation between surface winds, which are expected to control

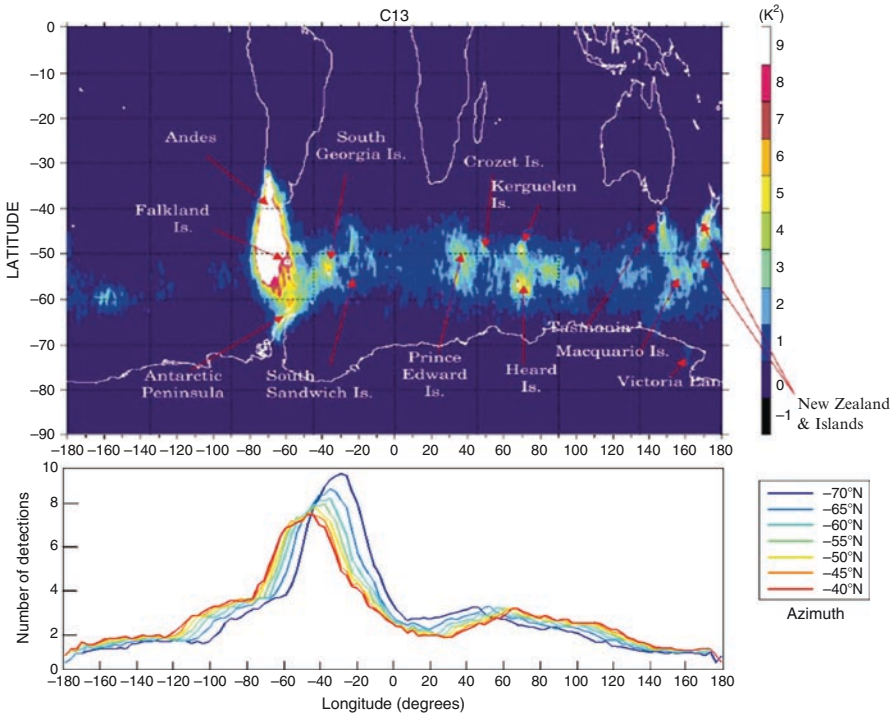

Fig. 21.8 Comparison between gravity waves observed by satellite in the stratosphere in June–August 2003 (Wu et al. 2006) and detected during the same period at the IS27 station. The source region (longitude) of gravity waves has been deduced from the detected azimuth, assuming that the source is located between latitudes ranging from 40 to 70°S

the orographic gravity wave activity, and the observed waves does not support this assumption.

Other observations in the lower Antarctica stratosphere with radiosondes report gravity waves with a downward energy transfer in winter and spring correlated with the stratospheric winds (Pfenninger et al. 1999; Yoshihi and Sato 2000). The origin, evoked by Yoshihi and Sato, could be gravity wave saturation, modification of the wave structure, or shift in the location of the polar vortex. The possibility of observing in the troposphere gravity waves from the stratosphere can then also be considered.

Such observations show that microbarometer measurements are important to determine the gravity wave behavior in the troposphere. Orographic and polar jet gravity waves or other stratospheric disturbances could be distinguished in the future by using several infrasound stations and other available stratospheric observations.

21.5.2 Effects of Thunderstorm Activity

Infrasound produced by lightning has been intensively studied from ground-based observations (Few 1986 and references therein). Low frequency infrasound and gravity waves related with severe weather were also observed in the ionosphere by HF radars (Davies and Jones 1972). More recently, new investigations in this topic were motivated by the discovery of transient luminous events called sprites, jets, or elves, which are the manifestation of intense energy exchanges between the troposphere, the stratosphere, and the mesosphere over thunderstorm areas (Sentman and Wescott 1993; Lyons and Armstrong 2004). Observations of sprites and mesospheric waves by airglow camera measurements, during thunderstorms producing sprites, showed that there is no distinctive signature in the airglow layer associated with sprites. However, upward propagating gravity waves with quasi-sinusoidal oscillations were observed over the convective cell associated to the thunderstorm (Sentman et al. 2003). The breaking of atmospheric waves generated by thunderstorms in the stratosphere excites short period secondary waves, which are trapped in the lower thermospheric duct and could explain the waves observed in the airglow imaging experiments (Snively and Pasko 2003; Snively 2008). Infrasound produced by sprites is characterized by a typical frequency dispersion (Liszka 2004, Farges et al. 2005). Weak air heating on the order of several degrees K has been estimated to be at the origin of the infrasound production (Pasko and Snively 2007).

The IMS infrasound network offers a unique opportunity for infrasound and gravity wave monitoring in relation with thunderstorm activity. During the coupling of atmospheric layers (CAL) project (Neubert et al. 2008), microbarometer observations were performed in an experimental station similar to the IMS infrasound stations. A large thunderstorm was crossing the station in the night of August 31, 2005. Fig. 21.9 presents the lightning locations given by the Météorage (French Lightning Detection Network) database in several successive 6 h maps from August 31st at 12hUT to September 1st at 12hUT. The upper part of the figure shows a wavelet analysis during the same period. The local wind measured at the station is indicated at the top of the figure. Between 12 and 18 h on August 31, the wind is very large inducing noise in infrasound observations. However, when the thunderstorm is over the station at 21:00 UT, the local wind speed and the related noise is weak.

A large gravity wave activity is observed when the thunderstorm is over the station. The wave period varies from 5 min up to 1 h at the maximum of the signal amplitude. The waves are then characterized by a broad frequency range. A large infrasound activity produced by lightning is also recorded when the thunderstorm is close to the station. Figure 21.10 shows the comparison between infrasound and gravity waves. The infrasound activity related to lightning is larger when the lightning impacts measured by Météorage (top of the figure) are close to the station, which is in agreement with previous observations (Farges 2008; Assink et al. 2008). The infrasound azimuth follows the thunderstorm motion approaching the station from 22:00 to 00:15 (azimuth 240°) and moving away in the opposite direction from 00:30 to 01:30 (azimuth 60°). Differently, the gravity wave activity is observed

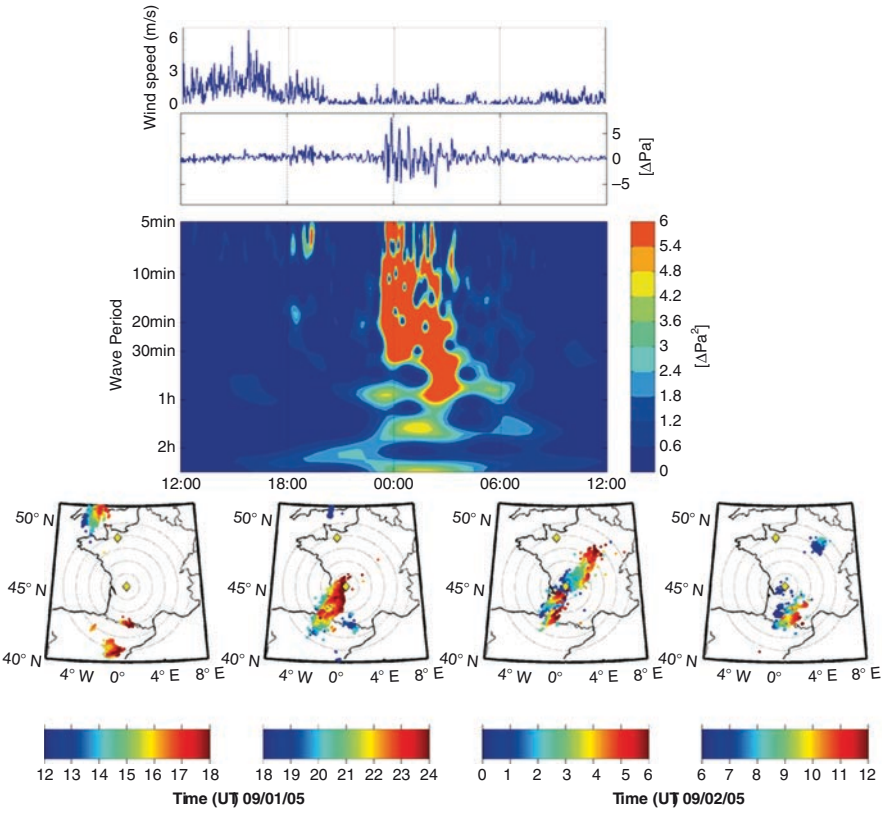

Fig. 21.9 Gravity waves observed during the thunderstorm of August 31–September 1, 2005. The *lower* part of the figure shows the thunderstorm displacement. The color scale codes the time. The wavelet analysis shows a large gravity wave activity when the storm is over the station. The *upper part* of the figure shows the surface wind speed measured at the station

from 23:30 to 04:00, while a weaker wave activity, with larger periods of about 1–2 h, persists up to 06:00. The azimuth of gravity waves only changes from 200° at the beginning of the thunderstorm to 220° when the thunderstorm moves away. The gravity waves are not related to the lightning activity. They arise from about the same area during the entire thunderstorm, while the lightning flashes moved from Southwest to Northeast following the thunderstorm motion over the station. A second thunderstorm front is observed at 03:00 with an azimuth slightly lower than the gravity wave azimuth. Gravity waves are probably originating from the stratiform region of the thunderstorm, decoupled from the first thunderstorm front (convective region) where larger number of lightning flashes are produced. No activity has been observed the other days, while other thunderstorms occurred at distances from 100 to 800 km from the station.

Such observations demonstrate that the IMS infrasound stations provide powerful means to characterize gravity wave systems produced by thunderstorm activity.

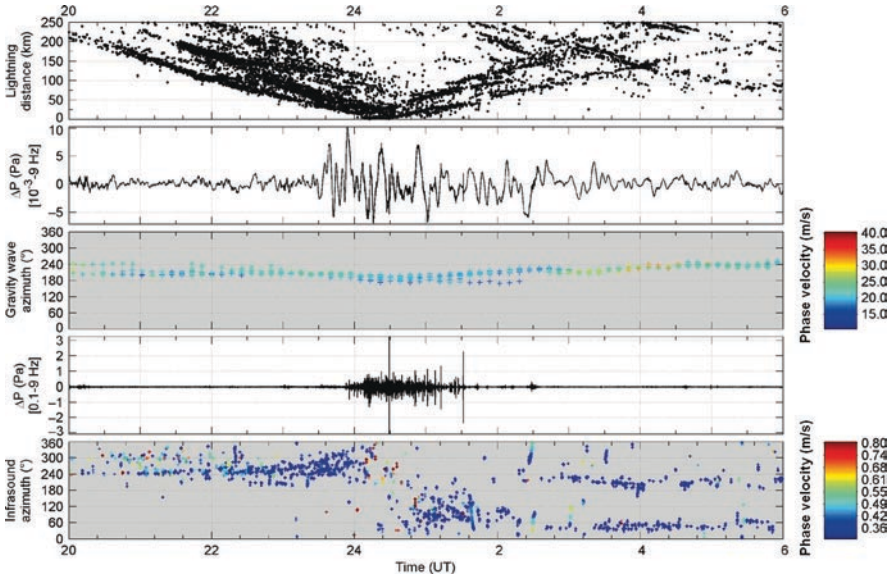

Fig. 21.10 Comparison between the characteristics of infrasound and gravity waves observed during the September 1, 2005 thunderstorm. The distance between the lightning impact and the station is given at the *top* of the Figure

Such observations are important in tropical regions where the thunderstorm activity is very large. Christian et al. (2003) showed that an average of 44 lightning flashes occur around the globe every second. The number of thunderstorms permanently active in the world is estimated to be between 1,000 and 2,000. Most of the activity is concentrated in tropical continental areas especially in Africa (about the third of the total activity). Since observations are difficult in these areas, the IMS network constitutes a relevant tool for the observation of wave activity in relation with thunderstorms.

21.6 Summary and Conclusions

It has been shown that the IMS network, mostly sensitive to infrasound in the range 0.02–5 Hz, can also measure gravity waves in spite of a limited frequency response of the sensors. Their amplitude reaches several tens of Pa after correction. It has been shown through different examples how the monitoring of infrasound and gravity waves can be used for a better understanding of the dynamics of the atmosphere. The first way is to study the variability of infrasound from quasi-continuous sources such as ocean swells or volcanoes in relation to changes in large scale atmospheric structures. The amplitude fluctuations of microbarom signals produced by ocean swells can be related to planetary waves which modulate the atmospheric wave

guide. The fluctuations are much larger in the Northern hemisphere than in the Southern hemisphere, because the largest planetary waves are produced over continental areas. The infrasound monitoring also reveals anomalies at a seasonal scale. For example, microbarom monitoring in Antarctica showed in the 2006 Austral winter unexpected changes in the temperature and/or wind changes in the stratosphere and mesosphere, which have been related to changes in the global atmospheric circulation in the stratosphere. The second way to study the atmospheric dynamics is the direct observation of large scale gravity waves. Four years of gravity wave observations at the Antarctica IS27 station showed a seasonal variation with larger amplitudes during the austral winter. The azimuth roughly coincides with the direction of Southern America and Antarctica peninsula where a large gravity wave activity is observed by satellite. However, the possibility of wave production from disturbances at higher altitudes in the stratosphere should also be considered. Another example shows the production of gravity waves by thunderstorms in Europe. Such studies can be performed over large periods of time and in several regions submitted to different geophysical influences. The infrasound network can then contribute to the understanding of the dynamics of the atmosphere at regional and global scales. As the CTBT network will provide long duration observations, it could provide relevant information about the evolution of the atmospheric wave activity in relation to climate change.

Acknowledgments The authors thank N. Brachet (CTBTO/PTS) for providing the PMCC detection lists for stations IS53 and IS27, and for much helpful discussions. The last chapter of this work was, in part, undertaken in the framework of the EU Research Training Network "Coupling of Atmospheric Layers," contract No.: HPRN-CT-2002-00216. The authors wish to thank the Météorage Company for real time access to lightning data over southern Europe.

References

Alcoverro B, Le Pichon A (2005) Design and optimization of a noise reduction system for infrasonic measurements using elements with low acoustic impedance. J Acoust Soc Am 117(4):1717–1727. doi:10.1121/1.1804966

Assink JD, Evers LG, Holleman I, Paulssen H (2008) Characterization of infrasound from lightning. Geophys Res Lett 35:L15802. doi:10.1029/2008GL034193

Baldwin MP, Dunkerton TJ (2001) Stratospheric harbingers of anomalous weather regimes. Science 294:581–584

Baldwin MP, Thompson DWJ, Shuckburgh EF, Norton WA, Gillet NP (2003a) Weather from the stratosphere? Science 301:317–319

Baldwin MP, Stephenson DB, Thompson DWJ, Dunkerton TJ, Charlton AJ, O'Neill A (2003b) Stratospheric memory and skill of extended-range weather forecasts. Science 301:636–640

Bass HE, Bhattacharyya J, Garcés MA, Hedlin M, Olson JV, Woodward RL (2006) Infrasound. Acoust Today 2006:9–19

Blanc E (1985) Observations in the upper atmosphere of infrasonic waves from natural or artificial sources: a summary, Ann. Geophysicae 3:673–687

Blanc E, Le Pichon A, Ceranna L, Farges T (2008) Infrasound monitoring, acoustic-gravity waves and global atmospheric dynamics. American Geophysical Union, Fall Meeting 2008, abstract #S11B-1736

Bowman HS, Bedard AJ (1971) Observations of Infrasound and Subsonic Disturbances Related to Severe Weather. Geophys J Int 26(1–4):215

Brachet N, Brown D, Le Bras R, Mialle P, Coyne J (2010) Monitoring the earth's atmosphere with the global IMS infrasound network. This volume, pp. 73–114

Bush GA, Ye A, Ivanov SN Kulichkov, Kuchayev AV, Pedanov MV (1989) Acoustic sounding of the fine structure of the upper atmosphere, Izv. Atmos Ocean Phys 25:251–256

Campus P, Christie DR (2010) Worldwide observations of infrasonic waves. This volume, pp. 181–230

Cansi Y (1995) An automatic seismic event processing for detection and location: the PMCC method. Geophys Res Lett 22:1021–1024

Ceranna L, Le Pichon A, Blanc E (2008) Microbarom Signals recorded in Antarctica: A measure for Sudden Stratospheric Warming? Geophysical Research Abstracts 10 EGU2008-A-08285, 2008, SRef-ID: 1607-7962/gra/EGU2008-A-08285, 2008 EGU General Assembly

Christian HJ, Blakeslee RJ, Boccippio DJ, Boeck WL, Buechler DE, Driscoll KT, Goodman SJ, Hall JM, Koshak WJ, Mach DM, Stewart MF (2003) Global frequency and distribution of lightning as observed from space by the Optical Transient Detector. J Geophys Res 108:4005. doi:10.1029/2002JD002347

Christie DR, Campus P (2010) The IMS infrasound network: design and establishment of infrasound stations. This volume, pp. 27–72

Chum J, Lastovicka J, Sindelarova T, Buresova D, Hruska F (2008) Peculiar transient phenomena observed by HF Doppler sounding on infrasound time scales. J Atmos Solar Terr Phys 70:866–878

Davies K, Jones JE (1972) Infrasound in the ionosphere generated by severe thunderstorms. J Acoust Soc Am 4(52):1087–1090

Delclos C, Blanc E, Broche P, Glangeaud F, Lacoume JL (1990) Processing and interpretation of microbarograph signals generated by the explosion of Mount St. Helens. J Geophys Res 95:5485–5494

Egger J, Wamser C, Kottmeier C (1993) Internal atmospheric gravity waves near the coast of Antarctica. Bound.-Layer Meteor 66:1–17

Evers LG, Haak HW (2001) Listening to sounds from an exploding meteor and oceanic waves. Geophys Res Lett 2:41–44

Farges T (2008) Infrasound from Lightning and Sprites. In: Betz HD, Schumann U, Laroche P (eds) Lightning: Principles, Instruments and Applications. Springer, Netherlands, pp 417–432

Farges T, LePichon A, Blanc E, Perez S (2003) Response of the lower atmosphere and the ionosphere to the eclipse of August 11, 1999. J Atmos Solar Terr Phys 65:717–726

Farges T, Blanc E, Lepichon A, Neubert T, Allin TH (2005) Identification of infrasound produced by sprites during the Sprite 2003 campaign. Geophys Res Lett 32:L01813. doi:10.1029/2004GL021212

Few AA (1986) Acoustic radiations from lightning. The earth's electrical environment. National Academy Press, Washington, pp 46–60

Fritts DC, Alexander MJ (2003) Gravity wave dynamics and effects in the middle atmosphere. Rev Geophys 41(1):1003. doi:10.1029/2001RG000106

Garcés M, Bass H, Drob D, Hetzer C, Hedlin M, Le Pichon A, Lindquist K, North R, Olson J (2004) Forensic studies of infrasound from massive hypersonic sources. Eos TransAGU 85(43):433

Garcés M, Caron P, Hetzer C, Le Pichon A, Bass H, Rob DD, Hattacharyya JB (2005) Deep Infrasound Radiated by the Sumatra Earthquake andTsunami. EOS, 86(35):317–320

Hauchecorne A, Bertaux JL, Dalaudier F, Russell JM, Mlynczak MG, Kyrölä E, Fussen D (2007) Large increase of NO2 in the north polar mesosphere in January–February 2004: Evidence of a dynamical origin from GOMOS/ENVISAT and SABER/TIMED data. Geophys Res Lett 34:L03810. doi:10.1029/2006GL027628

Hauchecorne A, Keckhut P, Chanin M-L (2010) Dynamics and transport in the middle atmosphere using remote sensing techniques from ground and space. This volume, pp. 659–678

Hertzog A, Boccara G, Vincent RA, Vial F, Cocquerez P (2008) Estimation of Gravity Wave Momentum Flux and Phase Speeds from Quasi-Lagrangian Stratospheric Balloon Flights Part II: Results from the Vorcore Campaign in Antarctica. J Atmos Sci 65:3056–3070. doi:10.1175/2008JAS2710.1

Hetzer CH, Waxler R, Gilbert KE, Talmadge CL, Bass HE (2008) Infrasound from hurricanes: Dependence on the ambient ocean surface wave field. Geophys Res Lett 35:L14609. doi:10.1029/ 2008GL034614

Hickey MP, Schubert G, Walterscheid RL (2001) Acoustic wave heating of the thermosphere. J Geophys Res 106(A10):21543–21548

Hines CO (1960) Internal atmospheric gravity waves. Can J Phys 38:1441–1481

Holton JR, Haynes PH, McIntyre ME, Douglass AR, Rood RB, Pfister L (1995) Stratosphere-troposphere exchange. Rev Geophys 33(4):403–439

Innis JL, Klekociuk AR, Vincent RA (2004) Interstation correlation of high-latitude lower-stratosphere gravity wave activity: Evidence for planetary wave modulation of gravity waves over Antarctica. J Geophys Res 109:D17106. doi:10.1029/2004JD004961

Kulichkov SN, Bush GA (2001) Rapid Variations in Infrasonic Signals at Long Distances from One-Type Explosions, Izvestiya. Atmos Oceanic Phys 37(3):306–313

Kulichkov S (2010) On the prospects for acoustic sounding of the fine structure of the middle atmosphere. This volume, pp. 505–534

Kuroda Y (2008) Effect of stratospheric sudden warming and vortex intensification on the tropospheric climate. J Geophys Res 113:D15110. doi:10.1029/2007JD009550

Le Pichon A, Garcés MA, Blanc E, Barthelemy M, Drob DP (2002) Acoustic propagation and atmosphere characteristics derived from infrasonic waves generated by the Concorde. J Acoust Soc Am 111:629–641

Le Pichon A, Guilbert J, Vallée M, Dessa JX, Ulziibat M (2003) Infrasonic imaging of the Kunlun Mountains for the great 2001 China earthquake. Geophys Res Lett 30(15):1814. doi:10.1029/2003GL017581

Le Pichon A, Blanc E, Drob D, Lambotte S, Dessa JX, Lardy M, Bani P, Vergniolle S (2005a) Infrasound monitoring of volcanoes to probe high-altitude winds. J Geophys Res 110:D13106. doi:10.1029/ 2004JD005587

Le Pichon A, Blanc E, Drob D (2005b) Probing high-altitude winds using infrasound. J Geophys Res 110:D20104. doi:10.1029/2005JD006020

Le Pichon A, Ceranna L, Garcés M, Drob D, Millet C (2006) On using infrasound from interacting ocean swells for global continuous measurements of winds and temperature in the stratosphere. J. Geophys Res 111:D11106.1–D11106.7. doi:10.1029/2005JD006690

Liszka L (1974) Long distance propagation of infrasound from articicial sources. J Acoust Soc Am 56(5):1383–1388

Liszka L (2004) On the possible infrasound generation by sprites. J Low Frequency Noise, Vibration Active Control 23:85–93

Lyons WA, Armstrong RA (2004) A review of electrical and turbulence effects of convective storms on the overlying stratosphere and mesosphere, in: AMS Symposium on Space Weather. AMS Annual Meeting, Seattle

Neubert T, Rycroft M, Farges T, Blanc E, Chanrion O, Arnone E, Odzimek A, Arnold N, Enell C-F, Turunen E, Bösinger T, Mika A, Haldoupis C, Steiner RJ, Van Der Velde O, Soula S, Berg OP, Boberg F, Thejll P, Christiansen B, Ignaccolo M, Füllekrug M, Verronen PT, Montanya J, Crosby N (2008) Recent Results from Studies of Electric Discharges in the Mesosphere. Surv Geophys 29(2):71–137. doi:10.1007/s10712-008-9043-1

Norris D, Gibson R, Bongiovanni K (2010) Numerical methods to model infrasonic propagation through realistic specifications of the atmosphere. This volume, pp. 535–568

Pasko VP, Snively JB (2007) Mechanism of infrasound radiation from sprites, In Abstracts of the American Geophysical Union, Fall Meeting 2007, #AE23A-0899.

Pfenninger M, Liu AZ, Papen GC, Gardner CS (1999) Gravity wave characteristics in the lower atmosphere at South Pole. J Geophys Res 104(D6):5963–5984

Plougonven R, Hertzog A, Teitelbaum H (2008) Observations and simulations of a large-amplitude mountain wave breaking over the Antarctic Peninsula. J Geophys Res 113:D16113. doi:10.1029/2007JD009739

Plumb RA (2002) Stratospheric transport. J Meteor Soc Japan 80:793–809

Ponomaryov EA, Sorokin AG, Tabulevich VN (1998) Microseisms and infrasound: a kind of remote sensing. Phys Earth Planetary inter 108:339–346

Rees JM, Denholm-Price JCW, King JC, Anderson PS (2000) A Climatological Study of Internal Gravity Waves in the Atmospheric Boundary Layer Overlying the Brunt Ice Shelf, Antarctica. J Atmos Sci 57:511–526

ReVelle DO (1976) On meteor-generated infrasound. J Geophys Res 81:1217–1230

Rind D (1977) Heating of the lower thermosphere by the dissipation of acoustic waves. J Atmos Terr Phys 39:445–456

Rind D (1978) Investigation of the lower thermosphere results of ten years of continuous observations with natural infrasound. J Atmos Terr Phys 40:1199–1209

Rind D, Donn WL (1975) Further use of natural infrasound as a continuous monitor of the upper atmosphere. J Atmos Sci 32:1694–1704

Rind D, Donn WL (1978) Infrasound observations of variability during stratospheric warmings. J Atmos Sci 35:546–553

Rind D, Donn WL, Dede E (1973) Upper air wind speeds calculated from observations of natural infrasound. J Atmos Sci 30:1726–1729

Rind D, Donn WL, Robinson W (1981) Stratospheric variability in summer. J Appl Meteor 20:900–909

Sentman DD, Wescott EM (1993) Observations of upper atmospheric optical flashes recorded from an aircraft. Geophys Res Lett 20:2857–2860

Sentman DD, Wescott EM, Picard RH, Winick JR, Stenbaek-Nielsen HC, Dewan EM, Moudry DR, S˜ao Sabbas FT, Heavner MJ, Morrill J (2003) Simultaneous observations of mesospheric gravity waves and sprites generated by a midwestern thunderstorm. J Atmos SolarTerr Phys 65:537–550

Snively Pasko (2008) Excitation of ducted gravity waves in the lower thermosphere by tropospheric sources. J Geophys Res 113:A06303. doi:10.1029/2007JA012693

Snively JB, Pasko VP (2003) Breaking of thunderstorm-generated gravity waves as a source of short-period ducted waves at mesopause. Geophys Res Lett 30(24):2254. doi:10.1029/2003GL018436

Thomas GE, Olivero J (2001) Noctilucent clouds as possible indicators of global change in the mesosphere, Adv. Space Res 28(7):937–946

Watanabe S, Sato K, Takahashi M (2006) A general circulation model study of the orographic gravity waves over Antarctica excited by katabatic winds. J Geophys Res 111:D18104. doi:10.1029/2005JD006851

Wilson CR (1973) Seasonal variations in auroral infrasonic wave activity. J Geophys Res 78:4801

Wilson CR (1975) Infrasonic wave generation by aurora. J Atmos Terr Phys 3(7):973–988

Wilson CR, Szuberla CAL, Olson JV (2010) High-latitude observations of infrasound from Alaska and Antarctica: mountain associated waves and geomagnetic/auroral Infrasonic signals. This volume, pp. 409–448

Wu DL, Preusse P, Eckermann SD, Jiang JH, de la Torre Juarez M, Coy L, Wang DY (2006) Remote sounding of atmospheric gravity waves with satellite limb and nadir techniques. Adv Space Res 37:2269–2277

Yoshihi M, Sato K (2000) A statisticasl tudy of gravity waves in the polar regions based on operational radiosonde data. J Geophys Res 105(D14):17995–18011

Chapter 22
Dynamics and Transport in the Middle Atmosphere Using Remote Sensing Techniques from Ground and Space

Alain Hauchecorne, Philippe Keckhut, and Marie-Lise Chanin

22.1 General Circulation

The region extending from about 10 to 90 km altitude is generally called the middle atmosphere. It is characterized by the dryness of the air as opposite to the lower atmosphere. It includes the stratosphere from 10 to 50 km, characterized by the presence of the ozone layer and a positive gradient of temperature, and the mesosphere from 50 to 90 km with a negative temperature gradient and a weaker vertical stability. Consequently, highest temperatures are reached at the stratopause (50 km) (Fig 22.1).

The vertical thermal structure of the middle atmosphere is controlled by the absorption of solar radiation by ozone, which is maximum at the stratopause. However, if one assumes that the thermal structure of the middle atmosphere is only controlled by radiative equilibrium, one obtains a much too cold temperature at winter pole and a much too warm one at summer pole. The deviation with the observed temperature increases with height from the tropopause to the mesopause. The geostrophic wind computed using the radiative temperature field, blowing from west in winter and from east in summer, increases continuously with height to reach unrealistic values in the upper mesosphere when the observed winds show a maximum in the lower mesosphere, around 60 km, and are reversed near the mesopause. This reversal of the wind is associated with a reversal of the temperature gradient between summer and winter poles. This indicates the fundamental role of the dynamics to control the whole thermal structure of the middle atmosphere. The observed thermal structure can only be explained with a global-scale mean meridional and vertical circulation from low-latitudes (ascent of air with adiabatic cooling) to high latitudes (descent of air with adiabatic warming) in the lower stratosphere known as the Brewer-Dobson circulation (Shepherd 2000), and from the summer hemisphere (ascent of air with strong adiabatic cooling) to the winter hemisphere (descent of air with strong adiabatic warming) in the upper

A. Hauchecorne (✉)
Université Versailles-Saint Quentin, CNRS/INSU, LATMOS-IPSL, BP3, 91371, Verrières-le-Buisson, Cedex, France

A. Le Pichon et al. (eds.), *Infrasound Monitoring for Atmospheric Studies*,
DOI 10.1007/978-1-4020-9508-5_22, © Springer Science+Business Media B.V. 2010

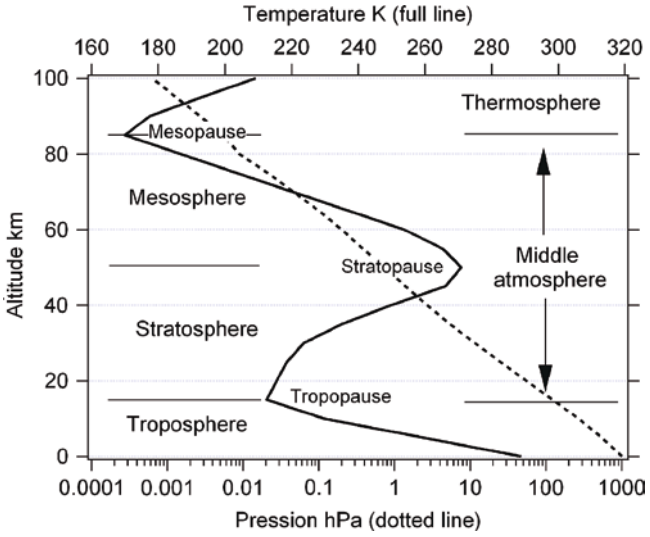

Fig. 22.1 Schematic representation of the thermal and pressure structure of the atmosphere with its different layers

stratosphere and the mesosphere. A global source of deceleration of the zonal wind is needed to maintain this so called "diabatic circulation" due to the fact that it transports air masses across isentropic surfaces. The diabatic circulation is essential in the redistribution of minor constituents in the whole middle atmosphere (Fig 22.2).

The deceleration of the zonal wind is due to the irreversible transport of momentum by atmospheric waves from their region of generation in the troposphere to their region of breaking in the middle atmosphere. The two most important types of waves interacting with the middle atmospheric zonal circulation are internal gravity waves, which have their origin in buoyancy forces in a vertically stable stratified atmosphere, and Rossby planetary waves, which have their origin in Coriolis forces in a meridional gradient of potential vorticity (McIntyre 1992). In the upper mesosphere, it is now well recognized that the dominant phenomenon to maintain the observed circulation is the breaking internal gravity waves (GW) generated in the troposphere and propagating upwards (Lindzen 1981; Holton 1982). The breaking occurs either statically, when the wave perturbation causes the adiabatic lapse rate to be exceeded, or dynamically, when the perturbation causes the wind shear to exceed a critical value. GW are selectively filtered by the mean wind at all levels, which leads to a prevalence of phase directions in the upper mesosphere opposite to the mean winds in the stratosphere and lower mesosphere (toward west in winter and toward east in summer). In the stratosphere, Rossby planetary waves play a major role in the evolution of the polar vortex in winter and are at the origin of sudden stratospheric warmings. Planetary waves can only propagate upwards in westerly winter winds, and in summer, the zonal easterly circulation is very quiet (Fig 22.3).

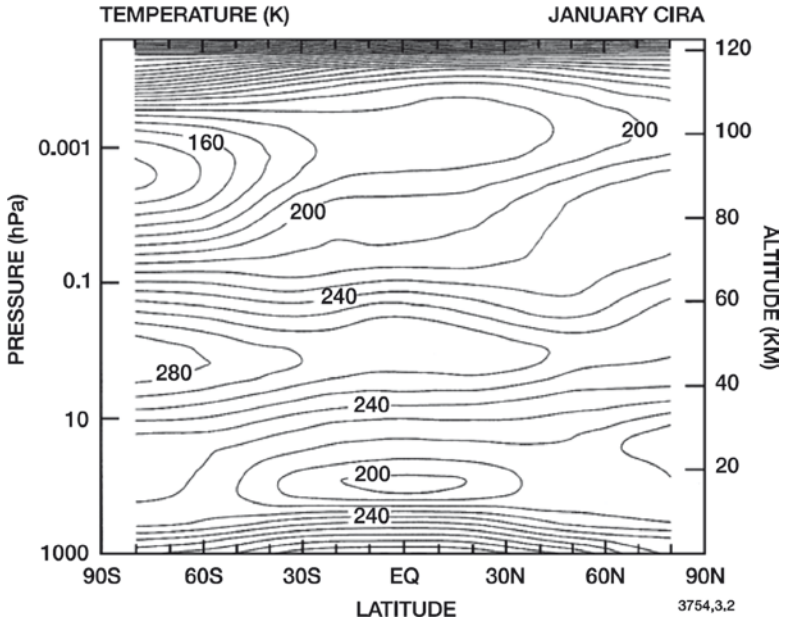

Fig. 22.2 Zonally averaged temperature (K) from the surface to approximately 120 km altitude in January, based on Fleming et al. (1988) Brasseur and Solomon (2006)

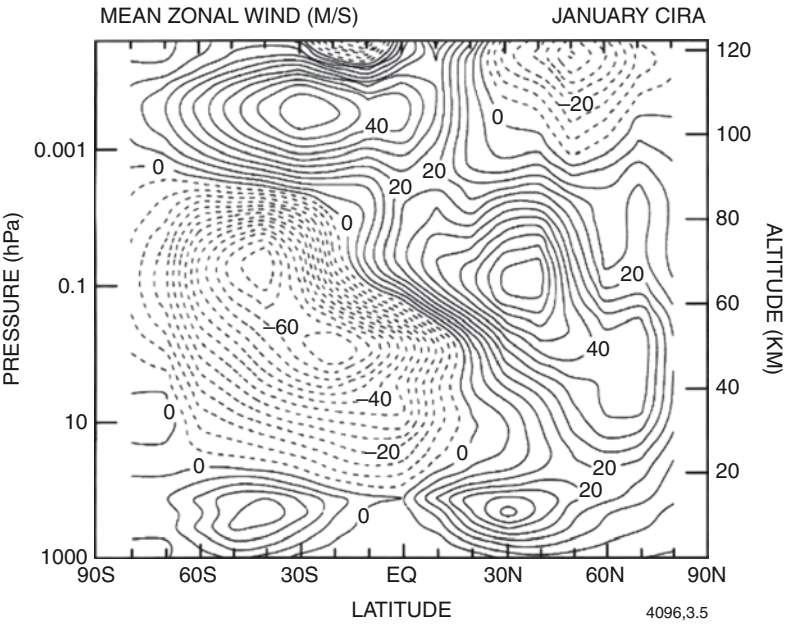

Fig. 22.3 Longitudinally averaged zonal wind (ms^{-1}) from the surface to approximately 120 km altitude in January, based on Fleming et al. (1988). Positive winds are blowing eastwards (westerlies) and negative winds are blowing westwards (easterlies) Brasseur and Solomon (2006)

Fundamental parameters in dynamical studies are those giving the physical state of the atmosphere, temperature, pressure, and the three components of the wind. Unfortunately, it is in general not possible to measure all these parameters at the same time and in the same volume. In particular, it is very difficult to get direct information on the vertical wind. Fortunately, it is possible to get some information on the 3D wind if constituents, which can be considered as passive tracers, are measured. The concentration of an atmospheric species is dependent on photochemical production and loss, and advection. The constituent should also present a gradient along the direction of the wind to be sensitive to the transport. The evaluation of the terms of the continuity equation for this species allows determining its chemical and dynamical lifetimes which depend on altitude, and to some extent, on latitude and season (Brasseur and Solomon 2006). A species can be considered as passive tracer if its dynamical lifetime is shorter than its chemical lifetime. The dynamical lifetime should be estimated according to the phenomenon that one wants to study. For the breaking of GW in the mesosphere, the typical time constant is one to a few days, while for the planetary waves in the winter stratosphere, the time constant is one to two weeks.

22.2 Atmospheric Dynamics

22.2.1 Extratropical Dynamics

22.2.1.1 Rossby Planetary Waves

The winter-time middle atmosphere at middle and high latitude is characterized by a large variability of temperature and winds. This variability is caused by the continuous propagation of Rossby planetary waves, which are generated in the troposphere by meridional motions due to the meridional gradient of the Coriolis parameter f. Rossby waves can propagate only westward relative to the mean flow and have a relatively slow phase speed (Charney and Drazin 1961). They are, therefore, blocked by easterly stratospheric winds in summer. In winter, planetary waves can propagate through the westerly stratospheric flow and, due to the exponential decrease of the atmospheric density with height, their relative amplitude increases until it reaches a critical amplitude leading to the wave breaking and a nonlinear interaction with the zonal flow at the origin of sudden warmings of the polar stratosphere.

Characteristic time scales of winter-time Rossby planetary waves are 10 to 20 days. Only larger horizontal waves (zonal modes 1 and 2 with dominant periods, respectively, around 16 and 12 days) can propagate up to the middle stratosphere and the mesosphere when shorter scale waves are dissipated in the lower stratosphere (Salby 1984). They are detected using analyses from numerical weather forecast models (Madden and Labitzke 1981), radiosonde data (Hirota and Hirooka 1983), and satellite data (Hirooka 2000), and are simulated by global circulation

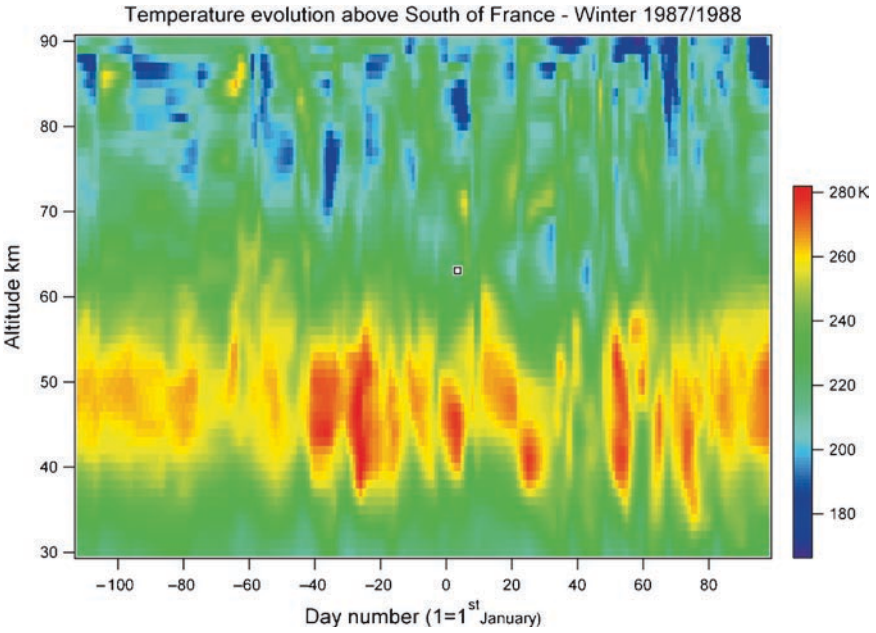

Fig. 22.4 Evolution of the temperature between 30 and 90 km as measured by Rayleigh lidar above South of Franceduring winter 1987–88. Day 1 corresponds to January 1, 1988. This plot is a composite from OHP and CEL lidar data

models (Pendlebury et al. 2008). A Rayleigh lidar (see section on ground-based remote sensing instruments) located in a site with favorable weather conditions like Observatoire de Haute-Provence (OHP, 44°N, 6°E) provides typically 3–4 mean temperature night-time profiles from 30 to 80 km per week, which allows a good survey of the evolution of planetary waves in the middle atmosphere (Hauchecorne and Chanin 1983; Hauchecorne et al. 1987). Figure 22.4 presents the evolution of temperature observed during one winter combining lidar measurements at OHP and on another French lidar site at the same latitude (Centre d'Essais des Landes, CEL, 44°, 1°W) and shows the succession of cold and warm perturbations due to the propagation of planetary waves. The survey of planetary waves activity is made at OHP since winter 1981/82, and the database covers now 27 years. A spectral analysis of the data reveals the presence of dominant modes around 12 days and 16 days identified as Rossby modes with wave numbers 2 and 1, respectively.

22.2.1.2 Stratospheric Warmings

A large interannual temperature variation is observed in the Northern Hemisphere winter stratosphere. The more spectacular phenomena are the sudden stratospheric warmings. During winters, the zonal-mean circulation can be significantly disrupted with polar stratospheric temperatures increasing by ~40–60 K in one week at

10 hPa (~30 km). When a reversal of the zonal-mean wind to an easterly direction is reached at 60°N down to 10 hPa (Labitzke 1977), these events are qualified as major stratospheric warmings. If they occur at the end of the winter March, they mark the transition between winter westerly winds and summer easterly winds, and are qualified as final warmings. Such extreme cases do not occur every winter, but are reported nearly for alternative winters, while minor events, not leading to a breakdown of the polar vortex, do occur 2–3 times each winter (Dunkerton and Baldwin 1991). The occurrence of sudden stratospheric warmings is mainly attributed to planetary wave breaking (Matsuno 1971; Hauchecorne and Chanin 1983). Schoeberl (1978) provided a review on the theory and observations of stratospheric warming using results reported from different places. He suggested that the major warming is confined to the Northern Hemisphere, but for the first time in 2002 a major warming was detected in the Southern Hemisphere (Baldwin et al. 2003).

22.2.2 Tropical Dynamics

22.2.2.1 Tape Recorder Effect

Global observations from space show that many chemical species have different tropical and extratropical mixing ratios along a same isentropic surface in the "overworld" lower stratosphere. This indicates the existence of a subtropical barrier with a strong gradient of potential vorticity that limits meridional exchanges, as at the border of the polar vortex. Holton et al. (1995) also describe the extratropical pumping of the tropical circulation. The breaking of planetary waves at middle and high latitudes induces a mean circulation from the tropics and an ascent of air in the intertropical region (Randel et al. 1993). This pumping controls the global rate of penetration of tropospheric air in the stratosphere which occurs mainly over convective clouds in the intertropical convergence zone. A very good demonstration of the upward motion in the tropical troposphere has been obtained using chemical tracers measured by HALOE and MLS on board UARS satellite (Mote et al. 1996). It has been possible to follow the ascent of water vapor seasonal minima and maxima for as long as 2 years up to 15 km above the tropopause ("tape recorder" effect). The very cold tropopause observed in this region (less than −80°C) explains the drying of the air injected in the stratosphere, but the detailed mechanism of drying is still under study. In particular, it is not well understood why the hygropause (altitude of minimum of water vapor mixing ratio) is a few km above the tropopause.

22.2.2.2 Tropical Planetary Waves

Near the equator, the Coriolis force decreases and free Rossby waves cannot develop. The theory predicts that long-period vertically propagating waves can exist. The two more important types are the eastward traveling Kelvin waves and

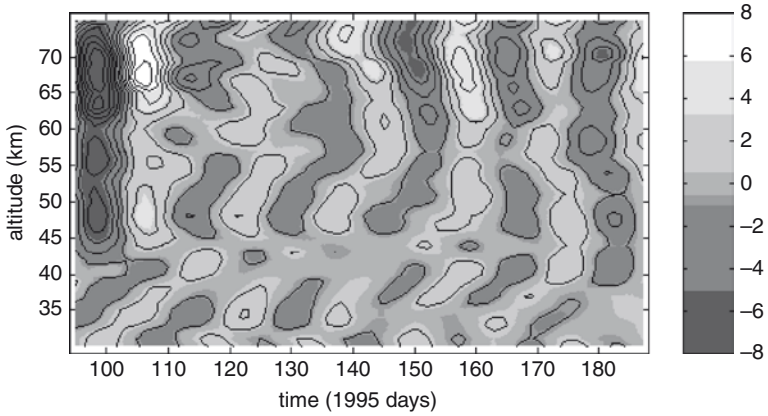

Fig. 22.5 Temperature perturbation (in K) observed by the Rayleigh lidar at Réunion Island from April to July 1995. Taken from Bencherif (1996)

the westward traveling Rossby-gravity waves (Holton 1979). These waves have a symmetric structure around the equator and their latitudinal extension is limited to about 25°S to 25°N. Contrary to midlatitude Rossby waves characterized by very long vertical wavelengths (40–50 km), equatorial Kelvin waves have a much shorter vertical wavelength, typically 5–10 km (Salby 1984). Such equatorial waves have been detected by a number of satellite and ground-based observations. As an example, we present temperature lidar observations at Réunion Island (21°S, 55°E), indicating that this site maybe under the influence of both tropical and extratropical planetary waves (Bencherif 1996). The phase of the perturbations observed in Fig. 22.5 seems to indicate the presence of Kelvin waves with short vertical wavelengths below 40 km and Rossby waves with long vertical wavelengths above this level. This interpretation is confirmed by the presence in UKMO (UK Meteorological Office) analyses of easterly winds below 40 km, which are favorable to the vertical propagation of Kelvin waves, and westerly winds above 40 km, which allow the propagation of Rossby waves from southern midlatitudes.

22.2.2.3 Quasi-Biennial Oscillation

The quasi-biennial oscillation (QBO) is a quasi-periodic oscillation of the equatorial zonal wind between easterlies and westerlies in the tropical stratosphere with a mean period of 28 months (Naujokat 1986). The alternating wind regimes develop at the top of the stratosphere and propagate downwards at about 1 km per month until they are dissipated at the tropical tropopause (see Fig. 22.6). This explanation of the phenomenon was first proposed by Holton and Lindzen (1972). Basically, the downward propagation of QBO is driven by two families of equatorial waves, Kelvin and Rossby-gravity waves propagating westward and eastward, respectively,

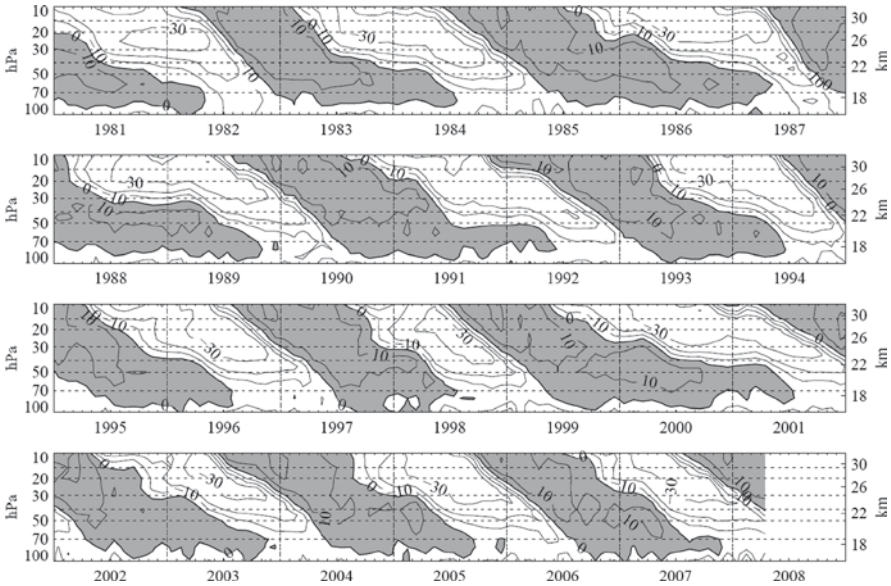

Fig. 22.6 Time-height of zonal wind at Singapore (1°N, 104°E). Westerly winds (and shaded) are positive and easterly winds are negative. A period of approximately 28 months (equatorial Quasi-Biennial Oscillation) is clearly visible. Extracted from Free University of Berlin Web site: http://www.geo.fu-berlin.de/met/ag/strat/produkte/qbo/index.html. Adapted from Naujokat (1986)

and accelerating the zonal wind in the direction of their propagation at their altitude of dissipation. Dunkerton (1997) found that forcing by GW should be also required to produce a realistic QBO in general circulation models. Baldwin et al. (2001) give a detailed review of the equatorial QBO and its interaction with extratropical dynamical phenomena as wintertime stratospheric polar vortices.

22.2.2.4 Semiannual Oscillation

The equatorial wind at the stratopause and in the lower mesosphere exhibits a semiannual oscillation (SAO) between eastward wind during equinox and westward wind during solstice with a peak amplitude of eastward wind up to 25 ms^{-1} and westward wind up to 25 ms^{-1} (Ray et al. 1998). This phenomenon was first noted by Reed (1966) using rocketsonde observations. Garcia et al. (1997) have used a variety of satellite, ground-based, and in-situ observations of wind and temperature to build a climatology of the SAO. The basic mechanism is as follows (Shepherd 2000): during solstice the strong meridional advection across equator creates a westward acceleration to conserve the angular momentum of advected air, while during equinox this mechanism does not act and the momentum deposition by equatorial Kelvin waves induces an eastward acceleration.

22.2.3 Gravity Waves, Mesospheric Inversions, and Tides

22.2.3.1 Internal Gravity Waves

As explained previously, internal GW play an important role in the driving of the middle atmosphere circulation (Lindzen 1981). They can only exist in a stable stratified atmosphere. Due to the gravity force, a parcel of air displaced vertically will start to oscillate. GW can propagate vertically and horizontally in the atmosphere when propagation conditions are favorable. They are formed in the troposphere above mountains (lee waves), convective clouds, and when the flow is not in geostrophic equilibrium as, for instance, in fronts. They can propagate upwards into the middle atmosphere until their phase speed is equal to the wind speed or they reach a critical amplitude with respect to the static or dynamical stability of the atmosphere. In the absence of breaking or dissipation, their amplitude $A(z)$ increases with altitude due to the exponential decrease of atmospheric density $\rho(z)$ in order to conserve the energy:

$$A(z) = p(z)^{-½}$$

Due to their relatively small vertical scales (a few tenths of km to a few km) and short periods (few minutes to few hours), GW are difficult to observe from space and radiosonde, and rocketsonde data give only snapshots of their characteristics. Continuous measurements using ground-based remote sensing instruments as Rayleigh temperature lidars (Wilson et al. 1991), Doppler wind lidars (Hertzog et al. 2001), MST radars (Allen and Vincent 1995; Venkat Ratnam et al. 2008), and natural emissions (Swenson and Gardner 1998) are then very valuable to study temporal and spectral characteristics of GW and to obtain a climatology of GW activity.

22.2.3.2 Mesospheric Inversions

In the mesosphere, the temperature is decreasing with height from the stratopause at 45–50 km to the mesopause at 85–95 km. However, temperature profiles show frequently an inversion layer around 70 km with a positive temperature gradient over several kilometers. The amplitude of the temperature inversion may reach values as high as 40 K. This phenomenon was first detected by Schmidlin (1976) using rocketsonde profiles, but without physical explanation. Hauchecorne et al. (1987) provided the first climatology and proposed a mechanism based on the breaking of GW, which leads to the vertical mixing of the atmosphere and a downward heat transport in the inversion layer. They showed that the inversion layer has an extension of at least several thousand km. Figure 22.7 presents a typical example of an inversion layer observed during one night at OHP, showing also the development and breaking of GW below the inversion. Leblanc and Hauchecorne (1997)

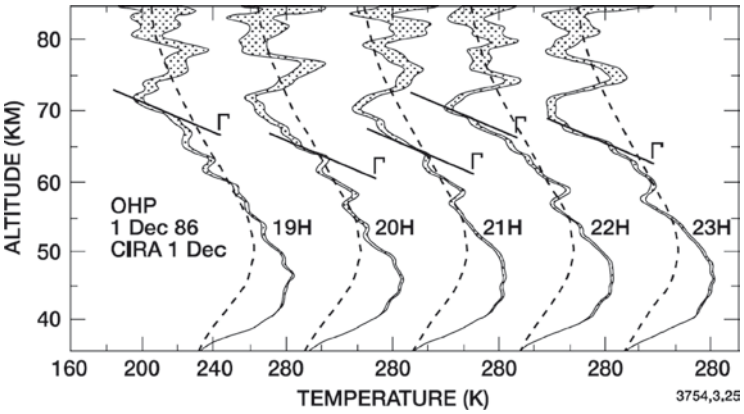

Fig. 22.7 Evolution of the temperature profile measured by the Rayleigh lidar at OHP showing the presence of gravity waves below 70 km reaching a critical amplitude indicated by the adiabatic lapse rate Γ and leading to a stable temperature inversion layer above 70 km. The two curves indicate the uncertainty of the temperature measurement (± 1 sigma) Hauchecorne et al. (1987)

confirmed the global extent of such inversions using temperature data from satellite instruments and showed that temperature inversions are enhanced in a midlatitude belt in winter above the region where the mesospheric jet is at maximum. Several mechanisms have been invoked and are reviewed in Meriwether and Gardner (2000). They include the breaking of GW, GW-tidal coupling, and chemical heating in the upper mesosphere. Salby et al. (2002) pointed out the role of the planetary wave structure in the development of inversion layers.

22.2.3.3 Thermal Tides

Thermal tides are temperature and wind oscillations forced by the heating due to the absorption of solar radiation by atmospheric gases, mainly ozone in the stratosphere and water vapor in the troposphere. Therefore, these periods are equal to the day (24 h, diurnal tide) or to its harmonics (semi-diurnal and ter-diurnal tides, respectively, 12 and 8 h). They have a planetary extension and, due to the exponential decrease of the density, their amplitude increases with height to reach very high values in the upper mesosphere-lower thermosphere where they are widely observed by MST radars between 70 and 100 km on horizontal wind components (Kishore et al. 2002). The theory of atmospheric tides was first presented by Lindzen (1966) and atmospheric tide models were developed to interpret radars observations (Forbes 1982). Their effect on the temperature can also be observed by lidar in the upper stratosphere and mesosphere (Keckhut et al. 1996). These authors pointed out the importance to take into account the temperature tidal component in the trend analysis in long temperature series from satellite instruments when the local hour of the measurements is changing with time.

22.3 Ground-Based Remote Sensing Measurements

Ground-based remote sensing instruments are used to probe the thermal and dynamical structure of the atmosphere. In particular, active instruments like radars and lidars allow determining the profile of wind and temperature in the atmosphere with a high vertical resolution. Due to the continuity of their measurements, they are very good tools to study periodic dynamical phenomena as gravity waves, planetary waves, and tides, and to infer the impact of such waves on the mean state of the atmosphere. We present here the main instruments used to monitor the structure of the middle atmosphere, Rayleigh and Raman lidars for temperature and Rayleigh Doppler lidars and MST radars for wind.

22.3.1 Rayleigh and Raman Lidars

The basic principle of a lidar is analogous to that of a radar, the radio waves being replaced by light waves from which comes the name of light detection and ranging (LIDAR) derived from the word radar. A lidar is made up of an emitter (a pulsed laser), a receiver (a collecting telescope), a detector (for instance, a photomultiplier), and a data acquisition system. Following the pioneering of Fiocco and Grams (1964), lidars have experienced a very large development for atmospheric studies. They are able to provide vertical profiles of physical parameters as temperature (Hauchecorne and Chanin 1980) and horizontal wind (Chanin et al. 1989) in the middle atmosphere. They are used also for the profiling of atmospheric constituents as, for instance, ozone (Godin et al. 1989) and aerosols (McCormick et al. 1978) in the stratosphere. Lidars allow continuous measurements in clear sky conditions. They are operated, in general, during night time to limit the level of background signal due to solar light scattered by the atmosphere. They are very good tools to study periodic dynamical phenomena as gravity waves, planetary waves, and tides, and to infer the impact of such waves on the mean state of the atmosphere.

The Rayleigh lidar is an instrument devoted to the measure of temperature in the middle atmosphere (30–90 km). Monochromatic laser pulses are sent vertically into the atmosphere and a temporal analysis of the backscattered light provides information about the vertical structure and composition of the atmosphere. Above the top of the stratospheric aerosols layer (about 30 km), the Mie scattering is negligible and the received signal due to the Rayleigh scattering is directly proportional to the atmospheric density. The temperature profile is deduced from the density profile assuming that the density is in hydrostatic equilibrium and obeys the perfect gas law (Hauchecorne and Chanin, 1980). The profile is limited upwards by the signal to noise ratio at 90–100 km. Keckhut et al. (1993) give a comprehensive review of characteristics and performances of Rayleigh lidars. These instruments provide unique information on the evolution of the density and temperature at time scales ranging from minutes to years. They are used for studies concerning atmospheric dynamics, climatology, and long-term trends at OHP where several lidars are

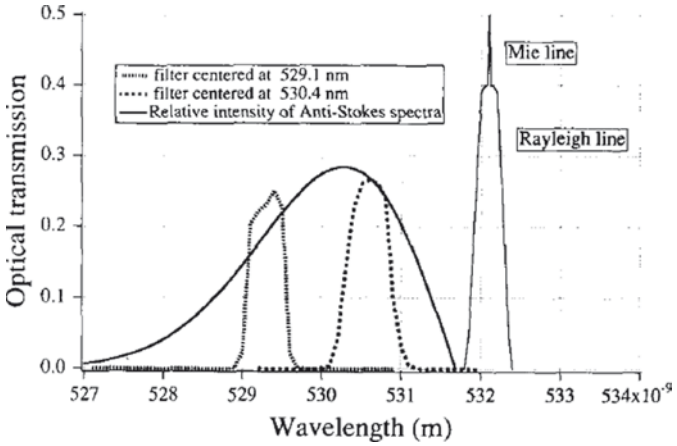

Fig. 22.8 Position of the filters used in the rotational Raman lidar and envelop of the rotational Raman AntiStokes lines for N2 and O2. When the temperature increases, the intensity increases in Raman lines near the Rayleigh line and decreases in those far from the Rayleigh line. The temperature is derived from the ratio between the signals filtered by the 2 filters Nedeljkovic et al. (1993)

operated routinely in the frame of the NDACC (Network for the Detection of Atmospheric Composition Changes) for the measurement of vertical profiles of ozone, temperature, water vapor, and aerosols.

It has been shown that below about 30 km, depending on the aerosols layer, it is not possible to use the Rayleigh scattering to measure the atmospheric density and temperature because of the contribution of the Mie scattering. It is, however, possible to extend the vertical profiles downwards using the Raman vibrational and rotational components of the scattering by the main gases of the atmosphere, N_2 and O_2 (Keckhut et al. 1990; Nedeljkovic et al. 1993). This technique can be used only on high power lidar systems due to the very low cross section of Raman scattering, about 3 orders of magnitude smaller than the Rayleigh cross section. Most of Rayleigh lidars are now equipped with Raman lidar channels to extend the vertical profiles downwards in the lower stratosphere and upper troposphere (Fig 22.8).

22.3.2 Rayleigh Doppler Wind Lidar

The Rayleigh Doppler lidar is an instrument designed to provide the horizontal wind field in the stratosphere where the backscattered signal is mainly due to Rayleigh scattering from air molecules (Chanin et al. 1989). The beam of a monochromatic pulsed laser is emitted in an oblique direction. The backscattered light is spectrally shifted when the illuminated air parcel is moving in the direction of the laser beam (Doppler shift). At the same time, the backscattered laser line is broadened by the Brownian motion of air molecules. As the vertical component of the wind is negligible in this region, the radial Doppler shift of the backscattered echo

is directly proportional to the projection of the horizontal wind on the line of sight. The Doppler shift is analyzed with a high-resolution spectral filter, for instance, a Fabry-Pérot interferometer. Very few ground-based Rayleigh Doppler lidars are in operation in the world. They provide vertical profiles of the 2 components of the horizontal wind and allow to study dynamical phenomena like GW (Souprayen et al. 1999). Figure 22.9 shows a nice example of a long period inertia-gravity wave with a downward propagating phase, a period of more than 7 h and an elliptic hodograph oriented south west – north east.

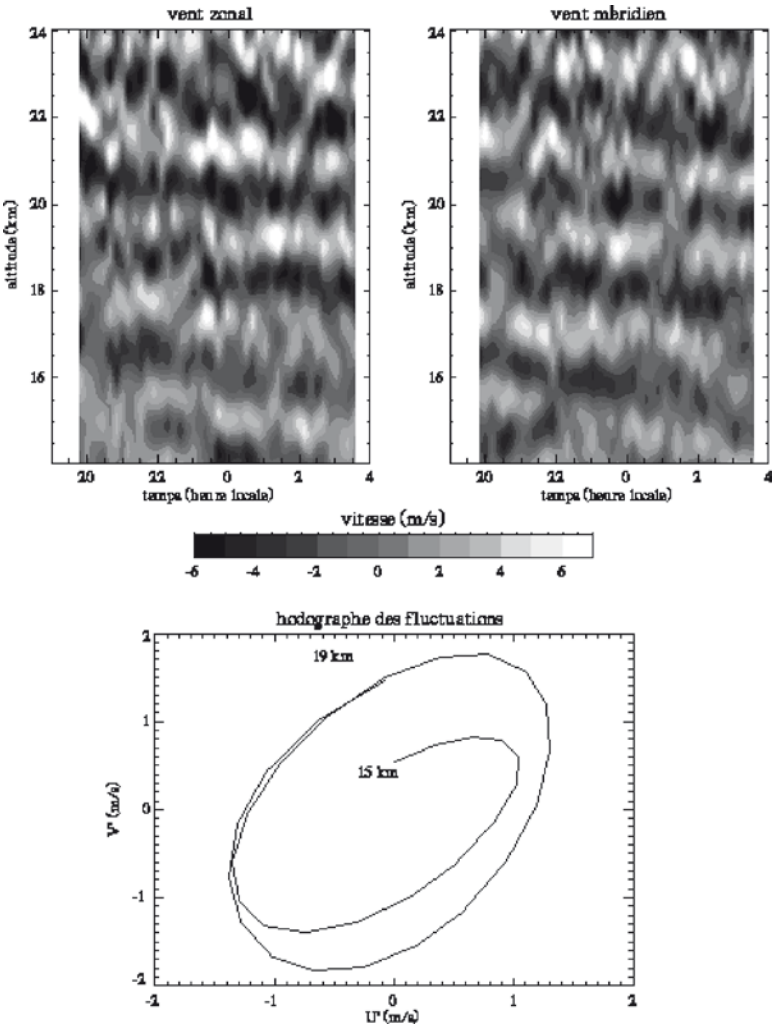

Fig. 22.9 Upper part, zonal and meridional components of the wind perturbations in ms^{-1} observed by the Doppler lidar at OHP during one night associated with the presence of an inertia-gravity wave and, lower part, hodograph of the gravity wave between 15 and 19 km

22.3.3 MST Radar

Mesosphere-stratosphere-troposphere (MST) radars are powerful instruments designed to study the dynamics of the middle atmosphere (Hocking, 1997). The principle is to observe the Doppler shift of a radio-wave beam scattered by refractive index inhomogeneities in the atmosphere. In the neutral atmosphere below 20 km, these inhomogeneities are due to air density or water vapor turbulent fluctuations. In the ionized atmosphere, above 60 km, they are due to fluctuations in electron density. In both cases, MST radar provides measurements of the radial wind as for the Doppler wind lidar. These radars can also provide turbulence parameters. Most MST radars are operated in the VHF band (typically 30–60 MHz, 5–10 m wavelengths). They provide information on the seasonal evolution of horizontal and vertical wind profiles, turbulence parameters, planetary waves, GW (Tsuda et al. 1990), and tides.

22.4 Remote Sensing from Space

Ground-based instruments provide very resolved temperature and wind data, but are operated in a limited number of site. In order to obtain a global view of the structure of the atmosphere, it is necessary to operate remote sensing instruments from space. They include infrared and microwave radiometers and GNSS radio-occultation receivers for temperature measurements, and in the near future, a space lidar for wind measurements.

22.4.1 Infrared and Microwave Radiometers

The global field of middle atmospheric temperature is measured by infrared and microwave radiometers on board operational and research meteorological satellites since 30 years (Nash and Brownscombe, 1983). The principle is to measure the thermal radiation emitted by the atmosphere at wavelengths corresponding to emission bands of an atmospheric constituent in constant mixing ratio in the atmosphere, in general, CO_2 in the infrared spectrum and O_2 in the microwave spectrum. The emission is then directly depending on temperature. For instruments looking at nadir, the vertical profile is obtained by looking in spectral bands emitted at different altitudes depending on their intensity, the stronger bands coming from the higher levels in the atmosphere. They cover mainly the troposphere and the lower stratosphere. For instruments looking at limb, the vertical profile is obtained with a scan of the tangent altitude. They provide temperature profiles mainly in the upper stratosphere and the mesosphere with a higher vertical resolution, but a poorer horizontal resolution than nadir sounders. Data of infrared and microwave operational sounders are assimilated in numerical weather forecast models. Data from stratospheric sounding unit (SSU) on board NOAA satellites since 1979 have been the

major source of upper stratospheric temperature until 1998. Since this date, they are replaced by the microwave advanced microwave sounding unit (AMSU) providing a better vertical resolution (Gelman et al. 2000).

22.4.2 GNSS Radio-Occultation

Global navigation satellite system (GNSS) radio-occultation provides vertical profiles of index of refraction in the atmosphere (Kursinski et al. 1997). The principle is to observe the Doppler shift of the radio signal emitted by GNSS satellites when the path is crossing the atmosphere and its length is increased by the refractive index change. Above 70 km in the ionized atmosphere, it allows to measure the electron content. In the neutral atmosphere, below 50 km, it provides the vertical profile of temperature in the troposphere and stratosphere, as well as humidity in the lower troposphere with a high vertical resolution (better than 500 m at the tropopause). The method is based on the measurement of time with a very high accuracy and is free from any systematic bias. This is an important point for climatological studies. GNSS radio occultation is now operational on several satellites, including the German satellite CHAMP, the operational European platform METOP, and the Taiwan-USA COSMIC/FORMOSAT-3 mission with 6 mini-satellites to improve the geographical coverage (Rocken et al. 2000). Comparisons of GNSS radio-occultation profiles with radiosonde profiles and ECMWF analyses have shown an excellent agreement in the upper troposphere and in the stratosphere up to 40 km (Fig. 22.10; Wickert et al. 2004). These data are now routinely assimilated in NWP models and are used for specific scientific studies like troposphere-stratosphere exchanges.

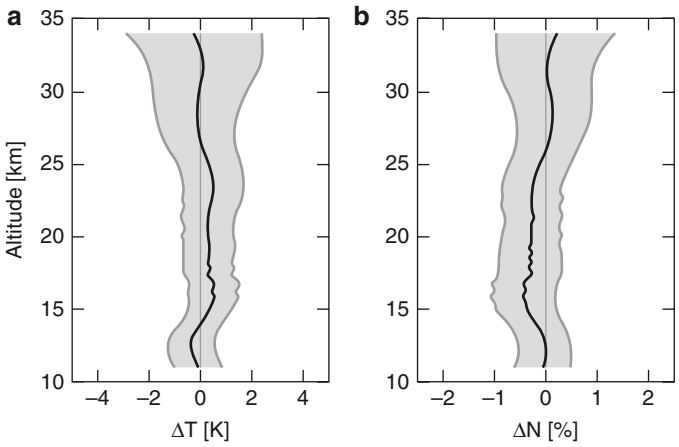

Fig. 22.10 Statistical comparison between 46,300 vertical (**a**) temperature and (**b**) refractivity profiles from CHAMP (GO) and corresponding ECMWF analysis data (CHAMP-ECMWF). From Wickert et al. 2004

22.4.3 ADM-AEOLUS Doppler Wind Lidar

The most important parameter for meteorological forecast is the wind measurement. However, this parameter is only measured by the network of radiosondes concentrated in continental areas. Except from radiosonde profiles, the wind is indirectly derived from temperature and humidity measurements assimilated in NWP. The Earth Explorer Atmospheric Dynamics Mission (ADM-Aeolus) planned to be launched in 2009 will be the first Doppler wind lidar in space (Stoffelen et al. 2005). It will provide global observations of wind profiles from space up to 30 km altitude to improve the quality of weather forecasts, and to advance the understanding of atmospheric dynamics and climate processes.

22.5 Conclusion

The middle atmosphere is a region where chemical, radiative, and dynamical processes are strongly coupled. This is also a region very sensitive to perturbations due to human activities. The polar stratospheric ozone hole is a striking example of this sensitivity. The observed global stratospheric and mesospheric cooling, linked to the warming of the lower atmosphere due to the increase of greenhouse gases, is another example. In order to understand all physical processes playing a role in this region, several remote sensing techniques from ground and from space have been developed and are operated routinely, including lidars, radars, radiometers, and radio-occultation receivers. The detection of infrasounds propagating in the middle atmosphere (Le Pichon et al. 2010; Blanc et al. 2010) is very promising to complement information on the structure and dynamics of this region and to probe atmospheric parameters in altitude ranges not easily accessible by other techniques (Drob et al. 2010).

References

Allen SJ, Vincent RA (1995) Gravity wave activity in lower atmosphere: Seasonal and latitudinal variations. J Geophys Res 100:1327–1350

Baldwin MP, Gray LJ, Dunkerton TJ et al (2001) The Quasi-Biennial Oscillation. Rev Geophys 39:179–229

Baldwin MP, Hirooka T, O'Neill A et al (2003) Major stratospheric warming in the southern hemisphere in 2002: dynamical aspects of the ozonehole split. SPARC Newsletter:20, 24–26

Bencherif H (1996) Observations de l'activité dynamique dans la moyenne atmosphère, par sondage LIDAR, au dessus du site de l'île de la Réunion, 20.8°S 55.5°E. Thèse de Doctorat de l'Université Paris 6, Paris

Brasseur GP, Solomon S (2006) Aeronomy of the middle atmosphere: chemistry and physics of the stratosphere and mesosphere, 3rd edn. Springer, Dordrecht, Netherlands

Blanc E, Le Pichon A, Ceranna L, Farges T, Marty J, Herry P (2010) Global scale monitoring of acoustic and gravity waves for the study of the atmospheric dynamics. This volume, pp. 641–658

Chanin ML, Garnier A, Hauchecorne A, Porteneuve J (1989) A Doppler Lidar for measuring winds in the middle atmosphere. Geophys Res Let 16:1273–1276
Charney JG, Drazin PG (1961) Propagation of planetary scale disturbances from the lower into the upper atmosphere. J Geophys Res 66:83–109
Drob DP, Meier RR, Picone JM, Garcés MM (2010) Inversion of infrasound signals for passive atmospheric remote sensing. This volume, pp. 695–726
Dunkerton TJ (1997) The role of gravity waves in the quasi-biennial oscillation. J Geoph Res 102:26053–2607
Dunkerton TJ, Baldwin MP (1991) Quasi-biennial Modulation of Planetary-Wave Fluxes in the Northern Hemisphere Winter. J Atmos Sci 48:1043–1061
Fiocco G, Grams G (1964) Observations of the aerosol layer at 20 km by optical radar. J Atmos Sci 21:323–324
Fleming EL, Chandra S, Schoeberl MR, Barnett JJ (1988) Monthly mean global climatology of temperature, wind, geopotential height, and pressure for 0-120 km. NASA Tech Memo 100697
Forbes JM (1982) Atmospheric Tides, 1, Model Description and Results for the Solar Diurnal Component. J Geophys Res 87:5222–5240
Garcia RR, Dunkerton TJ, Lieberman RS, Vincent RA (1997) Climatology of the semiannual oscillation, of the tropical middle atmosphere, J. Geophys. Res 102:26019–26032
Gelman ME, Miller AJ, Long CS et al (2000) The transition from SSU to AMSU data in CPC stratospheric analyses. SPARC Newslett 15:17–18
Godin S, Mégie G, Pelon J (1989) Systematic lidar measurements of the stratospheric ozone vertical distribution. Geophys Res Lett 16:547–550
Hauchecorne A, Chanin ML, Wilson R (1987) Mesospheric temperature inversion and gravity wave breaking. Geophys Res Lett 14:933–936
Hauchecorne A, Chanin ML (1980) Density and temperature profiles obtained by lidar between 30 and 70 km. Geophys Res Lett 7:564–568
Hauchecorne A, Chanin ML (1983) Mid-latitude observations of planetary waves in the middle atmosphere during the winter of 1981–1982. J Geophys Res 88:3843–3849
Hertzog A, Souprayen, Hauchecorne A (2001) Measurements of gravity waves activity in the lower stratosphere by DoppCler lidar. J Geophys Res 106:7879–7890
Hirota I, Hirooka T (1983) Normal mode Rossby waves observed in the upper stratosphere. Part I: First symmetric modes of zonal wavenumbers 1 and 2. J Atmos Sci 41:1253–1267
Hirooka T (2000) Normal mode Rossby waves as revealed by UARS/ISAMS observations. J Atmos Sci 57:1277–1285
Hocking, W.K. (1997) Strengths and limitations of MST radar measurements of middle-atmosphere winds. Ann. Geophysicae 15:1111–1122
Holton JR (1979) An introduction to Dynamic Meteorology, 2nd edn. Academic Press, London
Holton JR (1982) The role of gravity wave induced drag and diffusion in the momentum budget of the mesosphere. J Atmos Sci 40:2497–2507
Holton JR, Haynes PH, McIntyre ME et al (1995) Stratosphere-troposphere exchange. Rev Geophys 33:405–439
Holton JR, Lindzen RS (1972) An updated theory for the quasi-biennial cycle of the tropical stratosphere. J Atmos Sci 29:1076–1080
Keckhut P, Chanin ML, Hauchecorne A (1990) Stratospheric temperature measurements using Raman lidar. Appl Optics 29:5182–5186
Keckhut P, Hauchecorne A, Chanin ML (1993) A critical review of the data base acquired for the long term surveillance of the middle atmosphere by Rayleigh lidar. J Atm Ocean Tech 10:850–867
Keckhut P, Gelman ME, Wild JD et al (1996) Semi-diurnal and diurnal temperature tides (30–55 km): climatology and Effect on UARS-lidar data comparisons. J Geophys Res 101:10299–10310
Kishore P, Namboothiri SP S, Igarashi K et al (2002) MF radar observations of mean winds and tides over Poker Flat, Alaska (65.1_ N, 147.5_ W). Annales Geophysicae 20:679–690
Kursinski ER, Hajj GA, Schofield JT et al (1997) Observing Earth's atmosphere with radio occultation measurements using the Global Positioning System. J Geophys Res 102:23429–23465

Labitzke K (1977) Inter-annual variability of the winter stratosphere in the northern hemisphere. Mon Weather Rev 105:762–770
Leblanc T, Hauchecorne A (1997) Recent Observations of Mesospheric Temperature Inversions. J Geophys Res 102:19471–19482
Le Pichon A, Vergoz J, Cansi Y, Ceranna L, Drob D (2010) Contribution of infrasound monitoring for atmospheric remote sensing. This volume, pp. 623–640
Lindzen RS (1966) On the theory of the diurnal tide. Mon Wea Rev 94:295–301
Lindzen RS (1981) Turbulence and Stress Owing to Gravity Wave and Tidal Breakdown. J Geophys Res 86:9707–9714
McCormick MP, Swissler TJ, Chu WP, Fuller WH Jr (1978) Post-vocanic stratospheric aerosol decay as measured by lidar. J Atmos Sci 35:1296–1303
McIntyre ME (1992) Atmospheric Dynamics: Some Fundamentals with Observational Implications. Proceedings of Int School Phys Enrico Fermi CXV Course, JC Gille and G Visconti Eds, North-Holland, In
Madden RA, Labitzke K (1981) A free Rossby wave in the troposphere and stratosphered during January 1979. J Geophys Res 86:1247–1254
Matsuno T (1971) A dynamical model of the stratospheric sudden warming. J. Atmos Sci 28: 1479–1494
Meriwether W, Gardner CS (2000) A Review of the Mesosphere Inversion Layer Phenomena. J Geophys Res 105:12405–12416
Mote PW, Rosenlof KH, McIntyre ME et al (1996) An atmospheric tape recorder: The imprint of tropical tropopause temperatures on stratospheric water vapor. J Geophys Res 101:3989–4006
Nash J, Brownscombe JL (1983) Validation of the Stratospheric Sounding Unit. Adv Space Res 2:59–6
Naujokat B (1986) An update of the observed quasi-biennial oscillation of the stratospheric winds over the tropics. J Atmos Sci 43:1873–1877
Nedeljkovic N, Hauchecorne A, Chanin ML (1993) Rotational Raman lidar to measure the atmospheric temperature from the ground to 30 km. IEEE Transactions on Geoscience and Remote Sensing 31:91–101
Pendlebury D, Shepherd TG, Pritchard M, McLandress C (2008) Normal mode Rossby waves and their effects on chemical composition in the late summer stratosphere. Atmos Chem Phys 8:1925–1935
Randel WJ, Gille JC, Lahoz AE (1993) Stratospheric transport from tropics to middle latitudes by planetary wave mixing. Nature 365:533–535
Ray, E. A., M. J. Alexander, and J. R. Holton (1998), An analysis of the structure and forcing of the equatorial semiannual oscillation in zonal wind, *J. Geophys. Res.*, *103*(D2), 1759–1774.
Reed RJ (1966) Zonal wind behavior in the equatorial stratosphere and lower mesosphere. J Geophys Res 71:4223–4233
Rocken C, Kuo YH, Schreiner W et al (2000) COSMIC System Description. Terres Atmos Oceanic Sci 11:21–52
Salby ML (1984) Survey of Planetary-Scale Traveling Waves: The State of Theory and Observations. Rev Geophys 22:209–236
Salby M, Sassi F, Callaghan P et al (2002) Mesospheric inversions and their relationship to planetary wave structure. J Geophys Res 107. doi: 10.1029/2001JD000756
Schmidlin FJ (1976) Temperature Inversions near 75 km. Geophys Rev Lett 3:173–176
Schoeberl MR (1978) Stratospheric warmings: Observations and theory. Rev Geophys Space Phys 16:521–538
Shepherd TG (2000) The middle atmosphere. J Atmos Terr Sol Phys 62:1587–1601
Souprayen C, Garnier A, Hertzog A, Hauchecorne A (1999) Doppler wind lidar for stratospheric measurements. Part 1: Instrumental setup-validation-first climatological results. Appl Optics 38:2410–2431
Stoffelen A, Pailleux J, Källén E et al (2005) The atmospheric dynamics mission for global wind field measurement. Bull Amer Meteor Soc 86:73–87

Swenson GR, Gardner CS (1998) Analytical models for the responses of the mesospheric OH* and Na layers to atmospheric gravity waves. J Geophys Res 103: 6271–6294

Tsuda T, Kato S, Yokoi T et al (1990) Gravity waves in the mesosphere observed with the middle and upper atmospheric radar. Radio Sci 26:1005–1018

Venkat Ratnam MA, Narendra Babu A, Jagannadha Rao VVM et al (2008) MST radar and radiosonde observations of inertia-gravity wave climatology over tropical stations: Source mechanisms. J Geophys Res 113 D07109 doi:10.1029/2007JD008986

Wickert J, Schmidt T, Beyerle G et al (2004) The radio occultation experiment aboard CHAMP: operational data analysis and validation of atmospheric profiles. J Meteor Soc Jpn 82:381–395

Wilson R, Chanin ML, Hauchecorne A (1991) Gravity waves in the middle atmosphere by Rayleigh Lidar, Part. 2: Climatology. J Geophys Re 96:5169–5183

Chapter 23
The Representation of Gravity Waves in Atmospheric General Circulation Models (GCMs)

François Lott and Christophe Millet

23.1 Introduction

The technology of remote operational monitoring of nuclear tests has been established as a set of several detection techniques. The acoustic method is especially important because unauthorized tests may be conducted in the atmosphere, far away the national territory where the event of a nuclear explosion can be proved by a competent agency on site. While the location of underground tests may be determined by seismic methods with high accuracy, it is known that acoustic low-frequency waves generated by atmospheric tests can be deformed and masked by a plethora of waves of natural origin.

The possibility of propagation of acoustic low-frequency waves (or infrasounds) is explained by the existence of atmospheric channels, the vertical scales of which are large compared to the wavelength of infrasounds. Thus, the propagation models used for this purpose are mainly based on the acoustic wave equation and the use of asymptotic methods. Most numerical studies that have been carried out during the last decade used in length the ray tracing technique, the normal mode approach, and/or the resolution of the parabolic equation (see Part III of this book for a review).

Despite an overall good agreement with measurements associated with known events, a consensus seems to have emerged that these techniques cannot explain some important signals in the microbarograph measurements (see, e.g., Millet et al. 2007; Ponomarev et al. 2006 and Kulichkov et al. 2002, 2004a, 2004b). Indeed, long-range propagation of infrasounds is ensured mainly by low waveguide modes (Ponomarev et al. 2006), for which the vertical scales are comparable with the scales of atmospheric vertical inhomogeneity and, especially, with the scales of internal gravity waves. For such mode numbers, it is known that the ray optics approximation is not well-suited to acoustic propagation and fails to capture important atmospheric wave interactions. A consistent set of approximate equations for

F. Lott (✉)
Laboratoire de Météorologie Dynamique, Ecole Normale Supérieure, 24 rue Lhomond, 75231 Paris, France
e-mail: flott@lmd.ens.fr

A. Le Pichon et al. (eds.), *Infrasound Monitoring for Atmospheric Studies,*
DOI 10.1007/978-1-4020-9508-5_23, © Springer Science+Business Media B.V. 2010

large-scale waves may be obtained by a proper choice of dimensionless parameters in the primitive equations. However, such a scale analysis is no longer valid when waves of separate scales coexist and interact with one another.

To circumvent these difficulties, the future generation of infrasound propagation models will be based on the resolution of primitive equations of motion up to thermospheric altitudes. The most recent models become similar as the present Numerical Weather Forecasting Models (NWP) and Global Climate Models (GCM), except that they include compressible effects (For completeness, note that the NWP models still adopt approximations or numerical techniques that filter out a good fraction of the sound waves). Based on suitable numerical schemes, some of these models are able to capture acoustic waves as well as gravity waves, but still fail to compute wave motions in the same way as atmospheric motions. As a disturbance propagates upwards, the strong decrease of mean density with altitude gives rise to shock waves and gravity waves (GWs) that can no longer be ignored as high amplitude phenomena. Thus, whereas a simple rigid, free-slip surface is often employed in NWP models, one of the common issues of nonlinear acoustic-gravity wave propagation models deals with the treatment of radiation and outflow boundary conditions.

Internal GWs are ubiquitous in the atmosphere. They are observed, for instance, by the high-resolution radiosondes, which give vertical profiles of temperature and velocity (e.g., Dalaudier et al. 1994). Although GWs are quite coherent and predictible when they are produced by mountains, they are much more random when they are caused by other sources (convection, geostrophic adjustment in fronts, shear instabilities). This becomes particularly true in the middle atmosphere where the influence of waves coming from various independent sources can be felt at the same place. In this case, a statistical description is more adapted, and many measurements have shown that the GWs spectra in the vertical direction follow a spectral law given by $E \sim N^2\ m^{-3}$, where E, N, and m are respectively the kinetic or potential energy (expressed per unit mass), the Brunt-Vaisaala frequency, and the vertical wavenumber. These spectra are observed in the range of vertical wavelengths $2\pi/m$ between 100 m and few kilometers. When they break, which generally occur when we have $2\pi/m$ <100 m, the turbulence results in Kolmogoroff spectra. As these spectra are quite universal, most parameterizations of the nonorographic GW in GCMs are based on them (Hines 1997, Warner and McIntyre 1996). This makes them quite different from the parameterization of the mountain gravity waves, which use their more predictive nature (Lott and Miller 1997).

In General Circulation Models, quite substantial systematic errors have been reduced by including the parameterizations of orographic and nonorographic gravity waves. Historically, the orographic GWs routines have been introduced during the mid-eighties, when the global GCMs where limited to the troposphere and lower stratosphere resolution (Palmer et al. 1986). The nonorographic routines are more recent and have been introduced when the GCMs have begun to extent up to the mesosphere (Manzini et al. 1997). Such routines permit to correct the zonal mean wind and the zonal mean temperature at the summer mesopause.

The parameterization of mountain GWs alleviates systematic errors in GCM simulations of the tropospheric westerlies (Palmer et al. 1986). Miller et al. (1989)

extended this study, showing that the representation of orography in global models has an impact (positive or negative) on many of the large-scale structures mentioned before. Miller et al. (1989) and also Stephenson (1994) have shown that the vertical repartition of the mountain drag is an important issue for GCMs. These large-scale simulations obviously provide important applications for the 2-D (Clark and Peltier 1984; Durran 1987) and 3-D (Miranda and James 1992; Schar and Durran 1996) theoretical studies on mountain flow. Following these, Lott and Miller (1997) (hereafter LM97) have proposed a subgrid scale orographic (SSO) drag scheme which gives particular attention to the drag of the flow at levels that intersect the SSO. This scheme is also validated against the PYREX data (Bougeault et al. 1993) in all the situations for which the incident wind perpendicular to the ridge is strong.

Among the quasi-steady patterns that SSO parameterization schemes affect, the steady planetary wave is of particular interest because its simulation is rather difficult. For instance, Fig. A1 in D'Andrea et al. (1996) shows the steady geopotential height field for 15 different models: among them, many (but not all) are too zonal. To correct these errors, one has to determine which processes related to the mountains contribute to the steady planetary wave. For this purpose, the quasi geostrophic models are helpful because they have been extensively used in diagnosing the forcing of planetary waves (Held 1983). In these models, mountains induce vortex stretching, modifying the vorticity, but keeping the potential vorticity unchanged. Interestingly, the circulation over mountains associated to vortex stretching is driven by a force whose horizontal component is perpendicular to the incident flow in the linear quasi-geostrophic context and that is proportional to the mountain volume (Smith 1979). In the context of atmospheric models which do not use the quasi geostrophic approximation, the fact that vortex stretching can be eventually accounted for by a force that is quite predictable was used in Lott (1999) to reduce errors on the model simulation of the planetary waves.

Because this review is devoted to surface process, the recent progresses in developing new gravity wave drag schemes, which include nonorographic waves, are only mentioned here briefly and for completeness. Detailed impacts of such a scheme are, nevertheless, given in the Sect. 3.2. The need for such schemes follow that most GCMs now extend to the middle atmosphere, where the circulation is largely controlled by wave-induced forces (Rossby and Gravity waves) (Holton et al. 1995; Haynes et al. 1995). For the gravity wave part and in summer, mountain waves cannot provide these forces because they have good chances to encounter critical levels in the low stratosphere (Lindzen 1981). Furthermore, the forces needed in this season and near the mesopause are opposite in sign with the forces mountain waves can provide. Finally, observations suggest that steady GWs are seldom above about 20 km altitude. The general way by which nonorographic drag scheme is developed is grossly presented in Sect. 3.3, together with some results obtained in the LMD-GCM extended to the middle atmosphere and including the Hines (1997) parameterization scheme tested by Manzini et al. (1997) in the ECHAM4 model.

23.2 The Different Parameterizations

23.2.1 Subgrid-Scale Orographic Drag

The orographic drag scheme presented here is adapted from LM97 and used in Lott (1998). The SSO over one gridpoint region is represented by seven parameters, μ, γ, σ, θ, Z_{min}, Z_{max}, and Z_{mea}, which stand for the standard deviation, the anisotropy, the slope, the orientation, the minimum, the maximum, and the mean elevation of the orography, respectively. These seven parameters are evaluated over a grid point region from the US Navy dataset (on $10' \times 10'$ of degrees grids). The scheme uses values of low-level wind and static stability, which are partitioned into two parts. The first corresponds to the incident flow and is evaluated by averaging the wind, the Brunt-V\"ais\"al\"a frequency, and the fluid density between the model ground Z_{mean} and the mountain peaks Z_{max}. This low-level flow is referenced as $\boldsymbol{U}_H$, N_H, and ρ_H, respectively. The second part is the "blocked" flow, whose upper height Z_b is the highest level that satisfies the condition,

$$\int_{Z_b}^{Z_{max}} \frac{N}{U_p} dz \leq H_{NC}, \tag{23.1}$$

where the wind speed $U_p(z)$ is calculated by resolving the wind $\boldsymbol{U}(z)$ in the direction of the incident flow U_H. The parameter H_{NC} tunes the depth of the blocked flow layer and is of order one. Then, for each layer below Z_b, a force per unit volume is applied in the form

$$D_b(z) = -\rho C_d F \frac{Z_b - Z}{Z_b - Z_o} \frac{U|U|}{2}, \tag{23.2}$$

where F is given by

$$F = \left(2 - \frac{1}{r}\right) \frac{\sigma}{2\mu} \left[B(\gamma) \cos^2 \psi + C(\gamma) \sin^2 \psi \right], \tag{23.3}$$

if $r>1/2$, or by $F=0$, if $r<1/2$. In Eq.(22.3) the angle between the incident flow and the normal ridge direction is Ψ, the aspect ratio of the obstacle as seen by the incident flow is r. The functions $B(\gamma)$ and $C(\gamma)$ are of order 1 and take into account the anisotropy of the SSO (see LM97). The parameter C_d, which is typically of order unity from the literature on flow dynamics around bluff body, tunes the blocked flow drag amplitude.

On the supposition that when there is low-level flow blocking, the effective height of the SSO felt by the fluid is reduced to $Z_{max} - Z_b$, the gravity wave stress τ (which is a force per unit area) is reduced accordingly. After counting number of ridges within a grid point region, this stress becomes,

$$\tau = {}_{\rho H}\, GU_H N_H \left(Z_{\max} - Z_b\right)^2 \frac{\sigma}{4\mu}\begin{pmatrix} B\cos^2\psi_H + C\sin^2\psi_H \\ (B-C)\sin\psi_H\cos\psi_H \end{pmatrix}. \tag{23.4}$$

The parameter G tunes the GWs stress amplitude and is also of order 1. The vertical distribution of the gravity wave stress determines the levels at which the waves are dissipated and slow down the mean flow. First, the stress decays by a tunable factor $\beta < 1$ between the ground and the 850-hPa level to crudely account for the low-level dissipation of the trapped lee waves (see Miller et al. 1989 and the Appendix). Above, breaking occurs when the total Richardson number Ri falls below a critical value Ri_c, which is of order unity.

23.2.2 Orographic Lift

In the model itself, the lift representation consists of applying a force per unit volume $\boldsymbol{L}$ that is perpendicular to the wind at each level below the mountain maximum height $Z_{\max}$

$$\mathrm{L} = -{}_{\rho} C_l f \left(\frac{Z_{\max} - Z}{Z_{\max} - Z_o}\right) k \times u \tag{23.5}$$

In Eq. (23.5), f is the Coriolis frequency and C_l is a tunable parameter of order 1. When the incident wind is uniform in the vertical, Eq. (23.5) integrated from the model ground Z_{mea} to the mountain peak $Z_{\max}$ gives a stress,

$$L = -{}_{\rho} C_l f \left(\frac{Z_{\max} - Z_o}{2}\right) k \times u \tag{23.6}$$

which is near the lift stress exerted by an obstacle on a quasi-geostrophic flow (Smith 1979).

23.2.3 Nonorographic Waves

Because the nonorographic schemes include ensemble of waves with far different propagation properties, a convenient way to formulate them is to adopt a spectral representation. These differentiate them fundamentally from most current orographic schemes, where a representation in the physical space is necessary at low level, to account for nonlinearities. For mountain waves, the description in the physical space remains adequate aloft, providing the waves are hydrostatic. For nonorographic waves, the spectral representation is also motivated by the fact that

numerous observational studies suggest that GWs energy spectra have a slope at large vertical wavenumber m that is roughly independent of time and position.

Practical spectral GWs parameterization schemes (see for instance Hines 1997; Warner and Mc Intyre 1996, 2001) tend to describe gravity wave spectral evolution in terms of the vertical propagation and saturation of a spectrum, which is imposed at a given launch altitude. A good example of such a scheme is that of Warner and Mc Intyre (1996), where the evolution of the spectra from one altitude to the next is based on well-understood aspects of linear conservative GWs propagation. The saturation is then entirely empirical. When the spectra transported conservatively, present in the vertical wavenumber space, a saturated portion (i.e., the portion at "large" m) that exceed a given threshold, this threshold is imposed as the new spectra. To fit data, this threshold can include the m^{-3} slope suggested by observations. For historical reasons, in the LMD-GCM we have used until now the scheme proposed by Hines (1997), which try to include more sophisticated wave breaking models. In practice, nevertheless, it is likely that the schemes of Hines (1997) and Warner and Mc Intyre (1996, 2001) give comparable results.

23.3 Impacts on GCMs Runs

23.3.1 Subgrid-Scale Orographic Parameterization and Lift

The model used in this study is a tropospheric version of the LMDz GCM (Hourdin et al. 2006). It is a gridpoint model, and in the simulation presented, the gridpoints are regularly distributed in the longitude-latitude coordinates with resolution $3.75 \times 2.5°$. The version used has 19 vertical sigma-levels unevenly spaced to provide more resolution near the ground and in the lower stratosphere. In the experiment presented below, the different tunable parameters of the orographic forces scheme are: $H_{NC} = 1$, $C_d = 1$, $G = 1$, $\beta = 0.5$, $Ri_c = 0.25$, and $C_l = 1$. To perform simulations that can be compared to the observed climate and to ensure that the results presented are significant, the model is integrated over long periods and forced with observed sea-surface temperatures and sea-ice distribution.

In different set of experiments discussed with some details in Lott (1998), where the different parts of the orography parameterization scheme were each tested independently, it was found that the low-level blocked flow drag improves the low-level flow, but slightly degrades the steady planetary wave. Similar results were found for the gravity wave part of the scheme: GWs drag improves the westerlies at the upper levels (Palmer et al 1986) and at low levels where the trapped waves (Miller et al. 1989) reinforce the impact of the blocked drag. For the simulation of the steady planetary wave, the GWs drag is rather neutral, its impact is similar to that of the blocked flow drag. The lift scheme alone, on the other hand, appeared beneficial for the steady planetary wave, but does not affect the zonal wind very much.

The impact of the scheme on the model is represented on the differences map shown in Fig. 23.1 and 23.2. For both the zonal wind and the steady planetary wave, it appears that the model is closer to the climatology with the orographic

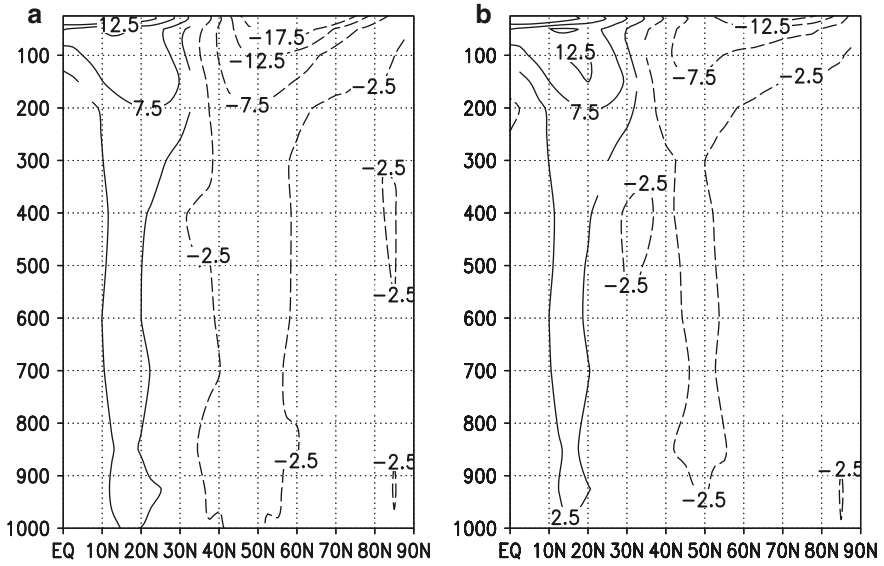

Fig. 23.1 Difference between the zonal wind of the NMC analysis and that of the GCM simulations: DJF 85-93. Zero line not shown, negative values are dashed. (**a**) Control run; (**b**) run with parameterization

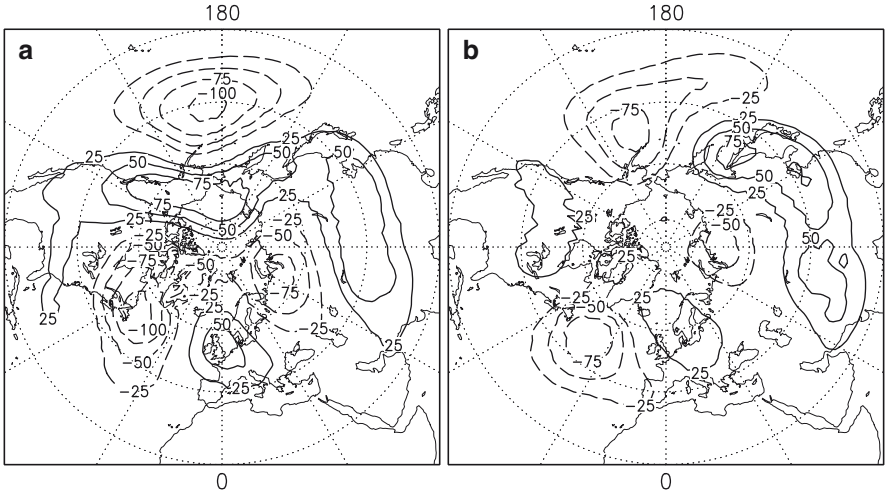

Fig. 23.2 Difference between the Geopotential height anomaly at 500 hPa of the NMC analysis fields and that of the GCM simulations: DJF 85-93. Zero line not shown, negative values are dashed. (**a**)Control run; (**b**)run with parameterization

parameterization. The parameterized drag tends to reduce errors at nearly all levels on the zonal wind. The benefits of the scheme are, nevertheless, the greatest at low-levels (below 900-hPa) where the drag is maximum and at high-levels (above 100-hPa), where the parameterized GWs break. The steady planetary waves differences are also reduced nearly everywhere in the northern hemisphere, and particularly over the continents. Improvements are, nevertheless, more evident over North America where the scheme efficiently improves the simulation of the ridge over the rocky mountains. The scheme is also helpful for the simulation of the steady planetary wave over northern Europe and northern Asia, but it does not reduce the errors south and east of the Himalaya plateau.

23.3.2 Nonorographic Gravity Waves Spectral Parameterization

23.3.2.1 Impacts in the midlatitudes

In comparison with the essentially tropospheric LMD-GCM used in Sect. 3.1, the extended LMD-GCM to the middle atmosphere spans all heights ranging from the surface to 0.01 mb (approximately 80 km), discretized into 50 levels of varying thickness (Lott et al. 2005). Layers are approximately 1.5 km thick between 10 and 60 km and then increase to about 8 km in the last two upper levels. A simple Rayleigh drag sponge layer is employed in the four upper layer at $z = 63.5$, 67.5, 72.5, and 81.25 km, with damping time constants equal 10 day^{-1}, 5 day^{-1}, 2.5 day^{-1} and 1.25 day^{-1} respectively. These Rayleigh-drags are applied to the nonzonal component of the flow only to prevent large-scale waves' downward reflection at the upper boundary, without violating Downward control principles (Shepherd et al. 1996).

The impact of the Gravity wave drag scheme on the simulated middle atmosphere circulation is evaluated by comparing two 5-years long (1993–1997) experiments, one with and the other without parameterized orographic and nonorographic gravity wave drag. The parameters used for the orographic GWs drag are the ones given in Sect. 3.1. The nonorographic Hines (1997) scheme is used with a low source strength, corresponding to an r.m.s. gravity-wave wind of 1 $m\,s^{-1}$ at the launch level. The launch level is the model ground.

Figure 23.3 shows the zonal mean wind in the model simulation in the absence of gravity wave drag for four different months. In this case, the model shows the usual enormous westerly biases in the simulated winds at midlatitude, and at nearly all levels above 20–30 km (for a comparison with climatology, see for instance Fig. 23.4 in Beagley et al. 1997). Figure 23.4 shows that these errors can be considerably reduced when introducing the gravity wave schemes, though discrepancies with observations still exist. In the tropics, the reduction of the biases from one experiment to the other does not appear clearly in Fig 23.3 and 23.4 as differences between the two simulations are less pronounced in this region.

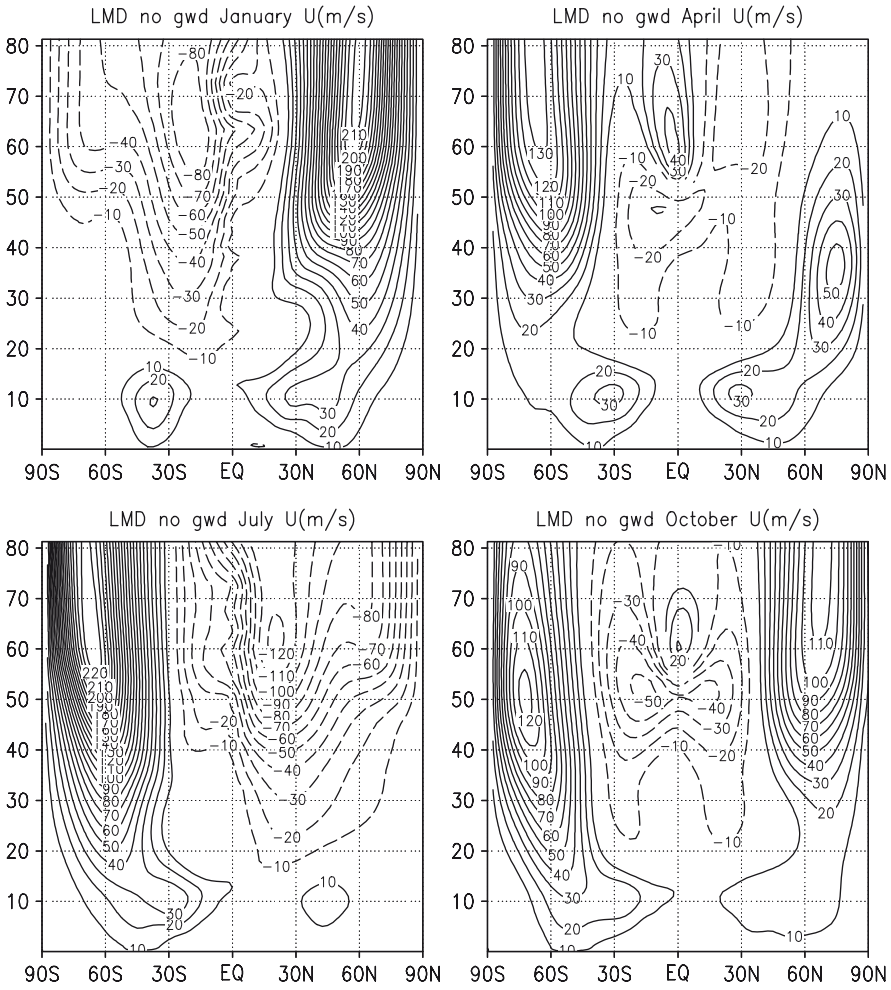

Fig. 23.3 Zonally averaged zonal wind field calculated from a 5-year run of the LMD-GCM with no gravity wave drag. Contour interval=10 $m\,s^{-1}$, negative values are dashed

23.3.2.2 Impact on the Tropical Oscillations

For a finer analysis, it is conventional to look at time-series of the zonal mean zonal wind at the equator and as a function of height. Figure 23.5 shows such a picture for both simulations for the year 1993. A semiannual oscillation is clearly evident in both model integrations above the stratopopause (around 60–70 km), extending down to 45–50 km into the upper stratosphere. We note, however, that the westerly phase is too weak and does not descend far enough compared with observations (see for instance Hamilton and Mahlman 1988). However, these defects are far more pronounced without GWs drag (Fig. 23.5a) than with GWs drag (Fig. 23.5b). Furthermore, the GWs parameterization also significantly reduce westerly biases.

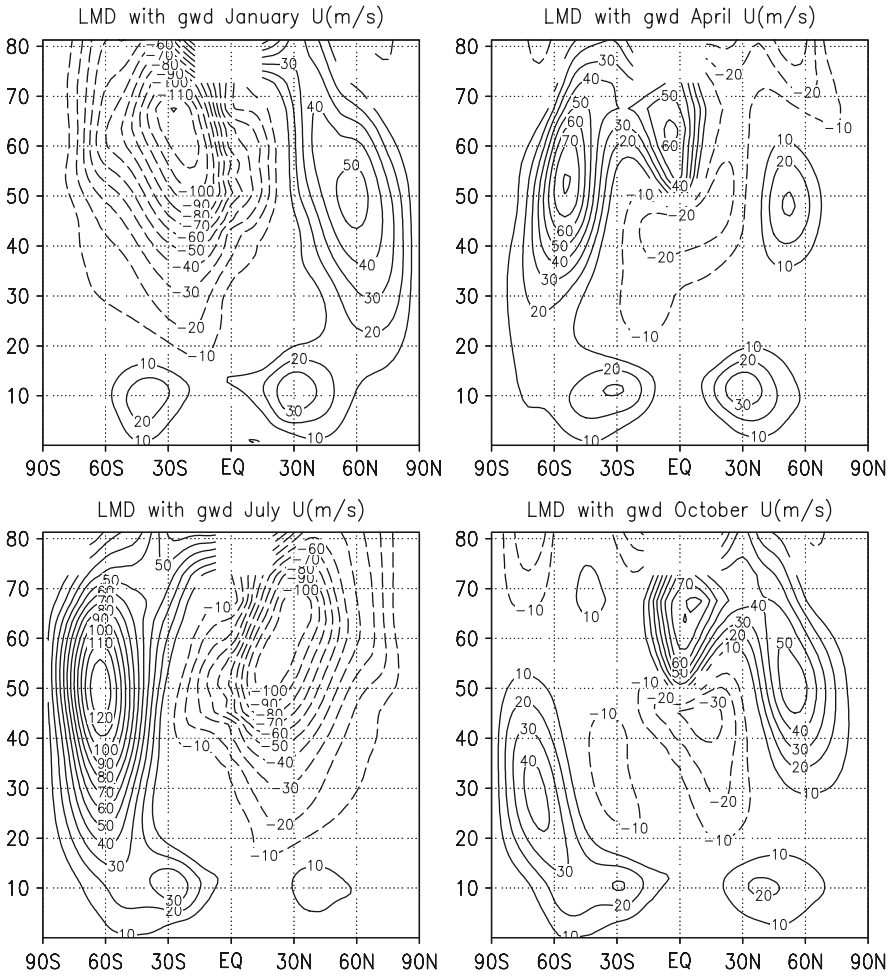

Fig. 23.4 Zonally averaged zonal wind field calculated from a 5-year run of the LMD-GCM with both nonorographic (Hines) and orographic (Lott and Miller) gravity waves (GWs) drag included. Contour interval=10 $m\,s^{-1}$, negative values are dashed

The fact that explicit simulation of tropical oscillations (semiannual oscillation and quasi-biennial oscillation) in GCMS of the middle atmosphere can be much improved by GWs drag parameterization is now illustrated. Because these oscillations need an accurate vertical resolution to be properly resolved, the simulations presented next are made with a version of the LMD-GCM that still include 50 vertical levels, but with the upper boundary placed at 65 instead of 80 km. Two simulations are made that differ from each other only in the source strength. In the first one (weak Hines), the source strength corresponds to a r.m.s. gravity-wave wind of 1 $m\,s^{-1}$ at the ground, while in the second one (strong Hines) it is 1.25 $m\,s^{-1}$.

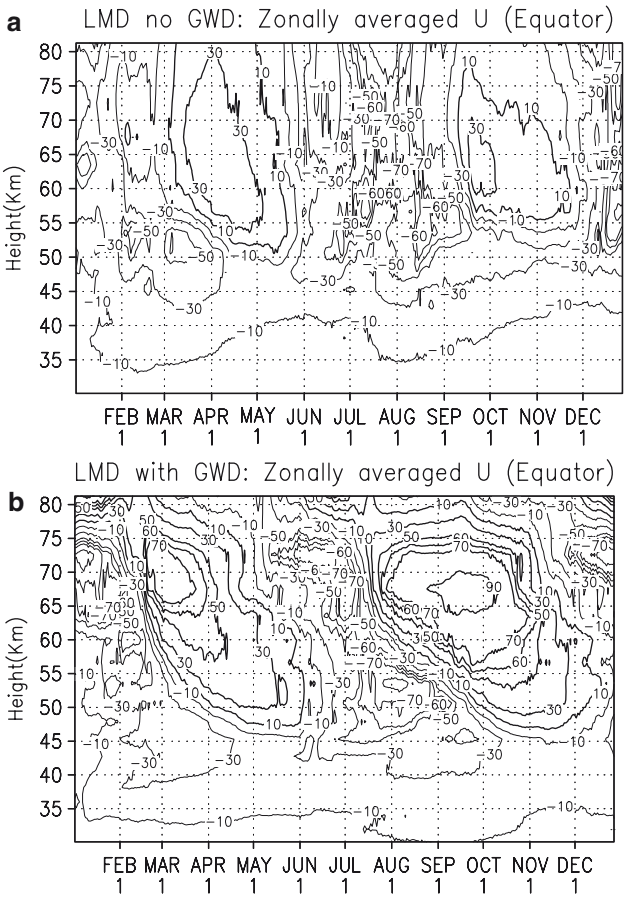

Fig. 23.5 (**a**)March of zonally averaged zonal wind at the equator for the year 1993 of the LMD-GCM integrations without GWs drag. (**b**)as (**a**) but for the integration with GWs drag. Contour interval = 20 $m\,s^{-1}$ in both panels. Positive values are thick solid, negative values are thin solid

Both simulations (Fig. 23.6a, b) exhibit a semiannual oscillation signal. However, the weak Hines experiment (Fig. 23.6a) shows a westerly phase that does not go beyond 45 km, while in the strong Hines experiment it descends down to 35 km, which is in far better agreement with the observations. Below these levels (i.e., including the quasi-biennial oscillation domain), the model presents a systematic easterly bias, and nearly no seasonal and inter-annual oscillations. Note, nevertheless, in the simulation with the strong Hines scheme and around 35–40 km, the adjacent westerly phase of the semiannual oscillation near coalesces between January and July of the second year and between July of the year 3 and January of the year 4. This indicates that the model is near producing an inter-annual tropical oscillation. It is too small, nevertheless, to maintain itself and descend further below 35 km: the model fails in producing a QBO in the 20–30 km region. Note

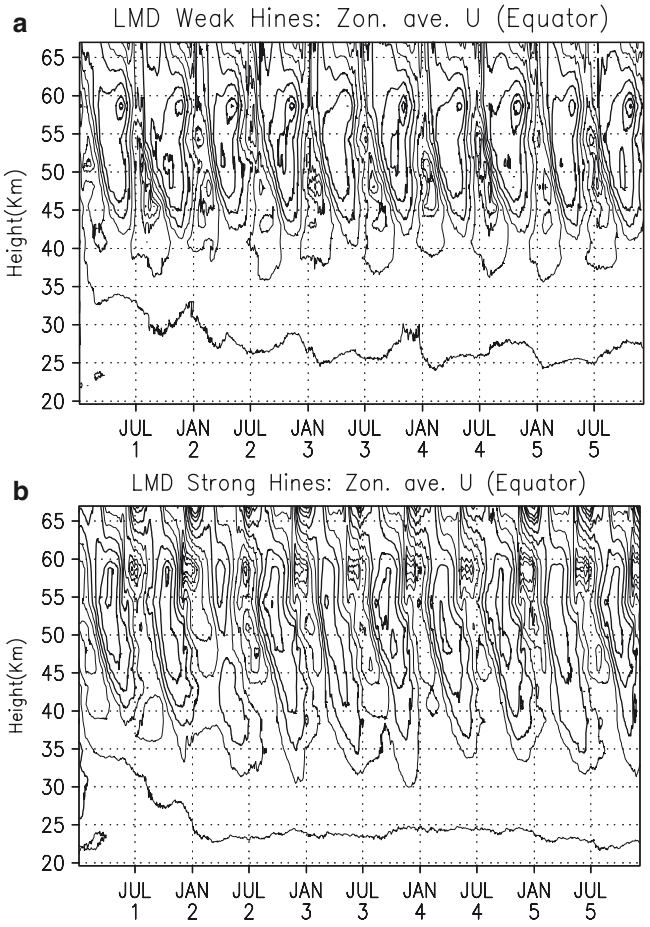

Fig. 23.6 (**a**)March of zonally averaged zonal wind at the equator for the period 1993–97 of the LMD-GCM integrations with GWs drag. (**b**)As (**a**) but for a stronger GWs forcing. Contour as in Fig. 23.5

here that this may be in good part due to the fact that the vertical resolution of the model in the low and middle stratosphere is not sufficiently refined. Models with higher resolution and GWs parameterization can today reproduce a quite realistic QBO (Giorgetta et al. 2006).

23.4 Concluding Remarks

During the 1990s, substantial progress was made in the understanding of the GWs generation by mountains as well as of their influence on the atmospheric general circulation. At almost the same time, it became clear that nonorographic GWs are

also significant for the climate, if we look at it in the middle atmosphere. The GWs up there being much less predictible, they are parameterized using techniques that are essentially statistical.

With the development of the International Monitoring System for the enforcement of the Comprehensive Nuclear Test Ban Treaty, there is a challenge to gain a still better understanding of the role of GWs in infrasound propagation. The primary need is to identify conditions for which GWs can be expected and how they can be represented in propagation models. Although the asymptotic methods that are used by the geophysical community permit to explain some basic properties of infrasonic signals observed during experiments, a fresh look at the problem starting with the GCM approach may prove to be fruitful. Both improvements of the parameterization of GWs and successful extensions of GCM to high altitudes make possible the use of GCM to locate the places where strong interactions between the acoustic disturbances and the atmospheric GWs can occur.

One of the most frustrating aspects of infrasound propagation research is our inability to predict the intensity of infrasonic arrivals. This follows that the acoustic waves are very sensitive to the state of the atmosphere and become nonlinear for even moderate amplitudes. Recent progress in "computational aeroacoustics," through the class of dispersion-relation-preserving numerical schemes or shock-capturing numerical schemes, could provide tools for a rigorous approach to this problem. By considering suited constitutive equations, this approach can include the relaxation processes and the absorption due to shear and bulk viscosity. Such numerical schemes could be used in GCM to capture the long-range propagation of shock waves generated by a pulse.

Finally, the main difficulty is to match, in a consistent scheme, different numerical models valid in widely different ranges of spatial and temporal scales. With the advent of large parallel computing systems and high resolution data, the assimilation of microbarograph data to correct the infrasound propagation may soon become reality.

References

Beagley SR, de Grandpré J, Koshyk JN, McFarlane NA, Shepherd TG (1997) Radiative Dynamical climatology of the first generation Canadian middle atmosphere model. Atmos Ocean 3:293–331

Bougeault P, Jansa A, Attie J, Beau I, Benech B, Benoit R, Bessemoulin P, Caccia J, Campins J, Carrissimo B, Champeaux J, Crochet M, Druilhet A, Durand P, Elkhafi A, Flamant P, Genoves A, Georgelin M, Hoinka K, Klaus V, Koffi E, Kotroni V, Mazaudier C, Pelon J, Petitdidier M, Pointin Y, Puech D, Richard E, Satomura T, Stein J, Tannhauser D (1993) The atmospheric momentum budget over a major mountain range: first results of the PYREX field program. Ann Geophys 11(395–418):1993

Clark TL, Peltier WR (1984) Critical level reflection and the resonant growth of nonlinear mountain waves. J Atmos Sci 41:3122–3134

Dalaudier F, Sidi C, Crochet M, Vernin J (1994) 1994, Direct evidence of "sheets" in the atmospheric temperature field. J Atmos Sci 51:237–248

D'Andrea F, Tibaldi S, Blackburn M, Boer G, Déqué M, Dix M, Dugas B, Ferranti L, Iwasaki T, Kitoh A, Pope V, Randall D, Roeckner E, Sraus D, Stern W, van der Dool H, Williamson D

(1996) Northern hemisphere atmospheric blocking as simulated by 15 atmospheric general circulation models in the period 1979-1988. Climate Dynamics 14:1979–1988

Durran DR (1987) Another look at downslope winds. Part 2: Nonlinear amplification beneath wave-overturning layers. J Atmos Sci 44:3402–3412

Fritts DC, Dunkerton TJ (1984) 1984, A quasi-linear study of gravity wave saturation and self-acceleration. J Atmos Sci 41:3272–3289

Giorgetta MA, Manzini E, Roeckner E, Esch M, Bengston L (2006) Climatology and forcing of the quasi-biennial oscillation in the MAECHAM5 model. J Clim 19:3882–3901

Hamilton K, Mahlman JD (1988) General Circulation Model simulation of the semi-annual oscillation of the tropical middle atmosphere. J Atmos Sci 45:3212–3235

Held IM (1983) Stationary and quasi-stationary eddies in the extratropical troposphere: Theory. In: Hoskins BJ, Pearce RP (eds) Large-scale Dynamical Processes in the Atmosphere. Academic Press, London, p 397

Hines CO (1997) Doppler-spread parameterization of gravity wave momentum deposit in the middle atmosphere. Part~2: Broad and quasi-monochromatic spectra and implementation. J Atmos Solar-Terrest Phys 59:387–400

Hourdin F, Musat I, Bony S, Braconnot P, Codron F, Dufresne J-L, Fairhead L, Filiberti M-A, Friedlingstein P, Grandpeix J-Y, Krinner G, Levan P, Lott F (2006) The LMDZ4 general circulation model: climate performance and sensitivity to parametrized physics with emphasis on tropical convection. Climate Dynamics 27:787–813. doi:10.1007/s00382-006-0158-0

Kulichkov SN, Bush GA, Svertilov AI (2002) New type of infrasonic arrivals in the geometric shadow region at long distances from explosions (2002), Izvestiya. Atmos Oceanic Phy 38(4):397–402

Kulichkov SN, Avilov KV, Bush GA, Popov OE, Raspopov OM, Baryshnikov AK, Re Velle DO, Whitaker RW (2004a) Onanomalously fast infrasonic arrivals at long distances from surface-explosions, Izvestiya. Atmos Oceanic Phy 40(1):1–9

Kulichkov SN, Avilov KV, Popov OE, Otrezov AI, Bush GA, Baryshnikov AK (2004b) Some results of simulation of long-range infrasonic propagation in the atmosphere, Izvestiya. Atmos Oceanic Phy 40(2):202–215

Lindzen RS (1981) Turbulence and stress due to gravity waves and tidal breakdown. J Geophys Res 86:9707–9714

Lott F (1995) 1995, Comparison between the orographic response of the ECMWF model and the PYREX 1990 data. Q J Roy Meteorol Soc 121:1323–1348

Lott F (1998) Linear mountain drag and averaged pseudo momentum profiles in the presence of trapped lee waves. Tellus 50A:12–25

Lott F (1999) Alleviation of stationary biases in a GCM through a mountain drag parameterization scheme and a simple representation of mountain lift forces. Monthly Weather Review 127:788–801

Lott F, Miller M (1997) A new subgrid scale orographic drag parameterization; its testing in the ECMWF model. Q J Roy Meteorol Soc 123:101–127

Lott F, Fairhead L, Hourdin F, Levan P (2005) The stratospheric version of LMDz: Dynamical Climatologies Arctic Oscillation, and Impact on the Surface Climate. Climate Dynamics 25:851–868. doi:10.1007/s00382-005-0064-x

Manzini E, McFarlane NA, McLandress C (1997) Impact of the Doppler Spread Parameterization on the simulation of the middle atmosphere circulation using the MA/ECHAM4 general circulation model. J Geophys Res 102:25751–25762

Miller MJ, Palmer TN, Swinbank R (1989) Parametrization and influence of subgridscale orography in general circulation and numerical weather prediction models. Meteorol Atmos Phy 40(84–109):1989

Millet C, Robinet JC, Roblin C (2007) On using computational aeroacoustics for long-range propagation of infrasounds in realistic atmospheres. Geophys Res Lett 34:L14814.1–L14814.5

Miranda PM, James IA (1992) Non-linear three dimensional effects on gravity-wave drag: splitting flow and breaking waves. Q J Roy Meteorol Soc 118:1057–1081

Palmer TN, Shutts GJ, Swinbank R (1986) Alleviation of systematic westerly bias in general circulation and numerical weather prediction models through an orographic gravity wave drag parameterization. Q J Roy Meteorol Soc 112(2056–2066):1986

Ponomarev EA, Rudenko GV, Sorokin AG, Dmitrienko IS, Lobycheva IY, Baryshnikov AK (2006) Using the normal-mode method of probing the infrasonic propagation for purposes of the comprehensive nuclear-test-ban-treaty. J Atmos Solar-Terrestrial Phy 68:599–614

Schar C, Durran DR (1996) Vortex formation and vortex shedding in continuously stratified flows past isolated topography. J Atmos Sci 54:534–554

Shepherd TG, Semeniuck K, Koshyck JN (1996) Sponge layer feedback in middle atmosphere models. J Geophys Res 101:23447–23464

Smith RB (1979) Some aspects of the quasi-geostrophic flow over mountain. J Atmos Sci 36:2385–2393

Stephenson DB (1994) The northern hemisphere tropospheric response to changes in the gravity-wave drag scheme in a perpetual January GCM. Q J Roy Meteorol Soc 120:699–712

Warner CD, Mc Intyre ME (1996) On the propagation and dissipation of gravity wave spectra through a realistic middle atmosphere. J Atmos Sci 53:3213–3235

Warner CD, Mc Intyre ME (2001) An ultra-simple spectral Spectral Parameterization for Nonorographic Gravity Waves. J Atmos Sci 58:1837–1857

Chapter 24
Inversion of Infrasound Signals for Passive Atmospheric Remote Sensing

Douglas P. Drob, R. R. Meier, J. Michael Picone, and Milton M. Garcés

24.1 Introduction

Atmospheric sound waves in the 0.01–20 Hz frequency band are known as infrasound. These waves can travel for thousands of kilometers through refractive ducts in the lower, middle, and upper atmosphere. Renewed scientific interest in infrasound follows recent advances in infrasound technology, in basic knowledge of the middle and upper atmosphere, in digital signal processing, and in the deployment and operation of the International Monitoring System (IMS) of the Comprehensive Nuclear-Test-Ban Treaty (CTBT) (Christie et al. 2001; Der et al. 2002; Bass et al. 2006; Christie and Campus 2010). Especially important is the role of atmospheric conditions that affect the propagation of acoustic waves. Substantial improvements in infrasound data acquisition and interpretation, coupled with unprecedented global coverage, lead to a capacity for retrieving the atmospheric state from infrasound observations. To provide context for the new concepts, we begin with a brief historical overview of atmospheric soundings.

Sound waves heard across the English Channel in 1901 were first used by Whipple (1926) to postulate the existence of the tropopause and the stratospheric temperature regime. The positive stratospheric temperature gradient remained an unproven hypothesis well into the mid-1940s (Cox 1947). Independent confirmation of the existence of the gradient was eventually obtained with the first peacetime use of V-2 rockets (Best et al. 1947; Gutenberg 1946). Physical understanding was then advanced with the demolition of fortifications on the Island of Helgoland on April 18, 1947 using a single detonation of five thousand tons of high explosive (Cox 1948). The resulting pressure perturbations were recorded on microbarographs strategically placed 66–1,000 km to the south-south-east (Cox 1949; Cox et al. 1949). The use of sound waves to probe the structure of the atmosphere continued through the mid-1950s with grenades ejected from rockets (Groves 1956).

D.P. Drob (✉)
Space Sciences Division, U.S. Naval Research Laboratory, 4555 Overlook Avenue, Washington, DC 20375, USA
e-mail: douglas.drob@nrl.navy.mil

A. Le Pichon et al. (eds.), *Infrasound Monitoring for Atmospheric Studies,*
DOI 10.1007/978-1-4020-9508-5_24, © Springer Science+Business Media B.V. 2010

These campaigns were carried out using microphones placed on the ground in close proximity to the rocket trajectory (Bowen et al. 1964). With the emergence of the space age, acoustic remote sensing was eventually superseded in terms of practicality, accuracy, and coverage by radiosondes (e.g. Durre et al. 2008), ground-based RADAR (e.g. Vincent 1984), LIDAR (e.g. Hauchecorne and Chanin 1980), GPS occultation (e.g. Poli et al. 2002), and various space-based optical techniques (e.g. Kaplan 1959; Klaes et al. 2007; Schwartz et al. 2008; Wang et al. 2005). Interestingly, optical and in situ measurements of atmospheric vertical profiles are still called "soundings" today.

Paralleling the evolution of optical and radar sounding systems, recent work on infrasound propagation has led to an innovative approach for extracting additional knowledge of the state of the upper atmosphere. Implemented properly, infrasound measurements have the potential to provide, independently or in conjunction with other atmospheric measurements, information about the upper atmosphere for both scientific research and numerical weather prediction. Infrasound research on this topic was revitalized by Donn and Rind (1971, 1972), Rind (1978), Rind and Donn (1975), and Rind et al. (1973). For a single station in Palisades, New York, they were able to relate the temporal variability of the amplitude of infrasound signals generated by ocean wave sources (known as microbaroms) in the North Atlantic to the seasonal and diurnal patterns of the stratosphere and lower thermosphere. More recently papers by Garcés et al. (2004) and Le Pichon et al. (2005a, b, 2006) showed renewed promise for this concept using infrasound generated by volcanoes and ocean waves. Like the previous studies, these efforts demonstrate that there are obvious seasonal and local time variations in infrasound propagation characteristics; in particular, they show that variations in the observed signal back azimuths and trace velocities can be directly correlated with changes in the atmospheric state. Le Pichon et al. (2005a, b) went one step further and derived corrections to the ground-to-space (G2S) atmospheric profiles needed to bring measured infrasound azimuth deviations in line with theory (Le Pichon et al. 2010). Thus, at a minimum, infrasound observations can provide a diagnostic technique for validating existing atmospheric specifications from numerical weather prediction systems and empirical models. More ambitiously, infrasound signals from known sources may be directly inverted to independently provide a measure of the atmosphere.

In contrast to the atmospheric science community, the seismic and hydroacoustic communities use acoustic tomography as the prime tool to determine the properties of the ambient media. The technical literature on tomography spans more than 30 years (e.g. Aki et al. 1977; Munk 1986; Munk and Wunsch 1979; Romanowicz 2008), and a number of academic textbooks have also been written on the subject (e.g. Menke 1989; Munk et al. 1995; Tarantola 2005; Wunsch 1996). In seismology, the medium (the solid earth) is basically static, i.e., the system effectively elicits the same response given the same inputs at different times. In hydroacoustics, the problem is mildly time dependent, where over few days a slightly different response can be observed given the same source location. For passive atmospheric remote sensing, the background medium has an appreciable time dependence on scales from minutes to months and includes the added complication of a dominant asymmetric

wind term which results in significant propagation anisotropy. However, one of the luxuries afforded to the atmospheric science community is that the properties of the medium can also be observed remotely from the ground and space, as well as in situ, by several different techniques.

This chapter investigates the possibility of utilizing long-range infrasound signals from impulsive natural and coincidental man-made events, in the process providing background knowledge on geophysical remote sensing theory, acoustic propagation, and atmospheric specifications. As in seismology and hydroacoustics, there are also direct applications to nuclear explosion detection, location, and characterization (DLC) activities. Scientific advances in these topic areas can, thus, improve the effectiveness of the Comprehensive Nuclear-Test-Ban Treaty Organization (CTBTO) verification activity.

Results are also presented from a numerical algorithms designed for passive acoustic remote sensing via infrasound. The objective of these numerical experiments is to determine whether currently available measurements are adequate to obtain meaningful information about the Earth's upper atmosphere. Infrasound observables are calculated for a series of fictitious point sources with a simple three dimensional (3D) Cartesian ray tracer and a set of atmospheric profiles spanning a range of geophysical conditions. These synthetic measurements are then inverted using optimal estimation theory in an attempt to estimate the original atmospheric background state. Calculation over a range of possible atmospheric configurations is necessary to understand the statistical robustness of the inversion procedure.

In Sect. 24.2, we will present the basic formalism for the passive acoustic remote sensing concept. In Sect 24.3, we describe the forward propagation model and atmospheric specifications, including a consideration of the pertinent statistical uncertainties in these *a priori* atmospheric fields relevant to the acoustic tomography problem. The limitations of current atmospheric specifications are the principal impetus for the development of acoustic tomography to measure winds and temperatures in the upper atmosphere. These limitations are discussed in some detail in Sect. 24.3.2. In Sect. 24.4, we describe one possible implementation of the acoustic remote sensing concept, presenting illustrative examples in Sect. 24.5. Lastly in Sect. 24.6, we summarize our results and suggest future directions for infrasonic tomography of the atmosphere.

24.2 Passive Acoustic Remote Sensing (Formalism)

A relationship between two sets of variables (x,y) may be expressed as $y \approx f(x;\beta)$ where y denotes the set of dependent response variables, x denotes a set of independent explanatory variables, and β a set of unknown model parameters. In traditional discrete inverse theory, the function f is called the forward model (or operator); for example, it could be an acoustic ray trace model that relates to a set of infrasound observables (y) to a source location (x) via the model parameters β. As written, the functional relationship between x and y is necessarily approximate because observational uncertainties can exist.

For the case of infrasound propagation from an arbitrary ground-truth event, there is typically some set of observable parameters from a network of receivers such as the wavefront normal arrival vector ($\mathbf{n}_{rcv}$), the signal arrival times (t_{rcv}), and the receiver locations ($\mathbf{r}_{rcv}$). The subscript rcv denotes an observed wave characteristics at a receiver. For the infrasound source location problem, the idea is to estimate the unknown source location $\mathbf{r}_{src}$ and origin time t_{src} (i.e. $\beta = [\mathbf{r}_{src}, t_{src}]$) from some set of observable parameters (e.g. Arrowsmith et al. 2008; Brown et al. 2002; Le Pichon et al. 2008). For the atmospheric remote sensing problem, we instead seek to estimate the state of the atmosphere (parameterized by some means β) using observed infrasound signals from an arbitrary ground-truth event. These observables may include the known source location $\mathbf{r}_{src}$, the receiver location $\mathbf{r}_{rcv}$, wavefront arrival vector $\mathbf{n}_{rcv}$, and travel time $t_\Delta = t_{rcv} - t_{src}$.

When the independent variables x are well-known and only the dependent variables y are subject to significant observational errors, ordinary least squares procedures can be applied to estimate the set of unknown model parameters β. The functional relationship can be rewritten as $y_i = f_i(x_i;\beta) + \varepsilon_i$, where ε_i are the actual but unknown uncertainties of the observations for some set of measurements $i = 1...n$. Optimal least-squares parameter estimation procedures are based on the minimization of some objective cost function such as

$$\chi^2 = \sum_{i=1}^{n} ([f_i(x;\beta) - y_i]^{\mathrm{T}} w_{\varepsilon_i} [f_i(x;\beta) - y_i]), \tag{24.1}$$

where χ^2 is a measure of the misfit between the data and model and w_ε representing the statistical weights of the observations, usually the reciprocal of the measurement variances $1/\sigma_i^2$. The textbooks of Menke (1989), Rodgers (2000), and Tarantola (2005) provide thorough discussions of how to characterize the information content of an observational system, calculate the maximum a posteriori estimate of the unknown model parameters, and the corresponding parameter uncertainties. These texts also present methodologies such as the Levenberg-Marquardt procedure (Marquardt 1963) for estimating model parameters when the forward model cannot be linearized, as well as for handling situations where the information content of the observational system is insufficient to estimate some of the unknown parameters.

The inversion procedure begins by choosing a reasonable candidate atmosphere parameterized by β, initializing a set of acoustic ray tracing equations with the observed location and wave normal of a detection [$\mathbf{r}_{rcv}$, $\mathbf{n}_{rcv}$], and integrating the acoustic ray equations backwards from time t_{src} with a negative time-step $-\Delta t$. At time $t = 0$ (t_{src}), we then have a model estimate of the source location $\mathbf{r}_{src}$ given the candidate atmospheric conditions. These can be compared against the true source location. The atmospheric profiles are then adjusted iteratively until all the signals converge at their point of origin, the true source location. This inverse methodology is illustrated pictorially in Fig. 24.1.

We can, therefore, search for an optimal set of atmospheric parameters β that minimizes the difference between our inverse calculations of the estimated source

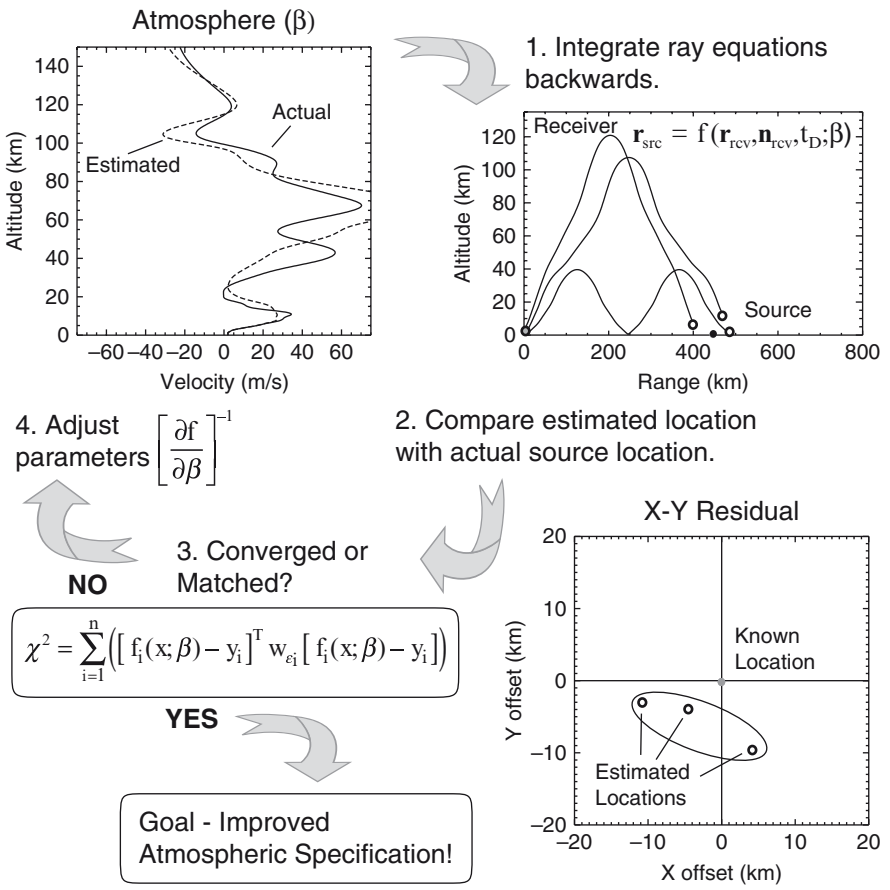

Fig. 24.1 A schematic of the infrasound inversion procedure formalism

location and the true source location. This approach works because the back propagated source location $\mathbf{r}_{src}$ is a function, albeit nonlinear, of the n detections $[\mathbf{r}_{rcv}, \mathbf{n}_{rcv}, t_\Delta]_i$ and the unknown model atmosphere. The atmospheric conditions can be estimated by minimizing the sum of squares of the miss distances

$$\chi^2 = \min_{\beta} \sum_{i=1}^{n} \left(\left[f_i(\mathbf{r_{rcv}}, \mathbf{n_{rcv}}, t_\Delta; \beta) - \mathrm{r}_{src,i} \right]^T w_{\varepsilon_i} \left[f_i(\mathbf{r_{rcv}}, \mathbf{n_{rcv}}, t_\Delta; \beta) - \mathrm{r}_{src,i} \right] \right) \quad (24.2)$$

via a nonlinear least-squares estimation procedure. The observables y_i of our infrasound acoustic tomography approach is the source origin $\mathbf{r}_{src}$, while the independent variables x_i of the forward model are the travel times t_Δ, wavefront arrival angles $\mathbf{n}_{rcv}$, and the receiver locations $\mathbf{r}_{rcv}$.

For the infrasound inversion procedure, the independent explanatory variables x_i for the forward acoustic propagation model are actually subject to comparable or

larger uncertainties than those of the dependent response variables y_i (i.e., the ground-truth event location $\mathbf{r}_{\text{src}}$). This is particularly true for the vertical component of the wave vector n_z, which in practice is difficult but not impossible to measure accurately (Szuberla and Olson 2004; Walker et al. 2008). The quantity n_z is derived from the trace velocity of the signal across the array and the local average ambient atmospheric conditions at the ground. It is also related to the classical ray parameter in the TauP method (Brown and Garcés 2009; Drob et al. 2009). The observed travel time t_Δ is also a independent variable and is typically well-known from ground-truth event information, but not always. When comparable observational uncertainties exist in both independent and dependent variables, the unknown model parameters β can be estimated with a modification of the nonlinear Levenberg-Marquardt procedure called weighted orthogonal distance regression (ODR) (Boggs et al. 1987, 1989; Zwolak et al. 2007). When considering the uncertainties in both the independent variables x and the response variables y, an explicit functional relationship between them can be written as $y_i = f_i(x_i + \delta_i; \beta) + \varepsilon_i$. The quantities δ_i and ε_i are the actual but unknown errors in the independent and dependent variables, respectively. The ODR procedure for multidimensional data seeks to minimize the objective cost function χ^2

$$\chi^2 = \min_{\beta,\delta} \sum_{i=1}^{n} \left(\left[f_i(x;\beta) - y_i \right]^{\mathrm{T}} w_{\varepsilon_i} \left[f_i(x;\beta) - y_i \right] + \delta^{\mathrm{T}}{}_i w_{\delta_i} \delta_i \right) \tag{24.3}$$

where w_ε represents some appropriate statistical weights (uncertainties) of the dependent variables (observations) and w_δ represents the statistical weights of the independent variables. In the ODR procedure, the unknown errors in the independent variables δ_i can also be estimated. The reader is referred to Boggs et al. (1989) and Zwolak et al. (2007) for details on the procedure. Additional details on the infrasound tomographic inversion, such as how the model atmosphere is parameterized via β, will be presented in Sect. 24.4.

24.3 Synthetic Data

In order to evaluate the inversion procedure, i.e., to understand how the spatiotemporal variability of infrasound propagation affects the inversion problem, we first create several realistic hypothetical observing scenarios and generate databases of synthetic infrasound signals. We then apply the inverse procedure to these synthetic data sets to see under what conditions we can retrieve the atmospheric profiles used in the forward simulations. This helps us to understand, design, and optimize the remote sensing system.

For expediency, the source and receiver configurations chosen for the present numerical experiments correspond to six infrasound calibration experiments described by Herrin et al. (2008). This choice allows us to prepare for the eventual application of the inversion methodology to the actual observation from the field

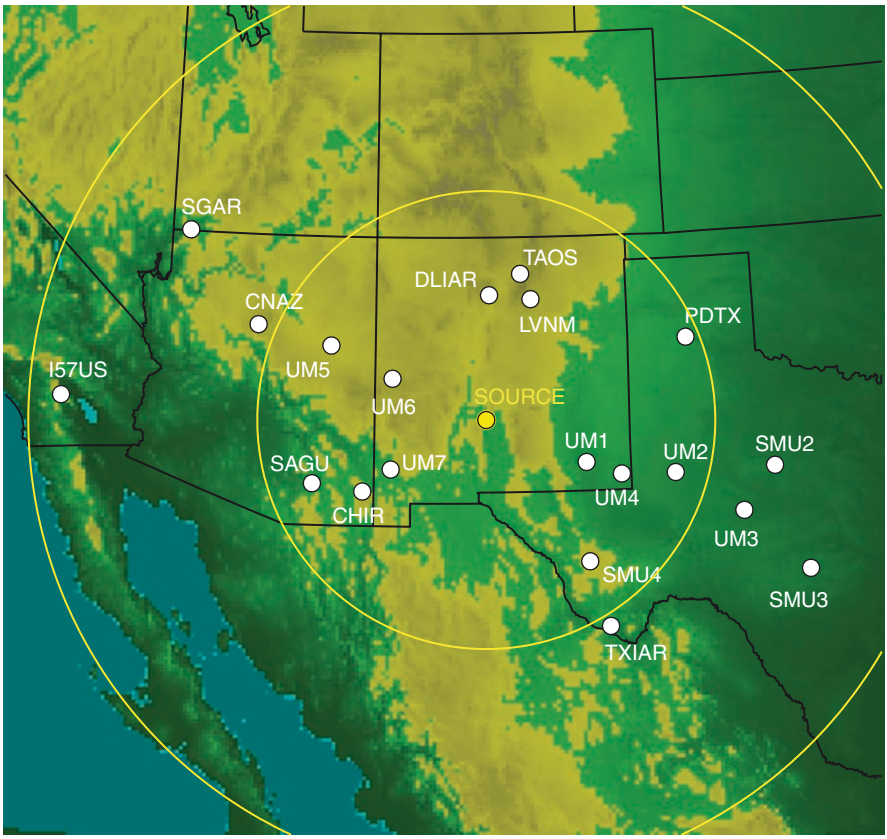

Fig. 24.2 Source and receiver configuration for the US Regional Infrasound Network used in the synthetic inversion experiments (see Herrin et al. 2008 for additional details)

experiments. Figure 24.2 shows the locations for the US regional infrasound network at the time of the calibration experiments, comprised of both permanent and temporary infrasound arrays. The observing system, thus, corresponds to the US regional infrasound network located in the Southwest United States, with the source located at the White Sands Missile Range (WSMR) at 32°N, 106°W. The concentric circles indicate ranges to the source of 500 and 1,000 km, respectively.

For each station $\mathbf{r}_{\text{rcv}}$, we compute a time series of infrasound observables, i.e., the acoustic travel times t_{Δ} and wavefront arrival vector $\mathbf{n}_{\text{rcv}}$. These are calculated via 3D Cartesian ray trace equations described below. For our synthetic experiments, we assume a simple single stationary acoustic point source that radiates an infrasound impulse isotropically in all directions. In practice, the idealized source may be of geophysical origin such as from a volcano, earthquake, or bolide; or of anthropogenic origin such as from a chemical explosion.

24.3.1 Forward Model

We make a number of approximations for the wave propagation physics in order to keep the numerical calculations simple. Geophysical effects resulting from atmospheric range dependence (Drob et al. 2003), attenuation (Bass et al. 2007), topography (Arrowsmith et al. 2007), and the scattering of acoustic energy by the atmosphere's internal gravity wave spectrum (Chunchuzov 2004; Ostashev et al. 2005) are ignored. The implications of these assumptions will be discussed later. The effects can be introduced incrementally and examined once we have a better understanding of the overall inverse problem. The underlying 3D Cartesian ray tracing equations expressed in terms of the front normal vector (**n**) are

$$\frac{\mathrm{d}\mathbf{r}}{\mathrm{d}t} = c\mathbf{n} + \mathbf{u}, \tag{24.4}$$

$$\frac{\mathrm{d}\mathbf{n}}{\mathrm{d}t} = (n\cdot\nabla(c + \mathbf{n}\cdot\mathbf{u}))\mathbf{n} - \nabla(c + \mathbf{n}\cdot\mathbf{u}), \tag{24.5}$$

where **r** is the wave position in Cartesian coordinates (x, y, z), c is the static sound speed ($c^2 = \gamma P/\rho$ with $\gamma = 1.4$ where P is atmospheric pressure and ρ is density), and **u** is the 3D wind vector; where **u** and c are both functions of (x, y, z). These equations represent the translation and rotation of an acoustic wavefront as it evolves with time. These equations can also be rewritten in phase velocity vector form (Lighthill 1978);

$$\frac{\mathrm{d}\mathbf{r}}{\mathrm{d}t} = c\frac{\mathbf{k}}{|\mathbf{k}|} + \mathbf{u}, \tag{24.6}$$

$$\frac{\mathrm{d}\mathbf{k}}{\mathrm{d}t} = -\mathbf{k}\frac{\partial \mathbf{u}}{\partial \mathbf{r}} - |\mathbf{k}|\frac{\partial c}{\partial \mathbf{r}}, \tag{24.7}$$

where **k** is the wave number vector such that $|\mathbf{k}| = 2\pi/\lambda$. A more elaborate set of ray tracing equations in spherical coordinates, including buoyancy oscillation terms, has been presented in a review by Gossard and Hooke (1975). For the present study (24.4) and (24.5) are preferable to (24.6) and (24.7) because infrasound arrays directly measure **n** as opposed to **k**. Equations (24.6) and (24.7) constitute a system of six ordinary differential equations that can be integrated numerically given the ambient environmental and initial conditions [$\mathbf{r}_{\mathrm{rcv}}$, $\mathbf{n}_{\mathrm{rcv}}$] to determine the position $\mathbf{r}_t$ and wavefront vector $\mathbf{n}_t$ at any time t.

To further simplify these equations, we assume a plane parallel, heterogeneous, range independent atmosphere so that **u** and c only vary in the vertical direction. The vector $\mathbf{u}(z)$ is composed of a zonal wind component $u(z)$ defined as positive eastward according to meteorological convention, and a meridional wind component $v(z)$ defined as positive northward. We also assume no vertical wind component, i.e., $w(z)$, is 0. In the present context, this is a reasonable assumption, i.e., for

idealized propagation over horizontal distances of less than about 750 km. With these approximations, (24.4) and (24.5) can also be expressed in an integral form as the TauP equations (Garcés et al. 1998; Drob et al. 2009).

24.3.2 Atmospheric Specifications

We use the local one dimensional atmospheric profiles from the global hybrid spectral G2S model of Drob et al. (2003) to compute the synthetic infrasound data. This system provides a unified global specification of $c(z)$ and $\mathbf{u}(z)$ from the Earth's surface to greater than 150 km by combining operational numerical weather prediction analysis fields and upper atmospheric empirical models. Mathematically, G2S is based on concepts from the empirical reference models of Hedin (1987) and Hedin et al. (1996), the vector spherical harmonic (VSH) thermospheric model of Killeen et al. (1987), and the SPHEREPACK 3.0 numerical global weather model development facility (Adams et al. 1999).

The G2S system has a moderate resolution four times (4×) daily output for automated near-real-time DLC applications, as well as a high-resolution product for detailed infrasound event analysis. The G2S specifications are provided as a compact VSH coefficient set that is applicable to a given calendar date and universal time. A computationally efficient application programming interface provides a streamlined mechanism for the direct utilization of these specifications in infrasound propagation codes. The G2S interface includes all the necessary platform independent data loading, interpolation, and file content management procedures. Linkable subroutines provide profiles of $c(z)$ and $\mathbf{u}(z)$ at any given location, be it a series of sites along a great circle, or a mesh covering the entire globe. As a convenient preprocessor for infrasound propagation calculations, the G2S system provides a post processor for existing numerical weather prediction fields. G2S also provides a placeholder for future operational numerical weather prediction models and assimilation systems (Akmaev et al. 2008) that are endeavoring to extend their upper boundary into the thermosphere.

In the present study, the observational data products which comprise the G2S coefficient sets are the 4× daily NOAA operational global forecast system (GFS) analysis products from 0 to 35 km (10 hPa) (Kalnay et al. 1990), the 4× daily stratospheric analysis from 15 to 55 km (100–0.2 hPa) from the NASA Goddard Space Flight Center, Goddard Earth Observing System GEOS-4 (Bloom et al. 1996), and above 45 km the HWM93 and MSISE-00 empirical models (Hedin et al. 1996; Picone et al. 2002). The G2S system can also incorporate analysis products with any resolution including those from the European Centre for Medium Range Weather Forecasting (ECMWF) (Courtier et al. 1998; Simmons et al. 2005), the United Kingdom Meteorology Office (UKMO) (Swinbank et al. 1998), and the Naval Operational Global Atmospheric Prediction System (NOGAPS) (Hogan and Rosmond 1991).

The numerical weather prediction specifications utilized in the region below of approximately 65 km represents a statistical combination of a large number of direct and indirect satellite-, ground-based, and in situ measurements (Simmons et al. 2005; Wu et al. 2002), with additional geophysical constrains provided by the governing equations for global fluid dynamics (Andrews et al. 1987; Holton 2004). The various numerical weather prediction specifications are widely accepted as providing an accurate representation of the day-to-day and hourly variability of the region at horizontal resolutions better than $1^\circ \times 1^\circ$. The early mathematical foundation of the various procedures employed by these systems is described by Daley (1991), with recent developments and techniques given by Joiner and Da Silva (1998), Migliorini et al. (2008), and Rabier (2005). Discussions of the state-of-the art in both the available satellite measurements and resulting global data fields are also described by Manney et al. (2008), Schwartz et al. (2008), and the references therein. For example, ECMWF has recently begun to produce specifications based on global satellite temperature soundings up to approximately 75 km altitude (0.01 hPa). The new NASA GEOS-5 system also provides near-real time specifications on 72 layers up to 0.01 hPa, resolving both the troposphere and stratosphere at a resolution of $1/2^\circ \times 2/3^\circ$ (Rienecker et al. 2008). A monumental reanalysis effort by the NASA Global Modeling and Assimilation Office (GMAO) called MERRA (Modern Era Retrospective-analysis for Research and Applications) will provide a high-resolution GEOS-5 time series at 6-h intervals from 1978 to current.

One important issue regarding these specifications is that above ~35 km, the wind fields are derived exclusively from the geophysical fluid dynamic balance of the global pressure fields, which are in turn determined from infrared temperature soundings. Diagnostic information does, however, enter indirectly through the observation and inner comparison of the global advection of passive observable tracers such as ozone. Furthermore, these derived wind fields are continuously evaluated against nonoperational research observations when and where they exist. Without directly measured atmospheric wind profiles, the resulting specifications may be subject to regional or temporal biases; however, as compared to existing empirical climatologies, the operational specifications are vastly superior. The typical stated geophysical uncertainty of these global numerical weather prediction analysis fields is 1.5 K for temperature and 2 m/s for winds near the surface, increasing to 2.5 K for temperature and greater than 5 m/s near the stratopause. With respect to these uncertainties, although the numerical prediction fields are not climatologies, they do represent regional and temporal averages, and as such, do not consider mesoscale contrasts and localized wind gusts.

Where reliable operational numerical weather prediction systems are limited to regions below the stratopause, the predominant morphology in the 65–150 km region of the G2S atmosphere is provided by the HWM93 and MSISE-00 empirical models (Hedin et al. 1996; Picone et al. 2002). These models include statistical parameterizations of the latitudinal, longitudinal, and seasonal variations of the general circulation and temperature structure of the atmosphere, including the diurnal patterns resulting from vertically propagating and in situ driven solar migrating tides. To a large extent, these seasonal variations and diurnal patterns dominate the

overall morphology of the mesosphere and lower thermosphere. The effects of Space Weather are also included above about 110 km. These two empirical models are based on four decades of satellite-, ground-based, and in situ atmospheric measurements, providing a robust statistical synopsis with estimated uncertainties on the order of 20–25 m/s for winds, and approximately 10–15 K for temperature in the region between 65 and 120 km. The exact nature of the uncertainties is a function of altitude, local-time, latitude, and season. As empirical models, there are two classes of errors in these specifications: statistical biases as compared to the true average state of the atmosphere resulting from shortcomings of the model formulation and/or the input data sets; and the systematic uncertainties resulting from random geophysical fluctuations that occur on spatiotemporal scales that are not resolved by observations or the empirical model.

The HWM93 model was recently upgraded to HWM07 by Drob et al. (2008) via the assimilation of recent upper atmospheric research satellite-based measurements (e.g. Hays et al. 1993; Shepherd et al. 1993) and ground-based measurements (e.g. Larsen 2002; Murayama et al. 2000; She 2004; Vincent and Lesicar 1991). The new model provides improved representations of the solar heating driven migrating tidal amplitudes and phases, including the seasonal variations thereof. The existing empirical models, however, do not fully include deterministic representations of the day-to-day tidal and planetary wave variability (Fritts and Isler 1994; Isler and Fritts 1995), or at present, nonmigrating tidal components (Forbes et al. 2003; Oberheide et al. 2006). When using these empirical models as a proxy for an instantaneous atmospheric profile, this geophysical variability accounts for a large portion of the random statistical error.

As detailed in a review by Fritts and Alexander (2003), the influence of atmospheric gravity waves on the upper atmosphere provides the second source of geophysical uncertainty for present-day global atmospheric specifications. A large fraction of the gravity wave spectrum in the operational numerical weather prediction models is filtered out during the data assimilation process, or simply just not resolved. Given the observed and predicted influence of gravity waves on the characteristics of infrasound propagation as described by Chunchuzov et al. (2005) and Kulichkov et al. (2008), the resolution of these waves through direct measurements or via an adequate semi-empirical spectral parameterization is an important challenge for the infrasound and atmospheric science research community. Given these caveats regarding the limitations of the present G2S model and other existing atmospheric specifications, example of environmental profiles of the wind velocity components and adiabatic sound velocity profiles from 0 to 150 km for WSMR (32°N, 106°W) on January 25, 2005, 18 UT are shown in Fig. 24.3.

24.3.3 Infrasound Observables

In order to calculate the infrasound observables from a given hypothetical event, a compact group of acoustic rays on a $0.05° \times 0.05°$ rectangular grid spanning $\pm 60°$ in

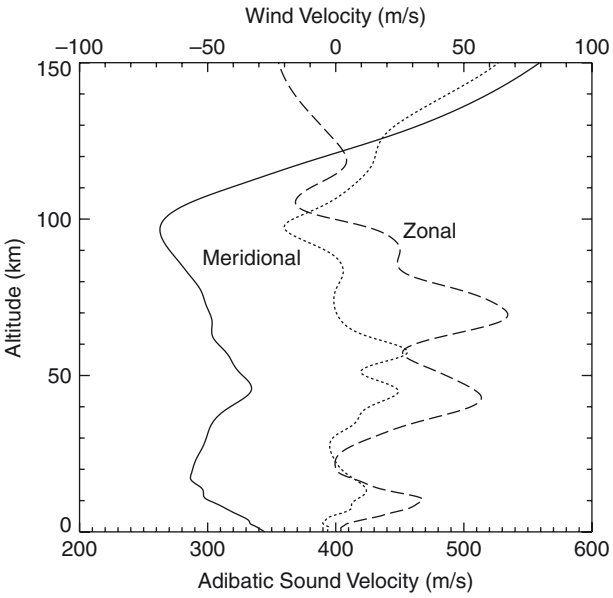

Fig. 24.3 Example environmental profiles of the static sound speed (*solid line*), zonal (*dashed line*), and meridional (*dotted line*) wind velocity components at 33°N, 106°W on 01/25/2005 at 18:00 UT

elevation and ±10.0° in back azimuth is integrated from an idealized point source toward each receiver. For the numerical integration of (24.4) and (24.5) for each ray, a fourth order Runge-Kutta method with a time step Δt of 0.1 s, changing to 0.05 s within 1,000 m of the surface, is used. Linear interpolation of the vertical G2S profiles and precomputed central finite differences is also used in the calculations. Any rays landing within 1,000 m of an infrasound array are counted as detections at $\mathbf{r}_{rcv}$, each with a corresponding travel time t_{Δ}, and wave front arrival angle $\mathbf{n}_{rcv}$.

The statistical robustness of each ray path to a detector, which depends on the atmospheric configuration and the numerical accuracy of the ray trace code, is checked by propagating each detection back again to the source, i.e., by integrating (24.4) and (24.5) in reverse with a negative time step ($-\Delta t$). This is also mathematically equivalent to reversing the sign of the background wind components. Rays returning to within some reasonable distance of their origin (e.g. ~1,000 m) are guaranteed to have an inherently stable path. This approach can also be used to establish the statistical robustness of raytracing results in DLC applications. The same reverse integration is also used in the inversion process. As an example of the results of the forward and backwards model calculations, the hypothetical ray paths for an acoustic source at the ground at WSMR on January 25, 2005 at 12:00 UT (see Fig. 24.3) are illustrated in Fig. 24.4.

With a multiyear archive of the G2S profiles, we then perform the forward model calculations for the network shown in Fig. 24.2 to create a synthetic observational

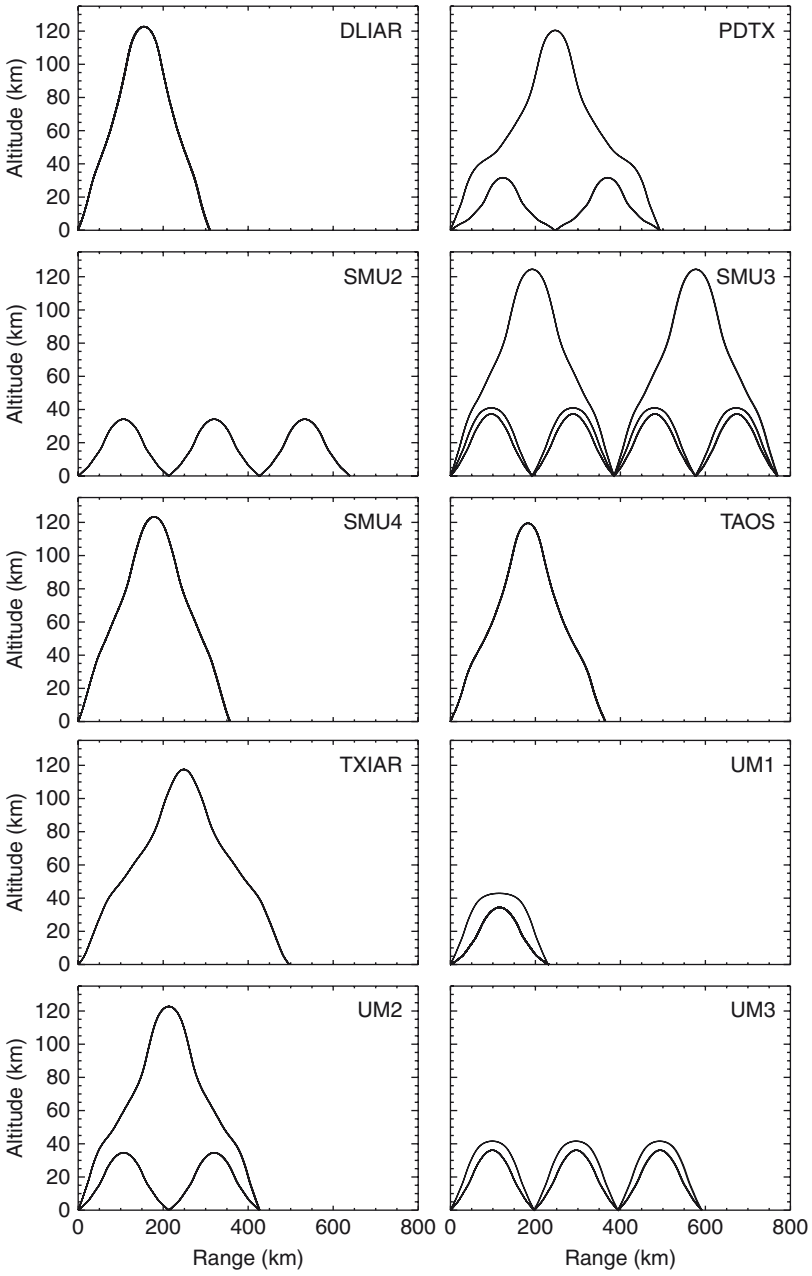

Fig. 24.4 Ray paths for the hypothetical detections by the US regional infrasound network on January 25, 2005 at 12:00 UTC given the G2S model atmospheric profiles

database. With this database, the statistical performance of a realistic infrasound atmospheric remote sensing network can be investigated over a complete range of environmental conditions (e.g. season, local-time, latitude), propagation modeling assumptions, and source types. As mentioned, such databases can also provide valuable insight into the spatiotemporal variability of infrasound propagation as recently described by de Groot-Hedlin et al. (2010) and Drob et al. (2009). Similar forward calculations investigating the signal from the volcanoes Yasur and Lopevi, located in the Vanuatu region of the south Pacific, by the IMS infrasound station I22FR have been performed by Antier et al. (2007) and Le Pichon et al. (2005b).

24.4 Inverse Procedures (Details)

Computational techniques for the tomography formalism introduced in Sect. 24.2 are now described. As mentioned, the least squares parameter estimation procedures provided by ODRPACK (Boggs et al. 1989) were chosen as they solve highly nonlinear, multivariate, weighted data fitting problems where significant uncertainties exist in both the dependent and independent variables. The software package also provides a complete range of statistical diagnostics as well as routines to evaluate the numerical derivatives of the forward model required by the nonlinear parameter estimation procedures. The most recent update of ODRPACK95 (Zwolak et al. 2007) also provides a means to specify upper and lower boundary constraints on the unknown model parameters.

24.4.1 Atmospheric Basis Functions

In this section, we present a parameterization of the model atmosphere used in the inversion procedure. We follow the empirical orthogonal functions (EOF) approach widely used by the seismic and hydroacoustic communities to parameterize the unknown background fields in tomographic inversion problems (Munk et al. 1995). EOFs utilize available *a priori* statistical information about the vertical structures and variability of the background fields in order to provide a versatile mathematical representation of historical observations or theoretical model results. EOFs are a convenient way to incorporate existing statistical knowledge about the spatiotemporal variability of the atmosphere to better condition the infrasound acoustic inversion and reduce the number of unknown quantities to be estimated.

The EOFs are readily determined by singular value decomposition (SVD) of the profiles of $c(z)$, $u(z)$, and $v(z)$ within a multiyear G2S time series. SVD is a simple algebraic decomposition whereby any $m \times n$ matrix M can be partitioned into the form $\mathbf{M} = \mathbf{U}\boldsymbol{\Sigma}\mathbf{V}^*$ where $\mathbf{U}$ is an $m \times n$ matrix of amplitudes, $\boldsymbol{\Sigma}$ is an $n \times n$ diagonal matrix of positive eigenvalues, and $\mathbf{V}^*$ is an $n \times n$ matrix of eigenvectors (see for example Wunsch 1996). The empirical orthogonal basis functions $\psi_j(z)$ are equivalent to the jth column from the $\mathbf{V}^*$ eigenvector matrix scaled by the appropriate diagonal

term in **Σ**. The linear scaling factors β_j correspond to the rows of the **U** matrix. The adiabatic sound velocity and wind profiles can now be represented by the sum of a set of linear EOFs $\psi_j(z)$, with unknown linear scaling factors β_j as

$$\tilde{u}(z) = \sum_j \beta_j \psi_j(z) + u_o(z), \tag{24.8}$$

where $u_o(z)$ is the multiyear average background state. When computing EOFs via an SVD transform, it is important to remove the average of the column vectors first.

In most instances, the complete set of EOFs can be truncated to provide an acceptable approximation; for example, with the first few basis functions 85% of the observed variance in the time dependent 1D G2S profiles can be represented, while 98.5% of the variance can be represented with the first dozen. With only six basis functions, the average maximum error over the entire multiyear time series for any one reconstructed zonal wind profile is approximately 14 m/s; with only 12 EOF functions it is 7 m/s, and with 18 EOFs it is 4 m/s. The first six vertical basis functions from a multiyear time series of zonal wind profiles from the G2S atmospheric specifications system are shown in Fig. 24.5. A set of empirical basis functions was also calculated for the time series of the HWM93 and MSISE-00 empirical atmospheres. As there is much less inherent natural variability represented by the empirical atmospheric specifications, 99.5% of the HWM93 model variance can be captured with the first dozen basis functions.

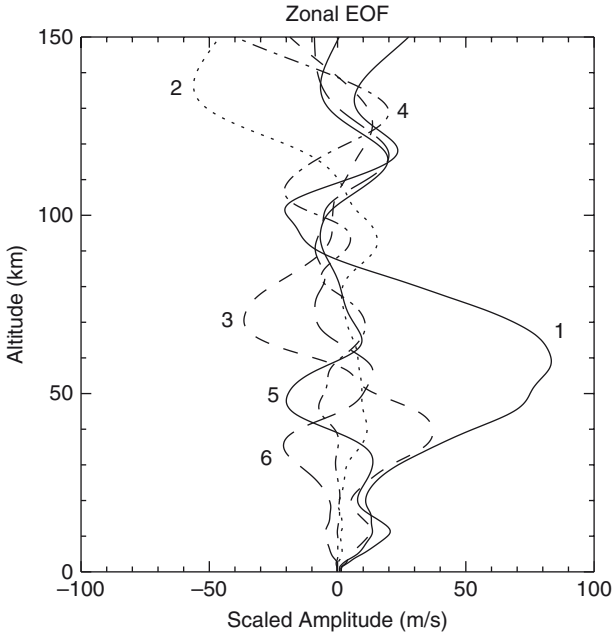

Fig. 24.5 Empirical Orthogonal Functions (EOF) of the zonal wind component from a 3-year time series (2003–2006) of G2S atmospheric profiles for 33° N, 106° W

24.4.2 Implementation and A Priori Information

Under the approximations described in Sect. 24.3.1, the local effective sound velocity profile $c_e(z) = c(z) + u_{\|}(z)$ establishes the first order characteristics of infrasound propagation (e.g., the ducting height, travel times, and ranges), where $u_{\|}(z)$ is the wind projected along the direction of propagation. In particular, the reflection height of the acoustic wavefront occurs at the altitude where its horizontal phase velocity V_θ equals the effective sound velocity $c_e(z)$ (e.g., Garcés et al. 1998; Drob et al. 2009). From simple geometric considerations, the ducting height influences the total path length and thus the average travel time, celerity, and even the spatial extent of near field shadow zones.

On average, the geophysical uncertainties in the adiabatic sound velocity are $\sigma_c \cong$ 1–3 m/s. This follows from the fact that typical uncertainties in atmospheric temperature T are $\sigma_T \cong$ 2–5 K where $c^2 \cong 401.875T$ to a very good approximation below 95 km. On the other hand, uncertainties in the wind components $\sigma_{u,v}$ are on the order of 25 m/s or more. Thus, when considering the uncertainties in the effective sound velocity, the uncertainties in the adiabatic sound velocity profiles are negligible compared to that of the winds. Given this, it is reasonable to assume that the adiabatic sound velocity profile $c(z)$ is already well-known and that only the wind velocity profiles $u(z)$ and $v(z)$ are to be estimated. This greatly simplifies our numerical inversion experiments. It is, however, acknowledged that at certain times and locations the statistical uncertainties of the climatological specifications of the mesosphere and lower thermospheric temperature profiles can be on the order of 10 K or more.

It is further assumed that the wind profile specifications below 15 km are already well known by some other means such as from an operational numerical weather prediction system or radiosonde profile. This *a priori* information can be incorporated into the existing framework by a modification of (24.8),

$$u(z) = \pi(z) \cdot \tilde{u}(z) + (1 - \pi(z)) \cdot u_a(z), \tag{24.9}$$

where $u_a(z)$ is the known *a priori* wind profile. The transition function $\pi(z)$ is defined as $\pi(z) = (1 + e^{-\alpha(z - \gamma)})^{-1}$ with the parameters α and γ chosen to be 0.1 km^{-1} and 15.0 km, respectively, for the case studies presented here. This modification helps to stabilize the inversion, particularly as the phase paths of ordinary differential equations are notoriously sensitive to initial conditions. As we shall see, this *a priori* information can also be folded into the tomographic inversion in other ways.

In addition to the consideration of the lower boundary of the model parameter space, no information above the maximum altitude of ducting can be obtained other than indirectly through limited continuity and extrapolation arguments. In fact, for weak sources over very long ranges, signals ducted in the thermosphere may not always be observed due to appreciable molecular attenuation above 120 km (e.g. Bass et al. 2007). Although we do not account for attenuation in the forward model, we have limited the propagation of the synthetic observations to altitudes below 130 km to partially address this issue.

By assuming that a reasonable *a priori* estimate of the winds between 130 and 150 km is also available, it is possible to further condition or regularize the solution space.

At any altitude in the inverse procedure, *a priori* information about the atmospheric profiles can be included by adding adjoint constraints to the objective cost function as such,

$$\chi^2 = \sum_{i=1}^{n} ([f_i(x;\beta) - y_i]^{\mathrm{T}} w_{\varepsilon_i} [f_i(x;\beta) - y_i]) + \sum_{l=1}^{m} ([u_l(\psi;\beta) - \hat{u}_l]^{\mathrm{T}} w_{u_l} [u_l(\psi;\beta) - \hat{u}_l]), \tag{24.10}$$

where $\hat{u}_l$ is a vector of m *a priori* wind measurements. We have omitted the extra term for the uncertainties in the independent variables x given in (24.4) for clarity. Note that $u_l(\psi;\beta)$ occurs in both the forward model $f_i(x;\beta)$ and the second term of (24.10). This strategy is akin to the approaches of Twomey (1963) and Tikhonov (1963) to account for additional error sensitivities and regularize difficult discrete inverse problems.

As reasonable wind profiles are readily available up to about 55 km in near-real-time, we include additional *a priori* constrains in two different altitude regions; one set in the 15–45 km altitude region with assigned statistical uncertainties of 10 m/s, and one set in the 120–150 km region with uncertainties of 15–20 m/s. Other variations on this theme can provide a means to limit the spurious amplitudes of higher order EOFs as well as any unwanted oscillations in other possible choices of basis functions.

Dual cost functions like the one presented in (24.10), again akin to the Twomey-Tikhonov method, are widely used in modern global atmospheric variational data assimilation systems (Rabier 2005). In these systems the cost function may be a combination of direct temperature and wind measurements, *a priori* global estimates from a previous 6-h forecast, and direct IR radiance observations, coupled with an appropriate forward radiative transfer model (Rabier 2005). Instead of assimilating independently inverted temperature profiles derived using incomplete *a priori* information – such as from a climatology and thus subject to possible statistical uncertainties and bias – the observational information content of satellite radiance measurements is directly integrated into the global atmospheric data assimilation system. In other words, in order to directly influence the global estimates of the atmospheric fields, the satellite radiance observation is simultaneously assimilated with the most up-to-date *a priori* atmospheric specifications, other corroborating measurements, and a suitable forward model. Infrasound travel times and arrival information could eventually be incorporated into future numerical weather prediction systems in this manner.

24.4.3 Observational Weighting and Basis Set Truncation

The synthetic observations for the inversion being described are arranged such that the dependent variable y is a matrix $[\mathbf{r}_{\mathrm{src}}]_i$ and the independent variable x is a matrix $[\mathbf{r}_{\mathrm{rcv}}, \mathbf{n}_{\mathrm{srv}}, t_{\Delta}]_i$. Assuming dispersed arrivals for our forward simulations, there are anywhere from 75 to 250 synthetic detections for the twenty stations in the regional

network. There are also 400 additional pseudo-data points from the adjoint constraints. In addition to the organization of the data, it is very important to obtain the proper balance between the various sources of information, weighting each one appropriately according to the error statistics (Rabier 2005). The correct specification of observational uncertainties can mean the difference between success and failure in the inversion process.

The assigned statistical uncertainties of the back propagated source location $\mathbf{r}_{\text{src}}$ are $\sigma_{r(x,y)} = 10$ km in the horizontal direction and $\sigma_{r(z)} = 5$ km in the vertical direction. The chosen values reflect the random statistical uncertainty introduced by the incompleteness of the EOF basis set used to represent the true atmosphere. Furthermore, in the absence of including implicit uncertainties for the independent variables in the ODR procedure, an artificial inflation of the uncertainties of the dependent variables ($\sigma_{\mathbf{r}}$) can represent the mapping of the uncertainties of the independent variables (σ_x) through the forward model. Slightly different results are obtained if the ODR procedure is run in the implicit mode (i.e. (24.3)) as opposed to as a standard Levenberg-Marquardt inversion (i.e. (24.2)). This finding testifies to the importance of assigning the proper statistical weights to the inversion variables. For the implicit ODR procedure, the specified uncertainties in the receiver location $\mathbf{r}_{\text{rcv}}$ are 1 km in the horizontal direction and 100 m in the vertical direction. The uncertainties in the wavefront arrival azimuth and elevation, functionally equivalent to $\mathbf{n}_{\text{rcv}}$, are set to $\sigma_{n(\varphi,\theta)} = 0.5°$. The uncertainties given for the travel times are $\sigma_{\Delta t} = 5$ s. When inverting actual observations, one does not have the luxury of choosing values in an ad hoc fashion. Thus, the values used for the present discussion may require additional investigation and refinement. Furthermore, at this point, no random noise or systematic biases have been explicitly added to the synthetic data sets; again to first incrementally develop the infrastructure needed to implement the inversion methodology. These issues need to be well understood before applying the inversion to any actual data sets.

Another important consideration for the inversion process is the selection of the total optimal number of basis functions to be estimated. The number of basis functions selected must not be so few that the inverted atmospheric profiles are crudely represented, or so many that spurious artifacts are created. As 98.5% of the observed variance can be represented with the first dozen basis functions, the inverse problem is easily over determined, i.e., the number of unknown parameters is much less than the number of observations. This does not guarantee, however, that the problem is well conditioned and the resulting parameter estimates are unique. In other words, in some instances, different atmospheric configurations might result in nearly identical sets of observed responses.

The ability of the inverse model to recover the unknown model parameters, given the truncation of the basis functions, can be investigated by running the inverse calculations with EOFs initialized with the true *a priori* values at various levels of truncation to verify the degree to which all of the rays converge successfully back at the origin. During this process, it was noticed that for some cases only a few basis functions were required. For these, changes in the minor details of the profile did not influence the robustness of the results, whereas in other cases the

slightest variations in the atmospheric profiles had significant consequences on the nature of the observed ray paths. Thus, more basis functions may be required.

24.4.4 Convergence

In the initial inversion experiments it was found that given an arbitrary set of initial values for β as the first guess, even with a sufficient number of EOFs and adjoint constraints, the inversion did not always converge to the global minimum, instead converge to some nearby local minimum. We determined, however, that the inversion does always converge to the global minimum given a very good first guess in close proximity to the true values. The inversion convergence also appeared to depend on the atmospheric configuration even though the experimental setup remained unchanged, with the forward model producing about the same number of synthetic detections. In particular, there appears to be a correlation between the convergence and the number of large-scale ducts and adjacent fine scale structures, also known as low velocity zones in the seismic literature (Bessonova et al. 1974).

Poor convergence in some instances could be due to the highly nonlinear nature of the forward model, limitations of the parameter estimation methodology, or the fact that for certain atmospheric configurations the problem is ill-posed or mixed determined (Menke 1989). For the atmospheric configurations which were problematic to invert, extra model parameters, adjustment of parameter weights, and several ad hoc schemes to search the solution space did not readily improve matters. Fortunately, the inversion converged acceptably for the vast majority of atmospheric configurations, particularly for the synthetic databases generated with the HWM93/MSISE-00 empirical models. The possibility that the convergence problem is related to the existence of nonlinear discontinuities in the forward model is discussed in more detail in the next section. Additionally, techniques involving the calculation of observational data and model resolution matrices (Menke 1989) may also yield insight.

Instances where the inversion fails are easily identified by large values of χ^2, i.e., by the fact that all of the signals do not converge back to the origin. Given the fact that the parameter estimation convergence is stable in the immediate vicinity of the true state space configuration, with enough computer time it should be possible to search the entire space through a brute force grid search or Monte Carlo method to clearly identify the original atmospheric state. To avoid the brute force approach, a hybrid method akin to simulated annealing or genetic programming is currently being considered.

In the hybrid approach, the state space search begins by estimating the amplitude of the first few basis functions of each wind velocity component. Furthermore, we choose known values for β corresponding to the EOF amplitudes of the same day and local time from exactly 1-year prior as an educated guess. An alternative approach might be to start off with average climatological

values of β corresponding to the local time and season of the observations being inverted, or those from an adjacent event. Then several sets of random perturbations are added to the parameters to create an ensemble of initial guesses. Next, the ODR procedure is run for each of the subsets in the ensemble. The subset with the lowest χ^2 is deemed the best β and is selected as the locus for the next ensemble of guesses. The number of unknown model parameters is also increased by two with one additional basis function for each wind component. This entire process is repeated until the number of unknown model parameters is on the order of ten to twenty.

In some instances the entire search process was not necessary as the ODR algorithm converged with the unknown model parameters set to reasonable values (and even in some cases zero). At the time of writing, there are, however, several examples where a reasonable estimate could not be found with the hybrid method. Again, those cases where the inversion fails are easily identified by large values of χ^2. Given that the parameters always converge in the immediate vicinity of the true state space configuration, with sufficient computational resources it should be possible to search the entire state space to determine the original atmospheric configuration that was used to create the synthetic data. A low value of χ^2 does not, however, indicate or guarantee that the resulting parameter estimates are unique. These topics are subjects for future scientific research by the infrasound community.

24.5 Results

Although we preformed the numerical inversion experiments over the entire multiyear time series of synthetic observations, a complete discussion is beyond the scope of this article. This chapter focuses on several illustrative examples. The first example shows the inversion results for typical winter time conditions as given by the HWM/MSIS empirical models for a hypothetical event occurring on 01/01/2005 at 00:00 UTC. Figure 24.6 shows the inversion results for three points in the iterative process. The first column shows the residual predictions of the back propagated source location on the x–y plane. The next column shows the residuals in the x–z plane. The last column shows the comparison of the estimated and true atmospheric zonal and meridional wind profiles. The first row shows the resulting residuals and atmospheric model profiles for the initial guess. The middle row shows the results at an intermediate stage in the parameter estimation process. The last row shows the converged, or best estimate profile.

For these conditions, the inversion works very well as the original profile is recovered successfully. In particular, the meridional wind component is well resolved, while between 70 and 100 km the zonal wind is only in error by a few m/s. This is not surprising as the amount of fine and intermediate scale structure in the original profiles is somewhat limited. The statistical uncertainties in $u(z)$ and $v(z)$, as calculated by the propagation of error of the estimated uncertainties in β

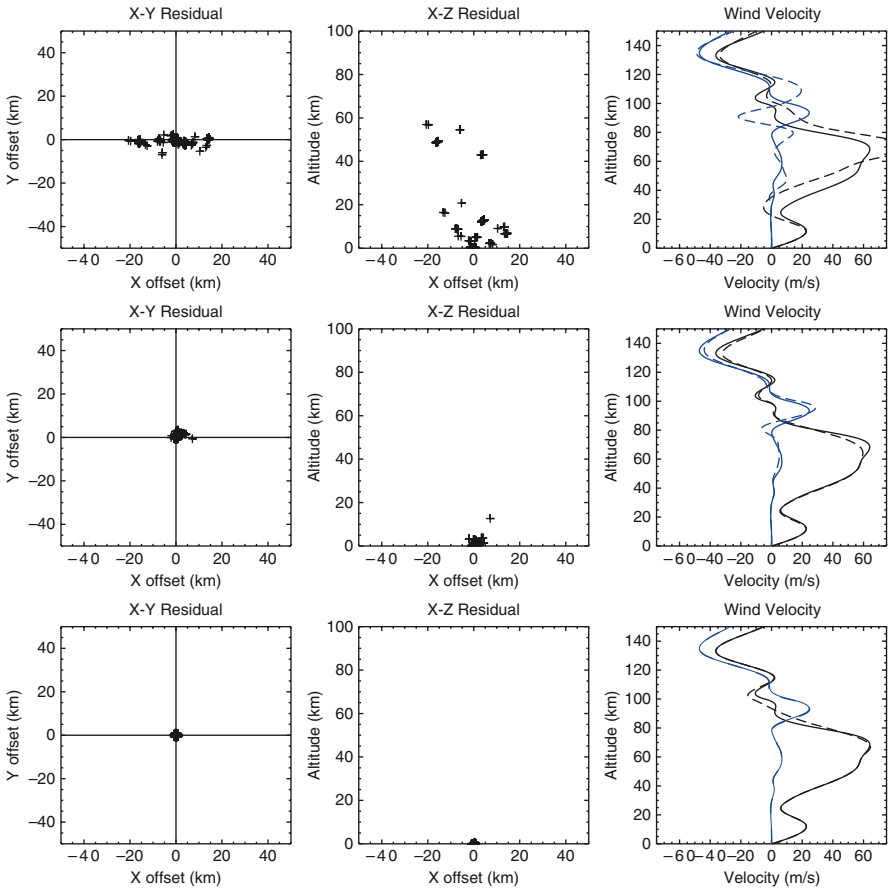

Fig. 24.6 Converged synthetic inversion results for a time 01/01/2005 at 12:00 UTC generated by the HWM/MSIS model. The *top row* shows the inversion results for a stage early in the process. The *second row* shows the results for an intermediate stage in the process. The *bottom row* shows best estimate of the atmospheric profile. The *left hand column* shows the *x–y* difference between the back-propagated and actual source location. The *middle column* shows the *x–z* plane of the residual. The *right hand column* shows the actual (*solid*) vs. estimated (*dashed*) wind profile. The zonal wind component exhibits the largest amplitude at the Stratopause (50–70 km)

from the ODR procedure, are omitted for clarity and brevity. They are on the order of 5 m/s, though they can be up to 15 m/s in some instances.

The next illustrative example shown in Fig. 24.7 presents the inversion results for the synthetic infrasound observations generated by the G2S model for a time of 01/25/2005 at 18:00 UTC. A significant double peaked structure in the stratospheric zonal wind jet is present. Despite this double peaked structure, the performance of the inversion is not dissimilar to the first example. The error in the zonal wind profiles is a only few m/s between 45 and 110 km. Errors of a few m/s between 70 and 100 km exist in the meridional wind profile.

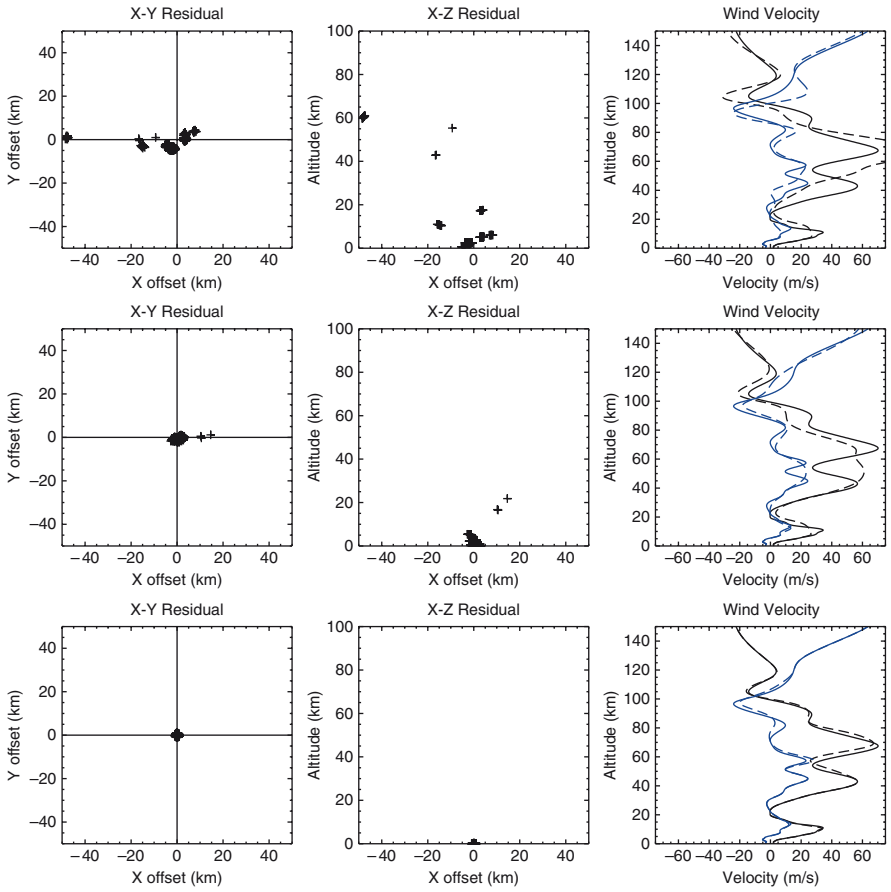

Fig. 24.7 Same as Fig. 24.6 for an atmospheric profile for 01/25/2005 at 18:00 UTC generated by the G2S model

In this example it is important to note that during the intermediate parameter estimation stage, reasonable convergence of back-propagated rays at the origin can be achieved despite the fact that the secondary stratospheric peak remains unresolved. The two outlying ray paths in the residual plots of the intermediate step are reflected at the secondary stratospheric peak. Fortunately, the ray paths and secondary maximum are eventually resolved by additional basis functions and estimation trials. Had the paths been not observed for whatever reason, it is possible that the upper duct would not have been properly resolved. This case raises the question of the possibility of nonuniqueness in the inversions, i.e., the possibility of a one-to-many mapping for a given collection of ray paths.

The third illustrative example shows the inversion results for typical summer time profiles as given by the MSIS/HWM empirical model for a hypothetical event occurring on 07/01/2005 at 00:00 UTC. Again the original profile is readily

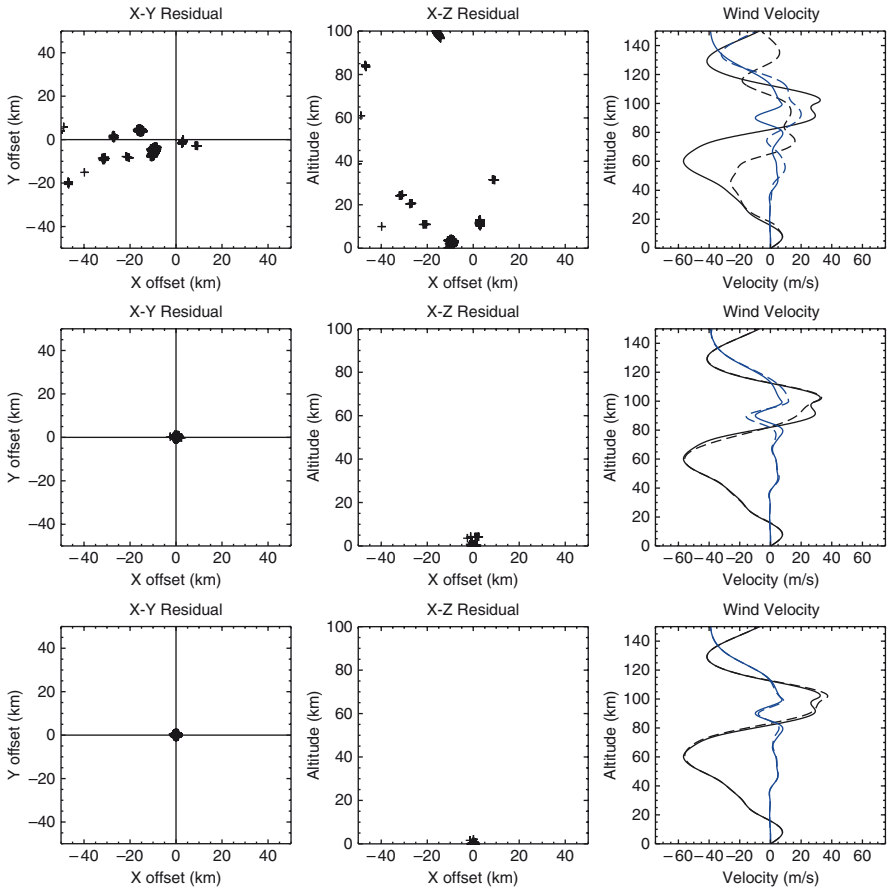

Fig. 24.8 Same as Fig. 24.6 for HWM/MSIS profiles generated for 07/01/2005 at 00:00 UTC

retrieved with convergence occurring early in the estimation process. Between approximately 70–105 km, the errors in the converged result are only a few m/s. Furthermore, as in the previous example, the meridional wind component is well recovered (Fig. 24.8).

The last example of the inversion results is for a G2S generated atmosphere for a hypothetical event occurring on 07/21/2005 at 18:00 UTC (Fig. 24.9). Again there is a double peak in the stratospheric zonal wind jet, though it is not as prominent as in the second example (Fig. 24.7). The agreement between the estimated and actual profiles is not as robust as in the previous examples. Above the refection point between 45 and 70 km, there are departures up to approximately 10 m/s. Furthermore, there is one ray path that does not converge back to the origin even though the profile near the reflection points is in good agreement. For this last example, the information content is weighted toward the atmospheric conditions near the refection height.

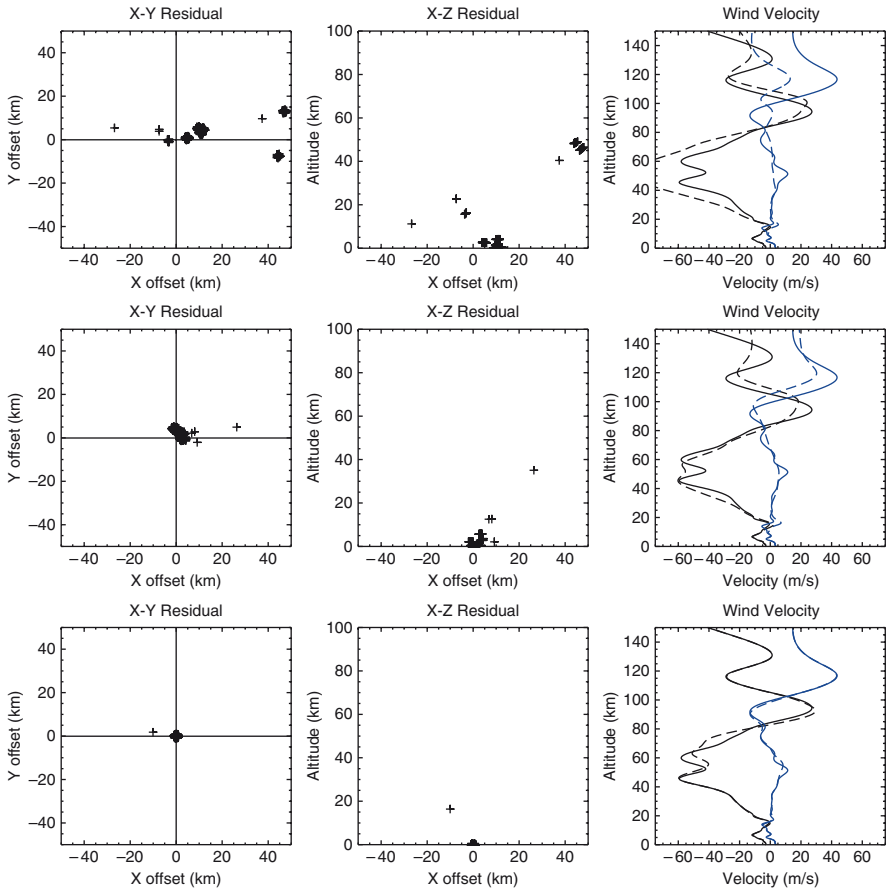

Fig. 24.9 Same as Fig. 24.6 for the G2S atmospheric profiles of 07/21/2005 at 18:00 UTC

24.6 Discussion

As the HWM93 and MSISE-00 empirical models contain less vertical structure than the G2S profiles, it is no surprise that it is much easier to successfully invert the synthetic observations generated by the empirical models. The presence of multiple ducts and low velocity zones appears to hamper the performance of the inversion. As shown in the second and fourth examples, some of the fine scale structure in the atmospheric profiles cannot always be resolved with only the first few basis functions. Even when starting the inversion off with a truncated basis set β, initialized to their true values, the parameter estimation procedure diverges to biased estimates in order to make up for the incompleteness of the truncated basis set (i.e., the missing information). The degree to which this is significant depends on the amount of randomness and covariance in the atmospheric system, which

may be quantified by the second order statistical moments of the atmospheric profiles. For problematic atmospheric conditions, some of the higher order basis functions may have large amplitudes, while during quiescent times when the profiles have limited vertical structure, the profiles can be well represented with only a few basis functions.

For certain atmospheric conditions, the difficulties that were encountered while trying to locate the global minimum may also be related to the nature of the acoustic ray paths near the transition point from a stratospheric to a thermospheric mode. In the vicinity of this transition point, a slight change in the background conditions can easily result in a vastly different phase path with a different travel time, range, and azimuth deviation. In other words, a possible reason for the poor performance of the inversion when multiple ducts are present is that the function $f_i(\mathbf{r}_{rcv}, \mathbf{n}_{rcv}, t_\Delta; \beta)$ is not a piecewise smooth function in β i.e., a slight change in β which implies a change in $u(z)$ or $v(z)$ can result in a large jump in $[\mathbf{r}_{src}, t_{src}]$ as the ray switches from a stratospheric mode to a tropospheric or thermospheric mode (or vice versa). The so-called fast or head-waves (e.g. Evers and Haak 2007) also reside in the vicinity of this region of the model parameter space. Interestingly, for an arbitrary source to receiver configuration, it can be shown mathematically that the waves in the vicinity of this saddle point have a greater probability of detection. As these issues are relevant to DLC methodologies, further research on these topics will help to improve source location accuracy, reduce network false alarm rates, and increase the detection threshold of existing infrasound monitoring networks.

There are a number of research challenges that are outstanding, among these are (a) inclusion of measurement noise and systematic biases within the synthetic observations and an investigation thereof, (b) a rigorous statistical survey of the inversion results from the batch processing of the entire synthetic database, (c) an estimation of the minimum number of stations that are needed to successfully perform an inversion, and (d) application of the inversion to an actual set of observations.

Also requiring consideration are the simplifying assumptions made in the wave propagation physics in order to keep the numerical experiments tractable. Geophysical effects such as atmospheric range dependence (Drob et al. 2003), attenuation (Bass et al. 2007), topographical effects (Arrowsmith et al. 2007), and the scattering of acoustic energy by the atmosphere's internal gravity wave spectrum (Chunchuzov 2004; Kulichkov et al. 2008; Ostashev et al. 2005) were neglected. The limitations of linear ray theory as compared to nonlinear full wave propagation as recently explored by Millet et al. (2007) are also relevant. The majority of these phenomena imply that there will likely be arrivals that would be observed in practice that might not be correctly mapped back to the source via the linear ray theory. A proper statistical treatment of potentially resulting outliers could, however, help to mitigate any negative impact on the inversion. With respect to gravity waves, initial tests indicate that their existence could actually improve the inversions because they can act as local refracting surfaces capable of creating multiple arrivals in the vicinity of the main duct. An inversion would then only provide an average estimate, with the fine scale structure not fully resolved.

Lastly by neglecting thermospheric attenuation, many of the thermospheric infrasound arrivals predicted for our hypothetical experiments may not be observed in practice, and thus, may not be available to provide information content about the upper atmosphere, particularly for weak infrasound sources.

Clearly the quality of the information obtained about the upper atmosphere from passive infrasound remote sensing depends on the precision, accuracy, and physics of the forward propagation modeling scheme. For example, given that the problem is highly nonlinear, small changes in the ray path within different propagation models will result in different model derivatives, i.e., different solutions (e.g. Husen and Kissling 2001). Certainly one possibility is to abandon the discrete linear ray tracing approach altogether and utilize full waveform synthesis methods such as can be provided by the parabolic equation method (Lingevitch et al. 2002) or a normal mode code (Pierce 1967). Given Moore's law predicting the doubling of computational resources every few years, the addition of full waveform propagation physics, including some of the neglected phenomena mentioned above, may become feasible in the near future.

24.7 Conclusion

This review presents a theoretical investigation into the possibility of utilizing ambient infrasound signals from natural geophysical and man-made impulsive sources to improve the present knowledge of upper atmospheric winds and temperatures. In the process, this discussion also provides background knowledge on basic geophysical remote sensing theory, linear acoustic wave propagation, and currently available global atmospheric specifications. We started the review with the early history of infrasound remote sensing and then presented the basic foundations of discrete inverse theory, outlining a simple infrasound travel time inversion scheme. We then discussed the generation of a time series of synthetic observations created for the purposes of evaluating the viability of a passive infrasound atmospheric remote sensing methodology. In this discourse, the state-of-the-art in atmospheric specifications, also required for performing infrasound DLC calculations, was reviewed. We then elaborated on the technical details of a possible inversion methodology and showed the results from several illustrative examples. Lastly, we discussed the limitations and consequences of the assumptions that were made to simplify the methodology, and proposed several ideas for how to proceed in the future. Through these numerical experiments we conclude that given suitable measurements of infrasound signals from a single impulsive event, passive infrasound remote sensing can, in theory, provide improved estimates of the state of the middle- and upper atmosphere with existing infrasound networks, and thus, improve current understanding, particularly in conjunction with other simultaneous atmospheric measurements.

Acknowledgements The authors would like to thank the NASA GSFC for making the GEOS-4 analysis fields for use in the G2S model for this scientific research. They would also like to thank

two anonymous reviewers for insightful comments on the initial drafts of this article. This work was supported by the Office of Naval Research. This chapter is dedicated to the memory of Dr. Hank Bass.

References

Adams JC, Swarztrauber PN (1999) Spherepack 3.0, 1999: a Model Development Facility. Month Weather Rev 127:1872–1878

Aki K, Christoffersson A, Husebye ES (1977) Determination of 3-dimensional seismic structure of lithosphere. J Geophys Res 82:277–296

Akmaev RA, Fuller-Rowell TJ, Wu F, Forbes JM, Zhang X, Anghel AF, Iredell MD, Moorthi S, Juang HM (2008) Tidal variability in the lower thermosphere: comparison of whole atmosphere model (WAM) simulations with observations from TIMED. Geophys Res Lett 35, doi:10.1029/2007GL032584

Andrews DG, Holton JR, Leovy CB (1987) Middle atmosphere dynamics. Academic Press, Orlando

Antier K, Le Pichon A, Vergniolle S, Zielinski C, Lardy M (2007) Multiyear validation of the NRL-G2S wind fields using infrasound from Yasur. J Geophys Res-Atmos 112, doi:10.1029/2007JD008462

Arrowsmith SJ, Drob DP, Hedlin MAH, Edwards W (2007) A joint seismic and acoustic study of the Washington State bolide: observations and modeling. J Geophys Res-Atmos 112, doi:10.1029/2006JD008001

Arrowsmith SJ, Whitaker R, Taylor SR, Burlacu R, Stump BW, Hedlin MAH, Randall G, Hayward C, Revelle DO (2008) Regional monitoring of infrasound events using multiple arrays: application to Utah and Washington State. Geophys J Int 175:291–300

Bass H, Bhattacharyya J, Garcés M, Hedlin M, Olson J, Woodward R (2006) Infrasound. Acoust Today 2(1):9–19

Bass HE, Hetzer CH, Raspet R (2007) On the speed of sound in the atmosphere as a function of altitude and frequency. J Geophys Res-Atmos 112, doi:10.1029/2006JD007806

Bessonova EN, Fishman VM, Ryaboyi VZ, Sitnikovn GA (1974) Tau method for inversion of travel times .1. Deep seismic sounding data. Geophys J R Astr Soc 36:377–398

Best N, Havens R, Lagow H (1947) Pressure and temperature of the atmosphere to 120 KM. Phys Rev 71:915–916

Bloom SC, Takacs LL, DaSilva AM, Ledvina D (1996) Data assimilation using incremental analysis updates. Month Weather Rev 124:1256–1271

Boggs PT, Byrd RH, Schnabel RB (1987) A stable and efficient algorithm for nonlinear orthogonal distance regression. SIAM J Sci Stat Comput 8:1052–1078

Boggs PT, Donaldson JR, Byrd RH, Schnabel RB (1989) Odrpack – software for weighted orthogonal distance regression. ACM Trans Math Software 15:348–364

Bowen PJ, Davies MJ, Stebbings RF, Groves GV, Boyd RLF, Dorling EB (1964) Upper atmosphere wind+temperature structure by skylark rocket-grenade experiments at Woomera Australia 1957-59. Proc Roy Soc Lond Math Phys Sci 280:170–184

Brown D, Garcés M (2009) Ray tracing in an inhomogeneous atmosphere with winds. In: Havelock D, Kuwano S, Vorländer M (eds) Handbook on signal processing in acoustics. Springer, ISBN: 978-0-387-77698-9

Brown DJ, Katz CN, Le Bras R, Flanagan MP, Wang J, Gault AK (2002) Infrasonic signal detection and source location at the Prototype International Data Centre. Pure Appl Geophys 159: 1081–1125

Christie DR, Veloso JAV, Campus P, Bell M, Hoffmann T, Langlois A, Martysevich P, Demirovic E, Carvalho J (2001) Detection of atmospheric nuclear explosions: the infrasound component of the International Monitoring System. Kerntechnik 66:96–101

Christie DR, Campus P (2010) The IMS infrasound network: design and establishment of infrasound stations. This volume, pp. 27–72

Chunchuzov IP (2004) Influence of internal gravity waves on sound propagation in the lower atmosphere. Meteorol Atmos Phys 85:61–76

Chunchuzov I, Kulichkov S, Otrezov A, Perepelkin V (2005) Acoustic pulse propagation through a fluctuating stably stratified atmospheric boundary layer. J Acoust Soc Am 117:1868–1879

Courtier P, Andersson E, Heckley W, Pailleux J, Vasiljevic D, Hamrud M, Hollingsworth A, Rabier E, Fisher M (1998) The ECMWF implementation of three-dimensional variational assimilation (3D-Var) I: formulation. Quart J R Meteorol Soc 124:1783–1807

Cox EF (1947) Microbarometric pressures from large high explosive blasts. J Acoust Soc Am 19:832–846

Cox EF (1948) Upper atmosphere temperatures from remote sound measurements. Am J Phys 16: 465–474

Cox EF (1949) Abnormal audibility zones in long distance propagation through the atmosphere. J Acoust Soc Am 21:6–16

Cox EF, Atanasoff JV, Snavely BL, Beecher DW, Brown J (1949) Upper-atmosphere temperatures from Helgoland big bang. J Meteorol 6:300–311

Daley R (1991) Atmospheric data analysis. Cambridge University Press, Cambridge, New York

de Groot-Hedlin CD, Hedlin MAH, Drob DP (2010) Atmospheric variability and infrasound monitoring. This volume, pp. 469–504

Der ZA, Shumway RH, Herrin ET (2002) Monitoring the comprehensive Nuclear-Test-Ban Treaty – Introduction. Pure Appl Geophys 159:907–908

Donn WL, Rind D (1971) Natural infrasound as an atmospheric probe. Geophys J R Astron Soc 26:111–133

Donn WL, Rind D (1972) Microbaroms and temperature and wind of upper-atmosphere. J Atmos Sci 29:56–172

Drob D, Emmert JT, Crowley G, Picone JM, Shepherd GG, Skinner W, Hays P, Niciejewski RJ, Larsen M, She CY, Meriwether JW, Hernandez G, Jarvis MJ, Sipler DP, Tepley CA, O'Brien MS, Bowman JR, Wu Q, Murayama Y, Kawamura S, Reid IM, Vincent RA (2008) An empirical model of the earth's horizontal wind fields: HWM07. J Geophys Res-Space Phys 113, doi:10.1029/2008JA013668

Drob DP, Garces M, Hedlin MAH, Brachet N (2009) The temporal morphology of infrasound propagation. Pure Appl Geophys in press

Drob DP, Picone JM, Garces M (2003) Global morphology of infrasound propagation. J Geophys Res-Atmos 108, doi:10.1029/2008JA013668

Durre I, Vose RS, Wuertz DB (2008) Robust automated quality assurance of radiosonde temperatures. J Appl Meteorol Climate 47:2081–2095

Evers LG, Haak HW (2007) Infrasonic forerunners: exceptionally fast acoustic phases. Geophys Res Lett 34, doi:10.1029/2007GL029353

Forbes JM, Zhang XL, Talaat ER, Ward W (2003) Nonmigrating diurnal tides in the thermosphere. J Geophys Res-Space Phys 108, doi:10.1029/2002JA009262

Fritts DC, Alexander MJ (2003) Gravity wave dynamics and effects in the middle atmosphere. Rev Geophys 41:64

Fritts DC, Isler JR (1994) Mean motions and tidal and 2-day structure and variability in the mesosphere and lower thermosphere over Hawaii. J Atmos Sci 51:2145–2164

Garcés MA, Hansen RA, Lindquist KG (1998) Traveltimes for infrasonic waves propagating in a stratified atmosphere. Geophys J Int 135:255–263

Garces M, Willis M, Hetzer C, Le Pichon A, Drob D (2004) On using ocean swells for continuous infrasonic measurements of winds and temperature in the lower, middle, and upper atmosphere. Geophys Res Lett 31,doi:10.1029/2004GL020696

Gossard EE, Hooke WH (1975) Waves in the atmosphere: atmospheric infrasound and gravity waves: their generation and propagation, Elsevier, Amsterdam

Groves GV (1956) Theory of the rocket-grenade method of determining upper-atmospheric properties by sound propagation. J Atmos Terr Phys 8:189–203

Gutenberg B (1946) Physical properties of the atmosphere up to 100 KM. J Meteorol 3:27–30
Hauchecorne A, Chanin ML (1980) Density and temperature profiles obtained by Lidar between 35-km and 70-km. Geophys Res Lett 7:565–568
Hays PB, Abreu VJ, Dobbs ME, Gell DA, Grassl HJ, Skinner WR (1993) The high-resolution Doppler imager on the upper-atmosphere research satellite. J Geophys Res-Atmos 98: 10713–10723
Hedin AE (1987) MSIS-86 thermospheric model. J Geophys Res-Space Phys 92:4649–4662
Hedin AE, Fleming EL, Manson AH, Schmidlin FJ, Avery SK, Clark RR, Franke SJ, Fraser GJ, Tsuda T, Vial F, Vincent RA (1996) Empirical wind model for the upper, middle and lower atmosphere. J Atmos Terr Phys 58:1421–1447
Herrin ET, Bass HE, Andre B, Woodward RL, Drob DP, Hedlin MA, Garcés MA, Golden PW, Norris DE, de Groot-Hedlin C, Walker KT, Szuberla CAL, Whitaker RW, Shields FD (2008) High-altitude infrasound calibration experiments. Acoust Today 4:12
Hogan TF, Rosmond TE (1991) The description of the navy operational global atmospheric prediction systems spectral forecast model. Month Weather Rev 119:1786–1815
Holton JR (2004) An introduction to dynamic meteorology. Elsevier Academic Press, Burlington, MA
Husen S, Kissling E (2001) Local earthquake tomography between rays and waves: fat ray tomography. Phys Earth Planet Int 125:171–191
Isler JR, Fritts DC (1995) Mean winds and tidal and planetary wave motions over Hawaii during airborne lidar and observations of Hawaiian Airglow Aloha-93. Geophys Res Lett 22:2821–2824
Joiner J, Da Silva AM (1998) Efficient methods to assimilate remotely sensed data based on information content. Quart J R Meteorol Soc 124:1669–1694
Kalnay E, Kanamitsu M, Baker WE (1990) Global numerical weather prediction at the National-Meteorological-Center. Bull Am Meteorol Soc 71:1410–1428
Kaplan LD (1959) Inference of atmospheric structure from remote radiation measurements. J Opt Soc Am 49:1004–1007
Killeen TL, Roble RG, Spencer NW (1987) A computer model of global thermospheric winds and temperatures. Adv Space Res 7:207–215
Klaes KD, Cohen M, Buhler Y, Schlussel P, Munro R, Luntama JP, von Engelin A, Clerigh EO, Bonekamp H, Ackermann J, Schmetz J (2007) An introduction to the EUMETSAT Polar System. Bull Am Meteorol Soc 88:1085–1096
Kulichkov SN, Chunchuzov IP, Bush GA, Perepelkin VG (2008) Physical modeling of long-range infrasonic propagation in the atmosphere. Izv Atmos Ocean Phys 44:175–186
Larsen MF (2002) Winds and shears in the mesosphere and lower thermosphere: results from four decades of chemical release wind measurements. J Geophys Res-Space Phys 107, doi:10.1029/2001JA000218
Le Pichon A, Blanc E, Drob D (2005a) Probing high-altitude winds using infrasound. J Geophy Res-Atmos 110, doi: 10.1029/2005JD006020
Le Pichon A, Blanc E, Drob D, Lambotte S, Dessa JX, Lardy M, Bani P, Vergniolle S (2005b) Infrasound monitoring of volcanoes to probe high-altitude winds. J Geophys Res-Atmos 110, doi: 10.1029/ 2004JD005587
Le Pichon A, Ceranna L, Garces M, Drob D, Millet C (2006) On using infrasound from interacting ocean swells for global continuous measurements of winds and temperature in the stratosphere. J Geophys Res-Atmos 111, doi:10.1029/2005JD006690
Le Pichon A, Vergoz J, Herry P, Ceranna L (2008) Analyzing the detection capability of infrasound arrays in Central Europe. J Geophys Res-Atmos 113, doi:10.1029/2007JD009509
Le Pichon A, Vergoz J, Cansi Y, Ceranna L, Drob D (2010) Contribution of infrasound monitoring for atmospheric remote sensing. This volume, pp. 623–640
Lighthill MJ (1978) Waves in fluids. Cambridge University Press, Cambridge
Lingevitch JF, Collins MD, Dacol DK, Drob DP, Rogers JCW, Siegmann WL (2002) A wide angle and high Mach number parabolic equation. J Acoust Soc Am 111:729–734

Manney GL, Kruger K, Pawson S, Minschwaner K, Schwartz MJ, Daffer WH, Livesey NJ, Mlynczak MG, Remsberg EE, Russell JM, Waters JW (2008) The evolution of the stratopause during the 2006 major warming: satellite data and assimilated meteorological analyses. J Geophys Res-Atmos 113, doi:10.1029/2007JD009097

Marquardt DW (1963) An algorithm for least squares estimation of nonlinear parameters. J Soc Indus Appl Math 11:431–441

Menke W (1989) Geophysical data analysis: discrete inverse theory. Academic Press, San Diego

Migliorini S, Piccolo C, Rodgers CD (2008) Use of the information content in satellite measurements for an efficient interface to data assimilation. Month Weather Rev 136:2633–2650

Millet C, Robinet JC, Roblin C (2007) On using computational aeroacoustics for long-range propagation of infrasounds in realistic atmospheres. Geophys Res Lett 34, doi:10.1029/2007GL029449

Munk W (1986) Acoustic monitoring of ocean gyres. J Fluid Mech 173:43–53

Munk W, Wunsch C (1979) Ocean acoustic tomography – scheme for large-scale monitoring. Deep-Sea Res 26:123-161

Munk WH, Worcester P, Wunsch C (1995) Ocean acoustic tomography. Cambridge University Press, Cambridge

Murayama Y, Igarashi K, Rice DD, Watkins BJ, Collins RL, Mizutani K, Saito Y, Kainuma S (2000) Medium frequency radars in Japan and Alaska for upper atmosphere observations. IEICE Trans Commun E83b:1996–2003

Oberheide J, Wu Q, Killeen TL, Hagan ME, Roble RG (2006) Diurnal nonmigrating tides from TIMED Doppler interferometer wind data: monthly climatologies and seasonal variations. J Geophys Res-Space Phys 111, doi:10.1029/2005JA011491

Ostashev VE, Chunchuzov IP, Wilson DK (2005) Sound propagation through and scattering by internal gravity waves in a stably stratified atmosphe*re*. J Acoust Soc Am 118:3420–3429

Picone JM, Hedin AE, Drob DP, Aikin AC (2002) NRLMSISE-00 empirical model of the atmosphere: statistical comparisons and scientific issues. J Geophys Res-Space Phys 107, doi: 10.1029/2002JA009430

Pierce AD (1967) Guided infrasonic modes in a temperature- and wind-stratified atmosphere. J Acoust Soc Am 41:597–611

Poli P, Joiner J, Kursinski ER (2002) 1DVAR analysis of temperature and humidity using GPS radio occultation refractivity data. J Geophys Res-Atmos 107, doi:10.1029/2001JD000935

Rabier F (2005) Overview of global data assimilation developments in numerical weather-prediction centres. Q J R Meteorol Soc 131:3215–3233

Rienecker MM, Suarez MJ, Todling R, Bacmeister J, Takacs L, Liu H-C, Gu W, Sienkiewicz M, Koster RD, Gelaro R, Stajner I, Nielsen JE (2008) The GEOS-5 data assimilation system – documentation of versions 5.0.1, 5.1.0, and 5.2.0, NASA/TM-2008-104606 27:93

Rind D (1978) Investigation of lower thermosphere results of ten years of continuous observations with natural infrasound. J Atmos Terr Phys 40:1199–1209

Rind D, Donn WL (1975) Further use of natural infrasound as a continuous monitor of upper-atmosphere. J Atmos Sci 32:1694–1704

Rind D, Donn WL, Dede E (1973) Upper air wind speeds calculated from observations of natural infrasound. J Atmos Sci 30:1726–1729

Rodgers CD (2000) Inverse methods for atmospheric sounding: theory and practice. World Scientific, Singapore

Romanowicz B (2008) Using seismic waves to image Earth's internal structure. Nature 451: 266–268

Schwartz MJ, Lambert A, Manney GL, Read WG, Livesey NJ, Froidevaux L, Ao CO, Bernath PF, Boone CD, Cofield RE, Daffer WH, Drouin BJ, Fetzer EJ, Fuller RA, Jarnot RF, Jiang JH, Jiang YB, Knosp BW, Kruger K, Li JLF, Mlynczak MG, Pawson S, Russell JM, Santee ML, Snyder WV, Stek PC, Thurstans RP, Tompkins AM, Wagner PA, Walker KA, Waters JW, Wu DL (2008) Validation of the aura microwave limb sounder temperature and geopotential height measurements. J Geophys Res-Atmos 113, doi:10.1029/2007JD008783

She CY (2004) Initial full-diurnal-cycle mesopause region lidar observations: diurnal-means and tidal perturbations of temperature and winds over Fort Collins, CO (41 degrees N 105 degrees W). J Atmos Solar-Terr Phys 66:663–674

Shepherd GG, Thuillier G, Gault WA, Solheim BH, Hersom C, Alunni JM, Brun JF, Brune S, Charlot P, Cogger LL, Desaulniers DL, Evans WFJ, Gattinger RL, Girod F, Harvie D, Hum RH, Kendall DJW, Llewellyn EJ, Lowe RP, Ohrt J, Pasternak F, Peillet O, Powell I, Rochon Y, Ward WE, Wiens RH, Wimperis J (1993) Windii, the wind imaging interferometer on the upper-atmosphere research satellite. J Geophys Res-Atmos 98:10725–10750

Simmons A, Hortal M, Kelly G, McNally A, Untch A, Uppala S (2005) ECMWF analyses and forecasts of stratospheric winter polar vortex breakup: September 2002 in the Southern Hemisphere and related events. J Atmos Sci 62:668–689

Swinbank R, Lahoz WA, O'Neill A, Douglas CS, Heaps A, Podd D (1998) Middle atmosphere variability in the UK Meteorological Office Unified Model. Q J R Meteorol Soc 124:1485–1525

Szuberla CAL, Olson JV (2004) Uncertainties associated with parameter estimation in atmospheric infrasound arrays. J Acoust Soc Am 115:253–258

Tarantola A (2005) Inverse problem theory and methods for model parameter estimation. Society for Industrial and Applied Mathematics, Philadelphia, PA

Tikhonov AN (1963) Solution of incorrectly formulated problems and regularization method. Doklady Akademii Nauk SSSR 151:501–504

Twomey S (1963) On numerical solution of Fredholm integral equations of first kind by inversion of linear system produced by quadrature. J ACM 10:97–101

Vincent RA (1984) Mf/Hf radar measurements of the dynamics of the mesopause region – a review. J Atmos Terr Phys 46:961–974

Vincent RA, Lesicar D (1991) Dynamics of the equatorial mesosphere – 1st results with a new generation partial reflection radar. Geophys Res Lett 18:825–828

Walker KT, Zumberge MA, Hedlin MAH, Shearer PM (2008) Methods for determining infrasound phase velocity direction with an array of line sensors. J Acoust Soc Am 124:2090–2099

Wang DY, von Clarmann T, Fischer H, Funke B, Gil-Lopez S, Glatthor N, Grabowski U, Hopfner M, Kaufmann M, Kellmann S, Kiefer M, Koukouli ME, Linden A, Lopez-Puertas M, Tsidu GM, Milz M, Steck T, Stiller GP, Simmons AJ, Dethof A, Swinbank R, Marquardt C, Jiang JH, Romans LJ, Wickert J, Schmidt T, Russell J, Remsberg E (2005) Validation of stratospheric temperatures measured by michelson interferometer for passive atmospheric sounding (MIPAS) on envisat. J Geophys Res-Atmos 110, doi:10.1029/2004JD005342

Whipple FJW (1926) Audibility of explosions and the constitution of the upper atmosphere. Nature 118:309–313

Wu WS, Purser RJ, Parrish DF (2002) Three-dimensional variational analysis with spatially inhomogeneous covariances. Month Weather Rev 130:2905–2916

Wunsch C (1996) The ocean circulation inverse problem. Cambridge University Press, Cambridge

Zwolak JW, Boggs PT, Watson LT (2007) Algorithm 869: ODRPACK95, 2007: a weighted orthogonal distance regression code with bound constraints. ACM Trans Math Software 33, doi:10.1145/1268776.1268782

Index